Springer Tracts in Civil Engineering

Sheng-Hong Chen

Computational Geomechanics and Hydraulic Structures

Springer

Springer Tracts in Civil Engineering

Springer Tracts in Civil Engineering (STCE) publishes the latest developments in Civil Engineering—quickly, informally and in top quality. The series scope includes monographs, professional books, graduate textbooks and edited volumes, as well as outstanding Ph.D. theses. Its goal is to cover all the main branches of civil engineering, both theoretical and applied, including:

Construction and Structural Mechanics
Building Materials
Concrete, Steel and Timber Structures
Geotechnical Engineering
Earthquake Engineering
Coastal Engineering
Hydraulics, Hydrology and Water Resources Engineering
Environmental Engineering and Sustainability
Structural Health and Monitoring
Surveying and Geographical Information Systems
Heating, Ventilation and Air Conditioning (HVAC)
Transportation and Traffic
Risk Analysis
Safety and Security
To submit a proposal or request further information, please contact: Pierpaolo Riva at Pierpaolo.Riva@springer.com, or Li Shen at Li.Shen@springer.com

More information about this series at http://www.springer.com/series/15088

Sheng-Hong Chen

Computational Geomechanics and Hydraulic Structures

Springer

Sheng-Hong Chen
School of Water Resources
and Hydropower Engineering
Wuhan University
Wuhan, Hubei
P.R. China

ISSN 2366-259X ISSN 2366-2603 (electronic)
Springer Tracts in Civil Engineering
ISBN 978-981-10-8134-7 ISBN 978-981-10-8135-4 (eBook)
https://doi.org/10.1007/978-981-10-8135-4

Library of Congress Control Number: 2018938778

Printed on acid-free paper

This Springer imprint is published by the registered company Springer Nature Singapore Pte Ltd.
part of Springer Nature
The registered company address is: 152 Beach Road, #21-01/04 Gateway East, Singapore 189721, Singapore

Foreword I

With the increasing demand of people for improved life quality, a large number of mega projects spring up in our modern society. The successful construction and sustainable operation of these mega projects mark not only the progress in modern science and technology but also the significant development of human society and civilization.

It is well known that the safety, reliability, and sustainability of a project depend on an elaborate, skillful, and accurate design. Structural computation is, in turn, a fundamental tool for its design, which provides the theories, methodologies, and procedures for profoundly understanding the structural performances of the project.

Over the past three decades, China, a populated country, has witnessed rapid economic and social development and risen to be a middle-income country. In the process, the mega projects, such as high dams, motorways, high-speed trains, ultra-long and deeply buried large-scale tunnels, and UHV grids, played crucial roles.

To exploit and utilize the hydro and water resources of the rivers, China has designed and built a great number of mega water resources and hydropower projects including the Three Gorges, Ertan, Xiaolangdi, Longtan, Xiaowan, Shuibuya, Pubugou, Guangzhao, Xiluodu, Jinping-I, Jinping-II, and South-to-North Water Diversion. These projects challenge the computational methods to tackle with high dams, high and steep cut slopes, large and long hydraulic tunnels with high velocity flow, deep overburden underground cavern clusters under complicated engineering and hydrogeological conditions.

Computational methods have experienced remarkable advancement over the past thirty years. They have evolved from the traditional empirical and semiempirical material mechanics methods as well as rigid body limit equilibrium methods to the nonlinear finite element method, non-continuum discrete element method, and other numerical calculation methods. This should be attributed to not only the development of modern computer technology but also the design and construction of various mega projects. On one hand, the computational methods offered credible and reliable scientific demonstration to the design of mega projects. On the other

hand, these mega projects promoted the development of modern geomechanics and computational methods.

Professor Chen Sheng-Hong has long been engaged in the research and development of computational methods and computer software for geomaterials and hydraulic structures. Paying special attention to laboratory experiments and in situ testing validation, he links the theories with practice and has made considerable innovative and practical research achievements. He harvested pragmatic results in the fields like standard adaptive software of the finite element method and initiated the block element analysis and composite element method which are influential both in China and abroad. These methods cover reinforcement analysis, feedback analysis, reliability analysis, seepage field and thermal field analysis, and multifield coupling analysis. He also has realized the synergy of methods, models, parameters, and hydraulic engineering structure safety. His theory and methodology have been verified and widely applied in the dam construction works, underground works, and artificial high slope works. They have offered solutions and scientific demonstrations to the crucial technological challenges in the design of the key national hydropower projects, such as Three Gorges, Longtan, Shuibuya, Guangzhao, Xiluodu, Jinping-I, Pubugou, Xiaowan, and contributed greatly to the success of project construction.

Professor Chen Sheng-Hong has won many science and technology awards of the provincial, ministerial, and national levels as well as those of national industry authorities and associations. He was honored as the Distinguished Professor of the Wuhan University of Hydraulic and Electric Engineering, and the Excellent Professor of Wuhan University, the Ministry of Water Resources, and the Ministry of Education. He is also granted the special government allowance of the State Council.

Professor Chen Sheng-Hong was invited as guest professor of Swiss Federal Institute of Technology in Lausanne (EPFL, Switzerland) and Parma University, Italy. He also worked as the guest professor in the Université des Sciences et Technologies de Lille (Université Lille1, France) on a long-term basis. He opens lectures overseas every year to teach advanced modern numerical computation methods and programs. Since 2000, he acted as the member of Computational Aspects of Analysis and Design of Dams, International Committee of Large Dam.

As the undergraduate and postgraduate schoolmate living in a same residence, as well as the partner in the construction of many mega hydraulic projects, I and Prof. Chen Sheng-Hong are good friends and colleagues. I am proud of his achievements in academic theory and engineering technology related to the geomechanics and hydraulic structures. I shall thank him for his valuable research findings to our breakthrough in the key technology projects of high dams, high and steep cut slopes, and large underground works. I am lucky to have read most of the manuscripts of this great book before publishing and deeply impressed by its rigorous

theory, clear logic, as well as innovative and pragmatic contents. The book has both historical texture and broad international vision. I am convinced that the book can not only serve as the reference to technicians engaged in geomechanics and hydraulic structures but also positively promote the health development of computational methods.

Beijing, China
November 2017

Prof. Zhou Jianping
Vice President, International
Commission on Large Dams;
Chief Engineer Power Construction
Corporation of China

Foreword II

During the visit of my friend Prof. Chen Sheng-Hong to Lille last year (June–July, 2017), he kindly presented me with an advanced draft of *Computational Geomechanics and Hydraulic Structures* and asked me to write a foreword. I was greatly impressed by the extensive area covered in this book, by the scientific and engineering basis of his works, and by the quality of the presentation. I accepted his invitation with great pleasure.

From our first encounter in 20 years ago at Lille when he worked in the Université des Sciences et Technologies de Lille (Université Lille 1, France) as the guest professor until today, we have met regularly either in China or in Europe, including his regular 1- to 3-month stay in Lille as guest professor in our university. We succeeded in building a strong cooperation through yearly academic visits, Ph.D. co-supervision, joint paper publication in international journals and conferences, and the organization of lectures for postgraduate students and young researchers. He is an enthusiastic, hardworking, and interdisciplinary engineering scientist and university educator. I highly appreciated the scientific and the engineering quality of the work of Professor Chen as well as that of his students. I am also proud of that for years our university has opportunity to provide resources for a portion of his theoretical researches and academic writings, which contribute to a part of the coverage in this book.

Through this book, Prof. Chen enhances our library by a synthesis of more than 30 years of academic and professional experience in the field of computational geomechanics and their use in the assessment of both the safety and performances of hydraulic structures throughout their lifecycle covering design, construction, and exploitation stages. At each stage, engineers have to deal with multiple analysis and decision-making challenges, which are related to the complexity of the hydraulic structures geometry, nonlinear behaviors of geomaterials, multiphysics and transient phenomena as well hydro-thermo-mechanical coupling. To cope with these challenges, engineers need to enhance the conventional analysis tools by advanced computational methods in order to consider complex issues, which could highly influence the safety and performances of hydraulic structures.

The works of this book resulted in significant advances in (i) the major issues of the finite element method (FEM) in the analyses of hydraulic structures inclusive error estimation and mesh refinement, thermomechanical and hydromechanical coupling, reinforcement mechanism and modeling, parametric inverse and feedback design, and safety calibration; (ii) the fundamentals of the block element analysis (BEA) and its enhancement inclusive hybrid techniques, seepage analysis and reinforcement analyses, as well as stochastic and dynamic analyses; (iii) the fundamentals of the composite element method (CEM) and its use in the reinforcement, seepage, and thermal analyses.

It is remarkable that Prof. Chen has conducted a huge state-of-the-art study in the field of computational geomechanics and hydraulic structures, and he crossed it with his own academic and professional expertise in the computation methods, laboratory tests and field observations, material properties and parametrical inverse, safety calibration, and countermeasure design. He also presents his research philosophy and skill with engineering cases such as the most famous hydraulic projects of Three Gorges, Longtan, Shuibuya, Xiaowan, Guangzhao, etc. All these resulted in this exceptional book, which I believe will be an important reference book in the field of computational geomechanics and hydraulic structures. I would like to outline that this book constitutes a kind of "encyclopedia" on the computational geomechanics methods and their applications.

In conclusion, this book should be found in every public or private engineering library, particularly in universities. Engineers and postgraduate students can find comprehensive information about the fundamentals of the computational methods in geomechanics as well as scientific and practical recommendations for the efficient use of these methods in the analysis of hydraulic structures. Thanks to Prof. Chen for this great contribution.

Lille, France
January 2018

Prof. Isam Shahrour
Distinguished Professor
former Vice President Université Lille 1

Preface

Hydraulic structures, particularly large underground caverns and high dams with their vicinal high cut slopes, play core roles in hydraulic projects. Following the rapid progress in the construction of mega hydraulic projects, China has reached international level in the theories and technologies related to the project investigation, research, design, construction, and management. The largest work completed in the world, the Three Gorges Project, is installed with electric power generator capacity of 22,400 MW; the world highest arch dam (Xiaowan, H = 294.5 m; Jinping-I, H = 305 m), the world highest concrete-faced rockfill dam (CFRD) (Shuibuya, H = 233 m), the world highest roller compacted concrete (RCC) gravity dam (Guangzhao, H = 200.5 m; Longtan, H = 192 m) are all erected in China.

Initiated in the 1960s and classified as a sub-discipline within computational mechanics, computational geomechanics uses numerical methods to study the phenomena governed by the principles of geomechanics. It is a successful paradigm of interdisciplinary development supported by the applied mathematics and mechanics as well as the computer science, and driven by engineering practices. Since the 1980s, Chinese scientists and engineers have made significant contributions to the research and application of computational geomechanics attributable to the impetus from the demands of civil engineering, environmental engineering, mining and transportation engineering, and hydraulic engineering. Today, modern computational geomechanics has profound influences on the design of giant and complex engineering structures that would be previously very difficult or even impossible to be appropriately analyzed using traditional calculation tools.

This book is mainly focused on the development and application of representative computational methods to estimate the performance and safety of hydraulic structures from their planning and design phases to construction and service phases, on which the author has been working since the mid-1980s. In addition, this book is intended to show how to achieve a good correlation between the numerical computation and the in situ behavior of the hydraulic structure, which is actually attributable to a close collaboration of the author and his colleagues, friends, and students with field engineers. In this book, the heuristic and visualized style is attempted to disseminate the research philosophy and road map. The organization

of various matters with typical methods (FEM, BEA, CEM) as warps and others (physical fields and engineering practices) as woofs is meant to clearly and logically elucidate the following aspects related to the subject of this book.

- Modeling of materials. The results of computational geomechanics for hydraulic structures are significantly dependent on the models of rock-like materials characterized by structure planes (rock discontinuities and concrete joints) and mitigation countermeasure components (e.g., reinforcement, drainage, and cooling). In the selection of constitutive models (relations) toward the definition of rock-like materials, these characteristics should be simplified in a rational way for the feasible and credible simulation of hydraulic structures (Chap. 2). This philosophy is followed throughout the generation of computation meshes (Chap. 3), the establishment of typical computational methods (Chaps. 4, 9 and 14), and the approaches of joints and reinforcement components (Chap. 6).
- Input of parameters. It is well known that the unsuccessful computation with regard to hydraulic structures is often blamed on the inappropriate input parameters defined in the material model. This is due to the difficulties arise from laboratory and in situ tests in addition to environmental (stress/water content/temperature) dependence. The laboratory test is suffered from stochastic variation whereas the in situ test possesses poor representativeness entailed by sample amount and high cost. Therefore, it is paramount to be involved in the investigation and experiment works as deeply as possible toward a correct interpretation of experimental data and a realistic evaluation of inputting parameters. On the aspects of computation technique, parametric back or inverse analysis is a supplementary approach to handle this issue subject to well-installed instruments, good understanding of construction procedure, as well as sufficient engineering experience (Chap. 7).
- Diversification of methods. Nowadays, there are a variety of modern computational methods available for geomechanics and hydraulic structures (Chap. 1), although only three of them are representatively elaborated in this book (i.e., FEM, BEA, and CEM). They may be roughly distinguished into entirely different two classes according to their conceptualization of rock-like materials, i.e., the continuum or discontinuum, each of them reflects one extreme aspect of the hydraulic structure encountered. The selection of the most representative ones is, however, an open question. This is actually dependent on the problem type, the material, the work situation, etc. Take a large rock block system for example, to understand its post-failure movements, the DDA or DEM would be a good choice because they permit decoupling of the block system. On the other hand, when the safety margins with respect to collapse/serviceability limit states are demanded, and suggestions concerning the seepage/stabilization countermeasures are expected, the BEA would be more appropriate attributable to its competent strength parameters and clearly allowable safety factors stipulated in the design codes/specifications.

Where the structural issue is very important and complex, it is suggestible to exercise diverse methods (at least two) in addition to traditional tools. This philosophy is followed throughout the whole book, and our readers will find that several typical projects are studied by the FEM or/and BEA (CEM) in addition to traditional LEM or/and TLM, plus geomechanical physical test.

Theoretically, "all-encompassing" methods covering continuum and discontinuum as well as finite and infinitesimal deformation, may be charming. Entailed by the professional experience of the author, however, I have to say that this is actually not very attractive and practical because it, if exists, would be too "precise" and "delicate" to be competent to the "roughly estimated parameters" and complex hydraulic structures.

- Standardization of preprocess. The computation procedure should been developed as not only to easily and reliably collect input data, but also to allow for the standardized discretization of the hydraulic structure. The mesh density (size) dependent on the structural configuration, exerted action, as well as the construction manner and sequence, will significantly affect the calibration of the local safeties (e.g., strength, allowable seepage gradient, cracking potentiality) of a hydraulic structure. This is why the automatic block identification and mesh generation (Chap. 3) and the adaptive refinement technology (Chap. 5) are looked at as important contents in this book. From the standpoint of a practitioner in the field of hydraulic engineering, automatic grid generation and adaptive refinement in grid-dependent computational methods (e.g., the FEM) may help to overcome the cumbersome preprocessing burden as well as to keep the balance between computation effort and precision, by appropriately stipulated discretization error tolerances in design codes/specifications for different structure types and grades, rather than to pursue computation precision solely.
- Coupling of fields. Very often, groundwater appears in and affects hydraulic structures. In addition, concrete placed onto the foundation undergoes strong temperature fluctuation before and after being loaded. As a result, hydraulic structures exhibit complex performances involving hydro-thermo-chemo-mechanical fields which demand appropriate handling. Although various and sophisticated coupling models with regard to the movement of water and heat through the material skeleton and fractures (discontinuities and joints) are available in the environmental engineering and nuclear power engineering, yet in the hydraulic engineering normally only partial coupling of temperature or/and seepage toward the deformation/stress needs to be taken into account attributable to the lower action level (Chap. 2). Full coupling, particularly of hydromechanical, is only sometimes encountered where the stress level in the rock mass is high (e.g., arch dam abutments). Under such circumstances, the coupling model should be rationally elaborated as simple as possible and its coupling parameters should be accessible by experiments (Chap. 2) or in situ back analysis (Chap. 8) subject to the conditions permitted for the project.

- Interpretation of results and calibration of safety. Once the analysis has been accomplished, it is necessary to display the results in such a way that they can be easily understood and interpreted, based on which the safety calibration with respect to the strength/seepage/temperature according to the design codes/specifications is undertaken. The calibration criteria may be both of local and/or overall (Chap. 4).
- Validation by test/observation and feedback. It is also highly important to check the validation of computational solutions by comparing them with in situ observed data. This is particularly presented in the study of Xiaowan Project (Chap. 8) where the comparison of the FEM computation with the instrumentation data is comprehensively carried out for the arch dam, and in the study of Longtan Project (Chap. 9) where an abutment slope failure accident is captured by the BEA.

This book may be looked at as an advanced continuation of the *Hydraulic Structures* by the author published in 2015 which mainly deals with the investigation, planning, design, construction, and management of hydraulic structures. I was planning to finish my professional activities by that book and to launch a new writing life that I have been dreaming since my childhood. However, the publication of the *Hydraulic Structures* was so welcome by the readers, and I was deeply touched and proud of. Encouraged by my friends, colleagues, and students that I am liable to further present the research achievements and engineering experiences of my team, I have to continue technical writing and now, I feel in relief by contributing this continuation book.

The basis of this book is established on my studies and practices conducted in China over the decades with the help of my students partially recited as Dr. Chen Shangfa, Dr. Wang Weiming, Dr. Xu Minyi, Dr. Fu Shaojun, Dr. Xu Qing, Dr. Wang Shufa, Dr. Qiang Sheng, Dr. Hu Jing, Dr. Cheng Zhao, Dr. Xia Huaixiao, Dr. Li Yongming, Dr. Fei Wenping, Dr. Qin Weixin, Dr. Feng Xuemin, Dr. Zheng Huifeng, Dr. He Zegan, Dr. Xu Guisheng, Dr. Peng Chengjia, Dr. Fu Chenghua, Dr. Xue Luanluan, and Dr. He Ji et al. I am so proud to see that most of them are now successful university professors, consultant engineers, and enterprise managers. In my engineering consultant and education works, I am very fortunate to have chance to collaborate with Prof. Zhou Jianping (Chief Engineer of Power Construction Corporation of China), Prof. Zou Lichun (Deputy President of Kunming Engineering Corporation Limited, PowerChina), Prof. Yang Jiaxiu (Deputy President of Guiyang Engineering Corporation Limited, PowerChina), Prof. Feng Shurong (President of Zhongnan Engineering Corporation Limited, PowerChina), Prof. Wang Renkun (Chief Engineer of Chengdu Engineering Corporation Limited, PowerChina), Prof. An Shengxun (Deputy President of Northwest Engineering Corporation Limited, PowerChina), et al. In the international education and academic activities, the collaboration with my lifetime friends, Prof. Peter Egger (EPFL, Switzerland) and Prof. Isam Shahrour (Lille University 1, France), is the most important. In addition, I am really grateful to Wuhan University for providing tolerant ivory tower and allowing time for me, to complete this book.

Greater challenges await us in the next prospective decades. From 2011 to 2050, under the state policy guidance for developing her vast western area, tens of mega hydropower projects will be built in China. For example, the Motuo hydropower project will be installed with generator capacity larger than 40,000 MW. These milestone projects will further give strong impetus to push the technology of hydraulic engineering in China up to an unprecedented level, and to provide ever vast room for the progress in computational geomechanics. By the publishing of this book, the author does wish to encourage our successors to take on historical responsibilities by conducting more advanced and practical researches on the relevant topics.

Wuhan, Hubei, P.R. China Sheng-Hong Chen

Contents

Chapter 1
Introduction

Abstract This chapter describes the connotation and denotation of computational geomechanics (CG), a sun-branch of computational methods or mechanics (CM) which is, in turn, the branch of modern mathematical modeling. The history of the CM is logically unfolded following the evolution of human civilization, and the state-of-the-art is examined with special reference to those who are most widely or potentially exercised in hydraulic engineering. This introductory chapter is concluded with comments and suggestions on the healthy development and successful application of the CG for hydraulic structures.

1.1 General

Under environmental actions (or exerted loads), effects such as deformations (deflections) and stresses will manifest within hydraulic structures. The failure will further be triggered if the action effects exceed the bearing capacity of the structure.

Since the beginning of human civilization, the design of hydraulic structures has evolved from primitive trial-and-error ventures to skillfully analytical approaches. Early hydraulic structure construction was an uncertain art resting on cumulative experiences. As the centuries unfolded, it was gradually merged with sciences and technologies. Particularly, the theories of mathematics and mechanics played increasingly important role in seeking safer design schemes. Nowadays, the analysis of action effects by means of laboratory physical modeling, field monitor modeling, and mathematical modeling, is indispensable in the design for important hydraulic structures (Chen 2015).

Physical modeling is a fundamental tool in the effect analysis of actions because it may give straight forward and intuitionistic answers concerning the deformation and failure of hydraulic structures. Even with the great progress in mathematical modeling of recent decades, the physical modeling is still effective in the study of structural problems with regard to cracking, sliding, and dynamic shaking for important hydraulic structures. Physical modeling may be generally distinguished

S.-H. Chen, *Computational Geomechanics and Hydraulic Structures*,
Springer Tracts in Civil Engineering, https://doi.org/10.1007/978-981-10-8135-4_1

as brittle material modeling, geo-mechanical modeling and emulation modeling according to the model materials used (Fumagalli 1973).

Technically, monitoring of hydraulic structures is related to instrumentation sciences, computer sciences, modern mathematics, and is one of the most essential branches of their safety management (ICOLD 1987, 1988; Dunnicliff 1990). A successful safety monitoring system for hydraulic structures (e.g. dams) consists of four functional components, i.e. instrumentation, data collection and management, data evaluation and calibration, and response plan. Monitor modeling for the interpretation and analysis of observed data is intended to answer the questions such as "what is the real state of the hydraulic structure?" and "how far is the real state shifted from the design stipulation and safety criteria?" Bearing these questions in mind, it is apparent that the monitoring modeling plays a crucial role in the construction and safety management of modern hydraulic structures (Ardito et al. 2008).

Mathematical modeling is another paramount tool in the analysis of action effects for modern hydraulic structures (ICOLD 2001a, b, 2013). It makes use of physical laws to build partial differential equations (PDEs) or their simplified versions such as the limit equilibrium modeling (LEM), which are solved under specific boundary and initial conditions. The major advantages of the mathematical modeling are:

- It is relatively easier to build for the simulation of construction and operation process;
- It may give prominence to the basic features of hydraulic structures, to adequately implement the analysis of their working principles and failure mechanism;
- It is sophisticated to carry out sensitive analysis by the adjustment of parameters and factors, to understand the tendency and extent of their influences on hydraulic structures, and to enlighten appropriate improvement- or/and counter-measures in the design and construction stages.

The back (inverse) analysis or its evolutionary product—feedback analysis, is actually a hybrid of monitor modeling and mathematical modeling in addition to other auxiliary tools such as computational intelligence (CI) and decision supporting system (DSS). It is prevalent in recent years for the dynamic design and construction of important hydraulic structures (e.g. dams, cut slopes, underground caverns and tunnels). Its researches and engineering practices have pushed the structural design and construction techniques up to an unprecedented level.

The main coverage of this book is much more closely related to the mathematical modeling, although physical modeling and monitor modeling are frequently demonstrated where the validations and engineering applications are addressed.

1.2 Mathematical Modeling

Typical mathematical modeling for hydraulic structures may be implemented by the following approaches.

(1) Analytical method

A closed-form (analytical) solution using the mathematical model represented by its specific PDE may be employed to directly calculate outputs after the plug of inputs into the formula. It possesses an unique advantage over the others, namely, accurate. Nevertheless, only under simple boundary and initial conditions such solution may be fortunately worked out. Nowadays, these precious closed-form solutions also play important roles in validating the computational solutions.

(2) Limit equilibrium method

The limit equilibrium method (LEM) makes use of a simplified version or a portion of PDE (e.g. neglecting deformation compatibility condition and constitutive relation), which is directly solved under the conditions of force or/and moment equilibrium solely, to provide the factor of safety (FOS) for the hydraulic structure concerned.

There are two approaches for determining the FOS against the loss of stability by means of the LEM. The first one is based on the condition of stress/force equilibrium at every point of a structure, the highest load or the lowest strength which does not lead to the loss of equilibrium of the structure is sought; the second one postulates the occurrence of a kinematically permitted failure mechanism, e.g. a sliding prone rock mass along a potential slip surface, the most adverse slip surface at which failure manifests, is sought (Bell 1968; Meyerhof 1984).

In the first approach, the state of stress in the structure must be pre-determined. Owing to the statically indeterminate feature of various hydraulic structures, deformation pattern must be taken into account. As a result, the stress-strain relation of material must be established beforehand, afterwards solutions are worked out by the application of computational methods (e.g. FEM). The main advantage of this approach is that the analysis itself indicates zones where potential slip surfaces may be evolved. Disadvantages lie in the extensive and complicated numerical computations. Hence this approach is desirable in particular problems where the structural deformation have to be explored.

The second approach consists of analyzing equilibrium along various kinematically potential slip surfaces and finding the most possible failure mode. It is generally exercised for the routine stability verification of structural profiles. Normally, this approach leads to a sufficiently convincible result and is very attractive in the routine design due to its simplicity.

To handle special cases where the stability of rock masses is dominated by the discontinuities, the key block theory (KBT) initiated independently by Warburton (1983, 1993), Goodman and Shi (1985), is prevalent. Instead of utilizing any stress/deformation analyses, it identifies “key blocks” in the rock mass formed by

discontinuities and exposure surfaces that are prone to sliding and rotating in certain directions. The key block theory, or simply block theory, enjoys wide applications in the tunnel and cut slope stabilization (Yow 1990; Shi and Goodman 1990; Chern and Wang 1993; Scott and Kottenstette 1993; Boyle and Vogt 1995; Nishigaki and Miki 1995; Lee and Park 2000; Lee and Song 1998).

Although LEM algorithms for the various stability issues of hydraulic structures (e.g. dam foundations, cut slopes) have been exercised for many years, yet it has been questionable that for a statically indeterminate structure, assumptions on the forces/moments are required to render the problem being statically determinate (Londe 1965; Guzina and Tucovic 1969; Chan and Einstein 1981; Chen 1984). Since such assumptions overlook several important factors lowering down the stability of hydraulic structures, therefore the reliability of the LEM is not always guaranteed and the risk of unsafe side design cannot be ruled out. A higher allowable safety factor is normally stipulated in the design specifications to compensate the deficits of the LEM, in an attempt to let engineers feel confidence that the stability safety has been assured.

(3) Computational methods

The mathematical modeling and problem-solving oriented computation techniques give birth to the discipline of "computation science" (CS). In practical use, it is typically the application of computer simulation and other forms of computation ranging from the numerical analysis for engineering structures to the solution for other various scientific problems.

Nowadays, as a result of the fast development of computer industry and computational techniques, the computation science is in parallel to the "theory" and "experiment" to form three "pillars" in an ambition to understand the nature, and of course, the hydraulic structures as well (Zhu 1998; Jing and Hudson 2002; Morton and Mayers 2005; Zienkiewicz et al. 2005, 2013; Bobet et al. 2009; Anandarajah 2010).

The computational method or computational mechanics (CM) is a branch of the computation science inter-disciplinarily supported by the mathematics, computer science, mechanics, etc. Important specializations in the hydraulic structures where the CM is widely exercised are the computational fluid dynamics, computational thermodynamics, and computational solid mechanics. As a sub-branch of CM, the computational geomechanics (CG) focusing on soils and rock-like materials (concrete and rocks), is the primary coverage of this book.

The subjects of mathematics mostly related to the CM are partial differential equations (PDEs), linear algebra, and numerical analysis. PDEs entail the mathematical model of various physical and mechanical phenomena in diverse subject areas such as fluid dynamics and solid mechanics. Very frequently, these PDEs are so complicated that finding their solutions in closed-form is neither possible nor practicable, and we have to resort to seeking numerical approximations. In this context, numerical analysis (NA)—the study of numerical approximation algorithms for PDEs, is an important underpinning in the CM.

1.3 Computational Methods for Engineering Structures

Scientists and engineers working in the field of computational methods for the mechanical process of engineering structures, particularly hydraulic structures targeted in this book, are customarily guided by the following task list.

- The pre-process for the real world entity representing a hydraulic structure is carried out. This is normally accomplished by modeling a solid structure inclusive its foundation, creating a discrete fracture network (DFN) inclusive joints in the structure (Wilcock 1996), identifying sub-domains (blocks), and if necessary (e.g. in FEM and FDM), discretizing the whole solid entity into a mesh (grid) system.
- The mathematical model simulating a physical phenomenon is constructed. This usually involves expressing the model in terms of PDEs. Of which, the constitutive equations (relations) for the construction materials (e.g. rock, soil, concrete) and their corresponding parameters are the most important factors dominating the computation results.
- The mathematical model is converted into a form suitable for digital computation. This is mostly related to the areas of linear algebra (LA) and numerical analysis (NA). Typically, this operation transfers a PDE (or a system thereof) into a corresponding algebraic equation set, and is called "discretization" because it creates an approximate discrete model from the original "accurate" model. There are various algorithms for such a discretization dependent on the basic conceptualizations and postulations with regard to the materials in the structure, such as the FEM for continua, the DEM for discontinua, and hybrid ones.
- Computer program is compiled (or revised) to solve the approximately discretized model using either direct methods (single marching scheme to obtain the next step solution) or iterative methods (start with a trial solution and arrive at the convergent solution by successively iterative refinement). The most widely exercised programming languages in the science and engineering communities are the Fortran and C++. Although they all possess well known popularity, yet the latter is becoming more and more prevalent because of its built-in visualization functions. The proprietary language/environment MATLAB is also widely employed, especially for a rapid application development and model verification. Depending on the nature of the problem, supercomputers or parallel computers may be demanded to run the program within acceptable time.
- Post-process and visualization. In order to help practitioners to understand, analyze, and debug computation results conveniently, as well as to add some fun to their works, it is extremely encouraged to develop well performed post-process software for vividly presenting the spatial-time distribution of physical and mechanical fields (e.g. temperature, hydraulic head and flow rate, deformation/stress and damage) in the structure concerned. All these are strongly dependent on the scientific visualization which is an interdisciplinary branch of computer science and has made rapid progress insofar (McCormick et al. 1987; Pickover 1994).

There are basically two ways to realize scientific visualization. The traditional and still effective approach is to run the computation software and save the output to a file, afterwards use is made of a special post-process program to hard print or to screen display the data. When the simulations are time consuming ("expensive"), or the data sets are very large, this is often advisable. The second approach is to do the visualization from within the computation program using language-callable routines. The Fortran language itself does not possess universal graphical constructs, as exists in the C++ language. In the former case, a wide selection of auxiliary software packages are now available (e.g. Dislin) where the emphasis is on realistic renderings of volumes, surfaces, illumination sources, and so forth, perhaps with a time component. In the latter case, many commercial software packages such as ABAQUS, NASTRAN, ADYNA, ANSYS, etc., are equipped with strong post-process modules.

– Safety calibration. For a hydraulic structure concerned, the run of computation program provides the hydraulic potential and its gradient, temperature variation and its gradient, deflection and stress, stability safety factor, etc. These indices should be assessed for the purpose of safe and economical design of the structure. There are basically three categories of safety criteria: those who possess the feature of "point" or "local" such as the computed stress against the allowable stress (strength), of "face" such as the slip driving force against the allowable resistance force with regard to a specified surface (planar or curved), and of "overall" such as the overall stability of the whole structure. It is relatively easier to construct a point criterion with the computed action effects (e.g. stress, hydraulic gradient) and correspondingly stipulated allowable indices. Although sometimes the singularity points may bring about the difficulties in the selection of appropriate action effects, yet the rendering processes such as the equivalent stress for arch dams (Chen 2015) may be employed to tackle the problem. Safety factor against sliding normally possesses a "face" feature. Although it is less disturbed by the singularity points, yet paradoxically it introduces difficulties in the construction of state function under the circumstances with curved slip surface due to the treatment of changeably directed shear stresses. Towards establishing an "overall" stability safety criterion for the structure using computational methods, either the "overload factor"—the ratio of the ultimate load to the actual load exerting on the structure to bring it to a state of limiting equilibrium, or the "strength reduction factor"—the ultimate strength (resistance) divided by the mobilized stress (failure driving) to bring the structure to a state of limiting equilibrium at incipient failure (Matsui and San 1992; Ugai and Leschinsky 1995; Dawson et al. 1999; Griffiths and Lane 1999), may be employed. The allowable (permissible) factor of safety (FOS) is stipulated according to the structure type and grade under definite load (action) combination. It is worthwhile to note that all the afore-defined safety factors exhibit different values, although in particular simple cases they could be identical.

The mathematical models, numerical procedures, and computer programs (codes, software) should be thoroughly verified using either experimental data or benchmarks (e.g. exact analytical solutions) available. Quite frequently, a new numerical or computational method is calibrated by comparing its outputs with those of existing well-established methods. It is appreciative that the "ICOLD Committee on Computational Aspects of Dam Analysis and Design" had made noteworthy contributions by organizing a series of "Benchmark Workshops" (altogether 14 until 2017) intended to offer dam engineers and researchers the opportunity to share their experiences of how to use computational methods properly.

1.4 History and State-of-the-Art of Computational Methods

The history of computation may date back to the dawn of human civilization (Klein 1972). The prehistory of arithmetic—precedence of computation, was limited to a small number of artifacts which may indicate the conception of addition and subtraction. The best-known is the "Ishango bone" from central Africa dating from between 20000 BC and 18000 BC, although its interpretation is still disputed (Rudman 2007).

According to the knowledge of the author, the development of computational methods may be roughly divided into 6 major periods according to the features of mathematics, mechanics, and computation tools, which will be summarized below.

1.4.1 3000 BC–300 BC

This is a dawn period of computational methods in the human history featured by arithmetic or elementary algebraic operations consisting of the study on numbers and basic operations between them, namely the addition, subtraction, multiplication and division (Struik 1987; Boyer 1991). The earliest written records indicate that the Egyptians and Babylonians were able to conduct all these elementary arithmetic operations as early as 2000 BC.

Complex calculations needed the assistance of tools such as counting board and abacus. One of the earliest mathematical writings on a Babylonian tablet (YBC 7289) from the Old Babylonian period (1830–1531 BC) gave a three significant sexagesimal digits (seven significant decimal digits) of $\sqrt{2}$ (Aaboe 2008), this means that with the help of counting board, they were able to compute the sides of a triangle (and hence square roots) which is extremely important in architecture and astronomy. In the period between 2700 BC and 2300 BC saw the first appearance of the Sumerian abacus, a table of successive columns which delimited the successive

magnitude orders of their sexagesimal number system. Abacus is a high efficient calculating tool that had been widely used in Europe, Russia, African and Eastern Asian countries (particularly prevalent in China) for centuries and may still find it application by merchants, traders and clerks in some parts of these countries. Sadly however, it is seldom to find the use of abacus in China since the 1980s due to the adoption and wide-spread of pocket electronic calculators, and recently, overwhelming smart mobile phones.

1.4.2 300 BC–1600 AD

This is a period initiated from the Hellenistic civilization of ancient Greece whose studies in mathematics overlapped with their philosophical and mystical beliefs.

Until the Hellenistic period the ancient Greeks lacked a symbol for zero, so they had to use three separate sets of symbols. One set for the unit's place, another for the ten's place, and the rest one for the hundred's place. For the thousand's place they would recur the symbols for the unit's place, and so on. Although the multiplication algorithm was slightly different, their addition and long division algorithms were identical to ours today. The square root algorithm once taught in school was known to Archimedes, who is believed as the inventor.

It is not very clear when the Chinese started to calculate with positional representation, but it is believed that definitely before 400 BC they possessed a similar positional notation based on the ancient counting rods. Coincidentally, they also lacked a symbol for zero and had one set of symbols for the unit's place, and a second set for the ten's place. For the hundred's place they would recur the symbols for the unit's place, and so on.

The ancient Hindu-Arabic people independently devised the place-value concept and positional notation. They combined the simpler computational methods with a decimal base numerals and the use of a digit representing zero (0), which eventually replaced all other old systems.

The milestone works were founded in the early 6th century AD by Aryabhata—an Indian mathematician who incorporated an existing version of computation system in his work, and in the 7th century AD by another Indian mathematician—Brahmagupta who established the use of zero (0) as a separate number and determined the results for the multiplication, addition and subtraction of zero and all other numbers, except for the result of division by 0.

The Arabs learned Indian new computation system. Although the Codex Vigilanus described an early form of Arabic numerals (without 0) by 976 AD, Leonardo of Pisa (Fibonacci) was primarily remembered for spreading their use throughout the European countries after the publication of his book "Liber Abaci" in 1202 AD. Styled as the "method of the Indians", he noted the significance of this "new" representation of numbers because it allowed for the computation system to consistently represent both large and small integers.

In the medieval period arithmetic was one of the seven liberal arts taught in European universities. The flourishing of algebra in the medieval Islamic world and in Renaissance Europe was an outgrowth of the crucial simplification in the computation through the decimal notation.

1.4.3 1600s–1800s

As the unfolding of human civilization, various higher performance calculating tools in addition to ancient abaci were created and used to assist in computation, including the slide rule invented around 1620–1630 AD by J. Napier, E. Gunter, E. Wingate, W. Oughtred, et al., the nomograms and mechanical calculators such as the Schickard's calculator invented in 1623 AD by W. Schickard, and the Pascal's calculator, also called as the "Pascaline", invented in 1642 AD by Blaise Pascal.

Mechanics is one of the most powerful demand-pulls of the progress in the computational method. The beginning of classical mechanics is generally attributable to Sir Isaac Newton and many contemporary natural philosophers in the 17th century, of which the solid mechanics mainly for the engineering structural design in its early time, was actually initiated by the "Hooke's law" in 1676—named after the British physicist Robert Hooke (Timoshenko 1953).

The next important step forward in the solid mechanics was made by Galileo Galilei who firstly developed a theory of beams, although recent studies argue that Leonardo da Vinci was the first to make the crucial observations. Leonhard Euler and Daniel Bernoulli were the first to established a simplified linear theory of elasticity that provides a tool for calculating the bearing capacity and deflection characteristics of beams.

The study of fluid mechanics may trace back at least to the days of ancient Greece, when Archimedes investigated fluid statics and buoyancy and formulated his famous law known now as the "Archimedes' principle"—generally considered to be the first major work on fluid mechanics. Rapid progress in fluid mechanics began with Leonardo da Vinci (observations and experiments), Evangelista Torricelli (invented the barometer), Isaac Newton (investigated viscosity) and Blaise Pascal (researched hydrostatics, formulated Pascal's law), and was continued until Daniel Bernoulli who established mathematical fluid dynamics (Massey and Ward-Smith 2005).

In 1715, Daniel Bernoulli systematized the virtual work principle and made explicit the concept of infinitesimal displacement to solve problems for both rigid bodies as well as fluids (Capecchi 2012). This is an important step towards the study on the mechanics of deformable bodies and the analysis for complex structures (Dym and Shames 1973).

At the end of this period, science and engineering were generally looked at as very distinct fields, and there was considerable doubt that a mathematical product of academia could be trusted for the safety assessment of engineering structures. Take the hydraulic structures for example, rational theories and criteria for the dam

design had few acceptance, problems encountered in its construction were ordinarily tackled in a style of trial and error (Chen 2015).

1.4.4 1800s–1940s

This is a period featured by the fast development in classical mechanics and mathematics under the impetus of the fast development in techniques for modern machinery manufacture industry and civil engineering inclusive hydraulic works.

Bridges and buildings continued to be constructed by precedent until the late 19th century, when the Eiffel Tower and the Ferris wheel demonstrated the validity of the mechanical theory on large scales. In the field of hydraulic structures, along with the invention and sophisticated application of climbing formwork, Portland cement, and modern concrete, Furens Dam (France, H = 50 m), a gravity dam accomplished in 1858, was designed according to the "gravity method"—a variant beam theory proposed by French engineer J Sazilly. New Croton Dam, also known as Cornell Dam (USA, H = 91 m), a gravity dam accomplished in 1905, was one of the first applications of American Portland cement. FA Noetzli summarized the works of the "crown cantilever method", a structural analysis algorithm for the arch-cantilever grid system initiated in 1905 by two US engineers GY Wisner and ET Wheeler, in a landmark paper by giving relatively simple formulas for calculating the cantilever and the arch actions, and then applied his formulations to the design of Pathfinder Dam (H = 65 m, USA), which was completed in 1909. In 1929, C Howell and AC Jaquith, both from the Bureau of Reclamation, formalized comprehensively the calculation method using various arches and cantilevers developed through scattered contributions, as the "trial-load method" (TLM).

Throughout this period, leading scientists in mechanics and mathematics had been involved in scientific studies and engineering applications of the continuum mechanics (fluid dynamics, heat transfer and solid mechanics) and related theory of partial differential equations (Florian 1928), and on many aspects their works had led to the discovery of modern numerical analysis and computational mechanics in use today.

On a microscopic scale, materials such as solids and fluids, are composed of particles (e.g. atoms and molecules) separated by "empty" space. On a mesoscopic or/and macroscopic scale, rock-like materials (concrete and rock) even contain voids, cracks and discontinuities. However, certain physical phenomena can be simply described by assuming the material as a continuum, i.e. in an object the matter is continuously distributed and fills the entire spatial domain it occupies. By the term of "continuum", it implies that the matter concerned can be continually sub-divided into infinitesimal elements with properties being identical to the original bulk one. On the length scales much greater than that of inter-particle distances, this conceptual (phenomenological) material model possesses high performance. Fundamental physical laws such as the conservation of mass, the conservation of momentum, the

conservation of energy, and the constitutive law (relation) of material properties, may be applied to derive PDFs governing the behaviors of object.

When the length scales does not hold, or when one wants to establish a continuum of finer resolution than that of the representative volume element (RVE) or representative element volume (REV) size, one has to employ a statistical volume element (SVE), which in turn, leads to random continuum fields. The latter may provide a micromechanics or mesomechanics basis for stochastic behaviors of materials. The levels of RVE (REV) and SVE link continuum mechanics to statistical mechanics, and they may be assessed only in a limited way via experimental testing when the constitutive response becomes spatially homogeneous (Ostoja-Starzewski 2007).

Continuum mechanics deals with the physical properties of solid and fluid which are independent of any particular coordinate system in which they are observed. These physical properties are then represented by tensors, which are mathematical objects with required properties independent of coordinate system. Basically, there are two formalisms in the classical field theory towards the continuum mechanics (Spencer 1980; Hutter and Jöhnk 2004), namely, the Lagrangian formalism and the Eulerian formalism.

The Lagrangian formalism seems a natural development from the Lagrangian mechanics established in 1788—a reformulation of the classical mechanics for discrete particle system with a finite degrees of freedom (DOF). To expand the Lagrangian formalism into the classical field theory of continuum which has an infinite number of DOF, the function of generalized coordinates—"Lagrangian", is replaced by a "Lagrangian density" that is the function of the field and its derivatives, and possibly of the space and time coordinates themselves. The independent variable t is replaced by an event in space-time (x, y, x, t) or still more generally, by a point on a "manifold". Often, the "Lagrangian density" is simply referred to as the "Lagrangian". In the Lagrangian formalism, an observer standing in the referential frame observes the changes in the position and physical properties as the material body moves through the space with the ongoing time.

The Eulerian formalism focuses on the current matter configuration, and what is occurring at a fixed point in the space with the time evolution, in lieu of giving attention to individual particles with regard to how they move through the space and time. This approach is conveniently applied in the study of fluid flow or solid deformation where the main interest is directed to the magnitude and rate at which the changes manifest, or to the gradient of the field rather than the shape of the body at a reference time.

In 1826, Claude-Louis Navier published an academic paper on the elastic behaviors of structures. He formulated the general theory of elasticity in a mathematically resoluble form with sufficient accuracy for the first time. He is therefore often respected as the founder of modern structural analysis. In 1873, Carlo Alberto Castigliano presented his dissertation with regard to compute displacements as the partial derivatives of strain energy, in his theorem the method of least work was a special case. In 1941 Alexander Hrennikoff discretely solved the elasticity plane

problems using a lattice framework in parallel to the "trial-load method" for arch dams.

In fluid dynamics, a set of quasilinear hyperbolic PDEs governing adiabatic and inviscid flow, the "Euler equations" named after Leonhard Euler, was formulated in his academic paper in 1757. Further mathematical justification was provided by Claude-Louis Navier and George Gabriel Stokes (Anderson 1995). The Navier-Stokes equations are also of great interest in a purely mathematical sense—it has not yet been proven that their three-dimensional solutions always exist, or that if they do exist, then they are smooth without any mathematical singularities. These are called the "Navier-Stokes existence and smoothness problems".

In 1822, Joseph Fourier published his seminal work on heat flow, in which he proposed his PDE for conductive diffusion of heat now being taught to students of mathematical physics and being the basis of thermal field analysis for concrete dams. Fourier also made a great contribution on purely mathematics by claiming that any function of a variable can be expanded in a sine series. Although his result is not correct without additional conditions, yet Fourier's observation that some discontinuous functions are the sum of infinite series was a breakthrough in the numerical analysis and computation.

The Darcy's law with regard to the rate of water seeping through a soil (permeability) was promulgated in 1856, and is still very relevant today. It is analogous to the Fourier's law in the field of heat conduction, the Ohm's law in the field of electrical networks, or the Fick's law in the diffusion theory, and therefore the similarity of governing PDEs exist between the heat conductivity and fluid permeability. The Darcy's law dictates how and where different types of earthfill materials can be used in an embankment dam. This is probably the first result in understanding two-phase problems, namely, fluid versus solid.

Field and laboratory testing for soil and rock materials began to emerge during the 1920s and early 1930s. In addition to the pioneering works on the topics such as soil permeability by Karl von Terzaghi who is generally respected as the father of soil mechanics, others contributed greatly, too, in the attempt to characterize these materials.

At the mid 20th century, the basic governing PDEs for solid mechanics, hydrodynamics, thermal conductivity, were all available. The ball was then passed to the scientists in mechanics and mathematics to find the solutions for specific issues arise from sciences and engineering.

In the whole 19th century, mathematical study on the numerical analysis and computation continued its long tradition of practical calculations. People did not seek exact answers that are often impossible to access in practice. Instead, they were highly interested in obtaining approximate solutions meanwhile maintaining reasonable bounds on errors. Many great mathematicians had been preoccupied by the issues of numerical analysis (Hildebrand 1956), and invented important algorithms with their big names like the Newton's method, the Lagrange interpolation polynomial, the Fourier series and transform, the method of Lagrange multipliers, the numerical quadratures of the Newton-Cotes formulas/Simpson's rule, the Euler's method, the iterative methods of Jacobi/Gauss-Seidel. Among them, C. F. Gauss is

an outstanding scientific giant (Dunnington 2012) attributable to his crucial works in least-squares data fitting in 1795, solution algorithm of linear equation sets (Gaussian elimination) in 1809, numerical quadrature (Gaussian quadrature) in 1814, as well as fast Fourier transform in 1805, though the last did not become widely known until its rediscovery by J. W. Cooley and J. Tukey in 1965.

Since around the 1900s, however, mathematicians were shifted to less conspicuous in the numerical analysis. This was a consequence of the great advances in scientific fields in which, for technical reasons, mathematical rigor had to be the heart of the subject. For example, many advances of the early 20th century sprang from mathematicians' new ability to reason rigorously about infinity, a subject relatively far from numerical analysis.

Before the advent of modern computers, numerical analysis often depended on hand interpolation in large printed tables. This was far from the sophisticated solution for complex structural problems governed by the PDEs and restrained by boundary and initial conditions. The computer for calculating the field functions, was highly solicitous of.

Charles Babbage, an English mechanical engineer, is considered the father of the computer by conceptualized the first mechanical analog computer in the early 19th century. After working on his revolutionary difference engines designed to aid in navigational calculations, in 1833 he realized that a much more general design, an "analytical engine", was possible (Goldstine 1972). The first modern analog computer was a tide-predicting machine invented by Sir William Thomson in 1872. The differential analyser, a mechanical analog computer designed to solve differential equations using wheel-and-disc mechanisms, was conceptualized in 1876 by James Thomson. The technology of mechanical analog computing reached its summit by H. L. Hazen and Vannevar Bush at MIT in 1927. A dozen of such devices were built before their obsolescence became obvious. By the 1950s the success of digital electronic computers had spelled the swan song for the most analog computing machines, but they remained in performance during the 1950s in some specialized applications such as university education.

1.4.5 1940s–1970s

It is an exciting era landmarked by the appearance of digital electronic computer and computational method towards the solution of PDEs arise from various science and engineering demands.

Humankind started the modern aviation times in 1939 by the first jet aircraft—the German Heinkel He 178. In 1943, the Messerschmitt Me 262, the first jet aircraft fighter, went into service in the German Luftwaffe. In October 1947, the Bell X-1 became the first aircraft to exceed the speed of sound. The first jet airliner—the de Havilland Comet, was introduced in 1952. The Boeing 707, the first widely successful commercial jet, had been in commercial service from 1958 to 2010. The

Boeing 747 was the world's biggest passenger aircraft from 1970 until 2005 when it was surpassed by the Airbus A380.

Although space flight had become an engineering possibility with the work of Robert H. Goddard in 1919 by his milestone paper "A Method of Reaching Extreme Altitudes", yet his work was not taken seriously by the public. Nonetheless, his paper was highly influential on the German "Von Braun's V-2", the first rocket to reach space at an altitude of 189 km in 1944. In the former USSR, the class of "Korolev's R-7 Semyorka" rockets was used to launch the world's first artificial Earth satellite "Sputnik 1" in October 1957, and later the "Vostok 1" with first human—Yuri Gagarin to orbit the Earth in April 1961. A class of rockets "Saturn" allowed the USA for sending the first two astronauts, Neil Armstrong and Buzz Aldrin, to the Moon and back the Earth on "Apollo 11", in July 1969.

In civil engineering, with the advances in construction material technology, skyscrapers (Empire State Building, USA, H = 381 m, 1931; World Trade Center, USA, H = 417 m, 1972; The Willis Tower—formerly Sears Tower, USA, H = 442 m,1974), bridges (George Washington Bridge, USA, L = 1450 m,1931; Lake Pontchartrain Causeway, USA, L = 38.442 km, 1956; Wuhan Yangtze River Bridge, China, L = 1670 m, 1957; Fremont Bridge, USA, L = 656.5 m, 1973), tunnels (Delaware Aqueduct, USA, L = 137 km,1945), and dams (Mauvoisin Arch Dam, Switzerland, H = 237 m,1957; Vajont Arch Dam, Italy, H = 265 m, 1959; Grande Dixence Gravity Dam, Switzerland, H = 285 m,1962; Glen Canyon Arch Dam, USA, H = 216 m,1964; Contra Arch Dam, Switzerland, H = 220 m, 1965; Oroville Earthfill Dam, USA, H = 235 m, 1967; Daniel Johnson Multi-arch Buttress Dam—Manicouagan No. 5 Dam, Canada, H = 214,1968; Mica Earthfill Dam, Canada, H = 242 m,1974; Dworshak Gravity Dam, USA, H = 219 m, 1976), continued to mount toward new height and/or length records.

All the above engineering activities required rational, reliable, and efficient computations for the structural issues with respect to the simulation and evaluation of high speed or/and high pressure flow, complex material deformation and strength (static and dynamic), strong temperature variation, as well as their coupling. Taking the civil engineering for example, the stability requirements on structure foundations and underground caverns gave impetus to the fast progress in rock mechanics founded by Leopold Müller. The evolution of soil mechanics and rock mechanics gave birth to and maturation of geotechnical engineering, as an important specialty of civil engineering. The use of a large stock of computers and computer programs jointly pushed by geotechnical engineers and computation scientists became a routine practice in the structural analysis and design to provide solution within a fairly short time.

It is fortunate that at the initiation of this period, the mathematical basis of approximation theory had been built. Today it has grown into one of the largest branches of mathematics encompassing classical questions of interpolation, series expansion, and harmonic analysis associated with the names of Newton, Fourier, Gauss, and others; semi classical problems of polynomial and rational minimax approximation associated with the names such as Chebyshev and Bernstein; and much newer topics including splines, radial basis functions, and wavelets.

In the early phase of this period, in addition to the traditional slide rules and mechanical calculators, large books were published with formulas and tables of data (e.g. interpolation points and function coefficients) for the purpose to facilitate computations by hand. The canonical work in the field is the NIST publication edited by Abramowitz and Stegun, a 1000-plus page book with a very large number of commonly used formulas and functions and their values at many points. Today, although these function values are no longer so useful as before when a computer is easily accessible, yet the large listing of formulas can still be very handy.

The principle of the modern computer was proposed by Alan Turing when he delivered a landmark paper in 1936 to the London Mathematical Society (Turing 1937) concerning a simple device called "universal computing machine"—now known as "universal Turing machine". It is capable of calculating any computable things by executing instructions (i.e. program) stored on tape, in this manner the programmable machine is allowed for. Modern computers are said to be "Turing-complete", which is to say, they possess the capability of algorithm execution equivalent to a universal Turing machine.

The mechanical calculator evolved into the electronic digital programmable computer when the "Colossus" was built in 1943, followed by the "ENIAC" built at the Moore School of Electrical Engineering, University of Pennsylvania (USA), by J. Presper Eckert and John Mauchly in 1945, as well as the "Manchester small-scale experimental machine" built at the Victoria University of Manchester (UK) in 1948 that is the first stored-program computer in the world.

John von Neumann, joined the ENIAC group in 1944, was a prestigious figure and he made the concept of a high-speed stored-program digital computer widely known through his writings and public addresses. As a result of his high profile in the field, it became customary to refer to electronic stored-program digital computers as "von Neumann machines". However, John Von Neumann himself acknowledged that the fundamental concept of the modern computer was the stored program by the Turing's design.

The final major event in this period of electronic computation history was the development of magnetic core memory. Once the absolute reliability, relative cheapness, high capacity and permanent life of ferrite core memory became apparent, it soon replaced other forms of high-speed memory. The IBM 704 and 705 computers (announced in May and October 1954, respectively) brought core memory into wide use.

Until the end of this period, mainframe computers such as IBM 7094 and IBM 7040/7044 were used primarily for critical applications and bulk data processing by large organizations/institutions, meanwhile less expensive minicomputers such as HP 2116A and PDP-8 were accessible by smaller agencies/schools.

New academic journals were founded such as the "Mathematics of Computation" since 1943 and the "Numerische Mathematik" since 1959. From this moment, numerical methods began to explode, computational science (also called scientific computing) became a "third way" besides the theoretical and experimental sciences.

Thanks to the efforts of these outstanding pioneers going back many decades, and thanks to the ever more powerful computers, we had reached at a level where most of the classical mathematical problems arise from physical sciences inclusive mechanics can be numerically solved to high efficiency and accuracy. Computational mechanics (CM), widely considered a branch of applied mechanics, was also considered a branch of computational science. Computational geomechanics (CG), a sub-branch of CM strongly backed up by the engineering fields of mining, transporting, building, etc., possesses more engineering proximate features attributable to its equalized demands on the material properties and safety margins in addition to computation algorithms.

Most of algorithms that make the CM powerful were invented since 1950, of which the classical versions of the finite difference method (FDM), the finite element method (FEM), and the boundary element method (BEM) based on the Eulerian formalism, are without doubt the zenith. For the field problems of low velocity fluid or infinitesimal deformation solid, the Eulerian formalism is more convenient and easier to incorporate the constitutive laws (relations) (e.g. Hooke's law, Darcy's law, Fourier's law) with regard to the physical/mechanical properties observed and summarized by our predecessors.

(1) FDM

It was firstly proposed by A Thom in the 1920s under the title of "the method of square" to solve nonlinear hydrodynamic equations. The FDM is based upon the approximations that permit substituting partial differential equations by finite difference equations, the latter are algebraic in form, and whose solutions are related to grid points (Morton and Mayers 2005).

Compared to the FEM and BEM, the most attractive merit of the FDM is that it is very easy to implement. The formation and solution of the equations are localized, which is more efficient for memory and storage handling in the computer program. No local trial (or interpolation) functions are demanded to approximate the PDE in the neighborhoods of the sampling points, as is done in the FEM and BEM. This also provides the additional advantage of more straightforward simulation of complex constitutive behaviors, such as plasticity and damage, without iterative algorithms using predictor-corrector mapping schemes for global matrix equation systems, as in the FEM and BEM.

The FDM is not as prevalent as the FEM in structural problems, although it is a major method in the fluid dynamics and hydraulics.

(2) BEM

Boundary integral is a classical tool for the solution of boundary value problems based on PDEs. The BEM is a numerical method of solving boundary integral equations applicable to problems for which the Green's functions can be established (Jaswon and Ponter 1963; Rizzo 1967; Cruse and Rizzo 1968; Brebbia et al. 1984).

The BEM initially sought a weak solution at the global level through the numerical solution of an integral equation derived using Betti's reciprocal theorem

and Somigliana's identity. The introduction of isoparametric elements using different orders of shape functions, in the same fashion as that in the FEM (Lachat and Watson 1976; Watson 1979), greatly enhanced the BEM's applicability for structural problems.

The BEM is more suitable for solving problems of fracturing in homogeneous and linearly elastic bodies because it possesses remarkable advantages over the FEM or FDM that:

- Only the boundary of the domain needs to be discretized. This reduces the model dimension by one and consequently allows for much simpler mesh generation and data input as well as smaller data storage.
- Exterior problems with unbounded domains are handled as easily as interior problems.
- In some cases, the physically relevant data are given not by the solution in the interior of the domain but rather by the boundary values of the solution or its derivatives. These data can be obtained directly from the solution of the BEM with high accuracy.
- Solutions inside the domain are continuously approximated with a rather high convergence rate and moreover, the same rate of convergence holds for all solution derivatives of any order in the domain.

Main difficulties with the BEM are that:

- Boundary integral equations require the explicit knowledge of a fundamental solution, or the Green's functions which are often problematic to obtain as they are based on the solution of system equations subject to a singularity load.
- For a given boundary value problem there exist different boundary integral equations, and to each of them there are several numerical approximations. Thus every BEM application requires several choices to be made.
- The classical theory of integral equations and their numerical solution concentrates on ordinary Fredholm integral equations of the second kind with regular kernel. However, the boundary integral equations frequently encountered may be of the first kind whose kernels are in general singular.
- It is not as efficient as the FEM in dealing with material heterogeneity because it cannot handle as many sub-domains (elements).
- It is not as efficient as the FEM in simulating non-linear behaviors (e.g. plasticity, damage) because domain integrals are often presented in these problems.

(3) FEM

The FEM in its practical application often known as the "finite element analysis" (FEA), is a numerical technique for finding approximate solutions to PDEs and (less often) integral equations (Zienkiewicz and Cheung 1967; Desai and Abel 1972; Gallagher 1975; Roy et al. 1976). The distinctive history of the FEM is its initial driving force from structural engineers who endeavored to the practical formulations and solution techniques in addition to the scientists in mathematics

and mechanics who laterly laid theoretical foundations with respect to the existence, stability, and uniqueness, of the solution and error analysis as well.

In numerical analysis, the Galerkin method converting a continuous operator problem governed by the PDE to a discrete one, is the equivalent of applying the variation operator to a function space (Yosida 1980) by converting the equation to a weak formulation. Use is then made of some constraints on the function space to characterize the space with a finite set of basis functions. This approach is usually credited to the Russian mathematician Boris Galerkin although it was firstly discovered by the Swiss mathematician Walther Ritz, to whom Galerkin referred (Pont 2012). Frequently, when referring to a Galerkin method, one also gives the name along with typical approximation methods used, such as the Bubnov-Galerkin method (after Ivan Bubnov), Petrov-Galerkin method (after Georgii I Petrov) or Ritz-Galerkin method after Walther Ritz (Ritz 1909; MacDonald 1933; Mikhlin 1964).

From the point view of mathematics, the FEM is a special case of more general Galerkin method with polynomial approximation functions. Its development can be traced back to the works by Hrennikoff (1941) and Courant (1943). Hrennikoff discretized the object domain by using a lattice analogy similar to the "trial-load method" for arch dams, whereas Courant divided the domain into finite triangular sub-regions to solve second order elliptic PDEs arise from the torsion problem of a cylinder.

The practical algorithm for the FEM was originated from the need for solving complex elastic structures in civil and aeronautical engineering (Argyris 1963). Between the later 1950s and early 1960s in China, Kang Feng proposed a systematic algorithm for the solution of PDEs, and studied the structural problem of Liujiaxia Gravity Dam (H = 147 m, 1974). His method was called the "finite difference method based on variation principle", which was latterly recognized as an independent invention of the finite element method (Lax 1993; Kang 1994). Although the approaches used by these pioneers are different, yet they share one essential feature—mesh discretization for a continuous domain into a set of discrete sub-domains usually called as "elements".

The FEM gained its ever stronger impetus in the 1960s and 1970s by the outstanding works of, for example, J. H. Argyris with co-workers at the University of Stuttgart, R. W. Clough with co-workers at the UC Berkeley, O. C. Zienkiewicz with co-workers at the University College of Swansea, and R. Gallagher with co-workers at Cornell University. Further driving was given in these years by available open source programs. US NASA sponsored the original version of NASTRAN, and the UC Berkeley made the SAP IV widely available. A rigorous mathematical basis to the FEM was eventually established in 1973 with the publication by Gilbert Strang and George J. Fix. The method has since been generalized for the numerical modeling of physical and mechanical systems in a wide variety of engineering disciplines (e.g. heat transfer, fluid dynamics, and solid mechanics).

Much development work in the FEM had been specifically oriented towards geotechnical structure problems, particularly in hydraulic engineering facing complex structural configurations, rock-like materials of heterogeneity and

non-linearity (plasticity), dynamic boundary conditions, and in situ geo-stresses (Naylor et al. 1981; Pande et al. 1990; Wittke 1990). The FEM out-performed the traditional FDM in the areas of hydraulic structures is attributable to its attractive merits of higher ability and flexibility.

1.4.6 1970s–Today

We are fortunate for having experienced such prosperous times featured by high performance computers and expansions of the FDM, FEM and BEM to various field problems, of which the FEM holds dominant position in the design of super engineering structures (e.g. super high dams). In addition, various new computational methods with regard to the issues of high-speed flow, large and discontinuous deformation, etc., have been booming propelled by engineering and other industry demands.

Activities in super tall skyscrapers move towards East, particularly the Asia (Petronas Towers, Malaysia, H = 452 m, 1996; Jin Mao Tower, China, H = 420.5 m, 1999; Taipei 101, Taiwan, H = 509.2 m, 2004; Burj Khalifa, United Arab Emirates, H = 829.8 m, 2009; Shanghai Tower, China, H = 632 m, 2015). Cable-stayed and suspension become prevalent types in the construction of long span and/or high bridges (Akashi Kaikyō Bridge, Japan, L = 3911 m, 1998; Baling River Bridge, China, L = 2237 m, 2009; Russky Bridge, Russia, L = 3100 m, 2012; Beipanjiang Bridge, China, L = 1341.4 m/H = 565 m, 2016). Long and/or large sectional tunnels are constructed world widely for transportation and water diversion (Seikan Tunnel, Japan, L = 53.85 km, 1988; Channel Tunnel, UK-France, L = 50.45 km, 1994; Lærdal Tunnel, Norway, L = 24.51 km, 2000; Lötschberg Base Tunnel, Switzerland, L = 34.57 km, 2007; Zhongnanshan Tunnel, China, L = 18.04 km, 2007; Eiksund Tunnel, Norway, L = 7.765 km, 2008; Gotthard Base Tunnel, Switzerland, L = 57.09 km, 2016).

In the areas of hydraulic structures, the traditional CVC gravity dams and earthfill dams continues to mount ever new height. Since the 1990s, the world has witnessed the boost of dam construction in China. Today, the world records of dam height kept by the country are the roller-compacted concrete (RCC) arch dam (Dahuashui, China, H = 134.5 m, 2008), the concrete faced rockfill dam (CFRD) (Shuibuya, China, H = 233 m, 2008), the RCC gravity dam (Longtan, China, H = 216 m, 2009), the conventional vibrated concrete (CVC) arch dam (Xiaowan, China, H = 294.5 m, 2012; Jinping-1, China, H = 305 m, 2014).

At the start of this period, use was widely made of the fourth generation (VLSI integrated circuits) computers such as the VAX with operating system "Digital's VAX/VMS" developed by the Digital Equipment Corporation (DEC) in the mid 1970s, and Alpha AXP with operating system "OpenVMS" developed by the DEC, too. Since then, the computer industry has been developing at a speed normally predicted by the "Moore's law" after Gordon Moore, the co-founder of the Fairchild Semiconductor and Intel. In 1965 he stated a doubling law every year in the number

of components per integrated circuit. In 1975, looking forward to the next decade, he revised his prediction to doubling every two years (Moore 1965, 1997). Insofar, advancements in computers are strongly linked to the Moore's law, particularly on the aspects such as quality-adjusted microprocessor prices and memory capacity, which throughout the late 20th and the early 21st centuries have contributed to world economic growth from all industry areas inclusive infrastructures. In this context, the Moore's law describes a driving force for technology and society change, and economic growth.

Today, computer hardware has to be designed in a multi-core manner to keep up with the Moore's law, and there is hot research to make computers out of many promising new types of technology, such as optical computers, DNA computers, neural computers, and quantum computers. Most computers are universal and able to calculate any computable functions limited only by their memory capacity and operating speed.

Since the 1970s, with the support of powerful computers and demands from industry such as hydraulic engineering, aircraft/airspace engineering, high-speed railway engineering, and marine engineering, new computational methods and their hybrid, sophisticated material models, various physical and chemical fields and their coupling, etc., have been developing fast. Some of them have only limited and short term influences, whereas the others have profound contributions to sciences and technologies until today. Complex structure systems that would be very difficult or impossible to handle with may be successfully simulated nowadays using the tools provided by the CM. The great expectation permeating in the whole industry, economy and society is that, with the incorporation of quantum, molecular and biological mechanics into new models, the CM is poised to play an even much more important role in the near future.

When the CM is expanded into the mechanics areas of compressible fluid dynamics with high flow speed, and of solid dynamics with separable/crackable and large deformation, the Lagrangian formalism starts to exhibit higher power although other intrinsic difficulties (e.g. counting/geometric shaping/interacting of particles) will manifest. In addition to the continuous and practical progress in the classical FDM, BEM and FEM (Zienkiewicz 2000), the most important events in this significant period are the invention of the generalized finite element method (GFEM), the discrete (distinct) element method (DEM), the discontinuous deformation analysis (DDA), the meshfree (meshless) method (MM), the numerical manifold method (NMM), and the smoothed particle hydrodynamics (SPH). Most of them are based on the Lagrangian formalism and therefore possess high potentialities towards the solutions of crack propagation/dislocation and particle detachment/flow for the geotechnical and hydraulic structures.

Attributable to selective methods available, we now have a wide spectrum of computational geomechanics for hydraulic structures related to complex rock-like materials (rock and concrete) of heterogeneous, anisotropic, and discontinuous, under different circumstances.

(1) The advancement in classical computational methods

1. FDM

The classical FDM with regular grid systems does suffer from restraints, most of all due to its inflexibility in dealing with fractures, complex boundary conditions and material heterogeneity. These make the standard FDM generally unfavorable for the solution of structural problems related to rock-like materials. Today however, significant progress has been made in the FDM with irregular meshes, such as triangular or Voronoi grid systems, which leads to the so-called finite volume method (FVM). Voronoi polygons grow from points to fill the space, as opposed to tessellations where the polygons are formed by lines cutting the plane, or by building up a mosaic from pre-existing polygonal shapes (Le Veque 2002).

The FVM can be formulated with basic variables (e.g. displacement) at the centers of cells (elements) or at the nodes (grid points) of unstructured grid. It is also possible to consider different material properties in different cells. The FVM is therefore as flexible as the FEM in handling material heterogeneity, mesh generation, and treatment of boundary conditions. It possesses similarities with the FEM and is hence regarded as a bridge between the FDM and FEM. The original concept and early code of the FVM for stress analysis can be traced back to the work of Wilkins (1963) who used a vertex-centered scheme with a quadrilateral grid.

Explicit representation of fractures is not easy in the FDM or FVM because they demand continuity in the functions between the neighborhood grid points. In addition, it is not possible to accommodate special "joint elements" in the FDM or FVM as in the FEM. In fact, this is the crucial weak point of them in the computational geomechanics. However, the FDM or FVM have been employed to study the mechanisms of fracturing processes, such as the shear-band formation and evolution of rock-like material samples (Fang 2001) and fault system formation and propagation as a result of tectonic loading (Poliakov 1999) without creating explicit discontinuity surfaces in the structures. This is achieved via a process of material failure or damage propagation at the grid points or cell centers.

Recently, the gradient smoothing method (GSM) has also been developed for computational fluid dynamics (CFD) problems (Liu et al. 2008; Zhang et al. 2008). It is similar to the FVM, but it uses gradient smoothing operations exclusively in nested fashions, namely gradient smoothing together with a directional derivative technique to develop the first-and second-order derivative approximations for a node of interest by systematically computing weights for a set of field nodes surrounding. A simple collocation procedure is then applied to the governing equations of strong form at each node using the approximate derivatives. In contrast with the FDM inheriting topological restrictions, the GSM can be easily applied to arbitrarily irregular meshes of complex geometry.

2. BEM

The original developments of the BEM towards computational geomechanics may be attributed to the works by Crouch and Fairhurst (1973), Bray and Brady (1978), Crouch and Starfield (1983). Followed and pushed further by many others (Hoek

and Brown 1982; Venturini and Brebbia 1983; Brebbia 1987; Pande et al. 1990; Beer and Watson 1992; Beer and Pousen 1995a, b; Cerrolaza and Garcia 1997; Birgisson and Crouch 1998), its applications to general stress and deformation analysis for underground excavation, soil-structure interaction, groundwater flow and fracturing process, etc., have been achieved. One of the most notable and specially formulated BEM, called the Galerkin BEM (GBEM), produces a symmetric coefficient matrix in the Galerkin sense of a weighted residual formulation (Bonnet et al. 1998; Wang et al. 2001a).

Inclusion of source terms, such as body forces, heat sources, fluid sink/source terms in potential problems, leads to domain integrals in the BEM. The same will also be manifested when considering in situ geo-stress fields and non-linear (e.g. plastic) material behaviors (Mukherjee 1982; Wang and Ma 1986). The traditional technique for dealing with such problems is the division of the domain into a number of internal cells or elements, which essentially undermines the advantages of "boundary only" discretization of the BEM. Different techniques have been developed over the years to handle this issue (Brebbia et al. 1984; Sugawara et al. 1988), of which the most notable is the dual reciprocity method (DRM) (Partridge et al. 1992; El Harrouni et al. 1997).

3. FEM

The FEM has become prevailing analysis tool in hydraulic structures for more than 40 years. Solutions to even very complicated stress problems, thermal problems, as well as seepage problems, can now be obtained routinely using the method (Chan et al. 1970; Hughes 1987; Cook et al. 1989; Crisfield 1997; Clough and Penzien 2003; Ern and Guermond 2004; Zienkiewicz et al. 2005, 2013; Krenk 2009). This is mainly attributable to its following advancements.

i. Representation of discontinuities (rock joints, concrete cracks and joints)

It was motivated by the needs of computational geomechanics since the late 1960s (Beer and Watson 1992). Today, the well-known "joint element" model (Goodman et al. 1968; Mahtab and Goodman 1970; Goodman 1976) has been widely implemented in FEM software and successfully applied to many practical engineering problems. The zero-thickness postulation of Goodman leading numerical ill-condition due to the large ratio of length to thickness of his element, was improved later by Zienkiewicz et al. (1970), Ghaboussi et al. (1973), Katona (1983), Desai et al. (1984), Gens et al. (1989, 1995), Buczkowski and Kleiber (1997). Since these element models are inherently formulated on continuum assumptions, therefore large-scale opening and sliding and complete detaching of elements, are not permitted. In addition, these element models suffer from the drawback that the global stiffness matrix is prone to ill-conditioned when many joint elements are incorporated.

ii. Automatic mesh generation

From the point view of practitioners inclusive the author of this book, mesh generation with complex interior structures and exterior boundaries, is a highly

demanding task when applying the FEM to hydraulic structures. It is truly critical when 3-D problems of complex geometry with a large amount of discontinuities are encountered.

Owe to the persistent and hard works throughout the 1980s, the breakthroughs have been completely made (Zienkiewicz and Phillips 1971; Thacker 1980; Ho 1988) using either triangular or quadrilateral element meshes for two-dimensional structures (Hermann 1976; Blacker et al. 1988). Algorithms for generating quadrilateral meshes are carried out "directly" or "indirectly". The latter creates quadrilateral elements by converting pre-generated triangular elements into quadrilateral ones by means of splitting or merging techniques (Zhu et al. 1991). When a direct algorithm is used, quadrilateral elements are constructed and placed directly into the domain. At the end of the 1980s, there had been a variety of sophisticated methods for the mesh generation towards two-dimensional domains of complex configuration, such as the octree method (Yerry and Shepard 1984), the Delauney triangulation (Sloan and Houlsby 1984), the paving method (Blacker and Stephenson 1991), the advancing front method (Lo 1985; Peraire et al. 1987; Löhner 1988; Jin and Wiberg 1990).

Started from the 1990s, three-dimensional grid discretization has achieved great progress propelled by the industry demands such as the CAD/CAM and the three-D print. Of which the advancing front technique (AFT) and the Delaunay triangulation method (DTM) are the most successful ones in generating tetrahedral meshes in sequence as well as in parallel. Since the AFT is able to well control the stretching direction of elements, it is more prevailing towards the general issues of fluid dynamics and special issues of solid mechanics (e.g. localization) (Löhner 1988; Peraire et al. 1992; Moller and Hansbo 1995). The author of this book also has exercised the AFT in the FEM study on hydraulic structures where the discontinuities and construction sequences are carefully taken into account (Chen et al. 1996, 2000; Cao et al. 1998).

However, the generation of hexahedral element mesh—superior to tetrahedral one in terms of analysis accuracy as well as amount of elements and nodes, is rather structured and offers less flexibility compared to the arbitrary unstructured tetrahedral mesh for the general purpose of adaptive FEM system. Existing algorithms with regard to this difficulty are still not very robust insofar.

One of afflictive problems in the generation of FE mesh is how to tackle the embedded macro-or/and meso-components due to the existence of discontinuities and the installation of reinforcement and drainage devices. Simulation of such components falls into two approach catalogues in the FEM: the implicit (equivalent) approach takes the influences of them into the compliance tensor and permeability tensor but neglects their exact positions (Barenblatt et al. 1960; Long et al. 1982; Pande and Gerrard 1983; Smith and Schwartz 1984; Dershowitz et al. 1985; Oda 1985; Bear et al. 1993; Dershowitz and Miller 1995; Jing and Stephansson 1996; Chen and Egger 1999), whereas the explicit (distinct) approach uses special elements to exactly simulate their geological and mechanical properties

(Endo et al. 1984; Long et al. 1985; Elsworth 1986a, b; Andersson and Dverstorp 1987; Dershowitz and Einstein 1987; Cacas et al. 1990; Swoboda and Marence 1991; Chen and Egger 1997). The former can be applied to very complex engineering problems with a large quantity of discontinuities and bolts as well as draining holes, whereas the latter has the potentiality to describe them in much more detail and consequently gives more precise solution. From the standpoint of engineering practitioners, major difficulties in the explicit approach of fractures and bolts/drainage holes lie in the pre-process to discretize the domain occupied by these components: on one hand, there are a large amount of discontinuities of different sizes, and a large amount of drainage holes or/and bolts of small diameter (e.g. 10 cm) installed within a small width and largely stretched zone (e.g. 3 m in distance between holes or/and bolts); on the other hand, the special elements at hand need certain nodes to be deployed along these components and some of them should be the common nodes of host solid elements. This, coupled with the complex configuration of hydraulic structures (e.g. dam foundation, cut slope and underground cavern), will lead to a time consuming and tedious pre-process overhead. Recently, the composite element method (CEM) proposed by the author (Chen et al. 2004b) may provide a promising solution for overthrowing this burden inherited in the explicit approach.

When simulating the process of fracture propagation, the FEM is further handicapped by the requirement of small element size and continuous re-meshing, to conform the fracture path and element edges. This makes the FEM less efficient in dealing with cracking problems than its BEM counterparts. Nevertheless, the importance of the FEM equipped with powerful mesh generators should not be and actually has not been neglected by hydraulic engineers. This is mainly because that the first concern in the design of a hydraulic structure is the safety calibration under the actions (loads) of normal or special combinations, where the limit states of serviceability or collapse are taken into account accompanied by stipulated allowable safety factors. Under such circumstances, the majority portion of discontinuities in the structure keeps closed and sliding deformation is only of minor. This is why the FEM attains dominant position in the routine design of hydraulic structures and is recommended as a principal computation tool in addition to traditional ones (e.g. gravity method, trial-load method) in the design specifications of China.

iii. Adaptive refinement and standardized software

Users of the FEM in hydraulic engineering also have been dreaming to assess the accuracy (refinement) of their computation results and to make the computation "standardized", to enable the FEM be prevailingly accepted as a principal analysis tool in routine design practices. However, before proceeding further we have to clarify the objectives of refinement and to specify "permissible error" or "error tolerance" for the practitioners. For instance, the naive statement that all displacement/stress, hydraulic potential and temperature as well as their gradients, should be given within specified tolerances, is not realistic. The reasons are that at

singularities, they will always be infinite and hence no acceptable error tolerance could be specified. Taking a gravity dam for example, its dam heel and toe are singularities where the strength conditions should be assessed according to the design specifications. Unfortunately, the denser of the elements around there, the higher of the stresses would manifest. Since the most procedures of doing refinement convergence are generally too expensive in frequent applications and decisions, therefore "experiences" of previous computations and rules on permissible element shapes and sizes have to be frequently exercised, leading the element refinement to be a kind of "magic". This, accompanied with many disastrous outcomes of computation, once led to the claim that only well trained and fully tested technical staff members would be permitted to apply the art of the FEM.

Today, the situation is changing attributable to the introduction of error estimators and adaptive techniques. This enables engineers to assess the discretization error of a FEM computation and to adaptively adjust mesh size with reasonable efforts. Such adaptive techniques were first introduced by I. Babuška and W. C. Rheinboldt in the late 1970s (1978), when they tried to find a process to refine the approximation with desired accuracy. At the present, there exist various procedures for the refinement of FE solutions broadly falling into two basic categories of h-version and p-version.

By the h-refinement, the elements of same class are continuously used but changed in size: in some locations they are made larger and in others smaller, to provide maximum economy in reaching the optimal solution (Zienkiewicz and Zhu 1987). The advantage is the FE software may be kept independent, but the software for mesh generation is demanded to handle the complex domain configuration and construction process. In addition, the h-refinement is slower in convergence, and not well performed in handling the problem of singularity.

By the p-refinement, we continue to use the same FE mesh of fixed element size and hierarchically increase the order of the polynomial used in the shape (basis) functions. It has been demonstrated for linear elastic fracture problems that the sequences of FE solutions with the p-refinement converge faster than that based on the h-refinement (Szabó and Mehta 1978). The theoretical foundations of the p-refinement were established in a paper of I. Babuška, B. A. Szabó and I. N. Katz published in 1981. For a large class of problems, the asymptotic convergence rate of the p-refinement in energy norm is at least twice that of the h-refinement, subject to quasi-uniform meshes are used. Further evidence of the faster convergence of the p-refinement was presented by Babuška and Szabó in 1982. The p-refinement is good at the singularity problems, but the structure of the FE software is complicated.

Nowadays, the adaptive FEM has been widely exercised in the computational geomechanics and hydraulic structures. The author of this book was also devoted in this area in the 1990s, and made practical contribution to the development of standard FEM software towards the routine design activities. Because personally, I tended to exploit the adaptive techniques for making the FE computation a standardized process, subject to the discretization error target or tolerance being stipulated after various "code calibrations" for existing hydraulic structures, taking it

for granted that these existing practices possess optimal discretization errors. Thereafter the FEM may be confidently embedded in CAD systems as an automatic computation toolkit for structural analysis, the very idea making personal experience in mesh discretization less important and permitting those who do not possess it to access the FEM more easily.

(2) The advancement in generalized finite element methods

In an attempt to develop special algorithms to overcome the deficits of traditional joint elements, the generalized FEM (GFEM) with discontinuous shape functions for fracture initiation and growth through bifurcation theory, was proposed by Texas School (Wan 1990; Melenk 1995; Duarte and Oden 1996; Melenk and Babuška 1996). The first work in the GFEM involved the global enrichments of approximation space.

In the year of 2000, local enrichments for singularities at sharp corners were also established (Duarte et al. 2000). It uses local function spaces to reflect the available information on the unknown solution, in this way to guarantee a good local approximation. A partition of unity is employed to "bond" these spaces together and to form the approximating sub-spaces. The treatment of discontinuities is at the element level. They are defined by distance functions so that their representation demands nodal function values solely by additional DOF in the trial functions—a kind of jump functions along the discontinuity tips. The motion of a discontinuity is simulated using the level set technique and no pre-defined joint elements are needed (Belytschko et al. 2001). It has been validated in problems with domains entailed by complicated boundaries (Belytschko and Black 1999; Strouboulis et al. 2000, 2001; Stolarska et al. 2001).

The GFEM performs well with both structured and unstructured meshes which can be independent of the problem geometry. Structured meshes are appealing for many studies in material science at the test sample level, where the interest is directed to determining the properties of a micro-or meso-element (unit cell) of the material. Unstructured meshes, on the other hand, tend to be widely exercised for the analysis of engineering structures at the prototype level since it is often desirable to conform the meshes to the external boundaries, although some methods under development today are able to tackle even complicated geometries with structured meshes (Belytschko et al. 2009).

The GFEM inspired a generation of researchers to develop variant methods distinguished as its family members.

1. SEM

The spectral element method (SEM) was introduced by Patera (1984). By expanding the solution in trigonometric series, a notable advantage of the SEM is its very high order. This approach relies on the fact that the trigonometric polynomial set—usually composed of orthogonal Chebyshev polynomials or very high order Legendre polynomials over non-uniformly spaced nodes, is an orthonormal basis. The computational error is reduced exponentially as the upgrade of the order

of approximating polynomials, therefore a fast convergence to the exact solution may be realized with fewer DOF in comparison with the classical FEM. The drawback of the SEM is the difficulty in modeling complex geometry, in contrast to the flexibility of the FEM.

The SEM uses a tensor product space spanned by nodal basis functions associated with Gauss-Lobatto points. In contrast, the p-refinement FEM spans a space of high order polynomials by nodeless basis functions.

2. NMM

The numerical manifold method (NMM) was founded by G. Shi in 1991 and further improved in 1997 (Shi 1992; Chen et al. 1998). It is in many aspects similar to the GFEM except for the treatment of discontinuities and discrete blocks by the truncated discontinuous shape functions in a unified form. It also may be looked at as the combination of the FEM and the DDA in a unified form to naturally bridge over the continuum and discontinuum representations: in handling discontinuities (faults, joints and cracks) the NMM takes over the advantages of the DDA, and for the strain-stress analysis in continuous material domains it is as powerful as the FEM.

The method is formulated using a node-based star covering system for constructing the trial functions, where a node is associated with a covering star which can be a set of standard finite elements associated with the node or be generated using least-square kernel technique with general shapes. The integration is performed analytically using the simplex integration technique.

In the application of the NMM, meshes also can be independent of domain geometry. Therefore mesh generation is greatly simplified and re-meshing is not demanded towards the simulation of fracture propagation (Salami and Banks 1996; Wang and Ge 1997; Wang et al. 1997; Amadei 1999; Ohnishi and Chen 1999).

3. XFEM

The name “extended finite element method” (XFEM)—a numerical technique based on the generalized finite element method (GFEM) and the partition of unity method (PUM), was coined by Northwestern School (Belytschko and Black 1999; Moës et al. 1999) in 1999. It also may be looked at as a variant of the FEM combined with some meshfree (meshless) aspects by extending the classical FEM through the enrichment of solution spaces with discontinuous functions. It is normally recognized that the development of the XFEM was an outgrowth of the extensive research in meshfree methods.

The XFEM enriches the approximation space so that it is able to naturally reproduce the challenging feature associated with the problems of, for example, the propagation of crack, the evolution of dislocation, and the evolution of phase boundary. It has been shown that such space enrichment can significantly improve the convergence rate and computation accuracy. Another advantage of the XFEM is that the computation mesh can be completely independent of the morphology of the domain concerned.

The XFEM has been implemented in the commercial code ABAQUS. It is increasingly adopted by other commercial software, with a few plug-ins and actual core implementations available (e.g. ANSYS, etc.).

4. S-FEM

The smoothed finite element method (S-FEM) is a particular class of the GFEM through carefully designed combination of the classical FEM and some of the techniques from the meshfree methods. The essential idea in the S-FEM is to use a finite element mesh (in particular triangular or tetrahedral) to construct a numerical algorithm of good performance. This is achieved by modifying the compatible strain field or by constructing a strain field with only the displacements. Such a modification/construction can be performed within elements but more often beyond the elements (i.e. meshfree concepts) to bring in the information from the adjacent elements. Naturally, the modified/constructed strain field has to satisfy certain conditions, and the standard Galerkin weak form needs to be modified accordingly to ensure the stability and convergence of solutions (Liu and Nguyen-Thoi 2010).

It has been proven that being softer than the classical FEM counterparts with identical mesh structure, the S-FEM often produces more accurate solutions with higher convergence rates and is much less sensitive to mesh distortion (Zeng and Liu 2016).

5. CEM

From the point view of practitioners, main disadvantage in the explicit simulation of a large amount of discontinuities and bolts as well as drainage holes lies in the pre-process to discretize the calculation domain. The composite element method (CEM) employs classical finite elements to cover the segments of discontinuities, bolts and draining holes embedded in the hydraulic structure. The shape functions may be of hierarchical, too, towards the p-refinement for desired computation accuracy. The sub-elements representing the segments of discontinuities, bolts and draining holes are detected and defined, and assigned with independent nodal displacements/hydraulic potentials/temperatures. Across the interfaces of these sub-elements, a jump in strain/stress or in gradient of head/temperature, is emerged naturally attributable to the independent nodal variables. These nodal variables may be solved from the governing equations similar to that of the classical FEM.

The CEM may be regarded as one of the simplified member of the GFEM in its initial work to explicitly simulate passive, fully-grouted rock bolts using simple meshes (Chen et al. 2004b, c). It possesses the potentiality to conveniently describe a large amount of discontinuities, bolts, draining holes and cooling pipes in much more detail and consequently gives more precise solution (Chen et al. 2004c, 2007b, 2008a, b, 2010b, 2011, 2012, 2015; Chen and Feng 2006; Chen and Shahrour 2008). The most remarkable feature of this method is to locate the discontinuities, bolts, drainage holes and cooling pipes, within the classical finite elements. In this manner less restraint is imposed on the mesh generation for complicated hydraulic structures.

The neglect of crack-tip performance leads to simpler algorithm and as a result, the CEM may be incorporated in the FEM software easily. However, the crack propagation phenomena cannot be handled well by the CEM at its present formulation, therefore it is suggestible to employ the CEM only for the hydraulic structures under the work situations where no widespread crack propagation is anticipatorily resulted in.

(3) The advancement in discrete element methods

In civil and hydraulic engineering, the problems with regard to the deformation and stability of rock foundations, dam abutments, underground caverns and cut slopes are truly important and difficult due to the discontinuity system traversing rock masses into blocks of various sizes, shapes and positions. Within the framework of the classical FEM, the implicit or equivalent approach is only valid in a very limited meaning whereas the explicit or distinct approach equipped by "joint elements" encounters overhead arise from huge pre-process effort and computer capacity.

The necessity to find new discontinuous models and correspondent algorithms had been aware long before by the researchers in the areas of geomechanics and geotechnical engineering. One of the pioneering works was provided by Trollope (1968) to deal with load transferring and structure deforming in a regular block system. From the 1970s to the 1990s, many researchers rushed into this area. To consider the deformation characteristics of rock masses, Cundall and his co-workers (Cundall 1971; Hart et al. 1988) established the "distinct element method" (DEM) that treats the rock block as rigid body but the discontinuity possesses deformation characteristics. In their formulation, the assumption of point to point-or edge-contact between blocks was adopted. Kawai (1978) proposed the "rigid body-spring element method" (RBSM) which takes the rock block as rigid body, too, but put some springs between blocks to describe the sliding or tensing of discontinuity planes. Chen (1984, 1987) developed a "block element method" or "block element analysis" (BEA) for deformable multi-blocky systems, with the assumption of face to face contact between blocks. Shi and his co-workers (Shi and Goodman 1985) founded the discontinuous deformation analysis (DDA) to handle the deformation and stability issues of rock masses. Use was made of the principle of energy, the assumptions of point to point-or edge-contact between blocks, and the linear interpolation of the displacement within a block, they established a set of equations to solve the deformation process of blocky rock systems.

The theoretical base of the discrete element methods is to formulate and solve the motion equations of rigid and/or deformable bodies using either implicit (based on the FEM discretization) or explicit (using the FDM/FVM discretization) approaches. Nowadays, a large family of numerical methods for simulating the motion of blocks (particles) is normally grouped in the category of the "discrete element methods" and is abbreviated as DEMs, although this term is also specially meant for the "distinct element method" proposed by Cundall.

1. DEM

The distinct element method (DEM) is the most famous one from which the family of discrete element methods was originated (Burman 1971; Cundall 1971; Chappel 1972; Byrne 1974). As one of the most rapidly developing areas of computational geomechanics (Sharma et al. 1999), it has been widely accepted as an effective method to address engineering problems in granular and discontinuous materials, especially in granular flows, powder mechanics, and rock mechanics.

The key concepts of the DEM are that the domain of interest is treated as an assemblage of rigid or deformable blocks/particles and that the contacts among them need to be identified and continuously updated during the entire deformation/motion process dominated by appropriate constitutive models (Cundall and Hart 1985, 1992; Cundall 1988; Hart et al. 1988). Intrinsically, the DEM is a force method which employs an explicit, time marching scheme to solve the equations of motion directly. Unbalanced forces drive the solution process, and damping is introduced to dissipate energy. To avert the distortion of the real vibration in dynamic problems, the amount and type of damping should be very carefully specified with the help of experiments. Nevertheless, if only a quasistatic solution is desired where the intermediate results are not of interest, the amount of damping and the type of relaxation scheme can be deliberately selected to obtain the highest solution efficiency.

The basic difference between the DEM and continuum-based methods (e.g. the FEM and CEM) is that the contact patterns between the components of a system are continuously changing with the deformation process for the former, but are fixed for the latter.

The representative explicit DEM computer codes for simulating jointed rocks are the UDEC (ITASCA Consulting Group Inc. 1992) and 3DEC (ITASCA Consulting Group Inc. 1994) for two-and three-dimensional problems, respectively.

To simulate the progressive failure mechanism, Cundall and Strack (1979) introduced a "particle flow code" (PFC) for the movement and interaction of disk-or spherical-particles using the principle of the DEM. A similar algorithm was developed by O. R. Walton et al. (Walton 1982; Heuze et al. 1990). In the PFC, discrete rigid particles bonded together to form an assemblage are capable of failure by progressive rupture of the contact bonds due to the shear and tension between these particles in terms of the friction coefficient. The failure behavior of a jointed rock can therefore be approached as either through the intact material or along the joints, or through a combination of these two mechanisms.

Well known PFC computer codes are the dynamic materials corporation (DMC) code (Taylor and Preece 1989, 1990), the PFC2D and PFC3D (ITASCA Consulting Group Inc. 1995a, b). The PFC has been widely exercised in diverse fields such as soil mechanics, non-metal material science, processing industry, and defense industry.

2. DDA

The discontinuous deformation analysis (DDA) was originally proposed by G. Shi and his co-workers (Shi and Goodman 1985; Shi 1988) where the rock blocks were postulated as "simply deformable", namely, first-order polynomials were employed for the displacement functions therefore the stresses and strains within a rock block were constant. The stress-displacement problems are solved by accounting for the interaction of independent particles (blocks) along discontinuities.

The DDA is typically formulated as a work-energy method, and can be derived by using the "principle of minimum potential energy" or by using the "Hamilton's principle" (MacLaughlin and Doolin 2006). Once the equations of motion are discretized, a step-wise time marching scheme in the Newmark family (Newmark 1965) is employed for their solution. The relation between adjacent blocks is governed by the contact interpenetration accounting for friction. The governing equation system so derived guarantees that equilibrium is held at all times. In addition, by passing the velocities of rock blocks at the end of a time marching step to the successive step, it offers dynamic solution with correct energy consumption.

Theoretically, the DDA is different from the DEM because the former is basically a displacement method using displacements as basic variables in an implicit formulation with opening-closing iterations within each time marching step to achieve the equilibrium of blocks under the constrains of contact. In addition, it does not require an artificial damping term to dissipate energy, and can easily incorporate other mechanisms for energy loss.

The DDA has been extended to a more comprehensive representation of discontinuities (Zhang and Lu 1998) and to the three-dimensional block system analysis (Shi 2001). It has been further improved for refined stress-deformation analysis using higher order elements (Ghaboussi 1988; Barbosa and Ghaboussi 1990, 1992; Shyu 1993; Chang 1994). Coupling of fluid flow across rock joints has been taken into account (Kim et al. 1999; Jing et al. 2001), too. Instead of originally penalty technique, its contact model has been improved by using the Lagrangian formalism (Lin et al. 1996; Ma et al. 1996; Hsiung 2001; Grayeli and Mortazavi 2006). A hybrid "finite-discrete element method" has been proposed to consider the fracturing and fragmentizing process of rocks (Munjiza et al. 1995, 1999; Munjiza and Andrews 2000; Munjiza 2004). To handle the non-linearity within and between blocks, a material non-linearity model using strain hardening/softening characteristics has been implemented (Ma 1999). Instead of its original formulation where a rock bolt was represented by a linear spring connecting two adjacent blocks, an advanced fully-grouted bolt/cable model with lateral (shear) constraint has been put forward (Te-Chin 1997; Moosavi and Grayeli 2006).

The engineering applications of the DDA to dams, tunnels, caverns, fragmentation processes of geological and structural materials, have been exercised since the 1990s (Lin et al. 1996; Jing 1998; Hatzor and Benary 1998; Yeung and Loeng 1997; Ohnishi and Chen 1999; Pearce et al. 2000; Hsiung and Shi 2001).

3. BEA

Attributable to its simplicity and experiences accumulated from engineering applications, the limit equilibrium method (LEM) is very useful in the stability analysis for rock foundations, abutments and cut slopes dominated by discontinuities. It has, however, certain limitations: the deformation of rocks cannot be considered; the factor of safety will be overestimated when the slip surface consists of multi-discontinuities, and postulations concerning the stress states on the slip surface have to be employed to render the problem statically determinate (Londe 1965).

In the early 1980s, to improve the LEM for the stability analysis of rock wedges in cut slopes, the deformation characteristics of discontinuities were introduced by the author of this book (Chen 1984). Later, the idea was generalized to the multi-blocky system giving rise to the "block element method" or "block element analysis" (BEA) (Chen 1987). With the assumption of face to face contact between blocks, the governing equations of the BEA were formulated by the consideration of the force and moment equilibrium condition, the deformation compatibility condition, and the elasto-viscoplastic constitutive relation on the discontinuities. In the time domain, the governing equations are implicitly and step-wisely solved to present the quasistatic/dynamic and non-linear (elasto-viscoplastic) evaluation of the whole block system. The BEA had been expanded further into the area of reinforcement and stochastic analyses (Chen 1993a, b; Chen et al. 1994). After the displacements in each block being interpolated by a set of polynomials of any order, and later by the overlap technique with classical finite elements, the BEA was able to tackle the complicated deformation pattern in rock blocks as well as on discontinuities (Chen et al. 2004a). The progress also had been achieved towards more systematical and practical algorithms, such as the unconfined seepage in discontinuity networks embedded with drainage and grouting curtain systems, the automatic identification of multi-block system for complicated domains with irregular ground surfaces, the engineering applications under complicated geological and structural conditions, the dam/foundation interaction and seismic responses, etc. (Xu et al. 2000; Chen et al. 2003, 2010a).

The BEA may be looked at as one of the simplified versions of the DDA because the assumption of infinitesimal deformation and related face-to-face contact of blocks through discontinuities where the contact updating during the block deflection/rotation process is neglected. This enables to easily handle various practical issues such as the coupling of fluid flow across rock joints, the simulation of reinforcement mechanism, the structural dynamic response under the action of seismic shakes, etc. It is also beneficial from the clear and accessible mechanical parameters which permit the experimental evaluation for a specific engineering case. It should remembered that, however, the BEA of infinitesimal deformation is mainly applicable for the routine structural analysis to solve the deformation, seepage, dynamic response, and safety margin with regard to serviceability and collapse limit states under normal and special action (load) combinations (Chen et al. 2007a).

The BEA has been recommended by the DL/T 5353-2006 «Design specification for engineering slopes in water resources and hydropower project» in China.

(4) The advancement in meshfree methods

Classical computational methods such as the FDM, BEM and FEM were originally defined on the mesh of data points (nodes). In such a mesh, each node has a fixed number of pre-defined neighborhood nodes, and its connectivity with neighborhood nodes can be employed to define mathematical operators (e.g. derivative). These operators are, in turn, used to construct the governing equations to simulate the physical or mechanical fields.

Where the material being simulated can move around (as in the computational hydrodynamics) or can deform finitely (as in the computational geomechanics), the connectivity of mesh points could be difficult to maintain without introducing error into the computation. If the mesh becomes tangled or degenerate during the simulation, the operators defined upon are no longer able to provide correct solutions. Although the domain may be re-meshed during the computation, yet this introduces additional error, since all the existing data points must be mapped onto a new set of data points.

A meshfree (or meshless, element free) method (MM) is that it does not require connection between the nodes in a domain concerned, but rather is based on the interaction of each node with all its neighborhood nodes. As a consequence, original extensive properties such as mass or kinetic energy are no more assigned to the elements but rather to the nodes. Significant advantage of the MM is therefore that it greatly simplifies the pre-process works.

As one of the earliest meshfree methods based on the Lagrangian formalism, the smoothed particle hydrodynamics (SPH) was proposed in 1977 (Gingold and Monaghan 1977; Lucy 1977). It divides the fluid into a set of discrete elements (cells) referred to as "particles" that possess a spatial distance known as the "smoothing length" over which their properties are "smoothed" by a kernel function. This means that the physical properties of any particle can be obtained by weighted averaging the relevant properties of all the particles which lie within the range of the kernel function according to their distance from the particle of interest, and their density as well. Kernel functions commonly used include the Gaussian function and the cubic spline function. Combined with an equation of state and an integrator, the SPH is able to simulate hydrodynamic flows efficiently. In 1990, L. D. Libersky and A. G. Petschek extended the SPH to solid mechanics (Libersky and Petschek 1990; Libersky et al. 1993). The main advantage of the SPH is its flexibility with regard to local distortion because the mesh dependence is naturally avoided. The main drawbacks of the SPH are inaccurate results near boundaries and tension instability (Swegle et al. 1995). Over the past years, different corrections have been introduced to improve the accuracy and tension stability of the SPH solutions.

Over the ensuing decades, much more MM algorithms have been emerged (Belytchko et al. 1996; Belytschko and Chen 2007), in which the trial functions are

no longer standard, but instead are generated from neighborhood nodes in a domain of influence by different approximations, such as the least squares technique. Although it has not outperformed the FEM in the routine structural problems, yet the MM exhibits great expectation due to its flexibility in the treatment of discontinuities and fracture growth in rock-like materials (Belytschko et al. 2000; Zhang et al. 2000; Li et al. 2001).

One recent advance in the MM is aimed at the computational tool for automated modeling and simulation. This is realized by the so-called weakened weak (W2) formulation based on the G space theory (Liu 2010) which offers possibilities to establish various models that work well with triangular meshes generated automatically and re-meshed easily. One typical W2 formulation is the smoothed point interpolation method (S-PIM) (Liu 2009).

(5) The advancement in computation intelligent methods

A significant event manifesting in this period is that the computational intelligence (CI) became a formal study area in computer science in the early 1990s (Attewell and Woodman 1982; Zadeh 1994). "Computational intelligence" (CI), also referred to as "soft computing" (SC), is normally looked at as a sub-branch of "bio-inspired computing" (BC) that relies heavily on the fields of biology, computer science and mathematics. The BC is, in turn, a branch of the "artificial intelligence" (AI) that was founded as an academic discipline in 1956 and has become an essential part of the technology industry. A significant milestone in the development of AI was erected in the 2017, when the AlphaGo won a three-game match with J. Ke, who at the time held the world No. 1 ranking.

The areas of CI study encompass a variety of machine learning inclusive artificial neural networks (ANN) and support vector machines (SVM); fuzzy logic (FL); evolutionary computation (EC) inclusive evolutionary algorithms (EA) and genetic algorithms (GA), swarm intelligence (SI) and ant colony optimization (ACO) and particle swarm optimization (PSO); and Bayesian network (BN), etc. The way in which CI differs from the traditional computational methods lies in its more evolutionary approach to learning, as opposed to what could be described by "rigorous PDEs".

Since the early 1990s, the computational intelligence, particularly the genetic algorithms (GA) and the artificial neural networks (ANN), have been provides as a broad way to address almost every challenging problem in geotechnical engineering (Neaupane and Adhikari 2006).

1. GA

Belonging to a larger class of evolutionary computation (EC), the genetic algorithm (GA) undertakes stochastic search that emulates biological evolution processes of natural selection. As one of the best-known heuristic search algorithms, the primary reason behind the use of GA lies in its ability to generate high-quality solutions for optimization and search problems attributable to bio-inspired operators such as mutation, crossover and selection (Gen and Cheng 1997).

The GA is well performed in solving large combinational design problems. For example, Simpson and Priest (1993) demonstrated the application of the GA for identifying the maximum discontinuity frequency in a complex rock structure for different problem sizes. S. Pal et al. (Pal et al. 1996; Javadi et al. 1999; Macari et al. 2005) employed the GA to identify optimal material parameters in constitutive models, and suggested that the use of the GA may overcome the difficulties arise from a large number of material parameters. Goh (1999) incorporated the GA to search for the critical slip surface in multi-wedge stability problems.

2. ANN

The artificial neural network (ANN) is a widely exercised computation intelligent algorithm for solving nonlinear complex problems. Unlike standard computational methods based on PDEs, it uses a parallel approach which is analogous to the functioning of the human brain. Its advanced version, the back-propagation neural network (BP-NN), is based on a supervised training technique that computes the difference between ANN-calculated output and corresponding desired output from the training dataset. The error is propagated backward through the net and the weights are adjusted during a number of iterations, named epochs. The training ceases when the calculated output values best approximate the desired values (Rumelhart et al. 1986).

Since the early 1990s, the ANN has been increasingly exercised as an effective tool in handling nonlinear relationship between parameters and variables for geotechnical and hydraulic engineering, both at the levels of prototype structure scale and test sample scale.

With respect of the prototype structure level, numerous literatures reveal that ANNs may be extensively used in the areas of geotechnical and hydraulic engineering such as the TBM performance (Ding et al. 2013), ground surface settlement due to tunneling (Kim et al. 2001), tunnel rock mass displacement (Yoo and Kim 2007), probable failure modes in underground cavern (Lee and Sterling 1992), tunnel support stability (Leu et al. 2001), dam displacement and settlement (Kim and Kim 2008; Joghataie and Dizaji 2011; Mata 2011), slope stability (Ni et al. 1996; Neaupane and Achet 2004; Ferentinou and Sakellariou 2007; Cho 2009).

The study at the test sample level is mostly focused on the constitutive relations of geomaterials (Adeli 2001), i.e. the neural network constitutive model (NNCM). For most constitutive models of geomaterials based on the classical elasticity and plasticity theories, the lack of physical understanding is customarily supplemented by either simplifying the problem or incorporating assumptions into the models, which would lead to the risk of complex formulation, exaggerative idealization, and excessive empirical parameters. The NNCM based on the data alone and trained on input-output data pairs to determine the structure and parameters of the model, does demand no simplifications/assumptions. In addition, the NNCM can be further updated, if new training examples as new data pairs become available.

Ghaboussi and Sidatra (1997) first developed a constitutive model for geotechnical materials by the ANN. They showed that the NNCM can be very

efficient in learning and generalizing the constitutive behavior of complex geomaterials and give better results. Under the encouragement of their pioneering work, many researchers proposed more advanced solutions as reliable and practical alternatives to modeling the failure criteria (Rafiai and Jafari 2011) and the constitutive behavior of geomaterials (Ellis et al. 1995; Goh 1995; Zhu et al. 1998; Basheer 2002; Habibagahi and Bamdad 2003; Fu et al. 2007).

Despite its good performance in many situations, the ANN suffers from drawbacks due to the lack of a robust theory by which the success in finding a good solution is always guaranteed. In addition to develop guidelines in the design process of the ANN and to give a comprehensive explanation of how it arrives at a prediction, a hybrid with classical computational methods such as the FEM, can make the relevant predictions for routine structure design with a competent accuracy and confidence.

(6) The advancement in hybrid methods

To handle the multi-phase or multi-scale (level) computations, the combination of the Lagrangian formalism and the Eulerian formalism gives rise to hybrid computational methods. In recent years, the combination of classical CM with modern CI unfolds a great expectation to provide much more powerful computation tools towards the challenges of future super projects.

1. Classical hybrid techniques

Hybrid methods are frequently desirable in geotechnical and hydraulic engineering, particularly when encountered with rock-like materials. There are various classical hybrid techniques dependent on the specific problem to be handled, of which the most useful and prevalent ones are the hybrid BEM/FEM, DEM/FEM, and DEM/BEM. The BEM is normally used for simulating far-field materials as equivalent elastic continua, whereas the FEM and DEM are intended to the non-linear and discontinuous rock-like materials at the vicinity fields where explicit representations for discontinuities and/or nonlinear behaviors are demanded.

The hybrid BEM/FEM was first proposed by O. C. Zienkiewicz and his co-workers (Zienkiewicz et al. 1977) then followed by B. H. G. Brady et al. (Brady and Wassyng 1981; Beer 1983; Elsworth 1986a, b) towards strain/stress and permeability analyses. It is customarily employed for simulating underground structures (Gioda and Carini 1985; Ohkami et al. 1985; Varadarajan et al. 1985; Swoboda et al. 1987; Von Estorff and Firuziaan 2000).

A hybrid FEM/DEM was described by Pan and Reed (1991), in which the FEM region exhibits nonlinear deformation and the DEM region consists of rigid blocks.

The hybrid DEM/BEM was implemented in the code group of UDEC and 3DEC (Lorig and Brady 1982; Lorig 1984; Lorig et al. 1986; Lemos 1987) for strain/stress analysis. Similar but different codes were developed and applied to various problems, such as rigid block motion (Hocking 1977; Taylor 1982), plate bending (Mustoe et al. 1987), and the RBSM (Kawai 1978; Kikuchi et al. 1992; Hu 1997; Li and Wang 1998). The hybrid DEM/BEM was used for coupled hydro-mechanical

analysis of jointed rock with the help of discrete fracture network (DFN) (Wei and Hudson 1988; Wei 1992).

The hybrid FEM/BEA and BEA/TLM were firstly proposed by the author and co-workers (Wang et al. 2001b; Chen et al. 2003) for the purpose to assess the arch dam strength and abutment stability simultaneously. Much earlier, a hybrid Beam/BEM was reported to simulate the support of underground openings (Pöttler and Swoboda 1986).

At present, the most well known computer code for the stress analysis in geotechnical and hydraulic engineering using the hybrid PFC/FDM is perhaps the FLAC3D (ITASCA Consulting Group Inc. 1993, 2002).

The hybrid DDA/SPH (Wang et al. 2016), CFD/DEM (Shan and Zhao 2014), and DEM/SPH (Wu et al. 2016; Tan and Chen 2017) also have been established towards the two-phase phenomena such as the fluid-structure interaction with free-surface flow and structural failure, the landslide movement and generated surge waves (tsunamis), etc.

Each of the aforementioned classical hybrid methods possesses inherited advantages, subject to special attention called to the continuity or compatibility conditions at the interfaces between regions with different methods.

2. Modern hybrid techniques

In the literatures with regard to the study on the hybrid of classical computational methods (CM) and modern computational intelligence (CA), two classes may be roughly distinguished, depending on the hybrid structure whether a CM is embedded in the CI (hybrid CI/CM) or a CI is embedded in the CM (hybrid CM/CA).

The "intelligent finite element method" (IFEM) is a good example of hybrid CM/CA which was proposed by AA Javadi and his co-workers through the incorporation of a NNCM in the finite element analysis (Javadi et al. 2003, 2009). In their work, they used test results to extract stress-strain relationship representing the mechanical responses of the geomaterial to applied loads through the training of a NNCM based on the BP-NN. The trained NNCM is then incorporated in the finite element analysis as a substitutive to classical constitutive relation.

McCombie and Wilkinson (2002) presented a good example of hybrid CA/CM, by a simple GA to seek the minimum safety factor in slope stability analysis based on the Bishop's simplified method, and showed that the GA can perform better than some traditional optimization methods such as the Monte-Carlo approach. Zolfaghari and his co-workers (2005) employed the GA to search for the critical non-circular failure surface in slope stability analysis based on the Morgenstern-Price method for a variety of slope geometries and loading conditions. Cui and Sheng (2005) also showed how a hybrid GA/FEM can be formulated towards the probability of structure failure. Similarly, the researches of the hybrid ANN/LEM and ANN/FEM for hydraulic structures may be found in literatures (Yi et al. 2004; Al-Suhaili et al. 2014), the latter is particularly prevalent today for the parametric back or inverse analysis (Sbarufatti et al. 2011; Zhou et al. 2015) and will be elaborated in Chap. 7.

1.5 Concluding Remarks on the Computational Geomechanics for Hydraulic Structures

Over the past decades, achievements in the application of computational geomechanics (CG), a sub-branch of computational mechanics (CM), for hydraulic structures, are impressive, especially on the aspects of continuum/discontinuum approaches related to discontinuities (faults, fractures, joints and interfaces), finite deformation related to dislocation, multi- phase/level computation related to micro-or/and meso-structure, etc. It is notable that the revolution in designing and building hydraulic structures was set, at least partially, in motion with the advancement of the CG. Today, hydraulic engineers are used to find answers to their problems with the help of computers.

In recent years nevertheless, the author of this book starts to feel a bit of worry over a somewhat Pollyanna atmosphere, particularly in the young students and engineers, that finer computations always lead to better designed performances of the structures. Sometimes, they show exaggerated passion to choose or to create an "universal method" which would "crown" all the existing methods. This situation is mainly blamed for that they, as beginners, tend to imagine but actually misunderstand, that scientists create formulas/equations and algorithms, and then, by inputting data into the corresponding software, computers turned out the desirable responses to the real world problems. In most cases what happens instead is that, although a fine algorithm may provide "precise" answers, yet they are only the answers to the imagined object probably far from the target we are looking forward to, as we used to make fun of our students that "rubbish in, rubbish out; finer rubbish in, finer rubbish out".

Taking the Chinese engineering practices for example, the primary analysis tools recommended in the design specifications/codes for dams, dam foundation/abutments, and cut slopes, are the classical LEM for stability calibration and the classical structural mechanics such as the gravity method (GM) and trial-load method (TLM) for strength calibration. The FEM is commonly ranked at the second position to handle special issues such as the local failure, the cracking risk, the interaction of complex foundation/dam body, etc., for "high dams or cut slopes". If we trace back the history of these classical methods of 100-plus years old and a number of prevalent modern computational methods since the 1970s, it will become clear that their most important and intrinsic talents are the intuitively formulated conceptualization of the problem in terms of mechanisms, material properties and parameters, execution processes, and other environmental perturbations. More important, after the building of their mathematical presentations, the permissible (allowable) factor of safety (reliability) might be matched convincingly via a wide range and extensive engineering exercises, through which the dominant factors with regard to the associated computation uncertainties arise from algorithm assumptions, geological exploration, laboratory and field tests, parametric evaluation, work situations stipulated (normal, check), project importance related to economy investment and society risk, are fully taken into account (Chen 2015).

The road ahead us is still long on which many obstacles exist before the CG may play leading role in the design of hydraulic structures. The author is convinced that this might be achieved only if we—researchers and practitioners, go forward "vis-à-vis" following the correct roadmap. For the researchers, they should avert to leave engineering practices, namely to avoid the risk of leaving their feet from the ground like Samson; whereas for the practitioners, it is advisable to keep an open mind for new advancements in computational methods and technologies. In what follows the author would like to put forward several comments and suggestions on the healthy development and successful application of CG in hydraulic structures, as the concluding remarks of this introductory chapter and the commencement of the main coverage chapters of this book.

1.5.1 Understand of Engineering Problems

There are various structure types in a hydraulic project (Chen 2015), each of them possesses unique features and corresponding concerns arise from the environmental settings, design processes and construction activities. We are neither able to fantasize an "all encompassing" model nor to find universal method for all major problems in hydraulic structures.

The safety is extremely respected by designers in hydraulic engineering. On the other hand, contractors and private owners prefer economical design with minimum labor effort and construction cost. Subsequently, implementation of robust optimization techniques which establish a trade-off between safety and total cost of projects is demanded in practice.

A successful and helpful computation is actually rely on the team work leading by those who are the experts of both hydraulic structure and modern computation, in addition to comprehensive knowledge and practice training in the fields of engineering geology, material science, construction or/and operation management, and even society or human sciences. Only in this manner, we may feel sufficient confidence to provide our computation results meeting the following requirements that:

- The geological and hydrogeological settings, such as in situ geo-stresses, seismic activities, rock strata and structures, are simulated as realistic as possible;
- The materials (soils, rocks, concrete) used in the structure and their properties, are studied in detail, permitted by the time and budget;
- The numerical representation of construction and operation processes, such as the sequences of foundation excavation and concrete placement, foundation treatment (grouting, draining and reinforcing), are appropriately simplified and simulated;
- The major concern over special difficulties encountered, their origins, consequences, possible solutions or remedial measures, are deliberated;

– The concerns and performances of the owner, design, contractor, even government agency, etc., might be more or less different in weighing the pros and cons with respect to the issues of reliability, convenience, economy, and society benefits/impacts, is fully realized.

1.5.2 Selection of Computational Methods

Today, we are happy but sometimes puzzled to have a large family of computational methods at hand.

In addition to classical methods (e.g. the LEM, the gravity method, the trial load method), the most prevalent computational methods commonly applied in hydraulic structures fall into continuum approaches (FDM, FEM, BEM, CEM), discomtinuum approaches (DEM, DDA, RBSM, BEA), and hybrid approaches. Since every computation method possesses its own merits and drawbacks and there is no one absolutely advantageous over the others, therefore it is an open question with respect to whether the discretization scheme (algorithm) of PDFs ranging from infinitesimal linear and continuous deformation (e.g. the FEM of elasticity) to finite nonlinear and discontinuous deformation (e.g. the DEM of block cluster), has been appropriately selected. The most relevant answer is dependent on the wisdom and cumulated experiences of the practitioners.

Based on the mainstream opinions of the experts in the areas of CG and the understanding of the author from the career practices in hydraulic structures, the first consideration in selecting one or more computational methods for a specific problem is the purpose of the computation task that:

– If the concern is only-or firstly focused on the stability against well defined failure modes (e.g. discontinuity-controlled planar or wedge slides, circular or nearly circular surface failure in “homogeneous” geomaterials), the LEM can normally give convincible and reliable judgment. The major advantages with the LEM are the simplicity in computation algorithm, full of experiences in the evaluation of parameters and in the selection of allowable safety factors.
– Classical computational methods such as the FEM is advisable towards further and more precise computations for the spatial-time distribution with regard to deformation/stress, hydraulic potential, and temperature, under various environmental actions following dynamic construction and operation agenda/schedule. They are also able to validate or give enlightenment relating the failure modes postulated in the LEM. If the analysis is intended for the jointed rock masses under normal or check (extreme) action (load) combinations, the BEA is a good computation tool attributable to its postulations of infinitesimal deformation and non-dislocation, which enable it to handle a large amount of discontinuities meanwhile to keep a consistent basis of the LEM and FEM with regard to the constitutive relations, mechanical parameters, and allowable safety factors (Chen et al. 2007a).

– The much more modern methods such as the DEM, DDA and SPH featured by discontinuous and finite deformation, have to be attempted when we are encountered with post-failure processes such as dam break, landslide, and their generated flood/surge waves. Under such circumstances, the constitutive relations and mechanical parameters, are certainly not identical to the situation when the integrity of the structure is maintained within the serviceability and collapse limit states. This issue is however, not well cared and addressed insofar within the knowledge scope of the author.
– Conceptual material models often indicate the availability of methods. Taking the FEM for example, it will be sophisticatedly exercised if only a few of large scale discontinuities (e.g. faults) are handled. It may also be successfully applied where the group joint sets exist, and they are sufficiently dense to guarantee the existence of small REV (RVE) compared to the characteristic dimension of the hydraulic structure. The latter case allows for the equivalent continuum constitutive relation by taking into account the influence of joints in mechanical parameters solely. At present, the CEM is very suitable for moderately jointed/fractured rock-like materials where the joint amount is rather large leading to difficulties in explicit discretization but not sufficiently large to guarantee the existence of the smaller REV.
– Where we are in the dilemma between more precise and higher ability methods, it is suggestible to try hybrid ones. Diverse exercise using representative methods is encouraged towards the overall understand of the problems.

1.5.3 Standardization of Computation Software

It has been bewildering for a long time that for a definite computation method towards a specific structure problem, significant difference may manifest originated from every task aspects in the whole computation procedure. For example, the element density or size of a FE mesh will influence the hydraulic potential and stress at the vicinity of a singularity. Such problem may partially overcome, from the point view of practitioners, through the standardization of computation algorithm instead of the accuracy.

Again, taking the FEM for example, the h-or p-version of refinement (adaptive technique) is suggestible to uniformly control the discretization precision of mesh, subject to the stipulation in the design specifications/codes of discrete error tolerances after a systematic “code calibration” analyses for various typical existing hydraulic structures. Some techniques of stress equivalence or singularity smear, such as the equivalent arch dam stresses at toe and heel (SL282-2003; DL/T5346-2006), may be further implemented to help the FEM become standard design tool competent to or even outperforming the classical trial-load method.

1.5.4 Evaluation of Material Models and Corresponding Parameters

It has been widely accepted that after the selection of computational methods for a specific hydraulic structure, the constitutive relation and corresponding input parameters should reflect the basic material properties while neglect the secondary and minor factors, and allow for the experimental validation. The evaluation of geological settings and engineering uncertainties, the homogenization and representation of material properties as equivalent continua and the existence of REV, etc., are routinely carried out. The back (inverse) analysis is always encouraged to tune the parameters or even further the constitutive relations.

Taking the FEM, BEA and CEM elaborated in this book for example, if we hope that they perform well as competent counterparts of classical design methods, the Mohr-Coulomb strength criterion or the mostly similar others are desirable. The strength parameters should be clearly specified as yield, peak and residual correspondent to the action combinations (normal, check) stipulated in the design specifications/codes.

In the dynamic and post-failure processes with large movement and certain block separate-crash due to the dam break and landslide, the strength and deformation parameters should be strongly dependent on the moving speed and lubricating effects of water (if exist). This issue has however, not sufficiently attracted attention and been well explored insofar.

1.5.5 Safety Calibration of Hydraulic Structures

Safety factors or factors of safety (FOS) obtained by modern computational methods will normally perform as auxiliary indices in addition to that by classical design methods, which will be helpful for engineers to make more convincible judgment concerning the structural safety. However, it should bear in the mind that in doing so, the action (load) combinations (normal or check) and the corresponding strength parameters (yield, peak, residual), as well as the allowable safety factor $[K]$ directly related to the risk and cost, are well defined or stipulated.

The allowable (permissible, design) safety factor should be stipulated on the considerations concerning the project class, the structure type and grade, the service life, the computation method, the definition of FOS, and even the state economy development level (Chen 2015).

Taking the rock slopes on reservoir banks far away from the hydraulic structures and communities/villages for instance, the creep movement of the slope or/and the local failure in the slope will be admitted during the service life of the reservoir, therefore a design with the FOS in its lower bound may be stipulated. In Chinese design specifications (SL386-2007; DL/T 5353-2006), the allowable safety factor $[K]$ for such slopes is ranged between 1.0 and 1.3 corresponding to the residual

strength parameters, dependent on the slope importance (grade and type), work situations (permanent, temporary, accidental), and the other indeterminate factors which cannot be taken into account in the computation solely (e.g. the quality and reliability of blasting and stabilizing operations in the construction, the difficulties with remedial treatment in case of unexpected accidents manifesting during the service, the experiences of designer particularly in case of lack of sufficient geologic exploration and experiment).

On the contrary, for the rock slopes at the vicinity of or above/under important hydraulic structures (e.g. dam abutments and foundation), a FOS approaching its upper bound is hence desirable in the design. In Chinese design specifications (SDL5108-1999; SL319-2005; SL282-2003; DL/T5346-2006), for dam foundation or abutment slopes the allowable safety factor $[K]$ is ranged between 2.3 and 3.5 correspondent to peak strength parameters, dependent on the dam importance (grade and type) and work situations.

1.5.6 Work Style of Scientists and Artists

Computational geomechanics, although on one hand has been widely recognized as a sub-branch of computing science, yet on the other hand it is similar to the art. Since there are unlimited variants and no "exact" solution, the layout and implementation of a computation task for a hydraulic structure is basically a creative activity relying on the engineer's talent. In other words, a successful computation for the hydraulic structure demands drawing on both the "left and right sides" of our brains.

We are supposed to possess a predictive capability that can only be attained after the key features of the reality have been well captured. At least the same important is the ability to compromise the drawbacks and to assimilate the merits of selective methods. This is why many Chinese design specifications/codes (dams, cut slopes, etc.) stipulate that for the important or complex hydraulic structure, at least two methods should be used in parallel.

Very often, the candidate computation methods are not necessarily to be high level in terms of mathematics and mechanics. As we will show in the hereinafter chapters, if we understand and handle the problem properly with the help of engineering experiences, a pertinent computation is able to provide quite satisfactory results. In this context, we, possessing divinity of creation and aesthetics, should be free of the worry that in the near future we will be replaced by "smart/intelligent" computation robots equipped by the "universal" computational algorithm.

References

Aaboe A. The culture of Babylonia: Babylonian mathematics, astrology, and astronomy. In: Boardman J, Edwards IES, Hammond NGL, Sollberger E, Walker CBF, editors. The Assyrian and Babylonian empires and other states of the near east, from the eighth to the sixth centuries BC. 2nd ed. Cambridge: Cambridge University Press; 2008. p. 276–92.

Adeli H. Neural networks in civil engineering: 1989–2000. Comput Aided Civ Infrastruct Eng. 2001;16(2):126–42.

Al-Suhaili RHS, Ali AAM, Behaya SAK. Artificial neural network modeling for dynamic analysis of a dam-reservoir-foundation system. Int J Eng Res Appl. 2014;4(1):121–43.

Amadei B, editor. Proceedings of the third international conferences on analysis of discontinuous deformation—from theory to practice (ICADD-III). Vail, Colorado: American Rock Mechanics Association; 1999.

Anandarajah A. Computational methods in elasticity and plasticity: solids and porous media. New York: Springer; 2010.

Anderson JD Jr. Computational fluid dynamics—the basics with applications. New York: McGraw-Hill; 1995.

Andersson J, Dverstop B. Conditional simulations of fluid flow in three-dimensional networks of discrete fractures. Water Resour Res. 1987;23(10):1876–86.

Ardito R, Maier G, Massaiongo G. Diagnostic analysis of concrete dams based on seasonal hydrostatic loading. Eng Struct. 2008;30(11):3176–85.

Argyris JH. Recent advances of matrix methods of structural analysis in aeronautical science, vol. 4. London: Pergamon Press; 1963.

Attewell PB, Woodman JP. Predicting the dynamics of ground settlement and its derivatives caused by tunneling in soil. Ground Eng. 1982;15(8):9–36.

Babuška I, Rheinboldt WC. A-posteriori error estimates for the finite element method. Int J Numer Methods Eng. 1978;12(10):1597–615.

Babuška I, Szabó BA. On the rates of convergence of the finite element method. Int J Numer Methods Eng. 1982;18(3):323–41.

Babuška I, Szabó BA, Katz IN. The p-version of the finite element method. SIAM J Numer Anal. 1981;18(3):515–45.

Barbosa R, Ghaboussi J. Discrete finite element method for multiple deformable bodies. Finite Elem Anal Des. 1990;7(2):145–58.

Barbosa R, Ghaboussi J. Discrete finite element method. Eng Computations. 1992;9(2):253–66.

Barenblatt GI, Zheltov LP, Kochina IN. Basic concepts in the theory of seepage of homogenous liquids in fissured rocks. J Appl Math Mech. 1960;24(5):1286–303.

Basheer IA. Stress-strain behavior of geomaterials in loading reversal simulated by time-delay neural networks. J Mater Civ Eng. 2002;14(3):270–3.

Bear J, Tsang CF, de Marsily G. Flow and contaminant transport in fractured rock. San Diego: Academic Press; 1993.

Beer G. Finite element, boundary element and coupled analysis of unbounded problems in elastostatics. Int J Numer Methods Eng. 1983;19(4):567–80.

Beer G, Pousen A. Efficient numerical modelling of faulted rock using the boundary element method. Int J Rock Mech Min Sci. 1995a;32(3):117A.

Beer G, Pousen A. Rock joints-BEM computations. In: Sevaldurai APS, Boulon MJ, editors. Mechanics of geomaterial interfaces. Amsterdam: Elsevier Science Publisher; 1995b. p. 343–73.

Beer G, Watson JO. Introduction to finite boundary element method for engineers. New York: Wiley; 1992.

Bell JM. General slope stability analysis. J Soil Mech Found Div ASCE. 1968;94(SM6):1253–70.

Belytschko T, Black T. Elastic crack growth in finite elements with minimal re-meshing. Int J Numer Methods Eng. 1999;45(5):601–20.

Belytschko T, Chen JS. Meshfree and particle methods. Hoboken: Wiley; 2007.

Belytschko T, Gracie R, Ventura G. A review of extended/generalized finite element methods for material modeling. Model Simul Mater Sci Eng. 2009;17(4) (featured article).

Belytschko T, Krongauz Y, Organ D, Fleming M, Krysl P. Meshless methods: an overview and recent developments. Comput Methods Appl Mech Eng. 1996;139(1–4):3–47.

Belytschko T, Organ D, Gerlach C. Element-free Galerkin methods for dynamic fracture in concrete. Comput Methods Appl Mech Eng. 2000;187(3–4):385–99.

Belytschko T, Moës N, Usui S, Parimi C. Arbitrary discontinuities in finite elements. Int J Numer Methods Eng. 2001;50(4):993–1013.

Birgisson B, Crouch SL. Elastodynamic boundary element method for piecewise homogeneous media. Int J Numer Methods Eng. 1998;42(6):1045–69.

Blacker TD, Stephenson MS. Paving: a new approach to automated quadrilateral mesh generation. Int J Numer Methods Eng. 1991;32(4):811–47.

Bobet A, Fakhimi A, Johnson S, Morris J, Tonon F, Ronald Yeung M. Numerical models in discontinuous media: review of advances for rock mechanics applications. J Geotech Geoenviron Eng ASCE. 2009;135(11):1547–61.

Blacker TD, Stephenson MB, Mitchiner JL, Phillips LR, Lin YT. Automated quadrilateral mesh generation: a knowledge system approach. ASME paper, 88-WA/CIE-4; 1988.

Bonnet M, Maier G, Polizzotto C. Symmetric Galerkin boundary element methods. Appl Mech Rev. 1998;51(11):669–704.

Boyer CB. A history of mathematics. 2nd ed. New York: Wiley; 1991.

Boyle WJ, Vogt TJ. Rock block analysis at Mount Rushmore National Memorial. In: Myer LR, Cook NGW, Goodman RE, Tsang CF, editors. Fractured and jointed rock masses. Rotterdam: AA Balkema; 1995. p. 717–23.

Brady BHG, Bray JW. The boundary element method for determining stress and displacements around long openings in a triaxial stress field. Int J Rock Mech Min Sci Geomech Abstr. 1978;15(1):21–8.

Brady BHG, Wassyng A. A coupled finite element-boundary element method of stress analysis. Int J Rock Mech Min Sci Geomech Abstr. 1981;18(6):475–85.

Brebbia CA, editor. Topics in boundary element research. Vol. 4: Applications in geomechanics. Berlin: Springer; 1987.

Brebbia CA, Telles JCF, Wrobel LC. Boundary element techniques: theory & applications in engineering. Berlin: Springer; 1984.

Buczkowski R, Kleiber M. Elasto-plastic interface model for 3D-frictional orthotropic contact problems. Int J Numer Methods Eng. 1997;40(4):599–619.

Burman BC. A numerical approach to the mechanics of discontinua. Ph.D. thesis. Australia: James Cook University of North Queensland; 1971.

Byrne RJ. Physical and numerical model in rock and soil-slope stability. Ph.D. thesis. Australia: James Cook University of North Queensland; 1974.

Cacas MC, Ledoux B, de Marsily G, Tillie B, Barbreau A, Durand E, Feuga B, Peaudecerf P. Modeling fracture flow with a stochastic discrete fracture network: calibration and validation, 1. The flow model. Water Resour Res. 1990;26(3):479–89.

Cao XH, Chen SF, Chen SH. Generation of tetrahedral meshes in 3-D domains by advancing front method. Eng J Wuhan Univ. 1998;31(1):16–20 (in Chinese).

Capecchi D. History of virtual work laws—a history of mechanics prospective. Milan: Springer; 2012.

Cerrolaza M, Garcia R. Boundary elements and damage mechanics to analyze excavations in rock mass. Eng Anal Bound Elem. 1997;20(1):1–16.

Chan HC, Einstein HH. Approach to complete limit equilibrium analysis for rock wedges—the method of "artificial supports". Rock Mech. 1981;14(2):59–86.

Chan SK, Tuba IS, Wilson WK. On the finite element method in linear fracture mechanics. Eng Fract Mech. 1970;2(1):1–17.

Chang QT. Nonlinear dynamic discontinuous deformation analysis with finite element meshed block systems. Ph.D. thesis. Berkeley: University of California; 1994.

Chappel BA. The mechanics of blocky material. Ph.D. thesis. Canberra: Australia National University; 1972.
Chen SH. The stability of a rock wedge in the slope. M.Sc. thesis. Wuhan: WUHEE; 1984 (in Chinese).
Chen SH. The elasto-plastic and elasto-viscoplastic analysis of the discontinuous rock masses. Ph. D. thesis. Wuhan: WUHEE; 1987 (in Chinese).
Chen SH. Numerical analysis and model test of rock wedge in slope. In: Pasamehmetoglu AG, et al., editors. Proceedings of the international symposium on assessment and prevention of failure phenomena in rock engineering. Rotterdam: AA Balkema; 1993a. p. 425–9.
Chen SH. Analysis of reinforced rock foundation using elastic-viscoplastic block theory. In: Ribeiro e Sousa L, Grossmann NF, editors. ISRM international symposium-EUROCK 93. Rotterdam: AA Balkema; 1993b. p. 45–51.
Chen SH. Hydraulic structures. Berlin: Springer; 2015.
Chen SH, Egger P. Elasto-viscoplastic distinct modeling of bolt in jointed rock masses. In: Yuan JX, editor. Proceedings of computer method and advances in geomechanics, vol. 3. Rotterdam: AA Balkema; 1997. p. 1985–90.
Chen SH, Egger P. Three dimensional elasto-viscoplastic finite element analysis of reinforced rock masses and its application. Int J Numer Anal Methods Geomech. 1999;23(1):61–78.
Chen SH, Feng XM. Composite element model for rock mass seepage flow. J Hydrodyn (Ser. B). 2006;18(2):219–24.
Chen SH, Shahrour I. Composite element method for the bolted discontinuous rock masses and its application. Int J Rock Mech Min Sci. 2008;45(3):384–96.
Chen SH, Shen BK, Huang MH. Stochastic elastic-viscoplastic analysis for discontinuous rock masses. Int J Numer Methods Eng. 1994;37(14):2429–44.
Chen SH, Wang JS, Zhang JL. Adaptive elasto-viscoplastic FEM analysis for hydraufic structures. J Hydraulic Eng. 1996;27(2):68–75 (in Chinese).
Chen G, Ohnishi Y, Ito T. Development of high-order manifold method. Int J Numer Methods Eng. 1998;43(4):685–712.
Chen SH, Chen SF, Cao XH. Three dimensional hexahedron mesh generation for rock engineering. In: Yafin SA, editor. Proceedings of the 3rd international conference on advance of computer methods in geotechnology and geoenvironment engineering. Moscow: AA Balkema; 2000. p. 203–6.
Chen SH, Xu MY, Shahrour I, Egger P. Analysis of arch dams using coupled trial load and block element methods. J Geotech Geoenviron Eng ASCE. 2003;129(11):977–86.
Chen SH, Li YM, Wang WM, Shahrour I. Analysis of gravity dam on a complicated rock foundation using an adaptive block element method. J Geotech Geoenviron Eng ASCE. 2004a;130(7):759–63.
Chen SH, Qiang S, Chen SF, Egger P. Composite element model of the fully grouted rock bolt. Rock Mech Rock Eng. 2004b;37(3):193–212.
Chen SH, Xu Q, Hu J. Composite element method for seepage analysis of geo-technical structures with drainage hole array. J Hydrodyn (Ser. B). 2004c; 16(3):260–6.
Chen SH, Qin WX, Shahrour I. Comparative study of sock slope stability analysis methods for hydropower projects. Mech Res Commun. 2007a;34(1):63–8.
Chen SH, Qin WX, Xu Q. Composite element method and application of trace simulation for strain localization bands. Chin J Rock Mechan Eng. 2007b;26(6):1116–22 (in Chinese).
Chen SH, Feng XM, Shahrour I. Numerical estimation of REV and permeability tensor for fractured rock masses by composite element method. Int J Numer Anal Methods Geomech. 2008a;32(12):1459–77.
Chen SH, Qiang S, Shahrour I, Egger P. Composite element analysis of gravity dam on a complicated rock foundation. Int J Geomech ASCE. 2008b;8(5):275–84.
Chen SH, Wang WM, Zheng HF, Shahrour I. Block element method for the seismic stability of rock slopes. Int J Geotech Geoenviron Eng ASCE. 2010a;136(12):1610–7.

Chen SH, Xue LL, Xu GS, Shahrour I. Composite element method for the seepage analysis of rock masses containing fractures and drainage holes. Int J Rock Mech Min Sci. 2010b;47(5):762–70.

Chen SH, Su PF, Shahrour I. Composite element algorithm for the thermal analysis of mass concrete: simulation of lift joint. Finite Elem Anal Des. 2011;47(5):536–42.

Chen SH, He J, Shahrour I. Estimation of elastic compliance matrix for fractured rock masses by composite element method. Int J Rock Mech Min Sci. 2012;49(1):156–64.

Chen SH, Zhang X, Shahrour I. Composite element model for the bonded anchorage head of stranded wire cable in tension. Int J Numer Anal Methods Geomech. 2015;39(12):1352–68.

Chern JC, Wang MT. Computing 3-D key blocks delimited by joint traces on tunnel surfaces. Int J Rock Mech Min Sci Geomech Abstr. 1993;30(7):1599–604.

Cho SE. Probabilistic stability analyses of slopes using the ANN-based response surface. Comput Geotech. 2009;36(5):787–97.

Clough RW, Penzien J. Dynamics of structures. 3rd ed. Berkeley: Computers & Structures Inc.; 2003.

Cook RD, Malkus DS, Plesha ME. Concepts and applications of finite element analysis. 3rd ed. New York: Wiley; 1989.

Courant R. Variational methods for the solution of problems of equilibrium and vibrations. Bull Amer Math Soc. 1943;49(1):1–23.

Crisfield MA. Non-linear finite analysis of solids and structures. New York: Wiley; 1997.

Crouch SL, Fairhurst C. Analysis of rock deformations due to excavation. In: Sikarskie DL, editor. Proceedings of the ASME symposium on rock mechanics, vol. 3. New York: ASME; 1973. p. 25–40.

Crouch SL, Starfield AM. Boundary element methods in solid mechanics. London: George Allen & Unwin; 1983.

Cruse TA, Rizzo FJ. A direct formulation and numerical solution of the general transient elastodynamic problem. Int J Math Anal Appl. 1968;22(1):244–59.

Cui LJ, Sheng DC. Genetic algorithms in probabilistic finite element analysis of geotechnical problems. Comput Geotech. 2005;32(8):555–63.

Cundall PA. A computer model for simulating progressive, large-scale movement in blocky rock system. In: Proceedings of the international symposium on rock fracture, vol. 1. Nancy: ISRM; 1971. p. 129–136 (paper no. II-8).

Cundall PA. Formulation of a three-dimensional distinct element model—part I: a scheme to detect and represent contacts in a system composed of many polyhedral blocks. Int J Rock Mech Min Sci Geomech Abstr. 1988;25(3):107–16.

Cundall PA, Hart RD. Development of generalized 2-D and 3-D distinct element programs for modelling jointed rock. ITASCA Consulting Group Misc. paper SL-85-1. Minneapolis: US Army Corps of Engineers; 1985.

Cundall PA, Hart DH. Numerical modelling of discontinua. Eng Comput. 1992;9(2):101–13.

Cundall PA, Strack ODL. A discrete numerical model for granular assemblies. Géotechnique. 1979;29(1):47–65.

Dawson EM, Roth WH, Drescher A. Slope stability analysis by strength reduction. Géotechnique. 1999;49(6):835–40.

Dershowitz WS, Einstein HH. Three dimensional flow modeling in jointed rock masses. In: Herget G, Vongpaisal S, editors. Proceedings of the 6th ISRM congress, vol. 1. Rotterdam: AA Balkema; 1987. p. 87–92.

Dershowitz WS, Miller I. Dual porosity fracture flow and transport. Geophys Res Lett. 1995;22 (11):1441–4.

Dershowitz WS, Gordon BM, Kafritsas JC. A new three dimensional model for flow in fractured rock. In: Proceedings of the international congress on hydrogeology on rocks of low permeability. Arizona: IAH; 1985. p. 441–8.

Desai CS, Abel JF. An introduction to the finite element method. New York: Van Nostrand Reinhold; 1972.

Desai CS, Zamman MM, Lightner JG, Siriwardane HJ. Thin layer element for interfaces and joints. Int J Numer Anal Meth Geomech. 1984;8(1):19–43.
Ding LY, Wang F, Luo HB, Yu M, Wu X. Feedforward analysis for shield-ground system. J Comput Civ Eng. 2013;27(3):231–42.
Duarte CA, Oden JT. An hp adaptive method using clouds. Comput Methods Appl Mech Eng. 1996;139(1–4):237–62.
Duarte CA, Babuška I, Oden JT. Generalized finite element methods for three-dimensional structural mechanics problems. Comput Struct. 2000;77(2):215–32.
Dunnicliff J. Twenty-five steps to successful performance monitoring of dams. Hydro Rev. 1990;9 (4):48–62.
Dunnington GW. Carl Friedrich Gauss, Titan of science: a study of his life and work. Whitefish: Literary Licensing, LLC; 2012.
Dym CL, Shames IH. Solid mechanics: a variational approach. New York: McGraw-Hill; 1973.
El Harrouni K, Ouazar D, Wrobel LC, Cheng AHD. Groundwater parameter estimation by optimization and DRBEM. Eng Anal Bound Elem. 1997;19(2):97–103.
Ellis GW, Yao C, Zhao R, Penumadu D. Stress-strain modeling of sands using artificial neural networks. J Geotech Eng ASCE. 1995;121(5):429–35.
Elsworth D. A model to evaluate the transient hydraulic response of three-dimensional sparsely fractured rock masses. Water Resour Res. 1986a;22(13):1809–19.
Elsworth D. A hybrid boundary-element-finite element analysis procedure for fluid flow simulation in fractured rock masses. Int J Numer Anal Methods Geomech. 1986b;10 (6):569–84.
Endo HK, Long JCS, Wilson CK, Witherspoon PA. A model for investigating mechanical transport in fractured media. Water Resour Res. 1984;20(10):1390–400.
Ern A, Guermond JL. Theory and practice of finite elements. New York: Springer; 2004.
Fang Z. A local degradation approach to the numerical analysis of brittle fracture in heterogeneous rocks. Ph.D. thesis. UK: Imperial College of Science, Technology and Medicine, University of London; 2001.
Ferentinou MD, Sakellariou MG. Computational intelligence tools for the prediction of slope performance. Comput Geotech. 2007;34(5):362–84.
Florian C. The early history of partial differential equations and of partial differentiation and Integration. Am Math Monthly. 1928;35(9):459–67.
Fourier J. Théorie analytique de la chaleur. Paris: Firmin Didot Père et Fils; 1822 (in French).
Fu Q, Hashash YMA, Hung S, Ghaboussi J. Integration of laboratory testing and constitutive modeling of soils. Comput Geotech. 2007;34(5):330–45.
Fumagalli E. Statical and geomechanical models. Wien: Springer; 1973.
Gallagher RH. Finite element analysis fundamentals. New Jersey: Prentice Hall, Inc.; 1975.
Gen M, Cheng RW. Genetic algorithm and engineering design. New York: Wiley-Interscience; 1997.
Gens A, Carol I, Alonso EE. An interface element formulation for the analysis of soil-reinforcement interaction. Comput Geotech. 1989;7(1–2):133–51.
Gens A, Carol I, Alonso EE. Rock joints: FEM implementation and applications. In: Sevaldurai APS, Boulon MJ, editors. Mechanics of geomaterial interfaces. Amsterdam: Elsevier; 1995. p. 395–420.
Ghaboussi J. Fully deformable discrete element analysis using a finite element approach. Int J Comput Geotech. 1988;5(3):175–95.
Ghaboussi J, Sidatra DE. New method of material modeling using neural networks. In: Pietruszczak S, Pande GN, editors. Proceedings of the 6th international symposium on numerical models in geomechanics. Rotterdam: AA Balkema; 1997. p. 393–400.
Ghaboussi J, Wilson EL, Isenberg J. Finite element for rock joints and interfaces. J Soil Mech Found Div ASCE. 1973;99(SM10):849–62.
Gingold RA, Monaghan JJ. Smoothed particle hydrodynamics—theory and application to non-spherical stars. Mon Not R Astron Soc. 1977;181(3):375–89.

Gioda G, Carini A. A combined boundary element-finite element analysis of lined openings. Rock Mech Rock Eng. 1985;18(4):293–302.
Goh ATC. Modeling soil correlations using neural networks. J Comput Civil Eng ASCE. 1995;9 (4):275–8.
Goh ATC. Genetic algorithms search for critical slip surface in multiwedge stability analysis. Can Geotech J. 1999;36(4):382–91.
Goldstine H. The computer from Pascal to von Neumann. Princeton: Princeton University Press; 1972.
Goodman RE. Methods of geological engineering in discontinuous rocks. San Francisco: West Publishing Company; 1976.
Goodman RE, Shi G. Block theory and its application to rock engineering. Englewood Cliffs: Prentice-Hall; 1985.
Goodman RE, Taylor R, Brekke TL. A model for the mechanics of jointed rock. J Soil Mech Found Div ASCE.1968;94(SM3):637–60.
Grayeli R, Mortazavi A. Discontinuous deformation analysis with second-order finite element meshed block. Int J Numer Anal Methods Geomech. 2006;30(15):1545–61.
Griffiths DV, Lane PA. Slope stability analysis by finite element. Géotechnique. 1999;49(3):387–403.
Guzina B, Tucovic I. Determining the maximum three dimensional stability of a rock wedge. Water Power. 1969;21(10):381–5.
Habibagahi G, Bamdad A. A neural network framework for mechanical behavior of unsaturated soils. Can Geotech J. 2003;40(3):684–93.
Hart R, Cundall PA, Lemos J. Formulation of three-dimensional distinct element model. Part 2. Mechanical calculations for motion and interaction of a system composed of many polyhedral blocks. Int J Rock Mech Min Sci Geomech Abstr. 1988;25(3):117–25.
Hatzor YH, Benary R. The stability of a laminated Voussoir beam: back analysis of a historic roof collapse using DDA. Int J Rock Mech Min Sci. 1998;35(2):165–81.
Hermann LR. Laplacian-isoparametric grid generation scheme. J Eng Mech ASCE. 1976;102 (EM5):749–56.
Heuze FE, Walton OR, Maddix DM, Shaffer RJ, Butkovich TR. Analysis of explosions in hard rocks: the power of discrete element modeling. In: Rossmanith HP, editor. Mechanics of jointed and faulted rocks. Vienna: AA Balkema; 1990. p. 21–8.
Hildebrand FB. Introduction to numerical analysis. New York: McGraw-Hill; 1956.
Ho LK. Finite element mesh generation methods: a review and classification. Comp Aided Des. 1988;20(1):27–38.
Hocking G. Development and application of the boundary integral and rigid block method for geotechnics. Ph.D. thesis. UK: University of London; 1977.
Hoek E, Brown ET. Underground excavations in rock. London: Institute of Mining and Metallurgy; 1982.
Howell C, Jaquith AC. Analysis of arch dams by trial-load method. Trans ASCE. 1929;93 (1):1191–225.
Hrennikoff A. Solution of problems of elasticity by the frame-work method. ASME J Appl Mech. 1941;8(1):A619–715.
Hsiung SM. Discontinuous deformation analysis (DDA) with nth order polynomial displacement functions. In: Elworth D, Tinucci JP, Heasley KA, editors. Proceedings of the 38th US symposium rock mechanics in the national interest. Washington: Swets & Zeitlinger Lisse; 2001. p. 1437–44.
Hsiung SM, Shi G. Simulation of earthquake effects on underground excavations using discontinuous deformation analysis (DDA). In: Elworth D, Tinucci JP, Heasley KA, editors. Proceedings of the 38th US symposium rock mechanics in the national interest. Washington: Swets & Zeitlinger Lisse; 2001. p. 1413–20.
Hu Y. Block-spring-model considering large displacements and non-linear stress-strain relationships of rock joints. In: Yuan JX, editor. Computer methods and advanec in geomechanics, vol. 1. Rotterdam: AA Balkema; 1997. p. 507–12.

Hughes TRJ. The finite element method. Englewood Cliffs: Prentice-Hall; 1987.
Hutter K, Jöhnk K. Continuum methods of physical modeling: continuum mechanics, dimensional analysis, turbulence. Berlin: Springer; 2004.
ITASCA. UDEC manual. Minneapolis: Itasca Consulting Group Inc.; 1992.
ITASCA. FLAC manuals. Minneapolis: Itasca Consulting Group Inc.; 1993.
ITASCA. 3DEC manual. Minneapolis: Itasca Consulting Group Inc.; 1994.
ICOLD. Dam safety guidelines (Bulletin 59). Paris: ICOLD; 1987.
ICOLD. Monitoring of dams and their foundations—state of the art (Bulletin 68). Paris: ICOLD; 1988.
ICOLD. Computational procedures for dam engineering—reliability and applicability (Bulletin 122). Paris: ICOLD; 2001a.
ICOLD. Design features of dams to resist seismic ground motion (Bulletin 120). Paris: ICOLD; 2001b.
ICOLD. Guidelines for use of numerical models in dam engineering (Bulletin 155). Paris: ICOLD; 2013.
ITASCA. PFC3D—particle flow code in 3-dimensions (Version 1.1), user's manual, vols. I & II. Minneapolis: Itasca Consulting Group Inc.; 1995a.
ITASCA. PFC-2D and PFC-3D manuals. Minneapolis: Itasca Consulting Group Inc.; 1995b.
ITASCA. FLAC—fast lagrangian analysis of continua, user's guide. Minneapolis: Itasca Consulting Group Inc.; 2002.
Jaswon MA, Ponter AR. An integral equation solution of the torsion problem. Proc Roy Soc London (Ser. A). 1963;273(1):237–46.
Javadi AA, Farmani R, Toropov VV, Snee CPM. Identification of parameters for air permeability of shotcrete tunnel lining using a genetic algorithm. Comput Geotech. 1999;25(1):1–24.
Javadi AA, Tan TP, Zhang M. Neural network for constitutive modeling in finite element analysis. Comput Assist Mech Eng Sci. 2003;10(4):523–9.
Javadi AA, Mehravar M, Faramarzi A, Alireza Ahangar-Asr A. An artificial intelligence based finite element method. ISAST Trans Comput Intell Syst. 2009;1(2):1–7.
Jin H, Wiberg NE. Two-dimensional mesh generation, adaptive remeshing and refinement. Int J Numer Methods Eng. 1990;29(7):1501–26.
Jing L. Formulation of discontinuous deformation analysis (DDA)—an implicit discrete element model for block systems. Int J Eng Geol. 1998;49(3–4):371–81.
Jing L, Hudson JA. Numerical methods in rock mechanics. Int J Rock Mech Min Sci. 2002;39 (4):409–27.
Jing L, Stephansson O. Network topology and homogenization of fractured rocks. In: Jamtveit B, editor. Fluid flow and transport in rocks: mechanisms and effects. London: Chapman & Hall; 1996. p. 91–202.
Jing L, Ma Y, Fang Z. Modelling of fluid flow and solid deformation for fractured rocks with discontinuous deformation analysis (DDA) method. Int J Rock Mech Min Sci. 2001;38 (3):343–55.
Joghataie A, Dizaji MS. Transforming results from model to prototype of concrete gravity dams using neural networks. J Eng Mech ASCE. 2011;137(7):484–96.
Kang F. Collected works of Feng Kang. Beijing: National Defense Industry Press; 1994 (in Chinese).
Katona MG. A simple contact-friction interface element with applications to buried culverts. Int J Numer Anal Methods Geomech. 1983;7(3):371–84.
Kawai T. New discrete models and their application to seismic response analysis of structures. Nucl Eng Des. 1978;48(1):207–29.
Kikuchi A, Kawai T, Suzuki N. The rigid bodies-spring models and their applications to three-dimensional crack problems. Comput Struct. 1992;44(1–2):469–80.
Kim YS, Kim BT. Prediction of relative crest settlement of concrete-faced rockfill dams analyzed using an artificial neural network model. Comput Geotech. 2008;35(3):313–22.

Kim Y, Amadei B, Pan E. Modelling the effect of water, excavation sequence and rock reinforcement with discontinuous deformation analysis. Int J Rock Mech Min Sci Geomech Abstr. 1999;36(7):949–70.
Kim CY, Bae GJ, Hong SW, Park CH, Moon HK, Shin HS. Neural network based prediction of ground surface settlements due to tunneling. Comput Geotech. 2001;28(6–7):517–47.
Klein M. Mathematical thought from ancient to modern time. New York: Oxford University Press; 1972.
Krenk S. Analysis of solids and structures. Cambridge: Cambridge University Press; 2009.
Lachat JC, Watson JO. Effective numerical treatment of boundary integral equations: a formulation for three-dimensional elastostatics. Int J Numer Methods Eng. 1976;10(5):991–1005.
Lax P. Feng Kang. SIAM News. 1993:26(11).
Le Veque JR. Finite volume methods for hyperbolic problems. Cambridge: Cambridge University Press; 2002.
Lee IM, Park JK. Stability analysis of tunnel key block: a case study. Tunn Undergr Space Technol. 2000;15(4):453–62.
Lee CI, Song JJ. Stability analysis of rock blocks around a tunnel. In: Rossmanith HP, editor. Mechanics of jointed and faulted rock. Rotterdam: AA Balkema; 1998. p. 443–8.
Lee C, Sterling R. Identifying probable failure modes for underground openings using a neural network. Int J Rock Mech Min Sci. 1992;29(1):49–67.
Lemos JV. A hybrid distinct element computational model for the half-plane. M.Sc. thesis. USA: University of Minnesota; 1987.
Leu SS, Chen CN, Chang SL. Data mining for tunnel support stability: neural network approach. Autom Constr. 2001;10(4):429–41.
Li G, Wang B. Development of a 3-D block-spring model for jointed rocks. In: Rossmanith HP, editor. Mechanics of jointed and faulted rock. Rotterdam: AA Balkema; 1998. p. 305–9.
Li S, Qian D, Liu WK, Belytschko T. A meshfree contact detection algorithm. Comput Methods Appl Mech Eng. 2001;190(24–25):3271–92.
Libersky LD, Petschek AG. Smooth particle hydrodynamics with strength of materials. In: Trease HE, Crowley WP, editors. Advances in the free-lagrange method (Lecture notes in physics, vol. 395. Berlin: Springer; 1990. p. 248–57.
Libersky LD, Petschek AG, Carney TC, Hipp JR, Allahdadi FA. High strain Lagrangian hydrodynamics—a three-dimensional SPH code for dynamic material response. J Comput Phys. 1993;109(1):67–75.
Lin CT, Amadei B, Jung J, Dwyer J. Extensions of discontinuous deformation analysis for jointed rock masses. Int J Rock Mech Min Sci Geomech Abstr. 1996;33(7):671–94.
Liu GR. Mesh free methods: moving beyond the finite element method. 2nd ed. Boca Raton: CRC Press; 2009.
Liu GR. A G space theory and a weakened weak (W2) form for a unified formulation of compatible and incompatible methods: Part I, theory. Int J Numer Methods Eng. 2010;81 (9):1093–126.
Liu GR, Nguyen-Thoi T. Smoothed finite element methods. Boca Raton: CRC Press; 2010.
Liu GR, Zhang J, Lam KY, Li H, Xu G, Zhong ZH, Li GY, Han X. A gradient smoothing method (GSM) with directional correction for solid mechanics problems. Comput Mech. 2008;41 (3):457–72.
Lo SH. A new mesh generation scheme for arbitrary planar domains. Int J Numer Methods Eng. 1985;21(8):1403–26.
Löhner R. Some useful data structures for the generation of unstructured grids. Commun Appl Numer Methods. 1988;4(1):123–35.
Londe P. Une method d'analyse a' trois dimensions de la stabilite d'une rive rocheuse. Ann Ponts Chaussees. 1965;135(1):37–60 (in French).
Long JCS, Remer JS, Wilson CR, Witherspoon PA. Porous media equivalents for networks of discontinuous fractures. Water Resour Res. 1982;18(3):645–58.
Long JCS, Gilmour P, Witherspoon PA. A model for steady fluid flow in random three dimensional networks of disc-shaped fractures. Water Resour Res. 1985;21(8):1105–15.

Lorig LJ. A hybrid computational model for excavation and support design in jointed media. Ph.D. thesis. USA: University of Minnesota; 1984.
Lorig LJ, Brady BHG. A hybrid discrete element-boundary element method of stress analysis. In: Goodman RE, Heuze FE, editors. Proceedings of the 23rd US symposium on rock mechanics. Berkeley; 1982. p. 628–636.
Lorig LJ, Brady BHG, Cundall PA. Hybrid distinct element-boundary element analysis of jointed rock. Int J Rock Mech Min Sci Geomech Abstr. 1986;23(4):303–12.
Lucy LB. A numerical approach to the testing of the fission hypothesis. Astron J. 1977;82 (12):1013–24.
Ma MY. Development of discontinuous deformation analysis, the first ten years; 1986–1996. In: Third international conference on analysis of discontinuous deformation—from theory to practice. Colorado: American Rock Mechanics Association; 1999. p. 17–32.
Ma MY, Zaman M, Zhu JH. Discontinuous deformation analysis using the third order displacement function. In: Salami MR, Banks D, editors. Proceedings of the first international forum discontinuous deformation analysis (DDA) and simulations of discontinuous media. Berkeley: TSI Press; 1996. p. 383–94.
Macari EJ, Samarajiva P, Wathugala W. Selection and calibration of soil constitutive model parameters using genetic algorithms. In: Yamamuro JA, Kaliakin VN, editors. Proceedings of the sessions geo-frontiers 2005 congress. Austin; 2005. p. 310–32.
MacDonald JK. Successive approximations by the Rayleigh-Ritz variation method. Phys Rev. 1933;43(10):830–3.
MacLaughlin MM, Doolin DM. Review of validation of the discontinuous deformation analysis (DDA) method. Int J Numer Anal Methods Geomech. 2006;30(4):271–305.
Mahtab M, Goodman RE. Three dimensional analysis of joint rock slope. In: Proceedings of the 2nd ISRM congress, vol. 3. Beograd: Privredni Pregled; 1970. p. 353–60.
Massey B, Ward-Smith J. Mechanics of fluids. 8th edn. London: Taylor & Francis; 2005.
Mata J. Interpretation of concrete dam behavior with artificial neural network and multiple linear regression models. Eng Struct. 2011;33(3):903–10.
Matsui T, San KC. Finite element slope stability analysis by shear strength reduction technique. Soils Found. 1992;32(1):59–70.
McCombie P, Wilkinson P. The use of the simple genetic algorithm in finding the critical factor of safety in slope stability analysis. Comput Geotech. 2002;29(8):699–714.
McCormick BH, DeFanti TA, Brown MD. Visualization in scientific computing. New York: ACM Press; 1987.
Melenk JM. On generalized finite element methods. Ph.D. thesis. USA: University of Maryland; 1995.
Melenk JM, Babuška I. The partition of unity finite element method: basic theory and applications. Comput Methods Appl Mech Eng. 1996;139(1–4):289–314.
Meyerhof GG. Safety factors and limit states analysis in geotechnical engineering. Can Geotech J. 1984;21(1):1–7.
Mikhlin SG. Variational methods in mathematical physics. New York: Macmillan; 1964.
Ministry of Water Resources of the People's Republic of China. (SL282-2003) Design specification for concrete arch dams. Beijing: China WaterPower Press; 2003 (in Chinese).
Ministry of Water Resources of the People's Republic of China. (SL319-2005) Design specification for concrete gravity dams. Beijing: China WaterPower Press; 2005(in Chinese).
Ministry of Water Resources of the People's Republic of China. (SL386-2007) Design code for engineering slopes in water resources and hydropower projects. Beijing: China WaterPower Press; 2007 (in Chinese).
Moës N, Dolbow J, Belytschko T. A finite element method for crack growth without remeshing. Int J Numer Methods Eng. 1999;46(1):131–50.
Moller P, Hansbo P. On advancing front mesh generation in three dimensions. Int J Numer Methods Eng. 1995;38(21):3551–69.
Moore G. Cramming more components onto integrated circuits. Electron Mag. 1965;38(8):114–7.

Moore G. The microprocessor: engine of the technology revolution. Commun ACM. 1997;40 (2):112–4.
Moosavi M, Grayeli R. A model for cable bolt-rock mass interaction: integration with discontinuous deformation analysis (DDA) algorithm. Int J Rock Mech Min Sci Geomech Abstr. 2006;43(4):661–70.
Morton KW, Mayers DF. Numerical solution of partial differential equations, an introduction. Cambridge: Cambridge University Press; 2005.
Mukherjee S. Boundary elements in creep and fracture. London: Applied Science Publishers; 1982.
Munjiza A. The combined finite-discrete element method. Chichester: Wiley; 2004.
Munjiza A, Andrews KRF. Penalty function method for combined finite-discrete element systems comprising large number of separate bodies. Int J Numer Methods Eng. 2000;49(11):1377–96.
Munjiza A, Owen DRJ, Bićanić N. A combined finite-discrete element method in transient dynamics of fracturing solid. Int J Eng Comput. 1995;12(2):145–74.
Munjiza A, Andrews KRF, White JK. Combined single and smeared crack model in combined finite-discrete element analysis. Int J Numer Methods Eng. 1999;44(1):41–57.
Mustoe GGW, Williams JR, Hocking G, Worgan KJ. Penetration and fracturing of brittle plates under dynamic impact. In: Proceedings of the NUMETA'87. Rotterdam: AA Balkema; 1987.
National Reform and Development Commission of the People's Republic of China. (DL/T 5346-2006) Design specification for concrete arch dams. Beijing: China Electric Power Press; 2006a (in Chinese).
National Reform and Development Commission of the People's Republic of China. (DL/T 5353-2006) Design specification for engineering slopes in water resources and hydropower projects. Beijing: China Electric Power Press; 2006b (in Chinese).
Naylor DJ, Pande GN, Simpson B, Tabb R. Finite elements in geotechnical engineering. Swansea: Pineridge Press; 1981.
Neaupane KM, Achet SH. Use of back propagation neural network for landslide monitoring: a case study in the higher Himalaya. Eng Geol. 2004;74(3–4):213–26.
Neaupane KM, Adhikari NR. Prediction of tunneling induced ground movement with the multi-layer perceptron. Tunn Undergr Space Technol. 2006;21(2):151–9.
Newmark NM. Effects of earthquakes on dams and embankments. Géotechnique. 1965;15(2):139–60.
Ni SH, Lu PC, Juang CH. A fuzzy neural network approach to evaluation of slope failure potential. Comput Aided Civ Infrastruct Eng. 1996;11(1):59–66.
Nishigaki Y, Miki S. Application of block theory in weathered rock. In: Myer LR, Cook NGW, Goodman RE, Tsang CF, editors. Fractured and jointed rock masses. Rotterdam: AA Balkema; 1995. p. 753–8.
Oda M. Permeability tensor for discontinuous rock masses. Géotechnique. 1985;35(4):483–95.
Ohkami T, Mitsui Y, Kusama T. Coupled boundary element/finite element analysis in geomechanics including body forces. Comput Geotech. 1985;1(4):263–78.
Ohnishi Y, Chen G. Simulation of rock mass failure with discontinuous deformation analysis. J Soc Mater Sci Japan. 1999;48(4):329–33.
Ostoja-Starzewski M. Microstructural randomness and scaling in mechanics of materials. Bosa Raton: Chapman & Hall/CRC; 2007.
Pal S, Wathugala GW, Kundu S. Calibration of a constitutive model using genetic algorithms. Comput Geotech. 1996;19(4):325–48.
Pan XD, Reed MB. A coupled distinct element-finite element method for large deformation analysis of rock masses. Int J Rock Mech Min Sci Geomech Abstr. 1991;28(1):93–9.
Pande GN, Gerrard CM. The behaviour of reinforced jointed rock masses under various simple loading states. In: Proceedings of the 5th ISRM congress. Melbourne: Brown Prior Anderson Pty Ltd; 1983. p. F217–23.
Pande GN, Beer G, Williams JR. Numerical methods in rock mechanics. New York: Wiley; 1990.
Partridge PW, Brebbia CA, Wrobel LC. The dual reciprocity boundary element method. Southampton and Boston: Computational Mechanics Publications and Elsevier; 1992.

Patera AT. A spectral element method for fluid dynamics—laminar flow in a channel expansion. J Comput Phys. 1984;54(3):468–88.
Pearce CJ, Thavalingam A, Liao Z, Bićanić N. Computational aspects of the discontinuous deformation analysis framework for modelling concrete fracture. Eng Fract Mech. 2000;65(2–3):283–98.
Peraire J, Vahdati M, Morgan K, Zienkiewicz OC. Adaptive remeshing for compressible flow computations. J Comput Phys. 1987;72(2):449–66.
Peraire J, Peiro J, Morgan K. Adaptive remeshing for three-dimensional compressible flow computations. J Comput Phys. 1992;103(2):269–85.
Pickover CA. Frontiers of scientific visualization. New York: Wiley; 1994.
Poliakov ANB. Modeling of tectonic problems with PAROVOZ: examples of lithospheric rifting and buckling. In: Detournay C, Hart R, editors. Proceedings of the 1st international FLAC symposium on numerical modeling in geomechanics. Rotterdam: AA Balkema; 1999. p. 165–72.
Pont JC, editor. Le destin douloureux de Walther Ritz (1878–1909), physicien théoricien de génie. Sion: Archives de l'Etat de Valais; 2012 (in French).
Pöttler R, Swoboda GA. Coupled beam-boundary element model (FE-BEM) for analysis of underground openings. Comput Geotech. 1986;2(4):239–56.
Rafiai H, Jafari A. Artificial neural networks as a basis for new generation of rock failure criteria. Int J Rock Mech Min Sci. 2011;48(7):1153–9.
Ritz W. Über eine neue Methode zur Lösung gewisser Variationsprobleme der mathematischen Physik. J Reine Angew Math. 1909;135:1–61 (in German).
Rizzo FJ. An integral equation approach to boundary value problems of classical elastostatics. Quart Appl Math. 1967;25:83–95.
Roy R, Bathe KJ, Wilson EL. Numerical methods in finite analysis. New Jersey: Prentice-Hall Inc.; 1976.
Rudman PS. How mathematics happened: the first 50,000 years. New York: Prometheus Books; 2007.
Rumelhart DE, Hinton GE, Williams RJ. Learning internal representations by error propagation. In: Rumelhart DE, McClelland JL, The PDP Group, editors. Parallel distributed processing: explorations in the microstructure of cognition, vol. 1. Foundations. Massachusetts: MIT Press; 1986.
Salami MR, Banks D, editors. Discontinuous deformation analysis (DDA) and simulations of discontinuous media. Albuquerque: TSI Press; 1996.
Sbarufatti C, Manes A, Gigliol M. Advanced stochastic fem-based artificial neural network for crack damage detection. In: Proceedings of forth international conference on computational methods for coupled problems in sciences and engineering; 2011. p. 1107–19.
Scott GA, Kottenstette JT. Tunnelling under the Apache trial. Int J Rock Mech Min Sci Geomech Abstr. 1993;30(7):1485–9.
Shan T, Zhao J. A coupled CFD-DEM analysis of granular flow impacting on a water reservoir. Acta Mech. 2014;225(8):2449–70.
Sharma VM, Saxena KR, Woods RD, editors. Distinct element modelling in geomechanics. Rotterdam: CRC Press; 1999.
Shi G. Discontinuous deformation analysis—a new numerical model for the statics and dynamics of block systems. Ph.D. thesis. Berkeley: University of California; 1988.
Shi G. Manifold method of material analysis. In: Transactions of the 9th army conference on applied mathematics and computing. Report No. 92–1. Minneapolis: US Army Research Office; 1991. p. 57–262.
Shi G. Discontinuous deformation analysis: a new numerical model for the statics and dynamics of deformable block structures. Eng Comput. 1992;9(2):157–68.
Shi G. Modeling rock joints and blocks by manifold method. In: Proceedings of the 33rd US symposium on rock mechanics. Rotterdam: AA Balkema; 1992. p. 639–48.
Shi G, Goodman RE. Two dimensional discontinuous deformation analysis. Int J Numer Anal Methods Geomech. 1985;9(6):541–56.

Shi G, Goodman RE. Finding 3-D maximum key blocks on unrolled joint traces of tunnel surfaces. In: Hustrulid WA, Johnson GA, editors. Rock mechanics contributions and challenges. Rotterdam: AA Balkema; 1990. p. 219–28.

Shi G. Three dimensional discontinuous deformation analysis. In: Elworth D, Tinucci JP, Heasley KA, editors. Proceedings of the 38th US symposium on rock mechanics in the national interest. Washington: Swets & Zeitlinger Lisse; 2001. p. 1421–8.

Shyu K. Nodal-based discontinuous deformation analysis. Ph.D. thesis. Berkeley: University of California; 1993.

Simpson AR, Priest SD. The application of genetic algorithms to optimisation problems in geotechnics. Comput Geotech. 1993;15(1):1–19.

Sloan SW, Houlsby GT. An implementation of Watson's algorithm for computing 2-dimensional Delauney triangulations. Adv Eng Softw. 1984;6(4):192–7.

Smith L, Schwartz FW. An analysis of the influence of fracture geometry on mass transport in fractured media. Water Resour Res. 1984;20(9):1241–52.

Spencer AJM. Continuum mechanics. London: Longman Group Limited; 1980.

State Economy and Trade Commission of the People's Republic of China. (DL5108-1999) Design specification for concrete gravity dams. Beijing: China Electric Power Press; 1999 (in Chinese).

Stolarska M, Chopp DL, Moës N, Belytschko T. Modeling crack growth by level sets in the extended finite element method. Int J Numer Methods Eng. 2001;51(8):943–60.

Strang G, Fix GJ. An analysis of the finite element method. Englewood Cliffs: Prentice-Hall; 1973.

Strouboulis T, Babuška I, Copps K. The design and analysis of the generalized finite element method. Comput Methods Appl Mech Eng. 2000;181(1–3):43–69.

Strouboulis T, Copps K, Babuška I. The generalized finite element method. Comput Methods Appl Mech Eng. 2001;190(32–33):4081–193.

Struik DJ. A concise history of mathematics. New York: Dover Publications; 1987.

Sugawara K, Aoki T, Suzuki Y. A coupled boundary element characteristics method for elasto-plastic analysis of rock caverns. In: Romana M, editor. Rock mechanics and power plants. Rotterdam: AA Balkema; 1988. p. 248–58.

Swegle JW, Hicks DL, Attaway SW. Smoothed particle hydrodynamics stability analysis. J Comput Phys. 1995;116(1):123–34.

Swoboda G, Marence M. FEM modelling of rockbolts. In: Beer G, et al., editors. Proceedings of computer methods and advance in geomechanics. Cairns: AA Balkema; 1991. p. 1515–20.

Swoboda G, Mertz W, Beer G. Rheological analysis of tunnel excavations by means of coupled finite element (FEM)-boundary element (BEM) analysis. Int J Numer Anal Methods Geomech. 1987;11(2):115–29.

Szabó BA, Mehta AK. p-convergent finite element approximations in fracture mechanics. Int J Numer Methods Eng. 1978;12(3):551–60.

Tan H, Chen SH. A hybrid DEM-SPH model for deformable landslide and its generated surge waves. Adv Water Resour. 2017;108:256–76.

Taylor LM. BLOCKS—a block motion code for geomechanics studies. Research Report SAND82-2373, DE83 009221. Albuquerque: Sandia National Laboratories; 1982.

Taylor LM, Preece SD. DMC—a rigid body motion code for determining the interaction of multiple spherical particles. Research report SAND-88-3482. Albuquerque: Sandia National Laboratories; 1989.

Taylor LM, Preece SD. Simulation of blasting induced rock motion using spherical element models. Eng Comput. 1990;9(2):243–52.

Te-Chin K. Improved modeling of rock bolting in DDA. In: Yuan JX, editor. Computer methods and advance in geomechanics. Rotterdam: AA Balkema; 1997.

Thacker WC. A brief review of techniques for generating irregular computational grids. Int J Numer Meth Eng. 1980;15(7):1335–41.

Timoshenko S. History of strength of materials. New York: McGraw-Hill; 1953.

Trollope DH. The mechanics of discontinua or clastic mechanics in rock problem. In: Stagg KG, Zienkiewicz OC, editors. Rock mechanics in engineering practice. New York: Wiley; 1968 (Chapter 9).
Turing AM. On computable numbers, with an application to the entscheidungs problem. Proc Lond Math Soc (Ser. 2). 1937;42:230–65.
Ugai K, Leschinsky D. Three dimensional limit equilibrium and finite element analyses: a comparison of results. Soil Found. 1995;29(4):1–7.
Varadarajan A, Sharma KG, Singh RB. Some aspects of coupled FEBEM analysis of underground openings. Int J Numer Anal Methods Geomech. 1985;9(6):557–71.
Venturini WS, Brebbia CA. Some applications of the boundary element method in geomechanics. Int J Numer Anal Methods Geomech. 1983;7(4):419–43.
Von Estorff O, Firuziaan M. Coupled BEM/FEM approach for non-linear soil/structure interaction. Eng Anal Bound Elem. 2000;24(10):715–25.
Walton OR. Explicit particle dynamics model for granular materials. In: Proceedings of the 4th international conference on numerical methods in geomechanics. Edmonton; 1982. p. 1261–68.
Wan RC. The numerical modeling of shear bands in geological materials. Ph.D. thesis. Edmonton: University of Alberta; 1990.
Wang S, Ge X. Application of manifold method in simulating crack propagation. Chin J Rock Mech Eng. 1997;16(5):405–10 (in Chinese).
Wang BL, Ma QC. Boundary element analysis methods for ground stress field of rock masses. Comput Geotech. 1986;2(5):261–74.
Wang Z, Wang S, Yang Z. Manifold method in analysis of large deformation for rock. Chin J Rock Mech Eng. 1997;16(5):399–404 (in Chinese).
Wang J, Mogilevskaya SG, Crouch SL. A Galerkin boundary integral method for non-homogenous materials with crack. In: Elsworth D, Tunicci JP, Heasley KA, editors. Rock mechanics in the national interest. Rotterdam: AA Balkema; 2001a. p. 1453–60.
Wang WM, Xu MY, Chen SH. Coupled method of block element and finite element for hydraulic structures. Chin J Rock Mech Eng. 2001b;20(Supp. 1):1029–33 (in Chinese).
Wang W, Chen G, Zhang H, Zhou S, Liu S, Wu Y, Fan F. Analysis of landslide-generated impulsive waves using a coupled DDA-SPH method. Eng Anal Bound Elem. 2016;64:267–77.
Warburton PM. Application of a new computer model for reconstructing blocky rock geometry, analysing single rock stability and identifying keystones. In: Proceedings of the 5th ISRM congress. Melbourne: ISRM, 1983. p. F225–30.
Warburton PM. Some modern developments in block theory for rock engineering. In: Hudson JA, editor. Comprehensive rock engineering, vol. 2. Oxford: Pergamon Press; 1993. p. 293–9.
Watson JO. Advanced implementation of the boundary element method for two-and three-dimensional elastostatics. In: Banerjee PK, Butterfield R, editors. Developments in boundary element methods, vol. 1. London: Applied Science Publishers; 1979. p. 31–63.
Wei L, Hudson JA. A hybrid discrete-continuum approach to model hydro-mechanical behaviour of jointed rocks. Eng Geol. 1988;49(3–4):317–25.
Wei L. Numerical studies of the hydromechanical behaviour of jointed rocks. Ph.D. thesis. UK: Imperial College of Science and Technology, University of London; 1992.
Wilcock P. The NAPSAC fracture network code. In: Stephansson O, Jing L, Tsang CF, editors. Coupled thermo-hydro-mechanical processes of fractured media. Rotterdam: Elsevier; 1996. p. 529–38.
Wilkins ML. Calculation of elasto-plastic flow. Research Report UCRL-7322. USA: University of California, Rev I Lawrence Radiation Laboratory; 1963.
Wittke W. Rock mechanics—theory and applications. Berlin: Springer; 1990.
Wu K, Yang D, Wright N. A coupled SPH-DEM model for fluid-structure interaction problems with free-surface flow and structural failure. Comput Struct. 2016;177:141–61.
Xu MY, Wang WM, Chen SH. Research on the dangerous sliding-block combination of rock slopes. Rock Soil Mech. 2000;21(2):148–51 (in Chinese).

Yerry MA, Shepard MS. Automatic 3-dimensional mesh generation by the modified octree technique. Int J Numer Methods Eng. 1984;20(11):1965–90.
Yeung MR, Loeng LL. Effects of joint attributes on tunnel stability. Int J Rock Mech Min Sci. 1997;34(3–4) (Paper No. 348).
Yi D, Xu MY, Chen SH, Ge XR. Application of neural network to back analysis of initial stress field of rock masses. Rock Soil Mech. 2004;25(6):943–6 (in Chinese).
Yoo C, Kim JM. Tunneling performance prediction using an integrated GIS and neural network. Comput Geotech. 2007;34(1):19–30.
Yosida Y. Functional analysis. 6th edn. Berlin: Springer; 1980.
Yow JL. Block analysis for preliminary design of underground excavations. In: Hustrulid WA, Johnson GA, editors. Rock mechanics contributions and challenges. Rotterdam: AA Balkema; 1990. p. 429–35.
Zadeh LA. Fuzzy logic, neural networks, and soft computing. Commun ACM. 1994;37(3):77–84.
Zeng W, Liu GR. Smoothed finite element methods (S-FEM): an overview and recent developments. Arch Comput Methods Eng. 2016;24:1–39.
Zhang X, Lu MW. Block-interfaces model for non-linear numerical simulations of rock structures. Int J Rock Mech Min Sci. 1998;35(7):983–90.
Zhang X, Lu MW, Wegner JL. A 2-D meshless model for jointed rock structures. Int J Numer Methods Eng. 2000;47(10):1649–61.
Zhang J, Liu GR, Lam KY, Li H, Xu G. A gradient smoothing method (GSM) based on strong form governing equation for adaptive analysis of solid mechanics problems. Finite Elem Anal Des. 2008;44(15):889–909.
Zhou CB, Liu W, Chen YF, Hu R, Wei K. Inverse modeling of leakage through a rockfill dam foundation during its construction stage using transient flow model, neural network and genetic algorithm. Eng Geol. 2015;187:183–95.
Zhu BF. Finite element method—principle and application. 2nd edn. Beijing: China WaterPower Press; 1998 (in Chinese).
Zhu JZ, Zienkiewicz OC, Hinton E, Wu J. A new approach to the development of automatic quadrilateral mesh generation. Int J Numer Methos Eng. 1991;32(4):849–66.
Zhu JH, Zaman MM, Anderson SA. Modeling of shearing behavior of a residual soil with recurrent neural network. Int J Numer Anal Methods Geomech. 1998;22(8):671–87.
Zienkiewicz OC. Achievements and some unresolved problems of the finite element methods. Int J Numer Methods Eng. 2000;47(special issue):9–28.
Zienkiewicz OC, Cheung YK. The finite element method in structural and continuum mechanics. London: McGraw-Hill Publishing Co; 1967.
Zienkiewicz OC, Zhu JZ. A simple error estimator and adaptive procedure for practical engineering analysis. Int J Numer Methods Eng. 1987;24(2):337–57.
Zienkiewicz OC, Phillips DV. An automatic mesh generation scheme for plane and curved surfaces by isoparametric coordinates. Int J Numer Methods Eng. 1971;3(3):519–28.
Zienkiewicz OC, Best B, Dullage C, Stagg K. Analysis of nonlinear problems in rock mechanics with particular reference to jointed rock systems. In: Proceedings of the 2nd ISRM congress, vol. 3. Belgrade: ISRM; 1970. p. 501–9.
Zienkiewicz OC, Kelly DW, Bettess P. The coupling of the finite element method and boundary solution procedures. Int J Numer Methods Eng. 1977;11(2):355–75.
Zienkiewicz OC, Taylor RL, Zhu JZ. The finite element method—its basis & fundamentals. 6th edn. Oxford: Elsevier Butterworth-Heinemann; 2005.
Zienkiewicz OC, Taylor RL, Fox DD. The finite element method for solid and structural mechanics. 7th edn. Oxford: Butterworth-Heinemann; 2013.
Zolfaghari AR, Heath AC, McCombie PF. Simple genetic algorithm search for critical non-circular failure surface in slope stability analysis. Comput Geotech. 2005;82(3):139–52.

Chapter 2
Preparation Knowledge of Material Properties

Abstract Termed as "rock-like materials" related to the subject of geomechanics in this book, rocks and concrete are mostly consumed in hydraulic structures whose properties are dependent on their micro-or/and meso-structures but usually described by phenomenological (conceptual) models on the macro-scale level. For the benefit of beginning students, different types of basic material properties related to hydraulics (permeability), thermodynamics (thermal stress), and mechanics (deformation and strength) are discussed in this chapter, with special reference to why and how the aggregate, cement paste, interfacial transition zone (ITZ), discontinuity, testing method, etc., affect these properties. The constitutive laws (relations, equations) related to the fields of permeability/temperature/mechanics ranging from linear to nonlinear until partial coupling of TM and HM, are concisely summarized. It is notable that the basic properties and constitutive laws elaborated in this chapter on one hand, presents preparation knowledge of rock-like materials and on the other hand, provides basic parametric inputs for the engineering cases as well as important constituents for the formulation of governing equations in the hereinafter chapters.

2.1 General

Termed as "rock-like materials" related to the subject of geomechanics in this book, rocks and concrete are mostly consumed in hydraulic structures whose physical and mechanical properties such as density, thermal conductivity, permeability, deformability and strength (Zienkiewicz 1968; Goodman 1989; Hudson and Harrison 1997; Young et al. 1998; Mehta and Monteiro 2006; Jaeger et al. 2007), must be comprehensively explored, tested and evaluated in order to design a hydraulic structure that is safe, feasible, and appropriate for the site conditions (Golzé 1977; Chen 2015). In addition, steel bars and black or HDPE pipes are widely used for the purposes of rock reinforcement and concrete cooling.

The properties of rock-like materials are dependent on their micro- or/and meso-structures but usually described by phenomenological (conceptual) models on

S.-H. Chen, *Computational Geomechanics and Hydraulic Structures*,
Springer Tracts in Civil Engineering, https://doi.org/10.1007/978-981-10-8135-4_2

the macro-scale level. It means a mathematical expression that relates several observated phenomena by "naked-eye" or/and instruments to each other, in a way consistent with fundamental physical theory, but not directly derived from microscopic or mesoscopic mechanism. Based on the thermodynamics of continuum (Malvern 1969; Irgens 2008), a rock-like material is thought to be composed of infinitesimal "representative elementary volume" (REV) or "representative volume element" (RVE). The magnitude of REV is normally defined as the minimum volume beyond which any matter element behaves essentially homogeneous like the whole material.

In the sense of phenomenological model, the properties of an elementary system are assigned to the volume elements. The phenomena appearing in the micro-or meso-structure of the material are represented in terms of state variables and conjugate thermodynamic forces, both attached to the elementary system. Cross-effects between phenomena on the micro-or meso-level and their macroscopic consequences may be determined from standard laboratory tests at the macro-scale level of engineering material samples. The phenomenological models most familiar to hydraulic engineers relate, for example, the strain versus stress, the temperature gradient versus heat flow, the hydraulic gradient versus seepage flow.

The concept of REV has drawn high attention since the early work by Hill (1963). As is common in continuum mechanics, several other definitions of REV are proposed by scientists for different purposes (Hashin 1983; Evesque 2000). The existence and size of REV have been studied by many scholars (Kanit et al. 2003; Stroeven et al. 2004; Gitman et al. 2007; Al-Raoush and Papadopoulos 2010; Skarzynski and Tejchman 2012).

Various studies have been carried out for a better understanding of the concrete REV. Robert (1998) demonstrated that sample dimension need to be at least 3 times the maximum aggregate size to representatively characterize electromagnetic properties of concrete. Huet (1999) suggested that the concrete REV should be not only dependent on the maximum aggregate size, but also on other the factors such as sample shape, aggregate content or the contrast between properties of the sample constituents. Van Vliet and Van Mier (2000) conducted a series of uniaxial tension experiments to study the size effect on the strength and fracture energy of concrete, they showed that the REV should be as large as 6–7 times the maximum aggregate size. A study using quantitative image analysis and computer simulation by Stroeven and Stroeven (2001) indicated that the concrete REV should exceed 4–5 times the maximum aggregate size for structure insensitive properties (such as stiffness) while it must be even larger for structure sensitive properties (such as fracture). Kim et al. (2009) proposed that for typical dense-graded asphalt concrete mixtures with a nominal maximum aggregate size of 19 mm, their effective non-damaged properties could be characterized by a REV size of 50 mm. Sebsadji and Chouicha (2012) concluded that, for laboratory concrete testing, standard sample dimension should be at least 3.5 times the nominal maximum aggregate size in the case of ordinary concrete mixtures. Based on these studies it may be rationally stipulated that the REV of concrete is 3–5 times the maximum aggregate size (Van Mier and Van Vliet 2003).

The story for rocks is, however, debatable due to their much larger and difficultly estimated REV. To make things even worse, the definition of REV for rocks is also ambiguous.

One of the rock REV definitions relates it to the sample size dependent on stochastic behaviors. On the basis of the crack tensor concept, Oda (1988) suggested that the rock REV must be at least three times the typical length of joint traces. This is normally applicable to fractured rock where the joint trace is smaller than 5 m. According to Müller (1974), the minimum size of the rock REV should be at least ten times the joint space.

Another rock REV definition relates it to the structure size, with regard to whether the equivalent continuum assumption is valid for the macroscopic phenomenological model. This is more difficult and less addressed until now. The applicability of phenomenological models is convincible with regard to mass concrete because the size of the elementary heterogeneity of concrete material is 10–120 mm (fully aggregated), which is considerably smaller than the structural dimensions—tens to hundreds in meter, taking dams for example. Towards rocks, Wilson and Witherspoon (1970) suggested a ratio 1/50 of the maximum joint space to the minimum structure boundary, to guarantee the validity of the equivalent continuum assumption. Louis (1974a, b) believed that where there are 1000-plus joints in the domain concerned, the REV does exist and the equivalent continuum assumption to construct a phenomenological model is valid for seepage analysis.

To the best of our knowledge insofar, only a limited works focusing on the determination of the REV size related to thermal and desorption isotherm of concrete and rocks are available for practical reference (Keskin et al. 2011; Zhou et al. 2013; Li et al. 2017; Xu et al. 2017).

The REV size is not necessarily unique for concrete and rocks since it depends sensitively on the material properties under investigation. Therefore, there is much room for its evaluation with regard to whether a macroscopic phenomenological model is valid for the structural problem encountered. Taking Xiaowan Arch Dam (H = 294.5 m, China) for example, its dam base width varying from the maximum 72.91 m (crown cantilever) to the minimum 12 m (crest arch abutments) may be looked at as the minimum structure boundary dimension; the maximum concrete aggregate size is 120 mm, the average trace length of dominant joint sets is 2.01–2.23 m, and the average space of dominant joint sets is 0.23–0.43 m, respectively. As a result, the corresponding minimum REV size is 360–600 mm for concrete according to Van Mier and Van Vliet, meanwhile for rocks it is 6 m according to Oda and 4.3 m according to Müller. This means that the physical and mechanical parameters should be evaluated by test samples larger than 600 mm for concrete and 6 m for rocks. We now easily realize that the latter requirement is nearly impossible to meet for the moment. Even if we success in doing so, the ratio of maximum joint space to the minimum structure boundary is 1/170–1/30, just spanning the criterion of Wilson and Witherspoon (1970) in between. This situation vividly presents the real difficulty we are encountered in the computational

geomechanics arise from rock-like materials, and explains why we should make compromise among the diverse applications of computation algorithms, material models, parametric evaluations, and, safety margins.

2.2 Rock-like Materials and Auxiliary Materials

2.2.1 Concrete

Concrete is a composite material that essentially consists of binding media within which are embedded particles or fragments of aggregate. The binder is formed from a mixture of hydraulic cement, flying ash, water, and several kinds of admixtures (Mehta and Monteiro 2006; ICOLD 2009).

Concrete containing natural sand and gravel or crushed-rock aggregates, generally weighing about γ_c = 2400 kg/m^3, is called "normal-weight concrete", and is the most prevalent for hydraulic structures. The normal-weight concrete in hydraulic structures is exposed to different physico-chemo-mechanical actions of either fresh or sea water. Such concrete is called "hydraulic concrete" which must possess certain properties capable of guaranteeing the stability and long service life of the hydraulic structure in addition to the good workability. These properties are high strength, high density, high impermeability, high water resistance (i.e. corrosion resistance); high abrasion resistance and cavitation resistance; high crack resistance.

Aggregates are the granular materials, such as sand, gravel, or construction/demolition waste that are mixed with a cementing medium to produce either concrete or mortar. According to the aggregate size, concrete is termed as "one-graded" with aggregate size of 5–20 mm, "two-graded" by the additional aggregate size of 20–40 mm, "three-graded" by the additional aggregate size of 40–80 mm, and "four-graded (fully aggregated)" by the additional aggregate size of 80–120 mm. In hydraulic structures, one-or two-graded concrete is employed for slim structures such as the tunnel lining, sluice and spillway pavement, this is mainly required by the construction technology; for mass structures such as dams, the fully-graded concrete is desirable to meet the requirements for the economy and temperature control.

Cement is a finely pulverized dry material which may develop the binding effect as a result of hydration. A cement is tagged "hydraulic" when its hydration products are stable in an aqueous environment. The most commonly consumed hydraulic cement is the Portland cement that consists of reactive calcium silicates forming the calcium silicate hydrates (C-S-H) primarily responsible for its adhesive characteristics, and is stable in aqueous environment.

Apart from aggregates, cement, and water, admixtures are commonly added to the concrete batch immediately before or during mixing. The use of admixtures in concrete may offer a variety of benefits such as to modify the setting and hardening characteristics of cement paste by chemically influencing the rate of cement

hydration, to plasticize fresh concrete mixtures through cutting the surface tension of water by water-reducing admixtures, to improve the durability of concrete exposed to cold weather by air-entraining admixtures, and to reduce thermal cracking in mass concrete by mineral admixtures such as pozzolan.

Mortar is a mixture of sand, cement, and water, but without coarse aggregates. Shotcrete is a mortar or concrete that is pneumatically transported through a hose and projected onto an excavated rock surface at high velocity for the purposes of its protection and reinforcement.

As a heterogeneous and multiphase material, there are various factors affecting concrete properties including the volume fraction, the characteristics of the principal constituents, and the characteristics of the "interfacial transition zone" (ITZ). In general, capillary voids and micro-cracks and oriented calcium hydroxide crystals are relatively more common in the ITZ than in the bulk cement paste matrix, therefore it often although not always, provides an important clue in the exploration of the properties of concrete.

Concrete mixes of different compositions are used depending on the engineering requirements, demanded by operating conditions of structures or their elements. Rational selection of the composition of concrete consists in obtaining good quality concrete at minimum cost, that is, obtaining long-life and economical concrete. In this respect, the specific consumption of cement for one cubic meter is a key index, namely, for a stipulated concrete grade it should be possibly minimum. This is also beneficial to reduce liberation of heat and to control the danger of cracking in concrete.

The property of place-ability (flow-ability) depends on the composition and water cement ratio (W/C) of concrete. The so-called settlement (slump) of a standard cone made from a concrete mix serves as an index of flow-ability: the larger settlement of the concrete mix cone after removing the form, the greater flow-ability of concrete placed in forms or sections. Use is made of different types of concrete mixes: dry and low-slump (slumps 1–2 cm) concrete mixes, they demand compaction by vibration for obtaining required strength, and are used in massive frames and structures; moderate-slump (slumps 2–4 cm) concrete mixes find application in reinforced massive frames; in reinforced concrete structures with up to 1% reinforcement ratio, consistent concrete mixes of 5–8 cm slumps may be required; 8–12 cm slumps are permitted for even larger proportions of reinforcement.

Although in practice most concrete is simultaneously subjected to a combination of compressive, shearing, and tensile stresses in two- or three-directions, the uni-axial compression test is most prevalent. The 28-day compressive strength of concrete determined by a standard uni-axial test using standard cubes ($150 \times 150 \times 150$ mm) is accepted universally as a primary index for concrete grading. Exclusive USA, strength grading of cement and concrete is exercised in China, Europe and many other countries characterized by the standard uni-axial compressive strengths in MPa. In the architecture industry of China, the strength grading is normally termed in a series of $C15$, $C20$, $C25$, $C30$, $C35$, $C40$, $C45$, $C50$, $C55$, $C60$, where the subsequence digit denotes the uni-axial compressive strength (in MPa) of standard cubes at the age of 28 days.

By uni-axial compressive strength, concrete may be divided into three general categories, namely, low-strength concrete whose compressive strength is lower than 20 MPa, moderate-strength concrete whose compressive strength is ranged from 20 to 40 MPa, and high-strength concrete whose compressive strength is higher than 40 MPa. Moderate-strength concrete, also referred to as ordinary or normal concrete, is mostly employed for hydraulic works.

Disregarding the effects such as crack formation (matter of early age) and chemical change due to AAR or aggressive water, the increase of concrete age is in general beneficial to the overall structural performance. An increase in the time dependent elastic modulus leads to a reduction in elastic deflection, and an increase in the time-dependent strength leads to an increase in structural safety. Attributable to the longer construction phase of hydraulic structures, the standards of China (GB50010-2010; SL191-2008) stipulate that in the design of concrete dams, the concrete grading may be specially termed with the uni-axial compressive strength of 85% guarantee rate that is tested by standard curing cubes at the design age of 90 days. Where the construction period is much longer, the design age may be equal to or even longer than 180 days subject to comprehensive study. Under such circumstances, the concrete strength grade is denoted as $C_{age(day)}Strength$ (MPa). For example, by grade $C_{180}40$ it means that the concrete possesses uni-axial compression strength 40 MPa of standard cubes (150 × 150 × 150 mm) tested at the age of 180 days.

For the compressive strength of three-graded or fully-graded concrete, the standard cubic specimen (150 × 150 × 150 mm) should be "wet-screened". In the process of such specimen, the aggregates larger than 40 mm are picked out.

The other requirements for testing sample size are stipulated in the design code SL352-2006 as follows:

- Wet-screened (two-or three graded). Standard cubes (150 × 150 × 150 mm) are demanded for compressive and splitting tension tests, in which the aggregates larger than 40 mm are screened. Beams by 100 × 100 × 400–600 mm are demanded for direct (axial) tension tests, whereas beams by 150 × 150 × 550 mm are demanded for three point bending tests. Cylinders of ϕ150 × 300 mm may be employed, too, particularly for axial compression strength and Young' modulus tests. Cylinders of ϕ150 × 450 mm or ϕ200 × 600 mm are employed for compressive creep tests, whereas those of ϕ150 × 500 mm are for tensile creep tests.
- Fully-graded (four-graded). Cubes larger than 450 × 450 × 450 mm are demanded for compression, splitting tension, and shear tests. Cylinders of ϕ450 × 900 mm also may be employed in compression tests. Beams by 450 × 450 × 1700 mm are normally used for three point bending tests.

Since the wet-screen of aggregates larger than 40 mm will greatly change the mortar content, the concrete parameters using wet-screened samples exhibit notable change with respect to that of the real fully-graded concrete in mass concrete structure. In recent years, the Chinese engineers supplementarily employ larger

Table 2.1 Strength values of fully-graded and wet-screened concretes: Xiaowan Arch Dam (28 days)

Strength grade	W/C	Maximum grain of aggregate (mm)	Sample size (cm/cubic)	Compressive strength (MPa)	Splitting tensile strength (MPa)
$C_{180}40$	0.40	40 (wet-screened/ two-graded)	15	35.0	2.40
		80 (wet-screened/ three-graded)	30	40.0	–
		150 (fully-graded)	45	40.5	2.12
$C_{180}30$	0.50	40 (wet-screened/ two-graded)	15	24.6	2.11
		80 (wet-screened/ three-graded)	30	29.0	–
		150 (fully-graded)	45	29.7	1.64

samples of real fully-graded concrete to help the selection of design parameters in addition to standard specimens. For dams higher than 200 m and other important hydraulic structures, such fully-graded concrete tests are normally demanded. The data listed in Table 2.1 may help us to understand that, compared to the standard cubic specimens of 150 × 150 × 150 mm, larger specimens will provide larger average compressive strength but smaller average tensile strength. When the size is increased beyond 450 mm, a much smaller variation in strength is observed. It is therefore validated that the strength of concrete possesses remarkable scale effects attributable to the heterogeneity at meso-scale level, and the REV size corresponding to fully-graded concrete strength would be approximately 450 mm.

In a hydraulic project, different portions of a mass concrete structure (e.g. dam) operate under different states of stress/seepage/temperature conditions. Hence for the purposes of achieving maximum correspondence of concrete grades to the operating conditions and of obtaining maximum economy, the so-called concrete grade zoning is customarily exercised in mass concrete structures (Chen 2015).

2.2.2 Rocks

At a granular level, rocks are composed of mineral grains held together by chemical bonds. Many rocks contain silica (SiO_2) forming crystals with other compounds, whose proportion in rock minerals is a major factor in determining their name and properties. Most brittle rocks comprise aggregates of crystal and amorphous particle bounded by varying amount of cementitious materials (Scholtz 1968; Ghaboussi and Gioda 1977; Barla 1995; Boukharov et al. 1995; Chen and Chugh 1996; Malan 2002; Schubert et al. 2003; Jaeger et al. 2007; Barla et al. 2010; Brantut et al. 2013).

Over the geologic history, rocks can be transformed from one type into another, which is called the rock cycle. These events produce three general classes of rocks, namely, igneous, sedimentary, and metamorphic:

- Igneous rocks are formed through the cooling and solidification of magma or lava;
- Sedimentary rocks are formed at the Earth's surface by the accumulation and cementation of fragments of earlier rocks, minerals, and organisms in water (sedimentation);
- Metamorphic rocks are formed by subjecting any rock types (i.e. sedimentary rock, igneous rock or another older metamorphic rock) to higher temperature or/and higher pressure conditions than those in which the original rock was formed.

In the modern civil engineering, rocks are generally described in the bore log by the following sequence of terms: drilling information, rock type, weathering, color, structure, rock quality designation (RQD), strength, and defects (Look 2007; Ulusay and Hudson 2007; Ulusay 2015).

Significant geological fractures such as faults, joints, bedding planes and fissures are commonly termed as "geological discontinuities" or "structural planes", which have certain shapes and sizes as well as orientations (attitudes). The overall geometrical feature of the major discontinuities in a rock mass is termed as "rock structure".

It is widely recognized that there are three basic peculiarities of rock masses compared to concrete:

- The rock mass comprises structural bodies surrounded by structural planes, therefore its engineering characteristics is co-decided by the material of structural body and various discontinuities, the latter are often dominant.
- The rock mass on which a hydraulic work rests has changeable stability states varying with stress conditions.
- The spatial characteristics of geological discontinuities, coupled with the properties and configurations of structural bodies, contribute to great disparity in the physical and mechanical properties of the rock mass.

Actually, there is another important basic peculiarity of rock mass—the virgin (un undisturbed, initial) in situ geo-stresses abbreviated as "in situ stresses" (or "geo-stresses"), that significantly affect its characteristics and engineering performances. As an important geologic setting of cut slopes, tunnels, and dam foundations, in situ stresses are the natural stresses that exist in the ground prior to any excavation. They determine the initial conditions for deformation/stress analysis and give rise to the stress adjustments accompanied by deformation when an opening/exposure surface is created (Goodman 1989; Jaeger et al. 2007).

The in situ stresses existing in a rock stratum can be decomposed into three principal compressive components, approximately one vertical and two horizontal, which are usually not equal. The vertical stress is mainly attributable to the

overburden weight exerting on the top of the stratum. The horizontal stresses are the result of the laterally restrained rock deformation plus externally applied tectonic actions and possible geothermal/ground water actions. The parameters that affect the magnitude of in situ stresses include overburden weight, fluid pore pressure, porosity, anomalies in the rock fabric (i.e. natural fractures), rock mechanical properties (such as the Poisson's ratio), tectonic activities (inclusive slip on fracture surfaces and viscoplastic flow throughout the rock), river trenching, terrestrial heating, chemical and physicochemical processes such as leaching, precipitation and re-crystallization of constituent minerals. Topographic conditions also significantly influence in situ stresses. In a deeply cut river valley, the in situ stress field is commonly distributed in 4 zones inclusive stress release zone, stress transition zone, stress concentration zone and, stable stress zone.

The foundations of various hydraulic structures should fully use the stress transition zone, partially use the stress–release zone and avoid as far as possible the stress concentration zone. The top of dam foundation bedrock should be adjusted appropriately so as to keep the ratio between the stress and the strength of rock within a range permitting only be fractured slightly; the axis of tunnel should be aligned as parallel as possible or be oblique slightly to the maximum principal stress; the surrounding rock mass of underground cavern should be reinforced when it is situated within the stress concentration zone. Full attention should be paid to the stress induced damages like rock burst and relaxation (scaling and fracturing).

Although some of the simplest clues to stress orientation can be estimated from the knowledge of a regional geology structure and its recent geologic history, yet quantitative information of in situ stresses requires the boundary and initial conditions, and field tests are the only true guide for important hydraulic structures (Goodman 1989; Yi et al. 2001; Yi and Chen 2003). To determine the magnitude and orientation of in situ stresses by the exploratory tests using a number of spatial reading points, much manpower and material resources are consumed. Basically, there are direct or indirect methods available for in situ stress testing. The former is represented by flat jack testing and hydraulic fracturing, which determines a circumferential normal stress component in the wall of a borehole; the latter is based on the determination of strain changes in the wall of a borehole, or other deformations of the borehole, induced by over coring that part of the hole containing the measuring device.

The in situ stresses tested in the same geology element commonly present scattered data by different methods. Even by a same test method, the data display large spatial dispersion, too. These are mainly blamed on the factors of discontinuity system, topography, erosion and denudation, apart from the errors resulted from test apparatus and operation.

(1) Intact rocks

It is also defined in engineering as "rock matrix" containing no naked-eye perceivable discontinuities. On the smaller scale however, it consists of grains with meso- or/and micro-structure governed by the geological events such as rock forming, water penetrating and weathering.

Table 2.2 Classification of rocks

Rock type		Example
Igneous rocks	Intrusives (plutonic)	Granite, Diorite, Porphyry
	Extrusives (volcanic)	Basalt, Rhyolite, Andesite, Tuff
Sedimentary rocks	Clastic sedimentary	Conglomerate, Sandstone, Shale
	Carbonatite	Limestone, Dolomite
	Weak and soft	Claystone
Metamorphic rocks	Ortho-rock	Gneiss, Hornblende schist
	Para-rock	Quartz, Marble, Slate, Phyllite, Chlorite schist

Three general classes of intact rocks are further subdivided into groups (see Table 2.2).

(2) Discontinuities

A discontinuity in geotechnical engineering is a plane or surface that marks a change in physical or chemical characteristics in a rock mass. There are three fundamental types of discontinuities, namely those who have been simply opened and are termed as “joints”, those who have been certain lateral movement and are termed as “shear zones” or “faults”, and those who emerge in sedimentary and layered volcanic rocks tightly linked with rock lithologic stratigraphy and are termed as “bedding planes”, “weak interlayers” or “intercalations”.

In geotechnical literatures, the term “fracture” is employed to denote the first and second types of discontinuities that are actually the separation in a geologic formation dividing the rock mass into several pieces. Fractures cause the rock to lose cohesion along its weakest plane and provide permeability networks for fluid movement.

Discontinuities possess many geometrical and mechanical features governing the overall properties of rock masses, particularly the anisotropy and heterogeneity in addition to the discontinuity with respect to their deformation, strength, and permeability.

1. Joints

A joint is a break (fracture) of natural origin in the rock most frequently manifesting as a member of joint sets. A joint set is a family of nearly parallel and evenly spaced joints that can be identified through mapping and analyzing their orientations, spacings, and physical properties. A joint system consists of at least two or more intersecting joint sets.

Joints are among the most universal geologic structures as they are found in the most exposures of the Earth crust. They vary greatly in appearance, dimension, and arrangement, and occur in quite different tectonic environments. Joints may be cleanly open or filled by various materials.

The stresses giving rise to joints were induced by the stretching of rock layers, the rise of pore fluid pressure, or the shrinkage due to cooling. Very often, the specific origin creating a joint set can be quite ambiguous and even controversial.

Joints result from brittle fracture of a rock mass may also be classified as "tensile joints" and "shear joints". Although it is possible to make such a discrimination by looking for the presence of slicken sides, yet from the standpoint of engineering it is not very necessary.

It is very important from the point view of engineering, that joints are described by their geometry features as follows:

- Spacing and frequency. Spacing is the distance between adjacent joint intersections with the measuring scan line. Frequency (i.e. the number per unit distance) is the reciprocal of the spacing.
- Orientation (trend, attitude). A joint is assumed to be planar whose dip direction (the compass bearing of the steepest line in the plane) and dip angle (the angle that this steepest line makes to the horizontal plane) uniquely define its orientation. It is either plotted on the stereonet and rose-diagram.
- Persistence. The extent of a joint in its own plane is commonly described using persistence, incorporated with the assumptions regarding the shape of the bounded plane and the associated characteristic dimensions (e.g. discontinuity discs of circular, ellipse, or rectangular).
- Roughness. The surface of the joint is usually uneven due to the existence of asperities and whose roughness may be defined either by reference to standard charts or mathematically (e.g. fractal geometry).
- Aperture. It is the perpendicular distance between the adjacent rock walls of a joint, which strongly dominates its permeability, nonlinear deformation and strength parameters as well.
- Sets. Joints occur for good mechanical reasons with some degree of clustering around preferred orientations associated with the formation mechanisms. Hence, it is untrivial to identify joint sets.

The stochastic characteristics of joint geometry features in the rock mass have been well studied and presented by Louis and Maini (1970), Baecher et al. (1977), Cruden (1977), Hudson and Priest (1983), Dershowitz (1984), Kulatilake and Wu (1984), Chiles (1988), Hakami and Larsson (1990), Kulatilake et al. (1993), Nicholl et al. (1999). These results lead to the selective probability distribution types and density functions for the center position, dip direction, dip angle, density, trace length, and aperture. However, in the practices of hydraulic engineering, the statistically average (or mean) value is always paramount in the structural design. Table 2.3 lists the available data of the dominant joint sets in Xiaowan Project in the phase of preliminary feasibility study.

Often imparting a well-developed permeability to rock masses, joints strongly influence, even dominate, the circulation of groundwater within bedrock. In addition, joints may have a significant influence on the mechanical behaviors (strength,

Table 2.3 Statistical data of the joint sets: Xiaowan Project (preliminary feasibility study)

Elevation (m)	Dominant attitude	Average space (m)	Average persistence (%)
<1050	N6°E, NW∠86°	0.42	82.3
	N10°W, NE∠30°	0.42	67.8
	N120°E, SE∠26°	0.24	57.85
	N7°E, SE∠87°	0.32	71.78
1050–1150	N10°E, NW∠83°	0.34	80.48
	N83°W, NE∠80°	0.43	90.02
	N14°E, SE∠30°	0.23	52.93
	N70°E, SE∠87°	0.26	63.21
>1150	N10°E, NW∠83°	0.33	77.70
	N83°W, NE∠80°	0.39	86.37
	N21°E, SE∠28°	0.25	54.03
	N70°E, SE∠87°	0.26	63.21

deformation, etc.) of rock masses in the construction of, for example, tunnels, dam foundations, and cut-slopes.

2. Faults

A fault is a large scale discontinuity in the rock mass, across which there had been significant displacement as a result of rock mass movement. Large faults within the Earth's crust result from the action of plate tectonic forces, with the largest ones forming the boundaries between the plates, such as subduction zones or transform faults. Energy release associated with rapid movement on active faults is the cause of most earthquakes.

A fault plane is normally represented by its mean fracture surface. A fault trace or fault line is the intersection of the fault plane with the ground surface commonly plotted on geologic maps.

Since faults usually do not consist of a single and clean fracture, geologists use the term "fault zone" when referring to the zone of complex deformation associated with the fault plane.

The two sides of a non-vertical fault are known as the hanging wall and footwall. By definition, the hanging wall occurs above the fault plane and the footwall occurs below. Slip is defined as the relative movement of geological features present on either side of a fault plane. Rocks within a fault zone are classified by their textures and their implied mechanism of deformation as:

- Cataclasite. A fault rock which is cohesive with poorly developed or even absent of planar fabric, or is incohesive and characterized by generally angular clasts and rock fragments in a finer-grained matrix of similar composition.
- Tectonic or fault breccia. A moderately-to coarsely grained cataclasite which contains >30% visible fragments.
- Fault gouge. An incohesive, clay-rich, finely-to ultrafinely grained cataclasite which may possess a planar fabric and contain <30% visible fragments.

- Clay-rich gouge. A fault rock formed in sedimentary sequence which contains clay-rich layers strongly deformed and sheared.
- Mylonite. A fault rock which is cohesive and characterized by a well-developed planar fabric resulted from tectonic reduction of grain size, and commonly contains rounded porphyroclasts and rock fragments of similar composition.
- Pseudotachylite. An ultrafine-grained and glassy-looking material, usually black and flinty in appearance.

In hydraulic engineering, a fault often forms a dominate discontinuity that may give rise to significant consequences on the mechanical behaviors (strength, deformation, etc.) of, for example, tunnels, dam foundations, or cut-slopes.

3. Intercalations

It is another kind of large scale discontinuities also termed as "weak (soft) interlayers". They primarily emerge in sedimentary and layered volcanic rocks and are tightly linked with the rock lithologic stratigraphy due to the deposition of weak materials into soft and sensitive stratum layers that are further disturbed by the interlayer shearing during tectonic folding movements followed by groundwater actions.

(GB50287-99) «Code for Water Resources and Hydropower Engineering Geological Investigation» (1999) distinguishes four weak interlayer types as argillic, clastic interbedded argillic, argillic interbedded clastic, clastics and crag (see Table 2.4).

(3) Rock masses

Engineers have developed various classification schemes for rock masses which are basically compromises between the use of a complete theory and the overlook of rock properties entirely (Brown 1981). All the existing rock mass classification schemes consider a few of the key features, and assign digital values to the classes (grades).

Table 2.4 Classification of weak interlayers (GB50287-99)

Type	Quantitative index		Shear strength parameters	
	Content of fine grain ($\leq$0.005 mm)	Content of clastics and crag ($\geq$2 mm)	f'	c' (MPa)
Clastics and crag	Non or few	>50%	0.55–0.45	0.250–0.100
Argillic interbedded clastic	0–10%	30–50%	0.45–0.35	0.100–0.050
Clastic interbedded argillic	10–30%	<30%	0.35–0.25	0.050–0.020
Argillic	>30%	–	0.25–0.18	0.005–0.002

These schemes may provide a short-cut to the rock mass properties that are more difficult to assess (e.g. the deformability), and provide direct guidance for engineering design (e.g. the type and amount of supporting required for a tunnel).

There are two prevalent classification schemes in the geotechnical engineering community essentially intended to estimate the supporting necessity of tunnels: one is the Q Method by Barton, another is the RMR System by Bieniawski (Hudson and Harrison 1997). Attempts also have been made to extend the classification systems, such as to the cut slopes (Romana 1993).

However, engineering practices for hydraulic projects have demonstrated that any classification systems, can only define the overall properties of rock masses within a limited spatial scope. It can by no means include those special geological elements of dominant significance which are difficult to be quantified by statistical data, e.g. the low-strength, thin-opening, and gently inclined discontinuities below the dam base which undermine the sliding resistant capacity of the dam.

In 1994, China promulgated the (GB50218-94) «Standard for Engineering Classification of Rock Masses». It includes the basic quality classification for rock mass applicable to assess the basic quality of rock mass, and the class identification of engineering rock masses intended to revise the basic quality index in conjunction with specific engineering undertakings.

The basic quality index (BQ) of rock mass is given by the formula

$$BQ = 3R_c + 250K_v \tag{2.1}$$

where R_c = uni-axial compression strength of saturated rock, MPa; K_v = index representing the rock mass integrity.

$$K_v = \left(\frac{V_{pm}}{V_{pr}}\right)^2 \tag{2.2}$$

where V_{pm} = primary wave velocity of rock mass, km/s; V_{pr} = primary wave velocity of rock matrix, km/s.

Equation (2.1) is subject to the following constraints:

- For a given K_v by Eq. (2.2), if $R_c > 90K_V + 30$, then assuming $R_c = 90K_v + 30$ for the calculation of BQ.
- For a given R_c, if $K_v > 0.04R_c + 0.4$, then assuming $K_v = 0.04R_c + 0.4$ for the calculation of BQ.

The rock mass quality classification based on the value of BQ is elaborated in Table 2.5.

In case of difficulty, the parameters R_c and K_v may be estimated using point load strength index $I_{(s)50}$ and volumetric joint count J_v of rock mass, according to Eq. (2.3) and Table 2.6.

Table 2.5 Standard for basic quality classification of engineering rock masses (GB50218-94)

Basic quality grade	1	2	3	4	5
Basic quality index BQ	>550	550–451	450–351	350–251	<251
Qualitative traits for basic quality classification	Hard and integral rock mass	① Hard/fairly integral rock mass; ② Fairly hard/integral rock mass	① Hard/fairly fissured rock mass; ② Fairly hard or alternating hard and soft/fairly integral rock mass; ③ Comparatively soft/integral rock mass	① Hard/fissured rock mass; ② Fairly hard/fairly fissured to fissured rock mass; ③ Fairly hard or alternating hard and soft rock predominated by soft rock/fairly -integral to fairly fissured rock mass; ④ Soft/very fissured rock mass	① Comparatively soft/fissured rock mass; ② Soft/fairly-fissured to fissured rock mass; ③ Very soft/very fissured rock mass

Table 2.6 Relationship between K_v and J_v (GB50218-94)

J_v (count/m^3)	<3	3–10	10–20	20–35	>35
K_v	>0.75	0.75–0.55	0.55–0.35	0.35–0.15	<0.15

$$R_c = 22.82 I_{(s)50}^{0.75} \tag{2.3}$$

where $I_{(s)50}$ = point load strength index using cylindrical sample (ϕ50 mm), MPa.

In the phase of planning or preliminary study, when the field testing data are unaccessible, the shear strength parameters of foundation rock may be selected according to the rock classification described above, subject to the revision taking into account of geologic settings, characteristics of discontinuities, recommendation of design specifications, as well as the data from analogue projects.

2.2.3 *Steel Bars and Wires*

Steel is an alloy of iron and other elements, primarily carbon, widely consumed in engineering structures and other applications attributable to its high tensile strength. The earliest known production of steel—pieces of iron ware excavated from an archaeological site in Anatolia (Kaman-Kalehoyuk), are nearly 4000 years old dating from 1800 BC (Akanuma 2005).

In the Chinese specifications (GB 1499) «Hot-rolled and ribbed steel bar used in reinforced concrete», steel bars fall into grade HRB400 and grade HRB335; in the Chinese specifications (GB 13013) «Hot-rolled and plain round steel bar used in reinforced concrete», steel bars grade HPB235 is noted as Q235 for hydraulic engineering; in the Chinese specifications (GB 13014) «Waste-heat treated steel bar used in reinforced concrete», steel bars RRB 400 is noted as KL400 for hydraulic engineering. By pre-stress steel strand it means the steel wire of stress–relieved, spiral ribbed and indented on three sides, as specified in (GB/T 5523) «Steel wires used in prestressed concrete». The mostly consumed steel materials in hydraulic structures for the purpose of reinforcement are steel bars (bolts) and wires (strands) summarized in Table 2.7. The digit following the letters is the characteristic value of tensile strength. For hot-rolled steel bars it is determined on the basis of yield strength f_{yk}. In contrast, the characteristic strength of pre-stress steel wires and heat-treated steel bars is determined on the basis of peak (ultimate) tensile strength f_{ptk}.

2.3 Density

Density (ρ) is one of the important properties of matters. It is defined as the ratio of mass by volume.

2.3.1 Concrete

The density of concrete may be adjusted or controlled through the selection of aggregates, by which the deformability as well as the resistance capacity (stability), may be "adjusted" to a certain extent.

Most natural mineral aggregates, such as sand and gravel, produce normal-weight concrete with an approximate density of 2400 (kg/m^3), which is subjected to slight variation within a range of 1.5% following the concrete grade—it is generally higher for higher grade concrete. This variation should be carefully studied, particularly for gravity dams, since the dam body size and corresponding expenditures will be significantly influenced by the concrete density.

2.3.2 Rocks

The rock density varies from the lowest 2.10 (g/cm^3) (e.g. standstone and limestone) to the highest 3.1 (g/cm^3) (e.g. granite and basalt) depending on its type and weathering degree. In Table 2.8 the density values of representative intact rocks are summarized (Wu and Zhou 2013).

Table 2.7 Characteristic tensile strength values for mostly used steel bars in hydraulic structures (GB 1499; GB/T 5523)

Type		Notation	Nominal diameter D (mm)	Elastic modulus E_s ($\times 10^5$ N/mm^2)	Poisson's ratio μ	Standard value of yield strength f_{yk} (N/mm^2)	Standard value of ultimate strength f_{ptk} (N/mm^2)	Elongation ratio δ_{gt} (%)
Hot rolled steel bar (bolt)	HPB235	Φ	6–22	2.10	0.3	235	375	>10
	HPB300	Φ	6–22	2.10	0.3	300	425	>10
	HRB335	Φ	6–50	2.0	0.3	335	455	>7.5
	HRB400	Φ	6–50	2.0	0.3	400	540	>7.5
	RRB400	Φ^R	8–40	2.0	0.3	400	540	>5.0
Strand wire (anchor cable)	1 × 3	Φ^S	8.6, 10.8, 12.9	1.95	–	–	1570, 1860, 1960	–
	1 × 7	Φ^S	9.5, 11.1, 12.7, 15.2, 17.8	1.90	–	–	1720, 1860, 1960	–
			21.6	1.95	–	–	1860	–

Table 2.8 Density values of intact rocks (Wu and Zhou 2013)

Rock type			Density (g/cm^3)
Igneous rocks	Intrusives (plutonic)	Granite	2.58–2.60
		Diorite	2.72–2.99
		Porphyry	2.60–2.89
	Extrusives (volcanic)	Basalt	2.5–3.1
		Rhyolite	2.28–2.70
Sedimentary rocks	Clastic sedimentary	Sandstone	2.20–2.71
		Shale	2.3–2.62
	Carbonatite	Limestone	2.66–2.71
		Dolomite	2.10–2.90
	Weak and soft	Claystone	2.24–2.6
Metamorphic rocks	Ortho-rock	Gneiss	2.30–2.98
	Para-rock	Quartz	2.4–2.8
		Marble	2.6–2.87
		Slate	2.50–2.90
		Phyllite	2.71–2.86
		Schist	2.77–3.01

2.3.3 Steel Bars and Wires

Steel comes in many different forms whose densities differ by type. The normally used steel bar exhibits a density of 7.85 (g/cm^3).

Due to very lower volumetric proportion in rocks and mass concrete, the weight of steel bars or/and strand wires is normally neglected in the structural computation.

2.4 Permeability

The foundation and dam materials are pervious to a certain extent, and seepage flow will occur attributable to the up-and down-stream head differences. Permeability is a mechanism of the ease with which a fluid (i.e. water) will flow through the porosity/fracture system of concrete and rock. Intact rocks and concrete exhibit lower permeability because the water does not flow easily through them. However, rock masses are commonly higher permeable where discontinuities (joints, faults, etc.) conduct water more readily.

Permeability is an important property as it will impose direct effects on the stability and can represent a significant cost, of the hydraulic structure (Louis and Maini 1970; Hsieh and Neuman 1985; Hsieh et al. 1985).

Permeability characteristics depend on the distribution, shape and orientation of the percolation network consisting in pores, ITZs, cracks and discontinuities, in a rock-like material. For the lower pervious concrete without serious construction

defects, it will take a long time (maybe several decades or even longer) to form a stable regime of seepage. On the contrary, attributable to a large amount of high permeable joints, fissures, and other structural planes, the foundation rock will take a much shorter time to form a stable seepage regime.

The water percolated into the rock-like materials builds up pore water pressure (Harza 1949; Keener 1950; Casagrande 1961; Cedergren 1989). The load due to pore water pressure exerting on the pervious dam/foundation is not a kind of boundary traction but rather a kind of volumetric force. Since the calculations in a volumetric way are relatively more complicated, hence it is often simplified as boundary traction, i.e. the "uplift", for the convenience of analysis. Another reason for the use of uplift lies in the fact that discontinuities in foundation rocks and construction joints in dam concrete are often weak faces dominating the water percolation, consequently the uplift action may by postulated as a interstitial water pressure having characteristics of boundary traction. Traditionally, only the pore water pressure which exerts upwards on a horizontal dam base or a horizontal section within the dam is named as uplift. Nowadays, this term is commonly referred to the resultant effective component of interstitial water pressure perpendicular to any plane, e.g. the dam/base interfaces, construction joints, or discontinuities within the underlying bedrock. However, this term and definition are not applicable in tunneling engineering. The uplift offsets a part of the selfweight of hydraulic structure, therefore it is unfavorable to the stability against sliding and the strength control. Although the built-up of pore water pressure and affected factors are quite complicated, yet after several decades of observation and research they are understandable and may be controlled well.

Other concepts related to the seeping water are the "excess pore pressure" and "effective stress". The importance of the forces transmitted through the soil skeleton from particles to particles was recognized in 1923 when Terzaghi presented the principle of effective stress transmitted through the soil skeleton only

$$\sigma = \sigma' + p \tag{2.4}$$

where p = pore water pressure or seepage pressure, MPa; σ = total stress, MPa; σ' = effective stress, MPa.

A just completed concrete dam manifests no seepage and usually $p = 0$. After a certain term of service when a portion of dam and foundation is saturated, the pore water pressure is built-up.

In the embankment dam design, the principle of effective stress is important in which the pore water pressure is denoted as u in lieu of p in Eq. (2.4). When a load is applied in a fully saturated soil, at beginning it may be resisted partially by inter particle forces and partially by the increased pressure of the pore water above the static value due to the deformation of solid skeleton. The component of pore water pressure u_e above the static value u_s is known as the "excess pore water pressure", i.e. $u = u_s + u_e$. The reduction in excess pore water pressure as drainage takes place is described as "dissipation". As the excess pore water pressure dissipates, the effective stress increases, accompanied by a corresponding reduction in volume.

When the dissipation of excess pore water pressure is completed, the increment of total stress will be carried entirely by the soil skeleton. This phenomenon is called "consolidation".

For dam concrete and foundation rocks, the transient state process of built-up and dissipation of excess pore water pressure is normally not considered in their quasistatic computation, i.e. $p = u = u_s$.

In general, neglecting the percolation threshold (Burgisser et al. 2017), the anisotropic seepage may be approximately described by the "Darcy's law", which linearly links the seepage velocity $\{\mathrm{v}\}$ and the gradient $\{J\}$ with regard to the hydraulic potential (water head) ϕ through a permeability tensor $[k]$ as

$$\{\mathrm{v}\} = [k]\{J\} \tag{2.5}$$

In which

$$\{v\} = [v_x \ v_y \ v_z]^T \tag{2.6}$$

$$\{J\} = [J_x \quad J_y \quad J_z]^T = -\left[\frac{\partial \phi}{\partial x} \quad \frac{\partial \phi}{\partial y} \quad \frac{\partial \phi}{\partial z}\right]^T \tag{2.7}$$

$$[\mathrm{k}] = \begin{bmatrix} k_{xx} & k_{xy} & k_{xz} \\ k_{yx} & k_{yy} & k_{yz} \\ k_{zx} & k_{zy} & k_{zz} \end{bmatrix} \tag{2.8}$$

Towards the formulation of governing equations related to PDEs and constitutive laws (relations) and boundary conditions, as well as corresponding algorithms, in the whole coverage of this book the global Cartesian coordinate system will be particularly defined using capital letters with its X-axis and Y-axis being horizontal, and Z-axis being upright. In addition, Y-axis points northward and X-axis points eastward. Whereas the axes using small letters (x, y, z) in Eqs. (2.6)–(2.8) form a local Cartesian coordinate system. Sometimes, a subscript is bound at the local coordinates or corresponding variables to indicate a specific material (e.g. j for joint, b for bolt, g for grout, w for stranded wire, p for cooling pipe), and if necessary (not always), a superscript is further employed to indicate whether the local coordinate system is of Cartesian (ca) or Cylindrical (cy).

The permeability tensor possesses an important and useful feature, namely the existence of permeability ellipsoid. The ellipsoid is defined with the semi-axes of $1/\sqrt{k_1}$, $1/\sqrt{k_2}$, and $1/\sqrt{k_3}$, where k_1, k_2 and k_3 are three principal permeability coefficients ($k_1 \geq k_2 \geq k_3$).

For the conceptual isotropic material at macro-scale level such as concrete or a large portion of intact rock, Eqs. (2.5)–(2.8) are simplified as

$$\begin{cases} v_x = -k\frac{\partial \phi}{\partial x} \\ v_y = -k\frac{\partial \phi}{\partial y} \\ v_z = -k\frac{\partial \phi}{\partial z} \end{cases} \tag{2.9a}$$

or

$$\begin{Bmatrix} v_x \\ v_y \\ v_z \end{Bmatrix} = -\begin{bmatrix} k & 0 & 0 \\ 0 & k & 0 \\ 0 & 0 & k \end{bmatrix} \begin{Bmatrix} \frac{\partial \phi}{\partial x} \\ \frac{\partial \phi}{\partial y} \\ \frac{\partial \phi}{\partial z} \end{Bmatrix} \tag{2.9b}$$

In which scalar k is termed as "permeability coefficient".

2.4.1 Concrete

The permeability coefficients of well cured modern concrete, which are strongly related to its density, usually vary between 10^{-5} and 10^{-9} cm/s.

Professional judgment in the design of hydraulic concrete should take into consideration not only the strength, deformation, and permeability, but also its durability that has serious implications for the life cycle of a hydraulic structure. Durability of concrete is defined as its service life under given environmental settings. Permeable concrete is, of course, less durable. Generally, watertight concrete endures for a long time. The excellent conditions of the 2000-plus years old concrete linings of several aqueducts in Europe built by the Romans provide a living testimony to the long-term durability of concrete in moist environments. It is obvious that there is a relationship between strength and durability since low strength is associated with high porosity (low density) and high permeability.

The permeability of concrete depends not only on the mix proportion, compaction, and curing, but also on the micro-or meso-scale cracks caused by the ambient temperature and humidity cycles. It also should be emphasized that the loss of mass by surface wear and cracking as well as leaching of the components of hardened cement paste due to soft water or acidic fluids (sulfate attack), would increase the porosity of concrete, which in turn, make the concrete more vulnerable to abrasion and erosion.

Instead of permeability coefficient, impermeability grade is normally employed as a key index in the durability design of hydraulic concrete. To meet the impermeability requirement, the water-cement ratio W/C must not exceed 0.5–0.55, and care should be taken to avoid separation of concrete mix into layers during handling and placing it in the framework.

In China, by the index of impermeability the concretes are classified into six impermeability grades *W*2, *W*4, *W*6, *W*8, *W*10 and *W*12 in which the subsequence digit indicates the pressure of water (in atmospheres) against which standard cured

samples of concrete at age of 28 days can withstand (for continuous 8 h) without allowing the water to percolate through them. Similar to the strength grading, a definition of 60, 90, 180 days, etc., may also be applicable with regard to the initial exerting time of head gradients on the hydraulic structure.

Impermeability grade testing employs cylindrical steel mould samples of ϕ450 mm × 450 mm for fully-graded concrete, and 150 mm high taper steel mould samples with top diameter ϕ170 mm and bottom diameter ϕ180 mm for wet-screened (two-graded) concrete. The procedure is specified in the design codes DL/T5150-2001 and SL352-2006.

The conventional impermeability test facilities may provide the relative permeability coefficient calculated according to the penetrating height and exerting pressure. Related to the absorption and unsaturated seepage mechanism, this relative permeability coefficient cannot be directly used in the seepage analysis of the concrete structures before appropriate revisions. The design codes DL/T5150-2001 and SL352-2006 advisably relate the impermeability grade to the permeability coefficient k (see Eqs. 2.9a, 2.9b) and allowable hydraulic gradient [J] (see Eq. 4.216) in Table 2.9, for the reference in preliminary design phases.

Table 2.10 gives the impermeability testing data of the concrete $C_{180}40$ for Xiaowan Arch Dam, China. From these data it is clear that a remarkable difference between the fully-graded and wet-screened (two-graded) concretes does exist in the relative permeability. It is also demonstrated that by adding aggregates to cement paste or mortar strengthens the permeability considerably, the larger of the aggregate size, the greater is the coefficient of permeability.

The explanation as to why the permeability of concrete is higher than that of the corresponding cement paste lies in the micro-and meso-cracks normally appearing in the "interfacial transition zone" (ITZ) between the aggregate and cement paste. During the early hydration period the ITZ is weak and vulnerable to cracking due to differential strains between the aggregate and the cement paste induced by drying shrinkage, thermal shrinkage, and externally applied load. These micro-and meso-scale cracks are too small to be perceived by the naked-eye, but are larger than most capillary cavities in the cement paste matrix. Later on, the propagation of these cracks establishes the interconnections for seeping water percolation.

Table 2.9 Relationship of concrete impermeability grade and permeability coefficient (DL/T5150-2001; SL352-2006)

Impermeability grade	*W*4	*W*6	*W*8	*W*10
Permeability coefficient k ($\times 10^{-8}$ cm/s)	0.783	0.419	0.261	0.177
Allowable hydraulic gradient [J]	$[J] < 10$	$10 \leq [J] < 30$	$30 \leq [J] < 50$	$[J] \geq 50$

Table 2.10 Data summarized from the impermeability grade test ($C_{180}40$): Xiaowan Arch Dam

Aggregate gradation	Impermeability grade	Penetration height (cm)	Relative permeability (10^{-7}m/s)
Fully-graded	>W14	3.93	7.74
Wet-screened (two-graded)	>W14	3.19	5.11
F/W ratio	–	1.23	1.51

2.4.2 Rocks

Study on the permeability properties of rocks may be accomplished by in situ tests and laboratory tests. In situ tests are normally conducted by pumping or packer techniques in a single borehole to get permeability coefficient. Although such tests are very valuable for understanding the permeability of rocks, yet a convincible evaluation of permeability coefficient could be the most difficult task, particularly for jointed rock masses, due to the heterogeneity of the foundations and the limitations of test procedures. By the postulations of three orthogonal sets of joints in a rock mass, triple hydraulic probe was proposed by Louis in 1970 for permeability tensor. Later on, cross-hole test was also proposed by Hsieh and Neuman in 1985 for the same purpose.

The concepts of primary permeability and secondary permeability in rock masses are widely accepted nowadays. The former refers to the rock matrix (intact rock) permeability, whereas the latter indicates the rock mass permeability dominated by discontinuities. Usually, the presence of discontinuities in a rock mass gives rise to a much higher secondary permeability than the primary one. Therefore, in most rock permeability problems encountered in hydraulic engineering, the secondary permeability plays much more important role in the cutoff and dewatering design.

(1) Intact rocks

For intact rocks, there are two testing types suggested by the Paris Laboratory (France), namely straight (axial) flow and radial flow. Since the former is restrained by the upper bound of $k = 10^{-8}$ cm/s, hence the latter is more popular. In the radial flow test, cylinder samples at a height of 150 mm and with a diameter of 60 mm are processed. Along the sample axis a hole of 125 mm deep with 12 mm diameter is drilled. The water pressure may be exerted either from its external or interior surface, the seeping water is flowing in radial direction.

The permeability coefficients of various intact rocks in Table 2.11 are collected from laboratory testing data available in a number of literatures (Brace et al. 1968; Farmer 1968; Serafim 1968; Jaeger et al. 2007; Wu and Zhou 2013). They range from approximately 10^{-3} (cm/s) (glenrose sandstone) to 10^{-11} (cm/s) (granite and shale).

Table 2.11 Permeability coefficients of intact rocks (Wu and Zhou 2013)

Rock type			Permeability coefficient k (cm/s)
Igneous rocks	Intrusives (plutonic)	Granite	5×10^{-11}–2×10^{-7}
		Diorite	8×10^{-11}–8×10^{-7}
		Porphyry	6×10^{-11}–2.5×10^{-7}
	Extrusives (volcanic)	Basalt	1.0×10^{-12}
		Rhyolite	1.0×10^{-11}–1.0×10^{-10}
Sedimentary rocks	Clastic sedimentary	Sandstone	1.6×10^{-7}–1.2×10^{-5}
		Shale	1.0×10^{-9}–5.0×10^{-13}
	Carbonatite	Limestone	7.0×10^{-10}–1.2×10^{-7}
		Dolomite	7.0×10^{-10}–1.2×10^{-7}
	Weak and soft	Claystone	6.0×10^{-7}–2.0×10^{-6}
Metamorphic rocks	Ortho-rock	Gneiss	4.0×10^{-12}–3.0×10^{-5}
	Para-rock	Quartz	1.8×10^{-10}–1.0×10^{-9}
		Marble	1.0×10^{-11}–1.0×10^{-10}
		Slate	7.0×10^{-11}–1.6×10^{-10}
		Phyllite	1.0×10^{-6}–1.0×10^{-5}
		Schist (fissured)	1.0×10^{-9}–5.0×10^{-8}

(2) Joints and interlayers

A rock joint may be unfilled or filled. An unfilled joint may, in turn, be opened or closed with asperity contact. Towards the estimation of its permeability, an unfilled joint is customarily simplified into two parallel smooth slabs with a determinative aperture. Lots of theories were proposed in light of this simplification, of which the "cubic law" firstly introduced by Boussinesq (1868) for the problem of the laminar flow of a viscous and incompressible fluid in two parallel smooth slabs, is the most classical and prevalent (Snow 1969).

For an open and smooth joint (see Fig. 2.1), the unit fluid flow rate q observes

$$q = -CJ = -k_f aJ \tag{2.10}$$

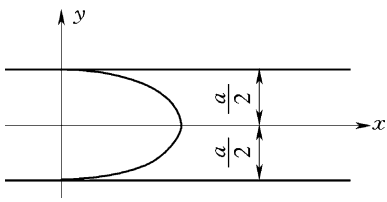

Fig. 2.1 Velocity pattern in a parallel and smooth joint

In which C is the hydraulic conductivity of joint, a is the hydraulic aperture of joint, and k_f is the equivalent permeability coefficient parallel to the joint surface calculated by the formula

$$k_f = \frac{ga^2}{12v} \tag{2.11}$$

where v = coefficient of water viscosity, cm^2/s.

Equation (2.10) is actually identical to the Darcy's law if we introduce the average velocity in joint as $v = \frac{q}{a}$.

Joint aperture is rather tiny but significantly influential to joint permeability, so it should to be gauged as precisely as possible in spite of difficulties (Kacewicz 1994).

Lomize (1951) experimentally validated the cubic law for laminar flow (Re < 500) using parallel glass plates. He also investigated the effect of roughness that accounted for the deviations from the ideal cubic law. Romm (1966) investigated fine (10–100 μm) and superfine (0.25–4.3 μm) joints by using various fluids, and he demonstrated that laminar flow in a joint observes the cubic law, at least, down to apertures of 0.02 μm. Witherspoon et al. (1980) studied the cubic law in both open and closed joints with regular asperity contact, and reported that the cubic law is held in the closed joint with aperture varying from 4 to 250 μm.

For rough joints with asperities (protuberances) on joint surfaces against permeability, modifications should be made for Eqs. (2.10) and (2.11) in order to take into account the surface roughness by introducing the contact area ratio (Louis 1969; Walsh 1981). Other famous works on the modification of the cubic law were worked out by Tsang and Witherspoon (1981), Barton et al. (1985), Fernandez and Moon (2010) introduced the hydraulic aperture into the cubic law as an appropriately weighted average aperture, which is a function of initial hydraulic joint aperture, joint aperture reduction factor and joint closure.

The author of this book proposed a "filled model" (Chen et al. 1989) which equates the asperities as a thin layer of evenly "filled" medium with certain deformation and permeability characteristics. In this manner, a unified model for both the filled and unfilled joints can be established, and Eq. (2.10) holds for the both joint types. For the filled joint, k_f is the permeability coefficient parallel to the joint surface of the natural filler medium, whereas for the unfilled and open joint, k_f is calculated according to the cubic law (see Eq. 2.11) or its modifications available; for the unfiled and closed joint, the asperities are looked at as a thin layer of virtual filler material with high porosity. This is simple and facilitates the computation algorithms, particularly in handling HM coupling problems.

In additional to the global coordinate system X–Y–Z in Fig. 2.2, a special local Cartesian coordinate system for the joint segment j is defined with its z_j-axis being perpendicular to the joint and upward, the y_j-axis being on the joint and pointing in the direction of dip, the x_j-axis being formed by the right hand rule (see Fig. 2.2). θ_j and ϕ_j are the dip angle and dip direction of the joint.

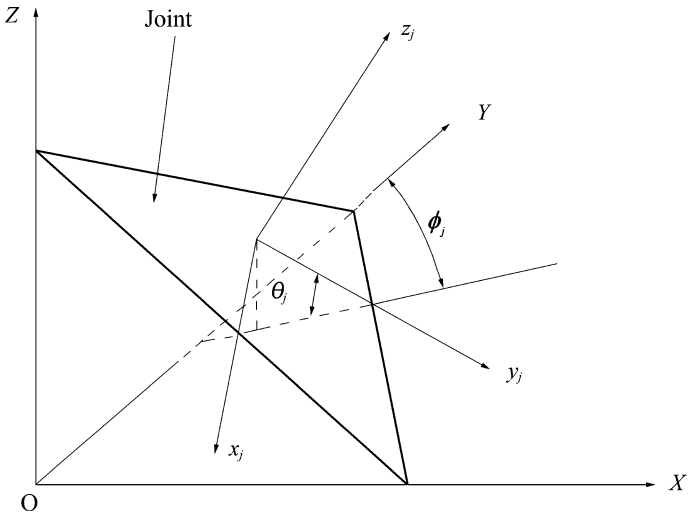

Fig. 2.2 Coordinate systems of joint segment j

The coordinate (displacement and velocity as well) transformation may be undertaken by

$$\begin{cases} \{x\}_j = \begin{Bmatrix} x_j \\ y_j \\ z_j \end{Bmatrix} = \begin{bmatrix} l_{11} & l_{12} & l_{13} \\ l_{21} & l_{22} & l_{23} \\ l_{31} & l_{32} & l_{33} \end{bmatrix} \begin{Bmatrix} X \\ Y \\ Z \end{Bmatrix} = [l]_j \{X\} \\ \{\mathrm{X}\} = \begin{Bmatrix} X \\ Y \\ Z \end{Bmatrix} = \begin{bmatrix} l_{11} & l_{21} & l_{31} \\ l_{12} & l_{22} & l_{32} \\ l_{13} & l_{23} & l_{33} \end{bmatrix} \begin{Bmatrix} x_j \\ y_j \\ z_j \end{Bmatrix} = [l]_j^T \{x\}_j \end{cases} \tag{2.12}$$

where

$$[l]_j = \begin{bmatrix} \cos\phi_j & -\sin\phi_j & 0 \\ \sin\phi_j \cos\theta_j & \cos\phi_j \cos\theta_j & -\sin\theta_j \\ \sin\phi_j \sin\theta_j & \cos\phi_j \sin\theta_j & \cos\theta_j \end{bmatrix} \tag{2.13}$$

Suppose the flow on the joint surface is isotropic, the Darcy's law with respect to the average velocity in the local coordinate system is

$$\begin{cases} v_x = -k_f \frac{\partial \phi}{\partial x} \\ v_y = -k_f \frac{\partial \phi}{\partial y} \\ v_z = -k_f \frac{\partial \phi}{\partial z} \end{cases} \tag{2.14a}$$

In which k_f is computed by the cubic law (see Eq. 2.11) for an open-and unfilled joint, or by the "filled model" for any joints using the permeability coefficient of the

virtual filler medium. Where the joint walls are impervious or the flow exchange between adjacent intact rock blocks is neglected, we have $v_z = 0$ and

$$\begin{cases} v_x = -k_f \frac{\partial \phi}{\partial x} \\ v_y = -k_f \frac{\partial \phi}{\partial y} \end{cases} \tag{2.14b}$$

(3) Rock masses

The secondary permeability of rock is several orders higher than the primary permeability in magnitude, due to the existence of discontinuity networks.

Usually, joints manifesting in sets are planar and in parallel. The aperture of joint ranges from 0.000001 to 0.01 m, the trace of joint varies from several meters to tens of meters. The real world model of the rock mass with complex discrete fracture network-porosity system is fairly difficult to be established (Kranz et al. 1979; Nuezil and Tracy 1981; Kolditz 1995; Singhal and Gupta 2010). In view of the much larger dimension of hydraulic structures (e.g. dams), equivalent continuum approach which smears the joints of high density, is commonly recognized as a reasonable compromise between the real world and research level related to the investigations, experiments and computations. Further, the laminar flow may be postulated on the safe side due to the tiny aperture of joint, hence the cubic law or/and Darcy's law holds. On these basic assumptions the beautiful linear constitutive Eqs. (2.5)–(2.11) relating seepage velocity and hydraulic gradient, may be employed.

However, it should bear in mind that these assumptions are actually problematic. A successful application of the equivalent continuum approach relies on the corner stone that a REV for the hydraulic behavior exists and its size is much smaller than the characteristic dimension of the structure concerned. Theoretically, the REV is defined as the size beyond which the rock hydraulic permeability tensor keeps unchanged. Practically, it is identified where the permeability components only exhibit minor fluctuation when the size of rock samples increases. Unfortunately insofar, this is a not well answered question and leaves a large room for the further study (vide Chap. 18).

1. Analytical solutions

Most joints in rock masses may be grouped into sets, each set is assumed with constant aperture, uniform spacing and dominant orientation. The rock mass permeability is contributed from individual joint set and intact rock matrix. Ignoring the water exchange between joint sets, the equivalent permeability tensor of a jointed rock mass is formulated by a "fracture tensor" (Snow 1969). Use is made of the expressions in Eqs. (2.9a, 2.9b)–(2.14a, 2.14b), we have

$$[K] = \sum_{j=1}^{n} \frac{g a_j^3}{12 b_j \nu} [l]_j^T [l]_j + [k_r] \tag{2.15}$$

In which n is the amount of joint sets; j is the serial number of joint sets; a_j is the hydraulic aperture of joint; b_j is the joint spacing; k_r is the primary permeability coefficient of intact rock matrix, which can be ignored if the intact rock is relatively impermeable.

In view of the finite size of joints in rock masses, Oda (1986a, b) revised Eq. (2.15) by introducing the connection coefficient ψ_j to give

$$[K] = \sum_{j=1}^{n} \psi_j \frac{g a_j^3}{12 b_j v} [l]_j^T [l]_j + [k_r] \tag{2.16}$$

Under the circumstances that the joint set j is persistence, $\psi_j = 1$.

Where the filled model for joints is employed, the corresponding permeability tensor may be simply generalized from Eq. (2.16) as

$$[K] = \sum_{j=1}^{n} \psi_j \frac{k_f a_j}{b_j} [l]_j^T [l]_j + [k_r] \tag{2.17}$$

Towards the influence of joint persistence on the permeability of rock mass, a simple relation between the connectivity ratio η and the connection coefficient ψ_j was established by He and Chen (2012) who postulated the distribution of joint segments in a manner schematically illustrated in Fig. 2.3, where the length of seepage path in joint j is $L_f = \sum_j L_{fj} = \eta L$, the length of seepage path in rock bridge is $L_r = \sum_j L_{rj} = (1 - \eta)L$, and the entire length of seepage path in rock mass is $L = \sum_j L_{fj} + \sum_j L_{rj}$ (connectivity ratio $0 \le \eta \le 100\%$).

The seepage path in the rock bridge is entailed within a zone whose quantification is difficult—it may be the Path 1, Path 2, Path 3 or even more complicated ones (see Fig. 2.4). This zone is therefore constrainedly simplified as a channel wider than a and parallel to the joint surface. The width of this potential seepage channel in rock bridge is assumed to be the product of the joint aperture a and the parameter m (m > 1) termed as "connection adjusting coefficient".

By the continuity principle of the seepage flow in joint segment and rock bridge channel, the relation between the connection coefficient ψ and the connectivity ratio η may be deduced as

$$\psi = \frac{1}{12} \frac{m k_r}{\eta m k_r + (1 - \eta) k_f} \tag{2.18}$$

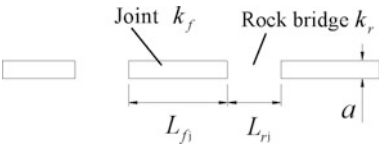

Fig. 2.3 Diagram to the simplification of joint connectivity ratio

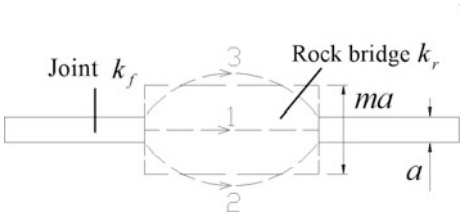

Fig. 2.4 Sketch of the seepage path in the rock bridge

where ψ = connection coefficient; η = connectivity ratio; m = connection adjusting coefficient; k_r = permeability coefficient of rock bridge; k_f = permeability coefficient of joint.

The connection adjusting coefficient may be evaluated by numerical testing at the sample level or the back analysis using field testing data. Dependent on the factors such as the rock type and joint connectivity ratio, m varies between 6 and 6000 (He and Chen 2012).

2. Field tests

Traditional tests towards the estimation of permeability are summarized by Hoek and Bray (1981). These include the borehole falling-head (pumping) test, the borehole recharge test and the borehole packer test. The last one is suitable to the case of lower underwater table and is mostly exercised in the China's hydraulic engineering. The (SL31-2003) «Code of Water Pressure Test in Borehole for Water Resources and Hydropower Engineering» stipulates that the borehole diameter should be 59–150 mm, for each packer segment the pressure should be increased by three incremental steps as 0.3, 0.6 and 1.0 MPa.

Through the borehole packer test, the unit filtration rate ω was traditionally computed to characterize the permeability of rock

$$\omega = \frac{\mathrm{Q}}{h_0 l} \tag{2.19}$$

where ω = unit filtration rate, L/(min m m); Q = gauged flow rate, L/min; h_0 = packer pressure, m; l = packer length in the borehole, m.

After the 1990s, ω has been replaced by the Lugeon [Lu L/(min m MPa)] to characterize the water percolation rate

$$q = \frac{\mathrm{Q}}{pl} \tag{2.20}$$

where p = pressure of the packer length, MPa; Q = gauged flow rate, L/min.

One unit water percolation rate (Lu) is equal to $\omega = 0.01$ L/(min m m).

Where the test segment is under water table and the unit water percolation rate is smaller than 10 Lu, the permeability coefficient may be estimated by the formula

$$k = \frac{Q}{2\pi l \Delta h} \ln \frac{l}{r_0} \tag{2.21}$$

where r_0 = radium of the bore hole, m; Δh = head difference between the injected water and groundwater, m.

Although such estimated permeability coefficient suffers from various deficiencies, it is very useful as a preliminary index in the evaluation of rock mass permeability in hydraulic engineering.

To test the principal permeability coefficients of rock masses on a larger scale (between boreholes), Louis (1974a, b) invented a technique that drills one injection hole and two monitoring holes, the shortest lines between monitoring holes and the injection hole are parallel to the rest two principal permeability coefficients. The pressure readings inside the monitoring holes make it possible to compute all the three unknown principal permeability coefficients.

Hsieh and Neuman (1985) improved the Louis's technique and termed it as "cross-hole testing". It consists of injecting water into (or withdrawing water from) the packed-off intervals in a number of boreholes meanwhile monitoring the transient head response in the similar intervals of neighborhood boreholes. The directions of the principal permeability tensor need not be known prior to the test, and the boreholes may possess arbitrary orientations. It also provides direct field information on whether it is proper to regard the medium as being homogeneous and anisotropic on the scale of test.

Table 2.12 summarizes the principal values of rock mass permeability tensors in a number of China's hydraulic projects, meanwhile Table 2.13 gives the full permeability tensors of granitic gneiss in the foundation and abutments of Xiaowan Arch Dam. They were all obtained from in situ tests and revised according to the geologic conditions.

Table 2.12 Principal values of rock mass permeability tensors of several China's hydraulic projects

Project	Position	Rock type	Dominant fracture sets	Principal values of equivalent permeability tensor (10^{-3} cm/s)		
				k_1	k_2	k_3
Three Gorges	Ship lock slope	Granite (slightly weathered)	3	0.0365	0.0321	0.0033
Longtan	Cut slope	Sandstone (slightly weathered)	5	0.007983	0.005438	0.005438
Pushihe	Dam foundation	Granite (weakly weathered)	3	0.355	0.143	0.133
Lingnan	Cut slope	Meta sandstone (weakly weathered)	4	0.740	0.287	0.181

Table 2.13 Permeability tensors of the granitic gneiss: Xiaowan Project, China

Elevation (m)		Permeability tensor (m/d)					
		Left bank			Right bank		
1245–1050	Shallow	0.0356	−0.0009	0.0096	0.0340	0.0097	−0.0190
		−0.0009	0.1769	−0.0030	0.0097	0.1727	−0.0029
		0.0096	−0.0030	0.1600	−0.0190	−0.0029	0.1598
	Middle	0.0024	−0.0001	0.0006	0.0019	0.0007	−0.0011
		−0.0001	0.0129	−0.0002	0.0007	0.0121	−0.0002
		0.0006	−0.0002	0.0117	−0.0011	−0.0002	0.0116
	Deep	0.0005	0.0000	0.0001	0.0004	0.0002	−0.0003
		0.0000	0.0030	0.0000	0.0002	0.0029	0.0000
		0.0001	0.0000	0.0027	−0.0003	0.0000	0.0027
1050–975	Shallow	0.0405	−0.0016	0.0053	0.0368	0.0096	−0.0170
		−0.0016	0.1770	−0.0017	0.0096	0.1727	−0.0035
		0.0053	−0.0017	0.1551	−0.0170	−0.0035	0.1570
	Middle	0.0028	−0.0001	0.0003	0.0021	0.0007	−0.0010
		−0.0001	0.0129	−0.0001	0.0007	0.0121	−0.0002
		0.0003	−0.0001	0.0114	−0.0010	−0.0002	0.0114
	Deep	0.0005	0.0000	0.0001	0.0004	0.0002	−0.0002
		0.0000	0.0030	0.0000	0.0002	0.0029	0.0000
		0.0001	0.0000	0.0027	−0.0002	0.0000	0.0027
975–950.5	Deep	0.0005	0.0000	0.0000	0.0005	0.0002	−0.0002
		0.0000	0.0030	0.0000	0.0002	0.0029	0.0000
		0.0000	0.0000	0.0026	−0.0002	0.0000	0.0026
Below 950.5	Deep	0.0006	0.0000	−0.0001	0.0006	0.0000	−0.0001
		0.0000	0.0030	0.0000	0.0000	0.0030	0.0000
		−0.0001	0.0000	0.0026	−0.0001	0.0000	0.0026

3. Numerical tests using DFN

In recent decades "numerical test" (NT) has been developed for stochastic rock samples containing "discrete fracture network" (DFN) (Wei and Hudson 1986; Wei et al. 1995; Zhang et al. 1996; Kulatilake and Panda 2000; Öhman and Niemi 2003; Min et al. 2004; Chen et al. 2008) to evaluate their permeability tensor and REV, which requires a large amount of computation efforts concerning different sample sizes and orientations.

This issue will be addressed in Chap. 18.

(4) Drainage holes

In addition to cutoff devices, drainage of seeping water is essential to prevent the built-up of high uplift in dams and their foundations during service period (Chen 2015).

Dam bodies are normally drained by an embedded array of porous concrete pipes of 15–20 cm in diameter, which run vertically through the full dam height. The spacing of these porous concrete pipes is 2–3 m. These drainage pipes discharge seeping water into the drainage gallery system first, afterwards the water is directed into sump wells and from therein further diverted into the downstream river by pumping or flowing automatically.

Drainage curtain of borehole array is conventionally installed in the dam foundation and abutment to control seepage and to relieve uplift as well as to prevent seepage hazards (e.g. piping). Foundation drainage holes are drilled and connected to the grouting gallery for releasing the seeping water to gutters, which is further gathered in sump wells. The foundation drainage holes should be 2–3 m in space and minimum 100–150 mm in diameter. The depth of holes is usually 40–60% of the grout curtain and no smaller than 10 m for high-to medium dams, which is related to the geologic and hydrogeologic conditions.

Groundwater in cut slopes is often a primary or contributory driving of slope failure, and a reduction in water pressures through sub-surface draining may improve the stability considerably, this comprises drilling a series of nearly horizontal drainage holes from the exposure faces. In large rock slopes, holes of 200–300 m in depth may be demanded to achieve ideal effects. For large and deep landslides, long drainage adits or tunnels may be driven from which a series of drainage holes are drilled into the saturated rock.

Sluices and low gravity dams may have to be founded on a preglacial valley with soft rocks, pervious alluvial or morainal deposits. Under seepage control for such foundations is, if necessary, by installing relief wells at the downstream toe. The wells, including screen and riser pipes, should possess a diameter which will permit the maximum design flow without excessive head losses, in no instance should the well's diameter be smaller than 15 cm. Seeping water from relief wells should be delivered into open ditches or into collector system outside of the dam base. Experience with relief wells indicates that with the ongoing of time their discharge function will be gradually undermined due to clogging of the well screen and/or reservoir siltation.

To uniformly handle the drainage holes and relief wells under the both circumstances of empty and clogging, the author of this book proposed an "air element" model (Hu and Chen 2003), by assuming that the hole/well is filled with an virtual filler material with much larger permeability coefficient. Where the hole/well is empty, the proportion $P = k_d/k_s$ ranges between 10^2 and 10^3 will guarantee a satisfactorily precise solution, in which k_d and k_s are the permeability coefficients of the virtual filler material and the surrounding host material (rock/soil/concrete), respectively. With the help of "air element", in the analysis of hydraulic structures the drainage hole may be simulated as a high permeable solid cylinder observing the Darcy's law.

Apart from the global coordinate system, a local Cartesian system (see Fig. 2.5a) is needed to simplify the formulation of computation algorithm for drainage holes in the subsequent chapters of this book: the z_d-axis is coincident with the axis of the drainage hole and points upward, the y_d-axis is perpendicular to the drainage hole

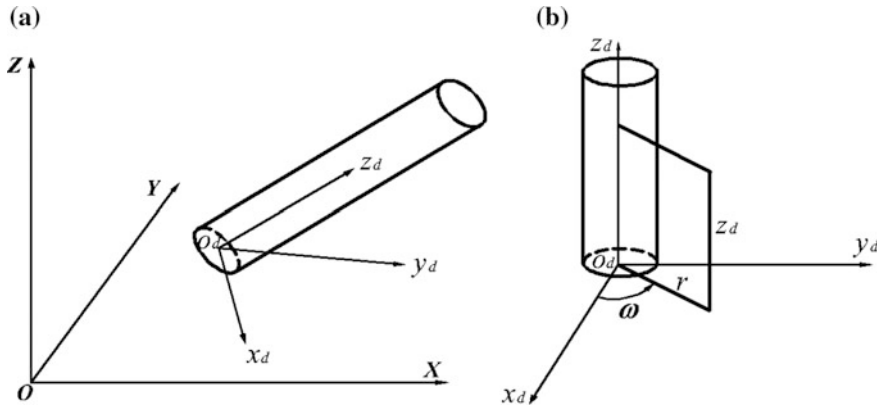

Fig. 2.5 Coordinate systems of drainage hole segment *d*. **a** Cartesian; **b** cylindrical

and points in the direction of dip, the x_d-axis is formed by the right hand rule. Based on this local Cartesian system, a local Cylindrical coordinate system is further defined in Fig. 2.5b for the purpose of further simplification in the computation algorithm.

The Darcy's law expressed in the local Cylindrical coordinate system is:

$$\begin{cases} v_r = -k_d \dfrac{\partial \phi}{\partial r} \\ v_\omega = -k_d \dfrac{1}{r} \dfrac{\partial \phi}{\partial \omega} \\ v_z = -k_d \dfrac{\partial \phi}{\partial z} \end{cases} \tag{2.22}$$

2.5 Thermal Conductivity

2.5.1 Concrete

The temperature rise in a concrete structure due to hydration process and thermal flow causes temperature fluctuations which in turn, produce thermal strains/stresses because of the restraints presenting in the structure. The most adverse effect of the thermal stress is the thermal cracking in surface lifts.

On the thin placed concrete lift the surface temperature is usually controlled by the atmosphere. When the initial temperature of the concrete is higher than the atmosphere temperature and the surface is not protected, the temperature jump (non-linear gradient) across the lift joint between old and new concrete lifts could be over 10 °C in the daytime with full sun, whereas in the night and rainy day it

could be only 2 °C. If the time of placing interval between two lifts is longer, the temperature jump would be even much larger, which will lead to the early age cracking in young concrete. Cracking may also emerge if the mean temperature varies considerably in the different parts of a casted structure. In both cases of early age cracking referred to above, the thermal movement due to hydration is the key clue (Carslaw and Jaeger 1985).

The thermal conductivity λ dominates the heat flux transmitted through a unit area of a material under a unit temperature gradient. For concrete, it is related to the mineralogical characteristics of aggregate, moisture content, density, and temperature.

The specific heat c is defined as the quantity of heat needed to raise the temperature of a unit mass of material by one degree. The specific heat of normal weight concrete is not very much affected by the type of aggregate, temperature, and other parameters. Typically, it varies within the range of 0.9–1.0 kJ/kg °C.

The thermal diffusivity a is the heat flowing rate through concrete from the hot side to the cold side. It is conventional estimated by the formula

$$\alpha = \frac{\lambda}{c\rho} \tag{2.23}$$

where ρ = density of concrete, g/cm^3.

The hydration heat of cement Q is the propulsion to "warm up" concrete, which may be represented by two kinds of formulas.

– Exponent

$$Q(\tau) = Q_0(1 - \mathrm{e}^{-m\tau}) \tag{2.24}$$

where $Q(\tau)$ = accumulated hydration heat at the age of τ, kJ/kg; Q_0 = total hydration heat, kJ/kg; τ = concrete age, day; m = constant related to cement and curing temperature.

– Hyperbolic

$$Q(\tau) = \frac{Q_0\tau}{n+\tau} \tag{2.25}$$

where: n = constant.

The hydration heat of cement should be tested for a specific project. For the moderate-heat Portland cement, the hydration heat usually does not exceed 210 kJ/kg after three days of hardening and 252 kJ/kg after seven days.

The thermal regime analysis often employs adiabatic temperature rise θ of concrete instead of the hydration heat Q of cement. It may be obtained either by direct or indirect methods.

For an important project, direct method using thermal rise test facilities on concrete samples is required, and the following formulas may be fitted using the tested data.

– Exponent

$$\theta(\tau) = \theta_0(1 - \mathrm{e}^{-\alpha\tau^{\beta}}) \tag{2.26}$$

– Hyperbolic

$$\theta(\tau) = \theta_0\tau^{\alpha}/(\beta + \tau^{\alpha}) \tag{2.27}$$

where θ_0 = final adiabatic temperature rise, °C; α, β = constants.

More complicated models (e.g. the maturity model) may also be established and exercised (Roy et al. 1994).

In short of tested data, use is made of indirect method based on the hydration heat and amount of cement, as well as the specific heat and density of mixtures, to estimate the adiabatic temperature rise by the formula

$$\theta(\tau) = \frac{Q(\tau)(W + kF)}{c\rho} \tag{2.28}$$

where W = amount of cement, kg/m^3; c = specific heat of concrete, kJ/(kg °C); ρ = density of concrete, kg/m^3; F = amount of mixture, kg/m^3; $Q(\tau)$ = hydration heat of cement, kJ/kg; k = fraction coefficient.

It is worthwhile to indicate that there is difficulty in the long-age test (e.g. 180 day or longer) for the final adiabatic temperature rise θ_0 of cement and concrete, blamed on the shortage of sensitive and reliable experimental equipments. The comparison study conducted on Xiaowan Project (see Fig. 2.6) shows that the final adiabatic temperature rise based on the long-age test ($C_{180}35$) is θ_0 = 39.2 °C, much higher than that of the conventional 28 days-age test ($C_{180}35$) θ_0 = 27.03 °C.

The surface exothermic coefficient β is an important parameter concerning the concrete/air contact face, which is demanded in defining the third type boundary condition (see Eq. 4.180).

Under the thermal action, the thermal strain is mainly governed by the coefficient of thermal expansion α, which is defined as the change in unit length per degree of temperature change. It is an important parameter towards the thermal stress and cracking control. Apart from the concrete composition design and humidity condition during curing, it is closely related to the aggregate type. In the phase of preliminary design, it can be estimated from the weighted average of the components, assuming 70–80% aggregate content in the concrete mixture. Since the thermal strain of concrete is significantly influenced by the thermal strain of

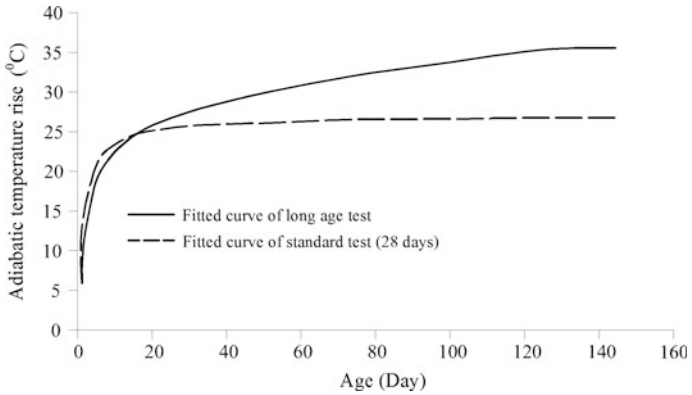

Fig. 2.6 Adiabatic temperature rise fitted by long-age and 28 days-age tests: Xiaowan Project, China

aggregate which is the primary constituent of concrete, therefore selecting an aggregate type with a low coefficient of thermal expansion (e.g. limestone), if it is economically feasible and technologically acceptable, may become a critical work for cracking prevention in mass concrete.

For important projects, all the aforementioned thermal parameters should be comprehensively studied by laboratory tests. In Table 2.14 the thermal parameters of several China's dam projects are summarized which may be referred to in the initial phases of design. Table 2.15 lists the surface exothermic coefficient tightly related with the wind speed.

2.5.2 *Rocks*

The thermal properties of rocks are mainly dependence upon their origins (types), composition, porosity, and geo-environmental settings (e.g. temperature) (Birch and Clark 1940; Danilova and Bogdanov 1967; Wu and Zhou 2013; Mielke et al. 2017), of which the most useful ones in hydraulic structures are their specific heat c and thermal conductivity λ. They participate the thermal analysis for concrete dams and tunnel linings during construction or/and operation phases where the heat exchange between concrete and rocks is taken into account. The data in Table 2.16 are collected from numerous literatures which exhibit large variation due to test methods, sample sizes and temperature, purposes of experiment, etc.

The coefficient of thermal expansion of commonly used rocks and minerals varies from about $\alpha = 5 \times 10^{-6}$ per °C (limestone and gabbros) to $\alpha = 12 \times 10^{-6}$ per °C (sandstone, natural gravel, and quartzite).

Table 2.14 Thermal parameters of typical China's dam concretes (Chen et al. 2011)

Project (aggregate rock)		W/C	Fly ash content (%)	Thermal diffusivity a ($\times 10^{-3}$ m^2/h)	Thermal conductivity λ (kJ/(m h °C))	Specific heat c (kJ/kg °C)	Coefficient of linear expansion α ($\times 10^{-6}$/°C)	Maximum adiabatic temperature rise θ_0 (°C)
Three-goreges (granite)		0.55	35	3.152	9.46	0.96	8.8	19.60
Three-goreges (granite)		0.50	20	3.23	9.46	1.013	8.8	24.20
Xiangjiaba (limestone)		0.55	40	2.88	7.33	0.929	5.46	26.25
Xiangjiaba (sandstone)		0.55	40	3.87	8.165	0.938	10.28	25.06
Wuqiangxi (quartz)		0.55	30	4.16	10.05	1.005	10.00	24.35
Longtan (limestone)		0.44	32	3.07	8.77	0.967	4.62	23.3
Xiaowan (gneiss)	$C_{180}30$	0.5	30	2.991	8.016	1.072	8.1	25
	$C_{180}35$	0.45	30	3.116	8.227	1.056	8.15	27
	$C_{180}40$	0.4	30	3.239	8.479	1.047	8.26	30

Table 2.15 Surface exothermic coefficients concerning concrete/air contact face (Chen et al. 2011)

Wind speed (m/s)	β (kJ/(m^2 h °C))		Wind speed (m/s)	β (kJ/(m^2 h °C))	
	Smooth surface	Rough surface		Smooth surface	Rough surface
0.0	18.4638	21.0596	5.0	90.1418	96.7151
0.5	28.6796	31.3591	6.0	103.2465	110.9921
1.0	35.7553	38.6442	7.0	116.0581	124.8922
2.0	49.4042	53.0049	8.0	128.5766	138.4575
3.0	63.0951	67.5750	9.0	140.7602	151.7296
4.0	76.7022	82.2288	10.0	152.6926	165.1274

Table 2.16 Thermal parameters of rocks (Wu and Zhou 2013)

Rock type			Temperature T (°C)	Specific heat c (J/(kg K))	Thermal conductivity λ (W/(m K))
Igneous rocks	Intrusives (plutonic)	Granite	50	787.1–975.5	2.17–3.08
		Diorite	20	837.4–1256.0	1.64–2.33
		Porphyry	20–40	900–910	2.1–2.6
	Extrusives (volcanic)	Basalt	0–300	908.5	1.60–2.18
		Rhyolite	0–300	870.9	1.04–2.80
Sedimentary rocks	Clastic sedimentary	Sandstone	50	762–1071	2.18–5.1
		Shale	0–300	774.6	1.72
	Carbonatite	Limestone	50	824.8–921.1	2.34–3.51
		Dolomite	50	921.1–1000.6	2.52–3.79
	Weak and soft	Claystone	50	908.5–925.3	2.32–3.23
Metamorphic rocks	Ortho-rock	Gneiss	0–300	736.9–1005	2.7–3.1
	Para-rock	Quartz	0–300	699.2–942.0	3.13–6.65
		Marble	0–300	795.5–879.2	2.11–2.80
		Slate	0–300	711.8	2.18
		Phyllite	20–40	850	1.9–3.2
		Schist	20–40	710–760	1.75–3.80

2.5.3 Cooling Pipes

There are many methods to alleviate, or even fully prevent, thermal cracking due to the built-up thermal stresses within concrete during casting and maturing, of which the often exercised one for reducing temperature gradients within a concrete structure, and thus also the risk of cracking, is to cool down the inner core with embedded cooling pipes. Normally, water is used as the cooling medium. Such a cooling technique was firstly employed to construct the Hoover Dam (H = 221.4 m, USA).

The types of cooling pipes are normally black or HDPE (high density polyethylene), in which the flowing water extracts heat from surrounding concrete.

For the simulation of cooling water and pipe, in addition to the global coordinate system, a local Cartesian system is needed to simplify the formulation of computation algorithms (see Fig. 2.7a): the z_p-axis is along the cooling pipe and upright, the y_p-axis is perpendicular to the cooling pipe and points in its dip direction, and the x_p-axis is formed by the right hand rule. On the basis of this local Cartesian coordinate system, a local Cylindrical coordinate system is further defined in Fig. 2.7b.

Specific heat c of both the black pipe and HDPE pipe is normally not taken into account in the thermal computation of mass concrete structures. In addition, the thermal conductivity λ is neglected for the black pipe, but it is suggestible as 1.66 kJ/(m h °C) for the HDPE pipe. The specific heat c and thermal conductivity λ of water are 2.1604 and 4.1868 (kJ/kg °C), respectively.

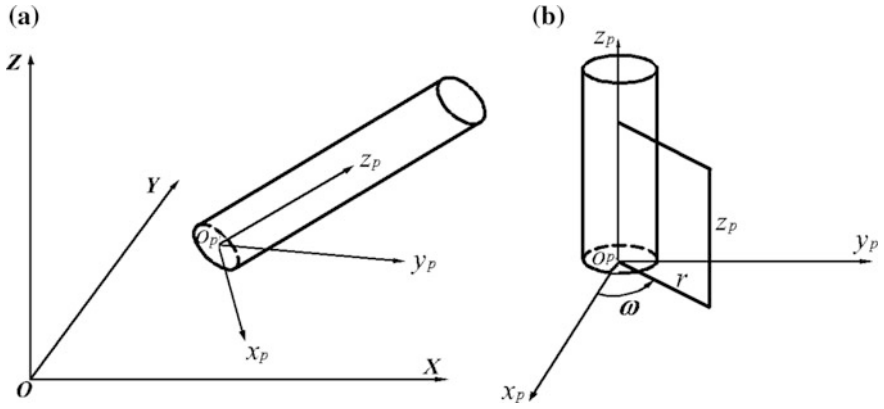

Fig. 2.7 Coordinate systems of cooling pipe segment p. **a** Cartesian; **b** cylindrical

2.6 Deformation

2.6.1 Quasistatic and Cyclic Loading

(1) Rock-like materials

1. Intact rocks and concrete

The conventional compressive test with or without confining pressure, in which a short, right cylinder is loaded axially, is one of the most widespread experiments (see Fig. 2.8) towards the studies on elastic behavior and strength, as well as on long term creep, of rock-like materials.

The most useful single description for the mechanical properties of rock-like materials is the complete stress–strain curve plotted in Fig. 2.8, using a right cylinder of material sample being confined laterally (σ_3) and compressed in axial direction (σ_1), where the abscissa axis exhibits lateral strain (ε_a) and the ordinate axis emerges deviate stress ($\sigma_1 - \sigma_3$). If $\sigma_3 = 0$ the test is called as uni-axial. This type of resultant curve, known as the "strain-controlled complete stress–strain curve", was firstly obtained in 1966 for rock, for the purpose to illustrate the very significant effect of the microstructure and the history on its mechanical behavior (Jaeger et al. 2007).

At the very beginning of loading, the curve covers an initial portion (OA) which could be concave upwards for rock, but also could be convex for concrete. This is mainly due to the deficit in the rock specimen preparation—the ends of the cylinder being non-parallel, and/or the closing of micro-cracks within the intact rock. After this initial portion, there is a portion of essentially linear behavior (AB). B may be defined as the "yield point" pinpointed by the "yield strength" σ_y, after this point plastic strain ε^p will manifest along with the continuous but gentler mounting of the loading curve, which is termed as the "hardening phase". The plastic strain may be detected by an unloading-reloading circle, F → Q → F for example, where the total

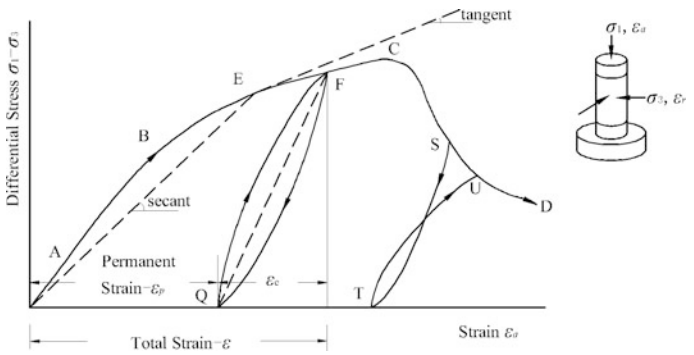

Fig. 2.8 Complete stress–strain curve of rock-like materials under constant confining pressure and quasistatic axial loading

strain is divided into the components of elastic and plastic, i.e. $\varepsilon = \varepsilon^e + \varepsilon^p$. After the peak point C tagged by the "peak strength" σ_p, also termed as the "ultimate strength" σ_u, the complete stress–strain curve enters a descending post-peak region (CD), which is named as the "softening phase". In this phase much more plastic strain may be found through unloading-reloading circle, such as S → T → U. For ductile materials or brittle materials under sufficient confining pressure, the point D may be sustained at a stable value following the continuous increase of strain, and finally the "residual strength" σ_r is declared. All the above defined characteristic points may be abbreviatedly termed as the "strength" σ_s where there is no risk of misleading.

There is approximately ten-fold augment in the deformation modulus and uni-axial strength from a strongly weathered rock to the fresh one. The geologic age also may considerably affect the deformation and strength parameters for sedimentary rocks.

Attributable to the major concern over the normal working situation and the difficulties in obtaining hardening/softening parameters, the yield strength is dominantly used in the computation for the design of hydraulic structures, and the perfect plasticity is postulated. The peak strength is sometimes employed where there exists difficulties to pinpoint the yield strength, under such circumstances the allowable safety factor should be somewhat higher than that uses the yield strength. The residual strength is only useful in the stability analysis for the structure where its deformation is of minor concern (e.g. a cut slope being neither a portion of nor closely adjacent to the dam).

2. Joints

Another very useful description for the mechanical behavior of rock-like materials is the complete strain-displacement curve under direct shear for discontinuities (joint, fault, fissure, etc), as shown in Fig. 2.9.

In compression (see Fig. 2.9b), the discontinuity is gradually pushed close, with an apparent limit when its two surfaces are contacted. The stiffness k_n associated with this compressive process exhibits strong nonlinearity linked to the applied normal stress and associated with the strength of the intact rock/concrete. When a

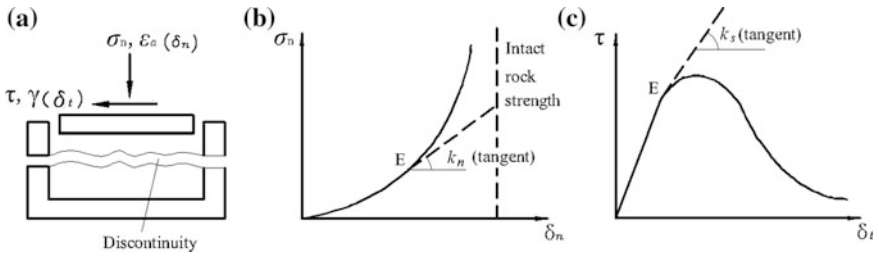

Fig. 2.9 Complete stress–strain curve of a discontinuity under constant normal pressure and quasistatic direct shear loading. **a** Schematic diagram to the test; **b** compressive behavior; **c** shear behavior

discontinuity is subjected to shear stress (see Fig. 2.9c), the curve is rather like the complete stress–strain curve of intact rock under axial compression, i.e., in addition to the shear stiffness k_s, there are the yield strength, the peak shear strength, and the post-peak failure region with the residual strength.

3. Rock masses

It has been widely recognized that joints are significantly influential to the gross response of the rock mass. While the intact rock may remain effectively elastic and undergo only small strain, irreversible slip at joints changes the overall stress distribution. In the first ISRM International Congress in 1966, Müller stated that discontinuity and anisotropy are the most characteristic properties of rock materials and that the properties of jointed media depend much more upon the joints of the unit rock block system than upon the rock material (Müller 1967; Brown 2011).

The actual mechanisms of joint deformations, are complex. Various minerals and gouges generated by sliding which fill joints, affect both their slip and compaction, or dilation. The presence of pore water alters the joint deformation process, too.

There was a period when scholars endeavored to conduct laboratory tests for the deformation and strength properties of jointed rock masses, through which several models of gross response taking into account of the effects of joint interaction and block interlock were correlated with experimental data. These experimental works were largely carried out with specimens of plaster materials containing multiple intersecting joint sets in order to simulate rock fracture and slip at low stress levels, and to facilitate preparation of joint surfaces (Einstein et al. 1969; John 1969). However, it is not clear that even the qualitative response of rock masses has been reproduced by such manner of tests (Barton 1972).

The term "modulus of deformation" or "deformation modulus" (E), a secant Young's modulus, signifies that its value is calculated from the data of the loading portion of the stress–strain curve comprising both elastic and permanent deformation. Nowadays as far as the deformation modulus (and the strength as well) of the rock mass is concerned, three approaches are exercised, i.e. either by computation using the properties of the intact rock and the discontinuities respectively, or via the direct in-situ tests, or through empirical formulae.

For highly jointed rock masses in which the joint spacings are much smaller than the characteristic dimension of the hydraulic structure concerned, it is very convenient to regard them as "equivalent" continua. Along this line, many works can be found from, for example, Salamon (1968), Morland (1974), Zienkiewicz and Pande (1977a, b), Amadei and Goodman (1981), Stephansson (1981), Gerrard (1982a, b), Amadei (1983), Pande and Gerrard (1983), Yoshinaka and Yamabe (1986), Chen and Pande (1994). Although various theoretical models are available for the computation of deformation modulus (and strength as well), yet they are all subjected to the verification and adjustment using the data from in situ tests, the engineering analogue, and the back analysis (if possible).

To avoid the effects of sampling disturbance, it is world widely demanded to determine the deformation modulus E and Poisson's ratio μ (or shear modulus G) mainly by the data from in situ testing. Four basic apparatus for in situ testing are prevalent towards the deformation modulus of rock mass.

- Borehole jacks and dilatometers;
- Flat jacks installed in slots cut into rock mass;
- Bearing plates;
- Radial jacks.

Expanding against the walls, jacks, designed to fit inside exploratory drill hole or slot and associated equipments for measuring dilation, can provide qualitative information on the rock deformability at depths of several hundred meters. Although they are quite useful, yet they are not sufficiently accurate in hard rock to provide quantitative design data for large hydraulic structures.

By plate bearing test, load increments are applied to a test plate, either in a shallow pit, or at the bottom of a large-diameter borehole, or on the walls of an adit, and the resulted displacements are measured. The value of the deformation modulus is then calculated using the relevant closed-form displacement solution.

Field testing is the most straight forward way to obtain the equivalent elastic deformation parameters, but it is costly and often involves uncertain errors related to the effects of hidden factors, the control of boundary conditions, the equipment installation, the test site preparation, the blasting damage, and the interpretation of results. These errors lead to the test data of rock masses with great inaccuracy and scatterness (Bieniawski 1978; Palmstrom and Singh 2001; Hoek and Diederichs 2006).

Empirical formulae establish certain relationships on the basis of rock mass classification (Barton 2002; Cai et al. 2004; Sonmez et al. 2004; Hoek and Diederichs 2006). Although they have gained extensive popularity for practical applications of engineering design, especially in tunneling, they often elicits estimations that are too conservative, largely because they make use of categorized parameters from case histories. Another shortcoming is that they lack a proper mathematical platform to establish constitutive relations. Furthermore, the anisotropy in the deformation properties cannot be properly represented in the tensor form that is a base of continuum mechanics.

(2) Steel bars

During monotonic loading (see Fig. 2.10), the uni-axial behavior of structural steel bar with yield plateau is essentially linear elastic from its virgin state (O) up to the sharp point of yield (A), followed by an abrupt yield drop and the yield plateau (AB). The plastic deformation along the yield plateau is caused by the "Lüders band propagation" (Hall 1970). From a macroscopic point of view, such a behavior can be handled as perfectly plasticity, and the length of the yield plateau can be quantified by the plastic strain at the end of the plateau. At the end of yield plateau (B), the material usually starts hardening nonlinearly up to the point (C)

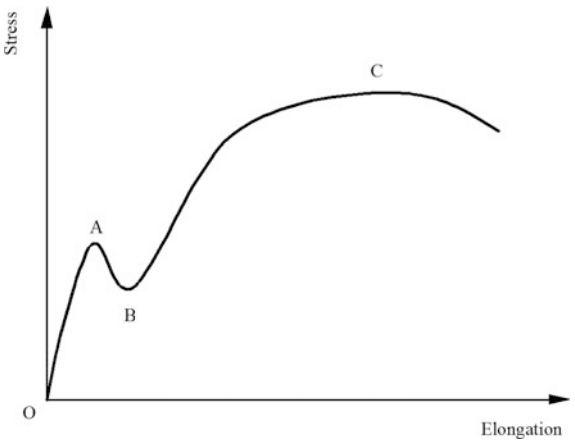

Fig. 2.10 Complete stress–strain curve of steel bar under monotonic and quasistatic tensile loading

corresponding to the ultimate strength when necking initiates. Afterwards, the true stress–strain relationship is almost linear, which indicates that the hardening modulus is approximately a constant (Bridgman 1952; Jia and Kuwamura 2014).

During cyclic loading, the material behavior of structural steel bar with yield plateau is much more complex than monotonic loading and is closely related to the strain amplitude of cycling (Hu et al. 2016). Generally, cyclic loops converge to a stabilized saturation dependent only on the loading amplitudes (Yamada et al. 2002; Matsumoto et al. 2005). This cyclic loading effect, however, is seldom considered in the hydraulic structures of mass concrete and rocks.

(3) Remarks

Although there exist various factors related to loading conditions (e.g. confining pressure in tri-axial tests) and loading rates which influence the shape of the complete stress–strain curve, yet there are always several features of importance to be indicated from Fig. 2.8 (Figs. 2.9 and 2.10 similar). The first one is the Young's modulus E of the material, either tangent or secant. The next one is the characteristic strength σ_s. The third one is the steepness of the descending portion (post-failure) which is an index of material brittleness. If the post-failure is in a form of steadily progressive strain at the same stress level, the material is termed as ductile, and a residual stress may be identified; if a sharp drop in the stress level down to zero occurs at the nearly same strain value, the material is brittle. In fact, the real situation is more complicated than these two extraordinary cases because a rock-like material usually exhibits obvious hardening phase under high confining pressure while softening phase may be completed abruptly under low confining pressure.

2.6.2 Sustained Loading

(1) Creep phenomena and mechanisms

The creep and stress relaxation have actually the same mechanisms emerged as two phenomena, the former exhibits a gradual increase in strain with the ongoing of time under a given level of sustained stress, the latter performs a gradual decrease in stress with the ongoing of time under a given level of sustained strain. Both manifestations are typical of viscoelastic or/and viscoplastic properties of rock-like materials, particularly the concrete in its young age.

The creep of concrete is originated from the calcium silicate hydrates (C-S-H) in the hardened Portland cement paste and theoretically occurs at all stress levels within the range of service actions (Wittmann 1982; Brooks 2005). It appears in early aging concrete mainly due to the loss and movement of a certain amount of physically adsorbed water in the C-S-H of paste matrix, and in mature aging concrete mainly caused by long-term relaxation of self-equilibrated micro-stresses in the nano-porous microstructure of the C-S-H. It is linearly dependent on the sustained stress under certain threshold value (e.g. 30% of uniaxial strength) if the pore water content is constant. The nonlinearity of the complete stress–strain curve of concrete, especially at stress levels greater than 30–40% of the ultimate stress, clearly shows the contribution of the ITZ and micro-cracks to creep. Additional creep strain occurs when a concrete is simultaneously exposed to the drying condition, which is caused by micro-cracking in the ITZ due to drying shrinkage.

The remarkable advance in the understanding and description of creep is the multi-level (scale) theory of coupled chemo-thermodynamics (Hellmich et al. 1999), by which the intrinsic material behaviors independent of field and boundary conditions can be determined. In this theoretical framework, material properties are not a function of time solely, but are related to their origin on the micro-level, namely the formation of C-S-H dependent on the temperature, moisture, age, etc. In the same framework, material functions relating autogenous (chemical) shrinkage, elastic stiffness, and creep compliance to the degree of hydration, may be derived (Sercombe et al. 2000), too.

The creep nature of rocks is mainly determined by their mineralogical and structural features (Cristescu and Gioda 1994). It has been shown that the time-dependent behavior of argillaceous rocks is attributed to creep, pore-pressure dissipation, swelling, and electrochemical effects. Meticulous investigations into creep of brittle rock using methods of electron microscopy (Boland and Hobbs 1973; Tappennier and Brace 1976; Dragon and Mróz 1979; Kranz 1979), acoustic emission (Ohnaka and Mogi 1982) and others have revealed that the long-term behavior of a polycrystalline rock depends, on one hand, upon the physical processes in each individual crystal grain as well as on the rock as a whole, and on the other hand, upon the interaction of the rock grains and other structural features. Therefore more precisely, intrinsic parameters such as mineralogy, porosity and water content, and extrinsic parameters such as deviatoric stress, strain rate, temperature and hygrometry, all influence the time-dependent behavior of rocks

(Maranini and Brignoli 1999; Auvray et al. 2004; Zhang and Rothfuchs 2004). Time-dependent behavior of the rock mass is an important aspect in the observation and prediction of land sliding movement (Bizjak and Zupančič 2007).

Creep deformations resulting from mechanical loading are normally studied through creep tests (deviatoric stress maintained constant over a long period) and relaxation tests (strain maintained constant over a long period), the former is more prevalent in the practices.

Figure 2.11 plots the creep curves using the tested data for a rock and a weak interlayer, respectively. It is remarkable that there is no strength threshold σ_0 for the soft rock or interlayer (see Fig. 2.11a), i.e., at any stress level, creep may be observed. Nevertheless, there is a strength threshold σ_0 for the hard rock (and concrete as well) (see Fig. 2.11b), creep deformation may be observed only if the threshold is exceeded.

A classical creep curve, as idealized in Fig. 2.12, represents the evolution of strain as the function of time under uni-axial stress at a constant temperature. In

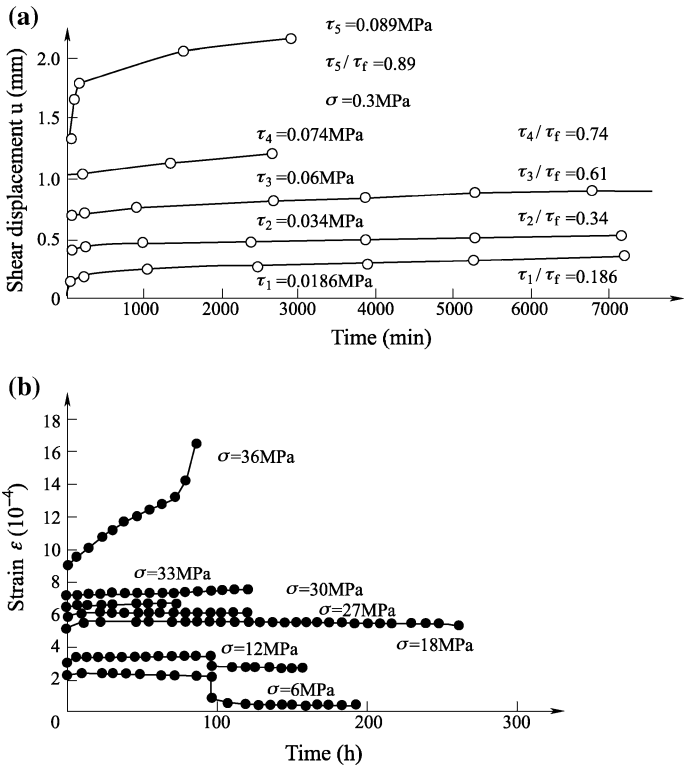

Fig. 2.11 Field tested creep curves of rocks. **a** Shear creep test of the argillaceous interlayer (Gezhouba Project); **b** compressive creep test of the granite (Three-gorges Project)

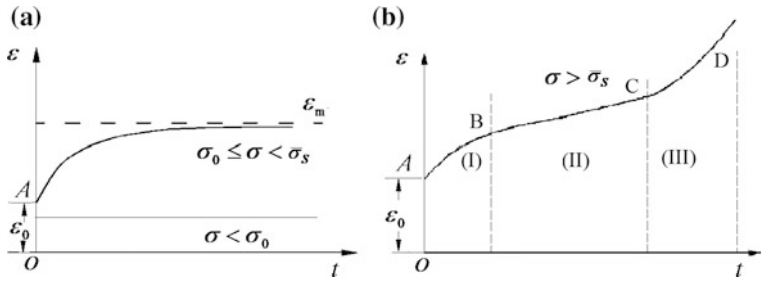

Fig. 2.12 Idealized creep curve of rock-like materials. **a** Convergent creep; **b** non-convergent creep

general, there are three phases in the creep history of rock (Kachanov 1958; Gruden 1971; Stagg and Zienkiewicz 1986; Betten 2008; Jaeger et al. 2007).

① The primary creep phase (also known as transient creep). Hardening of the material leads to the decrease in creep rate which is initially much higher. Where $\sigma_0 \le \sigma < \bar{\sigma}_s$, there is only primary creep emerging as a "convergent creep" shown in Fig. 2.12a.

② The secondary creep phase (also known as the steady state creep). Where $\sigma > \bar{\sigma}_s$, it follows the primary creep phase with a constant strain rate (see Fig. 2.12b).

③ The tertiary creep phase. There is an increase in the creep strain rate until the sample failure (see Fig. 2.12b).

The initiation of tertiary creep phase is due to the accumulation of irreversible deformation (creep damage), which has similar mechanism to the fatigue failure under cyclic loading (Ge et al. 2003).

It is worthwhile to indicate that for rock-like materials, the long term yield strength $\bar{\sigma}_s$ obtained from creep test is always smaller than σ_s from quasistatic test, this may be validated by the tested data illustrated in Tables 2.17 and 2.18.

The principal postulation is made that the creep of rock-like materials may be generally looked at as an integral manifestation of following three strain components (Boukharov et al. 1995):

- Elastic strain $\varepsilon^e(t)$. Depending on the bonding between the particles of each individual grain as well as on the bonding between grains (rock), the loss and movement of adsorbed water as well as the relaxation of self-equilibrated micro-stresses in the C-S-H (concrete);
- Plastic strain $\varepsilon^p(t)$. Resulting from the crystal (or C-S-H) dislocations movement and from the plastic deformation of cementitious materials;
- Brittle dilatancy $\varepsilon^b(t)$. Due to the micro-cracking process in individual crystal grains and between grains (rock), as well as in paste matrix and ITZ (concrete).

If we further postulate that micro-cracking does not contribute significant strain to the creep during the first two phases, a graphical decomposing of an integral

Table 2.17 Uni-axial compression strength values of rocks under sustained loading and quasistatic loading (laboratory)

Project	Rock	Quasistatic yield strength σ_s (MPa)	Creep yield strength $\bar{\sigma}_s$ (MPa)	Ratio $\bar{\sigma}_s/\sigma_s$
Three-gorges	Porphyritic granite (weakly weathered)	63.6	51.9	0.82
	Porphyritic granite (slightly weathered)	72.5	65.71	0.95
Shuibuya	Carbonaceous argillaceous limestone	22.85	12.59	0.55
	Carbonaceous argillaceous limestone	26.76	18.23	0.68
	Intercalation 031#	1.142	0.623	0.54
	Shale	18.39	11.33	0.62
	Limestone	70.31	52.73	0.75
Goupitan	Magenta claystone	18.05	13.01	0.72
	Celadon claystone	7.60	4.94	0.65

Table 2.18 Shear strength values of rocks under sustained loading and quasistatic loading (in situ)

Project	Rock	Quasistatic strength		Long term (creep) strength		Ratio	
		f′	c′ (MPa)	f_∞	c_∞ (MPa)	f_∞/f'	c_∞/c'
Three-gorges	Granite	2.2	2.7	2.0	2.2	0.91	0.81
	Joint (rough)	0.78	0.07	0.72	0.0	0.92	0
Gezhouba	Intercalation 202#	0.225	0.06	0.204	0.03	0.91	0.50
Baihetan	Intercalation 157-1	0.36	0.08	0.29	0.01	0.81	0.13

creep curve into elementary creeps using geometric subtraction may be illustrated in Fig. 2.13, which is further formulized by

$$\varepsilon(t) = \varepsilon^e(t) + \varepsilon^p(t) + \varepsilon^b(t) = \varepsilon_0 + \varepsilon^d(t) + \varepsilon^p(t) + \varepsilon^b(t) \tag{2.29}$$

where ε_0 = instant elastic deformation; $\varepsilon^d(t)$ = delayed elastic creep (e.g. creep of the young concrete at early age); $\varepsilon^p(t)$ = delayed plastic creep (e.g. perfect or work hardening visoplastic strain ε^{vp} of rock-like materials); $\varepsilon^b(t)$ = dilatant creep, or brittle creep (e.g. work softening viscoplastic strain of rock-like materials before rupture).

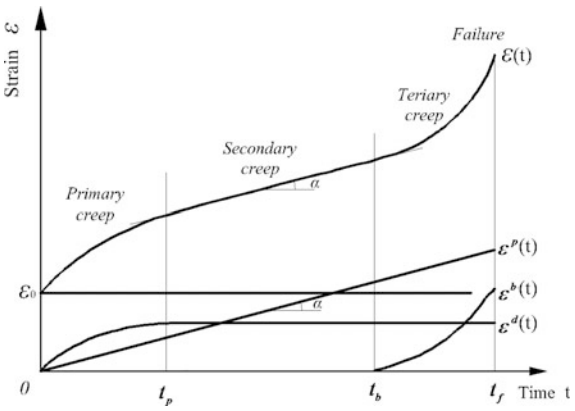

Fig. 2.13 Graphical decomposition of the creep curve for rock-like materials and discontinuities

There are some debates with regard to whether secondary creep exists as a distinct phase or simply as an inflexion between the primary and tertiary phases. Secondary creep, which is often observed on ice, salt or metallic alloys (Mott 1953; Stagg and Zienkiewicz 1986), is seldom observed on polycrystalline rocks and concrete. For example, during the test performed on brittle rocks, a transition from primary creep to tertiary creep without any stabilization of the strain rate may be observed. This is why some scholars (Gonze 1988; Dusseault and Fordham 1993) expressed doubts as to its existence. The author of this book believes that this phenomenon could be explained by the similarity between the creep failure mechanism and fatigue failure mechanism—they exhibit nearly identical threshold strength and the formation is entailed under the complete quasistatic stress–strain relation (Ge et al. 2003).

In the computation of hydraulic structures, the delayed elastic creep of young concrete at early age and the delayed plastic creep (i.e. visoplastic deformation) of rock are normally handled. The last phase of creep (brittle creep) is only considered where the post-failure performances of the hydraulic structures are of importance.

(2) Creep models

Researchers generally examine the aforementioned mechanisms and responses of creep through phenomenological approximation utilizing a postulated empirical formula or rheological model, of which the latter is more prevalent whose elastic response is represented in one-dimension by Hookean spring elements, rate-dependence behavior is represented by nonlinear dashpot elements, plastic performance is accounted for by adding sliding frictional elements.

One-dimensional rheological models for the phenomenological description of rock-like materials based on above spring-dashpot-slider elements consist of perfectly viscoplasticity, elasticity perfectly viscoplasticity, and hardening elasto-viscoplasticity. The elements may be connected in series or in parallel. Where the elements are connected in series the strain is additive meanwhile the

stress is equal in each element. In parallel connections, the stress is additive meanwhile the strain is equal in each element.

Prevalent phenomenological rheology models of one-dimension used in hydraulic structures for their creep deformation are illustrated in Table 2.19 (Wu and Zhou 2013), in which E is the modulus of elasticity, η is the viscosity of the dashpot, σ_s is the strength of the sliding element. These parameters are normally regarded as constant for practical reason. Where the young concrete of early age is handled, however, they are all time-dependent (vide Sects. 2.8.2 and 2.9.2). In case of necessary, expensive experiments are demanded to get the dependent relationship of these parameters with stress/strain rate as well as with inner variables (e.g. plastic strain), too. Table 2.20 gives the rheological models and corresponding constant parameters of the rocks for several hydraulic projects in China.

Table 2.19 Typical rheology models (Wu and Zhou 2013)

Name	Element connection	One-dimensional constitutive relation
Maxwell		$\sigma + \frac{\eta_2}{E_0}\dot{\sigma} = \eta_2 \dot{\varepsilon}$
Kelvin	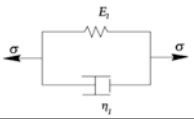	$\sigma = E\varepsilon + \eta_1 \dot{\varepsilon}$
Generalized Kelvin	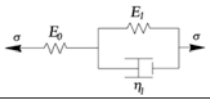	$\sigma + \frac{\eta_1}{E_0+E_1}\dot{\sigma} = \frac{E_0E_1}{E_0+E_1}\varepsilon + \frac{E_0\eta_1}{E_0+E_1}\dot{\varepsilon}$
Bonaitin-Thomson standard linear solid model	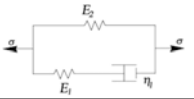	$\sigma + \frac{\eta_1}{E_1}\dot{\sigma} = E_2\varepsilon + \eta_1\left(1 + \frac{E_2}{E_1}\right)\dot{\varepsilon}$
Bergers	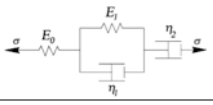	$\sigma + \left(\frac{\eta_2}{E_0} + \frac{\eta_1+\eta_2}{E_1}\right)\dot{\sigma} + \frac{\eta_1\eta_2}{E_0E_1}\ddot{\sigma} = \eta_2\dot{\varepsilon} + \frac{\eta_1\eta_2}{E_1}\ddot{\varepsilon}$
Viscoplastic	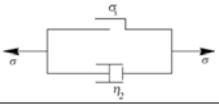	$\varepsilon = 0 \quad for \quad \sigma < \sigma_s$ $\dot{\varepsilon} = (\sigma - \sigma_s)/\eta_2 \quad for \quad \sigma \geq \sigma_s$
Bingham	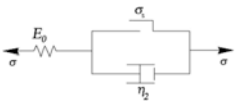	$\varepsilon = \frac{\sigma}{E_0}, \quad \dot{\varepsilon} = \frac{\dot{\sigma}}{E_0} \quad for \quad \sigma < \sigma_s,$ $\dot{\varepsilon} = \frac{\dot{\sigma}}{E_0} + \frac{(\sigma - \sigma_s)}{\eta_2} \quad for \quad \sigma \geq \sigma_s$
Mishihara	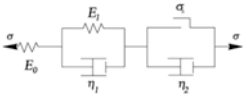	$\sigma + \frac{\eta_1}{E_0+E_1}\dot{\sigma} = \frac{E_0E_1}{E_0+E_1}\varepsilon + \frac{E_1\eta_1}{E_0+E_1}\dot{\varepsilon} \quad for \quad \sigma < \sigma_s$ $(\sigma - \sigma_s) + \left(\frac{\eta_2}{E_0} + \frac{\eta_1+\eta_2}{E_1}\right)\dot{\sigma} + \frac{\eta_1\eta_2}{E_0E_1}\ddot{\sigma} = \eta_2\dot{\varepsilon} + \frac{\eta_1\eta_2}{E_1}\ddot{\varepsilon}$ $for \quad \sigma < \sigma_s \geq \sigma_s$

Table 2.20 Rock rheological models and parameters for several hydraulic projects in China

Rock (Project)	Test method	Stress level (MPa)	Model	Parameter			
				E_1 (GPa)	E_0 (GPa)	η_1 (GPa h)	η_2 (GPa h)
Carbonaceous argillaceous limestone (Shuibuya)	Laboratory uni-axial	0.04–0.33	Bergers	0.550	0.024	2.658	55.433
Claystone (Goupitan)	Laboratory uni-axial	2.71–7.66	Bergers	27.6	5.26	67	4892
Limestone (Shuibuya)	Laboratory uni-axial	12.81–18.78	Generalized Kelvin	49.9	16.89	724	–
Granite (Three-gorges)	In situ uni-axial	6–33	Generalized Kelvin	1514.5	40.68	20,746.7	–
Altered Gneiss (Xiaowan)	Laboratory tri-axial (confine pressure = 2 MPa)	30–57.5	Burgers	160.44	11.29	8.407	63.333

2.7 Yield and Failure

2.7.1 Basic Strength Parameters

The stress–strain relation for linear elasticity is commonly known as the "Hooke's law". In its simplest form, the law defines the spring constant (or elasticity constant) in a scalar equation, stating the tensile/compressive force is proportional to the extended/contracted displacement and the material recovers its initial shape after unloading. In the context of plasticity, the applied force will induce non-recoverable (irreversible) deformations in the material when the stress reaches a critical magnitude, called as the "yield strength" or "elastic limit". The significance of the elastic limit in structural design lies in the fact that it represents the maximum allowable stress before the material undergoes permanent deformation.

(1) Concrete

Although the shape of complete stress–strain curve, the elastic modulus and the Poisson's ratio of concrete under uni-axial tension are similar to those under uni-axial compression, yet there is significant difference in its yield (and failure as well) mechanism: as the uni-axial tension state tends to arrest cracks much less frequently than the compressive state, the interval of stable crack propagation is anticipatorily much shorter.

There is evidence that the compressive and tensile strengths are closely related but there is no fixed proportion: as the compressive strength of concrete increases, the tensile strength also increases but at a lower rate. In other words, the tensile-to compressive strength ratio depends on the general level of the compressive strength. It appears that this ratio is approximately 10–11% for low-strength concrete, 8–9% for moderate-strength concrete, and 7% for high-strength concrete.

Most slim structural elements are designed under the assumption that the concrete would resist the compression but no tension, and use is made of steel bars to pick up tensile loads. With mass concrete structures however, tensile strength cannot be ignored because concrete cracking is frequently the outcome of a local tensile failure due to restrained shrinkages resulted either from lowering of concrete temperature or/and from drying of concrete moist. And it is impractical to resist all of the tensile failure by steel reinforcement. Therefore, an estimation of tensile strength (or ultimate tensile strain) is demanded, especially for judging the safety of a concrete dam under seismic actions. In addition, a combination of tensile, compressive, and shearing stresses determines the strength when the concrete is in three-dimensional loading state, such as in arch dams.

There exists a fundamental inverse relationship between concrete porosity and its strength. Since natural aggregates are generally dense and strong, therefore the porosity of the cement paste matrix as well as the ITZ will overwhelmingly determine the strength of normal-weight concrete.

Table 2.21 summarizes the concrete parameters of Xiaowan Arch Dam by laboratory experimental studies. It is evident that the strength and other related parameters depend on the concrete proportions related to the grade and the amount of cement as well as the amount of added water (i.e. W/C). Actually, they also depend on the characteristics of stone aggregate, curing age and conditions (temperature and moisture), loading conditions, test methods, etc. (Mehta and Monteiro 2006).

1. Aggregate

The influence of aggregates on concrete strength is not generally appreciated because aggregate strength is usually not a dominant factor in the normal-weight concrete. In other words, with most natural aggregates their strengths are hardly mobilized because the concrete failure is dominated by the other two phases. However, from theoretical considerations it may be anticipated that, independent of W/C, the size, the shape, the surface texture, and the mineralogy of aggregate particles would influence the characteristics of ITZ and, in turn, affect concrete strength.

A change in the maximum size of well-graded coarse aggregates imposes two opposing effects on the strength of concrete. With the same cement content and consistency, concrete mixtures containing larger aggregate particles require less mixing water. On the contrary, larger aggregates are prone to form weaker ITZ containing more micro-cracks. The net effect will vary with the W/C of concrete and the type of applied stress.

It has been observed that a concrete mixture containing rough-textured or crushed aggregates would show somewhat higher strength (especially tensile strength) at early ages. A stronger physical bond between the aggregate and the hydrated cement paste could be responsible for this phenomenon. At later ages however, when the chemical interaction between aggregates and cement paste begins to take effect, the influence of the surface texture of aggregate on strength may be reduced.

Table 2.21 Concrete parameters tested in Xiaowan Arch Dam, China

Strength grade	Aggregate percentage	Fly ash percentage (%)	W/C	Water content (kg/m^3)	Cementitious content (kg/m^3)	Compressive strength (MPa)				Tensile strength (MPa)			
						7 days	28 days	90 days	180 days	7 days	28 days	90 days	180 days
$C_{180}40$	5:5	30	0.4	92	230	19.7	30.5	42.9	48.6	1.91	2.49	3.33	4.09
$C_{180}35$		30	0.45	92	204	16.6	27.3	39.1	44.1	1.70	1.95	3.08	3.15
$C_{180}30$		30	0.5	92	184	15.8	26.6	38.8	43.8	1.28	1.85	2.63	2.91

Strength grade	Maximum tensile strain ($\times 10^{-6}$)				Young's modulus (GPa)				Adiabatic temperature rise (°C)		Impervious grade	Frozen grade
	7 days	28 days	90 days	180 days	7 days	28 days	90 days	180 days	28 days	Final		
$C_{180}40$	125.7	127.1	135.9	140.3	18.61	23.81	27.31	30.63	26.05	28.22	>W14	>F250
$C_{180}35$	103.1	110.9	115.3	126.8	16.99	23.55	26.62	30.60	25.58	27.03	>W14	>F250
$C_{180}30$	78.8	95.3	105.7	117.5	16.36	21.25	26.14	30.31	24.12	25.61	>W14	>F250

Differences in the mineralogical composition of aggregates are also known to affect the concrete strength. Reports show that, with identical mix proportions, the substitution of a calcareous aggregate for a siliceous aggregate can result in certain strength improvement. This may be due to the higher ITZ bond at later ages.

2. Curing conditions

The term "curing of concrete" involves a combination of growth conditions (time, humidity, and temperature) that promote the cement hydration immediately after the placement.

At a given W/C, the porosity of a hydrated cement paste is determined by the degree of cement hydration. Under normal temperature some of the constituent compounds of Portland cement begin to hydrate as soon as water is added, but the hydration reactions slow down considerably when the products of hydration coat the anhydrous cement grains. This is because hydration can proceed satisfactorily only under conditions of saturation. It almost stops when the vapor pressure of water in capillaries falls below 80% of the saturation humidity.

Diffusion of the adsorbed water and the water held by capillary tension in small pores (under 50 nm) of the hydrated cement paste into large capillary voids within the system or to the ambient environments, is a time-dependent process that takes place over long periods. An increase in the atmospheric humidity is expected to slow down the rate of moisture flow from the interior to the outer surfaces of concrete.

Like all chemical reactions, temperature has an accelerating effect on the hydration reactions. With moist-cured concrete the influence of temperature on strength depends on the temperature history from casting to curing.

i. Age

The evaluation of time-dependent strength (elastic modulus as well) is of great concern to structural engineers.

A minimum period of 7 days for moist-curing is generally demanded for the concrete containing normal Portland cement. It should be noted that the time versus strength relations in concrete generally assume moist-curing conditions and normal temperatures. At a given W/C, the longer time the moist curing period, the higher is the strength, subject to the hydration of anhydrous cement particles is still going on with sufficient water.

It has been reported that the strength and elastic modulus of concrete are not influenced to the same degree by curing age: at later ages (i.e. 3–12 months) the elastic modulus increases at a higher rate than the compressive strength. It is probably due to the beneficial effect of the density improvement of ITZ, as a result of slow chemical interaction between the alkaline cement pastes and aggregates, is more pronounced for the elastic modulus than for the compressive strength.

ii. Humidity

The strength of continuously moist-cured concrete is much greater than that of air-cured concrete. Moist-curing is provided either by water spraying/pounding, or by covering the concrete surface with wet mats of sand/sawdust/cotton. Since the amount of mixing water in a concrete mixture is usually more than needed for Portland cement hydration, proper application of an impermeable membrane soon after the concrete placement may offer an acceptable condition to maintain the strength development at a satisfactory rate.

It has been observed that regardless of mix proportions or curing age, concrete specimens that are tested in wet conditions exhibit about 15% higher elastic modulus than the corresponding specimens tested in a drying condition. On the contrary, the compressive strength of the specimen behaves in the opposite manner, i.e., the strength is higher by about 15% when the specimens are tested in drying condition. The explanation would be that: in a saturated cement paste the adsorbed water in the C-S-H is load-bearing, which contributes to higher elastic modulus; on the other hand, the disjoining water pressure in the C-S-H tends to reduce the van der Waals force of attraction, which in turn, to lower down the strength.

iii. Temperature

When concrete is casted and cured at a specific constant temperature in the range of 5–46 °C, it is generally observed that the higher of the temperature, the more rapid is the cement hydration and the strength development. It is reported that the 28-day strength of concrete specimens casted and cured at 5 °C is only about 80% of those casted and cured at 21–46 °C. At a curing temperature near freezing, this percentage is further lowered down to about one half. Therefore, adequate temperature must be maintained for a sufficient time, to provide enough activation energy for the hydration reactions to launch.

It has been observed, too, that within the temperature range 5–46 °C, the lower casting and curing temperature, the higher will be the ultimate strength. This is mainly attributable to a more uniform microstructure (especially the pore size distribution) of the hydrated cement paste.

3. Loading conditions

Loading conditions include stress level and duration. In addition, the advent and degree of nonlinearity in the complete stress–strain curve would obviously depend on the application rate of load.

The grading strength of concrete is tested in laboratory by uni-axial compression (SL352-2006) in which the load is progressively increased to crush the specimen within 2–5 min. In practice, most structural elements are subjected to a dead load for an indefinite period and, at times, to repeated loads or to impact loads. It is therefore, desirable to know the relationship between the concrete strength under laboratory loading conditions and actual loading conditions.

Table 2.22 Comparison of tensile strength values: Xiaowan Arch Dam, China

Strength grade	Age (days)	Wet-screened (two-graded) concrete (MPa)			Fully-graded (four-graded) concrete (MPa)		
		Splitting	Axial	Third-point flexural	Splitting	Axial	Third-point flexural
$C_{180}40$	28	2.40	2.75	3.62	2.12	1.41	2.71
	180	3.50	3.56	5.46	3.10	1.96	3.89
$C_{180}30$	28	2.11	2.20	3.41	1.64	1.09	2.53
	180	3.00	3.29	4.49	2.65	1.77	3.26

4. Scale effects

It has been widely accepted that the test results of concrete strength are significantly affected by the parameters involving in the test specimens including their shape and size.

5. Test methods

Direct tension test of concrete is seldom exercised, mainly because the specimen holding devices will introduce secondary stresses that cannot be ignored or revised. The most prevalent tests for estimating the tensile strength of concrete make use of splitting tension and third-point flexural (bending) loading.

Table 2.22 illustrates the comparison of tensile strengths in Xiaowan Arch Dam by different methods. It is evident that:

- For wet-screened concrete, axial tensile strength is the largest; on the contrary, for fully-grade concrete, axial tensile strength is the smallest.
- Third-point flexural loading tends to overestimate the tensile strength by 50–100%, probably because of the assumption of linear stress–strain relationship throughout the cross section of the bended beam and the fact that only a small portion near the specimen bottom is subjected to high tensile stress under the flexural loading.
- The tensile strength of fully-graded concrete is about 73–76% lower than that of wet-screened one.

In the design of hydraulic structures, the cracking resistance of concrete is primarily specified using an allowable value of tensile strain below which no apparent cracks manifest. This index is normally ranged between 0.00005 and 0.00007 apparently age dependent and specimen scale dependent. Taking Xiaowan Arch Dam for example (see Table 2.23), the maximum tensile strain increases with the age, and that of the fully-graded concrete is about 74–78% smaller than that of wet-screened one.

Table 2.23 Maximum tensile strain values: Xiaowan Arch Dam, China

Strength grade	Age (days)	Maximum tensile strain ($\times 10^{-6}$)	
		Wet-screened (two-graded) concrete	Fully-graded (four-graded) concrete
$C_{180}40$	28	123.9	97.0
	180	139.9	107.3
$C_{180}30$	28	114.2	89.8
	180	128.2	94.8

(2) Intact rocks

The uni-axial compressive strength of an intact rock is related to its type ranging from the lowest 40 MPa (phyllites) to the highest 170 MPa (rhyolites), according to Hoek and Bray (1981).

Mostly (>70%) but not always, the tensile strength tested by splitting $\sigma_{t,s}$ is larger than that by direct axial tension $\sigma_{t,d}$, the ratio $\sigma_{t,d}/\sigma_{t,s}$ is ranged within 0.60–1.43.

Instead of compressive and tensile strengths, the most important rock strength for hydraulic structures is the shear strength, particularly in the design of cut slopes and foundations of high concrete dams. Shear strength is a result of friction and interlocking of particles, and possibly cementation or bonding at particle contacts. It is evaluated in a comprehensive way using experiments, back analyses, and engineering analogues (empirical data). Laboratory tests employ shear box (direct shear test), tri-axial and unconfined (uni-axial) compressive apparatus, whereas in situ tests fall into vane shear and direct shear (Commission on Standardization of Laboratory and Field Tests (ISRM) 1974).

The Mohr envelope is primarily a graphic method to represent the results of a series of experiments on the shear of rock-like materials under varying external conditions, e.g. tri-axial tests under a series of confining pressures. In any experiments, the maximum and minimum principal stresses (σ_1 and σ_3) when failure takes place, are assumed to be known, and a Mohr circle for them can be drawn. If the conditions of test (e.g. confining pressure) are changed slightly, a slightly shifted Mohr circle (see Fig. 2.14) will be obtained. The envelope of all such circles, if exists, is the Mohr envelope for the rock-like material which is a curve relating normal stress σ and shear stress τ. In practice, only a limited portion of the envelope is available.

In a definite stress range, prior to the postulation of the principle of effective stress, the shear strength of material on a particular plane was expressed by Coulomb as a linear function of the normal stress. Therefore, in the stability analysis, it is generally assumed that the failure of material may be calibrated using the Mohr-Coulomb criterion, in which the shear strength is expressed in terms of parameters c (cohesion) and φ (angle of shearing friction) by the formula

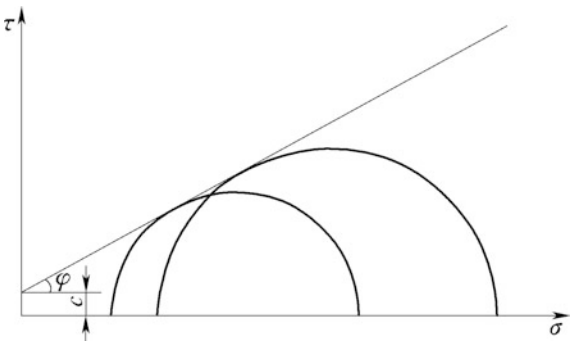

Fig. 2.14 Mohr-Coulomb strength envelope

$$\tau_f = c + \sigma \tan \varphi \tag{2.30}$$

where c and φ = total stress strength parameters representing the intercept at the ordinate axis and the slope of the Mohr-Coulomb shear envelope.

Use is made of tested data, graphs of shear stress against normal stress and shear displacement may be plotted to find c and φ corresponding to the yield, peak and residual shear strengths, which are selectively employed in the stability analysis taking into account of the types of hydraulic structures and the stipulated work situations. In the selection of strength parameters, the reservoir impounding induced rock softening should be foreseen, too.

Although the Mohr-Coulomb theory is not exactly true to rock-like materials, yet it offers a simple way to represent their failure under combined compressive-shear stress states from which an estimation of the shear strength can be easily obtained. In the preliminary phases of design, the shear strength parameters—the friction coefficient $f = \tan\varphi$ and cohesion c, may be roughly estimated by the compressive strength and tensile strength using Mohr rupture diagram.

It should be reminded that tests are always not able to simulate exact natural settings of rock-like materials, particularly the rock mass with discontinuities, therefore the testing data are normally not applied directly. They are subjected to revision taking into account of experimental conditions, sample representatives, computing methods, and natural conditions.

Assuming fresh to slightly weathered rock, the peak shear strength parameters range from the lowest sedimentary (triassic, coal, chalk) of c' = 1–20 MPa and φ' = 25°–35°, to the highest Igneous (granite) of c' = 30–50 MPa and φ' = 45°–55°. Strongly weathered rock will lead to significantly reduction in shear strengths (Look 2007).

Table 2.24 summarizes the shear strengths of typical intact rocks (Wu and Zhou 2013) and Table 2.25 gives the intact rock strengths and other parameters in Xiaowam Project.

Table 2.24 Strengths of intact rocks (Wu and Zhou 2013)

Rock type			Compressive		Tensile (splitting) (MPa)	Shear	
			Dry (MPa)	Wet (MPa)		c' (MPa)	φ' (°)
Igneous	Intrusives (plutonic)	Granite	150–230	110–210	7.5–16.5	10–35	45–65
		Diorite	180–270	140–250	7.5–17.5	12.4–16.7	54–61
		Porphyry	110–294	91–215	9.8–15.6	9.5–55	40–65
	Extrusives (volcanic)	Basalt	134–202	73–150	8.5–20.0	20–60	48–55
		Rhyolite	180–260	160–220	10.0–14.5	10–50	45–60
Sedimentary	Clastic sedimentary	Sandstone	18–80	8–68	2.0–5.5	8–40	35–50
		Shale	9–77	5–68	1.5–4.5	3.6–9.8	16–40
	Carbonatite	Limestone	80–235	32–174	6.0–14.1	10–50	35–50
		Dolomite	56–169	50–130	4.0–20.5	19.6–49.0	30–55
	Weak and soft	Claystone	20–59	2.0–32	3.5–5.5	7.5–11.5	18–30
Metamorphic	Ortho-rock	Gneiss	140	80	4.5–13.5	3–5	30–50
	Para-rock	Quartz	145–200	50.0–176.8	8.8–18.5	22–58	45–58
		Marble	70–140	50–118	5.0–14.5	15–30	35–50
		Slate	60–142	20–140	3.5–6.5	2–20	45–60
		Phyllite	73–111	68–111	3.5–5.5	1–20	26–65
		Schist	90–152	63–140	5.5–16.7	1–20	26–65

(3) Discontinuities

It is customarily assumed that the strength of a discontinuity is represented by the Mohr-Coulomb criterion (see Eq. 2.30). To give a general idea, at unfilled rock joints the friction angle ranges from $\varphi' = 20°–27°$ (schists, shale) to $\varphi' = 34°–40°$ (basalt, granite, limestone, conglomerate).

Table 2.25 Parameters of intact rocks (laboratory): Xiaowan Project, China

Rock type	Density (g/cm^3)	Porosity (%)	Water absorption (%)	Compressive strength (dry) (MPa)	Compressive strength (wet) (MPa)	Young's modulus E (GPa)	Poisson's ratio μ
Biotite granitic gneiss	2.63	2.23	0.4	171.6	169.8	38.0	0.27
Hornblende plagioclase gneiss	2.89	3.12	0.24	127.2	95.7	33.9	0.29
Hornblende schist	2.88	1.02	0.17	133.2	122.9	42.2	0.25

(4) Rock masses

Jointed rock masses are very often encountered in hydraulic structures (e.g. dams, tunnels, caverns, etc.). Their strength parameters are strongly dependent on the stress states in addition to the properties of each joint.

The determination of rock mass strength can be approached either via theoretical/computational analyses using the strengths of intact rocks and discontinuities, or via in situ tests directly.

In the first approach, researchers initially devoted themselves to the problems linked to stratified rock with regard to the elastic response and failure. The seminal work of Salamon (1968) on stratified materials consisting of isotropic layers was preceded by the works of Wardle and Gerrard (1972) who examined some restrictions to the values of equivalent elastic constants. In a work by Gerrard (1982a, b) orthorhombic constituents were considered, and Bourne (2003) presented an interesting discussion on global versus local stress states. Other works tackling the same problem with numerical approaches can be found in, for example, Adhikary and Dyskin (1998), Guz and Soutis (2001). Triantafyllidis and Gerolymatou (2014) formulated a solution covering both elasticity and failure in three dimensions.

Due to the fact that real world rock masses are discontinuous in most cases, tests conducted on small specimens in laboratory generally do not yield appropriate strength and deformation parameters (Bieniawski 1968a, b). The smaller of the specimen, the fewer discontinuities are presented and hence the stronger will be the specimen. A large specimen may, therefore, provide a better estimation of these characteristics. In situ tests are highly desirable for the strength evaluation of rock mass although difficulties arise from the extreme capacity demand of testing loads.

There are many types of large scale in situ tests such as compression tests and shear tests, etc. They are exercised throughout the world for various purposes and in various applications. For detailed messages our readers are referred to the book by Dunnicliff (1988).

It is also appropriate to suggest that laboratory or in situ testing is minimized until the decision on the site of the hydraulic structure has been made. In the early phases of design, the deformation modulus, uni-axial compression strength σ_c, uni-axial tensile strength σ_t, and shear strength parameters c and $\tan\varphi$ of the rock mass (weathered or intact) may be estimated using the rock classification indices of RBQ, RMR, and Q.

For dams, the basic quality index BQ can be used directly. However, the Chinese Standard (GB50218-94) requests a revision in BQ for underground structures and cut-slopes, the main factors taken into account of in the revision are the groundwater conditions, dominant structural planes, in situ geo-stresses. The Standard (GB50218-94) also suggests empirical relationships of BQ versus physical and mechanical parameters for rock masses, which are obtained from the statistic analysis relating the field tests of 47 typical hydraulic projects in China.

GB 50487-2008 «Code for Engineering Geological Investigation of Water Resources and Hydropower» also recommends shear strength parameters of rock

Table 2.26 Recommended shear strength and deformation parameters of rock masses (GB 50287-99)

Rock grade	Shear between concrete/ rock contact surface		Shear of rock		Deformation modulus
	f'	c' (MPa)	f'	c' (MPa)	E (GPa)
I	1.50–1.30	1.50–1.30	1.60–1.40	2.50–2.00	>20
II	1.30–1.10	1.30–1.10	1.40–1.20	2.00–1.50	20–10
III	1.10–0.90	1.10–0.70	1.20–0.80	1.50–0.70	10–5
IV	0.90–0.70	0.70–0.30	0.80–0.55	0.70–0.30	5–2
V	0.70–0.40	0.30–0.05	0.55–0.40	0.30–0.05	2–0.2

masses and discontinuities, according to the collected data from the extensive in situ and laboratory tests carried out in the China's hydraulic engineering.

Table 2.26 lists a portion of deformation and shear strength parameters recommended in the China's design codes for hydraulic projects (GB 50287-99), which may be referred to in the early phases of design. Table 2.27 gives the rock classification and corresponding parameters recommended for Xiaowan Project.

(4) Steel bars

The standard strengths of bolts (steel bar, strand wire anchor, earth nail) have been discussed previously in Sect. 2.2 (see Table 2.7).

2.7.2 Yield (Failure) Criteria

(1) Concept

From the uni-axial tests illustrated in Figs. 2.8, 2.9 and 2.10 it may be justified that a yield or ultimate stress can readily be determined. What if, however, there are bi-axial or tri-axial stresses exerting on a sample? Towards this question it is necessary to extend the definition from the uni-axial concept of a yield (failure) stress to a general three-dimensional state of yield (or failure) criterion (Michino and Findley 1976; Pisarenko and Lebedev 1976; Gurson 1977).

A "yield criterion" is a function of the strain/stress state and the material parameters defined either in strain or stress space, the latter is more prevalent, for deciding what combination of multi-axial stresses will bring about yield (Scheunemann 2004; Sakash et al. 2006; Wang and Lee 2006). It is expressed mathematically by a yield function F being equal to zero, i.e. $F = 0$. The material will perform elasticity where the yield function $F < 0$. The suitability of any proposed yield criteria must be validated by experiments and preferably, be supported by clear physical mechanism (Yu 2002).

Before the detailed works on the yield criteria and further the constitutive relations for rock-like materials hereinafter, it is essential that the terms "stress" and

Table 2.27 Classification and parameters recommended for Xiaowan Project, China

Rock grade		Structure	Geological characteristics	Suggestion on the parameters		
Grade	Sub-grade			Deformation modulus (GPa)	Shear strength	
					f'	c' (MPa)
I		Integrate	Slightly weathered—intact gneiss, non structural face of IV grade or above IV grade. In V grade structure face, joint sets are less or equal to 2. Seismic velocity Vp $\geq$ 5000 m/s	22–28	1.3–1.6	2.0–2.5
II		Blocky	Slightly weathered—intact gneiss, non structural face of IV grade or above IV grade. In V grade structure face, joint sets are 2–3, no filling. Seismic velocity Vp $\geq$ 4500 m/s	16–22	1.3–1.5	1.5–2.0
III	III_a	Inferior blocky	Weakly weathered, structural faces of IV grade are well developed. In V grade structure face, joint sets are above or equal to 3. Seismic velocity Vp = 4500–4000 m/s	12–16	1.1–1.3	1.1–1.5
	III_{b1}	Inferior blocky–blocky	Unloading rock of slightly weathered. Seismic velocity Vp = 4000–3500 m/s	8–12	1.2–1.3	0.9–1.1
	III_{b2}	Inferior blocky	Unloading rock of slightly weathered. Loosen joints are well developed and filled. Joints are well developed, open and filled by kaolinite clay. Seismic velocity Vp = 3000–2000 m/s	6–8	1.0–1.2	0.7–0.9

(continued)

Table 2.27 (continued)

Rock grade		Structure	Geological characteristics	Suggestion on the parameters		
Grade	Sub-grade			Deformation modulus (GPa)	Shear strength	
					f'	c' (MPa)
IV	IV_a	Jointed blocky	Weakly weathered. IV and V graded structural face are well developed. Joint opens. Seismic velocity Vp = 3500–2500 m/s	5–10	1.0–1.1	0.5–0.7
	IV_b	Mosaic	Fault influenced zone, joint concentrated zone, and erosion zone. IV and V grade structural faces are well developed. Joints are slightly open and filled	2–4	0.9–1.0	0.4–0.5
	IV_c	Cataclastic	Fault fragrant zone, strongly erosion zone. Structural faces are well developed and filled	0.5–2	0.8–0.9	0.3–0.4

"strain" are defined without ambiguity. Typically, two types of definitions are considered. The first type deals with materials only undergo small strains, whereas the second type deals with materials that are not limited to small strains. In the design of hydraulic structures, the first type is normally postulated, particularly for their normal working situation. Under such circumstances the Cauchy stress tensor corresponding to infinitesimal strain tensor is employed (Landau and Lipshitz 1970).

Towards the three dimensional expression of a yield criterion for rock-like materials, the following invariants with regard to stress and strain tensors are customarily employed (Nayak and Zienkiewicz 1972).

$$\begin{cases} I_1 = \sigma_x + \sigma_y + \sigma_z \\ I_2 = -\sigma_x\sigma_y - \sigma_y\sigma_z - \sigma_z\sigma_x + {\tau_{xy}}^2 + {\tau_{yz}}^2 + {\tau_{zx}}^2 \\ I_3 = \sigma_x\sigma_y\sigma_z + 2\tau_{xy}\tau_{yz}\tau_{zx} - \sigma_x\tau_{yz}^2 - \sigma_y\tau_{zx}^2 - \sigma_z\tau_{xy}^2 \end{cases} \tag{2.31}$$

$$\begin{cases} J_1 = 0 \\ J_2 = \frac{1}{6}\left[(\sigma_x - \sigma_y)^2 + (\sigma_y - \sigma_z)^2 + (\sigma_z - \sigma_x)^2 + 6({\tau_{xy}}^2 + {\tau_{yz}}^2 + {\tau_{zx}}^2)\right] \\ \quad = \frac{1}{3}(I_1^2 + 3I_2) \\ J_3 = \frac{1}{27}(2I_1^3 + 9I_1I_2 + 27I_3) \end{cases} \tag{2.32}$$

$$\begin{cases} \sigma_m = p = \frac{1}{3}(\sigma_x + \sigma_y + \sigma_z) = \frac{1}{3}I_1 \\ q = \sqrt{3J_2} \\ \theta_\sigma = \frac{1}{3}\arccos\left(\frac{3\sqrt{3}}{2}\frac{J_3}{J_2^{3/2}}\right) \end{cases} \tag{2.33}$$

The first invariant of stress tensor I_1 and the second invariant of deviatoric stress tensor J_2 are always positive, whereas the third invariant of deviatoric stress J_3 reverses in sign if the signs of all the stresses are reversed.

The Lode angle θ_σ is useful in the study of a yield surface on its π plane.

The hydrostatic stress p and the generalized shear stress q are customarily used in the study of yield criterion and corresponding constitutive relation in the classical plasticity theory, particular for soils.

(2) Yield criteria for rock-like materials

The behaviors of rock-like materials under multi-axial stress state are very complex and therefore, they normally have to be described from the phenomenological standpoint. Unlike the laboratory tests for determining the basic strength parameters of rock-like materials under uni-axial compression, splitting tension, and flexure loading, there is no standard test for them under multi-axial stress states.

Strength theory (inclusive yield criterion and failure criterion), as one of the most important components in constitutive relations, has been widely exercised in various computational geomechanics. Textbooks and monographs devoted to computational plasticity are referred to Brebbia (1985), Yu and Li (2012). Other related books and a brief history of nonlinear FEM before 2000 were summarized by Belytschko et al. (2000).

Yield criteria are usually noted in the forms of principal stresses or stress invariants as

$$\begin{cases} F(\sigma_1, \sigma_2, \sigma_3) = 0 \\ F(I_1, I_2, I_3) = 0 \\ F(I_1, J_2, J_3) = 0 \\ F(\sigma_m, J_2, \theta_\sigma) = 0 \\ F(p, q, \theta_\sigma) = 0 \end{cases} \tag{2.34}$$

A visual representation termed as the "yield surface" may be constructed in the principal stress space using the yield criterion in Eq. (2.34). Inside the surface the material is elastic whereas reaching the surface means the material initiates plastic deformation. It is physically impossible for a material to go beyond its yield surface.

For an isotropic material, the yield function F should be invariant with respect to the interchange operator for the coordinate axes, this means that the yield function is a symmetric function of the principal stresses σ_i (i = 1, 2, 3), namely, the yield function is tri-fold symmetric.

Nowadays, there have been numerous isotropic yield (failure) criteria for rock-like materials (see Table 2.28) falling into single-shear series (e.g. Tresca, Mohr-Coulomb), twin-shear series (e.g. Yu), and triple-shear series (e.g. von Mises, Drucker-Prager). In hydraulic structures, rock-like materials are normally regarded as frictional, and the Mohr-Coulomb criterion taking into account of the effects of friction and cohesion perhaps is the most prevalent one.

Although there is desperate need for anisotropic yield (failure) criteria with respect to jointed rock masses, yet credible and practical results are limitedly available except for simpler case with layered rocks (Mutschler and Fröhlich 1987; Taliercio and Landriani 1988; Ramamurthy 1993; Lai et al. 1999; Tien and Kuo 2001; Tien et al. 2006).

Physically, any yield surfaces for solid materials, if exist, should be smooth. But many of them artificially built focusing on one-or-two yield mechanisms solely may develop pointed pyramidal or conical vertices. For example, the single-shear criteria (e.g. the Mohr-Coulomb) are angular on the π-plane. Although theories of plasticity imply the formation of a vertex at the loading point on the yield surface (Hill 1967), yet experimental evidences suggest that, while relatively high curvature at the loading point is often observed, sharp vertices are seldom detected (Hecker 1976). Experimental data also indicate that the yield surfaces for metals are convex in Cauchy stress space, if elastic response within the yield surface is linear and unaffected by plastic flow.

Where there are pointed pyramidal or conical vertices on a yield surface, the flow vector of plastic strain is not uniquely defined. Before, these singularities give rise to constitutive models that are difficult to implement numerically. Koiter (1953) first provided limits within which the incremental plastic strain vector must lie. The singularities of the Mohr-Coulomb yield criterion can also be overcome by rounding off them or by employing a simple mathematical artifice in the numerical procedure (Owen and Hinton 1980). Other treatments of singularities in yield surfaces available are suggested by Ortiz and Popov (1985), Sloan and Booker (1986), de Borst (1987), Runesson et al. (1988), Simo and Hughes (1988), Pramono and Willam (1989), de Borst et al. (1991), Khan and Huang (1995), Larsson and Runesson (1996).

(3) Prevalent yield criteria in hydraulic structures

1. Von Mises criterion

This criterion is based on the Tresca criterion but takes into account the postulation that hydrostatic stresses do not contribute to material failure (Von Mises 1913; Timoshenko 1953)

$$J_2 = C \tag{2.35}$$

The von Mises yield surface in principal stress space circumscribes a cylinder around the hydrostatic axis (see Fig. 2.15).

Table 2.28 Isotropic yield (failure) criteria for rock-like materials

Criterion/ mechanism	Expression	Yield surface	Feature	Applicability
Tresca/single-shear	$\frac{\sigma_1 - \sigma_3}{2} = k$	Regular hexagonal pyramidal: on the π plane it is hexagon; on the meridian plane it is a pencil with parallel lines; there are ridges on the yield surface	Hydrostatic stress is not related to material failure	Metals or pure clays without friction
Mises/triple-shear (shear energy)	$J_2 = C$	Cylindrical surface: on the π plane it is circle; on the meridian plane it is pyrometric	Intermediate principal stress σ_2 is related to material failure	Metals or pure clays without friction
Drucker-Prager (D-P)/triple-shear (shear energy)	$\alpha I_1 + \sqrt{J_2} = k$	Circular conical surface: on the π plane it is circle; on the meridian plane it is pyrometric cone; there is conical vertex on the yield surface	Intermediate principal stress σ_2 is related to material failure	Widely exercised in rock-like materials with friction
Mohr-Coulomb (M-C)/singles-shear	$\tau_n = c + \sigma_n tg\varphi$ or $(\sigma_1 - \sigma_3) - (\sigma_1 + \sigma_3)\sin\varphi - 2c \cdot \cos\varphi = 0$	Irregular hexagonal prism: on the π plane it is irregular hexagon; on the meridian plane it is pyrometric cone; there are ridges and conical vertex on the yield surface	Difference in tension and compression is considered; intermediate principal stress σ_2 is not taken into account	Widely exercised in rock-like materials with friction

(continued)

Table 2.28 (continued)

Criterion/ mechanism	Expression	Yield surface	Feature	Applicability
Zienkiewicz-Pande (Z-P)/ shear-compressive	$\beta\sigma_m^2 + \alpha_1\sigma_m - k + \overline{\sigma}_+^2 = 0$	Curved-edge hexagonal prism: on the π plane it is hexagon with rounded corners; there are three types of second power function as failure curve on meridian plane	Intermediate principal stress σ_2 and hydrostatic stress are taken into account	Rock-like materials and soils with friction
Generalized twin-shear/ twin-shear	1. In general compressive state indicated by $\sigma_2 \leq \frac{1}{2}(\sigma_1 + \sigma_3) - \frac{1}{2}\beta(\sigma_1 - \sigma_3)$ The criterion is $f(\tau_{13}, \tau_{12}) = \tau_{13} + \tau_{12} - \beta(\sigma_{13} + \sigma_{12} - k_b) = \sigma_1 - \frac{1}{2}(\sigma_2 + \sigma_3) - \beta[\sigma_1 + \frac{1}{2}(\sigma_2 + \sigma_3)] - k_b = 0$ 2. In general tensile state indicated by $\sigma_2 \geq \frac{1}{2}(\sigma_1 + \sigma_3) - \frac{1}{2}\beta(\sigma_1 - \sigma_3)$ The criterion is $f'(\tau_{13}, \tau_{23}) = \tau_{13} + \tau_{23} - \beta(\sigma_{13} + \sigma_{23} - k_b) = \frac{1}{2}(\sigma_1 + \sigma_2) - \sigma_3 - \beta[\frac{1}{2}(\sigma_1 + \sigma_2) + \sigma_3] - k_b = 0$	Irregular hexagonal prism: on the π plane it is irregular hexagon; on the meridian plane it is pyrometric cone; there are ridges on the yield surfaces	Difference in tension and compression has been considered; yield does not occur under hydrostatic compression	Rock-like materials with friction
Lade/ shear-compressive	$\left(\frac{I_1^3}{I_3} - 27\right)\left(\frac{I_1}{p_a}\right)^m - k = 0$ $I_1^2 + 2I_2 - r^2 = 0$	Double surfaces: one is a group of triangular pyramid with curved edge; another is the concentric sphere	Difference in tension and compression has been considered	Rock-like materials and soils with friction
Willam-Warnke/ shear-compressive	$\frac{1}{3z}\frac{I_1}{\sigma_c} + \sqrt{\frac{2}{5}}\frac{1}{r(\theta)}\frac{\sqrt{J_2}}{\sigma_c} - 1 = 0$ In which $r(\theta) = \frac{u(\theta) + v(\theta)}{w(\theta)}$;	Uniquely and well defined first and second	Intermediate principal stress σ_2 is related to	Concrete

(continued)

Table 2.28 (continued)

Criterion/ mechanism	Expression	Yield surface	Feature	Applicability
	$u(\theta) = 2r_c(r_c^2 - r_t^2)\cos\theta$; $v(\theta) = r_c(2r_t - r_c)\sqrt{4(r_c^2 - r_t^2)\cos^2\theta + 5r_t^2 - 4r_t r_c}$; $w(\theta) = 4(r_c^2 - r_t^2)\cos^2\theta + (r_c - 2r_t)^2$; $r_c = \sqrt{\frac{6}{5}}\left[\frac{\sigma_b\sigma_t}{3\sigma_b\sigma_t + \sigma_c(\sigma_b - \sigma_t)}\right]$; $r_t = \sqrt{\frac{6}{5}}\left[\frac{\sigma_b\sigma_t}{\sigma_c(2\sigma_b + \sigma_t)}\right]$; $z = \frac{\sigma_b\sigma_t}{\sigma_c(\sigma_b - \sigma_t)}$	derivatives on every point of its surface	material failure; biaxial test is demanded	
Bresler-Pister/ extension of the Drucker-Prager criterion	$\sqrt{J_2} = A + BI_1 + CI_1^2$ $A = \sqrt{\frac{1}{3}}\frac{\sigma_c\sigma_t\sigma_b(\sigma_t + 8\sigma_b - 3\sigma_c)}{(\sigma_c + \sigma_t)(2\sigma_b - \sigma_c)(2\sigma_b + \sigma_t)}$; In which $B = \sqrt{\frac{1}{3}}\frac{(\sigma_c - \sigma_t)(\sigma_b\sigma_c + \sigma_b\sigma_t - \sigma_c\sigma_t - 4\sigma_b^2)}{(\sigma_c + \sigma_t)(2\sigma_b - \sigma_c)(2\sigma_b + \sigma_t)}$; $C = \sqrt{\frac{1}{3}}\frac{3\sigma_b\sigma_t - \sigma_b\sigma_c - 2\sigma_c\sigma_t}{(\sigma_c + \sigma_t)(2\sigma_b - \sigma_c)(2\sigma_b + \sigma_t)}$	Uniquely and well defined first and second derivatives on every point of its surface	Intermediate principal stress σ_2 is related to material failure; biaxial test is demanded	Concrete
Griffith/crack initiation of maximum strain energy release rate	1. For $3\sigma_3 + \sigma_1 < 0$ and the joint form included angle $\beta = 0$ with σ_3 The criterion is $\sigma_3 = -R_t$ 2. For $3\sigma_3 + \sigma_1 > 0$ and $\cos 2\beta = -\frac{1}{2}\cdot\frac{\sigma_1 - \sigma_3}{\sigma_1 + \sigma_3}$ The criterion is $(\sigma_1 - \sigma_3)^2 + 8R_t(\sigma_1 + \sigma_3) = 0$	—	Crack initiation and its direction may be predicted; intermediate principal stress σ_2 is not related to material failure	Splitting failure of rock-like materials
Hoek-Brown/ empirical	$\sigma_1 = \sigma_3 + \sigma_c\sqrt{m\frac{\sigma_3}{\sigma_c} + s}$	—	Intermediate principal stress σ_2 is not related to material failure	Rock-like materials with friction

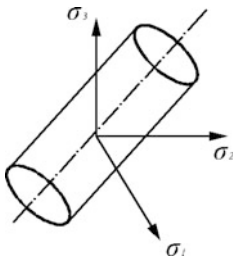

Fig. 2.15 Von Mises yield surface

The Von Mises criterion is used for the yield of rock bolts (steel bar and strand wire) in this book. Towards the expression of the yield criterion and further the establishment of the constitutive relation for the bolt b (stranded wire w and grout g as well) in the subsequent Chaps. 6 and 15, the local coordinate systems for the bolt segment are defined in Fig. 2.16. In the local Cartesian system (see Fig. 2.16a), the z_b-axis is along the bolt axis and upright, the y_b-axis is perpendicular to the bolt and points in the direction of dip, the x_b-axis is formed by the right hand rule. On the basis of the local Cartesian coordinate system, the local Cylindrical coordinate system is further defined in Fig. 2.16b.

The superscripts ca and cy are used to denote a variable in the local coordinate systems of Cartesian and Cylindrical respectively; the subscripts b in small letter and B in capital letter are used to denote the bolt related variables in the local coordinate system and global coordinate system, respectively.

Similar to Eqs. (2.12) and (2.13), the coordinate (displacement as well) transformation from the local Cartesian system to the global one is defined by

$$\begin{cases} \{x\}_b = \begin{Bmatrix} x_b \\ y_b \\ z_b \end{Bmatrix} = \begin{bmatrix} l_{11} & l_{12} & l_{13} \\ l_{21} & l_{22} & l_{23} \\ l_{31} & l_{32} & l_{33} \end{bmatrix} \begin{Bmatrix} X \\ Y \\ Z \end{Bmatrix} = [l]_b^{ca}\{X\} \\ \{\mathrm{X}\} = \begin{Bmatrix} X \\ Y \\ Z \end{Bmatrix} = \begin{bmatrix} l_{11} & l_{21} & l_{31} \\ l_{12} & l_{22} & l_{32} \\ l_{13} & l_{23} & l_{33} \end{bmatrix} \begin{Bmatrix} x_b \\ y_b \\ z_b \end{Bmatrix} = \left([l]_b^{ca}\right)^T \{x\}_b \end{cases} \tag{2.36}$$

where

$$[l]_b^{ca} = \begin{bmatrix} \cos\phi_b & -\sin\phi_b & 0 \\ \sin\phi_b\cos\theta_b & \cos\phi_b\cos\theta_b & -\sin\theta_b \\ \sin\phi_b\sin\theta_b & \cos\phi_b\sin\theta_b & \cos\theta_b \end{bmatrix} \tag{2.37}$$

In which ϕ_b and θ_b are the dip direction and dip angle of the bolt b, respectively.

The displacement transformation from the local Cartesian system to the local Cylindrical one, which will be useful in the works of subsequent Chaps. 15–17, is defined as

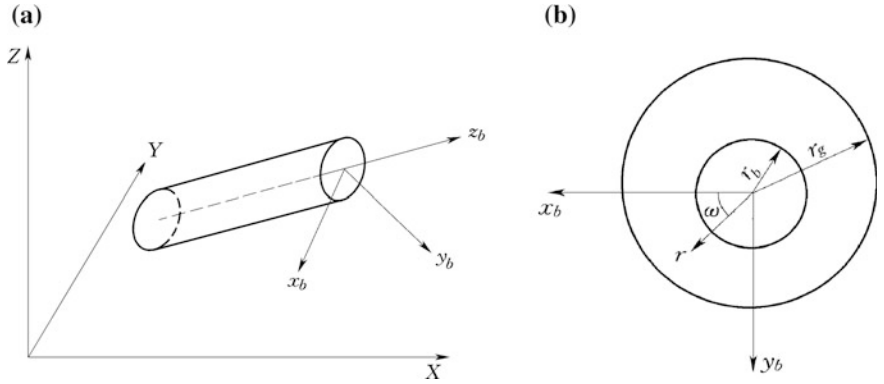

Fig. 2.16 Coordinate systems of bolt segment b. **a** Cartesian; **b** cylindrical

$$\{u\}_b^{cy} = \begin{Bmatrix} u_{rb} \\ u_{\omega b} \\ u_{zb} \end{Bmatrix} = \begin{bmatrix} \cos\omega & \sin\omega & 0 \\ -\sin\omega & \cos\omega & 0 \\ 0 & 0 & 1 \end{bmatrix} \begin{Bmatrix} u_{xb} \\ u_{yb} \\ u_{zb} \end{Bmatrix} = [l]_b^{cy}\{u\}_b^{ca} \tag{2.38}$$

The useful stress and strain transformation between the local Cartesian coordinate system to the global one is further defined by

$$\begin{cases} \{\varepsilon\}_b = [T]_b\{\varepsilon\}_B \\ \{\sigma\}_B = [T]_b^T\{\sigma\}_b \end{cases} \tag{2.39}$$

In which

$$[T]_b = \begin{bmatrix} l_{11}^2 & l_{21}^2 & l_{31}^2 & l_{21}l_{31} & l_{11}l_{31} & l_{11}l_{21} \\ l_{12}^2 & l_{22}^2 & l_{32}^2 & l_{22}l_{32} & l_{12}l_{32} & l_{12}l_{22} \\ l_{13}^2 & l_{23}^2 & l_{33}^2 & l_{23}l_{33} & l_{13}l_{33} & l_{13}l_{23} \\ 2l_{12}l_{13} & 2l_{22}l_{23} & 2l_{32}l_{33} & l_{22}l_{33}+l_{23}l_{32} & l_{12}l_{33}+l_{32}l_{13} & l_{12}l_{23}+l_{22}l_{13} \\ 2l_{11}l_{13} & 2l_{21}l_{23} & 2l_{31}l_{33} & l_{21}l_{33}+l_{23}l_{31} & l_{11}l_{33}+l_{13}l_{31} & l_{11}l_{23}+l_{21}l_{13} \\ 2l_{11}l_{12} & 2l_{21}l_{22} & 2l_{31}l_{32} & l_{21}l_{32}+l_{22}l_{31} & l_{31}l_{12}+l_{11}l_{32} & l_{11}l_{22}+l_{21}l_{12} \end{bmatrix} \tag{2.40}$$

Normally, there are only three stress components $\{\sigma\}_b = [\,\tau_{zxb} \quad \tau_{zyb} \quad \sigma_{zb}\,]^T$ to be taken into account in the formulation of the yield criterion and constitutive relation for bolts and strand wires. For example, the Von Mises yield function F_b of bolt is specifically expressed in the local Cartesian coordinate system by the formula

$$F_b = [3(\tau_{zxb}{}^2 + \tau_{zyb}{}^2) + \sigma_{zb}{}^2]^{1/2} - f_{yk} \tag{2.41}$$

In which f_{yk} is the yield strength of bolt b.

2. Drucker-Prager (D-P) criterion

Drucker and Prager (1952) proposed a generalized von Mises criterion in which the material friction is taken into account. It has been widely implemented in nonlinear FEM codes for geotechnical and hydraulic structures. Although substantial departures from the predictions of the D-P criterion that would give a rather poor approximation to the real failure conditions, had been observed (Humpheson and Naylor 1975; Zienkiewicz and Pande 1977a, b; Chen and Baladi 1985), yet this criterion are prevalent in the computation for hydraulic structures in China due to its

- Simplicity;
- Well defined and easily accessible parameters;
- Engineering convention;
- Comparable safety margin stipulated in the design codes/specifications.

The D-P criterion will be used for the yield of rock-like materials throughout this book. For isotropic intact rocks and concrete, it is expressed in the principal stress space with invariants as

$$F = aI_1 + \sqrt{J_2} - k = 0 \tag{2.42}$$

$$\begin{cases} a = \sin\varphi / [3(3 + \sin^2\varphi)]^{1/2} \\ k = \sqrt{3}c\cos\varphi / \sqrt{3 + \sin^2\varphi} \end{cases} \tag{2.43}$$

In which φ and c are the internal friction angle and cohesion of the material.

There are various expressions of α and k. It is conventionally to term any criterion expressed in Eq. (2.42) with different α and k as the "generalized Von Mises criterion" whose corresponding yield surface in the principal stress space circumscribes a circular conical surface around the hydrostatic axis (see Fig. 2.17),

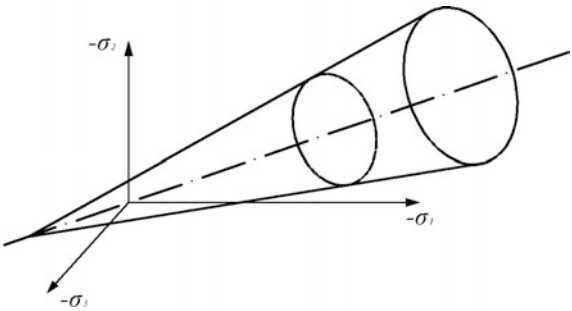

Fig. 2.17 Drucker-Prager yield surface

while with particular expressions of α and k in Eq. (2.43) as the Drucker-Prager criterion.

The D-P criterion will be retrogressed into the Von Mises criterion where $\varphi = 0$.

For the mortar grout segment g surrounding the bolt b (see Fig. 2.16), there are three stress components $\{\sigma\}_g = \begin{bmatrix}\tau_{zxg} & \tau_{zyg} & \sigma_{zg}\end{bmatrix}^T$ corresponding to $\{\sigma\}_b$ in the formulation of its yield criterion and constitutive relation. The D-P yield function F_g of grout g is specifically expressed in the local Cartesian coordinate system (see Fig. 2.16a) by the formula

$$\begin{cases} F_g = a\sigma_{zg} + \sqrt{\frac{1}{3}}\sqrt{\sigma_g^2 + 3(\tau_{zxg}^2 + \tau_{zyg}^2)} - k = 0 \\ a = \sin\varphi_g / \sqrt{3(3 + \sin^2\varphi_g)} \\ k = \sqrt{3}c_g \cos\varphi_g / \sqrt{3 + \sin^2\varphi_g} \end{cases} \tag{2.44}$$

In which φ_g and c_g are the friction angle and cohesion of the grout.

The D-P criterion will be used for the shotcrete lining in this book, too. Towards this purpose, in addition to the global coordinate system, a local Cartesian coordinate system is also needed to simplify the deduction (see Fig. 2.18). This local system is defined with its z_l-axis being perpendicular to the shotcrete layer l, the y_l-axis being on the shotcrete layer and coincident with the dip direction φ_l of the shotcrete layer and forming a dip angle θ_l with the horizontal plane, the x_l-axis being on the shotcrete layer and being orientated by the right hand rule.

The coordinate transformation from the local Cartesian system to the global one is identical to Eqs. (2.12) and (2.13) and Eqs. (2.36) and (2.37) in which the subscripts j and b are substituted by l.

Under the local Cartesian coordinate system, the stress vector of lining l is denoted as $\{\sigma\}_l = [\sigma_{xl}\ \sigma_{yl}\ \tau_{zyl}\ \tau_{zxl}]^T$. The stress transformation between the coordinate systems of lining is identical to Eqs. (2.39) and (2.40) in which the subscript b is substituted by l.

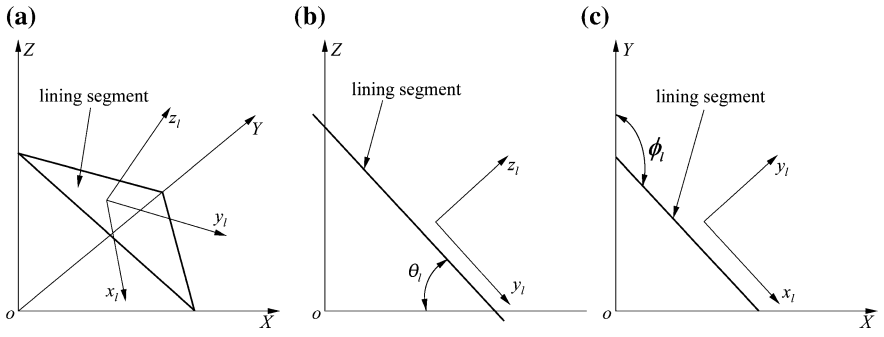

Fig. 2.18 Local coordinate system of lining segment l. **a** Three-dimensional view; **b** projected to dip direction; **c** projected on horizontal plane

The D-P yield criterion for the lining is given by the formula

$$\begin{cases} F_l = aI_1 + \sqrt{J_2} - k = 0 \\ a = \sin\varphi_l / [3(3 + \sin^2\varphi_l)]^{1/2} \\ k = \sqrt{3}c_l \cos\varphi_l / \sqrt{3 + \sin^2\varphi_l} \end{cases} \tag{2.45}$$

In which φ_l and c_l are the friction angle and cohesion of lining l.

The D-P criterion will also be applied to the joint element with thickness (Desai et al. 1985) in this book. Since the intercalations (fault, interlayer) are thin compared to their stretch or the characteristic dimension of the hydraulic structure, their deformation is restrained by the side rock walls. On the local Cartesian coordinate system defined in Fig. 2.2 we can assume that

$$\gamma_{xy}, \varepsilon_x, \varepsilon_y = 0 \tag{2.46}$$

and the stress vector may be denoted as $\{\sigma\}_j = [\ \tau_{zxj} \quad \tau_{zyj} \quad \sigma_{zj}]^T$. The D-P yield criterion may be reduced to

$$F_j = 3a\sigma_{zj} + \sqrt{(1 - 12a^2)(\tau_{zxj}^2 + \tau_{zyj}^2)} - k = 0 \tag{2.47}$$

It is interesting to find that the D-P criterion is actually identical to the Mohr-Coulomb criterion in case of joint element with thickness.

3. Mohr-Coulomb (M-C) criterion

In the principal stress space, the Mohr-Coulomb criterion for isotropic rock-like materials is expressed as

$$\frac{1}{3}I_1 \sin\varphi + \left(\cos\theta_\sigma - \frac{1}{\sqrt{3}}\sin\theta_\sigma \sin\varphi\right)\sqrt{J_2} - c\cos\varphi = 0 \tag{2.48}$$

In which the Lode angle θ_σ varies within $-\frac{\pi}{6} \le \theta_\sigma \le \frac{\pi}{6}$.

Equation (2.48) may be expressed in an alternative form

$$p\sin\varphi + \frac{1}{\sqrt{3}}q\left(\cos\theta_\sigma - \frac{1}{\sqrt{3}}\sin\theta_\sigma \sin\varphi\right) - c\cos\varphi = 0 \tag{2.49}$$

In which q and p are defined in Eq. (2.33).

The M-C yield surface in the principal stress space circumscribes an irregular hexagonal prism around the hydrostatic axis (see Fig. 2.19).

Disregard the disadvantage of the M-C criterion that the intermediate principal stress is not taken into account, it is widely exercised in China attributable to its remarkable advantages of clear physical mechanism, full-fledged parametric evaluation scheme, and rich practice experiences with competent safety margin stipulated in the design codes/specifications.

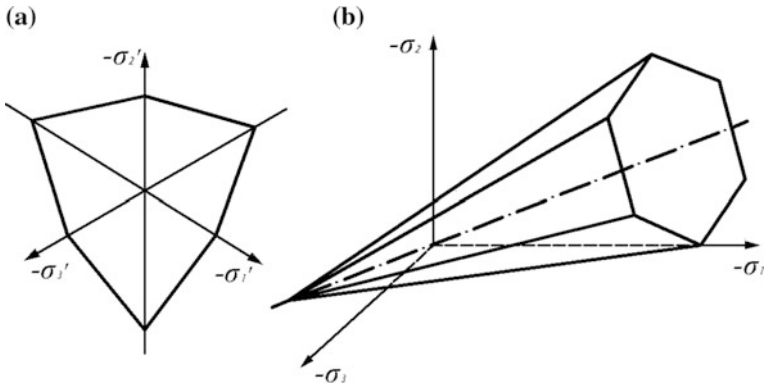

Fig. 2.19 Mohr-Coulomb yield surface. **a** On π-plane; **b** in principal stress space

Modifications of the C-M criterion with tension cut-off were suggested by Paul (1961), Chen and Drucker (1969). Multi-surface models combined with the Mohr-Coulomb criterion with a compressive cap were proposed by Simo et al. (1988), Lourenço and Rots (1997), Sutcliffe et al. (2001). Advanced smooth ridge models such as the Willam-Warnke criterion (1975), the Lade-Duncan criterion (1975), the Zienkiewicz-Pande criterion (1977a, b), and the others, are available (see Table 2.28).

In this book, tension cut-off will be adopted but the multi-surface (cap) models will not be taken into account because normally the hydrostatic pressure is not sufficiently large to bring about yield for the rock-like materials encountered in hydraulic structures.

The M-C criterion is also used for the yield of joint element without thickness, whose local Cartesian coordinate system has been defined in Fig. 2.2. The strain and stress transforming between the global and local coordinate systems of a joint segment j is identical to Eqs. (2.39) and (2.40) in which the subscript b is substituted by j. In the local coordinate system of joint j, the M-C criterion with tension cut-off is expressed by

$$\begin{cases} F_j = (\tau_{zxj}^2 + \tau_{zyj}^2)^{1/2} + \sigma_{zj} tg\varphi_j - c_j & for \quad \sigma_{zj} - \sigma_{Tj} < 0 \\ F_j = \sigma_{zj} - \sigma_{Tj} & for \quad \sigma_{zj} - \sigma_{Tj} \geq 0 \end{cases} \tag{2.50}$$

In which c_j, φ_j and σ_{Tj} are the cohesion, friction angle, and tension strength, respectively.

2.8 Constitutive Relations: Elasticity

2.8.1 Concept

In continuum mechanics, the "constitutive relation (equation, law)" or "equation of state" relates physical variables specific to a material, and approximates the response of that material to external stimuli such as applied fields or forces. Although constitutive relations may be derived from the first principle in physics, yet most of them used in the computation for hydraulic structures are simply phenomenological. They are combined with other governing equations (e.g. equilibrium, conservation, continuity) to solve mechanical/physical field problems. Taking the water percolation problem for instance, constitutive equation relates the seepage flow rate of water in rock-like materials to the water head (hydraulic potential) gradient (e.g. the Darcy's law). In the thermal conduction problem of concrete dams, it links the rate of heat flow with the gradient of temperature (e.g. the Fourier's law). Towards a structural problem, the connection between applied stresses or forces to emerged strains or deformations (e.g. the Hooke's law proposed in 1675) is necessarily built and often called as the "stress–strain relation". It deals with linear elastic materials which are able to resist actions and to return to their original size and shape when the actions are removed. The mechanism for elastic behavior can be quite different for different materials (Chen and Saleeb 1994).

A common approximate constitutive relation is frequently expressed as a simple proportionality through parameters representing the properties of the material, such as a spring constant in elasticity. However, it is often necessary to account for the directional dependence of the material, which demands a generalization from scalar parameters to a tensor. Constitutive relations are also modified to account for the rate of response and the non-linear performance of materials, if necessary.

There are various definitions of elastic moduli, such as the Young's modulus, the shear modulus, and the bulk modulus, all of them are the measures of the inherent elastic properties of a material as the resistance to deformation under an applied load. These moduli are corresponding to different kinds of deformation. For instance, the Young's modulus applies to extension/compression of a body, whereas the shear modulus applies to its torsion.

Perfect elasticity is only an approximation of the real world substance, and few rock-like materials stay purely elastic even after very small deformations. Regarding to the definition of the Young's modulus E which significantly influences the rigidity of hydraulic works, there are several prevalent expressions. The "tangent modulus" is given by the slope of a line drawn tangent to the stress–strain curve at any point, of which the initial tangent is the slope at initial stress. The elastic tangent modulus which is conventionally named as "elastic modulus", is the slope at any specified linear point (or near linear) on the stress–strain curve, but usually at a specified stress level (such as 50% for rock) of the maximum or peak stress. The "chord modulus" is given by the slope of a line drawn between two

points on the stress–strain curve. The "deformation modulus" is the slope of such a line between zero and a specified stress level with respect to the maximum or peak stress (e.g. 40% for concrete, 50% for rock, one-third for soil), which belongs to "secant modulus". The "recovery modulus" is the slope of unloading route.

For a sample subjected to simple axial load, i.e. the confining pressure $\sigma_3 = 0$ in Fig. 2.8, the ratio μ of the lateral strain ε_r to axial strain ε_a within the elastic range is called the "Poisson's ratio". It is generally not needed for the conventional design of concrete gravity dams. However, it is demanded for the structural analysis of tunnels, arch dams, and other statically indeterminate structures. In principle, the values of E of intact rocks and concrete, can be estimated from the curve relating principal stress difference and axial strain in appropriate laboratory tests. However, due to the effects of sampling disturbance, it is preferable to determine the Young's modulus E and Poisson's ratio μ (or shear modulus G) from the results of in situ tests.

(1) General form

The elastic constitutive relation is expressed in the form of increments throughout the rest coverage of this book. According to the convention prevalent in engineers, we use matrix notation for the fourth-order elastic tensor and vector notation for the second-order stress and strain tensors

$$\{\Delta\sigma\} = [\,\Delta\sigma_x \quad \Delta\sigma_y \quad \Delta\sigma_z \quad \Delta\tau_{yz} \quad \Delta\tau_{zx} \quad \Delta\tau_{xy}\,]^T \tag{2.51}$$

$$\{\Delta\varepsilon\} = [\,\Delta\varepsilon_x \quad \Delta\varepsilon_y \quad \Delta\varepsilon_z \quad \Delta r_{yz} \quad \Delta r_{zx} \quad \Delta r_{xy}\,]^T \tag{2.52}$$

The 6×6 elastic matrix $[D]^e$ linearly links above stress and strain vectors by the formula

$$\{\Delta\sigma\} = [D]^e\{\Delta\varepsilon^e\} \tag{2.53}$$

(2) Special cases

1. Discontinuity with thickness

For the discontinuity j with thickness (e.g. interlayer), its strain increment vector will be reduced with only three components in the local Cartesian coordinate system defined in Fig. 2.2 as

$$\{\Delta\varepsilon\}_j = [\,\Delta\gamma_{zxj} \quad \Delta\gamma_{zyj} \quad \Delta\varepsilon_{zj}\,]^T = \frac{1}{a_j}[\,\Delta u_{xj} \quad \Delta u_{yj} \quad \Delta u_{zj}\,]^T \tag{2.54}$$

$$\{\Delta\sigma\}_j = [\,\Delta\tau_{zxj} \quad \Delta\tau_{zyj} \quad \Delta\sigma_{zj}\,]^T \tag{2.55}$$

In which a_j is the aperture (thickness) of the discontinuity j.

The 3 × 3 elastic matrix $[D]_j$ linearly links above stress and strain vectors by the formula

$$\{\Delta\sigma\}_j = [D]_j^e \{\Delta\varepsilon^e\}_j \tag{2.56}$$

2. Discontinuity without thickness

For the discontinuity j without thickness (e.g. joint), the normal and shear forces applied across it can be scaled by the nominal area of the discontinuity to give normal and shear stresses, respectively, which give rise to normal and shear displacements. These displacements are related to the corresponding stresses by various parameters extensively studied (Barton et al. 1985), of which the model proposed primarily by Goodman et al. (1968), Mahtab and Goodman (1970) is the most prevalent in the design of hydraulic structures in many countries inclusive China. The so called "Goodman joint element" model simply links the stress increments in conjugate with the displacement increments in a linear form. Under such circumstances, the strain increment will be replaced by the relative displacement in the general form of the constitutive relation, which is expressed in the local Cartesian coordinate system defined in Fig. 2.2 as

$$\{\Delta u\}_j = [\,\Delta u_{xj} \quad \Delta u_{yj} \quad \Delta u_{zj}\,]^T \tag{2.57}$$

The 3 × 3 elastic matrix $[D]_j$ linearly links above stress and strain vectors by the formula

$$\{\Delta\sigma\}_j = [D]_j^e \{\Delta u^e\}_j \tag{2.58}$$

where it is demanded to describe the interfaces of grout/bolt and rock/grout, the local Cylindrical coordinate system defined in Fig. 2.16 might be employed to establish their constitutive relations. Under such circumstances Eq. (2.58) will hold but the stress and deformation vectors of the interface are replaced by

$$\{\Delta u\}_j = [\,\Delta u_{rj} \quad \Delta u_{\omega j} \quad \Delta u_{zj}\,]^T \tag{2.59}$$

$$\{\Delta\sigma\}_j = [\,\Delta\sigma_{rj} \quad \Delta\tau_{r\omega j} \quad \Delta\tau_{rzj}\,]^T \tag{2.60}$$

3. Grout

The elastic constitutive relation of grout g is expressed in the local Cartesian coordinate system defined in Fig. 2.16. Normally, only two shear stresses τ_{zxg} and τ_{zyg} perpendicular to the bolt axis and one axial tensile stress σ_{zg} are taken into account in the study of the constitutive relation for grout.

Denote the strain and stress incremental vectors in the local coordinate system as

$$\{\Delta\varepsilon\}_g = [\,\Delta\gamma_{zxg} \quad \Delta\gamma_{zyg} \quad \Delta\varepsilon_{zg}\,]^T \tag{2.61}$$

$$\{\Delta\sigma\}_g = [\,\Delta\tau_{zxg} \quad \Delta\tau_{zyg} \quad \Delta\sigma_{zg}\,]^T \tag{2.62}$$

The 3 × 3 elastic matrix $[D]_g$ linearly links above stress and strain vectors by the formula

$$\{\Delta\sigma\}_g = [D]_g^e \{\Delta\varepsilon^e\}_g \tag{2.63}$$

4. Bolt

The constitutive relation of bolt b is expressed in the local Cartesian coordinate system, too. Taking two shear stresses τ_{zxb} and τ_{zyb} perpendicular to the bolt axis and one axial tensile stress σ_{zb} into account and denoting the strain and stress incremental vectors in the local Cartesian coordinate system as

$$\{\Delta\varepsilon\}_b = [\,\Delta\gamma_{zxb} \quad \Delta\gamma_{zyb} \quad \Delta\varepsilon_{zb}\,]^T \tag{2.64}$$

$$\{\Delta\sigma\}_b = [\,\Delta\tau_{zxb} \quad \Delta\tau_{zyb} \quad \Delta\sigma_{zb}\,]^T \tag{2.65}$$

The 3 × 3 elastic matrix $[D]_b$ linearly links above stress and strain vectors by the formula

$$\{\Delta\sigma\}_b = [D]_b^e \{\Delta\varepsilon^e\}_b \tag{2.66}$$

5. Lining

Since the normal stress and strain perpendicular to the lining face may be neglected in the local coordinate system defined in Fig. 2.18, the stress and strain incremental vectors are denoted as

$$\{\Delta\sigma\}_l = [\,\Delta\sigma_{xl} \quad \Delta\sigma_{yl} \quad \Delta\tau_{zyl} \quad \Delta\tau_{zxl}\,]^T \tag{2.67}$$

$$\{\Delta\varepsilon\}_l = [\,\Delta\varepsilon_{xl} \quad \Delta\varepsilon_{yl} \quad \Delta\gamma_{zyl} \quad \Delta\gamma_{zxl}\,]^T \tag{2.68}$$

The elastic constitutive relation for lining l is expressed by the formula

$$\{\Delta\sigma\}_l = [D]_l^e \{\Delta\varepsilon^e\}_l \tag{2.69}$$

In which $[D]_l$ is the elastic matrix of 4 × 4.

The elastic matrices in Eqs. (2.53), (2.56), (2.58), (2.63), (2.66) and (2.69) will be specified in the hereinafter sections.

2.8.2 Concrete

The elastic modulus of natural aggregates of low porosity such as granite and basalt is in the range of 70–140 GPa, whereas with sandstone, limestone, and gravel, it varies from 21 to 49 GPa. The elastic moduli in the range of 7–28 GPa with hydrated Portland cement pastes have been reportedly determined by its porosity, which are similar to the elastic moduli of lightweight aggregates.

For concrete, the direct relationship between elastic modulus and strength does exist because they are both significantly affected by the porosity of the constituent phases, although not to the same degree (Swaddiwudhipong et al. 2003; Shen et al. 2016; Silva et al. 2016).

The Young's modulus used in preliminary phases of design may be estimated from empirical formulas that assume a direct dependence of the modulus on the strength and the density of concrete, or the concrete grade. Most design codes provide equation predicting Young's modulus of concrete in terms of compressive strength (ECS 2004; ACI 2008). As its first approximation, this estimation makes sense because the stress–strain behaviors of the three components of concrete, namely the aggregate, the cement paste matrix, and the ITZ, would actually be related to the deformation and ultimate strength of the concrete. According to the Chinese design codes GB50010-2010 and SL191-2008, the elasticity modulus of concrete can be determined by

$$E_c = \frac{10^5}{2.2 + \frac{34.7}{\sigma_c}} \tag{2.70}$$

where E_c = Young's modulus, MPa; σ_c = compression strength (28 days) of standard cubic sample, MPa.

The elastic modulus E_c of concrete in compression varies from 14 to 40 GPa. In the initial phases of design, the codes GB50010-2010 and SL191-2008 also suggest its reference values in relation to the concrete grade (see Table 2.29).

In the later design phases for an important project, the elastic modulus of concrete should be evaluated by experiments. Table 2.30 gives the testing results of the concrete in Xiaowan Arch Dam. It is found that there is a perceivable difference in

Table 2.29 Elastic modulus of concrete ($\times 10^4$ MPa) (GB50010-2010; SL191-2008)

Strength grade	*C*15	*C*20	*C*25	*C*30	*C*35	*C*40	*C*45	*C*50	*C*55	*C*60
E_c	2.20	2.55	2.80	3.00	3.15	3.25	3.35	3.45	3.55	3.60

Table 2.30 Young's modulus of concrete: Xiaowan Arch Dam, China

Strength grade	Age (days)	Compressive Young's modulus ($\times 10^4$ MPa)		Tensile Young's modulus ($\times 10^4$ MPa)	
		Wet-screened concrete (two-graded)	Fully-graded concrete	Wet-screened concrete (two-graded)	Fully-graded concrete
$C_{180}40$	28	2.383	2.412	2.972	3.437
	180	3.040	3.146	3.665	3.837
$C_{180}30$	28	2.131	2.261	2.655	2.997
	180	2.791	2.971	3.388	3.844

Table 2.31 Poisson's ratio of $C_{180}40$ concrete: Xiaowan Arch Dam, China

Aggregate gradation	Poisson's ratio
Fully-graded	0.17
Wet-screened, two-graded	0.21

the Young's modulus between fully-graded concrete and wet-screened concrete, and between the compressive and tensile loading as well.

The Poisson's ratio is not always needed for the conventional design of many hydraulic structures. However, it is demanded for tunnel linings, arch dams, and other statically indeterminate concrete structures.

Although there appears no consistent relationship between the Poisson's ratio and concrete characteristics such as W/C and curing age and aggregate gradation, yet it is generally lower in high strength concrete, and higher for saturated concrete and for dynamically loaded concrete. The values of the Poisson's ratio for concrete generally vary within 0.15–0.20, for ordinary concrete it may be assumed as $\mu = 0.167$ in the initial phases of design.

For an important project, the Poisson's ratio should be tested using steel cylindrical samples of $\phi 450$ mm $\times$ 900 mm for fully-graded concrete, and $\phi 150$ mm $\times$ 300 mm for wet-screened (two-graded) concrete. The test data of concrete $C_{180}40$ in Xiaowan Arch Dam are listed in Table 2.31. It is obvious that there is significant difference in the Poisson's ratio between fully-graded and wet-screened concretes.

Most concretes, particularly the "conventionally vibrated concrete" (CVC), may be looked at as an isotropic material whose elastic matrix in Eq. (2.53) is specified by

$$[D]_c^e = \begin{bmatrix} \frac{1}{E} & -\frac{\mu}{E} & -\frac{\mu}{E} & 0 & 0 & 0 \\ -\frac{\mu}{E} & \frac{1}{E} & -\frac{\mu}{E} & 0 & 0 & 0 \\ -\frac{\mu}{E} & -\frac{\mu}{E} & \frac{1}{E} & 0 & 0 & 0 \\ 0 & 0 & 0 & \frac{2(1+\mu)}{E} & 0 & 0 \\ 0 & 0 & 0 & 0 & \frac{2(1+\mu)}{E} & 0 \\ 0 & 0 & 0 & 0 & 0 & \frac{2(1+\mu)}{E} \end{bmatrix} \tag{2.71}$$

If necessary, the "roller compacted concrete" (RCC) may be looked at as a transversely isotropic symmetry material attributable to the existence of regular lift joints. To describe transversely isotropic elasticity, let s (e.g. x_j in Fig. 2.2) and t (e.g. y_j in Fig. 2.2) be any two perpendicular directions on the lift joint perpendicular to the axis of symmetry and let n (e.g. z_j in Fig. 2.2) be the direction parallel to the axis of symmetry, we have

$$[D]_c^e = \begin{bmatrix} \frac{1}{E_n} & -\frac{\mu_{sn}}{E_s} & -\frac{\mu_{sn}}{E_s} & 0 & 0 & 0 \\ -\frac{\mu_{sn}}{E_s} & \frac{1}{E_s} & -\frac{\mu_{st}}{E_s} & 0 & 0 & 0 \\ -\frac{\mu_{sn}}{E_s} & -\frac{\mu_{st}}{E_s} & \frac{1}{E_s} & 0 & 0 & 0 \\ 0 & 0 & 0 & \frac{1}{G_{ns}} & 0 & 0 \\ 0 & 0 & 0 & 0 & \frac{1}{G_{ns}} & 0 \\ 0 & 0 & 0 & 0 & 0 & \frac{2(1+\mu_{st})}{E_s} \end{bmatrix} \tag{2.72}$$

It is unique that the primary factors affecting thermal stress for young concrete, apart from the degree of restraint and temperature change, is the growth of the Young's modulus $E(\tau)$ with the ongoing of age in a basic form of exponent formula

$$E(\tau) = E_0(1 - e^{-a\tau}) \tag{2.73}$$

where τ = concrete age, day; E_0 = finial modulus when $\tau \to \infty$, MPa; a = constant.

In China, two improved forms of the Young's modulus $E(\tau)$ are prevailingly exercised (Zhu 1996).

– Composite exponent

$$E(\tau) = E_0(1 - e^{-a\tau^b}) \tag{2.74}$$

Table 2.32 Fitted constants of the Young's modulus

Concrete		Project	Hyperbolic		Composite exponent		
			E_0 (GPa)	q (d)	E_0 (GPa)	a	b
RCC	C15	Yantan	32.8	8.20	36.07	0.24	0.45
	C15	Three Gorges	35.6	28.00	35.00	0.061	0.70
	C20	Three Gorges	37.9	25.63	38.00	0.065	0.70
CVC	C20	Yantan	35.91	6.46	35.70	0.28	0.52
	C20	Three Gorges	34.25	8.59	34.25	0.24	0.50
	$C_{180}40$	Xiaowan	33	6.658	33	0.4804	0.3076
	$C_{180}35$	Xiaowan	32	7.098	32	0.4566	0.3154
	$C_{180}30$	Xiaowan	30	6.569	30	0.4375	0.3432

– Hyperbolic

$$E(\tau) = \frac{E_0 \tau}{q + \tau} \tag{2.75}$$

The practices in China validate that for CVC, the composite exponent function Eq. (2.74) exhibits higher precision, whereas for RCC, the hyperbolic function Eq. (2.75) is better performed. Table 2.32 summarized several fitted constants with regard to the Young's modulus evolution.

As a first approximation in the dam engineering, the mechanical properties of concrete are considered as directly proportional to the degree of hydration solely. It may be easily understood that the dependence on the temperature during curing has not been sufficiently investigated and taken into account in Eqs. (2.73)–(2.75). Since it has been widely accepted that the curing temperature has significant effects on the Young's modulus, Machida et al. (Machida and Uehara 1987; Majorana et al. 1990) postulated more advanced models by the concept of "concrete maturity", a temperature-and time dependent parameter, in the simulation of the growth of $E(\tau)$.

2.8.3 Rocks

(1) Intact rocks

The Young's modulus differs considerably for different rock types and at various stages of deformation. In compact igneous rocks, it is nearly constant until their failure. The commonly encountered secant Young's modulus, termed as the "deformation modulus", and the Poisson's ratio of fresh intact rocks are ranged from 80 GPa (granite porphyry, diorite, basalt porphyrite) to 3.0 GPa (shale, siltstone, conglomerate), and 0.15 (basalt porphyrite) to 0.33 (shale, siltstone, conglomerate). Generally speaking, the higher of the Young's modulus, the lower would be the Poisson's ratio.

In the design of hydraulic structures in China, intact rocks are mostly looked at as isotropic materials whose elastic matrix in formalism $[D]_r^e$ is identical to Eq. (2.71) subject to the subscript substituting for c by r.

The secant modulus E_{50} defined at 50% of the peak stress, is normally employed as the deformation modulus of rock, within this point the rupture does not manifest. The typical deformation parameters of intact rocks are summarized in Table 2.33 (Wu and Zhou 2013).

(2) Joints (interfaces)

There is a variety of testing procedures for the mechanical attributes of discontinuities, ranging from the simplest tilt tests, to the shear box tests, until the standard and tri-axial procedures and the sophisticated tests on servo-controlled equipments. By which a complete stress–displacement curve may be obtained (see Fig. 2.9).

Table 2.33 Deformation parameters of intact rocks (Wu and Zhou 2013)

Rock type			Deformation modulus E (GPa)	Poisson's ratio μ
Igneous rocks	Intrusives (plutonic)	Granite	50–71	0.17–0.25
		Diorite	55–75	0.2–0.28
		Porphyry	53–69	0.17–0.18
	Extrusives (volcanic)	Basalt	25–80	0.15–0.22
		Rhyolite	18–75	0.17–0.22
Sedimentary rocks	Clastic sedimentary	Sandstone	20–37	0.28–0.31
		Shale	3–10	0.28–0.33
	Carbonatite	Limestone	20–55	0.25–0.30
		Dolomite	39–58	0.23–0.25
	Weak and soft	Claystone	0.5–4	0.27–0.29
Metamorphic rocks	Ortho-rock	Gneiss	40–60	0.18–0.22
	Para-rock	Quartz	50–70	0.16–0.18
		Marble	18–60	0.24–0.28
		Slate	8–20	0.26–0.32
		Phyllite	10–15	0.28–0.33
		Schist	40–70	0.25–0.28

The elastic matrix for a joint element without thickness in Eq. (2.58) is specifically expressed by the formula

$$[D]_j^e = \begin{bmatrix} k_{sj} & 0 & 0 \\ 0 & k_{sj} & 0 \\ 0 & 0 & k_{nj} \end{bmatrix} \tag{2.76a}$$

where k_{nj} and k_{sj} = coefficients of normal stiffness and tangential stiffness of the joint j, MPa/m.

For an interface in its Cylindrical coordinate system whose stress and strain increments are denoted in Eqs. (2.59) and (2.60), the elastic matrix for corresponding joint element in Eq. (2.58) is written as

$$[D]_j^e = \begin{bmatrix} k_{nj} & 0 & 0 \\ 0 & k_{sj} & 0 \\ 0 & 0 & k_{sj} \end{bmatrix} \tag{2.76b}$$

As for the stiffness coefficients with respect to the joint compression and shear, there exists no linear relation mainly due to the closure and shear on its irregular wall surfaces. Among various approximations, Chen et al. (1989) had established a unified stiffness and permeability model which looks at the contacted asperities on joint walls as a thin layer of evenly "filled" virtual medium. This model applies for both the filled and unfilled discontinuities and is usually termed as "filled model".

(3) Weak interlayers

The elastic matrix for a joint element with thickness in Eq. (2.56) is dominated by the filler in the weak interlayer, i.e.

$$[D]_j^e = \begin{bmatrix} G_j & 0 & 0 \\ 0 & G_j & 0 \\ 0 & 0 & \lambda_j + 2G_j \end{bmatrix} \tag{2.77}$$

where G_j and λ_j = shear modulus and Lamé coefficients of the intercalated matter in the interlayer, MPa.

(4) Rock masses

The deformation properties of rock masses are closely related to the distribution of joints, fissures and bedding planes, which give rise to the anisotropy of rock mass deformation and strength. Consequently, in order to quantitatively study the equivalent deformation properties of rock masses, one of the most important procedures is the description of the spatial distribution of joints.

It is normally considered as orthotropic symmetry where there exist three mutual perpendicular directions of symmetry, referred to as principle symmetry directions (e.g. rock with three perpendicularly joint sets). Under such circumstances the elastic matrix in Eq. (2.53) is specifically expressed by

$$[D]_r^e = \begin{bmatrix} \frac{1}{E_x} & -\frac{\mu_{yx}}{E_y} & -\frac{\mu_{zx}}{E_z} & 0 & 0 & 0 \\ -\frac{\mu_{yx}}{E_y} & \frac{1}{E_y} & -\frac{\mu_{zy}}{E_z} & 0 & 0 & 0 \\ -\frac{\mu_{zx}}{E_z} & -\frac{\mu_{zy}}{E_z} & \frac{1}{E_z} & 0 & 0 & 0 \\ 0 & 0 & 0 & \frac{1}{G_{yz}} & 0 & 0 \\ 0 & 0 & 0 & 0 & \frac{1}{G_{zx}} & 0 \\ 0 & 0 & 0 & 0 & 0 & \frac{1}{G_{xy}} \end{bmatrix} \tag{2.78}$$

The Poisson's ratio μ_{ij} determines the normal strain in the symmetry direction j when a stress is added in another symmetry direction i. For the orthotropic rock mass we have

$$\frac{\mu_{ij}}{E_i} = \frac{\mu_{ji}}{E_j} \tag{2.79}$$

The nine independent constants are further reduced to five if the rock is isotropic within a plane (i.e. transversely isotropic). This is normally the case where two types of rocks are regularly interlayered. It also comes about when flat minerals like mica, talc, chlorite, graphite, serpentine, etc., are arrayed in parallel orientation, or when long minerals (e.g. amphiboles) are oriented with their long axes randomly pointed within parallel planes. The number of elastic constants is reduced to four for transversely isotropic symmetry attributable to one set of regular joints, for

example, parallel to bedding. In the local coordinate system defined in Fig. 2.2, the elastic matrix of a transversely isotropic rock is identical to that of the RCC in Eq. (2.72).

The prevalent continuum mechanics assumes that the REV is much smaller compared with the characteristic dimension of structure boundary or loading surface, this is equally to stipulate that traction gradients are much smaller on the element scale, and further, that relative displacements across joints are small compared with the joint spacing. Under such circumstances it is profitable to explore theories of gross response which average individual joint effects over a REV (Morland 1974).

An alternative continuum characterization of jointed rock masses by Singh (1973) treats the intact rock blocks and joints as two elastic phases of an overall linear elastic composite in which orthogonal parallel joint sets are considered, and stress gradients are assumed to be small over the REV. Stress concentration factors (ratio of mean joint stress to overall stress) are estimated for different staggered joint geometries in the REV subjected to simple boundary loads, both by analytic approximation and finite element calculation.

The "crack tensor" proposed by Oda in 1982 tries to quantitatively and comprehensively describe the spatial distribution of joints in a form of second-order or fourth-order crack tensor (Oda 1984, 1986a, b), through which an elastic constitutive relation may be formulated in terms of this tensor explicitly, taking into account the elastic behaviors of intact rock blocks and joints (Oda 1983; Oda et al. 1984, 1993, 2002).

Insofar, difficulties still exist in the practical evaluation of elastic matrix components for rock masses mainly due to:

- Stochastic features. Joints are dominant factors in the rock mass parameters, and their spatial distribution pattern (attitude, space or density, persistence) is actually random. In addition, rock blocks are composed of crystals and grains in a fabric that includes cracks and fissures. The in situ test may only comprise a portion of them and lack of full representation. The limited number of test samples and strongly fluctuated data obstruct us to conduct meaningful statistic analysis. How to explore the limited testing data from points to faces and further to a geological body is an unsolved issue, despite carefully layout testing locations.
- Scale effects. Smaller sample yields unnaturally higher deformation modulus (and strength as well). Take Three-gorges Project for example, the laboratory tests provided a deformation modulus of 69.6 GPa, the in situ tests lowered it down to 48.90 GPa, and the late phase back analyses gave an even lower deformation modulus of 32.10 GPa, for the granite in the ship lock cut slope. Coal, altered granite, shale, etc., with networks of fissures exhibit greater size effects—the ratio of laboratory tested strength to in situ tested one sometimes attains as high as of tens. Rather large sample size is hence demanded to get statistically complete collection of all the components influential to the deformation and strength. Ideally, a sample with at least 10 discontinuities

intersecting any of its edge might guarantee the REV with stable components of elastic matrix, but it would be very expensive, and under many circumstances, not realistic to accomplish such in situ tests due to the lack of technique capability.

- Dynamic evolution due to relaxation (EDZ). In the cut-slope at a height of 170 m for the ship lock in Three-gorges Project, the deformation modulus was deteriorated by 60% in the strongly relaxed zone within the depth of 5 m. Under the base of Goupitan Arch Dam, the deformation modulus was deteriorated by 40% in the strongly relaxed zone within the depth of 2 m.
- Environmental effects. The conventional test codes do not take into account of the factors of high in situ geo-stress, high hydraulic pressure, and high geo-thermal for deeply embedded rock masses.

Towards the estimation of deformation modulus, the codes (GB/T 50266-2013) stipulate a conventional procedure as follows.

- Engineering geological units are divided and followed by the rock classification. Then the configuration for experiment is accomplished comprising layout, sample number, and test methods.
- According to the design codes (GB/T 50266-99), (SL264-2001) and (DL/T5368-2007), the in situ deformation tests are carried out.
- The standard value is given through the statistical analysis of tested data. The mean arithmetical values may be looked at as the standard value of deformation modulus. When the sample number is sufficiently large, the standard value is defined as the 0.5 tantile of its probability distribution.
- After the further adjustment taking into account of the factors such as the geological representation and setting, as well as the test conditions, the recommended value is put forward.
- The design value is finally provided after the joint studies by a team engaged in structural design, geological investigation and tests. This study is based on the recommended value, the work situations of the hydraulic structure, the design and computation methods, as well as the similar engineering experiences.

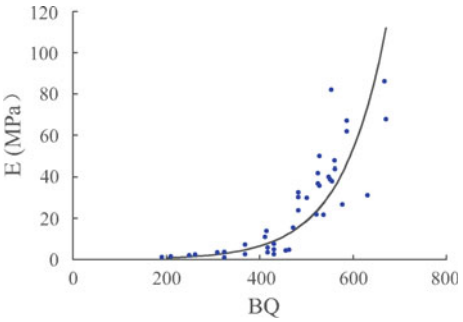

Fig. 2.20 Correlation of deformation modulus versus rock mass BQ

Through the statistic analysis conducted for 54 hydraulic projects in China, the BQ indices and the design values of deformation modulus are related in Fig. 2.20 and fitted in Eq. (2.80).

$$E = 0.0986\mathrm{e}^{0.0105[BQ]} \quad (R^2 = 0.8335) \tag{2.80}$$

When there are insufficient test data, the recommended deformation modulus of rock mass (see Table 2.26) based on the rock classification (GB50218-94) may also be selectively referred.

It should be emphasized again that all the Young's moduli estimated by in situ tests or/and engineering analogues at present engineering practices can only define isotropic elastic matrices. Further endeavors are desperately desirable to access a reliable anisotropic elastic matrix with both respect to the component values and principal directions. In this context a tight combination of geological explorations, theoretical/numerical analyses, and laboratory/field tests, is highly encouraged.

2.8.4 Others

(1) Grout

The elastic matrix in Eq. (2.63) is expressed in the local Cartesian coordinate system by the formula

$$[D]_g^e = \begin{bmatrix} G_g & 0 & 0 \\ 0 & G_g & 0 \\ 0 & 0 & \lambda_g + 2G_g \end{bmatrix} \tag{2.81}$$

where G_g and λ_g = shear modulus and Lamé coefficients of the grout mortar, MPa.

(2) Bolt

The elastic matrix in Eq. (2.66) is expressed in the local Cartesian coordinate system by the formula

$$[D]_b^e = \begin{bmatrix} G_b & 0 & 0 \\ 0 & G_b & 0 \\ 0 & 0 & \lambda_b + 2G_b \end{bmatrix} \tag{2.82}$$

where G_b and λ_b = shear modulus and Lamé coefficients of steel bar, MPa.

(3) Lining

The elastic matrix in Eq. (2.69) is expressed in the local Cartesian coordinate system by the formula

$$[D]_l^e = \begin{bmatrix} E_l & 0 & 0 & 0 \\ 0 & E_l & 0 & 0 \\ 0 & 0 & G_l & 0 \\ 0 & 0 & 0 & G_l \end{bmatrix} \tag{2.83}$$

where E_l and G_l = Young's modulus and shear modulus of lining, MPa.

2.9 Constitutive Relations: Viscoelasticity

2.9.1 Concept

In physics, creep is the tendency of a solid substance to move or deform slowly under actions, and over the typical history it may attain a strain rather larger than the initial (instantaneous) elastic strain (Hoff 2012). Where it occurs as a result of long-term exposure to the stresses that are still below the long term (creep) yield strength $\bar{\sigma}_s$ of the material and do not initiate a failure mode, it is termed as the "delayed elastic creep" or "elastic creep" in brief (see Fig. 2.12a).

The mechanism and computation of creep still being debated may be referred to the literatures and design handbooks (Troxell et al. 1958; Wittmann 1982; Neville et al. 1983; Bažant 1982, 1988; Mehta and Monteiro 2006; Chen et al. 2011). Phenomenologically, elastic creep simulated using rheological models falls into the category of viscoelasticity. While elasticity is usually the result of bond stretching along crystallographic planes in an ordered solid and does not dissipate energy in loading-unloading circles, viscosity is the result of the diffusion of atoms or molecules inside an amorphous material.

Use of more complex material laws of creep for large-scale applications requires appropriate treatment of the underlying constitutive relations. As for the so-called thermochemical problem in early age concrete, reference is made to Ulm and Coussy (1995), Ulm et al. (1998), Hellmich et al. (1999). The algorithmic basis for the implementation of creep laws has been well documented by Lechner et al. (2001). All of these algorithmically relevant studies contain extensions or derivates of classical algorithms for elasto-plasticity developed by Simo and Hughes (1998).

In service life, the stresses in hydraulic structures are normally limited within <40% of concrete strength and <50% of rock mass strength, in this case the stress–strain relation is approximately linear. This linearity postulation implies the principle of superposition (introduced by Boltzmann), and the elastic creep might thus be characterized by the linear viscoelasticity with the help of creep compliance function.

2.9.2 Concrete

When a deformation is suddenly imposed and held constant, creep causes relaxation of stress. After unloading, creep recovery might take place, but it is only partial, because of various factors such as the aging of concrete (Rhodes 1992).

In concrete structures, creep is sometimes welcomed because it relieves tensile stresses that might otherwise lead to cracking. Therefore, the creep of concrete, particularly the early age creep, is the most important phenomenon that should be well handled towards the prediction and mitigation of early concrete cracking.

Creep in early age concrete is driven by more than one mechanism. When a hydrated cement paste is subjected to a sustained stress of certain magnitude and duration, the C-S-H will lose a certain amount of physically adsorbed water, and the paste matrix will exhibit a creep strain. This is widely recognized as the most important scenario in concrete creep.

A saturated cement paste will not remain dimensionally stable when exposed to unsaturated ambient blamed on the loss of physically adsorbed water from C-S-H. Variations of pore water content due to drying or wetting processes give rise to significant volume changes of concrete in load-free specimens. They are called the "drying shrinkage" typically exhibiting negative strain increment (drying) between 0.0002 and 0.0005 in normal concrete and as high as 0.0012 in low strength concretes; or positive strain increment (wetting) <0.00005 in normal concrete and <0.00020 in high strength concrete. Drying shrinkage may be decomposed into reversible component which is a portion of total shrinkage that is reproducible on wetting-drying cycles and irreversible component which is the part of total shrinkage on first drying that cannot be reproduced on subsequent wetting-drying cycles, the latter is probably due to the development of chemical bonds within the C-S-H structure.

Both the drying shrinkage and creep strains in concrete are assumed to be correlated, because in practice they usually take place simultaneously and are mainly resulted from the removal of adsorbed water from the hydrated cement paste. The distinguishment is that in the former case the differential relative humidity between concrete and the environment is the driving force, whereas in the latter case it is the sustained applied stress. In addition, both the drying shrinkage and the creep phenomena in concrete exhibit a degree of irreversibility that has practical significance. It has been observed that when a concrete is simultaneously under loading and exposed to low relative humidity environment, the total strain increment is higher than any of the single factors.

Using the stoichiometric amount of water needed for complete hydration of the cement paste in a closed system, it can be shown that the volume of the hydration products would be less than the volumetric sum of the water and cement that is hydrated. Chemical shrinkage is the relative volume reduction by this phenomenon which is the measured deformation of cement paste in a closed system (Tazawa and Miyazawa 1995). Chemical shrinkage is also referred to as the "Le Chatelier contraction", in honor of the French scientist who first observed the phenomenon

(Davis 1940). In the hydraulic structures, chemical shrinkage is also termed as "autogenous shrinkage". The "Japanese Concrete Institute" defines autogenous shrinkage as the macroscopic volume reduction of cementitious materials when cement hydrates after initial setting.

1. Drying shrinkage

To separate shrinkages from creep, the load-free specimens are employed to get drying and autogenous components (Videla et al. 2008).

Drying shrinkage tests make use of cylindrical steel mould samples of ϕ450 mm $\times$ 900 mm for the fully-graded concrete, and of ϕ200 mm $\times$ 600 mm for the wet-screened (two-graded) one. In Xiaowan Arch Dam, the drying shrinkage of the concrete $C_{180}40$ was investigated with specimens of two different aggregates but identical W/C = 0.40. From the data listed in Table 2.34, we find that the shrinkage strain of fully aggregated concrete is much smaller than that of wet-screened one.

In the practical computation for hydraulic structures, the drying shrinkage strain increment is normally looked at as an initial strain whose time-dependent evolution is interpolated using the tested data directly (e.g. Table 2.34). The elastic constitutive relation taking into account of the initial strain will be in the form of

$$\{\Delta\varepsilon^s\} = [\,\Delta\varepsilon^s \quad \Delta\varepsilon^s \quad \Delta\varepsilon^s \quad 0 \quad 0 \quad 0\,]^T \tag{2.84}$$

$$\{\Delta\sigma\} = [D]_c^e(\{\Delta\varepsilon\} - \{\Delta\varepsilon^s\}) \tag{2.85}$$

2. Chemical (autogenous) shrinkage

The test for the autogenous shrinkage uses cylindrical steel mould samples of ϕ450 mm $\times$ 900 mm for the fully-graded concrete, and of ϕ200 mm $\times$ 600 mm for the wet-screened (two-graded) one. The tested results of the fully-graded concrete in Xiaowan Arch Dam are given in Table 2.35.

Similar to the drying shrinkage strain, the elastic constitutive relation taking into account of the initial strain attributable to autogenous shrinkage is in the form of

$$\{\Delta\varepsilon^a\} = [\,\Delta\varepsilon^a \quad \Delta\varepsilon^a \quad \Delta\varepsilon^a \quad 0 \quad 0 \quad 0\,]^T \tag{2.86}$$

$$\{\Delta\sigma\} = [D]_c^e\,(\{\Delta\varepsilon\} - \{\Delta\varepsilon^a\}) \tag{2.87}$$

3. Creep compliance function

In general, the influence of cement content and W/C of concrete on the creep (drying shrinkage as well) is direct, because an increase in the cement paste volume means a decrease in the aggregate fraction, and consequently a corresponding increase in the moisture-dependent deformations in concrete (Neville 1964; Counto 1964). For given cement content, with increasing W/C, both the drying shrinkage and creep are intensified.

Table 2.34 Drying shrinkage strain ($\times 10^{-6}$) of the concrete $C_{180}40$: Xiaowan Arch Dam, China

Item		Age (days)										
		3	5	7	15	28	45	60	90	120	150	180
Fully-graded	Clock gauge	6.11	14.43	21.65	42.18	74.37	93.1	109.34	137.36	148.19	162.62	175.10
	Strain gauge	13.83	22.27	27.53	44.14	63.34	80.48	95.08	120.67	140.58	154.72	152.14
Wet-screened (two-graded)	Clock gauge	86.51	110.42	132.23	201.86	292.24	344.46	377.34	412.86	422.35	431.85	440.29

Table 2.35 Autogenous volume deformation of the fully-graded concrete: Xiaowan Arch Dam, China

Strength grade	Autogenous volume deformation ($\times 10^{-6}$)															
	1 days	2 days	3 days	4 days	5 days	6 days	7 days	8 days	10 days	19 days	27 days	32 days	55 days	66 days	78 days	90 days
$C_{180}40$	−0.20	−0.31	−0.88	2.25	0.59	−1.10	0.57	−2.35	−3.95	−9.74	−12.09	−18.52	−25.98	−26.37	−24.55	−24.77
$C_{180}35$	−7.38	−7.50	−8.42	−8.77	−7.09	−7.27	−9.25	−9.25	−7.74	−11.79	−16.72	−16.96	−24.61	−26.56	−26.56	−20.71
$C_{180}30$	2.01	5.41	8.57	0.97	4.37	2.51	2.51	5.91	0.51	−1.41	−3.06	−6.75	−10.73	−14.47	−10.38	−7.37

Table 2.36 Creep degree of the concrete $C_{180}40$ (10^{-6}/MPa): Xiaowan Arch Dam, China

Grade	Age (days)	Loading duration (days)								
		1	3	7	10	15	30	45	60	90
Fully-graded	7	–	16.51	21.5	24.34	24.86	29.74	32.27	34.18	34.58
	28	–	13.27	16.4	16.91	19.05	21.21	23.74	23.68	25.46
	180	–	6.2	7.9	9.0	9.4	10.4	10.9	11.1	12.1
Wet-screened (two-graded)	7	20.4	27.8	34.1	38.0	42.7	48.8	53.4	57.4	61.0
	28	9.6	14.1	19.0	20.0	22.6	26.4	29.7	31.8	33.7
	180	5.9	7.6	9.4	10.2	10.7	12.3	13.9	14.4	15.6

Additional factors affecting creep are the curing history of concrete, temperature of exposure, and magnitude of applied stress. Depending on the curing history, creep strains in a real structure where wetting-drying cycles can enhance micro-cracking in the ITZ and thus increase the creep, may be significantly shifted from those in laboratory testing undertaken at a constant humidity and temperature.

Creep tests make use of cylindrical steel mould samples of ϕ450 mm × 900 mm for the fully-graded concrete, and of ϕ200 mm × 600 mm for the wet-screened (two-graded) one. The creep data of the concrete $C_{180}40$ in Xiaowan Arch Dam are presented in Table 2.36.

During the construction period, a hydraulic concrete at its early age is normally looked at as an elastic creep body whose stresses and strains [instantaneous and long term (creep)] are linearly related. The current and practically feasible state-of-the-art with phenomenological approximation of given creep curves is characterized by the "creep degree" or the "creep compliance function" $C(t-\tau)$ defined as the creep strain (i.e. the total strain minus shrinkages) manifested at time t by a unit sustained uni-axial stress applied at concrete age τ. It is gauged as the strain difference between the loaded and load-free specimens, and mostly represented by the hereditary theory of aging of the Russian school (Alexandrovskii 1966; Arutiunian and Kolmanovskii 1983; Bažant and Prasannan 1989).

The shortcomings of this solution are the disregard of the creep influence on the stresses after long loading period (e.g. one or two years) and the comparatively difficulties in determining the creep function parameters.

In China, the creep compliance function $C(t-\tau)$ customarily employed is in the form of

$$C(t-\tau)=\sum_{s}\psi_{s}\left(1-\mathrm{e}^{-r_{s}(t-\tau)}\right) \tag{2.88}$$

In which

$$\begin{cases}\Psi_{s}(\tau)=f_{s}+g_{s}\tau^{-p_{s}} & for \quad s=1\sim m-1\\ \Psi_{s}(\tau)=D\mathrm{e}^{-r_{s}\tau} & for \quad s=m\end{cases} \tag{2.89}$$

Equations (2.88) and (2.89) may be regarded as the semi-empirical form of non-linear Kelvin model series taking into account of the time-dependent features of elements, and is similar to the Alexandrovskii formula (Zhu 1985a, b).

Use is made of the test data for the concrete in Xiaowan Arch Dam, we get the following fitted creep compliance functions

– For concrete $C_{180}40$

$$C(t,\tau) = (2 + 56/\tau^{0.48})(1 - e^{-0.4(t-\tau)}) + (2.5 + 20/\tau^{2.5})(1 - e^{-0.05(t-\tau)}) + 32e^{-0.02\tau}(1 - e^{-0.02(t-\tau)}) \tag{2.90}$$

– For concrete $C_{180}35$

$$C(t,\tau) = (2 + 75/\tau^{0.48})(1 - e^{-0.4(t-\tau)}) + (3 + 20/\tau^{2.5})(1 - e^{-0.05(t-\tau)}) + 28e^{-0.02\tau}(1 - e^{-0.02(t-\tau)}) \tag{2.91}$$

The fitting quality of the creep compliance functions against the test data ($C_{180}40$) is verified in Fig. 2.21.

To generalize Eqs. (2.88) and (2.89) into tri-axial stress–strain state, postulations are made that (Santurjian and Kolarow 1996):

① The concrete is isotropic;
② The concrete is linear under tension nearly up to the point of rupture, meanwhile compressive stresses rarely reach half the compressive strength;
③ The Poisson's ratio is constant for both instantaneous and creep strains (e.g. $\mu = 0.17$);
④ The thermal expansion coefficient a is constant;

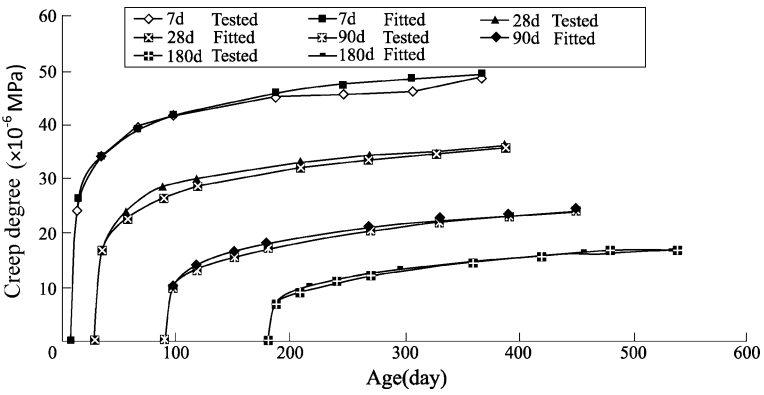

Fig. 2.21 Creep degree (compliance) of the $C_{180}40$ concrete: Xiaowan Arch Dam, China

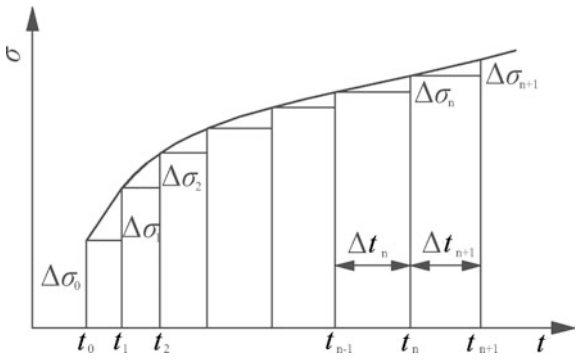

Fig. 2.22 Incremental scheme for creep algorithm

⑤ The creep compliance function $C(t-\tau)$ is unchanged in tensile and compressive loading;

⑥ The influence of the temperature during concrete hardening on the Young's modulus and creep, is taken into account by means of effective concrete age.

With these assumptions, volumetric and deviatoric stress–strain relations may be constructed in which $C(t-\tau)$ performs as the bulk and shear compliance functions.

To get the constitutive relation for concrete creep, the implicit scheme is employed (see Fig. 2.22) by the assumption that in the time interval Δt_n, the stress rate $\frac{\partial \sigma}{\partial t}$ = constant.

The incremental elastic strain $\{\Delta\varepsilon^e\}_t$ is given by the formula

$$\{\Delta\varepsilon^e\}_t = \frac{1}{E(\bar{\tau})}[Q]\{\Delta\sigma\}_t \tag{2.92}$$

In which $E(\bar{\tau})$ is the Young's modulus at the middle of age interval $\bar{\tau} = \tau - 0.5\Delta t_n$ (see Eqs. 2.74 and 2.75).

The creep strain increment $\{\Delta\varepsilon^c\}_t$ is expressed as

$$\begin{cases} \{\Delta\varepsilon^c\}_t = \{\eta\}_t + C(t,\bar{\tau})[Q]\{\Delta\sigma\}_t \\ \bar{\tau} = \tau - 0.5\Delta t_n \end{cases} \tag{2.93}$$

In which

$$\{\eta\}_t = \sum_s \left(1 - \mathrm{e}^{-r_s\Delta t_n}\right)\{\omega_s\}_t \tag{2.94}$$

and

$$\begin{cases} \{\omega_s\}_t = \{\omega_s\}_{t-\Delta t_n}\mathrm{e}^{-r_s\Delta t_{n-1}} + [Q]\{\Delta\sigma\}_{t-\Delta t_n}\Psi_s(\bar{\tau} - \Delta t_{n-1})\mathrm{e}^{-0.5r_s\Delta t_{n-1}} \\ \{\omega_s\}_{t_1} = [Q]\{\Delta\sigma\}_{t_0}\Psi_s(\tau_0) \end{cases} \tag{2.95}$$

For three-dimensional issue, the matrix $[Q]$ may be written as

$$[Q] = \begin{bmatrix} 1 & -\mu & -\mu & 0 & 0 & 0 \\ -\mu & 1 & -\mu & 0 & 0 & 0 \\ -\mu & -\mu & 1 & 0 & 0 & 0 \\ 0 & 0 & 0 & 2(1+\mu) & 0 & 0 \\ 0 & 0 & 0 & 0 & 2(1+\mu) & 0 \\ 0 & 0 & 0 & 0 & 0 & 2(1+\mu) \end{bmatrix} \tag{2.96}$$

The complete constitutive relation for concrete creep deformation is

$$\{\Delta\sigma\}_t = [\bar{D}]_t^e(\{\Delta\varepsilon\}_t - \{\eta\}_t) \tag{2.97}$$

In which $\{\eta\}_t$ may be regarded as the equivalent initial strain due to the creep of early age concrete corresponding to the equivalent elastic matrix $[\bar{D}]_t^e$

$$[\bar{D}]_t^e = \bar{E}_t[Q]^{-1} \tag{2.98}$$

$$\bar{E}_t = \frac{E(\bar{\tau})}{1 + E(\bar{\tau})C(t,\bar{\tau})} \tag{2.99}$$

2.9.3 Rocks

The reversible creep of rocks is normally neglected in the computation of hydraulic structures. For irreversible creep, the elasto-viscoplastic model may be employed which will be addressed later in Sect. 2.11.

2.10 Constitutive Relations: Plasticity

2.10.1 Classical Elasto-Plasticity Theory

Before the 1970s, numerical representations of rock-like materials in computational geomechanics often restricted displacements to elastic orders of magnitude. However, field observations of highly jointed rocks indicated that much larger displacements often manifest due to their plastic properties.

In material science, plasticity describes the deformation of a solid undergoing irreversible change of shape in response to exerted actions (Chen and Zhang 1991). The transition from an elastic behavior to the plastic behavior is called yield. Plasticity in a crystal of pure metal is primarily caused by two modes of deformation (slip and twinning) in the crystal lattice, whereas plastic deformations of

rocks and concrete at normal temperature are primarily caused by the formation of micro-cracks and sliding motions relative to these cracks (Harris 1992).

Research on classical plasticity theories started in 1864 with the work of Henri Tresca on the maximum shear criterion. An improved plasticity model was presented in 1913 by Von Mises which is now referred to as the von Mises yield criterion. Concepts such as the normality of plastic flow to the yield surface and the flow rule for plasticity were introduced by Prandtl (1924) and Reuss (1930).

In the classical plasticity theory, the total strain increment appearing in a loaded material is divided into elastic and plastic components such that

$$\{\Delta\varepsilon\} = \{\Delta\varepsilon^e\} + \{\Delta\varepsilon^p\} \tag{2.100}$$

In which the plastic strain increment is elaborated with the help of yield and load functions, flow rule, and hardening/softening law (Armstrong and Frederick 1966; Oden 1972; Miyoshi 1985; Owen et al. 1989; Simo and Hughes 1988; Doltsinis 1989; Inoue et al. 1990; Lemaitre and Chaboche 1990; Lubliner 1990; Chaboche 1991; Ohno and Wang 1993; Hill 1998; Han and Reddy 1999; Kolymbas 2000; Rappaz et al. 2003; Dunne and Petrinic 2005; de Souza Neto et al. 2009).

(1) Elastic behavior

The elastic strain increments, which are recoverable upon unloading, are calculated from the Hooke's law (see Eq. 2.53). The value of Poisson's ratio, being limited between zero and one half for most materials, is assumed to be constant.

(2) Yield/loading function

One consequence of yield is that as plastic deformation proceeds, an increase in stress is deeded to produce additional plastic strain. This phenomenon is known as "strain/work hardening". Plasticity materials with hardening necessitate increasingly higher stresses to result in further plastic deformation. On the contrary, "perfect plasticity" is a property of material to undergo irreversible deformation without any increase in stress or load.

Except perfect plasticity materials, the yield surface, as the plastic work increases, expands or shrinks until the current stress point is reached. Under such circumstances, the "loading function" ψ is defined as the subsequent yield function criterion

$$\psi(\sigma_{ij}, H_\alpha) = 0 \tag{2.101}$$

In which H_α is termed as "internal variable" which may be selectively adopted from those listed below, of which the plastic work is more commonly exercised.

- Plastic work $w^p = \int \{\sigma\}^T \{d\varepsilon\}^p$;
- Plastic strain ε^p;
- Equivalent (generalized) plastic shear strain $\bar{\gamma}^p = \int \sqrt{\frac{2}{3}(\{de\}^p)^T \{de\}^p}$;
- Plastic volumetric strain $\varepsilon_v^p = \varepsilon_x^p + \varepsilon_y^p + \varepsilon_z^p$.

There are three basic types of hardening to build a loading function ψ from corresponding yield function F, one is isotropic hardening shown in Fig. 2.23 and Eq. (2.102) where the only internal variable is $H_\alpha = w^p$.

$$\psi = F(I_1, J_2, \theta_\sigma) - C(H_\alpha) = 0 \tag{2.102}$$

Another is kinematic hardening shown in Fig. 2.24 and Eq. (2.103)

$$\psi = F((I_1, J_2, \theta_\sigma) - C(H_\alpha)) = 0 \tag{2.103}$$

The last one is mixed hardening (see Fig. 2.25 and Eq. 2.104) combined by that of isotropic and kinematic.

$$\psi = F((I_1, J_2, \theta_\sigma) - C_1(H_\alpha)) - C_2(H_\alpha) = 0 \tag{2.104}$$

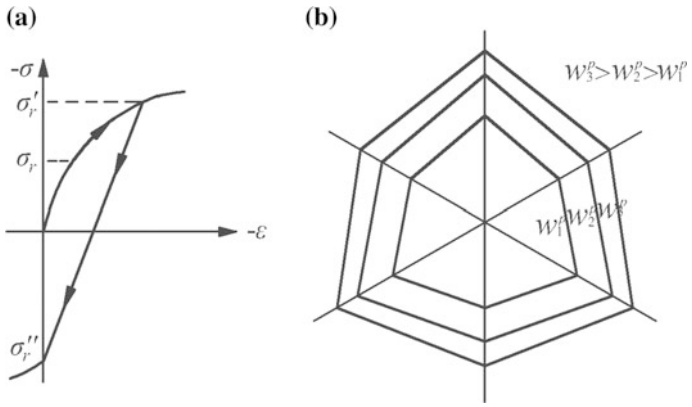

Fig. 2.23 Isotropic hardening. **a** Strain versus stress; **b** on the π-plane

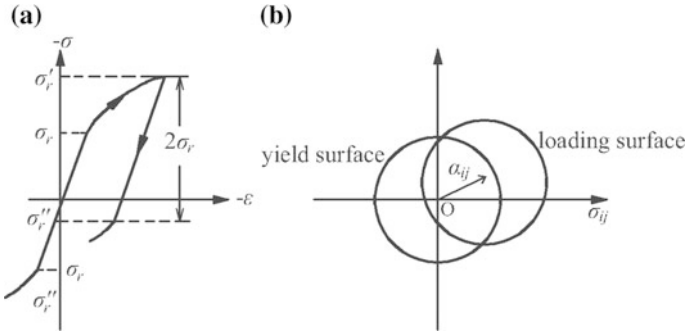

Fig. 2.24 Kinematic hardening. **a** Strain versus stress; **b** on the π-plane

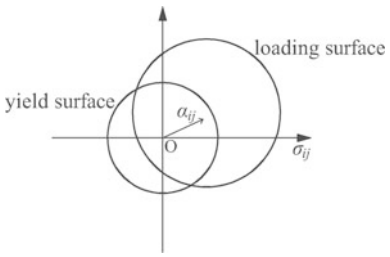

Fig. 2.25 Mixed hardening (on the π-plane)

Take the bolt (steel bar) for example, the Von Mises loading function of linear isotropic work hardening related to the generalized plastic shear strain is employed in this book, that

$$\begin{cases} \psi_b = [3(\tau_{zxb}{}^2 + \tau_{zyb}{}^2) + \sigma_b{}^2]^{1/2} - \sigma = 0 \\ \sigma = f_{yk} + (f_{ptk} - f_{yk})\bar{\gamma}^{vp}/\bar{\gamma}_u^{vp} \\ \bar{\gamma}_u^{vp} = \sqrt{2/3}\delta_{gt} \end{cases} \tag{2.105}$$

In which f_{yk}, f_{ptk}, δ_{gt}, $\bar{\gamma}^{vp}$ are the yield strength, ultimate strength, elongation ratio, and present plastic general shear strain, respectively.

Loading is defined as the situation under which increments of stress are greater than zero. If loading leads the stress vector across the plastic domain, then the increment of plastic strain occurs

$$\begin{cases} \psi = 0 \\ \left\{\frac{\partial \psi}{\partial \{\sigma\}}\right\}^T \{\Delta\sigma\} > 0 \end{cases} \tag{2.106}$$

The above equation, when it is equal to zero, indicates a state of neutral loading where the stress state moves along the loading (yield) surface without changing the plastic strain, i.e.

$$\begin{cases} \psi = 0 \\ \left\{\frac{\partial \psi}{\partial \{\sigma\}}\right\}^T \{\Delta\sigma\} = 0 \end{cases} \tag{2.107}$$

Unloading is defined as the situation when increments of stress are smaller than zero. The material stays in the elastic domain during unloading and no additional plastic strain is accumulated, namely

$$\begin{cases} \psi = 0 \\ \left\{\frac{\partial \psi}{\partial \{\sigma\}}\right\}^T \{\Delta\sigma\} < 0 \end{cases} \tag{2.108}$$

For perfect plasticity materials we have $\psi = F$ in Eqs. (2.106)–(2.108).

(3) Potential function and flow rule

Flow plasticity is a theory characterized by the assumption that the flow rule exists to determine the amount of plastic deformation. For hardening material, the work done of a loading-unloading cycle is positive or zero, this is called the "Drucker stability postulation". Although it eliminates the possibility of strain softening behavior that actually exists, yet if applicable, the "normality condition"—associated flow rule, that the plastic strain increment and the normal to the yield surface have the same direction, may be inferred. The use of the associated flow rule is a cornerstone in the so-called mathematical theory of plasticity which was formulated around 1950 by among others Hill, Drucker and Prager. This mathematical theory of plasticity contains some very attractive results such as the necessity of a convex yield surface and the existence of the limit theorems which have been used extensively in engineering computations (Lin and Bažant 1986).

Experimental data, however, indicate that the associated flow rule often fails to describe the plastic response of rock-like materials that exhibit shear dilatancy characterized by nonlinear volume change and associated with shear distortion, namely, they contract at low loading levels and dilate at higher loading levels. Some non-associated flow rules in which the loading (yield) and plastic potential functions are not identical, may be employed, if necessary.

Nowadays, associated and non-associated plastic strain flow rules are well-established concepts (Desai and Gioda 1990; Griffiths and Gioda 2000; Davis and Selvadurai 2002; Pivonka et al. 2003). The assumption of generalized associativity (or generalized normality) further relates the flow directions of all internal variables to a given loading surface (Rockafellar 1969; Halphen and Nguyen 1975; Jirásek and Bažant 2001; Frémond 2002).

Towards the plastic strain increment, we can without loss of generality assume that this can be derived from a plastic potential Q as

$$\{\Delta\varepsilon\}^p = \lambda\left\{\frac{\partial Q}{\partial\{\sigma\}}\right\} \tag{2.109}$$

$$\lambda = \frac{1}{A}\left\{\frac{\partial\psi}{\partial\sigma}\right\}^T\{\Delta\sigma\} \tag{2.110}$$

In which λ is a positive scalar of proportionality and $Q = \psi$ giving rise to the so called associated flow rule.

$Q = 0$ can be thought of as describing a surface in stress space. Since $\left\{\frac{\partial Q}{\partial\{\sigma\}}\right\}$ is a vector normal to this surface, the strain increment can be plotted as a vector normal to the surface with a length determined by λ.

The parameter A is dependent on the selection of internal variables.

– Hardening with plastic work w^p

$$A = -\frac{\partial \psi}{\partial w^p}\{\sigma\}^T\left\{\frac{\partial Q}{\partial \sigma}\right\} \tag{2.111}$$

– Hardening with plastic strain ε_{ij}^p

$$A = -\left\{\frac{\partial \psi}{\partial \varepsilon^p}\right\}^T\left\{\frac{\partial Q}{\partial \sigma}\right\} \tag{2.112}$$

– Hardening with generalized plastic shear strain γ^p

$$A = -\frac{\partial \psi}{\partial \gamma^p}\sqrt{\left\{\frac{\partial Q}{\partial \sigma}\right\}^T\left\{\frac{\partial Q}{\partial \sigma}\right\}} \tag{2.113}$$

– Hardening with plastic volumetric shear strain ε_v^p

$$A = -\frac{\partial \psi}{\partial \varepsilon_v^p}\frac{\partial Q}{\partial p} \tag{2.114}$$

The non-associated flow rule gives rise to non-symmetrical implicit matrix in the elasto-plastic and elasto-viscoplastic FEM, it in turn leads to the difficulties with equation solvers and higher computation overheads, although it may be additionally handled by the symmetrization operation proposed by Xiong (1993).

Generally, the expression for Q must be determined by experiment similarly to the yield function. This is, however, quite a demanding task, and as a first guess at Q it would be reasonable to make use of the yield criterion. For example, we may substitute a dilatancy angle ϕ for the friction angle φ in the yield functions of Drucker-Prager and Mohr-Coulomb, to obtain the corresponding potential functions (Goodman and Dubois 1972; Vermeer and de Borst 1984; Nemat-Nasser and Obata 1988; Manzari and Nour 2000). However, even for such a single additional parameter ϕ, difficulties do exist in its evaluation for engineering practices.

The non-associated potential functions occasionally used in this book are specified as follows.

1. Drucker-Prager (D-P) for rock-like materials

$$\begin{cases} Q = aI_1 + \sqrt{J_2} - k = 0 \\ a = \sin\phi/[3(3 + \sin^2\phi)]^{1/2} \\ k = \sqrt{3}c\cos\phi/\sqrt{3 + \sin^2\phi} \end{cases} \tag{2.115}$$

In which ϕ and c are the dilatancy angle and cohesion of the rock-like material, respectively.

2. Drucker-Prager (D-P) for joint element with thickness

$$Q_j = 3a\sigma_{zj} + \sqrt{(1-12a^2)(\tau_{zxj}^2 + \tau_{zyj}^2)} - k = 0 \tag{2.116}$$

$$\begin{cases} a = \sin\phi_j / [3(3+\sin^2\phi_j)]^{1/2} \\ k = \sqrt{3}c_j \cos\phi_j / \sqrt{3+\sin^2\phi_j} \end{cases} \tag{2.117}$$

In which ϕ_j and c_j are the dilatancy angle and cohesion of the interlayer, respectively.

3. Mohr-Coulomb (M-C) for rock-like materials

$$Q = \frac{1}{3} I_1 \sin\phi + \left(\cos\theta_\sigma - \frac{1}{\sqrt{3}}\sin\theta_\sigma \sin\phi\right)\sqrt{J_2} - c\cos\phi \tag{2.118}$$

Where $-\frac{\pi}{6} \le \theta_\sigma \le \frac{\pi}{6}$.
or

$$Q = p\sin\phi + \frac{1}{\sqrt{3}} q\left(\cos\theta_\sigma - \frac{1}{\sqrt{3}}\sin\theta_\sigma \sin\phi\right) - c\cos\phi \tag{2.119}$$

In which ϕ and c are the dilatancy angle and cohesion of the rock-like material, respectively.

4. Mohr-Coulomb (M-C) for joint element without thickness (joint, interface)

$$\begin{cases} Q_j = (\tau_{zxj}^2 + \tau_{zyj}^2)^{1/2} + \sigma_{zj} tg\phi_j - c_j & for \quad \sigma_{zj} - \sigma_{Tj} < 0 \\ Q_j = (\tau_{zxj}^2 + \tau_{zyj}^2 + \sigma_{zj}^2)^{1/2} & for \quad \sigma_{zj} - \sigma_{Tj} \ge 0 \end{cases} \tag{2.120}$$

In which c_j, ϕ_j, σ_{Tj} are the cohesion, dilatancy angle, and tension strength of the joint, respectively.

(4) Constitutive equation

In the elasto-plastic FEM one usually proceeds by applying a load increment which produces a displacement increment, and thus a total strain increment. The stress increment corresponding to this total strain increment can be determined by a constitutive relation similar to that of elasticity in formalism, i.e.

$$\begin{cases} \{\Delta\sigma\} = ([D]^e - [D]^p)\{\Delta\varepsilon\} = [D]^{ep}\{\Delta\varepsilon\} \\ [D]^p = \dfrac{[D]^e \dfrac{\partial Q}{\partial\{\sigma\}} \left\{\dfrac{\partial\psi}{\partial\{\sigma\}}\right\}^T [D]^e}{A + \left\{\dfrac{\partial\psi}{\partial\{\sigma\}}\right\}^T [D]^e \dfrac{\partial Q}{\partial\{\sigma\}}} \end{cases} \tag{2.121}$$

In which $[D]^p$ is termed as "plastic matrix" and $[D]^{ep}$ is termed as "elasto-plastic matrix". Such a relation was firstly derived and used in a finite element context by Zienkiewicz et al. (1969).

The elasto-plastic constitutive relation Eq. (2.121) defines the stress increment uniquely once the total strain increment and the current state of stress is known, whereas the a strain increment cannot be determined uniquely on the basis of a stress increment, i.e. $[D]^{ep}$ is singular. The use of Eq. (2.121) leads to a classical type of finite element nonlinearity where the current state and an increment are known. However, where the effect of the increment depends on the state that the increment gives rise to, an iterative procedure must be applied.

It should be emphasized that the positivity of $[D]^{ep}$ in Eq. (2.121) is only guaranteed for hardening matrieals. Following a material approaches to softening (see Figs. 2.8 and 2.9), its elasto-plastic constitutive law presents a descending branch which implies a local instability of the material. This local instability can progressively lead to irreversible strain localization, and eventually to global instability. When this behavior is introduced in a standard time-independent (e.g. elasto-plastic) constitutive relation some physically meaningless consequences arise for both initial and boundary value problems (Bažant et al. 1984), which in turn, causes the ill-posedness of the algorithm. When solved by means of computational methods (e.g. FEM), such an ill-posedness generally shows numerical instability and mesh dependence of the solution. This behavior may also emerge in elastic perfectly plastic materials in the presence of a non-associated flow rule (Rudnicki and Rice 1975). Associated to the formation of concentrated strain zones of limited thickness within the structures, the softening materials should be carefully handled taking into account of the condition governing the onset and the process of spread and coalescence of localization zones (Ortiz et al. 1987; Leroy and Ortiz 1989; Zienkiewicz et al. 1995; Desai and Toth 1996; Sterpi 1999; Chen et al. 2007).

The classical form of elasto-plastic constitutive relation (equation) in Eq. (2.121) has only been occasionally used in the exercises of computational geomechanics for hydraulic structures by the author of this book, because the solution using classical elasto-plastic constitutive equation may be identically accessed by using the elasto-viscoplastic constitutive equation of potential theory elaborated in the hereinafter Sect. 2.11. However, the framework and the components of the classical elasto-plastic theory such as the yield and loading functions, the potential function and flow rule, as well as the strain increment additivity, will form the theoretical base towards the building of the potential theory of elasto-viscoplasticity.

2.10.2 Remarks on Other Plasticity Theories

The classical elasto-plastic theory is a certain formalism treating the solid substance as "black box" which leads to difficulties in incorporating the internal structure of matter into the constitutive equation. Towards the improvement, generalized plasticity theories, endochronic models, continuum damage mechanics (CDM) offer the appealing frameworks for rock-like materials since they possess indicators of internal structures.

(1) Generalized plasticity theory

An important step towards the formulation of generalized plasticity is the idea of a plasticity model where loading and yielding surfaces are not coincident (Eisenberg and Phillips 1971). Starting from an axiomatic approach to describe inelastic behavior of materials, Lubliner proposed several simple generalized plasticity models that are able to represent observed experimental behaviors of metals (Lubliner 1974, 1980, 1984). In the generalized plasticity theory proposed by Zienkiewicz and Mróz (1984) for sands under monotonic and cyclic loading, neither yield surface nor plastic potential surface needs to be defined explicitly, and consistency law is not required to determine plastic modulus. The generalized plasticity has been successfully used for describing the shape memory alloy behavior (Lubliner et al. 1993; Lubliner and Auricchio 1996).

(2) Endochronic theory

Endochronic theory was developed during the 1970s and used for modeling the inelastic behaviors of metals (Valanis 1971; Valanis and Wu 1975), concrete and soils (Bažant and Bhat 1976; Bažant and Krizek 1976).

The endochronic stress evolution depends on the "intrinsic time" and is formulated by a convolution integral between the strain tensor and a scalar function of the intrinsic time called "memory kernel". When the kernel function is exponential, an incremental form of endochronic flow rule exists.

Bažant (1978) observed that for the endochronic theory the notion of loading surface can still be introduced, but it loses its physical meaning. Valanis (1980), Watanabe and Atluri (1986) proved that a non-linear kinematic (NLK) hardening model can be derived from an endochronic model by imposing a special intrinsic time definition. Moreover, a comparative study between the NLK hardening and the generalized plasticity theory has been presented by Auricchio and Taylor (1995). In view of there is a lack of unified theory framework on which formal comparisons between various plasticity theories could be based, new formulation of endochronic and NLK hardening models as well as generalized plasticity theory were suggested by Erlicher and Point (2006) using the classical notion of generalized normality (Halphen and Nguyen 1975), for the purpose to investigate the relationships between plasticity theories.

(3) Continuum damage theory

Continuum damage theory is focused on the damage representation suitable for making predictions with respect to the initiation and propagation of cracks (joints) in solid substances without resorting to a microscopic description that would be too complex for practical engineering computation (Kachanov 1982a, b, c; Krajcinovic 1983; Pijaudier-Cabot and Bažan 1987; Ju and Lee 1991; Swoboda and Yang 1999a, b). It offers a typical approaching strategy to simulate complex phenomena as indicated by Krajcinovic (1996) that "it is often argued that the ultimate task of engineering research is to provide not so much a better insight into the examined phenomenon but to supply a rational predictive tool applicable in design".

A damage activation criterion is needed to predict damage initiation (Lee et al. 1985). Most of the works use state variables to represent the effects of damage as a result of thermomechanical loading and ageing on the stiffness and remaining life of the material. These state variables may be measurable such as crack density, or inferred from the effect they have on some macroscopic property such as stiffness, coefficient of thermal expansion, remaining life, etc. They have conjugate thermodynamic forces that motivate further damage.

Since damage evolution does not progress spontaneously after initiation, therefore a damage evolution model is required. In plasticity-like formulations, it is controlled by a hardening function (Dragon and Mróz 1979; Murakami 1983, 1988; Kawamoto et al. 1988; Ju 1989; Chen and Schreyer 1995; Prat and Bažant 1997).

To tackle the problems arise from extending the phenomenological damage definition to rock-like materials, a second-order fabric tensor is normally incorporated to constitutive equations within the framework of continuum damage mechanics (Oda 1982). Since the damage-dependent elasticity tensor cannot be deduced on the hypothesis of strain equivalence, therefore the overall micromechanical analysis is necessary (Oda et al. 1984; Lemaitre 1990). From a phenomenological point of view, Cowin (1985) developed the most general fabric tensor-dependent elasticity tensor. The most important obstacles in the application of such damage theories are, probably the geometric measuation of anisotropic damage.

In computational geomechanics the damage is mostly regarded as the distributed micro-cracks (Budiansky and O'Connel 1976). However, this is mainly valid in a tensile stress dominated field. In addition, to describe the complicated mechanism with regard to the coupling of plastic flow in damage process, only conjugate-force-based damage evolution laws can keep a unitary and compact form (Rice 1971, 1975, 1978; Chow and Lu 1989). It is also debatable that the macroscopic stress/strain changes the contact manner (close or open) of crack surfaces which in turn, changes the crack propagation. To overcome the aforementioned difficulties for obtaining a practical formulation, some authors simply assume that the driving force behind the damage propagation is the net maximum tensile stress. Obviously, it is not a very convincible assumption because damage generally propagates not along the direction of its conjugate force.

2.11 Constitutive Relations: Viscoplasticity

2.11.1 Concept

Viscoplasticity is a theory in continuum mechanics that describes the rate-dependent inelastic behavior of solid substances. Rate-dependence in its context means that the deformation of the matter depends on the rate at which loads are applied. The main difference between the rate-independent plastic material and the rate-dependent viscoplastic material is that the latter exhibits not only permanent deformation but continues to demonstrating an irreversible creep as a function of time under the applied load.

The development of mathematical models in viscoplasticity may be dated back to 1910 with the representation of primary creep by Andrade's law. In 1929, Norton developed a one-dimensional dashpot model which linked the rate of secondary creep to the stress. In 1932, Hohenemser and Prager proposed the first model for slow viscoplastic flow relating the deviatoric stress for an incompressible Bingham (1922) solid. In 1934, Odqvist (1974) generalized the Norton's law to multi-axial cases.

Normally, viscoplasticity is treated as a consequence of subcritical crack growth or stress corrosion (Anderson and Grew 1977; Das and Scholz 1981; Atkinson 1984; Batra and Kim 1990; François et al. 1993; Lockner 1998; Amitrano and Helmstetter 2006; Haimson 2007; Gran et al. 2012; Xu et al. 2012; Brantut et al. 2013). Other possible mechanisms for viscoplasticity are the stress solution at crack tips (Rutter 1976), the diffusion of pore fluid pressure (Detournay and Cheng 1988), and the chemical interaction (Chen et al. 2003).

Nowadays, the concept of viscopalsticity is widely employed in the simulation of the secondary or/and tertiary creep (see Fig. 2.12), in which one-dimensional phenomenological models including the perfectly viscoplastic solid, the elastic perfectly viscoplastic solid, and the elasto-viscoplastic hardening solid (see Table 2.19), are constructed using spring-dashpot-slider elements. Many of these one-dimensional models can be generalized to three dimensional ones for the small strain regime through overstress formulations (Cristescu and Suliciu 1982; Mukherjee 1982), which are customarily categorized into two types (Simo and Hughes 1998), namely the Perzyna formulation and the Duvaut-Lions formulation. They all allow for stress to outgo beyond the rate-independent loading (yield) surface upon the application of a load and then to relax back on the surface over time. The loading (yield) surface is usually assumed to be rate-independent for quasistatic and earthquake related dynamic problems.

Perzyna, in 1963, introduced a viscosity coefficient that is temperature and time dependent. His phenomenological formulation was supported by the thermodynamics of irreversible processes. The ideas presented in his works have been the basis for most subsequent researches into rate-dependent viscoplasticity.

By the Perzyna formulation, if an elasto-viscoplastic computation reaches a stationary condition with respect to displacements, the solution to an equivalent

elasto-plasticity problem is obtained. The elasto-viscoplastic approach thus provides an alternative technique to solve elasto-plastic problems, which is found to possess considerable merits over other iterative processes (Zienkiewicz and Cormeau 1972, 1974). In particular, non-associated flow rules and strain softening can be handled with well without requiring specific numerical artifices.

The Perzyna formulation will be employed in the elasto-viscoplastic computation algorithms throughout this book.

2.11.2 Potential Theory

According to the principle of the Perzyna formulation, at time t_n, the implicit constitutive equation will take the following forms (Owen and Hinton 1980)

$$\begin{aligned}\{\Delta\sigma\}_t &= \left[\hat{D}\right]_t^e (\{\Delta\varepsilon\}_t - \{\dot{\varepsilon}^{vp}\}_t \Delta t) = \left[\hat{D}\right]_t^e (\{\Delta\varepsilon\}_t - \{\Delta\varepsilon^{vp}\}_t) \\ &= \left[\hat{D}\right]_t^e \{\Delta\varepsilon\}_t - \{\Delta\sigma^{vp}\}_t \end{aligned} \tag{2.122}$$

Or

$$\{\Delta\varepsilon\}_t = \left(\left[\hat{D}\right]_t^e\right)^{-1} \{\Delta\sigma\}_t + \{\dot{\varepsilon}^{vp}\}_t \Delta t = \left(\left[\hat{D}\right]_t^e\right)^{-1} \{\Delta\sigma\}_t + \{\Delta\varepsilon^{vp}\}_t \tag{2.123}$$

In which the implicit elasticity matrix $[\hat{D}]_t^e$ and elasto-viscoplastic strain rate $\{\dot{\varepsilon}^{vp}\}_t$ are

$$\begin{cases} [\hat{D}]_t^e = (([D]^e)^{-1} + [C]_t)^{-1} \\ [C]_t = \Theta \Delta t [H]_t \\ [H]_t = \left[\frac{\partial\{\dot{\varepsilon}^{vp}\}_t}{\partial\{\sigma\}_t}\right] \\ \{\dot{\varepsilon}^{vp}\}_t = \gamma \langle\psi\rangle \left\{\frac{\partial Q}{\partial\sigma}\right\}_t \end{cases} \tag{2.124}$$

where Δt = time marching step length, s; $[H]_t$ = implicit matrix; Θ = implicit parameter; γ = fluidity parameter, 1/(MPa s).

The function $<\psi>$ is defined as

$$<\psi> = \begin{cases} \psi & for \quad \psi > 0 \\ 0 & for \quad \psi \le 0 \end{cases} \tag{2.125}$$

In which ψ is the loading function. For perfect plasticity materials it is identical to the yield function F, i.e. $\psi = F$.

It is particularly notable that for discontinuities without thickness, the strain should be replaced by the relative displacement $\{\Delta u\}$, therefore we have

$$\begin{aligned}\{\Delta\sigma\}_t &= \left[\hat{D}\right]_t^e (\{\Delta u\}_t - \{\dot{u}^{vp}\}_t \Delta t) = \left[\hat{D}\right]_t^e (\{\Delta u\}_t - \{\Delta u^{vp}\}_t) \\ &= \left[\hat{D}\right]_t^e \{\Delta u\}_t - \{\Delta\sigma^{vp}\}_t \end{aligned} \tag{2.126}$$

Or

$$\{\Delta u\}_t = \left(\left[\hat{D}\right]_t^e\right)^{-1} \{\Delta\sigma\}_t + \{\dot{u}^{vp}\}_t \Delta t = \left(\left[\hat{D}\right]_t^e\right)^{-1} \{\Delta\sigma\}_t + \{\Delta u^{vp}\}_t \tag{2.127}$$

In which the implicit elasticity matrix $[\hat{D}]_t^e$ and elasto-viscoplastic strain rate $\{\dot{u}^{vp}\}_t$ are

$$\begin{cases} [\hat{D}]_t^e = (([D]^e)^{-1} + [C]_t)^{-1} \\ [C]_t = \Theta \Delta t [H]_t \\ [H]_t = \left[\frac{\partial\{\dot{u}^{vp}\}_t}{\partial\{\sigma\}_t}\right] \\ \{\dot{u}^{vp}\}_t = \gamma\langle\psi\rangle\left\{\frac{\partial Q}{\partial\sigma}\right\}_t \end{cases} \tag{2.128}$$

The implicit matrix in Eqs. (2.124) and (2.128) may be uniformly expressed as

$$\begin{cases} [H]_t = \gamma[\psi \frac{\partial\{q\}_t^T}{\partial\{\sigma\}_t} + \{a\}_t\{q\}_t^T] \\ \{a\}_t^T = \frac{\partial\psi}{\partial\{\sigma\}_t} \\ \{q\}_t^T = \frac{\partial Q}{\partial\{\sigma\}_t} \end{cases} \tag{2.129}$$

where $\Theta = 1$, we obtain a fully implicit or backward time marching scheme with the strain increment being determined from the strain rate corresponding to t_n, i.e. the end of the time marching step n.

$\Theta = 0.5$ yields implicit trapezoidal scheme and $\Theta \geq 0.5$ guarantees a time stepping scheme of unconditionally stable. This implies that the time marching scheme is numerically stable but does not guarantee the accuracy of the solution. To keep the balance between the time marching accuracy and the computation efforts, the adaptive time stepping technique based on the stepping error estimation may be employed (Zhang and Chen 1996, 1997).

On the other hand, $\Theta = 0$ gives the Euler time integration scheme which is also referred to as fully explicit or forward stepping scheme, since the strain increment is completely determined from the strain rate corresponding to the condition existing at t_{n-1}, i.e. the start of the time marching step n. Under such circumstances we have

$$[\hat{D}]_t^e = [D]^e \tag{2.130}$$

The explicit scheme is the simplest but is conditionally stable and numerical time integration can only be proceeded for a time interval Δt_n smaller than some critical values (Owen and Hinton 1980).

Depending on the materials encountered and coordinate systems defined, Eqs. (2.71), (2.72), (2.76a, 2.76b)–(2.78) and (2.81)–(2.83) may be selectively used for the corresponding elastic matrix $[D]^e$, and Eqs. (2.35), (2.41)–(2.45) and (2.47)–(2.50), may be selectively used as the corresponding yield criterion. The loading functions and non-associate potential functions, if necessary, may be found in Eqs. (2.105) and (2.115)–(2.120).

If the fluidity parameter γ may be evaluated by tests or in-situ back analyses, then the histories as well as the steady-state results concerning the deformation and stress of a hydraulic structure may be obtained. However, in many cases it is not easy to get the appropriate fluidity parameter or it is thought that only the elasto-plastic solution is of importance. Under such circumstances, we can simply assume that the fluidity parameter $\gamma = 1$, in this manner the calculated histories are not applicable, but the steady-state results with respect to deformation and failure are identical to the corresponding classical elasto-plastic solution (Zienkiewicz and Cormeau 1974), subject to appropriate time stepping scheme (implicit or explicit) and time stepping length to guarantee the computation accuracy and to avert numerical escalation.

2.12 Coupling Phenomenon

2.12.1 Concept

The coupling between the processes of heat transfer (T), fluid flow (H) and stress/deformation (M) in rock-like materials has become an increasingly important subject since the early 1980s (Tsang 1987, 1991), mainly attributable to the requirements from the design and performance assessment for underground radioactive waste repositories, and other engineering fields in which heat and water both play important roles, such as gas/oil recovery, hot-dry-rock thermal energy extraction, contaminant transport analysis and environment impact evaluation. The term "coupling" implies that the rock-like material response to the perturbations during the construction and operation of an engineering structure, cannot be predicted with confidence only by considering each process separately.

Although various computational techniques illustrated in Chap. 1 of this book may be employed for coupling problems, yet the representations using the FEM are the most prevalent for porous continua (Noorishad et al. 1992; Noorishad and Tsang 1996; Lewis and Schrefler 1998; Thomas and Missoum 1999; Borgesson et al. 2001; Rutqvist et al. 2001a, b; Hudson et al. 2001; Schrefler 2001). Other

applications are reported in the areas of advanced models and solution techniques for coupled THM models (Cervera et al. 1996; Wang and Schrefler 1998; Thomas and Cleall 1999; Thomas et al. 1999; Nithiarasu et al. 2000; Zimmerman 2000) inclusive flow and deformation of fractures (Selvadurai and Nguyen 1996, 1999) and double-porosity media (Masters et al. 2000).

The phenomenon of THM coupling is theoretically simulated using three inter-related PDEs with regard to the conservation of mass, energy and momentum. This belongs to the full coupling algorithm which is very rigorous involving the simultaneous solution of THM fields in a single simulator. It usually provides good solutions but demands extensive CPU-time consumption. In contrast, partial coupling algorithm solves a HTM field separately using three distinct simulators, but intermediate results must be passed between these simulators.

Partial coupling algorithm may be explicit or iterative. Taking the HM coupling for example, if the information obtained from the geomechanical simulator is not sent back to the flow simulator, the coupling is explicit. If the information is passed back and forth until the establishment of convergence, the coupling is iterative. Because of its reduced computing effort, explicit coupling is often exercised, if practically acceptable (Settari and Mourits 1994). Iterative algorithm is demanded when the HM coupling behavior is sensitive to joint/fracture compressibility (Samier et al. 2006).

In hydraulic structures, only the iterative HM coupling with regard to joint systems or/and explicit TM coupling with regard to solid skeleton phases are sometimes demanded, due to the lower stress or/and temperature level encountered.

2.12.2 Partial Coupling: Explicit Thermal to Stress/Strain

In general, solid substances expand on heating and contract on cooling. The strain associated with change in temperature will depend on the coefficient of thermal expansion of the matter and the magnitude of temperature drop or rise.

In mass concrete structures, the heat produced by cement hydration and relatively poor heat dissipation conditions result in a steep mount of temperature within a few days after the concrete placement. Before setting, the temperature rise related expansive deformation is not constrained and, therefore, it will result in only minor compressive stresses. As the rigid network of hydration products starts to build, subsequently cooling of concrete will give rise to higher shrinkage related tensile stresses due to the restraint appearing in concrete. Since the primary concern in the design and construction of mass concrete structures is that the completed structure stays a monolith free of cracks, every effort to control the temperature rise is made by the selection of proper cementitious materials and mix proportions, the implementation of artificial cooling, and the management of construction schedule.

Normally, concrete is supposed as isotropic elasticity and its free strain increment induced by the temperature increment is calculated by

$$\left\{\Delta\varepsilon^T\right\}_n = \begin{Bmatrix} \Delta\varepsilon_x^T \\ \Delta\varepsilon_y^T \\ \Delta\varepsilon_z^T \\ 0 \\ 0 \\ 0 \end{Bmatrix} = \begin{Bmatrix} \alpha\Delta T \\ \alpha\Delta T \\ \alpha\Delta T \\ 0 \\ 0 \\ 0 \end{Bmatrix} \tag{2.131}$$

where α = coefficient of thermal expansion, which is around 1.0×10^{-5} for concrete, 1/°C (see Table 2.14); ΔT = temperature variation, °C.

Under certain restraint, suppose the actual strain induced by ΔT is $\{\Delta\varepsilon\}_n$ (as yet unknown), the stress in the element is calculated by the coupling constitutive relation

$$\{\Delta\sigma\}_n = [D]_c^e \left(\{\Delta\varepsilon\}_n - \left\{\Delta\varepsilon^T\right\}_n\right) \tag{2.132}$$

where $[D]_c^e$ = elastic matrix; $\left\{\Delta\varepsilon^T\right\}_n$ = initial strain induced by temperature variation.

At the early age, as the on going of time after the placement and setting of concrete, its volume changes attributable to complex mechanical, physical and chemical processes. Apart from the direct relationship of the strain increment $\left\{\Delta\varepsilon^{\mathrm{T}}\right\}_n$ versus temperature variation in Eq. (2.131), the drying shrinkage $\left\{\Delta\varepsilon^s\right\}_n$ in Eq. (2.84), the autogenous shrinkage $\left\{\Delta\varepsilon^a\right\}_n$ in Eq. (2.86), and the creep strain $\left\{\Delta\varepsilon^c\right\}_n$ in Eq. (2.93), should be taken into account explicitly following the temperature history. Under such circumstances the total strain increment in the interval Δt_n is expressed by the formula

$$\{\Delta\varepsilon\}_t = \{\varepsilon(t)\} - \{\varepsilon(t-\Delta t_n)\} = \left\{\Delta\varepsilon^e\right\}_t + \left\{\Delta\varepsilon^c\right\}_t + \left\{\Delta\varepsilon^{\mathrm{T}}\right\}_t + \left\{\Delta\varepsilon^a\right\}_t + \left\{\Delta\varepsilon^s\right\}_t \tag{2.133}$$

where $\left\{\Delta\varepsilon^e\right\}_t$ = elastic strain increment; $\left\{\Delta\varepsilon^c\right\}_t$ = creep strain increment; $\left\{\Delta\varepsilon^{\mathrm{T}}\right\}_t$ = thermal strain increment; $\left\{\Delta\varepsilon^a\right\}_t$ = autogenous strain increment; $\left\{\Delta\varepsilon^s\right\}_t$ = drying shrinkage strain increment.

Instead of Eq. (2.132), the stress increment concerning thermal effects on the elastic performance of young concrete is expressed by the formula

$$\{\Delta\sigma\}_t = [\bar{D}]_t^e(\{\Delta\varepsilon\}_t - \left\{\Delta\varepsilon^c\right\}_t - \left\{\Delta\varepsilon^{\mathrm{T}}\right\}_t - \left\{\Delta\varepsilon^a\right\}_t - \left\{\Delta\varepsilon^s\right\}_t) \tag{2.134}$$

In which $[\bar{D}]_t^e$ is the equivalent elastic matrix of concrete within the time marching step interval Δt_n (see Eq. 2.98).

The strain/stress increments computed by Eqs. (2.133) and (2.134) are not necessarily sent back to the heat flow simulator.

2.12.3 Partial Coupling: Iterative Permeability to Stress/Strain

There are correlations between most of the rock properties, and the percolation of water through a jointed rock mass is without exception. It depends on the joint aperture, which in turn, will be related to the stresses exerting across the joint (Stratford et al. 1990; Ohnishi et al. 2001; Liu et al. 2016).

Basically, the seepage force (action) increment calculated by the flow simulator is passed to the geomechanical simulator to compute the corresponding changes in stresses, which are feedbacked to update the strain/stress dependent permeability tensor for the flow simulator.

Gangi (1978) had proposed a "bed of nails" model to determine the stress dependent permeability in jointed rock, in which the closure of joint under normal stress is described as an elastic compression of asperities. Attempts on the coupling relationship between normal stress and tangential seepage through the joint were also made by for example, Gale (1982), Raven and Gale (1985).

Rock joints may be filled or unfilled. An unfilled joint can be represented as two parallel plates in contact through asperities. These asperities may be looked at as a thin layer of equivalent granular material of high porosity clipped between the plates. Accordingly, Chen et al. (1989) proposed a "filled model", in which the asperities are replaced by an evenly "filled" virtual medium with certain deformation and permeability characteristics. In this manner, a uniform HM coupling model for both the filled and unfilled joints can be established.

There are normal and shear stresses on the joint surface in Fig. 2.26. Because the joint aperture is very small, a portion of strain components can be neglected, i.e.

$$\begin{cases} \varepsilon_{xj} = \varepsilon_{yj} = 0 \\ \gamma_{yxj} = 0 \end{cases} \tag{2.135}$$

Hence the elastic constitutive relation of the joint filler is expressed by three differential components

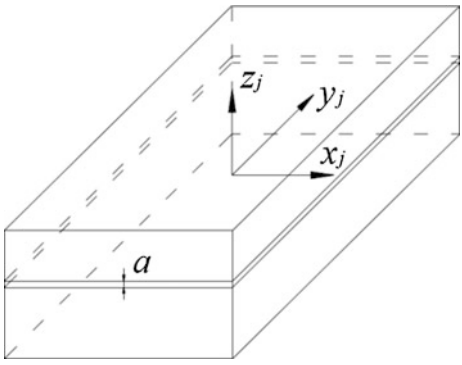

Fig. 2.26 Rock sample with a single joint segment

$$\begin{Bmatrix} d\tau_{zxj} \\ d\tau_{zyj} \\ d\sigma_{zj} \end{Bmatrix} = \begin{bmatrix} G & 0 & 0 \\ 0 & G & 0 \\ 0 & 0 & \lambda+2G \end{bmatrix} \begin{Bmatrix} d\gamma_{zxj} \\ d\gamma_{zyj} \\ d\varepsilon_{zj} \end{Bmatrix} \tag{2.136}$$

In which G_j and λ_j = shear modulus and Lamé coefficient of the filler matter (filled joint) or the equivalent asperity medium (unfilled joint), MPa.

Denoting the differential relative displacement of the joint walls as du_{xj}, du_{yj} and du_{zj}, Eq. (2.136) can be replaced by

$$\begin{Bmatrix} d\tau_{zxj} \\ d\tau_{zyj} \\ d\sigma_{zj} \end{Bmatrix} = \begin{bmatrix} k_s & 0 & 0 \\ 0 & k_s & 0 \\ 0 & 0 & k_n \end{bmatrix} \begin{Bmatrix} du_{xj} \\ du_{yj} \\ du_{zj} \end{Bmatrix} \tag{2.137}$$

In which

$$\begin{cases} k_s = \frac{G}{a} \\ k_n = \frac{\lambda+2G}{a} \end{cases} \tag{2.138}$$

where a = aperture of joint, m.

k_n and k_s are termed respectively as "normal and tangent stiffness coefficients" of the joint. According to Eq. (2.138), it is evident that even if the parameters λ and G are keeping constant, k_n and k_s are functions of normal stress, because the aperture a is related to the deformation u_{zj} which in turn, dependent on the normal stress σ_{zj}. When the joint exhibits a normal compression u_{zj}, the deformed joint aperture is calculated by the formula

$$a = a_0 + u_{zj} \tag{2.139}$$

where a_0 = initial joint aperture, m.

Introducing Eqs. (2.138) and (2.139) into Eq. (2.137), we have

$$d\sigma_{zj} = k_n du_{zj} = \frac{\lambda+2G}{a} du_{zj} = \frac{\lambda+2G}{a_0+u_{zj}} du_{zj} \tag{2.140}$$

By the integral throughout Eq. (2.140), it becomes

$$u_{zj} = a_0[\exp(\frac{\sigma_{zj}}{\lambda+2G}) - 1] \tag{2.141}$$

Denote

$$\xi = \frac{1}{\lambda+2G} \tag{2.142}$$

And take into account of Eqs. (2.139) and (2.141), the exponential relation between the joint aperture and the normal stress is given

$$a = a_0 + u_{zj} = a_0 \exp(\xi \sigma_{zj}) \tag{2.143}$$

where ξ = coupling coefficient.

Substituting for a from Eq. (2.143) in Eq. (2.138) results in

$$\begin{cases} k_s = k_{s0} \exp(-\xi \sigma_{zj}) \\ k_n = k_{n0} \exp(-\xi \sigma_{zj}) \end{cases} \tag{2.144}$$

where ξ = coupling coefficient; k_{n0} and k_{s0} = initial stiffness coefficients, MPa/m; σ_{zj} = normal stress on joint (negative for compression); MPa.

Since the virtual (equivalent) parameters λ and G are difficultly evaluated for unfilled joint, ξ is commonly estimated through the compression and direct shear tests.

By the exponential relation between the joint aperture and the normal stress in Eq. (2.143), and the hydraulic conductivity defined in Eq. (2.10), a simple relation of the hydraulic conductivity (either filled or unfilled joint) versus normal stress is obtained

$$C = k_f a_0 \exp(\xi \sigma_{zj}) = C_0 \exp(\xi \sigma_{zj}) \tag{2.145}$$

where ξ = coupling coefficient; C_0 = initial hydraulic conductivity of the joint, MPa/m; σ_{zj} = normal stress on the joint (negative for compressive), MPa.

The parameters in Eqs. (2.144) and (2.145) under the normal pressure <10 MPa may be estimated by the routine coupling tests for joints. Iwai (1976), Raven and Gale (1985) performed laboratory tests on the mechanical and hydraulic properties of tension fractures in basalt, granite, and marble. Cylindrical samples of intact rocks, 0.15 m in diameter, were diamond-cored from rock blocks, and a horizontal tension fracture was created in each sample using a modified "Brazilian" splitting method. A central hole, 0.022 m in diameter, provided access for outward radial flow of water. Use was made of their test data, Chen et al. (1989) evaluated the parameters in the "filled model" (see Table 2.37).

Table 2.37 Coupling parameters of joints (laboratory)

Coupling parameter	Granite (Raven and Gale 1985)	Granite (Iwai 1976)	Basalt (Iwai 1976)	Marble (Iwai 1976)
k_{n0} (MPa/m)	1.977×10^4	1.449×10^4	5.495×10^4	3.571×10^4
C_0 (m^2/s)	3.055×10^{-8}	6.4×10^{-8}	6.1×10^{-8}	6.1×10^{-9}
ξ	0.22	0.3	0.35	0.8

References

Adhikary D, Dyskin A. A continuum model of layered rock masses with non-associative joint plasticity. Int J Numer Anal Meth Geomech. 1998;22(4):245–61.

Akanuma H. The significance of the composition of excavated iron fragments taken from Stratum III at the site of Kaman-Kalehöyük, Turkey. Anatolian Archaeol Stud. 2005;14:147–58.

Alexandrovskii SV. Plane and reinforced concrete structures calculation under thermal and hygral effects. Moskow: Stroiizolat; 1966 (in Russian).

Al-Raoush R, Papadopoulos A. Representative elementary volume analysis of porous media using X-ray computed tomography. Powder Technol. 2010;200(1–2):69–77.

Amadei B. Rock anisotropy and the theory of stress measurements. Berlin: Springer; 1983.

Amadei B, Goodman RE. A 3-D Constitutive relation for fractured rock masses. In: Selvadurai APS, editor. Proceedings of international symposium, mechanical behaviour structured media. Ottawa, Canada. Amsterdam: Elsevier Scientific Publ Co; 1981. p. 249–68.

American Concrete Institute. (ACI 318-08) Building code for structural concrete. Detroit: ACI; 2008.

Amitrano D, Helmstetter A. Brittle creep, damage, and time to failure in rocks. J Geophys Res Solid Earth. 2006;111(B11):1–17.

Anderson OL, Grew PC. Stress corrosion theory of crack propagation with applications to geophysics. Rev Geophys. 1977;15(1):77–104.

Armstrong P, Frederick C. A mathematical representation of the multiaxial Bauschinger effect. GEGB report RD/B/N731; 1966.

Arutiunian NH, Kolmanovskii VB. Creep theory of inhomogeneous bodies. Moskow: Nauka; 1983 (in Russian).

Atkinson BK. Subcritical crack growth in geological materials. J Geophys Res Solid Earth. 1984;89(B6):4077–114.

Auricchio F, Taylor RL. Two material models for cyclic plasticity: nonlinear kinematic hardening and generalized plasticity. Int J Plast. 1995;11(1):65–98.

Auvray C, Homand F, Sorgi C. The aging of gypsum in underground mines. Eng Geol. 2004;74 (3):183–96.

Baecher GB, Lanney NA, Einstein HH. Statistical description of rock properties and sampling. In: Wang FD, Clark GB, editors. Proceedings of 18th US symposium rock mechanics. Colorado: Colorado School of Mines Press; 1977. p. 5c1–8.

Barla G. Squeezing rocks in tunnels. ISRM News J. 1995;2(3/4):44–9.

Barla G, Bonini M, Debernardi D. Time dependent deformations in squeezing tunnels. Int J Geoeng Case Histories. 2010;2(1):819–24.

Barton NR. A model study of rock-joint deformation. Int J Rock Mech Min Sci. 1972;9(5):579–82.

Barton NR. Some new Q-value correlations to assist in site characterisation and tunnel design. Int J Rock Mech Min Sci. 2002;39(2):185–216.

Barton NR, Bandis S, Bakhtar K. Strength, deformation and conductivity coupling of rock joints. Int J Rock Mech Min Sci Geomech Abstr. 1985;22(3):121–40.

Batra RC, Kim CH. Effect of viscoplastic flow rules on the initiation and growth of shear bands at high strain rates. J Mech Phys Solids. 1990;38(6):859–74.

Bažant ZP. Endochronic inelasticity and incremental plasticity. Int J Solids Struct. 1978;14 (9):691–714.

Bažant ZP. Mathematical models for creep and shrinkage of concrete. In: Bažant ZP, Wittman FH, editors. Creep and shrinkage in concrete structure. New York: Wiley; 1982.

Bažant ZP, editor. Mathematical modeling of creep and shrinkage of concrete. RILEM Committee TC 69 report. Chichester and New York: Wiley; 1988.

Bažant ZP, Bhat PD. Endochronic theory of inelasticity and failure of concrete. J Eng Mech Div ASCE. 1976;102(EM4):701–22.

Bažant ZP, Krizek RJ. Endochronic constitutive law for liquefaction of sand. J Eng Mech Div ASCE. 1976;102(EM2):225–38.

Bažant ZP, Prasannan S. Solidification theory for concrete creep. J Eng Mech. 1989;115(8): 1691–725.
Bažant ZP, Belytschko T, Chang TP. Continuum theory for strain-softening. J Eng Mech ASCE. 1984;110(12):1666–92.
Belytschko T, Liu WK, Moran B. Nonlinear Finite Elements for Continua and Structures. Chichester: Wiley; 2000.
Betten J. Creep mechanics, 3rd ed. Berlin: Springer; 2008.
Bieniawski ZT. Fracture dynamics of rock. Int J Fract Mech. 1968a;4(4):415–30.
Bieniawski ZT. The effect of specimen size on compressive strength of coal. Int J Rock Mech Min Sci. 1968b;5(4):325–35.
Bieniawski ZT. Determining rock mass deformability: experience from case histories. Int J Rock Mech Min Sci Geomech Abstr. 1978;15(5):237–47.
Bingham EC. Fluidity and plasticity. New York: McGraw-Hill; 1922.
Birch AF, Clark H. The thermal conductivity of rocks and its dependence upon temperature and composition. Am J Sci. 1940;238(8):529–58.
Bizjak KF, Zupančič A. Rheological investigation for the landslide Slano Blato near Ajdovscina (Slovenia). Geologija. 2007;50(1):121–9.
Boland JN, Hobbs BE. Microfracturing processes in experimentally deformed peridotite. Int J Rock Mech Min Sci. 1973;10(6):623–6.
Borgesson L, Chijimatsu M, Fujita T, Nguyen TS, Rutqvist J, Jing L. Thermo-hydro-mechanical characterization of a bentonite-based buffer material by laboratory tests and numerical back analysis. Int J Rock Mech Min Sci. 2001;38(1):95–104.
Boukharov GN, Chanda MW, Boukharov NG. The three processes of brittle crystalline rock creep. Int J Rock Mech Min Sci Geomech Abstr. 1995;32(4):325–35.
Bourne SJ. Contrast of elastic properties between rock layers as a mechanism for the initiation and orientation of tensile failure under uniform remote compression. J Geophys Res. 2003;108 (B8):2395.
Boussinesq J. Mémoire sur l'influence des frottements dans les mouvements réguliers des fluides. Journal de Mathématiques Pures et Appliquées. 1868;13(2e série):377–424 (in French).
Brace WF, Walsh JB, Frangos WT. Permeability of granite under high pressure. J Geophys Res. 1968;73(6):2225–36.
Brantut N, Heap MJ, Meredith PG, Baud P. Time-dependent cracking and brittle creep in crustal rocks: a review. J Struct Geol. 2013;52(7):17–43.
Brebbia CA, editor. Finite element systems (A handbook). Berlin: Springer; 1985.
Bridgman PW. Studies in large plastic flow and fracture: with special emphasis on the effects of hydrostatic pressure. New York: McGrawHill Book Company Inc; 1952.
Brooks JJ. 30-year creep and shrinkage of concrete. Mag Concrete Res. 2005;57(9):545–56.
Brown ET, editor. Rock characterization, testing and monitoring: ISRM suggested methods. Oxford: Pergamon Press; 1981.
Brown ET. Fifty years of the ISRM and associated progress in rock mechanics. In: Qian Q, Zhou XY, editors. Proceedings of 12th ISRM congress. Beijing: ISRM; 2011. p. 29–45.
Budiansky B, O'Connel RJ. Elastic moduli of a cracked solid. Int J Solids Struct. 1976;12(2): 81–97.
Burgisser A, Chevalier L, Gardner JE, Castro JM. The percolation threshold and permeability evolution of ascending magmas. Earth Planet Sci Lett. 2017;470:37–47.
Cai M, Kaiser PK, Uno H. Estimation of rock mass deformation modulus and strength of jointed hard rock masses using the GSI system. Int J Rock Mech Min Sci. 2004;41(1):3–19.
Carslaw HS, Jaeger JC. Conduction of heat in solids, 2nd ed. Oxford: Oxford University Press; 1985.
Casagrande A. First Rankine Lecture—control of seepage through foundations and abutment of dam. Géotechnique. 1961;11(3):161–82.
Cedergren HR. Seepage, drainage and flownets, 3rd ed. New York: Wiley; 1989.
Cervera M, Codina R, Galindo M. On the computational efficiency and implementation of block-iterative algorithms for non-linear coupled problems. Eng Comput. 1996;13(6):4–30.

Chaboche JL. On some modifications of kinematic hardening to improve the description of ratchetting effects. Int J Plast. 1991;7(7):661–78.
Chen SH. Hydraulic structures. Berlin: Springer; 2015.
Chen WF, Baladi GY. Soil plasticity: theory and implementation. Amsterdam: Elsevier; 1985.
Chen G, Chugh Y. Estimation of in situ visco-elastic parameter of weak floor strata by plate-loading tests. J Geotech Geol Eng. 1996;14(2):151–67.
Chen WF, Drucker DC. Bearing capacity of concrete blocks or rock. J Eng Mech ASCE. 1969;95 (EM4):955–78.
Chen SH, Pande GN. Rheological model and finite element analysis of jointed rock masses reinforced by passive, fully-grouted bolts. Int J Rock Mech Min Sci Geomech Abstr. 1994;31 (3):273–7.
Chen WF, Saleeb AF. Constitutive equations for engineering materials. 1: Elasticity and modeling, Revised ed. Amsterdam: Elsevier; 1994.
Chen Z, Schreyer HL. Formulation and computational aspects of plasticity and damage models with application to quasi-brittle materials. Contractor report, SAND95–0329. California: Sandia National Laboratories; 1995.
Chen WF, Zhang H. Structural plasticity: theory, problems and CAE software. New York: Springer; 1991.
Chen SH, Wang HR, Xiong WL. Study of the seepage characteristics of joint. J Wuhan Univ Hydraul Electr Eng (WUHEE). 1989;22(1):51–60 (in Chinese).
Chen G, Chenevert ME, Sharma MM, Yu M. A study of wellbore stability in shales including poroelastic, chemical, and thermal effects. J Petrol Sci Eng. 2003;38(3–4):167–76.
Chen SH, Qin WX, Xu Q. Composite element method and application of trace simulation for strain localization bands. Chin J Rock Mech Eng. 2007;26(6):1116–22 (in Chinese).
Chen SH, Feng XM, Shahrour I. Numerical estimation of REV and permeability tensor for fractured rock masses by composite element method. Int J Numer Anal Meth Geomech. 2008;32(12):1459–77.
Chen SH, Zhang GX, Zhu YM. Thermal stresses and temperature control of concrete. In: Zhou JP, Dang LC, editors. Handbook of hydraulic structure design, vol. 5. Concrete dams (Chapter 6). Beijing: China Water Power Press; 2011 (in Chinese).
Chiles JP. Fractal and geostatistical methods for modelling a fracture network. Math Geol. 1988;20 (6):631–54.
Chow CL, Lu TJ. On evolution laws of anisotropic damage. Eng Fract Mech. 1989;34(3):679–701.
Commission on Standardization of Laboratory and Field Tests. Suggested methods for determining shear strength (Document No. 1). Lisbon: ISRM; 1974.
Counto UJ. The effect of the elastic modulus of the aggregate on the elastic modulus, creep and creep recovery of concrete. Mag Concr Res. 1964;16(48):129–38.
Cowin SC. The relationship between the elasticity tensor and the fabric tensor. Mech Mater. 1985;4(2):137–47.
Cristescu ND, Gioda G, editors. Visco-plastic behaviour of geomaterials. Wien: Springer; 1994.
Cristescu ND, Suliciu I. Mechanics of plastix solids—viscoplasticity. Hague: Martinus Nijhoff Publishers; 1982.
Cruden DE. Describing the size of discontinuities. Int J Rock Mech Min Sci Geomech Abstr. 1977;14(3):133–7.
Danilova GN, Bogdanov SN. Determination of thermophysical properties of concretes and gravels used in the construction of concrete dams. Hydrotechnical Constr. 1967;1(4):326–9.
Das S, Scholz CH. Theory of time-dependent rupture in the Earth. J Geophys Res. 1981;86 (B7):6039–51.
Davis HE. Autogenous volume change of concrete. Proc ASTM. 1940;40:1103–10.
Davis RO, Selvadurai APS. Plasticity and geotechnics. Cambridge: Cambridge University Press; 2002.
de Borst R. Integration of plasticity equations for singular yield functions. Comput Struct. 1987;26 (5):823–9.

de Borst R, Pankaj P, Bićanić N. A note on singularity indicators for Mohr-Coulomb type yield criteria. Comput Struct. 1991;39(1–2):219–20.
de Souza Neto EA, Perić D, Owen DRJ. Computational methods for plasticity: theory and applications. New York: Wiley; 2009.
Dershowitz WS. Rock joint systems. Ph.D. thesis. Boston: Massachusetts Institute of Technology; 1984.
Desai CS, Gioda G, editors. Numerical methods and constitutive modeling in geomechanics. Wien: Springer; 1990.
Desai CS, Toth J. Disturbed state constitutive modeling based on stress–strain and nondestructive behavior. Int J Solids Struct. 1996;33(11):1619–50.
Desai CS, Drumm EC, Zaman MM. Thin layer element for interfaces and joints. J Geotech Eng ASCE. 1985;111(6):793–815.
Detournay E, Cheng AHD. Poroelastic response of a borehole in a nonhydrostatic stress field. Int J Rock Mech Min Sci. 1988;25(3):171–82.
Doltsinis IS, editor. Advances in computational nonlinear mechanics (CISM). Wien: Springer; 1989.
Dragon A, Mróz Z. A model for plastic creep of rock-like materials accounting for the kinetics of fracture. Int J Rock Mech Min Sci. 1979;16(4):235–59.
Drucker DC, Prager W. Soil mechanics and plastic analysis for limit design. Q Appl Math. 1952;10(2):157–65.
Dunne FPE, Petrinic N. Introduction to computational plasticity. Oxford: Oxford University Press; 2005.
Dunnicliff J. Geotechnicul instrumentation for monitoring field performance. Chichester: Wiley; 1988.
Dusseault MB, Fordham CJ. Time-dependent behavior of rocks. In: Hudson JA, editor. Comprehensive rock engineering: principles, practice, and projects, vol. 3. Oxford: Pergamon Press; 1993. p. 119–49.
Einstein HH, Nelson RA, Bruhn RW, Hirschfield RC. Model studies of jointed rock behaviour. In: Proceedings of 11th US symposium on rock mechanics (Chapter 6). Berkeley: Port City Press; 1969.
Eisenberg MA, Phillips A. A theory of plasticity with non-coincident yield and loading surfaces. Acta Mech. 1971;11(3):247–60.
Erlicher S, Point N. Endochronic theory, non-linear kinematic hardening rule and generalized plasticity: a new interpretation based on generalized normality assumption. Int J Solids Struct. 2006;43(14–15):4175–200.
European Committee for Standardization. (Eurocode 2) Design of concrete structures. Brussels: ECS; 2004.
Evesque P. Fluctuations, correlations and representative elementary volume (REV) in granular materials. Poudres Grains. 2000;11:6–17.
Farmer IW. Engineering properties of rocks. London: E & FN Spon Ltd; 1968.
Fernandez G, Moon J. Excavation-induced hydraulic conductivity reduction around a tunnel—Part 1: guideline for estimate of ground water inflow rate. Tunn Undergr Space Technol. 2010;25 (5):560–6.
François D, Pineau A, Zaoui A. Mechanical behaviour of materials. Volume II: viscoplasticity, damage, fracture and contact mechanics. Dordrecht: Kluwer Academic Publishers; 1993.
Frémond M. Non-smooth thermomechanics. Berlin: Springer; 2002.
Gale JE. The effects of fracture type (induced vs. natural) on the stress–fracture closure permeability relationships. In: Goodman RE, Heuze FE, editors. Proceedings of 23rd US symposium on rock mechanics. Rotterdam: AA Balkema; 1982. p. 290–8.
Gangi AF. Variation of whole and fractured porous rock permeability with confining pressure. Int J Rock Mech Min Sci Geomech Abstr. 1978;15(5):249–57.
Ge XR, Jiang Y, Lu YD. Testing study of fatigue deformation law of rock under cyclic loading. Chin J Rock Mech Eng. 2003;22(10):1581–5 (in Chinese).

Gerrard CM. Equivalent elastic moduli of a rock mass consisting of orthorhombic layers. Int J Rock Mech Min Sci Geomech Abstr. 1982a;19(1):9–14.
Gerrard CM. Elastic models of rock masses having one, two and three sets of joints. Int J Rock Mech Min Sci Geomech Abstr. 1982b;19(1):15–23.
Ghaboussi J, Gioda G. On the time-dependent effects in advancing tunnels. Int J Numer Anal Meth Geomech. 1977;1(3):249–69.
Gitman IM, Askes H, Sluys LJ. Representative volume: existence and size determination. Eng Fract Mech. 2007;74(16):2518–34.
Golzé AR, editor. Handbook of dam engineering. New York: Van Nostrand Reinhold Company; 1977.
Gonze P. Techniques de calcul utilisées en congé lation des terrains. In: La thermomé canique des roches. vol. 16. BRGM; 1988 (in French).
Goodman RE. Introduction to rock mechanics, 2nd ed. New York: Wiley; 1989.
Goodman RE, Dubois J. Duplication of dilatancy in analysis of jointed rocks. J Soil Mech Found Div ASCE. 1972;98(SM4):399–422.
Goodman RE, Taylor R, Brekke TL. A model for the mechanics of jointed rock. J Soil Mech Found Div ASCE. 1968;94(SM3):637–59.
Gran JD, Rundle JB, Turcotte DL. A possible mechanism for aftershocks: time dependent stress relaxation in a slider-block model. Geophys J Int. 2012;191(2):459–66.
Griffiths DV, Gioda G. Advanced numerical applications and plasticity in geomechanics. Wien: Springer; 2000.
Gruden DN. Single-increment creep experiments on rock under uniaxial compression. Int J Rock Mech Min Sci. 1971;8(2):127–42.
Gurson AL. Continuum theory of ductile rupture by void nucleation and growth. I. Yield criteria and flow rules for porous ductile media. J Eng Mater Technol. 1977;99(1):2–15.
Guz IA, Soutis C. A 3-D stability theory applied to layered rocks undergoing finite deformations in biaxial compression. Eur J Mech A Solids. 2001;20(1):139–53.
Haimson B. Micromechanisms of borehole instability leading to breakouts in rocks. Int J Rock Mech Min Sci. 2007;44(2):157–73.
Hakami E, Larsson E. Aperture measurement and flow experiments on a single natural fracture. Int J Rock Mech Min Sci Geomech Abstr. 1990;33(5):395–404.
Hall EO. Yield point phenomena in metals and alloys. New York: Plenum Press; 1970.
Halphen B, Nguyen QS. Sur les matériaux standards généralisés. Journal de Mécanique. 1975;14 (1):39–63 (in French).
Han W, Reddy BD. Plasticity: mathematical theory and numerical analysis. New York: Springer; 1999.
Harris D. Plasticity models for soils, granular and jointed rock materials. J Mech Phys Solids. 1992;40(2):273–90.
Harza LF. The significance of pore pressure in hydraulic structures. Trans ASCE. 1949;114 (1):193–214.
Hashin Z. Analysis of composite materials—a survey. J Appl Mech. 1983;50(3):481–505.
He J, Chen SH. A revised solution of equivalent permeability tensor for discontinuous fractures. J Hydrodyn Ser B. 2012;24(5):711–7.
Hecker SS. Experimental studies of yield phenomena in biaxially loaded metals. In: Stricklin JA, Saczalski KH, editors. Constitutive equations in viscoplasticity: computational and engineering aspects. AMD, vol. 20. New York: ASME; 1976. p. 1–33.
Hellmich Ch, Ulm FJ, Mang HA. Consistent linearisation in finite element analysis of coupled chemo-thermal problems with exo- or endothermal reactions. Comput Mech. 1999;24(4): 238–44.
Hill R. Elastic properties of reinforced solids: some theoretical principles. J Mech Phys Solids. 1963;11(5):357–72.
Hill R. The essential structure of constitutive laws for metal composites and polycrystals. J Mech Phys Solids. 1967;15(2):79–95.
Hill R. The mathematical theory of plasticity. Oxford: Oxford University Press; 1998.

Hoek E, Bray JW. Rock slope engineering, 3rd ed. London: Institution of Mining and Metallurgy; 1981.
Hoek E, Diederichs MS. Empirical estimation of rock mass modulus. Int J Rock Mech Min Sci. 2006;43(2):203–15.
Hoff NJ, editor. Creep in structures: IUTAM colloquium held at Stanford University (1962). Berlin: Springer; 2012.
Hsieh PA, Neuman SP. Field determination of the three-dimensional hydraulic conductivity tensor of anisotropic media. 1: Theory. Water Resour Res. 1985;21(11):1655–65.
Hsieh PA, Neuman SP, Stiles GK, Simpson ES. Field determination of the three dimensional hydraulic conductivity tensor of anisotropic media. 2: Methodology and application to fractured rocks. Water Resour Res. 1985;21(11):1667–76.
Hu J, Chen SH. Air element method for modeling the drainage hole in seepage analysis. Rock Soil Mech. 2003;24(2):281–7 (in Chinese).
Hu FX, Shi G, Shi YJ. Constitutive model for full-range elasto-plastic behavior of structural steels with yield plateau: calibration and validation. Eng Struct. 2016;118(7):210–27.
Hudson JA, Harrison JP. Engineering rock mechanics—an introduction to the principles. Oxford: Elsevier Science Ltd; 1997.
Hudson JA, Priest SD. Discontinuity frequency in rock masses. Int J Rock Mech Min Sci Geomech Abstr. 1983;20(2):73–89.
Hudson JA, Stephansson O, Andersson J, Jing L. Coupled T-H-M issues relating to radioactive waste repository design and performance. Int J Rock Mech Min Sci. 2001;38(1):143–61.
Huet C. Coupled size and boundary-condition effects in viscoelastic heterogeneous and composite bodies. Mech Mater. 1999;31(12):787–829.
Humpheson C, Naylor DJ. The importance of the form of the failure criterion. C/R/243/75. Swansea: University of Wales; 1975.
ICOLD. The specification and quality control of concrete for dams (Bulletin 136). Paris: ICOLD; 2009.
Inoue T, Kitagawa H, Shima S, editors. Computational plasticity. London: Elsevier; 1990.
Irgens F. Continuum mechanics. Berlin: Springer; 2008.
Iwai K. Fundamental studies of the fluid flow through a single fracture. Ph.D. thesis. Berkeley: University of California; 1976.
Jaeger JC, Cook NGW, Zimmerman R. Fundamentals of rock mechanics, 4th ed. MA: Wiley-Blackwell; 2007.
Jia LJ, Kuwamura H. Ductile fracture simulation of structural steels under monotonic tension. J Struct Eng ASCE. 2014;140(5):472–82.
Jirásek M, Bažant ZP. Inelastic analysis of structures. London: Wiley; 2001.
John KW. Strength and deformability of regularly jointed rocks (Chapter 5). Berkeley: Port City Press; 1969.
Ju JW. On energy-based coupled elastoplastic damage theories: constitutive modelling and computational aspects. Int J Solids Struct. 1989;25(7):803–33.
Ju JW, Lee X. Micromechanical damage models for brittle solid. Part I: tensile loadings and II: compressive loading. J Eng Mech ASCE. 1991;117(7):1495–536.
Kacewicz M. Model-free estimation of fracture apertures with neural networks. Math Geol. 1994;26(8):985–94.
Kachanov LM. Time of the rupture process under creep conditions. Izvestiya Akademii Nauk SSSR Otdelenie Tekniches. 1958;8:26–31.
Kachanov LM. A microcrack model of rock inelasticity. Part I: frictional sliding on microcracks. Mech Mater. 1982a;1(1):19–27.
Kachanov LM. A microcrack model of rock inelasticity. Part II: propagation of microcracks. Mech Mater. 1982b;1(1):29–41.
Kachanov LM. A microcrack model of rock inelasticity. Part III: time-dependent growth of microcracks. Mech Mater. 1982c;1(2):123–9.

Kanit T, Forest S, Galliet I, Mounoury V, Jeulin D. Determination of the size of the representative volume element for random composites: statistical and numerical approach. Int J Solids Struct. 2003;40(13–14):3647–79.
Kawamoto T, Ichikawa Y, Kyoya T. Deformation and fracturing behaviour of discontinuous rock mass and damage mechanics theory. Int J Numer Anal Meth Geomech. 1988;12(1):1–30.
Keener KB. Uplift pressures in concrete dams. Trans ASCE. 1950;116(1):1218–37.
Keskin RSO, Hover KC, Grigoriu M. Size effects in modeling diffusivity of hardened mortar. Comput Struct. 2011;89(9):713–23.
Khan AS, Huang S. Continuum theory of plasticity. New York: Wiley; 1995.
Kim YR, Lutif J, Allen D. Determining representative volume elements of asphalt concrete mixtures without damage. Transp Res Rec J Transp Res Board. 2009;2127(2):52–9.
Koiter WT. Stress–strain relations, uniqueness and variational theorems for elastic-plastic materials with singular yield surface. Q Appl Math. 1953;11(3):350–4.
Kolditz O. Modelling flow and heat transfer in fracture rocks: conceptual model of a 3-d deterministic fracture network. Geothermics. 1995;24(3):451–70.
Kolymbas D, editor. Constitutive modelling of granular materials. Berlin: Springer; 2000.
Krajcinovic D. Continuum damage mechanics revisited: basic concepts and definitions. J Appl Mech. 1983;52(4):829–34.
Krajcinovic D. Damage mechanics. Amsterdam: North Holland; 1996.
Kranz RL. Crack growth and development during creep of barre granite. Int J Rock Mech Min Sci. 1979;16(1):22–35.
Kranz RL, Frankel AD, Engelder T, Scholz CH. The permeability of whole and jointed barre granite. Int J Rock Mech Min Sci. 1979;16(4):225–34.
Kulatilake PHSW, Panda BB. Effect of block size and joint geometry on jointed rock hydraulics and REV. J Eng Mech ASCE. 2000;126(8):850–8.
Kulatilake PHSW, Wu TH. The density of discontinuity traces in sampling windows. Int J Rock Mech Min Sci Geomech Abstr. 1984;21(6):345–7.
Kulatilake PHSW, Wathugala DN, Stephansson O. Joint network modeling, including a validation to an area in Stripa Mine, Sweden. Int J Rock Mech Min Sci Geomech Abstr. 1993;30(5):503–26.
Lade PV, Duncan JM. Elastoplastic stress–strain theory for cohesionless soil. J Geotech Eng Div ASCE. 1975;101(GT10):1037–53.
Lai YS, Wang CY, Tien YM. Modified Mohr-Coulomb-type micromechanical failure criteria for layered rocks. Int J Numer Anal Meth Geomech. 1999;23(5):451–60.
Landau LD, Lipshitz EM. Theory of elasticity, 3rd ed. Oxford: Pergamon Press; 1970.
Larsson R, Runesson K. Implicit integration and consistent linearization for yield criteria of the Mohr-Coulomb type. Mech Cohesive-Friction Mater. 1996;1(4):367–83.
Lechner M, Hellmich CH, Mang NA. Short-term creep of shotcrete—thermochemoplastic material modeling and nonlinear analysis of a laboratory test and of a NATM excavation by the finite element method. In: Vermeer PA, Diebels S, Ehlers W, Herrmann HJ, Luding S, Ramm E, editors. Continuous and discontinuous modelling of cohesive-frictional materials. Lecture notes in physics, vol. 568. Berlin: Springer; 2001. p. 47–62.
Lee H, Peng K, Wang J. An anisotropic damage criterion for deformation instability and its application to forming limit analysis of metal plates. Eng Fract Mech. 1985;21(5):1031–54.
Lemaitre J. A course on damage mechanics, 2nd ed. Berlin: Springer; 1990.
Lemaitre J, Chaboche JL. Mechanics of solid materials. Cambridge: Cambridge University Press; 1990.
Leroy Y, Ortiz M. Finite element analysis of strain localization in frictional materials. Int J Numer Anal Meth Geomech. 1989;13(1):53–74.
Lewis RW, Schrefler BA. The finite element method in the static and dynamic deformation and consolidation of porous media. Chichester: Wiley; 1998.
Li XX, Chen SH, Xu Q, Xu Y. Modeling the three-dimensional unsaturated water transport in concrete at the mesoscale. Comput Struct. 2017;190:61–74.

Lin FB, Bažant ZP. Convexity of smooth yield surface of frictional material. J Eng Mech. 1986;112(11):1259–62.
Liu L, Xu WY, Wang HL, Wang RB, Wang W. Experimental studies on hydro-mechanical properties of metamorphic rock under hydraulic pressures. Eur J Environ Civil Eng. 2016;20 (1):45–59.
Lockner DA. A generalized law for brittle deformation of Westerly granite. J Geophys Res. 1998;103(B3):5107–23.
Ломизе М (Lomize M). Фильтрация в трещиноватых породах (Flow in fractured rocks). Госэнергоизат (Gosenergoizdat). Moscow; 1951 (in Russian).
Look BG. Handbook of geotechnical investigation and design tables. London: Taylor & Francis Group; 2007.
Louis C. A study of groundwater flow in jointed rock and its influence on the stability of rock masses. Rock mechanics research report 10. London: Imperial College; 1969.
Louis C. Rock hydraulics. In: Müller L, editor. Rock mechanics. Wien: Springer; 1974a. p. 299–387.
Louis C. Introduction a l'Hydraulique des Roches. Orleans: Bureau de Recherches Geologiques et Minieres; 1974b (in French).
Louis C, Maini YN. Determination of in-situ hydraulic parameters in jointed rock. In: Proceedings of 2nd ISRM congress. Belgrade: ISRM; 1970. p. 235–45.
Lourenço PB, Rots J. A multi-surface interface model for the analysis of masonry structures. J Eng Mech Div ASCE. 1997;123(EM7):660–8.
Lubliner J. A simple theory of plasticity. Int J Solids Struct. 1974;10(3):313–9.
Lubliner J. An axiomatic model of rate-independent plasticity. Int J Solids Struct. 1980;16(8): 709–13.
Lubliner J. A maximum-dissipation principle in generalized plasticity. Acta Mech. 1984;52 (3):225–37.
Lubliner J. Plasticity theory. NY: Macmillan Publishing Company; 1990.
Lubliner J, Auricchio F. Generalized plasticity and shape-memory alloys. Int J Solids Struct. 1996;33(7):991–1003.
Lubliner J, Taylor RL, Auricchio F. A new model of generalized plasticity and its numerical implementation. Int J Solids Struct. 1993;30(22):3171–84.
Machida N, Uehara K. Nonlinear thermal stress analysis of a massive concrete structure. Comput Struct. 1987;26(1–2):287–96.
Mahtab M, Goodman RE. Three dimensional analysis of joint rock slope. In: Proceedings of 2nd ISRM congress, vol. 3. Beograd: Privredni Pregled; 1970. p. 353–60.
Majorana CE, Zavarise G, Borsetto M, Giusepetti M. Nonlinear analyses of thermal stresses in mass concrete castings. Cem Concr Res. 1990;20(4):559–78.
Malan DF. Simulating the time-dependent behaviour of excavations in hard rock. Rock Mech Rock Eng. 2002;35(4):225–54.
Malvern LE. Introduction to the mechanics of a continuous medium. Englewood Cliffs: Prentice-Hall Inc; 1969.
Manzari MT, Nour MA. Significance of soil dilatancy in slope stability analysis. J Geotech Geoenviron Eng ASCE. 2000;123(1):75–80.
Maranini E, Brignoli M. Creep behaviour of a weak rock: experimental characterization. Int J Rock Mech Min Sci. 1999;36(1):127–38.
Masters I, Pao WKS, Lewis RW. Coupling temperature to a double-porosity model of deformable porous media. Int J Numer Anal Meth Geomech. 2000;49(3):421–38.
Matsumoto Y, Chung K, Yamada S. Experimental study on the hysteresis behavior of structural steel under multi-axial cyclic loading. J Struct Constr Eng. 2005;588:1881–8 (in Japanese).
Mehta PK, Monteiro PJM. Concrete: microstructure, properties, and materials, 3rd ed. New York: McGraw-Hill; 2006.
Michino MJ, Findley WN. An historical perspective of yield surface investigation for metals. Int J Non-linear Mech. 1976;11(1):59–82.

Mielke P, Bär K, Sass I. Determining the relationship of thermal conductivity and compressional wave velocity of common rock types as a basis for reservoir characterization. J Appl Geophys. 2017;140:135–44.
Min KB, Rutqvist J, Tsang CF, Jing LR. Stress–dependent permeability of fractured rock masses: a numerical study. Int J Rock Mech Min Sci. 2004;41(7):1191–210.
Miyoshi T. Foundations of the numerical analysis of plasticity. Lectures notes in numerical and applied analysis, vol. 7. Tokyo: Kynokunia Company Ltd; 1985.
Morland LW. Continuum model of regularly jointed mediums. J Geophys Res. 1974;79(2): 357–62.
Mott NF. A theory of work-hardening of metals. Part II: flow without slip-lines, recovery and creep. Phil Mag Ser 7. 1953;44(354):742–65.
Mukherjee S. Boundary elements in creep and fracture. London: Applied Science Publishers; 1982.
Müller L. Address to the opening session. In: Proceedings of 1st ISRM congress. Lisbon: LNEC; 1967. p. 80–3.
Müller L, editor. Rock mechanics. Wien: Springer; 1974.
Murakami S. Notion of continuum damage mechanics and its application to anisotropic creep damage theory. J Eng Mater Technol. 1983;105(2):99–105.
Murakami S. Mechanical modeling of material damage. J Appl Mech. 1988;55(2):280–6.
Mutschler TO, Fröhlich BO. Analytical calculation of the strength behaviour of interbedded rock mass. In: Herget G, Vongpaisal S, editors. Proceedings of 6th ISRM congress. Rotterdam: AA Balkema; 1987. p. 1167–71.
Nayak GC, Zienkiewicz OC. Convenient form of stress invariants for plasticity. J Struct Div ASCE. 1972;98(ST4):949–53.
Nemat-Nasser S, Obata M. A microcrack model of dilatancy in brittle materials. J Eng Mech ASCE. 1988;55(1):24–35.
Neville AM. Creep of concrete as a function of its cement paste content. Mag Concr Res. 1964;16 (46):21–30.
Neville AM, Diger WH, Brooks JJ. Creep of plain and structural concrete. London: Construction Press; 1983.
Nicholl MJ, Rajaram H, Glass RJ, Detwiler R. Saturated flow in a single fracture: evaluation of Reynolds equation in measured aperture fields. Water Resour Res. 1999;35(11):3361–73.
Nithiarasu P, Sujatha KS, Ravindran K, Sundararajan T, Seetharamu KN. Non-Darcy natural convection in a hydrodynamically and thermally anisotropic porous medium. Comput Methods Appl Mech Eng. 2000;188(1–3):413–30.
Noorishad J, Tsang CF. Coupled thermo-hydroelasticity phenomena in variably saturated fractured porous rocks—formulation and numerical solution. In: Stephansson O, Jing L, Tsang CF, editors. Coupled thermo-hydro-mechanical processes of fractured media. Rotterdam: Elsevier; 1996. p. 93–134.
Noorishad J, Tsang CF, Witherspoon PA. Theoretical and field studies of coupled hydromechanical behaviour of fractured rocks. 1: Development and verification of a numerical simulator. Int J Rock Mech Min Sci Geomech Abstr. 1992;29(4):401–9.
Nuezil CE, Tracy JV. Flow through fractures. Water Resour Res. 1981;17(2):191–9.
Oda M. Fabric tensor for discontinuous geological materials. Soils Found. 1982;22(4):96–108.
Oda M. A method for evaluating the effect of crack geometry on the mechanical behavior of cracked rock masses. Mech Mater. 1983;2(2):163–71.
Oda M. Similarity rule of crack geometry in statistically homogeneous rock masses. Mech Mater. 1984;3(2):119–29.
Oda M. An equivalent continuum model for coupled stress and fluid flow analysis in jointed rock masses. Water Resour Res. 1986a;22(13):1845–56.
Oda M. A stereological study on crack geometry of discontinuous rock masses. In: Ishizaka S, Kato Y, Takaki R, Toriwaki J, editors. Proceedings of 1st international symposium for science on form. Tokyo: KTK Scientific Publisher; 1986b. p. 183–9.

Oda M. A method for evaluating the representative elementary volume based on joint survey of rock masses. Can Geotech J. 1988;25(3):440–7.
Oda M, Suzuki K, Maeshibu T. Elastic compliance for rock-like materials with random cracks. Soils Found. 1984;24(3):27–40.
Oda M, Yamabe T, Ishizuka Y, Kumasaka H, Tada H, Kimura K. Elastic stress and strain in jointed rock masses by means of crack tensor analysis. Rock Mech Rock Eng. 1993;26(2):89–112.
Oda M, Katsube T, Takemura T. Microcrack evolution and brittle failure of Inada granite in triaxial compression tests at 140 MPa. J Geophy Res Solid Earth (1978–2012). 2002;107 (B10):ECV 9-1–17.
Oden JT. Finite elements of nonlinear continua. New York: McGraw-Hill; 1972.
Odqvist FKG. Mathematical theory of creep and creep rupture, 2nd ed. Oxford: Clarendon; 1974.
Öhman J, Niemi A. Upscaling of fracture hydraulics by means of an oriented correlated stochastic continuum model. Water Resour Res. 2003;39(10):1277.
Ohnaka M, Mogi K. Frequency characteristics of acoustic emission in rocks under uniaxial compression and its relation to the fracturing process to failure. J Geophys Res. 1982;87 (B5):3873–84.
Ohnishi Y, Tanaka M, Jing L. Hydro-mechanical response of a fractured granite rock mass to excavation of a test pit—the Kamaishi mine experiments in Japan. Int J Rock Mech Min Sci. 2001;38(1):79–94.
Ohno N, Wang JD. Kinematic hardening rules with critical states of dynamic recovery. Parts I and II. Int J Plast. 1993;9(3):375–403.
Ortiz M, Popov EP. Accuracy and stability of integration algorithms for elastoplastic constitutive relations. Int J Numer Meth Eng. 1985;21(9):1561–76.
Ortiz M, Leroy Y, Needleman A. A finite element method for localized failure analysis. Comput Meth Appl Mech Eng. 1987;61(2):189–214.
Owen DRJ, Hinton E. Finite elements in plasticity: theory and practice. Swansea: Pineridge Press Ltd; 1980.
Owen DRJ, Hinton E, Onate E. Computational plasticity: models, software and applications. Swansea: Pineridge Press Ltd; 1989.
Palmstrom A, Singh R. The deformation modulus of rock masses—comparisons between in situ tests and indirect estimates. Tunn Undergr Space Technol. 2001;16(2):115–31.
Pande GN, Gerrard CM. The behaviour of reinforced jointed rock masses under various simple loading states. In: Proceedings of 5th ISRM congress. Melbourne: Brown Prior Anderson Pty Ltd; 1983. p. F217–23.
Paul B. A modification of the Coulomb-Mohr theory of fracture. J Appl Mech. 1961;28(2):259–68.
Perzyna P. The constitutive equations for rate sensitive plastic materials. Q Appl Math. 1963;20 (4):321–32.
Pijaudier-Cabot G, Bažant ZP. Nonlocal damage theory. J Eng Mech Div ASCE. 1987;113 (10):1512–33.
Pisarenko GS, Lebedev AA. Deformation and strength of material under complex stressed state. Kiev: Naukova Dumka; 1976 (in Russian).
Pivonka P, Lackner R, Mang HA. Shapes of loading surfaces of concrete models and their influence on the peak load and failure mode in structural analyses. Int J Eng Sci. 2003;41 (13–14):1649–65.
Pramono E, Willam K. Implicit integration of composite yield surface with corners. Eng Comput. 1989;6(3):186–97.
Prandtl L, editor. Proceedings of 1st international congress for applied mechanics. Delft: IUTAM; 1924.
Prat PC, Bažant ZP. Tangential stiffness of elastic materials with systems of growing or closing cracks. J Mech Phys Solids. 1997;45(4):611–36.
Ramamurthy T. Strength and modulus responses of anisotropic rocks. In: Hudson JA, editor. Comprehensive rock engineering: fundamentals. Oxford: Pergamon Press; 1993. p. 313–29.
Rappaz M, Bellet M, Deville M. Numerical modeling in materials science and engineering. Berlin: Springer; 2003.

Raven KG, Gale JE. Water flow in a natural rock fracture as a function of stress and sample size. Int J Rock Mech Min Sci Geomech Abstr. 1985;22(4):251–61.

Reuss A. Berucksichtigung der elastichen, Formanderung in der Plastizitatstheorie. ZaMM. 1930;10:266 (in German).

Rhodes JA. Prediction of creep, shrinkage and temperature effects in concrete structures. ACI report 209R-92. Detroit: ACI Committee 209; 1992.

Rice JR. Inelastic constitutive relations for solids: an integral variable theory and its application to metal plasticity. J Mech Phys Solids. 1971;19(6):433–55.

Rice JR. Continuum mechanics and thermodynamics of plasticity in relation to microscale deformation mechanisms. In: Argon AS, editor. Constitutive equations in plasticity. Cambridge: MIT Press; 1975. p. 23–79.

Rice JR. Thermodynamics of quasi-static growth of Griffith cracks. J Mech Phys Solids. 1978;26 (2):61–78.

Robert A. Dielectric permittivity of concrete between 50 MHz and 1 GHz and GPR measurements for building materials evaluation. J Appl Geophys. 1998;40(1–3):89–94.

Rockafellar RT. Convex analysis. Princeton: Princeton University Press; 1969.

Ромм ЕС (Romm ES). Фильтрационные своиства трещиновтых горных пород (Flow characteristics of fractured rocks). Москва (Moscow): Издательство Недра (Nedra); 1966 (in Russian).

Romana MR. A geomechanical classification for slopes: slope mass rating. In: Hudson JA, editor. Comprehensive rock engineering. Oxford: Pergamon Press; 1993. p. 575–600.

Roy DM, Scheetz BE, Sabol S, Brown PW, Shi D, Licastro PH, Idom GM, Andersen PJ, Johanson V. Maturity model and curing technology. Washington DC: National Academy of Sciences; 1994.

Rudnicki JW, Rice JR. Conditions for the localization of deformation in pressure-sensitive dilatant materials. J Mech Phys Solids. 1975;23(6):371–94.

Runesson K, Sture S, Willam K. Integration in computational plasticity. Comput Struct. 1988;30 (1–2):119–30.

Rutqvist J, Borgesson L, Chijimatsu M, Kobayashi A, Jing L, Nguyen TS, Noorishad J, Tsang CF. Thermo-hydro-mechanics of partially saturated geological media: governing equations and formulation of four finite element models. Int J Rock Mech Min Sci. 2001a;38(1):105–27.

Rutqvist J, Borgsson L, Chijimatsu M, Nguyen TS, Jing L, Noorishad J, Tsang CF. Coupled thermo-hydro-mechanical analysis of a heater test in fractured rock and bentonite at Kamaishi mine—comparison of field results to predictions of four finite element codes. Int J Rock Mech Min Sci. 2001b;38(1):129–42.

Rutter EH. Kinetics of rock deformation by pressure solution. Philos Trans R Soc Lond. 1976; A283(1312):203–19.

Sakash A, Moondra S, Kinsey BL. Effect of yield criterion on numerical simulation results using a stress–based failure criterion. J Eng Mater Technol. 2006;128(3):436–44.

Salamon MDG. Elastic moduli of a stratified rock mass. Int J Rock Mech Min Sci. 1968;5(6): 519–27.

Samier P, Onaisi A, Fontaine G. Comparisons of uncoupled and various coupling techniques for practical field examples. SPE J. 2006;11(1):89–102.

Santurjian O, Kolarow L. A spatial FEM model of thermal stress state of concrete blocks with creep consideration. Comput Struct. 1996;58(3):563–74.

Scheunemann P. The influence of failure criteria on strength prediction of ceramic components. J Eur Ceram Soc. 2004;24(8):2181–6.

Scholtz CH. Mechanism of creep in brittle rock. J Geophys Res. 1968;73(10):3293–302.

Schrefler BA. Computer modelling in environmental geomechanics. Comput Struct. 2001;79 (22–25):2209–23.

Schubert W, Button EA, Sellner PJ, Solak T. Analyse zeitabhaengiger Verformungen im Tunnelbau (Analysis of time-dependent displacements of tunnels). Felsbau (Rock Soil Eng). 2003;21(5):96–103.

Sebsadji SK, Chouicha K. Determining periodic representative volumes of concrete mixtures based on the fractal analysis. Int J Solids Struct. 2012;49(21):2941–50.
Selvadurai APS, Nguyen TS. Scoping analyses of the coupled thermal-hydrological- mechanical behaviour of the rock mass around a nuclear fuel waste repository. Eng Geol. 1996;47(4): 379–400.
Selvadurai APS, Nguyen TS. Mechanics and fluid transport in a degradable discontinuity. Eng Geol. 1999;53(3–4):243–9.
Serafim JL. Influence of interstitial water on the behaviour of rock masses. In: Stagg KG, Zienkiewicz OC, editors. Rock mechanics in engineering practice. London: Wiley; 1968. p. 55–97.
Sercombe J, Hellmich CH, Ulm FJ, Mang HA. Modeling of early-age creep of shotcrete. I: model and model parameters. J Eng Mech ASCE. 2000;126(3):284–91.
Settari A, Mourits FM. Coupling of geomechanics and reservoir simulation models. In: Siriwardane HJ, Zeman MM, editors. Computer methods and advances in geomechanics. Rotterdam: AA Balkema; 1994. p. 2151–8.
Shen DJ, Shi X, Zhu SS, Duan XF, Zhang JY. Relationship between tensile Young's modulus and strength of fly ash high strength concrete at early age. Constr Build Mater. 2016;123:317–26.
Silva RV, de Brito J, Dhir RK. Establishing a relationship between modulus of elasticity and compressive strength of recycled aggregate concrete. J Clean Prod. 2016;112:2171–86.
Simo JC, Hughes TJR. Elastoplasticity and viscoplasticity—computational aspects. New York: Springer; 1988.
Simo JC, Hughes TJR. Computational inelasticity. NewYork: Springer; 1998.
Simo JC, Ju JW, Pister KS, Taylor RL. Assessment of cap model: consistency return algorithms and rate-dependent extension. J Eng Mech. 1988;114(2):191–218.
Singh B. Continuum characterization of jointed rock masses: Part I—the constitutive equations. Int J Rock Mech Min Sci Geomech Abstr. 1973;10(4):311–35.
Singhal BBS, Gupta RP. Applied hydrogeology of fractured rocks, 2nd ed. Dordrecht: Springer; 2010.
Skarzynski L, Tejchman J. Determination of representative volume element in concrete under tensile deformation. Comput Concr. 2012;9(1):35–50.
Sloan SW, Booker JR. Removal of singularities in Tresca and Mohr-Coulomb yield function. Comm Appl Num Meth. 1986;2(2):173–9.
Snow D. Anisotropic permeability of fractured media. Water Resour Res. 1969;5(6):1273–89.
Sonmez H, Gokceoglu C, Ulusay R. Indirect determination of the modulus of deformation of rock masses based on the GSI system. Int J Rock Mech Min Sci. 2004;41(5):849–57.
Stagg KG, Zienkiewicz OC, editors. Rock mechanics in engineering practice. NewYork: Wiley; 1986.
Stephansson O. The Nasliden Project–rock mass investigations. In: Stephansson O, Jones MJ, editors. Applications of rock mechanics to cut and fill mining. London: IMM; 1981. p. 145–61.
Sterpi D. An analysis of geotechnical problems involving strain softening effects. Int J Numer Anal Meth Geomech. 1999;23(13):1427–54.
Stratford RG, Herbert AW, Jackson CP. A parameter study of the influence of aperture variation on fracture flow and the consequences in a fracture network. In: Barton NR, Stephansson O, editors. Rock joints. Rotterdam: AA Balkema; 1990. p. 413–22.
Stroeven P, Stroeven M. Size of representative volume element of concrete assessed by quantitative image analysis and computer simulation. Image Anal Stereol. 2001;20(Suppl. 1):216–20.
Stroeven M, Askes H, Sluys LJ. Numerical determination of representative volumes for granular materials. Comput Meth Appl Mech Eng. 2004;193(30–32):3221–38.
Sutcliffe DJ, Yu HS, Page AW. Lower bound limit analysis of unreinforced masonry shear walls. Comput Struct. 2001;79(14):1295–312.
Swaddiwudhipong S, Lu HR, Wee TH. Direct tension test and tensile strain capacity of concrete at early age. Cem Concr Res. 2003;33(12):2077–84.
Swoboda G, Yang Q. An energy-based damage model of geomaterials. I: formulation and numerical results. Int J Solids Struct. 1999a;36(4):1719–34.

Swoboda G, Yang Q. An energy-based damage model of geomaterials. II: deduction of damage evolution laws. Int J Solids Struct. 1999b;36(4):1735–55.
Taliercio A, Landriani GS. A failure condition for layered rock. Int J Rock Mech Min Sci Geomech Abstr. 1988;25(5):299–305.
Tappennier P, Brace WF. Development of stress–induced microcracks in Westerly granite. Int J Rock Mech Min Sci. 1976;13(4):103–12.
Tazawa E, Miyazawa S. Experimental study on mechanism of autogenous of concrete. Cem Concr Res. 1995;25(8):1633–8.
Thomas HR, Cleall PJ. Inclusion of expansive clay behaviour in coupled thermo hydraulic mechanical models. Eng Geol. 1999;54(1–2):93–108.
Thomas HR, Missoum H. Three-dimensional coupled heat, moisture and air transfer in a deformable unsaturated soil. Int J Numer Meth Eng. 1999;44(7):919–43.
Thomas HR, Yang HT, He Y. A sub-structure based parallel solution of coupled thermo-hydro-mechanical modeling of unsaturated soil. Eng Comput. 1999;16(4):428–42.
Tien YM, Kuo MC. A failure criterion for transversely isotropic rocks. Int J Rock Mech Min Sci. 2001;38(3):399–412.
Tien YM, Kuo MC, Juang CH. An experimental investigation of the failure mechanism of simulated transversely isotropic rocks. Int J Rock Mech Min Sci. 2006;43(8):1163–81.
Timoshenko SP. History of strength of materials. New York: McGraw-Hill Book Company Inc; 1953.
Triantafyllidis T, Gerolymatou E. Estimation of the strength of stratified rock mass. Rock Mech Rock Eng. 2014;47(2):535–47.
Troxell GE, Raphael JM, Davis RE. Long-time creep and shrinkage tests of plain and reinforced concrete. Proc ASTM. 1958;58:1101–20.
Tsang CF, editor. Coupled processes associated with nuclear waste repositories. New York: Academic Press; 1987.
Tsang CF. Coupled thermomechanical and hydrochemical processes in rock fractures. Rev Geophys. 1991;29(4):537–48.
Tsang YW, Witherspoon PA. Hydromechanical behavior of a deformable rock fracture subject to normal stress. J Geophys Res. 1981;86(B10):9287–98.
Ulm FJ, Coussy O. Modeling of thermochemomechanical couplings of concrete at early ages. J Eng Mech ASCE. 1995;121(7):785–94.
Ulm FJ, Coussy O, Hellmich CH. Chemoplasticity: a review of evidence. In: de Borst R, Bićanić N, Mang R, Meschke G, editors. Computational modeling of concrete structures, Proceedings of EUROCK 1998. Rotterdam: AA Balkema; 1998. p. 421–40.
Ulusay R, editor. The ISRM suggested methods for rock characterization, testing and monitoring: 2007–2014. Cham: Springer; 2015.
Ulusay R, Hudson JA, editors. The complete ISRM suggested methods for rock characterization, testing and monitoring: 1974–2006. Ankara: ISRM Turkish National Group; 2007.
Valanis KC. A theory of viscoplasticity without a yield surface. Archiwum Mechaniki Stossowanej. 1971;23(4):517–51.
Valanis KC. Fundamental consequences of a new intrinsic time measure. Plasticity as a limit of the endochronic theory. Archiwum Mechaniki Stossowanej. 1980;32(2):171–91.
Valanis KC, Wu HC. Endochronic representation of cyclic creep and relaxation of metals. J Appl Mech ASME. 1975;42(1):67–73.
Van Mier JGM, Van Vliet MRA. Influence of microstructure of concrete on size/scale effects in tensile fracture. Eng Fract Mech. 2003;70(16):2281–306.
Van Vliet MRA, Van Mier JGM. Experimental investigation of size effect in concrete and sandstone under uniaxial tension. Eng Fract Mech. 2000;65(2.3):165–188.
Vermeer JPA, de Borst R. Non-associated plasticity for soils, concrete and rock. HERON. 1984;29 (3):3–64.
Videla CC, et al. Guide for modeling and calculating shrinkage and creep in hardened concrete. ACI report 209.2R-08. Farmington Hills: ACI Committee 209; 2008.

Von Mises R. Mechanik der Festen Korper im plastisch deformablen Zustand. Göttin Nachr Math Phys. 1913;1:582–92 (in German).
Walsh JB. Effect of pore pressure and confining pressure on fracture permeability. Int J Rock Mech Min Sci Geomech Abstr. 1981;18(5):429–35.
Wang L, Lee TC. The effect of yield criteria on forming limit curve prediction and deep drawing process simulation. Int J Mach Tools Manuf. 2006;46(9):988–95.
Wang XC, Schrefler BA. A multi-frontal parallel algorithm for coupled thermo-hydro-mechanical analysis of deformable porous media. Int J Numer Meth Eng. 1998;43(6):1069–83.
Wardle LJ, Gerrard CM. The "equivalent" anisotropic properties of layered rock and soil masses. Rock Mech Rock Eng. 1972;4(3):155–75.
Watanabe O, Atluri SN. Internal time, general internal variable, and multi-yield-surface theories of plasticity and creep: a unification of concepts. Int J Plast. 1986;2(1):37–57.
Wei ZQ, Hudson JA. The influence of joints on rock modulus. In: Tan ZY, editor. Proceedings of the international symposium on engineering in complex formations. Beijing: Science Press; 1986. p. 54–62.
Wei ZQ, Egger P, Descoeuders F. Permeability prediction for jointed rock masses. Int J Rock Mech Min Sci Geomech Abstr. 1995;32(3):251–61.
Willam KJ, Warnke EP. Constitutive models for the triaxial behavior of concrete. Proceedings of International Association for Bridge and Structural Engineering. Report 19, Section III. Bergamo: ISMES; 1975. p. 1–30.
Wilson CR, Witherspoon PA. An investigation of laminar flow in fractured porous rocks. Berkeley: University of California; 1970.
Witherspoon PA, Wang JSY, Iwai K, Gale JE. Validity of cubic law for fluid flow in a deformable rock fracture. Water Resour Res. 1980;16(6):1016–24.
Wittmann FH. Creep and shrinkage mechanisms. In: Bažant ZP, Wittmann FH, editors. Creep and shrinkage of concrete structures. London: Wiley; 1982. p. 129–61.
Wu AQ, Zhou HM. Rock mechanics. In: Liu ZM, Wang DX, Wang DG, editors. Handbook of hydraulic structure design, vol. 1. Fundamental theories (Chapter 5). Beijing: China Water Power Press; 2013 (in Chinese).
Xiong WL. Symmetric formulation of tangential stiffnesses for non-associated visco-plasticity with an implicit time integration scheme. Appl Math Mech. 1993;14(3):251–7 (in Chinese).
Xu T, Tang CA, Zhao J, Li L, Heap MJ. Modelling the time-dependent rheological behaviour of heterogeneous brittle rocks. Geophys J Int. 2012;189(3):1781–96.
Xu Y, Xu Q, Chen SH, Li XX. Self-restraint thermal stress in early-age concrete samples and its evaluation. Constr Build Mater. 2017;134:104–15.
Yamada S, Imaeda T, Okada K. Simple hysteresis model of structural steel considering the Bauschinger effect. J Struct Constr Eng Arch Inst Jpn. 2002;67(559):225–32 (in Japanese).
Yi D, Chen SH. Effect of the earth surface denudation on the initial stress back analysis of rock masses. Rock Soil Mech. 2003;24(2):254–6 (in Chinese).
Yi D, Xu MY, Chen SH. Application of genetic algorithms to back analysis of initial stress field of rock masses. Chin J Rock Mech Eng. 2001;20(Supp.2):1618–22 (in Chinese).
Yoshinaka R, Yamabe T. Jointed stiffness and the deformation behavior of discontinuous rock. Int J Rock Mech Min Sci Geomech Abstr. 1986;23(1):295–303.
Young JF, Mindness S, Gray RJ, Bentur A. The science and technology of civil engineering materials. NJ: Prentice Hall; 1998.
Yu MH. Advances in strength theories for materials under complex stress state in the 20th century. Appl Mech Rev ASME. 2002;55(3):169–218.
Yu MH, Li JC. Computational plasticity with emphasis on the application of the unified strength theory. Hangzhou: Zhejiang University Press; 2012.
Zhang JL, Chen SH. Study of time-stepping adaptivity in FEM analysis of time-dependent problems. J Wuhan Univ Hydraul Electr Eng (WUHEE). 1996;29(1):79–84 (in Chinese).
Zhang JL, Chen SH. An implicit scheme algorithm of elastic-viscoplastic FEM with time-stepping adaptive for bolted jointed rock masses. J Hydraul Eng. 1997;19(Supplement):168–75 (in Chinese).

Zhang C, Rothfuchs T. Experimental study of the hydro-mechanical behaviour of the Callovo-Oxfordian argillite. Appl Clay Sci. 2004;26(1–4):325–36.
Zhang X, Sanderson DJ, Harkness RM, Last NC. Evaluation of the 2D permeability tensor for fractured rock masses. Int J Rock Mech Min Sci Geomech Abstr. 1996;33(1):17–37.
Zhou C, Huang B, Shu X. Micromechanical model for predicting coefficient of thermal expansion of concrete. J Mater Civ Eng. 2013;25(9):1171–80.
Zhu BF. Computation of thermal stresses in mass concrete with consideration of creep effect. In: Proceedings of XV ICOLD congress (Lausanne). Paris: ICOLD; 1985a.
Zhu BF. The elastic modulus, creep compliance and stress relaxation coefficient of concrete. J Hydraul Eng. 1985b;15(9):54–61 (in Chinese).
Zhu BF. On the formula for modulus of elasticity of concrete. J Hydraul Eng. 1996;26(3):89–90 (in Chinese).
Zienkiewicz OC, editor. Rock mechanics in engineering practice. New York: Wiley; 1968.
Zienkiewicz OC, Cormeau IC. Viscoplasticity solution by finite element process. Arch Mech. 1972;24(5–6):873–88.
Zienkiewicz OC, Cormeau IC. Visco-plasticity and plasticity—an alternative for finite element solution of material nonlinearities. Computing methods in applied sciences and engineering (Part 1). Berlin: Springer; 1974. p. 259–87.
Zienkiewicz OC, Mróz Z. Generalized plasticity formulation and applications to geomechanics. In: Desai CS, Gallagher RH, editors. Mechanics of engineering materials. New York: Wiley; 1984. p. 655–79.
Zienkiewicz OC, Pande GN. Some useful forms of isotropic yield surfaces for soil and rock mechanics. In: Gudehus G, editor. Finite element in geomechanics. New York: Wiley; 1977a. p. 179–90.
Zienkiewicz OC, Pande GN. Time-dependent multilaminate model of rocks—a numerical study of deformation and failure of rock masses. Int J Numer Anal Meth Geomech. 1977b;1(3):219–47.
Zienkiewicz OC, Valliappan S, King IP. Elasto-plastic solutions of engineering problems “initial stress”, finite element approach. Int J Numer Meth Eng. 1969;1(1):75–100.
Zienkiewicz OC, Huang M, Pastor M. Localization problems in plasticity using finite element with adaptive remeshing. Int J Numer Anal Mech Geomech. 1995;19(2):127–48.
Zimmerman RW. Coupling in poroelasticity and thermoelasticity. Int J Rock Mech Min Sci. 2000;37(1):79–87.

Chapter 3
Geometrical Description and Discretization of Hydraulic Structures

Abstract Pre-processing towards the geometrical description and discretization is one of the prerequisites for the structural analysis using computational mechanics. Despite of tedious and time-consuming overheads, it must be handled carefully to obtain reasonable accuracy for the performance prediction of hydraulic structure. In this chapter, a robust identification algorithm of irregular block system is implemented with the help of the "directed body" concept and by taking into account of the existence of irregular ground surfaces (curved faults and dam surfaces as well) and grouting/drainage curtains. Use is made of the advancing front technique (AFT), a sophisticated element (triangular, quadrilateral, tetrahedral) discretization algorithm is further implemented for a structure domain identified previously or constructed by the technique with CAD/CAM software. These may be competently employed for the discrete approaches (e.g. BEA) and continuum approaches (e.g. FEM, CEM) elaborated in the hereinafter chapters towards hydraulic structures with complex discontinuity system and configuration.

3.1 General

3.1.1 Concept

In engineering practice, a numerical computation is commonly accomplished by three principal steps including pre-processing, structural response analysis, and post-processing. In this respect, the pre-processing towards the geometrical description and discretization is one of the prerequisites for the analysis of hydraulic structures. If a computation program has not been equipped with well performed pre-processing procedure and corresponding software, it will be difficult to be widely accepted by the practitioners.

The computation for a hydraulic structure using discrete approaches such as the distinct element method (DEM), the discontinuous deformation analysis (DDA), or the block element analysis (BEA) demands an identified discrete block system

S.-H. Chen, *Computational Geomechanics and Hydraulic Structures*,
Springer Tracts in Civil Engineering, https://doi.org/10.1007/978-981-10-8135-4_3

intersected by structural planes and the correspondent database concerning its geometry configuration.

Figure 3.1 shows the axonometric drawing of an integrated block system, and Fig. 3.2 shows the axonometric drawing of the corresponding decomposed blocks. Due to complicatedly distributed discontinuities, there are a variety of convex and concave blocks in the block system.

Where a continuum approach such as the finite element method (FEM) is exercised, the user should construct a FE mesh in which the whole structure domain is divided into a number of discrete sub-domains, namely "elements", connected at

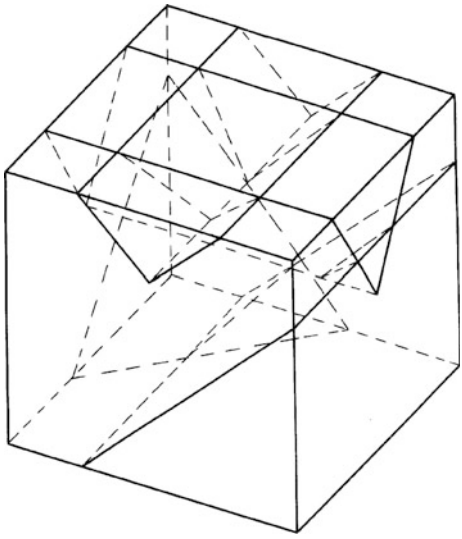

Fig. 3.1 Axonometric drawing of an integrated block system

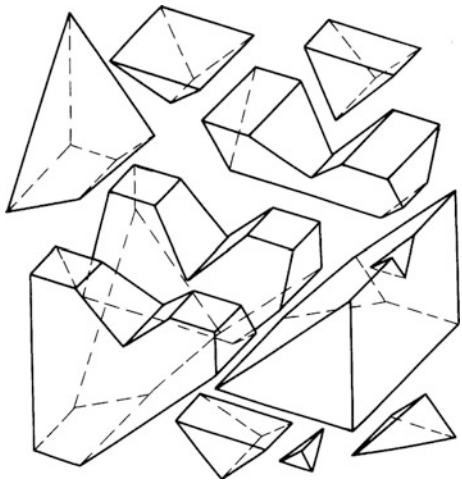

Fig. 3.2 Axonometric drawing of the decomposed blocks

discrete points called "nodes". Certain of these nodes will have fixed displacements, and others will have prescribed loads (Zienkiewicz et al. 2005). Use also may be made of the block system previously identified, to further produce standard solid elements from blocks and joint elements from structural planes (discontinuity segments). Figure 3.3 shows the discrete FE mesh for a gravity dam and its foundation.

The simplest type of two-dimensional solid elements is triangular. There are a variety types of three-dimensional solid elements (see Fig. 3.4; Table 3.1), of which the simplest one is tetrahedral. Usually, the curved-edge elements are more adaptive to the structure configuration and possess higher precision, but they need higher capacity and more efforts for computation.

In the analysis of shell structures such as thin arch dams and tunnel linings, shell elements are also available (see Fig. 3.5; Table 3.2).

Towards the simulation of structural planes such as faults and joints in rock masses, contact interfaces between concrete and rocks, cracks and joints in concrete dams, "joint elements" without thickness or with certain thickness are widely exercised. On such a joint element shown in Fig. 3.6, a local Cartesian coordinate system $(x_j y_j z_j)$ is defined (see also Fig. 2.2).

3.1.2 State of the Art

Discretization of a hydraulic structure with complex geometry into block system or even further to finite element system (mesh) may be one of the most tedious and time-consuming overheads. It must be handled carefully to obtain reasonable accuracy for its performance predictions.

(1) Block element system discretization

The study to develop a sophisticated description of sub-domains (e.g. rock blocks) began from the mid 1980s. Lin et al. (1987), Cundall (1988), Jing and Stephansson (1994) introduced geometrical identification algorithms for rock block system using

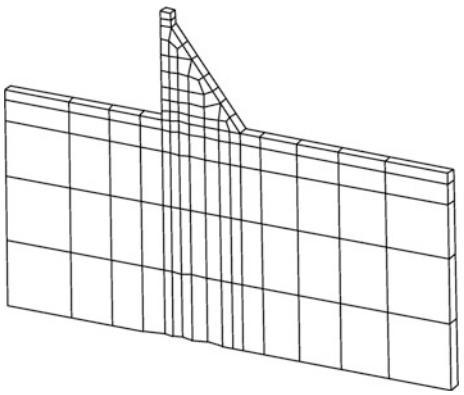

Fig. 3.3 Finite element mesh of a gravity dam

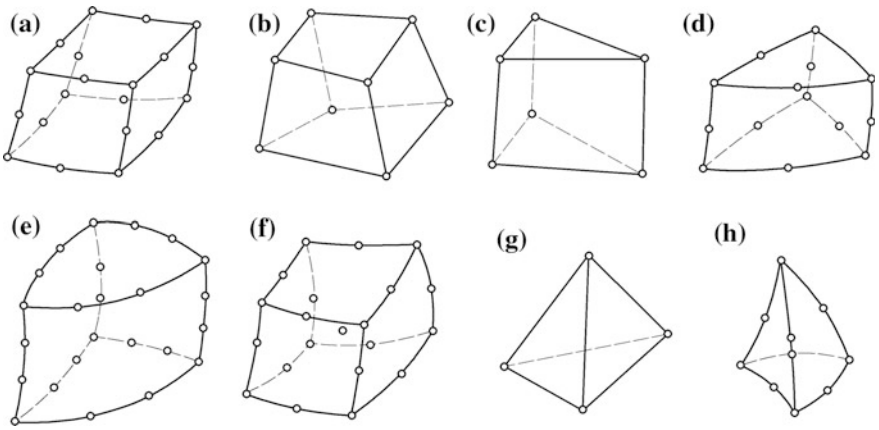

Fig. 3.4 Three-dimensional solid elements

Table 3.1 Three-dimensional solid elements

Type of element				Number of node	Freedom of element	Node number of edge	Remark
Three-dimensional isoparametric	Hexahedral	Quadratic curved edges		20	60	1	Figure 3.4a
		Straight edges		8	24	0	Figure 3.4b
		Variable nodes		8–21	24–63	0–1	Figure 3.4f
	Pentahedral	Straight edges		6	18	0	Figure 3.4c
		Curved edges	Quadratic	15	45	1	Figure 3.4d
			Cubic	24	72	2	Figure 3.4e
Tetrahedral	Straight edges			4	12	0	Figure 3.4g
	Curved edges			10	30	1	Figure 3.4h

topological techniques. Their methods are rather sophisticated, but unlikely to identify a system including concave blocks at that time. Heliot (1988) proposed a new approach to produce more realistic rock block system, in which a rock block is always decomposed into two convex blocks. In 1992, Ikegawa and Hudson made a breakthrough by the "directed body" concept to cope with both convex and concave blocks in the same identification procedure. After a check on the various existing methods, the author of this book realized that the directed body concept could be a solid base to establish a robust identification and pre-processing algorithm for the analysis of seepage, deformation and stability of complicated block system. During the implementation of the method, further improvements taking into account of the existence of irregular ground surfaces (curved faults and dam surfaces as well), the existence of the grouting and drainage curtains, etc., were made (Wang and Chen 1998). These enable us to carry out the pre-processing work more easily and more

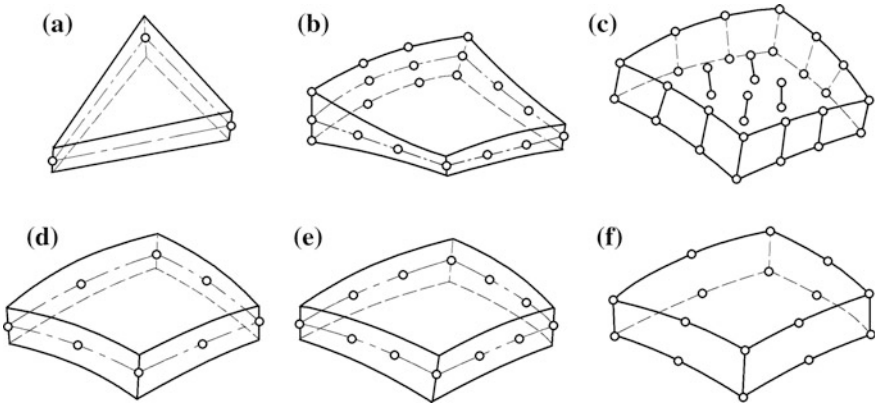

Fig. 3.5 Shell elements

Table 3.2 Shell elements

Type of element		Number of node	Freedom of element	Node number of edge	Remark
Thin shell		3	18	0	Figure 3.5a
Variable nodes	Thin shell	3–16	9–48	0–2	Figure 3.5b
	Thick shell	8–32	24–96	0–2	Figure 3.5c
Quadratic surface thick shell		8	40	1	Figure 3.5d
Cubic surface thick shell		12	60	2	Figure 3.5e
Isoparametric thick shell		16	48	1	Figure 3.5f

reliably. Our procedure on one hand, may be directly employed for the discrete approaches such as the BEA elaborated later in this book, on the other hand it may offer a well organized database for the further FE mesh generation, by discretizing each sub-domain (block) into a group of standard elements correctly connected. In the latter case, in addition to natural discontinuities and interfaces, artificial structural planes also may be supplementarily introduced to facilitate the FE mesh discretization by transforming a complex domain into a set of simplex blocks.

(2) Finite element system discretization

There are two groups of algorithms for the finite element mesh discretization, namely the structured meshing and unstructured meshing (Babuška et al. 1995). A structured mesh can be recognized by all its interior nodes possessing an equal number of adjacent elements. The mesh by a structured grid generator is typically

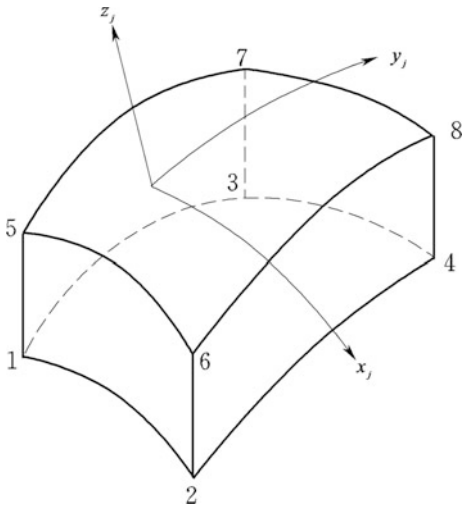

Fig. 3.6 Joint elements for structural planes/interfaces

all quad or hexahedral. Algorithms employed generally involve complex iterative smoothing techniques that attempt to align elements with boundaries or physical domains. Where non-trivial boundaries are required, "block structured" techniques can be employed which allow the user to break the domain up into topological blocks (sub-domains) by for example, the aforementioned block element system discretization. Structured grid generators are most commonly used within the CFD field, where strict alignment of elements is often required by the analysis code or necessary to capture physical phenomenon. Unstructured grid generator, on the other hand, relaxes the node valence requirement, allowing any number of elements to meet at a single node. Triangle and tetrahedral meshes are most commonly thought of when referring to unstructured meshing, although quadrilateral and hexahedral meshes can be unstructured, too (Owen 1998). Unstructured grid generators are more advantageous in the adaptive-refinement towards the FEM in structural computations, where strong concentration of stress/head gradient/temperature gradient demands rapid spatial variation in element sizes.

Initiated from the early 1970s when Buell and Bush (1973) used the computer for FE mesh discretization, after the intensive study of decades, various and sophisticated methods for two-dimensional domains had been available (Thacker 1980; Ho 1988), using either triangular or quadrilateral element meshes (Hermann 1976; Blacker et al. 1988). Algorithms for the generation of quadrilateral meshes can be either "direct" or "indirect". The indirect algorithm (Zhu et al. 1991; Owen et al. 1999; Merhof et al. 2007; De Berg et al. 2008) converts pre-generated triangular elements into quadrilateral ones by means of splitting or merging techniques). "Splitting" presumes inserting an additional node inside the triangle, splitting it into three triangles further being combined by pairs into quadrilaterals.

Techniques based on splitting may result in a poor mesh quality blamed on a large number of irregularly and badly positioned nodes. When the direct algorithm is used, quadrilateral elements are constructed and placed directly into the domain.

No sooner the success had been achieved in the two-dimensional FE mesh generation than the three-dimensional mesh discretization started to boom following the industry advance in CAD/CAM and three-D print. Of which advancing front technique (AFT) and Delaunay triangulation algorithm (DTA), are dominant in generating tetrahedral meshes. Since the AFT is able to control the stretching direction of elements well, it is prevalent in the general fields of fluid dynamics and the special fields of solid mechanics (e.g. localization) (Löhner 1988; Peraire et al. 1992; Moller and Hansbo 1995). The author of this book also had been involved in the application of the AFT to the FE mesh generation for hydraulic structures (Chen et al. 1996, 2000; Cao et al. 1998).

Hexahedral element meshes have been proved to be superior to tetrahedral ones in terms of higher computation accuracy. However, the rather structured feature of bricks (hexahedra) or prisms (pentahedra) leads to their exclusion from an adaptive meshing system of general purpose. The tetrahedral meshes, on the other hand, offer much greater flexibility.

1. Coordinate mapping method

This is one of the earliest and most classical direct methods (Zienkiewicz and Phillips 1971). It is based on the decomposition of a complex domain into simpler sub-domains which can be mapped on to the domains of simple geometry in a parametric space (Joe 1995). The most serious drawback with the mapping approach is that it can only be applied to a limited variety of geometry configurations and certain expertise is demanded for an appropriate decomposition of the primary domain.

2. Octree method

Spatial decomposition methods based on octree structures were originally proposed as approximate representations of geometric objects (Yerry and Shepard 1984). The basic concept of octree representation consists of placing the object of interest in a parallelepiped, typically a cuboid, which totally encloses the object. This parallelepiped is then subdivided into its eight octants which are then recursively sub-divided a number of times based on criteria defined by the application. The number of levels of sub-division typically varies throughout the domain. For example, when octrees are used to approximate a geometric object, octants either fully inside or outside the object are not sub-divided further, while those octants which contain a portion of the object's boundary continue to be subdivided to the finest level.

The mesh generation process is implemented by two steps, the first is the construction of octree and the second is the FE mesh generated within the octree.

3. Delauney triangulation method

The Delaunay triangulation is a geometric construction of long history (Sloan and Houlsby 1984). An efficient method for generating the Delaunay triangulation of a set of points was proposed by Watson, known as Watson's algorithm (1981).

The major difficulty in the Delaunay triangulation is to develop the points automatically within and on the boundary of a domain (Baker 1987). These points must be such generated as to avoid numerical difficulties, while producing a valid computational mesh compatible with the geometric representation of the object. Further requirements of controlling mesh density and associating the various sub-domains of the mesh, also pose difficulties.

4. Hybrid octree/Delauney method

Schroeder and Shephard (1990) proposed a hybrid octree/Delaunay approach for three-dimensional mesh generation. The basic motivation is to build an octree procedure for octant geometries that can then be tetrahedronized using Delaunay algorithm. This hybrid approach keeps the spatial addressability, localized mesh control, linear growth rate and geometric simplification features of the octree technique, meanwhile simultaneously takes the advantages of simple and optimal properties with the Delaunay triangulation. The major difficulty lies in maintaining the compatibility between octants because they are individually triangulated.

5. Paving method

The "paving method" (PM) is an alternative direct method to construct quadrilateral mesh (Blacker and Stephenson 1991), in which elements are propagated from the boundary to the interior of a physical domain. It demonstrates certain advantages over less straightforward methods and is actually preferred in many grid generators. Further studies on the paving method have been aimed at improving its robustness (White and Kinney 1997), functionality (Cass et al. 1996; Staten et al. 2005), computation efficiency (Lober et al. 1997), and mesh quality (Kinney 1997; Anderson 2009). For example, White and Kinney (1997) managed to enhance the robustness of the original algorithm by means of paving on the element-by-element basis instead of doing it row-by-row, this modification is claimed to be more immune to meshing process failures resulting in poor quality elements. Cass et al. (1996) extended the paving algorithm to arbitrary three-dimensional trimmed surfaces. To improve the quality of quadrilateral meshes, Kinney (1997) proposed a set of empirical clean-up routines to handle the connectivity, boundary, shape and size of elements.

6. Advancing front method

The "advancing front technique" (AFT) has been successful in generating unstructured meshes in both two-and three-dimensional cases (Lo 1985; Peraire et al. 1987; Löhner 1988; Löhner and Parikh 1988; Jin and Wiberg 1990; Jin and Tanner 1993).

The AFT creates new element together with the creation of new node, in this process the messages (e.g. the sizes and the stretching directions of the element) demanded for creating new node are stored in the background mesh. Setup of directed line segments (two-dimensional) or triangular surface patches (three-dimensional) on the domain boundary yields the initial front. After the finding of generation parameters (element size, element stretching direction) for the active front from the background mesh, the new element, point and faces are added to their respective lists, meanwhile the known line segment (or face patch) from the front is deleted, in this way the active front is updated. If there are any lines (or faces) left in the front, go to the beginning of the routine and recur the procedure until the front is empty.

7. Parallel mesh generation

Computational geomechanics sometimes require several meshes for different mechanical and physical fields of the structure. Parallel grid generator starting from a coarse volume mesh is a good strategy because it enables robust domain decomposition. In addition, the communication efforts can be minimized between processors because all the sub-domains can be easily defined beforehand and the mesh is generated on each sub-domain in parallel guided by the specific requirements for the mesh size and stretching direction.

The parallel mesh generation can be initiated from a surface mesh or a volume mesh. Löhner (2001) presented a "parallel advancing front technique" (PAFT) for distributed-memory machines. It sub-divides each sub-mesh into an interior region and interface regions. Each processor reads in a sub-mesh and refines the interior region independently. Once all the interior regions are refined, the processors refine the interface regions and, finally, the corners. An octree is employed in order to decompose the continuous geometry and to maximize code re-use for parallelizing the AFT on shared-memory computers. The PAFT is not efficient on large-scale distributed-memory parallel platforms blamed on the global synchronization at the beginning of each phase and the data movement for gathering (into a single node)/scattering (back to all nodes) the global octree before and after its sequential refinement and re-partition.

De Cougny and Shephard (1999) proposed a "parallel octree advancing front technique" (POAFT). It firstly generates a distributed coarse-grain octree using a "divide-and-conquer algorithm". The terminal octants and the geometric model of a domain define the sub-domains. The terminal octants are distinguished as interior, interface, boundary, and complete. Interface octants have at least one adjacent octant which is not local. Boundary octants include mesh entities from the input surface mesh while complete octants contain no front-faces. Before the boundary octants are refined and meshed, sometimes a re-partitioning is necessary. The meshing of boundary octants is one of the most challenging tasks. Every processor applies a tree-based face removal procedure in order to connect the input surface mesh with the volume mesh of the interior octants. In the POAFT, the sub-domain

limits or internal boundaries (i.e. interfaces between sub-domains) are specified beforehand so that no extra communication is required during the mesh generation in parallel.

Meshes automatically generated can contain strongly distorted poor elements, which cause numerical difficulties during the FE solution process. Therefore, the improvement procedure is indispensable to get a qualified finite element mesh (Dari and Buscaglia 1994; Zavattieri et al. 1996).

Commercial codes vie with one another to have the most user-friendly graphical "pre-processor". Some of these pre-processors can overlay a mesh on a pre-existing CAD file, so that the finite element analysis can be done conveniently as a part of the computerized drafting-and-design process.

3.2 Fitting of Curved Lines and Surfaces

The simplest curve is straight line and the simplest surface is plane. Next to lines and planes, there are conics and quadrics. Quadric surfaces, or quadrics for short, consist of ellipsoids, hyperboloids of one sheet, hyperboloids of two sheets, elliptic paraboloids, and hyperboloid paraboloids. Particular, two existing types of rank three quadrics-cones and cylinders, are the most useful. Cylinders fall into three sub-types of elliptic, hyperbolic and parabolic.

These 2000-plus years old conics and quadrics have been widely applied in the body configuration of hydraulic structures (arch dams, tunnels, for example) and are the familiar geometry objects in the FE mesh generation. However, sometimes we will be encountered with higher order curved lines and surfaces (e.g. arch dams) or even irregular surfaces (e.g. ground surfaces or large faults). They all demand appropriate geometry interpretation and discrete treatment in the FE mesh generation.

3.2.1 Curve Fitting

Curve fitting is the process of constructing a curve, or mathematical function that has the best fit to a series of spatial data points, possibly subject to constraints. Curve fitting involves either interpolation where an exact fit to the data is required, or smoothing where a "smooth" function is constructed that approximately fits the data. The customarily exercised curve fitting is to arrange representative points in sequence, afterwards the truncated polynomial interpolation is employed to undertake the fitting. For example, a third order polynomial may be used to fit the "Ferguson curve segment" by

$$r(v) = \begin{bmatrix} 1 & v & v^2 & v^3 \end{bmatrix} [C] \begin{Bmatrix} r^{(1)} \\ r^{(2)} \\ t^{(1)} \\ t^{(2)} \end{Bmatrix} \quad (0 \le v \le 1) \tag{3.1}$$

In which $r^{(1)}$ and $r^{(2)}$ = coordinates of the start and finish points, respectively; $t^{(1)}$ and $t^{(2)}$ = tangent vectors at the start and finish points, respectively.

According to the continuity requirement of C^1, the constant matrix $[C]$ is

$$[C] = \begin{bmatrix} 1 & 0 & 0 & 0 \\ 0 & 0 & 1 & 0 \\ -3 & 3 & -2 & -1 \\ 2 & -2 & 1 & 1 \end{bmatrix} \tag{3.2}$$

The cubic spline constructed below is a better alternative to analytically represent a curve, which demands less computational efforts and possesses higher numerical stability (Prenter 1975).

① Establishment of parameters

For $n+1 \quad (n > 3)$ vortices P_i $(i = 0, 1, \ldots, n)$, denote the ith chord length as $l_i = [P_i \quad P_{i-1}]$, where $t_i = \sum_{j=1}^{i} l_j$ and $t_0 = 0$.

② Establishment of m continuity equation by the "Hermite interpolation" in the interval $[t_{i-1}, t_i]$

$$\begin{cases} P(t) = P_{i-1}\dfrac{(t_i - t)^2[2(t - t_{i-1}) + l_i]}{l_i^3} + P_i\dfrac{(t - t_{i-1})^2[2(t_i - t) + l_i]}{l_i^3} \\ \qquad + m_{i-1}\dfrac{(t_i - t)^2(t - t_{i-1})}{l_i^2} + m_i\dfrac{(t - t_{i-1})^2(t - t_i)}{l_i^2} \\ P'(t) = 6\dfrac{P_i - P_{i-1}}{l_i^3}(t_i - t)(t_i - t_{i-1}) + m_{i-1}\dfrac{(t_i - t)(2t_{i-1} + t_i - 3t)}{l_i^2} \\ \qquad + m_i\dfrac{(t - t_{i-1})(2t_i + t_{i-1} - 3t)}{l_i^2} \\ P''(t) = 6\dfrac{P_i - P_{i-1}}{l_i^3}(t_i - t_{i-1} - 2t) + 2m_{i-1}\dfrac{3t - 2t_i - t_{i-1}}{l_i^2} + 2m_i\dfrac{3t - t_i - 2t_{i-1}}{l_i^2} \end{cases} \tag{3.3}$$

$P''(t)$ defined at t_i possesses an utmost left limit at the section i and an utmost right limit at the section $i+1$, i.e.

$$\begin{cases} P''(t_i-0)=\frac{2m_{i-1}}{l_i}+\frac{4m_i}{l_i}-6\frac{P_i-P_{i-1}}{l_i^2} \\ P''(t_i+0)=6\frac{P_{i+1}-P_i}{l_{i+1}^2}-\frac{2m_{i+1}}{l_{i+1}}-\frac{4m_i}{l_{i+1}} \end{cases} \tag{3.4}$$

In view of $P''(t_i-0)=P''(t_i+0)$, we have

$$\begin{cases} \mu_i m_{i-1}+2m_i+\lambda_i m_{i+1}=C_i, \\ C_i=3\left(\mu_i\frac{P_i-P_{i-1}}{l_i}+\lambda_i\frac{P_{i+1}-P_i}{l_{i+1}}\right) \\ \mu_i=\frac{l_{i+1}}{l_i+l_{i+1}} \\ \lambda_i=\frac{l_i}{l_i+l_{i+1}} \end{cases} \quad (i=1,2,\ldots,n-1) \tag{3.5}$$

③ Construction of boundary conditions m_0 and m_n

There are $n+1$ unknown variables in Eq. (3.5) comprising $n-1$ equations, therefore two boundary conditions m_0 and m_n need be constructed for the solution of these variables uniquely. With the help of third-order "Bezier curve" we have

$$\begin{cases} R_1(t)=P_0(1-t)^3+3Q_1(1-t)^2t+3Q_2(1-t)t^2+P_3t^3 \\ R_2(t)=P_{n-3}(1-t)^3+3Q_3(1-t)^2t+3Q_4(1-t)t^2+P_nt^3 \quad t\in[0,1] \end{cases} \tag{3.6}$$

And let

$$\begin{cases} R_1\left(\frac{l_1}{l_1+l_2+l_3}\right)=P_1 \\ R_1\left(\frac{l_1+l_2}{l_1+l_2+l_3}\right)=P_2 \\ R_2\left(\frac{l_{n-2}}{l_{n-2}+l_{n-1}+l_n}\right)=P_{n-2} \\ R_2\left(\frac{l_{n-2}+l_{n-1}}{l_{n-2}+l_{n-1}+l_n}\right)=P_{n-1} \end{cases} \tag{3.7}$$

We have

$$\begin{cases} Q_1=\frac{e_1(l_1+l_2)-e_2l_1}{l_2} \\ Q_2=\frac{e_1l_1-e_2(l_2+l_3)Q_1}{l_1} \\ Q_3=\frac{f_1(l_{n-2}+l_{n-1})-f_2l_{n-2}}{l_{n-1}} \\ Q_4=\frac{f_2(l_{n-1}+l_n)-f_1l_n}{l_{n-1}} \\ e_1=\frac{L_1^3P_1-(l_2+l_3)^3P_0-l_1^3P_3}{3(l_2+l_3)L_1l_1} \\ e_2=\frac{L_1^3P_2-l_3^3P_0-(l_1+l_2)^3P_3}{3l_3(l_1+l_2)L_1} \\ L_1=l_1+l_2+l_3 \\ f_1=\frac{L_2^3P_{n-2}-(l_{n-1}+l_n)^3P_{n-3}-l_{n-2}^3P_n}{3(l_{n-1}+l_n)l_{n-2}L_2} \\ f_2=\frac{L_2^3P_{n-1}-l_n^3P_{n-3}-(l_{n-2}+l_{n-1})^3P_n}{3l_n(l_{n-2}+l_{n-1})L_2} \\ L_2=l_{n-2}+l_{n-1}+l_n \end{cases} \tag{3.8}$$

In which

$$\begin{cases} m_0 = \frac{Q_1 - P_0}{|Q_1 - P_0|} \\ m_n = \frac{P_n - Q_4}{|P_n - Q_4|} \end{cases} \tag{3.9}$$

④ Solution of the m-continuity Eq. (3.5) in the matrix form of

$$[A]\{m\} = \{C\} \tag{3.10}$$

In which $[A]$ is a tri-diagonally dominant matrix, and

$$\begin{cases} [A] = \begin{bmatrix} 2 & \lambda_1 & & & \\ \mu_2 & 2 & \lambda_2 & & \\ & \mu_3 & 2 & \lambda_3 & \\ & \vdots & \vdots & \vdots & \\ & & \mu_{n-2} & 2 & \lambda_{n-2} \end{bmatrix} \\ \{m\} = [\, m_1 \quad m_2 \quad \ldots \quad m_{n-2} \quad m_{n-1} \,]^T \\ \{C\} = [\, C_1 - \mu_1 m_0 \quad C_2 \quad \ldots \quad C_{n-2} \quad C_{n-1} - \lambda_{n-1} m_n \,]^T \end{cases} \tag{3.11}$$

3.2.2 *Surface Fitting*

(1) Smooth surface

The interpretation of curved surfaces on an arch dam or in a tunnel is one of the key prerequisites in the generation of FE meshes. There are many methods to represent curved surfaces in terms of parametric coordinates (Thompson et al. 1974; Bornhill and Little 1984), of which the widely used one is "Coons patches". For defining these patches, the data concerning vortex coordinates $\{X\}$, tangent vectors $\{X_s\}$, $\{X_t\}$ and twist vector $\{X_{st}\}$, are needed. Where the twist vector $\{X_{st}\}$ cannot be obtained from the survey or design data directly in a mass hydraulic structure, several approximate methods such as the "Adini formula", are suggestible, or we may simply let $\{X_{st}\} = 0$.

In this book if necessary, the spline-blended surface interpolation proposed by Gordon (1969) is employed, where the boundary derivation condition of a surface is neglected, and the surface can be defined only with the coordinates of survey points without special demands on their location and amount.

A general form of smooth surface can be represented in terms of parametric coordinates

$$\begin{cases} X = X(u,v) \\ Y = Y(u,v) \\ Z = Z(u,v) \end{cases} \tag{3.12}$$

Let $Z = Z(u,v)$ be any continuous surface defined in the rectangular domain $R : [a,b] \times [c,d]$ on the parametric $u - v$ plane, and let $\pi : a = u_1 \le u_2 \le \cdots \le u_n = b$ and $\pi' : c = v_1 \le v_2 \le \ldots v_{n'} = d$ be the partitions of the intervals $I = (a,b)$ and $I' = (c,d)$. The surface Z and the vertical planes $u = u_i,\ v = v_j$ produce $n + n'$ univariate functions constructing a net work in a manner of

$$\begin{cases} f_j(u) = Z(u, v_j) & (j = 1, n') \\ g_i(v) = Z(u_i, v) & (i = 1, n) \end{cases} \tag{3.13}$$

There are two spline sets of odd degree meeting the cardinal conditions expressed by

$$\phi_i(u_k) = \delta_{ik} = \begin{cases} 0 & if\ i \neq k \\ 1 & if\ i = k \end{cases} \quad (i,\ k = 1, 2, \ldots, m_1;\ \ m_1 = n + 2p - 2) \tag{3.14}$$

$$\varphi_j(v_k) = \delta_{jk} = \begin{cases} 0 & if\ j \neq k \\ 1 & if\ j = k \end{cases} \quad (j,\ k = 1, 2, \ldots, m_2;\ \ m_2 = n' + 2p - 2) \tag{3.15}$$

Now let $p = 2$, the spline-blended surface will belongs to class C^2 (Prenter 1975). If the derivative condition at boundary is further neglected, namely

$$\begin{cases} Z_s(u_1, v) = 0 \\ Z_s(u_n, v) = 0 \\ Z_t(u, v_1) = 0 \\ Z_t(u, v_{n'}) = 0 \end{cases} \tag{3.16}$$

The surface interpolation can be derived by the formula

$$Z(u,v) = \sum_{i=1}^{n} \phi_i(u) g_i(v) + \sum_{j=1}^{n'} \varphi_j(v) f_j(u) - \sum_{i=1}^{n} \sum_{j=1}^{n'} \phi_i(u) \varphi_j(v) Z(u_i, v_j) \tag{3.17}$$

Obviously, the surface constructed in Eq. (3.17) will exhibit certain distortion near the boundary, but it is normally acceptable in “roughly shaped” hydraulic structures compared with “precisely shaped” machinery components.

(2) Arch dam surface

According to the shape of arch rings (see Fig. 3.7), arch dams may be distinguished as circular arch dams, multi-central arch dams, variable curvature arch dams, etc., (Chen 2015).

The upstream curve of crown cantilever (see Fig. 3.8) may be single arc or multi-arc, quadratic, cubic or other curve types (suitable for double curvature arch dams). It may also be vertical or inclined straight line, or poly line (suitable for single curvature arch dams). At the moment, the polynomial relating radial thickness Y and vertical altitude Z is widely exercised in the configuration of the profile of crown cantilever. For example, the upstream curve may be fitted by the formula

$$Y = a_1 Z + a_2 Z^2 + \cdots + a_n Z^n \tag{3.18}$$

The polynomial order n may be 2 in preliminary design phase, 3 in final design phase, and 4 in particular situation. The arch ring equation and cantilever equation may be converted into the univariate functions $f_j(u)$ and $g_i(v)$ to construct the arch dam surface Eq. (3.17).

(3) Irregular ground surface

The natural ground surfaces and faults are normally curved and irregular. To make the identification and pre-processing algorithms more realistic, the geological body bounded or delimited by several irregular surfaces should be handled.

Assume that the coordinates of the n points on one ground (or fault) surface are arranged in the following manner

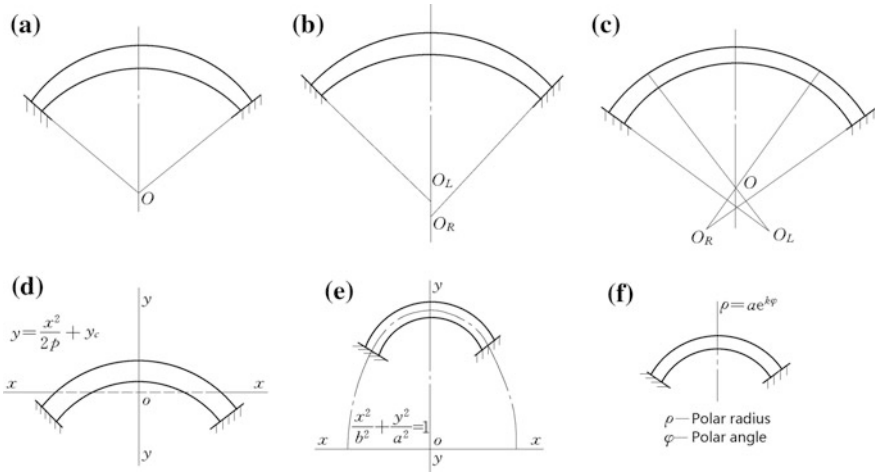

Fig. 3.7 Shapes of arch rings. **a** Circular arch; **b** double-central arch; **c** triple-central arch; **d** parabola arch; **e** ellipse arch; **f** logarithmic spiral arch

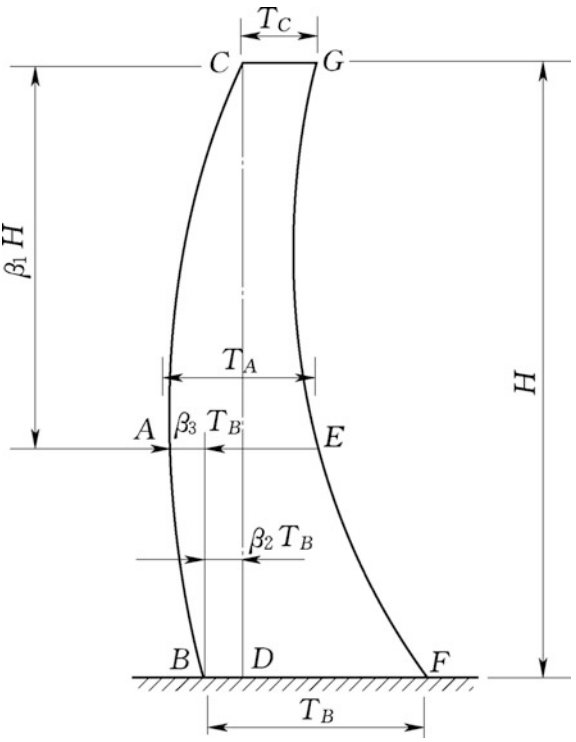

Fig. 3.8 Shape of crown cantilever

$$\begin{pmatrix} X_1 & X_2 & \dots & X_i & \dots & X_n \\ Y_1 & Y_2 & \dots & Y_i & \dots & Y_n \\ Z_1 & Z_2 & \dots & Z_i & \dots & Z_n \end{pmatrix}$$

Then the suggested surface formula is

$$Z(X,Y) = a_0 + a_1 X + a_2 Y + \sum_{i=1}^{n} t_i r_i^2 \ln(r_i^2 + \varepsilon) \tag{3.19}$$

In which

$$r_i = (X - X_i)^2 + (Y - Y_i)^2 \tag{3.20}$$

and ε is a small fraction (e.g. $\varepsilon = 0.001$). By inserting the coordinates of the n points into Eq. (3.19), n linear equations comprising $n+3$ coefficients $(a_0, a_1, a_2, t_1, t_2, \ldots, t_n)$ can be obtained. After supplemented by the following three conditions

$$\begin{cases} \sum_{i=1}^{n} t_i = 0 \\ \sum_{i=1}^{n} t_i X_i = 0 \\ \sum_{i=1}^{n} t_i Y_i = 0 \end{cases} \tag{3.21}$$

$n+3$ equations for solving the $n+3$ coefficients are established.

The mapping method can be applied to triangulate the surface of Eq. (3.19) parametrically expressed on the $u-v$ plane

$$\begin{cases} Z(u,v) = a_0 + a_1 u + a_2 v + \sum_{i=1}^{n} t_i r_i^2 \ln(r_i^2 + \varepsilon) \\ X = u \\ Y = v \\ r_i = (u - X_i)^2 + (v - Y_i) \end{cases} \tag{3.22}$$

3.2.3 Surface/Surface Intersection

The rest issue is the surface/surface intersection (SSI) in handling the irregular faults and ground surfaces. Since the SSI is an essential and well studied problem in the CAD/CAM (Shi and Cai 1996; Yu et al. 1999), we will merely find a reliable and simple algorithm practically implemented, that one surface possesses a parametric form meanwhile the other is in the implicit form. The former is inserted into the latter to get a nonlinear equation that can be solved by a routine procedure of contour extraction in a two-dimensional scalar field.

Define a parametric surface in Ω_g

$$\begin{cases} X = g_1(u,v) \\ Y = g_2(u,v) \\ Z = g_3(u,v) \end{cases} \tag{3.23}$$

And another implicit surface in Ω_f

$$f(X,Y,Z) = 0 \tag{3.24}$$

Introducing Eq. (3.23) into Eq. (3.24), the intersection line of these surfaces is interpreted by

$$f(g_1, g_2, g_3) = h(u, v) = 0 \tag{3.25}$$

Equation (3.25) is normally solved using the numerical algorithm of contouring. Denoting $\Omega = \Omega_f \cap \Omega_g$, the algorithm is implemented in the following steps.

① Establish regular grid on the parametric plane u–v shown in Fig. 3.9. Dividing this domain equally into n_u and n_v sections in the directions of u and v respectively, and let

$$\begin{cases} h_u = 1/n_u \\ h_v = 1/n_v \end{cases} \tag{3.26}$$

We have

$$\begin{cases} u_i = ih_u \quad (i = 0, 1, \ldots, n_u) \\ v_j = jh_v \quad (j = 0, 1, \ldots, n_v) \end{cases} \tag{3.27}$$

Each sell Δ_{ij} (see Fig. 3.9) in the grid possesses 4 vortices (u_i, v_j), (u_i, v_{j+1}), (u_{i+1}, v_j), and (u_{i+1}, v_{j+1}) $(i = 0, 1, \ldots, n_u - 1, j = 0, 1, \ldots, n_v - 1)$. The corresponding function $h(u, v)$ values at the vortices are $(h_{i,j}, h_{i,j+1}, h_{i+1,j}, h_{i+1,j+1})$.

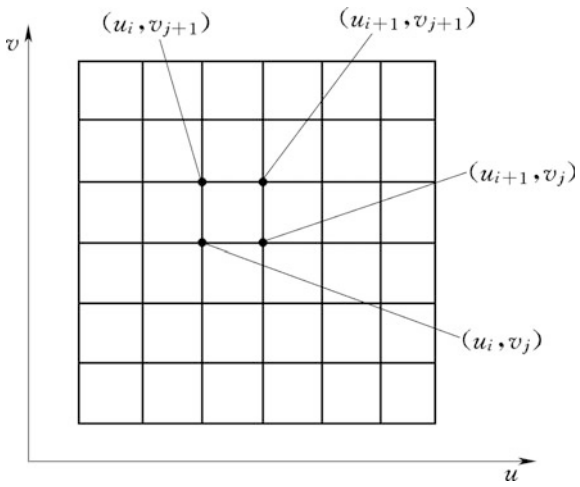

Fig. 3.9 Regular grid on the parametric plane u–v

② The cells are arranged sequentially and the contour segments are sought out in these sells. The key algorithm to locate a contour segment within Δ_{ij} is the intersection calculation of the contour and the grid cell. Suppose $h(u, v)$ varies linearly within Δ_{ij}, the following intersection calculation is carried out

- If $h_{i,j} \leq 0$, the vortex (u_i, v_j) is marked with "−", otherwise "+";
- If the 4 vortices are all marked with "+" or "−", the contour does not intersect with the cell, and the calculation goes back to the antecedent step, otherwise goes to the succedent step;
- For the cell with two vortices being marked with "+" at one edge and other two vortices being marked with "−" at the opposite edge, the linear interpolation is conducted to obtain the points where the cell edges are intersected by the contour. Take Fig. 3.10 for example where (u_i, v_j) is "−" and (u_i, v_{j+1}) is "+", the intersecting point is located at

$$\begin{cases} u_t = u_i \\ v_t = \frac{v_j h_{i,j+1} - v_{i+1} h_{i,j}}{h_{i,j+1} - h_{i,j}} \end{cases} \tag{3.28}$$

- For the cell Δ_{ij} with two "+" vortices and other two "−" vortices being located diagonally, the contour linkage may emerge two possibilities illustrated in Fig. 3.11. To overcome the ambiguity, St. Andrew cell may be employed using diagonal lines to subdivide the Δ_{ij} into four triangles (Fig. 3.12), the contour segments are judged and calculated in each triangle (see Fig. 3.13).

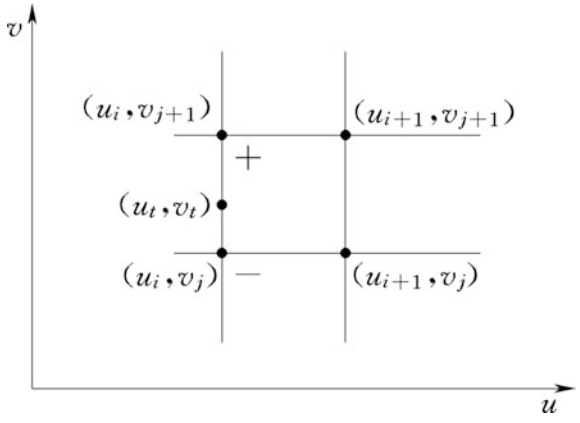

Fig. 3.10 Intersection of contour with a grid cell

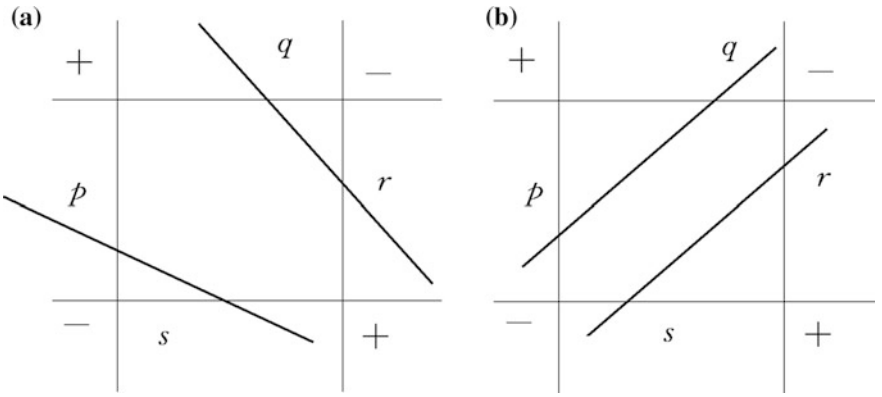

Fig. 3.11 Possible linkage of contour

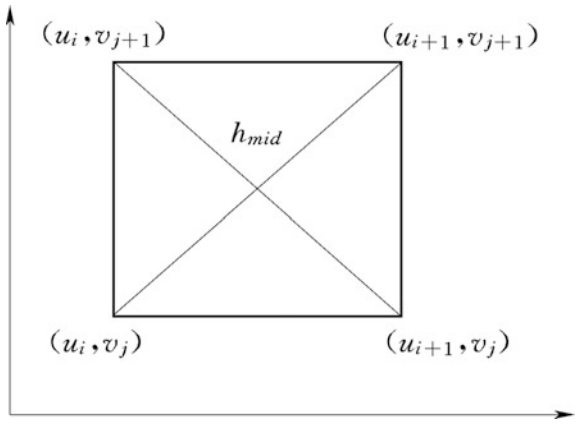

Fig. 3.12 St. Andrew sub-cells

3.3 Geometrical Description of Hydraulic Structures and Identification of Sub-domains

3.3.1 Concepts of Directed Geometrical Elements

A directed body is defined as the block enclosed by a number of directed faces Fig. 3.14b. A directed face has an external vector f^{ext} and an internal vector f^{int} perpendicular to the face and starting from the centroid of the face. The magnitude of the face vector is identical to the face area (Ikegawa and Hudson 1992).

A directed face is formed by a set of vertices arranged to make a right-handed system, with circular permutation, in terms of the external face vector (see Fig. 3.14a).

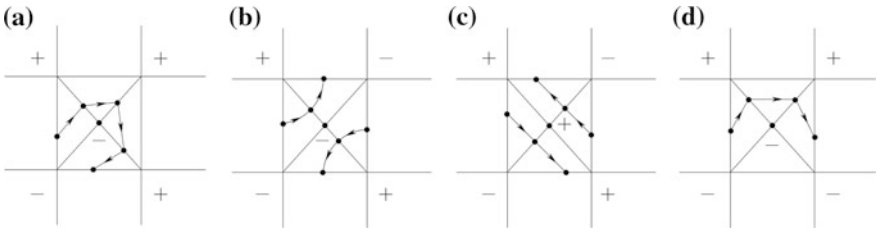

Fig. 3.13 Possibilities of contour segments in St. Andrew sub-cells

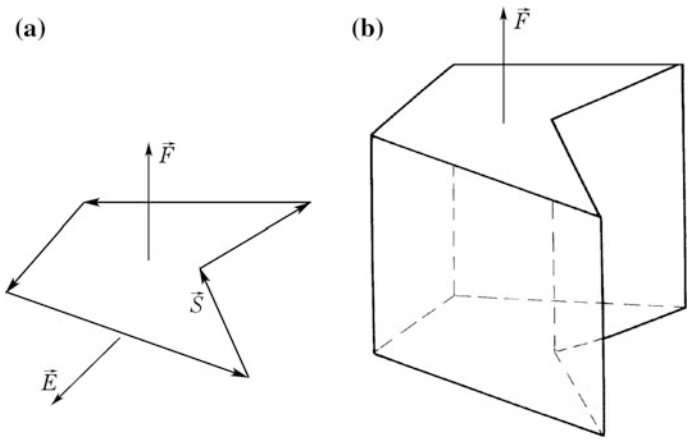

Fig. 3.14 Diagram showing directed body and directed face. **a** Directed face; **b** directed body

An edge has an external vector e^{ext} and an internal edge vector e^{int} perpendicular to both the external face vector and the edge, and starting from the middle of the edge. The magnitude of edge vector is identical to the edge length.

The directed body has a quite important geometrical invariant property that the resultant of all its external or internal face vectors is a null vector, i.e.

$$\sum_{i=1}^{n} \vec{F}_i = \vec{0} \tag{3.29}$$

In which i is the face sequence and n is the amount of all faces bounding the body. This is called the "body completion theorem" (Ikegawa and Hudson 1992).

The directed face also possesses a similar property that the resultant of all its external or internal edge vectors is a null vector, i.e.

$$\sum_{i=1}^{n} \vec{E}_i = \vec{0} \tag{3.30}$$

In which i is the edge sequence and n is the amount of all edges bounding the face. This is called the "face completion theorem" (Ikegawa and Hudson 1992).

Based on the above concepts, the automatic identification algorithm can be formulated for the blocky system containing both the convex and concave blocks.

3.3.2 Database Structures

The sub-domains (blocks) are identified in the global coordinate system and a four-leveled hierarchical structure of geometry element database for the block identification is constructed beforehand.

(1) Point

The coordinate (X_m, Y_m, Z_m) of each point P_m is input in sequence, and the message indicating if the point is in a structural surface or not, should be specified.

(2) Edge

For an edge E_k whose reference nodes $(P_1, P_2, P_3, \ldots, P_m, \ldots)$ are logically given, the type of the line segment and the message indicating if the edge is in a structural surface or not, should be specified.

(3) Directed face

For a directed face patch F_i, its type, reference points, and the line segments $(E_1, E_2, E_3, \ldots, E_k, \ldots)$ enclosing the face, should be specified.

(4) Directed body

Data describing the sub-domain B_j comprise its type, reference points, the face patches $(F_1, F_2, F_3, \ldots, F_i, \ldots)$ enclosing the body, the adjacent blocks B_i contacting the block B_j through the face patch F_i.

3.3.3 Identification Procedures

The flow chart of block identification is schematically formulated in Fig. 3.15.

(1) Generation of points

After reading the messages of all the surfaces (inclusive the irregular ground surface) by the sub-module of INPUT, a point is defined by the intersection of three or more structural surfaces and created by the sub-module POINT.

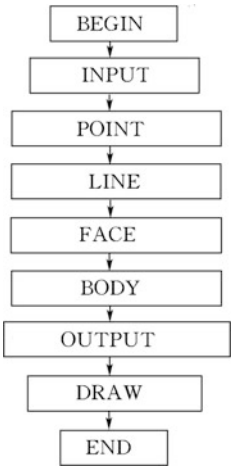

Fig. 3.15 Flow chart of block system identification

① Intersection loop over every three-surface combination is carried out;
② If there exists intersecting point of these tentative surfaces, the auxiliary examination is carried out to check if this is a superposition point;
③ If yes, the point is formed by at least four surfaces and should be abandoned, the process goes back to step ① for another tri-surface combination;
④ If no, the point is sorted as the new vortex point, and the process goes back to step ① for another tri-surface combination;
⑤ Steps ②–④ are recurred until all the tri-surface combinations have been covered;
⑥ Store the messages of all the generated vortices (inclusive their relations with the surfaces);
⑦ Turn to the next sub-module LINE.

(2) Generation of edges

The edge messages are produced after the completion of point generation. All the points related to a bi-surface combination are arranged in sequence, a edge comprising these points may be defined and messages indicating if it is in these two surfaces or not, is specified. If there are two edges possess identical messages, it means that there are at least three surfaces intersecting at the same edge, and one of them should be removed from the edge messages. The algorithm towards the edge generation is therefore formulated in the sub-module LINE as follows.

① Read in the stored messages of all the vortex points;
② Intersection loop over every bi-surface combination is carried out;
③ Sort out all the points that are related to a tentative bi-surface combination. If the number of points is smaller than 2, the process goes back to step ② for another bi-surface combination;

④ If these two surfaces are all planar, a straight edge is generated whose messages are created and recorded, then the process goes back to step ② for another bi-surface combination;
⑤ If at least one of the surfaces is curved, the curved edge segment is created and recorded, then the process goes back to step ② for another bi-surface combination;
⑥ Recur steps ②–⑤ until all the bi-surface combinations have been covered;
⑦ Store the messages of all the generated edges (inclusive their relations with the surfaces);
⑧ Turn to the next sub-module FACE.

(3) Generation of directed faces

The face messages are produced after the completion of edge generation. All the edges related to a structural surface (including ground surface) are arranged in sequence and anti-clockwise. The conjugated edges should form the smallest interior included angle (or largest exterior angle) (see Fig. 3.16). When directed edges form a closed face patch, i.e. the face completion theorem Eq. (3.30) is held, a directed face is generated. Any inner point located with the face should be judged as invalid.

Generally, each edge may be used twice as two directed edges (identical in quantity but negative in direction), so there are virtual directed faces to be deleted. Figure 3.17 shows 3 directed faces ABCDA, CEFDC, ADFECBA. Since the area of ADFECBA is negative and its quantity is the sum of ABCDA and CEFDC, therefore it is a virtual face and should be removed. The steps of the directed face generation in the sub-module FACE are detailed as follows.

① Read in the stored messages of all the edges;
② Loop over all the structural surfaces;
③ Loop over all the edges on a selected structural surface;
④ For a selected active edge, denote its end point as the start point of tentative new active edge, then

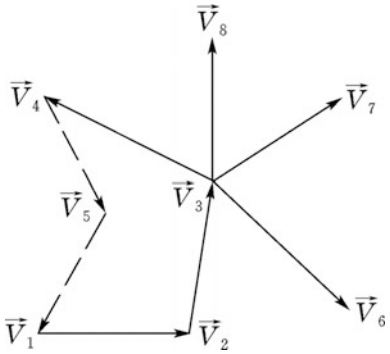

Fig. 3.16 Generation of a directed face

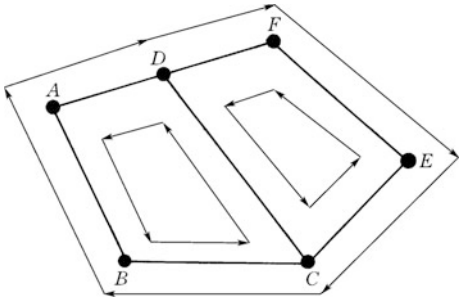

Fig. 3.17 Directed face patches on a structural surface

- Find out all the tentative edges started from this point, calculate their interior included angles with the active edge;
- The trial edge that forms the smallest interior included angle with the active edge is defined as the new active edge;
- If the end point of the new active edge is identical to the start point of the first active edge, a directed face is created, otherwise the process goes back to the step ④ for a new active edge;

⑤ If all the directed faces are created, the virtual faces are judged and removed, the valid directed faces are stored for the body generation;
⑥ A new structural surface is selected and the process from step ② to step ⑤ is recurred;
⑦ Steps ②–⑥ is repeated until all the structural surfaces are covered;
⑧ Turn to the next sub-module BODY.

(4) Generation of directed bodies

The body messages are produced after the completion of face generation. All the directed faces related to a common edge are arranged in sequence, the conjugated faces should form the smallest interior included angle (or largest exterior included angle) (see Fig. 3.18).

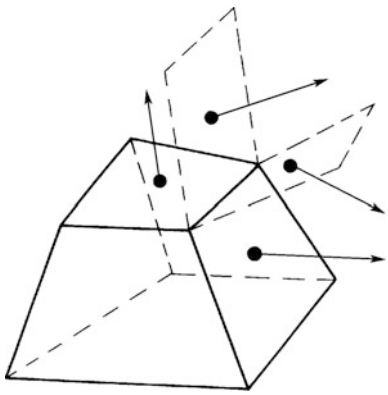

Fig. 3.18 Generation of a directed body

When a set of directed faces forms an closed entity, i.e. the body completion theorem Eq. (3.29) is held, a directed body is generated. Any inner point located within the entity should be judged as invalid. The steps of the directed body generation in the sub-module BODY are detailed as follows.

① Read in the stored messages of all the directed faces;
② Loop over all the directed faces;
③ For an active face, loop over all its directed edges;
④ For the selected edge, find all the faces it links, and calculate their interior included angles. The smallest interior included angle defines the new active face, and the process goes back to step ③;
⑤ If a new directed body meeting the completion theorem Eq. (3.29) is created, its messages are stored, the process goes back to step ②, otherwise goes back to step ③;
⑥ The virtual bodies with negative volume are removed by the auxiliary examination, the rest valid bodies are stored;
⑦ Turn to the next sub-modules OUTPUT and DRAW to output and visualize the block system.

3.3.4 *Handling of Special Cases*

(1) Removal of an invalid edge

Figure 3.19 schematically explains how to remove an invalid edge.

(2) Identification of a multiply connected face

A multiply connected face possesses two or more separately enclosed boundaries. The directed face shown in Fig. 3.20 has two enclosed boundaries ABCDA and EFGHE. Under such circumstances, three directed faces ABCDA, EFGHE, EHGFE will be generated according to the identification strategy, of which four interior points (E, F, G, H) within the face ABCDA create a virtual face EHGFE

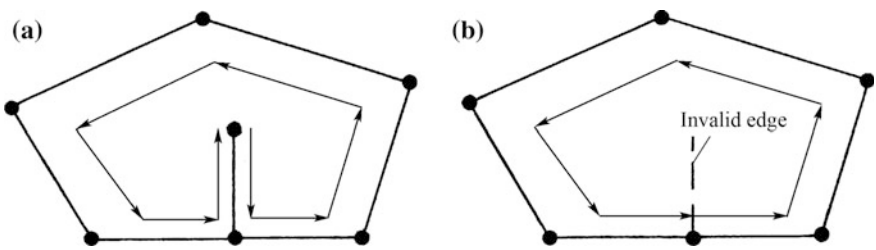

Fig. 3.19 Diagram showing the removal of invalid edge

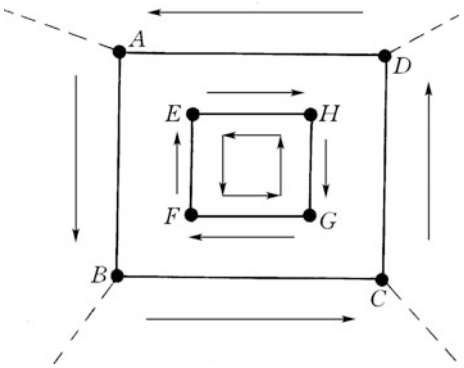

Fig. 3.20 Diagram showing the identification of multiply connected face

with negative area. After the removal of this invalid directed face, the multiply connected face ABCDA-EHGFE possesses two separate boundaries is identified.

(3) Generation of a directed face containing curved edges

Commonly, at least three directed edges are demanded to enclose a directed face. Where curved edges are permitted, however, two edges might be sufficient to form a directed face. In the generation process of directed face, the straight secant through the ends of a curved edge is employed. After the completion of the whole directed face, the secant is substituted by the original curve (see Fig. 3.21).

(4) Generation of a curved directed face

The curved surface should be projected on to a parametric plane. After the generation of all the directed faces on this parametric plane, the directed faces on the curved surface may be obtained by the inverse transformation.

Suppose a curved surface is expressed by the univalent function $Z(X, Y) = F(X, Y)$ and vertically projected on to the horizontal plane X–Y (see Fig. 3.22).

After the generation of a directed face, its edge vectors and face vector should be calculated (see Fig. 3.23). In doing so, the straight secant through the ends of the

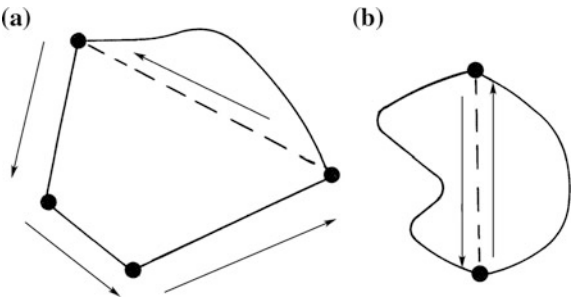

Fig. 3.21 Diagram showing the identification of directed face containing curved edges. **a** One curved edge; **b** two curved edges

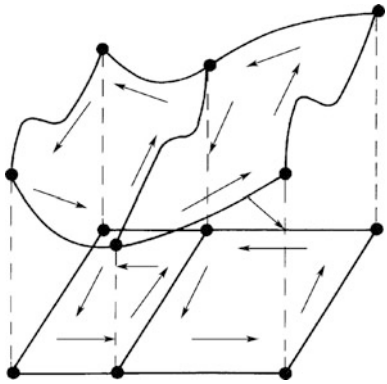

Fig. 3.22 Directed faces and edges on a curved structural surface

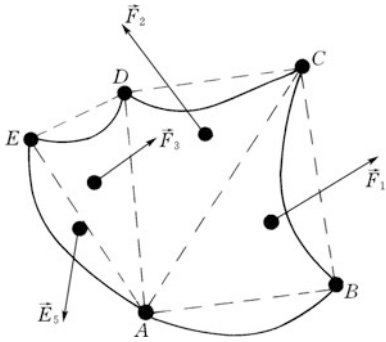

Fig. 3.23 Diagram showing the identification of curved directed face

curved edge is employed, then the curved face may be divided into ($nv - 2$) triangles (nv is the amount of the vortices on the face). The vectors of these curved edges and curved face are calculated using their straight and planar substitutes. These ($nv - 2$) vectors corresponding to triangles are superposed for the purpose of body identification. After the accomplishment of body generation, these planar triangles are back substituted by the original curved face.

(5) Generation of a body containing curved faces

Denote that the intersecting points of an irregular ground surface with structural planes as E, J, I, H and D, respectively (see Fig. 3.24). We substitute the triangles EJD, DJI and HDI for the curved face patch EJIHDE temporarily, in this manner the body completion theorem and face completion theorem can be applied to the equivalent body bounded by the substitute planar triangles and the identification algorithm can be carried out without major difficulties.

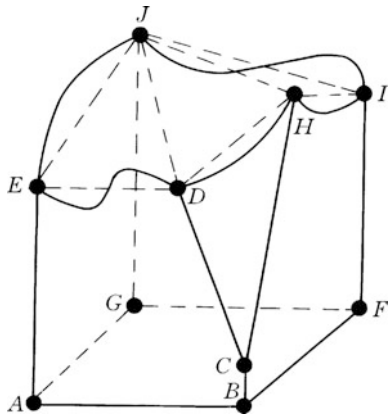

Fig. 3.24 Diagram showing the identification of a body containing curved face patch

3.3.5 Key Algorithms

(1) Intersection point of two planes with one curved surface

Suppose there are two non-parallel planes

$$\begin{cases} A_1X + B_1Y + C_1Z = D_1 \\ A_2X + B_2Y + C_2Z = D_2 \end{cases} \tag{3.31}$$

And their intersecting edge is given by

$$\begin{cases} Z = F_1(X) \\ Y = F_2(X) \end{cases} \tag{3.32a}$$

or

$$\begin{cases} Z = F_1(Y) \\ X = F_2(Y) \end{cases} \tag{3.32b}$$

Taking the intersecting edge Eq. (3.32a) for example, it is discretized along the X-axis into segments (i,j) with an interval length ΔX defined by the segment ends (X_i, Y_i, Z_i) and (X_j, Y_j, Z_j). Meanwhile, the curved surface formula in Eq. (3.19) provides $Z(X_i, Y_i)$ and $Z(X_j, Y_j)$.

If

$$(Z(X_i, Y_i) - Z_i) \cdot (Z(X_j, Y_j) - Z_j) < 0 \tag{3.33}$$

The segment (i,j) is intersected with the curved surface, and an interpolation between the two ends may indicate the exact intersecting point. Otherwise the next edge segment is trialed.

(2) Sequence of points on a curved edge

When a plane is intersected with the curved surface, a curved edge is produced. The iterative algorithm may be employed to find the points in sequence to form the messages of this curved edge.

Suppose a plane

$$AX + BY + CZ = D \tag{3.34}$$

is intersected with the ground surface interpreted in Eq. (3.19), we have

$$F(X, Y) = a_0 + a_1 X + a_2 Y + \sum_{i=1}^{n} t_i r_i^2 \ln(r_i^2 + \varepsilon) + \frac{A}{C} X + \frac{B}{C} Y - \frac{D}{C} = 0 \tag{3.35}$$

For a specified coordinate X (or Y), the coordinate Y (or X) may be solved by the iterative algorithm using the following formula deduced from Eq. (3.35)

$$Y = f(X, Y) \tag{3.36a}$$

or

$$X = f(X, Y) \tag{3.36b}$$

Starting from an initial vortex point (X_0, Y_0) on the edge, the coordinate X (or Y) is discretized into segments with interval length ΔX (or ΔY), then the iterative algorithm may be carried out to find corresponding Y_i (or X_i). The curved edge is defined by the initial vortex point (X_0, Y_0) and all the new detected vortex points (X_i, Y_i) (see Fig. 3.25).

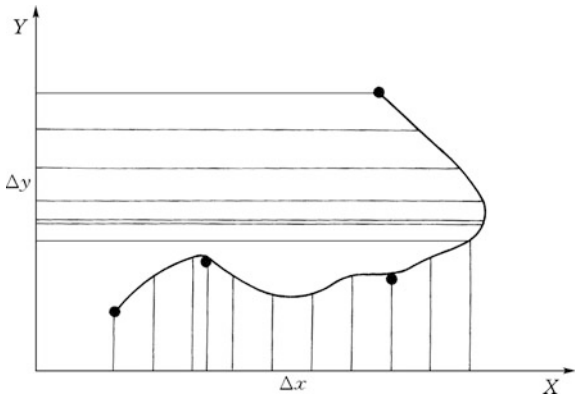

Fig. 3.25 Sequencing of the points on a curved edge

All the points of the edge calculated in sequence may be later employed in the area and volume computation (if necessary), ground contour drawing, as well as the FE mesh discretization.

(3) Judgment on the inclusion of a point within the polygon

The judgment on a point with regard to its relation to the polygon is indispensable in the directed face generation and discretization.

Giving any point P (corresponding to the vector $\vec{V}_P$) and directed polygonal face ABCDEFA (corresponding to the vector $\vec{F}$) (see Fig. 2.26). The edge $\vec{E}_{AB}$ of this face and the point P form an included angle

$$\theta_{AB} = \begin{cases} \arccos\left(\frac{(\vec{V}_A-\vec{V}_P)\cdot(\vec{V}_B-\vec{V}_P)}{|\vec{V}_A-\vec{V}_P|\cdot|\vec{V}_B-\vec{V}_P|}\right) & \left[(\vec{V}_A-\vec{V}_P)\times(\vec{V}_B-\vec{V}_P)\right]\cdot\vec{F}>0 \\ -\arccos\left(\frac{(\vec{V}_A-\vec{V}_P)\cdot(\vec{V}_B-\vec{V}_P)}{|\vec{V}_A-\vec{V}_P|\cdot|\vec{V}_B-\vec{V}_P|}\right) & \left[(\vec{V}_A-\vec{V}_P)\times(\vec{V}_B-\vec{V}_P)\right]\cdot\vec{F}<0 \end{cases} \tag{3.37}$$

All the included angles formed by the directed edges of the face with the point P are summed

$$\theta = \sum_{i=AB}^{FA} \theta_i \tag{3.38}$$

If $\theta = 0$, the point P is outside of the polygon ABCDEFA (see Fig. 3.26a), whereas $\theta = 360°$ means that the point P is within the polygon (see Fig. 3.26b).

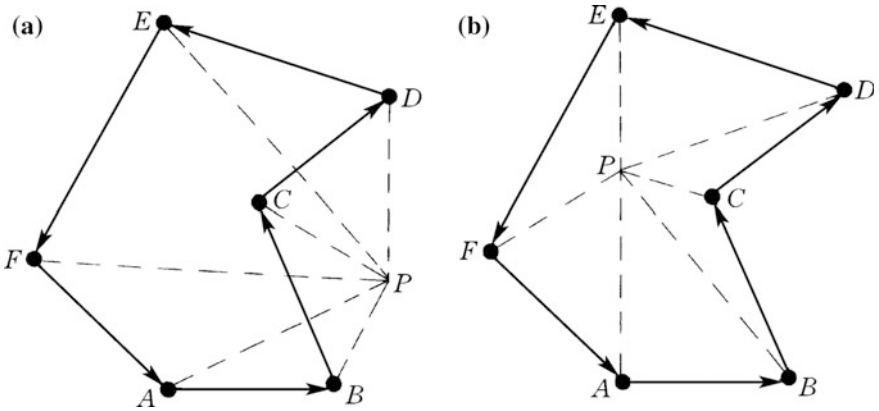

Fig. 3.26 Diagram to the inclusion judgment on the point with regard to a polygon. **a** *P* outside the polygon; **b** *P* within the polygon

3.4 Two-Dimensional Mesh Generation by the AFT

Attributable to the merit that the advancing front technique (AFT) is able to discretize 3D complex domains sophisticatedly, its use has been widely made to generate FE mesh, particularly towards the adaptive FEM (Peraire et al. 1992).

The AFT requires an initial front in order to start the discretization of a three-dimensional domain, this means that the surfaces enclosing the domain need to be defined, either by the identification algorithm of directed bodies and faces elaborated in Sect. 3.3, or by the entity construction technique using CAD/CAM software. Afterwards, the AFT grid generator performs two-dimensional mesh discretization on these surfaces (Moller and Hansbo 1995). It is well known that the quality of face discretization has a major impact on the quality of three-dimensional meshes, which in turn influences the quality of FEM computations. Of course, the two-dimensional problems encountered in the conventional design for several types of hydraulic structures (e.g. gravity dams and tunnels), rely on the two-dimensional mesh generation directly.

3.4.1 Database Structure

The database organizes geometrical elements (faces, edges, points) hierarchically (Beall and Shephard 1997). The underground cavern section shown in Fig. 3.27 may be used to elucidate such a database structure.

This cavern section consists of six sub-face patches: sub-face patch ① is distinguished due to its different rock stratum; sub-face patches ②–⑤ belong to the same rock stratum but they are divided by the faults F_1 and F_2; sub-face patch ⑥ is the excavated portion of the cavern.

Each sub-face is enclosed by straight or curved edge segments. Take sub-face patch ① for example, it is composed of edge segments 1, 10, 15 and 2. Edge 15 is straight and defined by points 4 and 3, edge 19 is a semi-circle and defined by points 9, 16 and 8.

Point is the elementary geometrical element defined by its coordinates solely.

This data structure enables to assign the material properties, excavation sequences (benches), concrete placement sequences (lifts), boundary conditions, etc., to the geometrical elements conveniently.

3.4.2 Generation of Triangular Element Mesh on Planar Surface

The triangular mesh generator detailed by Jin and Wiberg (1990) requires a separate input file as the background data of edge segments. Afterwards the generation of

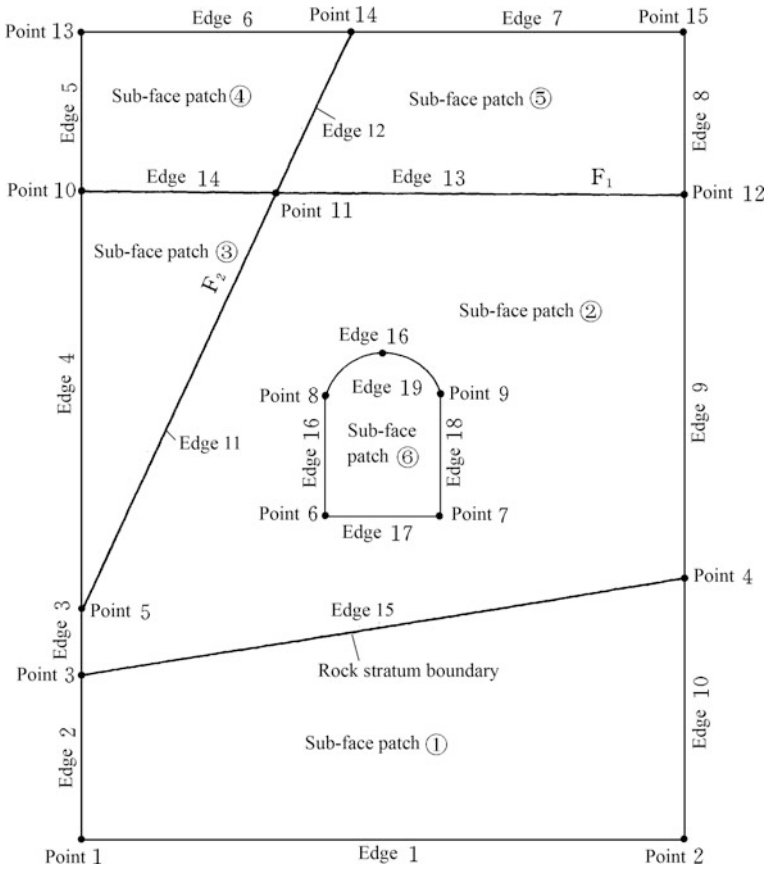

Fig. 3.27 Underground cavern and its geometrical elements

triangular element mesh on a planar surface using the AFT is implemented in the following steps.

① By discretizing the boundary, an initial front is created (see Fig. 3.28a).
② At any stage of node and element searching loop (see Fig. 3.28b, c), the shortest edge AB is selected as active edge (see Fig. 3.28, detailed drawing A).
③ Find the coordinates of midpoint D (see Fig. 3.28, detailed drawing A), the element size h at D is interpolated from the mesh density defined in the background mesh.
④ Calculate the coordinate of point C (see Fig. 3.28, detailed drawing A) that

- C is located at the interior side of edge AB;
- $|AC| \approx |BC| \approx$ h.

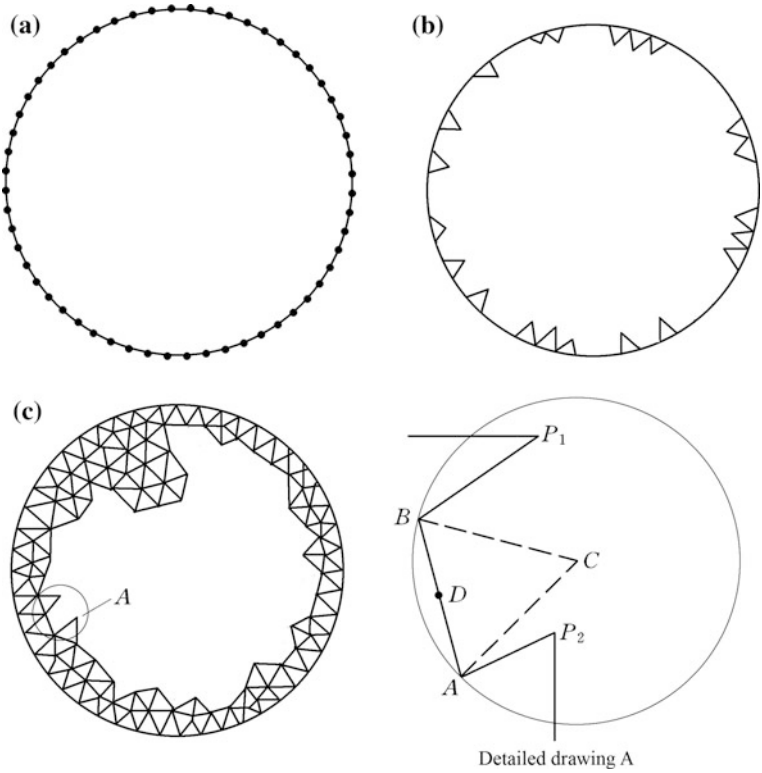

Fig. 3.28 Diagram to the generation of triangular element mesh

⑤ Create a point set N1 that

- Point P is located at the active front and at the interior side of edge AB;
- Point P is located within the circle centered on point C with a radius of h.

In the detailed drawing A of Fig. 3.28, N_1 contains two points (P_1 and P_2).

⑥ Construct the sub-set N2 of N1 that

- Apart from point P, ΔABP does not contain any point of set N1;
- Apart from AB, edge PD does not intersect with the active front;
- PA < nh, PB < nh (usually $n = 1.5$).

⑦ If N2 is not empty, the point which forms the largest included angle with AB ($\angle ABP$) is sorted as the new node to generate a new triangular element (ΔABP), the front is updated and the algorithm returns to step ②.

In the detailed drawing A of Fig. 3.28, point P_2 is finally selected as new node.

⑧ If N2 is empty, and C meets that

- ΔABC does not contain any points in N1;
- Apart from AB, CD does not intersect the active front;

Point C is sorted as the new node to generate a new triangular element (ΔABC), the front is updated and the algorithm returns to step ②.

⑨ If point C does not meet the requirements stipulated in step ⑧, the element generation fails and another active edge with second shortest length is alternatively attempted, then the algorithm returns to step ②.

⑩ If the active front is empty, the mesh generation is accomplished.

3.4.3 *Generation of Quadrilateral Element Mesh on Planar Surface*

The quadrilateral mesh generation using AFT for a planar surface patch may be formulated on the basis of triangular mesh generators (Lo 1989; Zhu et al. 1991; Zienkiewicz and Zhu 1991).

① By discretizing the boundary, the initial front is created (see Fig. 3.29a).

② The shortest edge segment (AB) is selected as active edge, a new triangular element (ΔABC) is created with the help of new node C according to the element size h defined at the background mesh (see Fig. 3.29b).

③ The active front is updated. In Fig. 3.29b, AC and BC are new active edges included in the updated active front, meanwhile AB is deleted from the active front.

④ From active edge AC or BC, another triangle is created, such as the triangle ΔBCD in Fig. 3.29c, and the active front is updated accordingly.

⑤ Two triangular elements ΔABC and ΔBCD are merged into a new quadrilateral element $ABCD$ (see Fig. 3.29c).

⑥ Steps ①–⑤ is recurred until the active front is empty.

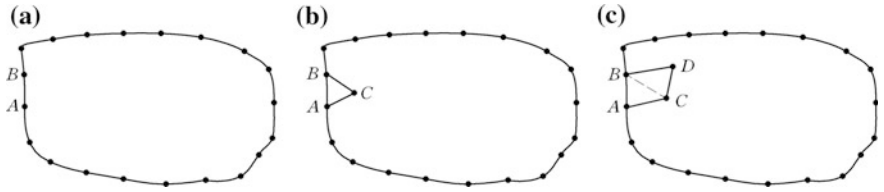

Fig. 3.29 Diagram to the generation of quadrilateral element mesh

3.4.4 Optimization of FE Mesh on Planar Surface

Independent of mesh generation, the so-called "smoothing techniques" have been developing for the improvement of already constructed meshes or their portions. Most of the smoothing algorithms insofar can be categorized into two groups: the Laplacian-based scheme (Blacker and Stephenson 1991; Hansbo 1995; George and Borouchaki 1998) and the optimization based scheme (Canann et al. 1993; Batdorf et al. 1997). The Laplacian scheme is straight forward and easy to implement, but often produces elements of rather poor quality. The optimization based scheme typically results in high-quality elements, but requires more computational overheads. In addition to the schemes mentioned above and their variants, the so-called angle-based optimization (Xu and Newman 2006) was also proposed.

3.4.5 Generation of Triangular Element Mesh on Curved Surface

Mesh generation on the curved surface is inevitable for the generation of three-dimensional meshes for the structures with curved interfaces or/and boundaries (Lo 1989; Nordsletten and Smith 2008).

Normally, a curved surface is first decomposed into a union of simple curved face patches, which may be generally undertaken together with the sub-domain decomposition using the technique for block system identification elaborated previously in this Chapter. Meshes are then generated on each of the face patch and finally stitched together into the whole discretized surface. Such an algorithm does give rather satisfactory results on the most types of curved surfaces in hydraulic structures.

To meet the requirement on the element sizes at different directions $\{e\}_1$, $\{e\}_2$, $\{e\}_3$ (see Fig. 3.30) (Moller and Hansbo 1995; Merhof et al. 2007), if necessary, one of the most widely exercised techniques is the transformation method, namely the mesh is first generated on a parametric plane and then mapped back onto the curved surface. This might produce reasonably good meshes for simple curved surfaces that are sufficiently smooth.

For tremendous complicated surfaces with strict requirement on discretization accuracy, Lau and Lo (1996) proposed a transformation method capable of generating high-quality meshes directly over curved face patches, taking into account of their curvature effect (see Fig. 3.31).

Denote

$$[\bar{g}] = \begin{bmatrix} \frac{1}{h_1} & 0 & 0 \\ 0 & \frac{1}{h_2} & 0 \\ 0 & 0 & \frac{1}{h_3} \end{bmatrix} \left[\{e\}_1, \{e\}_2, \{e\}_3\right]^{\mathrm{T}} \tag{3.39}$$

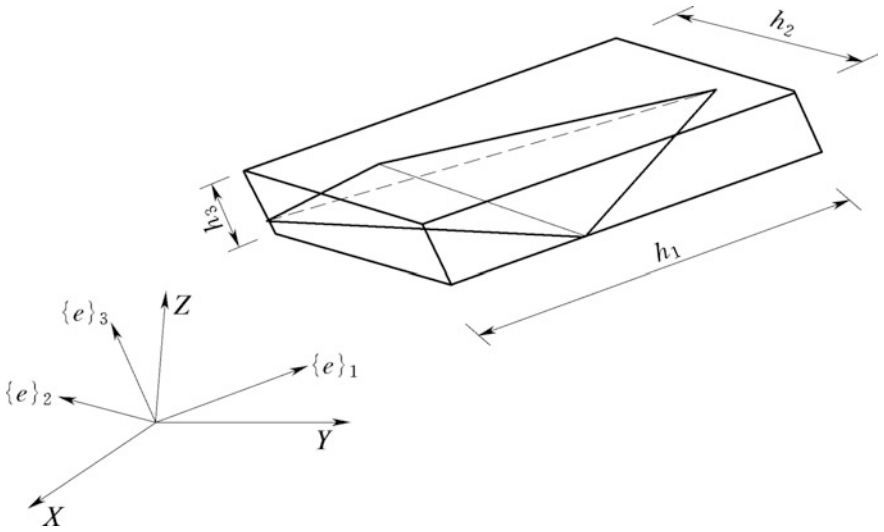

Fig. 3.30 Requirement for the element size on a curved surface

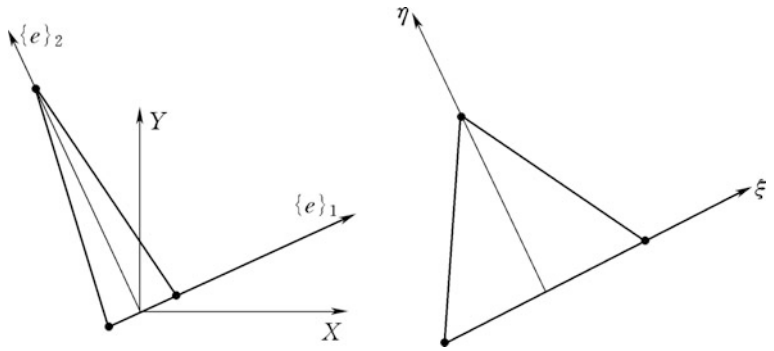

Fig. 3.31 Transformation from natural space to regular space

and let

$$[T] = \left([\bar{g}]^{\mathrm{T}} [\bar{g}] \right)^{\frac{1}{2}} \tag{3.40}$$

Transformation from natural space (X, Y, Z) to regular space (ξ, η, ζ) is conducted by

$$\begin{Bmatrix} d\xi \\ d\eta \\ d\varsigma \end{Bmatrix} = [T] \begin{Bmatrix} dX \\ dY \\ dZ \end{Bmatrix} \tag{3.41}$$

Peraire et al. (1992) define the transformation matrix in the manner of

$$[T'] = \sum_{i=1}^{3} \frac{1}{h_i} \{e\}_i \{e\}_i^T \tag{3.42}$$

It may be justified that $[T]$ is actually identical to $[T']$. $[T]$ or $[T']$ defines a transformation that eliminates the requirement of the directional element size on the mesh by mapping a directionally sized triangular element in the natural space (X, Y, Z) to an equilaterally unit triangular element in the regular space (ξ, η, ζ).

To transform the triangular element in the three-dimensional regular space (ξ, η, ζ) to the parametric plane (u, v), according to Eq. (3.23) we write

$$\begin{Bmatrix} dX \\ dY \\ dZ \end{Bmatrix} = \begin{bmatrix} \frac{\partial X}{\partial u} & \frac{\partial X}{\partial v} \\ \frac{\partial Y}{\partial u} & \frac{\partial Y}{\partial v} \\ \frac{\partial Z}{\partial u} & \frac{\partial Z}{\partial v} \end{bmatrix} \begin{Bmatrix} du \\ dv \end{Bmatrix} \tag{3.43}$$

Or simply

$$\{dX\} = [\{X_u\}, \{X_v\}]\{du\} \tag{3.44}$$

Introducing Eq. (3.44) into Eq. (3.41) leads to

$$\begin{Bmatrix} d\xi \\ d\eta \\ d\varsigma \end{Bmatrix} = [T][\{X_u\}, \{X_v\}] \begin{Bmatrix} du \\ dv \end{Bmatrix} \tag{3.45}$$

Define

$$[\bar{g}^*] = ([T][\{X_u\}, \{X_v\}])^{\mathrm{T}} ([T][\{X_u\}, \{X_v\}]) \tag{3.46}$$

The transformation from the directionally sized triangular element in the space (X, Y, Z) to the equilaterally unit triangular element in the two-dimensional parametric plane (ξ', η') is established

$$\begin{Bmatrix} d\xi' \\ d\eta' \end{Bmatrix} = ([\bar{g}^*])^{\frac{1}{2}} \begin{Bmatrix} du \\ dv \end{Bmatrix} \tag{3.47}$$

After the discretization in the space (ξ', η'), the inverse transformation is carried out from (ξ', η') back to (u, v) as

$$\begin{Bmatrix} du \\ dv \end{Bmatrix} = ([\bar{g}^*])^{-\frac{1}{2}} \begin{Bmatrix} d\xi' \\ d\eta' \end{Bmatrix} \tag{3.48}$$

3.5 Three-Dimensional Mesh Generation by the AFT

Lo (1985), Löhner and Parikh (1988) proposed an AFT towards the tetrahedral element generation for three-dimensional domains. Based on their algorithm, the author of this book also had developed a mesh generator (Cao et al. 1998; Chen et al. 2000; Xia and Chen 2001), in which particular attention is focused on the complex configuration of the dam/foundation containing irregular surfaces (e.g. discontinuities in rock masses and ground surfaces). However, insofar there are crucial difficulties to reliably implement the AFT for hydraulic structures by the transformation of tetrahedral mesh into whole-hexahedral mesh, although the latter is more effective and attractive for engineering practitioners.

3.5.1 General Considerations

(1) Flow chart

In the process of mesh generation flow charted in Fig. 3.32, a background mesh which completely covers the domain is defined to accommodate messages concerning the mesh density, material properties, boundary conditions, and actions.

To construct an initial front, the boundary surfaces are discretized beforehand using the two-dimensional mesh generator described previously in this Chapter. The initial generation front is a collection of all triangular faces discretized from the boundary surfaces of all the sub-domains in the block system identified.

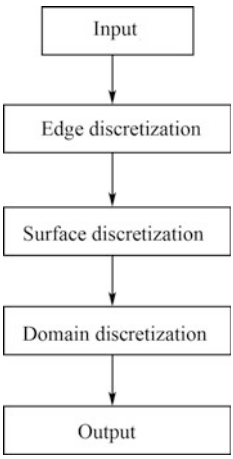

Fig. 3.32 Flow chart of tetrahedral element generation for three-dimensional domains

The face to be deleted from the list of active front always should be able to form the smallest tetrahedron element. A "best point" is created to form a tentative new tetrahedron element. If this tentative tetrahedron can pass through both the "validity test" to ensure the existent elements will not be intersected with the new element and the "auxiliary test" to ensure the qualified shape and position, it will be accepted as a new element. The new element, point and faces should be added to their respective lists to update the active front. The element generation process is terminated when the generation front is empty.

(2) Database structure

The data defining a complex domain are organized by simple sub-domains, each sub-domain possesses one material merely, or will be excavated/casted in one construction operation, or just supplementarily cut by artificial planes to facilitate the mesh generation (Löhner 1988). The local mesh will be generated in each sub-domain independently first, then all these local meshes will be "stitched" together to form the whole mesh.

A five-leveled hierarchical database structure for sorting and storing input data is presented in Fig. 3.33.

- First level. Data describing the domain, where the sub-domains (blocks, bodies) are denoted as $(B_1, B_2, B_3, \ldots, B_j, \ldots)$.
- Second level. Data listing the material parameters of sub-domain B_j, its excavation or replacement sequence, and face patches $(F_1, F_2, F_3, \ldots, F_i, \ldots)$ enclosing the sub-domain.

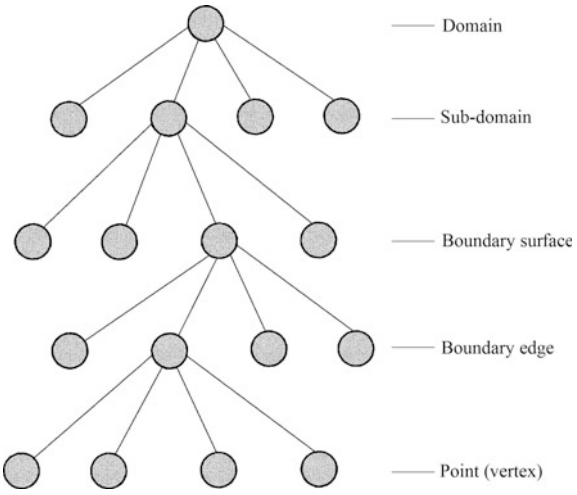

Fig. 3.33 Structure for sorting and storing input data

– Third level. Data of face patch F_i, inclusive its type, reference points, edge segments $(E_1, E_2, E_3, \ldots, E_k, \ldots)$ enclosing the face.
– Fourth level. Data of edge segment E_k inclusive its type and reference nodes $(P_1, P_2, P_3, \ldots, P_m, \ldots)$.
– Level five. The coordinates (X_m, Y_m, Z_m) and type of point P_m input in sequence.

3.5.2 *Treatment of Complex Domain*

The complexity in the FE mesh generation for hydraulic structures mainly arise from the material heterogeneity (faults and joints), the multiply connected domain (holes and pipes), as well as the sequential construction and operation processes.

(1) Multiply connected domain

Auxiliary line is customarily drawn for the multiply connected domain to transform it into simply connected domain (see Fig. 3.34).

If an auxiliary plane is employed to treat the three-dimensional multiply connected domain, the complicated intersecting computation with regard to surfaces is demanded. The author of this book had however, proposed an alternative way to handle multiply connected domain problems without the help of auxiliary lines/planes but rather by improving database structure (Cao et al. 1998).

(2) Discontinuity

Important discontinuities (joints, faults and interfaces) are simulated explicitly by joint elements with or without thickness in the FEM computation for hydraulic structures. In the mesh generation, firstly these discontinuities are looked as ordinary boundary face patches of sub-domains. After the triangulation of these faces, they will be duplicated in parallel, in this way the discontinuities can be discretized into triangular slab (prism) elements with or without thickness a (see Fig. 3.35).

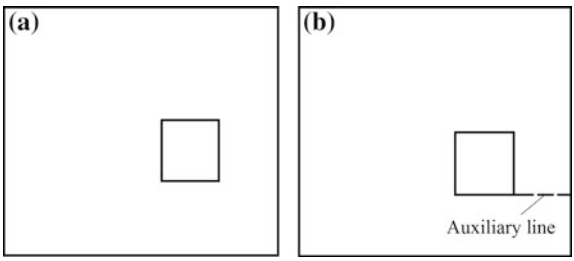

Fig. 3.34 Auxiliary line treatment. **a** Multiply connected domain; **b** simply connected domain

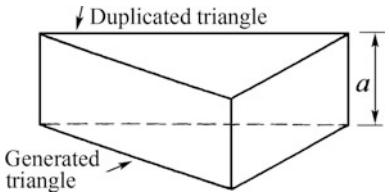

Fig. 3.35 Creation of triangular prism element by the duplication of a triangle

3.5.3 *Tetrahedral Mesh Generation*

After the input of background mesh and new mesh density data, the tetrahedral mesh generation using the AFT is carried out as follows (Nguyen-Van-Phai 1982; Peraire et al. 1992; Weatherill and Hassan 1994; Moller and Hansbo 1995).

① Triangulate each boundary surface using the two-dimensional AFT, all the triangular elements are organized to build the active front.
② Select a tentative triangle face (see Fig. 3.36) ΔABC from the active front for the purpose of new tetrahedral element generation.
③ From the background mesh the new tetrahedral element size h at mid-point E (see Fig. 3.36) is found.

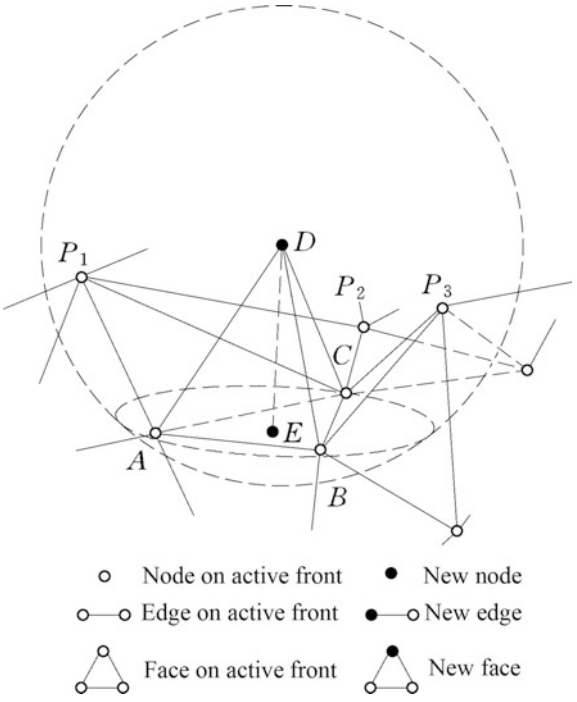

Fig. 3.36 Diagram to the generation of tetrahedral element mesh

④ Determine the coordinates of tentative node D (see Fig. 3.36) as the fourth node of the tentative tetrahedral element. Node D lies in the normal to the face of ΔABC through point E, and is approximately at a distance of h from each node of ΔABC, i.e. $|AD| \approx |BD| \approx |CD| \approx h$.

⑤ Check the validity of tentative tetrahedron $ABCD$ known as the "auxiliary test" that

- The angles between the active face and new faces are sufficiently large;
- The new faces do not intersect any of the existing faces on the active front.

⑥ If node D passes the auxiliary test, it forms a valid new tetrahedron and the process goes to the next step ⑦; otherwise, it is discarded and the process returns to step ④; if the point set of D is empty, the process goes to the step ⑧.

⑦ Once a new element has been generated the linked list forming the active front must be updated that

- New faces created during the generation of the new element are added into the list as active;
- Face ΔABC must be deleted from the active front.

⑧ Steps ①–⑦ is recurred until the active front is empty.

For more detailed algorithm with regard to geometry search and intersection, the readers are referred to Bonet and Peraire (1991), Peraire et al. (1992), Löhner (1988).

3.5.4 Tetrahedral Mesh Improvement

Algorithms for unstructured mesh improvement fall into three basic categories (Lo 1997; Lori and Carl 1997; Ito and Nakahashi 2004): point insertion/deletion to refine a mesh or to improve the local length scale of the mesh; local reconnection to change mesh topology by face or edge swapping for a given set of vertices; and smoothing operation to relocate mesh nodes to improve mesh quality without changing mesh topology. In general the latter two are conducted alternatively to achieve the desirable mesh optimization.

The frequently used configuration parameters of a tetrahedral element are the minimum solid angle θ, the radius ratio ρ of inscribed sphere to circumscribed sphere, and the parameter γ (Lo 1997).

For a tetrahedron $T(P_1P_2P_3P_4)$, denote l_{ij} as the length linking its vortices P_i and P_j, V as its volume, then the minimum solid angle θ is calculated by

$$\theta = \min(\theta_1, \theta_2, \theta_3, \theta_4) \tag{3.49}$$

In which

$$\sin\left(\frac{\theta_1}{2}\right) = \frac{12V}{\sqrt{\prod_{2 \le i \le j \le 4}\left[\left(l_{1i} + l_{1j}\right)^2 - l_{ij}^2\right]}} \tag{3.50}$$

Equation (3.50) is recurred for θ_2, θ_3, θ_4.

Radius ratio ρ of inscribed sphere to circumscribed sphere is defined as

$$\rho = \frac{3r}{R} \tag{3.51}$$

where r = radius of inscribed sphere, m; R = radius of circumscribed sphere, m.

γ parameter is calculated by the formula

$$\gamma = \frac{2\sqrt{3}V}{\left(\sum_{1 \le i < j \le 4} l_{ij}^2\right)^{1.5}} \tag{3.52}$$

Above parameters are actually correlated and any of them may be employed as an element quality index Q.

(1) Local mesh reconfiguration

Local mesh reconfiguration changes the connectivity of a part of mesh to improve mesh quality. It can be divided into two classes as face swapping and edge swapping (Lori and Carl 1997).

Face swapping reconnects two tetrahedral elements comprising five nodes and separated by a single interior face. A large number of non-overlapping tetrahedral configurations are possible with these five nodes, but only two can be legally reconnected, which enables a quick comparisons to find one with the higher quality.

Edge swapping reconfigures m tetrahedral elements incident on an edge through removing that edge to substitute the original m tetrahedral elements by new $2m - 4$ tetrahedral elements. The reconfiguration is performed only if every new tetrahedron exhibits better quality than the worst of m original tetrahedral elements. The effectiveness of edge swapping will be undermined dramatically following the increase of m (e.g. $m \ge 7$).

(2) Overall mesh smoothing

The most common approaches to mesh improvement are variants on Laplacian smoothing (Field 1988). This technique adjusts the location of each mesh node to the arithmetic mean (X_a, Y_a, Z_a) of its incident vertices. Let k vertices (nodes)

$(P_1, P_2, \ldots, P_k)$ be edge-incident to the vertex E_a. Laplacian smoothing defines new coordinates $\left(X_a^*, Y_a^*, Z_a^*\right)$ by the formulas

$$\begin{cases} X_a^* = \frac{\sum_{i \in k} X_i}{k} \\ Y_a^* = \frac{\sum_{i \in k} Y_i}{k} \\ Z_a^* = \frac{\sum_{i \in k} Z_i}{k} \end{cases} \tag{3.53}$$

In which X_i, Y_i, Z_i are spatial coordinates of each edge-incident vertex.

The new coordinates $\left(X_a^*, Y_a^*, Z_a^*\right)$ are immediately used for all subsequent Laplacian smoothing of other vertices.

Further improved algorithm seeks to maximize the minimum value of the mesh quality index Q in an overall (n dimensional) space. Suppose there are m elements in the mesh, the differentiable Q_{tol} may be defined as

$$Q_{tol} = \left(\prod_{i=1}^{m} Q_i \right)^{\frac{1}{m}} \tag{3.54}$$

It also may be defined as

$$Q_{tol} = \min Q_i \tag{3.55}$$

Since in the FE computation one highly distorted element solely may sufficiently give rise to very poor solution accuracy and high computation difficulty, Eq. (3.55) is more advisable and the interest of the smoother is directed to the maximum of function f

$$f = Q_{tol} = \min Q_i \tag{3.56}$$

For additional information on the solution of Eq. (3.56) using optimization process, readers are referred to the works of Polak (1987), Zavattieri et al. (1996).

3.5.5 *Hexahedral Mesh Generation*

The success of grid generation in two-dimensional domain by combining two triangles into one quadrilateral element naturally encourages researchers to find a similar way to recombine tetrahedral elements into hexahedron. One of the famous algorithms is named after Yamakawa and Shimada (2003), in which candidate hexahedral elements are stored in an array and sorted with respect to their geometrical quality. The algorithm then iterates through this array starting from the highest quality hexahedron. Hexahedral elements that are composed of available

tetrahedral elements and that preserve hexahedral conformity are successively added to the mesh.

Unfortunately, it is very complicated and difficult to guarantee the quality of full-hexahedral mesh or even hex-dominant mesh by the AFT (or DT) with recombination strategy (Baudouin et al. 2014). After more than two decades of concentrated research on the full-hexahedral grid generator, none of the methods satisfactorily comply with industrial requirements. Most of the methods lack geometric generality, and all-automatic methods are also very rare. Nowadays, the difficulty in producing all-hexahedral meshes leads researchers to develop new/or/hybrid algorithms (Sheffer et al. 1998; Ruiz-Gironés et al. 2012).

An attempt of subdividing a tetrahedron into four hexahedral elements was also proposed (Chen et al. 1998), according to the following rigorous routine.

- First, draw four straight lines from the center of the tetrahedron to the centers of its four triangular boundary faces;
- Then draw straight lines from the centers of triangular boundary faces to the middle points of the edge segments, respectively.

It can be proved that such sub-divided four hexahedral elements all have planar boundary faces. However, the perplexity in handle of poor mesh quality still exists (Chen et al. 1998).

Mesh generation, as a process of dividing a continuous physical domain into the grid for further numerical solution, is a crucial step before the FEM could be carried out. Although mesh generation and optimization had made remarkable progress in numerous in-house and/or commercial programs, yet many researchers are still persisting in. The Sandia National Laboratories 25th International Meshing Roundtable was just held in 2016, which reflects the related research history, current outcomes and existing problems.

3.6 Verification Examples

3.6.1 Example 1: Block System Identification

Figure 3.37 shows a valley segment which contains 6 faults, the corresponding block system identified is displayed in Fig. 3.38.

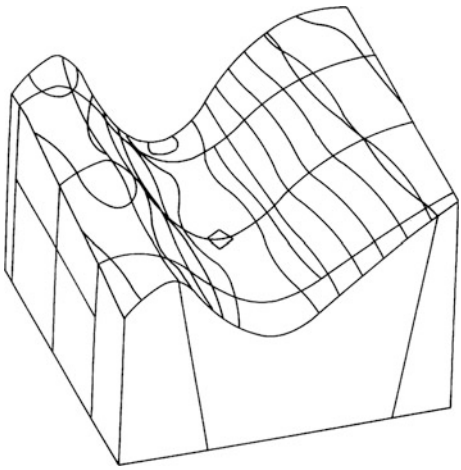

Fig. 3.37 Axonometric drawing of an integrated block system

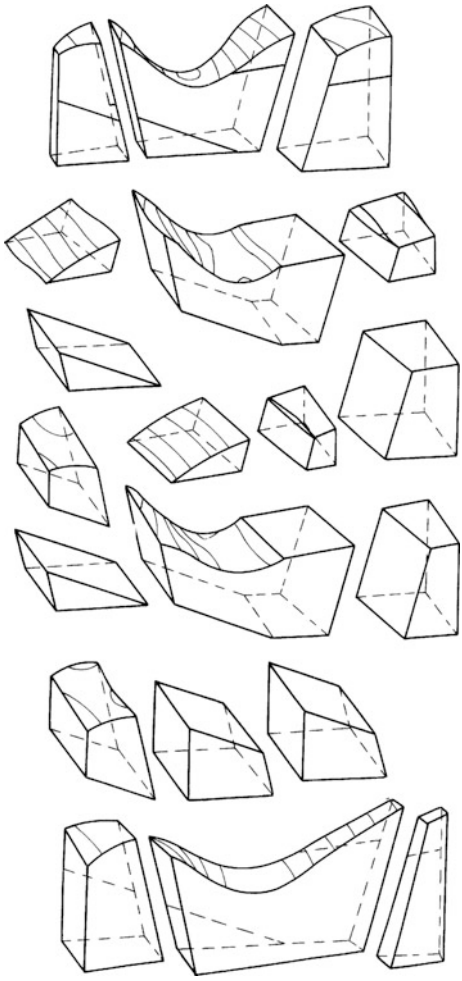

Fig. 3.38 Axonometric drawing of a decomposed blocks

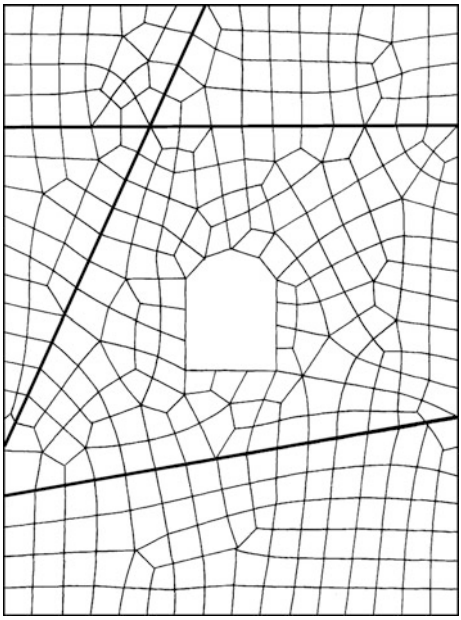

Fig. 3.39 Initial background mesh (375 elements; 421 nodes; e = 27%): two-dimensional cavern

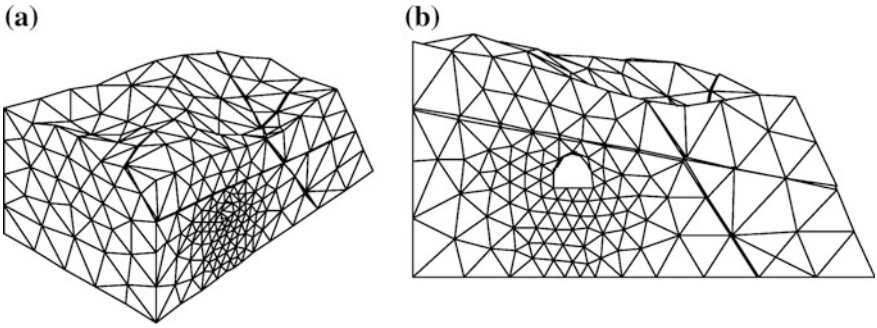

Fig. 3.40 Initial background mesh (6623 elements; 1826 nodes; e = 36%): three-dimensional cavern. **a** Axonometric view; **b** front view

3.6.2 Example 2: Quadrilateral Mesh Generation

For the shallowly embedded underground cavern in Fig. 3.27, if the initial mesh size is uniformly specified as h = 10 m, the mesh generator will output the background mesh in Fig. 3.39 comprising 421 nodes and 375 elements. The energy norm of error (Vide Chap. 5) corresponding to this mesh is e = 27%.

3.6.3 Example 3: Tetrahedral Mesh Generation

The problem being examined is a tunnel segment excavated under a rock slope with two intersected faults and an irregular ground surface. The mesh generator gives the initial background mesh shown in Fig. 3.40, its energy norm of error (Vide Chap. 5) is $e = 36\%$.

References

Anderson BD. Automated all quadrilateral mesh adaptation through refinement and coarsening. Master's thesis, Brigham Young University, Provo; 2009.

Babuška I, Henshaw WD, Oliger JE, Flaherty JE, Hopcroft JE, Tezduyar T. Modeling, mesh generation, and adaptive numerical methods for partial differential equations. New York: Springer; 1995.

Baker TJ. Three dimensional mesh generation by triangulation of arbitrary point sets. In: Proceedings of the AIAA 8th CFD conference. Swansea: Pineridge Press; 1987. p. 255–71.

Batdorf M, Freitag LA, Ollivier-Gooch C. Computational study of the effect of unstructured mesh quality on solution efficiency. In: Proceedings of the 13th annual computational fluid dynamics meeting. Reston: AIAA; 1997.

Baudouin TC, Remacle JF, Marchandise E, Henrotte F, Geuzaine C. A frontal approach to hex-dominant mesh generation. Adv Model Simul Eng Sci. 2014;1:8.

Beall MW, Shephard MS. A general topology-based mesh data structure. Int J Numer Methods Eng. 1997;40(9):1573–96.

Blacker TD, Stephenson MS. Paving: a new approach to automated quadrilateral mesh generation. Int J Numer Methods Eng. 1991;32(4):811–47.

Blacker TD, Stephenson MB, Mitchiner JL, Phillips LR, Lin YT. Automated quadrilateral mesh generation: a knowledge system approach. ASME paper; 1988. 88–WA/CIE–4.

Bonet J, Peraire J. An alternating digital (ADT) algorithm for 3-D geometric searching and intersecting problems. Int J Numer Methods Eng. 1991;31(1):1–17.

Bornhill RE, Little FF. Three and four-dimensional surfaces. Rochy Mt J Math. 1984;14(1): 77–102.

Buell WR, Bush BA. Mesh generation—a survey. J Int Eng Trans ASME. 1973;95(1):332–8 (Ser. B).

Canann SA, Stephenson MB, Blacker TD. Optismoothing: an optimization-driven approach to mesh smoothing. Finite Elem Anal Des. 1993;13(2–3):185–90.

Cao XH, Chen SF, Chen SH. Generation of tetrahedral meshes in 3-D domains by advancing front method. J Wuhan Univ Hydr Elec Eng (WUHEE). 1998;31(1):16–20 (in Chinese).

Cass RJ, Benzley SE, Meyers RJ, Blacker TD. Generalized 3D paving: an automated quadrilateral surface mesh generation algorithm. Int J Numer Methods Eng. 1996;39(9):1475–89.

Chen SH. Hydraulic structures. Berlin: Springer; 2015.

Chen SH, Wang JS, Zhang JL. Adaptive elasto-viscoplastic FEM analysis for hydraulic structures. J Hydraulic Eng. 1996;27(2):68–75 (in Chinese).

Chen SF, Chen SH, Cao XH. Automatic generation of unstructured hexahedron mesh for 3D complicated domain. Rock Soil Mech. 1998;19(4):46–51 (in Chinese).

Chen SH, Chen SF, Cao XH. Three dimensional hexahedron mesh generation for rock engineering. In: Yafin SA, (editor). Proceedings of 3rd international conference on advanced computer methods. Moscow: AA Balkema; 2000. p. 203–06.

Cundall PA. Formulation of three-dimensional distinct element model. Part 1. A scheme to detect and represent contacts in system composed of many polyhedral blocks. Int J Rock Mech Min Sci Geomech Abstr. 1988;25(3):107–16.

Dari EA, Buscaglia GC. Mesh optimization: how to obtain good unstructured 3-D finite element meshes with not-so-good mesh generators. Struct Optim. 1994;8(2):181–8.
De Berg M, Cheong O, van Kreveld M, Overmars M. Computational geometry: algorithms and applications. 3rd ed. Berlin: Springer; 2008.
De Cougny HL, Shephard MS. Parallel refinement and coarsening of tetrahedral meshes. Int J Numer Meth Eng. 1999;46(7):1101–25.
Field DA. Laplacian smoothing and Delaunay triangulations. Commun Appl Numer Methods. 1988;4(6):709–12.
George PL, Borouchaki H. Delaunay triangulation and meshing: application to finite elements. Paris: Hermes Science Publications; 1998. p. 230–4.
Gordon WJ. Spline-blended surface interpolation through curve networks. J Math Mech. 1969;18 (1):931–52.
Hansbo P. Generalized laplacian smoothing of unstructured grids. Commun Numer Methods Eng. 1995;11(5):455–64.
Heliot D. Generating a blocky rock mass. Int J Rock Mech Min Sci Geomech Abstr. 1988;25 (3):127–39.
Hermann LR. Laplacian-isoparametric grid generation scheme. J Eng Mech ASCE. 1976;102 (EM5):749–56.
Ho LK. Finite element mesh generation methods: a review and classification. Comp Aided Des. 1988;20(1):27–38.
Ikegawa Y, Hudson JA. A novel automatic identification system for three-dimensional multi-block systems. Eng Comput. 1992;9(2):169–79.
Ito Y, Nakahashi K. Improvements in the reliability and quality of unstructured hybrid mesh generation. Int J Numer Methods Fluids. 2004;45(1):79–108.
Jin H, Tanner RI. Generation of unstructured tetrahedral meshes by advancing front technique. Int J Numer Methods Eng. 1993;36(11):1805–23.
Jin H, Wiberg NE. Two-dimensional mesh generation, adaptive remeshing and refinement. Int J Numer Methods Eng. 1990;29(7):1501–26.
Jing L, Stephansson O. Topological identification of block assemblages for jointed rock masses. Int J Rock Mech Min Sci Geomech Abstr. 1994;31(2):163–72.
Joe B. Construction of three-dimensional improved-quality triangulations using local transformations. J Sci Comput SIAM. 1995;16(6):1292–307.
Kinney P. Clean up: improving quadrilateral finite elements meshes. In: Proceedings of the 6th international meshing roundtable. Park City: Sandia National Laboratories;1997. p. 449–61.
Lau TS, Lo SH. Finite element mesh generation over analytical curved surfaces. Comput Struct. 1996;59(2):301–9.
Lin D, Fairhurst C, Starfield AM. Geometrical identification of three dimensional rock block systems using topological techniques. Int J Rock Mech Min Sci Geomech Abstr. 1987;24 (6):331–8.
Lo SH. A new mesh generation scheme for arbitrary planar domains. Int J Numer Methods Eng. 1985;21(8):1403–26.
Lo SH. Generating quadrilateral elements on plane and over curved surfaces. Comput Struct. 1989;31(3):421–6.
Lo SH. Optimization of tetrahedral meshes based on element shape measures. Comput Struct. 1997;63(5):951–61.
Lober RR, Tautges TJ, Vaughan CT. Parallel paving: an algorithm for generating distributed, adaptive, all-quadrilateral meshes on parallel computers (Sandia report). Park City: Sandia National Laboratories; 1997.
Löhner R. Some useful data structures for the generation of unstructured grids. Commun Appl Numer Methods. 1988;4(1):123–35.
Löhner R. A parallel advancing front grid generation scheme. Int J Numer Methods Eng. 2001;51 (6):663–78.
Löhner R, Parikh P. Generation of three-dimensional unstructured grids by the advancing-front method. Int J Numer Methods Fluids. 1988;8(10):1135–49.

Lori A, Carl O. Tetrahedral mesh improvement using swapping and smoothing. Int J Numer Methods Eng. 1997;40(21):3979–4002.
Merhof D, Grosso R, Tremel U, Greiner G. Anisotropic quadrilateral mesh generation: an indirect approach. Adv Eng Softw. 2007;38(11–12):860–7.
Moller P, Hansbo P. On advancing front mesh generation in three dimensions. Int J Numer Methods Eng. 1995;38(21):3551–69.
Nguyen-Van-Phai. Automatic mesh generation with tetrahedron elements. Int J Numer Methods Eng. 1982;18(2):237–89.
Nordsletten D, Smith NP. Triangulation of p-order parametric surfaces. J Sci Comput. 2008;34 (3):308–35.
Owen SJ. A survey of unstructured mesh generation technology. In: Proceedings of the 7th international meshing roundtable. Dearborn: Sandia National Laboratories;1998. p. 239–67.
Owen SJ, Staten ML, Canann SA, Saigal S. Q-Morph: an indirect approach to advancing front quadrangle meshing. Int J Numer Methods Eng. 1999;44(9):1317–40.
Peraire J, Vahdati M, Morgan K, Zienkiewicz OC. Adaptive remeshing for compressible flow computations. J Comp Phys. 1987;72(2):449–66.
Peraire J, Peiro J, Morgan K. Adaptive remeshing for three-dimensional compressible flow computations. J Comp Phys. 1992;103(2):269–85.
Polak E. On the mathematical foundations of nondifferentiable optimization in engineering design. SIAM Rev. 1987;29(1):21–89.
Prenter PM. Splines and variational methods. New York: Wiley; 1975.
Ruiz-Gironés E, Roca X, Sarrate J. The receding front method applied to hexahedral mesh generation of exterior domains. Eng Comput. 2012;28(4):391–408.
Schroeder WJ, Shepard MS. A combined octree/delauney method for fully automatic 3-D mesh generation. Int J Numer Methods Eng. 1990;29(2):37–55.
Sheffer A, Etzion M, Rappoport A, Bercovier M. Hexahedral mesh generation using the embedded Voronoi graph. In: Proceedings of the 7th international meshing roundtable. Dearborn: Sandia National Laboratories; 1998. p. 347–64.
Shi JY, Cai WL. Visualization in scientific computing: algorithm and system. Beijing: Science Press; 1996 (in Chinese).
Sloan SW, Houlsby GT. An implementation of Watson's algorithm for computing 2-dimensional Delauney triangulations. Adv Eng Softw. 1984;6(4):192–7.
Staten ML, Owen SJ, Blacker TD. Unconstrained paving & plastering: a new idea for all hexahedral mesh generation. In: Hanks BW, editor. Proceedings of the 14th international meshing roundtable. Berlin: Springer; 2005. p. 399–416.
Thacker WC. A brief review of techniques for generating irregular computational grids. Int J Numer Methods Eng. 1980;15(7):1335–41.
Thompson JF, Thomas FC, Mastin CW. Automatic numerical generation of body fitted curvilinear coordinate system for field containing any number of arbitrary two-dimensional bodies. J Com Phys. 1974;15(3):299–319.
Wang WM, Chen SH. Automatic identification method for three-dimensional rock block systems. J Wuhan Univ Hydr Elec Eng (WUHEE). 1998;31(5):51–5 (in Chinese).
Watson DF. Computing the n-dimensional Delaunay tesselation with application to Voronoi polytopes. Comput J. 1981;24(2):167–72.
Weatherill NP, Hassan O. Efficient three-dimensional Delaunay triangulation with automatic point creation and imposed boundary constraints. Int J Numer Methods Eng. 1994;37(12):2005–39.
White DR, Kinney P. Redesign of the paving algorithm—robustness enhancements through element by element meshing. In: Proceedings of the 6th international meshing roundtable. Park City: Sandia National Laboratories; 1997. p. 323–35.
Xia HX, Chen SH. 3-D adaptive FEM in rock slope stability analysis. In: Desai CS et al. editors. Proceedings of the 10th international conference on computer methods and advances in geomechnics. Amsterdam: AA Balkema; 2001. p. 1635–9.
Xu H, Newman TS. An angle-based optimization approach for 2D finite element mesh smoothing. Finite Elem Anal Des. 2006;42(13):1150–64.

Yamakawa S, Shimada K. Fully-automated hex-dominant mesh generation with directionality control via packing rectangular solid cells. Int J Numer Methods Eng. 2003;57(15):2099–129.
Yerry MA, Shepard MS. Automatic 3-dimensional mesh generation by the modified octree technique. Int J Numer Methods Eng. 1984;20(11):1965–90.
Yu ZS, Peng QS, Ma LZ. An algorithm for intersection between parametric surface and implicit surface. J Comput Aided Des Comput Graph. 1999;11(2):97–9.
Zavattieri P, Dari EA, Buscaglia GC. Optimization strategies in unstructured mesh generation. Int J Numer Methods Eng. 1996;39(12):2055–71.
Zhu JZ, Zienkiewicz OC, Hinton E, Wu J. A new approach to the development of automatic quadrilateral mesh generation. Int J Numer Methods Eng. 1991;32(4):849–66.
Zienkiewicz OC, Phillips DV. An automatic mesh generation scheme for plane and curved surfaces by isoparametric coordinates. Int J Numer Methods Eng. 1971;3(3):519–28.
Zienkiewicz OC, Zhu JZ. Adaptive and mesh generation. Int J Numer Methods Eng. 1991;32 (4):783–810.
Zienkiewicz OC, Taylor RL, Zhu JZ. The finite element method—its basis & fundamentals. 6th ed. Oxford: Elsevier Butterworth-Heinemann; 2005.

Chapter 4
Fundamentals of the Finite Element Method

Abstract This chapter summarizes the principles, governing equations, and basic algorithms related to the finite element method (FEM), which has been the most general and powerful computation tool in the engineering design and analysis since the later 1960s. The "standard" and "hierarchical" shape functions using orthogonal polynomial series are elucidated in details, based on which the algorithms with regard to the fields of permeability, temperature, and deformation are elaborated. The solution techniques particularly important for hydraulic structures related to the issues of rock EDZ, phreatic surface, concrete hydration heating, reservoir water temperature, dynamic response, are addressed. This chapter is closed with the discussion on the safety criteria of hydraulic structures.

4.1 General

The finite element method (FEM) was initiated in a seminal work of Richard Courant (1943), and might be further traced back to the works by Hrennikoff (1941), but the relevance of their works was not recognized at the time until the early 1950s, when the method was rediscovered by engineers for solving complex elasticity and structure problems in civil and aeronautical engineering (Turner et al. 1956). Although the approaches proposed by these pioneers are different, yet they share one essential feature: mesh generation for a continuum domain into a set of discrete sub-domains, usually termed as "elements". The FEM obtained its real impetus in the 1960s (Argyris and Kelsey 1960). The term "finite element method" appeared firstly in a paper on the structural analysis by Clough (1960). Zienkiewicz and his co-workers (Zienkiewicz and Cheung 1964; Zienkiewicz et al. 1966, 1970; Zienkiewicz and Taylor 1967; Hinton and Irons 1968) and other outstanding scholars in the world gathered those works systematically and built the pioneering mathematical formalism of the FEM. Since then the FEM has been developed into one of the most general and powerful computational techniques towards the numerical solution of PDEs, and has been widely exercised in the engineering design and analysis.

S.-H. Chen, *Computational Geomechanics and Hydraulic Structures*,
Springer Tracts in Civil Engineering, https://doi.org/10.1007/978-981-10-8135-4_4

The FEM has been the prevalent computation tool in hydraulic structures for nearly 40 years. Solutions to even very complicated field problems of temperature, permeability, as well as strain/stress, now may be accessed routinely using the method. In this chapter, the concepts, principles, and basic algorithms will be expositorily summarized and according to various literatures (Owen et al. 1989; Babuška et al. 1995; Crisfield 1997; Wilson 1998; Zhu 1998; Clough and Penzien 2003; Zienkiewicz et al. 2005, 2013; Oden 2006), for the purpose to unfold the hereinafter chapters of this book.

4.2 Shape Functions and Interpolations

After the creation of FE mesh for a specified hydraulic structure as has been elaborated in Chap. 3, basic unknown state variables such as displacements [or temperatures, hydraulic potentials (water heads)] will be defined at the nodal points. A set of shape (also called basis) functions is chosen on reference elements to uniquely interpolate the nodal state variables onto the mapped elements of the mesh and its boundaries. To determine a one-to-one correspondence between the Cartesian coordinates in a reference element and the curvilinear coordinates in the real world element, the so-called isoparametric element is customarily employed which conducts coordinate mapping (transforming) between the reference element and stretched/distorted real world element. With the help of the principles of virtual work (or functional variation), an equation set of equivalent nodal forces (or fluxes) equilibrated by the boundary loads (or fluxes) is established, which may be algebraically solved to provide the basic state variables bound at the nodes. These solved basic state variables are further employed to calculate their gradient related variables such as strain/stress, seepage gradient, flow rate, temperature gradient, etc. (Babuška et al. 1995).

Traditional nodal shape (basis) functions of C_0 continuity as "standard" ones are prevalent in the most FE algorithms, which possess a well known property termed as "partition of unity" that each nodal shape function is equal to 1 at its binding node whereas at the other nodes it is equal to 0, and the summation of all the nodal shape functions is equal to 1.

A serious drawback exists, however, with these standard basis functions, when the element order is updated, the new shape functions have to be regenerated totally and hence all the calculations are repeated. It would be attractive to avoid this drawback by constructing the state variable interpolation as a series in which the nodal shape functions do not depend on the number of nodes in the element. This idea gives rise to "hierarchical" shape functions (Babuška et al. 1981).

4.2.1 One-Dimensional Elements

(1) Standard and hierarchical basis functions

Take the bar element illustrated in Fig. 4.1 for example. The traditional one-dimensional element of C_0 continuity entails the displacement interpolation along the bar by

$$u = N_1 u_1 + N_2 u_2 \tag{4.1}$$

In which the standard shape (basis) functions are

$$\begin{cases} N_1 = \varphi_1 = -\dfrac{1}{2}(\xi - 1) \\ N_2 = \varphi_2 = \dfrac{1}{2}(\xi + 1) \end{cases} \tag{4.2}$$

The normalized (parametric, simplex) coordinate ξ is a dimensionless geometrical variable with its origin at the middle of the element (see Fig. 4.1) and is calculated by the formula

$$\xi = \frac{2x - x_2 - x_1}{x_2 - x_1} \tag{4.3}$$

where x_1 = global coordinate of the left end; x_2 = global coordinate of the right end.

A progressively increasing number of nodes will improve the interpolation accuracy. To generate a set of standard shape functions using the polynomial of the 2nd order for the purpose of higher order interpolation, we can write

$$u = N_1 u_1 + N_2 u_2 + N_3 u_3 \tag{4.4}$$

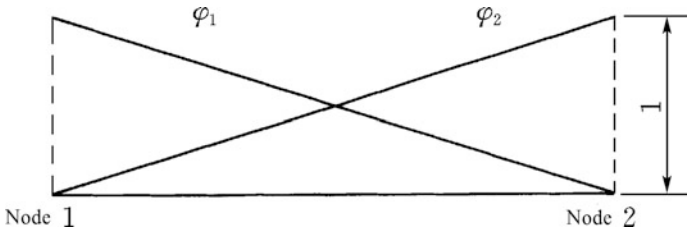

Fig. 4.1 One-dimensional element and basis functions

In which

$$\begin{cases} N_1 = \dfrac{1}{2}\xi(\xi - 1) \\ N_2 = \dfrac{1}{2}\xi(\xi + 1) \\ N_3 = \dfrac{1}{2}(1 - \xi)(1 + \xi) \end{cases} \tag{4.5}$$

u_1, u_2 and u_3 are exactly the nodal state variables, namely, the nodal displacements bound at the left end, right end and middle point. The standard shape functions N_1, N_2 and N_3 defined by the normalized coordinate ξ possess the property of the Lagrange interpolation, i.e. at the binding node it is equal to 1 whereas at the other points it is equal to 0, and the summation of all the shape functions is equal to 1. Compare Eq. (4.2) with Eq. (4.5) it is clear that the shape functions of different order will not be overlapped at all, this will result in the unpleasant consequence that the stiffness matrix of a lower order element is not the sub-matrix of the higher order ones. For a fixed mesh, if we try to use higher order element to improve the computation accuracy, the whole computation procedure should be re-started from the beginning, which results in low computation efficiency.

The hierarchical concept may also be well illustrated by the bar problem in Fig. 4.1. It keeps the linear interpolation Eq. (4.1) unchanged using the standard shape functions N_1 and N_2 defined in Eq. (4.2), meanwhile adds a polynomial basis function Φ_3 always so designed as to have zero values at the bar ends. The corresponding quadratic (2nd-order) interpolation is now in the form of

$$u = N_1\hat{u}_1 + N_2\hat{u}_2 + \Phi_3\hat{u}_3 \tag{4.6}$$

In which

$$\Phi_3 = (1 + \xi)(1 - \xi) \tag{4.7}$$

Contrast Eqs. (4.4) and (4.5) with Eqs. (4.6) and (4.7), the new state variables $\hat{u}_1$, $\hat{u}_2$, $\hat{u}_3$ may be expressed by

$$\begin{cases} \hat{u}_1 = u_1 \\ \hat{u}_2 = u_2 \\ \hat{u}_3 = u_3 - (u_1 + u_2)/2 \end{cases} \tag{4.8}$$

These new state variables are now not the explicit nodal ones (e.g. local displacements). In addition, the traditional properties such as the partition unity of shape functions, are no longer held. However, the final solution is identical because the interpolation of u within the bar element is unchanged.

As we have already noted, the above basis function Φ_3 is not obligated to be uniquely defined as $(1 - \xi^2)$, and many other possibilities exist in the quadratic expression subject to the null value restraint at both the ends of the bar element.

For a cubic (3rd-order) element, we further add an item related to Φ_4 to the quadratic expansion Eq. (4.6) where Φ_4 is any cubic (3rd-order) polynomial which is null at $\xi = \pm 1$ (i.e. at nodes 1 and 2). Again, a selective polynomial set is available. For example, we can write

$$\Phi_4 = \xi\left(1 - \xi^2\right) \tag{4.9}$$

The coordinate mapping (transforming) between the reference element and real world element holds by the standard shape functions identical to Eqs. (4.1)–(4.5).

Following a similar manner, we can define the much higher-order hierarchical element by adding the basis function series

$$\begin{cases} \Phi_5 = \xi^2\left(1 - \xi^2\right) \\ \Phi_6 = \xi^3\left(1 - \xi^2\right) \\ \qquad\qquad \cdots \end{cases} \tag{4.10}$$

As we have already emphasized that, the above polynomial set is not unique and many other possibilities exist. For example, an alternative series of the hierarchical basis functions may be conveniently built as

$$\Phi_p = \begin{cases} \frac{1}{(p-1)!}\left(\xi^{p-1} - 1\right) & (p = 3, 5, \ldots) \\ \frac{1}{(p-1)!}\left(\xi^{p-1} - \xi\right) & (p = 4, 6, \ldots) \end{cases} \tag{4.11}$$

Use is made of orthogonal polynomial series, a much better choice of hierarchical basis functions may be achieved to profit from their advantage that the stiffness matrix obtained is nearly diagonal and hence better matrix condition is implied (Babuška et al. 1989; Webb and Abouchacra 1995; Chilton and Suri 1997; Cheng and Chen 1999).

(2) Shape functions using orthogonal polynomials

1. Legendre polynomials

$$\Phi_p = \int_{-1}^{\xi} P_{p-2}(x)dx \quad (p = 3, 4, \ldots) \tag{4.12}$$

In which P_p is the p-order normalized Legendre polynomial

$$P_p(x) = \sqrt{\frac{2p+1}{2}} \frac{1}{2^{p-1}(p-1)!} \frac{d^p}{dx^p}\left(x^2-1\right)^p \tag{4.13}$$

The front items of Eq. (4.12) may be specified as follows

$$\begin{cases} \Phi_3 = \sqrt{\frac{3}{2}} \times \frac{1}{2}\left(\xi^2-1\right) \\ \Phi_4 = \sqrt{\frac{5}{2}} \times \frac{1}{2}\left(\xi^3-\xi\right) \\ \Phi_5 = \sqrt{\frac{7}{2}} \times \frac{1}{8}\left(5\xi^4-6\xi^2+1\right) \\ \Phi_6 = \sqrt{\frac{9}{2}} \times \frac{1}{8}\left(7\xi^5-10\xi^3+3\xi\right) \\ \Phi_7 = \sqrt{\frac{11}{2}} \times \frac{1}{16}\left(21\xi^6-35\xi^4+15\xi^2-1\right) \end{cases} \tag{4.14}$$

The corresponding functional curves are plotted in Fig. 4.2.

2. Jacobian polynomials

$$\Phi_p = (\xi^2-1)J_{p-3}^{(2,2)}(\xi) \quad (p=3,4,\ldots) \tag{4.15}$$

In which $J_p^{(2,2)}(x)$ is the Jacobian (2,2) orthogonal polynomial series of p-order

$$J_p^{(2,2)}(x) = \frac{1}{2^p p!} \cdot \frac{1}{(1-x)^2(1+x)^2} \cdot \frac{d^p}{dx^p}\left[(1-x)^2(1+x)^2\left(x^2-1\right)^p\right] \tag{4.16}$$

The front items of Eq. (4.15) are specified as follows

$$\begin{cases} \Phi_3 = \xi^2-1 \\ \Phi_4 = 3\xi^3-3\xi \\ \Phi_5 = 7\xi^4-8\xi^2+1 \\ \Phi_6 = 15\xi^5-20\xi^3+5\xi \\ \Phi_7 = \frac{15}{16}\left(33\xi^6-51\xi^4+19\xi^2+1\right) \end{cases} \tag{4.17}$$

The functional curves of the Jacobian polynomials are very similar to that of the Legendre polynomials (see Fig. 4.2).

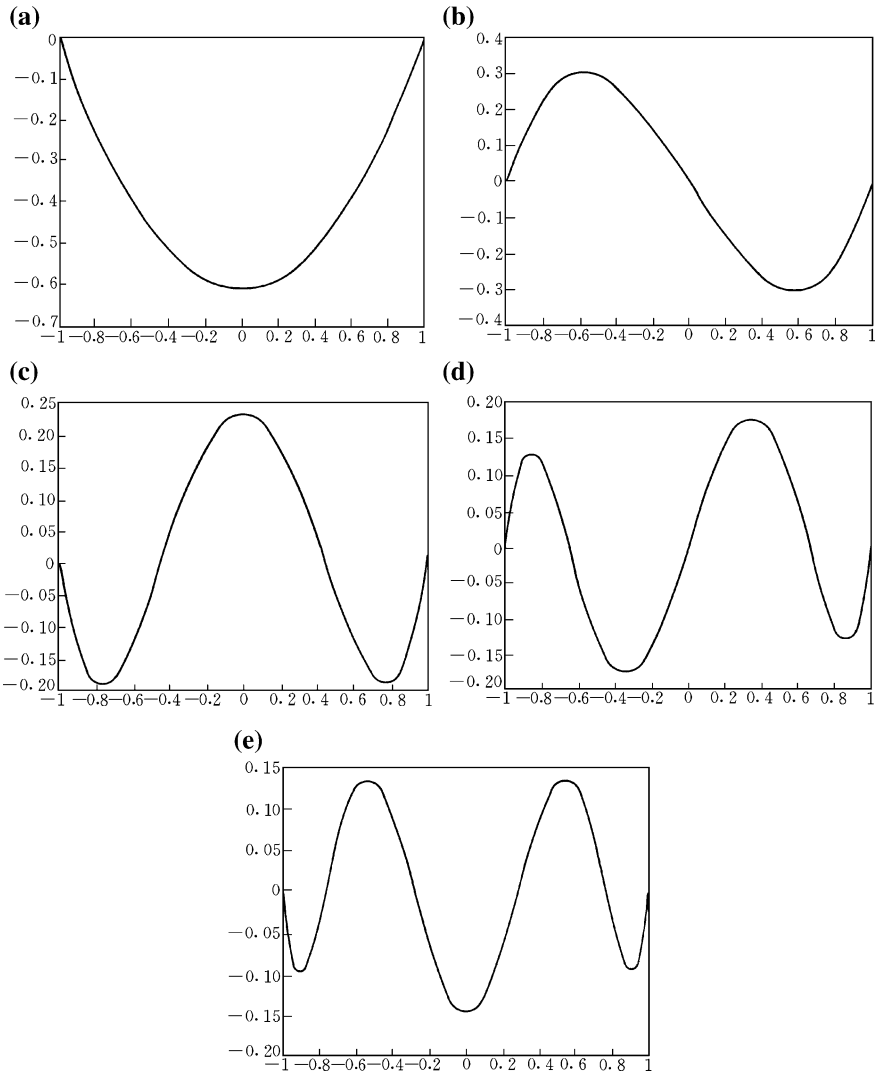

Fig. 4.2 Functional curves of the Legendre polynomials. **a** Φ_3; **b** Φ_4; **c** Φ_5; **d** Φ_6; **e** Φ_7

(3) Merits of orthogonal polynomial series as basis functions

Take the elastic problem of the bar element (see Fig. 4.1) for example, its stiffness matrix is computed by the formula

$$[K] = \int_0^l EA \frac{d[\Phi]^T}{dx} \frac{d[\Phi]}{dx} dx \tag{4.18}$$

Introducing Eqs. (4.2) and (4.14) into Eq. (4.18), we have

$$K = \frac{EA}{l}\begin{bmatrix} 1 & -1 & & & & \\ -1 & 1 & & & & \\ & & 1 & & & \\ & & & 1 & & \\ & & & & \cdot & \\ & & & & & 1 \end{bmatrix} \tag{4.19}$$

In which E, A, l are the Young's modulus, cross sectional area, and length of the bar, respectively.

It is clear that apart from the sub-matrix corresponding to the constant strain, the rest sub-matrix is diagonal, which is important for the purpose of saving computer memory and accelerating computation speed.

In addition, the stiffness matrix employing orthogonal polynomial series exhibits better condition number.

4.2.2 Two-Dimensional Elements

For the two-dimensional FEM, a standard element possesses nodal shape functions associated with its nodes which meet the condition of partition of unity. For hierarchical element two additional groups of shape functions are demanded. An edge shape function is associated with the edge enclosing the element. It is zero at other edges and the two ends of the edge itself. A face shape function is associated with the element itself, and it is zero at all the element edges and other elements.

(1) Triangular elements

1. Standard basis functions

A simplest two-dimensional finite element with triangular configuration is defined by its local nodes 1, 2, 3, and straight edge linking the nodes, as shown in Fig. 4.3. The choice of basic state variables, take the displacements for example, is of

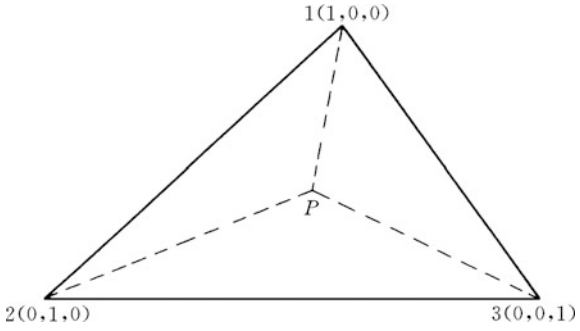

Fig. 4.3 Simplex coordinates of standard triangular element

paramount importance. The normalized coordinates for this element are defined using the element sub-division as simplex coordinates

$$\begin{cases} \xi_1 = \dfrac{S_{P23}}{S_{123}} \\ \xi_2 = \dfrac{S_{1P3}}{S_{123}} \\ \xi_3 = \dfrac{S_{12P}}{S_{123}} \end{cases} \tag{4.20}$$

It is obvious that ξ_1, ξ_2 and ξ_3 are defined within [0,1], and $\xi_1 + \xi_2 + \xi_3 = 1$.

Similar to the one-dimensional case, the traditional standard basis functions are employed to formulate nodal shape functions

$$N_i = \xi_i \quad (i = 1, 2, 3) \tag{4.21}$$

2. Hierarchical basis functions

Conventional polynomial sets may be employed to construct additional basis functions for the hierarchical element, if necessary.

– Edge basis functions

$$\begin{cases} E_{p(1-2)} = \begin{cases} \frac{1}{p!}\left[(\xi_2 - \xi_1)^p - (\xi_1 + \xi_2)^p\right] & (p = 2, 4, 6, \ldots) \\ \frac{1}{p!}\left[(\xi_2 - \xi_1)^p - (\xi_2 - \xi_1)(\xi_1 + \xi_2)^{p-1}\right] & (p = 3, 5, 7, \ldots) \end{cases} \\ E_{p(2-3)} = \begin{cases} \frac{1}{p!}\left[(\xi_3 - \xi_2)^p - (\xi_2 + \xi_3)^p\right] & (p = 2, 4, 6, \ldots) \\ \frac{1}{p!}\left[(\xi_3 - \xi_2)^p - (\xi_2 - \xi_3)(\xi_2 + \xi_3)^{p-1}\right] & (p = 3, 5, 7, \ldots) \end{cases} \\ E_{p(3-1)} = \begin{cases} \frac{1}{p!}\left[(\xi_1 - \xi_3)^p - (\xi_3 + \xi_1)^p\right] & (p = 2, 4, 6, \ldots) \\ \frac{1}{p!}\left[(\xi_1 - \xi_3)^p - (\xi_1 - \xi_3)(\xi_3 + \xi_1)^{p-1}\right] & (p = 3, 5, 7, \ldots) \end{cases} \end{cases} \tag{4.22}$$

– Face basis functions

$$F_p = \xi_1^i \xi_2^j \xi_3^k \quad (i + j + k = p; \quad i, j, k \geq 1) \tag{4.23}$$

If the orthogonal polynomial sets (e.g. the Jacobian) are employed, then we have

① Nodal basis functions where ($p \geq 1$)

$$N_i = \xi_i \quad (i = 1, 2, 3) \tag{4.24}$$

② Edge basis functions where ($p \geq 2$)

$$E_i(\alpha, \beta) = \alpha\beta J_{i-1}^{(2,2)}(\beta - \alpha) \quad (\alpha \neq \beta; \quad \alpha, \beta = \xi_1, \xi_2, \xi_3) \tag{4.25}$$

The orthogonal condition profitable in such a hierarchical element is

$$\int_0^1 E_i(\xi_k, (1-\xi_k)) E_j(\xi_k, (1-\xi_k)) d\xi_k = \delta_{ij} \frac{i(i+1)}{(i+3)(i+2)(2i+3)} \tag{4.26}$$

③ Face basis functions where ($p \geq 3$)

$$\begin{aligned} F_{pi} &= \xi_1 \xi_2 \xi_3 (1-\xi_3)^v J_i^{(2,2v+5)}(1-2\xi_3) J_v^{(2,2)}\left(\frac{\xi_2 - \xi_1}{1-\xi_3}\right) \\ &\quad (v = p-3-i; \quad i = 0, 1, \ldots p-3) \end{aligned} \tag{4.27}$$

The orthogonal condition profitable in such a hierarchical element is

$$\begin{aligned} \frac{1}{2S} \iint_S F_{pi} F_{qj} dS &= \int_{\xi_3=0}^{1} \int_{\xi_1=0}^{1-\xi_3} F_{pi} F_{qj} d\xi_1 \xi_3 \\ &= \delta_{pq}\delta_{ij} \frac{(v+1)(v+2)(i+1)(i+2)}{(2v+5)(v+4)(v+3)(2v+2i+8)(2v+i+7)(2v+i+6)} \end{aligned} \tag{4.28}$$

The front four items of the face basis functions are specified in Eq. (4.29) and Fig. 4.4.

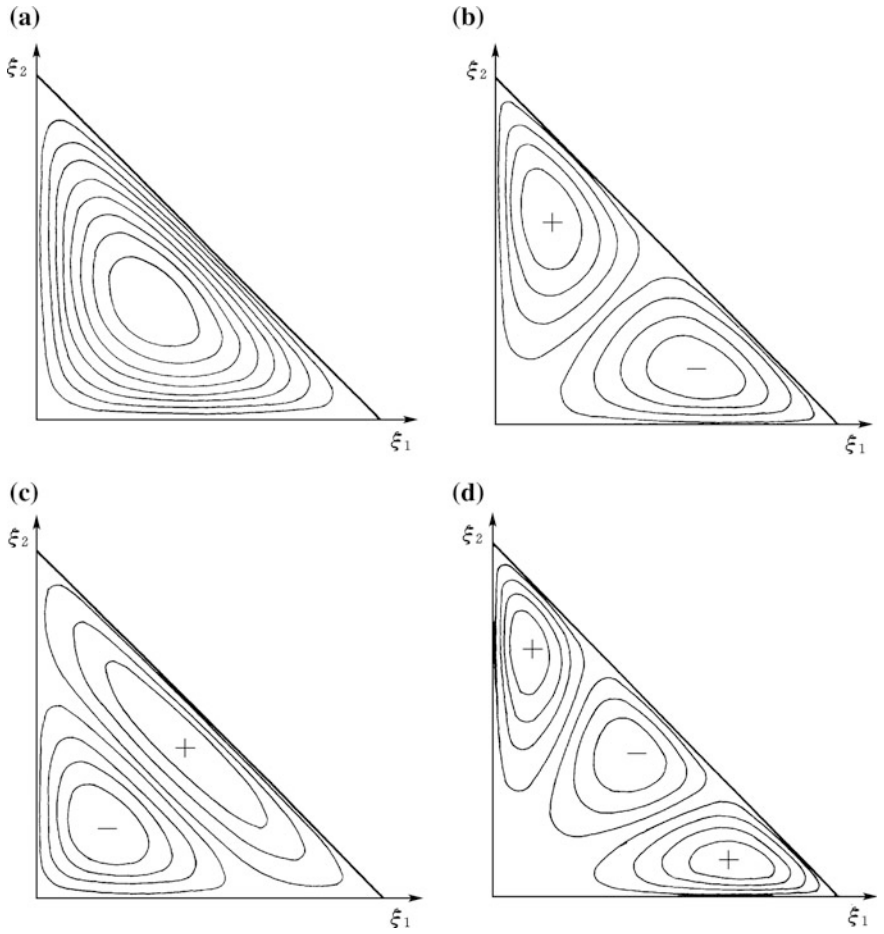

Fig. 4.4 Front four items of the face basis functions constructed with the Jacobian polynomials. **a** F_{30}; **b** F_{40}; **c** F_{41}; **d** F_{50}

$$\begin{cases} F_{30} = \xi_1\xi_2\xi_3 \\ F_{40} = 3\xi_1\xi_2\xi_3(\xi_2 - \xi_1) \\ F_{41} = 3\xi_1\xi_2\xi_3(1 - 3\xi_3) \\ F_{50} = \xi_1\xi_2\xi_3\left(-1 + 2\xi_3 - \xi_3^3 + 7\xi_2^2 - 14\xi_1\xi_2 + 7\xi_1^2\right) \end{cases} \tag{4.29}$$

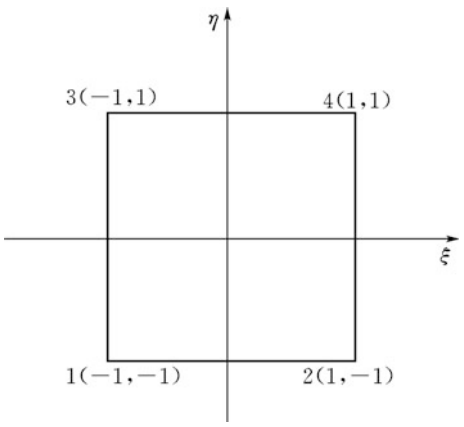

Fig. 4.5 Standard quadrilateral element

(2) Quadrilateral elements

1. Standard basis functions

A standard rectangular element defined by local nodes 1, 2, 3 and 4 is shown in Fig. 4.5. Any quadrilateral may be mapped into this standard element whose standard nodal basis functions are

$$N_i = \frac{1}{4}(1+\xi_0\xi)(1+\eta_0\eta) \quad (i=1,2,3,4) \tag{4.30}$$

In which ξ_0 and η_0 are the normalized coordinates of the node i

$$\begin{cases} \xi_0 = (-1)^i \\ \eta_0 = (-1)^{[i/2+0.5]} \end{cases} \tag{4.31}$$

2. Hierarchical basis functions

The additional basis functions for the hierarchical element are constructed as follows.

① Edge basis functions where ($p \geq 2$)

$$\begin{cases} E^p_{1-2} = \dfrac{1}{4}(1-\eta)\Phi_p(\xi) \\ E^p_{3-4} = \dfrac{1}{4}(1+\eta)\Phi_p(\xi) \\ E^p_{1-3} = \dfrac{1}{4}(1-\xi)\Phi_p(\eta) \\ E^p_{2-4} = \dfrac{1}{4}(1+\xi)\Phi_p(\eta) \end{cases} \tag{4.32}$$

In which Φ_p may be all the hierarchical basis functions available in one-dimensional case.

② Face basis functions where ($p \geq 4$)

$$F^p_{(i,j)} = \Phi_i(\xi)\Phi_j(\eta) \quad (i+j=p; \quad i,j \geq 2) \tag{4.33}$$

The above basis functions actually belong to the Serendipity family. If in lieu of $i + j = p$ we let $i, j \leq p$, they are transferred into the Lagrange family. The basis functions of the Serendipity family comprise fewer members than the Lagrange family, therefore this is advantageous to lower down the computation efforts. The hierarchical function curves of the simplest items for the quadrilateral element are plotted in Fig. 4.6.

4.2.3 Three-Dimensional Elements

For an isoparametric three-dimensional element, traditional standard shape functions are associated with the element nodes, and they meet the requirement on the partition of unity. Towards the hierarchical interpolation, additional three groups of hierarchical basis functions are demanded. An edge shape function is associated with the element edge, which is zero at other edges and the two ends of the edge itself. A face shape function is associated with the element face, which is zero at the four edges enclosing the face and the other faces. A body shape function (also called internal shape function) is associated with the element itself, which is zero on all the element faces.

(1) Tetrahedral elements

1. Standard basis functions

Any tetrahedral may be mapped into the standard element in Fig. 4.7, whose nodal basis functions are expressed in Eqs. (4.34) and (4.35) with the simplex coordinates define by the sub-division.

$$\begin{cases} \xi_1 = \dfrac{V_{P234}}{V_{1234}} \\ \xi_2 = \dfrac{V_{1P34}}{V_{1234}} \\ \xi_3 = \dfrac{V_{12P4}}{V_{1234}} \\ \xi_4 = \dfrac{V_{123P}}{V_{1234}} \end{cases} \tag{4.34}$$

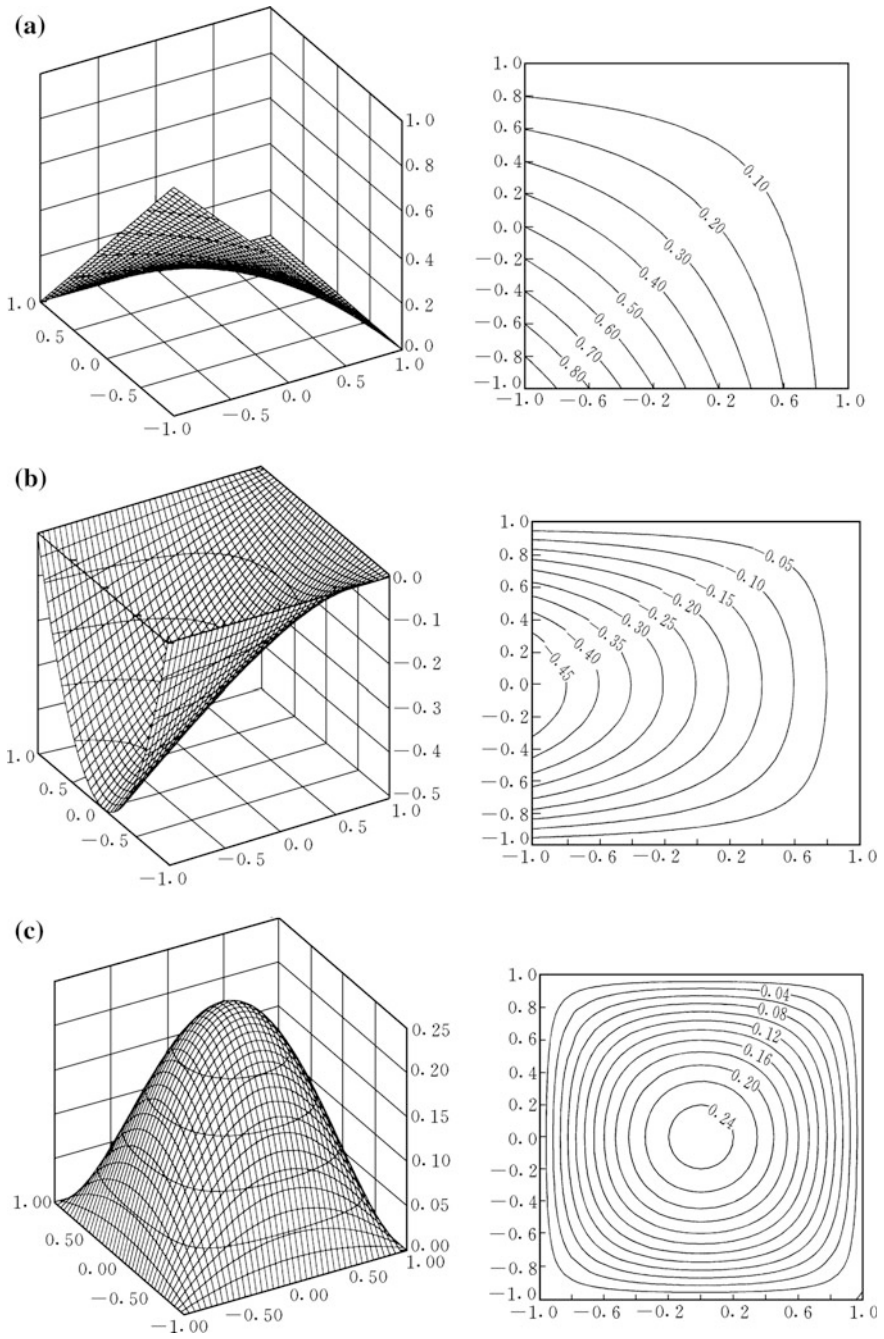

Fig. 4.6 Diagram showing the hierarchical basis functions for quadrilateral element. **a** Nodal function (N_i); **b** edge function $\left(E_i^2\right)$; **c** face function $\left(F_{(2,2)}^4\right)$

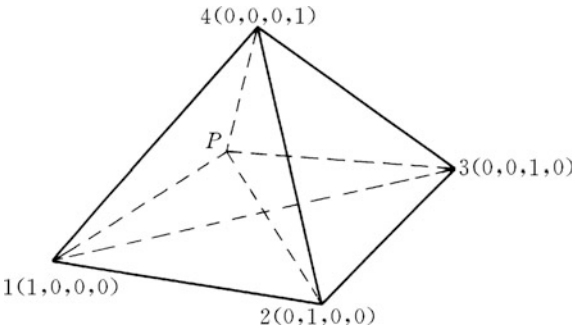

Fig. 4.7 Standard tetrahedral element

$$N_i = \xi_i \quad (i = 1, 2, 3, 4) \tag{4.35}$$

2. Hierarchical basis functions

The additional basis functions particular for the hierarchical element are constructed as follows.

① Basis function for the edge (r, s) where ($p \geq 2$)

$$E^p_{(r,s)} = -2\xi_r\xi_s G_{p-2}(\xi_r, \xi_s) \quad (r, s = 1, 2, 3, 4; r \neq s) \tag{4.36}$$

In which

$$G_m(x, y) = \sum_{i=0}^{m} (-1)^i \frac{1}{i+1} \binom{m}{i} \binom{m+1}{i} x^i y^{m-i} \tag{4.37}$$

The front items of edge functions are specified below

$$\begin{cases} E^2_{(r,s)} = -2\xi_r\xi_s \\ E^3_{(r,s)} = -2\xi_r\xi_s(\xi_r - \xi_s) \\ E^4_{(r,s)} = -2\xi_r\xi_s\left(\xi_s^2 - 3\xi_r\xi_s + \xi_r^2\right) \\ E^5_{(r,s)} = -2\xi_r\xi_s\left(\xi_s^3 - 6\xi_r\xi_s^2 + 6\xi_r^2\xi_s - \xi_r^3\right) \end{cases} \tag{4.38}$$

② Basis functions for the face (r, s, t) where ($p \geq 3$)

$$F^{(\alpha,\beta),t}_{(r,s,t)} = \xi_r\xi_s\xi_t H_{\alpha\beta}(\xi_r, \xi_s) \quad (\alpha + \beta = p - 3) \tag{4.39}$$

In which

$$H_{\alpha\beta}(x,y)=\sum_{i=0}^{\beta}\sum_{j=0}^{\alpha}\left(-\frac{1}{2}\right)^{i+j}i!j!(i+j)!\binom{\alpha}{j}\binom{\alpha+1}{j}\binom{\beta}{i}\binom{\beta+1}{i}\times\frac{1}{\prod_{k=1}^{i+j}[k(\alpha+\beta+2)-k(k-1)/2]}x^{\alpha-j}y^{\beta-i}\tag{4.40}$$

The front items of face functions are specified below

$$\begin{cases}F_{(r,s,t)}^{(0,0),3}=\xi_r\xi_s\xi_t\\ F_{(r,s,t)}^{(1,0),4}=\xi_r\xi_s\xi_t\left(\xi_r-\dfrac{1}{3}\right)\\ F_{(r,s,t)}^{(0,1),4}=\xi_r\xi_s\xi_t\left(\xi_s-\dfrac{1}{3}\right)\end{cases}\tag{4.41}$$

③ Body basis functions where ($p\geq 4$)

$$B^{(\alpha,\beta,\gamma),p}=\xi_1\xi_2\xi_3\xi_4 I_{(\alpha,\beta,\gamma)}(\xi_1,\xi_2,\xi_3)\quad(\alpha+\beta+\gamma=p-4)\tag{4.42}$$

In which

$$I_{(\alpha,\beta,\gamma)}(\xi_r,\xi_s,\xi_t)=\bar{I}_{(\alpha,0,0)}^{(\alpha+\beta+\gamma)}(\xi_r)\times\bar{I}_{(0,\beta,0)}^{(\beta+\gamma)}(\xi_r,\xi_s)\times\bar{I}_{(0,0,\gamma)}^{(\alpha,\beta,\gamma)}(\xi_r,\xi_s,\xi_t)\tag{4.43}$$

and

$$\begin{cases}\bar{I}_{(\alpha,0,0)}^{(m)}(\xi_r)=\sum\limits_{i=0}^{\alpha}(-1)^i i!\binom{\alpha}{i}\binom{\alpha+1}{i}\frac{(2m+5-i)!}{(2m+5)!}\xi_r^{\alpha-i}\\ \bar{I}_{(0,\beta,0)}^{(m)}(\xi_r,\xi_s)=\sum\limits_{i=0}^{\beta}(-1)^i i!\binom{\beta}{i}\binom{\beta+1}{i}\frac{(2m+3-i)!}{(2m+3)!}\xi_s^{\beta-i}(\xi_r-1)^i\\ \bar{I}_{(0,0,\gamma)}^{(m)}(\xi_r,\xi_s,\xi_t)=\sum\limits_{i=0}^{\gamma}i!\binom{\gamma}{i}\binom{\gamma+1}{i}\frac{(2m+1-i)!}{(2m+1)!}\xi_t^{\gamma-i}(\xi_s+\xi_r-1)^i\end{cases}\tag{4.44}$$

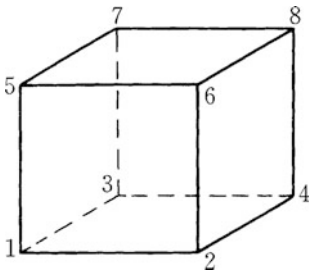

Fig. 4.8 Hexahedral element

The front items of body functions are specified below

$$\begin{cases} B^{(0,0,0),4} = \xi_r\xi_s\xi_t\xi_w \\ B^{(1,0,0),5} = \xi_r\xi_s\xi_t\xi_w\left(\xi_r - \frac{2}{7}\right) \\ B^{(0,1,0),5} = \xi_r\xi_s\xi_t\xi_w\left(\xi_s + \frac{2}{5}(\xi_r - 1)\right) \\ B^{(0,0,0),5} = \xi_r\xi_s\xi_t\xi_w\left(\xi_t + \frac{2}{3}(\xi_s + \xi_r - 1)\right) \end{cases} \tag{4.45}$$

(2) Hexahedral elements

1. Standard basis functions

For the standard hexahedral element illustrated in Fig. 4.8, we have traditional standard nodal shape functions defined as

$$N_i = \frac{1}{8}(1 + \xi_0\xi)(1 + \eta_0\eta)(1 + \zeta_0\zeta) \quad (i = 1, 2, \ldots, 8) \tag{4.46}$$

In which ξ_0, η_0, i are the normalized coordinates of node i

$$\begin{cases} \xi_0 = (-1)^i \\ \eta_0 = (-1)^{[i/2+0.5]} \\ \zeta_0 = (-1)^{[i/4+0.75]} \end{cases} \tag{4.47}$$

2. Hierarchical basis functions

The additional basis functions particular for the hierarchical element are constructed as follows.

① Edge basis element where ($p \geq 2$)

$$\begin{cases} E_1^p = \dfrac{1}{4}(1-\eta)(1-\zeta)\Phi_p(\xi) \\ E_2^p = \dfrac{1}{4}(1+\eta)(1-\zeta)\Phi_p(\xi) \\ E_3^p = \dfrac{1}{4}(1-\eta)(1+\zeta)\Phi_p(\xi) \\ E_4^p = \dfrac{1}{4}(1+\eta)(1+\zeta)\Phi_p(\xi) \\ E_5^p = \dfrac{1}{4}(1-\zeta)(1-\xi)\Phi_p(\eta) \\ E_6^p = \dfrac{1}{4}(1+\zeta)(1-\xi)\Phi_p(\eta) \\ E_7^p = \dfrac{1}{4}(1-\zeta)(1+\xi)\Phi_p(\eta) \\ E_8^p = \dfrac{1}{4}(1+\zeta)(1+\xi)\Phi_p(\eta) \\ E_9^p = \dfrac{1}{4}(1-\xi)(1-\eta)\Phi_p(\zeta) \\ E_{10}^p = \dfrac{1}{4}(1+\xi)(1-\eta)\Phi_p(\zeta) \\ E_{11}^p = \dfrac{1}{4}(1-\xi)(1+\eta)\Phi_p(\zeta) \\ E_{12}^p = \dfrac{1}{4}(1+\xi)(1+\eta)\Phi_p(\zeta) \end{cases} \tag{4.48}$$

In which Φ_p may be any hierarchical basis functions available in one-dimensional case.

② Face basis functions where ($p \geq 4$)

$$\begin{cases} F_1^{p(i,j)} = \dfrac{1}{2}(1-\xi)\Phi_i(\eta)\Phi_j(\zeta) \\ F_2^{p(i,j)} = \dfrac{1}{2}(1+\xi)\Phi_i(\eta)\Phi_j(\zeta) \\ F_3^{p(i,j)} = \dfrac{1}{2}(1-\eta)\Phi_i(\zeta)\Phi_j(\xi) \\ F_4^{p(i,j)} = \dfrac{1}{2}(1+\eta)\Phi_i(\zeta)\Phi_j(\xi) \\ F_5^{p(i,j)} = \dfrac{1}{2}(1-\zeta)\Phi_i(\xi)\Phi_j(\eta) \\ F_6^{p(i,j)} = \dfrac{1}{2}(1+\zeta)\Phi_i(\xi)\Phi_j(\eta) \end{cases} \quad (i,j \geq 2; i+j=p) \tag{4.49}$$

③ Body basis functions where ($p \geq 6$)

$$B^{p(i,j,k)} = \Phi_i(\xi)\Phi_j(\eta)\Phi_k(\zeta) \quad (i,j,k \geq 2; i+j+k=p) \tag{4.50}$$

The above basis functions belong to the Serendipity family. Similar to the two-dimensional case, if in lieu of $i + j = p$ and $i + j + k = p$, we let $i, j \leq p$ for face basis functions and $i, j, k \leq p$ for body basis functions respectively, they are transferred into the Lagrange family.

4.2.4 Generalized Interpolation of State Variables

Use is made of the foregoing basis functions, any basic state variables within an element may be interpolated. Take the displacement u in a hexahedral element for example, we have

$$\begin{aligned} u = &\sum_{i=1}^{8} N_i u_{Ni} + \sum_{p=2}\sum_{k=1}^{12} E_k^p u_{Ek}^p + \sum_{p=4}\sum_{i,j\geq 2}^{i+j=p}\sum_{k=1}^{6} F_k^{p(i,j)} u_{Fk}^{p(i,j)} \\ &+ \sum_{p=6}\sum_{i,j,k\geq 2}^{i+j+k=p} B^{p(i,j,k)} u_B^{p(i,j,k)} \end{aligned} \tag{4.51}$$

In which u_{Ni}, u_{Ek}^p, $u_{Fk}^{p(i,j)}$, and $u_B^{p(i,j,k)}$ are the general displacement variables, respectively corresponding to the nodes, edges, faces and body, of the element.

The right side of Eq. (4.51) may be truncated to leave only the first item merely, in this way the standard isoparametric element of 8 nodes is retrogressed.

If we assemble all the basis functions with respect to nodes, edges, faces, and body into a general shape function set (N_i) of the element e whose correspondent general node number is $f_e(p)$, any physical and mechanical variables, e.g. displacement u, head potential ϕ, and temperature T within the element with normalized coordinates (ξ, η, ζ) may be interpolated using the general nodal variables by the formulas

$$\begin{cases} u = \sum_{i=1}^{f_e(p)} N_i u_i \\ \phi = \sum_{i=1}^{f_e(p)} N_i \phi_i \\ T = \sum_{i=1}^{f_e(p)} N_i T_i \end{cases} \tag{4.52}$$

In the discussion hereinafter with respect to three-dimensional problems, $f_e(p) = 8$ means that the FE algorithm will be formulated using traditional standard isoparametric element of 8 nodes, otherwise the hierarchical technique will be addressed.

4.3 Quasistatic Strain/Stress Problems

4.3.1 Solid Elements

(1) Basic formulation for elasticity

The region concerned is discretized into an assemblage of sub-regions, each of which has its own approximating functions termed as basis or shape functions. Take the isoparametric hexahedral element e with 8 nodes (see Fig. 4.8) for instance. At time t, we denote the nodal displacement increment $\{\Delta\delta\}_t$ and the interior displacement increment $\{\Delta u\}_t$ as

$$\{\Delta\delta\}_t = \left[\begin{array}{ccccccc} \Delta u_{x1} & \Delta u_{y1} & \Delta u_{z1} & \cdots & \Delta u_{xf_e(p)} & \Delta u_{yf_e(p)} & \Delta u_{zf_e(p)} \end{array}\right]^T \quad (\text{for } p = 1, f_e(p) = 8) \tag{4.53}$$

and

$$\{\Delta u\}_t = [\Delta u_x \quad \Delta u_y \quad \Delta u_z]^T \tag{4.54}$$

where t is the time at the end of the nth time marching step.

There also exists nodal force increment

$$\{\Delta f\} = \left[\begin{array}{ccccccc} \Delta f_{x1} & \Delta f_{y1} & \Delta f_{z1} & \cdots & \Delta f_{xf_e(p)} & \Delta f_{yf_e(p)} & \Delta f_{zf_e(p)} \end{array}\right]^T \quad (\text{for } p = 1, f_e(p) = 8) \tag{4.55}$$

The approximation for the displacement within an element is an interpolation of the nodal displacements (as yet unknown) via shape functions.

$$\{\Delta u\}_t = [N]\{\Delta\delta\}_t \tag{4.56}$$

In which $[N]$ is termed as the "shape function matrix"

$$[N] = \left\lfloor N_1[I] \quad N_2[I] \quad \cdots \quad N_{f_e(p)}[I] \right\rfloor \quad (\text{for } p = 1, f_e(p) = 8) \tag{4.57}$$

where $[I]$ stands for 3×3 unit matrix.

For small deformation problems, we have

$$\begin{cases} \Delta\varepsilon_x = \partial\Delta u_x/\partial x \\ \Delta\varepsilon_y = \partial\Delta u_y/\partial y \\ \Delta\varepsilon_z = \partial\Delta u_z/\partial z \\ \Delta\gamma_{yz} = \partial\Delta u_z/\partial y + \partial\Delta u_y/\partial z \\ \Delta\gamma_{zx} = \partial\Delta u_x/\partial z + \partial\Delta u_z/\partial x \\ \Delta\gamma_{xy} = \partial\Delta u_y/\partial x + \partial\Delta u_x/\partial y \end{cases} \tag{4.58}$$

Inserting Eq. (4.56) into Eq. (4.58) leads to

$$\{\Delta\varepsilon\}_t = [B]\ \{\Delta\delta\}_t \tag{4.59}$$

In which $[B]$ is termed as the "strain matrix"

$$[B] = [[B_1] \quad [B_2] \quad \ldots \quad [B_{f_e(p)}]] \quad (\text{for } p = 1, f_e(p) = 8) \tag{4.60}$$

$$[B_i] = \begin{bmatrix} \frac{\partial N_i}{\partial x} & 0 & 0 \\ 0 & \frac{\partial N_i}{\partial y} & 0 \\ 0 & 0 & \frac{\partial N_i}{\partial z} \\ 0 & \frac{\partial N_i}{\partial z} & \frac{\partial N_i}{\partial y} \\ \frac{\partial N_i}{\partial z} & 0 & \frac{\partial N_i}{\partial x} \\ \frac{\partial N_i}{\partial y} & \frac{\partial N_i}{\partial x} & 0 \end{bmatrix} \tag{4.61}$$

According to the Hooke's law we have elastic constitutive relation

$$\{\Delta\sigma\}_t = [D]\ \{\Delta\varepsilon\}_t \tag{4.62}$$

In which $\{\Delta\sigma\}_t = \begin{bmatrix} \Delta\sigma_x & \Delta\sigma_y & \Delta\sigma_z & \Delta\tau_{yz} & \Delta\tau_{zx} & \Delta\tau_{xy} \end{bmatrix}_t^T$ is the stress incremental vector, $\{\Delta\varepsilon\}_t = \begin{bmatrix} \Delta\varepsilon_x & \Delta\varepsilon_y & \Delta\varepsilon_z & \Delta\gamma_{yz} & \Delta\gamma_{zx} & \Delta\gamma_{xy} \end{bmatrix}_t^T$ is the strain incremental vector, $[D]$ is the elastic matrix.

Inserting Eq. (4.59) into Eq. (4.62) gives rise to

$$\{\Delta\sigma\}_t = [S]\{\Delta\delta\}_t \tag{4.63}$$

In which $[S]$ is termed as the "stress matrix"

$$[S] = [D][B] \tag{4.64}$$

Suppose a small, virtual displacement $\{\Delta\delta^*\}_t$ occurs to the element e, it in turn produces a virtual strain $\{\Delta\varepsilon^*\}_t$ according to Eq. (4.59), then the virtual work principle may be written as

$$(\{\Delta\delta^*\}_t)^T\{\Delta f\} = \iiint_{\Omega_e} (\{\Delta\varepsilon^*\}_t)^T\{\Delta\sigma\}_t d\Omega \tag{4.65}$$

where

$$\{\Delta f\} = \iiint_{\Omega_e} [N]^T\{\Delta V\}d\Omega + \iint_{\Gamma_e} [N]^T\{\Delta p\}d\Gamma + [N]^T\{\Delta q\} \tag{4.66}$$

In which $\{\Delta V\}$, $\{\Delta p\}$ and $\{\Delta q\}$ are the nodal force incremental vectors corresponding to volumetric load, surface load, and concentrated load within the element or on the element boundaries.

Denoting

$$\{\varepsilon^*\}_t = [B]\{\delta^*\}_t \tag{4.67}$$

and use is made of Eq. (4.62), the virtual work principle Eq. (4.65) may be specified as

$$(\{\delta^*\}_t)^T\{\Delta f\} = \iiint_{\Omega_e} (\{\delta^*\}_t)^T[B]^T[D][B]\{\Delta\delta\}_t d\Omega \tag{4.68}$$

From Eq. (4.68) we have

$$[k]\{\Delta\delta\}_t = \{\Delta f\}_t \tag{4.69}$$

$$[k] = \iiint_{\Omega_e} [B]^T[D][B]d\Omega \tag{4.70}$$

In which $[k]$ is the stiffness matrix of the element e.

Gaussian quadrature for the numerical integration in Eqs. (4.66) and (4.70) is normally employed with the help of isoparametric element concept (Zienkiewicz et al. 2005).

Equation (4.69) is the governing equation for the element e. By looping over each element, the system stiffness matrix $[K]$ and force vector $\{\Delta F\}_t$ of the structure are assembled in a way similar to the "matrix truss method", then the governing (equilibrium) equation of the whole structure system is given by

$$[K]\{\Delta U\}_t = \{\Delta F\}_t \tag{4.71a}$$

After the solution for the system displacement vector $\{\Delta U\}_t$ of the discretized structure system, the strain increment $\{\Delta\varepsilon\}_t$ and stress increment $\{\Delta\sigma\}_t$ for each element may be computed individually using Eqs. (4.59)–(4.62).

In the following coverage throughout the whole book, $\{\Delta\delta\}_t$ will be used to note the system displacement vector in lieu of $\{\Delta U\}_t$, where there is no risk of misleading. Namely, instead of Eq. (4.71a), we may write

$$[K]\{\Delta\delta\}_t = \{\Delta F\}_t \tag{4.71b}$$

(2) Extended formulation for elasto-viscoplasticity

The constitutive relation of incremental form formulated in Chap. 2 (see Eqs. 2.122–2.125) will be implemented in the FEM algorithm for the purpose of elasto-viscoplastic analysis of hydraulic structures. The implicit symbol (superscript $\hat{}$) will be neglected in the hereafter discussions of this book, where no risk of misunderstanding will be led to.

The initial strain algorithm may be employed to solve the elasto-viscoplastic problem of hydraulic structures (Owen and Hinton 1980). Inserting Eq. (2.122) into Eq. (4.65), Eqs. (4.71a, 4.71b) will be transformed into

$$[K]\{\Delta\delta\}_t = \{\Delta F\}_t + \{\Delta F^{vp}\}_t \tag{4.72}$$

where the nodal equivalent (initial) load increment $\{\Delta F^{vp}\}_t$ attributable to viscoplastic deformation is assembled by the routine procedure of looping over $\{\Delta f^{vp}\}_t$ of each element

$$\{\Delta f^{vp}\}_t = \iiint_{\Omega_e} [B]^T [D]\{\Delta\varepsilon^{vp}\}_t d\Omega \tag{4.73}$$

4.3.2 *Joint Elements with Thickness*

Since the thickness of an interlayer or a fault j is rather small compared to its stretch, any two conjugate nodes of a joint element corresponding to its upper and lower faces [e.g. node 2 and node 6 in Fig. (3.6)] may employ the identical shape functions of isoparametric quadrilateral element (see Fig. 4.5) (Desai et al. 1985), namely

$$N_i = \frac{1}{4}(1+\xi_i\xi)(1+\eta_i\eta) \quad (i = 1,2,3,4) \tag{4.74}$$

where $\xi_i = (-1)^i$, $\eta_i = (-1)^{[i/2+0.5]}$.

The displacements on the joint walls are interpolated in a conjugate form

$$\begin{cases} \Delta u_{x,lower} = \sum_{i=1}^{4} N_i \Delta u_{xi} \\ \Delta u_{x,upper} = \sum_{i=1}^{4} N_i \Delta u_{xi+4} \end{cases} \tag{4.75}$$

Thus the displacement difference in the upper and lower walls is

$$\Delta u_x = \Delta u_{x,upper} - \Delta u_{x,lower} = \sum_{i=1}^{4} N_i (\Delta u_{xi+4} - \Delta u_{xi}) \tag{4.76}$$

Similarly, we have

$$\Delta u_y = \sum_{i=1}^{4} N_i \left(\Delta u_{yi+4} - \Delta u_{yi}\right) \tag{4.77}$$

$$\Delta u_z = \sum_{i=1}^{4} N_i (\Delta u_{zi+4} - \Delta u_{zi}) \tag{4.78}$$

Equations (4.76)–(4.78) may be expressed in the local coordinate system correspondent to the joint j using vector notations as

$$\{\Delta u\}_t = [l]_j [N] \{\Delta \delta\}_t \tag{4.79}$$

In which

$$[N] = [-N_1 I \quad -N_2 I \quad -N_3 I \quad -N_4 I \quad N_1 I \quad N_2 I \quad N_3 I \quad N_4 I] \tag{4.80}$$

$$\{\Delta \delta\}_t = [\Delta u_{x1} \quad \Delta u_{y1} \quad \Delta u_{z1} \quad \ldots \quad \Delta u_{x8} \quad \Delta u_{y8} \quad \Delta u_{z8}]^T \tag{4.81}$$

And the transformation matrix $[l]_j$ is defined in Eqs. (2.12)–(2.13).

There are three local strain components defined in Eqs. (2.54) and (2.55) which may be given in terms of the displacement interpolation Eq. (4.79)

$$\begin{cases} \{\Delta \varepsilon\}_t = \frac{1}{a_j} [l]_j [N] \{\Delta \delta\}_t = [B]_j \{\Delta \delta\}_t \\ [B]_j = \frac{1}{a_j} [l]_j [N] \end{cases} \tag{4.82}$$

According to the virtual work principle in Eq. (4.65) and the constitutive relation in Eq. (2.122), we obtain the governing equation of the joint element with thickness

$$[k]\{\Delta\delta\}_t = \{\Delta f\}_t + \{\Delta f^{vp}\}_t \tag{4.83}$$

In which

$$[k] = \iiint_{\Omega_e} [B]_j^T [D]_j [B]_j d\Omega = \frac{1}{a_j} \iint_{\Gamma_e} [N]^T [l]_j^T [D]_j [l]_j [N] d\Gamma \tag{4.84}$$

$$\{\Delta f^{vp}\}_t = \frac{1}{a_j} \iint_{\Gamma_e} [N]^T [l]_j^T [D]_j \{\Delta \varepsilon^{vp}\}_t d\Gamma \tag{4.85}$$

In which the elastic matrix $[D]_j$ is defined in Eq. (2.77).

Equations (4.83)–(4.85) may be assembled into Eqs. (4.72) and (4.73) in an identical manner of normal solid element.

4.3.3 Joint Elements Without Thickness

Where the joint thickness approaches zero, i.e. $a \to 0$, the stress increment may be postulated in proportional to the displacement difference of the conjugated nodes directly (Goodman et al. 1968; Mahtab and Goodman 1970), and the constitutive relation of joint will take the form in Eq. (2.126). Under such circumstances, the governing equation for the joint element without thickness is identical to Eq. (4.83) but in lieu of Eqs. (4.84) and (4.85), we have

$$[k] = \iint_{\Gamma_e} [N]^T [l]_j^T [D]_j [l]_j [N] d\Gamma \tag{4.86}$$

$$\{\Delta f^{vp}\}_t = \iint_{\Gamma_e} [N]^T [l]_j^T [D]_j \{\Delta u^{vp}\}_t d\Gamma \tag{4.87}$$

In which the elastic matrix $[D]_j$ is defined in Eq. (2.76a).

4.3.4 Simulation of Excavation Disturbed (Damage) Zone (EDZ)

(1) Concept

Stress redistribution and blasting impact during the excavation of underground cavern, slopes and dam foundations trigger relaxation in the surrounding rock

masses. As a result, excavation disturbed (damage) zone (EDZ) due to the relaxation will manifest along the excavation surface (Maejima et al. 2003; Martino and Chandler, 2004; Zhou et al. 2004; Malmgren et al. 2007).

It has been widely accepted that because of the stress redistribution during excavation, secondary cracks are induced around the initial rock fractures. Through the examinations by scanning electron microscope (SEM) and acoustic emission (AE), it is also revealed that the growth and nucleation of these cracks dominate the failure and macroscopic mechanical properties (Kwaśniewski 1993; Golshani et al. 2006; Corthésy and Leite 2008).

The spatial-time distribution of the relaxation is influenced by a variety of factors including the mechanical parameters of rocks, the characteristics of joints, the in situ geo-stresses, the excavation procedure, and the blasting technology. The EDZ is customarily further divided into the stress redistribution zone (SRZ) and the blasting impact zone (BIZ). The relaxation in SRZ is mainly induced by the tension and shear on the existing joints. The depth of this zone may range from 5 to 20 m. The relaxation in BIZ shows new cracks and fissures over a depth in the range of 0.5–2 m. Rock relaxation demonstrates the reduction of the Young's modulus (E), friction angle (φ), cohesion (c), and the augment of Poisson's ratio (μ) (Ramamurth 1993; Chen et al. 2001; Martino and Chandler 2004). The deterioration of the mechanical parameters is less pronounced in the SRZ than in the BIZ. Outside the EDZ the mechanical parameters of the rock mass undergo but a slight variation.

When the relaxation develops to certain degree, the spalling from the excavation surface will be triggered. Under certain geology conditions, the surface instability such as rock burst, or the appearance of larger extensive cracks along the excavation surface, will occur (Exadaktylos and Tsoutrelis, 1995). These phenomena have been mostly recognized and studied in the tunnelling engineering (Kaiser et al. 2010). The recent engineering practices also indicate that under certain circumstances such relaxation will affect the rock deformation and stability of excavated slopes, foundations and their adjacent structures (e.g. dams) remarkably.

Based on the damage theory, complete stress-strain relations for brittle rocks with crack propagation, have been explored, and the corresponding computation algorithms have been formulated for the rock deformation and failure taking the relaxation into account (Cai and Kaiser 2005; Moura et al. 2005; Exadaktylos et al. 2007; Jäger et al. 2008). This is a correct way, and, providing sufficient time and budget for the comprehensive tests to calibrate the corresponding parameters, the problems concerning the excavation-induced relaxation in EDZ could be well handled.

A rigorous engineering approach to the rock relaxation issue is somewhat, intractable, because of the intrinsic difficulties with the models and parameters for heterogeneous and anisotropic rock masses. Consequently, it is suggestible to take into account of a basic, rather than a detailed mechanism, towards the simplified and practical algorithm based on the conventional geology investigations and tests as well as the instrumentation observations. This is also because of the fact that a dam foundation excavated in hard and brittle rock under high in situ geo-stresses

may exhibit unexpected and rapid rock relaxation, leaving limited time for "mechanically perfect" analysis to help the countermeasure design.

Based on the above considerations we formulated a practical FE algorithm for the rock foundation excavation considering EDZ. A criterion to pinpoint EDZ using maximum tensile strain is introduced firstly, then the characteristics of the EDZ are described by the variation of the conventional mechanical parameters of the rock (E, μ, φ, c) pre- and post-relaxation. The algorithm is established on the elasto-viscoplastic potential theory, which is able to describe the deformation and stress adjustment history resulted from the deterioration of both the elastic and strength parameters.

(2) Relaxation mechanism and criterion

The relaxation criterion may be established using displacements, stresses, or internal variables (e.g. plastic strain) (Kaiser et al. 2010). It should be based on the mechanism understanding that after the excavation, the augment of rebound displacement and the reduction of stress perpendicular to the excavation surface will lead to the relaxation. The fracture mechanics and rock sample tests have shown that where the confining stress level is low, a hard rock performs in a way of brittle, and the failure means the initial micro-cracks propagating along the maximum compression stress (Kwaśniewski 1993; Golshani et al. 2006; Corthésy and Leite 2008). Therefore, the most inornate but applicable relaxation criterion makes use of the maximum tensile strain of rock, to claim that the excessive maximum tensile strain perpendicular to the maximum compressive stress is mainly blamed for the rock relaxation. This maximum stress is, nearly parallel to the excavation surface.

A rock sample under the principal compression stress σ_3 is shown in Fig. 4.9. The Poisson's effect will lead to the lateral tensile strain ε_1, which of course including the effect of micro-crack propagation. If the permissible (allowable) tensile strain ε_l can be experimentally obtained, the relaxation criterion can be simply expressed by the formula

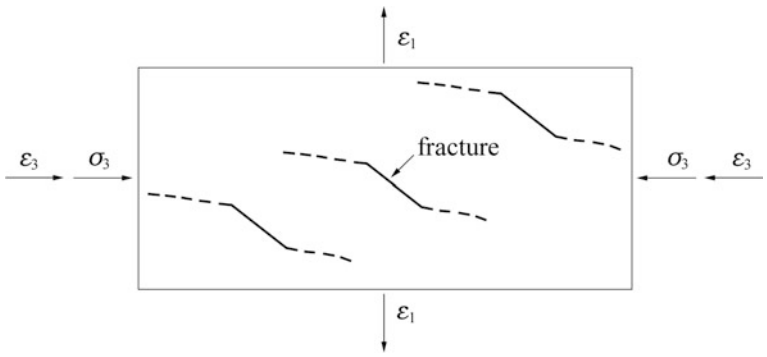

Fig. 4.9 Propagation of micro-cracks and development of tensile strain

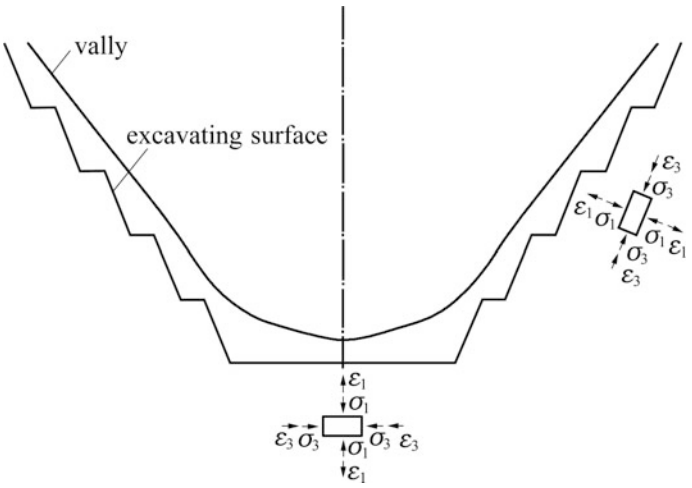

Fig. 4.10 Schematic diagram to dam foundation excavation

$$F = \varepsilon_1 - \varepsilon_l = 0 \tag{4.88}$$

Figure 4.10 shows the excavation surface of a dam foundation. As the ongoing of excavation, the compression stress σ_3 parallel to the excavation surface will be adjusted (increase or decrease), while the compression stress σ_1 perpendicular to the surface is definitely decreased (unloading). All these two factors put together will result in the tensile strain ε_1 perpendicular to the excavation surface. When the tensile strain exceeds the permissible value ε_l, rock relaxation occurs.

The maximum tensile strain criterion is one of the simplest strain-based failure criteria for rocks (Kwaśniewski and Takahashi 2010), which was initiated by Stacey (1981) in order to interpret the mechanism of sidewall slabbing in mine haulages and spalling from the face of bored tunnels. Stacy also suggested the value of permissible tensile strain $\varepsilon_l = 0.0073\%$ for a certain conglomerate reef and $\varepsilon_l = 0.0175\%$ for a diabase. The further researches were continued by Sakuri et al. (Sakurai 1981; Sakurai et al. 1995), Fujii et al. (1998), Li et al. (2000) towards the improvement of the criterion and the evaluation of ε_l. It was also reported to range between $\varepsilon_l = 0.1$–1% according to different laboratory testing resources (Kwaśniewski and Takahashi 2010).

However, the major difficulty lying in the evaluation of ε_l for a specific project has not been satisfactorily solved. This is resulted from two aspects: first, if the rock contains oriented joints (e.g. blind joints nearly parallel to the excavation surface), the permissible tensile strain ε_l will be much smaller than that from laboratory tests using intact rocks; second, the rock mass in the field has suffered from initial strain prior to the engineering disturbance, which is not so easy to be measured or computed. An alternative way to evaluate ε_l is, probably the back analysis

immediately undertaken after the starting of the rock excavation, using the messages of the relaxation depth obtained from the ultrasonic detection.

At any time t, the evolution of mechanical parameters may be simply expressed by the following formulas (Chen et al. 2012)

$$\begin{cases} E_t = E^* - \frac{E^* - E^{**}}{t_0} t & for \quad t \le t_0 \\ E_t = E^{**} & for \quad t > t_0 \end{cases} \tag{4.89}$$

$$\begin{cases} \mu_t = \mu^* + \frac{\mu^{**} - \mu^*}{t_0} t & for \quad t \le t_0 \\ \mu_t = \mu^{**} & for \quad t > t_0 \end{cases} \tag{4.90}$$

$$\begin{cases} \varphi_t = \varphi^* - \frac{\varphi^* - \varphi^{**}}{t_0} t & for \quad t \le t_0 \\ \varphi_t = \varphi^{**} & for \quad t > t_0 \end{cases} \tag{4.91}$$

$$\begin{cases} c_t = c^* - \frac{c^* - c^{**}}{t_0} t & for \quad t \le t_0 \\ c_t = c^{**} & for \quad t > t_0 \end{cases} \tag{4.92}$$

In which the initial (pre-relaxation) and final (post-relaxation) mechanical parameters are denoted as (E^*, μ^*, φ^*, c^*) and (E^{**}, μ^{**}, φ^{**}, c^{**}) respectively; the duration time of the relaxation is denoted as t_0. These parameters are evaluated by laboratory or/and field tests as well as back analyses.

(3) FE solution process considering EDZ

The FE computation for excavation effects involves the determination of nodal force vector $\{\Delta f\}_t$, which are equivalent to the tractions from the excavated elements adjacent to the excavation boundary

$$\{\Delta f\}_t = \iiint_{\Omega_e} [B]^T \{\sigma\}_t d\Omega - \iiint_{\Omega_e} [N]^T \gamma_r d\Omega \tag{4.93}$$

where γ_r = bulk unit weight of rock, kN/m^3; $[B]$ = strain matrix; $[N]$ = shape function matrix.

The integral of Eq. (4.93) covers the excavated elements merely, and only the forces corresponding to the nodes on the excavated surface are assembled in $\{\Delta f\}_t$.

The vector $\{\Delta f\}_t$ is then employed as a common load in the excavation simulation to obtain the adjusted stress field (Brown and Booker 1985), which is further followed by the relaxation computation.

The FEM algorithm for subsequent relaxation effects is established on the two sets of mechanical parameters (E_t, μ_t, c_t, φ_t) and ($E_{t+\Delta t}$, $\mu_{t+\Delta t}$, $\varphi_{t+\Delta t}$, $c_{t+\Delta t}$) at t and $t + \Delta t$, respectively (Chen et al. 2012).

1. Displacement and stress adjustment due to the deterioration of elastic parameters

Suppose the elastic parameters are deteriorated from (E_t, μ_t) down to ($E_{t+\Delta t}$, $\mu_{t+\Delta t}$), the elastic relaxation analysis is conducted by the "restraint-relaxation" procedure described as follows.

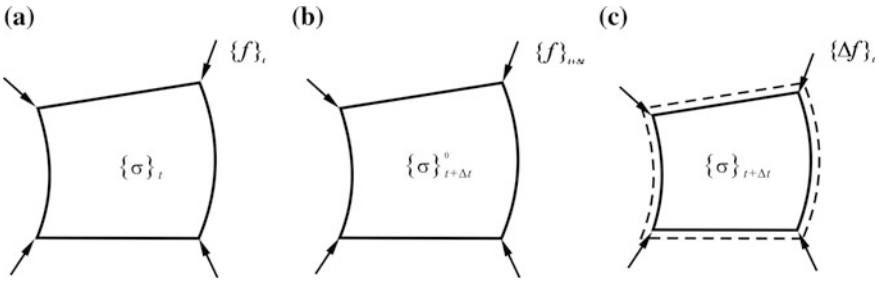

Fig. 4.11 Diagram to the calculation of unbalanced force. **a** Before relaxation; **b** after relaxation; **c** unbalanced force

① Calculate the strain $\{\varepsilon\}_t$ before relaxation

Figure 4.11a shows an element at time t, in which $\{f\}_t$ is the nodal force vector balanced by this element and the surrounding elements through the stress $\{\sigma\}_t$. The corresponding strain is

$$\{\varepsilon\}_t = [D]_t^{-1}\{\sigma\}_t \tag{4.94}$$

In which $[D]_t$ is the elastic matrix at time t.

② Calculate the clamped stress $\{\sigma\}^0_{t+\Delta t}$ after relaxation

Figure 4.11b shows the same element at time $t + \Delta t$ with deteriorated parameters. During the time interval Δt the elastic matrix varies from $[D]_t$ to $[D]_{t+\Delta t}$. Suppose the element is fully clamped, the stress $\{\sigma\}^0_{t+\Delta t}$ at time $t + \Delta t$ will become

$$\{\sigma\}^0_{t+\Delta t} = [D]_{t+\Delta t}\{\varepsilon\}_t \tag{4.95}$$

Figure 4.11b also displays the nodal force vector $\{f\}_{t+\Delta t}$ corresponding to this clamped stress state.

③ Calculate the unbalanced force $\{\Delta f\}_t$

Since the imagined clamp does not actually exist, the unbalanced nodal force vector before and after the relaxation will cause the strain and stress adjustment. Figure 4.11c shows the element before (in broken line) and after (in solid line) the adjustment where the unbalanced nodal force vector $\{\Delta f\}_t$ during the element relaxation is calculated by

$$\{\Delta f\}_t = \{f\}_{t+\Delta t} - \{f\}_t \tag{4.96}$$

The unbalanced nodal force $\{\Delta f\}_t$ can be further written as

$$\begin{aligned}\{\Delta f\}_t &= \{f\}_{t+\Delta t} - \{f\}_t = \iiint_{\Omega_e} [B]^T \{\sigma\}_t d\Omega - \iiint_{\Omega_e} [B]^T \{\sigma\}^0_{t+\Delta t} d\Omega \\ &= \iiint_{\Omega_e} [B]^T \left(\{\sigma\}_t - \{\sigma\}^0_{t+\Delta t}\right) d\Omega\end{aligned} \tag{4.97}$$

This unbalanced force $\{\Delta f\}_t$ will be employed to compute the increments of displacement, strain and stress due to the deterioration of elastic parameters by

$$[k]_t \{\Delta\delta\}_t = \{\Delta f\}_t \tag{4.98}$$

Equations (4.97) and (4.98) may be assembled into the system Eqs. (4.71a, 4.71b) in an identical manner of normal solid element. After the solution of $\{\Delta\delta\}_t$, the strain and stress increments due to elastic relaxation may be calculated by

$$\{\Delta\varepsilon\}_t = [B]\{\Delta\delta\}_t \tag{4.99}$$

$$\{\Delta\sigma\}_t = [D]_t \{\Delta\varepsilon\}_t \tag{4.100}$$

The displacement, strain and stress at time $t + \Delta t$ are accumulated by

$$\begin{cases} \{\delta\}_{t+\Delta t} = \{\delta\}_t + \{\Delta\delta\}_t \\ \{\varepsilon\}_{t+\Delta t} = \{\varepsilon\}_t + \{\Delta\varepsilon\}_t \\ \{\sigma\}_{t+\Delta t} = \{\sigma\}_t + \{\Delta\sigma\}_t \end{cases} \tag{4.101}$$

2. Displacement and stress adjustment due to the deterioration of strength parameters

Where the deterioration in strength parameters occurs, conventional non-linear FEM is conducted using the elasto-viscoplastic potential theory. The equivalent nodal force caused by the viscoplastic deformation is

$$\{\Delta f^{vp}\}_t = \iiint_{\Omega_e} [B]^T [D]_t \{\Delta\varepsilon^{vp}\}_t d\Omega \tag{4.102}$$

The increment of displacement is governed by

$$[k]_t \{\Delta\delta\}_t = \{\Delta f^{vp}\}_t \tag{4.103}$$

Equations (4.102) and (4.103) may be assembled into system Eqs. (4.72) and (4.73) in an identical manner of normal solid element. After the solution of $\{\Delta\delta\}_t$, the strain and stress increments due to viscoplastic relaxation may be calculated by

$$\{\Delta\varepsilon\}_t = [B]\{\Delta\delta\}_t \tag{4.104}$$

$$\{\Delta\sigma\}_t = [D]_t(\{\Delta\varepsilon\}_t - \{\Delta\varepsilon^{vp}\}_t) \tag{4.105}$$

The displacement, strain and stress at time $t + \Delta t$ are accumulated by

$$\begin{cases} \{\delta\}_{t+\Delta t} = \{\delta\}_t + \{\Delta\delta\}_t \\ \{\varepsilon\}_{t+\Delta t} = \{\varepsilon\}_t + \{\Delta\varepsilon\}_t \\ \{\sigma\}_{t+\Delta t} = \{\sigma\}_t + \{\Delta\sigma\}_t \end{cases} \tag{4.106}$$

3. Solution process considering the deterioration of both the elastic and strength parameters

The finite element solution process for the rock excavation considering the deterioration of both the elastic and strength parameters is formulated in the flow chart shown in Fig. 4.12, in which $K_{\max}$ is the amount of excavation benches.

4.4 Dynamic Strain/Stress Problems

4.4.1 Governing Equations

Structural analysis methods for earthquake effects are normally classified into two categories: approximate sliding stability analysis using an appropriate seismic coefficient (e.g. the pseudo-static method) and dynamic internal stress analysis (Severn 1978; Wilson 1998; ICOLD 2001, 2002; Clough and Penzien 2003; Chen et al. 2015) using site-dependent earthquake ground motions. The latter is obligatory for the hydraulic structures whose aseismic and fortifying design class is 1, and is optional for that with aseismic and fortifying design class 2 or 3 (DL 5073-2000).

By the virtual work principle and the D'Alembert's principle, the governing equation of the FEM for dynamic response under the exciting of earthquake is (Newmark 1959; Chopra and Chakrabarti 1981; Chopra 1987; Paulay and Priestley 1992)

$$[M]\left\{\ddot{\delta}(t)\right\} + [C]\left\{\dot{\delta}(t)\right\} + [K]\{\delta(t)\} = \{F\} \tag{4.107}$$

where $[M]$ = mass matrix; $[C]$ = damping matrix; $[K]$ = stiffness matrix; $\{\delta(t)\}$, $\left\{\dot{\delta}(t)\right\}$, $\left\{\ddot{\delta}(t)\right\}$ = vectors of displacement, velocity, and acceleration, respectively.

In Eq. (4.107) $\{F\}$ is the dynamic force vector, in the case of earthquake we have

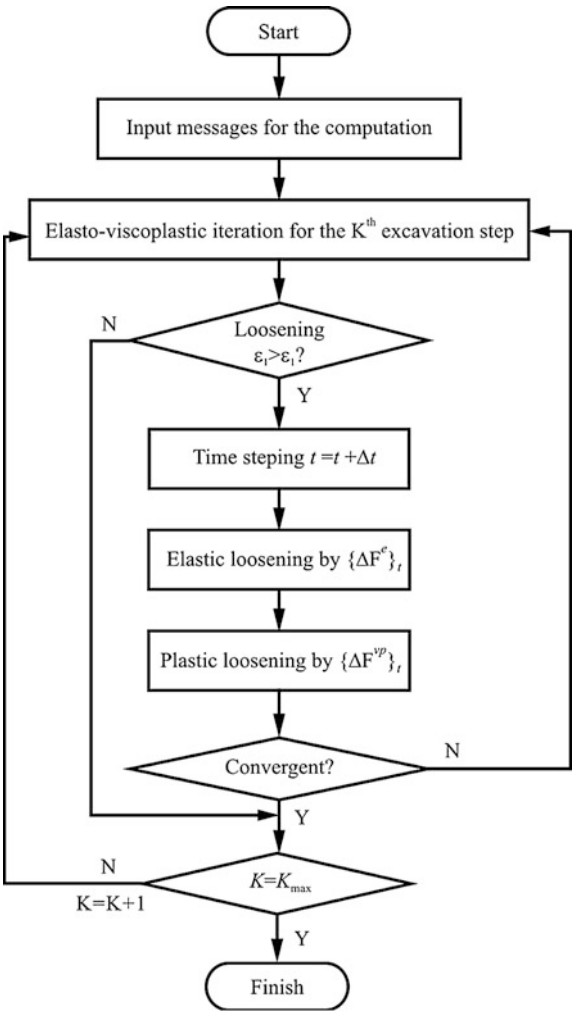

Fig. 4.12 Flow chart of the finite element solution process for EDZ effects

$$\{F\} = -[M]\left\{\ddot{\delta}_g(t)\right\} \tag{4.108}$$

where $\left\{\ddot{\delta}_g(t)\right\}$ = earthquake acceleration of ground motions.

The mass matrix $[M]$ of a structure system is assembled using $[m]^e$ of element e computed by the formula

$$[m]^e = \iiint_{\Omega_e} [N]^T \rho [N] d\Omega \tag{4.109}$$

where ρ = volumetric density of the material, kg/m^3.

Proportional damping (Rayleigh damping) is commonly stipulated (Caughey and Kelly 1965), that

$$[C] = \alpha_0[M] + \alpha_1[K] \tag{4.110}$$

In which α_0 and α_1 are found by the damping ratio through the formula

$$\begin{cases} \zeta_1 = \frac{a_0}{2\omega_1} + \frac{a_1\omega_1}{2} \\ \zeta_2 = \frac{a_0}{2\omega_2} + \frac{a_1\omega_2}{2} \end{cases} \tag{4.111}$$

In which ω_1 and ω_2 are the first and second natural frequencies.

4.4.2 Solution Techniques

Because the exact solutions for most dynamic problems do not exist or they demand an excessive efforts, two approximate approaches are normally employed to compute the dynamic responses of structural systems governed by Eq. (4.107). The first approach employs mode-superposition techniques in which the total response is expressed as a series of individual responses in the normal modes of vibration. Towards elastic hydraulic structures, this approach falls into the simplified response spectrum method and the finite element method using either a response spectrum or acceleration-time records for the dynamic input. It cannot be applied in non-linear structural system because of the superposition scheme involved, which requires that the system remains linear during the vibration process. The second approach termed as "time-history analysis" is applicable in the analysis of an arbitrary set of non-linear dynamic equations, and coupled linear modal equations are implemented by the direct time integration step-by-step. It enables the designer to determine the number of cycles of nonlinear behavior, the magnitude of excursion into the nonlinear range, and the time the structure remains nonlinear.

Dynamic analysis should be started with the simpler response spectrum method and progress to more refined ones, if needed. The time-history analysis is only required when important yielding (cracking) of the structure is indicated by, for example, a response spectrum analysis.

4.4.3 Modal Analysis

Since by experiences the damping has minor influence on the natural frequencies and modes, therefore it is ordinarily neglected in the modal analysis.

Let $[C] = 0$ and $\left\{\ddot{\delta}_g(t)\right\} = 0$ in Eq. (4.107), the governing equation of free vibration without damping is reduced

$$[M]\left\{\ddot{\delta}(t)\right\} + [K]\{\delta(t)\} = \{0\} \tag{4.112}$$

Assuming that the displacements are harmonically related with time

$$\{\delta(t)\} = \{\delta\}\sin(\omega t + \gamma) \tag{4.113}$$

where $\{\delta\}$ = vector of nodal displacement amplitudes; ω = natural frequencies; γ = initial phase angle.

Substituting for $\{\delta(t)\}$ and $\left\{\ddot{\delta}(t)\right\}$ from Eq. (4.113) in Eq. (4.112) that is divided by $\sin(\omega t + \gamma)$ at its two sides, we have

$$\left([K] - \omega^2[M]\right)\{\delta\} = \{0\} \tag{4.114}$$

This is a generalized eigenvalue equation, from which non-virtual solution for $\{\delta\}$ does exist only if

$$|\,[K] - \omega^2[M]| = 0 \tag{4.115}$$

For a three-dimensional problem with n nodes, this is a $3n$ order polynomial equation of ω^2, from which we can find $3n$ solutions (roots) ω_i as eigenvalues, of which the smallest ω_1 is called as the "fundamental frequency". For each ω_i Eq. (4.114) gives one solution of eigenvector $\{\delta\}_i$. The Jacobi method is normally applied to seek all the eigenvectors to form "natural modes". Since only few frontal (less than 20) modes might be important in the response spectrum analysis, therefore significant reduction in the size of system may be achieved. It is also worthwhile to indicate that for normal mode analysis, support (restraint) of the structure is unnecessary, and the magnitudes of eigenvectors and correspondent stresses bear no physical meaning.

4.4.4 Mode-Superposition

Supposing $s(\leq 20)$ natural frequencies ω_1 , ω_2, … ω_s and corresponding modes $\{\delta\}_1$, $\{\delta\}_2$ … $\{\delta\}_s$ have been found, the displacement of the structure is expressed by

$$\{\delta(t)\} = Y_1(t)\{\delta\}_1 + Y_2(t)\{\delta\}_2 + \cdots + Y_s(t)\{\delta\}_s \tag{4.116}$$

In which $Y_1(t)$, $Y_2(t)$ … $Y_s(t)$ are termed as "principal coordinates".

Substituting for $\{\delta(t)\}$, $\left\{\ddot{\delta}(t)\right\}$ and $\left\{\dot{\delta}(t)\right\}$ from Eq. (4.116) in Eq. (4.107) and using orthogonal conditions of natural modes, the coupled dynamic Eq. (4.107)

may be transformed to the uncoupled equation set with respect to the principal coordinates $Y_i(t)$

$$\ddot{Y}_i(t) + 2\omega_i\xi_i\dot{Y}(t) + \omega_i^2 Y_i(t) = -(\eta_{x_i}\ddot{\delta}_{g_x}(t) + \eta_{y_i}\ddot{\delta}_{g_y}(t) + \eta_{z_i}\ddot{\delta}_{g_z}(t)) \quad (i = 1, 2, \ldots, s) \tag{4.117}$$

In which η_{x_i}, η_{y_i}, η_{z_i} are the "mode-participation coefficients"; ξ_i is the "damping ratio".

$$\begin{cases} \eta_{x_i} = \frac{\{\delta\}_i^T[M]\{I_x\}}{\{\delta\}_i^T[M]\{\delta\}_i}, & \{I_x\} = [1 \quad 0 \quad 0 \quad 1 \quad \ldots]^T \\ \eta_{y_i} = \frac{\{\delta\}_i^T[M]\{I_y\}}{\{\delta\}_i^T[M]\{\delta\}_i}, & \{I_y\} = [0 \quad 1 \quad 0 \quad 0 \quad \ldots]^T \\ \eta_{z_i} = \frac{\{\delta\}_i^T[M]\{I_z\}}{\{\delta\}_i^T[M]\{\delta\}_i}, & \{I_z\} = [0 \quad 0 \quad 1 \quad 0 \quad \ldots]^T \\ \xi_i = \frac{\alpha_0}{2\omega_i} + \frac{\alpha_1\omega_i}{2} \end{cases} \tag{4.118}$$

Damping ratio is obtained by the vibration test of structures. According to the field observation data, the damping ratio of arch dams varies between 3 and 5%. For example, the damping ratio of Xiaowan Arch Dam (H = 294.5 m) is ξ_i = 5%. For the calculation of the parameters α_0 and α_1 in Eq. (4.111), the fundamental frequency ω_1 (1 Hz in the case of Xiaowan Arch Dam) and the threshold high frequency (12 Hz in the case of Xiaowan Arch Dam) are selected. The earthquake energy above threshold frequency may be neglected.

Equation (4.117) is called as "modal equations", which are a set of uncoupled, second order differential equations of $Y_i(t)$, and are much easier to be solved than the original Eq. (4.107). A famous solution of Eq. (4.117) was provided by the integration of Duhamel (1833)

$$\begin{aligned} Y_i(t) = &-\frac{1}{\bar{\omega}_i}\int_0^t (\eta_{x_i}\ddot{\delta}_{g_x}(t) + \eta_{y_i}\ddot{\delta}_{g_y}(t) + \eta_{z_i}\ddot{\delta}_{g_z}(t))e^{-\xi_i\bar{\omega}_i(t-\tau)}\sin\bar{\omega}_i(t-\tau)d\tau \\ &+ e^{-\xi_i\bar{\omega}t}(a_i\sin\bar{\omega}_i t + b_i\cos\bar{\omega}_i t) \end{aligned} \tag{4.119}$$

In which

$$\bar{\omega}_i = \omega_i\sqrt{1-\xi_i^2} \tag{4.120}$$

a_i and b_i are the constants calculated using the initial conditions (e.g. displacement, velocity) as follows

$$\begin{cases} a_i = Y_i(0) \\ b_i = \dfrac{\dot{Y}(0) + \xi_i \bar{\omega}_i Y_i(0)}{\bar{\omega}_i} \end{cases} \tag{4.121}$$

The numerical solution of Eq. (4.119) can be carried out by the linear interpolation between discrete time intervals and the calculation of the resulting integrals.

4.4.5 Response Spectrum

The FEM using response spectrum is able to simulate the linear dynamic response of structures by means of the natural (or characteristic) frequencies and corresponding normal modes (natural modes, mode shapes).

In Eq. (4.116), the function $Y_i(t)$ represents the proportion of the i mode in the vibration. For a certain earthquake action and damping, the solution of $Y_i(t)$ from Eq. (4.119) depends on ω_i. Let ω as abscissa axis and $Y_i(t)$ as ordinate axis, a group of scattered points called as "displacement response spectrum", may be plotted. Similarly, let $\dot{Y}(t)$ or $\ddot{Y}(t)$ as ordinate axis, and ω (or $T = \frac{2\pi}{\omega}$) as abscissa axis, "velocity response spectrum" or "acceleration response spectrum" also may be constructed. Because $Y_i(t)$, $\dot{Y}_i(t)$ and $\ddot{Y}_i(t)$ are time dependent, such response spectra are time dependent, too. Since in the practice the maximum earthquake response is the most concern, therefore $Y_{i\max}(t)$, $\dot{Y}_{i\max}(t)$ and $\ddot{Y}_{i\max}(t)$ are customarily used in lieu of the time dependent $Y_i(t)$, $\dot{Y}_i(t)$ and $\ddot{Y}_i(t)$ in the building of response spectra. With the help of such response spectra, it is no longer necessary to solve Eq. (4.119). Instead, $Y_{i\max}(t)$, $\dot{Y}_{i\max}(t)$ and $\ddot{Y}_{i\max}(t)$ may be inserted into Eq. (4.116) to obtain an estimation of the maximum responses (displacement, velocity, and acceleration), i.e. the bounds on the behaviors of a structure subjected to seismic loading (Chen 2015).

4.4.6 Time-History Analysis

The response spectrum solution, while providing much insight into the structural shake patterns, are in general not economical for the solution of transient problems in linear cases and not applicable where non-linearity declares its importance.

Towards the direct solution of Eq. (4.107), the classical Newmark-β algorithm and Wilson-θ algorithm (Newmark 1959; Bathe and Wilson 1972) basically belong to the particular case of a quadratic truncated Taylor series expansion with regard to time of the governing equation, are most prevalent for the dynamic analysis in hydraulic structures. The remarkable advantage of these algorithms in comparison

with the linear ones using the assumption of linear accelerate within the time interval $[t, t + \Delta t]$, is unconditionally stable in time marching steps.

By introduce a control parameter $\theta(\theta \geq 1)$, the Wilson-θ algorithm assumes that the accelerate is linear within the interval $[t, t + \theta\Delta t]$, and it is proved that the unconditional stable will be guaranteed when $\theta \geq 1.37$. In practical computation $\theta = 1.4$ is normally exercised.

At time $t + \tau$, the accelerate may be interpolated by the formula

$$\left\{\ddot{\delta}\right\}_{t+\tau} = \left\{\ddot{\delta}\right\}_t + \frac{\tau}{\theta\Delta t}\left(\left\{\ddot{\delta}\right\}_{t+\theta\Delta t} - \left\{\ddot{\delta}\right\}_t\right) \quad (0 \leq \tau \leq \theta\Delta t) \tag{4.122}$$

Integral the Eq. (4.122) and let $\tau = \theta\Delta t$ yields the velocity and displacement as follows

$$\begin{cases} \left\{\dot{\delta}\right\}_{t+\theta\Delta t} = \left\{\dot{\delta}\right\}_t + \frac{\theta\Delta t}{2}\left(\left\{\ddot{\delta}\right\}_{t+\theta\Delta t} + \left\{\ddot{\delta}\right\}_t\right) \\ \{\delta\}_{t+\theta\Delta t} = \{\delta\}_t + \theta\Delta t\left\{\dot{\delta}\right\}_t + \frac{(\theta\Delta t)^2}{6}\left(\left\{\ddot{\delta}\right\}_{t+\theta\Delta t} + 2\left\{\ddot{\delta}\right\}_t\right) \end{cases} \tag{4.123}$$

Equation (4.123) further provides the accelerate and velocity at time $\tau + \theta\Delta t$

$$\begin{cases} \left\{\ddot{\delta}\right\}_{t+\theta\Delta t} = \frac{6}{(\theta\Delta t)^2}\left(\{\delta\}_{t+\theta\Delta t} - \{\delta\}_t\right) - \frac{6}{\theta\Delta t}\left\{\dot{\delta}\right\}_t - 2\left\{\ddot{\delta}\right\}_t \\ \left\{\dot{\delta}\right\}_{t+\theta\Delta t} = \frac{3}{\theta\Delta t}\left(\{\delta\}_{t+\theta\Delta t} - \{\delta\}_t\right) - 2\left\{\dot{\delta}\right\}_t - \frac{\theta\Delta t}{2}\left\{\ddot{\delta}\right\}_t \end{cases} \tag{4.124}$$

Equation (4.124) is now introduced into Eq. (4.123) to give the displacement $\{\delta\}_{t+\theta\Delta t}$. Since the displacement $\{\delta\}_t$ and velocity $\left\{\dot{\delta}\right\}_t$ and accelerate $\left\{\ddot{\delta}\right\}_t$ at time t, as well as the displacement $\{\delta\}_{t+\theta\Delta t}$ at time $t + \theta\Delta t$, are all known, the velocity $\left\{\dot{\delta}\right\}_{t+\Delta t}$ and accelerate $\left\{\ddot{\delta}\right\}_{t+\Delta t}$ at time $t + \Delta t$ may be recurred.

To summarize, the following steps are specified for the implementation of the Wilson-θ algorithm

① Computation of system stiffness matrix $[K]$, damping matrix $[C]$ and mass matrix $[M]$;

② For the initial values of $\{\delta\}_0$, $\left\{\dot{\delta}\right\}_0$, and $\{F\}_0$, compute $\left\{\ddot{\delta}\right\}_0$ using the governing equation;

③ Let $\theta = 1.4$, calculate the constants

$a_0 = \frac{6}{(\theta\Delta t)^2}$, $a_1 = \frac{3}{\theta\Delta t}$, $a_2 = 2a_1$, $a_3 = \frac{\theta\Delta t}{2}$, $a_4 = \frac{a_0}{\theta}$

$a_5 = -\frac{a_2}{\theta}, a_6 = 1 - \frac{3}{\theta}, a_7 = \frac{\Delta t}{2}, a_8 = \frac{\Delta t^2}{6}$

④ Assemble the equivalent stiffness matrix

$$[\bar{K}] = [K] + a_0[M] + a_1[C] \tag{4.125}$$

⑤ Compute the equivalent load at time $t + \theta\Delta t$

$$\begin{aligned}\{\bar{F}\}_{t+\theta\Delta t} = \{F\}_{t+\theta\Delta t} + [M]\left(a_0\{\delta\}_t + a_2\left\{\dot{\delta}\right\}_t + 2\left\{\ddot{\delta}\right\}_t\right) \\ + [C]\left(a_1\{\delta\}_t + 2\left\{\dot{\delta}\right\}_t + a_3\left\{\ddot{\delta}\right\}_t\right)\end{aligned} \tag{4.126}$$

⑥ Compute the displacement at time $t + \theta\Delta t$

$$\{\delta\}_{t+\theta\Delta t} = [\bar{K}]^{-1}\{\bar{F}\}_{t+\theta\Delta t} \tag{4.127}$$

⑦ Compute the accelerate, velocity, and displacement at time $t + \Delta t$

$$\begin{cases}\left\{\ddot{\delta}\right\}_{t+\Delta t} = a_4\left(\{\delta\}_{t+\Delta t} - \{\delta\}_t\right) + a_5\left\{\dot{\delta}\right\}_t + a_6\left\{\ddot{\delta}\right\}_t \\ \left\{\dot{\delta}\right\}_{t+\Delta t} = \left\{\dot{\delta}\right\}_t + a_7\left(\left\{\ddot{\delta}\right\}_{t+\Delta t} + \left\{\ddot{\delta}\right\}_t\right) \\ \{\delta\}_{t+\Delta t} = \{\delta\}_t + \Delta t\left\{\dot{\delta}\right\}_t + a_8\left(\left\{\ddot{\delta}\right\}_{t+\Delta t} + 2\left\{\ddot{\delta}\right\}_t\right)\end{cases} \tag{4.128}$$

4.4.7 Dynamic Dam-Reservoir Interaction

The importance of reservoir water on the dynamic behavior of concrete dams was firstly demonstrated by Westergaard (1933) who gave hydrodynamic pressures at the vertical face of a rigid gravity dam subjected to harmonic ground motion. The incompressible water postulation and added mass concept had become standard in representing the reservoir/dam interaction, and various modifications have been made to apply the equivalent concept to arch dams.

Under the assumption of incompressible water, it is possible to write the dynamic equation of fluid as (Wilson and Khalvati 1983)

$$\frac{\partial^2 p}{\partial x^2} + \frac{\partial^2 p}{\partial y^2} + \frac{\partial^2 p}{\partial z^2} = 0 \tag{4.129}$$

With boundary conditions

$$\begin{cases} p = 0 & \text{on the surface of reservoir} \\ \partial p/\partial n = -\rho\ddot{\delta}_n & \text{on the contact face of structure/water} \end{cases} \tag{4.130}$$

where $\ddot{\delta}_n$ = absolute accelerate along the normal of the structure/water contact face; n = normal vector of the contact face.

Equations (4.129) and (4.130) may be discretized by the variation principle

$$[H]\{p\} = \{R\} \tag{4.131}$$

In which the matrix $[H]$ and vector $\{R\}$ of the reservoir system are assembled from that of element e

$$[h] = \iiint_{\Omega_e} [B]^T [B] d\Omega \tag{4.132}$$

$$\{r\} = -\iint_{\Gamma_e} \rho\ddot{\delta}_n [N]^T d\Gamma \tag{4.133}$$

where

$$\begin{cases} [B] = \lfloor [B_i] \quad [B_j] \quad \ldots \quad [B_m] \rfloor \\ [B_i] = [N_{i,x} \quad N_{i,y} \quad N_{i,z}]^T = \left[\dfrac{\partial N_i}{\partial x} \quad \dfrac{\partial N_i}{\partial y} \quad \dfrac{\partial N_i}{\partial z}\right]^T \end{cases} \tag{4.134}$$

Under the action of earthquake accelerate $\left\{\ddot{\delta}_g\right\}$, $\ddot{\delta}_n$ may be expressed by the formula

$$\ddot{\delta}_n = [l][\bar{N}]\left(\left\{\ddot{\delta}\right\} + \left\{\ddot{\delta}_g\right\}\right) \tag{4.135}$$

where $[\bar{N}]$ = shape function on the element face contacting reservoir water; $[l]$ = outward normal to the element face exerted by reservoir water expressed by

$$[l] = [\cos(n,x),\ \cos(n,y),\ \cos(n,z)] \tag{4.136}$$

Introducing Eq. (4.135) into Eq. (4.133) gives rise to

$$\{r\} = -[S]\left(\left\{\ddot{\delta}\right\} + \left\{\ddot{\delta}_g\right\}\right) \tag{4.137}$$

In which

$$[S] = \iint_{\Gamma_e} [N]^T \rho [l][\bar{N}] d\Gamma \tag{4.138}$$

On the other hand, the dynamic response of the structure system after the discretization is governed by

$$[M]\left\{\ddot{\delta}\right\} + [C]\left\{\dot{\delta}\right\} + [K]\{\delta\} = \{F\} + \{\bar{F}\} \tag{4.139}$$

In which $\{\bar{F}\}$ is the additional dynamic hydraulic pressure due to the reservoir water

$$\{\bar{F}\} = \iint_{\Gamma} [\bar{N}]^T [l]^T [N]\{p\} d\Gamma = 1/\rho [S]^T \{p\} \tag{4.140}$$

Summarizing Eqs. (4.108), (4.131), (4.137), (4.139) and (4.140) yields the equation set for the coupling problem

$$\begin{cases} [H]\{p\} = -[S]\left(\left\{\ddot{\delta}\right\} + \left\{\ddot{\delta}_g\right\}\right) \\ [M]\left\{\ddot{\delta}\right\} + [C]\left\{\dot{\delta}\right\} + [K]\{\delta\} = -[M]\left\{\ddot{\delta}_g\right\} + 1/\rho [S]^T \{p\} \end{cases} \tag{4.141}$$

The first row in Eq. (4.141) may be expressed as

$$\{p\} = -[H]^{-1}[S]\left(\left\{\ddot{\delta}\right\} + \left\{\ddot{\delta}_g\right\}\right) \tag{4.142}$$

Introducing Eq. (4.142) into the second row in Eq. (4.141) results in

$$\left([M] + [M_p]\right)\left\{\ddot{\delta}(t)\right\} + [C]\left\{\dot{\delta}(t)\right\} + [K]\{\delta(t)\} = -\left([M] + [M_p]\right)\left\{\ddot{\delta}_g\right\} \tag{4.143}$$

In which $[M_p]$ is termed as the "added mass matrix".

$$[M_p] = 1/\rho [S]^T [H]^{-1} [S] \tag{4.144}$$

Equation (4.143) is actually identical to Eq. (4.107) in formalism and may be solved by any available algorithms inclusive that elaborated above.

4.4.8 *Dynamic Dam-Foundation Interaction and Seismic Input*

The importance of dam-foundation interaction on the dam deflection and stress has long been recognized for static as well as for dynamic actions (Wilson and Button

1982). In the standard foundation model exercised towards the seismic response analysis in the 1970s, some appropriate supports/restraints were employed at all vertical boundaries of the FE mesh to approximate its response to each specified component of earthquake motion. For example, rollers at the sides that permit horizontal motion merely enable to simulate the response to a cross-canyon earthquake motion. However, in such a manner the earthquake excitation transmitted to the base of dam may be artificially amplified, and the vibration properties of the dam-foundation system may be significantly altered due to the inertial effects of the foundation mass.

A modified massless foundation was proposed in the late 1970s and has been employed extensively until today. By assuming that the deformable foundation region is massless, the foundation only performs as a system of springs. Obviously, the absence of mass allows for the earthquake excitation being transmitted instantaneously through the foundation rock to the dam base without any wave propagation effects. It is appropriate to apply a free-field surface motion as the earthquake input at the base rock because the same free-field motion would be observed if there were no dam-foundation interaction effects. Another feature of the massless foundation is that the dam vibrations are not affected by the foundation mass. Thus, the vibration of foundation do not tend to dominate the dynamic behavior of the dam, as will happen if a large volume of foundation rock with mass is included.

A deconvolution procedure for producing input of non-uniform free-filed motion along the canyon of dam site and a corresponding multiple-excitation technique (mainly for arch dams) were developed and exercised in the aseismic design of dams in China since the 1980s. Typically, it is postulated that the free-field motion is recorded at the infinitely extended surface of a horizontally stratified deformable foundation. A base rock input that might have produced the free-field motion at the surface of this layered rock is determined by the inverse operation with respect to the one-dimensional wave propagation equation. This deconvolved rock motion is applied at the base of dam-foundation system, underneath the foundation rock possesses mass as well as stiffness. With the later presence of dam on canyon, the motions are modified by reflection and refraction at the canyon and dam interface dominated by the FE algorithms.

Recently, a more effective and accurate approach to solve the dam-foundation interaction problem in time domain has been developed with the transmitting boundary techniques. The dam-foundation system can be divided into an interior region with a discrete dam and its adjacent near-field foundation enclosed by a far-field infinite foundation region with a set of artificial boundaries. At these artificial boundaries the outgoing waves from the interior region can be transmitted without reflection. The transmitting boundary technique may take following three important factors into account

- The spatial variation both in the amplitude and phase of a seismic input along the deep canyon;
- The energy dispersion of a seismic wave in the semi-infinite rock foundation;

– The effects of the topographical features of a canyon and the nonlinear properties of geological strata.

4.4.9 Dynamic Material Parameters

Another issue of paramount importance for dynamic analysis is the input of dynamic material parameters, particularly the Young's modulus and shear modulus. Theoretically, these parameters may be obtain by dynamic tests on the laboratory samples, but the heterogeneous and isotropic characteristics of rock often force engineers to turn to the field nondestructive tests or empirical correlations.

Sudden application of a concentrated force to the surface of a homogeneous elastic body generates body waves and surface waves. The body waves are distinguished as compressive (*P*) and shear (*S*), the latter is further decomposed into vertically polarized (*SV*) and horizontally polarized (*SH*). In rock-like materials the velocity V_p of the *P* wave is related to the dynamic Young's modulus, density, and Poisson's ratio, while the velocity V_s of the *S* wave is related to the shear modulus and density. The dynamic Young's modulus (E_d) can be solved from the following equations

$$\begin{cases} V_p = \sqrt{\dfrac{E_d}{\rho}\dfrac{(1-\mu)}{(1+\mu)(1-2\mu)}} \\ V_s = \sqrt{\dfrac{E_d}{\rho}\dfrac{1}{2(1+\mu)}} \end{cases} \tag{4.145}$$

where ρ = bulk density, kg/m^3; μ = Poisson's ratio.

The Poisson's ratio may be directly calculated by the formula

$$\mu = \frac{\frac{1}{2}(V_p/V_s)^2 - 1}{(V_p/V_s)^2 - 1} \tag{4.146}$$

In general, the dynamic Young's modulus is significantly larger than the static one. It has also been documented (Howarth 1984) that the discrepancy is much larger for soft rocks (e.g. sandstone) than for hard rocks (e.g. granite). The discrepancies between the dynamic modulus and static modulus are mostly attributable to the micro cracks and pores in materials.

The dynamic Young's modulus can be converted into static modulus, and vice versa, by empirical correlations (Lacy 1997; Du et al. 2001).

The Chinese design specifications (DL 5073-2000) stipulate that in the dynamic computation for concrete dams, the dynamic Young's modulus of concrete is amplified by 1.3 times static one, but there is no suggestion with regard to the

foundation rocks, although in the practice the widely accepted treatment is to identically amplify it by 1.3 times static modulus. In contrast, the US federal guidelines (FEMA 2005) stipulate that the dynamic Young's modulus of concrete is amplified by 1.5 times static one, and no modulus amplification for foundation rocks is demanded.

4.5 Seepage Problems

4.5.1 Governing Equations and Solution Techniques

The permeability study relies on the solution of hydraulic potential (or water head) function $\phi(x, y, x)$ based on the principles of fluid dynamics. For example, the steady state permeability theory for pervious continuum directly comes from the analogue of fluid dynamics for continuous flow.

The general form of the Darcy's law Eq. (2.5) is valid in any Cartesian coordinate system, and it is always possible to determine a coordinate system in which the matrix $[k]$ becomes diagonal, as shown in Eq. (2.9). Introducing Eq. (2.9) into the equation of continuity

$$\frac{\partial v_x}{\partial x} + \frac{\partial v_y}{\partial y} + \frac{\partial v_z}{\partial z} + q_0 = 0 \tag{4.147}$$

The governing equation of the seepage flow in perfectly saturated materials under the postulation that both material grains and pore water are incompressible, is associated with three orthogonal local axes as

$$\frac{\partial}{\partial x}(k_x \frac{\partial \phi}{\partial x}) + \frac{\partial}{\partial y}(k_y \frac{\partial \phi}{\partial y}) + \frac{\partial}{\partial z}(k_z \frac{\partial \phi}{\partial z}) + q_0 = 0 \tag{4.148}$$

In which q_0 is the rate of inner source.

Restricted to the materials that are homogeneous and isotropic, i.e. $k_x = k_y = k_z = k$, and where there is no inner source, Eq. (4.148) may be reduced to the famous Laplace differential equation

$$\frac{\partial^2 \phi}{\partial x^2} + \frac{\partial^2 \phi}{\partial y^2} + \frac{\partial^2 \phi}{\partial z^2} = 0 \tag{4.149}$$

Equation (4.148) or (4.149) is subject to appropriate boundary conditions (see Fig. 4.13).

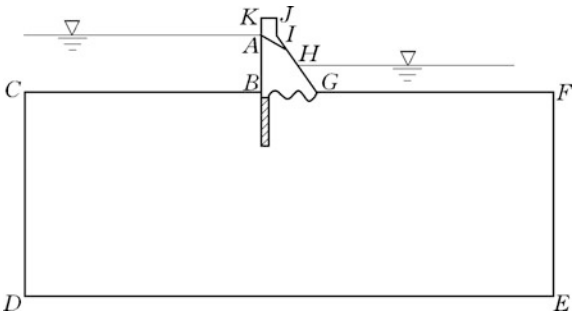

Fig. 4.13 Boundaries of the seepage regime of a gravity dam

1. First type boundary Γ_1 (Dirichlet)

This is the boundary on which the hydraulic potential is specified. For instance, the upstream surface (ABC), downstream exit surface (HI) and free discharge surface (FGH), are all the first type boundaries (see Fig. 4.13), on which

$$\phi(x,y,z)|_{\Gamma_1} = \phi_0(x,y,z) \tag{4.150}$$

where $\phi_0(x, y, z)$ = specified hydraulic potential, m.

2. Second type boundary Γ_2 (Neumann)

This is the boundary on which the normal gradient of hydraulic potential (or flow rate) is specified. For instance, on the boundary (CDEF) in Fig. 4.13 it is defined by

$$v_n = -k_n \cdot \left.\frac{\partial \phi}{\partial n}\right|_{\Gamma_2} = q(x,y,z) \tag{4.151}$$

where n = outside normal to the boundary surface; $q(x, y, z)$ = flow rate per unit area on the boundary surface, m/s, $q(x, y, z) = 0$ means the boundary is impervious.

3. Phreatic Γ_3 and outflow Γ_4 boundaries

Phreatic/free surface (AI) in Fig. 4.13 is a special boundary. Being a streamline of zero pressure, it should simultaneously satisfy the following conditions

$$\begin{cases} k_n \cdot \frac{\partial \phi}{\partial n}|_{\Gamma_3} = 0 \\ \phi(x,y,z)|_{\Gamma_3} = Z \end{cases} \tag{4.152}$$

On the outflow (exit) boundary (IH) in Fig. 4.13, we have

$$\begin{cases} k_n \cdot \frac{\partial H}{\partial n}|_{\Gamma_4} \neq 0 \\ \phi(x,y,z)|_{\Gamma_4} = Z \end{cases} \tag{4.153}$$

The solution of the governing Eq. (4.148) restrained by the boundary conditions in Eqs. (4.150)–(4.153) may provide the potential function $\phi = f(x, y, z)$ or conjugated stream function $q = g(x, y, z)$ of major practical interest, which may be further used to derive the seepage gradient J and seepage velocity v. However, complex boundaries make the exact analytical solution be very difficult, if not impossible, to access. The practical solution methods available are manual seepage flow net, physical model test, hydraulic method, numerical computation (e.g. FEM), and engineering analogue.

Towards the solution by the FEM, the above governing equation and boundary conditions are converted into the equivalent variational calculus (operator) for the function $I(\phi)$ (Yosida 1980) defined below

$$I(\phi) = \iiint_{\Omega} \left\{ \frac{1}{2} \left[k_x \left(\frac{\partial \phi}{\partial x} \right)^2 + k_y \left(\frac{\partial \phi}{\partial y} \right)^2 + k_z \left(\frac{\partial \phi}{\partial z} \right)^2 \right] - q_0 \phi \right\} d\Omega + \iint_{\Gamma_2} q \phi d\Gamma = \min \tag{4.154}$$

Since ϕ is a scalar, therefore the function $I(\phi)$ in Eq. (4.154) can be simply augmented from each element e in its bound coordinate system corresponding to principal permeability directions

$$\begin{aligned} I(\phi) &= \sum_{e}^{n_e} I^e(\phi) \\ &= \sum_{e}^{n_e} \left(\iiint_{\Omega_e} \left\{ \frac{1}{2} \left[k_x \left(\frac{\partial \phi}{\partial x} \right)^2 + k_y \left(\frac{\partial \phi}{\partial y} \right)^2 + k_z \left(\frac{\partial \phi}{\partial z} \right)^2 \right] - q_0 \phi \right\} d\Omega + \iint_{\Gamma_2} q \phi d\Gamma \right) \\ &= \min \end{aligned} \tag{4.155}$$

In which n_e stands the element amount in the structure system.

The function $I(\phi)$ in Eq. (4.155) is then discretized to obtain FE algorithm. Take the standard hexahedral element in Fig. 4.8 as example, on which there are 8 nodal potentials (ϕ_1, ϕ_2, …, ϕ_8) grouped into an element vector $\{\phi\}^e$. At any point within the element e, the hydraulic potential may be interpolated by

$$\begin{cases} \phi = [N]\{\phi\}^e \\ [N] = \begin{bmatrix} N_1 & N_2 & \dots & N_{f_e(p)} \end{bmatrix} \quad (for\, p = 1, f_e(p) = 8) \end{cases} \tag{4.156}$$

The flow velocity is calculated by the formula

$$\{\mathrm{v}\} = -[k][B]\{\phi\}^e \tag{4.157}$$

In which

$$\begin{cases} [B] = \lfloor [B_1] \quad [B_2] \quad \ldots \quad [B_{f_e(p)}] \rfloor \quad (for\, p = 1, f_e(p) = 8) \\ [B_i] = [N_{i,x} \quad N_{i,y} \quad N_{i,z}]^T = \left[\frac{\partial N_i}{\partial x} \quad \frac{\partial N_i}{\partial y} \quad \frac{\partial N_i}{\partial z} \right]^T \end{cases} \tag{4.158}$$

Introducing Eq. (4.156) into Eq. (4.155), the variational operator leads to

$$\frac{\partial I}{\partial \phi_i} = \sum_e^{n_e} \frac{\partial I^e}{\partial \phi_i} = 0 \quad (i = 1, 2, \ldots, DOF) \tag{4.159}$$

By looping over the elements around each node (freedom) i using Eq. (4.159), we get

$$[H]\{\phi\} = \{Q\} \tag{4.160}$$

In which the conductivity matrix $[H]$ and vector of discharge $\{Q\}$ arise from the boundary conditions of the structure system are assembled by their elementary components

$$[h]^e = \iiint_{\Omega_e} [B]^T [k][B] d\Omega \tag{4.161}$$

$$\{q\}^e = \iiint_{\Omega_e} [N]^T q_0 d\Omega - \iint_{\Gamma_2} [N]^T q d\Gamma \tag{4.162}$$

By the solved nodal potential $\{\phi\}$ from Eq. (4.160), the potential and the seepage flow velocity within an element may be calculated using Eqs. (4.156) and (4.157).

4.5.2 *Unconfined Seepage Problems*

The solution of an unconfined seepage problem demands the hydraulic potential (water head) within the regime enclosed by the boundaries and phreatic surface. The latter, being a special unknown boundary in the seepage regime, involves intrinsically geometrical nonlinearity and should be solved by certain iteration algorithms (France et al. 1971; Neumann 1973). However, where the unconfined seepage field manifests in a complex multi-connected domain, the nonlinearity due to the phreatic surface will be very intensive leading to difficulties in the convergence of iteration.

Algorithms for unconfined flow problems may be distinguished as fixed mesh and deformed mesh approaches (Bathe and Khoshgoftaar 1979). In the deformed

mesh approach, the computation is based on the domain below the phreatic surface solely that varies during the iterative process, while in the fixed mesh approach, however, the whole domain is taken into account and the phreatic surface is handled by setting different permeability properties for the portions below and above the surface. Essentially, the fixed mesh approach replaces the geometrical nonlinearity involved in the problem using material nonlinearity.

It is well known that many nonlinear boundary-value problems may be elegantly formulated using the theory of variational inequality, which has rigorous mathematics basis and provides a natural framework for the computation algorithm of flow through porous media. Take the unconfined seepage problem for example, use may be made of the continuous quasi-Heaviside function instead of the discontinuous stepwise Heaviside function, it is able to overcome mesh dependency and improve numerical stability much better (Chen et al. 2011b).

(1) Deformed mesh approach

With the deformed mesh approach, the element properties are held constant while the mesh is iteratively deformed to match the phreatic surface (Taylor and Brown 1967; Neumann and Witherspoon 1970; Chung and Kikuchi 1987; Fenton and Griffiths 1997). In this approach, an initial phreatic surface should be constructed according to the simplified analysis and engineering experiences, then the shape of elements is iteratively adjusted according to the results of the previous steps until the total water head at the phreatic surface is equal to the elevation head (i.e. null of pressure head).

High solution accuracy may be theoretically achieved but the mesh distortion appearing in the neighborhood of the phreatic surface may actually lead to high numerical errors. In addition, deformed mesh approach is often inflicted by the requirement of advanced theories which are unfamiliar to practical engineers.

(2) Fixed mesh approach: residual flow method

The residual flow method (Desai 1976) is a typical fixed grid approach where the boundary conditions on phreatic surface are met by the flow rate adjusting as follows.

① The whole domain is discretized and solved for nodal heads/potentials $\{\phi_r\}$.
② According to the condition $\phi_r = Z$, the tentative phreatic surface of the rth iteration is constructed.
③ The normal flow rate v_{nr} through the phreatic surface and the corresponding nodal flow vector $\{q_r\}$ are computed by

$$\{v_r\} = -[k][B]\{\phi_r\}^e \tag{4.163}$$

$$v_{nr} = \{l\}^T\{v_r\} \tag{4.164}$$

$$\{q_r\} = \iint_{\Gamma_3} [N]^T v_{nr} d\Gamma \tag{4.165}$$

In which $\{l\}$ is the outward normal unit vector of the rth tentative phreatic surface.

④ Solve the equation

$$[H]\{\Delta\phi_r\} = \{Q_r\} \tag{4.166}$$

In which $\{Q_r\}$ is the assemblage of the element residual flow rate $\{q_r\}$ (see Eq. 4.165).

⑤ Accumulate the total hydraulic potential after the rth iteration

$$\{\phi_{r+1}\} = \{\phi_r\} + \{\Delta\phi_r\} \tag{4.167}$$

⑥ The iteration will be terminated when $\{\Delta\phi_r\}$ is satisfactorily minor, otherwise let $r = r + 1$ and the iteration is recurred starting from step ②.

(3) Fixed mesh approach: initial flow rate method

Zhang et al. (1988) proposed a concept of initial flow, by adjusting the initial flow to enforce the zero flow through the phreatic surface. This method avoids the intersecting calculation of the phreatic surface in elements.

① The whole domain is discretized and solved for nodal heads/potentials $\{\phi_r\}$.
② According to the condition $\phi_r = Z$, the elements comprising tentative phreatic surface segment are recorded.
③ For each element containing phreatic surface segment, the initial flow rate is calculated by the integral over the dry portion (or saturated portion) only

$$\{q_r\} = -\iiint_{\Omega_e} [B]^T [k][B]\{\phi_r\}^e d\Omega \quad \text{(Gaussian point where } \phi_r < Z \text{ only)} \tag{4.168}$$

④ The initial flow rate $\{Q_r\}$ of the system is assembled using $\{q_r\}$, then we solve the potential increment by

$$[H]\{\Delta\phi_r\} = \{Q_r\} \tag{4.169}$$

⑤ Accumulate the total hydraulic potential after the rth iteration

$$\{\phi_{r+1}\} = \{\phi_r\} + \{\Delta\phi_r\} \tag{4.170}$$

⑥ The iteration will be terminated when $\{\Delta\phi_r\}$ is satisfactorily minor, otherwise let $r = r + 1$ and the iteration is recurred starting from step ②.

The initial flow rate method requires condensed Gaussian integration points to ensure the numerical accuracy and stability.

(4) Boundary pre-adjustment method

The initial (tentative) phreatic surface dominates the iterative efficiency in the fixed mesh approach. Where the boundary conditions are simple and the permeability properties of adjacent materials are similar, the solution of a confined seepage field in the same domain may be used to launch the iteration. However, there is the risk of non-convergence or very slow convergence because such an initial seepage field could depart from the exact solution significantly.

Boundary pre-adjustment method (Chen et al. 2000) is a useful strategy to handle the difficulties in defining initial tentative seepage field. It divides the boundary water level into n increments (see Fig. 4.14), then step by step, exerts them and solves the corresponding seepage field using fixed mesh approach. According to the seepage field related to the H_U^{i-1} of the $(i-1)$th incremental water level, use is made of its convergent phreatic surface as the tentative phreatic surface towards the next phase of iterative computation under the ith incremental water level H_U^i.

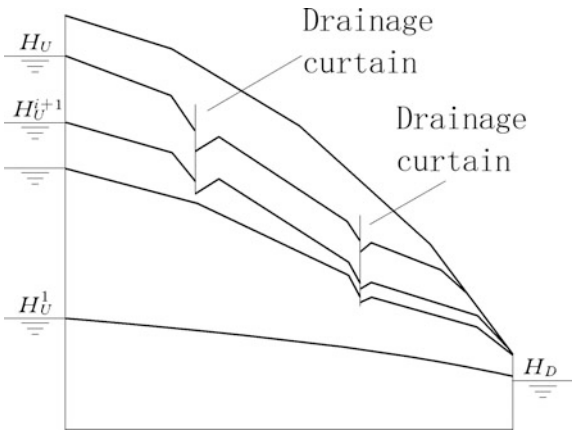

Fig. 4.14 Diagram to the phreatic surface iteration using boundary pre-adjustment method

4.5.3 Seepage Actions

As water seeps through porous or/and fractured materials it exerts a frictional drag on the material particles, which in turn, results in head losses. The frictional drag is termed as "seepage force" acting on materials, which is calculated as force per unit volume (it has the unit similar to that of weight).

$$f = \gamma_w \bar{J} \tag{4.171}$$

In which $\bar{J} = -grad(\phi)$ is the gradient of hydraulic potential.

This is an important concept to bear in mind that the volumetric seepage force is transferred from the hydrodynamic pressure of the percolated water, which is in turn, transferred from the boundary actions related to the up-and down-stream water. This concept may be helpful to prevent mistakes of neglecting or duplicating the action of seepage flow.

Suppose the hydraulic potential $\phi(x, y, z) = Z + \frac{p}{\gamma_w}$ has been solved in the regime, then the seepage force per unit volume may be computed by the formulas

$$\begin{cases} f_x = -\frac{\partial p}{\partial x} = -\gamma_w \frac{\partial \phi}{\partial x} \\ f_y = -\frac{\partial p}{\partial y} = -\gamma_w \frac{\partial \phi}{\partial y} \\ f_z = -\frac{\partial p}{\partial z} = -\gamma_w \frac{\partial \phi}{\partial z} + \gamma_w \end{cases} \tag{4.172}$$

where f_x, f_y, f_z = components of seepage force per unit volume, kN/m^3; γ_w = unit weight of water, kN/m^3; p = seepage pressure, kN/m^2.

The seepage force vector may be integrated over the element domain Ω_e

$$\{f\} = -\gamma_w \iiint_{\Omega_e} [N]^T \left[\frac{\partial \phi}{\partial x} \quad \frac{\partial \phi}{\partial y} \quad \frac{\partial \phi}{\partial z} - 1\right]^T d\Omega \tag{4.173}$$

Since

$$\left[\frac{\partial \phi}{\partial x} \quad \frac{\partial \phi}{\partial y} \quad \frac{\partial \phi}{\partial z}\right]^T = [B]\{\phi\}^e \tag{4.174}$$

We have

$$\{f\} = -\gamma_w \iiint_{\Omega_e} [N]^T [B]\{\phi\}^e d\Omega \gamma_w + \gamma_w \iiint_{\Omega_e} [N]^T \{I\} d\Omega, \quad \{I\} = [0 \quad 0 \quad 1]^T \tag{4.175}$$

4.6 Thermal and Thermal Stress Problems

4.6.1 Concept

To prevent early age cracking in concrete, one of the first concerned tasks for the engineers of concrete structures is the evaluation of the thermal field. Based on the evaluation the structural configuration and construction requirements inclusive protection and cooling measures can be designed or/and adjusted. Various methods are reported in literatures for the thermal problem of concrete, which are ranged from complex three-dimensional finite element analysis to simple manual calculation. Nowadays, the former is more and more prevalent.

Generally, the temperature history within concrete of hydraulic structures experiences three stages (Chen 2015).

① Early stage. This is a temperature mounting period, initiated from the casting and finished nearly at the end of the exothermic hydration of cement.
② Middle stage. This is a temperature falling period, commenced from nearly the end of the exothermic hydration of cement and terminated at the stable temperature. It often takes long time for exothermal concrete to lower down its temperature.
③ Late stage. This is the normal service period after totally cooling down of concrete. The zones underlying the surfaces (no deeper than 5–6 m from the surface) are exposed to seasonal temperature changes due to the temperature fluctuations of air and water and solar radiation, which is called as "quasi-stable temperature". In the portion deeper inside the mass structure, the fluctuations may be ignored and the temperature is actually stable assumed the mean annual temperature of the locality. For mass concrete structures such as gravity dams, the course reaches stable temperature is quite a long period ranged from several decades to more than one hundred years, if no artificial cooling measures would be carried out during the construction.

Due to both the development of the Young's modulus and the thermal action along with the ongoing of time, thermal stresses emerging within mass concrete structures also experience three stages as early stage thermal stresses, middle stage thermal stresses, and late stage thermal stresses. In temperature mounting period, the expansion of concrete lift is restrained by underneath foundation rock or old concrete. This restraint induces horizontal compressive stresses, which are of lower level because the Young's modulus at this stage has far from been fully developed. On the contrary, in the temperature falling period when concrete age exceeds 28 days and the Young's modulus is fairly developed, the shrinkage restraint results in higher horizontal tensile stresses, which give rise to net tensile stresses after the offset of early stage compressive stresses. If such a net tensile stress exceeds the tensile strength, undesirable cracking occurs. In addition, the surface radiation or

cold snap during mass concrete construction produces nonlinear temperature gradient from its surface to the internal portion, which also may result in surface cracking.

The analyses with regard to the thermal and thermal stress fields of mass hydraulic structures are accomplished by two steps: firstly, solve the thermal regime to obtain the temperature variation ΔT as a thermal action; then, apply the action ΔT to compute strain/stress increments in the structures (Fanelli and Giuseppetti 1975; Singh 1985; Tatro and Schrader 1985; Leger and Leclerc 2007).

4.6.2 Governing Equations and Solution Techniques

Temperature regime of a mass concrete structure, both in the construction period and operation period, may be solved by the heat transfer theory for continuum. The thermal action for a specified period is then defined as the temperature difference ΔT regarding the end and beginning of the period concerned (Zhu 1998; Zienkiewicz et al. 2005).

The governing equation of temperature $T(x, y, z, t)$ in the concrete structure is formulated on the basis of thermodynamics

$$\frac{\partial T}{\partial t} = a\left(\frac{\partial^2 T}{\partial x^2} + \frac{\partial^2 T}{\partial y^2} + \frac{\partial^2 T}{\partial z^2}\right) + \frac{\partial \theta}{\partial t} \tag{4.176}$$

where θ = adiabatic temperature rise (see Eq. 2.28), °C; a = thermal diffusivity (see Eq. 2.23), m^2/h.

The initial condition is specified as

$$T = T_0(x, y, z) \quad \text{When} \quad t = 0 \tag{4.177}$$

There are basically three types of boundary conditions (see Fig. 4.15).

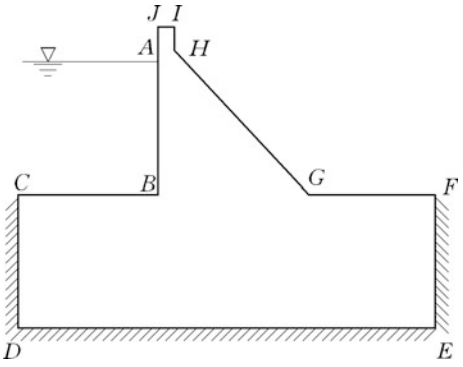

Fig. 4.15 Boundaries of the temperature regime of a gravity dam

1. First type boundary Γ_1 (Dirichlet condition, ABCDEF in Fig. 4.15)

$$T = T_b \tag{4.178}$$

For the dam face contacting reservoir water directly, T_b is the reservoir water temperature.

2. Second type Γ_2 (Neumann condition, FGHIJA in Fig. 4.15)

The normal component of flow (or flux) q_n is given as

$$q_n = -\lambda(\frac{\partial T}{\partial n}) = q(t) \tag{4.179}$$

where n = vector of direction cosines normal to the boundary surface; λ = thermal conductivity, kJ/(m h °C).

3. Third type Γ_3 (FGHIJA in Fig. 4.15)

$$q_n = -\lambda\frac{\partial T}{\partial n} = \beta(T - T_a) \tag{4.180}$$

where T_a = temperature of the water or air, °C; β = surface exothermic coefficient, kJ/(m^2 h °C).

If θ is zero meanwhile T_b, q and T_a are all constant, after a fairly long period the thermal field approaches a time independent state (i.e. $\frac{\partial T}{\partial t} = 0$), then we will encounter an particular case governed by the well known Laplace equation

$$\frac{\partial^2 T}{\partial x^2} + \frac{\partial^2 T}{\partial y^2} + \frac{\partial^2 T}{\partial z^2} = 0 \tag{4.181}$$

Similar to the permeability problem, we can get the following function $I(T)$ (Yosida 1980) whose minimization operator gives rise to identical governing equation and boundary conditions Eqs. (4.176)–(4.148).

$$\begin{aligned} I(T) = &\iiint_{\Omega} \left\{\frac{a}{2}\left[(\frac{\partial T}{\partial x})^2 + (\frac{\partial T}{\partial y})^2 + (\frac{\partial T}{\partial z})^2\right] + (\frac{\partial T}{\partial t} - \frac{\partial \theta}{\partial t})T\right\} d\Omega \\ &+ \iint_{\Gamma_2} \bar{q}T d\Gamma + \iint_{\Gamma_3} (\frac{\bar{\beta}}{2}T^2 - \bar{\beta}T_a T) d\Gamma \end{aligned} \tag{4.182a}$$

In which $\bar{\beta} = \beta/\lambda$ and $\bar{q} = q/\lambda$.

Normally in the thermal problem of concrete dams, the second type boundary does not presented. Under such circumstances we have

$$I(T) = \iiint_{\Omega} \left\{ \frac{a}{2} \left[(\frac{\partial T}{\partial x})^2 + (\frac{\partial T}{\partial y})^2 + (\frac{\partial T}{\partial z})^2 \right] + (\frac{\partial T}{\partial t} - \frac{\partial \theta}{\partial t})T \right\} d\Omega + \iint_{\Gamma_3} (\frac{\bar{\beta}}{2} T^2 - \bar{\beta} T_a T) d\Gamma \tag{4.182b}$$

A finite element solution in the space domain yields the semi-discrete set of ordinary differential equation, then a simple procedure in which the time domain is discretized by the central difference approximation gives rise to

$$([H] + \frac{2}{\Delta t}[R])\{T_{t+\Delta t}\} + ([H] - \frac{2}{\Delta t}[R])\{T_t\} + \{F_t\} + \{F_{t+\Delta t}\} = 0 \tag{4.183}$$

In which $[H]$ is the heat conductivity matrix of the structure system; $[R]$ is the heat capacity matrix; $\{F\}$ is the temperature load vector. They are assembled by the loop over each element using sub-matrices and vectors given by

$$\begin{cases} [h] = \iiint_{\Omega_e} a[B]^T[B] d\Omega \\ [r] = \iiint_{\Omega_e} [N]^T[N] d\Omega \\ \{f\} = \iiint_{\Omega_e} [N] \frac{\partial \theta}{\partial t} d\Omega - \iint_{\Gamma_3} [N]^T[N] \bar{\beta} d\Gamma + \iint_{\Gamma_3} [N] \bar{\beta} T_a d\Gamma \end{cases} \tag{4.184}$$

In which the matrices $[N]$ and $[B]$ are identical to that in Eqs. (4.156) and (4.158).

4.6.3 Temperature of Reservoir Water

The reliability and applicability of solutions using Eq. (4.183) are strongly dependent on the rationality in the evaluation of the thermal parameters related to the materials, the construction schedule, as well as the ambient factors such as the spatial-time variation of air temperature and reservoir water temperature, of which the last one (i.e. T_b) is quite complicated. Nowadays sufficient experiences have been accumulated for a good understanding of the water temperature in the majority of China's reservoirs (in temperate zone only) (Zhu 1998; Chen et al. 2011a).

(1) Features of reservoir water temperature

The temperature of reservoir water is an important boundary condition that entails the thermal performance of hydraulic structures (Raphael 1962), and is difficult to be exactly prescribed in the design phases. On the reservoir surface it often, although not always, fluctuates more than 10 °C, meanwhile in the middle and bottom regions the water body remains rather stable. The current methods for

studying the water temperature distribution in reservoirs include empirical or statistical formulas, engineering analogues and numerical computations (Huber et al. 1972; Orlob and Selna 1983).

Figures 4.16 and 4.17 display the water temperatures observed from two typical China's reservoirs, from which it may be concluded that

① During the warm season, superficial water is heated by shortwave solar radiation and air convection attributable to the sun shine. As a result, it is a bit of warmer than that of ambient temperature. In the cold season when the superficial water is frozen, thermal energy is more uniformly distribute in the reservoir water body due to the wind-induced turbulent diffusion and cloud albedo.

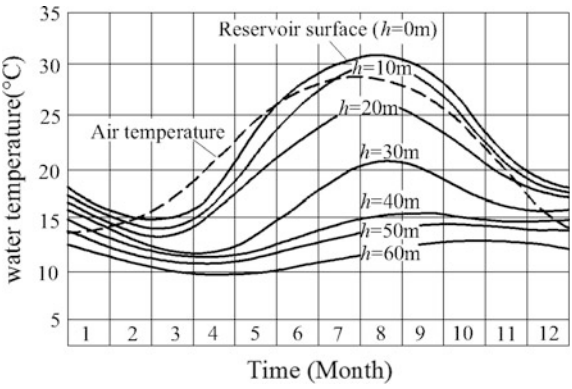

Fig. 4.16 Xinfengjiang reservoir, Guangdong Province, China

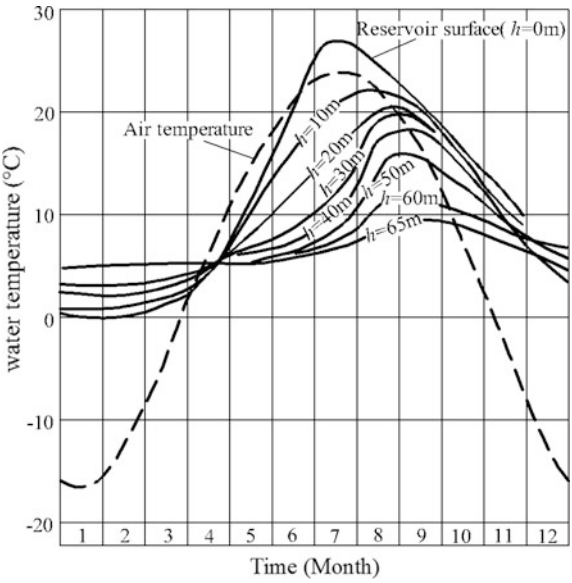

Fig. 4.17 Fengman reservoir, Jiling Province, China

② Generally, isothermal surfaces in the water body stay parallel with the reservoir surface.

③ At a certain depth, the periodic annual fluctuation manifests. The deeper of the water, the slighter will be the fluctuation extent. In addition, the temperature fluctuation of reservoir water body lags behind the ambient temperature. Generally, the fluctuation of reservoir temperature may be neglected in the reservoir water deeper than 80 m.

④ The reservoir bottom is dominated by the geothermy, inflow, and turbidity current. If there is no turbidity current and other special scenarios, the bottom temperature in the reservoir at chilly region is approximately 4–6 °C. For the reservoir at climate region, it is around the average ambient temperature of the coldest three-months in winter. Where the inflow is mainly from the melt water of snow mountains, or there is abnormal geo-heat sources, it is subject to an augment of ± (2–3) °C.

⑤ A stable cold sinking current causes the thermal stratification in the entire reservoir in a manner of

- Superficial layer (epilimnion). This is a layer of 10–20 m thick and is more sensitive to the meteorological conditions, particularly the seasonal ambient temperature fluctuation;
- Buffer layer (transition zone between epilimnion and hypolimnion). This is attributable to strong diffusion and convection of heat, the water intakes and other outlets assigned to the reservoir operation;
- Stable layer (hypolimnion). For a reservoir deeper than 100 m, the minor influence of ambient temperature and the sink of colder and denser water give rise to a relatively stable and low temperature layer, except for there is the influence of low level bottom outlets;
- Where there is the influence of turbidity current or initial deposition of thick slag/silt to dam heel, the local temperature near the reservoir bottom in front of the dam could be abnormally and significantly higher.

(2) Prediction of reservoir water temperature using semi-empirical correlations

Under periodical boundary conditions and with the 1-D thermal PDEs in hydrodynamics, the semi-empirical correlation Eq. (4.185) proposed by Zhu (1999) can be employed to forecast the 1-D distribution of the water temperature $T(h, t)$ (°C) along the reservoir depth h at time t (month)

$$T(h,t) = T_{\mathrm{m}}(h) + A(h)\cos\omega(t - t_0 - \varepsilon) \tag{4.185}$$

where $T_{\mathrm{m}}(h)$ = annual average temperature, °C; $A(h)$ = amplitude of temperature fluctuation at the depth of h, °C; ε = phase difference, (month); $\omega = 2\pi/\mathrm{P}$, circular frequency of temperature fluctuation (P = 12 months), °C; t_0 = emerging time of maximum annual ambient temperature, month.

1. Amplitude of temperature fluctuation $A(h)$ at water depth h

$$A(h) = A_0 \Sigma k_i e^{-\beta_i h} \tag{4.186}$$

Or

$$A(h) = A_0 e^{-\beta h^s} \tag{4.187}$$

In which k_i, β_i, β and s are the constants evaluated through the field observation data, and $\Sigma k_i = 1$.

According to the reservoir observation data collected in China, the following empirical formula may be used in the most China's reservoirs

$$A(h) = A_0 e^{-0.018h} \tag{4.188}$$

The amplitude of temperature fluctuation on the reservoir surface A_0 is normally postulated as

$$A_0 = A_a = (T_7 - T_1)/2 \tag{4.189}$$

where A_a = annually averaged ambient temperature, °C; A_7 = month average ambient temperature of the July (in China), °C; A_1 = month average ambient temperature of the January (in China), °C.

In chilly regions where the reservoir surface is frozen in the winter, we use following formula in lieu of Eq. (4.189)

$$A_0 = (T_7 + \Delta T)/2 = T_7/ + \Delta a \tag{4.190}$$

where Δa = influence of sun radiation, normally Δa = 1–2 °C.

2. Emerging time of the maximum annual ambient temperature t_0

It is normally postulated that in China t_0 = 6.5 (month), namely the highest temperature appears in between of June and July.

3. The phase difference ε

$$\varepsilon = 2.15 - 1.30 e^{-0.085h} \tag{4.191}$$

4. Annually average temperature $T_m(h)$ (°C)

$$T_m(h) = c + (T_s - c) e^{-0.04h} \tag{4.192}$$

$$\begin{cases} c = (T_b - T_s g)/(1 - g) \\ g = e^{-0.04H} \end{cases} \tag{4.193}$$

where H = depth of the reservoir in front of dam, m; T_s = annual average temperature on the reservoir surface, °C; T_b = annual average water temperature at the reservoir bottom, °C.

i. Annual average temperature on the reservoir surface T_s (°C)

In temperate region (annual average ambient temperature T_{am} = 10–20 °C) and hot area (T_{am} > 20 °C), where the reservoir surface is not frozen, T_s may be estimated by

$$T_s = T_{am} + \Delta b \tag{4.194}$$

In which Δb is the temperature augment due to sun radiation, normally Δb = 2–4 °C (temperate region) and Δb = 0–2 °C (hot area).

In chilly region where the reservoir surface is frozen in the winter, T_s may be estimated by

$$T_s = T'_{am} + \Delta b \tag{4.195}$$

$$T'_{am} = \frac{1}{12}\sum_{i=1}^{12} T_i \tag{4.196}$$

$$T_i = \begin{cases} T_{ai} & for \quad T_{ai} \geq 0 \\ 0 & for \quad T_{ai} < 0 \end{cases} \tag{4.197}$$

where T'_{am} = revised annual average ambient temperature, °C; T_{ai} = average ambient temperature of the ith month, °C.

Based on the field data collected in China, in chilly region we have Δb = 2 °C.

ii. Annual average water temperature at the reservoir bottom T_b (°C)

T_b is customarily evaluated by the engineering analogue using existing reservoirs of similar conditions. Where such analogue is absent in the preliminary phases of design, the data listed in Table 4.1 may be referred to. These data are merely applicable to the reservoirs deeper than 50 m in the mainland of China.

(3) Prediction of reservoir water temperature using numerical computations

Nowadays, computational methods such as the FEM have been extensively exercised to predict the temperature distribution of reservoir water by solving the vortex

Table 4.1 Annual average water temperature at reservoir bottom

Climate condition	Chilly (North-eastern China)	Chilly (Northern China, North-western China)	Temperate (Eastern China, Central China, South-western China)	Hot (Southern China)
T_b (°C)	4–6	6–7	7–10	10–12

motion of incompressible viscous fluid governed by the thermal convection-diffusion equations (Imberger et al. 1978). Of all the methods available, the 3-D model is the most powerful (Zhang and Baptista 2008) because it can provide detailed temporal and spatial patterns of reservoir temperature taking into account of the in-and out-flows, although the 1-D and 2-D models are still prevalent.

Methods using one-dimensional approach were initiated in the 1970s, when Stefan and Ford (1975) developed a deterministic, process-oriented, unsteady model for lake water quality. It uses a one-dimensional vertical transport equation to predict temperature as a function of depth and time under a wide range of meteorological conditions. The surface wind mixing, vertical turbulent diffusion, convective heat transfer, and heat flux from solar radiation, are all incorporated into his model by the regression analysis of field data.

Lei and Patterson (2002) proposed a two-dimensional approach using the Navier-Stokes and energy equations as well as the Boussinesq approximation to study the natural convection in a reservoir sidearm subject to solar radiation. Bednarz et al. (2009) used a similar approach to investigate the transient flow response to periodic temperature changes at reservoir water surface.

Compared with empirical formulas, the computational methods can strike a balance between accuracy, efficiency, economy, and applicability, which makes them very powerful for the reservoir temperature estimation. However, the effort for the computation is huge. In addition, vigilance is reminded that where there is numerical dispersion or oscillation due to improper treatments concerning the convection terms, the prediction quality would be even inferior to those by empirical formulas.

4.6.4 *Actions of Temperature: Elastic Analysis*

The initial strain $\{\Delta\varepsilon^T\}$ attributable to temperature variation ΔT under the circumstance without any restraint is related through the coefficient of thermal expansion α (see Eq. 2.131). In the appearance of restraint, the actual strain $\{\Delta\varepsilon\}$ (as yet unknown) and the stress $\{\Delta\sigma\}$ induced by ΔT in a finite element are related by the formula

$$\{\Delta\sigma\} = [D]\left(\{\Delta\varepsilon\} - \left\{\Delta\varepsilon^T\right\}\right) = [D]\,[B]\{\Delta\delta\} - [D]\left\{\Delta\varepsilon^T\right\} \tag{4.198}$$

where $[D]$ = elastic matrix; $[B]$ = strain matrix; $\{\Delta\delta\}$ = nodal displacement vector.

According to the virtual work principle Eq. (4.65) where $\{\Delta f\}$ is null, the governing equation for the solution of nodal displacement vector is given by

$$[K]\{\Delta\delta\} = \{\Delta F\} \tag{4.199}$$

In which the overall stiffness $[K]$ of the structure system is identical to that of Eqs. (4.71a, 4.71b), and the overall equivalent force vector $\{\Delta F\}$ due to temperature variation is assembled by the loop over each element using

$$\{\Delta f\} = \iiint_{\Omega_e} [B]^T [D]\{\Delta\varepsilon^T\} d\Omega \tag{4.200}$$

After the solution of the overall displacement vector $\{\Delta\delta\}$, the elastic stress increment due to thermal action may be computed using Eq. (4.198).

4.6.5 *Actions of Temperature: Viscoelastic Analysis (Creep)*

The concrete may deform continuously as the time goes on, which are resulted from mechanical, physical and chemical processes including:

- Temperature change. It is a very important action on concrete structures, of which two distinct phenomena need to be cared over. One is the hydration of the cement which warms up the structure during its setting and hardening, another is the fluctuation of ambient temperature under the construction and normal service conditions. All these may lead to cracking in concrete. In both cases the analyses of the thermal field in a structure and the consequently induced stresses need data on the adiabatic temperature rise, conductivity and diffusivity, specific heat and coefficient of thermal expansion (vide Chap. 2).
- Volume change. It is mainly due to the moisture variation and the consequent drying shrinkage in addition to the chemical reaction and the consequent autogenous shrinkage. The effect of drying shrinkage of mass concrete reduces rapidly along the thickness and become negligible at a depth of about 0.50 m.
- Creep. It is a kind of time-dependent deformation under sustained loading generally accepted as a rheological phenomenon associated with the gel-like component in the cement paste (Troxell et al. 1958; Nasser and Neville 1965; Neville et al. 1983). Creep phenomenon also can be partially explained in terms of viscoelastic and/or viscoplastic deformation of the cement paste and the gradual transfer of load from cement paste to aggregate. Creep properties are of particular relevance to understand the mechanism of potential thermal cracking of mass concrete, this is why the most extensive use of creep data is in the thermal stress analysis for concrete dams (Mehta and Monteiro 2006; Chen et al. 2011a). In recent decades it has been found that some forms of enhanced creep due to alkali-aggregate reactions can significantly affect the long term deflections and stresses of concrete structures, but for the moment this issue will not be addressed in this book.

Creep effects (short and long terms) need to be well handled, especially for structures of static indetermination such as arch dams, because they lead to the redistribution of stresses.

For the short term creep problem accompanied with temperature and volume changes, the incremental algorithm discretizes the time domain in a series of intervals (t_1, t_2 … t_n) with $\Delta t_n = t_n - t_{n-1}$ (see Fig. 2.22). In the interval Δt_n the strain and stress increments are expressed in Eqs. (2.133) and (2.134). The element equilibrium equation may be derived from the virtual work principle

$$\{\Delta f\}_t = \iiint_{\Omega_e} [B]^T \{\Delta\sigma\}_t d\Omega \tag{4.201}$$

Introducing Eq. (2.134) into Eq. (4.201) yields

$$\{\Delta f\}_t = [k]_t \{\Delta\delta\}_t - \{\Delta f^c\}_t - \{\Delta f^T\}_t - \{\Delta f^a\}_t - \{\Delta f^s\}_t \tag{4.202}$$

where $\{\Delta f^c\}_t$ = incremental element nodal load vector due to creep; $\{\Delta f^T\}_t$ = incremental element nodal load vector due to temperature; $\{\Delta f^a\}_t$ = incremental element nodal load vector due to autogenous shrinkage; $\{\Delta f^s\}_t$ = incremental element nodal load vector due to drying shrinkage.

The element stiffness matrix in term of $[\overline{D}]_t$ (see Eq. 2.98) is computed by

$$[k]_t = \iiint_{\Omega_e} [B]^{\mathrm{T}} [\overline{D}]_t [B] d\Omega \tag{4.203}$$

And the equivalent nodal force increments are computed by the formulas

$$\{\Delta f^c\}_t = \iiint_{\Omega_e} [B]^{\mathrm{T}} [\overline{D}]_t \{\eta\}_t d\Omega \tag{4.204}$$

$$\{\Delta f^T\}_t = \iiint_{\Omega_e} [B]^{\mathrm{T}} [\overline{D}]_t \{\Delta\varepsilon^T\}_t d\Omega \tag{4.205}$$

$$\{\Delta f^a\}_t = \iiint_{\Omega_e} [B]^{\mathrm{T}} [\overline{D}]_t \{\Delta\varepsilon^a\}_t d\Omega \tag{4.206}$$

$$\{\Delta f^s\}_t = \iiint_{\Omega_e} [B]^{\mathrm{T}} [\overline{D}]_t \{\Delta\varepsilon^s\}_t d\Omega \tag{4.207}$$

Following the routine procedure the governing equation of the structure system is assembled

$$[K]_t\{\Delta\delta\}_t = \{\Delta F\}_t + \{\Delta F^c\}_t + \{\Delta F^T\}_t + \{\Delta F^a\}_t + \{\Delta F^s\}_t \tag{4.208}$$

In which the system stiffness matrix and load vectors are assembled using that of all the elements in the discrete system

$$[K]_t = \sum_{\mathrm{e}} [k]_t \tag{4.209}$$

$$\begin{cases} \{\Delta F^c\}_t = \sum\limits_{\mathrm{e}} \{\Delta f^c\}_t \\ \{\Delta F^T\}_t = \sum\limits_{\mathrm{e}} \{\Delta f^T\}_t \\ \{\Delta F^a\}_t = \sum\limits_{\mathrm{e}} \{\Delta f^a\}_t \\ \{\Delta F^s\}_t = \sum\limits_{\mathrm{e}} \{\Delta f^s\}_t \end{cases} \tag{4.210}$$

Substituting for the nodal displacement increment $\{\Delta\delta\}_t$ in Eqs. (4.59) and (2.134) from the solution of Eq. (4.208) yields the incremental strain $\{\Delta\varepsilon\}_t$ and stress $\{\Delta\sigma\}_t$, then the stress at time t is accumulated by

$$\{\sigma\}_{t_n} = \{\Delta\sigma\}_{t_1} + \{\Delta\sigma\}_{t_2} + \cdots + \{\Delta\sigma\}_{t_n} = \Sigma\{\Delta\sigma\}_{t_i} \tag{4.211}$$

4.7 Safety Criteria

4.7.1 Concept

The structural performance is customarily assessed by means of calibration models using structural analyses (e.g. computation) based on physical understanding and empirical data. Due to idealized modeling, inherent physical uncertainties and inadequate or insufficient data, these models themselves and the parameters entering the models (e.g. material parameters and load characteristics), are uncertain.

The limited ability of engineers to calibrate structural performance is bridged by a variety of design criteria. These may be broadly classified as safety factor or factor of safety (FOS) and reliability index (RI), depending on the extent of the application of probability theory and statistics in the treatment of stochastic characteristics encountered in engineering (Cornell 1969; Hasofer and Lind 1974; Ellingwood et al. 1982; Ang and Tang 1984; Madsen et al. 1986; Chen 2015).

The FOS, generally noted as K to calibrate if a structure is stability or not, belongs to the philosophy of deterministic design. It treats the stochastic parameters deterministically using empirical methods. For example, for the loads of extreme adverse, small probability oriented values are used, whereas for the material

strength, conservative and high dependability (assurance factor) oriented values are adopted. When the FOS evaluated by computations or experiments is equal to or larger than the specified value (i.e. allowable safety factor or design safety factor), the structure is considered as safe.

Structural reliability theory belongs to the philosophy of indeterministic design. It uses probabilistic modeling for the uncertainties and provides methods for the quantification of the probability that a structure does not fulfill the performance criteria. In this way uncertainties can be related quantitatively to the design reliability of a structure. To facilitate the applications and to attend the habits of engineers, Chinese design codes or specifications recommend partial safety factor method base on limit state equation. In its mathematical principles, the partial safety factor method is a deterministic way to analyze limit state equation. However, it does consider the uncertainty by introducing a group of so-called partial safety factors larger than or equal to 1.

Nowadays in China, a fairly large portion of new version design codes or specifications for hydraulic structures are based on limit-state reliability analysis using partial safety factors, which are exercised particularly by the design institutes formerly belong to the State Electrical Ministry, Energy Ministry, or State Electrical Cooperation. On the other hand, the institutes belong to the Water Resources Ministry are used to adhere the design codes or specifications mainly based on the traditional FOS analysis (Chen 2015). The latter, which will be customarily employed throughout the whole coverage of this book, makes use the FOS of point, face, and global (overall), respectively.

4.7.2 Definition of Safety Factors

For each type of hydraulic structures, running FEM software produces the solutions with respect to displacement and stress, hydraulic potential and its gradient, temperature and its gradient, etc. These indices should be calibrated for the purpose of safe and economical design of the structure concerned.

(1) Point FOS K_p

Take the gravity dam in Fig. 4.18 for example. The Chinese design specifications demand following calibration works (Chen 2015).

① That the allowable stresses in the dam concrete or in the foundation rock shall not be exceeded. Particularly, the vertical stresses in the foundation rock and principal stresses in the dam concrete at the dam heel (A) and toe (C) are strictly limited within the corresponding allowable stress values (gravity method).

i. The tensile vertical stress at the dam heel, if any, should be lower than or equal to the allowable tensile stress of rock

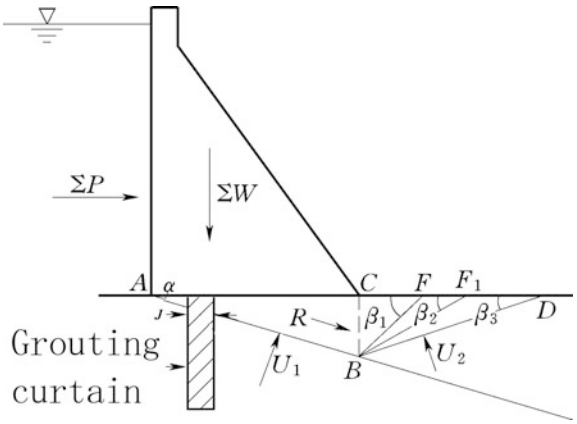

Fig. 4.18 Diagram to the stability assessment for a gravity dam

$$\sigma_{z,dam\quad heel} - [\sigma_l] \leq 0 \tag{4.212}$$

where $[\sigma_l]$ = allowable tensile stress of rock, MPa. It is usually zero in the gravity method.

ii. The compressive vertical stress at the dam toe should be lower than or equal to the allowable compressive stress of rock

$$\sigma_{z,dam\quad toe} - [\sigma_a] \leq 0 \tag{4.213}$$

where $[\sigma_a]$ = allowable compressive stress of rock that is defined as the ratio of the uni-axial compressive strength of rock to its correspondent FOS (K_p). K_p = 20–25 for hard and fractured rock, K_p = 10–20 for medium hard rock, K_p = 5–10 for lower strength rock, or soft rock.

iii. The point safety factor K_p is normally used in the FE computation for hydraulic structures, too. It is defined with yield (or failure) criterion in terms of yield resistance R and yield driving S

$$K_p = \frac{R}{S} \tag{4.214}$$

Take the Drucker-Prager criterion (see Eqs. 2.42 and 2.43) for example, we have

$$\begin{cases} K_p = \frac{aI_1 - k}{\sqrt{J_2}} \\ a = \sin\varphi / [3(3 + \sin^2\varphi)]^{1/2} \\ k = \sqrt{3}c\cos\varphi / \sqrt{3 + \sin^2\varphi} \end{cases} \tag{4.215}$$

In which φ and c are the internal friction angle and cohesion of the rock-like material.

It is notable that there is no clear stipulation in the Chinese design specifications for hydraulic structures with respect to the allowable point safety factor $[K_p]$. The widely but not unanimously accepted one for dam structures is $[K_p] = 2.0$ where only small and isolated portions below $[K_p]$ are permitted.

② That the allowable potential gradients in the dam concrete or foundation rock shall not be exceeded. Particularly, the potential gradients in the foundation grouting curtain are strictly limited within the corresponding allowable gradient, i.e.

$$J \leq [J] \tag{4.216}$$

where $[J]$ = allowable seepage gradient. For the rock foundation of a concrete dam, $[J]$ = 20–15 where dam height >100 m, $[J]$ = 15–10 where dam height 50–100 m, $[J] \leq 10$ where dam height <50; whereas for the dam concrete itself, $[J]$ is stipulated in Table 2.9.

The criteria stated in Eqs. (4.212)–(4.216) possess "point" or "local" feature. Normally, it is relatively easy to construct a local criterion and to specified its correspondent allowable index (right side item), but sometimes the singularities may bring about the difficulties in the selection of action effects such as the maximum stress and seepage gradient (left side item).

(2) Face FOS K_f

Again, we take the gravity dam for example. The Chinese design specifications demand the safety against sliding on any horizontal (e.g. AC in Fig. 4.18) or near-horizontal plane within the dam, at the base, or on any rock seam in the foundation (e.g. ABF, ABF_1, ABD in Fig. 4.18).

When the sliding prone surface AC is horizontal, the FOS is defined as the ratio of the total resistance to the resultant horizontal thrust along the surface, namely

$$K_f = \frac{f'(\sum V - U) + c'A}{\sum H} \tag{4.217}$$

where f' = shear friction factor; c' = shear cohesion factor; A = area of sliding surface; $\sum H$ = resultant horizontal loads; $\sum V$ = resultant vertical loads; U = uplift.

In the study of slope stability using FEM, Wright et al. (1973), Yamagami and Ueta (1988) defined the FOS as the ratio of the total shear resistance mobilized on a potential slip surface to the total slip driving force on the same surface, as

$$K_f = \frac{\sum_{i=1}^{n} (f_i \sigma_i + c_i) l_i}{\sum_{i=1}^{n} \tau_i l_i} \tag{4.218}$$

where σ_i = normal stress on the slip surface segment embedded in the element i; τ_i = shear stress on the slip surface segment embedded in the element i; f_i = friction coefficient of the slip surface segment i; c_i = cohesion representing the unit shearing strength of the slip surface segment i; l_i = length of the slip surface segment i.

The definition in Eq. (4.218) may also be termed as the "stress resultant method" (SRM) or "finite element method + limit equilibrium method" (FEM + LEM) and is most familiar to hydraulic engineers, although the calculated result often exhibits remarkably shift from that by the conventional limit equilibrium methods.

Normally, the face FOS K_f against sliding is less disturbed by the singularity problem, but paradoxically it introduces other difficulties in the construction of criterion and the sought of minimization.

(3) Overall FOS K

An overall FOS K may be further distinguished as overload factor or strength reduction factor.

1. Overload factor

The overload factor K is defined as the ratio of the ultimate load to the actual load exerting on the structure, to bring it to a state of limiting equilibrium at incipient failure. The critical (minimal) K is sought using trial and error procedure. For each tentative K, the finite element computation is carried out under the multiplied actions (by K). The critical K is looked at as the overload FOS for the structure under a specified work situation.

2. Strength reduction factor

The strength reduction factor K is defined as the ratio of the ultimate strength (resistance) divided by the mobilized stress (failure driving) to bring the structure to a state of limiting equilibrium at incipient failure (Matsui and San 1992; Ugai and Leschinsky 1995; Dawson et al. 1999; Griffiths and Lane 1999; Chen et al. 2007). The critical (minimal) K is sought using trial and error procedure. For each tentative K, the finite element computation is carried out under the reduced strength parameters (by K). The critical K is looked at as the FOS for the structure under a specified work situation.

In China, the strength reduction factor is widely accepted in the design of cut slope and embankment slope for hydraulic projects, because

- The loads on slopes are relatively more clear and easier to be prescribed. On the contrary, the strength parameters of rocks and soils exhibit larger variation and are more difficult to evaluate. Therefore it would be wise to use strength reduction factor to have a good understanding of the safety margin with regard to the parametric uncertainty.
- Self weight is a predominant load on slopes. Since it gives rise to both the driving force and resistance force, therefore overload factor is not very appropriate in the definition of the safety margin for slopes.

On the contrary, the concrete dam design prefers the overload factor by multiplying the reservoir water thrust solely, this is attributable to that

① The most important action is the reservoir water pressure laterally exerting on the concrete dam. This action possesses large variation following the reservoir water level fluctuation, particularly where the considerations on the landslide induced surge waves are demanded.
② The self weight of dam and foundation are relatively more clear and easier to be evaluated.

It is notable that for a definite computation method, significant difference in foregoing definitions for the FOS may manifest, although in particular simple cases they could be identical.

4.7.3 Searching for Overall Safety Factors

The most intractable question in the search of minimal overall safety factor is "how to pinpoint whether a hydraulic structure starts to enter a state of limit equilibrium at incipient failure"?

The loss of structural stability is actually identical to the loss of strength at the critical portion or surface in the structure. Accompanied by the loss of stability, the stress-deformation curve exhibits an extreme point, i.e. this is belong to the instability problems with extreme point. Prevalent detection algorithms for the incipient failure are related to the non-convergence in computation, penetration of plastic zone, catastrophe in displacement (or energy), and limit shear resistance.

(1) Non-convergence of solution

This is most commonly exercised (Dawson et al. 1999; Griffiths and Lane, 1999; Lechman and Griffiths 2000; Sloan 2013). When a structure reaches at the critical state (i.e. the limit equilibrium state), non-convergence will occur and the solution could escalate during the iterative process. However, because the convergence in nonlinear finite element computation is subjectively controlled by the tolerance magnitude of out-of-balance forces and/or the tolerance of nodal displacements specified by users, and by many other additional factors as well, non-convergence does not necessarily mean the collapse of structures.

(2) Penetration of plastic zone

Luan et al. (2003) (Zheng et al. 2008) suggested that a structural failure might take place as the moment at which there exists a plastic band going through the structure in such a manner that all the elements in the band enter plastic state. The major problem is, however, the mesh size and stretching dependent of the plastic zone.

(3) Catastrophe criterion (displacement, energy)

It says (Snitbhan and Chen 1978; Manzari and Nour 2000; Fu and Chen 2008; Chen et al. 2013; Liu et al. 2016) that when a structure reaches at the critical state, some characteristic points within the structure would enter a flow state deforming considerably in a manner described by the catastrophe theory (Zeeman 1977). This is theoretically correct but, in reality we are often puzzled that the moment entering the flow state would be changeable for these characteristic points.

(4) Limit shear resistance

The stress field corresponding to the reduced shear strength parameters or amplified loads (actions) is computed by the FEM, then the minimum stress resultant factor $K_{f,\min}$ in Eq. (4.218) is sought by optimization technique. When $K_{f,\min} = 1$, the structure is looked at as being brought into a state of limit equilibrium (Duncan 1996; Kim and Lee 1997; Farias and Naylor 1988).

References

Ang AH-S, Tang WH. Probability concepts in engineering planning and design, vol. I & II. New York: Wiley; 1984.

Argyris JH, Kelsey S. Energy theorems and structural analysis. London: Butterworth Scientific Publications; 1960.

Babuška I, Szabó BA, Katz IN. The p-version of the finite element method. SIAM J Numer Anal. 1981;18(3):515–45.

Babuška I, Griebel M, Pitkäranta J. The problem of selecting the shape functions for a p-type finite element. Int J Numer Meth Eng. 1989;28(8):1891–908.

Babuška I, Henshaw WD, Oliger JE, Flaherty JE, Hopcroft JE, Tezduyar T. Modeling, mesh generation, and adaptive numerical methods for partial differential equations. New York: Springer; 1995.

Bathe KJ, Khoshgoftaar MR. Finite element free surface seepage analysis without mesh iteration. Int J Numer Anal Meth Geomech. 1979;8(3):13–22.

Bathe KJ, Wilson EL. Stability and accuracy analysis of direct integration methods. Earthquake Eng Struct Dynam. 1972;1(3):283–91.

Bednarz TE, Lei CW, Patterson JC. Unsteady natural convection induced by diurnal temperature changes in a reservoir with slowly varying bottom topography. Int J Therm Sci. 2009;48 (10):1932–42.

Brown PT, Booker JR. Finite element analysis of excavation. Comput Geotech. 1985;1(3):207–20.

Cai M, Kaiser PK. Assessment of excavation damaged zone using a micromechanics model. Tunn Undergr Space Technol. 2005;20(4):301–10.

Caughey TH, Kelly MEJ. Classical normal modes in damped linear dynamic systems. J Appl Mech ASME. 1965;32(3):583–8.

Chen SH. Hydraulic structures. Berlin: Springer; 2015.

Chen SH, Wang WM, She CX, Xu MY. Unconfined seepage analysis of discontinuous rock slope. J Hydrodyn. 2000;12(3):75–86.

Chen SH, Chen SF, Shahrour I, Egger P. The feedback analysis of excavated rock slope. Rock Mech Rock Eng. 2001;34(1):39–56.

Chen SH, Qin WX, Shahrour I. Comparative study of sock slope stability analysis methods for hydropower projects. Mech Res Commun. 2007;34(1):63–8.

Chen SH, Zhang GX, Zhu YM. Thermal stresses and temperature control of concrete. In: Zhou JP, Dang LC, editors. Handbook of hydraulic structure design, vol. 5. Concrete dams (Chapter 6). Beijing: China Water Power Press; 2011a (in Chinese).

Chen YF, Hu R, Zhou CB, Li DQ, Rong G. A new parabolic variational inequality formulation of Signorini's condition for non-steady seepage problems with complex seepage control systems. Int J Num Anal Meth Geomech. 2011b;35(9):1034–58.

Chen SH, Wang GJ, Zhou H, Wang WM, Zou LC. Evaluation of excavation-induced relaxation and its application to an arch dam foundation. Int J Numer Anal Meth Geomech. 2012;36 (1):166–81.

Chen GQ, Huang RQ, Zhou H, et al. Research on progressive failure for slope using dynamic strength reduction method. Rock Soil Mech. 2013;34(4):1140–6 (in Chinese).

Chen HQ, Wu SX, Dang FN. Seismic safety of high arch dams. Beijing: Academic Press; 2015.

Cheng Z, Chen SH. Three dimensional hierarchical finite element method for hydraulic structure. J Hydraul Eng. 1999;21(12):53–8 (in Chinese).

Chilton L, Suri M. On the selection of a locking-free hp element for elasticity problems. Int J Numer Meth Eng. 1997;40(11):2045–62.

Chopra AK. Simplified earthquake of concrete gravity dam. J Struct Div ASCE. 1987;113 (ST8):1688–708.

Chopra AK, Chakrabarti P. Earthquake analysis of concrete gravity dams including dam-water-foundation rock interaction. Earthquake Eng Struct Dynam. 1981;9(4):363–83.

Chung KY, Kikuchi N. Adaptive methods to solve free boundary problems of flow through porous media. Int J Num Anal Meth Geomech. 1987;11(1):17–31.

Clough RW. The finite element in plane stress analysis. J Struct Div ASCE (Proceedings of the 2nd ASCE conference on electronic computation). 1960;23:345–78.

Clough RW, Penzien J. Dynamics of structures, 3rd ed. Berkeley: Computers & Structures Inc; 2003.

Cornell CA. A probability based structural code. ACI J. 1969;66(12):974–85.

Corthésy R, Leite MH. A strain-softening numerical model of core discing and damage. Int J Rock Mech Min Sci. 2008;45(3):329–50.

Courant R. Variational methods for the solution of problems of equilibrium and vibration. Bull Am Math Soc. 1943;49(1):1–61.

Crisfield MA. Non-linear finite element analysis of solid and structures, vol. 2. New York: Wiley; 1997.

Dawson EM, Roth WH, Drescher A. Slope stability analysis by strength reduction. Géotechnique. 1999;49(6):835–40.

Desai CS. Finite element residual schemes for unconfined flow. Int J Numer Meth Eng. 1976;10 (6):1415–8.

Desai CS, Drumm EC, Zaman MM. Thin layer element for interfaces and joints. J Geotech Eng ASCE. 1985;111(6):793–815.

Du L, Du L, Peng S, Wang Y. Back calculations of formation elastic properties in VTI media. World Geol. 2001;20(4):396–416.

Duhamel JMC. Mémoir sur la méthode générale relative au movement de le chaleur dans les corps solides plongers dans des milieux dont la temperature varie avec le temps. J de L' École Polytechnique Paris. 1833;14:20–77.

Duncan JM. State of the art: limit equilibrium and finite element analysis of slopes. J Geotech Geoenviron Eng ASCE. 1996;122(7):577–96.

Ellingwood B, MacGregor JG, Galambos TV, Cornell CA. Probability based load criteria: load factors and load combinations. J Struct Div ASCE. 1982;108(ST5):978–97.

Exadaktylos G, Tsoutrelis CE. Pillar failure by axial splitting in brittle rocks. Int J Rock Mech Min Sci Geomech Abstr. 1995;32(6):551–62.

Exadaktylos G, Tsouvala S, Liolios P, Barakos G. A three-dimensional model of an underground excavation and comparison with in situ measurements. Int J Num Anal Meth Geomech. 2007;31(3):411–33.

Fanelli DIM, Giuseppetti G. Techniques to evaluate effects of internal temperatures in mass concrete. Water Power Dam Constr. 1975;27(7):226–30.
Farias MM, Naylor DJ. Safety analysis using finite element. Comput Geotech. 1988;22(2):165–81.
FEMA. Federal guidelines for dam safety: earthquake analyses and design of dams. Washington, DC: FEMA; 2005.
Fenton GA, Griffiths DV. A mesh deformation algorithm for free surface problems. Int J Num Anal Meth Geomech. 1997;21(12):817–24.
France PW, Parekh CJ, Peters JC. Numerical analysis of free surface seepage problems. J Irrig Drainage Div ASCE. 1971;97(1):165–79.
Fu CH, Chen SH. Study on instability criteria of surrounding rock of underground engineering cavern based on catastrophe theory. Rock Soil Mech. 2008;29(1):167–72 (in Chinese).
Fujii Y, Kiyama T, Ishijima Y, Kodama J. Examination of a rock failure criterion based on circumferential tensile strain. Pure Appl Geophys. 1998;152(3):551–77.
Golshani A, Okui Y, Oda M, Takemura T. A micromechanical model for brittle failure of rock and its relation to crack growth observed in triaxial compression tests of granite. Mech Mater. 2006;38(4):287–303.
Goodman RE, Taylor R, Brekke TL. A model for the mechanics of jointed rock. J Soil Mech Found Div ASCE. 1968;94(SM3):637–60.
Griffiths DV, Lane PA. Slope stability analysis by finite element. Géotechnique. 1999;49(3):387–403.
Hasofer AM, Lind NC. An exact and invariant first order reliability format. J Eng Mech Div ASCE. 1974;100(EMl):111–21.
Hinton E, Irons B. Least squares smoothing of experimental data using finite elements. Strain. 1968;4(3):24–7.
Howarth DF. Apparatus to determine static and dynamic elastic moduli. Rock Mech Rock Eng. 1984;17(4):255–64.
Hrennikoff A. Solution of problems of elasticity by the frame-work method. ASME J Appl Mech. 1941;8(1):A619–715.
Huber WC, Harleman DRF, Ryan PJ. Temperature prediction in stratified reservoirs. J Hydraul Div ASCE. 1972;98(4):645–66.
ICOLD. Computational procedures for dam engineering—reliability and applicability (Bulletin 122). Paris: ICOLD; 2001.
ICOLD. Seismic design and evaluation of structures appurtenant to dams (Bulletin 123). Paris: ICOLD; 2002.
Imberger J, Patterson J, Hebbert B, Loh I. Dynamics of reservoir of medium size. J Hydraul Div ASCE. 1978;104(HY5):725–43.
Jäger P, Schmalholz SM, Schmid DW, Kuhl E. Brittle fracture during folding of rocks: a finite element study. Philos Mag. 2008;88(28–29):3245–63.
Kaiser PK, Amann F, Steiner W. How highly stressed brittle rock failure impacts tunnel design. In: Zhao J, et al., editors. Rock mechanics in civil and environmental engineering. Lausanne: ISRM; 2010. p. 27–38.
Kim JK, Lee SR. An improved search strategy for the critical slip surface using finite element stress fields. Comput Geotech. 1997;21(4):295–313.
Kwaśniewski M. Mechanical behavior of anisotropic rocks. Compr Rock Mech. 1993;4(1):16–22.
Kwaśniewski M, Takahashi M. Strain-based failure criteria for rocks: state of the art and recent advances. In: Zhao J, et al., editors. Rock mechanics in civil and environmental engineering. Lausanne: ISRM; 2010. p. 45–56.
Lacy LL. Dynamic rock mechanics testing for optimized fracture designs. In: SPE annual technical conference and exhibitions. San Antonio, TX: Society of Petroleum Engineers; 1997. p. 23–36 (Paper SPE38716).
Lechman JB, Griffiths DV. Analysis of the progression of failure of earth slopes by finite elements. In: Griffiths DV, et al., editors. Geotechnical special publication: slope stability. Denver, Colorado: ASCE; 2000. p. 250–65.

Leger P, Leclerc M. Hydrostatic, temperature, time-displacement model for concrete dams. J Eng Mech ASCE. 2007;133(3):267–77.
Lei CW, Patterson JC. Natural convection in a reservoir sidearm subject to solar radiation: a two-dimensional simulation. Numer Heat Transfer Part A. 2002;42(1–2):13–32.
Li X, Wu Z, Takahashi M, Yasuhara K. An experimental study on the failure strain-based failure criteria of brittle materials. J Appl Mech. 2000;3(8):387–94.
Liu XR, Tu YL, Zhong ZL, Liu YQ. Slope's failure criterion based on energy catastrophe in shear strength reduction method. J Central South Univ (Sci Technol). 2016;47(6):2065–72 (in Chinese).
Luan MT, Wu YJ, Nian TK. A Criterion for evaluating slope stability based on development of plastic zone by shear strength reduction FEM. J Disaster Prev Mitig Eng. 2003;23(3):1–8.
Madsen HO, Krenk S, Lind NC. Methods of structural safety. Englewood Cliffs: Prentice Hall; 1986.
Maejima T, Morioka H, Mori T, Aoki K. Evaluation of loosened zones on excavation of a large underground rock cavern and application of observational construction techniques. Tunn Undergr Space Technol. 2003;18(2):223–32.
Mahtab M, Goodman RE. Three dimensional analysis of joint rock slope. In: Proceedings of the 2nd ISRM congress, vol. 3. Beograd: Privredni Pregled; 1970, p. 353–60.
Malmgren L, Saiang D, Töyrä J, Bodare A. The excavation disturbed zone (EDZ) at Kiirunavaara mine, Sweden—by seismic measurements. J Appl Geophys. 2007;61(1):1–15.
Manzari MT, Nour MA. Significance of soil dilatancy in slope stability analysis. J Geotech Geoenviron Eng ASCE. 2000;123(1):75–80.
Martino JB, Chandler NA. Excavation-induced damage studies at the Underground Research Laboratory. Int J Rock Mech Min Sci. 2004;41(8):1413–26.
Matsui T, San KC. Finite element slope stability analysis by shear strength reduction technique. Soils Found. 1992;32(1):59–70.
Mehta PK, Monteiro PJM. Concrete: microstructure, properties, and materials, 3rd ed. New York: McGraw-Hill; 2006.
Moura A, Lei XL, Nishisawa O. Prediction scheme for the catastrophic failure of highly loaded brittle materials or rocks. J Mech Phys Solids. 2005;53(11):2435–55.
Nasser KW, Neville AM. Creep of concrete at elevated temperatures. ACI J. 1965;62(12): 1567–79.
Neumann ST. Saturated-unsaturated seepage by finite element. J Hydraul Div ASCE. 1973;99 (12):2233–50.
Neumann ST, Witherspoon PA. Finite element method of analyzing of steady seepage with a free surface. Water Resour Res. 1970;6(3):889–97.
Neville AM, Diger WH, Brooks JJ. Creep of plain and structural concrete. London: Construction Press; 1983.
Newmark NM. A method of computation for structural dynamics. J Eng Mech Div ASCE. 1959;85(EM3):67–94.
Oden JT. Finite elements of nonlinear continua. New York: Dover Publications; 2006.
Orlob GT, Selna IG. Temperature variation in deep reservoirs. J Hydraul Div ASCE. 1983;108 (HY3):301–25.
Owen DRJ, Hinton E. Finite elements in plasticity: theory and practice. Swansea: Pineridge Press Ltd; 1980.
Owen DRJ, Hinton E, Onate E. Computational plasticity: models, software and applications. Swansea: Pineridge Press Ltd; 1989.
Paulay T, Priestley MJN. Seismic design of reinforced concrete and masonry buildings. New York: Wiley; 1992.
Ramamurth T. Strength and modulus response of anisotropic rocks. Compr Rock Mech. 1993;4 (1):23–8.
Raphael JM. Prediction of temperatures in rivers and reservoirs. J Power Div ASCE. 1962;88 (2):157–81.

Sakurai S. Direct strain evaluation technique in construction of underground opening. In: Proceedings of the 22nd US symposium on rock mechanics. Cambridge: MIT; 1981, p. 278–82.
Sakurai S, Kawashima I, Otani T. A criterion for assessing the stability of tunnels. In: Ribeiro e Sousa L, Grossmann NF, editors. Proceedings of the 1993 ISRM international symposium EUROCK 93. Rotterdam: AA Balkema; 1995, p. 969–73.
Severn RT. The aseismic design of concrete dams (part one). Int J Water Power Dam Constr. 1978;28(1):37–8 (Part one), 28(2):41–6 (Part two).
Singh M. State-of-the-art finite element computer programs for thermal analysis of mass concrete structures. Civil Eng Practicing Des Eng. 1985;4(1):129–36.
Sloan SW. Geotechnical stability analysis. Géotechnique. 2013;63(7):531–72.
Snitbhan N, Chen WF. Elasto-plastic large deformation analysis of soil slopes. Comput Struct. 1978;9(6):567–77.
Stacey TR. A simple extension strain criterion for fracture of brittle rock. Int J Rock Mech Min Sci Geomech Abstr. 1981;18(6):469–74.
Stefan HG, Ford DE. Temperature dynamics in dimictic lakes. J Hydraul Div ASCE. 1975;101 (1):97–114.
Tatro SB, Schrader EK. Thermal considerations for roller-compacted concrete. ACI J. 1985;82 (2):119–28.
Taylor RL, Brown CB. Darcy flow solutions with a free surface. J Hydraul Div ASCE. 1967;93 (HY2):25–33.
Troxell GE, Raphael JM, Davis RE. Long-time creep and shrinkage tests of plain and reinforced concrete. Proc ASTM. 1958;58(3):1101–20.
Turner MJ, Clough RW, Martin HC, Topp LJ. Stiffness and deflection analysis of complex structures. J Aeronaut Sci. 1956;23(9):805–23.
Ugai K, Leschinsky D. Three dimensional limit equilibrium and finite element analyses: a comparison of results. Soil Found. 1995;29(4):1–7.
Webb JP, Abouchacra R. Hierarchal triangular elements using orthogonal polynomials. Int J Numer Meth Eng. 1995;38(2):245–57.
Westergaard HM. Water pressure on dams during earthquakes. Trans ASCE. 1933;98(2):418–33.
Wilson EL. Three dimensional static and dynamic analysis of structures: a physical approach with emphasis on earthquake engineering, 2nd ed. Berkeley, CA: Computers and Structures Inc; 1998.
Wilson EL, Button MR. Three-dimensional dynamic analysis for multi-component earthquake spectra. Earthquake Eng Struct Dyn. 1982;10(3):471–6.
Wilson EL, Khalvati M. Finite elements for the dynamic analysis of fluid-solid systems. Int J Numer Meth Eng. 1983;19(11):1657–68.
Wright G, Ulhawwy H, Duncan JM. Accuracy of equilibrium slope stability analysis. J Soil Mech ASCE. 1973;99(SN10):783–91.
Yamagami T, Ueta Y. Search for critical slip lines in finite element stress fields by dynamic programming. In: Proceedings of the 6th international conference on numerical methods in geomechanics. Rotterdam: AA Balkema; 1988, p. 1335–9.
Yosida Y. Functional analysis, 6th ed. Berlin: Springer; 1980.
Zeeman EC. Catastrophe theory: selected papers 1972–1977. Massachusetts: Addison Wesley Publishing Co; 1977.
Zhang YL, Baptista AM. SELFE: a semi-implicit Eulerian-Lagrangian finite element model for cross-scale ocean circulation. Ocean Model. 2008;21(3–4):71–96.
Zhang YT, Chen P, Wang L. Residual flow method for seepage problem with free surface. J Hydraul Eng. 1988;10(8):18–26 (in Chinese).
Zheng H, Liu DF, Li CG. On the assessment of failure in slope stability analysis by the finite element method. Rock Mech Rock Eng. 2008;41(4):629–39.
Zhou HM, Sheng Q, Li WS. Excavation-disturbed zone and weaken degree of mechanical properties for rock mass of TGP shiplock slope. Chin J Rock Mech Eng. 2004;23(7):1078–81 (in Chinese).

Zhu BF. Finite element method—principle and application, 2nd ed. Beijing: China Water Power Press; 1998 (in Chinese).
Zhu BF. Thermal stresses and temperature control of mass concrete. Beijing: China Electric Power Press; 1999 (in Chinese).
Zienkiewicz OC, Cheung YK. The finite element method for analysis of elastic isotropic and orthotropic slabs. Proc Inst Civil Eng. 1964;28(4):471–88.
Zienkiewicz OC, Taylor RL. The finite element method for solid and structural mechanics. New York: McGraw Hill; 1967.
Zienkiewicz OC, Mayer P, Cheung YK. Solution of anisotropic seepage by finite elements. J Eng Mech Div ASCE. 1966;92(1):111–20.
Zienkiewicz OC, Irons BM, Scott IC, Cambell JS. Three-dimensional stress analysis. In: Proceedings of the IUTAM symposium on high speed computing of elastic structures. Liege: University of Liege Press; 1970, p. 413–33.
Zienkiewicz OC, Taylor RL, Zhu JZ. The finite element method—its basis & fundamentals, 6th ed. Oxford: Elsevier Butterworth-Heinemann; 2005.
Zienkiewicz OC, Taylor RL, Fox DD. The finite element method for solid and structural mechanics, 7th ed. Oxford: Butterworth-Heinemann; 2013.

Chapter 5
Adaptive Techniques in the Finite Element Method

Abstract In computational methods, particularly the FEM, the adaptive refinement indicates an automatic convergence process. The motivations of adaptive study for hydraulic structures elucidated in this chapter are multi-fold inclusive pre-process facilitation and software standardization, of which the latter is more attractive because it may enable engineers to control the computation error tolerance for different grades of hydraulic structures, in lieu of optional and ambiguous consideration and discussion on the adequate mesh size. Towards this target, the most prevalent adaptive refinement schemes, namely, the h-version to control the error of approximation by means of element size and the p-version to control the error of approximation through the polynomial shape functions, are elaborated in this chapter. To be more practical for hydraulic structures, the issues of viscoplastic deformation, phreatic surface, refinement strategy, equation solver, etc., are specifically handled. This chapter is closed with a variety of validation examples (underground cavern, embankment dam, concrete dam, sluice) and two engineering application cases (cut slope, landslide).

5.1 General

In computational methods, particularly the FEM, the adaptive refinement indicates an automatic convergence process. The most commonly used adaptive refinement strategies fall into h-, p-, and hp-version. The approach to control the error of approximation by means of the element size h is called the h-version of refinement or simply the h-refinement. The approach to control the error of approximation through the augment of polynomial shape functions with progressively increasing degree p is called the p-version of refinement or simply the p-refinement. The latter possesses more rapid exponential convergence rates for a given number of variables subject to appropriate mesh design. The combination of h-version and p-version gives rise to the hp-refinement, in this procedure both the sizes of elements h and their degrees of polynomials p are altered (Guo and Babuška 1986a, b; Zienkiewicz et al. 1989).

S.-H. Chen, *Computational Geomechanics and Hydraulic Structures*,
Springer Tracts in Civil Engineering, https://doi.org/10.1007/978-981-10-8135-4_5

5.1.1 H-Version of Refinement

There are basically three sub-classes of h-refinement (Babuška and Rheinboldt 1978; Zienkiewicz and Zhu 1991).

(1) Element subdivision (enrichment)
If existing elements show too large approximation (discrete) error, they are simply divided into smaller ones keeping the original element boundaries intact. Such a process is cumbersome as many hanging points might be created where an element with mid-side nodes is joined to its adjacent linear element without such nodes. Local constraints at the hanging points are demanded and the calculations become more involved. Nevertheless, this refinement is quite welcome where its drawbacks are overcome by appropriate sub-division strategies.

(2) Complete mesh regeneration or re-meshing
Here, on the basis of a given solution using old mesh, a new element size is predicted and a totally new mesh is regenerated. In this way the refinement and de-refinement are simultaneously permitted. Of course this could be expensive, especially in three-dimensional cases where mesh generation is difficult for certain types of elements. In addition, it also presents a problem of transferring data from one mesh to another. For many practical engineering problems however, particularly for that the element shape will be severely distorted during the analysis, complete mesh regeneration is a natural choice. This refinement will be employed in this book in the elaboration of h-refinement algorithm.

(3) R-refinement
Also termed as s-refinement, it keeps the total number of nodes and the topology of mesh unchanged but adjusts nodal position to obtain an optimal approximation. Although this procedure is theoretically of interest, yet it is difficult to use in practice and there is little to recommend it.

5.1.2 P-Version of Refinement

By p-refinement we stay with the same element size and mesh topology but simply increase, hierarchically in general, the order of polynomials used in the shape functions. Although the FE software structure is more complicated, yet it had been demonstrated on the basis of elastic fracture mechanics that the sequences of solutions based on the p-refinement converge faster than the sequences based on the h-refinement (Szabó and Mehta 1978). The theoretical foundations of the p-refinement were established in a paper by Babuška et al. in 1981 where they shown that for a large class of problems the asymptotic convergence rate of the p-version in terms of energy norm is at least twice that of the h-refinement, subject

to quasi-uniform meshes. Additional computational results and evidences of faster convergence of the p-refinement were presented by Babuška and Szabó in 1982. In addition, the p-refinement performs well in handling singularities. The p-refinement algorithms fall into three sub-classes (Cheng and Chen 1999), too.

(1) Complete refinement
The polynomial order is increased uniformly throughout all the elements in the whole discretized domain.
(2) Element refinement
The polynomial order is adjusted locally with respect to each element in the whole discretized domain.
(3) Degree of freedom (DOF) refinement

DOF refinement is theoretically the most rigorous algorithm of p-refinement. It introduces more important DOFs to effectively control the discretization error.

5.1.3 Motivations of Adaptive Study for Hydraulic Structures

The motivations of adaptive study for hydraulic structures are multi-fold inclusive the facilitation in the pre-process and the software standardization in the design specifications. Particularly the latter may enable engineers to control the computation error tolerance e_t for different grade of hydraulic structures, in lieu of optional and ambiguous consideration and discussion on the adequate mesh size. Towards this target, the author believe that the specified error tolerance e_t may be eventually "check analyzed" from existing structures in service by the experienced engineers and scholars, towards the design specifications of new generation.

5.2 H-Version of Refinement in Space Domain: Strain/Stress Problems

5.2.1 Frameworks

The domain must be defined and covered by an initial background mesh. A finite element analysis carried out on this background mesh launches the iterative refinement, which is implemented by the following main steps (De et al. 1983; Zienkiewicz and Zhu 1991):

① A mesh is generated according to the given mesh size.
② A FE solution is obtained and the corresponding discretization error is estimated.

③ If the error does not meet the stipulated tolerance, the new mesh size related to the error is evaluated towards the next iterative refinement, then recur from step ①, otherwise the refined mesh and corresponding computation results are output to collapse the iteration.

The major functional modules in the h-refinement procedure are implemented to undertake following missions that:

- The mesh is generated by a well performed pre-process procedure;
- The discretization error is estimated reasonably and easily at all iterative stages;
- The transfer of mechanical and physical variables between tentative meshes is reliable and accurate.

A wide variety of algorithms has been devised for the generation of unstructured grids of complex geometrical representations (Babuška and Rheinboldt 1978, 1979) covering elasticity (Zienkiewicz and Zhu 1991), fluid dynamics (Peraire et al. 1987; Probert et al. 1991), metal process (Zienkiewicz et al. 1988), groundwater permeability (Rank and Werner 1986; Chung and Kikuchi 1987; Burkley and Bruch 1991; Chen 1996). A more detailed discussion on the issue of automatic mesh generation may be found in Chap. 3.

Two classes of discretization error estimators are currently available (Targowski et al. 1990). The first class introduced by Babuška and Rheinboldt (1978, 1989) is based on evaluating the residuals of approximate solution to obtain local, more accurate answers; the second class introduced by Zienkiewicz and Zhu (1987) estimates the error in gradient-based norms simply by improved values of gradient using available recovery process (Z^2 or ZZ-estimator). The latter is rather prevalent in the applications of h-refinement.

Obviously, the validation of the ZZ-estimator depends on the accuracy of the recovered value of gradient such as the stress denoted by $\{\sigma^*\}$. It customarily utilizes the discontinuous nature of the gradient across element boundaries to define an approximation of error. The earliest recovery technique made use of L_2 projection (Hinton and Campbell 1974; Kelly et al. 1983a, b; Babuška and Miller 1984a, b, c) and, even simpler, of averaging procedure. Later, it was found that reliable error estimators of the mesh discretization can be achieved by using the interpolation of recovered nodal values, of which the famous one is the Super-convergent Patch Recovery (SPR) (Zienkiewicz and Zhu 1992a, b; Wiberg and Abdulwahab 1993; Wiberg et al. 1994; Wiberg and Li 1994). In the SPR method, a patch of elements adjacent to a node is constructed, and the least squares fitting is performed at specific points within the element patch. The locations where the gradients are sampled are referred to as "super-convergent", implying that the accuracy order at these specific locations is higher than at arbitrary locations within the element. The high efficiency of the SPR has been proven (Zienkiewicz and Zhu 1995). A more general one is the Recovery by Equilibrium of Patches (REP) (Boroomand and Zienkiewicz 1997a, b), in which the original PDE (or equilibrium equation) is expressed in terms of the field we seek to recover, and then the PDE is solved in least squares sense over a patch of

elements adjacent to a given node (Tabbara et al. 1994). The REP has the advantage over the SPR in that it is applicable for any element type.

The data transfer between meshes (Ortiz and Quigley 1991; Zienkiewicz et al. 1995; Deb et al. 1996a, b; Cramer et al. 1999) is indispensable for adaptive h-refinement because that:

- The refined meshes for the stress computation and seepage computation are not overlapped;
- The different phases of rock excavation and concrete placement demand different meshes;
- Spatial-time characteristics attributable to the crack propagation (Wang 1987; Tradegard et al. 1998) or/and localization (Leroy and Ortiz 1990; Needleman 1992; Chen et al. 2007) need mesh adjustment and data transfer.

5.2.2 *Error and Element Size Estimators*

Towards the adaptive FEM computation of h-version refinement, the posteriori error and element size estimator is most essential.

Normally, the exact solution demanded in approximation error estimation is not accessible. In the ZZ-estimator, stress gradient error is approximated by the difference between the recovered solution $\{\sigma^*\}$ of higher order and the original FE solution $\{\sigma_h\}$ on the mesh with element size h.

Take the linear elastic problem for example, the governing equation of Eq. (4.71) may be reduced in terms of total displacement

$$[K]\{\delta\} = \{F\} \tag{5.1}$$

The total strain and stress hold the same forms in Eqs. (4.59) and (4.62) but neglect the incremental prefix Δ and time subscript t.

Under a certain family of elements with polynomial interpolation order p and mesh size h, denote the FE computed outcomes as $\{u_h\}, \{\varepsilon_h\}, \{\sigma_h\}$, and the precise solutions as $\{u\}, \{\varepsilon\}, \{\sigma\}$, then the error vectors are calculated by

$$\begin{cases} \{e_{u,h}\} = \{u\} - \{u_h\} \\ \{e_{\varepsilon,h}\} = \{\varepsilon\} - \{\varepsilon_h\} \\ \{e_{\sigma,h}\} = \{\sigma\} - \{\sigma_h\} \end{cases} \tag{5.2}$$

The point-wise definitions of errors $\{e\}$ are cumbersome in view of application, so various integral scales $\|e\|$, such as the so-called L_2-norm and the energy norm, are used.

– Energy norm

$$\|e_h\| = \left(\iiint_{\Omega} \left([B]\{e_{u,h}\}\right)^T [D] \left([B]\{e_{u,h}\}\right) d\Omega \right)^{\frac{1}{2}}$$
$$= \left(\iiint_{\Omega} \left(\{e_{\sigma,h}\}\right)^T [D]^{-1} \left(\{e_{\sigma,h}\}\right) d\Omega \right)^{\frac{1}{2}} \tag{5.3}$$

– L_2-norm

$$\|e_h\| = \left(\iiint_{\Omega} \left(\{e_{\sigma,h}\}\right)^T \left(\{e_{\sigma,h}\}\right) d\Omega \right)^{\frac{1}{2}} \tag{5.4}$$

The energy norm of the error in Eq. (5.3) will be employed in this book, based on which the error energy $U(u - u_h)$ is conventionally denoted as

$$U(u - u_h) = \|e_h\|^2 \tag{5.5}$$

The asymptotic convergence rate of the finite element solution (Zienkiewicz and Zhu 1991) states that

$$\begin{cases} \|e_h\| = O(h^l) \\ l = \min(p, \lambda) \end{cases} \tag{5.6}$$

Where p = order of the polynomials used in the shape functions; $\lambda < 1$ = intensity of singularities (if present).

Since the precise solution $\{\sigma\}$ cannot be accessed, therefore it is substituted by a "best guess" $\{\sigma^*\}$ in Eq. (5.3) to get

$$\|e_h\| \approx \|\tilde{e}_h\| = \left(\iiint_{\Omega} (\{\sigma^*\} - \{\sigma_h\})[D]^{-1} (\{\sigma^*\} - \{\sigma_h\}) d\Omega \right)^{\frac{1}{2}} \tag{5.7}$$

In hydraulic engineering, rock-like materials are often inhomogeneous, and discontinuities (e.g. faults, joints) frequently appear. Since the stress continuity is not guaranteed on a discontinuity surface, therefore it is advisable that the error estimator Eq. (5.7) should be worked out separately in different matter sub-domains. If the SPR procedure (Zienkiewicz and Zhu 1992a, b) is conducted in each material domain separately, the recovered stress field $\{\sigma^*\}$ is continuous in each sub-domain but exhibits jump across the sub-domain boundaries.

The effective index θ of the estimator is defined by

$$\theta = \frac{\|\tilde{e}_h\|}{\|e_h\|} \quad (0 \le \theta \le 1) \tag{5.8}$$

When $\theta \approx 1$, the estimator performs with the highest efficiency.
We express Eq. (5.7) in a way of

$$\|\tilde{e}_h\| = \|\sigma^* - \sigma_h\| = \|(\sigma^* - \sigma) - (\sigma_h - \sigma)\| \tag{5.9}$$

Then according to the characteristics of energy norm, we have

$$\|\sigma^* - \sigma\| - \|\sigma_h - \sigma\| \le \|\tilde{e}_h\| \le \|\sigma^* - \sigma\| + \|\sigma_h - \sigma\|$$

or

$$\|e_h\| - \|e^*\| \le \|\tilde{e}_h\| \le \|e_h\| + \|e^*\| \tag{5.10}$$

In which $\|e^*\|$ is the error norm between the "best guess" and precise solution. According to Eqs. (5.8) and (5.10) we get

$$\left(1 - \frac{\|e^*\|}{\|e_h\|}\right) \le \theta \le \left(1 + \frac{\|e^*\|}{\|e_h\|}\right) \tag{5.11}$$

Since $\frac{\|e^*\|}{\|e_h\|} \to 0$ following the refinement iteration, therefore according to Eq. (5.11) it may be confirmed that $\theta \to 1$.

5.2.3 *Practical Algorithm*

Due to the non-linear deformation, the simple relation between the displacement and the energy norm [see Eqs. (5.1)–(5.3)] no longer exists. Under such circumstances, we need more complicated procedures for the error and element size estimator (Stone and Babuška 1998; Boroomand and Zienkiewicz 1999). However, from the standpoint of hydraulic engineering application, a practical algorithm via "pseudo energy norm" is suggestible (Chen 1996; Xia and Chen 2001).

Suppose under the present mesh (with size h^{old}) the elasto-viscoplastic solutions $\{u_h\}, \{\varepsilon_h\}, \{\sigma_h\}$ are given where

$$\{u_h\} = [N]\{\delta_h\} \tag{5.12}$$

And the definition of error vector in Eq. (5.2) is held.

The pseudo energy norm of error is defined in an analogue way similar to Eq. (5.7).

$$\|e_h\| = \left(\iiint_{\Omega} \{e_\sigma\}^T \{e_\varepsilon\} d\Omega \right)^{1/2} \tag{5.13}$$

Equation (5.13) is integrated on the whole domain Ω but also may be accumulated by the summation of all the contributions from individual element i in the square form

$$\|e_h\|^2 = \sum_{i=1}^{n_e} \|e_h\|_i^2 \tag{5.14}$$

In which $\|e\|_i$ represents the contribution from element i, n_e is the element amount. The estimated relative error is

$$e = \|e_h\| / \|u\| \tag{5.15}$$

In which $\|u\|$ is the corresponding energy norm of the exact (precise) solution calculated by

$$\|u\| = \left(\iiint_{\Omega} \{\sigma\}^T \{\varepsilon\} d\Omega \right)^{1/2} \tag{5.16}$$

Where the error is uniformly distributed in each element and the error tolerance e_t is specified, we have

$$\|e_h\|_i^2 = \|e_h\|^2 / n_e \quad (i = 1, 2, \ldots, n_e) \tag{5.17}$$

Introducing Eqs. (5.15) and (5.16) into Eq. (5.17) leads to

$$\|e_h\|_i = e_t \|u\| / \sqrt{n_e} \quad (i = 1, 2, \ldots, n_e) \tag{5.18}$$

We may define a refinement parameter ξ_i as follows

$$\xi_i = \sqrt{n_e} \, \|e_h\|_i / (e_t \|u\|) \quad (i = 1, 2, \ldots, n_e) \tag{5.19}$$

For all the element i, $\xi_i = 1$ entails the optimal mesh and the h-refinement is accomplished. Otherwise the new element size h_i^{new} towards the next iterative refinement is calculated by the formula

$$h_i^{new} = h_i^{old} / \xi_i^{1/l} \quad (i = 1, 2, \ldots, n_e) \tag{5.20}$$

In which $l = \min(p, \lambda)$, p is the order of the shape functions and $\lambda < 1$ is the intensity of the singularity.

The new element size h_i^{new} may be looked at as being located at the center of the old element i, which is assembled into the database as a portion of back ground messages for the generation of new mesh.

5.2.4 Data Transfer

For a large class of nonlinear problems the mesh configuration needs to change (Kato et al. 1993). Upon re-meshing, material history data and internal variables in addition to strains/stresses have to be mapped from the old mesh to a new one. In practice, this involves transferring state variables from a discrete number of points (nodes or/and integral points) in the old mesh to another set of points in a new mesh.

The data that need to be transferred in the elasto-viscoplastic computation may be uniformly termed as

$$\Lambda_{h,t} = \left(\{u_h\}_t, \{\varepsilon_h\}_t, \{\sigma_h\}_t, \{H_{a,h}\}_t\right) \tag{5.21}$$

Where $\{u_h\}_t$ = displacement; $\{\varepsilon_h\}_t$ = strain; $\{\sigma_h\}_t$ = stress; $\{H_{a,h}\}_t$ = internal variable related to viscoplasticity.

These variables may be located at nodes (e.g. displacements) or at integral points (e.g. stresses, strains, internal variables), respectively.

Several important aspects of the transfer operation ought to be well cared are:

- Consistency with the constitutive equations;
- Equilibrium of the system;
- Compatibility with the displacement field on the new mesh;
- Compatibility with evolving boundary conditions;
- Minimization of the numerical diffusion of state variables.

Since state variables may be stored at the integral points or/and nodes, two different types of transfer operators are generally needed. Suppose at time instant $t + \Delta t$ the state variable $\Lambda_{h,t+\Delta t}$ is solved, and the error estimation indicates the refinement of $h + 1$, the data transfer operators are defined below according to Perić et al. (1996).

$$\{u_{h+1}\}_{t+\Delta t} = \Gamma_1\left(\{u_h\}_{t+\Delta t}\right) \tag{5.22}$$

$$\left(\{\sigma_{h+1}\}_{t+\Delta t}, \{\varepsilon_{h+1}\}_{t+\Delta t}, \{H_{a,h+1}\}_{t+\Delta t}\right) = \Gamma_2\left(\{\sigma_h\}_{t+\Delta t}, \{\varepsilon_h\}_{t+\Delta t}, \{H_{a,h}\}_{t+\Delta t}\right) \tag{5.23}$$

The transfer operator Γ_1 is simple because it links the old nodes directly to the new nodes. The operator Γ_2 corresponding to Gaussian quadrature points is more complex involving the steps depicted in Fig. 5.1. It transfers Λ to the nodes first, then further to the Gaussian quadrature points.

(1) Extrapolation of a continuous state variable field on the old mesh (see Fig. 5.1a)

Use is made of standard nodal extrapolation and average, a continuous state variable $\Lambda^N_{h,t}$ may be get from the original discrete values $\Lambda^G_{h,t}$ at the integration points

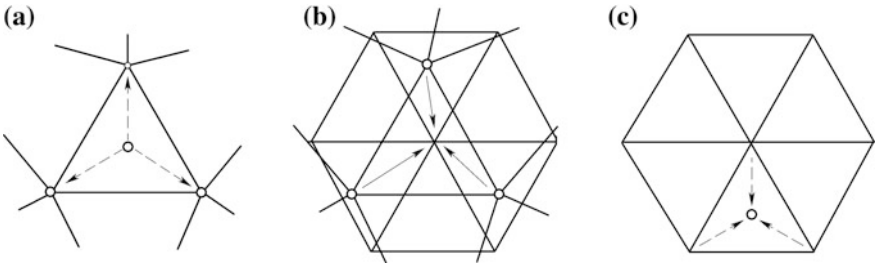

Fig. 5.1 Steps of the operator Γ_2 (linear triangle element)

$$\Lambda_{h,t}^{N} = \Gamma_2^1 \Lambda_{h,t}^{G} \tag{5.24}$$

In which the superscripts N, G indicate the nodal and Gaussian points, respectively.

Evidently, this step constitutes an important source of numerical diffusion. More advanced techniques similar to the SPR to construct a smooth field meanwhile to cut down transfer diffusion are for instance, the global least squares approximation (Hinton and Campbell 1974) and the iterative procedure (Loubignac et al. 1977).

(2) Interpolation of a continuous state variable field on the new mesh (see Fig. 5.1b)

For each new node, the element of the old mesh containing this new node is determined in terms of its normalized coordinates. The new nodal values $\Lambda_{h+1,t}^{N}$ are then easily computed using the old shape functions and the field of continuous state variable $\Lambda_{h,t}^{N}$ on the old mesh

$$\Lambda_{h+1,t}^{N} = \Gamma_2^2 \Lambda_{h,t}^{N} \tag{5.25}$$

This is implemented through three detailed steps as follows.

① For the node j in the new mesh $(h+1)$ with coordinate $\{x_{h+1}\}_j$, the background element $\Omega_{h,e}$ is sought in the old mesh (h) (see Fig. 5.2), i.e. $\{x_{h+1}\}_j \in \Omega_{h,e}$.

– Search an old node most close to the new node j, all the old elements related to this old node are grouped as candidate elements.
– The normalized coordinates $\{R_h\}_j = [\xi_{hj} \quad \eta_{hj} \quad \zeta_{hj}]^T$ of the node j corresponding to each candidate element are calculated using the Newton-Raphson iterative procedure

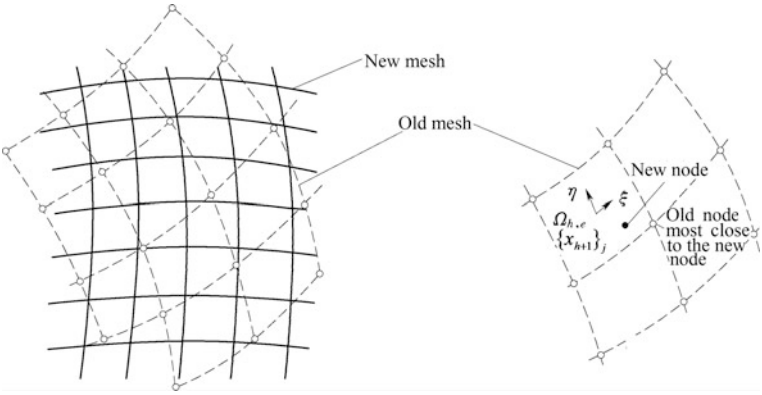

Fig. 5.2 Identification of element

$$\{G\} = \{x_{h+1}\}_j - \sum_{i=1} N_i\Big(\{R_h\}_j\Big)\{x_h\}_i = 0 \tag{5.26}$$

In which $\{x_h\}_i$ are the nodal coordinates of the candidate element and $N_i\big(\{R_{h,j}\}\big)$ is the ith shape function of the candidate element.

If $0 \le R_{h,j} \le 1$ (for triangular and tetrahedral element)
$-1 \le R_{h,j} \le 1$ (for quadrilateral and hexahedral element)

The candidate element is selected as the target element.

② The shape functions of the old mesh (h) are employed to interpolate the state variable defined at the new node j

$$\Lambda^N_{h+1,t} = \sum_{i=1} N_i\Big(\{R_h\}_j\Big)\Big(\Lambda^N_{h,t}\Big)_i \tag{5.27}$$

③ The shape functions of the new mesh ($h+1$) are employed to interpolate the state variable at the new Gaussian quadrature point (see Fig. 5.1c)

$$\Lambda^G_{h+1,t} = \sum_{i=1} N_i\big(\{R^G_{h+1}\}\big)\Big(\Lambda^N_{h+1,t}\Big)_i \tag{5.28}$$

The above procedure makes use of shape function interpolation and least squares minimization, which will more or less bring about data diffusion, i.e. localization features might be smoothed. Data diffusion can be further brought about by computing the state variable on new integration (quadrature) points directly from the continuous state variable field on the old mesh (Lee and Bathe 1994). All these

introduce inconsistencies (Pavana Chand and Krishna Kumar 1998). Consistency here refers to the correct mutual dependencies between the transferred state variables on the basis of governing equations. Ortiz and Quigley (1991) showed that by applying the Hu-Washizu principle, a consistent transfer operator for the state variables from the old Gaussian quadrature point directly to a new one, can be derived.

5.3 H-Version of Refinement in Space Domain: Seepage Problems

Adaptive FEM was firstly implemented for the steady state seepage problems in 1986 (Rank and Werner 1986; Chung and Kikuchi 1987). In 1991, Burkley and Bruch established an adaptive FE algorithm for the unconfined seepage problem through a homogeneous earth fill dam with triangle mesh. Chen et al. (1996), Feng and Chen (2003) generalized it into the practical algorithm with 2-D quadrilateral mesh and 3-D tetrahedral mesh. Since the Z^2 or ZZ-estimator aiming at the elasticity problem (Zienkiewicz and Zhu 1987) possesses clear physical concept and can be easily implemented, therefore the mesh error and size estimator for seepage problem was similarly proposed by these pioneering researchers.

Denote the exact solution of hydraulic potential and flow rate as ϕ and $\{v\}$, and the corresponding FE solution on the mesh of size h^{old} as ϕ_h and $\{v_h\}$. Error is therefore defined as the difference between the exact solution and the approximate solution

$$\begin{cases} e_{\phi,h} = \phi - \phi_h \\ e_{v,h} = \{v\} - \{v_h\} = -[k]\left[\frac{\partial}{\partial x} \quad \frac{\partial}{\partial y} \quad \frac{\partial}{\partial z}\right]^T e_{\phi,h} \end{cases} \tag{5.29}$$

It is convenient to scale the error in terms of "energy norm" in the form of

$$\|e_h\| = \left(\iiint_{\Omega} \{e_{v,h}\}^T [k]^{-1} \{e_{v,h}\} d\Omega \right)^{1/2} \tag{5.30}$$

In which $[k]$ is the permeability matrix.

Since we cannot get the exact solutions with regard to ϕ and $\{v\}$ in Eq. (5.29) unless under very simple boundary conditions, the estimation of mesh error involves the comparison of the approximate solution with other more precise solution $\{v^*\}$ termed as the "best guess" of $\{v\}$. $\{v^*\}$ may be given by a similar procedure of SPR, or even simply by the average surrounding the nodes using the recovered nodal values on element-base, i.e.

$$\{v^*\}_i = [N]\{\bar{v}^*\}_i^N \tag{5.31}$$

The nodal vector $\{\bar{v}^*\}_i^N$ of the element i is given by

$$\{\bar{v}^*\}_i^N = \frac{1}{m}\sum_{j=1}^{m}\{v^*\}_j^N \tag{5.32}$$

In which j runs over m elements around the node N concerned, and

$$\iiint_{\Omega_j} [N]^T([N]\{v^*\}_j^N - \{v_h\}_j)d\Omega = 0 \tag{5.33}$$

The energy norm of error in Eq. (5.30) is defined in the entire domain Ω and normally calculated by the square summation of all the elements n_e in the discrete domain

$$\|e_h\|^2 = \sum_{i=1}^{n_e}\|e_h\|_i^2 \tag{5.34}$$

A good approach of the total energy norm of ϕ can be postulated as

$$\|\phi\|^2 \approx \|\phi_h\|^2 + \|e_h\|^2 \tag{5.35}$$

In which

$$\|\phi_h\| = \left(\iiint_{\Omega} \{v_h\}^T[k]^{-1}\{v_h\}d\Omega\right)^{1/2} \tag{5.36}$$

In general, the error is scaled in terms of an overall percentage energy norm, i.e.

$$e = \frac{\|e_h\|}{\|\phi\|} \tag{5.37}$$

If this error is equal to the tolerance specified by the user, namely

$$e = e_t \tag{5.38}$$

The optimal mesh has been obtained, otherwise the element size h should be refined by distributing the error evenly among elements, i.e.

$$\|e_h\|_i^2 = \|e_h\|^2/n_e \quad (i = 1, 2, \ldots, n_e) \tag{5.39}$$

Substituting $\|e_h\|^2$ from Eq. (5.37) in Eq. (5.39) yields

$$\|e_h\|_i = e_t\|\phi\|/\sqrt{n_e} \quad (i = 1, 2, \ldots, n_e) \tag{5.40}$$

We may define a refinement parameter ξ_i as

$$\xi_i = \sqrt{n_e}\|e_h\|_i/(e_t\|\phi\|) \quad (i = 1, 2, \ldots, n_e) \tag{5.41}$$

For all the element i, $\xi_i = 1$ entails the optimum mesh. Otherwise the new element size h_i^{new} towards the next iterative refinement is calculated by the formula

$$h_i^{new} = h_i^{old}/\xi_i^{1/l} \quad (i = 1, 2, \ldots, n_e) \tag{5.42}$$

In which $l = \min(p, \lambda)$, p is the order of the shape function and $\lambda < 1$ is the intensity of the singularity.

In Fig. 5.3 we construct the flow chart towards the seepage analysis using the h-refinement FEM. It comprises 4 major modules for mesh generation, seepage analysis, error and mesh size estimation, and post process, respectively.

5.4 H-Version of Refinement in Time Domain: Elasto-Viscoplasticity Problems

5.4.1 Concept

For problems of parabolic types (e.g. viscoplastic deformation, transient heat conduction, unsteady seepage and transport) and hyperbolic types (e.g. dynamic response), the discretization and integration (marching, stepping) scheme in time domain plays a crucial role in preserving computation convergence and efforts (Zienkiewicz et al. 1984; Zienkiewicz and Taylor 1985; Selman 1992; Wiberg et al. 1992; Wiberg and Li 1994). At specific time t_i where the subscript i denotes the sequence of discrete time steps taken to reach t_i, most of direct time integration schemes require the solution to be specified in the previous instant t_{i-1}. The time-stepping (marching) length $\Delta t_i = t_i - t_{i-1}$ should be prescribed, too. These schemes can be categorized into heuristic methods, in which the time-step is controlled by either the rate of convergence of the solution or the rate of variation of a state variable, and adaptive methods, in which an estimator for time-stepping error is employed to adaptively set/adjust the time-stepping length.

It is troublesome to choose an appropriate time-stepping length for the direct time integration process with heuristic methods. Selecting smaller time-stepping length provides more detailed and stable description of the response, but spends larger computation resources. The correct choice of time-stepping length must consider the conflict between the demands of solution accuracy in addition to the

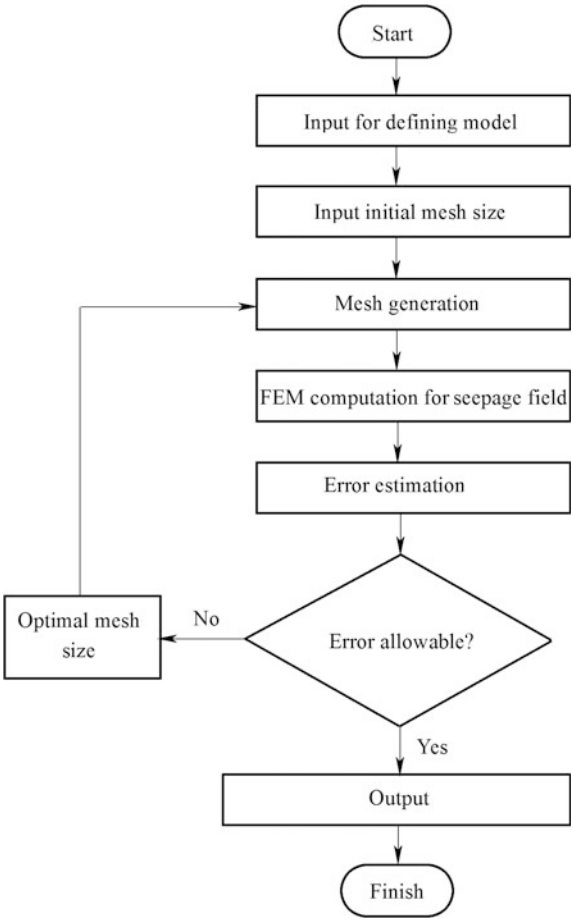

Fig. 5.3 Flow chart for the seepage analysis of h-refinement

numerical stability (in some cases) and computational effort. Unfortunately, the optimal time-stepping length may change considerably during the computation due to the changes in actions and/or system nonlinearities. Thus, although the fixed time-stepping scheme is prevalent and its length choice is frequently based on intuition and experience, the desirable approach is adaptive (automatic) strategy seeking the largest possible time-stepping length while maintaining a prescribed accuracy efficiently.

Adaptive time-stepping algorithms for parabolic and hyperbolic problems available may be distinguished into three types as follows (Rossi et al. 2014).

– Current characteristic frequency (Park and Underwood 1980). It was initially a strategy based on a scale of the residual force vector computed at the midpoint of the time interval, and was further developed by Bergan and Mollestad (1985) to estimate time-stepping length using an expression similar to the Rayleigh quotient.

- Local error estimator (Zienkiewicz and Shiomi 1984; Zienkiewicz and Xie 1991; Zhang and Chen 1996, 1997). It is based on a simple expression as an indicator of local error obtained at little computational effort. Hulbert and Jang (1995), Chung et al. (2003) proposed a priori error estimator and automatic time-stepping algorithms applied to the integration process for generalized Newmark-α method. It uses only information in the previous and current time steps without a feedback process, which is required in most conventional a posteriori error estimators.
- Indicator of curvature (Lages et al. 2013). It is a strategy that employs an estimator based on the geometric indicator of displacement history curvature. This estimator is obtained at little computational effort and is applicable to various existing direct time integration methods.

For structural dynamic analyses, Bergan and Mollestad (1985) suggested a set of criteria to evaluate control strategies for time-stepping length. Briefly, these are

- The optimized time-stepping length should not be influenced by the initial stepping length;
- The time-stepping length should remain constant during a linear stationary response;
- The time-stepping length should not be influenced by the selection of physical units or by the DOFs in the dynamic equations;
- All of the input parameters should be easily described;
- The additional computational cost for time-stepping length selection should be as small as possible;
- The time-stepping length should react immediately to sudden changes in a dynamic response analysis;
- The time-stepping length should not change without necessity.

In the following coverage of this section, only elasto-viscoplastic problems are addressed to give our readers the general idea with regard to the automatic time-stepping algorithms based on the adaptive refinement.

5.4.2 Refinement Strategies

Refinement strategies can control the time-stepping length using either a posteriori or a priori estimators of the truncation error. A posteriori refinement calculates the error based on the result just obtained (Babuška and Rheinboldt 1978), using for example, the extrapolation technique (Abbasian and Carey 1997; Belfort et al. 2007). A priori refinement (Schneid et al. 2004) attempts to determine a bound on the truncation error beforehand. The latter is however, difficult to ensure accuracy and depends on the convergence rate as well as the derivate of the function.

In the elasto-viscoplastic potential theory (Owen and Hinton 1980), the viscoplastic strain increment may be expressed by

$$\{\Delta\varepsilon^{vp}\}_t = \left[(1-\Theta)\{\dot{\varepsilon}^{vp}\}_t + \Theta\{\dot{\varepsilon}^{vp}\}_{t+\Delta t}\right]\Delta t \tag{5.43}$$

In which $\{\dot{\varepsilon}^{vp}\}_{t+\Delta t}$ and $\{\dot{\varepsilon}^{vp}\}_t$ are the viscoplastic strain rates that occur at the beginning and the end of the time step, respectively.

We also have

$$\{\dot{\varepsilon}^{vp}\}_{t+\Delta t} = \{\dot{\varepsilon}^{vp}\}_t + [H]_t\{\Delta\sigma\}_t \tag{5.44}$$

In which $[H]_t$ is the implicit matrix [see Eq. (2.129)] and $\{\Delta\sigma\}_t$ is the stress increment in the interval Δt.

$$[H]_t = \frac{\partial\{\dot{\varepsilon}^{vp}\}_t}{\partial\{\sigma\}_t} \tag{5.45}$$

$$\{\Delta\sigma\}_t = ([H]_t)^{-1}(\{\dot{\varepsilon}^{vp}\}_{t+\Delta t} - \{\dot{\varepsilon}^{vp}\}_t) \tag{5.46}$$

In Eq. (5.43), an implicit parameter $\Theta \geq 1/2$ guarantees unconditional numerical stability. Although this means that Δt may be selected without worries over the noise producing unaccepted oscillation or even abnormal collapse in computation, yet the time-stepping length is additionally restrained to keep the balance between the computation effort and accuracy.

In elasto-viscoplastic problems when the time-stepping is unconditionally stable, the accuracy is customarily ascertained by the heuristic strategies. Use is often made of minimum and maximum time-stepping lengths, time-step reduction, enlargement factor, and a maximum number of iterations. Two fractional values of the maximum number of iteration are also exercised for determining when the time-stepping length is adjusted: if the solution converges in fewer iterations than the lower fractional value, the time-stepping length is reduced and vice versa (Owen and Hinton 1980). Towards the more clever adjustment of time-stepping length, and further, the standardized computational software for practitioners, adaptive time-stepping is recognized as a better strategy (Zienkiewicz and Shiomi 1984; Zienkiewicz and Taylor 1985; Zhang and Chen 1997).

5.4.3 *Error Estimators*

Introducing Eq. (5.44) into Eq. (5.43), we have (Zhang and Chen 1997)

$$\{\Delta\varepsilon^{vp}\}_t = \{\dot{\varepsilon}^{vp}\}_t\Delta t + \Theta\Delta t[H]_t\{\Delta\sigma\}_t \tag{5.47}$$

Since at any time $t+\Delta t$, the viscoplastic strain $\{\varepsilon^{vp}\}_{t+\Delta t}$ is cumulated by $\{\varepsilon^{vp}\}_{t+\Delta t} = \{\varepsilon^{vp}\}_t + \{\Delta\varepsilon^{vp}\}_t$, we have

$$\{\varepsilon^{vp}\}_{t+\Delta t} = \{\varepsilon^{vp}\}_t + \{\dot{\varepsilon}^{vp}\}_t \Delta t + \Theta \Delta t [H]_t \{\Delta\sigma\}_t \tag{5.48}$$

Equation (5.48) gives "extrapolation solution" or "differential solution" of $\{\varepsilon^{vp}\}_{t+\Delta t}$ with 1st-order in terms of the truncation of the Taylor series.

Suppose that at the start of time marching we hold an accurate solution $\{\varepsilon^{vp}\}_t$, then with the Taylor series expansion we may get the higher order solution of $\{\varepsilon^{vp}\}_{t+\Delta t,ex}$ as the "best guess" of the exact solution $\{\varepsilon^{vp}\}_{t+\Delta t}$ at the end that

$$\{\varepsilon^{vp}\}_{t+\Delta t,ex} = \{\varepsilon^{vp}\}_t + \{\dot{\varepsilon}^{vp}\}_t \Delta t + \frac{1}{2}\Delta t^2 \{\ddot{\varepsilon}^{vp}\}_t + o\left(\Delta t^3\right) \tag{5.49}$$

The time-stepping error can be calculated using high-order items in the Taylor series by the subtraction operation between the "extrapolation solution" Eq. (5.48) and the "exact solution" Eq. (5.49) as

$$\{\varepsilon^{vp}\}_{t,error} = \{\varepsilon^{vp}\}_{t+\Delta t} - \{\varepsilon^{vp}\}_{t+\Delta t,ex} = \Theta [H]_t \{\Delta\sigma\}_t \Delta t - \frac{1}{2}\Delta t^2 \{\ddot{\varepsilon}^{vp}\}_t + o\left(\Delta t^3\right) \tag{5.50}$$

Introducing Eq. (5.46) into Eq. (5.50), we have

$$\{\varepsilon^{vp}\}_{t,error} = \Theta \Delta t \left(\{\dot{\varepsilon}^{vp}\}_{t+\Delta t} - \{\dot{\varepsilon}^{vp}\}_t\right) - \frac{1}{2}\Delta t^2 \{\ddot{\varepsilon}^{vp}\}_t + o\left(\Delta t^3\right) \tag{5.51}$$

The truncated Taylor series for $\{\dot{\varepsilon}^{vp}\}_{t+\Delta t}$ is employed to calculate the second order derivation $\{\ddot{\varepsilon}^{vp}\}_t$ in Eq. (5.51), i.e.

$$\{\dot{\varepsilon}^{vp}\}_{t+\Delta t} = \{\dot{\varepsilon}^{vp}\}_t + \Delta t \{\ddot{\varepsilon}^{vp}\}_t + o\left(\Delta t^2\right) \tag{5.52}$$

From Eq. (5.52) we get

$$\{\ddot{\varepsilon}^{vp}\}_t = \frac{1}{\Delta t}\left(\{\dot{\varepsilon}^{vp}\}_{t+\Delta t} - \{\dot{\varepsilon}^{vp}\}_t\right) + o(\Delta t) \tag{5.53}$$

Insert Eq. (5.53) into Eq. (5.51) and neglect the 3rd-order item gives rise to

$$\{\varepsilon^{vp}\}_{t,error} = (\Theta - \frac{1}{2})\Delta t \left(\{\dot{\varepsilon}^{vp}\}_{t+\Delta t} - \{\dot{\varepsilon}^{vp}\}_t\right) \tag{5.54}$$

Equation (5.54) is the local error estimator of second order defined at Gaussian quadrature points. It is found that Eq. (5.54) does not hold where Θ = 1/2 because in this case the time-stepping scheme Eq. (5.43) intrinsically possesses higher order accuracy, hence a similar deduction gives rise to a substitute error estimator of higher order as

$$\{\varepsilon^{vp}\}_{t,error} = (\Theta - \frac{1}{3})\Delta t(\{\dot{\varepsilon}^{vp}\}_{t+\Delta t} - \{\dot{\varepsilon}^{vp}\}_t) - \frac{1}{6}\Delta t^2\{\ddot{\varepsilon}^{vp}\}_t \tag{5.55}$$

5.4.4 Implementation

The Euclid norm of the local error is used to scale the error η (Zhang and Chen 1997).

$$\eta = \left\|\{\varepsilon^{vp}\}_{t,error}\right\| = \sqrt{(\{\varepsilon^{vp}\}_{t,error})^T\{\varepsilon^{vp}\}_{t,error}} \tag{5.56}$$

The normalized dimensionless error is further defined by the formula

$$e = \frac{\eta}{\left\|\{\Delta\varepsilon^{vp}\}_{\max}\right\|} \times 100\% \tag{5.57}$$

In which $\left\|\{\Delta\varepsilon^{vp}\}_{\max}\right\|$ is the Euclid norm of the maximum viscoplastic strain increment. Since the error e is different in each Gaussian quadrature point, the maximum error $e_{\max}$ is selected to control the time-stepping length for the whole structure system

$$e_{\max} = \underset{i,g}{Max}(e) \tag{5.58}$$

In which i and g cover all the elements and Gaussian points emerging viscoplastic deformation.

After the specification of error tolerance (allowable or permissible error) e_t, the time-stepping length at each step is controlled according to

$$\begin{cases} e_{\max} = e_t \\ e_{\max} < e_t \\ e_{\max} > e_t \end{cases} \tag{5.59}$$

- $e_{\max} = e_t$. The solution is accepted and the marching process proceeds to the next time increment without changing its stepping length.
- $e_{\max} < e_t$. The time-stepping length can be raised. However, it is advisable to execute the augment only for the next time-stepping, and the solution from the current step is accepted.
- $e_{\max} > e_t$. The time-stepping length is subject to reduction. The current solution is discarded, and a new solution is re-computed using a smaller stepping length Δt_{new} calculated by the formulas

$$\begin{cases} \Delta t^{new} = (e_t/e_{\max})^{1/2}\Delta t^{old} & 2 \text{ - order estimator} \\ \Delta t^{new} = (e_t/e_{\max})^{1/3}\Delta t^{old} & 3 \text{ - order estimator} \end{cases} \tag{5.60}$$

5.5 P-Version of Refinement in Space Domain: Strain/Stress Problems

5.5.1 Concept

It is well known that the accuracy of FE solution depends on both the mesh refinement and the dimension of basis function space, and the hierarchical upgrade of basis functions is an effective way to realize the p-convergence. Denote H^{p_i} as the p_i-order hierarchical space where the element size is unchanged, according to the hierarchical concept, the lower order space is the subset of the higher order space, i.e. $H^{p_1} \subset H^{p_2} \subset \ldots \subset H^{p_i} \subset \ldots \subset H^{p_n} (p_1 < p_2 < \ldots < p_i < \ldots p_n)$.

In the middle of the 1970s, the Washington University compiled a p-refinement FEM program COMET-X with the concept of hierarchical elements. Babuška, Szabó and Katz firstly analyzed the theory of p-refinement in 1981 and pointed out that in the p-version of refinement using quasi-uniform mesh, the rate of convergence is higher than that in the h-version of refinement. When the singularities are at the element boundaries in a quasi-uniform mesh, the rate of convergence of the p-refinement is twice that of the h-refinement (Rahulkumar et al. 1997). In 1985, the first commercial software PROBE of p-refinement is published by Noetic.

In the following years the research was booming in the area of computation techniques for the p-refinement FEM (Wiberg and Möller 1988). Typically, Hinnant (1994) proposed a vector integral scheme which specifically takes advantage of the nature of p-version element matrices, to minimize the computational effort. Since the 1990s, scholars made remarkable progress in the p-refinement inclusive solution strategy towards various field problems (Morris et al. 1992; Papadrakakis and Babilis 1994; Fei and Chen 2004).

So far, most studies on the p-refinement are focused on the theories and applications within the range of elastic and homogenous materials. Since rock-like materials are mostly heterogeneous, non-linear, and discontinuous, there is still much room for the improvements towards the solution of complicated hydraulic structure problems using the FEM of p-version refinement.

5.5.2 Error Analysis and Refinement Strategies for Elastic Problems

Use is made of all the basis functions with respect to nodes, edges, faces, and body to formulate a general shape function set N_i with a certain degree of freedom (DOF), the displacement u within the element specified by the normalized coordinates (ξ, η, ζ) may be interpolated using the corresponding nodal displacements (state variables) by Eq. (4.52). Under such nomenclature convention, the approximation for the displacement within an element [see Eq. (4.56)], the strain related to the general nodal displacements [see Eq. (4.59)], the stress related to the general nodal displacements [see Eq. (4.63)], as well as the governing equations [see Eqs. (4.69)–(4.70)], do hold.

For the linear elasticity problem under certain mesh and basis functions of order p, denote $\{u_p\}, \{\varepsilon_p\}, \{\sigma_p\}$ as the computational solutions by FEM, and $\{\mu\}, \{\varepsilon\}, \{\sigma\}$ as the correspondent exact solutions, the error vectors are defined as (Babuška et al. 1994a, b).

$$\begin{cases} \{e_{u,p}\} = \{u\} - \{u_p\} \\ \{e_{\varepsilon,p}\} = \{\varepsilon\} - \{\varepsilon_p\} \\ \{e_{\sigma,p}\} = \{\sigma\} - \{\sigma_p\} \end{cases} \tag{5.61}$$

The error norm is defined accordingly

$$\|e_p\| = \begin{cases} \|u - u_p\| \\ \|\varepsilon - \varepsilon_p\| \\ \|\sigma - \sigma_p\| \end{cases} \tag{5.62}$$

A particular notation U for the displacement error in the elastic problem has been conventionally used for many years, i.e.

$$\begin{cases} U = \|u - u_p\|^2 \\ U_p = \|u_p\|^2 \\ U_u = \|u\|^2 \end{cases} \tag{5.63}$$

The energy norm are usually employed under the circumstances of elastic deformation

$$\begin{aligned} \|e_p\| &= \left(\iiint_{\Omega} \left([B]\{e_{u,p}\}\right)^T [D] \left([B]\{e_{u,p}\}\right) d\Omega \right)^{\frac{1}{2}} \\ &= \left(\iiint_{\Omega} \left(\{e_{\sigma,p}\}\right)^T [D]^{-1} \left(\{e_{\sigma,p}\}\right) d\Omega \right)^{\frac{1}{2}} \end{aligned} \tag{5.64}$$

This definition may be of overall covering all the elements or of local covering element i only, and they are related in a manner of

$$\left\|e_p\right\|^2 = \sum_{i=1}^{n_e} \left\|e_p\right\|_i^2 \tag{5.65}$$

It has been verified that these errors can be well characterized by a function of the degree of freedom abbreviated as *DOF*, or simply as N if there is no risk of misleading.

The p-refinement algorithms fall into the "complete refinement" by which all elements are refined, the "element refinement" by which only the elements whose precisions cannot meet the requirement are refined, and the "*DOF* refinement" by which the *DOF* s prone to reduce the error remarkably are refined (Cheng and Chen 1999). Generally speaking, the complete refinement is the simplest, but it has an obvious disadvantage that those elements sufficiently accurate are forced to upgrade. The *DOF* refinement may be regarded as the most rigorous method but it is too complicated to implement. The element refinement is a good compromise between the complete refinement and the *DOF* refinement.

(1) Complete refinement

It has been shown by Zienkiewicz et al. (1970, 1983) that, the error energy norm in Eq. (5.64) will approach zero monotonously following the mesh refinement or the basis function upgrade. The problem now is, how to estimate the energy norm (U_u) of exact solution. It may be handled by the strategies of residual-based, recovery-based, goal-oriented, and a variety of practical (Grätsch and Bathe 2005).

1. Residual-based error estimator

It aims to improve the quality of computational solution by minimizing the discretization error with the help of some global scales (i.e. norm). Whilst it is possible to compute the discretization error via solving the exact solution or very accurate solution on an extremely well resolved mesh, in practical applications the essential idea stems from the definition of the residual of variational problems. Giving a well discretized mesh, the convergent rate of p-refinement is

$$\left\|e_p\right\| = \left\|u - u_p\right\| \le C/N_p^{\beta} \tag{5.66}$$

In which β is dependent on the smoothness of the solution. For the h-refinement FEM without the existence of singularity, we have $\beta = p/2$.

Therefore

$$\left|U_u - U_p\right| = U\left(u - u_p\right) \approx C^2/N_p^{2\beta} \tag{5.67}$$

Where N_p is the *DOF* when the polynomial order is p.

Equation (5.67) contains three unknown variables U_u, C and β. Towards the solution of U_u we write

$$\begin{cases} |U_u - U_p| \approx C^2/N_p^{2\beta} \\ |U_u - U_{p-1}| \approx C^2/N_{p-1}^{2\beta} \\ |U_u - U_{p-2}| \approx C^2/N_{p-2}^{2\beta} \end{cases} \tag{5.68}$$

Taking into account of the monotony feature of U

$$\frac{\log\left(\frac{U_u - U_p}{U_u - U_{p-1}}\right)}{\log\left(\frac{U_u - U_{p-1}}{U_u - U_{p-2}}\right)} = \frac{\log\frac{N_{p-1}}{N_p}}{\log\frac{N_{p-2}}{N_{p-1}}} \tag{5.69}$$

And denoting

$$\frac{\log\frac{N_{p-1}}{N_p}}{\log\frac{N_{p-2}}{N_{p-1}}} = Q \tag{5.70}$$

We have

$$\frac{U_u - U_p}{U_u - U_{p-1}} \approx \left(\frac{U_u - U_{p-1}}{U_u - U_{p-2}}\right)^Q \tag{5.71}$$

From Eq. (5.71) the strain energy of exact solution U_u may be estimated.

The adaptive strategy is established by at least three continuous successive orders p of hierarchical upgrade, where the relative error is calculated by the energy norms of the exact solution U_u and error $U(u - u_p)$

$$e = \frac{\|e_p\|}{\|u\|} = \sqrt{\frac{U(u - u_p)}{U_u}} \tag{5.72}$$

The adaptive refinement is terminated if $e \leq e_t$, otherwise the basis functions should be upgraded using polynomials of higher order.

2. Recovery-based error estimator

One of the classical techniques to define an error estimator is via the construction of higher order solution to approximate discretization error. As stated previously, this could be somewhat impractical or expensive to compute with high resolution. A recovery-based error estimator attempts to construct an approximation to the error via a higher precise solution $\{u^*\}$ in comparison to $\{u_p\}$. The philosophy is that since $\{u^*\}$ converges to the exact solution faster than $\{u_p\}$, the error given by $\{e_p\} = \{u^*\} - \{u_p\}$ is a meaningful approximation of the discretization error in an appropriate norm.

The recovery estimator that utilizes the discontinuous nature of the gradient of finite element solution across element boundaries to define an approximation of the error, has been addressed in Sect. 5.2.

3. Goal-oriented error estimator

It seeks to modify the finite element mesh, with the objective of improving the numerical approximation of a specific quantity of interest (e.g.$\{u_p\}$) (Babuška and Rheinboldt 1978; Prudhomme and Oden 1999; Becker and Rannacher 2001; Chung et al. 2016).

4. Practical estimator

Since the main purpose of adaptive refinement in the works of this book is to make the computation software be standardized towards the design of hydraulic structures, rather than to unilaterally pursue the "computational accuracy", a practical algorithm of *p*-refinement will be proposed hereinafter. (Fei and Chen 2003a, b).

We define the energy norm

$$\|e_p\| = \left(\iiint_{\Omega} \left(\{\sigma\} - \{\sigma_p\}\right)^T \left(\{\varepsilon\} - \{\varepsilon_p\}\right) d\Omega \right)^{\frac{1}{2}} \tag{5.73}$$

In which $\{\sigma_p\}$ and $\{\varepsilon_p\}$ are respectively the stress and strain computed with certain shape functions of grade p, $\{\sigma\}$ and $\{\varepsilon\}$ are respectively the exact stress and strain. It is supposed that the stress and strain of higher grade $p+1$ is the "best guess" of the exact stress and strain. For a mesh system containing n_e elements, the error energy norm in Eq. (5.73) can be rewritten as

$$\|e_p\| = \sum_{i}^{n_e} \|e_p\|_i = \sum_{i}^{n_e} \left(\iiint_{\Omega_i} \left(\{\sigma_{p+1}\} - \{\sigma_p\}\right)^T \left(\{\varepsilon_{p+1}\} - \{\varepsilon_p\}\right) d\Omega \right)^{\frac{1}{2}} \tag{5.74}$$

and the total energy norm of exact solution is computed by the formula

$$\|u\| = \sum_{i}^{n_e} \left(\iiint_{\Omega_i} \left(\{\sigma_{p+1}\}\right)^T \left(\{\varepsilon_{p+1}\}\right) d\Omega \right)^{\frac{1}{2}} \tag{5.75}$$

The following relative error is therefore established

$$e = \frac{\|e_p\|}{\|u\|} \tag{5.76}$$

If the error e is smaller than or equal to the error tolerance e_t, i.e.

$$e \leq e_t \tag{5.77}$$

The calculation results is accepted as practical satisfactory, otherwise the order p of the shape functions should be upgraded.

The complete refinement demands a "well" designed mesh. The problem is, where there is a singularity, how to well discretize the domain? Szabó (1986) suggested that the element size around the singularity is shrunk by a fraction scale of 0.15 (see Fig. 5.4).

(2) Element refinement

The element refinement is intended to avoid the unnecessary upgrade for those elements with gentle stress gradient.

1. Error estimator

Since in Eq. (5.66) $\beta = \frac{1}{2}p$ for h-refinement and generally the convergent rate is higher in p-refinement, therefore an acceptable β_p in Eq. (5.66) for p-refinement may be

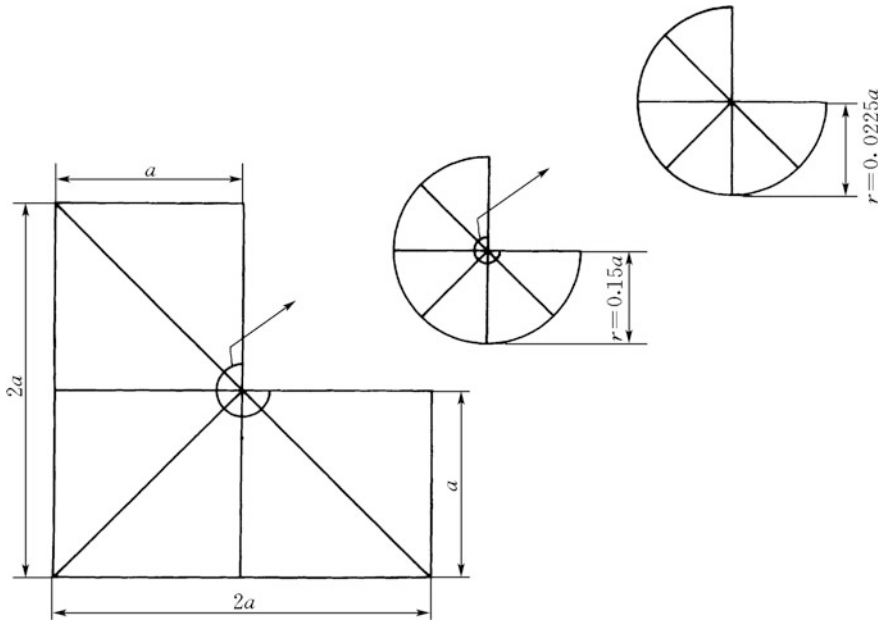

Fig. 5.4 Mesh design surrounding a singularity (by Szabó)

$$\beta_p = \frac{\phi}{2} p \tag{5.78}$$

In which $\phi \geq 1$.
Similar to the Eq. (5.78), the higher order (grade) of $p+1$ gives rise to

$$\beta_{p+1} = \frac{\phi}{2}(p+1) \tag{5.79}$$

For the problem without singularity, combine Eqs. (5.78) and (5.79) we obtain

$$\frac{p}{p+1} \approx \frac{\beta_p}{\beta_{p+1}} \tag{5.80}$$

Equation (5.80) may be used to estimate the convergent rate of element because we can relate the error norm of order p to that of order $p+1$ in a manner of

$$\left\|e_{p+1}\right\| = \left(\frac{N_p}{N_{p+1}}\right)^{\beta_{p+1}} \left\|e_p\right\| = \left(\frac{N_p}{N_{p+1}}\right)^{\beta_p \frac{p+1}{p}} \left\|e_p\right\| \tag{5.81}$$

Similarly, from order $p+1$ to order $p+2$ we have

$$\left\|e_{p+2}\right\| = \left(\frac{N_{p+1}}{N_{p+2}}\right)^{\beta_{p+2}} \left\|e_{p+1}\right\| = \left(\frac{N_{p+1}}{N_{p+2}}\right)^{\beta_p \frac{p+2}{p}} \left\|e_{p+1}\right\| \tag{5.82}$$

Introducing Eq. (5.81) into Eq. (5.82) leads to

$$\left\|e_{p+2}\right\| = \left(\frac{N_{p+1}}{N_{p+2}}\right)^{\beta_p \frac{p+2}{p}} \left(\frac{N_p}{N_{p+1}}\right)^{\beta_p \frac{p+1}{p}} \left\|e_p\right\| \tag{5.83}$$

or

$$\left\|e_{p+2}\right\| = \left[\left(\frac{N_p}{N_{p+2}}\right)^{p+2} \left(\frac{N_{p+1}}{N_p}\right)\right]^{\beta_p \frac{1}{p}} \left\|e_p\right\| \tag{5.84}$$

Inductive approach gives rise to

$$\left\|e_{p+n}\right\| = \left[\left(\frac{N_p}{N_{p+n}}\right)^{p+n} \left(\frac{\left(N_{p+n-1}\right)\left(N_{p+n-2}\right)\cdots\left(N_{p+1}\right)}{N_p^{n-1}}\right)\right]^{\beta_p/p} \left\|e_p\right\| \quad \forall n > 1 \tag{5.85}$$

Equation (5.85) may be employed to estimate the energy norm of error under different order of basis functions, where there is no singularity in the element concerned.

If a node on the element is the singularity, we have $\beta = \lambda$ = constant, in which λ is dependent on the intensity of the singularity. Under such circumstances, following the similar procedure of Eqs. (5.81)–(5.85), we get

$$\left\|e_{p+1}\right\| = \left(\frac{N_p}{N_{p+1}}\right)^{\beta} \left\|e_p\right\| \tag{5.86}$$

$$\left\|e_{p+2}\right\| = \left(\frac{N_{p+1}}{N_{p+2}}\right)^{\beta} \left\|e_{p+1}\right\| \tag{5.87}$$

$$\left\|e_{p+n}\right\| = \left(\frac{N_p}{N_{p+n}}\right)^{\beta} \left\|e_p\right\| \tag{5.88}$$

2. Practical algorithms

① For the element i, the stress $\{\sigma_p\}_i$ of order p is obtained.

② The computation of order $p+1$ is carried out to get a higher order stress $\{\sigma_{p+1}\}_i$ that is directly looked at as the "best guess" of the exact solution. The relative error of the element i is calculated by the formula

$$e_i = \frac{\left\|e_p\right\|_i}{\left\|\sigma_{p+1}\right\|_i} = \frac{\left\|\sigma_{p+1} - \sigma_p\right\|_i}{\left\|\sigma_{p+1}\right\|_i} \tag{5.89}$$

③ If $e_i \le e_t$, the polynomial order $p+1$ is kept for the element i, otherwise we use Eq. (5.85) or Eq. (5.88) to estimate the tentative order $p = p+n$ and return to step ①.

④ Repeat steps ①–③ until for all the elements the following criterion is met

$$e_i \le e_t \quad (i = 1, \ldots, n_e) \tag{5.90}$$

(3) *DOF* refinement

Towards the purpose of *DOF* refinement, we write the governing equation of the FEM for an element in the hierarchical form of

$$[k_p]\{\delta_p\} = \{f_p\} \tag{5.91}$$

Denote the additional displacement sub-vector attributable to the p-refinement as $\{\delta_a\}$, and

$$\{\delta^*\} = [N]\{\delta_p\} + [N_a]\{\delta_a\} \tag{5.92}$$

$$\begin{bmatrix} [k_p] & [k_{pa}] \\ [k_{ap}] & [k_{aa}] \end{bmatrix} \begin{Bmatrix} \{\delta_p\} \\ \{\delta_a\} \end{Bmatrix} = \begin{Bmatrix} \{f_p\} \\ \{f_a\} \end{Bmatrix} \tag{5.93}$$

The error with respect to the displacement is termed as

$$\{e_{u,p}\} = [N](\{\delta\} - \{\delta_p\}) + [N_a]\{\delta_a\} \tag{5.94}$$

In which $\{\delta\}$ is the exact solution of the nodal displacement and $[N_a]$ is the additional sub-matrix of the shape function due to the hierarchical upgrade. A convincible postulation might be

$$\{\delta_p\} \approx \{\delta\} \tag{5.95}$$

The second row of Eq. (5.93) gives the solution of $\{\delta_a\}$

$$\{\delta_a\} = ([k_{aa}])^{-1}(\{f_a\} - [k_{ap}]\{\delta\}) \tag{5.96}$$

To operate the inverse of $[k_{aa}]$ in Eq. (5.96), we introduce one *DOF*, for example, j. Since there is only one scalar member $\delta_{a,j}$ of $\{\delta_a\}$, we have

$$([k_{aa}])^{-1} \equiv \frac{1}{k_{a,jj}} \tag{5.97}$$

There are two manners to scale the error in Eq. (5.94) using the energy norm. One is to link it with the strain and stress increments in a form of

$$\|e_{u,p}\|^2 = (\{\delta_a\})^T \iiint_{\Omega_i} [B_a]^T [D][B_a] d\Omega \{\delta_a\} \tag{5.98}$$

Another is to link it with the residual $\{r\}$ related to the exact and FE solutions by

$$[k]\{e_{u,p}\} \equiv [k](\{\delta\} - \{\delta_p\}) = \{r\} \tag{5.99}$$

$$\|e_{u,p}\|^2 = C_j^2 = \frac{\left(\iiint_{\Omega_i} ([N_a])^2 d\Omega\right)\left(\iiint_{\Omega_i} (\{r\})^2 d\Omega\right)}{k_{a,jj}} \tag{5.100}$$

By the *DOF* refinement, it is to introduce those *DOFs* with larger C_j. For example, the *DOF* j added in the next refinement iteration may be selected according to

$$C_j \geq \gamma C_{\max} \tag{5.101}$$

Obviously, $\gamma = 0$ in Eq. (5.101) leads to the complete refinement.

Too smaller of γ may introduce not very important *DOFs*, on the contrary, too larger of γ may neglect important *DOFs*. Both of these cases will undermine the refinement efficiency. Hence it is advisable that

$$10\% \leq \gamma \leq 25\% \tag{5.102}$$

5.5.3 *Error Analysis and Refinement Strategies for Elasto-Viscoplastic Problems*

The p-refinement taking into account of elasto-viscoplasticity (viscoelasticity as well) is basically similar to that of linear elasticity, the difference mainly lies in the much more complicated error estimator and refinement strategy (Wilson et al. 1992; Holzer and Yosibash 1996). Towards the purpose of standardization of FEM software for hydraulic structures, a practical algorithm is suggestible (Chen and Cheng 2001; Fei and Chen 2003).

Theoretically, at each time step the shape functions should be adjusted through the raise and lower down of the polynomial order p. Although there are no essential difficulties, yet the computation effort is huge. The author had tried two approaches in the practices for hydraulic structures, namely, the p-refinement is carried out after every prescribed time steps, or conducted at the time-marching end corresponding to one load increment solely. Since these two approaches do not make significant difference in the sense of algorithm, therefore the latter will be elucidated as follows with the element refinement strategy.

For one load increment

$$\{f\} = \iiint_{\Omega_i} \left[N_{p-1}\right]^T \{V\} d\Omega + \iint_{\Gamma_i} \left[N_{p-1}\right]^T \{p\} d\Gamma + \left[N_{p-1}\right]^T \{q\} \tag{5.103}$$

Suppose that after the accomplishment of a successive time step, the steady state solutions $\{\delta_{p-1}\}, \{\varepsilon_{p-1}\}$ and $\{\sigma_{p-1}\}$ of order $p-1$ demand upgrade for the basis functions of element i, the refinement iteration is recurred according to

① Giving the solution $\{u_p\}_t$ and $\{\sigma_p\}_t$ of order p at time t, the equivalent load increment due to viscoplastic flow at time $t + \Delta t$ is computed by

$$\left\{\Delta f_p^{vp}\right\}_{t+\Delta t} = \iiint_{\Omega_i} \left[B_p\right]^T [D] \left\{\Delta \varepsilon_p^{vp}\right\}_{t+\Delta t} d\Omega \tag{5.104}$$

② Solve the equilibrium equation of the structural system

$$[K_p]\{\Delta U_p\}_{t+\Delta t} = \left\{\Delta F_p^{vp}\right\}_{t+\Delta t} \tag{5.105}$$

③ Calculate the element strain increment at $t+\Delta t$

$$\{\Delta\varepsilon_p\}_{t+\Delta t} = [B_p]\{\Delta\delta_p\}_{t+\Delta t} \tag{5.106}$$

④ Calculate the element stress increment at $t+\Delta t$

$$\{\Delta\sigma_p\}_{t+\Delta t} = [D]\left(\{\Delta\varepsilon_p\}_{t+\Delta t} - \left\{\Delta\varepsilon_p^{vp}\right\}_{t+\Delta t}\right) \tag{5.107}$$

⑤ Accumulate the vectors of nodal displacement, element strain, and stress at $t+\Delta t$

$$\begin{cases} \{\delta_p\}_{t+\Delta t} = \{\delta_p\}_t + \{\Delta\delta_p\}_{t+\Delta t} \\ \{\varepsilon_p\}_{t+\Delta t} = \{\varepsilon_p\}_t + \{\Delta\varepsilon_p\}_{t+\Delta t} \\ \{\sigma_p\}_{t+\Delta t} = \{\sigma_p\}_t + \{\Delta\sigma_p\}_{t+\Delta t} \end{cases} \tag{5.108}$$

⑥ Repeat steps ①–⑤ until the steady state solutions $\{\delta_p\}$, $\{\varepsilon_p\}$, and $\{\sigma_p\}$ are reached.
⑦ Repeat steps ①–⑥ until all the load increments are exerted.
⑧ Calculate the element error e_i according to Eq. (5.89).
⑨ If $e_i \le e_t$ for all the elements in the structural system, the refinement iteration collapses with an acceptable order of p. Otherwise let the unsatisfied elements be upgraded by $p = p+1$, then repeat steps ①–⑧.

5.5.4 *Key Algorithms*

The p-refinement possesses several peculiarities with its algorithms such as the generation of topologic messages, the integral of matrices (vectors), and the solution of governing equation set (Morris et al. 1992; Carnevali et al. 1993; Hinnant 1994; Papadrakakis and Babilis 1994).

(1) Generation of topologic messages

The program TOPO flow-charted in Fig. 5.5 comprises three major modules: point generation for an edge by the NODE-EDGE; edge generation for a face by the EDGE-FACE, and face generation for an element by the FACE-BODY.

The topologic messages for p-refinement need be sequentially organized in a manner of

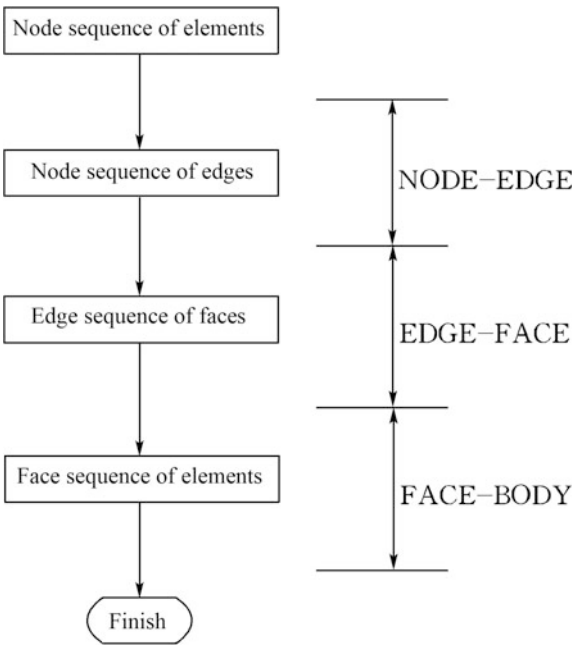

Fig. 5.5 Flow chart of the program TOPO

- Nodal sequence and corresponding coordinates as well as elementary sequence and their nodal sequence, are generated by pre-process modules elaborated in Chap. 3;
- Point sequence of each edge, is demanded and generated by the TOPO;
- Edge sequence of each element surface, is demanded and generated by the TOPO;
- Surface sequence of each element, is demanded and generated by the TOPO.

(2) Handling of boundary conditions

Standard FEM assigns a boundary constraint to the real nodes. Since the face and edge possess own basis functions in the p-refinement, so they contribute to the *DOFs* of an element and should be looked at as "virtual *DOFs*". These virtual *DOFs* are equally treated as the "real *DOFs*", and they are uniformly termed as generalized *DOFs*. In this manner, the general basis functions corresponding to general nodes are formulated by grouping the functions of point, edge, face and body. Suppose for instance, a face is restrained by a type of boundary condition, then the virtual nodes assigned to the face as well as the edge on this face are imposed with the boundary restraint in addition to the real node geometrically defining the face. Since there are no face basis functions where $p<4$ nor edge basis functions where $p<2$, therefore there are no restraints under such circumstances.

Figures 5.6 and 5.7 illustrate the differences between the standard and hierarchical FEM in handling totally restrained face and partially restrained edge.

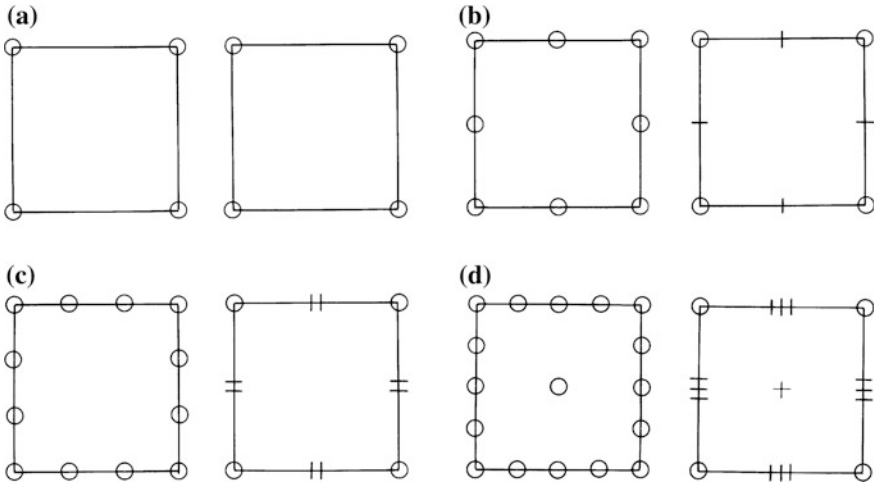

Fig. 5.6 Handling of totally restrained face (left—standard; right—hierarchical) **a** $p = 1$; **b** $p = 2$; **c** $p = 3$; **d** $p = 4$

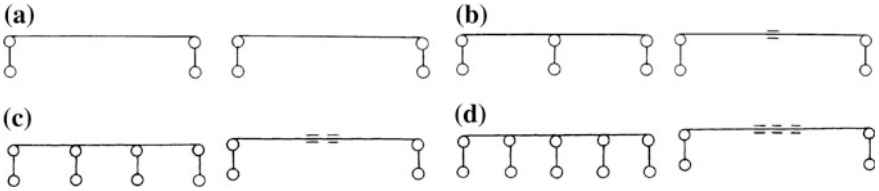

Fig. 5.7 Handling of partially restrained edge (left—standard; right—hierarchical) **a** $p = 1$; **b** $p = 2$; **c** $p = 3$; **d** $p = 4$

(3) Assembling of stiffness matrix and load vector

1. Element stiffness matrix

Take the hexahedral element for example. When $p = 1$, the points 1–8 are taken as the real nodes with correspondent standard basis functions N_{1-8}; when $p = 2$, the edges 1–12 are assigned with the virtual nodes 9–20 corresponding to the basis functions E^2_{1-12}; when $p = 3$, the edges 1–12 are additionally assigned with the virtual nodes 21–32 corresponding to the basis functions E^3_{1-12}; when $p = 4$, the edges 1–12 are additionally assigned with the virtual nodes 37–44 corresponding to the basis functions E^4_{1-12}, and the faces 1–6 are assigned as the virtual nodes 44–50 with the correspondent basis functions $F^{4(2,2)}_{1-6}$; when $p = 5$, the edges 1–12 are additionally assigned with the virtual nodes 51–62 corresponding to the basis functions E^5_{1-12}, and the faces 1–6 are additionally assigned with the virtual nodes 67–74 corresponding to the basis functions $F^{5(2,3)}_{1-6}$ and $F^{5(3,2)}_{1-6}$; when $p = 6$, the

edges 1–12 are additionally assigned with the virtual nodes 75–86 corresponding to the basis functions E^{6}_{1-12}, the faces 1–6 are additionally assigned with the virtual nodes 87–104 corresponding to the basis functions $F^{6(2,4)}_{1-6}$,$F^{6(3,3)}_{1-6}$ and $F^{6(4,2)}_{1-6}$, and one body is assigned with the virtual node 105 corresponding to the basis function $B^{6(2,2,2)}$; and so forth.

The above $f_e(p)$ basis functions are uniformly termed as N_i $(1 \le i \le f_e(p))$ to concisely express the element interpolation

$$\begin{cases} u_{xp} = \sum\limits_{i=1}^{f_e(p)} N_i u_x \\ u_{yp} = \sum\limits_{i=1}^{f_e(p)} N_i u_y \\ u_{zp} = \sum\limits_{i=1}^{f_e(p)} N_i u_z \end{cases}$$

Or

$$\begin{cases} \{u_p\} = [N_p]\{\delta_p\} \\ [N_p] = [N_1[I] \quad N_2[I] \ldots N_{f_e(p)}[I]] \end{cases} \tag{5.109}$$

In which $[I]$ stands for 3×3 unit matrix.

The coordination interpolation keeps the isoparametric form using the nodal shape functions only

$$\begin{cases} x = \sum\limits_{i=1}^{8} N_i x_i \\ y = \sum\limits_{i=1}^{8} N_i y_i \\ z = \sum\limits_{i=1}^{8} N_i z_i \end{cases} \tag{5.110}$$

We have the element stiffness of order p

$$[k_p] = \iiint\limits_{\Omega_e} [B_p]^T [D][B_p] d\Omega = \int\limits_{-1}^{1}\int\limits_{-1}^{1}\int\limits_{-1}^{1} [B_p]^T [D][B_p] |J| d\xi d\eta d\zeta \tag{5.111}$$

In which the matrix of strain $[B_p]$ is

$$\begin{cases} [B_p] = \left[[B_1] \quad [B_2] \ldots [B_{f_e(p)}] \right] \\ [B_i]^T = \begin{bmatrix} N_{i,x} & 0 & 0 & 0 & N_{i,z} & N_{i,y} \\ 0 & N_{i,y} & 0 & N_{i,z} & 0 & N_{i,x} \\ 0 & 0 & N_{i,z} & N_{i,y} & N_{i,x} & 0 \end{bmatrix} \end{cases} \quad (i = 1, 2, \ldots, f_e(p)) \tag{5.112}$$

2. Overall stiffness matrix of the structural system

If we look at the whole structure system as a "big element" comprising N_n real nodes, N_e edges, N_f faces, and N_b bodies, the overall stiffness of the structure system assembled in this sequence is hierarchical, and the amount of general nodes in the structure system is

$$\begin{aligned} f_t(p) = & N_n + \max(0, p-1) N_e + \max\left(0, \frac{1}{2}(p-2)(p-3)\right) N_f \\ & + \max\left(0, \sum_{k=6}^{p} \frac{1}{2}(k-4)(k-5)\right) N_b \end{aligned} \tag{5.113}$$

3. Load transfer

Load transfer to the element nodes is similar to the standard FEM. Take the volumetric force for example, we have

$$\{\Delta f_p\} = \iiint_{\Omega_e} [N_p]^T \{\Delta V\} d\Omega = \int_{-1}^{1} \int_{-1}^{1} \int_{-1}^{1} [N_p]^T \{\Delta V\} |J| \, d\xi d\eta d\zeta \tag{5.114}$$

It is notable that virtual nodal forces are self-balanced and merely the forces transferred to the real nodes shall take part in the balance against exerted loads.

Figure 5.8 shows the hierarchical structure of the stiffness matrix and the load vector.

(4) Numerical integration

Some matrix and vector functions should be integrated over the whole or partial domain of a finite element in order to get element matrices and vectors. Numerical integration (quadrature) is so intimately related to the performance of FE analysis, that the selection of its scheme and order is a portion of the definition of a particular finite element. Following the upgrade of polynomial order, higher order integration demands larger computer capacity. Some scholars (Douglas Jr and Olsen 1989) even thought that the p-version technique would be intrinsically limited below, for example, $p = 4$, due to the large amount of time required to complete integrations.

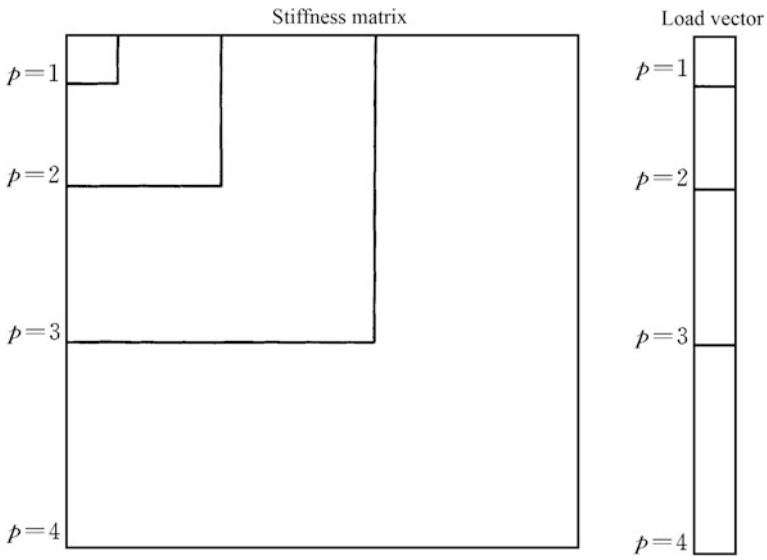

Fig. 5.8 Diagram showing hierarchical structure of stiffness matrix and load vector

In recent decades however, several advanced integration schemes have been proposed to reduce the effort for integral computation considerably.

1. Strategy to reduce integration computation

Irons (1969) introduced a technique to reduce the number of floating point operations during element integration. His work was further enhanced by Gupta and Mohraz (1972) by using tensor notation and bringing the material constants outside of the integral. Both the works make use of the fact that the strain matrix is relatively sparse and hence avoid multiplications by zero. Bardell (1989) and Yagawa et al. (1990) showed that the symbolic pre-computation of certain quantities could significantly accelerate the integration process. These works are all applicable to the Gaussian integration (quadrature). Taking the element stiffness matrix $\left[k_p\right]$ in Eq. (5.111) for example, its sub-matrix relating freedom i and j is

$$\left[k_{ij}\right] = \begin{bmatrix} (\lambda+2G)R_{xx}+G\left(R_{yy}+R_{zz}\right) & (\lambda+G)R_{xy} & (\lambda+G)R_{yz} \\ (\lambda+G)R_{yx} & (\lambda+2G)R_{yy}+G(R_{zz}+R_{xx}) & (\lambda+G)R_{yz} \\ (\lambda+G)R_{zx} & (\lambda+G)R_{zy} & (\lambda+2G)R_{zz}+G\left(R_{xx}+R_{yy}\right) \end{bmatrix}$$

$$(i,j=1,2,\ldots,f_e(p)) \tag{5.115}$$

In which

$$R_{st} = \int_{-1}^{1}\int_{-1}^{1}\int_{-1}^{1} \frac{\partial N_i}{\partial s}\frac{\partial N_j}{\partial t}|J|d\xi d\eta d\zeta \quad s,t \in \{x,y,z\};\ (i,j = 1,2,\ldots,f_e(p)) \tag{5.116}$$

and

$$[J] = \begin{bmatrix} \frac{\partial N_1}{\partial \xi} & \frac{\partial N_2}{\partial \xi} & \cdots & \frac{\partial N_8}{\partial \xi} \\ \frac{\partial N_1}{\partial \eta} & \frac{\partial N_2}{\partial \eta} & \cdots & \frac{\partial N_8}{\partial \eta} \\ \frac{\partial N_1}{\partial \zeta} & \frac{\partial N_2}{\partial \zeta} & \cdots & \frac{\partial N_8}{\partial \zeta} \end{bmatrix} \cdot \begin{bmatrix} x_1 & y_1 & z_1 \\ x_2 & y_2 & z_2 \\ \vdots & \vdots & \vdots \\ x_8 & y_8 & z_8 \end{bmatrix} \tag{5.117}$$

Since

$$\begin{Bmatrix} \frac{\partial N_i}{\partial x} \\ \frac{\partial N_i}{\partial y} \\ \frac{\partial N_i}{\partial z} \end{Bmatrix} = [J]^{-1} \begin{Bmatrix} \frac{\partial N_i}{\partial \xi} \\ \frac{\partial N_i}{\partial \eta} \\ \frac{\partial N_i}{\partial \zeta} \end{Bmatrix} = \begin{bmatrix} c_{xx} & c_{xy} & c_{xz} \\ c_{yx} & c_{yy} & c_{yz} \\ c_{zx} & c_{zy} & c_{zz} \end{bmatrix} \begin{Bmatrix} \frac{\partial N_i}{\partial \xi} \\ \frac{\partial N_i}{\partial \eta} \\ \frac{\partial N_i}{\partial \zeta} \end{Bmatrix} \quad (i = 1,2,\ldots,f_e(p)) \tag{5.118}$$

Therefore we get

$$\frac{\partial N_i}{\partial s}\cdot\frac{\partial N_j}{\partial t} = \left(c_{sx}\frac{\partial N_i}{\partial \xi} + c_{sy}\frac{\partial N_i}{\partial \eta} + c_{sz}\frac{\partial N_i}{\partial \zeta}\right)\left(c_{tx}\frac{\partial N_j}{\partial \xi} + c_{ty}\frac{\partial N_j}{\partial \eta} + c_{tz}\frac{\partial N_j}{\partial \zeta}\right) \quad (i,j = 1,2,\ldots,f_e(p)) \tag{5.119}$$

The following strategies for the reduction of integral calculation efforts make use of hierarchical natures.

- Take advantages of the sparsity of $[B]$ and $[D]$. The algebra computation for $[B_i]^T[D][B_j]$ is conducted first, then the integration scheme is carried out for each nonzero member in the resultant matrix.
- Members with different order in the matrix are integrated using different Gaussian integration orders.
- For a member in the stiffness matrix, different coordinate directions may possess different polynomial orders, therefore different Gaussian integration orders are advisable.

2. Vector integration scheme

The one-dimensional structural problem is used to elucidate the vector integration scheme, which exploits the structure of the matrix in order to reduce the computational effort (Hinnant 1994). Instead of Eq. (5.115), we write

$$k_{ij} = \int_{-1}^{1} \frac{\partial \sigma_k}{\partial u_i} \frac{\partial \varepsilon_k}{\partial u_j} |J| dx \quad (i,j = 1,2,\ldots,f_e(p)) \tag{5.120}$$

The stiffness in Eq. (5.120) is actually the dot product of two functions. One is entirely dependent upon the row index i, while the other is dependent only upon the column index j.

Since each term in the dot product of Eq. (5.120) can be integrated individually, it is convenient to express Eq. (5.120) in a simpler generic form

$$k_{ij} = \int_{-1}^{1} g_i(x) h_j(x) dx \quad (i,j = 1,2,\ldots,f_e(p)) \tag{5.121}$$

The philosophy of vector integration is to operate integration on the $g_i(x)$ and $h_j(x)$ separately for all i and j, then combine the operation results. Since the specific values of i and j are not relevant to our discussion, they will be dropped for notational simplicity. Thus the object of study becomes,

$$\int_{-1}^{1} g(x) h(x) dx \tag{5.122}$$

The orthonormal curve fitting of g and h with, for example, the Legendre or Jacobian polynomial series, can be written as

$$\begin{cases} g(x) = \sum_{I=0}^{\infty} c_I P_I(x) \\ h(x) = \sum_{J=0}^{\infty} d_J P_J(x) \end{cases} \tag{5.123}$$

In which

$$\begin{cases} c_I = \int_{-1}^{1} g(x) P_I(x) dx \\ d_J = \int_{-1}^{1} h(x) P_J(x) dx \end{cases} \tag{5.124}$$

Introducing Eq. (5.123) into Eq. (5.122), we get

$$\int_{-1}^{1} g(s)h(x)dx = \sum_{I=0}^{\infty} c_I d_I \tag{5.125}$$

Equation (5.125) justifies that the integral of g times h can be calculated by the dot product of two vectors $\{c\}$ and $\{d\}$.

For more details our readers are referred to the creative work of Hinnant (1994).

(5) Solvers for linear equation system emerged from p-refinement

The FEM utilizes basis shape functions vanishing outside of the reference element to transform a PDE into the discrete system governed by an algebraic equation set. Take the linear problem for example, the correspondent equation set is also linear and can be expressed simply by

$$[A]\{x\} = \{b\} \tag{5.126}$$

In which $\{b\}$ and $\{x\}$ are N-dimensional vectors representing the forces and the unknown basic state variables (e.g. displacement, hydraulic potential, temperature), $[A]$ is an N $\times$ N non-singular, sparse, and positive definite matrix representing the discrete form of the differential operator.

Solution algorithms to obtain $\{x\}$ fall into two basic classes of direct and iterative. Interested readers are referred to Golub and Loan (1996) and Saad (2003) where these algorithms are discussed in more detail.

1. Direct methods

In the context of direct method, we need the calculation of $[A]^{-1}\{b\}$ directly. Naively, one could consider the possibility to explicitly assemble the matrix $[A]^{-1}$ and then perform the foregoing matrix-vector product. Nevertheless, this approach is seldom ever advocated. The alternative and realistic way is that we seek a method to apply operation action of the inverse of $[A]$ on a vector.

Efficient direct solution methods factorize the original matrix $[A]$ into several components, for which the operation of inverse applied to a vector is trivial. For example, the LU decomposition factorizes $[A]$ in a form of $[A] = [L][U]$, where $[L]$ and $[U]$ are lower and upper triangular matrices of same dimension. Following the factorization, the solution is obtained via first performing $\{y\} = [L]^{-1}\{b\}$ (forward), and then computing $\{x\} = [L]^{-1}\{y\}$ (backward).

Modern prevalent factorization techniques can further exploit the sparsity in the FE operator $[A]$. To perform the factorization, sparse direct methods require $O(N^{3/2})$ floating point operations in two-dimension problems, and $O(N^2)$ operations in three-dimension ones. In addition, the forward and backward procedures demand $O(N \log N)$ and $O(N^{4/3})$ floating point operations in two-and three-dimensional problems, respectively (Li and Widlund 2006).

The memory usage and CPU time required for the solution using factorization techniques can become prohibitively expensive when the number of unknown state variables becomes large. In addition, high-resolution is not always guaranteed, even with the usage of double-precision and super computer.

2. Iterative methods

In contrast to direct methods which produce the solution $\{x\}$ in a "two-step" (factorize-forward/backward solution) procedure, iterative methods pursue updates to the solution via a sequence of iterative operations. A simple iterative method (e.g. Richardson's method) is constructed below to explain their features.

① Set the iteration counter $k = 0$ and choose the initial guess for the solution $\{x^0\} = 0$.
② Update the solution

$$\{x^{k+1}\} = \{x^k\} + (\{b\} - [A]\{x^k\}) \tag{5.127}$$

③ Update the counter $k = k + 1$ then return to step ②.
At each iteration step, a collapse condition is prescribed to terminate the iterative sequence when $\{x^k\}$ is sufficiently accurate. Typically it may be related to the residual in a manner of

$$\{r\} = \{b\} - [A]\{x^k\} \tag{5.128}$$

Iterative methods exhibit an attractive property that only matrix-vector and vector-vector product operations are employed to obtain the solution. Thus in terms of memory usage, they could be much cheaper compared to direct methods.

Nowadays, a large number of robust iterative methods are available. We are able to choose an appropriate one according to the properties of the matrix $[A]$ encountered, e.g. symmetric or non-symmetric, positive definite or non-positive definite, etc. For an implementation "catalog" of different iterative methods the work by Barrett et al. (1994) is recommended.

In all cases, the number of iterations needed to reach a convergent solution can be rather large, and will generally increase as the resolution of the finite element mesh is refined. To accelerate the convergence of iterative procedure, use is prevalently made of pre-conditioners. In the example of the aforementioned Richardson's method, the iterative Eq. (5.127) is reformed by a pre-conditioner $[B]$:

$$\{x^{k+1}\} = \{x^k\} + [B]^{-1}(\{b\} - [A]\{x^k\}) \tag{5.129}$$

Intuitively we can infer that $[B]$ should be a close approximation to $[A]$, and the cost (memory usage and CPU time) should be much cheaper to undertake the action of its inverse than that of $[A]$.

An optimal pre-conditioner is one in which the number of iterations to reach convergence is independent of the mesh resolution. The pre-conditioners which

possess this property are called multi-level pre-conditioners. An excellent coverage of the theory and implementation concerning multi-level pre-conditioners can be found within the works by Wesseling (1992), Briggs et al. (2000), Trottenberg et al. (2001), and Falgout (2006).

A multi-level pre-conditioner tries to construct a hierarchical representation of $[A]$ containing multi-levels (two or more). At the top of this hierarchy is the operator $[A]$, and on each subsequent level we have a "coarser" representation of the operator from the level above. The under-lying principle of such multi-level algorithms is that we use solutions from the coarser level to accelerate the convergence on the finer levels. Information concerning the solution is passed between different levels in the hierarchy via interpolant (fine → coarse) and prolongation (coarse → fine) operators.

3. SSOR-PCG method for general purpose

The method of "symmetric successive over-relaxation pre-conditioned conjugate gradient" (SSOR-PCG) (Lin 1997), as a well preformed solver of iterative for Eq. (5.126), is presented as follows.

① Let R represent the real N-dimensional vector space, and suppose $[M] = \left([S]^T[S]\right)^{-1}$ is a symmetric and positive definite matrix, the Eq. (5.126) is transformed in the PCG (pre-conditioned conjugate gradient) form

$$\begin{cases} [A']\{x'\} = \{b'\} \\ [A'] = [S][A][S]^T \\ \{b'\} = [S]\{b\} \\ \{x'\} = [S]^{-T}\{x\} \end{cases} \tag{5.130}$$

② Towards the iterative procedure, we set the initial values

$$\begin{cases} \{x^0\} \\ \{g^0\} = [A]\{x^0\} \\ \{h^0\} = [M]^{-1}\{g^0\} \\ \{d^0\} = -\{h^0\} \\ k = 0 \end{cases} \tag{5.131}$$

$$R:\ \delta = \left(\{g^k\}, \{h^k\}\right)$$

③ If $\delta \leq \varepsilon$, the iteration collapses, otherwise

$$\begin{cases} \tau_k = \frac{(\{g^k\},\{h^k\})}{(\{d^k\},[A]\{d^k\})} \\ \{x^{k+1}\} = \{x^k\} + \tau_k\{d^k\} \\ \{g^{k+1}\} = \{g^k\} + \tau_k[A]\{d^k\} \\ \{h^{k+1}\} = [M]^{-1}\{g^{k+1}\} \\ \beta_k = \frac{(\{g^{k+1}\},\{h^{k+1}\})}{(\{g^k\},\{h^k\})} \\ \{d^{k+1}\} = -\{h^{k+1}\} + \beta_k\{d^k\} \\ k = k+1 \end{cases} \tag{5.132}$$

The convergent rate of equivalent Eq. (5.130) is dependent on the $Cond([A'])$. If $[M]$ is a unit matrix, then Eq. (5.132) becomes the "conjugate gradient" (CG) iterative scheme with convergent rate depending on $Cond([A])$. Normally, $Cond([A])$ is rather large and we may expect that $Cond([A']) \ll Cond([A])$. The matrix $[M]$ so selected is termed as the pre-conditioner of $[A]$. A good pre-conditioner should meet the following requirements

- $Cond(A') \ll Cond(A)$;
- Compared with $[A]$, it does not demand too large additional memory;
- It is much easier to solve $[M]\{h\} = \{g\}$ than to solve $[A]\{x\} = \{b\}$.

Where the decomposition matrices of the "symmetric successive over-relaxation (SSOR) method are used to construct the $[M]$ in a manner of

$$[M] = (2-\omega)^{-1}([D]/\omega + [L])([D]/\omega)^{-1}([D]/\omega + [L])^T \tag{5.133}$$

The PCG algorithm employing $[M]$ in Eq. (5.133) is termed as the SSOR-PCG method. In Eq. (5.133), $[D]$ is the diagonal matrix of $[A]$,$[L]$ is the lower triangular matrix of $[A]$, i.e.$[A] = [D] + [L] + [L]^T$, $0 < \omega < 2$ is the relaxation factor.

The selection of appropriate relaxation factor ω is still problematic because there is no theoretical support to get the optimal relaxation factor for the matrix $[A]$ derived from complex engineering problems. As a result, empirical values based on computation experiences are widely exercised. For caution, ω should be very close to 1.0, and $\omega = 1.0$–1.1 is commonly advisable.

4. SSOR-PCG method for the p-refinement FEM

The foregoing SSOR-PCG method is revised to take into account of the hierarchical properties of the p-refinement FEM (Fish and Guttal 1997), i.e. the lower order solution may be employed in the successive higher order solution.

i. Iterative algorithm

Denote the algebra equation set from the FEM of order p as

$$[A_p]\{x_p\} = \{b_p\} \tag{5.134}$$

In which

$$\begin{cases} [A_p] = \begin{bmatrix} [A_{p-1}] & [A_{p-1,a}] \\ [A_{a,p-1}] & [A_{a,a}] \end{bmatrix} \\ \{x_p\} = \begin{Bmatrix} \{x_{p-1}\} \\ \{x_a\} \end{Bmatrix} \\ \{b_p\} = \begin{Bmatrix} \{b_{p-1}\} \\ \{b_a\} \end{Bmatrix} \end{cases} \tag{5.135}$$

Similarly, the corresponding equation of order $(p-1)$ is

$$[A_{p-1}]\{x_{p-1}\} = \{b_{p-1}\} \tag{5.136}$$

Suppose the solution of Eq. (5.136) is $\{x_{p-1}^0\}$, the iterative marching for Eq. (5.134) launches

$$\begin{cases} [A_{a,a}]\{x_a^{s+1}\} = \{b_a\} - [A_{a,p-1}]\{x_{p-1}^s\} \\ [A_{p-1}]\{x_{p-1}^{s+1}\} = \{b_{p-1}\} - [A_{p-1,a}]\{x_a^{s+1}\} \end{cases} \tag{5.137}$$

In which s is the iterative step using the SSOR-PCG method. Computation experiences show that the iterative convergent rate of Eq. (5.137) is high, and s is normally smaller than 5.

ii. Initial value

Another use is made of initial value assignment. Suppose the algebra equation from the p-refinement FEM is N_{p-1} dimension in the previous upgrade of order $(p-1)$ and is $N_p = N_{p-1} + N_a$ dimension during the present upgrade of order p. Let $\{x^0\}$ in Eq. (5.131)

$$\{x^0\} = \begin{Bmatrix} \{x_{p-1}\} \\ \{0\} \end{Bmatrix} \tag{5.138}$$

In which $\{x_{p-1}\}$ is the previous FE solution of $p-1$ order and $\{0\} = [0 \quad \dots \quad 0]_{N_a \times 1}^T$. This may give rise to remarkable acceleration effect in the iteration because the $\{x^0\}$ constructed in Eq. (5.138) is rather close to the solution of Eq. (5.134).

5.6 P-Version Refinement in Space Domain: Permeability Problems

5.6.1 Error Estimator

The element refinement strategy is taken as the example to elucidate the p-version refinement FEM for permeability problems (Fei and Chen 2004).

Suppose the basis functions are of p-order, then the flow velocity is calculated by the formula

$$\{q_p\} = -[k][B_p]\{\phi_p\}^e \tag{5.139}$$

The higher order $(p+1)$ solution of flow velocity is regarded as the "best guess" of the exact solution, then similar to Eq. (5.30), the "energy norm" for the element i may be computed by the formula

$$\|e_p\|_i = \sqrt{\iiint_{\Omega_i} (\{q_{p+1}\} - \{q_p\})^T [k]^{-1} (\{q_{p+1}\} - \{q_p\}) d\Omega} \tag{5.140}$$

And the total energy norm of the element i is

$$\|\phi\|_i = \sqrt{\iiint_{\Omega_i} \{q_{p+1}\}^T [k]^{-1} \{q_{p+1}\} d\Omega} \tag{5.141}$$

The relative error e_i is a dimensionless scale of the error

$$e_i = \|e_p\|_i \Big/ \|\phi\|_i \tag{5.142}$$

5.6.2 Basic Solution Procedure

When the solution $\{\phi_{p-1}\}$ of order p-1 has been accomplished, the iterative procedure for the unconfined seepage field $\{\phi_p\}$ of successive higher order p is carried out as follows.

① Suppose at the rth phreatic surface iterative step, the potential function $\{\phi_{p,r}\}$ is solved.

② According to the condition $\phi_{p,r} = Z$, the tentative phreatic surface is constructed.

③ For each element i in which a patch of phreatic surface is embedded, its contribution to the residual nodal flow rate is calculated using

$$\{q_{p,r}\} = -\iiint_{\Omega_i} [B_p]^T [k][B_p]\{\phi_{p,r}\}^e d\Omega \text{ (Gaussian point where } \phi_{p,r} < Z \text{ only)} \tag{5.143}$$

④ The overall residual flow rate $\{Q_{p,r}\}$ is assembled, afterwards the potential increment is solved by

$$[H_p]\{\Delta\phi_{p,r}\} = \{Q_{p,r}\} \tag{5.144}$$

⑤ The adjusted potential after the $r+1$th iteration is accumulated by

$$\{\phi_{p,r+1}\} = \{\phi_{p,r}\} + \{\Delta\phi_{p,r}\} \tag{5.145}$$

⑥ Where $\{\Delta\phi_{p,r}\}$ is sufficiently small, the phreatic surface iteration loop collapses, and we return to step ⑦; otherwise let $r = r+1$ and go back step ①.
⑦ The error e_i of element i is evaluated using Eqs. (5.140)–(5.142).
⑧ If $e_i \le e_t$ for all the elements, the p-refinement is collapsed with an acceptable order of p; Otherwise, let $p = p+1$ for unqualified elements and let $r = 1$, steps ①–⑦ are recurred.

5.7 Verifications and Applications

5.7.1 Adaptive Time-Stepping (H-Refinement)

The bar element fixed at two ends in Fig. 5.9a is assigned with unit parameters E = 10000, σ_y = 0, γ = 0.001, and L = 1. An initial displacement δ = 0.1 is suddenly imposed at its lower end. The analytical solution for this simplest stress relax problem plotted in Fig. 5.9b is well known from the elementary theory of rheology. The computational results with implicit parameter Θ = 0.85 and variable e_t are plotted in this figure, too. It demonstrates that the strategy of automatic marching with adaptive time step length yields the satisfactory accuracy when the error tolerance is prescribed as e_t = 5%.

5.7.2 Two-Dimensional Underground Cavern (H-Refinement)

For the underground cavern of shallowly embedded in Fig. 3.27 whose in situ stress field is dominated by the gravity actions of the surrounding rocks and the

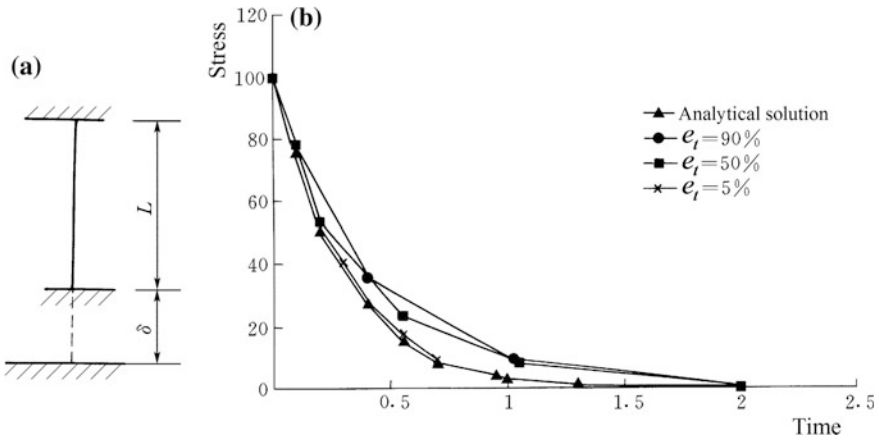

Fig. 5.9 Stress relax history of the bar element ($\Theta = 0.85$)

excavation is postulated to be accomplished in one bench, we input the background mesh size $h = 10$ m, the mesh generator creates an uniformly distributed background mesh (see Fig. 3.39) comprising 375 elements and 421 nodes ($e = 27\%$).

The iterative computation using the h-refinement FEM on the foregoing background mesh with prescribed error tolerance $e_t = 15\%$ produces the refined mesh (see Fig. 5.10) comprising 2862 elements and 2898 nodes ($e = 14.1\%$). Since it is close to the prescribed error tolerance e_t, the adaptive iteration is collapsed after the output of corresponding results.

The mesh distribution is automatically adjusted with the help of the specified error tolerance, and it is obvious that the elements are concentrated around the cavern attributable to the strong stress concentration (gradient) in this area. In Fig. 5.11 we draw the contours of local (point) safety factor K_p based on the Drucker-Prager criterion [see Eq. (4.215)], it is evident that the area of concentrated elements is mostly overlapped with the area enclosed by the contour of local safety factor $K_p = 2.0$.

5.7.3 *Three-Dimensional Underground Cavern (H-Refinement)*

For the tunnel excavated under a rock slope with initial background mesh ($e = 36\%$) (see Fig. 3.40), we specify the error tolerance $e_t = 15\%$. After two iteration steps, the refined mesh is reached with actual error $e = 12.3\%$(see Fig. 5.12).

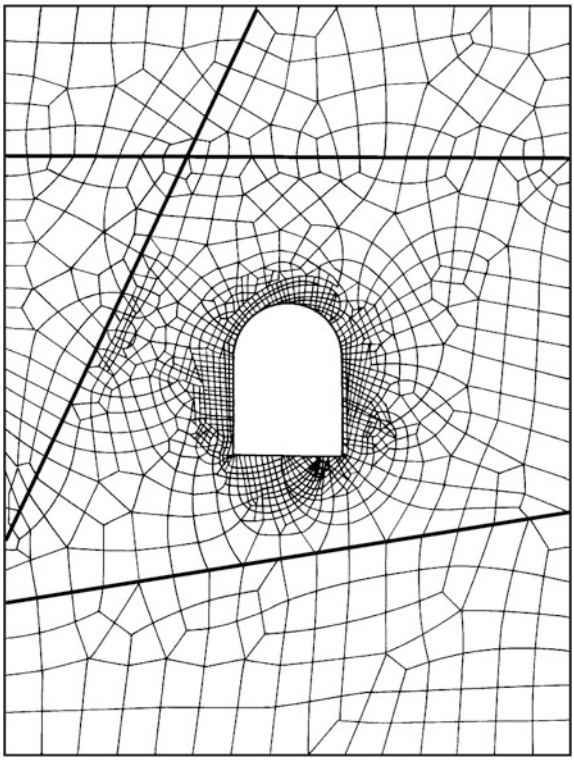

Fig. 5.10 Refined mesh (2862 elements; 2898 nodes; $e = 14.1\%$): two-dimensional cavern

5.7.4 *Two-Dimensional Embankment (H-Refinement)*

The embankment in Fig. 5.13 is installed with horizontal drain device. Input the initial background mesh size $h = 5$ m, the back ground mesh is generated in Fig. 5.14 with $e = 17.2\%$. Specify the error tolerance $e_t = 10\%$, the optimal mesh is obtained after two iteration steps with actual error $e = 9.7\%$ (see Fig. 5.15).

Table 5.1 lists the gradient J of hydraulic potential at the left extremity of the horizontal drainage. Figure 5.16 gives the phreatic surface by the analytical solution (Polubarinova-Kochina 1962) and the FE solution on the refined mesh, Fig. 5.17 illustrates the flow velocity field on the refined mesh.

5.7.5 *Three-Dimensional Sluice Foundation (H-Refinement)*

Figure 5.18 presents a pervious foundation supporting the impervious concrete bottom slab of a sluice. The foundation soil is homogeneous and isotropic with the

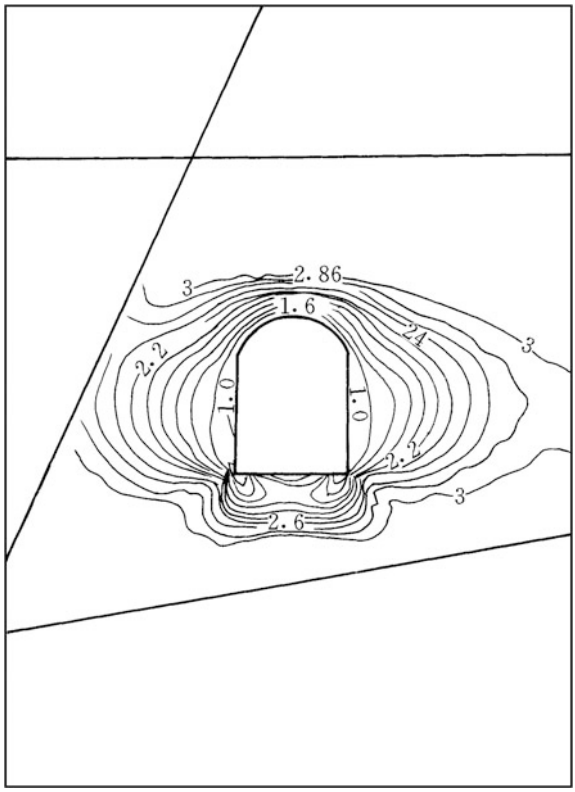

Fig. 5.11 Contours of point safety factor K_p

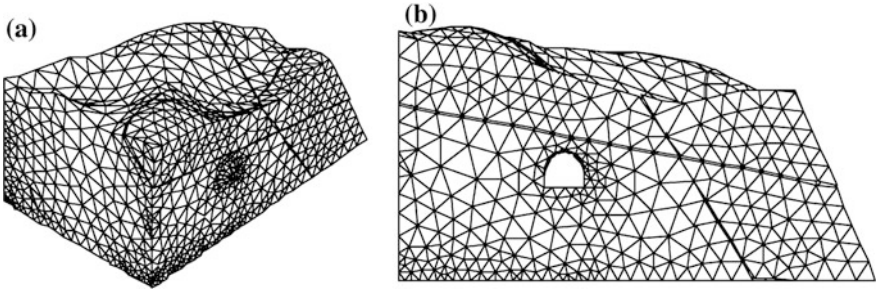

Fig. 5.12 Refined mesh (13,114 elements; 3762 nodes; $e = 12.3\%$): there-dimensional cavern. **a** Axonometric view; **b** front view

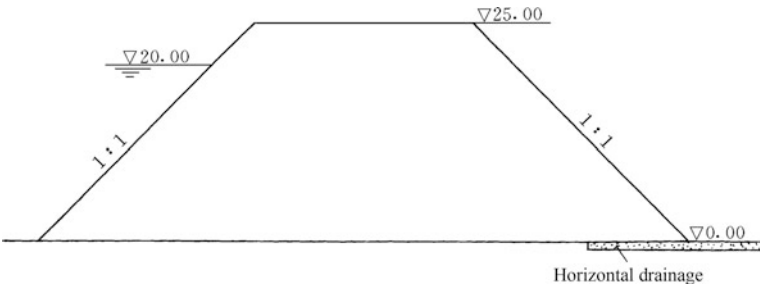

Fig. 5.13 Homogeneous embankment with a horizontal drain

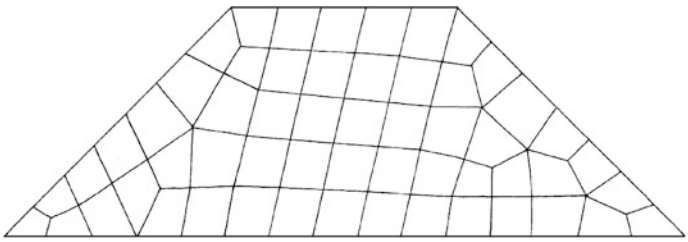

Fig. 5.14 Initial background mesh (56 elements, 74 nodes, e = 17.2%)

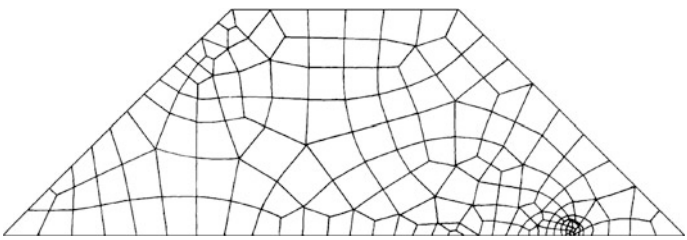

Fig. 5.15 Refined mesh (198 elements; 232 nodes; $e = 9.7\%$)

Table 5.1 Gradient of the hydraulic potential at the left extremity of the horizontal drainage

Mesh error e	17.2% (initial)	9.7% (refined)
Gradient J	0.9377	6.0876

permeability coefficients $k = k_x = k_y = k_z = 1.0 \times 10^{-3}$ m/s. Head water is 5 m and tail water is 0 m. Input the initial mesh size $h = 3$ m, the initial background mesh is generated in Fig. 5.19 with error e = 31.1%. Specify the error tolerance e_t = 10%, the refined mesh is obtained only after two iteration steps with e = 9.3%. Figure 5.20 is the axonometric view of the refined mesh and Table 5.2 displays the error following the adaptive iteration. Figures 5.21 and 5.22 draw the potential contours and the flow velocities in the longitudinal section.

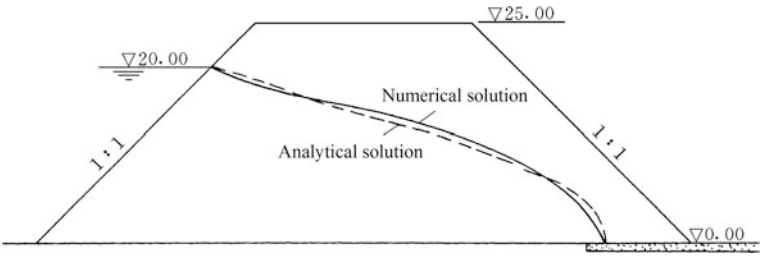

Fig. 5.16 Phreatic surface

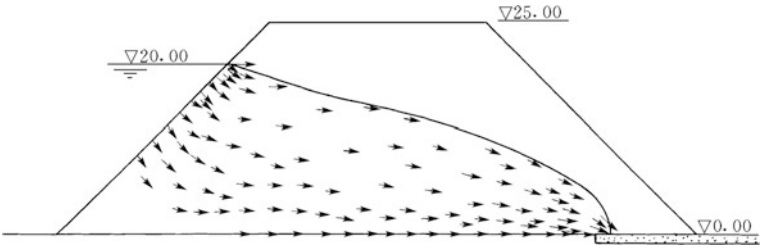

Fig. 5.17 Distribution of flow velocity on the refined mesh

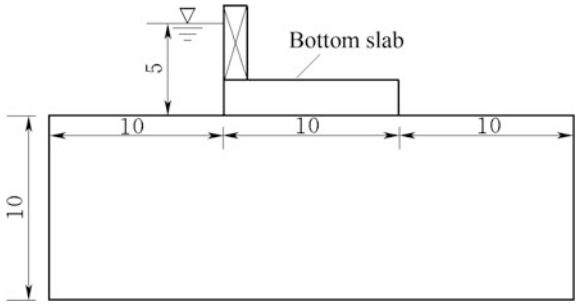

Fig. 5.18 Sluice foundation with impermeable concrete bottom slab

5.7.6 Jointed Sample Under Uni-Axial Pressure (Complete P-Refinement)

The sample is initially discretized into three big elements (see Fig. 5.23): element ① and element ② are solid elements, whereas element ③ is a joint element with thickness. The top of sample is exerted by an uniform pressure of 1.0 MPa, and the bottom is fixed completely. The material parameters are listed in Table 5.3. The error tolerance is specified as e_t = 3.0%, and the variation of nodal displacement following the p-refinement is illustrated in Table 5.4.

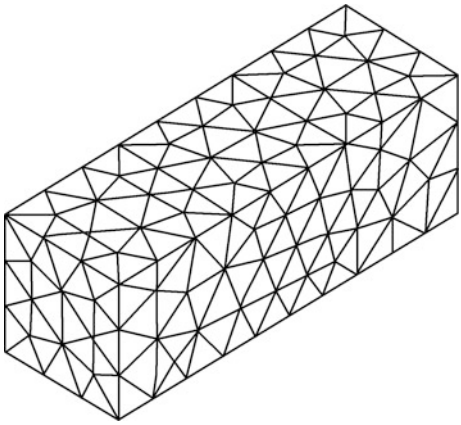

Fig. 5.19 Initial background mesh (797 elements; 236 nodes; e = 31.1%)

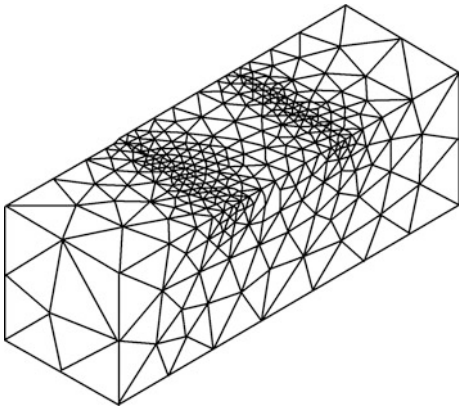

Fig. 5.20 Refined mesh (2397 elements; 621 nodes; e = 9.3%)

Table 5.2 Variation of mesh discretization errors

–	Initial background	First refinement iteration	Second refinement iteration
Mesh size h (m)	3.0	0.7–4.5	0.2–5.0
Mesh error e (%)	31.1	18.8	9.3

In parallel, we subdivide the coarse mesh in Fig. 5.23 into a finer mesh in Fig. 5.24 (octree method) for the cross-reference using h-refinement. On this higher resolution mesh the same problem is solved using standard 8-nodal hexahedral elements. The results of nodal displacement are also listed in the last column of Table 5.4 (last column).

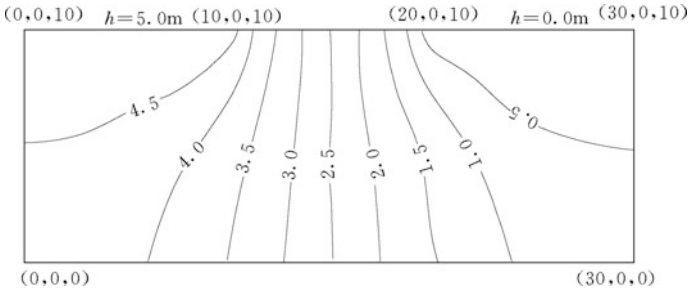

Fig. 5.21 Potential contours on the refined mesh

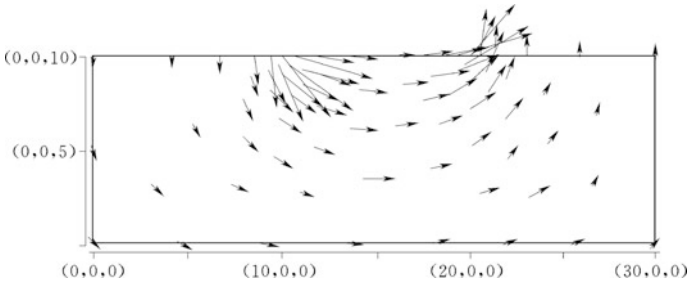

Fig. 5.22 Flow velocity on the refined mesh

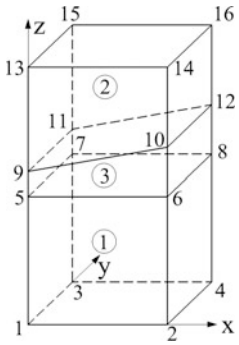

Fig. 5.23 Jointed sample: coarse mesh for p-refinement

Table 5.3 Material parameters

–	Young's modulus E (GPa)	Poisson's ratio μ	Cohesion c (MPa)	Friction angle φ (°)
Solid element	30	0.2	2.8	40
Joint element	15	0.15	1.6	45

Table 5.4 Variation of nodal displacements (unit: mm)

Method		p-refinement				h-refinement ($h^{new} = h^{old}/2$) ($p = 1$)
		$p = 1$	$p = 2$	$p = 3$	$p = 4$	
Error		–	7.12%	3.44%	2.02%	
Node 5	u_x	−0.004325	−0.003284	−0.003646	−0.003519	−0.003515
	u_y	−0.004255	−0.003139	−0.003505	−0.003377	−0.003383
	u_z	−0.032110	−0.033100	−0.033330	−0.032760	−0.032930
Node 6	u_x	0.004437	0.003210	0.003646	0.003480	0.003485
	u_y	−0.004339	−0.003126	−0.003553	−0.003374	−0.003393
	u_z	−0.032230	−0.033030	−0.033370	−0.032720	−0.032910
Node 9	u_x	−0.004322	−0.003915	−0.004036	−0.004077	−0.004055
	u_y	−0.003632	−0.003213	−0.003337	−0.003368	−0.003361
	u_z	−0.038410	−0.039310	−0.039360	−0.039150	−0.039220
Node 10	u_x	0.002973	0.002580	0.002714	0.002728	0.002720
	u_y	−0.003545	−0.003242	−0.003341	−0.003362	−0.003355
	u_z	−0.044920	−0.045500	−0.045610	−0.045440	−0.045500

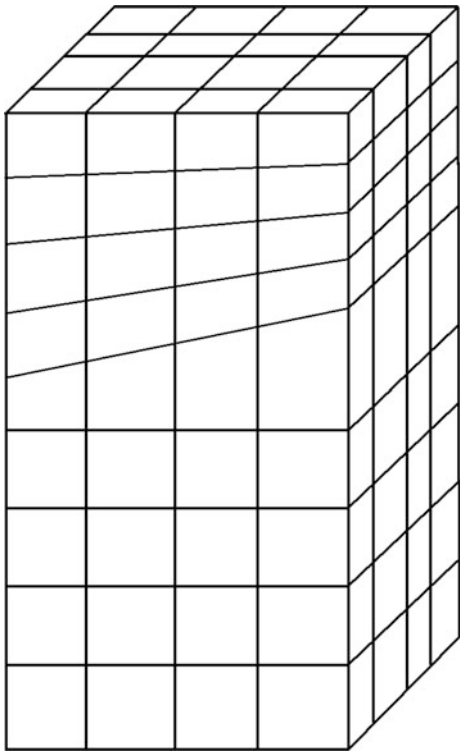

Fig. 5.24 Jointed sample: h-refined mesh

5.7.7 Three-Dimensional Gravity Dam on a Homogenous Foundation (Complete P-Refinement)

Figure 5.25 shows a gravity dam at a height of 100 m whose crest width is 10 m. The material parameters for the computation are:

- Dam concrete. Volumetric weight $\gamma_c = 0.024$ MN/m^3, Young's modulus E_c = 25 GPa, Poisson's ratio $\mu_c = 1/6$.
- Foundation rock. Volumetric weight $\gamma_r = 0.026$ MN/m^3, Young's modulus $E_r = 75$ GPa, Poisson's ratio $\mu_r = 0.25$.

A dam monolith of 10 m thick is discretized into 114 hexahedral elements and 284 real nodes (see Fig. 5.26). Specifying the error tolerance $e_t = 10\%$, the complete p-refinement is carried out until the error is under the control when $p = 3$. The variation of p-refinement indices is presented in Table 5.5 and Fig. 5.27, respectively.

5.7.8 Two-Dimensional Gravity Dam on a Heterogeneous Foundation (Element P-Refinement)

Figure 5.28 shows the computation mesh (projected on the plane $X - Z$) for the gravity dam identical to Fig. 5.25, but there are additional two faults F_1 and F_2 embedded in its foundation which should be discretized using joint element without thickness. In addition, the contact surface J of dam/foundation is also simulated. There are 160 elements and 384 real nodes. The material parameters are listed in Table 5.6.

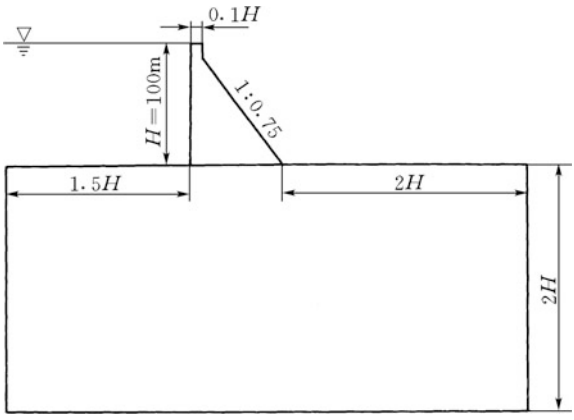

Fig. 5.25 Gravity dam on a homogenous foundation

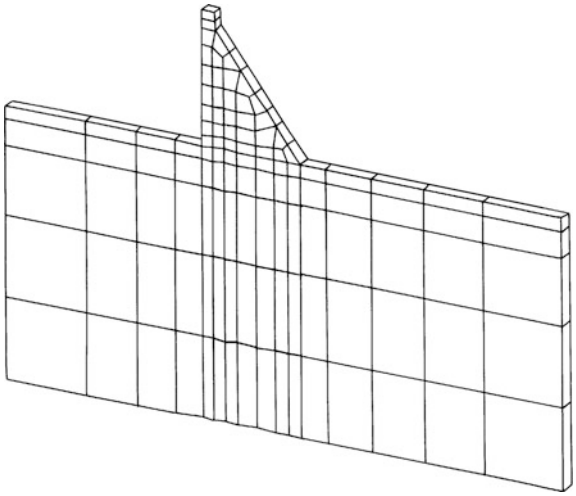

Fig. 5.26 Computation mesh (114 elements; 284 nodes; 652 edges; 484 faces)

Table 5.5 Variation of p-refinement indices

p	General nodes of element $f_e(p)$	General nodes of the whole structure $f_t(p)$	Overall *DOF*	Density of overall stiffness (%)	Error energy norm e (%)
1	8	284	510	5.786	27.04
2	20	936	1875	4.049	16.69
3	32	1588	3240	3.795	9.93

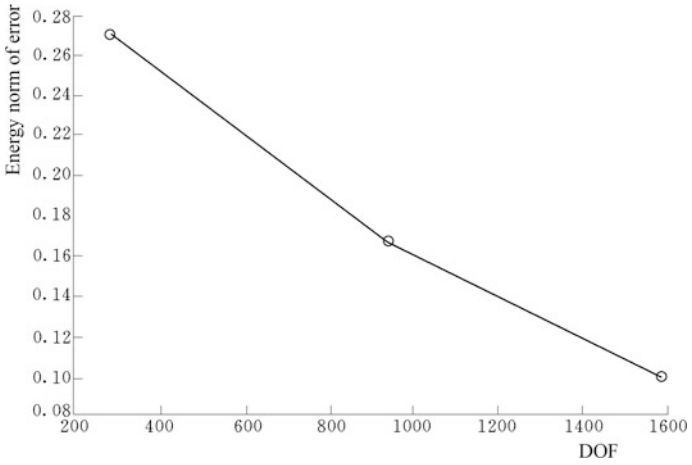

Fig. 5.27 *DOF* versus error e

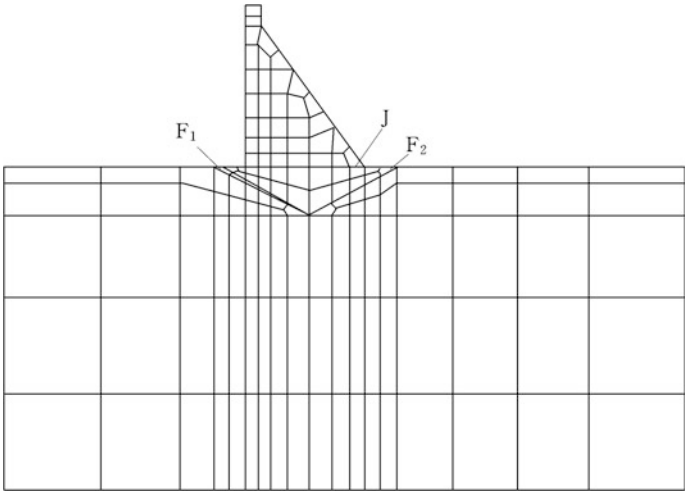

Fig. 5.28 Computation mesh projected on the plane $X-Z$ for the gravity dam with faults F_1 and F_2

Table 5.6 Material parameters

–	Foundation	Dam	F_1	F_2	J
Unit weight γ (MN/m^3)	0.026	0.024	0.025	0.025	–
Young's modulus E (GPa)	25	28	24	24	–
Poisson's ratio μ	0.2	0.167	0.2	0.2	–
Cohesion c (MPa)	1.2	1.6	1.0	1.0	2.0
Friction angle φ (°)	45	40	45	45	45
Tension strength σ_T (MPa)	0.2	0.18	0.2	0.2	0.2
Dip angle θ (°)	–	–	153.43	33.69	0
Dip orientation ϕ (°)	–	–	180	180	180
Normal stiffness k_n (MN/m^3)	–	–	–	–	25
Shear stiffness k_s (MN/m^3)	–	–	–	–	10

Table 5.7 Variation of p-refinement indices

p	Refined elements	General nodes of the whole structure $f_t(p)$	Overall DOF	Density of overall stiffness (%)	Error energy norm e (%)
1	–	384	706	4.147	–
2	160	1278	2599	2.663	10.38
3	97	1939	4058	2.499	0.37

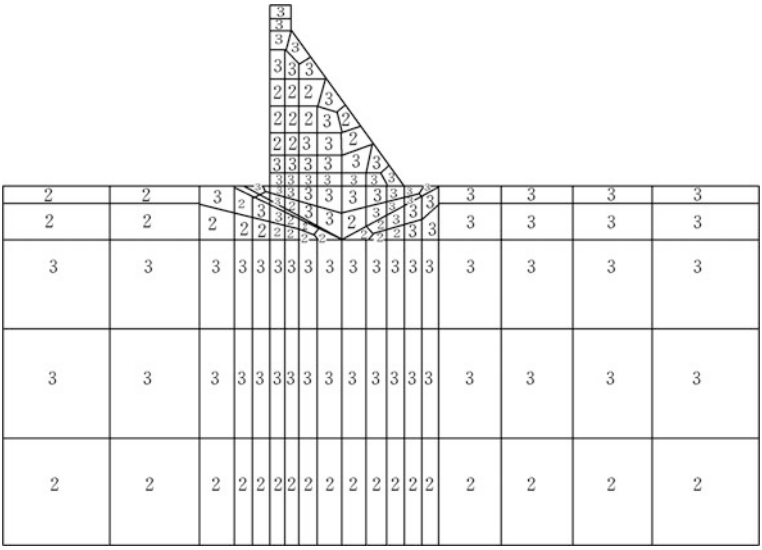

Fig. 5.29 Distribution of shape function order p after the refinement

We prescribe the error tolerance $e_t = 5\%$, the element refinement is terminated when $p = 3$. The variation of p-refinement indices is listed in Table 5.7, and Fig. 5.29 shows the distribution of shape function order after the element refinement.

We subdivide each solid element in Fig. 5.29 into eight finer elements (Octree method), and each joint element into four finer elements as well. In this way a simple h-refinement FEM is implemented whose principal stresses are compared with that by the p-refinement in Table 5.8.

The computation results validate that the p-refinement is prone to raise the principal stresses at the crucial points (singularities) where strength safety should be calibrated in the dam design. The results of $p = 2$ is rather close to that of h-refinement ($h^{new} = h^{old}/2$, $p = 1$) through the uniform octree sub-division.

Table 5.8 Principal stresses computed by the p-refinement and h-refinement FEM (Unit: MPa)

Principal stress		p-refinement			h-refinement ($h^{new} = h^{old}/2$) ($p = 1$)
		$p = 1$	$p = 2$	$p = 3$	
Dam heel	σ_1	1.193751	1.789498	2.096205	1.835808
	σ_3	−0.717360	−0.712321	−0.722489	−0.566757
Dam toe	σ_1	−0.223288	−0.188617	−0.032742	−0.0327781
	σ_3	−3.000112	−3.924229	−4.669299	−3.557305
Generatrix point of downstream slope	σ_1	−0.085366	−0.061472	−0.059228	−0.119863
	σ_3	−0.409060	−0.598107	−0.676079	−0.622786

5.7.9 *Excavation of Slope: Ship Lock, Three Gorges Project, China*

(1) Presentation of the project

Three Gorges Project (see Fig. 5.30) dams the Yangtze River in the Hubei Province, China. It is the world's largest water resources project in terms of installed turbine generator capacity (22,500 MW). The dam was completed and fully functional on July 4, 2012, when the last of the main turbine generators in the underground plant began production.

As well as to produce electricity, the project is intended to increase the Yangtze River's shipping capacity and to reduce the risk of downstream floods. In addition to the ship lift completed in December 2015 and started to trial running from September 2016, the ship locks play a principal role in raising annual river shipping capacity from ten million tons to 100 million tons.

There is double-lane and five tandem ship lock installed near the left dam abutment. It comprises up-and down-stream approach channels, ship lock chambers, water conveyance system and drainage system located in the mountain around (see Fig. 5.31). The total length of the ship lock from the entrance of the upstream approach channel to the exit of the downstream approach channel is 6442 m. The main structure of the ship lock (inclusive six lock chambers) is 1621 m in length.

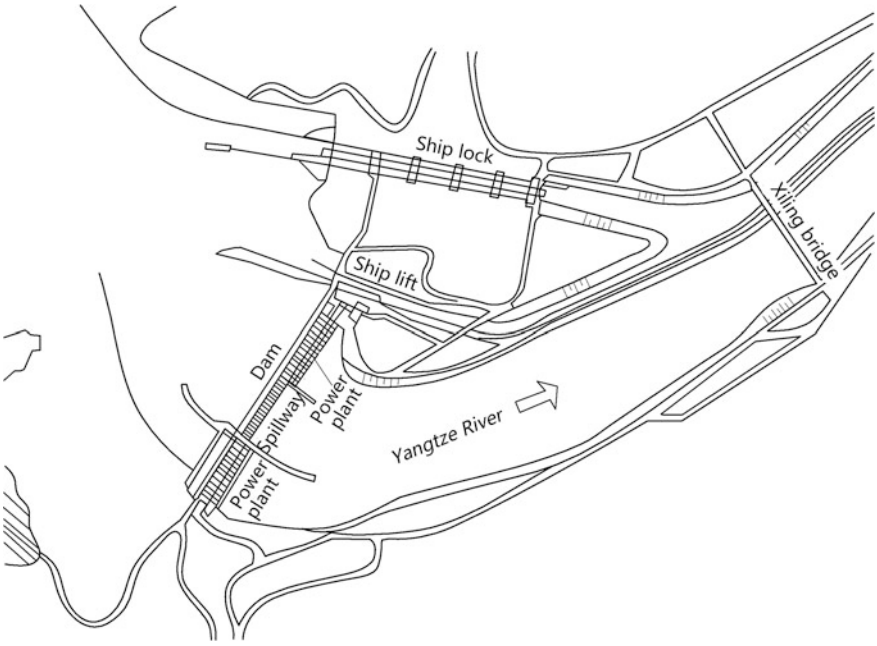

Fig. 5.30 Plan of Three-Gorges Water Resources Project (gravity dam), China

The highest slope cutting is 170 m, altogether 41.96 million m^3 open cut and 980,000 m^3 tunnel cut were undertaken. A rock pillar wall of 54–57 m wide is left between the two lock lanes serving as the middle-isolated wall (pier). The side walls of the ship lock chambers are of thin concrete lining back-tied on the vertical slopes, in this way the rock mass also performs as an integrity component of the ship lock structure.

The rock mass in the ship lock area consists of amphibole granite (Pre Sinian Period), occasionally of schist, with 4 dominant sets of joints dipping at 50°–75°. Pegmatitic dikes are commonly encountered, which may potentially result in local wedge failures. The maximum principal in situ geo-stress is nearly horizontal in the ship lock area forming an small included angle (about 30°) with the cut slope. The horizontal in situ geo-stress within the excavation channels is at a relatively lower level of 4–11 MPa.

(2) Characteristics of the computation

The representative section of the second stage of the ship lock (see Fig. 5.32, chainage 15,600 m) is taken for the deformation and stability analysis using the elaso-viscoplastic FEM of h-refinement.

There are more than ten faults in the section concerned, of which the most adverse ones are f_{229}, f_{204} and F_8. They, together with the Pegmatitic dyke ex, are explicitly taken into account in the mesh discretization. The excavation is simulated by six benches corresponding to the elevation of 170.0, 155.0, 140.0, 125.0, 112.9, and 92.5 m, respectively.

(3) Mesh refinement

Firstly, the geometrical messages of the ship lock, mechanical properties of the rock masses, the excavation benches, are prepared in the input data file. The error tolerance is specified as $e_t = 5\%$ (the initial stress is taken into account of the total energy norm). The refined meshes corresponding to excavation benches are shown in Figs. 5.33, 5.34, 5.35, 5.36, 5.37 and 5.38. It is notable that near the exposure face, particularly at the break point of the cut slope surface, elements are concentrated. In addition, at different excavation benches, the stress concentration zones are shifted downwards, and the mesh is adjusted in correspondence.

The displacements, the stresses, the safety factors, and the reinforcement schemes of the ship lock were comprehensively studied using above refined meshes in its preliminary design phases (Chen 1998; Chen and Chen 2001).

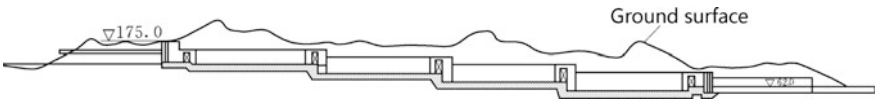

Fig. 5.31 Longitudinal section of the dual-lane and five-tandem ship lock in Three-Gorges Project

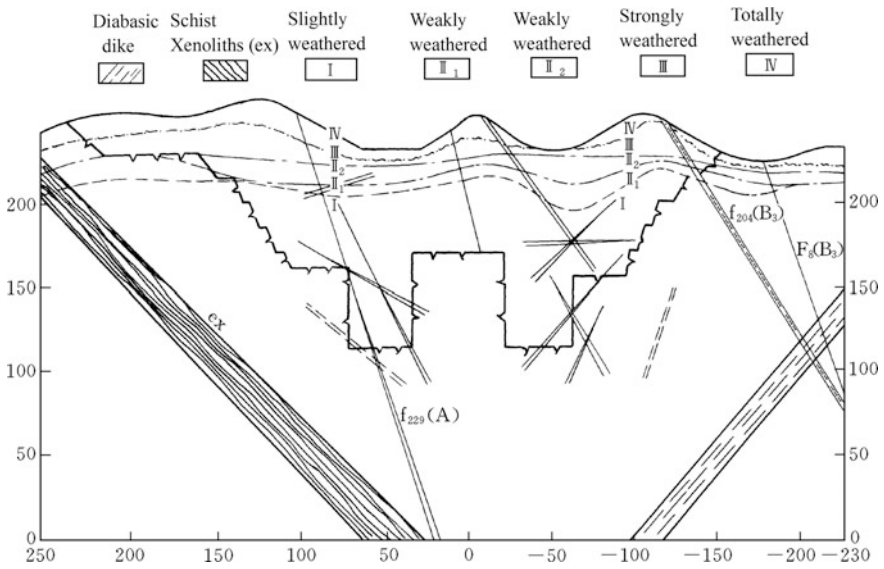

Fig. 5.32 Geology profile of the representative section (chainage 15,600 m)

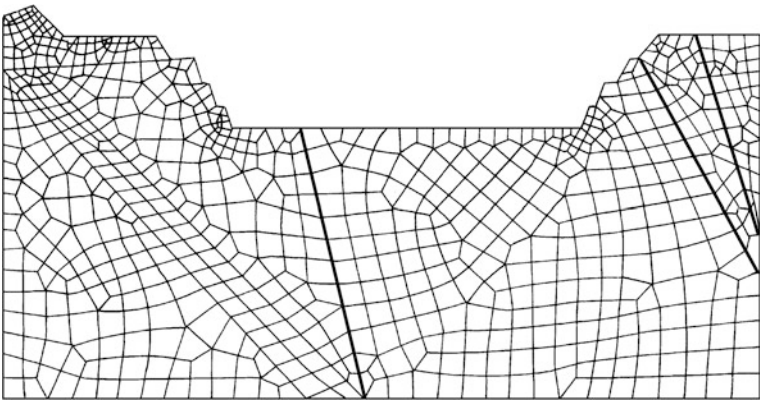

Fig. 5.33 Refined mesh after the first bench excavation (787 elements; 865 nodes)

5.7.10 Stabilization of Landslide: Shuibuya Project, China

(1) Presentation of the project

Located on the Qingjiang River, Hubei Province, China, Shuibuya Project comprises a concrete faced rockfill dam (CFRD), a bank-type spillway controlled by five 14 m × 21.8 m gates with maximum discharge of 16,300 m^3/s, an

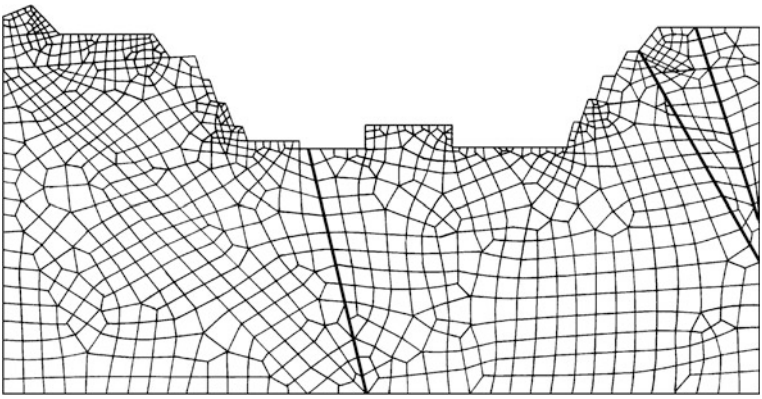

Fig. 5.34 Refined mesh after the second bench excavation (1080 elements; 1178 nodes)

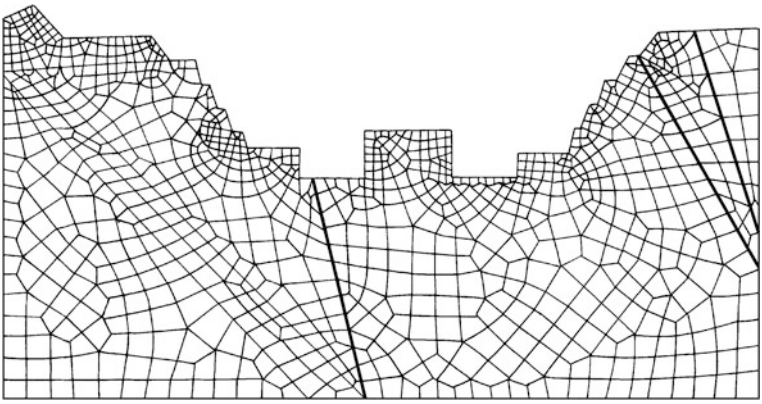

Fig. 5.35 Refined mesh after the third bench excavation (1009 elements; 1111 nodes)

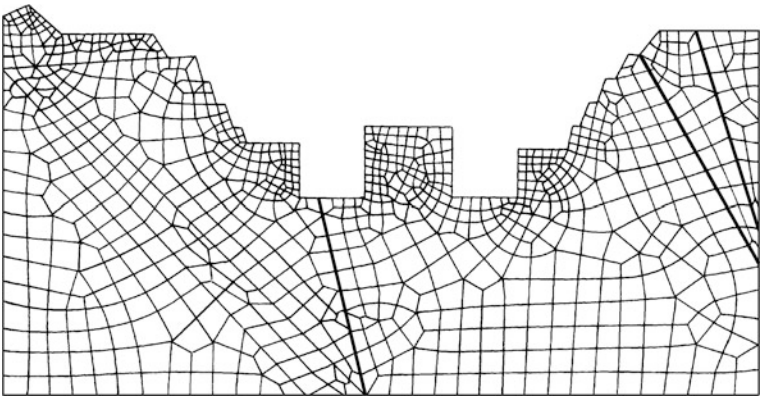

Fig. 5.36 Refined mesh after the fourth bench excavation (908 element; 1008 nodes)

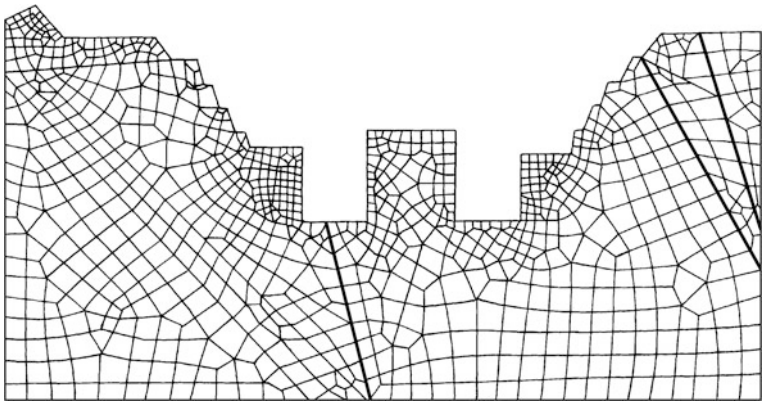

Fig. 5.37 Refined mesh after the fifth bench excavation (937 elements; 1042 nodes)

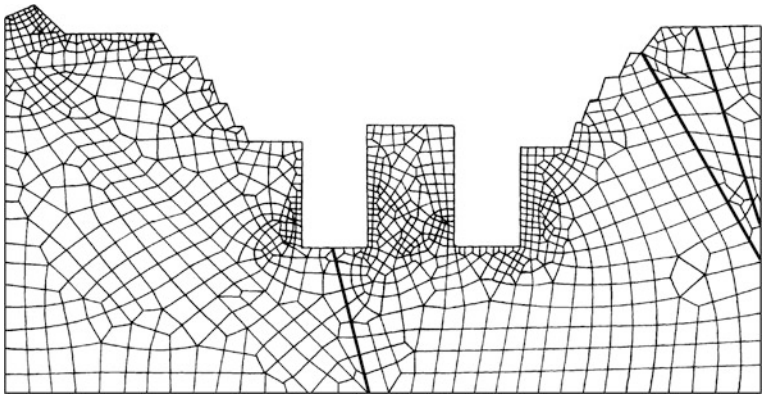

Fig. 5.38 Refined mesh after the sixth bench excavation (1109 elements; 1228 nodes)

underground power station installed with four turbine generator units (4 × 460 MW) (see Fig. 5.39).

The major purpose of the project is hydroelectricity generation in addition to flood mitigation, navigation, tourism and fishery. The project possesses the tallest CFRD in the world (H = 233 m) containing 15,640,000 m^3 rockfill materials. Construction on the project was authorized in January 2002 and began soon thereafter. On August 12, 2006, the dam reached its maximum height of 233 m and by July 2007, its first turbine generator was operational. The whole project was completed later in 2008.

Dayantang landslide (see Figs. 5.39 and 5.40a) is located at the downstream left abutment of the CFRD, 800 m to the dam axis and 300 m to the flip bucket nose of the shore spillway (Chen et al. 2002). It is evolved from an ancient bedded rock landslide on the slightly dip-away single slip surface, during that event the slide

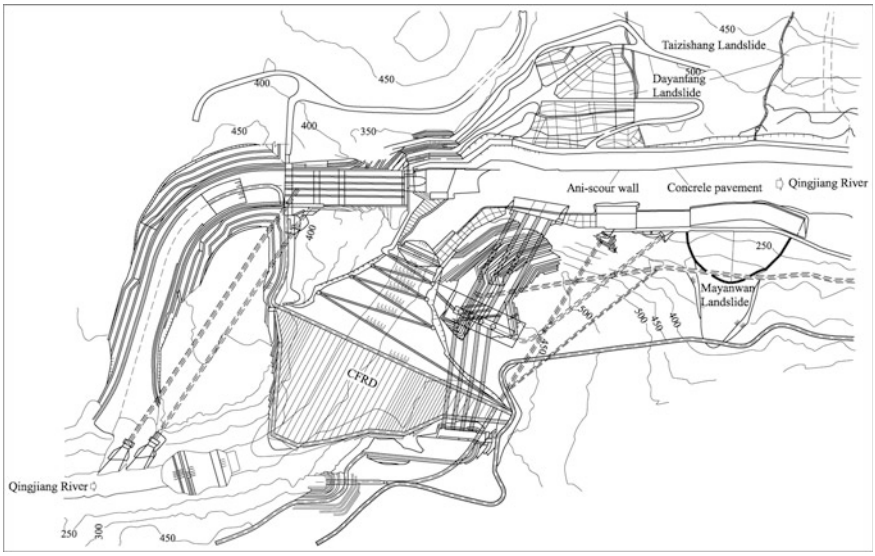

Fig. 5.39 Plan of Shuibuya Project, China

body was dismissed into a fragmented structure. The present landslide surface is 0.196 km^2, the thickness of the slide body is 25–64.8 m and the total slide volume is 5.88 $\times$ 10^6 m^3.

Under the natural condition, Dayantang landslide is stable. However, since it is situated at the vicinity of the spillway, the project construction and operation will give rise to adverse effects in the following aspects:

- The excavation of the plunge pool cuts a portion of the bedrock from the landslide toe, which will bring down its slide stability and erosion resistance.
- The atomization rainfall due to flood discharge through the spillway will further bring down its stability.
- The construction activities will damage the surface vegetation on the slide body, which will in turn, undermine its stability due to stronger infiltration.

The stabilization scheme of this landslide was designed and implemented according to the comprehensive analysis with respect to its overall and local stability.

(2) Characteristics of the computation

The principal section B-B of Dayantang landslide is shown in Fig. 5.40b.

The major stabilization countermeasure includes two rows of lateral resistance piles near the toe. The space of piles is 10 m, the cross sectional area of each pile is 3 $\times$ 4 m. At the top of each pile, a pre-stress anchor cable of 4000 kN is installed to tie back the pile towards the bedrock beneath the slide body.

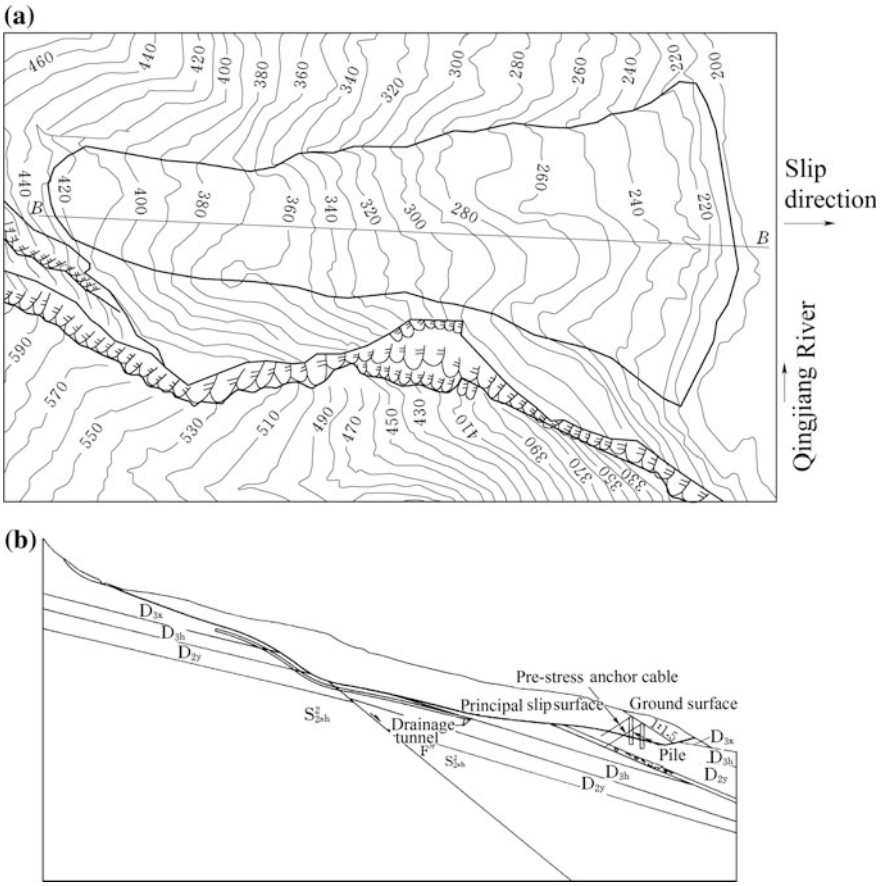

Fig. 5.40 Dayantang landslide. **a** Plan; **b** principal section B-B

Three work situations were studied including

① Self-weight + Steady seepage field (natural).
② Excavation.
③ Reinforcement + Excavation.

The physical and mechanical parameters used in the study are listed in Table 5.9.

(3) Results and discussions

1. Mesh refinement
   Figure 5.41 is the initial background mesh with error of energy norm $e = 6.3\%$ (in situ geo-stress is taken into account in the total energy norm). Prescribing the error tolerance as $e_t = 2\%$, the refined mesh is generated in Fig. 5.42. The

Table 5.9 Physical and mechanical parameters of Dayantang landslide

–	Dry unit weight γ (kN/m^3)	Young's modulus E (MPa)	Poisson's ratio μ	Cohesion c (kPa)	Friction angle φ (^{o})
Slide body	23.0	29	0.40	19.5	22.0
Slip surface	23.0	19	0.40	10.0	18.0
Bedrock	26.0	2500	0.34	650.0	35.0
Pile concrete	24.0	24000	0.17	2000.0	45.0

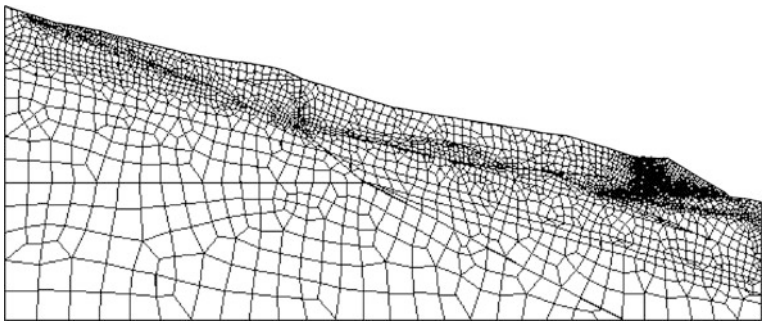

Fig. 5.41 Initial background mesh (3662 elements; 3782 nodes)

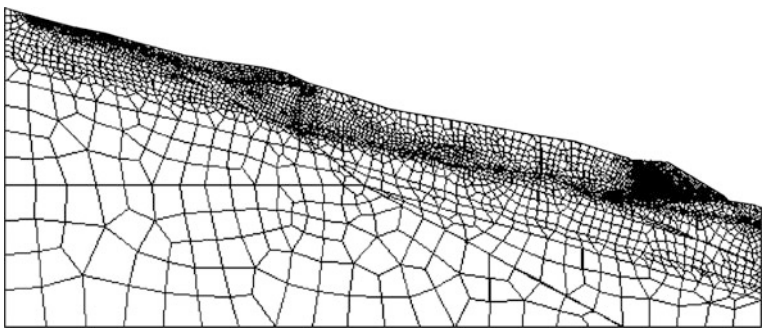

Fig. 5.42 Refined mesh (5316 elements; 5487 nodes)

elements tend to concentrate around the toe of the slide body, attributable to the severe plastic deformation around this area.

2. Stresses
   Figure 5.43 shows the principal stresses under the work situation of ③ Reinforcement + Excavation. The first principal stresses range between 0 and

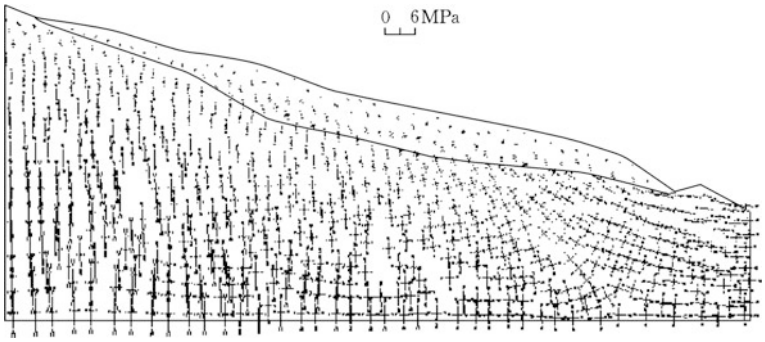

Fig. 5.43 Principal stresses under the work situation ③ Reinforcement + Excavation

−0.67 MPa, the second principal stresses range between 0 and −1.10 MPa. The maximum stress emerges on the slip surface where the slide body is the thickest.

3. Deformation
   Where there is no reinforcement (i.e. under the work situation of ② Excavation), there will be a continuous downwards creep after the plunge pool excavation, and no convergent solution can be obtained. Nevertheless, the slip deformation may be well controlled by the installation of two-row piles strengthened by the pre-stress anchor cables at their top before the plunge pool excavation. Figure 5.44 illustrates the convergent displacements due to excavation after the reinforcement (i.e. work situation ③). At the toe of the landslide, the maximum horizontal and vertical displacements are 14.5 and 15.7 cm, respectively.
4. Plastic zones and stability safety factor against sliding
   The computation reveals that if there are no reinforcement countermeasures before the plunge pool excavation, there will be a large plastic zone in the front of the slide body, and the FE computation is divergent. This plastic zone develops from the toe towards the up portion of the slide body until an overall

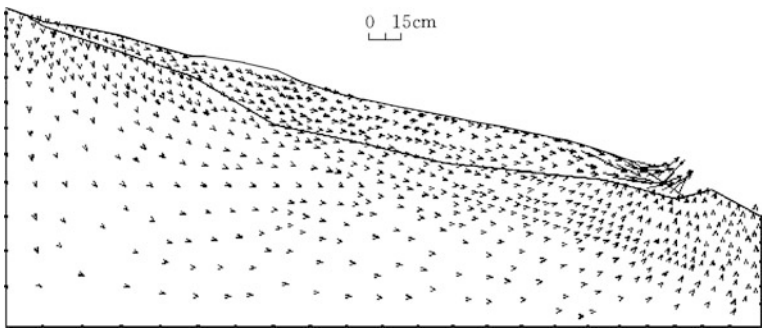

Fig. 5.44 Convergent displacements under the work situation ③ Reinforcement + Excavation

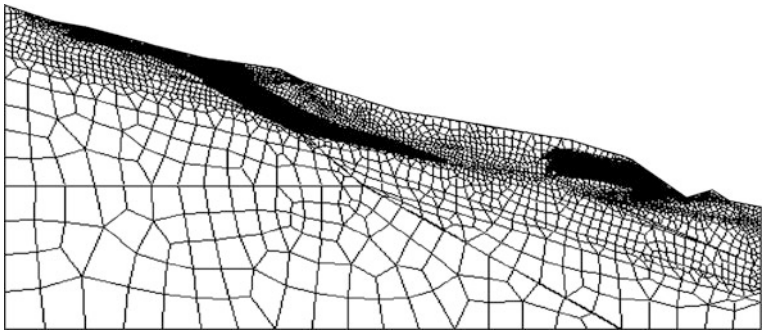

Fig. 5.45 Plastic zones (in black) under the work situation ③ Reinforcement + Excavation

slip failure is triggered. This validates that the reinforcement scheme is effective and indispensable to ensure the stability of Dayantang landslide. Figure 5.45 draws the plastic zones (in black) after the reinforcement and followed by the plunge pool excavation.

The strength reduction factor under the natural work situation ① is $K = 1.28$, whereas after the reinforcement followed by the excavation (i.e. work situation ③) it is approximately maintained at $K = 1.24$, which actually meets the design specifications (SL 386-2007) which stipulate the allowable safety factor $[K] = 1.25$ for grade 1 slopes and landslides.

References

Abbasian RO, Carey GF. A note on Richardson extrapolation as an error estimator for non-linear reaction diffusion problems. Commun Numer Meth Eng. 1997;13(7):533–40.

Babuška I, Miller A. The post-processing approach in the finite element method—Part 1: calculation of displacements, stresses and other higher derivatives of the displacements. Int J Numer Meth Eng. 1984a;20(6):1085–109.

Babuška I, Miller A. The post-processing approach in the finite element method—Part 2: the calculation of stress intensity factors. Int J Numer Meth Eng. 1984b;20(6):1111–29.

Babuška I, Miller A. The post-processing approach in the finite element methods—Part 3: a posteriori error estimates and adaptive mesh selection. Int J Numer Meth Eng. 1984c; 20(12):2311–24.

Babuška I, Rheinboldt WC. A-posteriori error estimates for the finite element method. Int J Numer Meth Eng. 1978;12(10):1597–615.

Babuška I, Rheinboldt WC. Adaptive approaches and reliability estimations for finite element analysis. Comp Meth Appl Mech Eng. 1979;17(18):519–40.

Babuška I, Rheinboldt WC. Error estimates for adaptive finite element computations. SIAM J Numer Anal. 1989;15(4):736–54.

Babuška I, Szabó BA. On the rates of convergence of the finite element method. Int J Numer Meth Eng. 1982;18(3):323–41.

Babuška I, Szabó BA, Katz IN. The p-version of the finite element method. SIAM J Numer Anal. 1981;18(3):515–45.

Babuška I, Strouboulis T, Upadhyay CS. A model study of the quality of a posteriori error estimators for linear elliptic problems. Error estimation in the interior of patchwise uniform grids of triangles. Comp Meth Appl Mech Eng. 1994a;114(3–4):307–78.

Babuška I, Strouboulis T, Upadhyay CS, Gangaraj SK, Copps K. Validation of a posteriori error estimators by numerical approach. Int J Numer Meth Eng. 1994b;37(7):1073–123.

Bardell NS. The application of symbolic computing to the hierarchical finite element method. Int J Numer Meth Eng. 1989;28(5):1181–204.

Barrett R, Berry M, Chan TF, Demmel J, Donato J, Dongarra J, Eijkhout V, Pozo R, Romine C, van der Vorst H. Templates for the solution of linear systems: building blocks for iterative methods. Philadelphia, USA: SIAM; 1994.

Becker R, Rannacher R. An optimal control approach to a posteriori error estimation in finite element methods. In: Iserles A, editor. Acta numerica. Cambridge, UK: Cambridge University Press; 2001. p. 1–102.

Belfort B, Carrayrou J, Lehmann F. Implementation of Richardson extrapolation in an efficient adaptive time stepping method: applications to reactive transport and unsaturated flow in porous media. Transp Porous Media. 2007;69(1):123–38.

Bergan PG, Mollestad E. An automatic time-stepping algorithm for dynamic problems. Comput Meth Appl Mech Eng. 1985;49(3):299–318.

Boroomand B, Zienkiewicz OC. Recovery by equilibrium in patches (REP). Int J Numer Meth. Eng. 1997a;40(1):137–64.

Boroomand B, Zienkiewicz OC. An improved REP recovery and effectivity robustness test. Int J Numer Meth Eng. 1997b;40(17):3247–77.

Boroomand B, Zienkiewicz OC. Recovery procedures in error estimation and adaptivity. Part 2: adaptivity in nonlinear problems of elasto-plasticity behaviour. Comput Meth Appl Mech Eng. 1999;176(1–4):127–46.

Briggs WL, Henson VE, McCormick SF. A multigrid tutorial. 2nd ed. Philadelphia, USA: Society for Industrial and Applied Mathematics; 2000.

Burkley VJ, Bruch JC Jr. Adaptive error analysis in seepage problems. Int J Numer Meth Eng. 1991;31(7):1333–56.

Carnevali P, Morris RB, Tsuji Y, Taylor G. New basis functions and computational procedures for p-version finite element analysis. Int J Numer Meth Eng. 1993;36(22):3759–79.

Chen SH. Adaptive FEM analysis for two-dimensional unconfined seepage problems. J Hydrodyn. 1996;19(1):60–6.

Chen SH. Elasto-viscoplastic adaptive finite element analysis of the navigation lock in Three Gorges Project. Rock Soil Mech. 1998;19(1):13–9 (in Chinese).

Chen SH, Chen SH. Application of adaptive elasto-viscoplastic finite element method in stability analysis of landslide. Chin J Rock Mech Eng. 2001;20(Sup 2):1596–9 (in Chinese).

Chen SH, Cheng Z. Study on the p-version adaptive finite element method for the hydraulic structures. J Hydraul Eng. 2001;23(11):62–9 (in Chinese).

Chen SH, Wang JS, Zhang JL. Adaptive elasto-viscoplastic FEM analysis for hydraulic structures. J Hydraul Eng. 1996;19(2):68–75 (in Chinese).

Chen SF, She CX, Chen SH. Adaptive elasto-viscoplastic finite element analysis of the stability of Dayantang slope. Chin J Rock Mech Eng. 2002;21(2):169–75 (in Chinese).

Chen SH, Qin WX, Xu Q. Composite element method and application of trace simulation for strain localization bands. Chin J Rock Mech Eng. 2007;26(6):1116–22 (in Chinese).

Cheng Z, Chen SH. Three dimensional hierarchical finite element method for hydraulic structure. J Hydraul Eng. 1999;21(12):53–8 (in Chinese).

Chung KY, Kikuchi N. Adaptive methods to solve free boundary problems of flow through porous media. Int J Numer Anal Meth Geomech. 1987;11(1):17–31.

Chung J, Cho EH, Choi KA. A priori error estimator of the generalized -α method for structural dynamics. Int J Numer Meth Eng. 2003;57(4):537–54.

Chung ET, Leung WT, Pollock S. Goal-oriented adaptivity for GMsFEM. J Comp Appl Math. 2016;296:625–37.

Cramer H, Findeiss R, Steinl G, Wunderlich W. An approach to the adaptive finite element analysis in associated and non-associated plasticity considering localization phenomena. Comput Meth Appl Mech Eng. 1999;176(1–4):187–202.

De SR, Gago JP, Kelly DW, Zienkiewicz OC. A posteriori error analysis and adaptive processes in the finite element method: Part 2—adaptive mesh refinement. Int J Numer Meth Eng. 1983; 19(11):1621–56.

Deb A, Loret B, Prevost JH. Automated band identification procedure for dynamic strain localization. Comput Meth Appl Mech Eng. 1996a;137(3–4):307–30.

Deb A, Prevost JH, Loret B. Adaptive meshing for dynamic strain localization band identification procedure for dynamic strain localization. Comput Meth Appl Mech Eng. 1996b; 137(3–4):285–306.

Douglas Jr J, Olsen ET. Computational efficiency of the p-version of the finite element method: a comparison with the h-version. Technical report. West Lafayette (USA): Purdue University; 1989.

Falgout RD. An introduction to algebraic multigrid. Comput Science Eng. 2006;8(6):24–33.

Fei WP, Chen SH. Elasto-viscoplastic dynamic analysis by 3D p-version adaptive FEM for hydraulic structures. Eng J Wuhan Univ. 2003a;36(2):20–4 (in Chinese).

Fei WP, Chen SH. 3-D p-version elasto-viscoplastic adaptive FEM model for hydraulic structures. J Hydraul Eng. 2003b;25(3):64–70 (in Chinese).

Fei WP, Chen SH. Solution of 3-D p-version adaptive finite element method containing joint elements. J Hydraul Eng. 2003c;25(4):58–66 (in Chinese).

Feng XM, Chen SH. H-version adaptive finite element method for three-dimensional seepage problem. J Hydrodyn Ser B. 2003;31(3):122–6 (in Chinese).

Fei WP, Chen SH. 3D steady seepage analysis using p version adaptive FEM. Rock Soil Mech. 2004;25(2):201–15 (in Chinese).

Fish J, Guttal R. Adaptive solver for the p-version of finite element method. Int J Numer Meth Eng. 1997;40(10):1767–84.

Golub GH, Loan CFV. Matrix computations. Baltimore, USA: Johns Hopkins University Press; 1996.

Grätsch T, Bathe KJ. A posteriori error estimation techniques in practical finite element analysis. Comput Struct. 2005;83(4–5):235–65.

Guo B, Babuška I. The h-p version of the finite element method—Part 1: basic approximation results. Comp Mech. 1986a;1(1):21–41.

Guo B, Babuška I. The h-p version of the finite element method—Part 2: general results and application. Comp Mech. 1986b;1(2):203–26.

Gupta A, Mohraz B. A method of computing numerically integrated stiffness matrices. Int J Numer Meth Eng. 1972;5(1):83–9.

Hinnant HE. A fast method of numerical quadrature for p-version finite element matrices. Int J Numer Meth Eng. 1994;37(21):3723–50.

Hinton E, Campbell JS. Local and global smoothing of discontinuous finite element functions using a least squares method. Int J Numer Meth Eng. 1974;8(3):461–80.

Holzer SM, Yosibash Z. The p-version of the finite element method in increment elasto-plastic analysis. Int J Numer Meth Eng. 1996;39(11):1859–78.

Hulbert GM, Jang I. Automatic time step control algorithms for structural dynamics. Comp Meth Appl Mech Eng. 1995;126(1–2):155–78.

Irons BM. Economical computer techniques for numerically integrated finite elements. Int J Numer Meth Eng. 1969;1(2):201–3.

Kato K, Lee NS, Bathe KJ. Adaptive finite element analysis of large strain elastic response. Comput Struct. 1993;47(4–5):829–55.

Kelly DW, De SR, Gago JP, Zienkiewicz OC, Babuška I. A posteriori error analysis and adaptive processes in the finite element method: Part 1—error analysis. Int J Numer Meth Eng. 1983a;19(11):1583–619.

Kelly DW, De SR, Cago JP, Zienkiewicz OC, Babuška I. A posteriori error analysis and adaptive processes in the finite element method: Part II—adaptive mesh refinement. Int J Numer Meth Eng. 1983b;19(11):1621–56.

Lages EN, Silveira ESS, Cintra DT, Frery AC. An adaptive time integration strategy based on displacement history curvature. Int J Numer Meth Eng. 2013;93(12):1235–54.

Lee NS, Bathe KJ. Error indicators and adaptive remeshing in large deformation finite element analysis. Finite Elem Anal Des. 1994;16(2):99–139.

Leroy Y, Ortiz M. Finite element analysis of transient strain localization phenomena in frictional solids. Int J Numer Meth Eng. 1990;14(2):93–124.

Li J, Widlund O. FETI-DP, BDDC and block Cholesky methods. Int J Numer Meth Eng. 2006; 66(2):250–71.

Lin SZ. Improved iterative format of symmetric successive over relaxation-preconditioned conjugated radiant method. J Numer Meth Comp Appl. 1997;18(4):266–70 (in Chinese).

Loubignac G, Cantin G, Touzot G. Continuous stress fields in finite element analysis. AIAA J. 1977;15(11):1645–7.

Morris RB, Tsuji Y, Carnevali P. Adaptive solution strategy for solving large systems of p-type finite element equations. Int J Numer Meth Eng. 1992;33(7–10):2057–71.

Needleman A. Analysis of plastic flow localization in metals. Appl Mech Rev. 1992;45(3):3–18.

Ortiz M, Quigley JJ. Adaptive mesh refinement in strain localization problems. Comp Meth Appl Mech Eng. 1991;90(1–3):781–804.

Owen DRJ, Hinton E. Finite elements in plasticity: theory and practice. Swansea, UK: Pineridge Press Ltd; 1980.

Papadrakakis M, Babilis GP. Solution techniques for the p-version of the adaptive finite element method. Int J Numer Meth Eng. 1994;37(8):1413–31.

Park KC, Underwood PG. A variable-step central difference method for structural dynamics analysis—part 1. theoretical aspects. Comput Meth Appl Mech Eng. 1980;22(2):241–58.

Pavana Chand Ch, Krishna Kumar R. Remeshing issues in the finite element analysis of metal forming problems. J Mat Process Technol. 1998;75(1–3):63–74.

Peraire J, Vahdati M, Morgan K, Zienkiewicz OC. Adaptive remeshing for compressible flow computations. J Comp Phys. 1987;72(2):449–66.

Perić D, Hochard CH, Dutko MD, Owen DRJ. Transfer operators for evolving meshes in small strain elasto-plasticity. Comp Meth Appl Mech Eng. 1996;137(3–4):331–44.

Polubarinova-Kochina PY. Theory of ground water movement. Princeton (Translated from the Russian edition by Roger de Wiest JM), NJ (USA): Princeton University Press; 1962.

Probert EJ, Hassan O, Morgan K, Peraire J. An adaptive finite element method for transient compressible flows with moving boundary. Int J Numer Meth Eng. 1991;32(4):751–65.

Prudhomme S, Oden JT. On goal-oriented error estimation for elliptic problems: application to the control of point wise errors. Comput Meth Appl Math. 1999;176(1–4):313–31.

Rahulkumar P, Saigal S, Yunus S. Singular p-version finite elements for stress intensity factor computations. Int J Numer Meth Eng. 1997;40(6):1091–114.

Rank E, Werner H. An adaptive finite element approach for the free surface seepage problem. Int J Numer Meth Eng. 1986;23(7):1217–28.

Rossi DF, Ferreira WG, Mansur WJ, Calenzani AFG. A review of automatic time-stepping strategies on numerical time integration for structural dynamics analysis. Eng Struct. 2014; 80(12):118–36.

Saad Y. Iterative Methods for Sparse Linear Systems. Philadelphia, USA: SIAM; 2003.

Schneid E, Knabner P, Radu F. A priori error estimates for a mixed finite element discretization of the Richards' equation. Numer Math. 2004;98(2):353–70.

Selman A. Adaptive mesh refinement procedure for static and dynamic problems. Ph.D. thesis. Swansea, UK: University College of Swansea; 1992.

Stone TJ, Babuška I. A numerical method with a posteriori error estimation for determining the path taken by a propagating crack. Comp Meth Appl Mech Eng. 1998;160(3–4):245–71.

Szabó BA. Mesh design for the p-version of the finite element method. Comp Meth Appl Mech Eng. 1986;55(1–2):181–97.

Szabó BA, Mehta AK. p-convergent finite element approximations in fracture mechanics. Int J Numer Meth Eng. 1978;12(3):551–60.
Tabbara M, Blacker T, Belytschko T. Finite element derivative recovery by moving least square interplants. Comp Meth Appl Mech Eng. 1994;117(1–2):211–23.
Targowski R, Guerlement G, Lamblin D. Geometrical interpretation for error estimation in finite element analysis. Comp Meth Appl Mech Eng. 1990;80(2):117–28.
Tradegard A, Nilsson F, Östlund S. FEM-remeshing technique applied to crack growth problems. Comp Meth Appl Mech Eng. 1998;160(1–2):115–31.
Trottenberg U, Oosterlee CW, Schüller A. Multigrid. Orlando, USA: Academic Press Inc; 2001.
Wang R. Experiment and finite element simulation of X-type shear fractures from a crack in marble. Tectonophysics. 1987;144(1–3):141–50.
Wesseling P. An introduction to multigrid methods. Chichester, UK: Wiley; 1992.
Wiberg NE, Abdulwahab F. A posteriori error estimation based on superconvergent derivatives and equilibrium. Int J Numer Meth Eng. 1993;36(16):2703–24.
Wiberg NE, Li XD. Superconvergent patch recovery of finite element solution and posteriori norm error estimate. Comp Meth Appl Mech Eng. 1994a;10(4):313–20.
Wiberg NE, Li XD. A post-processed error estimate and an adaptive procedure for the semi-discrete finite element method in dynamic analysis. Int J Numer Meth Eng. 1994b;37(21):3585–603.
Wiberg NE, Möller P. Formulation and solution of hierarchical finite element equations. Int J Numer Meth Eng. 1988;26(5):1213–33.
Wiberg NE, Zeng LF, Li XD. Error estimation and adaptivity in elastodynamics. Comp Meth Appl Mech Eng. 1992;101(1–3):369–95.
Wiberg NE, Abdulwahab F, Saulius Ziukas S. Enhanced superconvergent patch recovery incorporating equilibrium and boundary conditions. Int J Numer Meth Eng. 1994;37(20):3417–40.
Wilson CJ, Carnevali P, Morris RB, Tsuji Y. Viscoelastic damping calculations using a p-type finite element code. ASME J Appl Mech. 1992;59(3):696–9.
Xia HX, Chen SH. 3-D adaptive FEM in rock slope stability analysis. In: Desai CS, editor. Proceedings of 10th international conference on computer methods and advances in geomechanics. Amsterdam, Netherlands: AA Balkema; 2001. p. 1635–9.
Yagawa G, Ye GW, Yoshimura S. A numerical integration scheme for finite element method based on symbolic manipulation. Int J Numer Meth Eng. 1990;29(7):1539–49.
Zhang JL, Chen SH. Study of time-stepping adaptivity in FEM analysis of time-dependent problems. J Wuhan Univ Hydraul Electr Eng (WUHEE). 1996;29(1):79–84 in Chinese.
Zhang JL, Chen SH. An implicit scheme algorithm of elastic-viscoplastic FEM with time-stepping adaptive for bolted jointed rock masses. J Hydraul Eng. 1997;19(Supplement):168–75 (in Chinese).
Zienkiewicz OC, Irons BM, Scott IC, Cambell JS. Three-dimensional stress analysis. In: Proceedings of IUTAM symposium on high speed computing of elastic structures. Liege (Belgium); 1970.
Zienkiewicz OC, Shiomi T. Dynamic behaviour of saturated porous media, the generalized Biot formulation and its numerical solution. Int J Numer Meth Geomech. 1984;8(1):71–96.
Zienkiewicz OC, Taylor RL. Coupled problems—a simple time-stepping procedure. Commum Appl Numer Meth. 1985;1(2):233–9.
Zienkiewicz OC, Xie YM. A simple error estimator and adaptive time stepping procedure for dynamic analysis. Earthq Eng Struct Dyn. 1991;20(9):871–87.
Zienkiewicz OC, Zhu JZ. A simple error estimator and adaptive procedure for practical engineering analysis. Int J Numer Meth Eng. 1987;24(2):337–57.
Zienkiewicz OC, Zhu JZ. Adaptive and mesh generation. Int J Numer Meth Eng. 1991;32(4):783–810.
Zienkiewicz OC, Zhu JZ. The surperconvergent patch recovery and a posteriori error estimates. Part 1: the recovery technique. Int J Numer Meth Eng. 1992a;33(7):1331–64.

Zienkiewicz OC, Zhu JZ. The surperconvergent patch recovery and a posteriori error estimates. Part 2: error estimates and adaptivity. Int J Numer Meth Eng. 1992b;33(7):1365–82.
Zienkiewicz OC, Zhu JZ. Superconvergence and the superconvergent patch recovery. Finite Elem Anal Des. 1995;19(1–2):11–23.
Zienkiewicz OC, De SR, Gago JP, Kelly DW. The hierarchical concept in finite element analysis. Comp Struct. 1983;16(1–4):53–65.
Zienkiewicz OC, Wood WL, Hine NW, Taylor RL. A unified set of single step algorithms. Part 1: general formulation and applications. Int J Numer Meth Eng. 1984;20(8):1529–52.
Zienkiewicz OC, Liu YC, Huang GC. Error estimation and adaptivity in flow formulation for forming problems. Int J Numer Meth Eng. 1988;25(1):23–42.
Zienkiewicz OC, Zhu JZ, Gong NG. Effective and practical h-p version adaptive analysis procedures for the finite element method. Int J Numer Meth Eng. 1989;28(1–6):879–91.
Zienkiewicz OC, Huang MS, Pastor M. Localization problems in plasticity using finite elements with adaptive remeshing. Int J Numer Meth Eng. 1995;32(5):127–48.

Chapter 6
Reinforcement Analysis Using the Finite Element Method

Abstract Earth anchors inclusive solid bars (bolt, rebar) and stranded wire cables, have been extensively exercised in a wide range of geotechnical engineering. Shotcrete is also prevalent for the purpose to restrain rock exposures from excessive deforming and loosening. The relationships of meso-structure property are at the heart of the FEM towards the performance of reinforced hydraulic structures. Based on experimental studies, this chapter presents comprehensive studies inclusive explicit (distinct) approach and implicit (equivalent) approach of reinforcement components and joints. Either of them exhibits intrinsic advantages and disadvantages. The former uses special elements to individually discretize joints and reinforcement components to extract detailed behaviors of reinforced structures, whereas the latter elaborates an equivalent constitutive relation neglecting the exact positions of joints and reinforcement components to provide the overall structural response. One of the major advancements achieved in this chapter is that the localized shear deformation at the intersection points of bolts/shotcrete layers with joints is taken into account, which enables to describe the behaviors of bolt/shotcrete at the joint in much more detail even with implicit approach. The other important advancement is the consideration of the interface between equivalent bolt-grout material and host rock, which makes it possible to simulate the pull-out mechanism of bolt with explicit approach. In addition to a number of validation examples interspersed within the context, this chapter is closed with three engineering application cases (underground cavern, cut slope, dam foundation).

6.1 General

6.1.1 Reinforcement Types and Mechanisms

Earth anchors have been extensively employed in a wide range of geotechnical engineering—more than 500 million reinforcement units are installed in the world per annum (Windsor 1997). They can be distinguished as two main categories: solid bar (bolt, rebar) and stranded wire cable (Stillborg 1994). The former is normally

S.-H. Chen, *Computational Geomechanics and Hydraulic Structures*,
Springer Tracts in Civil Engineering, https://doi.org/10.1007/978-981-10-8135-4_6

used for the systematic surface protection in combination with shotcrete, whereas the latter is customarily installed to provide large pre-stress and deep reinforcement.

Penetrating into rock about 4–12 m deep to form a reinforced layer around the tunnel or along the slope surface, rock bolts are installed to stabilize the rock mass by tying back the movable rock blocks that are likely to fail around the excavation area, as well as to reduce the deformability and to maintain the strength of the rock mass (see Fig. 6.1b–d). There are various types of rock bolts falling into active and passive ones. Active rock bolts exert a positive force to the rock mass and are made of steel bars or stranded wires that are anchored in the rock on one extremity with a plate and fixed by a nut on the other extremity. They are always tensioned after installation and may be sealed by grout or resin for long-term applications against corrosion. The anchorage may either be punctual at the end of borehole at which it is installed or distributed along the entire length of the bolt, either through a sealing grout product or rock/bolt friction. Passive rock bolts can be punctually anchored to (through mechanical anchorage or localized grouting) or fully bonded to (along

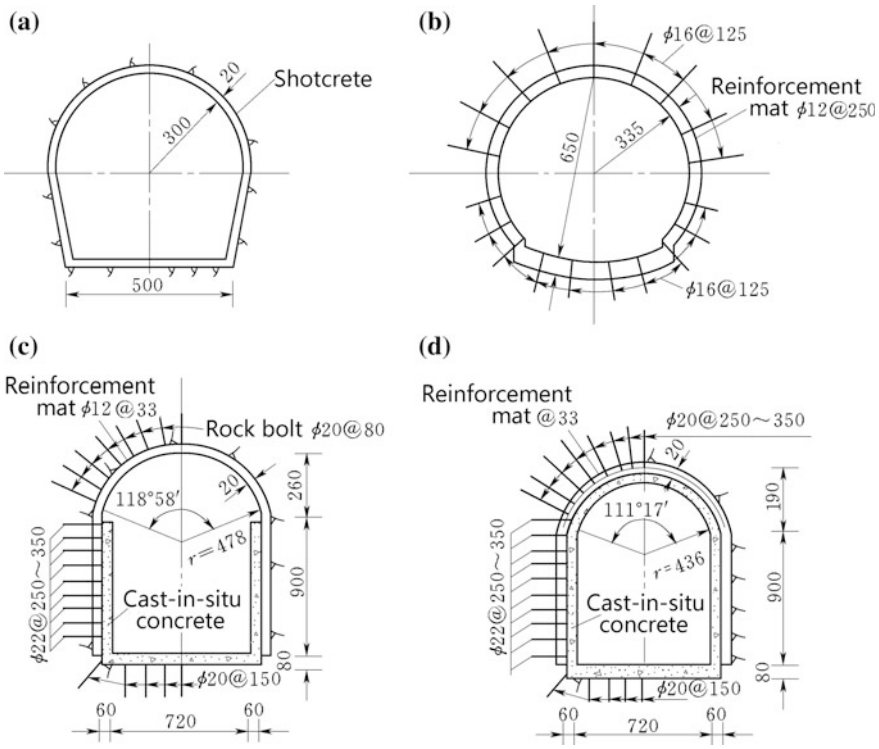

Fig. 6.1 Types of bolt and shotcrete supporting (Unit: cm). **a** Shotcrete; **b** rock bolt; **c** rock bolt + shotcrete + steel mesh; **d** rock bolt + shotcrete + steel mesh + concrete lining

their entire length either through friction or a sealing grout product) the rock mass. They only react to the deformation therefore must be installed before a significant movement of rock mass taking place. For rock masses reinforced with passive, fully-grouted bolts, it is widely accepted that the principal reinforcing mechanism of the bolt is the raise of shear resistance along the joints, which is, in common terms, expressed in three parts, i.e. tension force in the bolt, friction as a consequence of increased normal stress, and dowel effect (Bjurstrom 1974; Azuar 1977; Egger and Fernandes 1983; Goris and Conway 1987; Spang and Egger 1990; Egger and Pellet 1991; Egger and Zabuski 1991; Bawden et al. 1992; Hyett et al. 1992; Kaiser et al. 1992; Yazici and Kaiser 1992; Jalalifar and Aziz 2010a, b).

Applying immediately after the advance of cut face, shotcrete (also called spray-concrete) protection of a thin layer (5–20 cm thick) which works together in time with the surrounding rock mass (see Fig. 6.1a), is intended to restrain rock from excessive deforming and loosening. A portion of shotcrete penetrated into rock fractures may also multilaterally contribute to the bonding of loosen rock, the protecting of rock weathering, the blocking of seepage path, the filling of deficit, and the smoothing of surface. Being a flexible supporting structure, it also helps to transfer loads to the rock bolts.

For low strength or poor integrity rock masses, combination of rock bolts and shotcrete is desirable. For even worse situation of weak or strongly fractured rock masses, steel mesh may be installed before the spray of shotcrete, which may enhance the integrity and strength of shotcrete and reduce the thermal induced cracks (see Fig. 6.1b–d).

Composed of 2, 3, 7 or more (up to 19) high strength and stress-relieved (stabilized) steel wires, stranded wire cables actually belong to the category of active rock bolts with large pre-stress tonnage for deep reinforcement. Restrained by the construction techniques however, the length of such cables is usually limited within 50 m. In addition, for loosen or fragment rock slopes, due to the difficulties with the borehole drilling and grouting operation, the pre-stress cable was seldom employed. Anyway, this restraint is less rigorous nowadays attributable to the breakthrough of construction techniques. For example, altogether 1380 pre-stress cables had been installed for the Yingshuigou ancient landslide in Xiaowan Project by the “casing while drilling technique”, the average depth of borehole is 65 m, of which the maximum one is 92 m.

Two types of stranded wire cables may be roughly distinguished as in compression and in tension. A typical tension cable generally consists of three parts (see Fig. 6.2): the bonded inside anchorage head with certain bonded length, the free length and the out-laid anchor head. The tension load is transferred from the anchor’s free length to the surrounding rock mass through the bonded inside anchorage head in a form of shear at the interfaces of grout/stranded wire and rock/grout, attributable to a combined mechanism inclusive chemical adhesion, mechanical interlocking and frictional resistance (Fuller and Cox 1975).

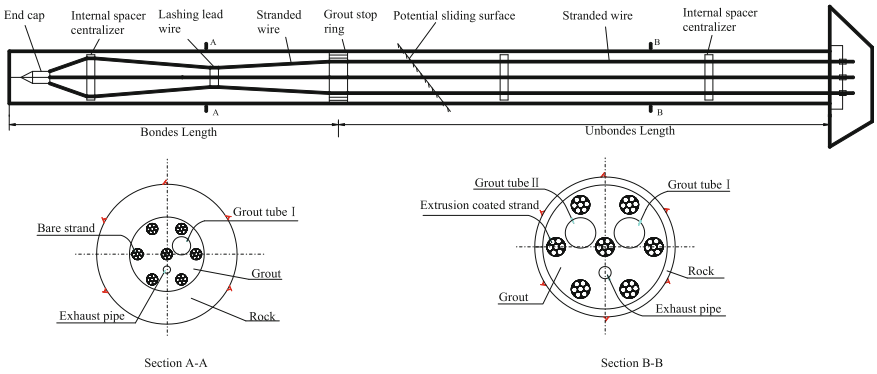

Fig. 6.2 Configuration of a tension anchor cable with 7 stranded wires

6.1.2 History and State-of-the-Art

Rock bolts were initially used in mining in the 1890s, whereas the systematic use was documented at the St. Joseph Lead Mine (USA) in the 1920s. In the late 1940s, rock bolts were started their applications to the civil tunnel supporting in USA and Australia. Shotcrete was invented in 1907 by American taxidermist Carl Akeley to repair the crumbling facade of the Field Columbian Museum in Chicago (Pietro 2002). Bolt and shotcrete supporting was invented much later between 1957 and 1965 in Austria with the development of the "New Austrian Tunneling Method (NATM)" that is actually an approach or philosophy to tunneling rather than a set of excavation and supporting techniques (Rabcewicz 1964, 1965; Hagenhofer 1990; Müller 1990; Kovári 1994). The stabilization of rock masses by bolts and shorcrete now have been widely exercised in open/underground excavations and foundation engineering (Hoek and Bray 1981; Pande et al. 1990; Bickel et al. 1996; Kropik and Mang 1996; Ng et al. 2004).

In hydraulic projects, combination of rock bolts and shotcrete is commonly exercised in the initial or temporary supporting for permanent works such as dam abutments, or for the temporary works such as diversion tunnels. Stranded wire cables are particularly employed in the deep and active reinforcement for high cut slopes, high side walls of large span underground caverns, and downstream dam abutments at the vicinity of dam toe. The first temporary supporting practice with rock bolts in China was the hydraulic tunnel constructed in Luhun Project in the 1950s, followed by the temporary supporting with bolts and shotcrete in the excavation of the 80 m high surge shaft in Bikou Project. Thereafter bolts and shotcrete have been prevalently and successfully applied as permanent supporting in the underground caverns, free flowing tunnels, as well as the pressure tunnels of medium-to low head (e.g. the Projects of Huilongshan, Yuzixi, Fengjiashan).

The simulation of reinforcement components is particularly laborious. To achieve a prescribed degree of displacement control in the immediate vicinity of the

structure concerned, it requires that the effect of any reinforcement is defined in a quantitative manner, and the interactive nature of reinforcement mechanism should be represented adequately. This in turn, demands comprehensive studies inclusive experimental, analytical and numerical methods, of which the last one falls into explicit (distinct) approach (Weerasinghe and Littlejohn 1977; ST. John and Van Dillen 1983; Aydan et al. 1987; Aydan 1989; Swoboda and Marence 1991, 1992; Marence and Swoboda 1995; Chen and Egger 1997; Qiang and Chen 2001; Benmokrane et al. 1995a, b; Barley 1997a, b) and implicit (equivalent) approach (Pietruszczak and Mróz 1981; Larsson and Olofsson 1983; Pande and Gerrard 1983; Stillborg 1984; Larsson et al. 1985; Sharma and Pande 1988; Kaiser et al. 1992; Chen and Pande 1994; Jarrel and Haberfield 1997; Woods and Barkhordari 1997; Chen and Egger 1999) of reinforcement components and joints. Either of them exhibits intrinsic advantages and disadvantages. The former uses special elements to individually discretize joints and reinforcement components (bolts, lining, anchors), whereas the latter elaborates an equivalent constitutive relation neglecting the exact positions of joints and reinforcement components to provide the overall response of reinforced structures.

6.2 Equivalent Approach of Jointed Rock Masses Reinforced by Fully Grouted Bolts

Usually, postulations concerning the interactions of reinforcement components within the REV (representative element volume) are made for the formulation of an equivalent constitutive relation. If the reinforced rock masses behave elastically, a number of equivalent methods available would be quite effective. In the presence of plastic deformation however, it will be cumbersome to get their rationally response. Hence it is essential to develop an equivalent nonlinear constitutive relation of jointed rock masses which appropriately takes into account the influence of bolts.

In the following coverage of this section, we present a road map showing how to get a more detailed description of the bolting effects on joints by means of an implicit (equivalent) rheological model (Chen and Pande 1994; Chen and Egger 1999), guided by the laboratory and field tests.

6.2.1 Reinforcement Mechanism and Rheological Models

A number of researchers have conducted shear tests for the purpose of determining the contribution of a bolt to the shear strength and the stiffness of joints, most of them were carried out by direct shear on natural or artificial rock (or concrete) joints. For example, a series of laboratory tests were conducted at EPFL

(Egger and Fernandes 1983; Spang and Egger 1990; Egger and Pellet 1991; Egger and Zabuski 1991) by conventional shear box containing parallelepipedic blocks of 220 mm × 200 mm × 150 mm and 150 mm × 150 mm × 130 mm (see Fig. 6.3). Tests on reinforced samples by 2-D or 3-D stresses can also be found in literatures (Grasselli 2005).

These tests reveal that the deformations and stresses are localized near the portion where the bolt intersects a joint, and that the deflection of the included angle between the bolt and joint due to shear deformation could be significant. Specifically

– For samples with a bolt forming small included angle with the normal of the joint, bending of the bolt becomes predominant even when the shearing force is small, which will create two hinges above and below the joint plane (see Fig. 6.4). As the stress level is approximately constant in the zone between the two hinges, the exact location of failure cannot be predicted. Failure may occur by bending in one of the plastic hinges or by combined shear and tension near the shear surface. Results show the occurrence of both failure types for tests

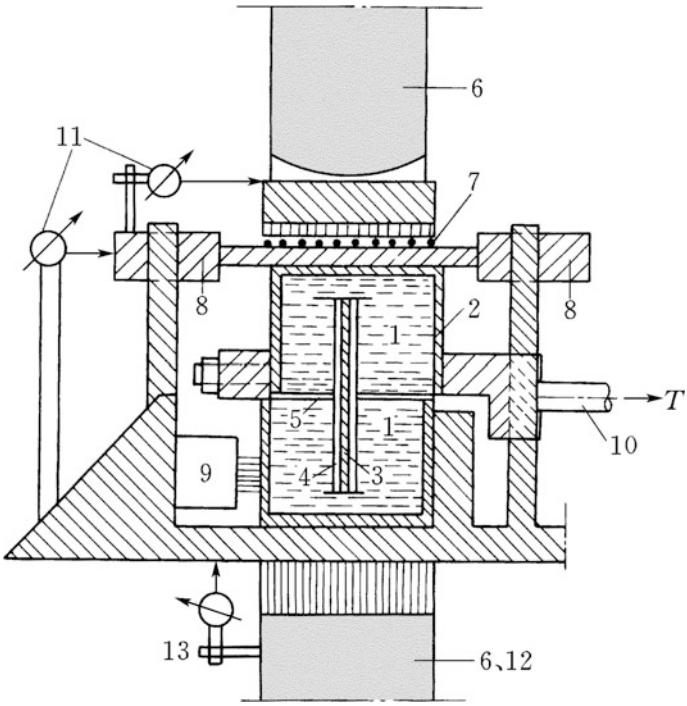

Fig. 6.3 Configuration of direct shear testing device of bolted joint. 1—parallelepipedic block; 2—steel box; 3—bolt; 4—cement mortar; 5—shear surface; 6—vertical jack; 7—frictionless upper support; 8—guided cam; 9—horizontal jack; 10—transducer of shear force; 11—transducer of shear force displacement; 12—transducer of normal force; 13—transducer of vertical displacement

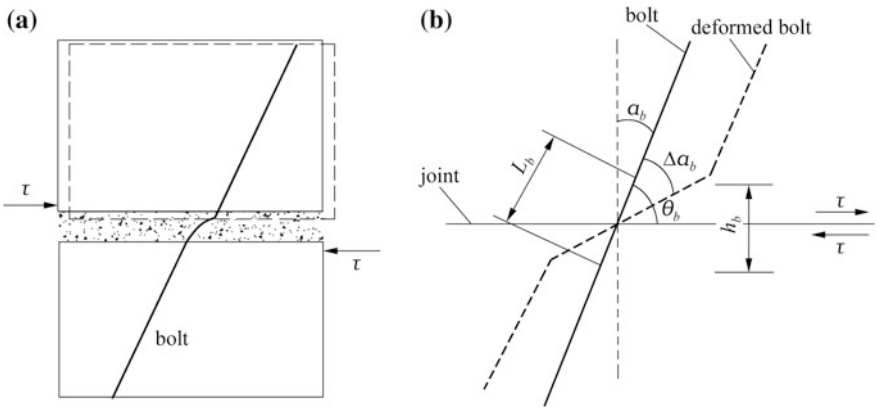

Fig. 6.4 Deformation of bolt near a joint. **a** Schematic; **b** quantitative notation

under apparently the same conditions, the ultimate loads and displacements at failure are nearly identical.

- For samples with a bolt being inclined at a large included angle to the normal of the joint, two hinges also emerge in the tests, but the bending phenomena are not so strong. The great majority of the inclined bolts fail in tension near the shear surface.
- The vertical height of a bended bolt is about 2–4 times the bolt diameter d_b, i.e. $h_b = (2{-}4)d_b$. It is termed as "effective height", corresponding to an "effective length" of $L_b = h_b/\cos\alpha_b$ (see Fig. 6.4). This height depends on the quality of the rock (or the grout mortar) and bolt, as well as on the bolt's diameter and inclined angle, etc.
- The samples in which the bolt forms a small included angle with the normal of the joint show larger shearing displacements, i.e. the inclined bolts react in a stiffer way than normal ones. In addition, the maximum shear resistance of the bolted joint increases which the inclination of the bolt, provided there is considerable friction along the joint.
- Large bolt diameters reduce the shearing displacements demanded for mobilizing a given shearing force, and the maximum shearing force increases linearly with the sectional area of the bolt.

All of the test results available give us a fairly deep insight into the reinforcement mechanism of passive, fully grouted bolts on joints. On one hand, they permit the development of analytical or semi-empirical formulas to predict the effect of bolts on the shear resistance along a joint, which is very useful in the conventional reinforcement design. On the other hand, they provide a solid base to develop numerical models for the purpose of more detailed analysis of the deformation and stress states in complicated structures.

A number of useful and simple equivalent models have been proposed to simulate the reinforced jointed rock masses. Zienkiewicz and Pande (1976) firstly

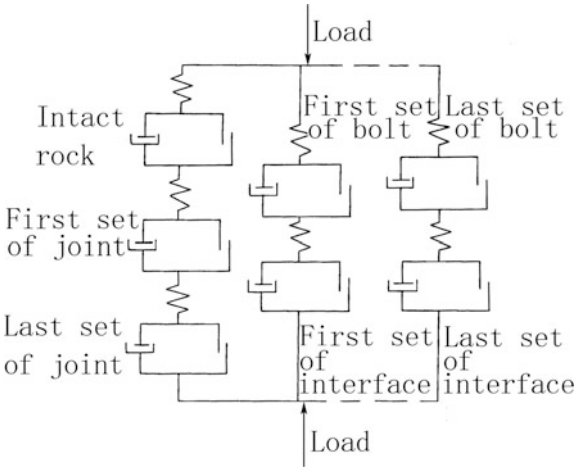

Fig. 6.5 Conventional rheological model of the REV containing joints and bolts

proposed an elasto-viscoplastic "multi-laminate" model for jointed rock masses. Later, Pande and Gerrard (1983), Sharma and Pande (1988) modified the model to cover reinforced cases. Larsson and Olofsson (1983) proposed a similar approach. Their approaches may be illustrated by the rheological model in Fig. 6.5 (Sharma and Pande 1988) whose advantage is simple and easy to implement whereas disadvantage is that the reinforcement mechanism cannot be well interpreted.

Take the REV containing two sets of joints and one set of bolts shown in Fig. 6.6a for example. Under the action of uniform vertical pressure, the intersection points of the bolt with the joint set 1 and joint set 2 manifest different stresses due to different deformation. However, the model constructed in Fig. 6.5 will provide identical stresses attributable to the homogenization assumption. Again, take the REV containing two joint sets with identical dip angle 45° but opposite dip direction, and one horizontal bolt set (see Fig. 6.6b), for example. Since there is no

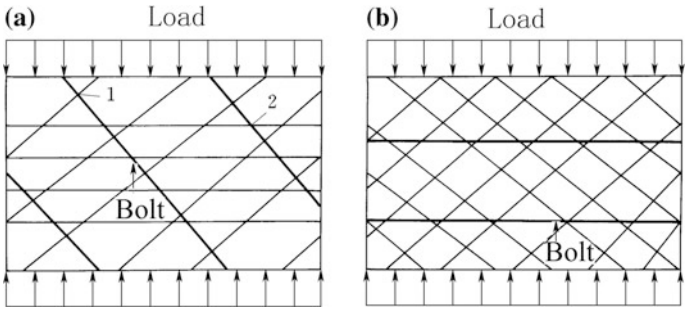

Fig. 6.6 Typical REVs containing two joint sets and one bolt set

homogenized shear stress in the whole REV according to the model in Fig. 6.5, therefore there is no localized shear stress in the bolt apart from tension. However, such localized shear stresses at the intersection points of bolts with joints do actually exist, overlooking of them will lead to the underestimation of the reinforcement effects of rock bolts.

We proposed a new rheological model shown in Fig. 6.7 (Chen and Pande 1994; Chen and Egger 1999). The advantage with the new model is that it enables us to describe the bolt's behavior at the joint in more detail even with an equivalent approach. For example, from the observation of test samples it is clear that the bolts have undergone an intensive localized shear and tension deformations. Such phenomenon can be taken into account in the new rheological model to some extent if the test results can be correctly interpreted into the constitutive relation of the bolted joint.

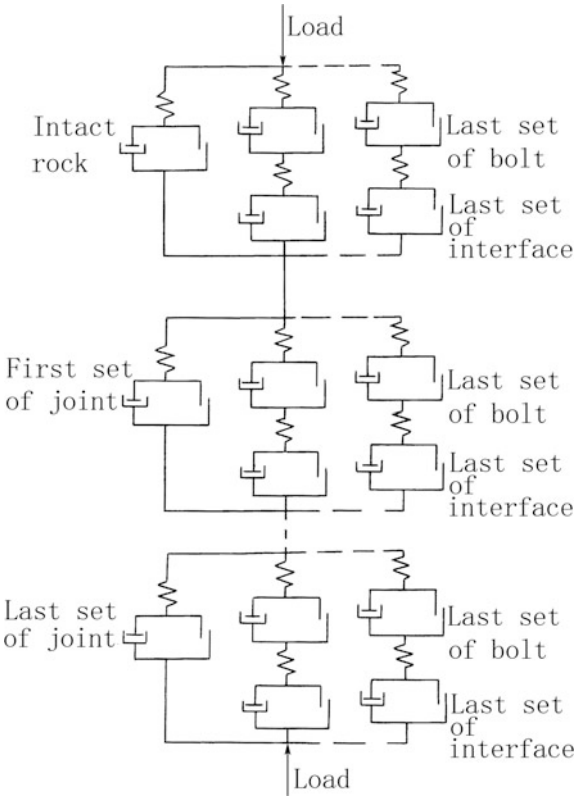

Fig. 6.7 New rheological model of the REV containing joints and bolts

6.2.2 Basic Assumptions and Formularization

For fully-grouted rock bolts, the primary concern is the effect of bolt on the shear resistance of a joint, therefore the influence of interfaces may be normally neglected in the equivalent study. The proposed rheological model in Fig. 6.7 infers following four basic assumptions which reflect the major findings from laboratory tests, that

① The strain increment of the jointed rock with bolt is given as the sum of the incremental strains of the reinforced rock material and the reinforced joints.
② The load increment is shared among the bolt and rock material in the reinforced rock material, the same applies to the reinforced joint.
③ The mean stress in the bolted rock material is equal to that in the bolted joint.
④ The strain of the bolt is equal to that of the rock material in the bolted rock material, similarly, the relative displacement of the two bolt hinges (see Fig. 6.4) is equal to that of the joint walls.

Under the coordinate systems for the joint j and bolt b defined in Figs. 2.2 and 2.16 respectively, these assumptions can be mathematically formulated as follows.

① Assumption 1—strain addition

$$\{\Delta\varepsilon\} = \{\Delta\varepsilon\}_{\mathrm{R(B)}} + \sum_{J} \{\Delta\varepsilon\}_{J(B)} \tag{6.1}$$

② Assumption 2—stress share

$$\begin{cases} \{\Delta\sigma\}_{R(B)} = A_R\{\Delta\sigma\}_R + \sum\limits_b A_b[T]_b^T\{\Delta\sigma\}_{(br)} \\ \{\Delta\sigma\}_{j(b)} = A_R\{\Delta\sigma\}_j + \sum\limits_b A_b[T]_{(bj)}^T\{\Delta\sigma\}_{(bj)} \\ [T]_{(bj)}^T = ([T]_j^T)^{-1}[T]_b^T \end{cases} \tag{6.2}$$

In which A_R and A_b are the volumetric ratios of rock and bolt in a REV, and we have

$$A_R + \sum_b A_b = 1$$

③ Assumption 3—stress consistency

$$\{\Delta\sigma\} = \{\Delta\sigma\}_{R(B)} = \{\Delta\sigma\}_{J(B)} \tag{6.3}$$

④ Assumption 4—strain consistency

$$\begin{cases} \{\Delta\varepsilon\}_{R(B)} = \{\Delta\varepsilon\}_R = \{\Delta\varepsilon\}_{(BR)} \\ \{\Delta\varepsilon\}_{j(b)} = \{\Delta\varepsilon\}_j = [T]_{(bj)}\{\Delta\varepsilon\}_{(bj)} \end{cases} \tag{6.4}$$

In Eqs. (6.1)–(6.4), any quantities without subscript belong with the equivalent material; the subscripts r, j, and b denote the rock material, the joint set, and the bolt set, respectively; the subscripts (br) and (bj) denote the bolt b in the rock material and in the joint set j; the subscripts $r(b)$ and $j(b)$ denote the reinforced rock material and the reinforced joint set j. All the subscripts written in small letters imply the local coordinate system, while the same subscripts written in capital letters imply the global system. The transformation matrix $[T]_b$ has been defined in Eq. (2.40), and the form of matrix $[T]_j$ is identical to $[T]_b$ but the subscript b should be substituted by the subscript j.

6.2.3 Constitutive Equations

According to the potential theory of elasto-viscoplasticity summarized in Chap. 2, at time t the constitutive equation will take the form of Eqs. (2.122)–(2.129). In the following deduction, the superscript $(\hat{})$ denoting implicit time-stepping scheme, the subscript (t) or (n) denoting time or stepping sequence, will be neglected where there is no risks of misleading.

(1) Intact rock

See Eqs. (1.122)–(1.125).

(2) Joint

On the local Cartesian coordinate system of joint defined in Fig. 2.2, only normal stress σ_{zj} and shear stresses τ_{zxj} and τ_{zyj} can be transmitted. According to Eqs. (2.126)–(2.129), the contribution of joint deformation to the strain of the equivalent material is given by

$$\{\Delta\sigma\}_j = [D]_j(\{\Delta\varepsilon\}_j - \{\dot{\varepsilon}^{vp}\}_j\Delta t) \tag{6.5}$$

where

$$\begin{cases} [D]_j = s_j \begin{bmatrix} 0 & 0 & 0 & 0 & 0 & 0 \\ 0 & 0 & 0 & 0 & 0 & 0 \\ 0 & 0 & k_{nj} & 0 & 0 & 0 \\ 0 & 0 & 0 & k_{sj} & 0 & 0 \\ 0 & 0 & 0 & 0 & k_{sj} & 0 \\ 0 & 0 & 0 & 0 & 0 & 0 \end{bmatrix} \\ \{\dot{\varepsilon}^{vp}\}_j = \frac{\{\dot{u}^{vp}\}_j}{s_j} = \frac{\gamma_j}{s_j} < F_j > \left\{\frac{\partial Q_j}{\partial\{\sigma\}_j}\right\} \end{cases} \tag{6.6}$$

In which the yield function F_j and potential function Q_j are expressed by the cohesion c_j, friction angle φ_j, dilation angle ϕ_j and tension strength σ_{Tj} [see Eqs. (2.50) and (2.120)]; s_j is the joint spacing; k_{nj} and k_{sj} are the normal stiffness and tangential stiffness.

(3) Bolt

On the local Cartesian coordinate system of bolt in Fig. 2.16, only normal stress σ_{zb} and shear stresses τ_{zxb} and τ_{zyb} can be transmitted. We express Eq. (2.122) in the "true" stress and strain as

$$\{\Delta\sigma\}_b^* = [D]_b^*(\{\Delta\varepsilon\}_b^* - \{\dot{\varepsilon}^{vp}\}_b^*\Delta t) \tag{6.7}$$

In which the yield function, the loading function, and the elastic matrix may be found in Eqs. (2.41), (2.105) and (2.82), subject to the dimension expansion of the elastic matrix from 3 × 3 to 6 × 6 in a similar manner of joint [see Eq. (6.6)].

1. Bolt at joint

Use is made of the assumption ④ for the equivalent material, the relative displacement between the two hinges is equal to the relative displacement of the joint walls at the intersection point. For the tension stress σ_b in this hinge segment, the uniform distribution along the effective length L_b seems a good and reasonable postulation (see Fig. 6.8a), for the shear stress τ_b, we postulate two applicable types of distribution shown in Fig. 6.8b, c.

Within the effective length, the "true" strain of the bolt in Eq. (6.7) should be made equivalent to that of the rock mass according to the effective length and joint spacing through the transformation $\{\Delta\varepsilon\}_b = \frac{L_b}{s_j}\{\Delta\varepsilon\}_b^*$, therefore the equivalent constitutive relation for the bolt at joint is

$$\{\Delta\sigma\}_{(bj)} = [D]_{(bj)}(\{\Delta\varepsilon\}_{(bj)} - \{\dot{\varepsilon}^{vp}\}_{(bj)}\Delta t) \tag{6.8}$$

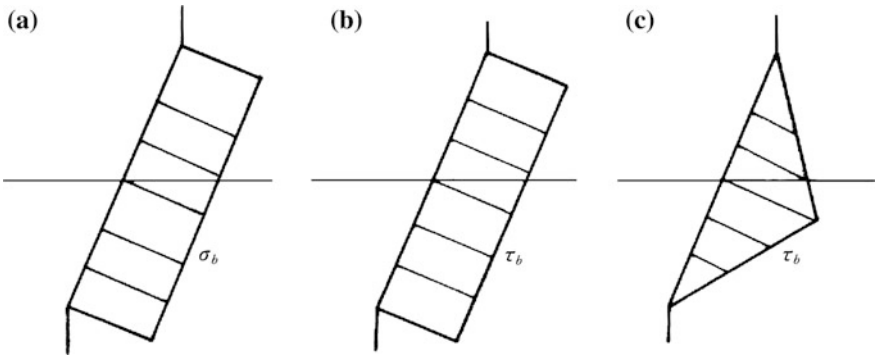

Fig. 6.8 Diagram to the simplification of stress distribution along the effective length. **a** Normal stress; **b** shear stress (uniform); **c** shear stress (triangular)

In which

$$\begin{cases} [D]_{(bj)} = \frac{s_j}{L_b}[D]_b^* \\ \{\dot{\varepsilon}^{vp}\}_{(bj)} = \frac{L_b}{s_j}\{\dot{\varepsilon}^{vp}\}_b^* \end{cases} \tag{6.9}$$

It is emphasized that in the implementation of Eqs. (6.8) and (6.9), attention should be paid on the localized deflection of bolt at joint, namely the deflections $\Delta\theta_b$ of the dip angle θ_b and $\Delta\phi_b$ of the dip direction ϕ_b, should be taken into account. In our practical algorithm, during the viscoplastic iteration the effective length L_b, the dip direction ϕ_b and the dip angle θ_b are updated at certain time steps by

$$\begin{cases} L_b(t+\Delta t) = L_b(t) + s_j \Delta\varepsilon_{zb} \\ \phi_b(t+\Delta t) = \phi_b(t) + \arctan\left(\frac{s_j \Delta\gamma_{zxb}}{L_b(t)}\right) \\ \theta_b(t+\Delta t) = \theta_b(t) - \arctan\left(\frac{s_j \Delta\gamma_{zyb}}{L_b(t)}\right) \end{cases} \tag{6.10}$$

2. Bolt in rock

For a bolt in rock, the stress and strain demand no equivalent treatment, and Eq. (6.7) may be used directly, but the subscript b should be replaced by (br) and the superscript * should be deleted.

(4) Equivalent material

Substituting the constitutive equation of each component into Eq. (6.2), and making strain transformation defined by Eqs. (2.39) and (2.40), the constitutive equations of bolted rock and bolted joint are obtained as

$$\begin{cases} \{\Delta\sigma\}_{R(B)} = A_R[D]_R\{\Delta\varepsilon\}_R - A_R[D]_R\{\dot{\varepsilon}^{vp}\}_R\Delta t \\ \qquad + \sum_b A_b[T]_b^T[D]_{(br)}[T]_b\{\Delta\varepsilon\}_{(BR)} - \sum_b A_b[T]_b^T[D]_{(br)}\{\dot{\varepsilon}^{vp}\}_{(br)}\Delta t \\ \{\Delta\sigma\}_{j(b)} = A_R[D]_j\{\Delta\varepsilon\}_j - A_R[D]_j\{\dot{\varepsilon}^{vp}\}_j\Delta t \\ \qquad + \sum_b A_b[T]_{(bj)}^T[D]_{(bj)}[T]_{(bj)}\{\Delta\varepsilon\}_{(bj)} - \sum_b A_b[T]_{(bj)}^T[D]_{(bj)}\{\dot{\varepsilon}^{vp}\}_{(bj)}\Delta t \end{cases} \tag{6.11}$$

Taking Eq. (6.4) into account, the above constitutive equations can be reduced to

$$\begin{cases} \{\Delta\sigma\}_{R(B)} = [D]_{R(B)}\{\Delta\varepsilon\}_{R(B)} - \{\Delta\sigma^{vp}\}_{R(B)} \\ \{\Delta\sigma\}_{j(b)} = [D]_{j(b)}\{\Delta\varepsilon\}_{j(b)} - \{\Delta\sigma^{vp}\}_{j(b)} \end{cases} \tag{6.12}$$

or

$$\begin{cases} \{\Delta\varepsilon\}_{R(B)} = [D]_{R(B)}^{-1}\{\Delta\sigma\}_{R(B)} + [D]_{R(B)}^{-1}\{\Delta\sigma^{vp}\}_{R(B)} \\ \{\Delta\varepsilon\}_{j(b)} = [D]_{j(b)}^{-1}\{\Delta\sigma\}_{j(b)} + [D]_{j(b)}^{-1}\{\Delta\sigma^{vp}\}_{j(b)} \end{cases} \tag{6.13}$$

In which

$$\begin{cases} [D]_{R(B)} = A_R[D]_R + \sum\limits_b A_b[T]_b^T[D]_{(br)}[T]_b \\ [D]_{j(b)} = A_R[D]_j + \sum\limits_b A_b[T]_{(bj)}^T[D]_{(bj)}[T]_{(bj)} \end{cases} \tag{6.14}$$

and

$$\begin{cases} \{\Delta\sigma^{vp}\}_{R(B)} = A_R[D]_R\{\dot{\varepsilon}^{vp}\}_R\Delta t + \sum\limits_b A_b[T]_b^T[D]_{(br)}\{\dot{\varepsilon}^{vp}\}_{(br)}\Delta t \\ \{\Delta\sigma^{vp}\}_{j(b)} = A_R[D]_j\{\dot{\varepsilon}^{vp}\}_j\Delta t + \sum\limits_b A_b[T]_{(bj)}^T[D]_{(bj)}\{\dot{\varepsilon}^{vp}\}_{(bj)}\Delta t \end{cases} \tag{6.15}$$

Transforming the constitutive equation of the bolted joint [the second row of Eq. (6.15)] using the matrix $[T]_j$, then introducing it together with the constitutive equation of the bolted rock material [the first row of Eq. (6.15)] into Eq. (6.1), the equivalent constitutive equation of the jointed rock mass with bolts is finally formulated as

$$\{\Delta\varepsilon\} = [S]\{\Delta\sigma\} + \{\Delta\varepsilon^{vp}\} \tag{6.16}$$

In which

$$[S] = [D]_{R(B)}^{-1} + \sum_j \left([T]_j\right)^{-1}[D]_{j(b)}^{-1}\left([T]_j^T\right)^{-1} \tag{6.17}$$

and

$$\{\Delta\varepsilon^{vp}\} = [D]_{R(B)}^{-1}\{\Delta\sigma^{vp}\}_{R(B)} + \sum_j [T]_j^{-1}[D]_{j(b)}^{-1}\{\Delta\sigma^{vp}\}_{j(b)} \tag{6.18}$$

6.2.4 *Verification and Parametric Study*

The direct shear sample illustrated in Fig. 6.3 is made of concrete with size of 220 mm × 200 mm × 150 mm. The mesh for the calculation is illustrated in Fig. 6.9a (projected on the $X-Z$ plane, thickness = 200 mm in the direction of Y axis). Since the "equivalent" approach is adopted in the constitutive relation, and

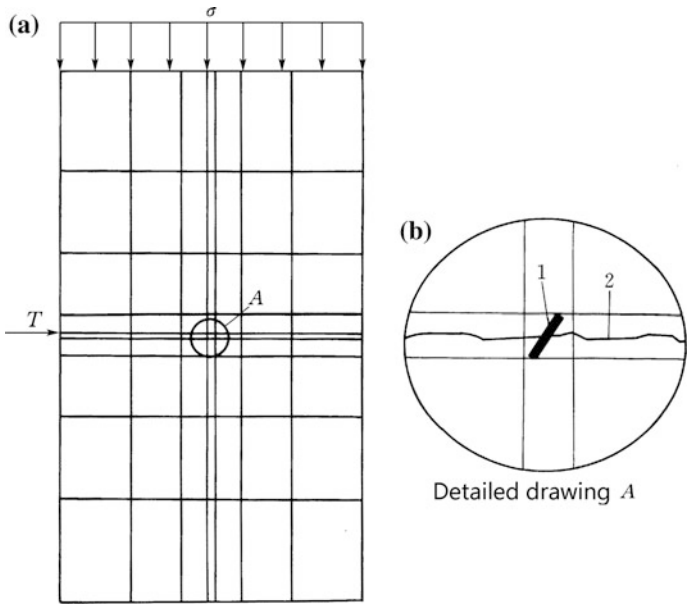

Fig. 6.9 Mesh of the test sample projection on the $X-Z$ plane

there are only one joint plus one bolt in the sample, therefore it is wise to deploy thin elements to accommodate the joint and bolt (see Fig. 6.9b). For the element containing a joint, the thickness of element should be specified as the joint spacing; similarly, for the element containing a bolt, the volumetric proportion should be specified as the ratio of the bolt's volume to the element's volume.

In Tables 6.1 and 6.2, the parameters of the concrete block, joint and bolt, are listed respectively. Since only the quasistatic (elasto-plastic) behaviors are of interest in the test, the fluidity parameters are all assumed as $\gamma = 1.0$ in the computation.

Table 6.1 Parameters of concrete

E (GPa)	μ	c (MPa)	φ (°)	ϕ (°)
17.8	0.2	12.5	45.0	45.0

Table 6.2 Parameters of joint and bolt

Joint					Bolt						
k_n (MN/m^3)	k_s (MN/m^3)	c (MPa)	φ (°)	ϕ (°)	E (GPa)	μ	f_{yk} (MPa)	f_{ptk} (MPa)	δ_{gt} (%)	θ (°)	d_b (mm)
1000	300	0	34.0	0	210	0.3	630	670	27.0	60.0	8.0

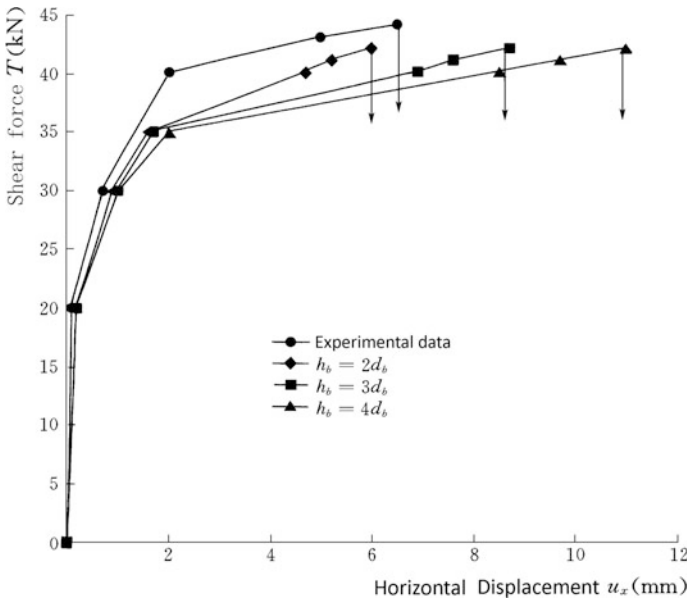

Fig. 6.10 Shear force versus displacement of the sample Vnr1.40 (bolt normal to joint)

In the laboratory test and numerical analysis, a normal pressure σ = 0.2 MPa is exerted at the top of the sample first, then the shear force T is raised step by step until the failure of the sample. Tentative values of the "effective length" or "effective height" ($h_b = (2-4)d_b$) are trialed to find the best curve fitting for shear force T versus displacement u_x. In Fig. 6.10, we find that if the "effective length" or "effective height" of a bolt at joint could be correctly specified by the tests, both the deformation and strength of the reinforced joint can be well predicted.

6.3 Equivalent Approach of Jointed Rock Masses Reinforced by Fully Grouted Bolts and Shotcrete Lining

Quantification of stress state in a tunnel shell made of shotcrete is of great importance for the safety of tunnel and other underground openings (e.g. power house caverns), both during the excavation process and service period (Aydan et al. 1992). Early methods dealing with this issue reported in the literatures normally discretize the tunnel shell by means of finite beam elements or shell elements (Timoshenko 1940). In situ monitoring of displacement plays crucial role in the estimation of the load at shell and in the implementation of NATM (Zachow 1995; Rokahr et al. 2002; Schubert et al. 2002).

In the following coverage of this section, we extend the equivalent rheological model established previously to cover the jointed rock mass reinforced by the combination of bolts and shotcrete (Chen et al. 2009).

6.3.1 Reinforcement Mechanism and Rheological Models

It has been confirmed that there are two hinges attributable to bending in the bolt near a joint, between the hinges the bolt undergoes strong localized shear and tensile deformations. With these ongoing deformations the dip angle of the bolt as well as the included angle between the bolt and the normal of joint will be deflected. This phenomenon, together with the hardening of the steel bar, will enable the bolt to mobilize larger shear resistance along the joint until the plastic deformation reaches a certain criterion depending on the steel quality.

On the analogy of bolt, it sounds rather reasonable to postulate that the shotcrete lining is a thin layer pasted on the rock surface whose major function is to restrain the joints near the shotcrete from shear and tension deformations. Two hinges due to bending in the lining near joint may manifest (see Fig. 6.11) with an "effective length". Between the hinges the lining undergoes strong localized shear and tensile deformations. With these ongoing deformations the dip angle of the lining as well as the included angle between the lining and the normal of joint will be deflected (see Fig. 6.11b). This mechanism enables the lining to mobilize shear resistance along the joint until the plastic deformation reaches a certain criterion.

Figure 6.12 shows four REVs around an excavated cavern. Element A contains joints only, element B contains joints and shotcrete lining, element C contains joints and bolts, element D contains joints, shotcrete lining and bolts. The last one, i.e. the element D will be particularly addressed hereinafter.

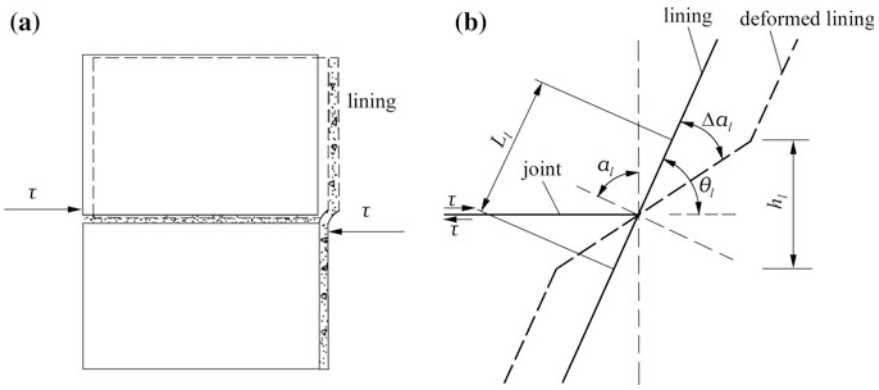

Fig. 6.11 Deformation of shotcrete lining patch near a joint. **a** Schematic; **b** quantitative notation

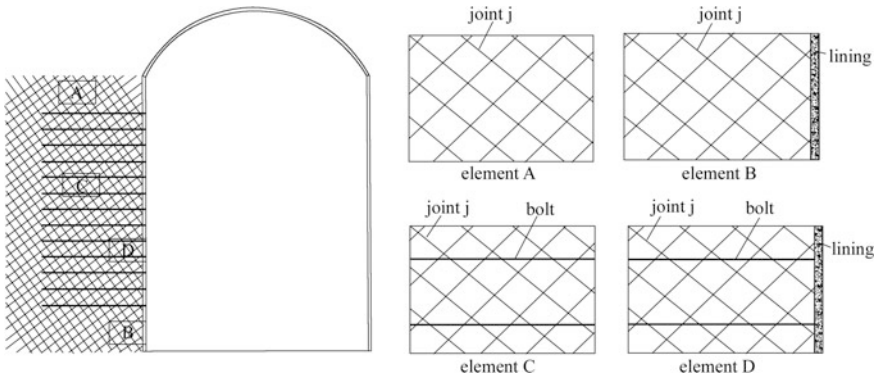

Fig. 6.12 Typical REVs around an excavated cavern

The generalized rheological model of the jointed rock mass reinforced by fully grouted bolts and lining is constructed in Fig. 6.13. It is notable that the interfaces of steel/grout and grout/rock are not taken into account in this model. It also should be reminded that the joint persistence is indirectly handled with the average out deformation and strength parameters over the joint and the "rock bridge".

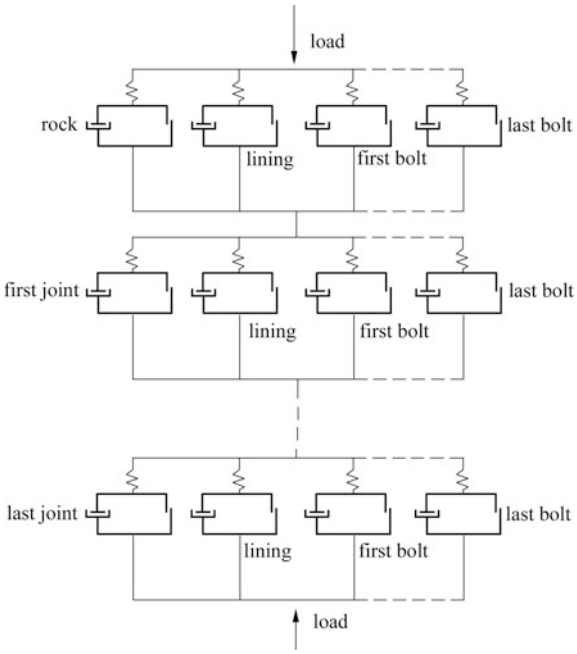

Fig. 6.13 Rheological model for the REV contains joints + bolts + shotcrete lining

6.3.2 Basic Assumptions and Formularization

According to the rheological model in Fig. 6.13, a bolt (or lining) segment in the REV can exhibit different stresses at joint and within (or on) intact rock. In this manner, the localized deformation of bolt and shotcrete lining at joint can be simulated. This rheological model implies four assumptions as follows.

① Assumption 1—strain addition
It states that the strain increment of the jointed rock mass reinforced by shotcrete and bolts (element D) is the sum of the incremental strains of the reinforced intact rock and reinforced joints. This assumption is mathematically formulated in the global coordinate system as

$$\{\Delta\varepsilon\} = \{\Delta\varepsilon\}_{R(LB)} + \sum_{J} \{\Delta\varepsilon\}_{J(LB)} \tag{6.19}$$

In which $\{\Delta\varepsilon\}$ is the equivalent strain increment of the jointed rock mass containing bolts and lining; $\{\Delta\varepsilon\}_{R(LB)}$ is the equivalent strain increment of intact rock containing bolts and lining; $\{\Delta\varepsilon\}_{J(LB)}$ is the equivalent strain increment of joint containing bolts and lining.

② Assumption 2—stress share
It states that the load increment is shared among the bolt, shotcrete, and intact rock in the reinforced intact rock, the same applies to the reinforced joint. The corresponding formulas are

$$\begin{cases} \{\Delta\sigma\}_{R(LB)} = A_R\{\Delta\sigma\}_R + \sum\limits_b A_b[T]_b^T\{\Delta\sigma\}_{(br)} + A_l[T]_l^T\{\Delta\sigma\}_{(lr)} \\ \{\Delta\sigma\}_{j(lb)} = A_R\{\Delta\sigma\}_j + \sum\limits_b A_b[T]_{(bj)}^T\{\Delta\sigma\}_{(bj)} + A_l[T]_{(lj)}^T\{\Delta\sigma\}_{(lj)} \\ [T]_{(bj)}^T = ([T]_j^T)^{-1}[T]_b^T \\ [T]_{(lj)}^T = ([T]_j^T)^{-1}[T]_l^T \end{cases} \tag{6.20}$$

In which A_R, A_l and A_b are the volumetric proportions of the intact rock, shotcrete lining, and bolt in the REV considered, and we have

$$A_R + \sum_b A_b + A_l = 1$$

③ Assumption 3—stress consistency
It states that the average stress in the reinforced intact rock is equal to that in the reinforced joint, mathematically

$$\{\Delta\sigma\} = \{\Delta\sigma\}_{R(LB)} = \{\Delta\sigma\}_{J(LB)} \tag{6.21}$$

④ Assumption 4—strain consistency
It states that the strains of the bolt and shotcrete are equal to that of the intact rock in the reinforced intact rock; similarly, the relative displacements of the two hinges of the bolt and shotcrete are equal to that of the reinforced joint walls, mathematically

$$\begin{cases} \{\Delta\varepsilon\}_{R(B)} = \{\Delta\varepsilon\}_{R} = \{\Delta\varepsilon\}_{(BR)} = \{\Delta\varepsilon\}_{(LR)} \\ \{\Delta\varepsilon\}_{j(b)} = \{\Delta\varepsilon\}_{j} = [T]_{(bj)}\{\Delta\varepsilon\}_{(bj)} = [T]_{(lj)}\{\Delta\varepsilon\}_{(lj)} \end{cases} \tag{6.22}$$

The local coordinate systems of joint, bolt, and lining have been defined in Figs. 2.2, 2.16, and 2.18. In Eqs. (6.19)–(6.22) all quantities without subscript belong with the equivalent material. Let the subscripts r, j, b and l denote the rock, joint set, bolt set and shotcrete lining, respectively; the subscripts (br), (bj), (lr) and (lj) denote the bolt in the intact rock and at the joint set, the shotcrete lining at the intact rock and the joint set, respectively; the subscripts $r(lb)$ and $j(lb)$ denote the intact rock r and joint set j reinforced by bolt b and shotcrete lining l together. All the above subscripts written in small letters imply the local Cartesian coordinate system, whereas the same subscripts written in capital letters imply the global coordinate system.

The transformation matrix $[T]_b$ has been defined in Eq. (2.40), the forms of matrices $[T]_j$ and $[T]_l$ are identical to $[T]_b$ but the subscript b should be replaced by j and l.

6.3.3 Constitutive Equations

The constitutive equations of rock, joint and bolt are identical to that in Sect. 6.2.3. In the following only the constitutive equation of shotcrete lining is additionally elaborated.

(1) Shotcrete lining at joint

As has been illustrated in Fig. 6.11a, a lining patch would undergo bending process during the shear of the joint. The bending height h_l termed as "effect height" or the corresponding "effective length" $L_l = h_l / \sin\alpha_l$ (see Fig. 6.11b) is related to various factors such as the properties of rock, joint, and shotcrete. It is postulated that along the effective length, the normal stresses σ_{xl} and σ_{yl} are uniformly distributed, the

shear stresses τ_{zxl} and τ_{zyl} are uniformly distributed, too. Within the effective length, the constitutive equation can be given by the "true" strain $\{\Delta\varepsilon\}_l^*$

$$\{\Delta\sigma\}_l^* = [D]_l^*(\{\Delta\varepsilon\}_l^* - \{\dot{\varepsilon}^{vp}\}_l^*\Delta t) \tag{6.23}$$

Since the equivalent strain contributed from the joint set j is

$$\{\Delta\varepsilon\}_{(lj)} = \frac{L_l}{s_j}\{\Delta\varepsilon\}_l^*$$

or

$$\{\Delta\varepsilon\}_l^* = \frac{s_j}{L_l}\{\Delta\varepsilon\}_{(lj)} \tag{6.24}$$

Therefore we have the constitutive equation given by the equivalent strain

$$\{\Delta\sigma\}_{(lj)} = [D]_{(lj)}(\{\Delta\varepsilon\}_{(lj)} - \{\dot{\varepsilon}^{vp}\}_{(lj)}\Delta t) \tag{6.25}$$

In which

$$\begin{cases} [D]_{(lj)} = \frac{s_j}{L_l}[D]_l^* \\ \{\dot{\varepsilon}^{vp}\}_{(lj)} = \frac{L_l}{s_j}\{\dot{\varepsilon}^{vp}\}_l^* \end{cases} \tag{6.26}$$

In Eqs. (6.24) and (6.26) L_l is the effective length of the lining at joint and s_j is the spacing of the joint set j. During the viscoplastic deformation, the effective length L_l, the dip direction ϕ_l and the dip angle θ_l should be updated at certain time steps by the formulas

$$\begin{cases} L_l(t+\Delta t) = L_l(t) + s_j\Delta\varepsilon_{yl} \\ \phi_l(t+\Delta t) = \phi_l(t) + \arctan\left(\frac{s_j\Delta\gamma_{zxl}}{L_l(t)}\right) \\ \theta_l(t+\Delta t) = \theta_l(t) - \arctan\left(\frac{s_j\Delta\gamma_{zyl}}{L_l(t)}\right) \end{cases} \tag{6.27}$$

(2) Shotcrete lining at rock

For the shotcrete lining at rock, Eq. (6.23) may be used directly, but the subscript l should be replaced by (lr) and the superscript * should be deleted.

(3) Equivalent material

In the first step, the constitutive equations of the rock, joint, shotcrete lining, bolt are introduced in the stress share Eq. (6.20) simultaneously. After the corresponding coordinate transformations we get

$$\begin{cases} \{\Delta\sigma\}_{R(LB)} & = A_R[D]_R\{\Delta\varepsilon\}_R - A_R[D]_R\{\dot{\varepsilon}^{vp}\}_R\Delta t \\ & \quad + A_l[T]_l^T[D]_{(lr)}[T]_l\{\Delta\varepsilon\}_{(LR)} - A_l[T]_l^T[D]_{(lr)}\{\dot{\varepsilon}^{vp}\}_{(lr)}\Delta t \\ & \quad + \sum_b A_b[T]_b^T[D]_{(br)}[T]_b\{\Delta\varepsilon\}_{(BR)} - \sum_b A_b[T]_b^T[D]_{(br)}\{\dot{\varepsilon}^{vp}\}_{(br)}\Delta t \\ \{\Delta\sigma\}_{j(lb)} & = A_R[D]_j\{\Delta\varepsilon\}_j - A_R[D]_j\{\Delta\dot{\varepsilon}^{vp}\}_j\Delta t \\ & \quad + A_l[T]_{(lj)}^T[D]_{(lj)}[T]_{(lj)}\{\Delta\varepsilon\}_{(lj)} - A_l[T]_{(lj)}^T[D]_{(lj)}\{\dot{\varepsilon}^{vp}\}_{(lj)}\Delta t \\ & \quad + \sum_b A_b[T]_{(bj)}^T[D]_{(bj)}[T]_{(bj)}\{\Delta\varepsilon\}_{(bj)} - \sum_b A_b[T]_{(bj)}^T[D]_{(bj)}\{\dot{\varepsilon}^{vp}\}_{(bj)}\Delta t \end{cases} \tag{6.28}$$

Next, we take the strain consistency Eq. (6.22) into account, the Eq. (6.28) becomes

$$\begin{cases} \{\Delta\sigma\}_{R(LB)} = [D]_{R(LB)}\{\Delta\varepsilon\}_{R(LB)} - \{\Delta\sigma^{vp}\}_{R(LB)} \\ \{\Delta\sigma\}_{j(lb)} = [D]_{j(lb)}\{\Delta\varepsilon\}_{j(lb)} - \{\Delta\sigma^{vp}\}_{j(lb)} \end{cases} \tag{6.29}$$

or

$$\begin{cases} \{\Delta\varepsilon\}_{R(LB)} = [D]_{R(LB)}^{-1}\{\Delta\sigma\}_{R(LB)} + [D]_{R(LB)}^{-1}\{\Delta\sigma^{vp}\}_{R(LB)} \\ \{\Delta\varepsilon\}_{j(lb)} = [D]_{j(lb)}^{-1}\{\Delta\sigma\}_{j(lb)} + [D]_{j(lb)}^{-1}\{\Delta\sigma^{vp}\}_{j(lb)} \end{cases} \tag{6.30}$$

In which

$$\begin{cases} [D]_{R(LB)} = A_R[D]_R + A_l[T]_l^T[D]_{(lr)}[T]_l + \sum_b A_b[T]_b^T[D]_{(br)}[T]_b \\ [D]_{j(lb)} = A_R[D]_j + A_l[T]_{(lj)}^T[D]_{(lj)}[T]_{(lj)} + \sum_b A_b[T]_{(bj)}^T[D]_{(bj)}[T]_{(bj)} \end{cases} \tag{6.31}$$

$$\begin{cases} \{\Delta\sigma^{vp}\}_{R(LB)} = A_R[D]_R\{\dot{\varepsilon}^{vp}\}_R\Delta t + A_l[T]_l^T[D]_{(lr)}\{\dot{\varepsilon}^{vp}\}_{(lr)}\Delta t + \sum_b A_b[T]_b^T[D]_{(br)}\{\dot{\varepsilon}^{vp}\}_{(br)}\Delta t \\ \{\Delta\sigma^{vp}\}_{j(lb)} = A_R[D]_j\{\dot{\varepsilon}^{vp}\}_j\Delta t + A_l[T]_{(lj)}^T[D]_{(lj)}\{\dot{\varepsilon}^{vp}\}_{(lj)}\Delta t + \sum_b A_b[T]_{(bj)}^T[D]_{(bj)}\{\dot{\varepsilon}^{vp}\}_{(bj)}\Delta t \end{cases} \tag{6.32}$$

The constitutive equation of joint containing lining and bolt [the second row of Eq. (6.30)] is transformed with $[T]_j$, afterwards its resultant is introduced into the strain addition Eq. (6.19) together with the constitutive equation of the rock with lining and bolt [the first row of Eq. (6.30)], the equivalent constitutive equation of the jointed rock mass containing lining and bolts is finally formulated

$$\{\Delta\varepsilon\} = [S]\{\Delta\sigma\} + \{\Delta\varepsilon^{vp}\} \tag{6.33}$$

In which

$$[S] = \left([D]_{R(LB)}\right)^{-1} + \sum_j \left([T]_j\right)^{-1} \left([D]_{j(lb)}\right)^{-1} \left([T]_j^T\right)^{-1} \tag{6.34}$$

$$\{\Delta\varepsilon^{vp}\} = [D]_{R(LB)}^{-1}\{\Delta\sigma^{vp}\}_{R(LB)} + \sum_j [T]_j^{-1}[D]_{j(lb)}^{-1}\{\Delta\sigma^{vp}\}_{j(lb)} \tag{6.35}$$

where the REV contains no shotcrete lining, Eqs. (6.33)–(6.35) will be degenerated back to the constitutive equation of the jointed rock mass reinforced by the bolt only [see Eqs. (6.16)–(6.18)].

6.3.4 *Verification and Parametric Study*

Figure 6.14 presents a sample of jointed rock for the verification study. It comprises two joint sets spaced at 0.5 m and with dip angle of 45° and −45°, respectively. The sample is loaded by the uniform pressure P on its top. One horizontal bolt set (diameter d_b = 30 mm, spacing = 1 m × 1 m) or/and two lining layers on its left and right vertical surfaces (thickness of lining δ_l = 10 cm), are deployed. Under such testing configuration, the equivalent stress and strain within the sample are uniformly distributed.

Towards the verification, three FE models are constructed.

① FE model 1. The intact rock, joints, linings and bolts are all approached explicitly. The joints are discretized by joint elements without thickness (Goodman et al. 1968; Mahtab and Goodman 1970), intact rock, bolts and

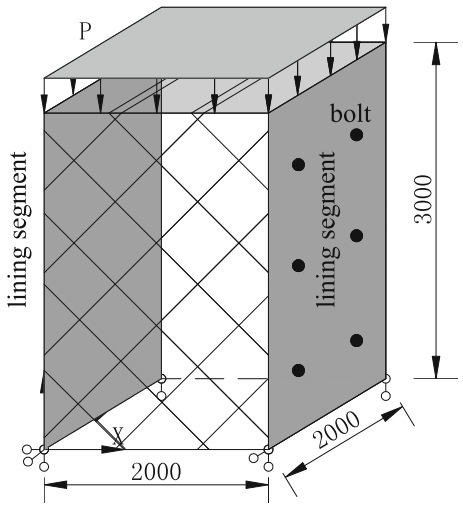

Fig. 6.14 Numerical test sample (Unit: mm)

linings are all discretized by solid elements. The mesh includes 4446 elements and 5340 nodes.

② FE model 2. The sample is regarded as one solid equivalent element, the effect of joints, bolts and linings are simulated using the equivalent approach elaborated in this section.

③ FE model 3. The sample is discretized into 96 elements and 175 nodes, the effect of joints, bolts and linings are all simulated by the equivalent approach elaborated in this section.

FE model 1 simulates the joints, linings and bolts explicitly and is able to provide more precise solution. Therefore, it performs as a "benchmark" to validate the equivalent solutions by FE models 2 and 3. The only difference between FE models 2 and 3 lies in their mesh density.

The material parameters of the rock and shotcrete as well as joints and bolts used in the computation are listed in Tables 6.3 and 6.4.

The following four reinforcement cases are studied with regard to the above three FE models.

- Case 1. Without reinforcements.
- Case 2. One horizontal bolt set only, without shotcrete linings.
- Case 3. Two lining patches on its left and right vertical surfaces, without bolts.
- Case 4. Two lining patches on its left and right vertical surfaces + one horizontal bolt set.

The pressure P is incrementally raised until the failure of the samples. The curves relating the pressure P and the vertical displacement u_z at the top center point plotted in Figs. 6.15, 6.16 and 6.17 validate that

- The results by equivalent FE models 2 and 3 are close to the results of the explicit approach by FE model 1. However, it is obvious that FE model 1 needs more complex mesh;
- Use of shotcrete linings or fully-grouted bolts independently may raise the overall strength of samples;
- It seems that the bolt is more effective in the improvement of sample strength than shotcrete lining under the specified design parameters;

Table 6.3 Parameters of rock and shotcrete

Material	E (GPa)	μ	c (MPa)	φ (°)	ϕ (°)
Shotcrete	25	0.18	2.0	50.0	50.0
Rock	28	0.20	205	56.0	56.0

Table 6.4 Parameters of joints and bolts

Joint					Bolt						
k_n (MN/m^3)	k_s (MN/m^3)	c (MPa)	φ (°)	ϕ (°)	E (GPa)	μ	f_{yk} (MPa)	f_{ptk} (MPa)	δ_{gt} (%)	θ (°)	d_b (mm)
60,000	20,000	0.1	25.0	0	210	0.18	340	370	10.0	0.0	30.0

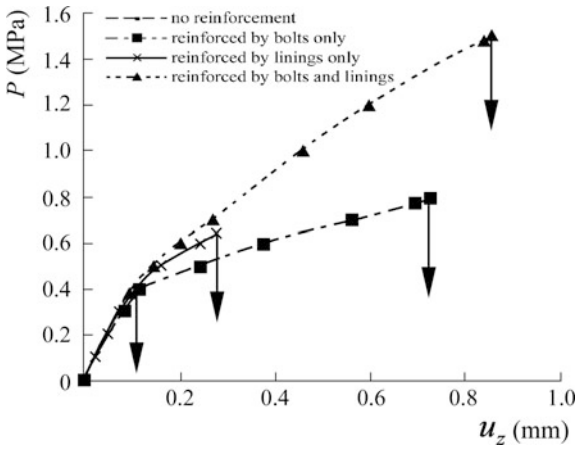

Fig. 6.15 $P-u_z$ relationship of FE model 1

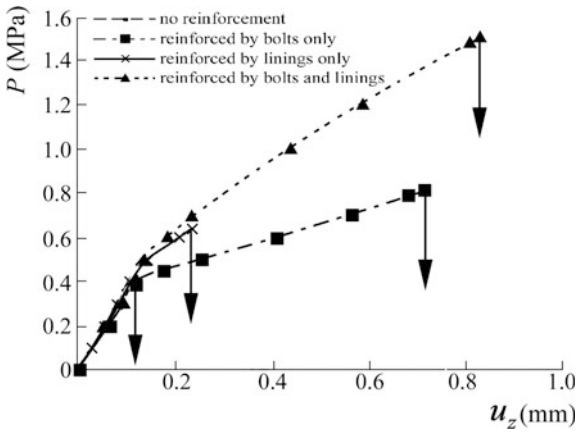

Fig. 6.16 $P-u_z$ relationship of FE model 2

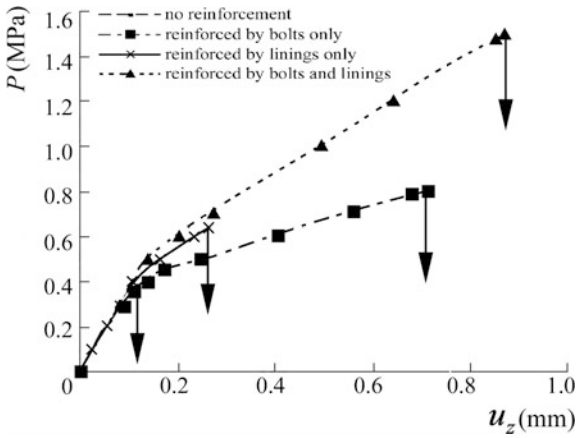

Fig. 6.17 $P-u_z$ relationship of FE model 3

– However, combination of shotcrete lining and bolt may increase the sample strength much more remarkably.

Similar to the parameter "effective height" h_d or "effective length" L_d of the bolt at joint, the "effective height" h_l or "effective length" L_l of the shotcrete lining at joint in Eqs. (6.23)–(6.27) is dominated by various factors.

A numerical test procedure using the samples in Fig. 6.14 is further carried out to study the effective height of the lining at joint (Chen et al. 2009).

① The Young's modulus of rock, the strength parameters of joint, the dip angle of joint, the thickness of lining, are selected as the main factors influencing the effective height. The upper and inferior bounds of these parameters are prescribed.
② Within the upper and inferior bounds, m_i tentative values are designed for each factor, then by the orthogonal design method, N combinations of the factors are prepared.
③ According to these N factor combinations, numerical test samples are discretized by explicit FE model 1 and equivalent FE model 3, respectively.
④ For each test sample, the result from FE model 1 is looked at as a benchmark solution.
⑤ For each test sample, tentative effective heights of the lining are trialed until the best fitting between FE model 3 and FE model 1 is obtained. In this manner the value of the effective height of the lining at joint under a specified factor combination is estimated.
⑥ All the factor combinations are grouped as input data set, and the corresponding effective heights are grouped as output data set in the training of artificial neural network (ANN) (Haykin 1999). The trained ANN will provide the relationship between the factors and the effective height of the lining at joint.
⑦ An empirical relation between the effective height and the thickness of shotcrete lining can be empirically suggested as $h_l = \alpha \cdot \delta_l = 0.1{-}2.0\delta_l$. Compared with the empirical relation between the effective height and the diameter of bolt ($h_b = \alpha \cdot d_b = 2.0{-}4.0d_b$), it can be justified that the parameter α is rather smaller for the shotcrete lining, mostly due to a much lower ductility of the shotcrete lining.

6.4 Distinct Approach of Jointed Rock Masses Reinforced by Fully Grouted Bolts

6.4.1 Basic Assumptions and Formularization

To deal with very complicated stabilization problems, a combination of equivalent and distinct approaches is more powerful than to make use of either one only. Therefore, the interest of this section is directed to the distinct approach for rock bolts.

In 1989 Aydan proposed a three-dimensional bolt element with 8 nodal points. Two of them are connected to the bolt, whereas the six others are connected to host rock. The number of nodes in two-dimensional cases is reduced to six. Swoboda and Marence (1991, 1992) modified the formulation by assigning different coordinates for the bolt nodes and the nodes of rock/grout interfaces. Thus, the bolt and rock displacements are different at the bolt-joint intersection, and the parameters in the stiffness matrix are not constant. They depend on the joint displacement and are independently calculated by an iterative procedure.

We proposed a bolt element using the technique of assemblage in which the bolt and grout are simplified as a kind of equivalent material (see Fig. 6.18), and the interface between equivalent bolt-grout material and host rock is taken into account (Chen and Egger 1997; Qiang and Chen 2001).

For the simplicity of discussion, the 8-node bolt element schematically illustrated in Fig. 6.19 is taken as an example, for which the basic assumptions are postulated that

① The load increment is shared among bolt and grout.
② The strain of bolt is equal to that of grout.
③ Along the axial direction, the displacement of bolt-grout material is linearly distributed.

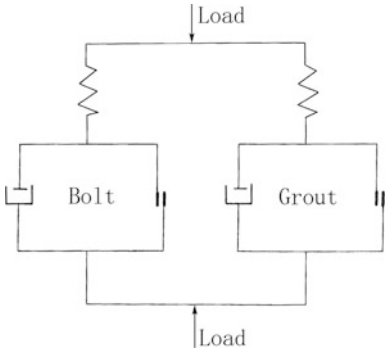

Fig. 6.18 Rheological model of the equivalent bolt-grout material

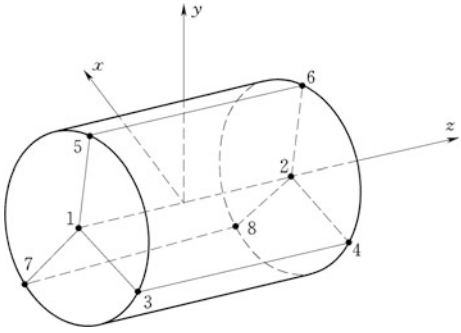

Fig. 6.19 8-node bolt element

④ Along the radial direction, the stress of bolt-grout is uniform.
⑤ Normal stress along the axis is transmitted by bolt-grout material.
⑥ Shear stresses perpendicular to the axis is transmitted by bolt-grout material, too.
⑦ Shear stress along the axis is transmitted through the interfaces between grout and rock.
⑧ The relative displacement on the interface of grout and rock perpendicular to the axis is step-wisely distributed along the circumferential direction.

6.4.2 Constitutive Equations

(1) Equivalent bolt-grout material

The rheological model of the equivalent bolt-grout material in Fig. 6.18 is actually a simplified case of Fig. 6.7 where the rock is replaced by the grout and there are no joints. Hence on the local Cartesian coordinate system (see Fig. 2.16) it may be routinely given by the formula

$$\{\Delta\sigma\}_{(bg)} = [D]_{(bg)}\{\Delta\varepsilon\}_{(bg)} - \{\Delta\sigma^{vp}\}_{(bg)} \tag{6.36}$$

where the subscript (bg) means the equivalent grout-bolt material, and

$$[D]_{(bg)} = A_b[D]_b + A_g[D]_g \tag{6.37}$$

$$\{\Delta\sigma^{vp}\}_{(bg)} = A_b[D]_b\{\dot{\varepsilon}^{vp}\}_b\Delta t + A_g[D]_g\{\dot{\varepsilon}^{vp}\}_g\Delta t \tag{6.38}$$

In which A_g and A_b are the volumetric ratios of grout and bolt respectively observing

$$A_g + A_b = 1$$

The elastic matrices $[D]_g$ and $[D]_b$ have been given in Eqs. (2.81) and (2.82), the viscoplastic strain rates $\{\dot{\varepsilon}^{vp}\}_b$ and $\{\dot{\varepsilon}^{vp}\}_g$ have been given in Eqs. (2.122)–(2.125).

(2) Interface between the equivalent bolt-grout material and host rock

Figure 6.20 shows an interface patch and corresponding local Cylindrical coordinate system. The relative displacement and stress increments are identical to Eqs. (2.126)–(2.129) where the cohesion c, friction angle φ, dilation angle ϕ and tension strength σ_T are specified for the interface between the equivalent bolt-grout material and host rock.

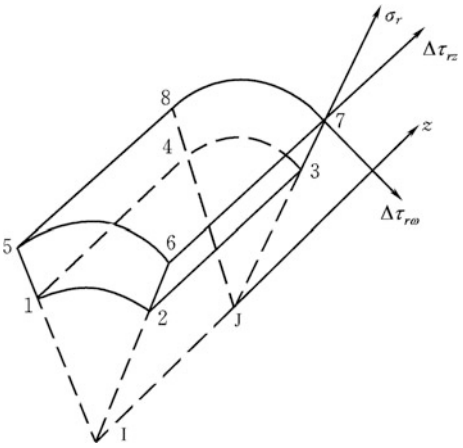

Fig. 6.20 Interface patch simulated by joint element

6.4.3 Governing Equations of the Bolt Element

(1) Equivalent bolt-grout material

The displacement increment $\{\Delta u\}_{(bg)}$ of the equivalent bolt-grout material on its local Cartesian coordinate system (see Fig. 6.20) is related to the nodal displacement increment $\{\Delta\delta\}_{(bg)}$ at the nodes I and J as

$$\{\Delta u\}_{(bg)} = [l]_b^{ca}[M]_{(bg)}\{\Delta\delta\}_{(bg)} \tag{6.39}$$

In which the transformation matrix $[l]_b^{ca}$ has been defined in Eq. (2.36) and

$$[M]_{(bg)} = \begin{bmatrix} N_I & 0 & 0 & N_J & 0 & 0 \\ 0 & N_I & 0 & 0 & N_J & 0 \\ 0 & 0 & N_I & 0 & 0 & N_J \end{bmatrix} \tag{6.40}$$

$$\begin{cases} N_I = -\frac{\xi-1}{2} \\ N_J = \frac{1+\xi}{2} \\ \xi = \frac{z}{L_b/2} \end{cases} \tag{6.41}$$

$$\begin{cases} \{\Delta u\}_{(bg)} = \begin{Bmatrix} \Delta u_{x(bg)} \\ \Delta u_{y(bg)} \\ \Delta u_{z(bg)} \end{Bmatrix} \\ \{\Delta\delta\}_{(bg)} = \begin{Bmatrix} \Delta u_{xI} \\ \Delta u_{yI} \\ \Delta u_{zI} \\ \Delta u_{xJ} \\ \Delta u_{yJ} \\ \Delta u_{zJ} \end{Bmatrix} \end{cases} \tag{6.42}$$

The strain increment of the equivalent bolt-grout material is

$$\{\Delta\varepsilon\}_{(bg)} = [B]_{(bg)}\{\Delta\delta\}_{(bg)} \tag{6.43}$$

In which

$$[B]_{(bg)} = \frac{1}{L_b}\begin{bmatrix} 0 & 0 & 1 \\ 1 & 0 & 0 \\ 0 & 1 & 0 \end{bmatrix}[l]_b^{ca}\begin{bmatrix} -1 & 0 & 0 & 1 & 0 & 0 \\ 0 & -1 & 0 & 0 & 1 & 0 \\ 0 & 0 & -1 & 0 & 0 & 1 \end{bmatrix} \tag{6.44}$$

Taking into account of Eqs. (6.36) and (6.43) and application of the virtual work principle gives rise to

$$[k]_{(bg)}\{\delta\}_{(bg)} = \{\Delta f\}_{(bg)} + \{\Delta f^{vp}\}_{(bg)} \tag{6.45}$$

In which

$$[k]_{(bg)} = \pi r_g^2 \int_{-L_b/2}^{L_b/2} [B]_{(bg)}^T [D]_{(bg)} [B]_{(bg)} dz \tag{6.46}$$

$$\{\Delta f^{vp}\}_{(bg)} = \pi r_g^2 \int_{-L_b/2}^{L_b/2} [B]_{(bg)}^T \{\Delta\sigma^{vp}\}_{(bg)} dz \tag{6.47}$$

(2) Interfaces between the equivalent bolt-grout material and surrounding elements of host rock

The relative displacement $\{\Delta u\}_j$ of the interface on its local Cylindrical coordinate system (see Fig. 6.20) is related to the nodal displacement increment $\{\Delta\delta\}_j$ as

$$\{\Delta u\}_j = [B]_j\{\Delta\delta\}_j = [l]_j^{cy}[l]_j^{ca}[M]_j\{\Delta\delta\}_j \tag{6.48}$$

In which the transformation matrices $[l]_j^{ca}$ and $[l]_j^{cy}$ have been defined in Eqs. (2.36)–(2.38) but the subscript b should be replaced by j, and

$$\begin{cases} \{\Delta u\}_j = \begin{Bmatrix} \Delta u_r \\ \Delta u_\omega \\ \Delta u_z \end{Bmatrix} \\ \{\Delta\delta\}_j = \begin{Bmatrix} \Delta u_{x1} \\ \Delta u_{y1} \\ \Delta u_{z1} \\ \vdots \\ \Delta u_{x4} \\ \Delta u_{y4} \\ \Delta u_{z4} \end{Bmatrix} \end{cases} \tag{6.49}$$

$$[M]_j = \begin{bmatrix} -N_1 & 0 & 0 & -N_2 & 0 & 0 & -N_3 & 0 & 0 & -N_4 & 0 & 0 \\ 0 & -N_1 & 0 & 0 & -N_2 & 0 & 0 & -N_3 & 0 & 0 & -N_4 & 0 \\ 0 & 0 & -N_1 & 0 & 0 & -N_2 & 0 & 0 & -N_3 & 0 & 0 & -N_4 \\ N_5 & 0 & 0 & N_6 & 0 & 0 & N_7 & 0 & 0 & N_8 & 0 & 0 \\ 0 & N_5 & 0 & 0 & N_6 & 0 & 0 & N_7 & 0 & 0 & N_8 & 0 \\ 0 & 0 & N_5 & 0 & 0 & N_6 & 0 & 0 & N_7 & 0 & 0 & N_8 \end{bmatrix} \tag{6.50}$$

$$\begin{cases} N_i = \frac{1}{4}(1+\xi_i\xi)(1+\eta_i\eta) \\ N_{i+4} = N_i \\ \xi = \frac{z}{L_b/2} \\ \eta = \frac{\omega}{\omega_0} \end{cases} \quad (i = 1{-}4) \tag{6.51}$$

Taking into account of Eqs. (6.48) and (2.216)–(2.219), the virtual work principle will give the relationship between the nodal force increment and the nodal displacement increment of the interface as follows

$$[k]_j\{\delta\}_j = \{\Delta f\}_j + \{\Delta f^{vp}\}_j \tag{6.52}$$

In which

$$[k]_j = r_g \int_{-L_b/2}^{L_b/2} \int_{-\omega_0}^{\omega_0} [B]_j^T [D]_j [B]_j \, d\omega dz \tag{6.53}$$

$$\{\Delta f^{vp}\}_j = r_g \int_{-L_b/2}^{L_b/2} \int_{-\omega_0}^{\omega_0} [B]_j^T [D]_j \{\dot{u}^{vp}\}_j \Delta t \, d\omega dz \tag{6.54}$$

(3) Assemblage of explicit bolt element considering grout and interface

The whole bolt element is assembled by one bar element representing the bolt-grout equivalent material and n_j joint elements representing the interface patches related to the surrounding elements of host rock. Suppose the bar element possesses nodes I and J (see Fig. 6.21), then the interior nodes (1–4) of the joint (interface) element are all assembled to the node I and J, meanwhile the exterior nodes (5–8) of the same joint element are assembled to the host rock elements.

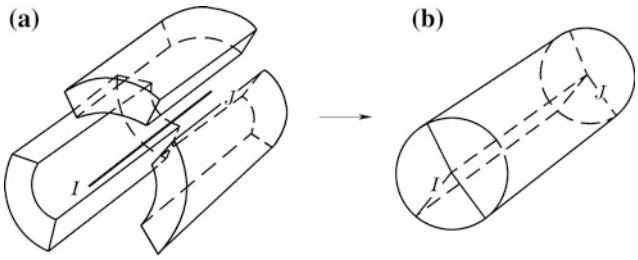

Fig. 6.21 Assemblage of an explicit bolt element considering interfaces

6.5 Distinct Approach of Stranded Wire Cables

For a hydraulic structure installed with a large amount of stranded wire cables, the primary task in the optimal layout design for reinforcement scheme is the simulation of reinforcement effects on the structure safety due to the pre-stress and additional stiffness of the cable (Stheeman 1982; Hassani and Rajaie 1990; Mitri and Rajaie 1990; Hassani et al. 1992; Mitri et al. 1993; Kim 2003).

It is normally recommended that on the out-laid anchor head, a concentrated force or distributed pressure of certain pattern is exerted to simulate the pre-stress, meanwhile a concentrated force equalizing pre-stress is exerted in the bonded inside anchorage head as "bar" or "beam" element with definite length. Since the exerting position at the bonded inside anchorage head is difficultly pinpointed, it is customarily postulated at the intersection of the bonded inside anchorage head with the free length, for the safe side consideration.

The free length can be approached by an additional stiffness matrix of the anchor element bound to the structure system which links the out-laid anchor head and the bonded inside anchorage head.

6.5.1 Basic Assumptions and Formularization

Figure 6.22 shows a cable element c with free length L_c and sectional area A_c. It links solid elements e_i and e_j whose geometry parameters are

- Dip direction ϕ_c and dip angle θ_c;
- Global coordinates (X_{ci}, Y_{ci}, Z_{ci}) and corresponding normalized coordinates $(\xi_{ci}, \eta_{ci}, \zeta_{ci})$ of the out-laid anchor head A (in the element e_i);
- Global coordinates $\left(X_{cj}, Y_{cj}, Z_{cj}\right)$ and corresponding normalized $\left(\xi_{cj}, \eta_{cj}, \zeta_{cj}\right)$ of the bonded inside anchorage head B (in the element e_j);

The mechanical parameters and variables of this free length element are the Young's modulus E_c, inner force increment ΔR_c and deformation increment $\Delta\delta_c$.

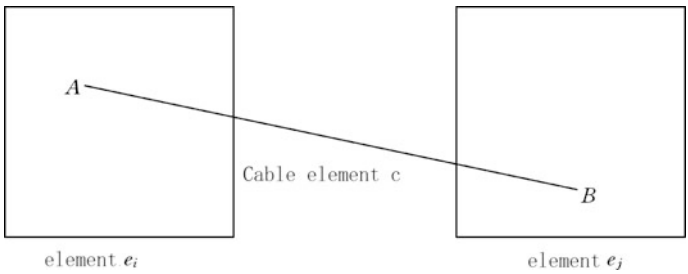

Fig. 6.22 Anchor element for the free length AB

The displacement increments at points A and B are related to their adjoin solid elements by

$$\{\Delta u\}_A = [N]_i\big|_A \{\Delta\delta\}_i \tag{6.55}$$

$$\{\Delta u\}_B = [N]_j\Big|_B \{\Delta\delta\}_j \tag{6.56}$$

where $[N]_i$ and $[N]_j$ = shape function matrices of e_i and e_j; $\{\Delta\delta\}_i$ and $\{\Delta\delta\}_j$ = nodal displacement increments of e_i and e_j.

The deformation increment $\Delta\delta_c$ of the free length L_c between A and B is calculated by

$$\Delta\delta_c = [l]_c^T(\{\Delta u\}_A - \{\Delta u\}_B) \tag{6.57}$$

In which $[l]_c$ is the directional cosine of the cable element c.

$$[l]_c = [\sin\phi_c \sin\theta_c \qquad \cos\phi_c \sin\theta_c \qquad \cos\theta_c]^T \tag{6.58}$$

Suppose the cable element is elastic, the constitutive equation relating its inner force increment and deformation increment may be simply given

$$\Delta R_c = A_c E_c \Delta\delta_c / L_c \tag{6.59}$$

6.5.2 Governing Equations of the Cable Element

The virtual work of the cable reinforced system is

$$W_F = \sum_{i=1}^{n_e} W_i + \sum_{c=1}^{n_c} W_c \tag{6.60}$$

where W_F = virtual work of the structure system due to external actions; W_i = virtual work contributed by the solid element e_i; W_c = virtual work contributed by the cable element c; n_e = amount of the solid elements in the system; n_c = amount of the anchor cables.

(1) Virtual work contributed by external actions

$$W_F = \sum_{i=1}^{ne} \{\Delta\delta^*\}_i^{\mathrm{T}} \{\Delta f\}_i \tag{6.61}$$

where $\{\Delta\delta^*\}_i$ = virtual displacement of the element e_i; $\{\Delta f\}_i$ = external action increment at the element e_i.

(2) Virtual work contributed by the solid element e_i

$$W_i^e = \iiint_{\Omega_i} \{\Delta\varepsilon^*\}_i^{\mathrm{T}} \{\Delta\sigma\}_i \, d\Omega \tag{6.62}$$

where $\{\Delta\varepsilon^*\}_i$ = virtual strain increment of the solid element e_i; $\{\Delta\sigma\}_i$ = stress increment of the solid element e_i.

(3) Virtual work contributed from the cable element c

$$W_c = \Delta\delta_c^* \Delta R_c \tag{6.63}$$

where $\Delta\delta_c^*$ = virtual strain increment of the anchor cable element c.

Equations (6.55)–(6.63) may be simultaneously employed in the routine operator of the virtual work principle, to provide

$$\begin{cases} \{\Delta f\}_i = \iiint\limits_{\Omega_i} [B]_i^{\mathrm{T}} [D]_i [B]_i \{\Delta\delta\}_i d\Omega + \dfrac{A_c E_c}{L_c} [N]_i^{\mathrm{T}}\big|_A \{l\}_c \{l\}_c^T [N]_i\big|_A \{\Delta\delta\}_i \\ \qquad\qquad - \dfrac{A_c E_c}{L_c} [N]_i^{\mathrm{T}}\big|_A \{l\}_c \{l\}_c^T [N]_j\Big|_B \{\Delta\delta\}_j \\ \{\Delta f\}_j = \iiint\limits_{\Omega_j} [B]_j^{\mathrm{T}} [D]_j [B]_j \{\Delta\delta\}_j d\Omega + \dfrac{A_c E_c}{L_c} [N]_j^{\mathrm{T}}\Big|_B \{l\}_c \{l\}_c^T [N]_j\Big|_B \{\Delta\delta\}_j \\ \qquad\qquad - \dfrac{A_c E_c}{L_c} [N]_j^{\mathrm{T}}\Big|_B \{l\}_c \{l\}_c^T [N]_i\big|_A \{\Delta\delta\}_i \end{cases} \tag{6.64}$$

The existence of cable element c therefore contributes to its linked solid elements e_i and e_j in a form of additional stiffness matrices

$$\begin{cases} [k]_{ii} = \frac{A_c E_c}{L_c} [N]_i^{\mathrm{T}}\big|_A \{l\}_c \{l\}_c^T [N]_i\big|_A \\ [k]_{jj} = \frac{A_c E_c}{L_c} [N]_j^{\mathrm{T}}\Big|_B \{l\}_c \{l\}_c^T [N]_j\Big|_B \end{cases} \tag{6.65}$$

$$\begin{cases} [k]_{ij} = -\frac{A_c E_c}{L_c} [N]_i^{\mathrm{T}} \big|_A \{l\}_c \{l\}_c^T [N]_j \big|_B \\ [k]_{ji} = -\frac{A_c E_c}{L_c} [N]_j^{\mathrm{T}} \big|_B \{l\}_c \{l\}_c^T [N]_i \big|_A \end{cases} \tag{6.66}$$

These matrices are assembled in the overall stiffness matrix of the reinforced structure system identical to the conventional FEM algorithm.

6.5.3 Remarks

To handle with the interface failure (slippage and separation) mechanism of bonded inside anchorage head (Yazici and Kaiser 1992; Briaud et al. 1998), different interface models established by Goodman et al. (1968), Ghaboussi et al. (1973), Hermann (1978), Desai et al. (1984, 1986), Beer (1985), Griffiths (1985), Hyett et al. (1995) are available and recently, an important breakthrough using fine finite element grid to simulate the interfaces of soil/grout and grout/strand wire has been achieved (Kim et al. 2007). In order to overcome the pre-process difficulties with the discretization of the bonded inside anchorage head, the composite element method (CEM) also has been formulated by the author (Chen et al. 2015) to explicitly simulate rock, grout, stranded wire, rock/grout interface and grout/stranded wire interface. This study will be presented later in Chap. 15.

6.6 Engineering Applications

6.6.1 Underground Cavern: Pubugou Project, China

(1) Presentation of the project

Pubugou Hydropower Project is located on the Daduhe River, a tributary of the Yangtze River in Sichuan Province, China. The main purpose of the project is power generation with total installation capacity of 3300 MW (6 × 550 MW). Its construction started on March 30, 2004, the first generator was put into operation in December 2009 and the rest by March 2010.

The underground power house is located in the sound granite. Figure 6.23 shows the plan of the underground power house, on which six gauge points (POINT 1–POINT 6) for in situ geo-stress aggression are marked.

(2) Characteristics of the computation

The stabilization study for the 6th turbine generator section shown in Fig. 6.24 is presented.

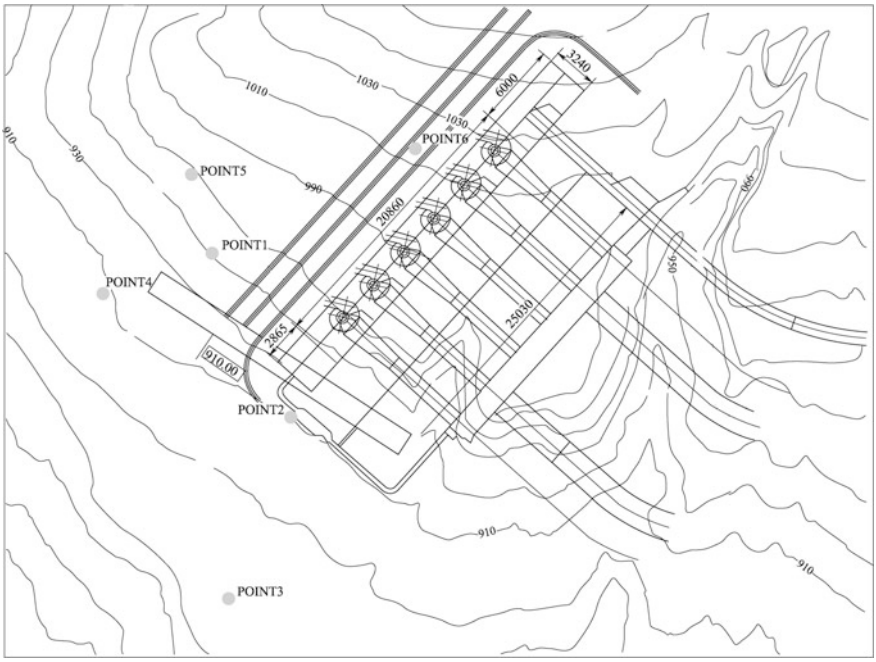

Fig. 6.23 Plan of the underground power house: Pubugou Project, China

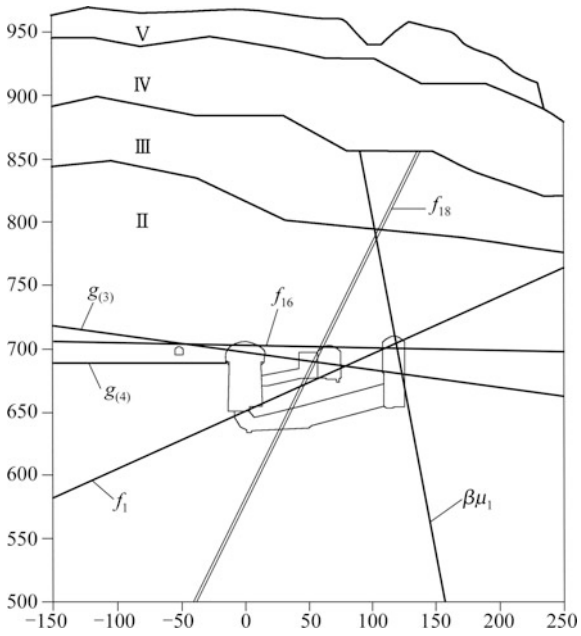

Fig. 6.24 Geological profile of the 6th turbine generator section

The main faults explicitly simulated in the computation are $f1$, $f16$, $f18$, $g(3)$, $\beta\mu1$, $g(4)$. The joint sets implicitly simulated are

- First set. Dip angle = 11°, spacing = 1.5 m, normal stiffness k_n = 209,000 GPa/m, shear stiffness k_s = 104,500 GPa/m, cohesion c = 1.3 MPa, friction angle φ = 41.78°, tensile strength σ_T = 1.3 MPa.
- Second set. Dip angle = −51°, spacing = 2 m, normal stiffness k_n = 209,000 GPa/m, shear stiffness k_s = 104,500 GPa/m, cohesion c = 1.3 MPa, friction angle φ = 41.78°, tensile strength σ_T = 1.3 MPa.

The parameters of the rock masses provided by the designer are summarized in Table 6.5.

The parameters of the final reinforcement scheme are elaborated as follows.

1. Bolts for the generator chamber
   - Crest crown. Φ28@1200 × 1200 mm, L = 7 m; Φ32@1200 × 1200 mm, L = 9 m.
   - Side wall. Φ28@1500 × 1500 mm, L = 7 m.
2. Bolts for the transmission chamber
   - Crest crown. Φ28@1200 × 1200 mm, L = 6 m.
   - Side wall. Φ28@1500 × 1500 mm, L = 7 m.
3. Bolts for the tail water gate chamber
   - Crest crown. Φ28@1200 × 1200 mm, L = 6 m.
   - Side wall. Φ28@1500 × 1500 mm, L = 7 m.
4. Shotcrete lining for the generator chamber
   - Crest crown.δ_l = 120 mm.
   - Side wall.δ_l = 150 mm.

Table 6.5 Parameters of rock masses

Material	Young's modulus E (GPa)	Poisson's ratio μ	Cohesion c (MPa)	Friction angle φ (°)	Tensile strength σ_T (MPa)
Rock class IV + V	2	0.30	0.5	40.03	0.4
Rock class III + IV	10	0.26	1.2	47.85	1.0
Rock class II + III	20.9	0.21	2.2	56.12	1.6
Faults $f1$, $f16$, $f18$, $g(3)$, $\beta\mu1$, $g(4)$	1.66	0.35	0.7	32.25	0.4
Shotcrete	26	0.2	2.0	50.19	1.6

5. Shotcrete lining for the transmission chamber δ_l = 120 mm.
6. Shotcrete lining for the tail water gate chamber δ_l = 120 mm.

The "effective height" of the shotcrete lining at joint is 0.8 times the shorcrete thickness, and the "effective height" of the bolt at joint is 3 times the bolt diameter.

The mesh generated for the computation contains 37,055 elements and 37,246 nodes. Figure 6.25 shows a portion of the FE mesh around the caverns.

(3) Excavation procedure

The excavating benches in Fig. 6.26 are simulated by nine computation steps.

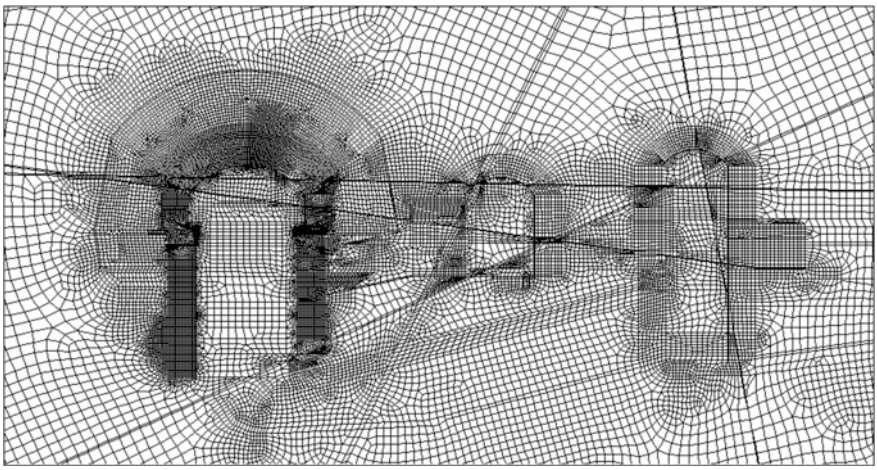

Fig. 6.25 Portion of the FE mesh around the caverns

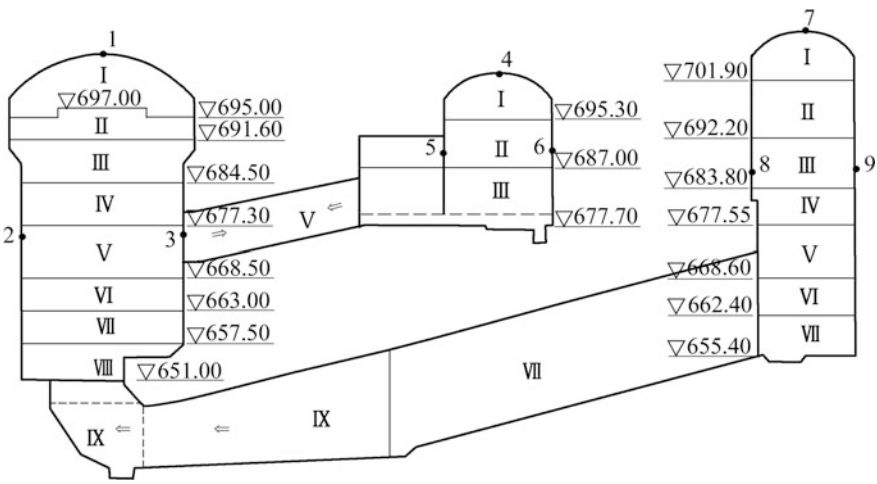

Fig. 6.26 Excavation benches and the representative points

- Step 1. Generator chamber bench I (see Fig. 6.27), tail water gate bench chamber I.
- Step 2. Generator chamber bench II, tail water gate chamber bench II, transmission chamber bench I, generator chamber bench III.
- Step 3. Transmission chamber bench II, tail water gate chamber bench III.
- Step 4. Generator chamber bench IV, transmission chamber bench III.
- Step 5. Generator chamber bench V, tail water gate chamber bench IV.
- Step 6. Tail water gate chamber bench V, generator chamber bench VI.
- Step 7. Generator chamber bench VII.
- Step 8. Tail water gate chamber bench VI, generator chamber bench VIII (see Fig. 6.28).
- Step 9. Tail water gate chamber bench VII.

(4) Computation results and discussions

Two cases are studied by the FEM with regard to two extraordinary reinforcement schemes:

- Case 1. Neither shotcrete nor bolt are considered.
- Case 2. The combined shotcrete and bolt reinforcement is implemented only one step lagging behind of the excavation.

The accumulated displacements at the representative points (see Fig. 6.26) are summarized in Table 6.6 which validate that

Fig. 6.27 Generator chamber after the bench I

Fig. 6.28 Generator chamber after the bench VIII

Table 6.6 Accumulated displacements at representative points (unit: mm)

Point	Accumulated displacement	Case	Excavation step			
			STEP 3	STEP 5	STEP 7	STEP 9
1	$\sum u_y$	1	−47.191	−52.687	−57.594	−62.260
		2	−43.589	−46.634	−49.292	−52.373
2	$\sum u_x$	1	4.879	26.894	47.433	54.809
		2	4.869	26.524	46.384	53.795
3	$\sum u_x$	1	−1.318	−14.488	−38.602	−39.952
		2	−1.256	−14.202	−37.756	−38.799
4	$\sum u_y$	1	−59.209	−84.569	−109.982	−131.215
		2	−53.455	−63.869	−76.797	−87.930
5	$\sum u_x$	1	29.782	52.033	49.831	59.160
		2	29.836	49.616	45.683	54.305
6	$\sum u_x$	1	−4.733	−17.286	−14.048	−3.523
		2	−4.553	−16.228	−12.407	−1.454
7	$\sum u_y$	1	−29.033	−34.254	−38.091	−39.828
		2	−27.331	−31.335	−34.301	−35.523
8	$\sum u_x$	1	16.200	19.859	28.821	43.220
		2	16.345	19.844	28.642	42.953
9	$\sum u_x$	1	−16.448	−29.189	−39.463	−47.706
		2	−16.299	−28.866	−39.065	−47.298

– The reinforcement scheme (Case 2) remarkably reduces the deformation of the caverns.
– Since the reinforcement is implemented one excavation step lagging behind, therefore the difference between the reinforced case 2 and the unreinforced case 1 at the lower elevation (e.g. points 2,3,8,9) are not so significant as that at the higher elevation (e.g. points 1,4,7).

6.6.2 *Cut Slope: Longtan Project, China*

(1) Presentation of the project

Longtan Project is located on the Hongshuihe River—a tributary of the Pearl River, Guangxi Zhuang Autonomous Region, China.

The project is intended for hydroelectric power generation, flood control and navigation. It (see Fig. 6.29) comprises a large roller-compacted concrete (RCC) gravity dam of 216.2 m high and 849.44 m long; a flood discharge structure arranged in the river-bed dam monoliths consisting of 7 surface spillways and 2 bottom outlets; a left-bank underground power-generation system installed with 9 generator units of 6426 MW in total capacity; and a right-bank navigation structure equipped with two-tandem vertical ship-lifts. Its construction started on July 1, 2001, the river closure was completed by November 2003, the impoundment was initiated in October 2006, the first turbine generator unit was put into operation by May 2007, and the whole project was completed by December 2009.

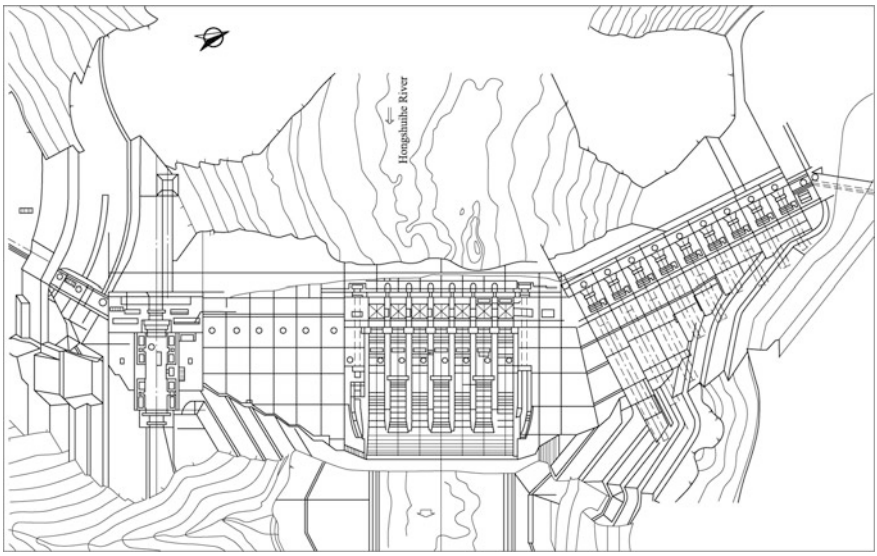

Fig. 6.29 Plan showing the layout of Longtan Project, China

(2) Characteristics of the computation

The underground powerhouse in the left bank mountain diverts water from headrace intake of power tunnels situated under a high slope of layered rocks. Long term observation revealed the bending and toppling creep in the rocks under natural conditions. The depth exhibiting time-dependent deformation is 30–76 m, the corresponding volume of the creep body is 12 million m^3.

The excavation of headrace intakes created a 420 m high and 400 m long cut slope with surface area of 0.18 million m^2 (see Figs. 6.30 and 6.31). The bending and toppling deformation and the stability of slope, the rationality and validity of reinforced scheme, as well as the influences of long term creep deformation on the intake structures during its service period, were thoroughly studied before and during the slope excavation.

The Sect. 9.9 of the 9th turbine generator (see Figs. 6.30 and 6.32) is presented to illustrate the studies conducted. The representative faults in this section are F_1, F_{12}, F_5, F_{28} and F_{32}. The rock masses can be classified into 6 types according to the degree of weathering: surface layer (eluvium), totally weathered, strongly weathered, weakly weathered, slightly weathered, and fresh (intact).

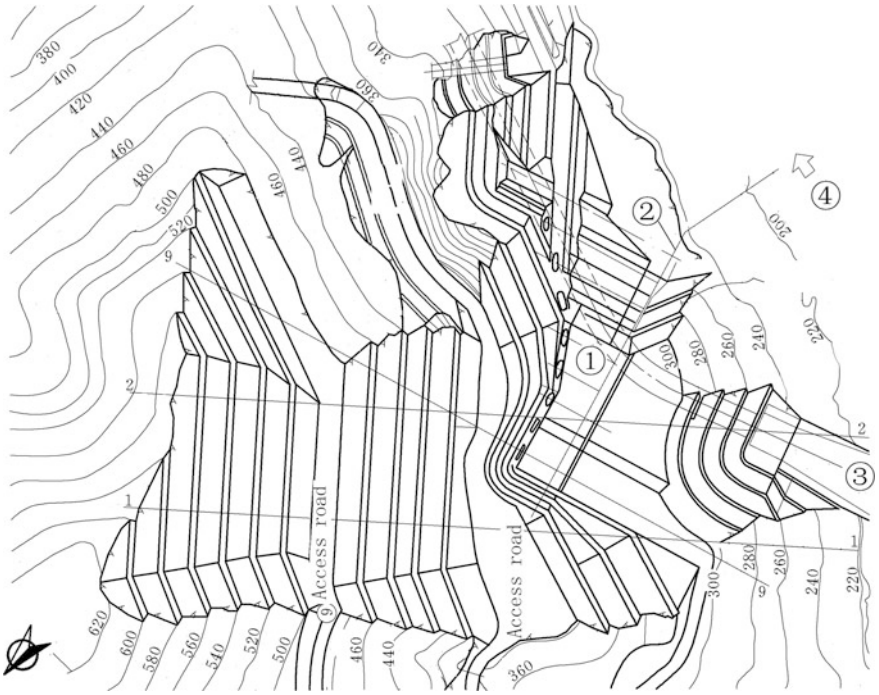

Fig. 6.30 Plan showing the left bank intakes of power tunnels: Longtan Project, China. ①—dam foundation; ②—dam axis; ③—left bank diversion tunnel; ④—Hongshuihe River

Fig. 6.31 Downstream-right bank view of the intake slope (cut elevation 440 m)

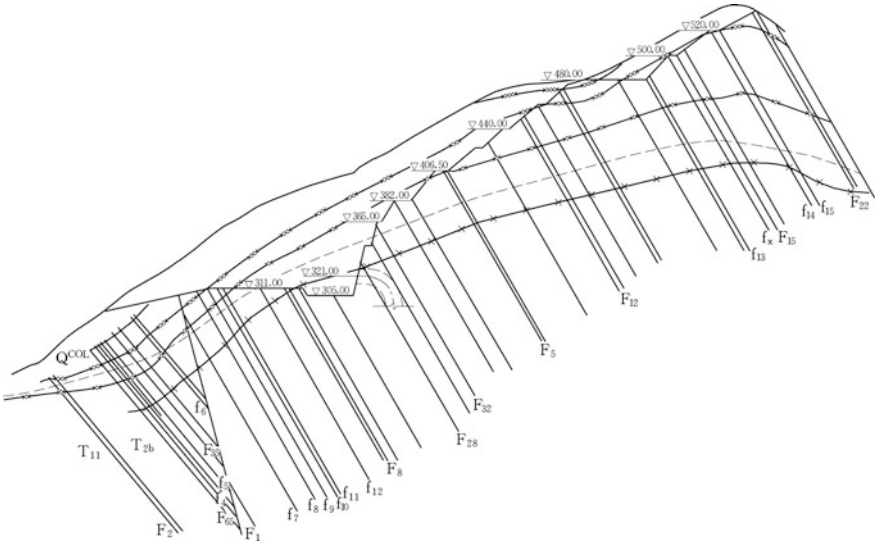

Fig. 6.32 Geological section of the power tunnel intake (9th turbine generator unit)

In situ geo-stress field of the natural rock mass consists of gravitational and tectonic components. For deep underground structures, tectonic stresses must be taken into account in the computation. In Longtan Project however, the excavated portions of slope are mainly surface loose rocks, totally weathered and strongly weathered rocks. The in situ geo-stress field is dominated by the gravity action of rocks and therefore back analyzed using their self volumetric weight only.

(3) Excavation procedure

According to the construction schedule, the Sect. 9.9 was excavated by 12 benches from the beginning (August, 2001) to the end (September, 2003). Figure 6.33 shows the excavation benches and Table 6.7 lists the reinforcement scheme.

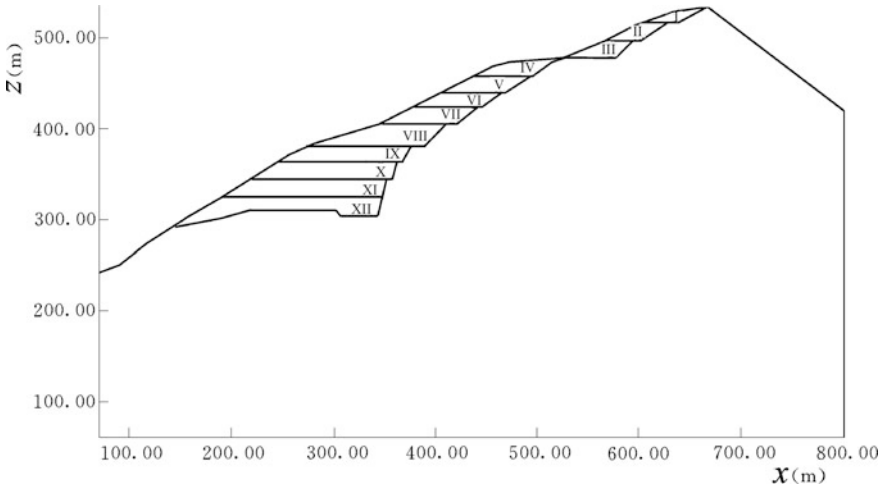

Fig. 6.33 Excavation benches

Table 6.7 Reinforcement scheme

Bench sequence	Bench elevation (m)	Pre-installed bolt	Systematic bolt	Pre-stress anchor cable
I	520.00	ϕ 32@2000–15000	ϕ25@2000 × 2000–5000	1 × 2000kN@6000
II	500.00	ϕ32@2000–15000	ϕ25@2000 × 2000–5000	1 × 2000kN@6000
III	480.00	ϕ32@2000–15000	ϕ25@2000 × 2000–5000	1 × 2000kN@6000
IV	460.00	ϕ32@4000–25000	ϕ25@2000 × 2000–5000	1 × 3000kN@6000
V	440.00	ϕ32@2000–15000	ϕ25@2000 × 2000–5000	1 × 2000kN@6000
VI	425.00	ϕ32@1500–15000	ϕ25@2000 × 2000–5000	1 × 3000kN@6000
VII	406.50	ϕ32@1500–15000	ϕ25@1500 × 1500–9000	1 × 2000kN@6000
VIII	382.00	ϕ32@1500–15000	ϕ25@2000 × 2000–5000	2 × 2000kN@6000 1 × 3000kN@6000
IX	365.00	0	ϕ25@2000 × 2000–5000	5 × 2000kN@6000
X	345.00	0	ϕ25@2000 × 2000–5000	5 × 2000kN@6000
XI	325.00	0	ϕ25@2000 × 2000–5000	4 × 2000kN@6000
XII	305.00	0	ϕ25@2000 × 2000–5000	0

(4) Computation results and discussions

The FE mesh is so discretized as to simulate all types of weathered rock, the main faults, the EDZ, the reinforcement components inclusive bolts and pre-stress stranded wire cables, and the excavation procedure step by step. The mesh contains 5068 elements and 5148 nodes (see Fig. 6.34), of which 156 are explicit elements for pre-installed bolts and cables, 1190 are implicit elements containing systematic bolts.

1. Back analysis of mechanical parameters

The back (inverse) analysis of mechanical parameters whose principles and methods will be elaborated in Chap. 7, had been carried out. The back analyzed parameters are presented in Tables 6.8 and 6.9.

2. Displacements

The displacement increments at the representative excavation bench XI and the accumulated displacements after the completion of slope excavation are displayed in Figs. 6.35 and 6.36. The incremental and accumulated displacements on the slope surface by the computation and monitor are cross-referenced in Table 6.10, in which the positivity of displacements means that u_x points inside the mountain, or u_z points upright.

The excavation induced displacements exhibit following features

– The horizontal displacements by computation and monitor generally agree with each other. However, it is a pity that there are no vertical displacement observations available for this slope section.

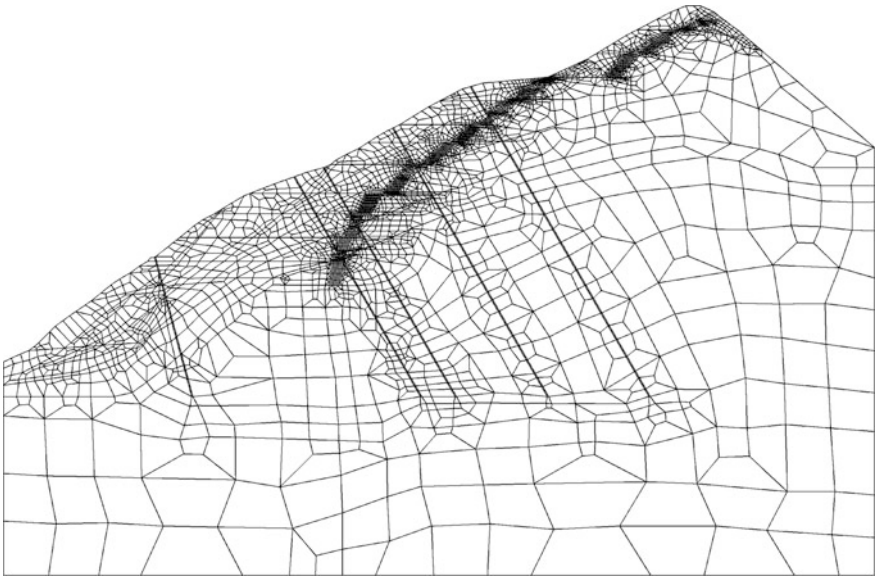

Fig. 6.34 Finite element mesh

Table 6.8 Mechanical parameters of rocks

Rock	E (MPa)	μ	c (MPa)	φ(°)	σ_T (MPa)
Eluvium	250[a]	0.35[a]	0.15[a]	24.23[a]	0.000[a]
Totally weathered	400[a]	0.34[a]	0.20[a]	26.60[a]	0.000[a]
Strongly weathered 1	1000	0.34[a]	0.20	26.60	0.100[a]
Strongly weathered 2	1250	0.34[a]	0.29	30.96	0.100[a]
Weakly weathered 1	4000	0.28[a]	0.49	34.99	0.500[a]
Weakly weathered 2	5500	0.27[a]	0.70	41.99	0.800[a]
Slightly weathered	11,000[a]	0.27[a]	0.98[a]	45.00[a]	0.800[a]
Intact	13,000[a]	0.26[a]	1.23[a]	48.50[a]	1.150[a]
Intact and integrated	15,000[a]	0.25[a]	1.48[a]	52.43[a]	1.500[a]

[a]indicates the parameter belonging with original design (without back analysis)

Table 6.9 Mechanical parameters of discontinuities

Discontinuity	c (MPa)	φ (°)
Joint in strongly weathered rock	0.200	28.000
Joint in weakly weathered rock	0.200	30.96
Joint in slightly weathered rock	0.200	30.96
Joint in intact rock	0.200	30.96
Fault	0.030[a]	14.40[a]
Gentle dip joint	0.180[a]	28.81[a]

[a]indicates the parameter belonging with original design (without back analysis)

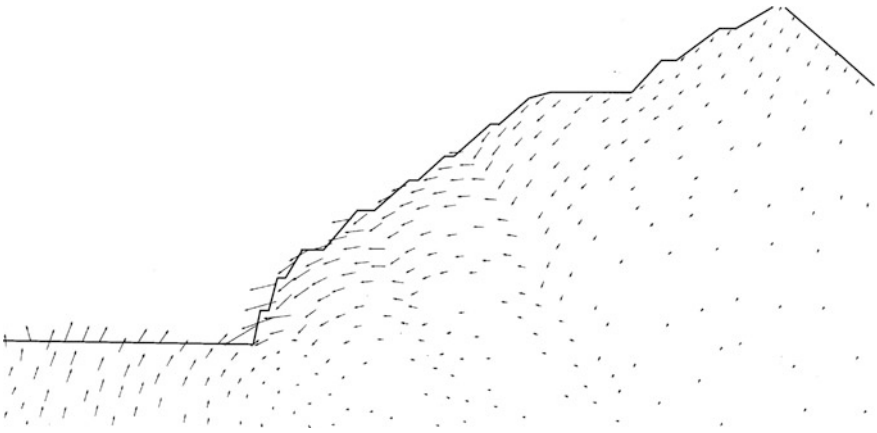

Fig. 6.35 Displacement increments (Bench XI)

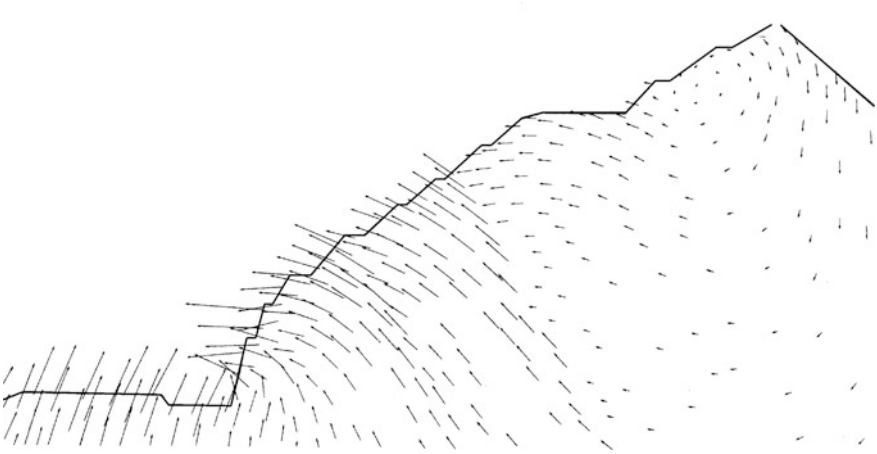

Fig. 6.36 Accumulated displacements (Bench XII)

Table 6.10 Incremental and accumulated displacements

Bench	Elevation (m)	Computation (mm)				Monitor (mm)	
		Δu_x	$\sum \Delta u_x$	Δu_z	$\sum \Delta u_z$	$\sum \Delta u_x$	$\sum \Delta u_z$
VIII	520	0.6	0.6	−0.4	−0.4	0.4	N/A
IX	520	0.5	1.1	−0.8	−1.2	−2.0	N/A
X	520	−2.1	−1.0	−3.0	−4.2	−2.5	N/A
XI	520	−3.6	−4.6	−4.8	−9.0	−3.6	N/A
	480	−8.7	−8.7	−3.6	−3.6	2.5	N/A
	425	−10.6	−10.6	−4.8	−4.8	−0.8	N/A
	382	−12.3	−12.3	−6.8	−6.8	−13.6	N/A
XII	520	−0.8	−5.4	−0.6	−9.6	Damaged	N/A
	480	−1.2	−9.9	−0.5	−4.1	Damaged	N/A
	425	−1.6	−12.2	−0.9	−5.7	Damaged	N/A
	382	−1.7	−14.0	−1.2	−8.0	Damaged	N/A

- From bench I to bench VI, the displacements on the slope surface are basically dominated by elastic rebound directing upright and into the mountain; the maximum accumulated horizontal and vertical displacements are 1.6 and 5.0 mm, respectively; from the bench VII, the displacement direction starts to shift down-and-outward, this indicates that the stability of the slope starts to undermine.
- After the completion of excavation, large accumulated displacements emerge between the EL. 305–440 m.

– The portion manifesting accumulated horizontal displacements in excessive of 20 mm is located between the EL. 305–420 m with an average depth 25.0 m; the maximum depth is 40 m at the EL. 382 m.
– Joint slippage extensively occurs in the interlayer rock masses, the maximum slippage displacement is 2 mm. This is a typical feature of slope with flexural toppling creep.

3. Stresses of bolts

Table 6.11 gives the stresses of typical bolts on 19 November 2002, when the excavation bench reached at the EL. 365 m, from the data listed in the table it may be concluded that

Table 6.11 Computed and monitored bolt's stresses

Bolt element	Elevation (m)	Computed axial stress (MPa)	Computed shear stress (MPa)	Sequence of the bolt reinforcement meter	Monitored axial stress (MPa)
3162	478.00	2.496	−1.250	AS_2^3-3	1# 14.00 2# −12.00 3# 20.00
3160		2.319	−0.300		
3157		1.852	0.250		
3155		0.868	0.439		
3152		11.143	4.549		
3093	470.00	−2.302	−0.486	AS_2^3-4	1# 1.40 2# 1.75 3# 0.35
3086		−0.652	−0.200		
3077		0.102	−0.101		
3063		0.210	−0.084		
2647		4.330	−1.322		
2577	442.00	−1.164	−2.419	AS_2^3-5	1# 4.00 2# 1.34 3# 2.84
2571		5.334	−2.374		
2568		5.582	−2.048		
2567		5.872	−1.815		
2563		5.991	−1.530		
2084	408.50	15.539	−4.446	AS_2^3-9	1# 6.67 2# 6.67 3# 0.90
2079		18.488	−4.771		
2076		18.963	−4.914		
2071		16.560	−4.951		
2056		14.966	4.342		
1919	392.00	10.748	−6.014	AS_2^3-11	1# 24.03 2# 40.05 3# 12.02
1914		13.131	−5.545		
1910		14.547	−5.157		
1907		14.507	−6.271		
1904		15.987	−5.880		

– The bolts layout horizontally are in tension but that vertically are in compression.
– The stress of bolt near the slope surface undergoes larger increase than that deeper into the slope.
– The maximum tensile stress of bolt is 20 MPa, far below from the strength of the steel bar.

4. Stresses and plastic zones in slope

Figures 6.37 and 6.38 draw the principal stresses and yield zones after the completion of slope excavation. It may be concluded that

– The maximum stress at the bottom corner (EL. 295 m) is 9.12 MPa, this concentrated stress is nearly 3.1 times the in situ geo-stress.
– There is a tensile zone between the EL. 325.0–406.5 m whose maximum depth is 12.0 m and the maximum tensile stress is 0.25 MPa.
– Interlayer slippage is the dominant factor affecting the deformation and stability of the headrace intake slope in a form of local flexural toppling. Particularly, when the excavation bench reaches down to the EL. 325 m, the slippage of interlayer and fault between the EL. 325–382 m gives rise to a penetrated bending-shear plastic zone (see the black portion in Fig. 6.38), and the likelihood of a local slip body just over the subsequently excavated intake tunnels, is rather high.

5. Remedial suggestions

– The pre-stress cable reinforcement should be strengthened, and their free length should be elongated. The depth and amount of pre-installed bolts are increased, too.
– The instrumentation system should be improved, particularly for the portion below the EL. 382 m.

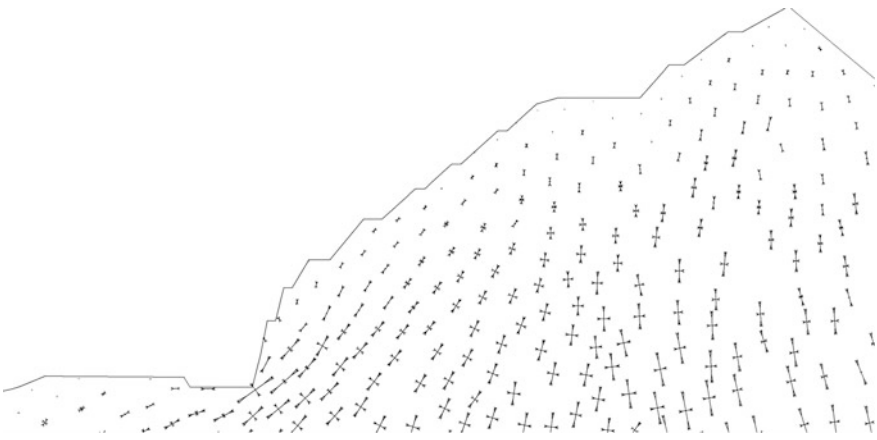

Fig. 6.37 Principal stresses (Bench XII)

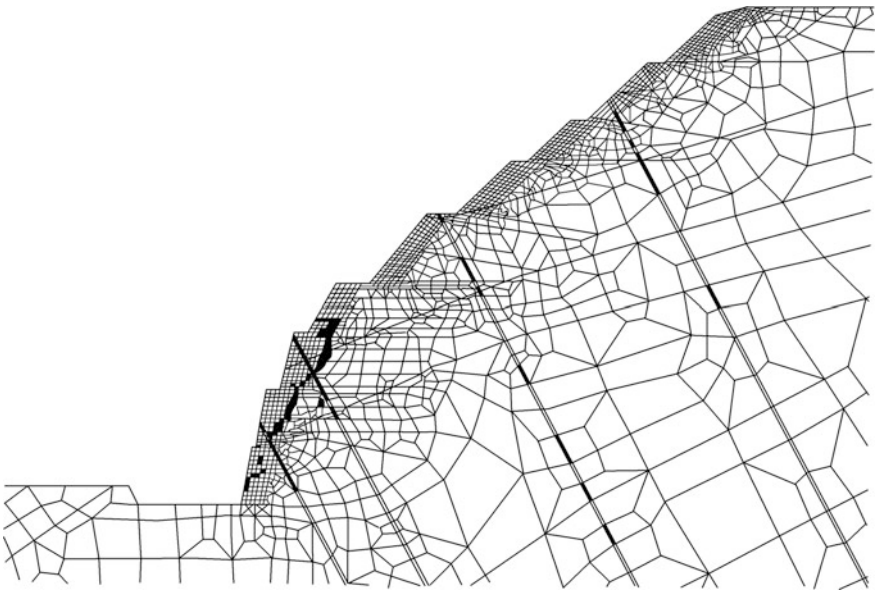

Fig. 6.38 Yield zones of faults and rock (Bench XII)

– The blast operation, particularly for the portion below the EL. 382 m and beneath the intake tunnel portal, should be controlled more strictly than beforehand stipulated according to the conventional construction regulations.

These suggestions had been accepted and observed by the designer and contractor, the slope had been cut successfully and has been in service normally insofar.

6.6.3 Dam Foundation: Xiaoxi Project, China

(1) Presentation of the project

Rock bolt reinforcement is also applicable to concrete dam foundation, particularly during the excavation when it is found that the geological conditions are much more adverse than anticipated. If the evidences indicate that the foundation grouting has limited improvements, the deeper excavation and the dam body enlargement are also restrained by the cofferdams, this countermeasure exhibits remarkable advantages. The pioneering work of rock bolt reinforcement for dam foundation is Tirso Gravity Dam (Italy) (Egger 1992) whose foundation rocks are composed of micaschist, gneiss and granite. After the excavation down to the dam base level, it was found that the rock was strongly weathered and poor in quality, therefore the

rock bolt reinforcement on the whole foundation (20,000 m^2) was installed. This dam has been completed and operated normally.

In China, a number of concrete dams were installed with rock bolts in the foundations, but in the design phases they were not taken into account for the safety margin calibration, and the bolting parameters (e.g. inclination, diameter, length) were not designed deliberately. Xiaoxi Hydropower Project (XHP) is the first concrete dam installed with rock bolts as the principal measure for the foundation stabilization in China.

Xiaoxi Dam is located at the middle reach of the Zijiang River, Hunan Province, China. The normal storage level (NSL) (normal water level, NWL) is 198.0 m corresponding to a total reservoir capacity of 141 million m^3, the installed generator capacity is 135 MW. From right bank to left bank the project is sequentially layout in a manner of (see Fig. 6.39a) power house monoliths + spillway monoliths + solid dam monoliths.

(2) Characteristics of the computation

The rock masses are mainly Cambrian system (∈) and Devonian system (D) whose deformation and strength parameters are listed in Table 6.12. There are 11 faults near or beneath the foundation, of which the largest one is the regional fault F_1 passing through the center of the river bed (see Fig. 6.39b). Nearly all the 8 spillway dam monoliths are located on this regional fault which dips to the left bank (dip angle 67°–78°) and has a cracked zone of 180 m wide. In the fault F_1 there are irregularly distributed black limestone lenses, calcareous shale intercalated with limestone lenses, quartz sandstone intercalated with shale lenses, argillaceous siltite intercalated with shale lenses, carbon slurry plate shale intercalated with calcite gangues and conglomerations. Their deformation and strength parameters are listed in the Table 6.12, too.

Since the fault F_1 may result in serious problems of uneven settlement and low stability with the dam foundation, in addition to conventional laboratory and field tests conducted in the design phases, field direct shear tests and ultrasonic wave inspections were also undertaken particularly within the fault F_1 before the placement of dam concrete (see Table 6.13).

The purpose of direct shear testing is to evaluate the shear resistance of dam/foundation interface (Lo et al. 1991). Each group of direct shear tests intended to determine the deformation/strength properties of concrete/rock interface comprises 5 samples, whereas each group of direct shear tests for determining the deformation/strength properties of rock/rock interface comprises 6 samples. The sample size is 20 cm × 15 cm × 20 cm (length × width × height), and the maximum normal stress is $\sigma_{max} = 0.3$MPa. The testing configuration and procedure are stipulated by the GB/T50266.99 (1999). The test results revealed that a majority of sliding failures occurred 2–10 cm beneath the concrete/rock interface, leading to a shear strength nearly identical to that of rock/rock interface, i.e. the shear resistance of the dam/foundation interface at the fault F_1 is totally dominated by the shear strength of rock itself.

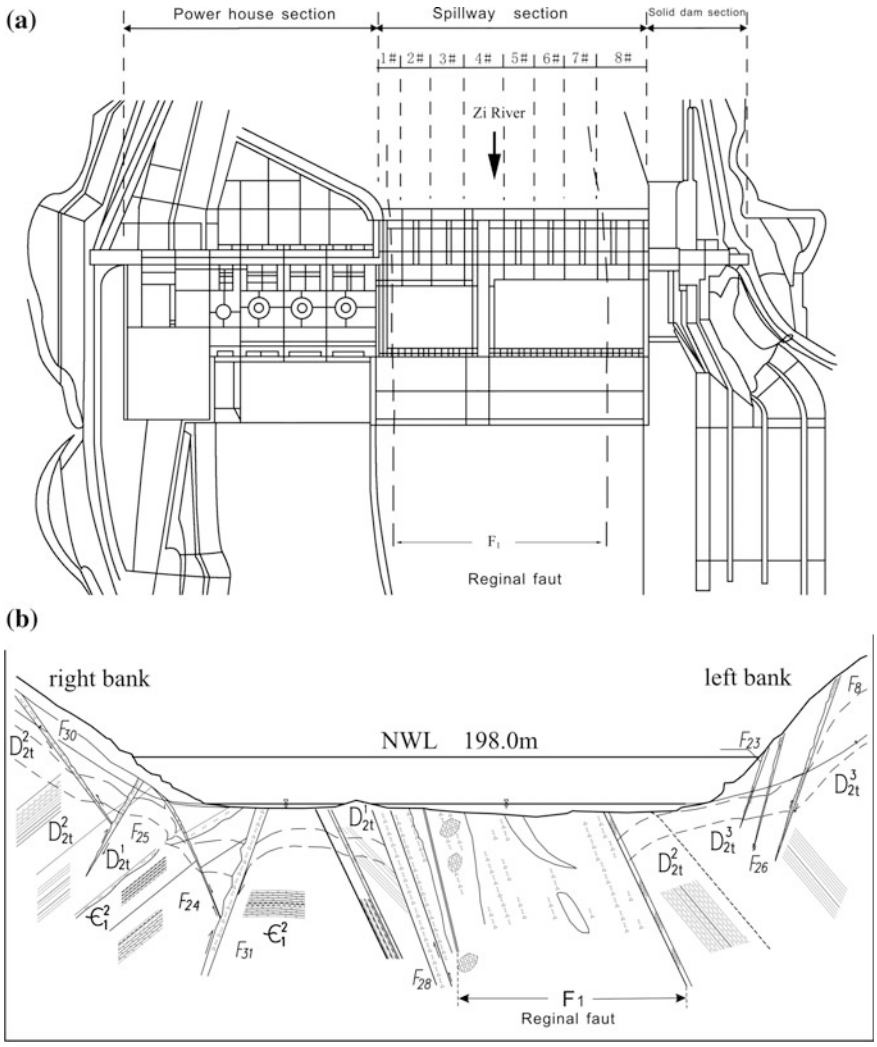

Fig. 6.39 Xiaoxi Hydropower Project, China. **a** Layout of the project; **b** geology section along the dam axis (downstream view)

The main purpose of the ultrasonic wave inspections is to evaluate the effectiveness of consolidation grouting. Each group of ultrasonic inspections using longitudinal wave comprises through-transmission between three vertical boreholes triangularly arranged, the distance and depth of the boreholes are 1.2–3 m and 7–18 m, respectively. The result data showed an average speed V_p = 2450–3440 m/s before the consolidation grouting. The grouting could raise the V_p by 5.6–12.6%, which means that the effectiveness of the consolidation grouting is not very remarkable for the fault F_1.

Table 6.12 Mechanical parameters of foundation rock masses

Rock formation	Rock type	Young's modulus E (GPa)	Poisson's ratio μ	Cohesion c (MPa)	Friction angle φ (°)	Volumetric weight (MN/m^3)
$\in_1^2$	Siliceous plate shale	0.45	0.3	0.45	36.9	0.025
	Carbon slurry plate shale	0.5	0.3	0.15	24.2	0.026
$\in^2$	Black limestone lens	7	0.3	0.75	43.5	0.027
	Calcareous shale intercalated with limestone lens	4.2	0.3	0.42	33.0	0.027
D_{2t}^1 D_{2t}^3	Quartz sandstone intercalated with shale lens	4.5	0.3	0.45	35.8	0.027
D_{2t}^2	Argillaceous siltite intercalated with shale lens	4.0	0.3	0.4	35.0	0.25
Rock within the fractured and disturbed zone of the fault F_1	Quartz sandstone intercalated with shale lens	1.2	0.3	0.2	29.2	0.026
	Quartz sandstone intercalated with shale lens	1.1	0.3	0.18	27.5	0.026
	Argillaceous siltite intercalated with shale lens	0.65	0.35	0.15	27.5	0.025
	Argillaceous siltite intercalated with shale lens	0.6	0.35	0.13	25.6	0.025
	Carbon slurry plate shale intercalated with calcite gangues and conglomerations	0.35	0.35	0.05	19.3	0.026
	Siliceous plate shale intercalated with limestone lens	0.63	0.35	0.15	26.6	0.025
	Silicalite lens	1	0.3	0.18	28.4	0.026

Table 6.13 Additional field tests conducted before the placement of concrete

Rock	Test type		
	Direct shear test		Ultrasonic wave inspections
	Concrete/rock interface	Rock/rock interface	
Before consolidation grouting	1 (group)	2 (group)	51 (group)
After consolidation grouting	1 (group)	0	35 (group)

Since the rocks in the fault F_1 are weak and irregularly distributed, and the shear resistance of the dam/foundation interface is mainly dominated by the rocks, therefore the shear strength parameters of the dam/foundation interface (see Table 6.14) are evaluated as average values of shear properties according to the daylight area proportions of rocks on the dam foundation surface.

(3) Stability analysis using the gravity method: before bolting

In the gravity method, sliding stability is calibrated in terms of a face FOS against sliding [see Eq. (4.217)]. When the potential sliding surface is horizontal, this face FOS particularly termed as K' in China's design specifications is defined as the ratio of the total resistance to the resultant horizontal loads

$$K' = \frac{f'(\sum V - U) + c'A}{\sum H} \tag{6.67}$$

where f' = shear friction factor;c' = shear cohesion factor; A = area of sliding surface; $\sum H$ = resultant horizontal loads; $\sum V$ = resultant vertical loads; U = uplift.

Applied to a concrete gravity dam, K' on a horizontal plane should not be lower than 3.0 for the normal load combinations. K' should not be lower than 2.5 under the extreme load combinations. When seismic effect is taken into account, K' should be at least higher than 2.3 (Chen 2015).

To guarantee the stability of the dam foundation, the designer had proposed and implemented a series of stabilization measures such as:

Table 6.14 Average shear strength parameters of the dam/rock interface before reinforcement

Parameters	Dam monolith							
	$1^{\#}$	$2^{\#}$	$3^{\#}$	$4^{\#}$	$5^{\#}$	$6^{\#}$	$7^{\#}$	$8^{\#}$
Friction coefficient f'	0.537	0.511	0.492	0.525	0.532	0.529	0.526	0.643
Cohesion c' (MPa)	0.186	0.155	0.159	0.168	0.167	0.161	0.174	0.387

– Enlarge the dam section, move the grout curtain towards upstream, intensify drainage all over the dam foundation. These provisions were expected to increase the vertical force, and in turn, the slide resistance in Eq. (6.67);
– Excavate the dam foundation dipping in the direction of upstream, which was expected to bring down the slide driving force in Eq. (6.67);
– Link the dam body with the downstream still basin and approaching walls, to make use of their additional resistance.

Two important load combinations are considered in the stability calibration of the dam.

– The normal load combination includes

Gravity + silt pressure from the reservoir + static hydraulic pressure from the reservoir and tail water at the NSL + uplift at the NSL + wave pressure at the NSL.

In this case the safety factor K' should not be lower than 3.0 stipulated by the design specifications.

– The extreme (special) load combination includes

Gravity + silt pressure from the reservoir + static hydraulic pressure from the reservoir and tail water at the reservoir level during the catastrophe flood + uplift at the reservoir level during the catastrophe flood + wave pressure at the reservoir level during the catastrophe flood.

In this case the safety factor K' should not be lower than 2.5 stipulated by the design specifications.

According to the shear strength parameters in Table 6.14 and by the formula in Eq. (6.67), the safety factors K' against the sliding of spillway dam monoliths $2^{\#}$–$7^{\#}$ are not satisfied (see Table 6.15).

The computation results made the point that since the cofferdams had been completed when the poor characteristics of the fault F_1 were fully understood, all the above measures merely had limited effectiveness in the improvement of the dam stability because of the limited space within the cofferdams.

Eventually, the rock bolt reinforcement had to be adopted. Since the key issue in the reinforcement design using the gravity method is to determine the contribution from rock bolts to the shear cohesion c' in Eq. (6.67), hence supplementary field direct shear tests with regard to bolting effects had been undertaken to safeguard the reinforcement design.

Table 6.15 Stability safety factors against sliding by the gravity method: before bolting

Dam monolith	$1^{\#}$	$2^{\#}$	$3^{\#}$	$4^{\#}$	$5^{\#}$	$6^{\#}$	$7^{\#}$	$8^{\#}$
Normal load combination	3.29	2.20	2.09	2.71	2.37	2.32	2.49	3.26
Extreme load combination	2.95	2.09	1.98	2.28	2.22	2.17	2.34	3.24

(4) In situ tests of bolted rock masses

1. Semi-empirical formula for bolting effects

The semi-empirical formula to determine the reinforcement effect using the index T_0 was proposed by Spang and Egger (1990)

$$T_0 = P_t[1.55 + 0.011\sigma_c^{1.07}\sin^2(\alpha+\phi)]\sigma_c^{-0.14}(0.85 + 0.45\tan\varphi) \tag{6.68}$$

where T_0 = shear resistance due to the rock bolt ($T_0 = T - T_N$), MN; T = shear force acting along a definite rock joint or slip surface containing bolts, MN; T_N = shear resistance of the joint or slip surface without bolt, MN;P_t = tensile strength of the bolt, MPa; σ_c = compressive strength of the rock, MPa; ϕ and φ = dilation angle and friction angle of the rock joint or potential sliding surface, °; α = inclination of the bolt, °.

Equation (6.68) is subject to the following conditions (Spang and Egger 1990):

- Rock bolt is made of plain steel bar or screwed reinforcement bar, and is grouted by cement mortar;
- The diameter of the drill hole is approximately twice that of the bolt;
- The compressive strength of the rock mass is $\sigma_c > 10$ MPa;
- The inclination of the bolt is $0° \le \alpha \le 45°$.

For important project where it is possible, a series of field tests is desirable to validate the formula in Eq. (6.68) and adjust the related parameters.

2. Test configuration

In situ direct shear tests were carried out just before the final design phase of the bolting reinforcement for the spillway foundation. These direct shear tests are intended to check the semi-empirical formula in Eq. (6.68), which is paramount crucial to the design of bolted foundation. Three large direct shear samples of bolted rock masses were processed, accompanied with one large direct shear sample without bolt. These test samples are located on the rocks of siltite and cataclasite within the fault F_1 under spillway dam section $1^{\#}$–$3^{\#}$, respectively.

The sample size is 100 cm (length) × 80 cm (width) × 100 cm (height), and is made of concrete identical to that of the dam. The bolting parameters are listed in Table 6.16. Figure 6.40 shows the configuration of the test.

Table 6.16 Bolting parameters of in situ test samples

Sample's sequence		$1^{\#}$	$2^{\#}$	$3^{\#}$
Bolting parameters	Diameter of steel bar (mm)	1Φ36	2Φ36	3Φ36
	Inclination of steel bar (°)	15	25	15
	Length of steel bar (m)	9	12	16
	Diameter of the borehole (mm)	75	110	110

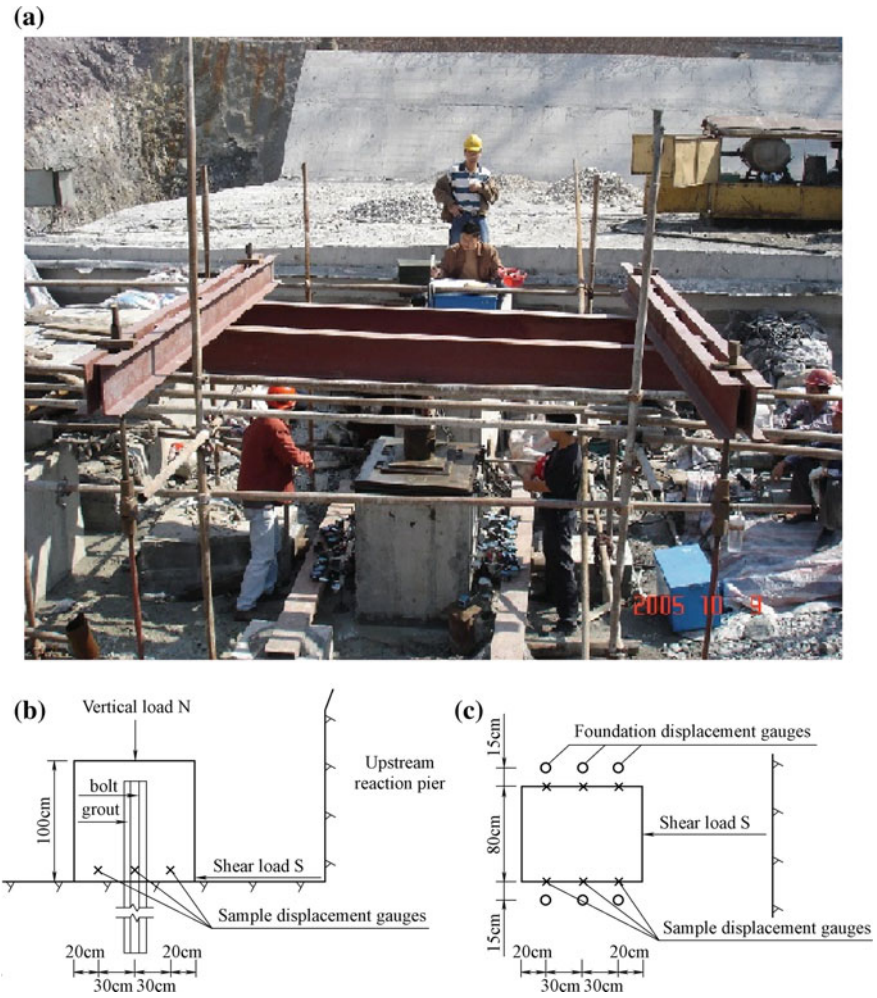

Fig. 6.40 Configuration of the field shear test. **a** Photo; **b** left side view; **c** plan view

The vertical pressure on the top of samples is supplied by one jack, the reaction of this pressure is transferred to the ground through four rock bolts around the sample (9 m long, diameter 2Φ32). The maximum vertical pressure is $\sigma_{max} = 0.3$ MPa and the corresponding maximum vertical load is $N_{max} = 0.3\ \text{MPa} \times 1\ \text{m} \times 0.8\ \text{m} = 0.24$ MN.

The horizontal shear force is applied by two jacks (maximum shear load $S_{max} = 2 \times 3$ MN) installed at the upstream side of the sample, the reaction of this pressure is transferred to the ground through the reaction pier excavated in the rock.

At both the left and right sides of the sample there are three gauge points lined-up from upstream to downstream, which are used to monitor the horizontal

and vertical displacements. These gauges are installed at the level of the third height of the sample. To monitor the foundation displacement which is necessary for the evaluation of the relative shear displacement between sample and foundation, gauges are also installed at the foundation rock surface.

3. Test procedure and results

The vertical pressure ($\sigma_{\max} = 0.3$ MPa) is exerted in 5 incremental steps, in each step the pressure should be maintained for a period of at least 10 min, during which at least two readings are taken. If the displacement difference between these readings is smaller than 0.1 mm, the pressure is raised up to the next step of loading.

When the vertical pressure reaches $\sigma_{\max} = 0.3$ MPa, the gauges are adjusted to zero as new initial reading, then the horizontal shear stress starts to apply in step sequences. In each step, at least 20 min is demanded to maintain the pressure, during which at least five readings are taken. If the displacement difference is smaller than 0.1 mm, the pressure is raised to the next step of loading.

From the direct shear test sample without bolt, the average shear strength at the concrete/rock interface is 0.61 MPa, i.e. the shear resistance without bolt is $T_N = 0.61\ \text{MPa} \times 1\ \text{m}\,(length) \times 0.8\ \text{m}\,(width) = 0.488\ \text{MN}$.

Three different scenarios in the samples containing bolt are observed:

- Sample $1^{\#}$. When the shear stress at concrete/rock interface reached 1.559 MPa (i.e. $T = 1.559\ \text{MPa} \times 1\ \text{m}\,(length) \times 0.8\ \text{m}\,(width) = 1.247\ \text{MN}$), the displacements mounted suddenly after 8 min, accompanied with the decrease of shear stress down to 1.427 MPa. In the attempt to raise the pressure of the horizontal jacks, a loud bang accompanied with further dramatic drop of the horizontal pressure ended the test. This is a very successful sample, by which the deformation and failure of the bolted rock are well documented. The shear resistance contributed from the bolt is $T_0 = T - T_N = 0.759\,\text{MN}$.
- Sample $2^{\#}$. When the shear stress at the concrete/rock interface reached 1.888 MPa (i.e.$T = 1.888\ \text{MPa} \times 1\ \text{m}\,(length) \times 0.8\,\text{m}\,(width) = 1.510\,\text{MN}$), the reaction pier supporting the horizontal jacks failed, leading to an unexpected ending of the test. This is not a very successful sample since the ultimate shear strength contributed from bolt cannot be pinpointed. However, it infers that the ultimate shear strength of the bolted sample should be higher than 1.888 MPa, i.e. the shear resistance contributed from the bolt is $T_0 = T - T_N \geq 1.022$ MN.
- Sample $3^{\#}$. When the shear stress at the concrete/rock interface reached 1.386 MPa (i.e. $T = 1.386\ \text{MPa} \times 1\,\text{m}\,(length) \times 0.8\,\text{m}\,(width) = 1.109\,\text{MN}$), the concrete sample itself cracked, and the test had to be stopped. This test did not provide reasonable information concerning the ultimate shear strength of the bolted sample. However, it provide a lower bound of T_0 that $T_0 = T - T_N \geq 0.661$ MN.

The relations of shear stress versus shear displacement are plotted in Figs. 6.41, 6.42 and 6.43. The displacements of the foundation surface are given in these figures, too, which can be used to calculate the relative displacement between the sample and the foundation.

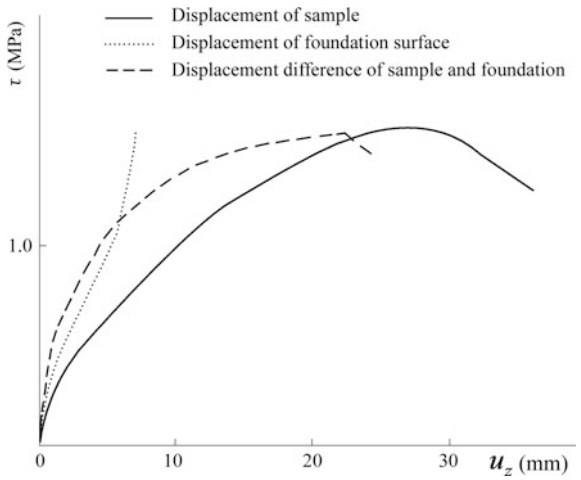

Fig. 6.41 Shear stress versus shear displacement: sample 1#

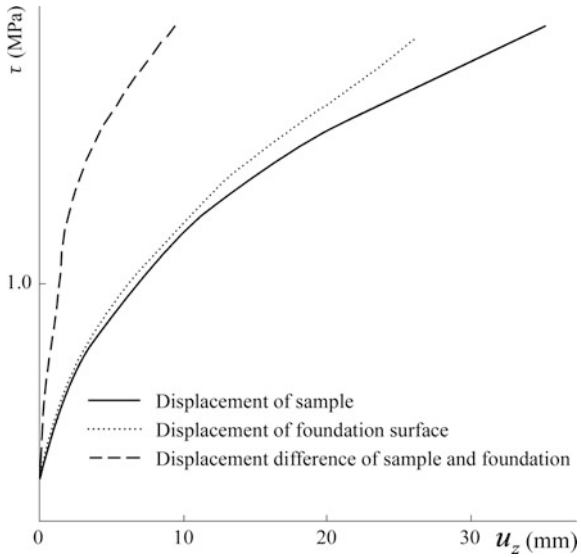

Fig. 6.42 Shear stress versus shear displacement: sample 2#

A cross-reference of the shear resistance due to the bolt (T_0) by the foregoing direct shear tests and the semi-empirical formula [see Eq. (6.68)] is made in Table 6.17. As has been explained above, sample 3# provides lower contribution of bolt to the shear strength, because of too early termination of the test due to sample concrete rupture.

(5) Reinforcement design

The total length of the 8 spillway dam monoliths is 142.5 m. With the average shear strength parameters of the foundation rocks in Table 6.14 and taking into account of all the aforementioned measures for dam stability apart from bolting, the safety

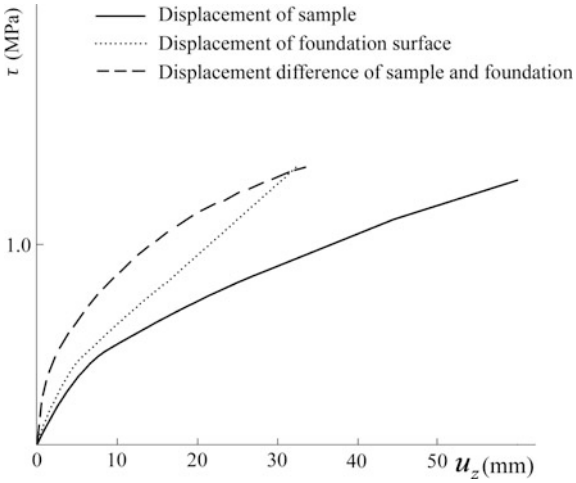

Fig. 6.43 Shear stress versus shear displacement: sample 3#

Table 6.17 Shear resistance by the direct shear tests and the semi-empirical formula

Sample sequence		1#	2#	3#
Shear resistance T_0 (kN)	In-situ direct shear test	759	≥1022	≥661
	Semi-empirical formula [see Eq. (6.68)]	389	790	1168
	Difference in the test and the formula (%)	+95	≥+29	≤−47

factors of the spillway dam monoliths 2#–7# against sliding are not satisfactory (see Table 6.15). Therefore, rock bolts are installed in the foundation of these dam monoliths (see Figs. 6.44 and 6.45).

Each rock bolt (3Φ32@2 m) is made of three steel bars with diameter of 32 mm. The distance between rock bolts is 2 m. The length of bolts is 12 m, of which 10.5 m is in the rock and 1.2 m is in the dam. The boreholes for bolt installation are Φ130 in the diameter, their inclinations are alternatively varied (15° or 25°).

(6) Stability analysis using the gravity method: after bolting

Supposing the control area per bolt is S, the contribution of a bolt can be thought of as the additional cohesion c_b to a joint or slip surface

$$c_b = T_0/S \tag{6.69}$$

Hence the factor of safety against sliding is calculated by the formula

$$K' = \frac{f'(\sum V - U) + c'A + c_bA}{\sum H} \tag{6.70}$$

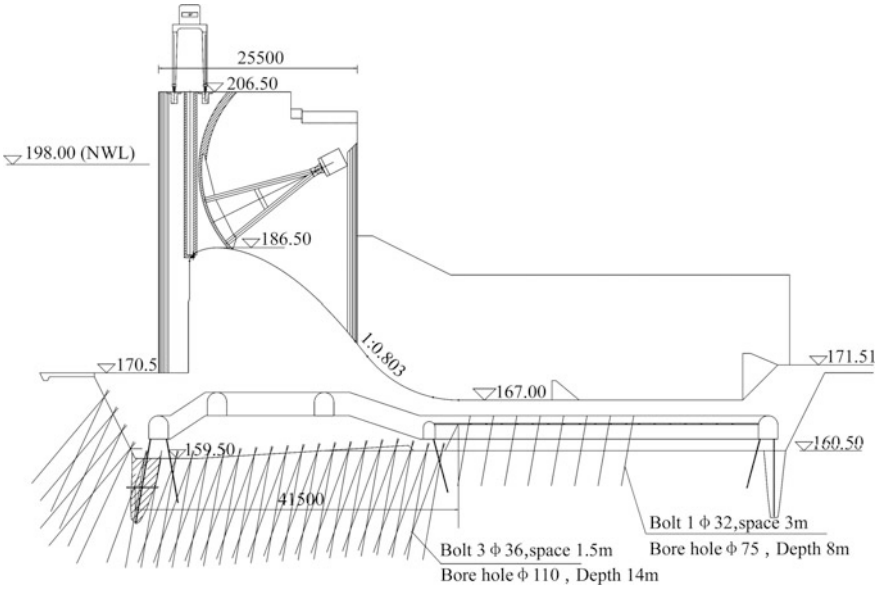

Fig. 6.44 Layout of the rock bolts at the spillway dam foundation

Fig. 6.45 Rock bolts under the construction

Table 6.18 Equivalent shear cohesion c_b contributed from the bolts

Arrangement of bolts	Inclination angle (°)	Shear force T_0 (kN)	Shear cohesion c_b (kPa)
Three steel bars with diameter of 32 mm; the distance between rock bolts is 2 m (3Φ32@2 m)	15	878	110
	25	886	

Table 6.19 Stability safety factors against sliding by the gravity method: after bolting

Dam monolith	$1^{\#}$	$2^{\#}$	$3^{\#}$	$4^{\#}$	$5^{\#}$	$6^{\#}$	$7^{\#}$	$8^{\#}$
Normal load combination	–	3.20	3.08	3.40	3.04	2.99	3.16	–
Extreme load combination	–	3.09	2.97	2.93	2.91	2.86	3.02	–

The equivalent shear cohesion c_b contributed from the bolts in Table 6.18 is evaluated by the semi-empirical Eqs. (6.68) and (6.69).

Table 6.19 lists the safety factors against sliding after bolting. It is happy that with all the countermeasures taken into account including the bolt reinforcement, the spillway dam monoliths $2^{\#}$–$7^{\#}$ satisfy the safety criterion stipulated in the design specifications. Since a portion of the dam monoliths $1^{\#}$ and $8^{\#}$ is already located outside of the fault F_1, their safety standard is met without bolts.

(7) Stability analysis using the finite element method

The 8 spillway dam monoliths including their foundation are discretized into 351,703 hexahedral or tetrahedral elements (foundation 291,235, dam body 60,468) and 369,042 nodes (see Fig. 6.46).

The loads exerted on the dam/foundation are in situ geo-stresses calculated by the volumetric weight of the rocks and lateral pressure ratio $K_0 = 0.47$; seepage forces in the foundation calculated by the FEM (the hydraulic potential in the foundation is plotted in Fig. 6.47); dam weight calculated by the volumetric weight of concrete; hydraulic pressure calculated by the static water pressure under the actions of NSL and correspondent tail water level.

Three cases are analyzed using the FEM with regard to the NSL.

- Case 1. Without bolt reinforcement, the 8 spillway dam monoliths work independently (the transverse joints are permanent without closure grouting).
- Case 2. With bolt reinforcement, the 8 spillway dam monoliths work independently (the transverse joints are permanent without closure grouting).
- Case 3. With bolt reinforcement, the 8 spillway dam monoliths are linked by closure grouting the key slots and installing steel bars through the transverse joints.

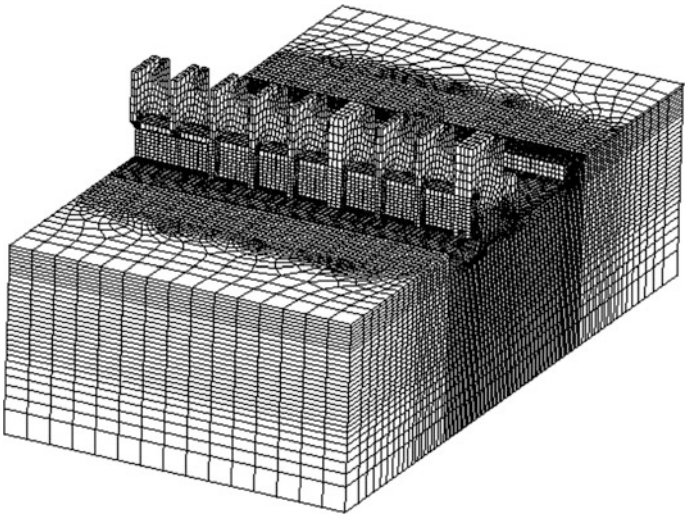

Fig. 6.46 FE mesh of the spillway dam and foundation

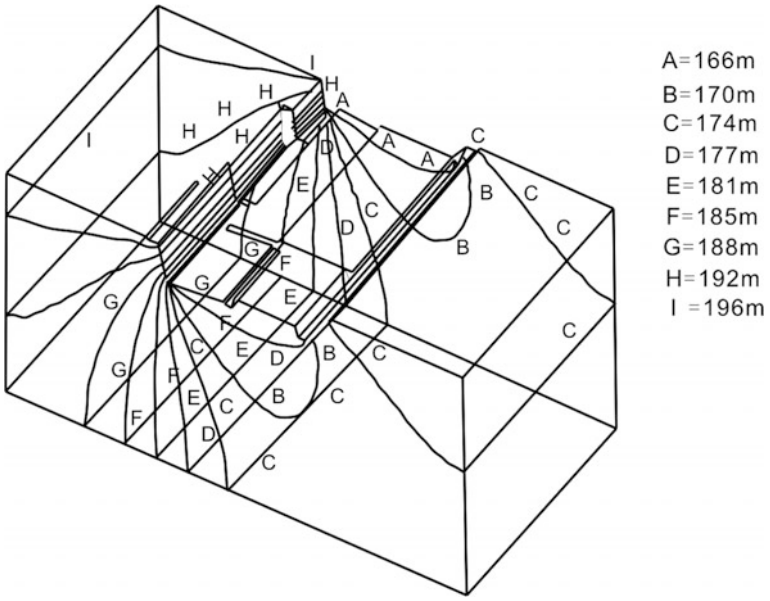

Fig. 6.47 Contours of the hydraulic potential in the foundation

1. Displacements

– Case 1. The maximum displacement towards downstream is 13 mm.
– Case 2. The maximum displacement towards downstream is reduced to 12 mm.
– Case 3. The maximum displacement towards downstream is further reduced to 3.2 mm.

2. Stresses

The maximum tensile and compressive stresses at the dam heel and toe are critical strength indices for gravity dam design. By the computation it is found that

– Case 1. The maximum tensile and compressive stresses under the NSL are 1.22 and −10.3 MPa, respectively.
– Case 2. The bolts can "homogenize" the stress distribution in the straggly interpenetrated rock fault. The maximum tensile and compressive stresses under the NSL are reduced to 1.19 and −8.99 MPa, respectively.
– Case 3. The stress distribution at the dam foundation can be further "homogenized" by the closure of the transverse joints. In this case the maximum tensile and compressive stresses under the NSL are further reduced to 1.06 and −4.83 MPa, respectively.

3. Stability

The strength reduction factor is employed as the safety index instead of conventional overloading factor, this is mainly due to the worry over the abnormally poor of the foundation geologic conditions.

– Case 1. The minimum strength reduction factor is approximately 2.0, which is much lower than 3.0 stipulated in the design specifications.
– Case 2. The bolts can increase the minimum strength reduction factor up to approximately 2.8. These indices are not far from 3.0 stipulated in the design specifications.
– Case 3. The overall strength reduction factor of the spillway comprising 8 dam monoliths with closed transverse joints can be further raised up to approximately 3.5.

Fig. 6.48 Xiaoxi project in service

The dam with bolted foundation was accomplished and started operation in January, 2008 (see Fig. 6.48). Insofar it has been performing well. For example, the monitored displacements are within the range of computational data; there are no serious cracks and leakage in the dam and foundation.

The final account of the bolt reinforcement cost is approximately 38 Million RMB (5.7 Million USD).

References

Aydan O. The stabilisation of rock engineering structures by rockbolts. Ph.D. thesis, Nagoya University, Japan; 1989.

Aydan O, Kyoya T, Ichikawa Y, Kawamoto T. Anchorage performance and reinforcement effects of fully grouted rockbolts on rock excavations. In: Proceedings of the 6th ISRM congress (vol. 2). Montreal: ISRM; 1987. p. 757–60.

Aydan O, Sezaki M, Kawamoto T. Mechanical and numerical modelling of shotcrete. In: Pande GN, Pietruszcak S, editors. NUMOG IV—international symposium on numerical models in geomechanics. Rotterdam: AA Balkema; 1992. p. 757–64.

Azuar JJ. Stabilisation de massifs rocheux fissures par barres d'acier scellees. Rapport de recherche No. 73. Paris: Laboratoire Central des Ponts et Chaussees; 1977.

Barley AD. Properties of anchor grout in a confined state. In: Littlejohn GS, editor. Ground anchorages and anchored structures—Proceedings of the international conference on institution of civil engineers (ICE). London: Thomas Telford; 1997a. p. 13–22.

Barley AD. The single bore multiple anchor system. In: Littlejohn GS, editor. Ground anchorages and anchored structures—Proceedings of the international conference on institution of civil engineers (ICE). London: Thomas Telford; 1997b. p. 67–75.

Bawden WF, Hyett AJ, Lausch P. An experimental procedure for the in situ testing of cable bolts. Int J Rock Mech Min Sci Geomech Abstr. 1992;29(5):525–33.

Beer G. An isoparametric joint/interface element for finite element analysis. Int J Numer Methods Eng. 1985;21(4):585–600.

Benmokrane B, Chekired M, Xu H. Monitoring behavior of grouted anchors using vibrating-wire gauges. J Geotech Eng ASCE. 1995a;121(6):466–75.

Benmokrane B, Chennouf A, Mitri HS. Laboratory evaluation of cement based grouts and grouted rock anchors. Int J Rock Mech Min Sci Geomech Abstr. 1995b;32(7):633–42.

Bickel JO, Kuesel TR, King EH. Tunnel engineering handbook. 2nd ed. New York: Chapman & Hall; 1996.

Bjurstrom S. Shear strength of hard rock jointed reinforced by grouted untensioned bolts. In: Proceedings of the 3rd ISRM congress (vol. 2). Washington: National Academy of Science; 1974. p. 1194–9.

Briaud JL, Powers WF, Weatherby DE. Should grouted anchors have short tendon bond length? J Geotech Geoenviron Eng ASCE. 1998;124(2):110–9.

Chen SH. Hydraulic structures. Berlin: Springer; 2015.

Chen SH, Egger P. Elasto-viscoplastic distinct modelling of bolt in jointed rock masses. In: Yuan JX, editor. Proceedings of the computer methods and advance in geomechanics. Wuhan, Rotterdam: AA Balkema; 1997. p. 1985–90.

Chen SH, Egger P. Three dimensional elasto-viscoplastic finite element analysis of reinforced rock masses and its application. Int J Numer Anal Methods Geomech. 1999;23(1):61–78.

Chen SH, Pande GN. Rheological model and finite element analysis of jointed rock masses reinforced by passive, fully-grouted bolts. Int J Rock Mech Min Sci Geomech Abstr. 1994;31 (3):273–7.

Chen SH, Fu CH, Shahrour I. Finite element analysis of jointed rock masses reinforced by fully-grouted bolts and shotcrete lining. Int J Rock Mech Min Sci. 2009;46(1):19–30.

Chen SH, Zhang X, Shahrour I. Composite element model for the bonded anchorage head of stranded wire cable in tension. Int J Numer Anal Methods Geomech. 2015;39(12):1352–68.

Desai CS, Zaman MM, Lightner JG, Siriwardane HJ. Thin-layer element for interfaces and joints. Int J Numer Anal Methods Geomech. 1984;8(1):19–43.

Desai CS, Muqtadir A, Scheele F. Interaction analysis of anchor-soil systems. J Geotech Eng ASCE. 1986;112(5):537–53.

Egger P. Ground improvement by passive rock bolts, experimental and theoretical studies, example. Memorie GEAM. 1992;29(1):5–10.

Egger P, Fernandes H. Nouvelle presse triaxiale-etude de modeles discontinus boulonnes. In: Proceedings of the 5th ISRM congress (vol. 1, Theme A). Melbourne: Brown Prior Anderson Pty Ltd.; 1983. p. A171–5.

Egger P, Pellet F. Strength and deformation properties of reinforced jointed media under true triaxial conditions. In: Wittke W, editor. Proceedings of the 7th ISRM congress. Rotterdam: AA Balkema; 1991. p. 215–20.

Egger P, Zabuski L. Behaviour of rough bolted joints in direct shear tests. In: Wittke W, editor. Proceedings of the 7th ISRM congress. Rotterdam: AA Balkema; 1991. p. 1285–8.

Fuller PG, Cox RHT. Mechanics of load transfer from steel tendons to cement based grout. In: Grundy P, Stevens LK, editors. Proceedings of the 5th Australian conference on the mechanics of structures and materials. Melbourne: Melbourne and Monash Universities; 1975. p. 189–203.

Ghaboussi J, Wilson EL, Isenberg J. Finite element for rock joint interfaces. J Soil Mech Found Div ASCE. 1973;99(SM10):833–48.

Goodman RE, Taylor RL, Brekke TL. A model for the mechanics of jointed rock. J Soil Mech Found Div ASCE. 1968;94(SM3):637–59.

Goris JM, Conway JP. Grouted flexible tendons and scaling investigation. In: Proceedings of the 13th world mining congress. Rotterdam: AA Balkema; 1987. p. 783–92.

Grasselli G. 3D behaviour of bolted rock joints: experimental and numerical study. Int J Rock Mech Min Sci. 2005;42(1):13–24.

Griffiths DV. Numerical modeling of interfaces using conventional finite element. In: Kawamoto T, Ichikawa Y, editors. Proceedings of the 4th international conference on numerical methods in geomechanics. Rotterdam: AA Balkema; 1985. p. 837–44.

Hagenhofer F. NATM for tunnels with high overburden. Tunnels Tunn. 1990;22(5):51–2.

Hassani FP, Rajaie H. An investigation into the optimization of a shotcrete cable bolt support systems. In: Proceedings of the 14th congress of the Council of Mining and Metallurgical Institution. London: IMM; 1990. p. 119–29.

Hassani FP, Mitri HS, Khan UH, Rajaie H. Experimental and numerical studies of cable bolt support systems. In: Kaiser PK, McCreath DR, editors. Proceedings of the international symposium on rock supports in mining and underground construction. Rotterdam: AA Balkema; 1992. p. 411–7.

Haykin S. Neural networks: a comprehensive foundation. New Jersey: Prentice Hall; 1999.

Hermann LR. Finite element analysis of contact problems. J Soil Mech Found Div ASCE. 1978;104(EM5):1043–57.

Hoek E, Bray JW. Rock slope engineering. 3rd edition. London: Institute of Mining and Metallurgy; 1981.

Hyett AJ, Bawden WF, Reichert RD. The effect of rock mass confinement and the bond strength of fully grouted cable bolts. Int J Rock Mech Min Sci Geomech Abstr. 1992;29(5):503–24.

Hyett AJ, Bawden WF, Macsporran GR, Moosavi M. A constitutive law for bond failure of fully grouted cable bolts using a modified Hoek cell. Int J Rock Mech Min Sci Geomech Abstr. 1995;32(1):12–36.

Jalalifar H, Aziz N. Analytical behaviour of bolt-joint intersection under lateral loading conditions. Rock Mech Rock Eng. 2010a;43(1):89–94.

Jalalifar H, Aziz N. Experimental and 3D numerical simulation of reinforced shear joints. Rock Mech Rock Eng. 2010b;43(1):95–103.

Jarrel DJ, Haberfield CM. Tendon/Grout interface performance in grouted anchors. In: Proceedings of the conference on ground anchorages and anchored structures. London: Institution of Civil Engineers (ICE); 1997.

Kaiser PK, Yazici S, Nose J. Effect of stress change on the bond strength of fully grouted cables. Int Rock Mech Min Sci Geomech Abstr. 1992;29(3):293–306.

Kim NK. Performance of tension and compression anchors in weathered soil. J Geotech Geoenviron Eng ASCE. 2003;129(12):1138–50.

Kim NK, Park JS, Kim SK. Numerical simulation of ground anchors. Comput Geotech. 2007;34(6):498–507.

Kovári K. Erroneous concepts behind the new Austrian tunnelling method. Tunnels Tunn. 1994;26(11):38–42.

Kropik C, Mang HA. Computational mechanics of the excavation of tunnels. Eng Comput. 1996;13(7):49–69.

Larsson H, Olofsson T. Bolt action in jointed rock. In: Proceedings of the international symposium on rock bolting. Rotterdam: AA Balkema; 1983. p. 33–46.

Larsson H, Olofsson T, Stephansson O. Reinforcement of jointed rock mass—a non linear continuum approach. In: Proceedings of the international symposium on fundamentals of rock joints. Bjorkliden: Centek Publishers; 1985. p. 567–77.

Lo KY, Ogawa T, Lukajic B, Dupak DD. Measurement of strength parameters of concrete-rock contact at the dam-foundation interface. Geotech Test J. 1991;14(4):383–94.

Mahtab M, Goodman RE. Three dimensional analysis of joint rock slope. In: Proceedings of the 2nd ISRM congress (vol. 3). Beograd: Privredni Pregled; 1970. p. 353–60.

Marence M, Swoboda G. Numerical model for rock bolts with consideration of rock joint movements. Rock Mech Rock Eng. 1995;28(3):145–65.
Ministry of Construction of the People's Republic of China. (GB/T50266-99) Standard for tests method of engineering rock masses. Beijing: Research Institute of standards and norms (MOC); 1999 (in Chinese).
Mitri HS, Edrissi R, Henning J. Finite element modelling of cable-bolted slopes in hard rock underground mines. In: Proceedings of the SME annual meeting. Alburquerque: SME; 1993. p. 94–116.
Mitri HS, Rajaie H. Stress analysis of rock mass with cable support—a finite element approach. In: Proceedings of the conference on stresses in underground structures. Ontario: CANMET; 1990. p. 110–9.
Müller L. Removing the misconceptions on the new Austrian tunnelling method. Tunnels Tunn. 1990;22(special issue):15–18.
Ng CWW, Lee KM, Tang DKW. Three-dimensional numerical investigations of new Austrian tunneling method (NATM) twin tunnel interactions. Can Geotech J. 2004;41(3):523–39.
Pande GN, Gerrard CM. The behaviour of reinforced jointed rock masses under various simple loading states. In: Proceedings of the 5th ISRM congress. Melbourne: Brown Prior Anderson Pty Ltd. 1983;F217–23.
Pande GN, Beer G, Williams JR. Numerical methods in rock mechanics. New York: Wiley; 1990.
Pietro T. Carl Akeley—a tribute to the founder of Shotcrete. Shotcrete. 2002, summer:10–12.
Pietruszczak ST, Mróz Z. Finite element analysis of deformation of strain softening materials. Int J Numer Methods Eng. 1981;17(3):327–34.
Qiang S, Chen SH. A new three-dimensional element model of rock bolt. Chin J Rock Mechan Eng. 2001;20(supp 2):1476–82 (in Chinese).
Rabcewicz L. The new Austrian tunnelling method (part two). Water Power. 1964;16(12):511–5.
Rabcewicz L. The new Austrian tunnelling method (part three). Water Power. 1965;17(1):19–24.
Rokahr RB, Stark A, Zachow R. On the art of interpreting measurement results. Felsbau. 2002;20(2):16–21.
Schubert W, Steindorfer A, Button EA. Displacement monitoring in tunnels—an overview. Felsbau. 2002;20(2):7–15.
Sharma KG, Pande GN. Stability of rock masses reinforced by passive, fully-grouted bolts. Int J Rock Mech Min Sci Geomech Abstr. 1988;25(5):273–85.
Spang K, Egger P. Action of fully-grouted bolts in jointed rock and factors of influence. Rock Mech Rock Eng. 1990;23(2):201–29.
ST. John CM, Van Dillen DE. Rockbolts: a new numerical representation and its application in tunnel design. In: Proceedings of the 24th US symposium on rock mechanics. New York: AEG; 1983. p. 13–25.
Stheeman WH. A practical solution to cable bolting problems at the Tsumeb Mine. CIM Bull. 1982;75(838):65–77.
Stillborg B. Experimental investigation of steel cable for rock reinforcement in hard rock. Ph.D. thesis, Lulea University of Technology, Sweden; 1984.
Stillborg B. Professional users handbook for rock bolting. 2nd edition. Clausthal-Zellerfeld: Trans Tech Publications Limited; 1994.
Swoboda G, Marence M. FEM modelling of rockbolts. In: Proceedings of the computer methods and advance in geomechanics. Rotterdam: AA Balkema; 1991. p. 1515–20.
Swoboda G, Marence M. Numerical modelling of rock bolts in intersection with fault system. In: Proceedings of the numerical models in geomechanics, NUMOG 5. Swansea: Pineridge Press Ltd.;1992. p. 729–38.
Timoshenko S. Theory of plates and shells. New York: McGraw-Hill; 1940.
Weerasinghe RB, Littlejohn GS. Load transfer and failure of anchorages in weak mudstone. In: Littlejohn GS, editor. Proceedings of the conference on ground anchorages and anchored structures. London: Thomas Telford, Institution of Civil Engineers (ICE); 1977. p. 23–4.
Windsor CR. Rock reinforcement systems. Int J Rock Mech Min Sci. 1997;34(6):919–51.

Woods RI, Barkhordari K. The influence of bond stress distribution on ground anchor design. In: Littlejohn GS, editor. Proceedings of the conference on ground anchorages and anchored structures. London: Thomas Telford, Institution of Civil Engineers (ICE); 1997. p. 55–65.

Yazici S, Kaiser PK. Bond strength of grouted cable bolts. Int J Rock Mech Min Sci Geomech Abstr. 1992;29(3):279–92.

Zachow R. Dimensionierung zweischaliger Thnnel in Fels auf der Grund lage von in-situ Messungen (Dimensioning of bicoque tunnels in rock masses based on in situ measurements). Technical report 16. Hannover: University of Hannover; 1995 (in German).

Zienkiewicz OC, Pande GN. Time dependent multi-laminated model of rocks—a numerical study of deformation and failure of jointed rock masses. Int J Numer Anal Methods Geomech. 1976;1(3):219–47.

Chapter 7
Inverse and Feedback Analyses Based on the Finite Element Method

Abstract To undertake a successful computation task concerning the construction and operation process of hydraulic structures, one of the mostly concerned obstacles is the limited or incomplete sets of input data. This chapter presents the study on the inverse and feedback analyses for hydraulic structures using the FEM, intended to provide another parametric solution in addition to traditional ones (e.g. field exploration and investigation, laboratory experiment and field test, as well as engineering analogue). The principles and strategies with regard to the specific issues of in situ geo-stresses and material parameters (mechanical, permeable and thermal), are elaborated. The mathematical tools, particularly the algorithms for constrained nonlinear optimization problems arise from the inverse analysis, are presented. The aggression belonging to mathematical programming algorithms and the ANN belonging to heuristic search algorithms are implemented and validated in detail. In addition to a number of validation examples interspersed within the context, this chapter is closed with two engineering application cases (dam foundation, cut slope).

7.1 General

7.1.1 Concept

General-purposed numerical computation methods (e.g. the FEM) have been fully developed since the 1960s to become powerful tools in the design of hydraulic structures today. They have, as in other engineering fields, been performed mostly to undertake the comprehensive simulation of construction and service processes in details. However, difficulties with these methods were soon realized by engineers who tried to predict the behaviors of structures through limited or incomplete sets of input data. Many lessons have been taught that the unsuccessful numerical computation is most likely resulted from the improper inputting with regard to the constitutive relation and corresponding parameters or the boundary and initial conditions (e.g. ground water table, geo-stress). We are often, although not always,

S.-H. Chen, *Computational Geomechanics and Hydraulic Structures*,
Springer Tracts in Civil Engineering, https://doi.org/10.1007/978-981-10-8135-4_7

puzzled that under certain circumstances the difference between the computation and observation may be larger than ten times.

The performances of a hydraulic structure depend on many factors related to the materials, geological settings, construction procedure and operation schedule. In the design phases, these factors are evaluated by the comprehensive studies through the field exploration and investigation, laboratory and field tests, and engineering analogue.

However, by laboratory and in situ tests it is merely theoretically possible to reach a convincible interpretation for the parameters of rock-like materials that make up the full-scale hydraulic works, because it is impossible to fully take into account of the representation of test samples in light of the discontinuities, nonhomogeneities, and a variety of environmental factors (e.g. seepage pressure). In addition, it is expensive for large scale field investigation and tests, and difficult with the control of field test conditions. The tests results are also strongly influenced by the factors such as sampling methods, sample preparations, test methods and facilities as well as procedures. All these rule out the possibility of detailed investigation and tests during the design phases and in turn, introduce the possibility of large performance difference between the designed work state and real world one.

Hoek (1990) discussed the difficulties in determining shear strength of rock masses and concluded that the usefulness of the information obtained from field or laboratory tests in the decision making for parameters would be very limited. Practical engineers actually, tried various new solutions by turning to other means such as establishing empirical criteria (Hoek and Brown 1980), comparing the materials under consideration with those of the similar works whose parameters have been well understood (i.e. engineering analogue). Among all of their approaches, "back (or inverse) analysis" has become more and more prevalent in help them to determine the physical and mechanical parameters of rock-like materials.

For a large hydraulic project, some small cut slope failures might be encountered during the construction of access roads, excavation of tunnel portals and pits at the borrow areas, etc. Such failure incidents, similar to large scale direct shear tests performed on the similar ground materials, present cases for back analysis, from which lessons learnt are valuable in assessing the material strength parameters.

For an inactive ancient landslide, the back analysis is based on the judgment of its present stability safety factor and the formulation of the equilibrium equations for the typical sections. The solution of these equations provides shear strength parameters c or/and φ. According to the engineering experiences, when a landslide is in creep compression state, constant slip state, and accelerate slip state, the stability safety factor may be estimated as 1.01–1.10, 1.0, and 0.95–0.98, respectively.

Launching of construction and continuing throughout the whole operation period, new geological features (e.g. discontinuities and rock weathering) may be revealed, and monitored data concerning action effects (e.g. stresses, displacements, temperatures, uplifts) can be collected, all these provide precious messages with respect to the real state of the structure.

Many countries such as Canada, USA, Australia, France, Russia, Italy, Austria, China, etc., have enacted safety laws at the national level which are practiced in the safety management inclusive inspecting and monitoring activities of hydraulic structures, particularly dams, during their construction and operation phases. These activities may also provide data for the purpose to evaluate relevant physical and mechanical variables (e.g. the material properties of rock/concrete or the exerting loads), or to refine their values postulated at the design phases.

7.1.2 State of the Art

An "inverse problem" in science is the process from a set of observations to the causal factors that produced them. It is also called the "back analysis" problem because it starts with the results and then calculates the causes. It is one of the most important disciplines of mathematics purposed to provide us intrinsic parameters that we cannot directly observe. This field was firstly explored in 1929 by Soviet-Armenian physicist Viktor Ambartsumian who dealt with determining the equations of a vibrating string by a given family of eigenvalues (Lynden-Bell and Gurzadyan 1998). Nowadays, back analysis finds applications in communication, medical imaging, geophysics, remote sensing, machine learning, nondestructive testing, and many other fields.

Over the past 50 years or longer, attention has been focused on the solutions with which to determine the properties of rock-like materials (e.g. mechanical parameters, in situ geo-stresses, permeability, etc.), from the field observations and readings available (Sakurai 1981; Sakurai and Takeuchi 1983; Gioda and Sakurai 1987; Romanov 1987). Intended to find the values of parameters characterizing the material, back analysis leads to results (e.g. displacements, stresses, etc.) as close as possible to their in situ readings. However, it is notable that not all problems are invertible because we are not guaranteed to possess sufficient information to uniquely determine the solution of a corresponding equation. It is also necessary to remind that in most physical systems, we do not ever have enough information to uniquely constrain our solutions. Therefore, most inverse problems are considered as "underdetermined" (Groetsch 1993).

The back analysis has long been exercised in geotechnical engineering as a critical technique for estimating the hydraulic properties of large scale geological formations, such as the permeability and porosity, subject to the assumption of hydraulic constitutive laws for porous media, e.g. the Darcy's law or other non-Newtonian fluid models. Although complexity is enhanced when thermal processes are further involved in multiple-phased flow of fluids with various states of saturation (Lesnic et al. 1997; Russo 1997; Hanna and Jim Yeh 1998; Nutzmann et al. 1998; Roth et al. 1998; Wang and Zheng 1998; Chen et al. 1999; Finsterle and Faybishenko 1999; Katsifarakis et al. 1999; Mayer and Huang 1999; Wen et al. 1999, 2002; Fatullayev and Can 2000; Li and Yang 2000; Vasco and Karasaki 2001; Jhorar et al. 2002), yet it is fortunate for us, as hydraulic engineers, to neglect

such complexity because only the TM coupling and the HM coupling are normally considered, attributable to the fact that the levels of stress and hydraulic pressure as well as temperature encountered in surface founded or shallow embedded hydraulic structures, are relatively lower.

A comprehensive review of the subject is given by de Marsily et al. (1999) with the history of inverse methods in the past 50 years, especially the applications of the stochastic approach using geo-statistics.

Since the displacements by extensometers with multiple anchors, and the convergent displacements of tunnel walls, are the most directly in situ measurable and computational variables, they have been used extensively to derive material properties over the years (Sakurai and Takeuchi 1983; Gens et al. 1996; Ledesma et al. 1996a, b; Yang et al. 1996, 2000, 2001; Ai-Homoud et al. 1997; Hojo et al. 1997; Kim and Lee 1997; Mello Franco et al. 1997; Okui et al. 1997; Rossmanith and Uenishi 1997; Sakurai 1997; Singh et al. 1997; Sonmez et al. 1998; Ohkami and Swoboda 1999; Guo 2000; Obara et al. 2000; Pelizza et al. 2000; Chi et al. 2001; Krajewski et al. 2001).

A large and important family of back analysis techniques in hydraulic engineering is focused on the efficiency of computation and the uniqueness of solution. The essence is to derive unknown material properties (or system geometry, boundary condition, initial conditions) based on a limited number of laboratory or routinely field observed dada of some key variables, using optimization techniques (e.g. mathematical programming) of error minimization.

One of successful approaches towards this mission can be undertaken by the FEM combined with the optimization techniques, with the help of the understanding of instrumentations and construction procedures, as well as the engineering experiences. The principles and algorithms will be addressed in the hereinafter coverage.

7.2 Back Analysis Issues in Hydraulic Structures

The history of back analysis in geotechnical engineering shows that its techniques fall onto one route in terms of program structure and fundamental concepts. Differences only lie in the selection of the material constitutive laws, the simplification of the geological structure, the treatment of multi-stage rock excavation and concrete placement, the inclusion of measurement errors, and the way the results of back analysis are utilized (e.g. feedback analysis and dynamic design).

To perform a back analysis, in general terms, it is necessary to use stress/seepage/thermal computation procedures (e.g. the FEM) for determining the distribution of a physical field concerned with regard to the problem at hand. Because the direct inversion of the field problem is normally impossible, the techniques of optimization are frequently employed (Sakurai and Akutagawa 1995; Chen et al.

2001). To do so, a goal, also known as a target mathematically represented by an "objective function", should be defined beforehand. This is a function that measures how close the predicted data from the FEM fit the observed data.

7.2.1 In Situ Geo-Stresses

The common exercises are that based on the measured data of geo-stresses at several positions through field investigations and tests, the stress functions or the interior/external loads are used to produce the in situ geo-stress field. The displacements observed may be employed, too, subject to the clearly specified deformation parameters (e.g. Young's modulus) beforehand.

For the in situ geo-stress back analysis, we construct the objective function $f(\{\mathrm{x}\})$ to be minimized

$$f(\{\mathrm{x}\}) = \sum_{i=1}^{n} (\sigma_i - \sigma_i^*)^2 = f(x_i, y_i, z_i, E, \mu, \gamma_r, \Delta, U, V, W, T, \ldots) \tag{7.1}$$

where

n	amount of measured messages;
σ_i	geo-stress being back analyzed;
σ_i^*	measured geo-stress;
x_i, y_i, z_i	coordinates of the position concerned;
E,μ, γ_r	Young's modulus, Poisson's ratio, volumetric weight of the rock, respectively;
Δ	self-weight factor;
U, V, W	regional tectonic actions;
T	geothermal.

Normally, the mechanical parameters (e.g. E, μ, γ_r) are specified previously. A set of boundary load combinations is defined corresponding to the regional FE model (see Fig. 7.1), in which the factors to be back analyzed are self-weight factor Δ; regional tectonic actions U, V, W; and geothermal T. In Fig. 7.1, U and V may be the boundary actions in terms of displacement u, loads p and q (or alternatively boundary stresses σ and τ).

7.2.2 Material Parameters

The parameters related to the fields of elasticity, plasticity, viscoplasticity, permeability, thermal, etc., are inversed using the messages monitored during the construction (e.g. rock excavation, concrete placement) or/and service

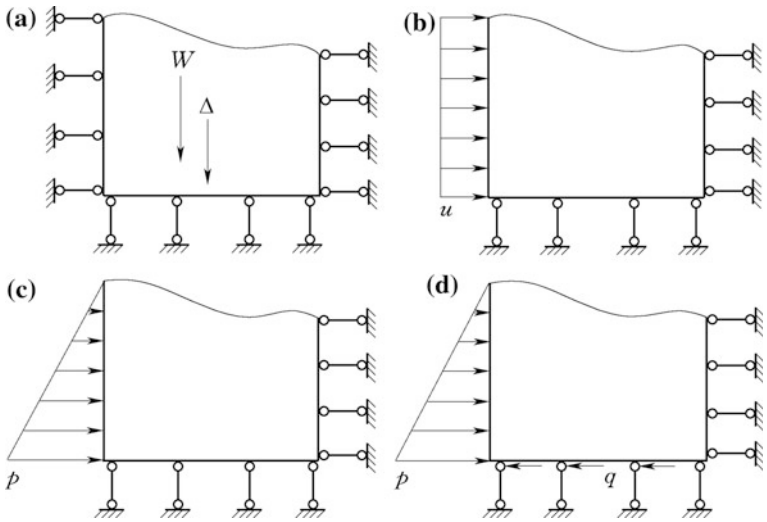

Fig. 7.1 Diagram to the notation of boundary conditions

(e.g. reservoir water level fluctuation) periods. This is sophisticatedly exercised in the practices subject to the models are appropriately prescribed in the computation software.

(1) Mechanical parameters

The objective function to be minimized is conventionally constructed using the computed and monitored displacements as

$$f(\{\mathrm{x}\}) = \sum_{i=1}^{n} (u_i - u_i^*)^2 = f(x_i, y_i, z_i, \sigma, E, \mu, c, \varphi, \gamma_r, \phi, \Delta T, \ldots) \tag{7.2}$$

where

n	amount of measured messages;
u_i	computed displacement;
u_i^*	monitored displacement;
σ	initial geo-stress;
x_i, y_i, z_i	coordinates of the position concerned;
$E, \mu, c, \varphi, \gamma_r$	Young's modulus, Poisson's ratio, cohesion, friction angle, volumetric weight;
ϕ	hydraulic potential;
ΔT	temperature variation.

Normally, the in situ geo-stress field is previously defined by a set of boundary load combinations corresponding to the regional FE model (see Fig. 7.1), so the

factors to be back analyzed the moment are mainly the mechanical parameters such as E and μ.

(2) Permeability and thermal parameters

We construct the objective function to be minimized for the thermal back analysis problem as

$$f(\{\mathrm{x}\}) = \sum_{i=1}^{n} (T_i - T_i^*)^2 = f(x_i, y_i, z_i, \alpha, \theta_0, T_0, T_a, T_b, \beta, c, \ldots) \tag{7.3}$$

where

n	amount of measured messages;
T_i	computed temperature;
T_i^*	monitored temperature;
T_0	initial temperature;
x_i, y_i, z_i	coordinates of the position concerned;
c	specific heat of concrete;
θ_0	adiabatic temperature rise;
β	surface exothermic coefficient
a	thermal diffusivity;
T_b	water temperature.
T_a	air temperature.

Most permeability back analysis problems may be constructed using the following objective function

$$f(\{\mathrm{x}\}) = \sum_{i=1}^{n} (\phi_i - \phi_i^*)^2 = f(x_i, y_i, z_i, \phi_0, q, k, \psi_j, a_j, \ldots) \tag{7.4}$$

where

n	amount of measured messages;
ϕ_i	computed hydraulic potential;
ϕ_i^*	monitored hydraulic potential;
x_i, y_i, z_i	coordinates of the position concerned;
k	principal permeability coefficient of intact rock;
ψ_j	connection coefficient of the joint set j;
a_j	hydraulic aperture of the joint set j.

Sometimes, use is made of multi-or single-hole packer tests (see Fig. 7.2) towards the permeability back analysis (Louis and Maini 1970; Hsich and Neuman 1985; Hsich et al. 1985). In this case the objective function may be constructed as

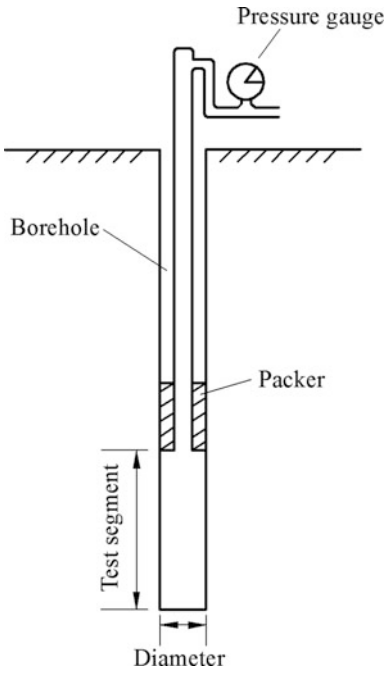

Fig. 7.2 Diagram to the single-hole test with single packer

$$f(\{\mathrm{x}\}) = \sum_{i=1}^{n} (Q_i - Q_i^*)^2 = f(x_i, y_i, z_i, P, k, \psi_j, a_j, \ldots) \tag{7.5}$$

where

n	amount of measured messages;
Q_i	computed inject flow;
Q_i^*	monitored inject flow;
x_i, y_i, z_i	coordinates of the position concerned;
k	permeability coefficient of intact rock;
P	inject pressure;
ψ_j	connection coefficient of joint set j;
a_j	hydraulic aperture of joint set j.

Normally by Eq. (7.5), the most difficultly evaluated parameters such as the connection adjusting coefficients ψ_i and the hydraulic apertures a_i, are back analyzed subject to the prescribed other parameters.

Figure 7.3 is the sketch of the boundary conditions at the axial section of a borehole that is generally stipulated in the back analysis, where AFE is the borehole wall, GFE is the test segment, AB and BC are the overflow boundaries, and DC is impervious.

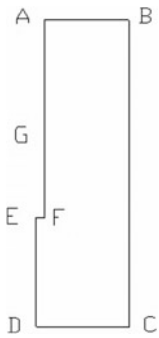

Fig. 7.3 Sketch of the boundary conditions for single-hole packer test

7.2.3 Model Recognition

A forward analysis starts with the definition of a mechanical model and correspondent parameters. The results would be cross-referenced with the monitored (measured, observed) data relating the current state of the structure. If necessary, parameter tuning may be performed for better agreement between computed and monitored data.

Under certain circumstances, parametric tuning solely would not lead to a better representation of the reality. It then becomes necessary to adjust the mechanical model (e.g. constitutive relation, failure mode) itself. Such a model tuning through back analysis enables to achieve a better agreement between computed and monitored data.

7.2.4 Mathematical Tools

(1) Formulation of constrained nonlinear optimization problems

Generally, the parametric identification process involves solving a certain kind of constrained nonlinear optimization problem. Take the deformation parametric back analysis using observed displacements for example, the optimization problem is formulated with following general statement:

$$\min f(\{\mathrm{x}\}) \tag{7.6}$$

Subject to the governing equation for the observed field data (e.g. u, σ, T, ϕ)

$$x \subseteq D_x$$

where

$f(\{\mathrm{x}\})$ objective function defined in Eq. (7.2);
$\{\mathrm{x}\}$ parameter vector;
D_x admissible set of the parameters.

Admissible set of the parameters is normally defined in the form of upper and lower bounds indicated by the superscript l and u on the parameters concerned, according to laboratory and field experiments as well as engineering analogue

$$\begin{cases} E^l \le E \le E^u \\ \mu^l \le \nu \le \mu^u \\ c^l \le c \le c^u \\ \varphi^l \le \varphi \le \varphi^u \\ \ldots\ldots\ldots\ldots\ldots\ldots\ldots \end{cases} \tag{7.7}$$

It may be automated with the help of mathematical optimization algorithms to form a generalized parameter model tuning tool. This, as it is general one, may be applied to a wide range of linear and non-linear problems arise from the nature of hydraulic structures.

(2) Optimization algorithms

The parametric identification process is a special treatment for the governing equation of the FEM through a core routine relating the measured data to a list of unknown parameters. It can be handled as an optimization problem (Gioda 1990) which can be solved by the techniques of mathematical programming algorithms, optimality criteria methods and heuristic search algorithms.

1. Mathematical programming algorithms

Many kinds of mathematical programming available are customarily classified in two categories of linear and non-linear. In the linear programming, the objective function and the associated constraints are represented in a linear combination of design variables. The linearization of objective function or constraints is not always easy and if the linearization techniques are used, the error in the linearized representation is inevitable (Moses 1964; Erbatur and Al-Hussainy 1992). On the other hand, the nonlinear programming was initially developed for un-constrained non-linear problems. The incidence of the optimal solution is shown by the proof of Kuhan-Tucker conditions (KT) (Kuhn and Tucker 1951) which are the necessary conditions for the justification of the optimal solution. However, the application of KT conditions is enormously difficult for the most of engineering problems (Camp et al. 1998).

Aggression is the most prevailing method for the linear objective function with regard to the parameters. Traditional regression techniques include simple linear regression, multiple linear regression, principal component regression, stepwise regression, etc. (Draper and Smith 1966; Chattefuee and Hadi 2006). Each of them can be employed to analyze the relationship between dependent variables and independent variables. Among them, stepwise regression is the most prevalent one in the issue of dam deformation.

Non-linear optimization may be further distinguished as the gradient type and the direct search type (Gioda and Sakurai 1987).

As a benefit from the gradient information, the gradient-type methods are characterized by fast and smooth convergence, of which the Gauss-Newton method is reported to be most effective (Nocedal and Wright 1999). The direct search methods are advantageous where the analytical expression of the gradient cannot be determined, especially when the system equation is nonlinear (Engl et al. 1996). In addition, it is quite flexible in the solution of back analysis problems, because these methods can provide the optimal solution by means of only successive evaluations of the objective function. A typical and popular direct search method is the Nelder-Mead variable polyhedron search method (Nelder and Mead 1965), which is an extension of the simplex method (Spendley et al. 1962). In some cases, however, the Nelder-Mead method generates an irregular simplex, which may provide some fake local solutions. To overcome this drawback, Box (1965) proposed the complex method.

2. Optimality criteria methods

The optimality criteria methods (OCMs) are developed based on the combination of KT conditions from nonlinear mathematical programming and Lagrangian multipliers. In this approach, KT conditions support the necessary desires for the optimal solution while Lagrangian multipliers guarantee the satisfaction of constrains in the optimization problem. OCMs are used vastly in engineering problems including the continuous and discontinuous design variables (SriVidya and Ranganathan 1995; Kuhn 2014; Yi and Lu 2016).

3. Heuristic search algorithms

In recent years the heuristic search algorithms based on the computational intelligences (CI), such as the artificial neural networks (ANN) (Yang and Zhang 1998; Yi and Wanstedt 1998; Yi et al. 2004b), the evolutionary algorithms (EA) and the genetic algorithm (GA) (Goldberg 1989; Yi et al. 2001, 2004a), are prevailingly employed as a nonlinear modeling tools to fit the complex relationship between inputs and outputs (Millar and Hudson 1994; Kim et al. 2001; Leu et al. 2001).

Being independent of objective function or/and constraint gradients, heuristic search algorithms do not require an explicit relationship between the objective function and constraints. With the probabilistic searching algorithm, they may save computational time in contrast to, for example, the gradient based methods that normally cost a considerable part of computational effort in sensitivity analysis phase (McCall 2005). They also can be easily implemented in discrete, continuous, and mixed optimization problems with minor adaptations. In addition, the open format for constraint statements and the possibility of defining multiple scenarios in the optimization process fascinate many researchers to implement heuristic search algorithms in engineering design optimization (Lagaros et al. 2002).

7.3 Feedback Analysis Issues in Hydraulic Structures

On the basis of back analysis, feedback analysis may be further undertaken towards the revolution from static design to the dynamic design during the construction period of hydraulic projects. This is normally founded on the combination of the numerical computation (e.g. FEM), field monitor, CAD, and decision supporting system.

There are a large number of computation methods available for hydraulic structures, each of them possesses its special merits and drawbacks. In the hereinafter coverage of this chapter, only the FEM with the elasto-viscoplastic potential theory and supplemented by special elements (e.g. joint element) is employed to construct the feedback analysis system.

Towards a routine design, the mechanical parameters are suggested beforehand by the comprehensive studies comprising laboratory and field tests and the engineering analogue. So far, the situation is discontented because there are intrinsic disadvantages with this methodology of parametric evaluation, mainly:

- High cost for large scale investigations and tests;
- Hard to control the conditions in the field tests and poor representation of the laboratory samples;
- Impossible to investigate every details in the design phases.

All of these might cause poor representation of the parameters compared to the advanced mechanical models and computational methods, and as a result, poor prediction might be offered by the computation.

It is natural, therefore, that those who work on the computation for hydraulic structures shift their focus towards finding ways to identify the missing information from the results of field readings “ex post facto”. This trend of utilizing updated information from engineering site effectively has led to the birth and growth of the feedback analysis and dynamic design during the construction and service stages.

During the construction, new geology features may be revealed, and the construction methods such as excavation and reinforcement procedures could be changed, too. More important, a lot of monitored data will provide the messages about the real state of the structure. All of these lead us to consider the questions such as: what is the real state of the structure? How far is the reality shifted from the previous postulation in design phases? Is it necessary and possible to revise/adjust the design in time? The answer is now “yes” for both the researchers and practitioners. In the tunneling engineering, the NATM provides a typical and successful example of feedback analysis and dynamic design. Since the 1990s, the philosophy has been expanded into the areas of cut slope and dam structures in hydraulic engineering (Chen et al. 2001) attributable to the progresses in

- The survey and monitor technologies;
- The database management and analysis methods;
- The computational geomechanics;
- The CAD/CAM technologies;
- The decision supporting with high performance computers.

7.4 Regression Methods

7.4.1 Multiple Linear Regression

A monitored effect value y [e.g. u^*, T^*, ϕ^*, Q^* in Eqs. (7.2)–(7.5)] may be looked at as a continuous random variable that observes normal distribution with mathematical expectation E and variance σ^2.

Suppose the relationship between the dependent or response variable y and $n-1$ predictor (or explanatory) variables $x_1, x_2, \ldots, x_{n-1}$ is formulated by the linear model

$$\begin{cases} y = a + b_1 x_1 + b_2 x_2 + \cdots + b_{n-1} x_{n-1} + \varepsilon \\ \varepsilon \sim N(0, \sigma^2) \end{cases} \tag{7.8}$$

or

$$y \sim N(a + b_1 x_1 + b_2 x_2 + \cdots + b_{n-1} x_{n-1}, \sigma^2) \tag{7.9}$$

The conditional mathematical expectation $E\{y|x_1, x_2, \ldots, x_{n-1}\}$ of y observes the following regression equation

$$E\{y|x_1, x_2, \ldots, x_{n-1}\} = \beta_0 + \sum_{i=1}^{n-1} \beta_i x_i \tag{7.10}$$

In which β_i is the regression parameter.

Suppose there are m observations for $x_1, x_2, \ldots, x_{n-1}$, the regression equation based on these observations is

$$\hat{y}(t) = b_0 + \sum_{i=1}^{n-1} b_i x_i \tag{7.11}$$

In which $\hat{y}$ is the regression of the monitored effect value y, which is the unbiased estimation for E of the parent body y under the environmental factors; b_i $(i = 0, 1, \ldots, n-1)$ are constants referred to as the model partial regression coefficients (or simply as the regression coefficients), which is the unbiased estimation for the parameters β_i $(i = 0, 1, \ldots, n-1)$ of the parent body.

Where $m < n-1$, Eq. (7.11) cannot be solved. On the contrary when $m > n-1$, Eq. (7.11) has more than one solution, under such circumstances the least square method may be employed to get the optimal solution of Eq. (7.11) by minimizing the sum of the squares of the errors, which represents the L_2—norm of the misfit between the observed data and the predicted data from the model

$$Q = \sum_{j=1}^{m} \left[y_j - (a + b_1 x_{1,j} + b_2 x_{2,j} + \cdots + b_{n-1} x_{n-1,j}) \right]^2 \tag{7.12}$$

In Eq. (7.12) Q is actually the special form of the objective function F in Eqs. (7.2)–(7.5). The role of the objective function is to minimize the difference between the predicted and observed data.

To minimize the objective function (i.e. solve the inverse problem) we should make use of its gradients

$$\frac{\partial Q}{\partial b_i} = \frac{\sum_{j=1}^{m} \left[y_j - \hat{y}_j \right]^2}{\partial b_i} = 0 \quad (i = 1, 2, \ldots, n-1) \tag{7.13}$$

It can be shown that the least square estimates b_i $(i = 0, 1, \ldots, n-1)$ are given by the solution of a set of linear equations

$$([C][C]^T) \begin{Bmatrix} a \\ b_1 \\ b_2 \\ \vdots \\ b_{n-1} \end{Bmatrix} = [C] \begin{Bmatrix} y_1 \\ y_2 \\ y_3 \\ \vdots \\ y_m \end{Bmatrix} \tag{7.14}$$

In which

$$[C] = \begin{bmatrix} 1 & 1 & 1 & \ldots & 1 \\ x_{1,1} & x_{1,2} & x_{1,3} & \ldots & x_{1,m} \\ x_{2,1} & x_{2,2} & x_{2,3} & \ldots & x_{2,m} \\ \vdots & \vdots & \vdots & \vdots & \vdots \\ x_{n-1,1} & x_{n-1,2} & x_{n-1,3} & \ldots & x_{n-1,m} \end{bmatrix} \tag{7.15}$$

The expression Eq. (7.14) is known as the "Normal Equation" and gives us a possible solution to the inverse problem. Because the units of $x_{i,j}$ $(i = 1, 2, \ldots, n-1; j = 1, 2, \ldots, m)$ in Eq. (7.14) are not consistent, therefore they should be non-dimensionally normalized.

7.4.2 *Stepwise Regression*

Stepwise regression is a composite method using forward and backward multiple regressions, which removes and adds the predictive variables to the regression model through a sequence of tests, so that the best subset of the predictors can be

identified. It is very prevalent in China for the purpose of constructing the relationship between dam deformation and environmental variables.

The stepwise regression is essentially a forward selection (FS) procedure, but with the added proviso that at each stage the possibility of deleting a variable as in backward elimination (BE), is considered (Chattefuee and Hadi 2006). In this procedure a variable that entered in the earlier stages of selection may be eliminated at later stages. The procedure is terminated, when dropping a variable does not lead to any further improvement in the regression accuracy. The final regression equation obtained by the stepwise regression is

$$\hat{y} = b_0 + \sum_{i=1}^{k} b_i x_i \tag{7.16}$$

In which k is the finial number of predictor (or explanatory) variables, $(k \leq n-1)$.

7.4.3 Model Tests and Diagnostics

(1) Multiple correlation coefficient (R)

Multiple correlation coefficient R $(0 \leq R \leq 1)$ is an important index to check the validation of the regression. It is used as a summary gauge to judge the fitness of the linear model y for a given body of data $x_i (i = 1, 2, \ldots, k)$

$$R = \sqrt{\sum_{j=1}^{m} (\hat{y}_j - \bar{y})^2 / \sum_{j=1}^{m} (y_j - \bar{y})^2} \tag{7.17}$$

where

$\bar{y}$ mean of the effect value $y(t)$

When the model fits the data well, i.e. the observed values and predicted values close to each other, R approaches to unity. On the other hand, if there is no linear relationship between $y(t)$ and the predictive variables $x_i(t) (i = 1, 2, \ldots, k)$, i.e. the linear model gives a poor fitting, R approaches to zero.

(2) Residual standard deviation (S)

$$S = \sqrt{\sum_{j=1}^{m} [y_j - \hat{y}_j]^2 / (m - k - 1)} \tag{7.18}$$

The number $m - k - 1$ in the denominator of Eq. (7.18) is termed as the "degrees of freedom" (DOF). It is equal to the number of observations minus the number of estimated regression coefficients. Residual standard deviation S is also an important index to check the quality of regression equation. The smaller of the S, the better fitting obtains for the regression equation.

(3) Fitting residual ε_j

Theoretically, the residual $\varepsilon_j (j = 1, 2, \ldots, m)$ between the standard deviations of the regressed response variable $\hat{y}_j$ and the observed one y_j, is a stochastic series that observes normal distribution $N(0, \sigma^2)$. If $\varepsilon_j (j = 1, 2, \ldots, m)$ does not observe normal distribution and in which there are the periodical or trend terms, the regression equation shall be improved by measures including to revise original predictive variables.

Using statistical models, the relationship between input and output signals can be formulated only in the sense of regression and/or correlation analysis without physical significance. If an observation in excess of history record (e.g. a reservoir level higher than the maximum history level), the statistical model may lose the capability to predict and explain the monitored data, i.e. the reliability of extrapolated prediction cannot be guaranteed. This is why sometimes such a model is termed by "black box".

7.4.4 *Verification Example: In Situ Geo-Stresses*

Where the rock is elastic, the regression technique and the FEM can be combined to back analyze the in situ geo-stress field using the tested in situ stresses before the excavation. The basic procedure is illustrated as follows.

- Establish regional FE model with effort to simulate joints, fractures and terrain.
- Define a set of boundary load (or displacement) combinations with regard to the regional FE model (see Fig. 7.1), in which the factors to be back analyzed are self-weight factor Δ; regional tectonic actions U, V, W; and geothermal T.
- For each boundary load combination, undertake the FE analysis to obtain the computed stresses at the in situ testing points.
- The computed stresses at the in situ testing points and the corresponding boundary load combinations are grouped into samples for regression procedure to get the self-weight factor, regional tectonic actions and geothermal.

Suppose the unit initial stresses $(\sigma_\Delta, \sigma_U, \sigma_V, \sigma_W, \sigma_T, \ldots)$ have been computed under the actions of unit boundary condition as illustrated in Fig. (7.1). According to the principle of linear superposition, the actual geo-stress is calculated by

$$\sigma = b'_{\Delta}\sigma_{\Delta} + b'_{U}\sigma_{U} + b'_{V}\sigma_{V} + b'_{W}\sigma_{W} + b'_{T}\sigma_{T} + \cdots \tag{7.19}$$

The regression algorithm is carried out towards Eq. (7.19) to obtain the regression coefficients $b'_{\Delta}, b'_{U}, b'_{V}, \ldots$.

For the simple example illustrated in Figs. 7.4 and 7.5, the boundary conditions and mechanical parameters are prescribed first, then the stress field in the domain is computed by the FEM. This stress field is regarded as the "actual in situ geo-stresses". Five points are selected as the testing points whose computed stresses are extracted as the "measured in situ geo-stresses". These measured stresses are employed to back analyze the whole geo-stress field using the stepwise regression as elaborated above. This regressed geo-stress field is compared with (post-check) the actual in situ geo-stress field, to validate the method.

In the computation mesh (see Fig. 7.4), the actual in situ geo-stress field is produced by the volumetric weight $\gamma_r = 0.027$ MN/m^3, boundary actions of surface pressure $U = 3$ MPa, $V = 2$ MPa, and $W = 0$ (see Fig. 7.5).

There are two sets of measured geo-stresses, those who used for the back analysis are displayed in Table 7.1, whereas those who used for the post-check of the inverse accuracy are displayed in Table 7.2.

The regression operator gives regression coefficients $b'_{\Delta} = 1.00003$, $b'_{U} = 29.99990$, $b'_{V} = 20.00000$, i.e. the actions on the slope are back analyzed as $\gamma'_r = b'_{\Delta}\,\gamma_r = 0.02700$ MN/m^3, $U' = b'_{U}\,U = 2.99999$ MPa, $V' = b'_{V}\,V = 2.00000$ MPa. They are very close to the boundary actions previously exerted. Table 7.3 presents the contrast between the actual and back analyzed in situ stresses.

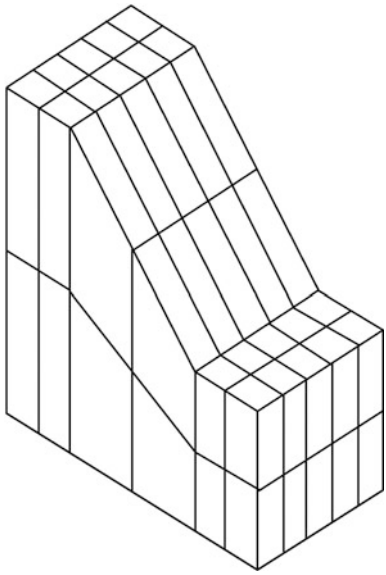

Fig. 7.4 Computation mesh

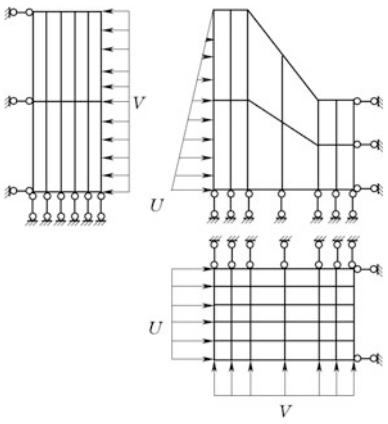

Fig. 7.5 Loads and boundary conditions

Although the regression method elaborated in this section is simple and practical, yet it is subject to the limitation of elastic performance. Under the circumstances where the non-linear deformation is not negligible, more sophisticated computation intelligence (CI) techniques such as ANN and GA, are demanded.

7.5 Computation Intelligence Methods

7.5.1 Concept

Since traditional optimization methods encounter difficulties in the solution of nonlinear and non convex systems, computation intelligent (CI) methods have been more and more prevalent for determining relations between process parameters. This is attributable to their significant advantages such as powerful capability in learning, non-linear and non-local mapping, memory and self-recognition; high precision; low computation effort, etc. (Sklavounos and Sakellariou 1995). There are a large category of the CI algorithms inclusive the immune system (Joshi 1995), the artificial bee colony (Karaboga and Ozturk 2011), the genetic algorithm (Mitsuo and Cheng 1997), the artificial neural network (Rumelhart et al. 1986), etc. Among them the artificial neural network abbreviated as ANN, is the most prevalent in the parametric back analysis for hydraulic structures.

7.5.2 Artificial Neural Networks

An artificial neural network (ANN) is a mathematical model that simulates the structure and function of biological neural networks (e.g. human brain) (see Fig. 7.6).

Table 7.1 Measured in situ geo-stresses and corresponding computed unit stresses for back analysis

Testing point	In situ geo-stress (MPa)							
			σ_x	σ_y	σ_z	τ_{yz}	τ_{zx}	τ_{xy}
1#	Measured		−1.995553	−0.602550	−0.141329	−0.369256	−0.374999	0.386997
	Unit stresses	σ_Δ	0.000792	−0.002887	−0.067124	0.001147	−0.000614	0.000700
		σ_U	0.000020	−0.020203	−0.002379	−0.012404	−0.012453	0.012810
		σ_V	−0.099848	0.000321	−0.000141	0.000085	−0.000040	0.000100
2#	Measured		−1.998233	−1.978698	−0.113484	−0.007485	−0.049248	0.387586
	Unit stresses	σ_Δ	0.000544	0.001746	−0.104932	−0.000185	−0.000166	0.002737
		σ_U	−0.000573	−0.065509	−0.000368	−0.000292	−0.002162	0.012957
		σ_V	−0.099079	−0.000759	0.000124	0.000074	0.000789	−0.000193
3#	Measured		−1.981295	−1.584942	0.150831	−0.014313	−0.002199	0.107110
	Unit stresses	σ_Δ	0.001632	0.004494	−0.130171	0.000411	−0.000509	0.002030
		σ_U	0.001298	−0.053184	0.009791	−0.000270	0.000052	0.003114
		σ_V	−0.101093	0.000304	0.000583	−0.000332	−0.000162	−0.000636

N.B. Unit stress is the stress at the measuring point under the action of $\gamma_r = 0.027$ MN/m^3, U = 0.1 MPa and V = 0.1 MPa

Table 7.2 In situ geo-stresses for the post-check of accuracy

Testing point	In situ geo-stresses (MPa)						
		σ_x	σ_y	σ_z	τ_{yz}	τ_{zx}	τ_{xy}
4#	Measured	−1.736928	−2.349351	−0.298544	0.020894	0.468770	0.522997
5#	Measured	−1.765756	−1.641396	0.255387	−0.026980	−0.018258	0.063837

It is a parallel processing network to determine the complex nonlinear relationships between independent (predictor) and dependent (response) variables (Zeidenberg 1990).

In Fig. 7.6, w_i is the weight representing the sense ability of the ith neuron for the received messages, and $f(z)$ is termed as the output or "activation function". Mathematically, it is defined as a composition of functions, the latter may further be defined as a composition of other functions. A widely used type of composition is the nonlinearly weighted sum in Eq. (7.20) where f may be predefined as the hyperbolic tangent or sigmoid function [see Eq. (7.21)].

$$y = f(z) = f\left(\sum_{i=1}^{n} w_i x_i - \theta\right) \tag{7.20}$$

$$f(z) = \frac{1}{1 + e^{-z}} \tag{7.21}$$

where

θ threshold

The important characteristics of the activation function is that it provides a smooth transition as the input values change, i.e. a small change in the input produces a small change in the output. An ANN employing the activation function in Eq. (7.20) is also termed as the "threshold network".

Where the w_i has been fixed (by training) for a certain input set $(x_1, x_2, \ldots, x_n)^T$, Eq. (7.20) gives output. If we expect that for every permissible input, a rational output is provided, the model of ANN should be appropriately established and the corresponding weight w_i should be well trained.

The ANN has been found to be very effective in non-linear mapping among the parameters involved in numerical computation and the nonlinear optimization problem arise from the back analysis for hydraulic structures.

(1) Basic structure of the ANN

Basic ANN model possesses three layers of input, hidden, and output. Each layer consists of several processing components, called as neurons (see Fig. 7.7).

The ANN architecture constructs the connections between the layers and neurons. The role of the hidden layers is to adjust input data set to the new data set of outputs. At first, specific random weights are assigned to inputs. This step is called

Table 7.3 Contrast between the actual and back analyzed in situ geo-stresses

Measuring point	In situ geo-stresses (MPa)						
		σ_x	σ_y	σ_z	τ_{yz}	τ_{zx}	τ_{xy}
1#	Measured	−1.995553	−0.602550	−0.141329	−0.369256	−0.374999	0.386997
	Back analyzed	−1.995554	−0.602549	−0.141329	−0.369255	−0.374997	0.386996
	Relative error (%)	−0.00005	−0.00017	0.00000	−0.00027	−0.00053	0.00026
2#	Measured	−1.998233	−1.978698	−0.113484	−0.007485	−0.049248	0.387586
	Back analyzed	−1.998235	−1.978691	−0.113484	−0.007485	−0.049248	0.387584
	Relative error (%)	−0.00010	−0.00035	0.00000	0.00000	0.00000	0.00052
3#	Measured	−1.981295	−1.584942	0.150831	−0.014313	−0.002199	0.107110
	Back analyzed	−1.981296	−1.584935	0.150830	−0.014313	−0.002201	0.107109
	Relative error (%)	−0.00005	−0.00044	0.00066	0.00000	−0.09087	0.00093
4#	Measured	−1.736928	−2.349351	−0.298544	0.020894	0.468770	0.522997
	Back analyzed	−1.736931	−2.349345	−0.298544	0.020894	0.468768	0.522995
	Relative error (%)	−0.00017	−0.00026	0.00000	0.00000	0.00043	0.00038
5#	Measured	−1.765756	−1.641396	0.255387	−0.026980	−0.018258	0.063837
	Back analyzed	−1.765752	−1.641385	0.255388	−0.026980	−0.018258	0.063837
	Relative error (%)	−0.00023	−0.00067	0.00039	0.00000	0.00000	0.00000

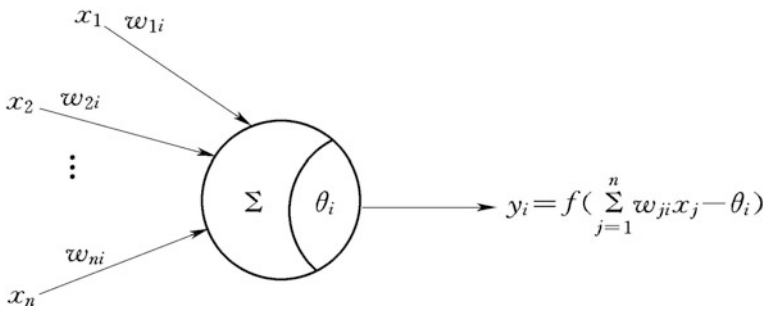

Fig. 7.6 Schematic diagram for a neuromime

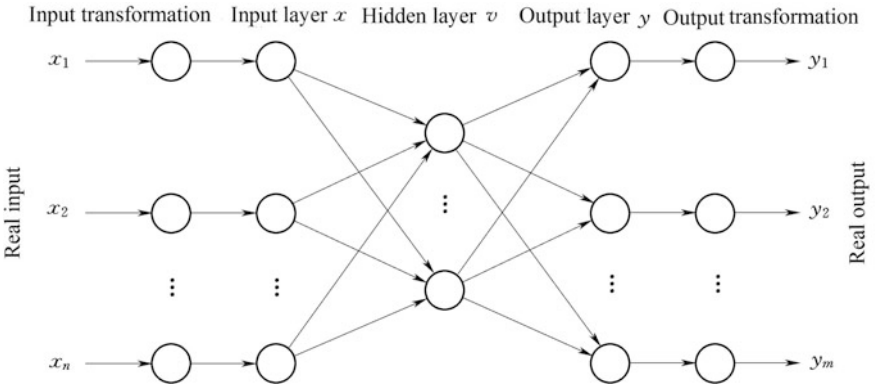

Fig. 7.7 Sketch of the ANN with single hidden layer

as the training of ANN. In this step, the extracted errors from experiments and predicted values are returned to the beginning of the network where all corrections to weights are made. This procedure is continued until the desired outcome has been extracted.

The back-propagation (BP) artificial neural network commonly used in the study of the back analysis, is a supervised training technique that computes the difference between the ANN calculated output and the corresponding desired output from the training data set (Werbos 1994). It uses the gradient descent algorithm to modify the network weights Δw for minimizing the network error E.

$$\Delta w(t+1) = \eta(-\frac{\partial E}{\partial w(t)}) + \alpha \Delta w(t-1) \tag{7.22}$$

$$E = \frac{1}{2}\sum_{i=1}^{n}(o_i^* - o_i)^2 \leq \varepsilon \tag{7.23}$$

where

w network weight;
t tth learning cycle (iteration);
η learning rate;
α momentum factor;
o_i output;
o_i^* desired output;
n number of output unit;
ε target error

The error is then propagated backward through the net and the weights are adjusted during a number of iterations, named "epochs". The training ceases when the calculated output values best approximate the desired values (Rumelhart et al. 1986).

The procedure of back propagation is summarized as follows.

- Initialize the weights of the network with small random values;
- Take the inputs of each training pattern into the network, then calculate the outputs using the inputs and the current weights of the network;
- Compare the calculated outputs to the desired outputs, and compute the network error E by the formula in Eq. (7.23);
- Calculate how much lower or higher the weights should be adjusted to match the calculated outputs and the desired outputs, using the gradient descent algorithm in Eq. (7.22);
- Adjust the weights backwards, i.e. from the output neurons to the inner neurons;
- Repeat the iteration with the modified weights, until the stopping criterion of the network error [see Eq. (7.23)] is satisfied.

(2) Training of the BP network

The primary goal of training is to minimize the error function E by searching for a set of connection weights and threshold values that enable the ANN to produce outputs equal or close to targets. After the training has been accomplished, the ANN is then capable of generating reasonable output results given new inputs.

Suppose p sets of training samples

$$\{x_1, x_2, \ldots, x_n; T_1, T_2, \ldots, T_m\}^k \quad (k = 1, 2, \ldots, p) \tag{7.24}$$

In which

$$\{T_1, T_2, \ldots, T_m\}^k \quad (k = 1, 2, \ldots, p) \tag{7.25}$$

is the kth output set comprising m members.

For each iteration (epoch), the input is executed to generate output. At the end of each training epoch, the differences between the outputs generated by the ANN and target outputs are calculated. The error, in turn, serves as the feedback of the next

learning process, which is used to adjust the weights and thresholds. The training continues until the network error falls below a specified target error ε.

The selection of an appropriate input vector that will allow for an ANN to be successfully mapped to the desired output vector is not a trivial task. Unlike traditional physically-based models, the set of variables that influence the system are not known beforehand. In this sense an ANN should not be considered as merely a black box, instead, to understand well the engineering needs under consideration is an important prerequisite for the successful application of ANN. This will help to avoid not only the loss of information if key input variables are omitted, but also the inclusion of spurious inputs that tends to confuse the training process.

The learning rate η is a dominant parameter in the network training which controls the step size when weights are iteratively adjusted. The momentum constant α whose value ranges between 0 and 1, is usually introduced into the training step to accelerate the convergence. The target error (or permissible error) ε is specified to collapse the training iteration where the values of the error function for all the training samples are smaller than this target error.

With regard to the number of neurons in the hidden layer of BP network, it is important to note that this is obtained mainly through the accumulated experience and the in situ test data gathered from past projects without an exact analytical expression. Recently, other optimization techniques (e.g. the GA), have been used to optimize the number of neurons as well as the weights (Johari et al. 2011), resulting in "hybrid optimization algorithms".

7.5.3 *Verification Example: In Situ Geo-Stresses*

For the slope example with boundary conditions illustrated in Figs. 7.4 and 7.5, the actual in situ geo-stresses are produced by the volumetric weight $\gamma_r = 0.027$ MN/m^3, boundary actions $U = 3$ MPa, $V = 4$ MPa, and $W = 0$. Five points whose computed stresses are extracted as the tested in situ geo-stresses, are collected in Table 7.4. Then these stresses are employed to back analyze the in situ geo-stress field using the BP-ANN specifically illustrated as follows.

- Construct a set of boundary loading combinations.
- For each combination, the normal FE computation is carried out to extract the stresses in the points as input set, meanwhile the boundary loads are grouped into output set.
- A sample is composed of one input and one corresponding output.
- Train the network using the samples.
- Input the tested (measured) in situ geo-stresses into the trained ANN, the output outcomes as back analyzed boundary load combination.
- According to the back analyzed boundary load combination provided by the ANN, the non-linear FE computation is undertaken to give the back analyzed in situ geo-stress field.

Table 7.4 Contrast of the back analyzed and measured in situ geo-stresses

Measuring point	In situ geo-stresses (MPa)						
		σ_x	σ_y	σ_z	τ_{yz}	τ_{zx}	τ_{xy}
1#	Measured	−3.679611	0.041274	0.038974	−0.321166	−0.485432	0.365396
	Back analyzed	−3.724485	0.054649	0.043216	−0.320502	−0.495994	0.369437
	Relative error (%)	1.21953	32.4054	10.8842	0.206745	2.17579	1.10593
2#	Measured	−3.988565	−1.930467	−0.060973	−0.006259	−0.024110	0.375838
	Back analyzed	−4.048194	−1.942932	−0.047513	−0.006444	−0.024023	0.380695
	Relative error (%)	1.49500	0.645699	22.0753	2.95575	0.360848	1.29231
3#	Measured	−3.985236	−1.540377	0.267294	−0.022934	−0.020398	0.139954
	Back analyzed	−4.046083	−1.551194	0.293117	−0.023350	−0.021303	0.143429
	Relative error (%)	1.52681	0.702226	9.66090	1.81391	4.43671	2.48296
4#	Measured	−3.756996	−2.357433	−0.288854	0.028006	0.481456	0.529777
	Back analyzed	−3.814430	−2.380053	−0.286619	0.028620	0.486648	0.534707
	Relative error (%)	1.52872	0.959517	0.773746	2.19239	1.07839	0.930584
5#	Measured	−3.701597	−1.683440	0.396349	−0.023635	−0.116458	0.096350
	Back analyzed	−3.764859	−1.699429	0.421722	−0.024164	−0.120758	0.099413
	Relative error (%)	1.70905	0.949785	6.40168	2.23821	3.69232	3.17904

28 samples are grouped to train the ANN, and 229,561 training epochs are conducted before the error target is met. The input of measured in situ geo-stress gives rise to back analyzed boundary load output $\gamma_r' = 0.026$ MN/m^3, $U' = 3.03$ MPa, $V' = 4.06$ MPa. According to these loads, the non-linear FE computation provides the back analyzed in situ geo-stress field. The cross-reference of the back analyzed and measured in situ geo-stresses in Table 7.4 exhibits an average relative error 4%.

7.6 Back Analysis of Permeability Tensor: Xiaowan Project, China

7.6.1 Presentation of the Project

Vide Sect. 8.1.

7.6.2 Characteristics of the Computation

There are three dominant sets of fractures in the dam foundation/abutments whose attitudes have been presented in Table 2.3. In addition, the permeability of the intact rock matrix and the hydraulic aperture of joints are $k = 6.8 \times 10^{-8}$ m/s and $a = 0.02$ mm, respectively.

In order to study the permeability of the rock masses in the dam foundation/abutments, a series of directional single-hole packer tests had been conducted. ZK13-4, ZK13-3 and ZK107 are the three of them in different directions whose positions and information are displayed in Fig. 7.8 and Table 7.5. The second segment of ZK13-4, the second segment of ZK13-3 and the sixth segment of ZK107 are closely located in the same family of rock mass (granite gneiss). The packer pressure within the range of $P = 0.3$–1.5 MPa produces linear curves of pressure $\sim$ flow that are employed for back analyzing the equivalent permeability tensor of the rock mass around the area nearby.

7.6.3 Procedures of the Back Analysis

Parameters in the equivalent permeability tensor [see Eqs. (2.15)–(2.17)] mostly difficult to evaluate are the connection adjusting coefficient ψ_j and the aperture a_j of the joint set j, provided that other parameters may be specified beforehand by field investigations and tests. The procedure towards the back analysis for ψ_j or/and a_j is launched by a set of ψ_j (or a_j) tentatively supposed. Then for each ψ_j or/and a_j the

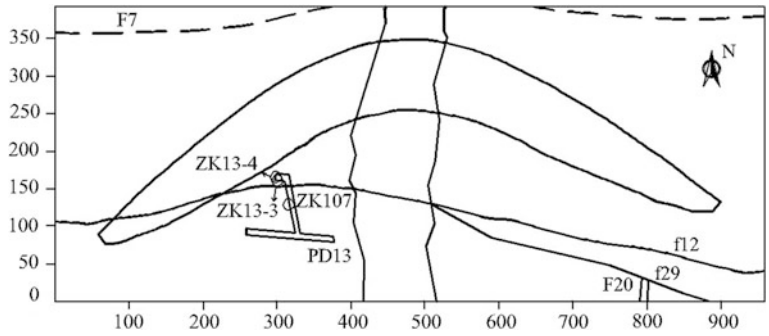

Fig. 7.8 Diagram to the position of packer tests (unit: m)

relevant flow rate Q_i are computed by the FEM for multi-or single-hole packer tests (see Figs. 7.2 and 7.3). These ψ_j or/and a_j and Q_i are grouped to create training samples for the ANN to fit their relationship. After the training, the parameter ψ_j or/and a_j can be back analyzed by inputting the in situ injected flow rate Q_i^*.

(1) Choice of single-hole packer test segments

Since Q_i^* is the only observed data for each single-hole packer test, therefore in order to back analyze ψ_j (or a_j) from Q_i^*, the number of single-hole packer tests should be equal to or more than that of fracture sets. In addition, to avoid the linear correlation of joint sets, three joint sets are the maximum to be taken into account in the permeability back analysis. Similarly, to avoid the linear correlation of Q_i^*, the packer test holes should be drilled in different directions.

Suppose the number of single-hole packer tests is equal to that of joint sets in a geological unit. Each packer test provides one test segment with outcomes in a form of linear pressure $\sim$ flow curve.

(2) Establishment of FE models

According to the depths, diameters, orientations and test segment locations of the boreholes, we establish FE models for each single-hole packer test in the global coordinate system with X-axis being eastward, Y-axis being northward, and Z-axis being upright. If the rock mass contain three joint sets, three FE models should be built (see Fig. 7.9). The boundary conditions are illustrated in Fig. 7.3.

(3) Preparation of ANN training samples

- Determine the amount of samples and estimate the ranges (upper and lower bounds) of the sample variables (ψ_j or a_j) according to the field investigation.
- Uniformly parameterize the sample variables within their ranges, and discretize them by the uniform design technique (Fang et al. 2000).

Table 7.5 Information of the packer tests: Xiaowan Project, China

Packer test	Test segment		Diameter (m)	Elevation of the borehole entrance (m)	Dip direction	Dip angle (°)	Test pressure (MPa)	Injected flow ($\times 10^{-5}$ m^3/s)	P ~ Q curve
	No.	Position (m)							
ZK13-4	2	8.56–13.69	0.075	1009.98	N80°W	5	0.6	328	Linear
ZK13-3	2	8.36–13.49	0.075	1009.78	S10°W	7	0.6	159	Linear
ZK107	6	51.81–61.98	0.056	1049.42	–	90	0.48	133	Linear

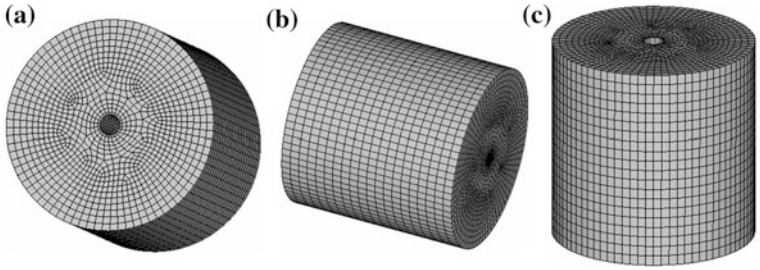

Fig. 7.9 Sketch of the FE models for single-hole packer tests

- Simulate the packer tests by the FEM to extract the injected flow Q_i under the pressure P_i, in this procedure the equivalent permeability tensor [see Eqs. (2.15)–(2.17)] containing ψ_j or/and a_j, is employed.
- Organize the samples consist of ψ_j or/and a_j and Q_i for network training.

(4) Training of the ANN

The injected flows are the network inputs, and the connection adjusting coefficients (or the apertures) are the network outputs.

(5) Back analysis of the connection adjusting coefficients ψ_i or/and apertures a_i

Input the in situ injected flows Q_i^* into the trained ANN, the network output gives the back analyzed outcomes of the connection adjusting coefficients or the apertures. With the back analyzed ψ_i or/and a_i, the equivalent permeability tensor of the rock mass is calculated using Eqs. (2.16) or (2.17).

7.6.4 Computation Results

The connection adjusting coefficient ψ_j to be back analyzed ranges from 10 to 200 for the joint sets 1 and 2, and 3000 to 6000 for the joint set 3, which are all discretized by 30 intervals. The hidden units in the hidden layer are 30, the momentum factor is 0.2 and the learning rate is 0.8, the target error is stipulated as $\varepsilon_k = 10^{-6}$. The back analyzed connection adjusting coefficient ψ_j and corresponding permeability tensor are given in Table 7.6.

Table 7.6 Back analyzed results of the equivalent permeability tensor

Joint set	Connection coefficient (ψ_j)	Permeability tensor ($\times 10^{-9}$ m/s)		
1	42.6	106	−1.54	−17.2
2	20.5	−1.54	114	−3.38
3	5992.7	−17.2	−3.38	76.7

Based on a systematic study by the geologists according to their investigations, experiences and engineering analogue, and by the back analysis works inclusive the example illustrated above, the permeability tensors for the major rock strata in the site of Xiaowan Project are elaborated (see Table 2.14). These tensors are further subject to feedback analysis and dynamic adjustment after the impounding of the reservoir (vide Chap. 8).

7.7 Feedback Analysis of Excavated Rock Slope: Three Gorges Project, China

7.7.1 Presentation of the Project

Three Gorges Project and its ship locks have been presented in Chap. 5 (Sect. 5.7.9). In view that the Yangtze River is a China's golden waterway, the overall and local stability of the ship locks must to be guaranteed. In addition, the time-dependent creep deformation of the ship lock slopes during the service period has to be strictly constrained within 5 mm, in order to meet the requirements for the normal operation of the miter gates.

Comprehensive studies had been conducted before the excavation by the designers and researchers inclusive the author, which concluded that there would be no danger of massive instability of the slope. During the construction, local failures along discontinuities and caused by blasting damage as well as by stress relief were, however, perceived to happen frequently. It is worthwhile to note that the studies were unable to yield consistent results regarding the deformation of the slope. For example, the predicted maximum displacement ranged from several centimeters to over one hundred centimeters. Therefore, the designers and the author undertook a supplementary study by means of the feedback analysis for the prediction of deformations and stresses, and the dynamic stabilization design for the slope during the construction and operation periods.

7.7.2 Characteristics of the Computation

(1) Engineering geology

The 20-20 section located at the gate chamber of the third step lock is chosen as a typical section to present the works (see Fig. 7.10). The rock masses are classified into 5 types according to the weathering degree: totally weathered, strongly weathered, weakly weathered, slightly weathered and fresh. In addition, there are two main faults f_{1222}, f_{1007}, the corresponding fragmentized bands, the trespasser rock *ex*.

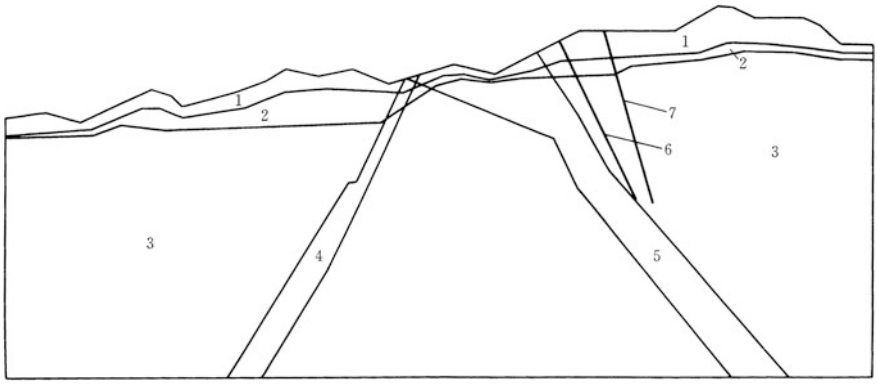

Fig. 7.10 Schematic geology profile of Sect. 20-20. 1—totally weathered rock and strongly weathered rock; 2—weakly weathered rock; 3—slightly weathered rock and intact rock; 4—fragmentized band; 5—trespasser rock *ex*; 6—fault f_{1222}; 7—fault f_{1007}

(2) In situ geo-stresses

The in situ geo-stress field in the slightly weathered and intact rocks is back analyzed. The back analyzed boundary actions are expressed by the boundary stresses of overburden depth dependent

$$\begin{cases} \sigma_x = -4.3867 - 0.1184H \\ \sigma_y = -4.5344 - 0.01129H \\ \sigma_z = -1.4629 - 0.03031H \\ \tau_{yz} = 0.04623 + 0.00002H \end{cases} \tag{7.26}$$

where

H overburden depth, m

The in situ geo-stresses in the totally weathered and strongly weathered rocks are dominated by the gravity action and calculated by the formulas

$$\begin{cases} \sigma_x = 0 \\ \sigma_y = -\frac{\mu}{1-\mu} \quad \gamma_r H \\ \sigma_z = -\gamma_r H \\ \tau_{yz} = 0 \end{cases} \tag{7.27}$$

where

γ_r volumetric weight of rock, kN/m^3;
μ Poisson's ratio;
H overburden depth, m

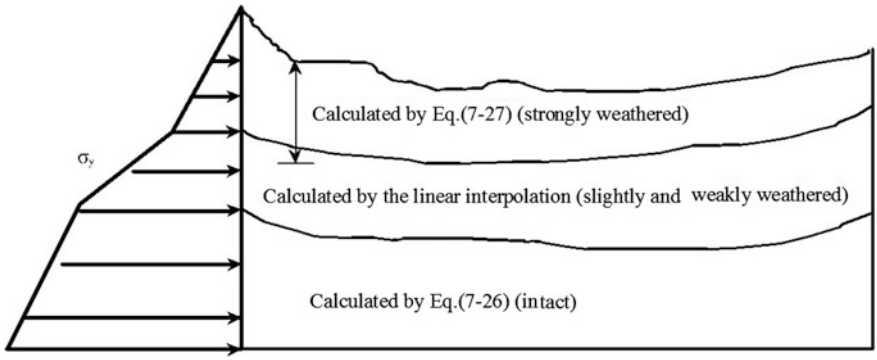

Fig. 7.11 Boundaries with regard to the in situ geo-stress field

In the weakly weathered rock masses, the in situ geo-stress field is calculated according to a linear interpolation between the strongly weathered rock masses governed by Eq. (7.27) and slightly weathered rock masses governed by Eq. (7.26), as illustrated in Fig. 7.11.

(3) Excavation benches and executive schedule

According to the construction schedule, the section was excavated by 15 benches whose levels and the corresponding executive times are illustrated in Fig. 7.12. Figure 7.13 shows the excavated southern slope in the February, 1998.

(4) Blasting damage relaxation band and stress relief relaxation band

According to the ultrasonic detection in the field, two sub-zones, namely the blasting impact zone (BIZ) and the stress redistribution zone (SRZ) of the EDZ whose mechanical parameters were deteriorating with the ongoing excavation, were

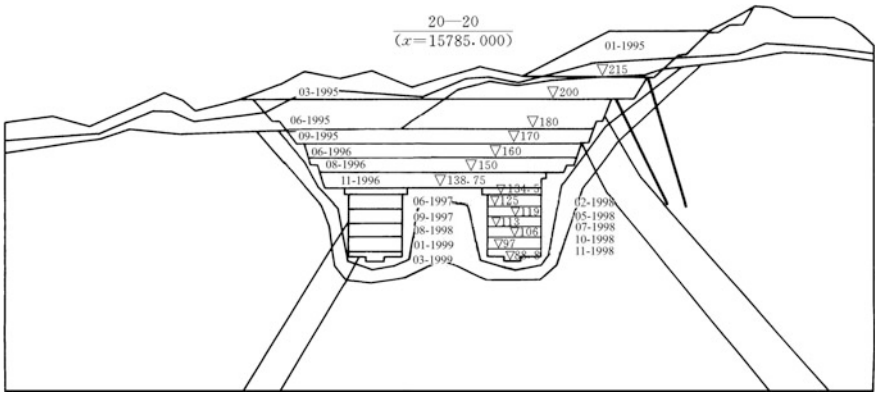

Fig. 7.12 Excavation benches and their executive times

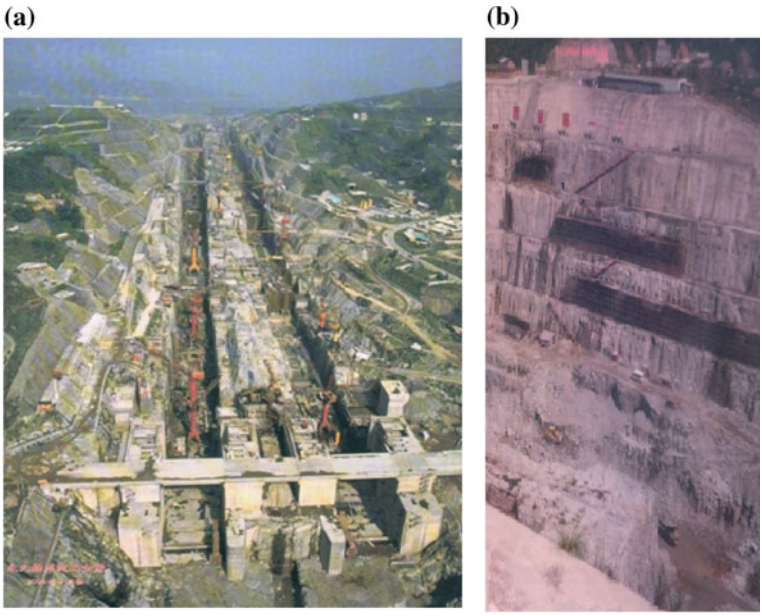

Fig. 7.13 Ship lock in the construction, **a** Bird eye view; **b** southern slope in February, 1998

defined along the excavation face. The depth of the BIZ which is induced by both the blasting damage and the stress relief, is approximately 5 m. The depth of the SRZ which is mainly induced by stress relief, is approximately 20 m. The boundary between these two sub-zones is plotted in Fig. 7.14. The stability of the excavated slope was strongly influenced by the EDZ: local failure might frequently occur and rock bolts were systematically installed depending on the probable characteristics of the EDZ.

(5) Instrumentation layout for displacement monitoring

It is well known that a successful parametric identification should explore the measured data on which the parameters have great impact. From this standpoint it is suggestible to measure displacements with high system sensitivity (Murakami et al. 1991). However, it can hardly help where more than one parameter need to be identified (Haftka et al. 1998). So far, there is no widely accepted criterion for designing the optimal instrumentation layout.

During the excavation construction of the ship lock, comprehensive instrumentation was implemented. The monitoring object (gauge) points used in the back analysis are illustrated in Fig. 7.14 and detailed in Tables 7.7, 7.8 and 7.9.

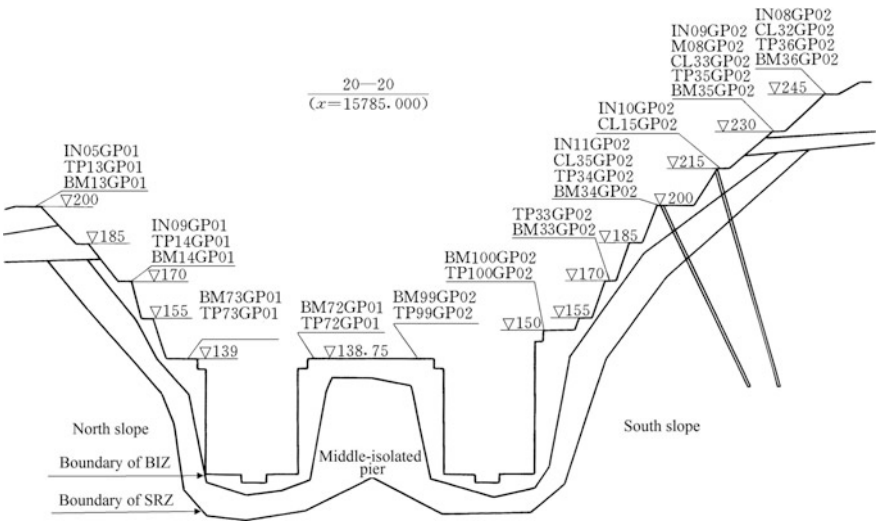

Fig. 7.14 Installation of the object points for displacement monitoring

Table 7.7 Object point layout for the surface displacements of section 20-20

Object point		Elevation (m)	Initial date of reading	Rock type
Northern slope	TP13GP01 BM13GP01	200	June 1995	Strongly and totally weathered
	TP14GP01 BM14GP01	170	August 1996 April 1996	Slightly weathered and intact
Separation pier	TP72GP01 BM72GP01 (Northern wall)	139	November 1997	Slightly weathered and intact
	TP99GP02 BM99GP02 (Southern wall)	139	January 1998	Slightly weathered and intact
Southern slope	TP100GP02 BM100GP02	150	December 1997	Slightly weathered and intact rock
	TP33GP02 BM33GP02	170	December 1996	Slightly weathered and intact
	TP34GP02 BM34GP02	200	November 1995	Slightly weathered and intact
	TP35GP02 BM35GP02	230	March 1995	Strongly and totally weathered
	TP36GP02 BM36GP02	245	December 1994	Strongly and totally weathered

Table 7.8 Borehole inclinometer layout of section 20-20

Object point		Top elevation of the borehole (m)	Depth of the borehole (m)	Initial date of reading	Rock type
Northern slope	IN05GP01	200	35.5	January 1996	Strongly and totally weathered
	IN09GP01	170	35.0	May 1996	Slightly weathered and intact
Separation pier	IN03CZ32 (Northern wall)	139	50.0	December 1997	Slightly weathered and intact
	IN04CZ32 (Southern wall)	139	50.0	December 1997	Slightly weathered and intact
Southern slope	IN14GP02	173	25.0	December 1996	Slightly weathered and intact
	IN11GP02	200	30.5	December 1995	Weakly weathered
	IN10GP02	215	20.5	December 1995	Weakly weathered
	IN09GP02	230	20.5	June 1995	Strongly and totally weathered
	IN08GP02	245	20.5	June 1995	Strongly and totally weathered

Table 7.9 Extensometer layout of section 20-20

Object point	Top elevation of the borehole (m)	Distance from the gauge point to the top of the borehole (m)						Rock type
		1#	2#	3#	4#	5#	6#	
Southern slope M08GP02	230	33.2	27.8	22.4	17.0	11.6	6.2	Strongly and totally weathered

(6) The FE mesh and main feedback analysis procedure

The FE mesh (see Fig. 7.15) used in the calculation is carefully created to simulate the excavation procedure step by step, and to let all the object points be located at the nodes. The mesh contains 2250 elements and 2322 nodes.

Since the mechanical parameters of the fresh rock, slightly weathered rock, faults f_{1222} and f_{1007}, the fragmentized bands and the rock dyke are less influenced by the relaxation due to blasting damage and stress relief, they are fixed after the

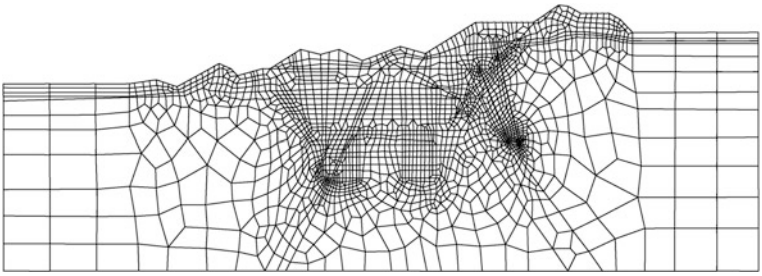

Fig. 7.15 FE mesh of the section 20-20

first three steps of feedback analysis. From the fourth step of excavation, the attention is focused on the evolution of mechanical parameters in the BIZ and SRZ, which are taken into account of in the subsequent deformation and stability predictions.

7.7.3 Strategies of Feedback Analysis

Suppose the *i*th excavation step is handled using the parameters and the stress field obtained by the $(i-1)$th step feedback analysis. The elasto-viscoplastic FEM analysis yields the predicted displacements, stresses as well as the stability of the slope due to the *i*th step of excavation. After the *i*th excavation step has been executed, and the monitored data have been read, the precision of the prediction can be checked and the back analysis is conducted afterwards. An updated set of parameters are therefore available for the prediction of the next $(i+1)$th excavation step.

During the feedback analysis, problems may give rise which cannot be solved by the computational method and displacement messages solely, and the knowledge from the investigation as well as the engineering expertise would be very helpful.

(1) Local minimum versus global minimum

Since the objective function f defined in Eq. (7.2) is not linear, it is liable to be trapped in a local minimum in lieu of to get the demanded global one (see Fig. 7.16) during the optimization analysis. The existing mathematical methods to

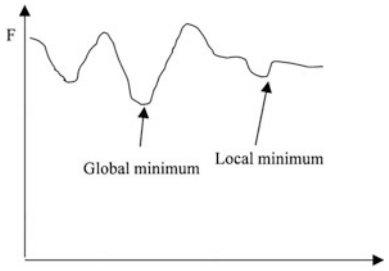

Fig. 7.16 Local minimum and global minimum

identify if a point emerges local minimum and swift away from this point in time, is not robust attributable to the strong nonlinearity and implicit of the function f.

To deal with this difficulty it is suggestible that:

- To de-couple the parameters, i.e. do not try to identify all parameters at one stroke;
- To define the upper and inferior bounds of the parameters according to the values obtained by experiments and engineering analogues.

(2) Parameter de-coupling

Although the observation indicated no obvious creep deformation in the slope, yet designers had been worrying that after the accomplishment of the excavation there could be creep displacements large enough affecting the normal operation of the miter gates in the ship lock, so eventually it was decided that the fluidity parameter should be back analyzed. As a result, the back analysis mainly concerns five parameters γ, E, μ, c and φ which are coupled. If all parameters in all types of rocks are expected to be dynamically updated, it will be found that there is no definite solution. For a set of observation data, a possible combination may yield a high value of E but low values of c and φ, or low E but high c and φ. In addition, c and φ are coupled, too. For the moment, the problem cannot be solved merely by mathematical and mechanical theories. Therefore the following approaches are advisable.

① With fluidity parameter $\gamma = 1$, the strain/stress histories are not applicable by the potential elasto-viscoplastic theory, but the steady-state results are identical to the conventional static elasto-plastic solution. Therefore, the parameters E, μ, c and φ can be back analyzed firstly using the convergent displacements, then the displacement history will be simulated to get real fluidity parameter γ.

② Since the Poisson's ratio μ is relatively less important than the other parameters, it may be fixed to the data used in the design phases from the beginning of the back analysis. After a certain steps when nearly all the other parameters are updated, one step may be used to check the parameter μ and to make the update, if necessary. During this step all the other parameters are fixed.

③ Since at the beginning of the excavation there are no or only limited plastic (yield) zones in the rock slope, the monitored data of the first few steps can be used to evaluate the elastic modulus E only. In this calculation, the strength parameters c and φ are fixed to the data used in the design phases. Then, as the going on of excavation, the parameters c and φ will be back analyzed. After a certain calculation steps, the data of one step may be used to check the E and to make the update, if necessary.

④ Since there are many types of rock masses and faults with different strength parameters in a slope, it is not appropriate to evaluate all strength parameters

of all rock masses simultaneously. At each step of back analysis, the attention should be focused on the strength parameters of the rock situated close to the present excavation surface. In this way, the strength parameters are back analyzed sequentially from the upper portion to the lower portion of the slope, along with the ongoing excavation.

⑤ Since the angle of friction φ is more stable, it is suggestible to fix this parameter in antecedent step referring to the data used in the design phases, and to conduct the back analysis with respect to the cohesion c. In the subsequent step the cohesion c is fixed, and the new displacement readings may be employed to adjust the friction angle φ, if necessary. This iteration is expected to offer a good and stable estimation of the strength parameters.

7.7.4 Computation Results

(1) Back analyzed parameters

According to the engineering geological conditions and the displacement readings from the monitoring instruments, the feedback analysis had been carried out successfully during the excavation of the ship lock. The mechanical parameters back analyzed are summarized in Tables 7.10 and 7.11 and Figs. 7.17, 7.18 and 7.19, in which the data used in the design phases are also provided for the sake of comparison. It can be found that for the slightly weathered and fresh rocks, weakly weathered rocks, faults f_{1222} and f_{1007}, the fragmentized bands, and the rock dyke *ex* whose mechanical parameters are supposed to be fixed in the design phases, the back analyzed parameters are a bit of lower. For the rock masses in the BIZ and SRZ, the mechanical parameters back analyzed undermine remarkably as the going down of the slope cutting.

Table 7.10 Mechanical parameters of the rock masses

Rock type	Young's modulus E (MPa)	Cohesion c (MPa)	Friction angle φ (°)	Poisson's ratio μ
Totally and strongly weathered	300[a]	0.2[a]	36[a]	0.35[a]
Weakly weathered	5000[a]	0.8[a]	47[a]	0.25[a]
Slightly weathered	32000	1.72	58.68	0.2[a]
Fragmentized bands	11500	1.10	44.1	0.25[a]
Rock dyke (Trespasser) *ex*	8300	1.2	55	0.25[a]
f_{1222}	3500[a]	0.5[a]	35[a]	0.3[a]
f_{1007}	3500[a]	0.5[a]	35[a]	0.3[a]

N.B. Superscript [a]indicates the parameter belonging with original design (without back analysis)

Table 7.11 Fluidity parameters of the rock masses

Rock type	Totally and strongly weathered	Weakly weathered	Slightly weathered and fresh	Fragmentized bands	Rock dyke *ex*	BIZ	SRZ	f_{1222} f_{1007}
Fluidity $\frac{1}{\gamma}(GPa.d)$	24.9	35.0	221.0	84.6	55.7	103.0	167.4	24.0

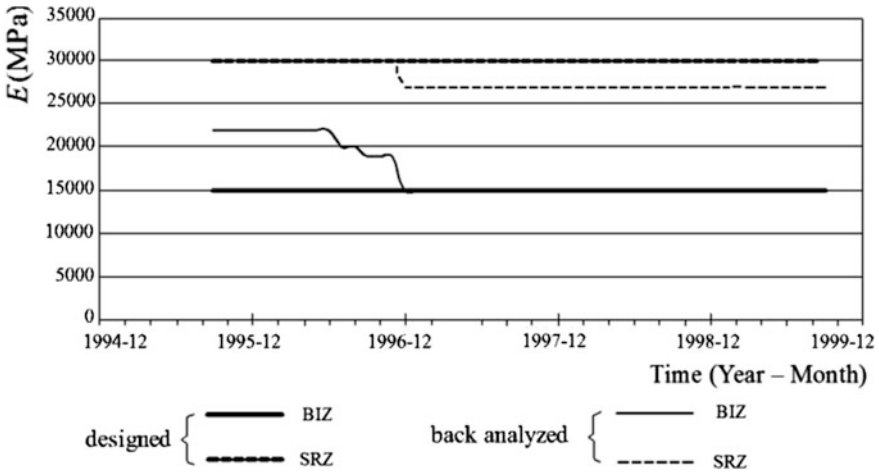

Fig. 7.17 Young's modulus E of the EDZ

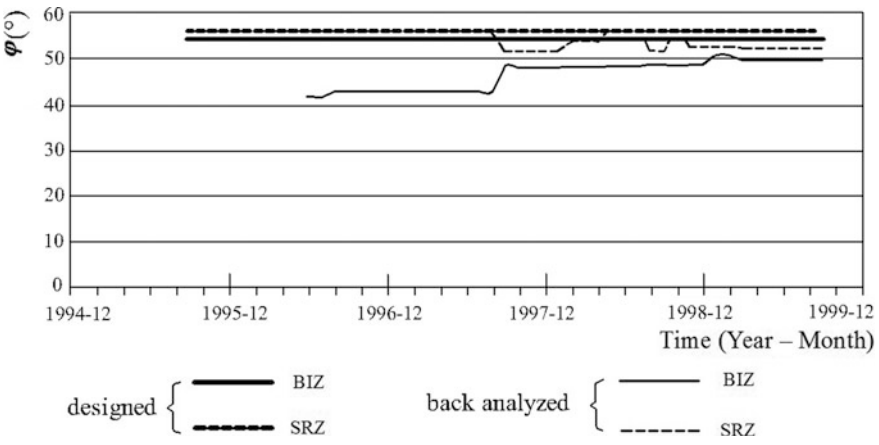

Fig. 7.18 Friction angle φ of the EDZ

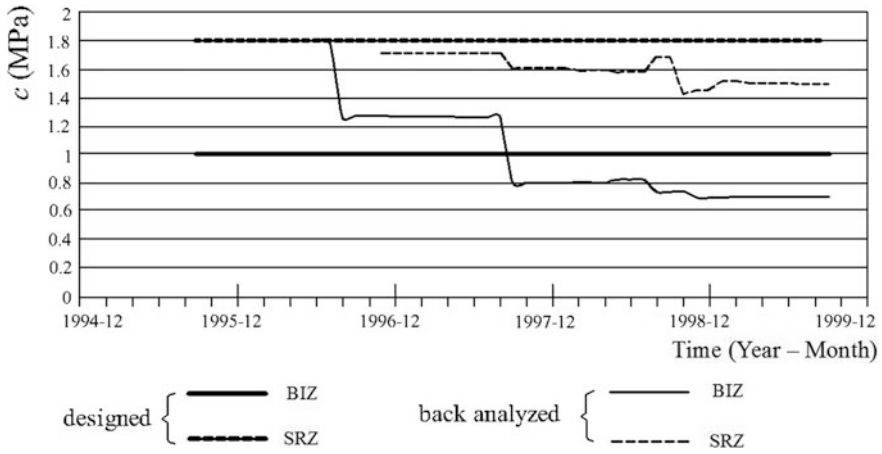

Fig. 7.19 Cohesion c of the EDZ

(2) Forecasted displacements

Figure 7.20 displays the accumulated displacements of the section 20-20 at April 1999, when the excavation of entire ship lock was just completed. The feedback analysis outcomes indicate that the maximum displacement is 71.63 mm which will occur at the southern slope. The elasto-viscoplastic analysis forecasts that there is maximum 1.42 mm time-dependent displacement which will be converged within 7–8 months after the completion of the excavation, therefore the conclusion may be made that if the miter gates are installed after the end of 1999, there is no risk of hazardous displacement adverse to the normal operation of the gates. It is proud to indicate that the field observation data so far have verified above predictions.

The displacement histories at some typical object points predicted by the feedback analysis are plotted in Figs. 7.21, 7.22, 7.23 and 7.24. Compared with the observed displacement histories in the same figures it can declare that the feedback analysis provides good prediction for the displacements of the ship lock slope.

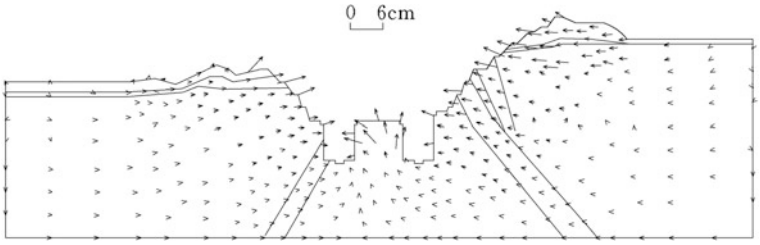

Fig. 7.20 Accumulated displacements (April 1999)

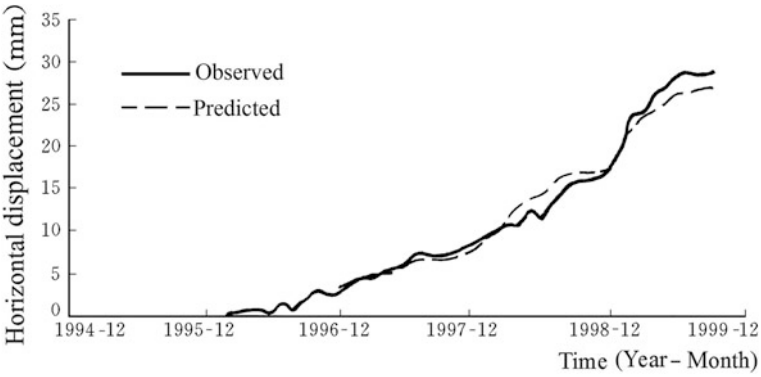

Fig. 7.21 Horizontal displacement at TP/BM13GP01

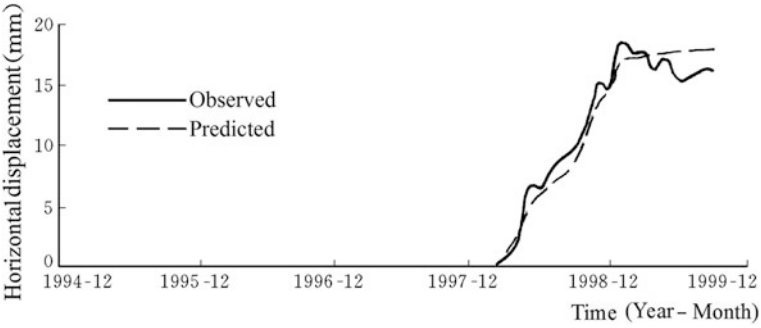

Fig. 7.22 Horizontal displacement at TP/BM99GP02

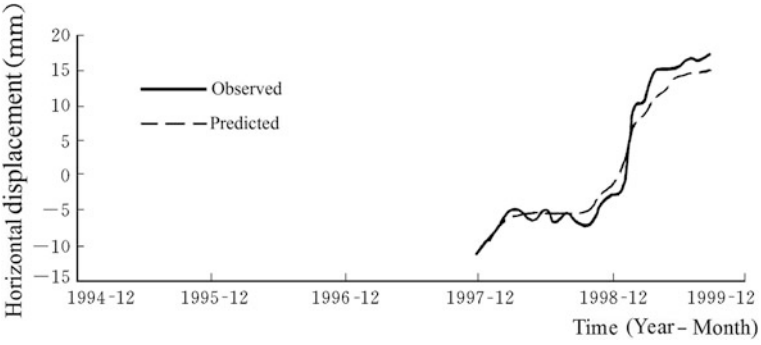

Fig. 7.23 Horizontal displacement at TP/BM72GP01

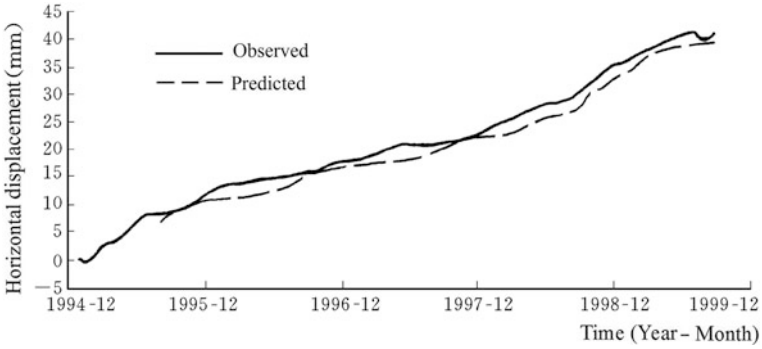

Fig. 7.24 Horizontal displacement at TP/BM36GP02

(3) Forecasted stresses and stability

Figure 7.25 displays the stress distribution after the accomplishment of the slope cutting. According to the prediction of the 17th step when the excavation of the entire ship lock is just completed, the maximum stress at the bottom corner of the southern slope is 24.7 MPa, and that at the bottom corner of the northern slope is 24.1 MPa. Since the long term creep strength $\bar{\sigma}_s$ of rocks around these areas is approximately 50 MPa, there is no risk of long term creep deformation which could jeopardize the long term operation of the miter gates.

The analysis results also show that there are tensile stresses in the separation pier of the double-lane ship lock with maximum value of 0.817 MPa and maximum depth of 28 m from the top of the pier. It means that cracking and local failure could occur frequently during the excavation construction, therefore more attention should be paid to the reinforcement of this area.

The contours of the point safety K_p (see Fig. 7.26) calculated by Eq. (4.215) justify that plastic deformation manifests at the southern and northern slopes as well as at the middle pier. The dominant plastic zones are located in the southern slope and the separation pier with maximum depth of 30 m. Since the viscoplastic iteration is convergent, therefore the overall stability of the slope is held.

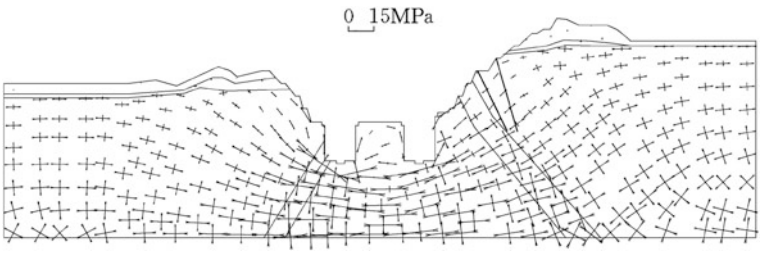

Fig. 7.25 Stress distribution after the completion of excavation

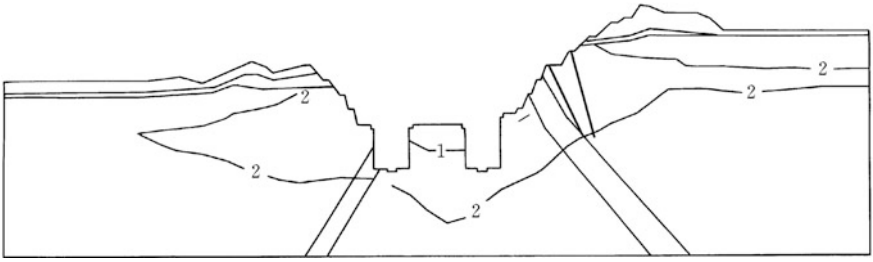

Fig. 7.26 Contours of the point safety factor

(4) Discussions

The techniques of back analysis shine a bright light on the numerical computation for a variety of hydraulic structures, of which the parametric identification strategies are specially emphasized in this chapter. The feedback analysis further provides a realistic way to overcome the indetermination of the parameters in the investigation and design stages. Use is made of the data extracted from the monitoring instrumentation system during the project construction, both the parameters and the structural design may be justified and revised in time, if necessary.

Every parametric identification method possesses its unique merits and drawbacks. The selection among optimization methods is determined by the specific situation. The methods presented in this chapter are not complicated from the standpoint of mathematics and mechanics. However, as we have elucidated in the feedback analysis of excavated rock slope (Three Gorges Project), problems such as the local minimum and global minimum, the parameter de-coupling, etc., cannot be solved merely by the computation directly because of the complicity of hydraulic structures. Anyway, if we handle the problems properly with the help of investigation instruments and the understanding of the construction procedure, as well as the engineering experiences, the feedback analysis can provide quite satisfactory results (Fig. 7.27).

Fig. 7.27 Accomplished ship lock: Three Gorges Project, China

References

Ai-Homoud AS, Tai AB, Taqieddin SA. A comparative study of slope stability methods and mitigative design of a highway embankment landslide with a potential for deep seated sliding. Eng Geol. 1997;47(1–2):157–73.

Box MJ. A new method of constrained optimization and a comparison with other methods. Comput J. 1965;8(1):42–52.

Camp C, Pezeshk S, Cao GZ. Optimized design of two-dimensional structures using a genetic algorithm. J Struct Eng. 1998;124(5):551–9.

Chattefuee S, Hadi AS. Regression analysis by example. 4th ed. New Jersey, USA: Wiley; 2006.

Chen J, Hopmans JW, Grismer ME. Parameter estimation of two-fluid capillary pressure-saturation and permeability function. Adv Water Resour. 1999;22(5):479–93.

Chen SH, Chen SF, Shahrour I, Egger P. The feedback analysis of excavated rock slope. Rock Mech Rock Eng. 2001;34(1):39–56.

Chi SY, Chern JC, Lin CC. Optimized back-analysis for tunnelling-induced ground movement using equivalent ground load model. Tunn Undergr Space Technol. 2001;16(3):159–65.

de Marsily G, Delhomme JP, Delay F, Buoro A. 40 years of inverse solution in hydrogeology. Earth Planet Sci. 1999;329(2):73–87 (in French).

Draper NR, Smith H. Applied regression analysis. New York, USA: Wiley; 1966.

Engl HW, Hanke M, Neubauer A. Regularization of inverse problems. Dordrecht, Netherlands: Kluwer Academic Publishers; 1996.

Erbatur F, Al-Hussainy M. Optimum design of frames. Comput Struct. 1992;45(5–6):887–91.

Fang KT, Lin DKJ, Winker P, Zhang Y. Uniform design: theory and application. Technometrics. 2000;42(3):237–48.

Fatullayev A, Can E. Numerical procedure for identification of water capacity of porous media. Math Comput Simul. 2000;52(2):113–20.
Finsterle S, Faybishenko B. Inverse modelling of a radial multistep outflow experiment for determining unsaturated hydraulic properties. Adv Water Resour. 1999;22(5):431–44.
Gens A, Ledesma A, Alonso EE. Estimation of parameters in geotechnical back analysis. II: application to a tunnel problem. Comput Geotech. 1996;18(1):29–46.
Gioda G. Some applications of mathematical programming in geomechanics. In: Desai CS, Gioda G, editors. Numerical methods and constitutive modelling in geomechanics. New York, USA: Springer; 1990. p. 319–50.
Gioda G, Sakurai S. Back analysis procedures for the interpretation of field measurements in geomechanics. Int J Numer Anal Meth Geomech. 1987;11(6):555–83.
Goldberg DE. Genetic algorithm in search, optimization and machine learning. 2nd ed. Reading, MA, USA: Addison-Wesley; 1989.
Groetsch CW. Inverse Problems in the mathematical sciences. New York, USA: Springer; 1993.
Guo WD. Visco-elastic consolidation subsequent to pile installation. Comput Geotech. 2000;26 (2):113–44.
Haftka RT, Scott EP, Cruz JR. Optimization and experiments: a survey. Appl Mech Rev. 1998;51 (7):435–48.
Hanna S, Jim Yeh TC. Estimation of co-conditional moments of transmissivity, hydraulic head and velocity fields. Adv Water Resour. 1998;22(1):87–95.
Hoek E. Estimating Mohr-Coulomb friction and cohesion values from the Hoek-Brown failure criterion. Int J Rock Mech Min Sci Geomech Abstr. 1990;12(3):227–9.
Hoek E, Brown ET. Empirical strength criterion for rock masses. J Geotech Eng Div, ASCE. 1980;106(GT9):1013–35.
Hojo A, Nakamura M, Sakurai S, Akutagawa S. Characterization of non-elastic ground behavior of a large underground power house cavern by back analysis. Int J Rock Mech Min Sci. 1997;34(3–4): Paper No. 008.
Hsich PA, Neuman SP. Field determination of the three dimensional hydraulic conductivity tensor of anisotropic media 1, theory. Water Resour Res. 1985;21(11):1655–65.
Hsich PA, Neuman SP, Stiles GK, Simpson ES. Field determination of the three dimensional hydraulic conductivity tensor of anisotropic media 2, methodology and application to fractured rocks. Water Resour Res. 1985;21(11):1667–76.
Jhorar RK, Bastiaanssen WGM, Fesses RA, Van Dam JC. Inversely estimating soil hydraulic functions using evapor transpiration fluxes. J Hydrol. 2002;258(1):198–213.
Johari A, Javadi AA, Habibagahi G. Modelling the mechanical behaviour of unsaturated soils using a genetic algorithm-based neural network. Comput Geotech. 2011;38(1):2–13.
Joshi RR. Immune network memory: an inventory approaches. Comput Oper Res. 1995;22 (6):575–91.
Karaboga D, Ozturk C. A novel clustering approach: artificial bee colony (ABC) algorithm. Appl Soft Comput. 2011;11(1):652–7.
Katsifarakis KL, Karpouzos DK, Theodossiou N. Combined use of BEM and genetic algorithms in groundwater flow and mass transport problems. Eng Anal Bound Elem. 1999;23(7):555–65.
Kim YT, Lee SR. An equivalent model and back-analysis technique for modelling in situ consolidation behavior of drainage-installed soft deposits. Comput Geotech. 1997;20(2):125–42.
Kim CY, Bae GJ, Hong SW, Park CH, Moon HK, Shin HS. Neural network based prediction of ground surface settlements due to tunnelling. Comput Geotech. 2001;28(6–7):517–47.
Krajewski W, Edelmann L, Plamitzer R. Ability and limits of numerical methods for the design of deep construction pits. Comput Geotech. 2001;28(6–7):425–44.
Kuhn HW. Nonlinear programming: a historical view. In: Giorgi G, Kjeldsen TH, editors. Traces and emergence of nonlinear programming. Basel, Switzerland: Springer; 2014. p. 393–414.
Kuhn HW, Tucker AW. Nonlinear programming. In: Proceedings of 2nd Berkeley symposium on mathematics, statistics and probability. Berkeley (USA): University of California Press; 1951. p. 481–92.

Lagaros ND, Papadrakakis M, Kokossalakis G. Structural optimization using evolutionary algorithms. Comput Struct. 2002;80(7–8):571–89.
Ledesma A, Gens A, Alonso EE. Estimation of parameters in geotechnical back analysis. I: maximum likelihood approach. Comput Geoetch. 1996a;18(1):1–27.
Ledesma A, Gens A, Alonso EE. Parameter and variance estimation in geotechnical back-analysis using prior information. Int J Numer Anal Meth Geomech. 1996b;20(2):119–41.
Lesnic D, Elliott L, Ingham DB, Clennell B, Knipe RJ. A mathematical model and numerical investigation for determining the hydraulic conductivity of rocks. Int J Rock Mech Min Sci. 1997;34(5):741–59.
Leu SS, Chen CN, Chang SL. Data mining for tunnel support stability: neural network approach. Autom Constr. 2001;10(4):429–41.
Li HL, Yang QC. A least-square penalty method algorithm for inverse problems of steady-state aquifer models. Adv Water Res. 2000;23(8):867–80.
Louis C, Maini YN. Determination of in-situ hydraulic parameters in jointed rock. In: Proceedings of 2nd ISRM congress. Belgrade, Yugoslavia: ISRM; 1970. p. 235–45.
Lynden-Bell D, Gurzadyan V. Victor Amazaspovich Ambartsumian. Biographical Mem Fellows Roy Soc. 1998;44:23.
Mayer AS, Huang C. Development and application of a coupled-process parameter inversion model based on the maximum likelihood estimation method. Adv Water Res. 1999;22(8):841–53.
McCall J. Genetic algorithms for modelling and optimisation. J Comput Appl Math. 2005;184 (1):205–22.
Mello Franco JA, Assis AP, Mansur WJ, Telles JCF, Santiago AF. Design aspects of the underground structures of the Serra da Mesa hydroelectric power plant. Int J Rock Mech Min Sci. 1997;34(3–4):Paper No. 016.
Millar DL, Hudson JA. Performance monitoring of rock engineering systems using neural networks. In: Symposium of artificial intelligence in the minerals sector. University of Nottingham, UK: Institute of Mining Metallurgy; 1994. p. A3–A16.
Mitsuo G, Cheng RW. Genetic algorithm and engineering design. New York, USA: Wiley-Interscience; 1997.
Moses F. Optimum structural design using linear programming. J Struct Div, ASCE. 1964;90:89–104.
Murakami A, Hasegawa T, Sakaguchi H. Interpretation of ground performances based on back analysis results. In: Beer G, Booker JR, Carter JP, editors. Computer methods and advances in geomechanics. Rotterdam, Netherlands: AA Balkema; 1991. p. 1011–5.
Nelder JA, Mead R. A simplex method for function minimization. Comput J. 1965;7(4):308–13.
Nocedal J, Wright SJ. Numerical optimization. New York, USA: Springer; 1999.
Nutzmann G, Thiele M, Maciejewski S, Joswig K. Inverse modelling techniques for determining hydraulic properties of coarse-textured porous media by transient outflow methods. Adv Water Res. 1998;22(3):273–84.
Obara Y, Nakamura N, Kang SS, Kaneko K. Measurement of local stress and estimation of regional stress associated with stability assessment of an open-pit rock slope. Int J Rock Mech Min Sci. 2000;37(8):1211–21.
Ohkami T, Swoboda G. Parameter identification of viscoelastic materials. Comput Geotech. 1999;24(4):279–95.
Okui Y, Tokunaga A, Shinji M, Mori M. New back analysis method of slope stability by using field measurements. Int J Rock Mech Min Sci. 1997;34 (3–4): Paper No. 234.
Pelizza S, Oreste PP, Pella D, Oggeri C. Stability analysis of a large cavern in Italy for quarrying exploitation of a pink marble. Tunn Undergr Space Technol. 2000;15(4):421–35.
Romanov VG. Inverse problems of mathematical physics. Utrecht, Netherlands: VNU Science Press; 1987.

Rossmanith HP, Uenishi K. Post-blast bench block stability assessment. Int J Rock Mech Min Sci. 1997; 34(3–4): Paper No. 264.

Roth C, Chiles JP, de Fouquet C. Combining geostatistics and flow simulators to identify transmissivity. Adv Water Res. 1998;21(7):555–65.

Rumelhart DE, Hinton GE, Williams RJ. Learning internal representations by error propagation. In: Rumelhart DE, McClelland JL, editors. Parallel distributed processing, vol. 1. Massachusetts, USA: MIT Press; 1986. p. 318–62.

Russo D. On the estimation of parameters of log-unsaturated conductivity covariance from solute transport data. Adv Water Res. 1997;20(4):191–205.

Sakurai S. Lessons learned from field measurements in tunnelling. Tunn Undergr Space Technol. 1997;12(4):453–60.

Sakurai S, Akutagawa S. Some aspects of back analysis in geotechnical engineering. In: Ribeiro e Sousa L, Grossmann NF, editors. Proceedings on 1993 ISRM international symposium–EUROCK 93. Rotterdam, Netherlands: AA Balkema; 1995. p. 1130–40.

Sakurai S. Direct strain evaluation technique in construction of underground openings. In: Proceedings on 22nd US symposium of rock mechanics. Cambridge, MA, USA: MIT Press; 1981. p. 278–82.

Sakurai S, Takeuchi K. Back analysis of measured displacement of tunnels. Rock Mech Rock Eng. 1983;16(3):173–80.

Singh B, Viladkar MN, Samadhiya NK, Mehrotra VK. Rock mass strength parameters mobilised in tunnels. Tunn Undergr Space Technol. 1997;12(1):47–54.

Sklavounos P, Sakellariou M. Intelligent classification of rock masses. In: Adey RA, Rzevski G, Tasso C, editors. Applications of artificial intelligence in engineering—proceedings of the tenth international conference on applications of artificial intelligence in engineering. Udine, Italy: Computational Mechanics Publications; 1995. p. 387–93.

Sonmez H, Ulusay R, Gokceoglu C. A practical procedure for the back analysis of slope failure in closely jointed rock. Int J Rock Mech Min Sci. 1998;35(2):219–33.

Spendley W, Hext GR, Himsworth FR. Sequential application of simplex designs in optimization and evolutionary operation. Technometrics. 1962;4(4):441–61.

SriVidya A, Ranganathan R. Reliability based optimal design of reinforced concrete frames. Comput Struct. 1995;57(4):651–61.

Vasco DW, Karasaki K. Inversion of pressure observations: an integral formulation. J Hydrol. 2001;253(1–4):27–40.

Wang PP, Zheng C. An efficient approach for successively perturbed groundwater models. Adv Water Res. 1998;21(6):499–508.

Wen XH, Capilla JE, Deutsch CV, Gomez-Hernandez JJ, Cullick AS. A program to create permeability fields that honour single-phase flow rate and pressure data. Comput Geosci. 1999;25(3):217–30.

Wen XH, Deutsch CV, Cullick AS. Construction of geostatistical aquifer models integrating dynamic flow and tracer data using inverse technique. J Hydrol. 2002;255(1–4):151–68.

Werbos PJ. The roots of back propagation: from ordered derivatives to neural networks and political forecasting. New York, USA: Wiley; 1994.

Yang Y, Zhang Q. Application of neural networks to rock engineering systems (RES). Int J Rock Mech Min Sci. 1998;35(6):727–45.

Yang L, Zhang K, Wang Y. Back analysis of initial rock stress and time-dependent parameters. J Rock Mech Min Sci Geomech Abstr. 1996;33(6):641–5.

Yang Z, Lee CF, Wang S. Three-dimensional back-analysis of displacements in exploration adits-principles and application. Int J Rock Mech Min Sci. 2000;37(3):525–33.

Yang ZF, Wang ZY, Zhang LQ, Zhou RG, Xing NX. Back-analysis of viscoelastic displacements in a soft rock road tunnel. Int J Rock Mech Min Sci. 2001;38(3):331–41.

Yi CJ, Lu M. A mixed-integer linear programming approach for temporary haul road design in rough-grading projects. Autom Constr. 2016;71(2):314–24.

Yi H, Wanstedt S. The introduction of neural network system and its applications in rock engineering. Eng Geol. 1998;49(3–4):253–60.
Yi D, Xu MY, Chen SH. Application of genetic algorithms to back analysis of initial stress field of rock masses. Chin J Rock Mech Eng. 2001;20(Supp. 2):1918–22 (in Chinese).
Yi D, Chen SH, Ge XR. A methodology combining genetic algorithm and finite element method for back analysis of initial stress field of rock masses. Rock Soil Mech. 2004a;25(7):1077–80 (in Chinese).
Yi D, Xu MY, Chen SH, Ge XR. Application of neural network to back analysis of initial stress field of rock masses. Rock Soil Mech. 2004b;25(6):943–6 (in Chinese).
Zeidenberg M. Neural network models in artificial intelligence. New York, USA: Ellis Horwood; 1990.

Chapter 8
Comprehensive Application of the Finite Element Method: Xiaowan Project

Abstract Concrete arch dam exhibits remarkable spatial-time characteristics because its working state might be evolved dramatically attributable to the dynamic construction process and operation environment. To overcome the limitations of routine design and analysis approaches for the high arch dam due to predetermined modes and assumptions, further advanced study is demanded to demonstrate the adequacy of structural analysis theories and calibration standards, as well as to evaluate its safety credibly. In this chapter, the systematic study on Xiaowan Arch Dam at a height of 294.5 m is exhibited, which covers the whole process from the back analysis of in situ geo-stress to the excavation/reinforcement of abutment/foundation, followed with the concrete placement/cooling/grouting operation until the reservoir impoundment/service. This study is supported by a toolkit termed as the "Digitized System of Xiaowan Arch Dam" (DSXAD) which is the combination of the instrumentation system, the FEM system towards the fields of permeability/temperature/deformation, and the decision making system towards engineering judgment. The evolution of the real working state of the arch dam has been thoroughly revealed, and a series of difficult technical issues such as the foundation rock EDZ and dam concrete cracks emerged during its construction, are successfully solved under the guidance of the DSXAD.

8.1 General

From the initial batch of arch dams over the height of 100 m in the late 1980s to the completion of 250 m high Ertan Arch Dam in 1995, plentiful experiences concerning the investigation, design, research, construction and operation of high arch dams had been accumulated in China. Since the new Millennium, the "Development of the West Regions" policy of China has further accelerated the high arch dam construction in the country. For example, the completion of Xiaowan Arch Dam (H = 294.5), Jinping 1 Arch Dam (H = 305 m) and Xiluodu Arch Dam (H = 278 m) established a landmark as one of the Chinese great achievements (Pan and He 2000; Jia 2013).

S.-H. Chen, *Computational Geomechanics and Hydraulic Structures*,
Springer Tracts in Civil Engineering, https://doi.org/10.1007/978-981-10-8135-4_8

As a slim shell structure flexibly based on its deformable foundation, concrete arch dam exhibits remarkable spatial-time characteristics. This is prominent since the working state might be evolved dramatically attributable to the dynamic construction process and the operating environment, particularly for high double-curvature arch dams with huge thrust actions from reservoir water (Chen 2015). However, the routine design and analysis approaches are limitedly available due to the predetermined modes and assumptions postulated in these approaches, which may only partially reflect the real working state of the arch dam under the supposed boundary conditions. For this reason, further study is demanded to reveal the evolution mechanism of spatial-time characteristics of high arch dams, so as to demonstrate the adequacy of the structural analysis theories and the correspondent calibration standards, as well as to evaluate the safety, reliability, economy and rationality of the arch dam which is under construction or putting into operation.

At a height of 294.5 m and total hydraulic thrust force of 18 million tons, Xiaowan Arch Dam was the most challenging hydropower project in China (Zou 2010) facing crucial difficulties (e.g. complicated geological conditions) beyond the existing design codes/specifications and the experiences in many aspects. Attributable to its special leading position and current technology situation, explorations and studies for Xiaowan Dam had been continuously conducted throughout the whole process from the early design phases to the execution and operation periods. Particularly, in the initial period of construction, the information-based dynamic design concept was well accepted and the systematic instrumentation was arranged for the dam. Therefore, this dam is an ideal and precious object for the study on the spatial-time characteristics of high double-curvature arch dams, because it is able to provide abundant, detailed and accurate field data for the verification.

In this chapter, the systematic study on Xiaowan Arch Dam by the FEM is presented, which covers the whole procedure from the in situ geo-stress back analysis to the abutment excavation and concrete placement until the reservoir impoundment operation. The study is elaborated by the combination of the instrumentation system, the numerical computation, and the engineering judgment, in a toolkit termed as the “Digitized System of Xiaowan Arch Dam” (DSXAD). With the help of the DSXAD, the evolution of the real working state of the dam during its construction period as well as service period has been revealed, and a series of difficult technical issues emerged during the construction of the dam are successfully solved (Zou et al. 2016).

8.2 Presentation of the Project

8.2.1 Layout

The main hydraulic structures layout in the project are the double curvature arch dam, plunge pool, auxiliary weir, flood release and diversion tunnels, and underground power plant system (see Fig. 8.1). The river bed is at the EL. 950.5 m and the dam crest is at the EL. 1245 m. The dam thickness varies from 12 m at the crest to 72.9 m at the base of the crown cantilever (Zou 2010).

The main accessory works comprised in the arch dam are 5 overflow spillways, 6 middle elevation orifices, 2 drawing down bottom outlets, 3 diversion orifices, 2 diversion bottom outlets, drainage galleries and drainage holes, and concrete aprons at the upstream and downstream respectively, etc. (see Fig. 8.2).

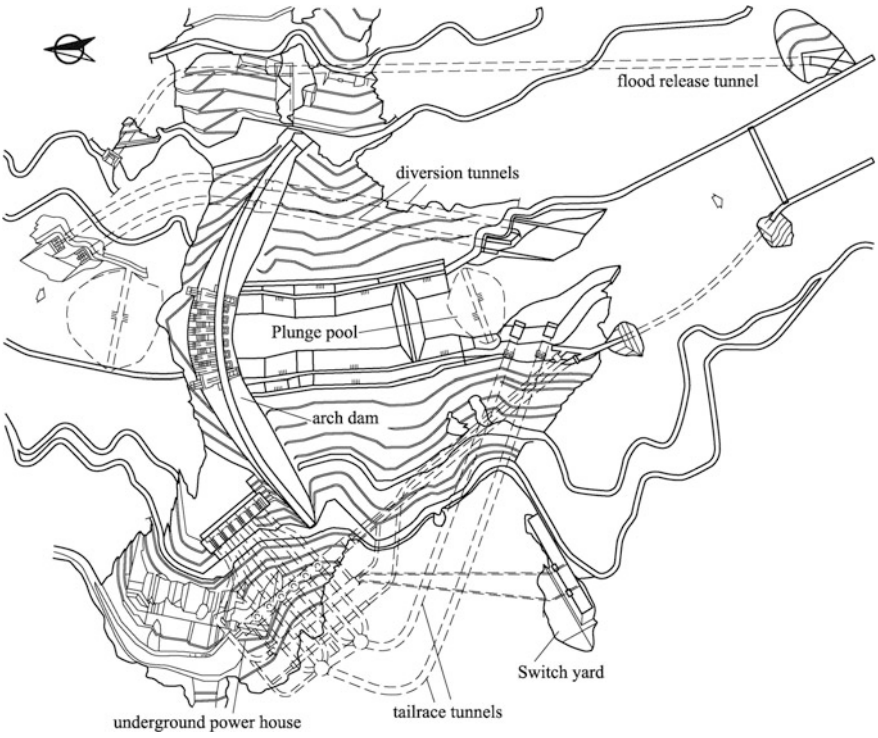

Fig. 8.1 Plan showing the layout of Xiaowan Project

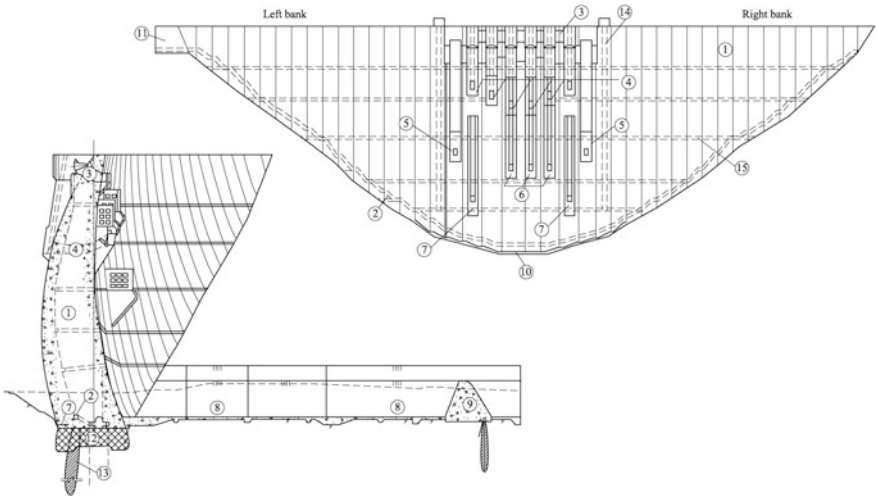

Fig. 8.2 Cantilever profile and upstream elevations of Xiaowan Arch dam. ①—arch dam; ②—foundation grouting gallery; ③—overflow spillway; ④—orifice spillway; ⑤—drawing down bottom outlet; ⑥—diversion orifice; ⑦—diversion bottom outlet; ⑧—plunge pool; ⑨—auxiliary weir; ⑩—bottom inducing joint; ⑪—abutment thrust pier; ⑫—consolidation grout; ⑬—curtain grout; ⑭—lift shaft; ⑮—inspection gallery

8.2.2 Engineering Geology

The project is located in a V-shaped valley stretching 2300 m long where the gullies are deeply cut, the mountains are steep and nearly 1000 m high above the natural river water. During dry seasons, the river water is 80–120 m wide. A number of high and steep slopes, especially the 700 m high cut slope along the abutment sections, have to be handled towards the layout of the permanent and temporary structures and construction sites.

The bedrocks distributed in the project area is of moderately-to deeply metamorphic rock system which consists mainly of granite, gneiss and hornblende plagioclase gneiss, intercalated with discontinuous and thin layered schist. The rock formations trend perpendicular to the river in a form of monolithic structure, and dip towards upstream. The rock is weathered on its superficial layer. The base boundary of the moderately weathered rock under the dam site is changeable from 30 m deep (in the riverbed) to 35–50 m deep (in the two banks).

Stress release is one of the major engineering geological features. The superficial rocks on both bank slopes had been relaxed due to the stress release during the river trenching history: opening fissures are fully developed; most of the schist intercalations are normally argillified or softened. The depth of the stress release zone is closely related with topography. For example, it is much deeper in the mountain ridges with well developed opening shear fissures, whereas in the portions of gullies very thick Quaternary topping deposits are distributed.

In the dam site, there exist one grade II fault (F_7) with the strike angle nearly EW and dip angle N∠74°–90°, fragment width 18.6–37 m, principal fracture width 0.8–2.5 m. The nearest distance from the fault F_7 to the dam heel is 50 m.

There are more than 20 grade III faults (e.g. F_{11}, F_{10}, F_5, F_{20}, F_3), of which only F_{20} with strike angle nearly SN belongs to tensile-torsion fault, the others are all compression-torsion faults with strike angles N75°–80°W and dip angles NE∠75°–90°. The width of the grade III fault is normally 0.5–4 m.

A number of grade IV and V structural planes such as f and gm are grouped into two sets: the high dip angle ones are well developed (f_{12}, f_{34}, f_{30}, f_{15}) while the low dip angle ones are not fully developed. The high dip angle f and gm are further distinguished according to their strikes into two sub-sets as nearly EW trending (strike angle N70°–85°W) with average space 15 m, and nearly SN trending (strike angle N10°W–N20°E) with average space 20 m.

There are 5 geological erosion zones in the resistance bodies influencing the deformation and stability of dam abutments, of which E_8 is in the left abutment, E_1, E_4, E_5 and E_9 are in the right abutment. They are all nearly NS trending.

In addition, there also exist three sets of dominant joints:

① High dip angle joints across the river;
② High dip angle joints along the river; and
③ Middle/low dip angle joints along the river.

Figure 8.3 is the geological plan of the dam site. The geological features used in the design are summarized in Tables 8.1, 8.2, 8.3 and 8.4.

According to the field explorations and tests, the maximum in situ geo-stress near the river bed is σ_1 = 26.7 MPa.

The natural underground water table is approximately 40–60 m below the ground surface.

8.2.3 Concrete Materials

Through the optimal study on the concrete composition (cement, flying ash, aggregate, admixture), the dam body is casted in three concrete zones of A ($C_{180}40$), B ($C_{180}35$), C ($C_{180}30$). They possess properties idealized as "high strength, high ultimate tensile strain, moderate elastic modulus, low heat productivity and shrinkage". However, for the implementation of the DSXAD, several special studies had been carried, such as the comparative studies on the traditional wet-screened concrete versus fully-graded concrete, the comparative studies on the adiabatic temperature rise obtained from the concretes of long-age (180 days) versus standard 28 days-age, as well as the creep degree and volumetric deformation of the concretes. In addition, the temperatures of reservoir water and ambience were fitted by the long term field observation. Attributable to these studies, the spatial-time characteristics of the concrete materials are fully available in a manner of simulating computation by dynamic assignment of the concrete material properties.

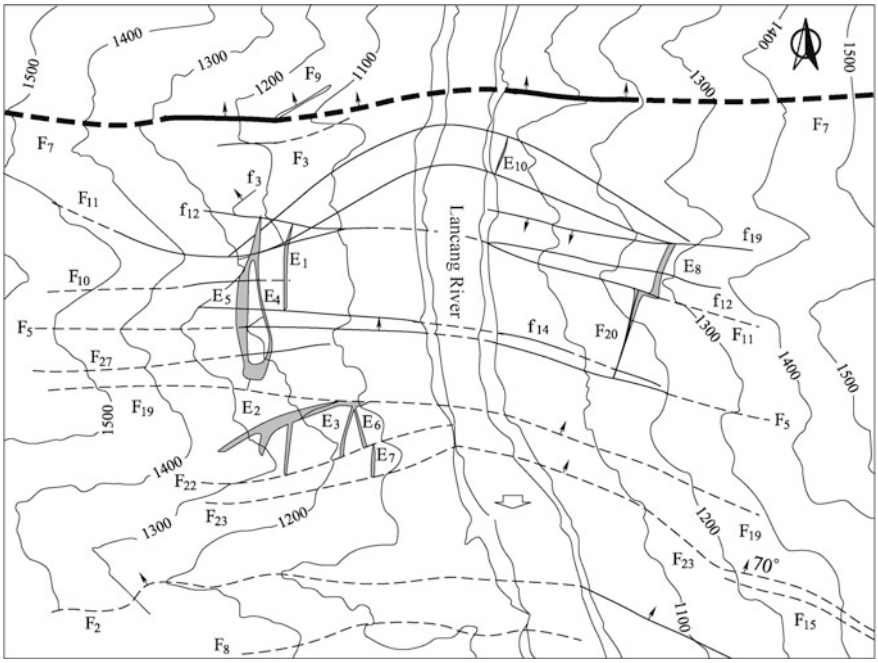

Fig. 8.3 Geological plan of the dam site

(1) Comparative study on the wet-screened concrete versus fully-graded concrete

The properties of concrete that affect the behaviors of the arch dam mainly involve several relevant indices with regard to heat, permeability, and deformation. According to the conventional tests on wet-screened concrete, the concrete designed for Xiaowan Dam possesses ideal properties. After the start of the concrete placement, however, by the fully-graded concrete tests it was verified that the concrete actually placed in the dam are subject to remarkable variations in contrast to wet-screened tests, these are

① A compressive strength variation about 85–117%;
② A split tensile strength variation about 78–95%;
③ An axial tensile strength variation about 50–80%;
④ An ultimate tensile strain variation about 55–78%;
⑤ A creep strain variation about 50–98% (under load at 7th day–180th day); and
⑥ An elasticity modulus variation about 95–127%.

In terms of the cracking-resistance performance of concrete, the fully-graded concrete is poorer than that of wet-screened concrete.

Table 8.1 Attitudes of the joint sets (feasibility study)

Elevation (m)		Strike (°)	Dip angle (°)	Strong weathered			Weakly weathered			Slightly weathered		
				Space (m)	Aperture (mm)	Persistence (%)	Space (m)	Aperture (mm)	Persistence (%)	Space (m)	Aperture (mm)	Persistence (%)
Left bank	975.0–950.5	90	88	0.30	0.80	85	0.40	0.16	70	0.50	0.08	50
		10	80	0.35	0.05	95	0.45	0.02	80	0.45	0.01	60
		270	16	0.93	0.80	80	1.34	0.16	60	1.84	0.08	25
Right bank		95	88	0.30	0.80	85	0.40	0.16	70	0.50	0.08	50
		10	80	0.35	0.05	95	0.45	0.02	80	0.55	0.01	60
		90	19	1.02	0.80	80	1.94	0.16	60	2.14	0.08	25
River bed under 950.5		90	88	0.30	0.80	85	0.40	0.16	70	0.50	0.08	50
		10	80	0.35	0.05	95	0.45	0.02	80	0.45	0.01	60
		90	0	0.93	0.80	80	1.34	0.16	60	1.84	0.08	25

Table 8.2 Attitudes of the faults (feasibility study)

Sequence	Dip direction (°)	Dip angle (°)	Coordinates of mean point (m)			Thickness (m)
			X	Y	Z	
F_7	357	85	1000	957	1245	3.00
F_{19}	12	77	−100	510	990	0.50
F_{11}	10–30	83–90	700	630	930	0.30
F_5	9	80	1000	368	1245	0.46
F_{10}	5	85	0	640	990	0.11
F_{20}	280	85	740	500	1150	0.20
F_{27}	10	75	0	510	1150	0.15
f_{12}	8	83	300	730	930	0.32
f_{14}	10	80	1000	370	1245	0.30
f_{11}	10	80	0	600	1150	0.45
f_{21}	8	70	800	530	1150	0.10
f_{33}	270	90	880	450	1150	0.17
f_{29}	90	87	770	500	1150	0.20
f_{19}	200	75	700	690	1150	0.06
f_{10}	10	85	0	640	1150	0.20
f_{15}	95	90	230	650	990	0.15
f_{36}	245	80	200	560	1070	0.10
f_{17}	5	90	850	665	1190	0.15
f_{30}	300	90	800	620	1190	0.11
f_{34}	275	88	880	650	1190	0.50
f_{32}	65	85	780	660	1190	0.20
f_9	10	81.5	100	680	1110	0.16

Table 8.3 Attitudes of the erosion bands (feasibility study)

Sequence	Dip direction (°)	Dip angle (°)	Coordinates of mean point (m)			Thickness (m)
			X	Y	Z	
E_1	276	87	110	650	1150	0.25–7.0
E_5	265–280	90	50	650	1150	3.50–20.0
E_4	265	87	40	500	1150	0.30–13.5
E_8	300	90	800	620	1190	2.0–12.0

Table 8.4 Attitudes of the loosen fissure bands (feasibility study)

Sequence	Dip direction (°)	Dip angle (°)	Coordinates of mean point (m)			Thickness (m)
			X	Y	Z	
L_1	275	28	758	726	1170	0.05
L_2	275	28	810	700	1210	0.05
R_1	85	26	82	688	1170	0.05
R_2	85	26	42	664	1210	0.05

(2) Comparative study on the adiabatic temperature rise of long-age versus 28 days-age

According to the test data of 28 days-age (stipulated in the design specifications), the thermal parameters and its related characteristics of concrete in Table 8.5 are employed in the feasibility study phase.

It is necessary to emphasize that the comparison study shows that the final adiabatic temperature rise based on the long-age test ($C_{180}35$, with final fitted value of 39.2 °C) is 12.17 °C higher than that of the conventional 28 days-age test ($C_{180}35$, with final fitted value of 27.03 °C) (see Fig. 2.6).

(3) Creep degree and volume deformation

Fitting of creep degree and volume deformation of concrete had been carried out based on the tested data (see Fig. 2.21; Tables 2.40 and 2.41), for the purpose to fully describe the time dependent characteristics of the dam.

(4) Temperatures of reservoir water and ambience

The temperatures of reservoir water and ambience are fitted by the long term field readings. Figure 8.4 gives the monitored and fitted reservoir water temperatures at two typical object points.

The daily variation of ambient temperature is exactly provided by the local meteorological station and inputted for the thermal field analysis during the

Table 8.5 Thermal parameters of the concretes in Xiaowan Dam (feasibility study)

Grade	Adiabatic temperature rise θ_t (°C)	Thermal diffusivity a (m^2/h)	Volumetric weight γ (kg/m^3)	Specific heat c (kJ/kg °C)	Coefficient of thermal expansion α ($\times 10^{-6}$/°C)	Surface exothermic coefficient β (kJ/m^2 h °C)
$C_{180}40$	$\theta_t = 30t/(3.8 + t)$	0.00319	2500	1.036	8.2	47.1
$C_{180}35$	$\theta_t = 27t/(4.0 + t)$	0.0032				
$C_{180}30$	$\theta_t = 25t/(4.0 + t)$	0.0032				

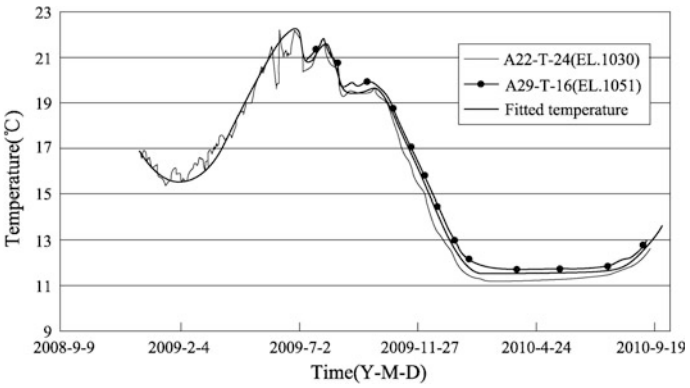

Fig. 8.4 Monitored and fitted temperatures of the reservoir water

construction period of dam. For the purpose of long term performance forecast, according to the SL282-2003 «Design specification for concrete arch dams» the annual variation of ambient temperature is fitted by the monthly average temperature observed in the dam site. Using the observed data since December 13, 2005, the local meteorological station provided the fitted annual variation of the ambient temperature (with the correlation index $\rho = 0.991$) in the formula

$$T = 20.584 + 5.74 \times \cos[0.516(t - 6.7)] \tag{8.1}$$

where t = accumulated months since December, 2005.

8.2.4 Construction Procedure

(1) Dam foundation and abutment excavation

The excavation of the dam foundation and abutments is undertaken following the sequential benches that

- Above the EL. 1030 m, 20 m for each cut bench;
- Below the EL. 1030 m, 10 m for each cut bench.

Altogether 19 cut benches are carried out.

(2) Dam body placement

Figure 8.5 shows the placement procedure of the typical dam monolith 22# (crown cantilever).

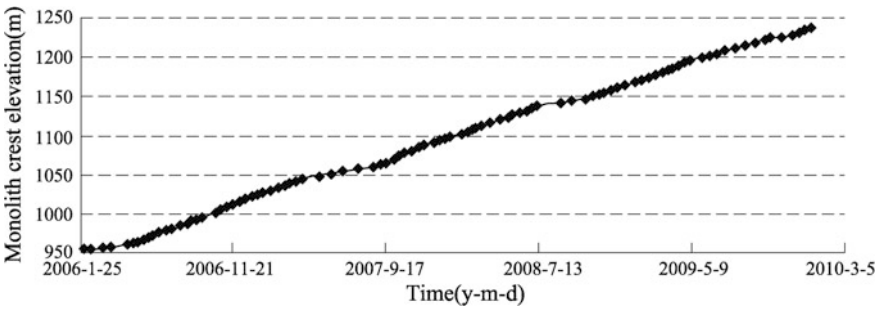

Fig. 8.5 Placement schedule of the crown cantilever dam monolith 22#

(3) Cooling scheme

Both the metal (black) cooling pipes (coefficient of heat conductivity = 262.8 kJ/m h °C) and plastic (HDPE) cooling pipes (coefficient of heat conductivity = 1.66 kJ/m h °C) are employed. The cooling pipes are serpentinely layout, the space between pipes are

– 1.5 m × 1.5 m (horizontal × vertical) in restraint zone (near the base); and
– 1.5 m × 3.0 m (horizontal × vertical) in non-restraint zone.

8.2.5 Instrumentation

The whole dam is monitored by the installation of 215 object points for deformation (plumb line, diffraction alignment, geometric leveling, GPS), 208 object points for stress/strain/temperature (differential resistor sensor), 145 object points for seepage pressure (vibrating wire sensor). The accuracy and reliability of the data extracted from the instrumentation system in the DSXAD are rigorously checked during the manufacture and installation of the instruments by the Chinese National Specifications (e.g. DL/T5211-2005 «Technical specification for dam safety monitoring automation», SL268-2001 «Fundamental specification of equipment of automation system for dam safety monitoring»).

In the evaluation of the dam performance hereinafter, the relative difference $\|e\|_r$ and absolute difference $\|e\|_a$ between the observed and computed variables (e.g. temperature, hydraulic head, deformation, stress) are defined

$$\begin{cases} \|e\|_r = \left| \dfrac{\delta_{observation} - \delta_{computation}}{\delta_{observation}} \right| \\ \{|e\|_a = \left| \delta_{observation} - \delta_{computation} \right| \end{cases} \tag{8.2}$$

where $\delta_{observation}$ = observed variable; $\delta_{computation}$ = computed variable.

8.3 Back Analysis of the In Situ Geo-Stresses in the Dam Site

In situ geo-stress field is an important factor in the arch dam design with regard to the abutment deformation and stability. To determine its magnitude and orientation by field testing, much manpower and material resource are requested. Based on the field readings, the stress regression method should be designed to determine the in situ geo-stress field by means of regression method, least-squares method and others (Fairhurst 2003). In recent decades, the research shows that the hybrid artificial neural network (ANN) and FEM performs well towards the back analysis of in situ geo-stress field using tested stresses (Yi et al. 2004). The ANN belongs to computation intelligence (CI) prevalently used for nonlinear data mapping to fit the complex relationship between inputs and outputs (vide Chap. 7). The mainstream steps towards the back analysis of the in situ geo-stress field in Xiaowan Dam site are briefly summarized as follows.

① Establish 3D regional FE model with effort to reflect joints, fractures and terrain.
② Define a set of boundary load combinations for the regional FE model corresponding to the tectonic activities.
③ For each boundary load combination, implement FE analysis to obtain the stresses at the field testing points.
④ The computed stresses at the field testing points and the corresponding boundary load combinations are grouped into training samples for the ANN, in which the stresses are inputs and the boundary load combinations are outputs.
⑤ The ANN training is carried out using the samples defined in step ④.
⑥ Input the stress readings by the field tests into the trained ANN leads to the "best guess" of the boundary load combination.
⑦ Apply the "best guess" of boundary load combination to the 3D regional FE model, the in situ geo-stress field outcomes as the initial condition in the subsequent simulation of slope and dam abutment excavation.

8.3.1 In Situ Geo-Stress Tests

All the tests were conducted using stress relief method. Two-dimensional geo-stress tests employ single borehole with dip angle of 5°–8°; Three-dimensional geo-stress tests employ three crossed boreholes, whose dip angles are 5°–8°.

The in situ geo-stress test indicates that the maximum principal stress is nearly SN trending at the shallow overburden, and shifted towards NWW at the depth of the underground cavern (machine house) with maximum value 10–25 MPa.

Table 8.6 Tested in situ geo-stresses at Xiaowan Dam site for back analysis

Point	Overburden depth (m)	Stress components (MPa)					
		σ_x	σ_y	σ_z	τ_{yz}	τ_{zx}	τ_{xy}
σ_7	134.4	−2.90	−8.20	−6.60	2.80	−0.80	3.60
σ_{104}	100.7	−6.10	−6.80	−5.60	−3.50	3.80	0.10
σ_{13}	91.9	−6.90	−14.40	−8.40	−2.50	−3.30	−0.40
PD15	169.1	−8.40	−27.60	−12.50	−0.80	3.70	2.80
Machine chamber 1	395.5	−17.80	−15.60	−19.90	5.90	−7.10	3.30
Machine chamber 2	283.1	−11.10	−10.00	−13.70	2.40	−2.80	0.30
Machine chamber 3	407.4	−15.10	−14.70	−16.50	3.60	−4.10	0.10
PD57-3	55.9	−5.13	−7.67	−5.61	0.99	−2.22	4.26

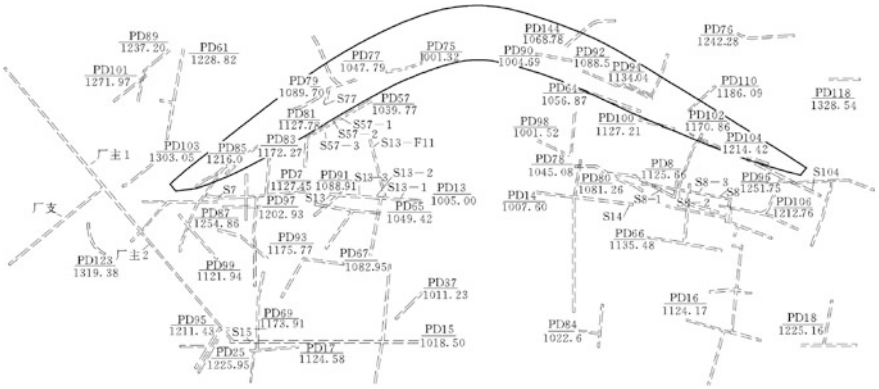

Fig. 8.6 Plan showing the layout of test points for in situ geo-stresses

Table 8.6 lists the three-dimensional in situ geo-stresses of the 8 object points for the back analysis. They are all located in the fresh (intact) or slightly weathered rocks (see Fig. 8.6).

8.3.2 Characteristics of the Computation

(1) Computation domain

The back analysis is carried out in a domain by dividing the dam site from north to south in a length of 6500 m, from east to west in a width of 3000 m, the bottom elevation is −300 m.

(2) Faults

The largest faults F_5, F_7 are discretized explicitly using the joint element with thickness.

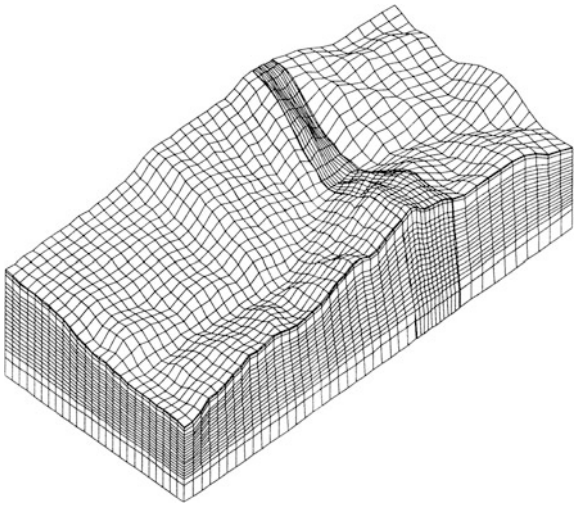

Fig. 8.7 FE mesh for the back analysis of in situ geo-stresses

(3) Boundary conditions

The eastern and northern sides are horizontally constrained meanwhile the bottom is vertically (Z-direction) supported. On the western and southern sides, the linearly distributed boundary pressures are exerted for the purpose to simulate the tectonic action of the Earth crust, whose values are back analyzed.

(4) Physical and mechanical properties

Elided.

(5) FE mesh

The mesh for the back analysis in Fig. 8.7 is discretized using hexahedral elements of 8-nodes for rocks, and joint elements with thickness for faults F_5, F_7. It contains 25,000 elements and 27,846 nodes.

8.3.3 Results and Discussions

Use is made of the 8 field test points (see Table 8.6), the in situ geo-stress field is back analyzed with the optimal weight factors respect to gravity $\Delta = 1.57$, EW tectonic pressure $U = 0.42$ MPa, NS tectonic pressure $V = 7.02$ MPa.

Figures 8.8 and 8.9 show the distribution of geo-stresses on the sections across the river stream. Table 8.7 lists the relative error of back analyzed geo-stresses with regard to that of measured. The average error is approximately 18%.

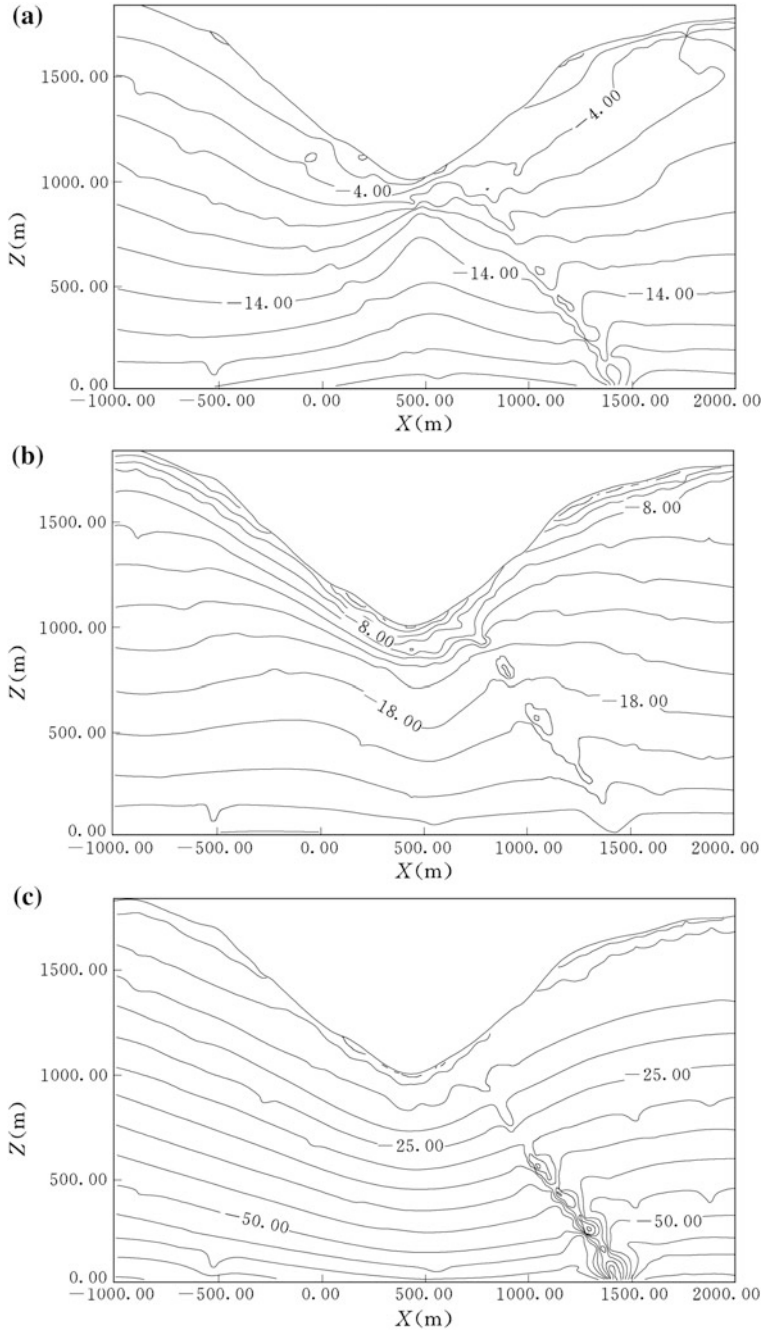

Fig. 8.8 Contours of geo-stresses at the vertical section Y = 500 m across the river (Unit: MPa). **a** σ_1; **b** σ_2; **c** σ_3

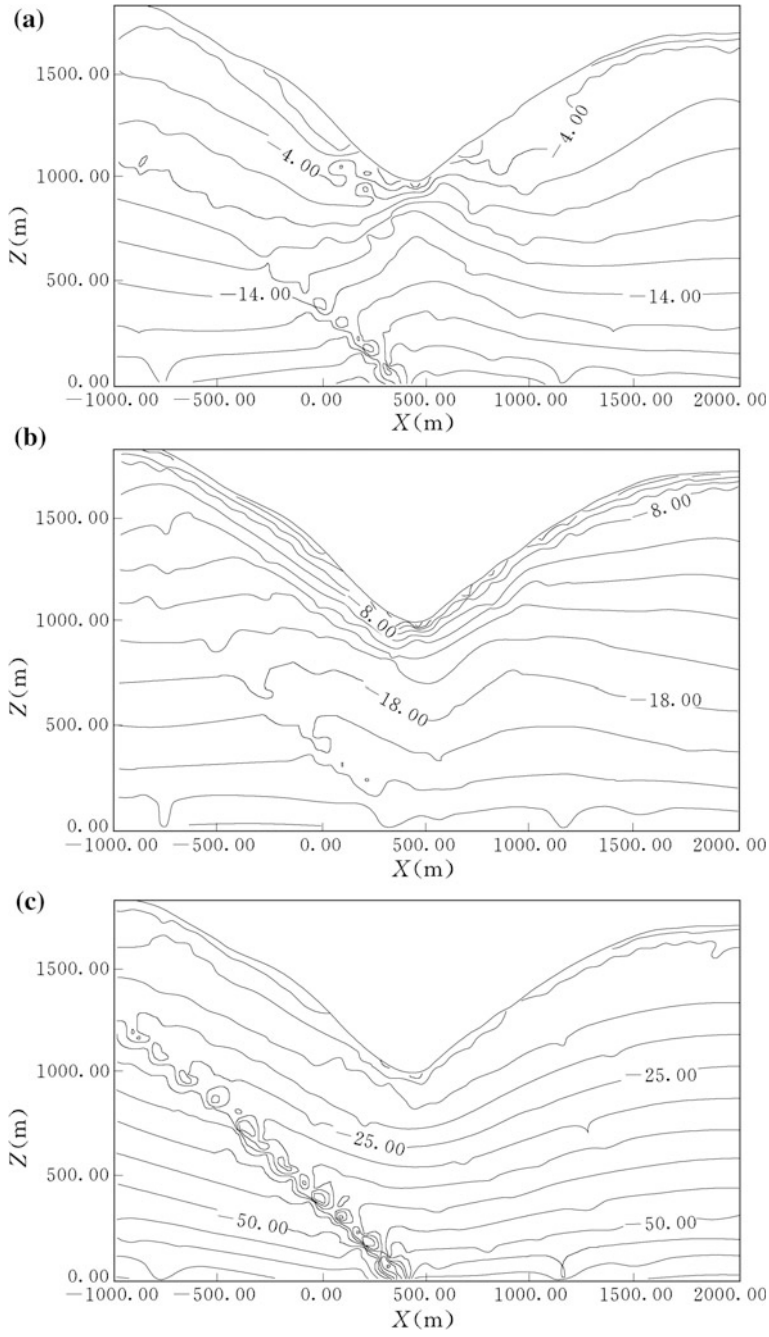

Fig. 8.9 Contours of geo-stresses at the vertical section Y = 700 m across the river (Unit: MPa). **a** σ_1; **b** σ_2; **c** σ_3

Table 8.7 Relative error of the back analyzed in situ geo-stresses

Point	Back analyzed geo-stress components (MPa)			Relative error		
	σ_x	σ_y	σ_z	σ_x	σ_y	σ_z
σ_7	−2.90	−8.43	−6.74	0.001	0.027	0.021
σ_{104}	−5.32	−6.79	−7.36	−0.128	−0.001	0.315
σ_{13}	−9.22	−13.09	−8.92	0.337	−0.091	0.062
PD15	−7.15	−11.82	−10.51	−0.149	−0.572	−0.159
Machine chamber 1	−7.15	−13.18	−15.26	−0.598	−0.155	−0.233
Machine chamber 2	−8.01	−12.81	−13.11	−0.279	0.281	−0.043
Machine chamber 3	−7.62	−13.44	−16.77	−0.495	−0.086	0.017
PD57-3	−5.17	−7.81	−4.53	0.008	0.019	−0.192

8.4 Excavation and Reinforcement of the Dam Abutments

8.4.1 Dominant Factors Influencing the Deformation and Stability of the Dam Abutments

(1) Abutment resistance bodies

There are four grade III faults (F_{11}, F_{10}, F_5, F_{20}) across the downstream of the dam abutments, which may potentially affect the deformation and stability of the abutment resistance bodies.

The erosion zones E_8 located at the left abutment and E_1, E_4, E_5, E_9 located at the right abutment, may influence the deformation and stability of the abutment resistance bodies, too.

These discontinuities should be taken into account of in the design of deep reinforcement scheme for the abutments.

(2) At the vicinity of dam abutments

The dominant factors adverse to the excavated slopes at the vicinity of abutment surfaces are the low-dip joints of SN-trending, the high-dip joints and erosion zones of SN-trending, and the EW-trending faults of steep-inclined (e.g. grade III faults F_3 and F_{11}).

These discontinuities might give rise to various unstable rock blocks. According to the excavation layout and geological conditions, the major failure modes of unstable blocks or their combinations are

- Toppling from the exposure surface into the excavated pit;
- Planar slip along the low-to-middle inclined structural planes towards the river channel or excavated pit;
- Collapse or slip of the cut slope in front of the dam.

8.4.2 Characteristics of the Reinforcement Analysis

(1) Computation domain

The analysis is carried out for the domain enclosing the dam site, which is 1000 m from north to south, 1600 m from east to west. Bottom restraints are imposed at the EL. 700 m. Figure 8.10 is the plan showing the major discontinuities explicitly simulated in the FE mesh.

(2) Excavation bench

All together 28 benches (20 m high for each) are excavated. Figure 8.11 is the plan of the excavated bench surface. Figures 8.12 and 8.13 show the left and right abutments in December, 2004.

(3) Layout of reinforcement schemes

1. Layout of the deep reinforcement within the dam abutments

After the systematic study on the 8 representative reinforcement schemes, the scheme with shear keys + concrete replacement for the fault F_{11} + downstream dam heel filet, is finally recommended and implemented. Figure 8.14 is the diagram showing the layout of this reinforcement scheme in the right abutment at the EL. 1130 m.

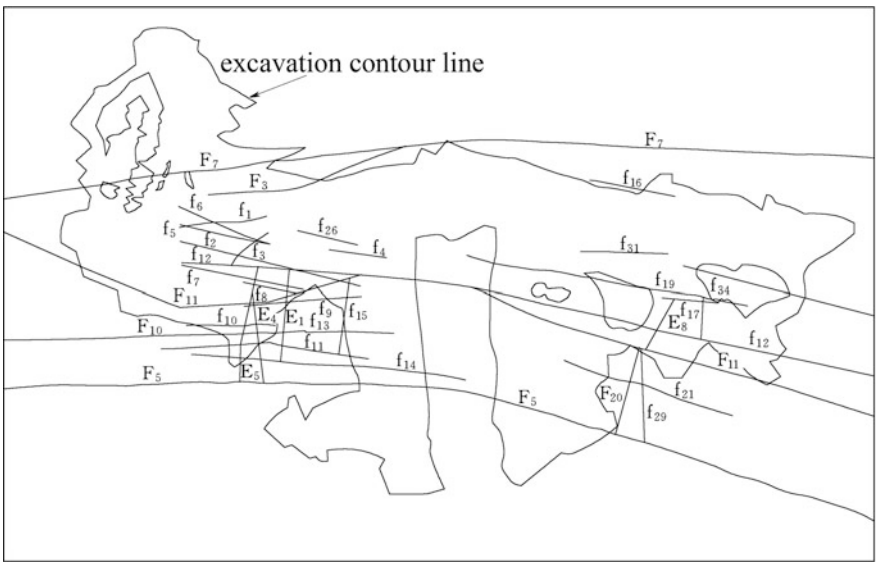

Fig. 8.10 Major discontinuities explicitly simulated in the FE mesh

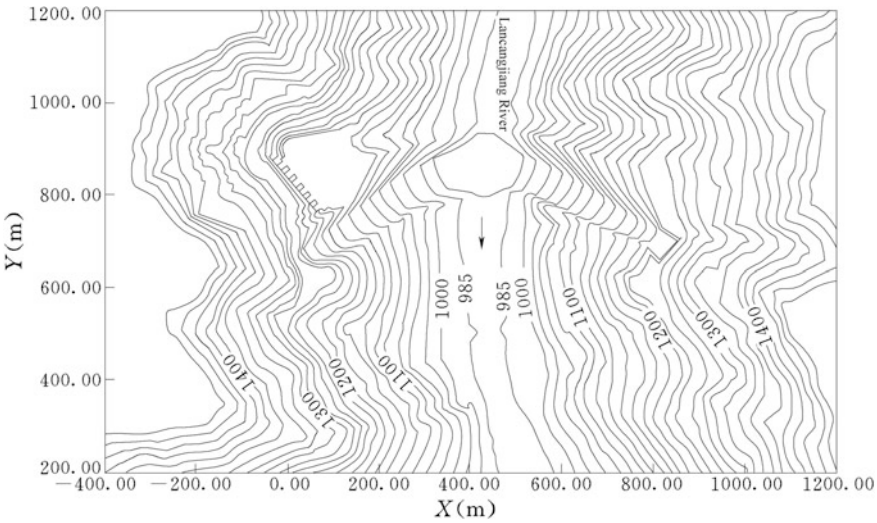

Fig. 8.11 Diagram of the plan showing excavated bench surfaces

Fig. 8.12 Left abutment excavation (2004–12)

Fig. 8.13 Right abutment excavation (2004–12)

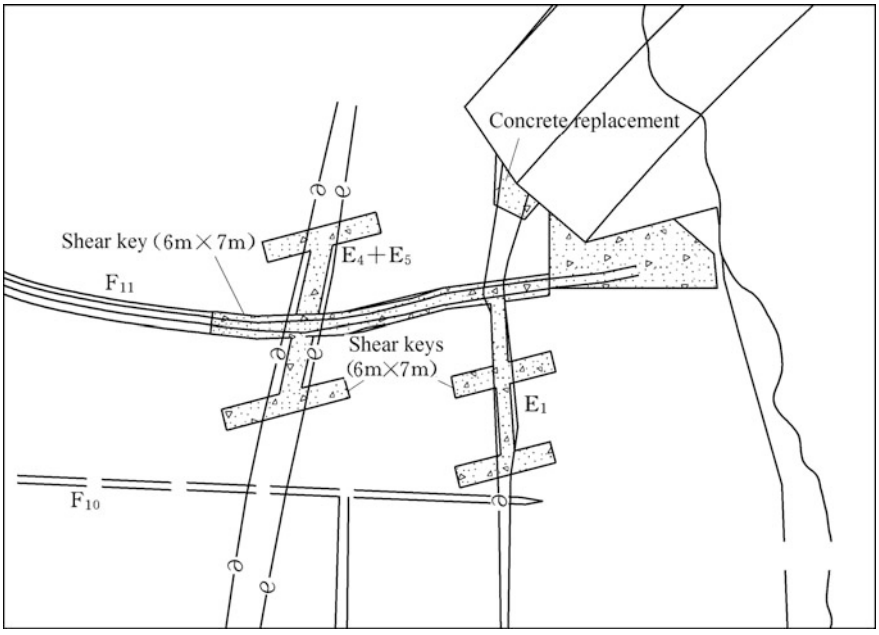

Fig. 8.14 Diagram showing the final deep reinforcement scheme at the EL. 1130 m (shear keys + concrete replacement for the fault F_{11} + downstream dam heel filet)

2. Layout of the shallow reinforcement at the vicinity of abutment surfaces

After the systematic study on the 2 representative reinforcement schemes using both the FEM and BEM (vide Chap. 13), the finial reinforcement scheme at the shallow vicinity of abutment surfaces focused on both the construction period and operation period, is proposed (see Fig. 8.15; Tables 8.8, 8.9 and 8.10). Altogether more than 60,000 fully grouted bolts and more than 8000 pre-stress stranded wire cables, are installed.

(4) FE mesh (see Fig. 8.16).
(5) Physical and mechanical parameters
Elided.

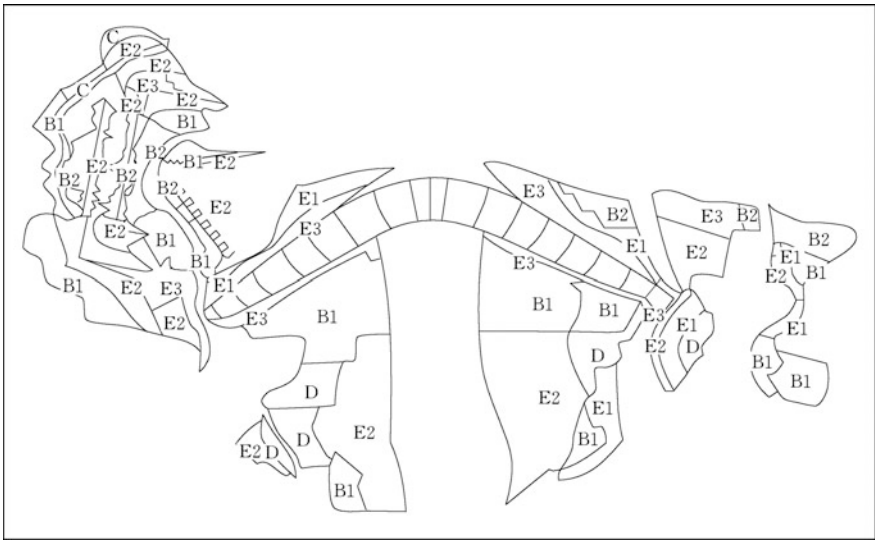

Fig. 8.15 Plan showing the final shallow reinforcement scheme

Table 8.8 Zoning of the final shallow reinforcement scheme

Zone	A	B1	B2	C	D	E1	E2	E3
Pre-stress cable (MN)	6	3	3	1.8	1	–	–	–
Full-grouted bolt	Φ25	Φ25	–	Φ25	Φ25	Φ32	Φ25	Random

Table 8.9 Parameters of pre-stress anchor cables of the final shallow reinforcement scheme

Pre-stress (MN)	6	3	1.8	1
Length (m)	80	30–60	30–50	30–45
Horizontal space (m)	4	4–6	5	5–6
Vertical space (m)	4	4–6	8–12	4

Table 8.10 Parameters of fully-grouted bolts of the final shallow reinforcement scheme

Diameter	Φ32	Φ25
Length (m)	9	3–6
Horizontal space (m)	2.5	2.5–3
Vertical space (m)	2	1.5–3

Note All the cables and bolts are installed at a downwards dip angle 15°

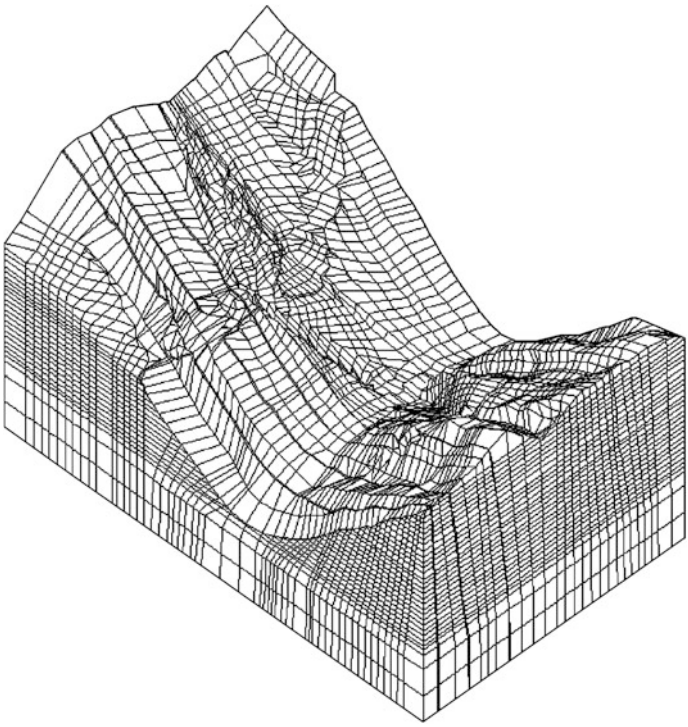

Fig. 8.16 FE mesh of the arch dam foundation and abutments (29,638 elements; 32,533 nodes): bid design

(6) In situ geo-stress field.

The in situ geo-stress field of the dam site has been back analyzed previously (Sect. 8.3) in a fair large overlay domain to eliminate the boundary effects with regard to the tectonic action distribution, but consequently the effects of small faults of grade III and IV as well as the erosion zones are over looked. Therefore, towards the computation of abutment deformation and stability, the secondary back analysis using smaller domain taking into account of all important III and IV grade faults as well as the erosion zones, is demanded. The boundary conditions in the form of deformation or stress are specified using the corresponding results obtained in the first phase of back analysis with the larger overlay domain (Qin et al. 2008).

8.4.3 Results and Discussions

The benchmark scheme without reinforcement indicates that the abutment slope fails at the 13th excavation bench down to the EL. 1245 m, when the convergence in the viscoplastic iteration does not hold.

The finial reinforcement layout scheme performs well with respect to the deformation and stability. Figure 8.17 plots the plastic zones on the excavating surface, Figs. 8.18 and 8.19 display the accumulated displacement and the adjusted stress at the EL. 1170 m after the completion of the abutments and foundation excavation.

(1) Displacements

In general, the displacement is lager on the upstream slope than on the downstream slope. Taking the left abutment at the EL. 1190 m for example, the upstream slope deflection is 2.8 cm, whereas it is 1.6 cm on the downstream slope. They are all directed towards the cut pit. Nevertheless, the displacements of the right abutment are all directed towards upstream, particularly at the portion of higher elevation. This is mainly attributable to the cut of the headrace intake for the underground power house. At the EL. 1190 m the upstream slope deflection is 1.8 cm and downstream slope deflection is 3.5 cm.

The excavation of the headrace intake slope for the underground power house results in perpendicular-trending but upstream-shifted deflection, of which the maximum displacement 8.6 cm emerges at the EL. 1190 m.

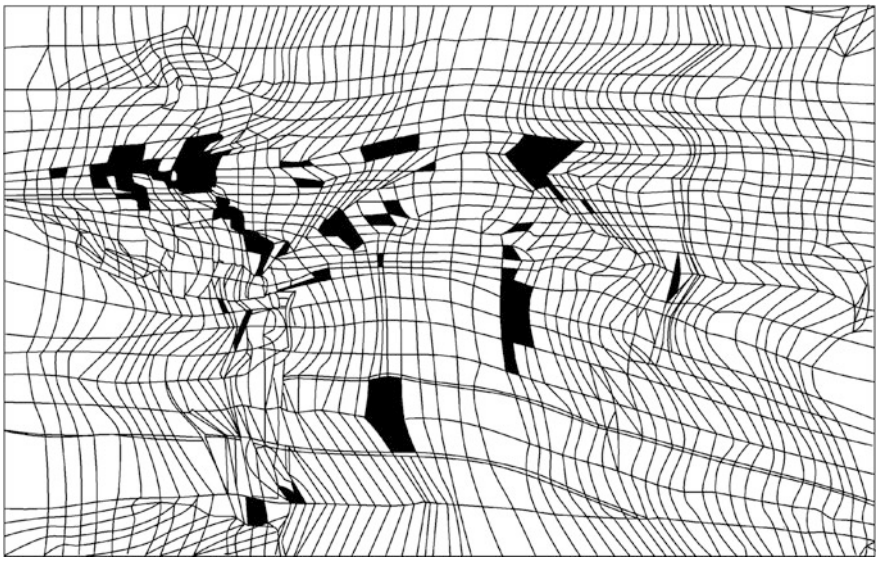

Fig. 8.17 Plastic zone on the excavating surface: final reinforcement scheme

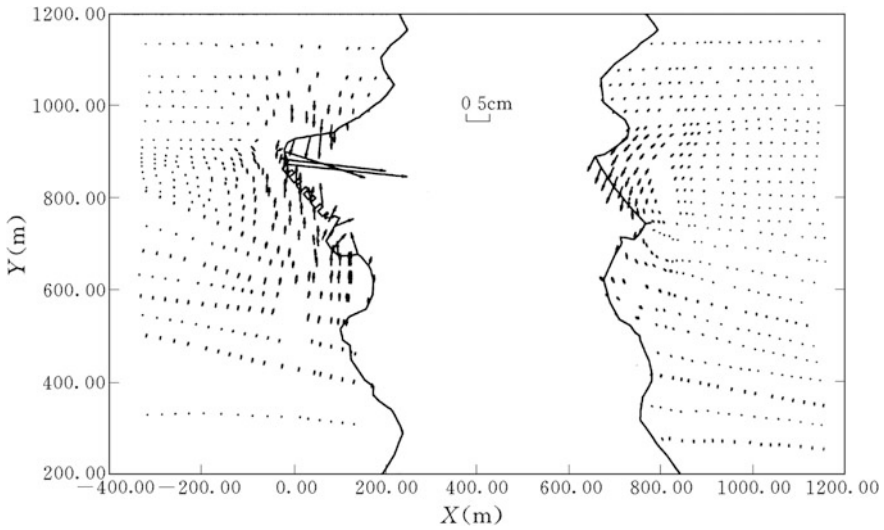

Fig. 8.18 Accumulated displacements at the EL. 1170 m: final reinforcement scheme

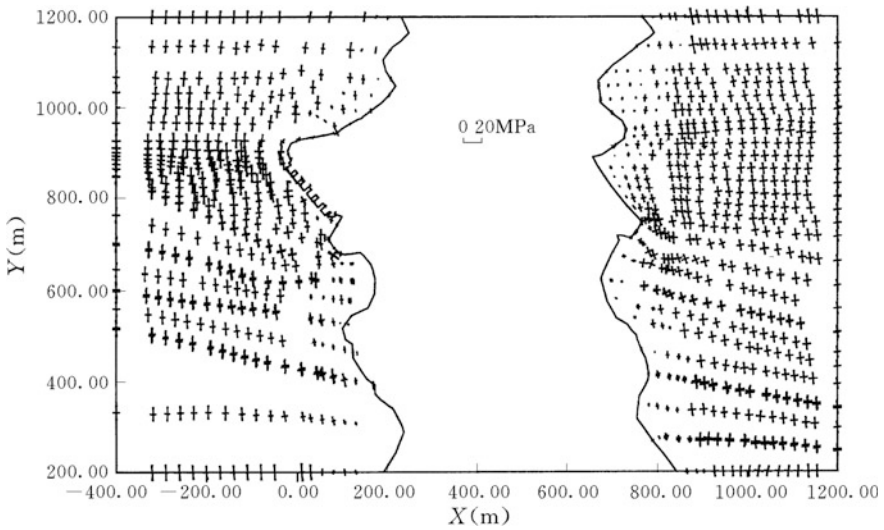

Fig. 8.19 Principal stresses at the EL. 1170 m: final reinforcement scheme

The plunge pool excavation exhibits typical unloading performance: the displacements are all directed towards the river channel, but those of the left bank are larger than the right bank. At the EL. 1050 m the maximum excavating induced displacement is 9.8 cm.

(2) Stresses

From the excavation surface, the EW-trending stress decays quickly due to the unloading effect, whereas the NS-trending stress decays rather slowly. Higher stress level emerges at the upstream portion of the headrace intake for power tunnels.

(3) Point safety factors

From the inside of mountain towards the exposure surface, the point safety factor K_p defined in Eq. (4.215) decays, but it may be maintained at around 1.2–1.8 near the slope surface. Therefore, the point safety on the shallow portion of the slope is basically satisfied after the reinforcement.

(4) Plastic zones

The major plastic zones near the exposure surface appear at the convex portion of the upstream slope near the left abutment at the EL. 1070 m, the left and right slopes of the downstream plunge pool at the EL. 1050 m, the headrace intake slope of the power tunnels at the EL. 1170 m, and the concave portion of the intake slope near the fault F_7. All these may bring about local failures during the cut construction, and the random bolts are demanded in time.

8.5 Excavation Induced EDZ

8.5.1 General Description

At near the completion of the abutment and foundation excavation, it is found that the in situ geo-stress near the river bed exceeds 30 MPa (20 MPa at the stage of feasibility study stage), and there is an additional set of blind joints parallel to the valley's surface. These factors resulted in serious excavation relaxation in the dam foundation. Figure 8.20 shows the cracking emerged on the excavation surface, Fig. 8.21 shows the cracking before and after the excavation revealed by the borehole camera within the river bed.

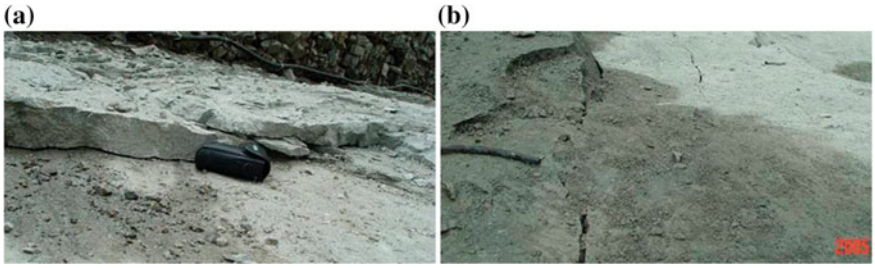

Fig. 8.20 Cracks on the excavation surface. **a** Cracks along the excavation surface; **b** cracks perpendicular to the excavation surface

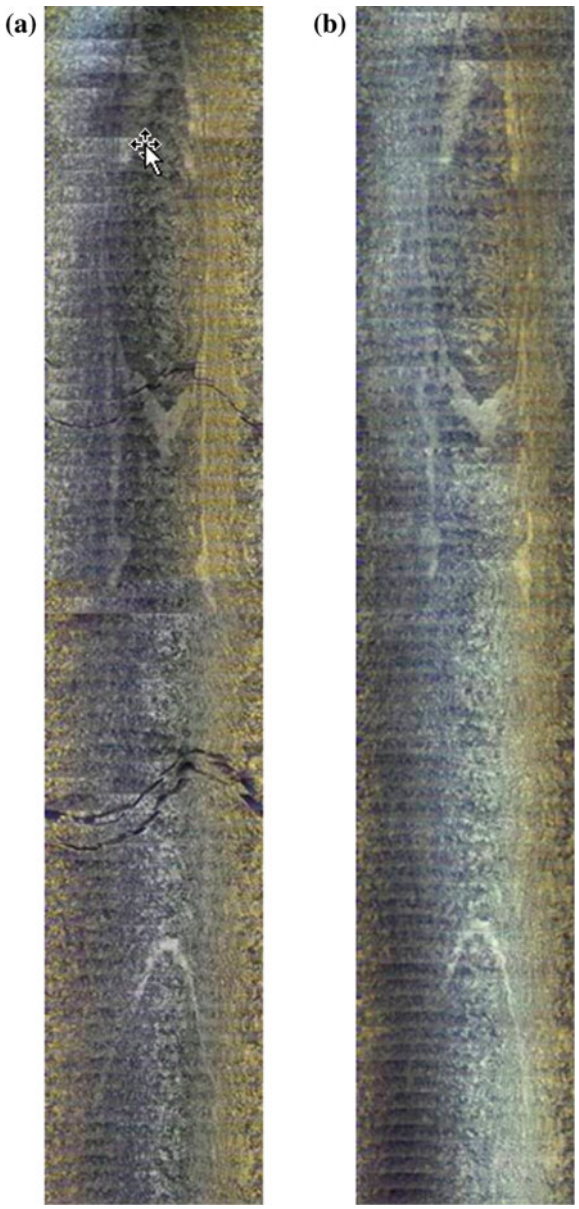

Fig. 8.21 Cracks revealed by the borehole camera. **a** After excavation; **b** before excavation

The degradation of rock mass quality is found to be strongly time-dependent. In Figs. 8.22 and 8.23, we find that

– As the going on of time, the quality of rock mass in the shallow layer is subject to further degradation;
– The degradation depth of rock mass increases quickly within 60 days;

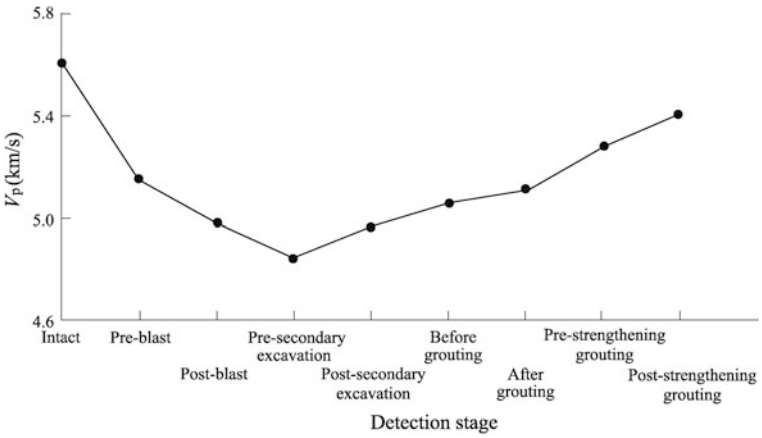

Fig. 8.22 Acoustic velocity variation below the dam base (within 5 m)

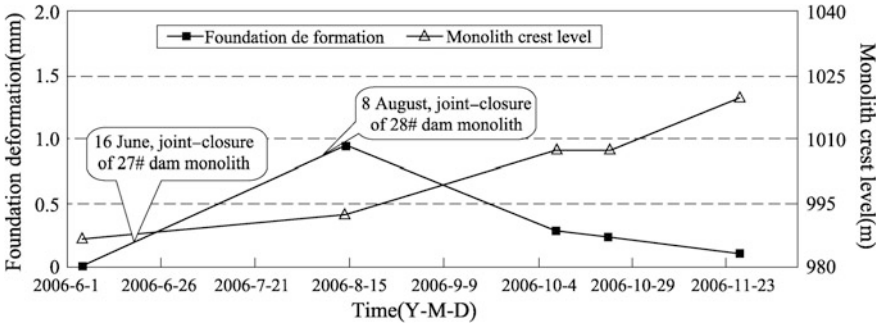

Fig. 8.23 Typical deformation history of the dam foundation

– The acoustic velocity of rock mass basically becomes stable after 180 days.

Degradation coefficient β and recovery coefficient δ are defined to quantitatively evaluate the degree of rock degradation and recovery

$$\begin{cases} \beta = \frac{V_{p1} - V_{p2}}{V_{p1}} \\ \delta = \frac{V_{p3} - V_{p2}}{V_{p1} - V_{p2}} \end{cases} \tag{8.3}$$

where V_{p1} = velocity of longitudinal wave of the intact rock mass, m/s; V_{p2} = velocity of longitudinal wave of the rock mass after degradation, m/s; V_{p3} = velocity of longitudinal wave of the rock mass after recovery, m/s.

Consolidation grouting may enhance the homogeneity and raise the wave velocity (see Fig. 8.22). In addition, along with the concrete placement of the dam, the degraded rock mass is gradually compacted and recovered (see Fig. 8.23) under the action of concrete weight.

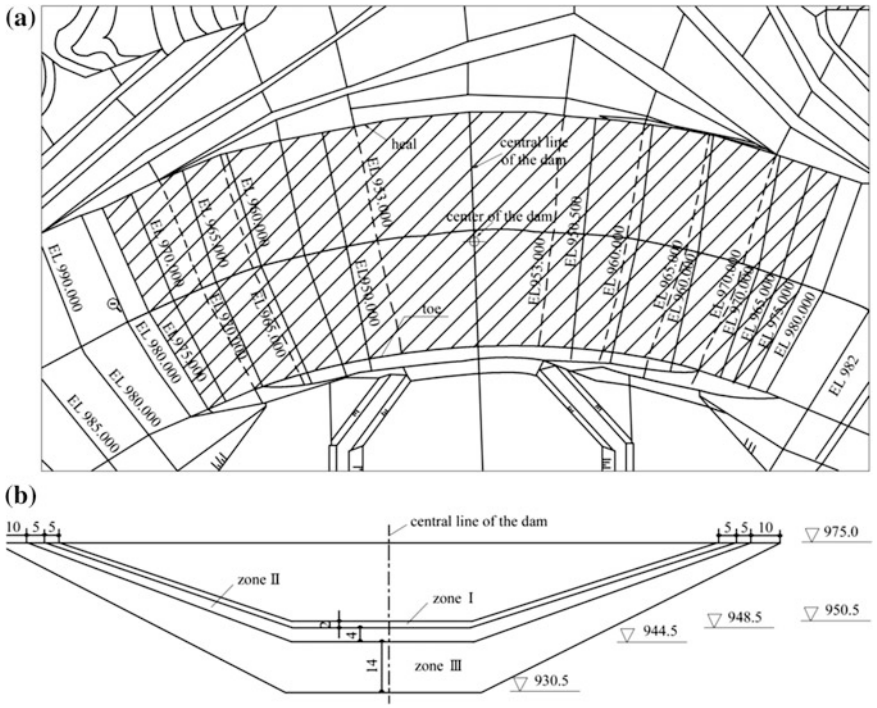

Fig. 8.24 Simplified diagram to the foundation relaxation below the EL. 975 m. **a** Plan; **b** vertical section along the dam axis

According to the field investigation (ultrasonic, borehole camera, etc.) along the dam axis, the foundation relaxation mainly manifests below the EL. 975 m which can be divided into three zones (see Fig. 8.24). The deformation and strength parameters before and after the relaxation are listed in Table 8.11.

Table 8.11 Mechanical parameters before and after relaxation (below the EL. 975 m)

	E (GPa)	c (MPa)	$f = tg\varphi$	Relaxation zones
Before relaxation	20	1.8	1.40	–
After relaxation	11	1.0	1.15	Zone I
	14	1.2	1.20	Zone II
	18	1.8	1.43	Zone III

8.5.2 Preparations for Analysis

Mixed hexahedral and tetrahedral elements are used in the discretization of the foundation and abutments. In the FE mesh shown in Fig. 8.25, 4 faults (F_5, F_7, F_{10}, F_{11}) and 4 alteration zones (E_1, E_8, E_9, E_{10}) are explicitly discretized by the joint elements with thickness.

The excavation procedure is simulated as follows: above the EL. 1030 m, 20 m for one excavation bench, below the EL. 1030 m, 10 m for one excavation bench. Altogether 19 excavation steps are simulated using the algorithm considering EDZ (vide Chap. 4).

8.5.3 Results and Discussions

(1) Spatial characteristics of the relaxation

First, the conventional nonlinear FE computation (without relaxation) simulating the foundation excavation is conducted. Next, cross-reference the calculated tensile strain distribution in the foundation and the investigated relaxation zones (using ultrasonic, borehole camera, etc.), the permissible tensile strain is back analyzed as $\varepsilon_l = 0.015\%$ for the hard rock. The relaxation analysis is further carried out following the flow chart in Fig. 4.12, to adjust the strain and stress fields within the relaxation zones indicated by the maximum tensile strain criterion Eq. (4.88).

In Fig. 8.26, we find that the maximum tensile strain at the vicinity of the excavation surface below the EL. 975 m is 0.04–0.05%, whereas above the EL. 975 m it is 0.02–0.03%. In the central portion of the foundation influenced by the alteration zone E_{10}, the tensile strain approaches 0.1%. This means that the risk of

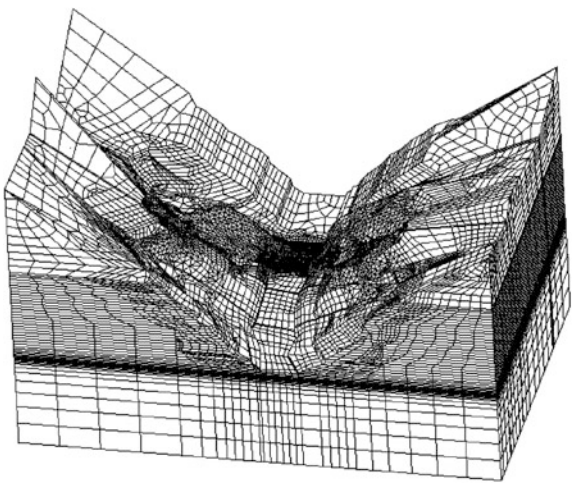

Fig. 8.25 FE mesh of the dam foundation and abutments (370,145 elements; 156,282 nodes): construction phase

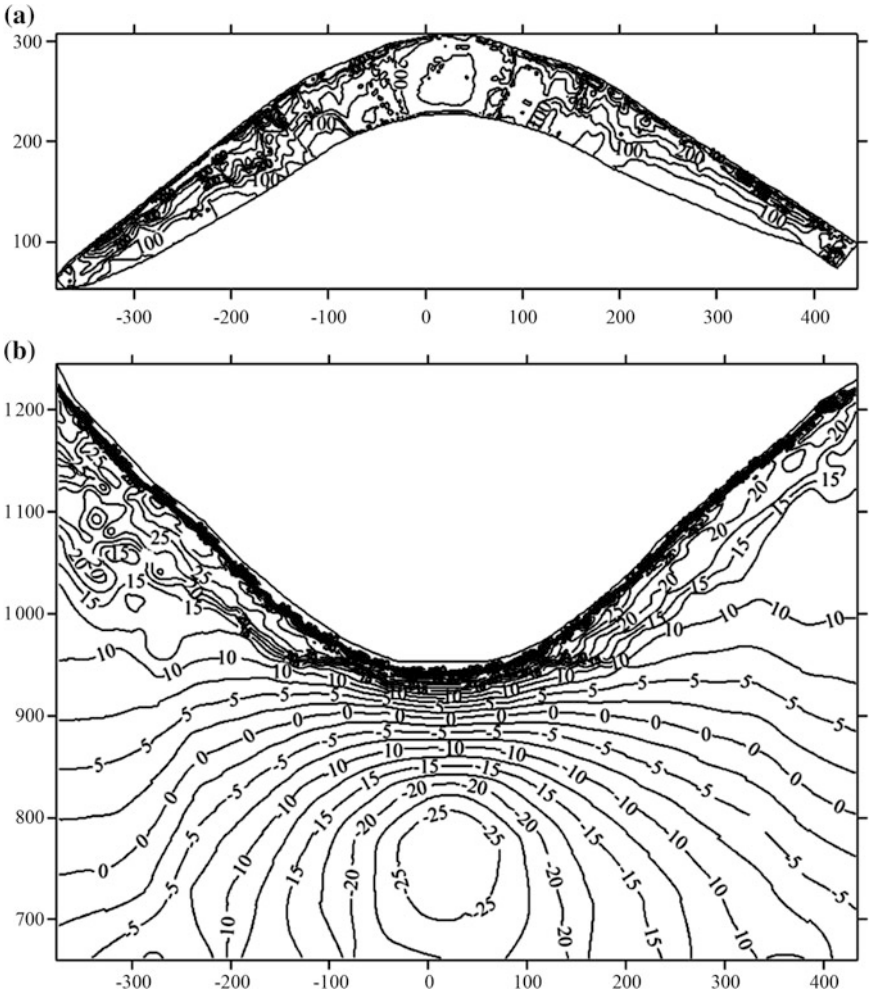

Fig. 8.26 Contours of maximum principal strain (Unit: $\times 10^{-5}$). **a** Plan; **b** vertical section along the dam axis

strong relaxation becomes higher and higher with the ongoing excavation down to the river bed. It is also found that the excavating induced tensile strain decays with the increase of the overburden rock depth, this means that the relaxation will occur only at the vicinity of the foundation excavating surface.

Figure 8.27 shows the principal tensile strain and principal compress stress along the vertical direction beneath the crown cantilever. Since the permissible tensile strain for the hard rock is 0.015%, the conclusion can be made from Fig. 8.27a that the rock below the elevation of 950.5 m (foundation surface) will be degraded down to a maximum depth of 22 m. This judgment agrees well to the field observation.

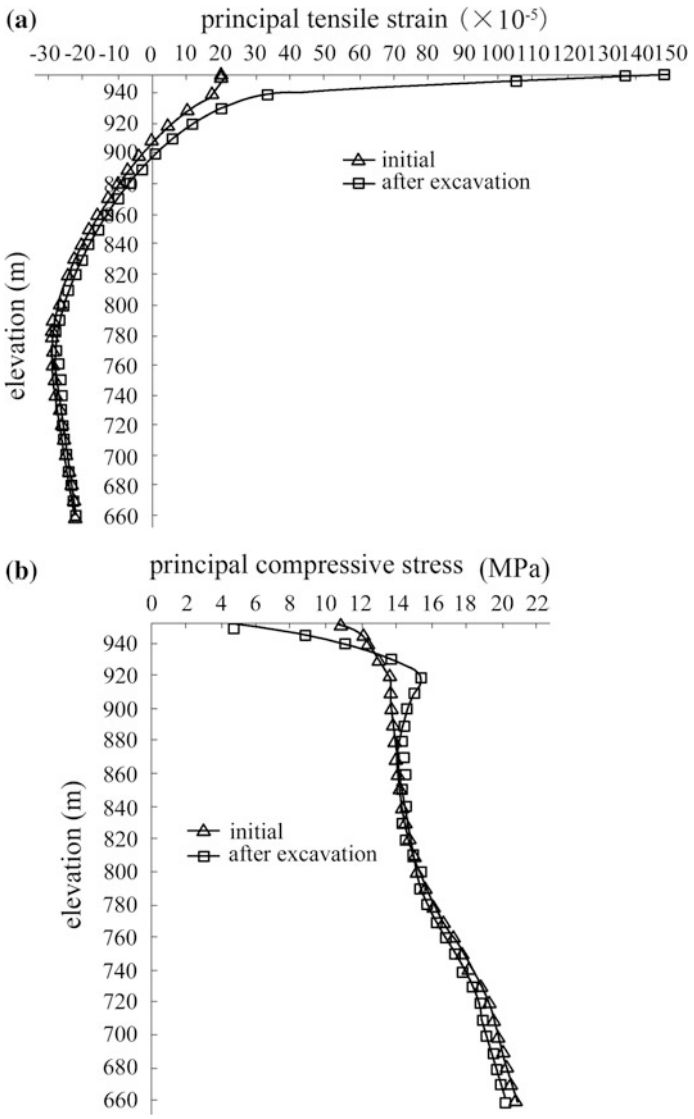

Fig. 8.27 Maximum principal tensile strain and compressive stress beneath the crown cantilever. **a** Principal tensile strain; **b** principal compressive stress

It also can be found from Fig. 8.27b that as the deterioration of the mechanical parameters below the EL. 950.5 m (excavating surface), the stress at the shallow portion undergoes interesting adjustment: At the EL. 950.5 m, the principal stress is reduced from 10.2 MPa (initial stress) to 6.8 MPa (adjusted after relaxation); However, when the overburden depth is over 17 m from the excavating surface (EL. 932.5 m), the adjusted stress starts to exceed the initial stress; There is a point

(overburden depth of 33 m from the excavation surface) at which the difference in the adjusted stress and initial stress reaches maximum value (initial 12.6 MPa vs. adjusted 15.0 MPa). After this point when the overburden depth keeps increase, the difference in the initial stress and relaxed (adjusted) stress becomes smaller and smaller. At the overburden depth of 100 m (EL. 850.5 m), they are nearly identical.

The above results concerning the rock relaxation portion, range and depth, as well as the stress distribution characteristics, are all justified by the in situ investigations.

(2) Temporal characteristics of the relaxation

The deformation arise from the relaxation exhibits significant time-dependent characteristics, to which high attention has been focused on because it is hazardous to the dam construction and operation.

Sliding micrometers are installed to monitor the foundation deformation. From their readings, the back analysis is carried out to find the fluidity parameter γ of the foundation rocks: $\gamma = 2.1 \times 10^{-5}$ $(\text{MPa day})^{-1}$ for the relaxed rock and $\gamma = 20.5 \times 10^{-5}$ $(\text{MPa day})^{-1}$ for the rest ones.

With the back analyzed fluidity parameters the deformation history can be well predicted. Figures 8.28 and 8.29 present the vertical displacement histories at the center of the cantilever dam section (dam monolith 22#), the monitored data by the sliding micrometers are also given in these figures.

Figure 8.30 plots the predicted vertical displacement history according to the back analyzed fluidity parameters if there were no dam concrete placement. It is interesting to learn that the maximum vertical displacement $u = 16$ mm would be asymptotically approached at the end of 2006. Since the dam concrete started to pour at the end of 2005, when the vertical displacement only had completed a small portion $u = 4$ mm, therefore the necessity of the study concerning the interaction between the dam body and rebounded foundation during the dam concrete placement, is highlighted.

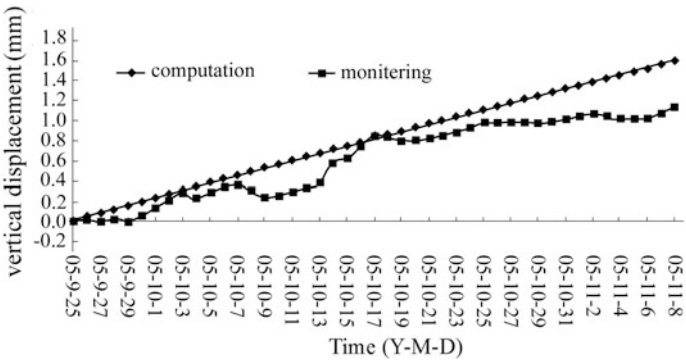

Fig. 8.28 History of the vertical displacement at the EL. 950 m (0.5 m below the foundation surface, $\|e\|_r = 24\%$, $\|e\|_a = 0.38$ mm)

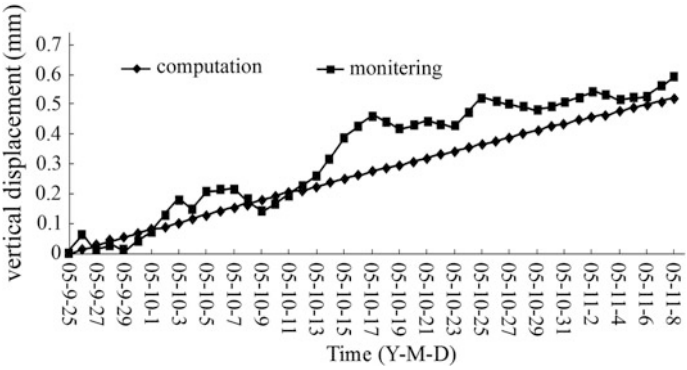

Fig. 8.29 History of the vertical displacement at the EL. 947 m (3.5 m below the foundation surface, $\|e\|_r = 41\%$, $\|e\|_a = 0.18$ mm)

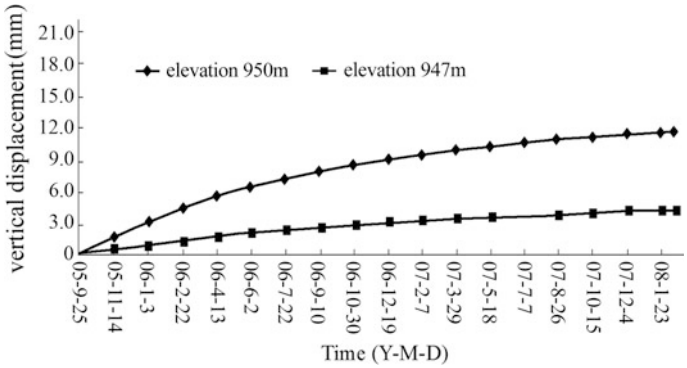

Fig. 8.30 Predicted history of the vertical displacement: without dam

8.6 Dam Concrete Placement and Reservoir Impoundment

8.6.1 Generation of the Computation Meshes

To handle the multi-field issues involved in the dam, three computation meshes are constructed with regard to the fields of temperature, seepage, and strain/stress, respectively (see Fig. 8.31).

The mesh for the temperature field (see Fig. 8.31a) completely emulates the temperature rise process of different dam monoliths. For this purpose the mesh is strictly built using brick elements of 0.6–1.0 m thick. The temperature control measures and ambient boundary conditions are inputted according to the field data from the reports of surveillance and safety review.

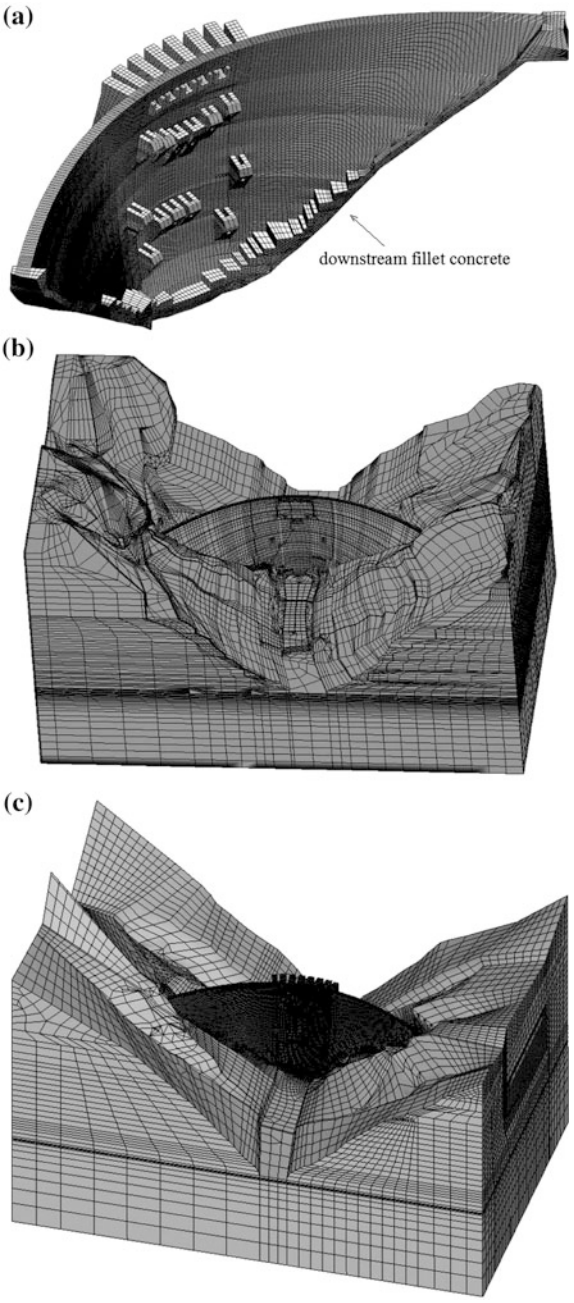

Fig. 8.31 FE meshes of the dam and foundation/abutments: construction phase. **a** Temperature analysis (448,966 elements; 505,958 nodes); **b** seepage analysis (1058,610 elements; 791,986 nodes); **c** stress/strain analysis (1,163,662 elements; 942,608 nodes)

The appurtenant features taken into account of the mesh for the seepage field (see Fig. 8.31b) include:

- Grouting curtains in the dam foundation and abutments;
- Drainage systems in the dam body, dam foundation, dam abutment and downstream resistance body (rock); and
- Major faults and alteration defects.

The mesh for the stress/strain field (see Fig. 8.31c) emulates the geological features as follows:

- Lithology, weathering, replacement and consolidation grouting of resistance body rock, tunnel plugs and shaft plugs (concrete replacements) in the abutments, are all exactly discretized;
- Three sets of rock joints, and systematic rock bolts are implicitly approached;
- Faults F_7, F_{11}, F_{10}, F_5 and E_{10} are explicitly approached;
- Relaxed rock zone in dam foundation induced by excavation (20 m deep) is sub-divided into 3 layers (i.e. 0–2, 2–6 and 6–20 m);
- Interface between the concrete and rock, base joint at the dam heel, grout curtains, and all galleries/tunnels, are approached explicitly;
- Dam body orifices, gate piers, main galleries, all the 43 transverse joints, and all the pre-stressed anchor cables, are approached explicitly;
- Thermal-induced concrete cracks are embedded in the dam body according to the time of their occurrence and identified spatial distribution;
- Mesh is so designed with element sizes around 1 m, in accordance with the actual placing process of each dam monolith;
- Abutment excavation is implemented by 19 benches and the element thickness near the foundation surface is controlled within 2 m, for the purpose to well simulate the EDZ.

8.6.2 Back Analysis Strategies

The physical and mechanical parameters involved in the computation are numerous while the observation object points in the instrumentation system and the samples for the physical (laboratory and field) tests are limited, so dominant parameters subject to the feedback adjustment should be carefully selected according to their variation degree and impact on the performance of the structure (Chen et al. 2001):

- For the temperature field, the premier parameter being back analyzed is the adiabatic temperature rise with greater variation and the second parameter is related to the temperature control measures (e.g. cooling water);
- For the seepage field, the premiere parameter being back analyzed is the difficultly gauged hydraulic aperture of rock joint and the second parameter is the joint connectivity;

- For the strain/stress field, the premier parameter being back analyzed is the deformation modulus with remarkable consequence and the second parameter is the cohesion with greater variation;
- The in situ geo-stress field regression is firstly performed on larger area based on the tested values but ignoring most structural planes, then more structural planes are incorporated and the size of computation domain is reduced for the secondary regression, so as to perform the cross-reference between the calculated and measured values of the in situ geo-stress locally influenced by the existence of these structural planes. In the secondary regression, the stresses or/and displacements extracted from the precedent larger domain are interpolated to the successive smaller domain as the input boundary conditions;
- After the launch of dam foundation excavation, the back analysis of rock parameters should be focused on the EDZ near the excavation surface (Chen et al. 2012a);
- After the launch of dam concrete placement, in addition to continuously focusing on the spatial-time evolution characteristics of the EDZ, the back analysis and adjustment of the mechanical parameters of dam concrete should be put on agenda in time.

The Artificial Neural Network (ANN) algorithm is combined with the FEM to create the connection between the monitoring data and the parameters that significantly influence the fields of temperature/seepage/deformation by establishing a highly nonlinear mapping model to accomplish the back analysis (vide Chap. 7). On this basis, the forecast of the structural performance and corresponding safety is carried out. The necessity and possibility to revise the design schemes and/or construction techniques, are further feedback analyzed.

8.6.3 Iterative Actions of Dam Foundation and Dam Body

The performances of the dam foundation and dam body are interconnected, showing spatial heterogeneity in addition to obvious temporal evolution features according to the results provided by the computation and instrumentation.

- The stresses around the two abutments are basically symmetrical.
- During the concrete placement period and the initial reservoir impounding, higher compressive stress emerges near the dam heel. Meanwhile lower compressive stress, even with locally tensile stress, emerges near the dam toe. The bedrock undergoes compressive deformation and recovery of rock quality, particularly near the dam heel.
- With the completion of dam concrete placement and the rise of impounding reservoir level, the compressive stress near the dam heel is gradually declined with locally tensile stress. Meanwhile compressive stress near the dam toe

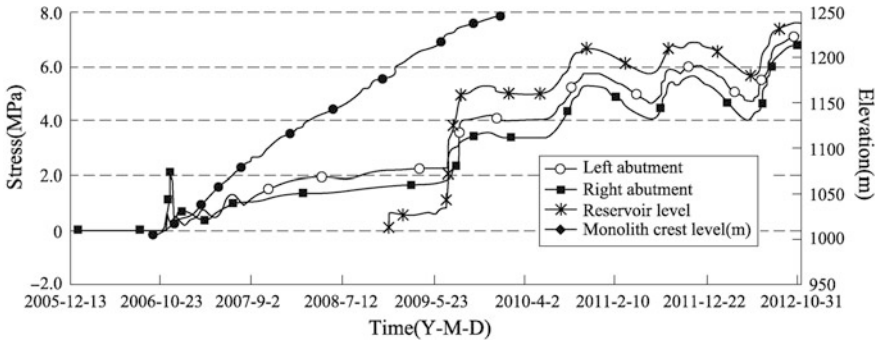

Fig. 8.32 Principal compressive stresses on the dam toe at the EL. 1010 m

gradually climbs. During these periods, the rock mass exhibits certain degree of re-degradation near the dam heel.

– Under the normal operation, the characteristics of foundation rock mass show spatial-time periodical variation along with the periodical fluctuation of reservoir water level, but the extent of such fluctuation is negligible.

Figure 8.32 exhibits the histories of the principal compressive stresses on the dam toe at the EL. 1010 m where it bears greater load. It is apparent that

– Before the dam concrete is placed up to the EL. 1210 m and the water level rises to the EL. 1125 m, the stress level on the abutment is low;
– As the dam concrete placement goes on and the water level rises, the load on the abutment increases gradually;
– When the dam concrete is placed up to the crest and the reservoir water rises to the normal storage level (NSL), the maximum principal compressive stress in the left abutment is approximately −7.0 MPa and that in the right abutment is approximately −6.2 MPa.

8.6.4 Spatial-Time Characteristics of the Dam Body

(1) Temperature

The temperature of concrete varies along with the concrete placement and the implementation of temperature control measures. The longest placing block for Xiaowan Dam is almost 100 m. At the initial stage of dam concrete placement, the temperature control measures were determined in accordance with the routine algorithmic method specified in the existing design codes. However, the actual temperature pickup is excessively high in the period between the end of the Stage I cooling and the beginning of the Stage II cooling. In addition, the temperature drop range and

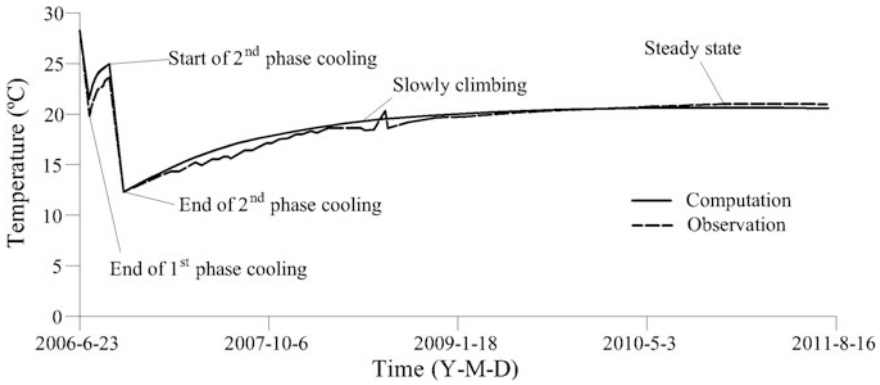

Fig. 8.33 Typical temperature history: routine design of temperature control measures ($\|e\|_r$ = 8.6%, $\|e\|_a$ = 1.5 °C)

rate are very sharp during the Stage II cooling. These phenomena are revealed by both the computation and the field observation with the help of the DSXAD (see Fig. 8.33).

After the timely adjustment of temperature control measures in light of the actual spatial-time evolution of dam body temperature and the cracking mechanism, the temperature field has been controlled effectively. To be specific, the temperature basically remains unchanged when the Stage I cooling is over and drops steadily along with the Stage II cooling, and the temperature picks up at a certain degree when the Stage II cooling is over and the final stabled temperature is reached around 19 °C (see Fig. 8.34). As a result, the principal tensile stress during the construction period is limited within 0.5–0.8 MPa at the most locations (see the stress envelope over the EL. 1110 m in Fig. 8.45).

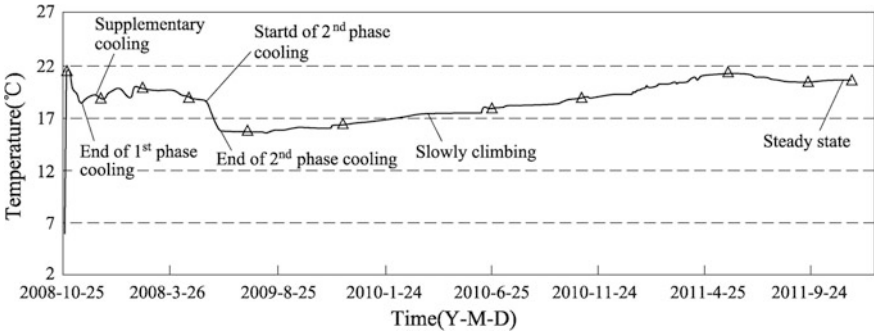

Fig. 8.34 Typical temperature history: after the adjustment of temperature control measures according to the DSXAD

(2) Seepage

Figure 8.35 draws the isopotential contours with respect to hydraulic head under the normal storage level (NSL) 1240 m. It can be seen that the contours near the grout curtain are concentrated, meanwhile the hydraulic head declines significantly beneath the cushion pool. This means that the grout curtain and the drainage system play important roles in the control of hazardous seepage flow.

Figure 8.36 cross-references the computed and observed hydraulic heads on the EL. 950.5 m of the dam monolith 22# (December 16, 2008 is the first day of reservoir impounding). It demonstrates that they agree with each other well.

(3) Uplift distribution on the dam base

The uplift on the dam base is usually not important for arch dam design. However, due to the intensive EDZ, the local shear resistance of the dam base becomes one of the most concerns, which is associated closely with the uplift on the dam base.

Figure 8.37 shows the uplift distribution on the EL. 948.5 m under the crown cantilever section (dam monolith 22#), where the uplift is expressed by the height of water column. The dashed line represents design uplift, where H_1 is the head water level and H_2 is the tail water level. The solid line represents computed uplift. We find that

- The distribution pattern of both the design uplift and the computed uplift is consistent; and
- The computed uplift is lower than the design uplift on the whole.

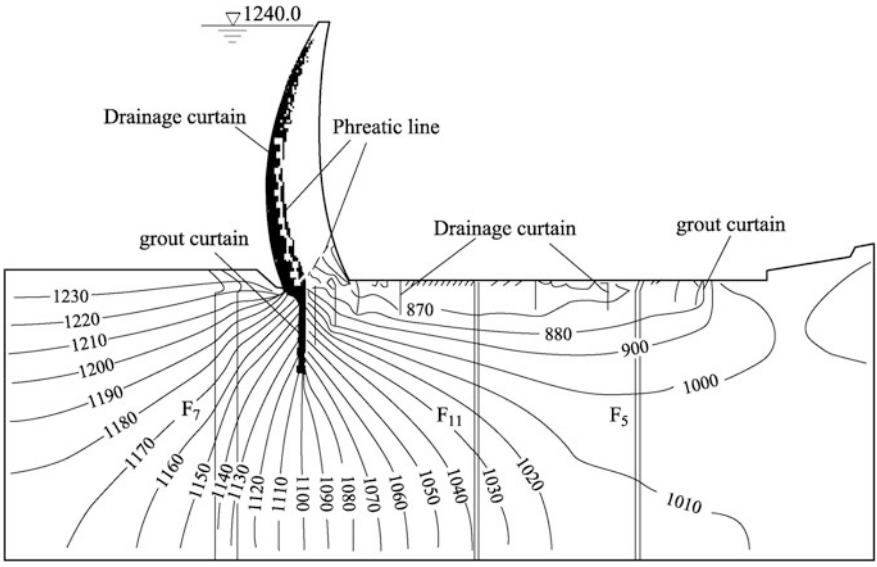

Fig. 8.35 Isopotential contours of the crown cantilever dam monolith 22# under the NSL 1240 m

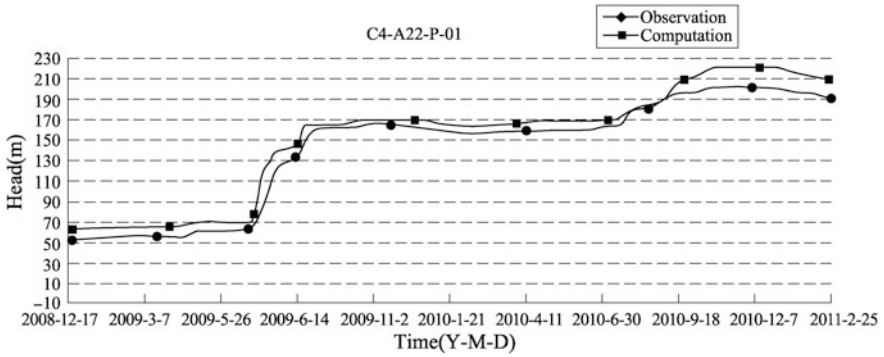

Fig. 8.36 Computed and observed hydraulic heads (EL. 950.5 m, dam monolith 22#, $\|e\|_r$ = 9.5%, $\|e\|_a$ = 19 m)

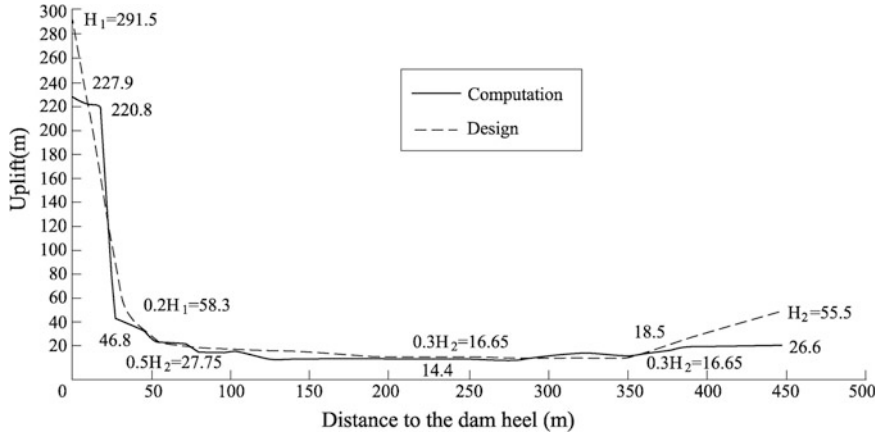

Fig. 8.37 Uplift on the EL. 948.5 m under the crown cantilever section (dam monolith 22#)

These demonstrate that the design uplift on the dam base is adequately stipulated and it contributes to certain additional safety margin with regard to the local shear resistance along the dam base.

(4) Seepage flow

To design drainage equipments and to select pump capacity economically and efficiently, the seepage flow evaluation of each specified area is undertaken. Table 8.12 lists the seepage flow through the whole project area under NSL 1240.0 m by the computation.

It is worthwhile to indicate that the computed flow discharge is nearly twice as large as that of gauged. After the comprehensive comparison of the computed and

Table 8.12 Seepage flow discharge under NSL 1240 m (m^3/day)

Flow discharge computed	Flow discharge gauged
467.14	240.3

gauged results concerning the seepage flows through different areas in addition to that through the whole project area, it is confirmed that

– The effectiveness of seepage control installation is guaranteed, and;
– The permeability coefficients of the foundation rock masses might be a bit of over-estimated in the computation.

(5) Deformation

Since the vertical plumb used for the displacement monitoring of the dam body is installed and put into operation lag in the concrete placement, the measured displacement is solely relative one while the calculated one may be either relative or absolute (see Fig. 8.38). However, when a spatial-time relation is built using the calculated and monitored relative displacements, the consistence and agreement may be verified. Therefore, it may be concluded that the displacements and their

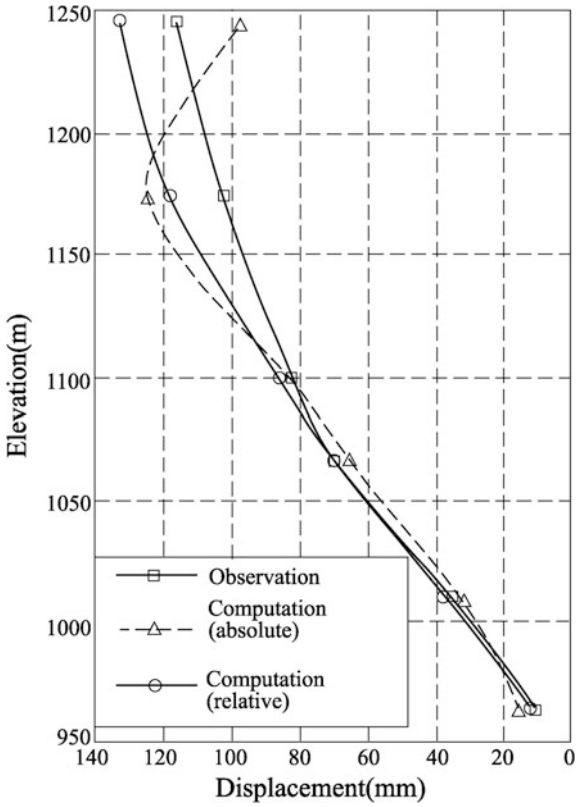

Fig. 8.38 Computed and monitored radial displacements of the crown cantilever (dam monolith 22#) under NSL 1240 m ($\|e\|_r$ = 13.6%, $\|e\|_a$ = 16 mm)

distribution pattern of the dam body may be well interpreted by the computation results, under the premise that full consideration is given to the spatial-time evolution characteristics of foundation rocks and dam concrete.

The most remarkable deformation features of Xiaowan Dam are summarized below.

- It moves toward upstream at the beginning along with the concrete placement of the dam body. When the dam concrete placing height is about 200 m, the deformation toward upstream reaches the maximum (about 18 mm);
- As the reservoir impounding and the dam concrete placing go on, the deformation along the river course gradually tends to the downstream direction;
- When the impounding is proceeded up to the normal storage level, the maximum displacement (about 138 mm) appears at near the EL. 1210 m (see Fig. 8.39);
- It exhibits periodical fluctuations after the project is putted into normal operation.

(6) Stress

When the concrete of Xiaowan Dam is placed up to near the EL. 1180 m, the dam overhanging reaches the maximum. As a result, the stress emerging in the dam body is compressive at the dam heel and tensile at the dam toe (see Fig. 8.40a). When the concrete is placed to the dam crest (EL. 1245 m) and the water level rises to the EL. 1181 m, the dam body is in an ideal stressing state, namely the maximum compressive stresses at the dam heel and dam toe are limited within −4.0 MPa (see Fig. 8.40b). When the water level continues to climb, the compressive stress at the dam heel reduces but that at the dam toe climbs. When the water level reaches the normal storage level, the compressive stress at the dam toe reaches its maximum and a certain tensile stress manifests at the dam heel (see Fig. 8.40c).

A structural-induced joint (i.e. bottom inducing joint, or base joint) is installed along the heel of Xiaowan Dam at the maximum height of 7 m above the dam base. The dam body below the joint is placed monolithically and strengthened with the upstream and downstream fillet concrete (see Fig. 8.31a). The relief effect of tensile stress at the dam heel is remarkable: the maximum tensile stress is concentrated at

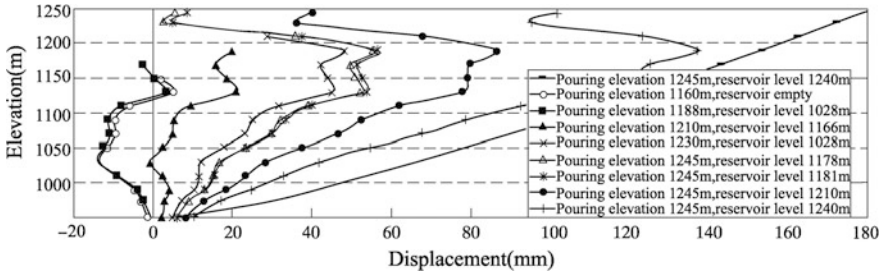

Fig. 8.39 Displacements along the river course of the crown cantilever (dam monolith 22#)

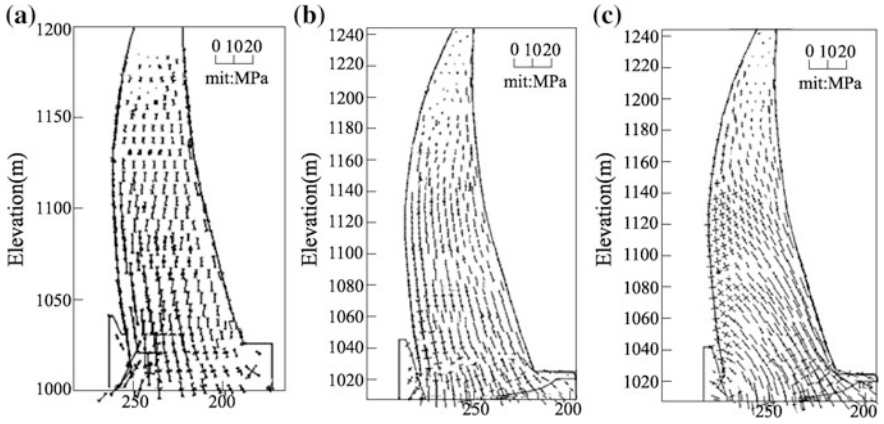

Fig. 8.40 Stresses of the crown cantilever (dam monolith 22#). **a** Pouring elevation 1188 m, reservoir level 1028 m; **b** pouring elevation 1245 m, reservoir level 1181 m; **c** pouring elevation 1245 m, reservoir level 1240 m

the elevation where the induced joint is installed in lieu of at the dam base. As the ongoing of the dam concrete placement followed by the reservoir impoundment and until the normal operation, the stress at the induced joint varies gradually (see Fig. 8.41). When the reservoir water reaches the normal storage level (EL. 1240 m), the vertical stress close to the upstream dam face and surrounding the induced joint is nearly null (see Fig. 8.42).

To sum up, the stressing state of the double-curvature arch dam varies all the time in the history from the concrete placement to the normal operation, showing remarkable spatial-time characteristics. The dam exhibits two crucial periods, namely

– When the reservoir is completely empty during construction. The maximum compressive stress at the dam heel is smaller than the allowable compressive strength and the tensile stress at the dam toe is limited within the allowable tensile strength of the dam concrete, and;

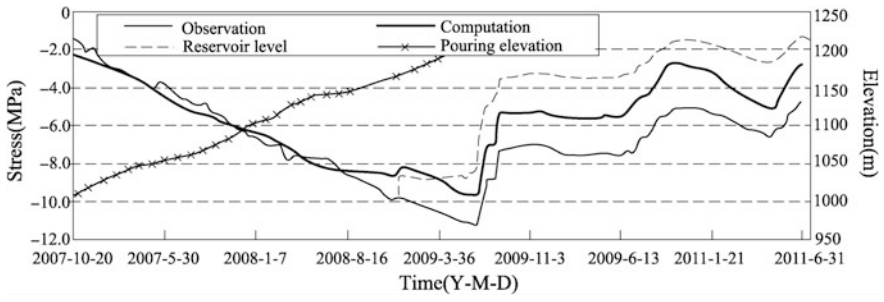

Fig. 8.41 History of vertical stress on the induced joint ($\|e\|_r$ = 48%, $\|e\|_a$ = 2.6 MPa)

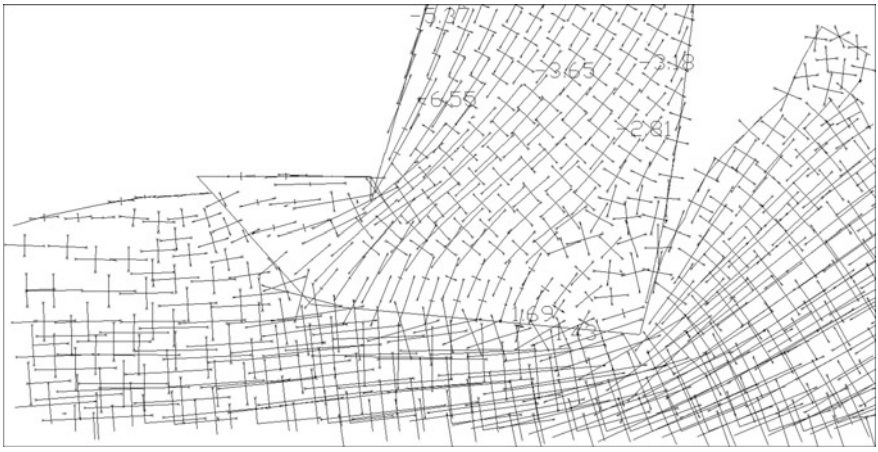

Fig. 8.42 Stresses of the crown cantilever (dam concrete placed to the crest EL. 1245 m; NSL 1240 m)

– When the reservoir is at NSL 1240 m. The maximum tensile stress is centralized at the elevation where the induced joint is installed rather than at the dam base, and the maximum compressive stress on the downstream dam toe is under the control by the allowable strength value.

The stress field is smoothly and symmetrically distributed at other periods, and in general the dam is under three-dimensional compression. These spatial-time features revealed by the DSXAD fully demonstrate that the double-curvature structure of Xiaowan Dam is under an optimal working state, and the dam design/construction is very successful.

8.6.5 Key Issues Solved with the Help of the DSXAD

(1) Foundation relaxation

1. Safety calibration

The study indicates that after the rock relaxation due to foundation excavation, although the overall stability of the dam/foundation system is not seriously affected, yet the local shear resistance at the shallow depth will be remarkably undermined, which in turn, would be hazardous to the seepage control system of the dam foundation.

According to the (SL282-2003) «Design specification for concrete arch dams», both the point and surface safety factors (K_{p2} and K_{f2}) postulating friction mechanism are stipulated in the local shear calibration, i.e.

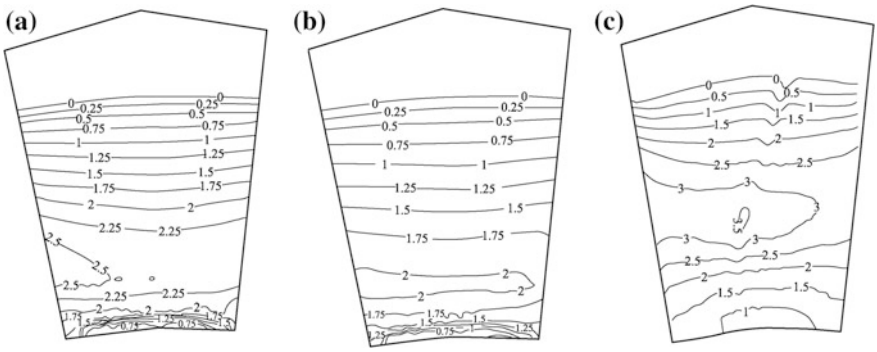

Fig. 8.43 Point safety factor K_{p2} on the EL. 948.5 m under the dam monolith 22#. **a** Before relaxation; **b** after relaxation; **c** after treatment

$$\begin{cases} K_{p2} = \dfrac{\sigma_i f_i}{\tau_i} \\ K_{f2} = \dfrac{\sum \sigma_i f_i A_i}{\sum \tau_i A_i} \end{cases} \tag{8.4}$$

The allowable safety factors are $[K_{p2}] = 1.1$ and $[K_{f2}] = 1.5$, respectively.

By the computation, it is found that the point and surface safety factors are reduced by more than 30% due to the relaxation (see Fig. 8.43; Table 8.13).

2. Countermeasures

① Excavation and clearance. Apart from conventional excavation and clearance, the additional excavation and clearance are undertaken consisting of the removal of obviously relaxed rock, fragrant rock cut by open joints, and the thin layered rock.

The depth of the additional foundation clearance is approximately 1 m, with the locally deepest of 3 m. It is worthwhile to mention that according to the analysis, too deep of additional clearance will trigger more serious and deeper relaxation, therefore it is wise to treat the EDZ embedded deeper by bolting, then to pour the concrete monolith as early as possible, to stop the residual time-dependent relaxation.

② Consolidation grouting. After the additional foundation clearance, to compensate the reduction in the deformation modulus of the relaxed rock shallowly embedded under the dam base, the meticulous and high quality consolidation is carried out after the placement of base concrete, by grouting through boreholes arranged in a pattern of grid. The

Table 8.13 Surface safety factor K_{f2} on the EL. 948.5 m under the dam monolith 22#

Case	Friction safety factor K_{f2}
Before relaxation	1.98
After relaxation	1.43
After treatment	2.17

minimum overlay concrete monolith is over 5–6 m for the dam monoliths on the river stream, and 4.5 m for the dam monoliths on the abutments. The split-spacing method by reducing the grout hole interval is followed until the final spacing (2–4 m), which should be determined during grouting operations on the basis of the results being monitored from these operations.

The grouting quality is controlled by the acoustic velocity. The acceptance standard of the velocity of longitudinal wave through rock mass after grouting V_{p3} is: depth 0–2 m, V_{p3} = 4750 m/s; depth 2–5 m or even deeper, V_{p3} = 5000 m/s.

③ Reinforcement. Bolting is employed in the dam foundation to raise its shear resistance. Fully grouted, passive dowels comprising steel bars are installed in the grouting holes under the dam monoliths 12#–32#. These steel bars perform as rigid shear pins across any planes of discontinuities in the rock, in this way to improve the shear resistance along the discontinuities in three different mechanisms: tension force in the bolt, friction as a consequence of the increase in the normal stress, and dowel effect (Egger 1992; Chen et al. 2012b). The rock bolts (3Φ32) used in Xiaowan Dam foundation is 12 m long, of which 9 m is in the rock. Altogether 6720 rock bolts are installed.

In recent years, pre-stress stranded anchor cables installed in the abutment slopes at the downstream vicinity of the arch dam toe, are widely exercised in China and the other countries (Chen et al. 2015). The pre-stress reinforcement prevents or limits the hazardous deformation and dilation of the foundation rock that might lead to failure.

The layout of these pre-stress cables is dependent on the computation results. They are all dispersion-type tensile cables, whose parameters are given in Table 8.14.

3. Effect of the treatment countermeasures

The average velocity V_{p3} of longitudinal wave through the rock mass after grouting is higher than 5000 m/s, this means that the grouting quality reaches the design target.

The immediate concrete placement after the additional foundation clearance is justified as a rather wise decision, to control the evolution of dam foundation

Table 8.14 Parameters of pre-stress anchor cables installed at the dam toe

Cable capacity (kN)	Installation elevation (m)	Number (unit)	Borehole depth (m)	Inclination	Dip angle (°)
6000	965–1085	366	41–80	From dam toe toward upstream	60–78
4000	1021–1142	136	40–65	From dam toe toward upstream	46–60

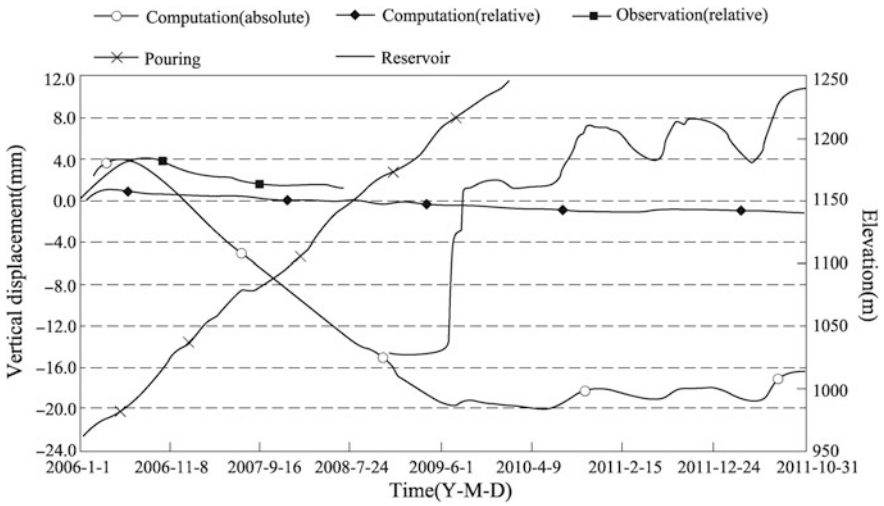

Fig. 8.44 Vertical displacement history at the EL. 950 m (0.5 m below the base) ($\|e\|_r$ = 71.2%, $\|e\|_a$ = 2.8 mm)

relaxation effectively (see Fig. 8.44). The concrete with a thickness of about 10 m may constrain the rebounding of dam foundation rock mass at the riverbed dam monoliths, whereas that with a thickness of about 20–30 m may constrain the rebounding of dam foundation rock mass at the bank slope dam monoliths. When the height of the concrete monolith is raised up to 30–40 m, the upward rebounding deformation is totally stopped and followed with a downward re-compression deformation. However, the continuous up-rise of the foundation causes somewhat early age cracking in the base concrete. This gives us a new lesson that more reasonable placement time should be further studied, to make a good compromise between the requirements of relaxation control and concrete cracking prevention.

The safety factors after the treatments are shown in Fig. 8.43c and Table 8.13 (row 4), it is clear that the shear resistance is improved considerably by the foregoing countermeasure.

(2) Dam cracking

1. Scenarios of dam cracking

In the early batch of dam concrete designed according to the conventional specifications, the spatial gradient and temporal variation of temperature cause high tensile stress—as high as 1.2–2.2 MPa (see the principal tensile stress envelope below the EL. 1110 m in Fig. 8.45). Since the actual tensile strength of the dam concrete is merely about 1.4 MPa, therefore temperature-induced cracks manifested and extended significantly during the early phase of dam concrete placement (Fu et al. 2011; Wang et al. 2011). The chemical grouting treatment was undertaken for these temperature-induced cracks immediately after their detection, meanwhile

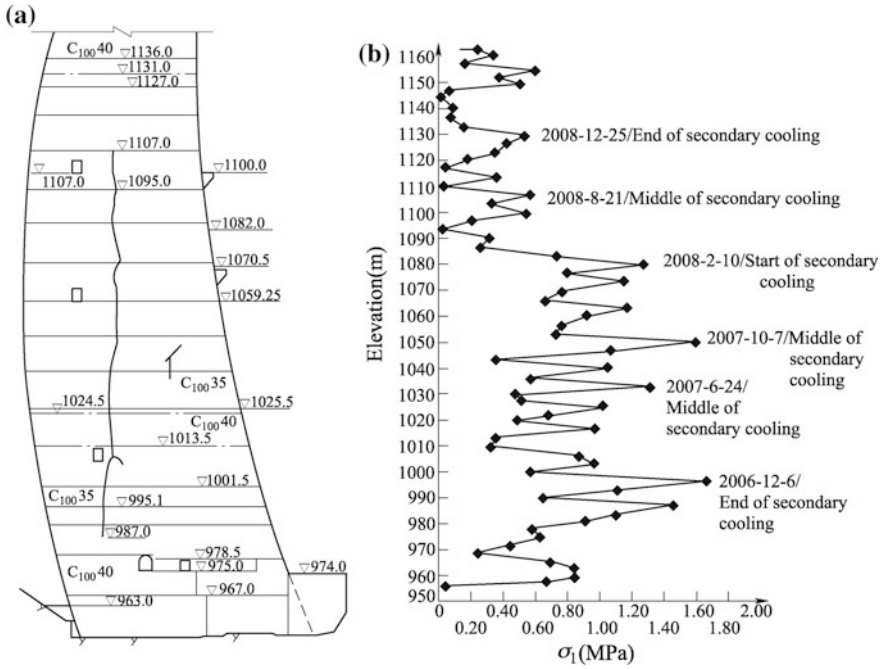

Fig. 8.45 Envelope of the tensile principal stresses and cracking of the dam monolith 22#. **a** Cracks; **b** envelope of the tensile principal stresses

the new, high-quality post-cooling scheme was feedback analyzed and designed for the later batch of dam concrete, both under the guidance of the DSXAD.

The tensile stresses in cracks are gradually re-compressed (see Fig. 8.46) as the ongoing of the continuously dam concrete placement and reservoir impoundment. At the NSL, the cracks are tightly closed. For this reason, the higher operating water level, the higher stability conditions attains for the dam cracks.

In addition to help the successful control of the occurrence of new temperature-induced cracks in Xiaowan Dam, the following understandings are also provided by the computational results:

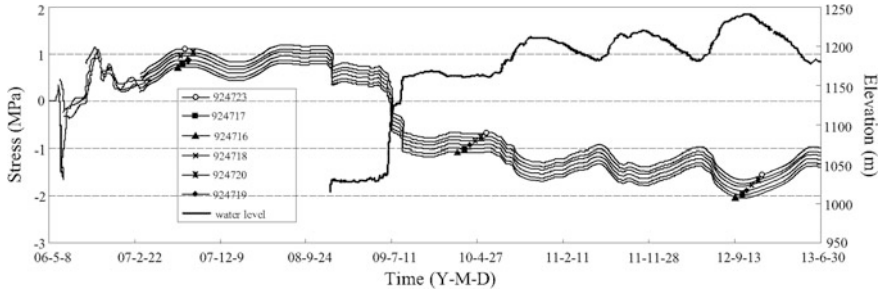

Fig. 8.46 History of the normal stress on the 24# crack

– The routine way suggested in the design codes/specifications cannot well display the thermal stress in the arch dam with respect to its spatial-time evolution during the construction process. Particularly, the conventionally calculated tensile stress is rather under-estimated;
– For the high arch dam, an allowable safety factor 1.3–1.8 against cracking stipulated in the design specifications is not sufficient when the design parameters are determined using wet-screened concrete tests;
– At present, the test method is unable to accurately trace the whole heat releasing process of concrete, so exact judgment is difficultly made concerning the hydration heat releasing and temperature field evolving of the concrete, particularly in the stage of temperature drop;
– The creep index and the coefficient of stress relaxation (approximately taken as 0.5) that are obtained from standard laboratory tests and suggested by the design codes/specifications, are under-estimated.

2. Risks and countermeasures for dam cracking

To demonstrate the computation precision with respect to the temperature cracks and to their stability under higher water levels, a number of typically monitoring object points are selected and the computational results are cross-referenced with their readings.

Figures 8.47 and 8.48 show the compressive stresses of two typical points on the interface of dam and foundation. The point A is located at the EL. 950.5 m below the dam monolith 22#, which is in the middle of the river bed. The point B is located at the EL. 1004 m below the 15# dam monolith, which is on the right bank abutment. Figures 8.49 and 8.50 show the relative displacements along the river course of two typical points in the arch dam. The point C is located at the EL. 1010 m in dam monolith 22#. The point D is located at the EL. 1100 m in dam monolith 15#. It can be found that the computed results agree the monitored readings well, which validates the reliability of the computation.

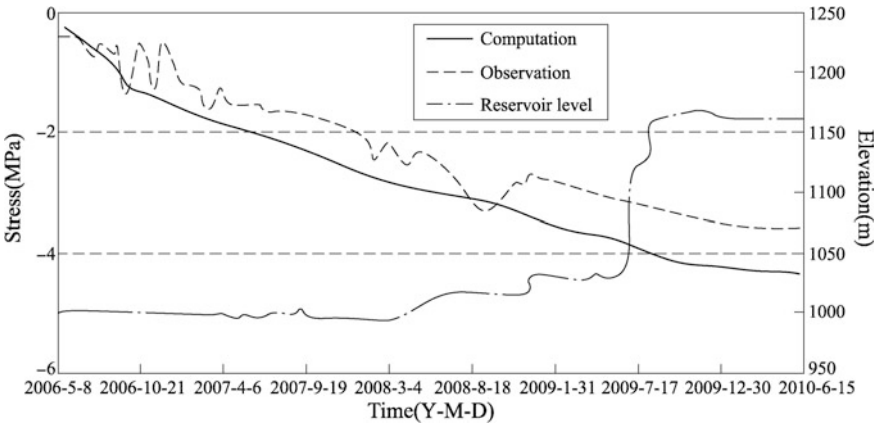

Fig. 8.47 History of the compressive stress at point A ($\|e\|_r$ = 23%, $\|e\|_a$ = 0.81 MPa)

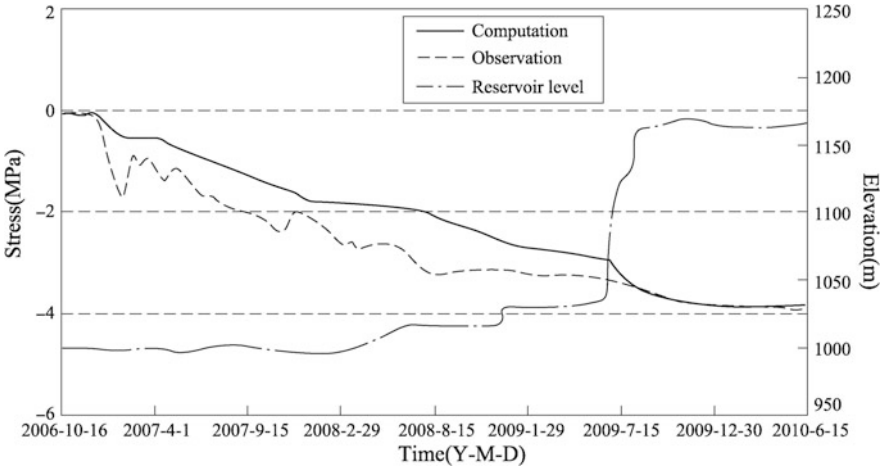

Fig. 8.48 History of the compressive stress at point B ($\|e\|_r$ = 28%, $\|e\|_a$ = 0.92 MPa)

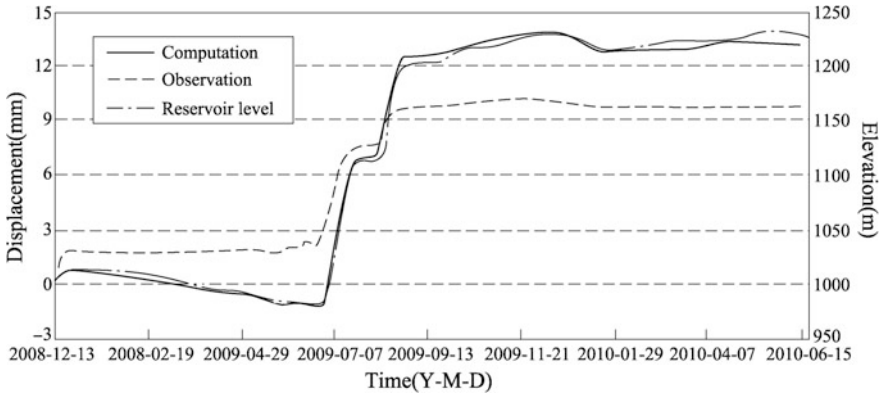

Fig. 8.49 History of the relative displacement along river course at point C ($\|e\|_r$ = 4%, $\|e\|_a$ = 0.6 mm)

Although there are no readings to pinpoint the cracking initiation and its early propagation, the computation results related to the initiation and open/closure process of the cracks generally agree with the early inspection of engineers. Further verification with regard to the crack initiation and early propagation by the computation may be indirectly provided by the instrumentation readings from the object points installed on the transverse joints between dam monoliths. A typical point E located at the EL. 960 m on the transverse joint 22# is selected for this purpose whose computed and monitored open/closure is cross-referenced in Fig. 8.51. This transverse joint experienced a complicated open/closure process shortly after the concrete pouring,

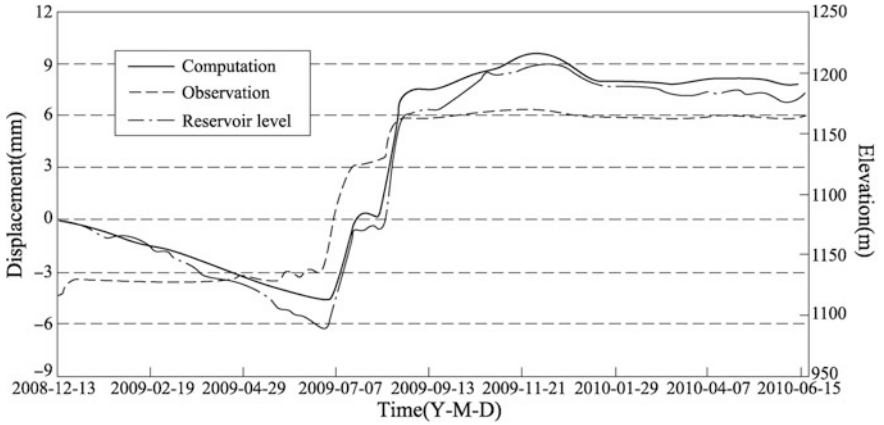

Fig. 8.50 History of the relative displacement along river course at point D ($\|e\|_r$ = 25%, $\|e\|_a$ = 1.5 mm)

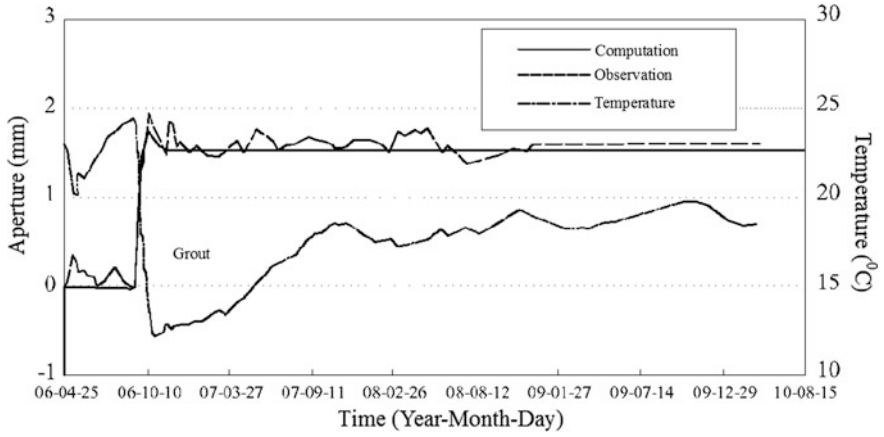

Fig. 8.51 Open/closure history of the crack at point E ($\|e\|_r$ = 11%, $\|e\|_a$ = 0.26 mm)

then followed with a continuous open process during the second stage post-cooling, and finally a steady state was reached after the joint closure grouting.

The risks of further crack propagation during the later phase construction, reservoir impoundment, and service under NSL, are calibrated with the help of the Stress Intensity Factors (SIFs K_{I}, K_{II}, K_{III}) in the fracture mechanics (Chan et al. 1970; Linsbaurer et al. 1989a, b; Dhondt 1998).

Figure 8.52 shows the evolution of the SIF on the point F (EL. 1010 m) located at the lower crack tip in the dam monolith 21#. K_{I} exhibits a sharp drop shortly after the tip element cracks, afterwards it rebounds gradually. However, when the dam is poured to the EL. 1150 m, K_{I} begins to drop again. After the chemical grouting,

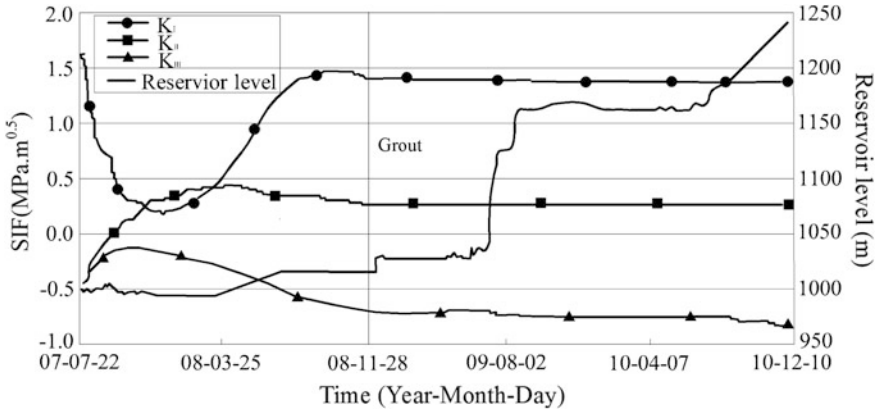

Fig. 8.52 History of the stress intensity factor at point F

K_I continues to drop slowly. The history of K_{II} is similar to that of K_I before the dam is poured to the EL. 1150 m, but after that K_{II} continues to mount. The chemical grouting slows down the rise of K_{II} remarkably. The evolution of K_{III} is opposite to that of K_{II}, and the value of K_{III} during the reservoir impounding is much smaller than those of K_I and K_{II}. Since all these three SIFs do not exceed the fracture toughness of the dam concrete, i.e. 1.5 MPa $m^{1/2}$, this crack will be stable during the whole reservoir impoundment and service periods.

Figure 8.53 displays the history of the SIF on point G (EL. 980 m) located at the lower crack tip in the dam monolith 25#. The evolution of K_I is similar to that of K_{II}. They all rapidly drop to zero shortly after the tip element cracks, then they maintain a small value all along. Therefore, this crack also will be stable during the water impounding process and in the service period.

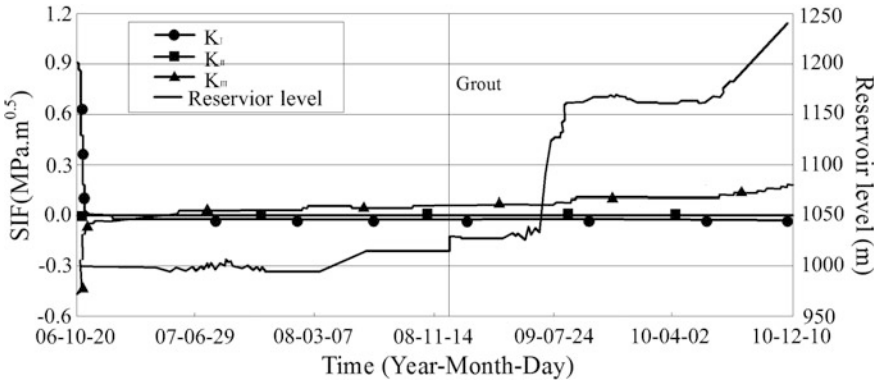

Fig. 8.53 History of the stress intensity factor at point G

According to all of the analyses concerning the SIFs, the most significant conclusion is made that the cracks in Xiaowan Arch Dam are stable during the water impounding process and service period. This has been verified by the monitored data during the reservoir impounding and the normal operation since December 16, 2008 (the first day of reservoir impounding).

8.7 Concluding Remarks

The concept of spatial-time evolution of Xiaowan Arch Dam is comprehensively introduced into the whole computational procedure. Following the progress of construction, the dynamic input of the parameters related to structure growth, temperature field, permeability field and deformation/stress field, as well as their coupling via actions, are studied in an intention to explore the performance of high arch dams. The Digitized System of Xiaowan Arch Dam (DSXAD) is then formulated by the combination of the instrumentation system, the spatial-time simulation, and the engineering judgment, which may be applied to describe the evolution of the arch dam during its construction period as well as service period. It has been fully demonstrated that this double-curvature structure is in an optimal working condition under huge hydraulic thrust, and the design/construction is very successful (Fig. 8.54).

In the execution of Xiaowan Arch Dam, a series of difficult technical issues, such as the dam foundation relaxation and dam body cracking, are successfully solved with the help of the DSXAD. Through these practices important theoretical insights are obtained and a new milestone for the high arch dam construction in China is founded. In addition, these valuable experiences will provide a solid base for the further revision and improvement of related design codes and specifications.

Fig. 8.54 Xiaowan Project in service

References

Chan SK, Tuba IS, Wilson WK. On the finite element method in linear fracture mechanics. Eng Fract Mech. 1970;2(1):1–17.

Chen SH. Hydraulic structures. Berlin: Springer; 2015.

Chen SH, Chen SF, Shahrour I, Egger P. The feedback analysis of excavated rock slope. Rock Mech Rock Eng. 2001;34(1):39–56.

Chen SH, Wang GJ, Zhou H, Wang WM, Zou LC. Evaluation of excavation-induced relaxation and its application to an arch dam foundation. Int J Numer Anal Meth Geomech. 2012a;36(1):166–81.

Chen SH, Yang ZM, Wang WM, Shahrour I. Study on the rock bolt reinforcement for the gravity dam foundation. Rock Mech Rock Eng. 2012b;45(1):75–87.

Chen SH, Zhang X, Shahrour I. Composite element model for the bonded anchorage head of stranded wire cable in tension. Int J Numer Anal Meth Geomech. 2015;39(12):1352–68.

Dhondt G. Automatic 3D mode I crack propagation calculations with finite elements. Int J Numer Meth Eng. 1998;41(4):739–57.

Egger P. Ground improvement by passive rock bolts, experimental and theoretical studies, example. Memorie GEAM. 1992;29(1):5–10.

Fairhurst C. Stress estimation in rock: a brief history and review. Int J Rock Mech Min Sci Geomech Abstr. 2003;40(7–8):957–73.

Fu SJ, He T, Wang GJ, Zhang SH, Zou LC, Chen SH. Evaluation of cracking potential for concrete arch dam based on simulation feedback analysis. Sci China Technol Sci. 2011; E54(3):565 –72.

Jia JS. Dam construction in China—a sixty year review. Beijing: China Water Power Press; 2013.

Linsbaurer HN, Ingraffea AR, Rossmanith HP, Wawrzynek PA. Simulation of cracking in large arch dam: Part 1. J Struct Eng ASCE. 1989a;115(7):1599–615.

Linsbaurer HN, Ingraffea AR, Rossmanith HP, Wawrzynek PA. Simulation of cracking in large arch dam: Part 2. J Struct Eng ASCE. 1989b;115(7):1616–30.

Pan JZ, He J. Large dams in China—a fifty year review. Beijing: China Water Power Press; 2000.

Qin WX, Fu CH, Wang WM, Chen SH. Refined simulation of initial geostress field based on sub-model method. Chin J Geotech Eng. 2008;30(6):930–4 (in Chinese).

Wang WM, Ding JX, Wang GJ, Zou LC, Chen SH. Stability analysis of the temperature cracks in Xiaowan arch dam. Sci China Technol Sci. 2011;E54(3):547–55.

Yi D, Xu MY, Chen SH, Ge XR. Application of artificial neural network to back analysis of initial stress field of rock masses. Rock Soil Mech. 2004;25(6):943–6 (in Chinese).

Zou LC. Challenge and thinking of constructing Xiaowan Hydropower Project. J Hydroelectric Eng. 2010;36(12):15–9 (in Chinese).

Zou LC, Chen SH, Wang GJ, Fu SJ, Tang XL, Xu Q, Zhao ZY, Wang WM, Xie M, He J. Simulation for the spatial-time characteristics of high arch dam. Geotech Geol Eng. 2016;34(4):949–80.

Chapter 9
Fundamentals of the Block Element Analysis

Abstract In this chapter, the principles and basic algorithms of the block element analysis (BEA) are presented, to show how a practical method in computational geomechanics may be inspired and established through a simple engineering problem. An attempt to improve the limit equilibrium method (LEM) for a more rational solution of rock wedge stability in slope gives rise to the consideration of the deformation characteristics of slip planes. The governing equations for the block system are formulated by taking into account of the force and moment equilibrium condition for rigid blocks, the deformation compatibility condition between blocks, and the elasto-viscoplastic constitutive relation of discontinuities. Since the seepage flow imposes a remarkable influence on the stability of rock masses, the interest is further directed to establishing a seepage analysis algorithm competent to the BEA. With the basic assumption that the seepage is merely permitted in discontinuities whereas the rock blocks are impervious, and use is made of the messages provided by the block system identification, the variational function of the seepage flow in discontinuity network can be automatically discretized and solved. Two engineering application cases related to the natural and cut slopes demonstrate unique merit of the BEA, namely, it possesses both the reliability of the FEM and the simplicity of the LEM.

9.1 General

In the early 1980s, due to a number of unexpected slope failure accidents encountered in the engineering consultant works, the author was attracted to a kind of classical and simple slope problem—rock wedge stability. An attempt to improve the limit equilibrium method of rigid body had given rise to the consideration of the deformation characteristics of slip planes through discontinuities (Chen 1984). Later, the idea was developed into the multi-blocky system as "Block Element Analysis" (BEA), with the assumption of face to face contact between blocks. The governing equations for the blocky rock system were formulated by taking into account of the force and moment equilibrium condition for rigid blocks, the deformation

S.-H. Chen, *Computational Geomechanics and Hydraulic Structures*,
Springer Tracts in Civil Engineering, https://doi.org/10.1007/978-981-10-8135-4_9

compatibility condition between blocks, and the elasto-viscoplastic constitutive relation of discontinuities (Chen 1987, 1992; Chen et al. 1988). The methodology was further expanded into the areas of reinforcement analysis, stochastic analysis, seepage analysis, hybrid analysis, and dynamic analysis (Chen 1991, 1993a; Chen et al. 1994, 2000, 2010; Wang et al. 2001). Towards the systematical and practical demand of hydraulic structures, the automatic identification of multi-block system for complicated domain with irregular ground surface, drainage and grouting curtains, reinforcement components, etc., had been developed, too (Chen et al. 2002).

After the displacement in each block being interpolated by a set of polynomial of any order, the method was finally generalized into the area where the complicated deformation pattern in rock blocks as well as at discontinuities, can be incorporated (Chen 1993b, 1994). A more refined BEA has also be implemented by taking into account of the rock block deformations using hierarchical refinement of p-version, in which an overlapped hierarchical element contains a deformable block (Chen et al. 2004).

The BEA has been recommended by the DL/T 5353–2006 "Design specification for engineering slopes in water resources and hydropower project".

9.2 Stability Problems of the Rock Wedge in Slope

Let's start from the basic stability problem in the slope engineering—a rock wedge with potentiality of slide on its two structural planes. Although the limit equilibrium method (LEM) is very useful in the routine stability analysis of slope due to the simplicity and the experiences accumulated in many years of applications, yet it has certain limitations: the deformation of the rock is neglected; and the safety factor could be overestimated when the slip surface consists of equal to or more than two discontinuities. Postulations concerning the stress state on the slip surface often although not always, have to be employed to make the problem statically determinate (Chan and Einstein 1981; Chen 1984).

9.2.1 Limit Equilibrium Method for the Wedge Stability Analysis

Figure 9.1a shows a rock wedge which possesses the potentiality of slide along the intersecting line CD included by the two discontinuity planes. The LEM of rigid body has been widely exercised in the stability analysis of such wedge in slope engineering. However, since the LEM has overlooked some important factors undermining the stability of rock wedge, its reliability is suspicious because sometimes it will lead to unsafe judgment on the wedge's stability. Indeed, a higher permissible (allowable) safety factor in the design can be employed to overcome

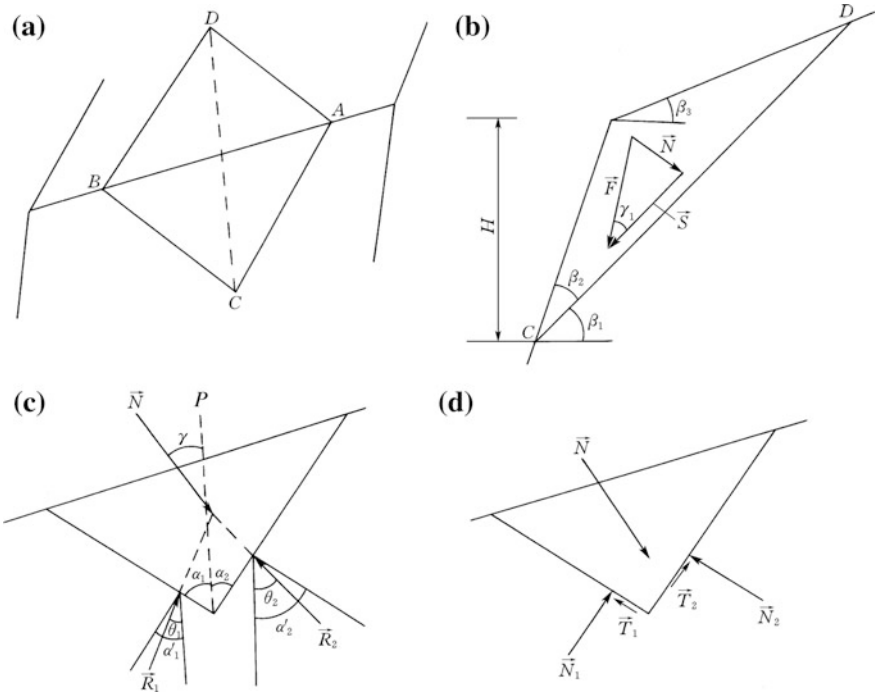

Fig. 9.1 Diagram to the stability analysis for a rock wedge in slope

this drawback, but we still feel no full confidence in whether the stability safety is appropriately guaranteed.

Assume the load E includes an angle γ_1 with the line CD and an angle γ with the line P (see Fig. 9.1b, c). The load is resolved into the S component along CD and the N component perpendicular to CD by the formulas

$$\begin{cases} \mathrm{S} = \mathrm{E}\cos\gamma_1 \\ \mathrm{N} = \mathrm{E}\sin\gamma_1 \end{cases} \tag{9.1}$$

The component N forms an equilibrium force system with the reaction forces R_1 and R_2 on the slip planes. These reactions R_1 and R_2, in turn, can be resolved into the shear forces T_1 and T_2 as well as the normal forces N_1 and N_2 on the slip planes (see Fig. 9.1d)

$$\begin{cases} \mathrm{N}_1 = \sin(\theta_2 - \gamma)\cos(\alpha_1' - \theta_1)/\sin(\theta_1 + \theta_2) \\ \mathrm{N}_2 = \sin(\theta_1 + \gamma)\cos(\alpha_2' - \theta_2)/\sin(\theta_1 + \theta_2) \\ \mathrm{T}_1 = \sin(\theta_2 - \gamma)\sin(\alpha_1' - \theta_1)/\sin(\theta_1 + \theta_2) \\ \mathrm{T}_2 = \sin(\theta_1 + \gamma)\sin(\alpha_2' - \theta_2)/\sin(\theta_1 + \theta_2) \end{cases} \tag{9.2}$$

Denoting A_1, A_2, f_1, f_2, c_1, c_2 as the areas, the friction coefficients and the cohesions of the slip planes 1 and 2, respectively, then the safety factor against sliding is calculated by the formula

$$K_f = \frac{\sqrt{(N_1 f_1 + A_1 c_1)^2 - (K_f T_1)^2} + \sqrt{(N_2 f_2 + A_2 c_2)^2 - (K_f T_2)^2}}{S} \tag{9.3}$$

Two basic problems arise from the above equations.

① Since the angles θ_1 and θ_2 are unknown, so the reactions T_1, T_2, N_1, N_2 are also unknown, therefore K_f is actually unsolved. It is normally postulated in the engineering practice that

$$\begin{cases} \theta_1 = \alpha_1' \\ \theta_2 = \alpha_2' \end{cases} \tag{9.4}$$

This assumption turns out

$$\begin{cases} \mathrm{N}_1 = N \sin(\alpha_2' - \gamma) / \sin(\alpha_1' + \alpha_2') \\ \mathrm{N}_2 = N \sin(\alpha_1' + \gamma) / \sin(\alpha_1' + \alpha_2') \\ \mathrm{T}_1 = T_2 = 0 \end{cases} \tag{9.5}$$

and we have

$$K_f = \frac{N_1 f_1 + A_1 c_1 + N_2 f_2 + A_2 c_2}{S} \tag{9.6}$$

Equation (9.4) is the well known "normal resolution assumption" (Londe 1965) and is equally to assume that T_1 and T_2 perpendicular to the slip direction are zero, in this manner the calculated K_f by Eq. (9.6) is larger than that by Eq. (9.3), i.e. there is the danger in overestimating stability factor.

② In the deduction, only the condition of force equilibrium has been taken into account. Overlooking of momentum will lead to unsafe calculation outcomes, too (Chan and Einstein 1981).

A number of methods for minimum safety factor such as the "partition method" (PM) (Guzina and Tucovic 1969; Copen et al. 1977), had been proposed for the improvement. Unfortunately, they are normally too conservative, in some cases the safety factor calculated by Eqs. (9.1) and (9.6) will be several times larger than the "minimum safety factor" (Chen 1984).

9.2.2 Inspiration from the Finite Element Analysis

To throw a light in the problem about whether the shear forces T_1 and T_2 exist or not, use may be made of the finite element method. For example, Goodman et al. analyzed the elastic stress distribution on the slip planes of wedge (Goodman et al. 1968; Mahtab and Goodman 1970). However, to understand the stress state on the slip planes under limit equilibrium condition, a non-linear analysis is desirable.

Typical rock wedges studied by the elasto-viscoplastic FEM (Chen 1984, 1990) leads to the following findings.

① The relationship between the stress state on the slip planes and the rock properties of the wedge and foundation is not significant. Even if the elastic modulus and strength parameters become very large, i.e., the wedge and foundation are actually rigid bodies, the stresses on the slip planes only undergo a minor variation.

② The main influencing factors towards the stress state on the sliding planes are

- The angle $\alpha_1 + \alpha_2$ formed by the two slip planes. If the other parameters are fixed, the smaller of $\alpha_1 + \alpha_2$, the larger of T_1 and T_2. When $\alpha_1 + \alpha_2$ approaches to 180°, both the T_1 and T_2 approach to zero.
- The deformation of the slip planes characterized by the ratio of normal stiffness to tangential stiffness $R = k_n/k_s$. If the other parameters are fixed, the larger of R, the smaller of the T_1 and T_2. When R approaches to infinitely large, both the T_1 and T_2 approach to zero.
- As the strength parameters of the slip planes are reduced until the wedge reaches limit equilibrium state, T_1 and T_2 are reduced, too. But they will not approach to zero, i.e. the shear forces T_1 and T_2 still exist in the limit equilibrium state, in other words, the "normal resolution" is not correctly postulated.

9.2.3 Improvement of the Limit Equilibrium Method

The FEM is a more suitable computation tool towards the stability analysis of rock wedge in slope, but its pre-and post-processing is much more complicated than the classical LEM, especially in 3-D situation where a slope contains a large number of wedges or rock blocks. Can we look for a new method which possesses both the merits of the FEM's reliability and the LEM's simplicity?

It has been previously revealed by the elasto-viscoplastic FEM that the main influence factors to the stress state on the slip planes are the geometry and the deformation characteristics of the slip planes themselves. In the wedge's case, if the rock slope fails by the sliding along discontinuities, the rock block's characteristics plays minor role in the stability analysis. In light of these findings an improved LEM can be formulated taking into account of the deformation on slip planes and

neglecting that of wedge rock. The governing equations comprising the equilibrium equation of the wedge, the deformation compatibility equation between the slip planes and wedge, and the constitutive equation of slip planes, have been established (Chen 1984, 1990).

An example of the rock wedge analyzed by the different existing methods inclusive the improved method (IM) by the author is presented for the validation. The computation parameters are listed in Tables 9.1, 9.2 and 9.3.

The calculated safety factors by the FEM, the conventional LEM, the partition method (PM) (Copen et al. 1977) and the improved method (IM), are all plotted in Fig. 9.2. It can be seen that the results by the FEM and the IM are quite close to

Table 9.1 Geometric parameters of the rock wedge (see Fig. 9.1)

α_1 (°)	α_2 (°)	β_1 (°)	β_2 (°)	β_3 (°)	H (m)
60	45	20	40	10	50

Table 9.2 Mechanical parameters of the slip planes

φ_1 (°)	φ_2 (°)	c_1 (kPa)	c_2 (kPa)	$R_n = k_{n1}/k_{n2}$	$R_s = k_{s1}/k_{s2}$	$R = k_n/k_s$
20	25	20	20	0.48	0.48	Variable

Table 9.3 Mechanical parameters of the rock wedge

E (MPa)	μ	c (MPa)	φ (°)	γ_r (kN/m^3)
220,000	0.16	0.16	35	27

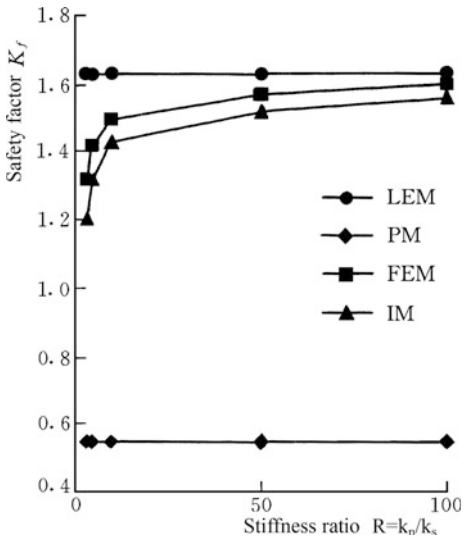

Fig. 9.2 Safety factor K_f of the wedge versus stiffness ratio R of the slip planes

each other. The classical LEM with "normal resolution assumption" and the PM provide upper and inferior bounds for the safety factor.

9.3 Establishment of the Block Element Analysis

Through the study of the rock wedge in slope it is demonstrated that apart from the strength parameters, the deformation parameters such as the normal stiffness and tangential stiffness of slip planes have significant influence on the stability of the wedge. The main mechanism is that if there are two or more slip planes, the reaction forces on the slip planes are statically indeterminate, in this case the deformation parameters will influence the stress distribution remarkably.

Also by the rock wedge study, we have been taught that if merely the deformation and strength parameters of slip planes are taken into account, an improved method which is simpler than the FEM and more precise than the LEM can be established. This encouraged us to have a further try to extend the improvement LEM into the case where the rock masses consist of substantial rock blocks, and luckily, the idea was realized in a form of work initially termed as "elasto-viscoplastic block theory" (Chen 1987) and now we call it as the "block element analysis" (BEA). It is mathematically the simplification version of the DDA (Shi 1992) where only face-to-face contact is permitted between the rock blocks. The other contact patterns are not considered because such deformation patterns, for the moment, are not allowed for in the limit states for hydraulic structures, other than to complicate the governing equations and algorithm as well as parametric evaluation.

9.3.1 Coordinate Systems

In Fig. 9.3 the block r_l is taken as a representative block element, the boundary plane of the block is denoted by $j_{rl,rm}$, the adjoining block contacting the block r_l through the plane $j_{rl,rm}$ is denoted by r_m.

The block in Fig. 9.4 is delimited by seven discontinuities, the strikes, dips and mean points of each discontinuity can be decided through geological investigation. Let the Y-axis of global coordinate system point to the north and keep horizontal; the X-axis point to the east and keep horizontal, too; the Z-axis be upright. For each discontinuity patch a local coordinate system is also needed to facilitate the mechanical deduction. The origin of the local coordinate system of plane $j_{rl,rm}$ is at the plane's centroid, the $z_{j_{rl,rm}}$-axis is perpendicular to the plane, the direction of the $x_{j_{rl,rm}}$-axis and $y_{j_{rl,rm}}$-axis are coincident with the strike and dip directions respectively, in addition, the $x_{j_{rl,rm}}$-axis must keep horizontal.

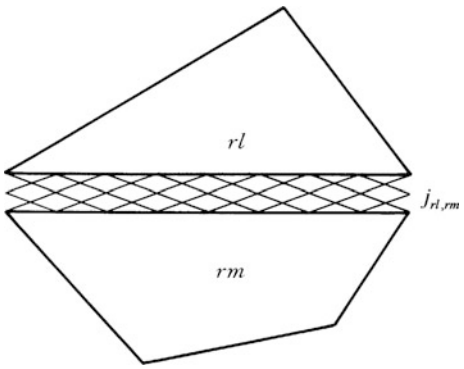

Fig. 9.3 Contact of block elements r_l and r_m

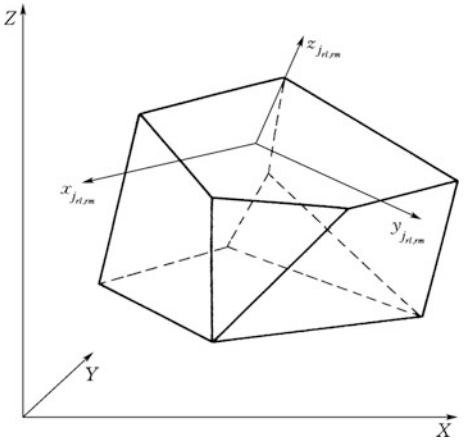

Fig. 9.4 Global and local coordinate systems of the representative block r_l

The origin of local coordinate system is located at the geometry center of discontinuity patch $j_{rl,rm}$ whose coordinate is denoted as $(X^0_{j_{rl,rm}}, Y^0_{j_{rl,rm}}, Z^0_{j_{rl,rm}})$, the coordinate of the geometry center of block *rl* is denoted as $(X^0_{rl}, Y^0_{rl}, Z^0_{rl})$.

Under the global coordinate system, the planar structural face $j_{rl,rm}$ may be expressed by equation

$$A_{j_{rl,rm}}X + B_{j_{rl,rm}}Y + C_{j_{rl,rm}}Z = D_{j_{rl,rm}} \tag{9.7}$$

In which $A_{j_{rl,rm}}, B_{j_{rl,rm}}, C_{j_{rl,rm}}, D_{j_{rl,rm}}$ are the functions of the dip direction, dip angle, and the global coordinates of, for example, its mean point.

The coordinate transformation is defined by the matrix $[l]_{j_{rl,rm}}$ in Eqs. (2.12) and (2.13) where the subscript j is replaced by $j_{rl,rm}$. At any point with local coordinate $\begin{pmatrix} x_{j_{rl,rm}} & y_{j_{rl,rm}} \end{pmatrix}$ on plane $j_{rl,rm}$, the stress and deformation (relative displacement) increments are denoted as

$$\begin{cases} \{\Delta\sigma\}_{j_{rl,rm}} = [\,\Delta\tau_{zx} \quad \Delta\tau_{zy} \quad \Delta\sigma_z\,]^T \\ \{\Delta u\}_{j_{rl,rm}} = [\,\Delta u_x \quad \Delta u_y \quad \Delta u_z\,]^T \end{cases} \tag{9.8}$$

All external load increments exerting at the centroid of block *rl* are expressed in the global coordinate system as (see Fig. 9.5)

$$\{\Delta F\}_{rl} = [\,\Delta F_X \quad \Delta F_Y \quad \Delta F_Z \quad \Delta M_X \quad \Delta M_Y \quad \Delta M_Z\,]^T \tag{9.9}$$

The deflection increments of the block *rl* are also expressed in the global coordinate system as (see Fig. 9.5)

$$\{\Delta U\}_{rl} = [\,\Delta U_X \quad \Delta U_Y \quad \Delta U_Z \quad \Delta W_X \quad \Delta W_Y \quad \Delta W_Z\,]^T \tag{9.10}$$

9.3.2 Governing Equations

(1) Force and moment equilibrium equation

Integrating the stress increments on each plane $j_{rl,rm}$ into the resultant force with respect to the centroid of block r_l (see Fig. 9.5), we get the equilibrium equation

$$\{\Delta F\}_{rl} - \sum_{j_{rl,rm}} J(j_{rl,rm}) \iint_{\Gamma_{j_{rl,rm}}} [P]_{j_{rl,rm}} \{\Delta\sigma\}_{j_{rl,rm}} dx_{j_{rl,rm}} dy_{j_{rl,rm}} = 0 \quad (r_l = 1, 2, \ldots, n_r)) \tag{9.11}$$

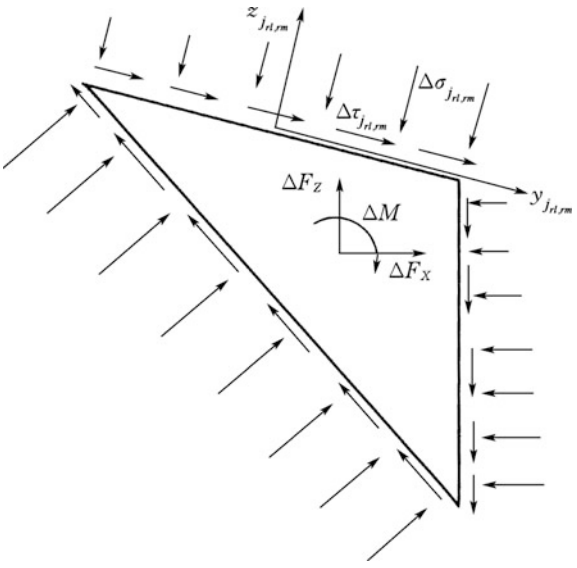

Fig. 9.5 Diagram to the equilibrium of representative block r_l

In which function $J(j_{rl,rm})$ is defined as

$$J(j_{rl,rm}) = \begin{cases} 1 & \text{for block } r_l \text{ above plane } j_{rl,rm} \\ -1 & \text{for block } r_l \text{ under plane } j_{rl,rm} \end{cases} \tag{9.12}$$

and $[P]_{j_{rl,rm}}$ is a 6×3 matrix defined as

$$[P]_{j_{rl,rm}} = \begin{bmatrix} [l]^{-1}_{j_{rl,rm}} \\ [l]^{-1}_{j_{rl,rm}}[P_1]_{j_{rl,rm}} + [P_2]_{j_{rl,rm}}[l]^{-1}_{j_{rl,rm}} \end{bmatrix} \tag{9.13}$$

in which

$$[P_1]_{j_{rl,rm}} = \begin{bmatrix} 0 & 0 & y_{j_{rl,rm}} \\ 0 & 0 & -x_{j_{rl,rm}} \\ -y_{j_{rl,rm}} & x_{j_{rl,rm}} & 0 \end{bmatrix} \tag{9.14}$$

$$[P_2]_{j_{rl,rm}} = \begin{bmatrix} 0 & -(Z^0_{j_{rl,rm}} - Z^0_{rl}) & (Y^0_{j_{rl,rm}} - Y^0_{rl}) \\ (Z^0_{j_{rl,rm}} - Z^0_{rl}) & 0 & (X^0_{j_{rl,rm}} - X^0_{rl}) \\ -(Y^0_{j_{rl,rm}} - Y^0_{rl}) & (X^0_{j_{rl,rm}} - X^0_{rl}) & 0 \end{bmatrix} \tag{9.15}$$

In Eq. (9.15) $\{X^0\}_{j_{rl,rm}} = \begin{bmatrix} X^0_{j_{rl,rm}} & Y^0_{j_{rl,rm}} & Z^0_{j_{rl,rm}} \end{bmatrix}^T$ is the global coordinate of the discontinuity $j_{rl,rm}$ on the block rl, and $\{X^0\}_{rl} = \begin{bmatrix} X^0_{rl} & Y^0_{rl} & Z^0_{rl} \end{bmatrix}^T$ is the global coordinate of the centroid of the block rl.

(2) Deformation compatibility equation

The displacement increments of the blocks r_l and r_m will give rise to deformation increment $\{\Delta u\}_{j_{rl,rm}}$ on the plane $j_{rl,rm}$ (see Fig. 9.6). According to kinematics they may be related by the formula

$$\{\Delta u\}_{j_{rl,rm}} = J(j_{rl,rm})[l]_{j_{rl,rm}}([M]_{rl}\{\Delta U\}_{rl} - [M]_{rm}\{\Delta U\}_{rm}) \tag{9.16}$$

in which

$$\begin{cases} [M]_{rl} = \begin{bmatrix} 1 & 0 & 0 & 0 & (Z - Z^0_{rl}) & -(Y - Y^0_{rl}) \\ 0 & 1 & 0 & -(Z - Z^0_{rl}) & 0 & (X - X^0_{rl}) \\ 0 & 0 & 1 & (Y - Y^0_{rl}) & -(X - X^0_{rl}) & 0 \end{bmatrix} \\ \begin{Bmatrix} X \\ Y \\ Z \end{Bmatrix} = [l]^{-1}_{j_{rl,rm}}\{x\}_{j_{rl,rm}} + \{X^0\}_{rl} \end{cases} \tag{9.17}$$

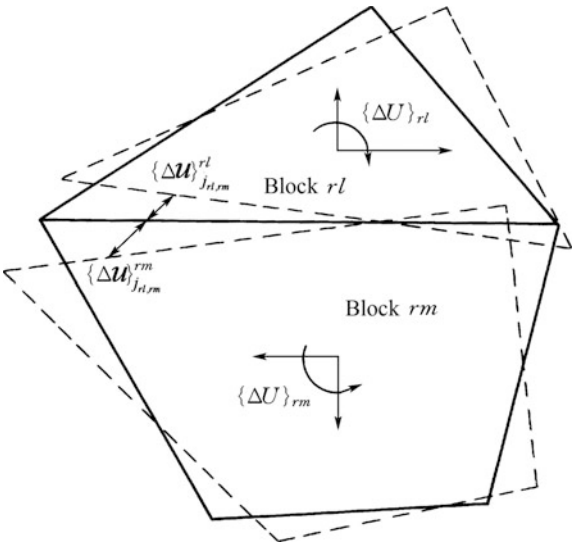

Fig. 9.6 Deformation of discontinuity $j_{rl,rm}$ attributable to adjacent blocks rl and rm

$$\begin{cases} [M]_{rm} = \begin{bmatrix} 1 & 0 & 0 & 0 & (Z - Z^0_{rm}) & -(Y - Y^0_{rm}) \\ 0 & 1 & 0 & -(Z - Z^0_{rm}) & 0 & (X - X^0_{rm}) \\ 0 & 0 & 1 & (Y - Y^0_{rm}) & -(X - X^0_{rm}) & 0 \end{bmatrix} \\ \begin{Bmatrix} X \\ Y \\ Z \end{Bmatrix} = [l]^{-1}_{j_{rl,rm}} \{x\}_{j_{rl,rm}} + \{X^0\}_{rm} \end{cases} \tag{9.18}$$

(3) Constitutive equation

According to the potential formulation (Owen and Hinton 1980), the deformation and stress increments at any point $\begin{pmatrix} x_{j_{rl,rm}} & y_{j_{rl,rm}} \end{pmatrix}$ on the discontinuity plane $j_{rl,rm}$ shall observe the elasto-viscoplastic constitutive relation in Eqs. (2.126)–(2.129).

(4) Equilibrium equation of the whole block system

Substituting Eqs. (2.126) and (9.16) into Eq. (9.11), the equilibrium equation of the block r_l becomes

$$[K]_{rl,rl}\{\Delta U\}_{rl} + \sum_{rm} [K]_{rl,rm}\{\Delta U\}_{rm} = \{\Delta F\}_{rl} + \{\Delta F^{vp}\}_{rl} \qquad (r_l = 1, 2, \ldots, n_r) \tag{9.19}$$

where r_m over loops all the adjoin blocks of the block r_l in corresponding to the plane $j_{rl,rm}$, and

$$\begin{cases} [K]_{rl,rl} = \sum\limits_{j_{rl,rm}} \iint\limits_{\Gamma_{j_{rl,rm}}} [P]_{j_{rl,rm}} [D]_{j_{rl,rm}} [l]_{j_{rl,rm}} [M]_{rl} dx_{j_{rl,rm}} dy_{j_{rl,rm}} \\ [K]_{rl,rm} = -\iint\limits_{\Gamma_{j_{rl,rm}}} [P]_{j_{rl,rm}} [D]_{j_{rl,rm}} [l]_{j_{rl,rm}} [M]_{rm} dx_{j_{rl,rm}} dy_{j_{rl,rm}} \\ \{\Delta F^{vp}\}_{rl} = \sum\limits_{j_{rl,rm}} J(j_{rl,rm}) \iint\limits_{\Gamma_{j_{rl,rm}}} [P]_{j_{rl,rm}} \{\Delta\sigma^{vp}\}_{j_{rl,rm}} dx_{j_{rl,rm}} dy_{j_{rl,rm}} \end{cases} \tag{9.20}$$

For the other blocks there also exist foregoing equations, assembling all of such equations in a similar way to the FEM, the equilibrium equation set of the block system is finally constructed

$$[K]\{\Delta U\} = \{\Delta F\} + \{\Delta F^{vp}\} \tag{9.21}$$

In which

$$\begin{cases} \{\Delta U\} = [\{\Delta U\}_1^T \ldots \{\Delta U\}_{n_r}^T]^T \\ \{\Delta F\} = [\{\Delta F\}_1^T \ldots \{\Delta F\}_{n_r}^T]^T \\ \{\Delta F^{vp}\} = [\{\Delta F^{vp}\}_1^T \ldots \{\Delta F^{vp}\}_{n_r}^T]^T \end{cases} \tag{9.22}$$

are the displacement increment, the load increment, and the viscoplastic equivalent force increment, of the block system, respectively.

At any time step, we solve Eq. (9.21) firstly. Then use is made of the displacement increment of the block system $\{\Delta U\}$ to calculate the deformation and stress increments by Eqs. (9.16) and (2.126). Next, identify the yield points on the discontinuities. If yield occurs, calculate the viscoplastic strain/stress increments and corresponding equivalent load increments using Eqs. (2.126)–(2.129) and Eq. (9.20), afterwards go to the next time marching step.

9.3.3 Numerical Integration on Discontinuity Network

Calculation of the matrices $[K]_{rl,rl}$ and $[K]_{rl,rm}$ as well as the equivalent load vector $\{\Delta F^{vp}\}_{rl}$ in Eq. (9.20) requires the numerical integration (quadrature) on discontinuities. To get the resultant load vector attributable to the volumetric force of rock block, and in the case where the deformation of rock blocks is taken into account (vide Chap. 10), we need to integrate throughout entire entity blocks, too. It is difficult to give a closed-form of the integration result, since the shapes and sizes of discontinuity patches and rock blocks are changeable. We present here a Gaussian quadrature method on the discontinuity as well as in the block entity as follows.

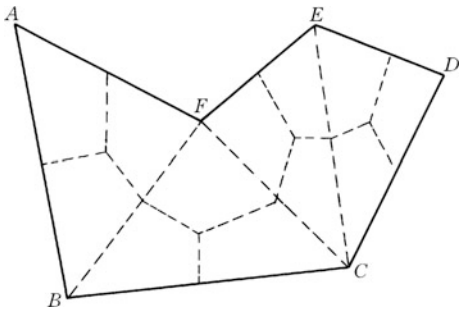

Fig. 9.7 Element dividing on a discontinuity plane towards quadrature

(1) Quadrature on discontinuities

Figure 9.7 shows a discontinuity plane $j_{rl,rm}$ on block r_l whose vortex coordinates are known. The plane is firstly divided into triangles. For each triangle, we draw lines from its centroid to the middle points of its edges, the plane is divided into a set of quadrilaterals. Then Eq. (9.20) can be additively calculated using the Gaussian quadrature on the normalized coordinates ξ and η of every element e

$$\begin{cases} [K]_{rl,rl} = \sum\limits_{j_{rl,rm}} \sum\limits_{e} \int\limits_{-1}^{1} \int\limits_{-1}^{1} [P]_{j_{rl,rm}} [D]_{j_{rl,rm}} [l]_{j_{rl,rm}} [M]_{rl} |J| d\xi d\eta \\ [K]_{rl,rm} = -\sum\limits_{e} \int\limits_{-1}^{1} \int\limits_{-1}^{1} [P]_{j_{rl,rm}} [D]_{j_{rl,rm}} [l]_{j_{rl,rm}} [M]_{rm} |J| d\xi d\eta \\ \{\Delta F^{vp}\}_{rl} = -\sum\limits_{j_{rl,rm}} \sum\limits_{e} J(j_{rl,rm}) \int\limits_{-1}^{1} \int\limits_{-1}^{1} [P]_{j_{rl,rm}} \{\Delta\sigma^{vp}\}_{j_{rl,rm}} |J| d\xi d\eta \end{cases} \tag{9.23}$$

In which e is the amount of quadrilaterals discretized from plane $j_{rl,rm}$ and $|J|$ is the Jacobian determinant. Usually, two Caussian sampling points in each direction may sufficiently guarantee the integral accuracy.

(2) Quadrature in blocks

Firstly the block is divided into tetrahedrons. For each tetrahedron the following subdivide are conducted (see Fig. 9.8): drawing lines from block centroid to the centroids of its surfaces, and drawing lines from surface centroids to the middle points of edges. In this manner the tetrahedron will be subdivided into four hexahedra. After making coordinate transform, the three-dimensional Gaussian quadrature can be implemented for any function $F(X, Y, Z)$ defined in the block rl as

$$\iiint F(X,Y,Z)dXdYdZ = \sum_{e} \int\limits_{-1}^{1} \int\limits_{-1}^{1} \int\limits_{-1}^{1} F(\xi,\zeta,\eta)|J|d\xi d\zeta d\eta \tag{9.24}$$

In which e is the amount of integration element produced in block rl.

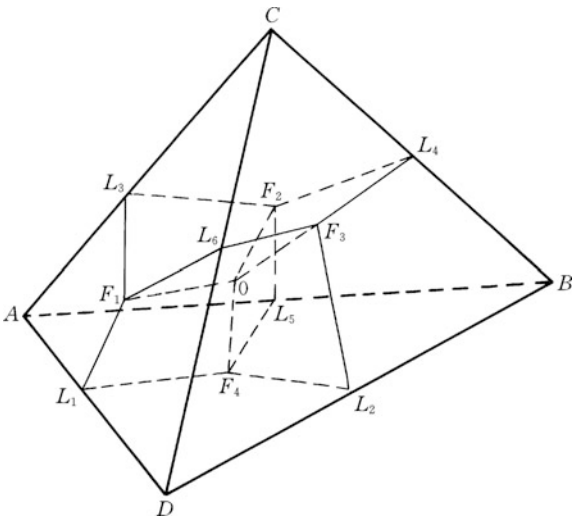

Fig. 9.8 Element dividing in a tetrahedron towards quadrature

9.3.4 Searching for Safety Factors

A potential failure case (mode) is defined as a portion of the slope formed by one block or by the combination of several blocks whose safety factor is comparatively lower than that stipulated in the design codes. If a slope contains a large amount of blocks, theoretically there will have substantial failure cases whose search for safety calibration will cost huge computer resources. To minimize the search effort, a heuristic search strategy called "intelligent search method" (Xu et al. 2000) had been proposed. The strategy is that only the possible block combinations enlightened by the previously calibrated block combinations, are to be considered in the successive search.

9.4 Seepage Field for the Block Element Analysis

Seepage flow imposes a great influence on the stability of rock masses. Hence the interest of this section is directed to establishing a seepage analysis algorithm, which may be easily incorporated into the deformation and stability analysis using the elasto-viscoplastic BEA elaborated above.

Although the seepage problem is well formulated in the FEM, yet for discontinuity networks there still exist issues with regard to the discontinuity network discretization, the iteration algorithm of unconfined flow, the consideration of the drainage and grouting curtains.

The basic assumption adopted in the study is that the seepage is merely permitted in discontinuities whereas the rock blocks are impervious. With the help of

this assumption, the variational equation of the seepage flow in the discontinuity network can be discretized into two-dimensional finite element system automatically using the messages provided by the block system identification.

9.4.1 Governing Equations

Denote the hydraulic potential as $\phi = Z + p/\gamma$, the governing equation of the seepage field in Eq. (4.148) may be rewritten in the form of

$$\{S\}^T[k]\{S\}\phi + q_0 = 0 \tag{9.25}$$

or

$$L\phi + q_0 = 0 \tag{9.26}$$

In which the permeability tensor $[k]$ has been defined in Eq. (2.9).

The solution of the PDE in Eq. (9.25) is subject to the boundary conditions defined in Eqs. (4.150)–(4.153) which will be re-expressed as follows.

1 First type (Dirichlet)

$$\phi|_{\Gamma_1} = \phi_0 \tag{9.27}$$

where ϕ_0 = specified hydraulic potential, m.

2 Second type (Neumann)

$$v_n = -\{n\}^T[k]\{S\}\phi|_{\Gamma 2} = q \tag{9.28}$$

where q = flow rate per unit area on the boundary surface, m/s, q = 0 means the boundary is impervious; {n} = unit normal vector outward of the boundary.

$$\{\mathrm{n}\}^{\mathrm{T}} = [\,l_x \quad l_y \quad l_z\,] \tag{9.29}$$

3 Phreatic type

$$\begin{cases} \phi|_{\Gamma 3} = Z \\ \{\mathrm{n}\}^{\mathrm{T}}[\mathrm{k}]\{\mathrm{S}\}\phi|_{\Gamma 3} = 0 \end{cases} \tag{9.30}$$

4 Outflow type

$$\begin{cases} \phi|_{\Gamma 4} = Z \\ \{\mathrm{n}\}^{\mathrm{T}}[\mathrm{k}]\{\mathrm{S}\}\phi|_{\Gamma 4} \neq 0 \end{cases} \tag{9.31}$$

In Eqs. (9.25)–(9.31), L and $\{S\}$ are the differential operators

$$\begin{cases} \mathrm{L} = \{S\}^{\mathrm{T}}[\mathrm{k}]\{S\} \\ \{S\} = \left[\frac{\partial}{\partial X} \quad \frac{\partial}{\partial Y} \quad \frac{\partial}{\partial Z}\right]^{T} \end{cases} \tag{9.32}$$

The above governing equation and boundary conditions lead to the variational problem in Eq. (4.154). Since the rock block is assumed impervious so the permeability coefficient k in rock block is zero. In addition, since ϕ is a scalar so the variational function $I(.)$ in Eq. (4.154) can be segmentally expressed in the local coordinate system of each discontinuity plane $j_{rl,rm}$ as

$$\begin{aligned} I(\phi) = \sum_{j_{rl,rm}} \iiint_{\Omega} \left(\frac{1}{2}(\{S\}_{j_{rl,rm}}\phi)^{T}[k]_{j_{rl,rm}}(\{S\}_{j_{rl,rm}}\phi) - q_0\phi\right) dx_{j_{rl,rm}} dy_{j_{rl,rm}} dz_{j_{rl,rm}} \\ + \iiint_{\Gamma_2} q\phi d\Gamma = \min \end{aligned} \tag{9.33}$$

In which the summation index $j_{rl,rm}$ runs over all the discontinuities. The differential operator $\{S\}_{j_{rl,rm}}$ and the permeability coefficient matrix $[k]_{j_{rl,rm}}$ are expressed in the local coordinate system

$$\begin{cases} \mathrm{L} = (\{S\}_{j_{rl,rm}})^{\mathrm{T}}[\mathrm{k}]_{j_{rl,rm}}\{S\}_{j_{rl,rm}} \\ [k]_{j_{rl,rm}} = \begin{bmatrix} k & 0 & 0 \\ 0 & k & 0 \\ 0 & 0 & k \end{bmatrix} \\ \{S\}_{j_{rl,rm}} = \left[\frac{\partial}{\partial x_{j_{rl,rm}}} \quad \frac{\partial}{\partial y_{j_{rl,rm}}} \quad \frac{\partial}{\partial z_{j_{rl,rm}}}\right]^{T} \end{cases} \tag{9.34}$$

Usually the thickness (hydraulic aperture) $a_{j_{rl,rm}}$ of the discontinuity is much smaller than the size of blocks, therefore it can be assumed that

$$\frac{\partial \phi}{\partial z_{j_{rl,rm}}} = 0 \tag{9.35}$$

Thus, Eq. (9.33) is reduced to the two-dimensional form on the discontinuity patches

$$I(\phi) = \sum_{j_{rl,rm}} \iint_{\Omega_{j_{rl,rm}}} \left(\frac{1}{2} (\{S\}_{j_{rl,rm}} \phi)^T [k]_{j_{rl,rm}} (\{S\}_{j_{rl,rm}} \phi) - a_{j_{rl,rm}} q_0 \phi \right) dx_{j_{rl,rm}} dy_{j_{rl,rm}} + \int_{\Gamma_2} q\phi d\Gamma = \min. \tag{9.36}$$

Where the differential operators $\{S\}_{j_{rl,rm}}$ and permeability $[k]_{j_{rl,rm}}$ are

$$\begin{cases} \{S\}_{j_{rl,rm}} = \left[\frac{\partial}{\partial x_{j_{rl,rm}}} \quad \frac{\partial}{\partial y_{j_{rl,rm}}} \right]^T \\ [k]_{j_{rl,rm}} = a_{j_{rl,rm}} \begin{bmatrix} k_f & 0 \\ 0 & k_f \end{bmatrix} \end{cases} \tag{9.37}$$

The parameter k_f in Eq. (9.37) is termed as equivalent permeability coefficient of the structural plane (see Eq. (2.11)).

9.4.2 Discretization of Governing Equations

Equation (9.36) can be discretized using the finite element mesh over the discontinuity network. Taking the discontinuity plane $j_{rl,rm}$ shown in Fig. 9.7 for example, it is firstly divided by triangles, then for each triangle drawing lines from its centroid to the middle points of its edges, the triangle is divided into quadrilaterals. For each element the shape function of the four-node isoparametric element is employed to give the interpolation

$$\phi = [N]\{\phi\}^e \tag{9.38}$$

In which the shape function $[N]$ is defined in Eq. (4.30).

Use is made of Eq. (9.36) to conduct the variational operation, the governing equation towards the solution of seepage field is

$$[H]\{\phi\} = \{Q\} \tag{9.39}$$

In which $[H]$ is the hydraulic conductivity matrix of the system composed of all the patched faces. It is assembled from $[h]^e$ of each element $e_{j_{rl,rm}}$ on the discontinuity $j_{rl,rm}$

$$[h]^e = \iint_{e_{j_{rl,rm}}} \left(\{S\}_{j_{rl,rm}} [N] \right)^T [k]_{j_{rl,rm}} (\{S\}_{j_{rl,rm}} [N]) dx_{j_{rl,rm}} dy_{j_{rl,rm}} \tag{9.40}$$

$\{Q\}$ is flow vector contributed from the inner source and boundary assembled from that $\{Q\}^e$ of each element $e_{j_{rl,rm}}$ on the discontinuity $j_{rl,rm}$

$$\{Q\}^e = a_{j_{rl,rm}} \iint\limits_{e_{j_{rl,rm}}} ([N])^T q_0 dx_{j_{rl,rm}} dy_{j_{rl,rm}} - \int\limits_{\Gamma_2} ([N])^T q d\Gamma \tag{9.41}$$

9.4.3 Key Algorithms

(1) Unconfined seepage problem

The principle of the "residual flow rate" for the unconfined seepage in the FEM (vide Chap. 4) is revised accordingly to solve the discontinuity network seepage field.

① Solve Eq. (9.39) firstly to get the element hydraulic potentiality $\{\phi\}^e$.

② Use is made of Eq. (9.38) to get the hydraulic potentiality at each Gaussian point. The phreatic surface divides a discontinuity plane $j_{rl,rm}$ into two parts, namely the portion $\Omega^1_{j_{rl,rm}}$ above the phreatic surface and the portion $\Omega^2_{j_{rl,rm}}$ below the phreatic surface, which are judged by the following conditions:

– If $\phi_r < Z$ (Z is the vertical global coordinate of the point concerned), the Gaussian point belongs to $\Omega^1_{j_{rl,rm}}$;

– If $\phi_r > Z$, the Gaussian point belongs to $\Omega^2_{j_{rl,rm}}$.

In this manner a tentative phreatic surface can be constructed by a set of its embedding elements.

③ For each element e that contains phreatic surface, the Gaussian points in $\Omega^1_{j_{rl,rm}}$ contribute to its nodal "residual flow rate" $\{Q_r\}^e$ as

$$\{Q_r\}^e = -\iint\limits_{\Omega^1_{j_{rl,rm}}} \left(\{S\}_{j_{rl,rm}}[N]\right)^T [k]_{j_{rl,rm}} \left(\{S\}_{j_{rl,rm}}[N]\right) \{\phi_r\}^e d\Omega \tag{9.42}$$

④ Accumulate the contributions from all the Gaussian points in $\Omega^1_{j_{rl,rm}}$ to form the global "residual flow rate" $\{Q_r\}$, then the rth iteration for the unconfined seepage field is carried out accordingly

$$[H]\{\Delta\phi_r\} = \{Q_r\} \tag{9.43}$$

⑤ Solution of Eq. (9.43) gives rise to the updated hydraulic potential by

$$\{\phi_{r+1}\} = \{\phi_r\} + \{\Delta\phi_r\}$$

⑥ Let $r = r + 1$, steps ②–⑤ are recurred until the following collapse criteria are met

– That the total number of Gaussian points in the domain where $\phi < Z$ is unchanged between the successive two iteration steps;
– That the increment of the nodal hydraulic potentiality in $\Omega^2_{jrl,rm}$ is sufficiently smaller than a specified fraction tolerance.

(2) Simulation of grout curtain and drainage curtain

The grouting curtain is looked at as a special block with small width and large stretch, whose spatial location and other messages are generated in the block identification procedure. Also in the identification for a block system, each discontinuity patch should be checked if it is intersected with the grouting curtain. This intersecting portion is only a narrow stripe on the discontinuity and assigned with much lower hydraulic conductivity compared to the rest portion. Usually a fraction of 100–1000th is advisable.

The drainage curtain is approached by an equivalent discontinuity patch whose hydraulic conductivity can be decided by the equivalent principle of flow rate related to the rock's conductivity, the diameter and spacing of drainage holes. For dam engineering, an amplification of 10–100 times that of surrounding host material, is advisable.

9.4.4 *Verification Example*

Figure 9.9 shows a block delimited by four surfaces (1, 2, 3, 7). Their permeability coefficients are identically $k = 1.0 \times 10^{-4}$ m/s. The upstream water level is 12 m and the downstream water level is 0. Near the upstream a grouting curtain is installed whose permeability coefficient is $k = 1.0 \times 10^{-5}$ m/s.

Figure 9.10 gives the phreatic line and flow velocity on surface 2, it is found that the phreatic line drops dramatically through the curtain.

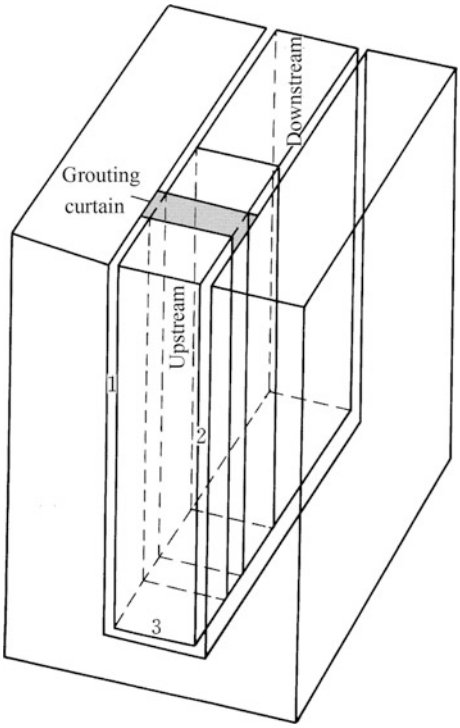

Fig. 9.9 Block with grouting curtain

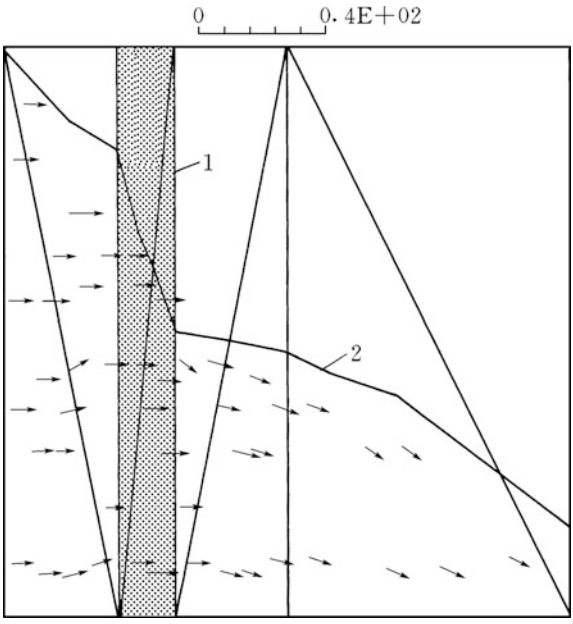

Fig. 9.10 Seepage field on surface 2

9.5 Engineering Applications

9.5.1 Natural Slope: Baozhusi Project, China

(1) Presentation of the Project

Baozhusi Project (see Fig. 9.11) is located on the Bailongjiang River, Sichuan Province, China. Construction on the dam began in 1984, the generators were operational between 1996 and 1998 while the rest of the facilities were complete in 2000. The project is purposed for hydroelectric power generation, flood control and water supply towards irrigation and industrial uses. The 132 m tall and 524.48 m long concrete gravity dam creates a 2550 million m^3 reservoir. On either side of power station at the dam's base, there are two gate-controlled chute spillways. In addition, there are two pairs of orifice spillways. Below the left orifice there are two bottom outlets. The total discharge capacity of the spillways and openings is 16,060 m^3/s. The dam type power station is installed with 4 × 175 MW Francis turbine-generators.

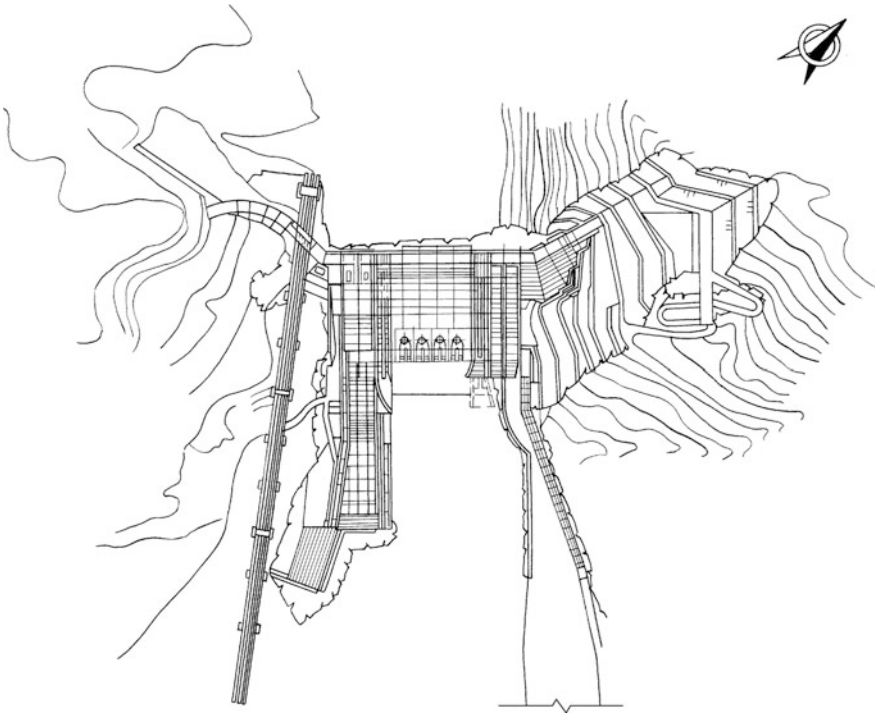

Fig. 9.11 Plan of Baozhusi Project, China

(2) Characteristics of the computation

The slope at the downstream left abutment of the Baozhusi Gravity Dam is illustrated in Fig. 9.12. Under the natural condition, two argillic intercalations (D_1, D_3) and three faults (f_{10}, F_4, F_{10}) delimit 4 potential slip blocks whose axonometric drawings are displayed in Fig. 9.13.

Since the underground water table is below the EL. 500 m, therefore only the saturated seepage flow attributable to rainfall is taken into account in the stability analysis. Table 9.4 lists the parameters used in the computation.

(3) Computation results

The strength reduction is carried out until one block or block combination reaches critical (limit) state. Altogether four failure modes are detected whose corresponding safety factors are listed in Table 9.5.

The block combination of block element 1 + block element 3 possesses the lowest safety factor. This is justified by the field observation that the rock mass in this portion exhibits time-dependent deformation and relaxation, the local rock collapse and rock fall had created a gully.

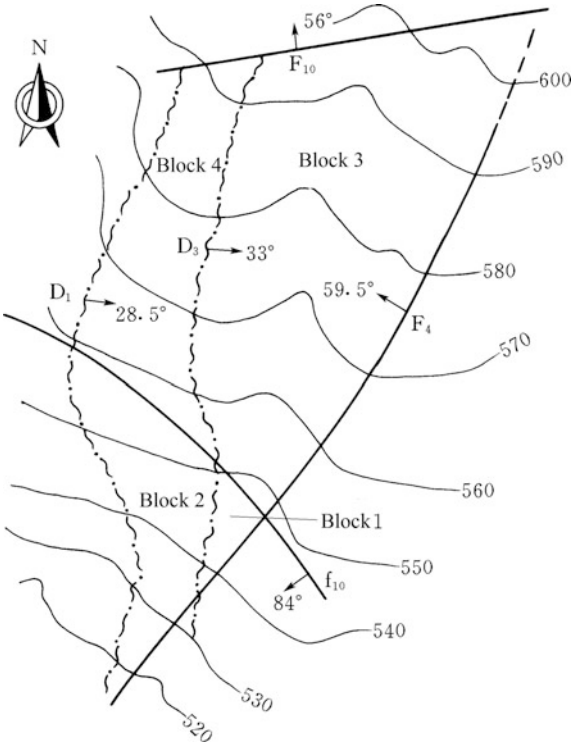

Fig. 9.12 Geology plan of the abutment slope: Baozhusi Project, China

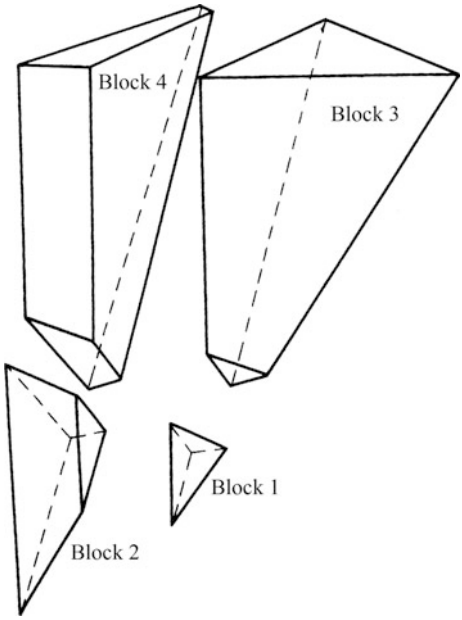

Fig. 9.13 Axonometric drawing of the decomposed movable block system in the slope

Table 9.4 Parameters used in the computation

–		D_1	D_3	F_4	F_{10}	f_{10}
Strike (°)		70.0	70.0	15.0	60.0	145.0
Dip angle (°)		SE28.5	SE33.0	NW59.5	NW56.0	SW84.0
Stiffness (MN/m^3)	k_n	22.4	15.0	29.9	9.11	150.0
	k_s	6.41	4.27	8.55	2.6	42.7
Strength	c (kPa)	10.0	10.0	0.0	20.0	0.0
	φ (°)	14.0	14.0	16.7	24.2	16.7
	σ_T (kPa)	1.0	1.0	0.0	2.0	0.0
Volumetric weight of rock γ_r = 26.4 kN/m^3						

Table 9.5 Failure modes and corresponding safety factor K

Failure mode	Load combination	
	Self weight	Self weight + seepage
Block 1	1.75	1.45
Block 1 + Block 2	1.70	1.40
Block 1 + Block 3	1.40	1.05
Block 1 + Block 2 + Block 3 + Block 4	1.45	1.15

9.5.2 *Cut Slope: Longtan Project, China*

(1) Presentation of the Project

Vide Chap. 6 (Sect. 6.6.2).

(2) Characteristics for the computation

Entailed by the project layout, the right dam abutment was excavated in a complicated configuration (see Fig. 9.14). During the excavating, a local collapse occurred and the failure risk of a series movable block combinations were alarmed. The revised excavation was carried out successfully under the guidance of comprehensive studies inclusive the BEA illustrated hereinafter.

1 Structural planes

The large faults F_{89}, $F_{90}(F_{90-1})$, F_{136}, F_{60}, $F_{345-1}(F_{330-6})$, f_6 and the random interlayer faults as well as the low dip angle joints, are taken into account in the analysis. Their locations and occurrences are shown in Fig. 9.15 and detailed in Table 9.6.

2 Specific block elements with high slip potentiality

The analysis identifies 5 dangerous block elements.

i. Small block

This is enclosed by the faults F_{136} and F_{89} and random interlayer fault (see Figs. 9.16 and 9.17).

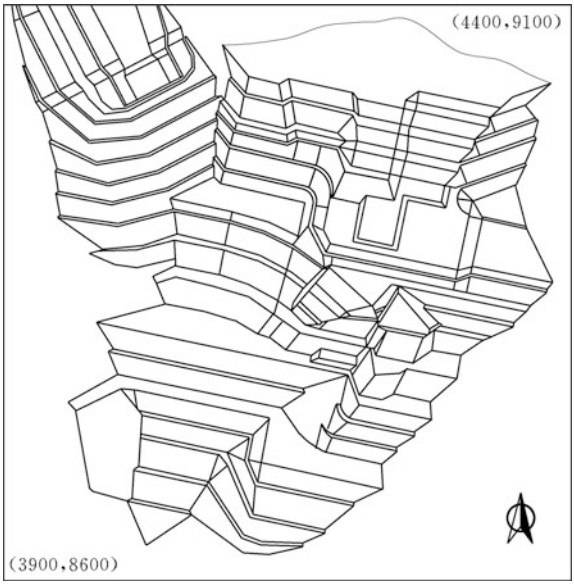

Fig. 9.14 Plan showing the layout of excavation benches (right dam abutment after local collapse)

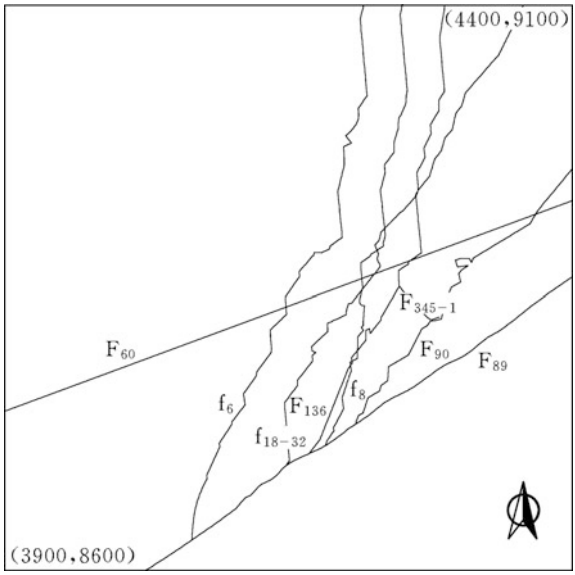

Fig. 9.15 Plan showing the location of major structural planes

Table 9.6 Occurrence of the major structural planes

Structural planes		Strike direction	Dip direction	Dip angle (°)
F_{60}		N70°E	NW/SE	90
F_{89}		N65°E	NW	75
F_{90}		N59°E	NW	60
F_{136}		N40°E	NW	65
F_{345-1}		N20°E	NW	32
F_{330-6}			NW	
Interlayer fault and f_6		N5°W	NE	57
Low dip angle structural planes	Joint	N70°E	NW	30
	Fault + joint	N15°E	NW	30

ii. Medium block

This is enclosed by the faults F_{136}, F_{89}, f_6 and the low dip angle joint, the outcrop elevation is 330 m (see Figs. 9.18 and 9.19).

iii. Large block 1

This is enclosed by the faults F_{90} (F_{90-1}), F_{89}, f_6 and the low dip angle joint, the outcrop elevation is 330 m (see Figs. 9.20 and 9.21).

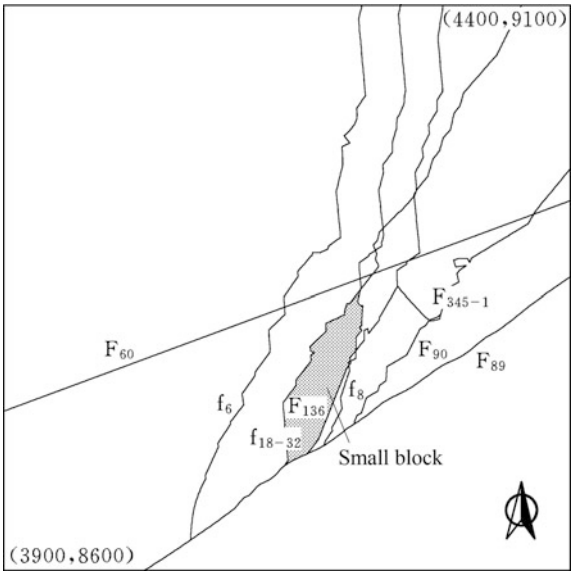

Fig. 9.16 Location of the small block element

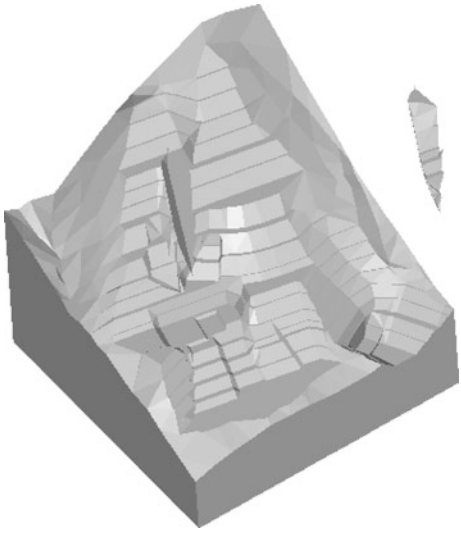

Fig. 9.17 Axonometric drawing of the decomposed small block element in the slope

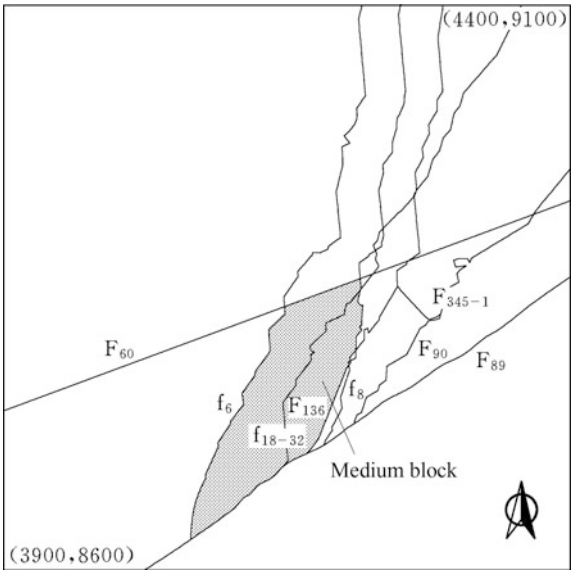

Fig. 9.18 Location of the medium block element

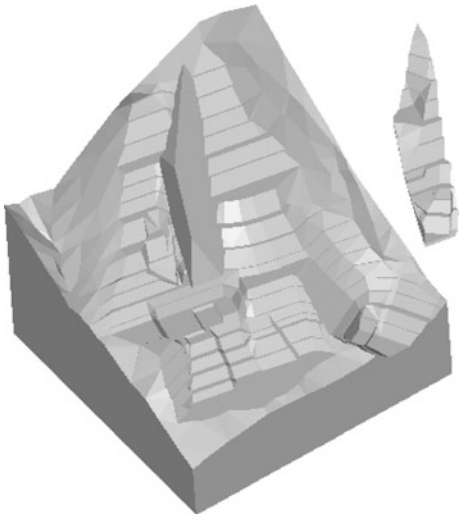

Fig. 9.19 Axonometric drawing of the decomposed medium block element in the slope

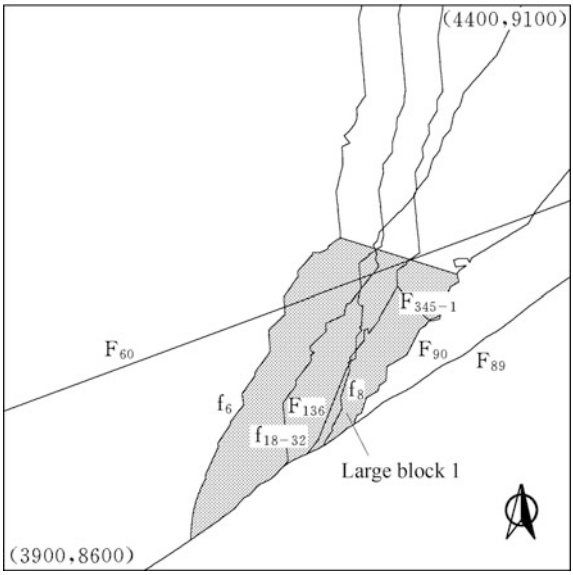

Fig. 9.20 Location of the large block element 1

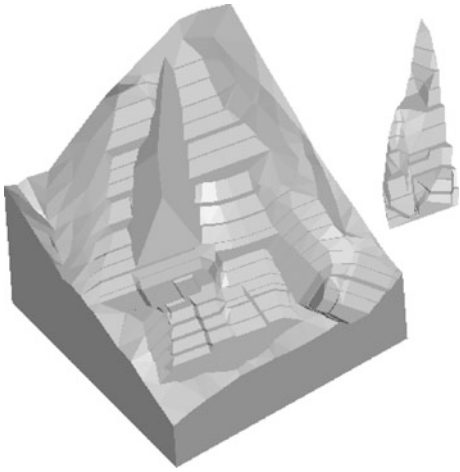

Fig. 9.21 Axonometric drawing of the decomposed large block element 1 in the slope

iv. Large block 2

This is enclosed by the faults F_{90} (F_{90-1}), F_{89}, f_6 and the low dip angle joint, the outcrop elevation is 297 m (see Figs. 9.22 and 9.23).

v. Local collapse body

This is enclosed by the faults F_{90}, f_8 and F_{330-6} (F_{345-1}), and was collapsed on November 20, 2002 (see Figs. 9.24, 9.25, 9.26 and 9.27).

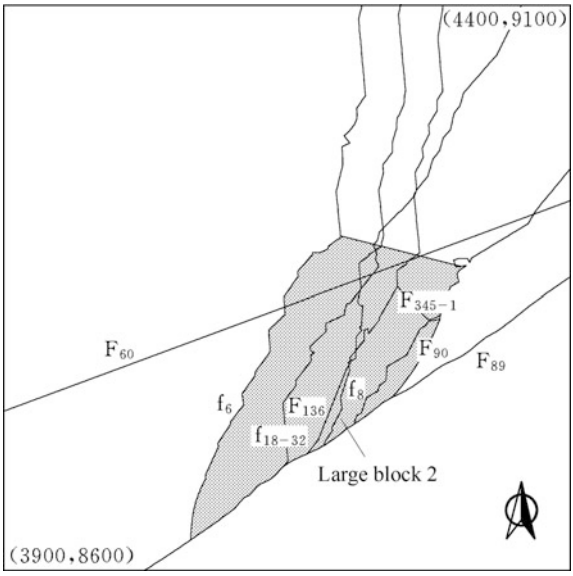

Fig. 9.22 Location of the large block element 2

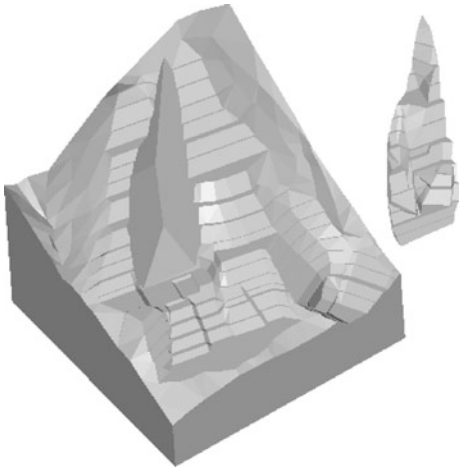

Fig. 9.23 Axonometric drawing of the decomposed large block element 2 in the slope

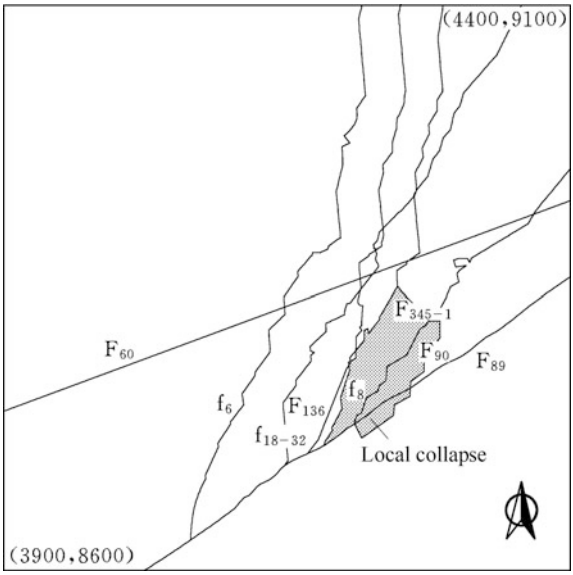

Fig. 9.24 Location of the local collapse body

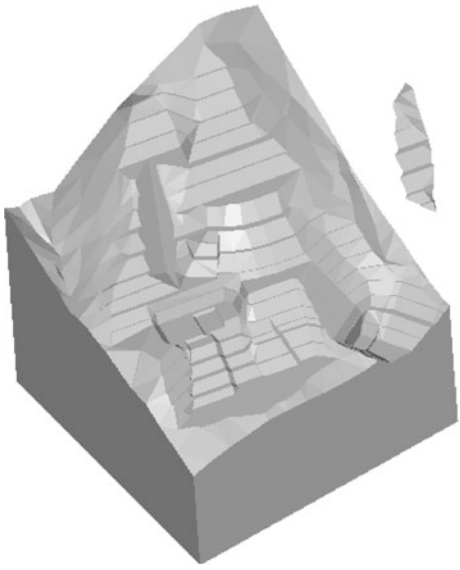

Fig. 9.25 Axonometric drawing of the local collapse body

Fig. 9.26 Right abutment slope before the local collapse

(3) Mechanical parameters

Elided.

(4) Loads

1 Volumetric weight

$$\gamma_r = 26.5 \text{ kN/m}^3.$$

2 Groundwater

The monitored groundwater table during the construction period is employed.

3 Seismic action

The intensity of design earthquake is 7 (modified Mercalli), with corresponding acceleration a = 0.1 g. The pseudo-static method, that conducts the static analysis by using the results of dynamic analysis indirectly, is employed. The inertia forces equivalent to additional static loads are calculated in terms of the maximum earthquake acceleration stipulated for design (Chen 2015), whose direction is identical to the slip direction of the block concerned.

(5) Results and conclusions

The main results extracted from the BEA are summarized below:

Fig. 9.27 Right abutment slope after the local collapse

- The safety factors against sliding of the block elements concerned may be arranged in sequence from the lowest (small block) to the highest (large block), with the medium block being in between (see Table 9.7).
- The local collapse body exhibits a lower safety factor of 1.092, this explains why it failed during the excavation before the additional reinforcement. This may be looked at as the benchmark solution by the field test. Any block elements or their combinations with safety factors lower than that of the local collapse body may be calibrated as unstable.
- The safety factor of small block is definitely insufficient by the initial reinforcement design using fully grouted bolts, therefore the additional pre-stress cables are demanded.

Table 9.7 Safety factors against sliding

Load combination		Small block	Medium block	Large block 1		Large block 2		Local collapse body
		–	–	F_{60} transmits residual force	F_{60} is looked at as exposure face	F_{60} transmits residual force	F_{60} is looked at as exposure face	–
Without reinforcement	Weight	0.861	1.175	1.724	1.716	1.814	1.670	1.092
	Weight + earthquake	0.746	1.007	1.436	1.429	1.526	1.429	–
	Weight + groundwater	0.861	1.166	1.693	1.683	1.800	1.684	1.092
Surface reinforcement by fully grouted bolts	Weight	0.950	1.216	1.875	1.787	1.853	1.708	–
	Weight + earthquake	0.818	1.040	1.492	1.490	1.570	1.470	–
	Weight + groundwater	0.861	1.206	1.778	1.758	1.855	1.730	–

- The safety factor of medium block is nearly satisfied. However, under the circumstances of earthquake, blast vibration, or heavy rain, its possibility of failure does exist, therefore the additional pre-stress cables are demanded, too.
- The safety factor of large block is held, therefore the additional pre-stress cables are not necessary.

Based on the foregoing study, the additional pre-stress cables were further optimally designed and installed. All the pre-stress stranded wire cables are horizontally installed along the direction of slip, and their lengths are entailed by the depth of small and medium blocks.

After the additional reinforcement, the abutment has been performing well from the construction period until the service period insofar.

References

Chan HC, Einstein HH. Approach to complete limit equilibrium analysis for rock wedges—the method of "artificial supports". Rock Mech. 1981;14(2):59–86.

Chen SH. The stability of a rock wedge in the slope. MSc thesis, WUHEE, Wuhan (China); 1984 (in Chinese).

Chen SH. The Elasto-plastic and Elasto-viscoplastic analysis of the discontinuous rock masses. PhD thesis, WUHEE, Wuhan (China); 1987 (in Chinese).

Chen SH. Stability analysis of rock wedge in slope. J Hydraulic Engng. 1990;12(6):18–26 (in Chinese).

Chen SH. Analysis of seepage flow in rock masses with block structure. J Hydraulic Engng. 1991;13(10):27–31 (in Chinese).

Chen SH. Block-fault model and its application in the elasto-viscoplatic analysis of rock slope. J Hydraulic Engng. 1992;14(7):9–15 (in Chinese).

Chen SH. Analysis of reinforced rock foundation using elastic-viscoplastic block theory. In: Ribeiro e Sousa L, Grossmann NF, editors Proc 1993 ISRM Int Symp—EUROCK 93. Rotterdam (Netherlands): AA Balkema; 1993a. p. 45–51.

Chen SH. Numerical analysis and model test of rock wedge in slope. In: Pasamehmetoglu AG, et al., editors. Proc int symp on assessment and prevention of failure phenomena in rock engineering. Rotterdam (Netherlands): AA Balkema; 1993b. p. 425–9.

Chen SH. A new development in elastic-viscoplastic block theory of rock masses. In: Siriwardane HJ, Zaman MM, editors. Proc 8th Int Conf Comp Meth Adv Geomech. Rotterdam (Netherlands): AA Balkema; 1994. p. 2235–40.

Chen SH, Li YM, Wang WM, Shahrour I. Analysis of gravity dam on a complicated rock foundation using an adaptive block element method. J Geotech Geoenviron Engng, ASCE. 2004;130(7):759–63.

Chen SH, Shahrour I, Egger P, Wang WM. Elasto-viscoplastic block element method and its application to arch dam abutment slopes. Rock Mech Rock Engng. 2002;35(3):171–93.

Chen SH, Shen BK, Huang MH. Stochastic elastic-viscoplastic analysis for discontinuous rock masses. Int J Numer Meth Engng. 1994;37(14):2429–44.

Chen SH, Wang HR, Xiong WL. Elasto-plastic and elasto-viscoplastic block element theory of jointed rock masses. In: Yuan JX editors Proc 3rd Chinese Conf Numer Anal Meth Geotech Engng. Zhuhai (China):1988; 684–701 (in Chinese).

Chen SH, Wang WM, She CX, Xu MY. Unconfined seepage analysis of discontinuous rock slope. J Hydrodynamics. 2000;12(3):75–86.

Chen SH, Wang WM, Zheng HF, Shahrour I. Block element method for the seismic stability of rock slopes. Int J Geotech Geoenviron Engng, ASCE. 2010;136(12):1610–7.

Copen MD, Lindholm EA, Tarbox GS. Design of concrete dams. In: Golzé AR, editor. Handbook of Dam Engineering. New York (USA): Van Nostrand Reinhold; 1977.

Goodman RE, Taylor R, Brekke TL. A model for the mechanics of jointed rock. J Soil Mech Found Div, ASCE.1968,94(SM3):637–660.

Guzina B, Tucovic I. Determining the maximum three dimensional stability of a rock wedge. Water Power. 1969;21(10):381–5.

Londe P. Une methode d'analyse a trois dimensions de la stabilite d'une rive rocheuse. Ann Ponts Chaussees. 1965;135(1):37–60.

Mahtab M, Goodman RE. Three dimensional analysis of joint rock slope. In: Proc 2nd ISRM congress, vol. 3. Beograd (Yugoslavia): Privredni Pregled, 1970; 353–360.

Owen DRJ, Hinton E. Finite elements in plasticity: theory and practice. Swansea (UK): Pineridge Press Ltd; 1980.

Shi GH. Discontinuous deformation analysis: a new numerical model for the statics and dynamics of deformable block structures. Eng Comput. 1992;9(2):157–68.

Wang WM, Xu MY, Chen SH. Analysis method of network seepage for blocky rock mass with complicated boundary condition. Chinese J Rock Mech Engng. 2001;20(4):473–6 (in Chinese).

Xu MY, Wang WM, Chen SH. Research on the dangerous sliding-block combination of rock slopes. Rock and Soil Mechanics. 2000;21(2):148–51 (in Chinese).

Chapter 10
Adaptive Techniques in the Block Element Analysis

Abstract This chapter begins with a laboratory experiment showing that the conventional BEA performs well in the safety calibration for the rock wedge, but it is not equally competent in the deformation assessment. Since the foundation deformation could be important for indeterminate structures (e.g. arch dams), a pertinent improvement is desirable. The crucial breakthrough is achieved by the displacement interpolation within the block element using mapped nodal displacements bound at an overlay element. Then, with the deformation compatibility condition of rock blocks and discontinuities as well as their elasto-viscoplastic constitutive relation, the operation of the virtual work principle produces the governing equation for the solution of these mapped nodal displacements. A practical *p*-refinement strategy is further implemented by checking and controlling the energy norm error tolerance of each block element. This chapter is closed with a number of validation examples (cantilever, gravity dam) and one engineering application case concerning dam-foundation system, to the latter a parallel physical test is demonstrated for cross-reference.

10.1 General

In dam foundations and abutment slopes (resistance bodies) there usually exist a number of discontinuities which cut the rock masses into blocks of various sizes, shapes and positions. Computation methods such as the well known DEM (Cundall 1971; Cundall 1988; Hart et al. 1988) and DDA (Shi 1992) already possess intrinsic abilities to solve the problems of stability and discontinuous deformation for such rock masses reasonably. To consider the complicated displacement and stress patterns as well as the rupture in blocks, remarkable advancements also have been achieved by the high-order polynomial interpolation or the sub-division using classical standard finite elements in blocks (Shyu 1993; Chang 1994; Koo and Chern 1996; Lin and Lee 1996).

The block element analysis (BEA) established in the previous Chap. 9 of this book looks at the rock blocks as rigid bodies meanwhile the discontinuities possess

S.-H. Chen, *Computational Geomechanics and Hydraulic Structures*,
Springer Tracts in Civil Engineering, https://doi.org/10.1007/978-981-10-8135-4_10

elasto-viscoplastic characteristics. To consider the phenomena of rock block deformation and rupture in the BEA, a preliminary attempt was made by the polynomial interpolation of the displacement field in rock blocks (Chen 1994), but the further study showed that it only performs well when the order of polynomials p is lower than 3, further upgrade of polynomial order will fail because of numerical instability. Later, a new strategy had been proposed by defining a classical standard finite element as overlay element to include the block element (Wang and Chen 2001; Chen et al. 2004): the displacement within the block element is interpolated from the mapped nodal displacements bound at the overlay element; with the deformation compatibility conditions of rock blocks and discontinuities as well as their elasto-viscoplastic constitutive relations, the application of the virtual work principle produces the governing equation to solve the mapped nodal displacements on the overlay element. A practical p-version adaptive refinement was further implemented by checking and controlling the energy norm error tolerance of each block element.

10.2 Inspiration from Physical Experiments

10.2.1 Experimental Configuration

Figure 10.1 shows the configuration for the physical model tests using two wedges (Chen 1993) whose geometry features are summarized in Table 10.1.

The foundation and wedges are casted by the Gypsum, the slip planes (faults) are casted by the geo-mechanical material with much lower strength (Chen 2015), whose mechanical parameters are listed in Table 10.2.

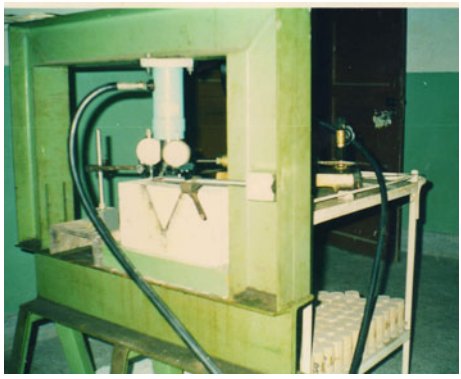

Fig. 10.1 Configuration of the test model

Table 10.1 Geometric features of wedges made of Gypsum (see Fig. 9.1)

Model sequence	α_1 (°)	α_2 (°)	β_1 (°)	β_2 (°)	β_3 (°)	H (m)
1	35	35	55	35	0	0.1
2	45	45	55	35	0	0.1

Table 10.2 Mechanical parameters of the faults made of the geo-mechanical material

k_n (MN/m^3)	k_s (MN/m^3)	c (kPa)	$tg\varphi$
38,000	15,660	110	0.8

10.2.2 Test and Computation Results

Under each loading step, the vertical displacement at the outer edge of wedge is recorded after an interval of ten minutes allowing for the stability of the test system. Where the ultimate load is reached, the oil pressure for the vertical jack cannot be maintained and the wedge collapses.

Plotting of the vertical displacements by computation and test produces curves in Fig. 10.2. They exhibit remarkable features that

– The vertical displacement of model 1 is larger than that of model 2, this is due to the fact that the included angle between two slip planes in model 1 is smaller than that in model 2;

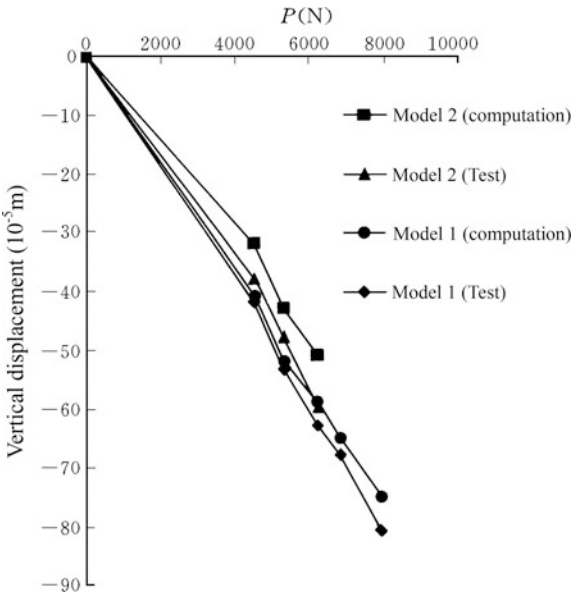

Fig. 10.2 Vertical displacement at the edge of wedge versus vertical jack pressure

Table 10.3 Maximum loads by the experiment and computation

Model sequence	Experiment (N)	Computation (N)	
		LEM	BEA
1	7348–7910	49,470	7910–8480
2	6217–6782	6400	6217–6782

– There is certain discrepancy between the computed and experimented displacements. The tested displacements of either model 1 or model 2 are larger than of the computed ones, this is due to the overlook of the block deformation in the conventional BEA formulated in the previous Chap. 9;
– There is a knee point in the curve of displacement versus vertical load P, the wedge fails after the load exceeding this point. For model 1, the knee point is around P = 6217–7348 N by experiment, whereas the computation indicates a knee point around P = 6782–7910 N; For model 2, the knee point is around P = 5652–6217 N by both the experiment and computation.

The maximum vertical loads calculated by the LEM for these two models are cross-referenced with these knee point loads in Table 10.3. We find that the BEA formulated in Chap. 9 provides reasonable safety index of the wedge against sliding. In addition, the safety of wedge will be raised as the reduction of the included angle between its two slip planes, but the LEM exhibits exaggerated mounting in the wedge safety.

10.3 Deformable Block Elements

10.3.1 Concept

The experimental study illustrated above validates that the conventional BEA performs well in the safety calibration for the rock block, but its performance in the deformation calibration is not equally competent. Since the foundation deformation could be important for indeterminate structures (e.g. arch dams), a better description of rock block deformation is desirable.

A preliminary attempt to introduce block deformation into the BEA was made by the complete polynomial interpolation of the displacement field within blocks (Chen 1994). Later, the displacement of the block was revolutionarily interpolated from the nodal displacements of its overlay element, to attain much better numerical stability and to allow for the adaptive refinement.

10.3.2 Overlay Element

We choose the block *rl* as the representative block, and denote its adjoin block as the block *rm* connecting with the block *rl* through the discontinuity $j_{rl,rm}$. The deformation and stress increments on the discontinuity $j_{rl,rm}$ are denoted as

$$\{\Delta u\}_{j_{rl,rm}} = [\,\Delta u_x \quad \Delta u_y \quad \Delta u_z\,]^T_{j_{rl,rm}} \tag{10.1}$$

$$\{\Delta \sigma\}_{j_{rl,rm}} = [\,\Delta \tau_{zx} \quad \Delta \tau_{zy} \quad \Delta \sigma_z\,]^T_{j_{rl,rm}} \tag{10.2}$$

The displacement, strain, and stress increments of the block *rl* are denoted as

$$\{\Delta u\}_{rl} = [\,\Delta u_x \quad \Delta u_y \quad \Delta u_z\,]^{\mathrm{T}}_{rl} \tag{10.3}$$

$$\{\Delta \varepsilon\}_{rl} = [\,\Delta \varepsilon_x \quad \Delta \varepsilon_y \quad \Delta \varepsilon_z \quad \Delta \gamma_{yz} \quad \Delta \gamma_{zx} \quad \Delta \gamma_{xy}\,]^{\mathrm{T}}_{rl} \tag{10.4}$$

$$\{\Delta \sigma\}_{rl} = [\,\Delta \sigma_x \quad \Delta \sigma_y \quad \Delta \sigma_z \quad \Delta \tau_{yz} \quad \Delta \tau_{zx} \quad \Delta \tau_{xy}\,]^{\mathrm{T}}_{rl} \tag{10.5}$$

For an irregular rock block shown in Fig. 10.3, a standard or hierarchical finite element is endued to circumscribe the block. This finite element is termed as "overlay element". The overlay elements corresponding to the different blocks can be inter-overlapped. The displacements $\{\Delta u\}_{rl}$ in block *rl* are interpolated from the nodal displacements $\{\Delta \delta\}_{rl}$ bound at the overlay element by the formula

$$\{\Delta u\}_{rl} = [N]_{rl}\{\Delta \delta\}_{rl} \tag{10.6}$$

In which

$$\{\Delta \delta\}_{rl} = [\,\Delta \delta_{x1} \quad \Delta \delta_{y1} \quad \Delta \delta_{z1} \ldots \Delta \delta_{xf_{rl}(p)} \quad \Delta \delta_{yf_{rl}(p)} \quad \Delta \delta_{zf_{rl}(p)}\,]^{\mathrm{T}}_{rl} \tag{10.7}$$

and $[N]$ is termed as "shape function matrix"

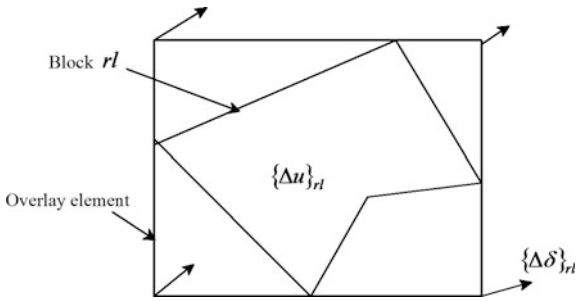

Fig. 10.3 Diagram showing the block *rl* and circumscribed overlay element

$$[N]_{rl} = \begin{bmatrix} N_1[I] & N_2[I] & \dots & N_{f_e(p)}[I] \end{bmatrix} \quad (\text{for } p = 1,\ f_e(p) = 8) \tag{10.8}$$

where $[I]$ stands for 3×3 unit matrix.

In Eqs. (10.6)–(10.8), $[N]_{rl}$ is defined in the whole overlay element, $\{\Delta\delta\}_{rl}$ is the general displacement vector corresponding to the general degree of freedoms, $f_{rl}(p)$ is the number of the general nodes, N_i is a point, edge, face, or body shape function as the case may be (vide Chap. 4). It should be emphasized that the interpolation expressed in Eq. (10.6) is only valid within each inscribing block element.

10.3.3 Deformation Compatibility Equation

Within the block element *rl*, we have

$$\{\Delta\varepsilon\}_{rl} = [B]_{rl}\{\Delta\delta\}_{rl} \tag{10.9}$$

in which $[B]_{rl}$ is the strain matrix

$$[B]_{rl} = \begin{bmatrix} [B_1]_{rl} & [B_2]_{rl} & \dots & [B_{f_{rl}(p)}]_{rl} \end{bmatrix} \tag{10.10}$$

$$[B_i]_{rl} = \begin{bmatrix} N_{i,x} & 0 & 0 \\ 0 & N_{i,y} & 0 \\ 0 & 0 & N_{i,z} \\ 0 & N_{i,z} & N_{i,y} \\ N_{i,z} & 0 & N_{i,x} \\ N_{i,y} & N_{i,x} & 0 \end{bmatrix}_{rl} \quad (i = 1, 2, \dots, f_{rl}(p)) \tag{10.11}$$

The relative displacement increment on the discontinuity plane $j_{rl,rm}$ is

$$\{\Delta u\}_{j_{rl,rm}} = J(j_{rl,rm})[l]_{j_{rl,rm}} \left([N]_{rl}\{\Delta\delta\}_{rl} - [N]_{rm}\{\Delta\delta\}_{rm}\right) \tag{10.12}$$

In which the matrix $[l]_{j_{rl,rm}}$ has been defined in Eqs. (2.12) and (2.13), and $J(j_{rl,rm})$ has been defined in Eq. (9.12).

10.3.4 Constitutive Equation

Use is made of the potential elasto-viscoplastic theory (Owen and Hinton 1980), the stress and strain increments in block *rl* expressed by Eq. (2.122) can be restated as

$$\{\Delta\sigma\}_{rl} = [D]_{rl}\{\Delta\varepsilon\}_{rl} - \{\Delta\sigma^{vp}\}_{rl} \tag{10.13}$$

In which the elastic matrix $[D]_{rl}$ is the function of the Young's modulus and Poisson's ratio (see Eq. (2.78)); the viscoplastic stress increment $\{\Delta\sigma^{vp}\}_{rl}$ is given according to the associated flow rule with Drucker-Prager yield criterion.

Meanwhile the deformation and stress increments at any point on the discontinuity plane $j_{rl,rm}$ will observe Eq. (2.126) which is restated as

$$\{\Delta\sigma\}_{j_{rl,rm}} = [D]_{j_{rl,rm}}\{\Delta u\}_{j_{rl,rm}} - \{\Delta\sigma^{vp}\}_{j_{rl,rm}} \tag{10.14}$$

In which the elastic matrix $[D]_{j_{rl,rm}}$ is the function of the normal and tangential stiffness coefficients (see Eq. (2.76)); the viscoplastic stress increment $\{\Delta\sigma^{vp}\}_{j_{rl,rm}}$ is given according to the non-associated flow rule with the Mohr-Coulomb yield criterion.

10.3.5 Governing Equations

(1) The virtual work principle

The virtual work principle for the block system is mathematically constructed as

$$\sum_{rl=1}^{n_r} W_{rl} + \sum_{j_{rl,rm}=1}^{n_j} W_{j_{rl,rm}} = W_F \tag{10.15}$$

In which W_{rl} is the virtual work contributed from block rl, $W_{j_{rl,rm}}$ is the virtual work contributed from discontinuity $j_{rl,rm}$, W_F is the virtual work of external forces, n_r and n_j are the amounts of blocks and discontinuities in the whole rock block system, respectively.

If the blocks rl and rm demonstrate virtual nodal displacement vectors $\{\Delta\delta^*\}_{rl}$ and $\{\Delta\delta^*\}_{rm}$, then the virtual displacements inside the block elements are $\{\Delta u^*\}_{rl}$ and $\{\Delta u^*\}_{rm}$, the corresponding virtual strains are $\{\Delta\varepsilon^*\}_{rl}$ and $\{\Delta\varepsilon^*\}_{rm}$, the virtual deformation on the discontinuity $j_{rl,rm}$ is $\{\Delta u^*\}_{j_{rl,rm}}$. They must observe following restraints

$$\{\Delta u^*\}_{rl} = [N]_{rl}\{\Delta\delta^*\}_{rl} \tag{10.16}$$

$$\{\Delta u^*\}_{rm} = [N]_{rm}\{\Delta\delta^*\}_{rm} \tag{10.17}$$

$$\{\Delta\varepsilon^*\}_{rl} = [B]_{rl}\{\Delta\delta^*\}_{rl} \tag{10.18}$$

$$\{\Delta\varepsilon^*\}_{rm} = [B]_{rm}\{\Delta\delta^*\}_{rm} \tag{10.19}$$

$$\{\Delta\delta^*\}_{j_{rl,rm}} = J(j_{rl,rm})[l]_{j_{rl,rm}}\left([N]_{rl}\{\Delta\delta^*\}_{rl} - [N]_{rm}\{\Delta\delta^*\}_{rm}\right) \tag{10.20}$$

1 Contribution from block rl

$$W_{rl} = \iiint_{\Omega_{rl}} \{\Delta\varepsilon^*\}_{rl}^{\mathrm{T}}\{\Delta\sigma\}_{rl}d\Omega \tag{10.21}$$

2 Contribution from discontinuity $j_{rl,rm}$

$$W_{j_{rl,rm}} = \iint_{\Gamma_{j_{rl,rm}}} \{\Delta\delta^*\}_{j_{rl,rm}}^{\mathrm{T}}\{\Delta\sigma\}_{j_{rl,rm}}dx_{j_{rl,rm}}dy_{j_{rl,rm}} \tag{10.22}$$

3 Virtual work of external forces

$$W_F = \sum_{rl=1}^{n_r} \{\Delta\delta^*\}_{rl}^{\mathrm{T}}\{\Delta f\}_{rl} \tag{10.23}$$

In Eq. (10.23) $\{\Delta f\}_{rl}$ is the general load vector transferred from the loads exerting on block element rl to the respective overlay element, which will be presented later.

(2) Equilibrium equation

Introducing Eqs. (10.9), (10.12)–(10.14) and (10.16)–(10.23) into Eq. (10.15), and recall that $\{\Delta\delta^*\}_{rl}$ is arbitrary, a set of equilibrium equations will be extracted as

$$\begin{aligned}\{\Delta f\}_{rl} = {} & \iiint_{\Omega_{rl}} [B]_{rl}^{\mathrm{T}}[D]_{rl}[B]_{rl}\{\Delta\delta\}_{rl}d\Omega - \iiint_{\Omega_{rl}} [B]_{rl}^{\mathrm{T}}\{\Delta\sigma^{vp}\}_{rl}d\Omega \\ & + \sum_{j_{rl,rm}} \iint_{\Gamma_{j_{rl,rm}}} \Big([N]_{rl}^{\mathrm{T}}[l]_{j_{rl,rm}}^{\mathrm{T}}[D]_{j_{rl,rm}}[l]_{j_{rl,rm}}[N]_{rl}\{\Delta\delta\}_{rl} \\ & - [N]_{rl}^{\mathrm{T}}[l]_{j_{rl,rm}}^{\mathrm{T}}[D]_{j_{rl,rm}}[l]_{j_{rl,rm}}[N]_{rm}\{\Delta\delta\}_{rm} \\ & - J(j_{rl,rm})[N]_{rl}^{\mathrm{T}}[l]_{j_{rl,rm}}^{\mathrm{T}}\{\Delta\sigma^{vp}\}_{j_{rl,rm}}\Big)dx_{j_{rl,rm}}dy_{j_{rl,rm}} \end{aligned} \quad (r_l = 1, 2, 3, \ldots, n_r) \tag{10.24}$$

In which the subscript $j_{rl,rm}$ runs over all the discontinuities around block rl, and the subscript rm runs over all the adjoin blocks around block rl corresponding to discontinuity $j_{rl,rm}$. Assemble Eq. (10.24) of every block into the equilibrium equation set of the whole block system in a similar routine to that of the FEM, we have

$$\begin{bmatrix} [k]_{r1,r1} & [k]_{r1,r2} & \cdots & [k]_{r1,n_r} \\ [k]_{r2,r1} & [k]_{r2,r2} & \cdots & [k]_{r2,n_r} \\ \vdots & \vdots & \vdots & \vdots \\ [k]_{n_r,r1} & [k]_{n_r,r2} & \cdots & [k]_{n_r,n_r} \end{bmatrix} \begin{Bmatrix} \{\Delta\delta\}_{r1} \\ \{\Delta\delta\}_{r2} \\ \vdots \\ \{\Delta\delta\}_{n_r} \end{Bmatrix} = \begin{Bmatrix} \{\Delta f\}_{r1} \\ \{\Delta f\}_{r2} \\ \vdots \\ \{\Delta f\}_{n_r} \end{Bmatrix} \tag{10.25}$$

or

$$[K]\{\Delta\delta\} = \{\Delta F\} \tag{10.26}$$

In Eq. (10.26), $[K]$ is the global stiffness matrix assembled from the elementary sub-matrices

$$\begin{cases} [k]_{rl,rl} = \iiint\limits_{\Omega_{rl}} [B]_{rl}^T [D]_{rl} [B]_{rl} d\Omega + \sum\limits_{j_{rl,rm}} H(rl,rm) \iint\limits_{\Gamma_{j_{rl,rm}}} [N]_{rl}^T [l]_{j_{rl,rm}}^T [D]_{j_{rl,rm}} [l]_{j_{rl,rm}} [N]_{rl} dx_{j_{rl,rm}} dy_{j_{rl,rm}} \\ [k]_{rl,rm} = -H_1(rl,rm) \iint\limits_{\Gamma_{j_{rl,rm}}} [N]_{rl}^T [l]_{j_{rl,rm}}^T [D]_{j_{rl,rm}} [l]_{j_{rl,rm}} [N]_{rm} dx_{j_{rl,rm}} dy_{j_{rl,rm}} \\ H(rl,rm) = \begin{cases} 1 & \textit{If} \quad rl \quad \textit{and} \quad rm \quad \textit{are} \quad \textit{adjacent} \\ 0 & \textit{If} \quad rl \quad \textit{and} \quad rm \quad \textit{are} \quad \textit{not} \quad \textit{adjacent} \end{cases} \end{cases} \tag{10.27}$$

In which $\{\Delta\delta\}$ is the global general displacement increments vector defined below

$$\{\Delta\delta\} = \begin{bmatrix} \{\Delta\delta\}_1^{\mathrm{T}} & \{\Delta\delta\}_2^{\mathrm{T}} & \cdots & \{\Delta\delta\}_{n_r}^{\mathrm{T}} \end{bmatrix}^{\mathrm{T}} \tag{10.28}$$

and $\{\Delta F\}$ is the correspondent global general load vector

$$\begin{cases} \{\Delta F\} = \begin{bmatrix} \{\Delta F\}_1^{\mathrm{T}} & \{\Delta F\}_2^{\mathrm{T}} & \cdots & \{\Delta F\}_{n_r}^{\mathrm{T}} \end{bmatrix}^{\mathrm{T}} \\ \{\Delta F\}_{rl} = \{\Delta f\}_{rl} + \{\Delta f^{vp}\}_{rl} \end{cases} \tag{10.29}$$

$$\{\Delta f^{vp}\}_{rl} = \iiint\limits_{\Omega_{rl}} [B]_{rl}^T \{\Delta\sigma^{vp}\}_{rl} d\Omega + \sum_{j_{rl,rm}} J(j_{rl,rm}) \iint\limits_{\Gamma_{j_{rl,rm}}} [N]_{rl}^{\mathrm{T}} [l]_{j_{rl,rm}}^{\mathrm{T}} \{\Delta\sigma^{vp}\}_{j_{rl,rm}} dx_{j_{rl,rm}} dy_{j_{rl,rm}} \tag{10.30}$$

With the solved nodal displacements $\{\Delta\delta\}_{rl}$ from Eq. (10.26), the displacements and the strains as well as the stresses in block rl and on discontinuity $j_{rl,rm}$, can be calculated by Eqs. (10.6), (10.12), (10.13) and (10.14).

(3) Nodal loads

There are two types of nodal load increments in Eq. (10.29). One is the equivalent load $\{\Delta f^{vp}\}_{rl}$ due to viscoplastic deformation given in Eq. (10.30). Another is the external load $\{\Delta f\}_{rl}$, which can be obtained on the virtual work consideration with regard to the load balance.

1 Point force

If a point force $\{\Delta q\} = [\,\Delta q_x \quad \Delta q_y \quad \Delta q_z\,]^{\mathrm{T}}$ exerts on block *rl*, and the coordinate of acting point is $(\,x_q \quad y_q \quad z_q\,)$, then its virtual work is

$$\{\Delta u^*\}_{rl}^{\mathrm{T}}\{\Delta q\} = \{\Delta\delta^*\}_{rl}^{\mathrm{T}}[N]_{rl}^{\mathrm{T}}\big|_{(\,x_q \quad y_q \quad z_q\,)}\{\Delta q\} \tag{10.31}$$

It must be equal to the virtual work of the external load $\{\Delta f\}_{rl}$ in a manner of

$$\{\Delta\delta^*\}_{rl}^{\mathrm{T}}\{\Delta f\}_{rl} = \{\Delta\delta^*\}_{rl}^{\mathrm{T}}[N]_{rl}^{\mathrm{T}}\big|_{(\,x_q \quad y_q \quad z_q\,)}\{\Delta q\} \tag{10.32}$$

Therefore we have

$$\{\Delta f\}_{rl} = [N]_{rl}^{\mathrm{T}}\big|_{(\,x_q \quad y_q \quad z_q\,)}\{\Delta q\} \tag{10.33}$$

2 Surface distributed force

The surface force $\{\Delta p\} = [\,\Delta p_x \quad \Delta p_y \quad \Delta p_z\,]^{\mathrm{T}}$ exerting on the discontinuity $j_{rl,rm}$ of block *rl* can be transferred into a general load vector in the same way as

$$\{\Delta f\}_{rl} = \iint\limits_{\Gamma_{j_{rl,rm}}} [N]_{tl}^{\mathrm{T}}\{\Delta p\}dx_{j_{rl,rm}}dy_{j_{rl,rm}} \tag{10.34}$$

3 Volumetric force

The volumetric force $\{\Delta v\} = [\,\Delta v_x \quad \Delta v_y \quad \Delta v_z\,]^{\mathrm{T}}$ of block *rl* can also be balanced by the corresponding nodal load vector

$$\{\Delta f\}_{rl} = \iiint\limits_{\Omega_{rl}} [N]_{rl}^{T}\{\Delta v\}d\Omega \tag{10.35}$$

10.4 Procedure for Adaptive P-Refinement

Towards the formulation of a practical p-refinement BEA, the error estimation and upgrade of the shape function order may be carried out on the block element separately.

For the block element *rl*, there exist exact solutions with respect to the displacement $\{u\}_{rl}$, strain $\{\varepsilon\}_{rl}$ and stress $\{\sigma\}_{rl}$, whose corresponding BEA solutions with the shape function order of p are $\{u_p\}_{rl}$, $\{\varepsilon_p\}_{rl}$, and $\{\sigma_p\}_{rl}$, respectively. Hence we have three error definitions

$$\begin{cases} \{e_u\}_{rl} = \{u\}_{rl} - \{u_p\}_{rl} \\ \{e_\varepsilon\}_{rl} = \{\varepsilon\}_{rl} - \{\varepsilon_p\}_{rl} \\ \{e_\sigma\}_{rl} = \{\sigma\}_{rl} - \{\sigma_p\}_{rl} \end{cases} \tag{10.36}$$

To get a unified scale of the error, the error energy norm and total energy norm are defined as

$$\|e\|_{rl} = \iiint_{\Omega_{rl}} \{e_\sigma\}_{rl}^T \{e_\varepsilon\}_{rl} d\Omega \tag{10.37}$$

$$\|u\|_{rl} = \iiint_{\Omega_{rl}} \{\sigma\}_{rl}^T \{\varepsilon\}_{rl} d\Omega \tag{10.38}$$

The dimensionless relative error will be

$$e_{rl} = \frac{\|e\|_{rl}}{\|u\|_{rl}} \times 100\% \tag{10.39}$$

where the relative error e_{rl} is equal to or smaller than the error tolerance e_t, i.e.

$$e_{rl} \le e_t \tag{10.40}$$

The order p of the shape functions is appropriately accepted.

The rest problem is how to get the exact solutions in Eq. (10.36). To simplify the algorithm, use is made of the successive upgrade results of order $p+1$ as the "best guess" for the exact solutions. This approximate treatment is advantageous attributable to less requirement for computation effort. Suppose the strains and stresses are obtained using the shape functions of orders p and $p+1$, respectively. Then the "best guess" for the exact solutions in Eq. (10.36) will be

$$\{\varepsilon\}_{rl} = \{\varepsilon_{p+1}\}_{rl} \tag{10.41}$$

$$\{\sigma\}_{rl} = \{\sigma_{p+1}\}_{rl} \tag{10.42}$$

where the error tolerance is met according to Eq. (10.40), the order of block *rl* will be fixed as $p+1$. The p-refinement iteration is accomplished after the error tolerances of all the block elements are met.

10.5 Verification Examples

10.5.1 Cantilever Beam

An elastic cantilever beam (length $L = 6.0$ m; width $b = 0.5$ m; height $h = 1.0$ m) exerted by a concentrated force $P = 0.5$ MPa at its free end is studied (see Fig. 10.4). The elastic parameters used in the study are the elastic modulus $E = 10000$ MPa and the Poisson's ratio $\mu = 0.17$.

Both the p-refinement BEA and the classical FEM are employed to solve this problem. In the former the cantilever is looked at as one block element, whereas in the latter it is divided uniformly along the length and height into 12 sections and 4 layers (i.e. 48 elements).

Figure 10.5 shows the computed and analytically solved flexural curves of the beam axis, and Fig. 10.6 shows the normal stress distribution on the fixed end section. In the BEA, the shape function order p along the width is fixed to 1, meanwhile along both the length and height directions it is adaptively upgraded

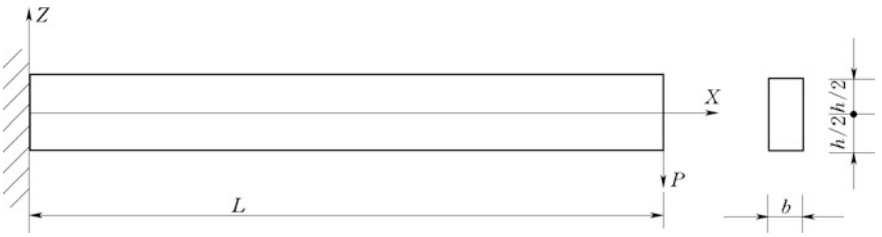

Fig. 10.4 Diagram of an elastic cantilever beam

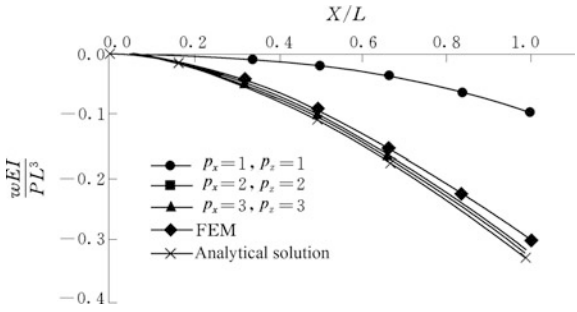

Fig. 10.5 Flexural curve of beam axis (I = sectional inertia moment)

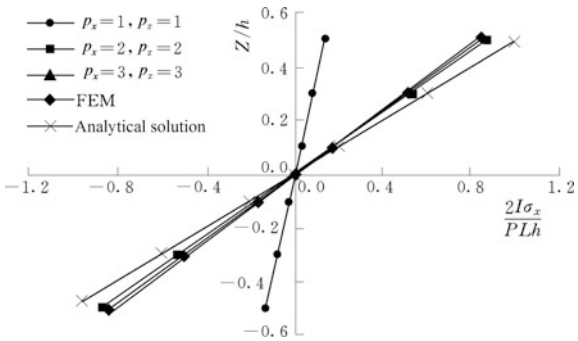

Fig. 10.6 Normal stress distribution on the fixed end section (I = sectional inertia moment)

Table 10.4 Variation of p-refinement indices of the cantilever beam

Adaptive step	p	System DOF	Energy norm	Relative error (%)	Flexure (m)
1	1	24	0.0679009	96.68	0.004610
2	2	48	0.2658887	44.12	0.070694
3	3	72	0.2962777	0.35	0.087778
4	4	102	0.2962795	–	0.087782

from 1 until to 4. The degree of freedom (DOF), energy norm, relative error, and the flexure are summarized in Table 10.4.

10.5.2 Simplified Gravity Dam

A simplified gravity dam, whose profile and block element system are illustrated in Fig. 10.7, has been studied. The mechanical parameters of the foundation rock and dam concrete are listed in Table 10.5. The mechanical parameters of the discontinuities are listed in Table 10.6.

The dam is analyzed in parallel using both the BEA and FEM. A slice of 10 m along the Y direction is cut for the study and the corresponding FE mesh in Fig. 10.8 is its projection on the $X - Z$ plane.

Towards the computation using the BEA, the shape function order p along the Y-direction is fixed to $p = 1$, but those along the X and Z directions are upgraded adaptively until up to $p = 5$. The degree of freedom, the energy norm, the relative error, and the displacements of the upstream dam top are summarized in Tables 10.7 and 10.8 shows the optimal shape function orders of all the 14 block

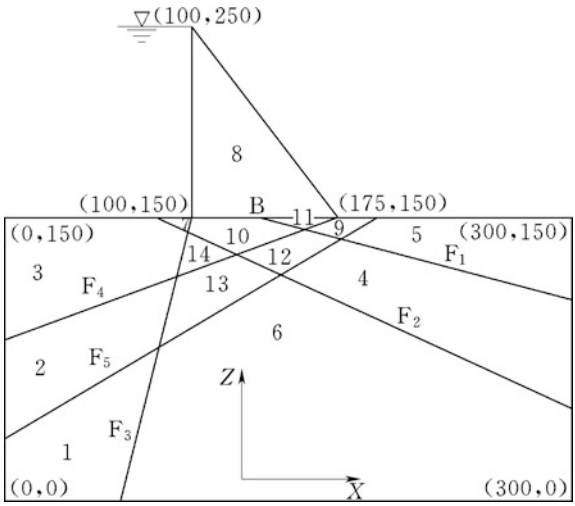

Fig. 10.7 Profile of a simplified gravity dam

Table 10.5 Mechanical parameters of the foundation rock and dam concrete

Parameters	Rock	Concrete
Young's modulus E (GPa)	15	20
Poisson's ratio μ	0.20	0.15
Angle of friction φ (°)	45.0	45.0

Table 10.6 Mechanical parameters of the discontinuities

Parameters	F_1	F_2	F_3	F_4	F_5	B
Normal stiffness k_n (GN/m^3)	2.0	2.0	2.0	2.0	2.0	2.0
Tangential stiffness k_s (GN/m^3)	0.87	0.87	0.87	0.87	0.87	0.87
Angle of friction φ (°)	40	40	40	40	40	45
Cohesion c (MPa)	0.02	0.02	0.02	0.02	0.02	0.2
Strength of tension σ_T (MPa)	0.02	0.01	0.01	0.02	0.02	0.02

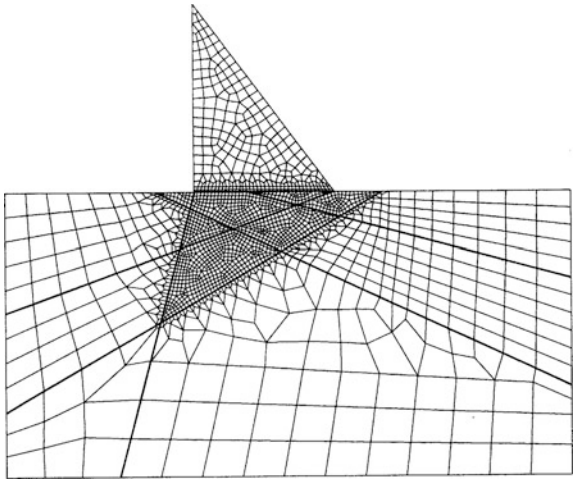

Fig. 10.8 FE mesh of the simplified gravity dam projected on the $X - Z$ plane (2109 elements; 4358 nodes)

Table 10.7 Variation of p-refinement indices of the simplified gravity dam

Adaptive step	p	System DOF	Energy norm	Relative error (%)	Displacements of the upstream dam crest	
					u_X (m)	u_Z (m)
1	1	336	3.485523	39.41	0.0218	0.00347
2	2	672	3.792542	17.59	0.0346	0.00674
3	3	1008	3.852612	11.88	0.0384	0.00793
4	4	1248	3.880075	7.46	0.0382	0.00791
5	5	1392	3.890929	–	0.0390	0.00816

Table 10.8 Optimal shape function order and degree of freedom

Block element	1	2	3	4	5	6	7	8	9	10	11	12	13	14
p	3	3	5	4	4	5	3	5	4	5	3	3	4	3
Element DOF	72	72	138	102	102	138	72	138	102	138	72	72	102	72

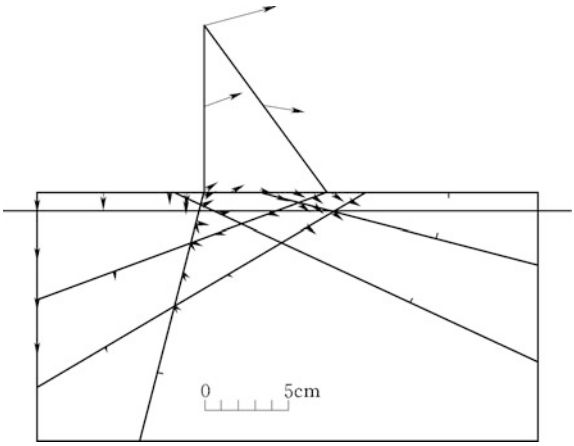

Fig. 10.9 Displacements by the BEA

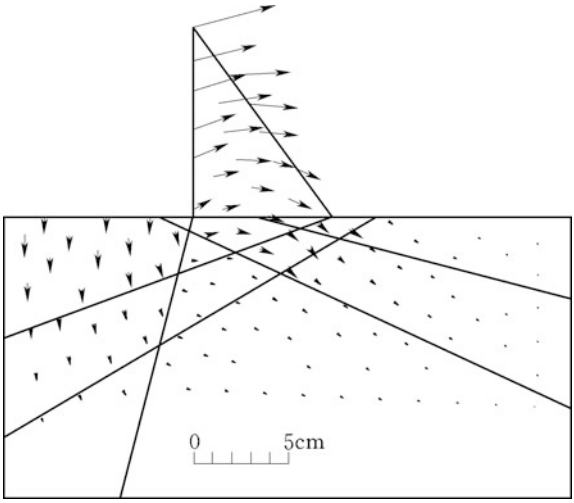

Fig. 10.10 Displacements by the FEM

elements. The displacement in the $X - Z$ plane obtained from the BEA and FEM are given in Figs. 10.9 and 10.10, meanwhile the principal stresses in the $X - Z$ plane are given in Figs. 10.11 and 10.12.

10.6 Engineering Application: Baozhusi Project, China

10.6.1 Presentation of the Project

Vide Chap. 9 (Sect. 9.5.1).

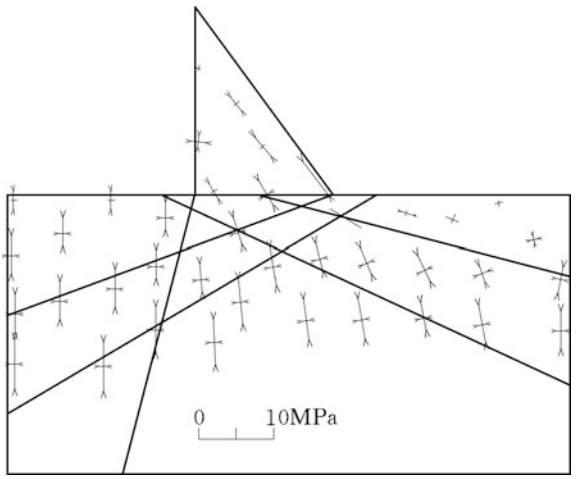

Fig. 10.11 Principal stresses by the BEA

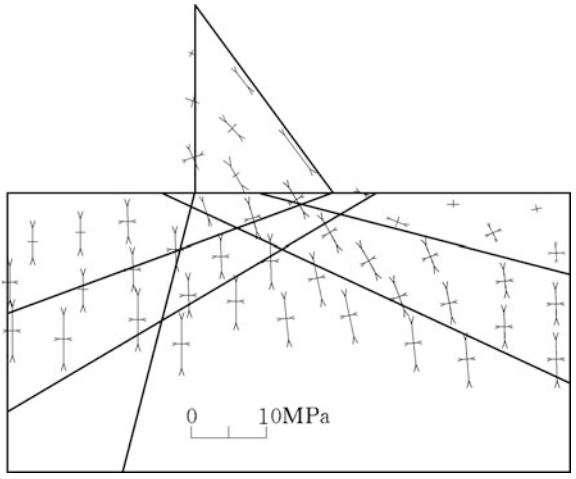

Fig. 10.12 Principal stresses by the FEM

10.6.2 Characteristics of the Computation

The 17th dam monolith of 21.5 m thickness and 131 m high is shown in Fig. 10.13, in which a penstock is installed. The width of the dam's base is 92 m (exclusive the powerhouse). The rock mass under the dam foundation is Ordovician sand stone and at the downstream of the dam is Silurian shale (S_1). The main discontinuities are faults (F_4, F_2) and argillic intercalated layers (D_5, $D_{7,8}$, D_1, D_3, D_6).

Preliminary studies showed that the safety of the dam foundation against sliding was insufficient. The designer then revised the structural design by replacing the open and permanent joint between the dam and powerhouse with a bonded

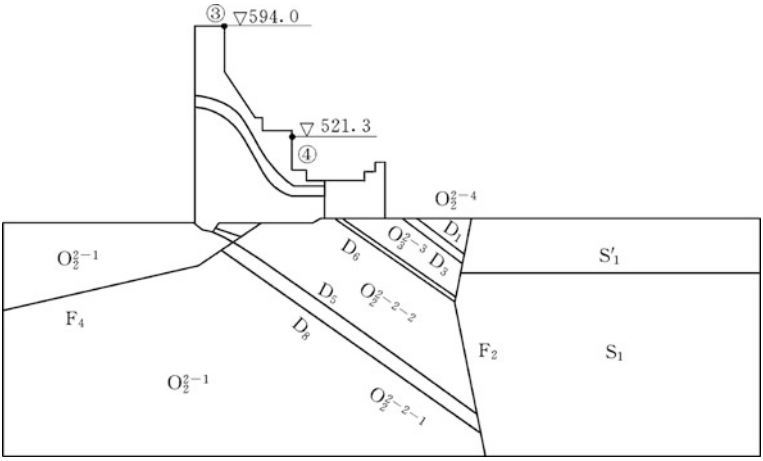

Fig. 10.13 Dam monolith 17#: Baozhusi Project, China ③ and ④—displacement gauge (object) points

temporary joint, in this manner the dam and powerhouse were supposed to work together resisting the reservoir water thrust. Before the impounded reservoir level had risen to the EL. 550.0 m, the dam and power house were kept separate from each other and both worked independently; after the impounded level of the EL. 550.0 m, the joint between the dam and powerhouse was grouted to link them together.

The computation study was carried out for the revised design to analyze the deformation and stress of the dam/foundation system, which is expected to answer the questions with regard to "what is the failure mechanism of the structure (sliding within the foundation or cracking in the dam body)"? "Is the safety of the dam sufficient"? A parallel laboratory physical test was carried out, too. The main prototype mechanical parameters used in the computation and test are listed in Tables 10.9 and 10.10.

Table 10.9 Prototype mechanical parameters of the rock masses and concrete

Rock	Unit weight γ_r (kN/m^3)	Friction angle φ (°)	Cohesion c (MPa)	Deformation modulus E (Gpa)	Poisson's ratio μ	Tensile strength σ_t (kPa)
O_2^{2-1}	23.52	45.0	0.6	7.53	0.27	10.0
O_2^{2-2-1}	25.97	45.0	0.6	2.89	0.30	6.6
O_2^{2-2-2},O_2^{2-3}	25.48	45.0	1.0	18.70	0.18	47.6
O_2^{2-4}	25.87	45.0	0.8	11.90	0.25	29.0
S_1	25.48	26.6	0.4	4.00	0.30	22.0

Table 10.10 Prototype mechanical parameters of the discontinuities

Discontinuity	Deformation modulus E (Mpa)	Poisson's ratio μ	Friction angle φ (°)	Cohesion c (MPa)	Thickness t (m)	Remark
D_1,D_3	30.0	0.40	20.8	0.01	0.01	–
D_6	50.0	0.40	19.3	0.02	0.01	–
$D_{7,8}$	50.0	0.40	21.8	0.01	0.01	Upstream side of F_4
$D_{7,8}$	300.0	0.30	21.8	0.02	0.01	Downstream side of F_4
D_5	40.0	0.40	14.0	0.01	0.01	Upstream side of F_4
D_5	300.0	0.30	16.7	0.02	0.01	Downstream side of F_4

According to the equality principle with respect to the relative displacement of discontinuity walls, the stiffness coefficients k_n and k_s input in the BEA computation are related to the Young's modulus E and Poisson's ratio μ of discontinuity filler by the formulas

$$\begin{cases} k_n = \frac{E}{t} \\ k_s = \frac{1}{t}\frac{E}{2(1+\mu)} \end{cases} \tag{10.43}$$

In which t is the thickness of the discontinuity.

Figure 10.14 shows the block system consisting of 28 block elements. The block elements in the foundation are exactly defined by the discontinuities, whereas the dam body and powerhouse are discretized by dummy discontinuity faces. In the discretization of dam, the penstock and the dam/powerhouse joint are taken into account. For the dummy discontinuity faces in the dam body and power house, the

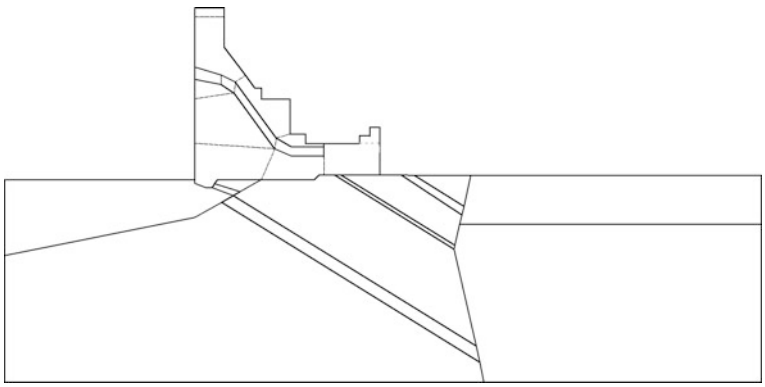

Fig. 10.14 Block element system for the BEA computation (28 blocks)

stiffness coefficients and strength should be high enough to ensure the computation precision. The error tolerance e_t in the adaptive upgrade for the shape function order p is stipulated as $e_t = 5\%$.

10.6.3 Test Configuration and Procedure

The physical model is made of geo-mechanical material with high specific weight and low elasticity and strength, which is ideal for the study of the displacement and failure mechanism of the dam/foundation system (Fig.10.15). However, the stress in this kind of structural model cannot be well gauged by the conventional instruments.

The principal coefficients of scaling (Chen 2015) in the model test are

- Geometry, 170;
- Young's modulus, 170;
- Volumetric weight, 1;
- Displacement, 17;
- Friction coefficient, 1.

The static hydraulic pressure of the reservoir is equalized by a series of jacks arranged along the upstream dam face, the output of jacks can be controlled to simulate the reservoir water level fluctuation. The overloading process is implemented in 7 steps (see Table 10.11) to extract the failure mechanism and correspondent safety factor of the dam, where the overload increments and overload factors are calculated by the formulas

$$P_i = \frac{1}{2}\gamma(2H_i - H)H \tag{10.44}$$

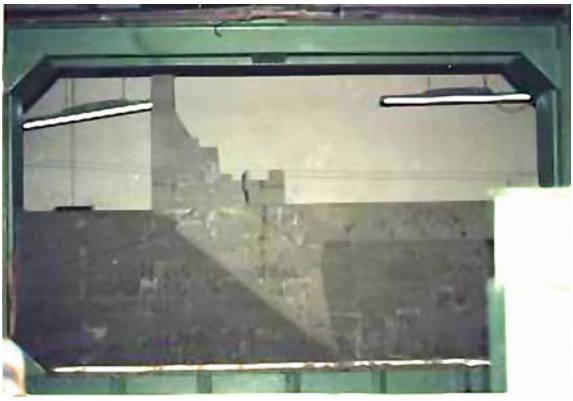

Fig. 10.15 Gravity dam model made of geo-mechanical materials

Table 10.11 Overloading steps

Overloading step	Upstream water level (m)	Upstream water depth H_i (m)	Overload increment P_i (mN)	Overload factor K_i	Remark
1	594.70	130.70	–	1.00	–
2	610.38	146.38	103.90	1.24	–
3	626.07	162.07	124.01	1.48	–
4	646.98	182.98	150.82	1.80	–
5	654.82	190.82	160.88	1.92	–
6	659.50	195.50	166.87	1.99	–
7	660.05	196.05	156.83	2.00	Upstream cracking near penstock

$$K_i = 2\frac{H_i}{H} - 1 \tag{10.45}$$

In which H is the upstream normal water depth at the beginning of overloading, H_i is the overloading water depth at the ith overloading step.

Altogether 7 displacement object points are layout in the dam and powerhouse. In addition, a number of strain gauges are deployed on the upstream dam face to detect dam cracking.

10.6.4 Computation Results

(1) Displacements

Figure 10.16 gives the calculated displacement increments when the overload factor K is equal to 2.0. The displacement increments against K at the gauge points ③ and ④ (see Fig. 10.13) are plotted in Fig. 10.17.

(2) Stresses

Figure 10.18 gives the calculated principal stresses when the overloading factor K is equal to 2.0. Unfortunately, in the geo-mechanical material test the strain cannot be measured credibly by conventional instruments, hence there is no cross-reference between the computation and test with regard to the strains and stresses.

(3) Failure mechanism and safety

The overloading factor K can be regarded as a safety index of dams. In the physical model test, it was found that the first crack appeared at the upstream dam body near the penstock (EL. 558.4 m) when the overloading factor K = 2.0. After the overloading factor exceeded 2.0, several cracks appeared between the penstock

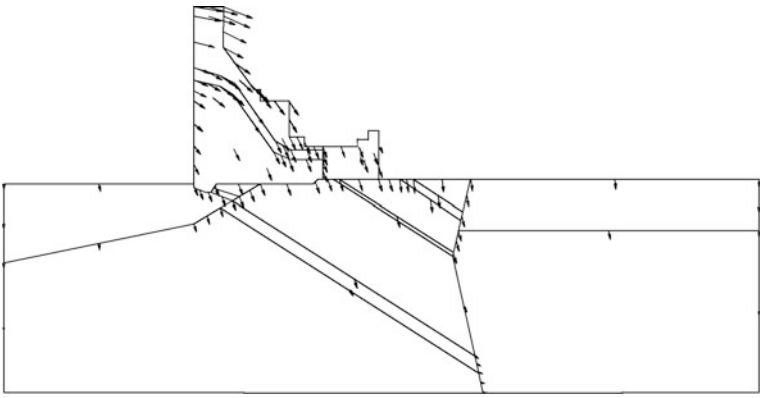

Fig. 10.16 Accumulated displacements (computed)

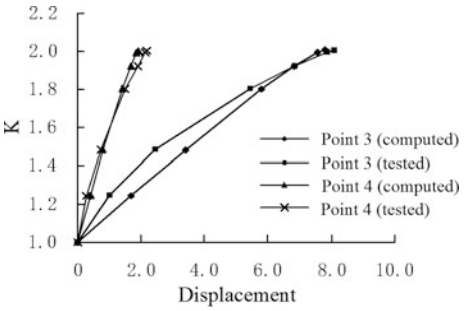

Fig. 10.17 Displacements at the gauge points versus overload factor K

and the dam heel. The crack near the penstock propagated fast and the upstream jack pressure in the test could not be sustained, leading to the failure of the dam. The corresponding safety factor can therefore be defined as equal to 2.0. It can therefore be confirmed that the failure mechanism is cracking in the dam, and the stability against the sliding in the foundation is no longer dominant consideration after the revision of design.

Figure 10.19 shows the tensile yield zones when $K = 2.0$ by the BEA, which are the areas enclosed by the contour of point safety factor equal to unit and the upstream boundary. It is clear that the failure mechanism can be well revealed by the BEA. The computation gives a safety factor of $K = 2.3$, which is higher than that from the physical model test. This is mainly attributable to the perfect plasticity (no hardening and softening) and associated flow rule postulated in the computation.

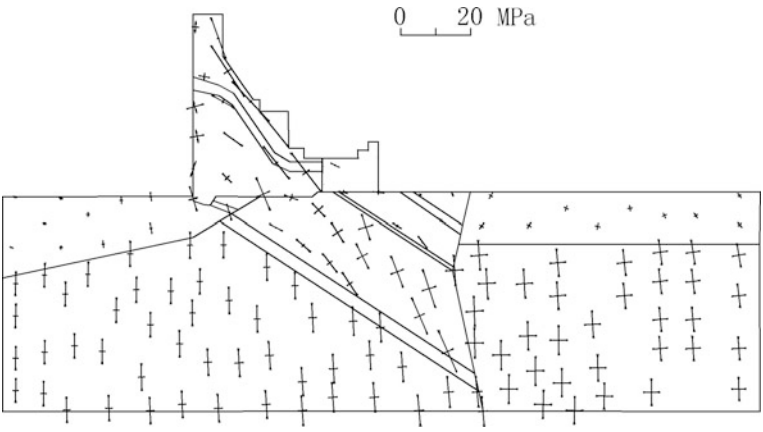

Fig. 10.18 Principal stresses (computed)

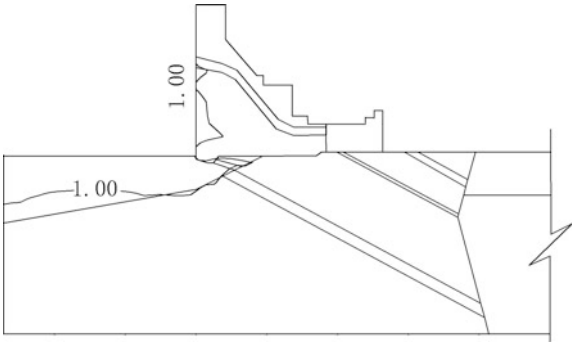

Fig. 10.19 Tensile yield zones under the overload factor $K = 2$ (computed)

The computation also indicates that at the upstream riverbed there is a tensile cracking zone. It will propagate along with the overloading process, too, but much slower than that occurs in the dam body. Therefore it is not the dominated factor entailing the safety of the dam.

References

Chang CT. Nonlinear dynamic discontinuous deformation analysis with finite element meshed block system. Ph.D. thesis, University of California at Berkeley (USA); 1994.

Chen SH. Numerical analysis and model test of rock wedge in slope. In: Pasamehmetoglu AG, et al., editors. Proc Int Symp on Assessment and Prevention of Failure Phenomena in Rock Engineering. Rotterdam (Netherlands): AA Balkema; 1993. p. 425–9.

Chen SH. A new development in elastic-viscoplastic block theory of rock masses. In: Siriwardane HJ, Zaman MM, editors. Proc 8th Int Conf Comp Meth Adv Geomech. Rotterdam (Netherlands): AA Balkema; 1994. p. 2235–40.

Chen SH. Hydraulic structures. Berlin, Germany: Springer-Verlag; 2015

Chen SH, Li YM, Wang WM, Shahrour I. Analysis of gravity dam on a complicated rock foundation using an adaptive block element method. J Geotech Geoenviron Eng, ASCE. 2004;130(7):759–63.

Cundall PA. A computer model for simulating progressive, large-scale movement in blocky rock system. In: Rock fracture, Proc Symp ISRM. Nancy (USA): ISRM; 1971. p. 129–136.

Cundall PA. Formulation of three-dimensional distinct element model. Part 1. A scheme to detect and represent contacts in system composed of many polyhedral blocks. Int J Rock Mech Min Sci & Geomech Abstr. 1988;25(3):107–116.

Hart R, Cundall PA, Lemos J. Formulation of three-dimensional distinct element model. Part 2. Mechanical calculations for motion and interaction of a system composed of many polyhedral blocks. Int J Rock Mech Min Sci & Geomech Abstr. 1988;25(3):117–125.

Koo CY, Chern JC. The development of DDA with third order displacement function. In: Salami R, Banks D, editors. Proc of the 1st international forum on discontinuous deformation analysis (DDA) and simulations of discontinuous media. Albuquerque (USA): TSI Press; 1996. p. 342–9.

Lin JS, Lee DH. Manifold method using polynomial basis function of any order. In: Salami R, Banks D, editors. Proc of the 1st international forum on discontinuous deformation analysis (DDA) and simulations of discontinuous media. Albuquerque (USA): TSI Press; 1996. p. 365–72.

Owen DRJ, Hinton E. Finite elements in plasticity: theory and practice. Swansea (UK): Pineridge Press Ltd; 1980.

Shi GH. Discontinuous deformation analysis: a new numerical model for the statics and dynamics of deformable block structures. Eng Comput. 1992;9(2):157–68.

Shyu K. Nodal based discontinuous deformation analysis. PhD thesis, University of California at Berkeley (USA); 1993.

Wang WM, Chen SH. A new implementation of elastic-viscoplastic block theory for rock masses. In: Kundu T, Desai CS, editors. Proc. 10th international conference on computer method and advances in geomechanics. Rotterdam (Netherlands): AA Balkema; 2001, 417–422.

Chapter 11
Hybrid Methods Related to the Block Element Analysis

Abstract In this chapter, hybrid methods are elaborated meant to solve the interaction problem of the hydraulic structure resting on its rock foundation/abutment. The foundation/abutment is simulated with block elements whereas the structure is discretized using arch/cantilever elements in orthodoxy, or more flexible finite elements. On the contact surface between the structure and the foundation/abutment, the displacement compatibility of the structure element and the foundation element are enforced, in this manner the hybrid governing equation set may be assembled to solve the displacements and stresses of the structure as well as the stability of the foundation/abutment simultaneously. At the end of this chapter, a successful engineering application case (arch dam) is presented.

11.1 General

There are two basic safety targets in the design of hydraulic structures (e.g. dams), namely, the control of the strength and deformation of the structure itself, as well as the control of the stability and deformation of its foundation or/and abutments (Chen 2015).

Take the arch dam design for example. The conventional analysis tool for arch dams is the "trial load method" (TLM) put forward by the United States Department of the Interior Bureau of Reclamation (USBR) in the 1930s (Copen et al. 1977). Following the appearance and the advancement of the computer industry, the method has been improved at various aspects with regard to the solution techniques, the precise consideration of the deflections of the arches and cantilevers, etc. (Suresh and Natarajan 1981; Lin and Yang 1987; Zhu et al. 1987). The TLM discretizes the arch dam with a series of arches and cantilevers, at which the exerted loads are shared by these components respectively, and their stresses are calculated separately according to the shared loads. Theoretically, the TLM may provide rather competent stresses for arch dam design, but it leaves a questionable assumption that the rock in its foundation/abutments is an elastic and homogeneous half space. Based on this assumption the relationship between the deformation of the

S.-H. Chen, *Computational Geomechanics and Hydraulic Structures*,
Springer Tracts in Civil Engineering, https://doi.org/10.1007/978-981-10-8135-4_11

foundation/abutments and the thrust from the dam can be established, to cope with the arch dam as a system of arches and cantilevers supported on the elastic foundation. Actually, this is rather problematic in the arch dams with complicated geology conditions.

The handling of the stability and deformation of foundation and abutments gives rise to another difficulty in the arch dam design. Generally, there exist a number of discontinuities which cut the rock masses into blocks of various sizes, shapes and positions. Attributable to its simplicity and the experiences accumulated in the engineering practices for long time, the conventional design makes the application of the limit equilibrium method (LEM) taking into account of the arch dam's thrust calculated by the TLM. It has, however, certain limitations: the deformation of the abutments cannot be solved, and the stability safety factor [or factor of safety (FOS)] would be overestimated when the slip surface is composed of two or more discontinuities (Londe 1965; Guzina and Tucovic 1969; Copen et al. 1977; Chan and Einstein 1981; Chen 1984, 1993).

In addition, since the stability of dam abutments is dependent on the dam's thrust strongly, an optimal design scheme of the dam using the TLM without the consideration of the stability of abutments is not the true optimal design. If the stability analysis of the dam abutments by the LEM under the dam's thrust gives unfavorable safety condition, we have to revise the dam's layout to improve the abutment stability, subject to new optimal design procedure for the dam body with correspondent new dam's thrust. This revision should be iteratively repeated several times to get an acceptable optimal design scheme compromising between the strength of the dam's body and the stability of the abutments. It is time costing and, the final design is strongly dependent on the initial design scheme.

The finite element method (FEM) is advantageous in handling very complicated configurations of the hydraulic structure and its foundation, as well as various loading and construction procedures. Good description of discontinuities and reinforcement components can be achieved if special elements (joint elements, bolt elements, etc.) are properly used. Although there are no competent permissible (allowable) strengths and overall stability criteria for the FEM in the design codes/specifications at the moment, yet the FEM is very helpful and already widely exercised in the study of special problems arise from the design for hydraulic structures.

The block element analysis (BEA) presented previously is able to handle the abutment slopes containing numerous discontinuities of various scales and orientations easily. It possesses peculiarities inclusive a powerful pre-processing toolkit for the complicated abutment slope with irregular ground surface, a comprehensive mechanical computation module dealing with various construction and loading processes, an intelligent searching strategy for the potential failure cases formed by the block combinations. Nevertheless, it has to admit that this method is far from perfect for the stability problems of arch dam. One of the main drawbacks is that it takes the thrust loads from the arch dam as constant forces calculated by the TLM. The reality is however, that as the deformation evolution of the dam and abutments, these thrust loads will change in both the direction and magnitude. Furthermore, since it treats the abutment separately from the dam, a real optimal design is cumbersome to reach.

Hybrid methods are therefore elaborated in our study, which is meant to solve the interaction problem of hydraulic structure and its foundation/abutments. The foundation will be simulated with block elements whereas the structures will be discretized by arch/cantilever elements in orthodoxy (Xu and Chen 2001; Chen et al. 2003), or more flexible finite elements (Wang et al. 2001). Towards each element, the stiffness matrix can be used to relate its displacements and loads. On the contact surface between the structure and the foundation, the displacements of the structure element and the foundation element are obligatorily compatible. With these considerations, the hybrid governing equation set may be assembled to solve the displacements and stresses of the structure system as well as the stability of the foundation/abutments simultaneously.

11.2 Formulation of the Trial Load Method

11.2.1 Concept

The modern procedure of the TLM has been well formulated in a various literatures (Chen 2015).

The whole arch dam will be divided into orthogonal arch-cantilever system (see Fig. 11.1). As a compromise between the computation accuracy and efficiency, normally 5–7 arch rings and 9–13 cantilevers are demanded. The number of arch rings and cantilevers should be compatible. Suppose that the amount of arch rings is n and the amount of cantilevers is m, very often the relation $m = 2n - 1$ is met to let any node at foundation be a common one (conjugate point) of the arch and cantilever. The conjugate nodes are as uniformly distributed as possible to cover the whole dam body.

At each conjugate node there is six deformation components (see Fig. 11.2), i.e. three linear deflections and three angle deflections, which are arranged in sequence according to their importance as the radial deflection v, tangential deflection u, angle deflection θ_z around axis z, angle deflection θ_t around tangential axis t, vertical deflection w, angle deflection θ_r around radial axis r. The correspondent external loads on arches or cantilevers are the radial load p, tangential load q, vertical load s, horizontal moment m_z, vertical moments m_t and m_r. These deflections and external loads may be grouped into correspondent vectors $\{\Delta\delta\}_{ac}$ and $\{\Delta f\}_{ac} = \{\Delta f\}_a + \{\Delta f\}_c$ $(ac = 1, 2, \ldots, n_{ac})$.

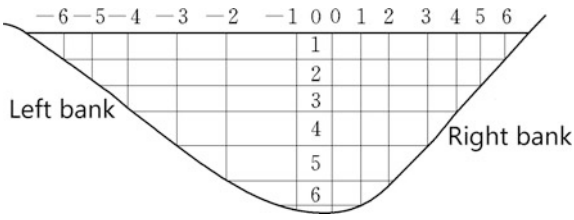

Fig. 11.1 Arch-cantilever system of an arch dam

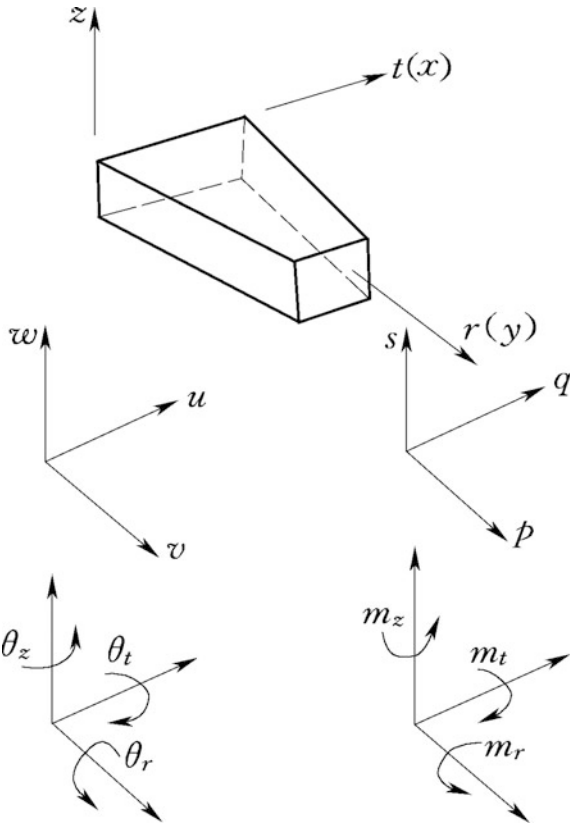

Fig. 11.2 Deflections and loads at a conjugate node

Theoretically, all these six deflections and their compatibility are taken into account to get an exact load division between arches and cantilevers, which is termed as "six directional (whole) adjustment". However, in practice the first three deflections are customarily adopted as independent variables through which the rest three deflections are expressed indirectly. These three key independent variables are solved by their deformation compatibility conditions at the conjugate nodes, which is termed as "three-directional adjustment". Similarly, four- or five-directional adjustment may be exercised.

It is worthwhile to remind that the strength criteria of arch dams are based on the three- or four-directional adjustment in the Chinese design codes for concrete arch dams.

Suppose that the loads at an arch dam are co-carried or shared by the arches and cantilevers respectively according to their stiffness coefficients, and use is made of the displacement compatibility conditions at all the nodes formed by the intersection of the arches with cantilevers, a set of equilibrium equation of the arch dam is established by which the nodal displacements may be solved. These displacements are further employed to calculate the internal forces and in turn, the stresses,

according to the arch and cantilever theory. The stresses are checked and calibrated by their permissible (allowable) tensile and compressive values. The thrust forces are also calculated from the internal forces of the arches and cantilevers contacting the abutments and foundation, which will be further passed to the LEM/BEA/FEM analysis to calibrate the abutment stability.

If the strength of the dam's body or/and the stability of the abutments are not held, the layout of the dam or/and the reinforcement of abutments should be modified, and the above analysis shall be recurred.

At the beginning of the 1930s when the method was initiated, the solution of an equation set with large freedom was a difficult overhead, so the load sharing between the arches and cantilevers should be "guessed" firstly, after the displacements of the arches and cantilevers were calculated separately, the displacement compatibility (equality) condition would be employed to check the correctness of the load partition. Usually, a number of repeated iterations should be carried out to get the acceptably correct load partition permitted by the displacement compatibility condition. Therefore, the researchers and engineers labeled the method with "trial load".

11.2.2 Governing Equations of Arch-Cantilever System

In Fig. 11.3, a shell patch is simplified on to its neutral surface whose four nodes possess linear and angular deflections. The directions along the arch and cantilever are defined as

$$\vec{v}_a = \vec{c}_2 - \vec{c}_1 \tag{11.1}$$

$$\vec{v}_b = \vec{c}_4 - \vec{c}_3 \tag{11.2}$$

Thus the radial direction is defined by

$$\vec{v}_r = \vec{v}_a \times \vec{v}_b \tag{11.3}$$

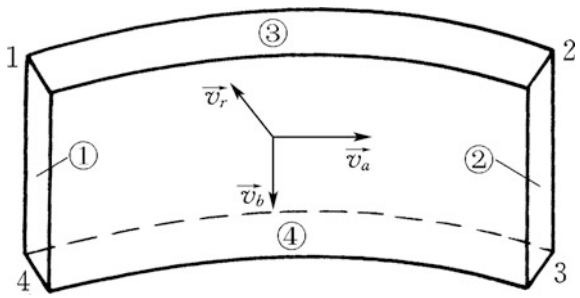

Fig. 11.3 Arch-cantilever element

In this way a locally orthogonal coordinate system is established.

We group the displacement increments of the element nodes in the global coordinate system into a vector $\{\Delta\delta\}_{ac}$. The global displacement increments $\{\Delta\delta\}_a$ and $\{\Delta\delta\}_c$ along the arch and cantilever directions are

$$\{\Delta\delta\}_a = [H]_a\{\Delta\delta\}_{ac} \tag{11.4}$$

$$\{\Delta\delta\}_c = [H]_c\{\Delta\delta\}_{ac} \tag{11.5}$$

In which $[H]_a$ and $[H]_c$ are the interpolation functions along the arch and cantilever directions, respectively. The above displacements can be transformed into the local coordinate system as

$$\{\Delta\delta\}'_a = [T]_a\{\Delta\delta\}_a = [T]_a[H]_a\{\Delta\delta\}_{ac} \tag{11.6}$$

$$\{\Delta\delta\}'_c = [T]_c\{\Delta\delta\}_c = [T]_c[H]_c\{\Delta\delta\}_{ac} \tag{11.7}$$

where $[T]_a$ and $[T]_c$ are the transformation matrices defined by

$$[T]_a = [\,-\vec{v}_b \quad \vec{v}_a \quad \vec{v}_r \quad -\vec{v}_b \quad \vec{v}_a\,]^T \tag{11.8}$$

$$[T]_c = [\,\vec{v}_a \quad \vec{v}_b \quad \vec{v}_r \quad \vec{v}_a \quad \vec{v}_b\,]^T \tag{11.9}$$

At the arch and cantilever directions, the displacement increments $\{\Delta\delta\}'_a$ and $\{\Delta\delta\}'_c$ are linked to the load increments $\{\Delta f\}'_a$ and $\{\Delta f\}'_c$ by the stiffness matrices $[k]'_a$ and $[k]'_c$ as follows

$$\{\Delta f\}'_a = [k]'_a\{\Delta\delta\}'_a \tag{11.10}$$

$$\{\Delta f\}'_c = [k]'_c\{\Delta\delta\}'_c \tag{11.11}$$

These load increments $\{\Delta f\}'_a$ and $\{\Delta f\}'_c$ are transformed into the global coordinate system noted as $\{\Delta f\}_a$ and $\{\Delta f\}_c$. Recall the invariance of the virtual work and use is made of Eq. (11.6), we have

$$\begin{aligned}\{\Delta\delta\}^T_{ac}\{\Delta f\}_a &= \{\Delta\delta\}^{'T}_a\{\Delta f\}'_a = ([T]_a[H]_a\{\Delta\delta\}_{ac})^T\{\Delta f\}'_a \\ &= \{\Delta\delta\}^T_{ac}[H]^T_a[T]^T_a\{\Delta f\}'_a\end{aligned} \tag{11.12}$$

Therefore

$$\{\Delta f\}_a = [H]^T_a[T]^T_a\{\Delta f\}'_a \tag{11.13}$$

Performing the similar deduction gives

$$\{\Delta f\}_c = [H]_c^T [T]_c^T \{\Delta f\}_c' \tag{11.14}$$

According to the principle of the TLM, the total load increment $\{\Delta f\}_{ac}$ is simply the summation of the contribution from the arch $\{\Delta f\}_a$ and the cantilever $\{\Delta f\}_c$, i.e.

$$\begin{aligned}\{\Delta f\}_{ac} &= \{\Delta f\}_a + \{\Delta f\}_c \\ &= [H]_a^T [T]_a^T \{\Delta f\}_a' + [H]_c^T [T]_c^T \{\Delta f\}_c' \\ &= [H]_a^T [T]_a^T [k]_a' [T]_a [H]_a \{\Delta\delta\}_{ac} + [H]_c^T [T]_c^T [k]_c' [T]_c [H]_c \{\Delta\delta\}_{ac} \\ &= ([H]_a^T [T]_a^T [k]_a' [T]_a [H]_a + [H]_c^T [T]_c^T [k]_c' [T]_c [H]_c)\{\Delta\delta\}_{ac}\end{aligned} \tag{11.15}$$

Denote

$$[k]_{ac} = [H]_a^T [T]_a^T [k]_a' [T]_a [H]_a + [H]_c^T [T]_c^T [k]_c' [T]_c [H]_c \tag{11.16}$$

We obtain the governing equation of the arch-cantilever element relating the displacement and load increments through the stiffness matrix $[k]_{ac}$ in a manner of

$$\{\Delta f\}_{ac} = [k]_{ac} \{\Delta\delta\}_{ac} \tag{11.17}$$

Equation (11.17) can be assembled by a routine procedure similar to the FEM into the governing equation set of the arch-cantilever system

$$\{\Delta F\}_{dam} = [K]_{dam} \{\Delta\delta\}_{dam} \tag{11.18}$$

After the load increments (water pressure, temperature, etc.) exerting on the dam are transferred into the nodal load vector $\{\Delta F\}_{dam} = \left[\{\Delta f\}_1^{\mathrm{T}}, \{\Delta f\}_2^{\mathrm{T}}, \{\Delta f\}_3^{\mathrm{T}}, \ldots, \{\Delta f\}_{n_{ac}}^{\mathrm{T}}\right]^T$, the displacement increments $\{\Delta\delta\}_{dam} = \left[\{\Delta\delta\}_1^{\mathrm{T}}, \{\Delta\delta\}_2^{\mathrm{T}}, \{\Delta\delta\}_3^{\mathrm{T}}, \ldots, \{\Delta\delta\}_{n_{ac}}^{\mathrm{T}}\right]^T$ may be solved by Eq. (11.18). Afterwards the element stress increments are calculated with these displacement increments simply by the theory of elastic beam and arch.

11.3 Hybrid of Block Element System with Arch-Cantilever Element System

Towards the hybrid system of block elements for foundation/abutments and arch-cantilever elements for arch dam, their displacement increments must be related with the help of contact (interactive) conditions. A simple treatment is to

postulate that the contact face is rigid so that the displacement increment of an arch-cantilever element on the contact face is identical to that of its connected block element, namely the nodal displacement increment of the arch-cantilever element *ac* contacting the block element *rl* should be expressed by

$$\{\Delta\delta\}_{ac} = [T]\{\Delta U\}_{rl} \tag{11.19}$$

In this manner the arch-cantilever nodal freedoms are replaced by that of the connected block element. The transformation matrix $[T]$ in Eq. (11.19) is defined as

$$\begin{cases} [T] = \begin{bmatrix} [I] & [A] \\ [0] & [I] \end{bmatrix} \\ [A] = \begin{bmatrix} 0 & Z_{rl}^0 - Z_{ac} & -(Y_{rl}^0 - Y_{ac}) \\ -(Z_{rl}^0 - Z_{ac}) & 0 & X_{rl}^0 - X_{ac} \\ Y_{rl}^0 - Y_{ac} & -(X_{rl}^0 - X_{ac}) & 0 \end{bmatrix} \end{cases} \tag{11.20}$$

In which $[I]$ is a 3×3 unit matrix, $(X_{rl}^0, Y_{rl}^0, Z_{rl}^0)$ is the centroid coordinate of the block *rl* and (X_{ac}, Y_{ac}, Z_{ac}) is the nodal coordinate of the arch-cantilever element which contacts the block *rl*. If a node does not contact the block element *rl*, $[T]$ is a unit matrix.

Similarly, the nodal load increment $\{\Delta f\}_{ac}$ of the arch-cantilever element *ac* can be transferred to the centroid of its contacting block element *rl* by

$$\{\Delta f\}_{rl} = [T]^T\{\Delta f\}_{ac} \tag{11.21}$$

Introducing Eqs. (11.17) and (11.19) into Eq. (11.21), the nodal displacement and load increments of the arch-cantilever element *ac* contacting the block element *rl* are related by

$$\{\Delta f_{hybrid}\}_{rl} = [T]^T[k]_{ac}[T]\{\Delta U\}_{rl} = [k]_{hybrid}\{\Delta U\}_{rl} \tag{11.22}$$

In which

$$[k]_{hybrid} = [T]^T[k]_{ac}[T] \tag{11.23}$$

Equations (11.22), (9.19) and (11.17) are assembled according to the freedoms of all the block elements and the rest freedoms of the arch-cantilever elements, the hybrid governing equation set of the dam and foundation system will take the form of

$$[K]\{\Delta\delta\} = \{\Delta F\} + \{\Delta F^{vp}\} \tag{11.24}$$

In which $[K]$ is the system stiffness matrix, and

$$\begin{cases} \{\Delta\delta\} = \left[\{\Delta\delta\}_1^{\mathrm{T}}, \{\Delta\delta\}_2^{\mathrm{T}}, \ldots, \{\Delta\delta\}_{n_{ac}}^{\mathrm{T}}, \{\Delta U\}_1^{\mathrm{T}}, \{\Delta U\}_2^{\mathrm{T}}, \ldots, \{\Delta U\}_{n_r}^{\mathrm{T}}\right]^T \\ \{\Delta F\} = \left[\{\Delta f\}_1^{\mathrm{T}}, \{\Delta f\}_2^{\mathrm{T}}, \ldots, \{\Delta f\}_{n_{ac}}^{\mathrm{T}}, \{\Delta f\}_1^{\mathrm{T}}, \{\Delta f\}_2^{\mathrm{T}}, \ldots, \{\Delta f\}_{n_r}^{\mathrm{T}}\right]^T \\ \{\Delta F^{vp}\} = \left[\{0\}_1^{\mathrm{T}}, \{0\}_2^{\mathrm{T}}, \ldots, \{0\}_{n_{ac}}^{\mathrm{T}}, \{\Delta f^{vp}\}_1^{\mathrm{T}}, \{\Delta f^{vp}\}_2^{\mathrm{T}}, \ldots, \{\Delta f^{vp}\}_{n_r}^{\mathrm{T}}\right]^T \end{cases} \tag{11.25}$$

11.4 Hybrid of Block Element System with Finite Element System

The subscripts *rl* and *ei* are used to denote the deformable block element and finite element, $j_{rl,ei}$ is used to denote the interface (contact face) between *rl* and *ei*. The other nomenclatures are identical to that in the foregoing chapters.

We recall that the displacement of block element *rl* using hierarchical shape functions for overlay element is

$$\{\Delta u\}_{rl} = [N]_{rl}\{\Delta\delta\}_{rl} \quad (rl = 1, 2, \ldots, n_r) \tag{11.26}$$

In which $[N]_{rl}$ and $\{\Delta\delta\}_{rl}$ are the hierarchical shape function matrix and general displacement vector of the block element *rl*, respectively.

In a finite element, it is well known that

$$\{\Delta u\}_{ei} = [N]_{ei}\{\Delta\delta\}_{ei} \quad (ei = 1, 2, \ldots, n_e) \tag{11.27}$$

In which $[N]_{ei}$ and $\{\Delta\delta\}_{ei}$ is the hierarchical shape function matrix and general displacement vector of the finite element *ei*, respectively.

If the block element *rl* and finite element *ei* adjoins through the interface $j_{rl,ei}$, the relative displacement of this interface is

$$\{\Delta u\}_{j_{rl,ei}} = J\left(j_{rl,ei}\right)[l]_{j_{rl,ei}}\left([N]_{rl}\{\Delta\delta\}_{rl} - [N]_{ei}\{\Delta\delta\}_{ei}\right) \tag{11.28}$$

In which the coordinate transformation matrix $[l]_{j_{rl,ei}}$ of the interface has been defined in Eqs. (2.12) and (2.13) where the subscript *j* shall be replaced by $j_{rl,ei}$, and the function $J\left(j_{rl,ei}\right)$ has been defined in Eq. (9.12).

The strain increments of *rl* and *ei* are

$$\{\Delta\varepsilon\}_{rl} = [B]_{rl}\{\Delta\delta\}_{rl} \tag{11.29}$$

$$\{\Delta\varepsilon\}_{ei} = [B]_{ei}\{\Delta\delta\}_{ei} \tag{11.30}$$

The constitutive relations of the block element and finite element as well as the interface have been discussed in the foregoing chapters.

The virtual work of a structural system comprising block element sub-system and finite element sub-system is

$$W_F = \sum_{rl}^{n_r} W_{rl} + \sum_{ei}^{n_e} W_{ei} + \sum_{j}^{n_j} W_j \tag{11.31}$$

where W_F = virtual work contributed from the external actions; W_{rl} = virtual work contributed from the block element rl; W_{ei} = virtual work contributed from the finite element ei; W_j = virtual work contributed from the structural plane j (inclusive the interfaces between block elements and finite elements); n_r = amount of the block elements; n_{ei} = amount of the finite elements; n_j = amount of the structural planes (inclusive the interfaces between block elements and finite elements).

$$W_{rl} = \iiint_{\Omega_{rl}} \{\Delta\varepsilon^*\}_{rl}^T \{\Delta\sigma\}_{rl} d\Omega \quad (rl = 1, 2, \ldots, n_r) \tag{11.32}$$

$$W_{ei} = \iiint_{\Omega_{ei}} \{\Delta\varepsilon^*\}_{ei}^T \{\Delta\sigma\}_{ei} d\Omega \quad (ei = 1, 2, \ldots, n_e) \tag{11.33}$$

$$W_j = \iint_{\Gamma_j} \{\Delta\delta^*\}_j^{\mathrm{T}} \{\Delta\sigma\}_j dx_j dy_j \quad (j = 1, 2, \ldots, n_j) \tag{11.34}$$

$$W_F = \sum_{rl}^{n_r} \{\Delta\delta^*\}_{rl}^{\mathrm{T}} \{\Delta F\}_{rl} + \sum_{ei}^{n_e} \{\Delta\delta^*\}_{ei}^{\mathrm{T}} \{\Delta F\}_{ei} \tag{11.35}$$

In which the superscript * indicates the virtual quantity.

Introducing Eqs. (11.32)–(11.35) into Eq. (11.31), after the arrangement it gives rise to the hybrid governing equation set of the structure system as follows

$$[K]\{\Delta\delta\} = \{\Delta F\} \tag{11.36}$$

In which $[K]$, $\{\Delta\delta\}$ and $\{\Delta F\}$ are the stiffness matrix, displacement vector and load vector of the whole hybrid system.

$[K]$ is assembled by four types of sub-matrices, namely $[k]_{rl,rl}$, $[k]_{rl,rm}$, $[k]_{ei,ei}$, $[k]_{rl,ei}$. They are respectively the contributions from block element rl solely, the interaction of block elements rl and rm, finite element ei solely, and the interaction of block element rl and finite element ei. For the first three types our readers are referred to the Chaps. 4, 5 and 10, whereas for the last one it may be given as

$$[K]_{rl,ei} = -H(rl,ei)\iint\limits_{\Gamma_{j_{rl,ei}}} [N]_{rl}^{\mathrm{T}}[l]_{j_{rl,ei}}^{\mathrm{T}}[D]_{j_{rl,ei}}[l]_{j_{rl,ei}}[N]_{ei}dx_{j_{rl,ei}}dy_{j_{rl,ei}} \tag{11.37}$$

$$H(rl,ei) = \begin{cases} 1 & if \quad rl \quad and \quad ei \quad are \quad adjacent \\ 0 & if \quad rl \quad and \quad ei \quad are \quad not \quad adjacent \end{cases} \tag{11.38}$$

The system displacement and load vectors are simply assembled as

$$\{\Delta\delta\} = \left[\{\Delta\delta\}_{r1}^{\mathrm{T}} \quad \ldots \quad \{\Delta\delta\}_{n_r}^{\mathrm{T}} \quad \{\Delta\delta\}_{e1}^{\mathrm{T}} \quad \ldots \quad \{\Delta\delta\}_{n_e}^{\mathrm{T}}\right]^T \tag{11.39}$$

$$\{\Delta F\} = \left[\{\Delta F\}_{r1}^{\mathrm{T}} \quad \ldots \quad \{\Delta F\}_{n_r}^{\mathrm{T}} \quad \{\Delta F\}_{e1}^{\mathrm{T}} \quad \ldots \quad \{\Delta F\}_{n_e}^{\mathrm{T}}\right]^T \tag{11.40}$$

In Eq. (11.40) the load increments $\{\Delta F\}_{rl}$ and $\{\Delta F\}_{ei}$ are composed of two portions

$$\{\Delta F\}_i = \{\Delta f\}_i + \{\Delta f^{vp}\}_i \quad (i = rl, ne) \tag{11.41}$$

11.5 Verifications and Applications

11.5.1 Cantilever Beam Example

For the cantilever beam in Fig. 10.4, the left half portion is simulated by one deformable block element whose shape function order is p = 1 along the thickness direction Y, whereas the right half portion is discretized into 24 finite elements (see Fig. 11.4). The artificial interface between the block element and finite elements is supposed to possess very high stiffness coefficients with $k_n = 2 \times 10^7$ MPa/m and $k_s = 1 \times 10^7$ MPa/m, to eliminate its influence on the computation results.

Figure 11.5 gives the deflection distribution along the cantilever and Fig. 11.6 shows the cross sectional distribution of the normal stress. When along both the

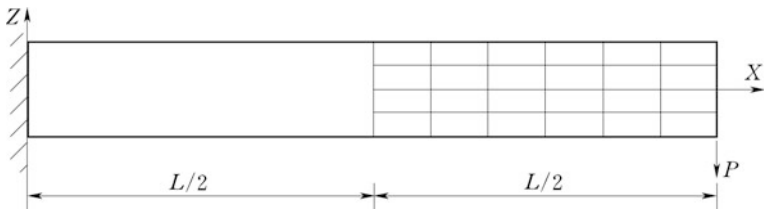

Fig. 11.4 Hybrid block element and finite element system on the $X - Z$ plane

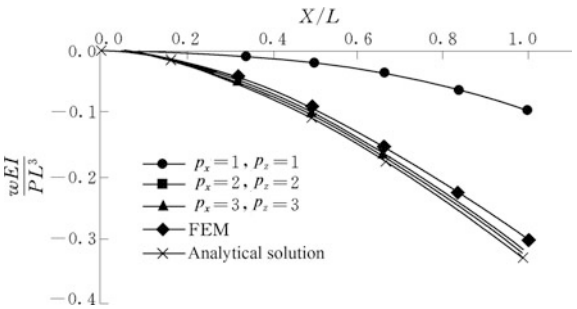

Fig. 11.5 Flexural curves of the beam axis (I = sectional moment of inertia)

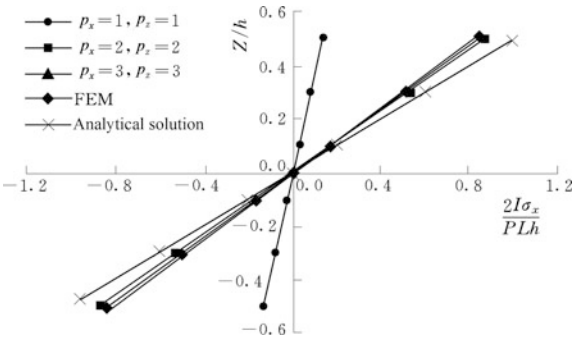

Fig. 11.6 Normal stress distribution of the fixed end section (I = sectional moment of inertia)

directions X and Z the shape function order of finite elements is $p = 2$ and that of block element is $p = 3$, the computation and analytical results are very close to each other.

11.5.2 Engineering Application: Dahuashui Project, China

(1) Presentation of the Project

Dahuashui Project is located on the Qingshuihe River, Guizhou Province, China. It is spanned by of a RCC double-curvature arch dam (parabolic arch ring) with a gravity block on the left bank (see Fig. 11.7).

The main purposes of the project are the hydroelectric power generation and flood control. The dam creates a gross reservoir storage of 276×10^6 m^3 which supplies water to a power station installed with two 200 MW turbine generators. Construction on the dam was launched in December 2003 and was expectantly completed in May 2007, but a lack of funding delayed project completion until its initial operation in January 2008.

The dam is located in a non-symmetric valley trenched in limestone (see Fig. 11.8): during dry seasons, the river surface is 37 m wide at the EL. 755 m; at the EL. 815 m the valley is 101 m wide; at the EL. 868 m (NSL) the river valley is

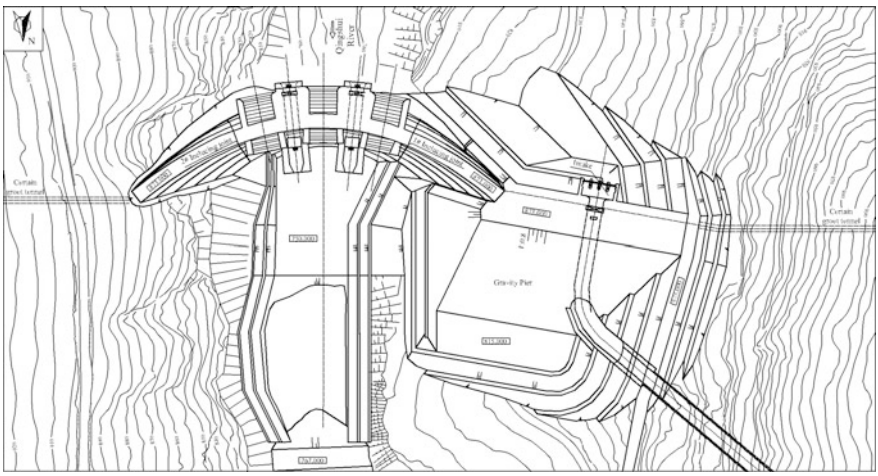

Fig. 11.7 Plan showing the layout of Dahuashui Project

256 wide. As a result, a gravity block pier is installed at the left abutment (see Fig. 11.9).

The limestone bedrocks under and near the dam are intersected by the faults f_1, f_2, f_3, f_{23}, f_{30}, f_4. By the borehole exploration and geophysical CT investigation, there are no large Karst features (e.g. karrens, solution cavities, cenotes, sinkholes, dolines, underground rivers) apart from small ones (size < 0.5–3.0 m).

The attitude of rock stratum is N10°W, SW ∠27°. The comprehensive studies on the occurrences and mechanical properties of discontinuities, the valley topography, as well as the thrust forces exerted by the arch dam, allowed for the definition of those discontinuities which should be included in the analysis as follows:

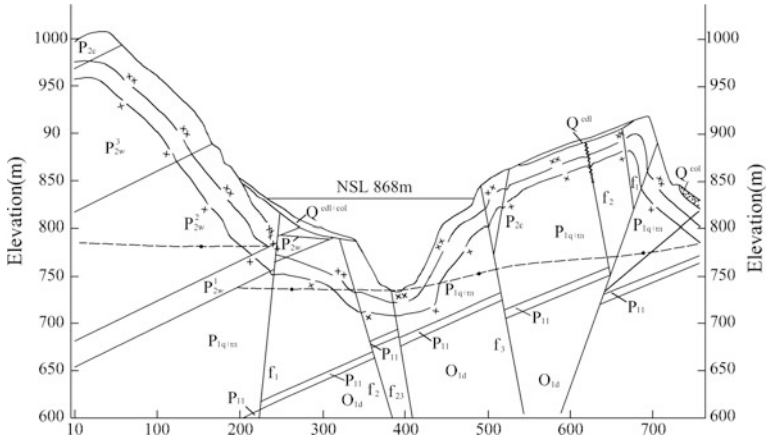

Fig. 11.8 Geologic section of Dahuashui Project along the dam axis

Fig. 11.9 Start of the gravity pier construction

- Three joint sets. ① N60°–90°E, NW (SE) ∠70°–90°;② N60°–90°W, SW (NE) ∠70°–90°;③ N0°–30°E, NW (SE) ∠60°–90°.
- Eleven faults whose geological parameters are listed in the Table 11.1.

After routine works, the designer presented the final optimal design. The crest width is 7.00 m and the length of crest is 256.19 m; the crest elevation and the bottom elevation of the gravity block are 837.00 and 800.00 m, respectively; the dam bottom thickness is 28.0 m and the correspondent thickness-height ratio is 0.208. With the crest elevation at 873.00 m and the bottom elevation at 738.5 m, the maximum dam height is 134.50 m which ranked it the highest RCC arch dam in the world. Figure 11.10 illustrates the horizontal arch rings at different elevations.

(2) Characteristics of the computation

The hybrid BEA/TLM method elaborated in this chapter has been employed during each design phase to evaluate the strength and stability of the candidate dam schemes. In the following a part of the results for the finally optimized dam design will be briefly presented.

1. Mechanical parameters

The mechanical parameters of the discontinuities are assigned on the basis of a comprehensive study including the geological investigations, the laboratory and

Table 11.1 Geological parameters of the faults

Sequence	Attitude	Type	Stretching (m)	Width of fractured zone (m)
f_1	N80°W, NE ∠70°–85°	Compression-torsion	>200	0.20–0.50
f_2	N75°–90°E, NW ∠70°–85°	Compression-torsion	>200	1.00–2.00
f_3	N55°–68°W, NE ∠70–85°	Compression-torsion	190	0.50–1.20
f_4	N70°–90°E, SE ∠80°	Compression-torsion	>200	0.50–1.60
f_5	N70°–90°E, SE ∠80°	Compression-torsion	>200	0.20–0.50
f_6	N70°–90°E, SE ∠80°	Compression-torsion	>200	0.10–0.40
f_8	N65°–85°E, SE ∠70°–85°	Compression-torsion	>200	0.20–1.50
f_{23}	N0°–15°E, SE ∠60°–85°	Compression	>200	0.50–2.50
f_{24}	N35°E, SE ∠60°	Compression	>150	0.05–0.10
f_{25}	N38°W, SW ∠50°–70°	Compression	>200	0.50
f_{26}	N72°E, NW ∠82°	Compression	>200	2.50–3.50

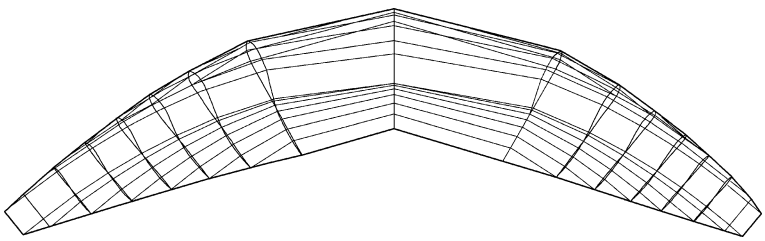

Fig. 11.10 Layout of dam arch rings

field tests, and engineering analogue. The key parameters are the normal and shear stiffness coefficients, the cohesion and the friction angle, of the various discontinuities.

The elastic behavior is stipulated for the dam concrete with the Young's modulus E = 20.78 GPa and the Poisson's ratio $\mu = 0.18$.

2. Block and arch-cantilever sub-systems

The foundation is discretized into block element sub-system (see Figs. 11.11, 11.12 and 11.13) meanwhile the arch-cantilever sub-system for the dam is also constructed. The whole system includes 70 arch-cantilever elements (8 arch rings

and 15 cantilever columns) and 4808 block elements (inclusive 85 blocks for the gravity block pier).

3. Load combinations

The calculation is carried out with respect to two load combinations.

– Basic load combination. Volumetric weight of dam body + normal head water level + corresponding tail water level + silt pressure + temperature drop.

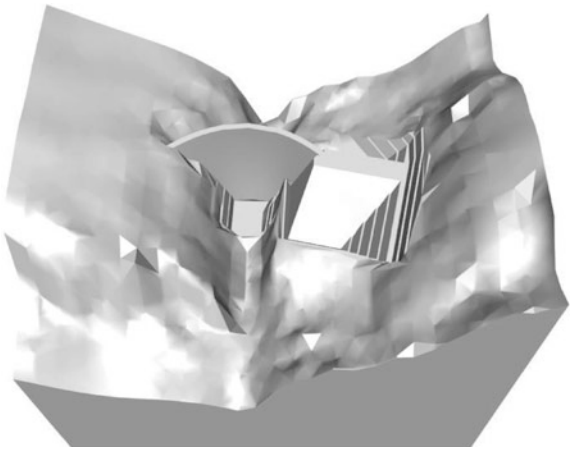

Fig. 11.11 Dam and foundation system: axonometric perspective view

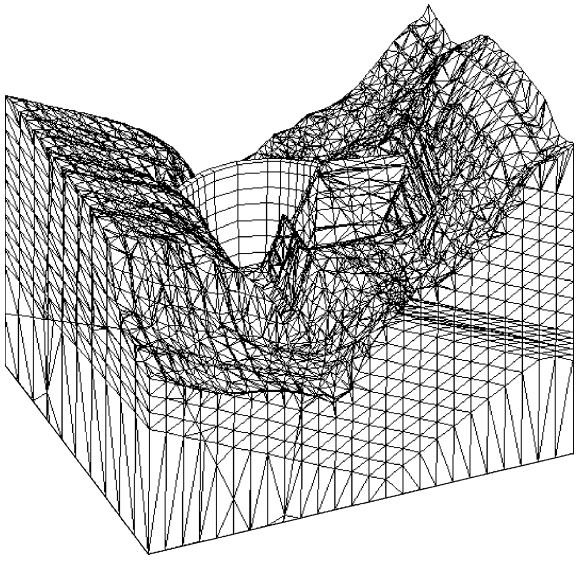

Fig. 11.12 Block and arch-cantilever system: view from downstream right bank

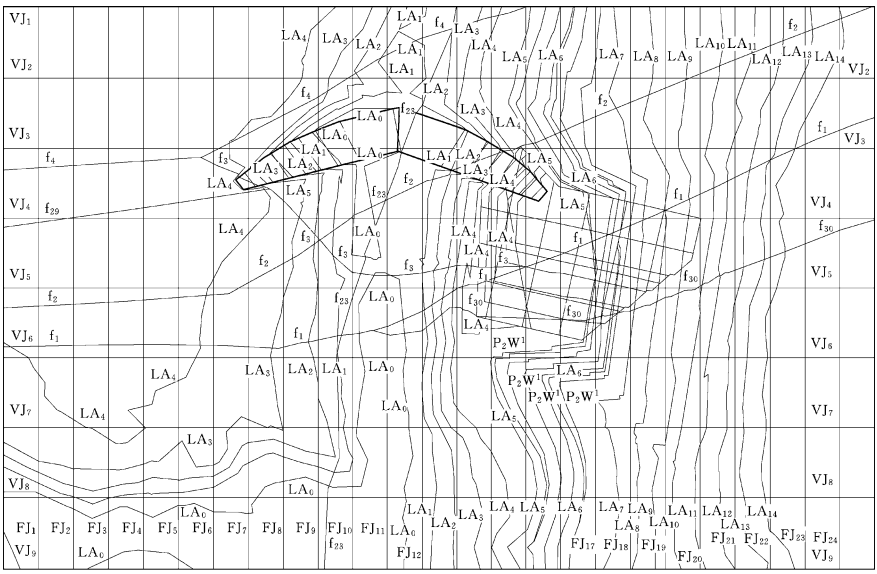

Fig. 11.13 Block and arch-cantilever system: plan

– Special load combination. Volumetric weight of dam body + catastrophe flood water level + corresponding tail water level + silt pressure + temperature rise.

It is a routine to calculate the self-weight, the water pressure, the silt pressure and the temperature drop or rise in the dam (Chen 2015). The seepage flow in the discontinuity network taking account of the seepage control devices such as the drainage and grout curtains however, should be analyzed by the method illustrated in Chap. 9.

(3) Results

1. Dam body displacements

Figures 11.14 and 11.15 give the displacement increments at the EL. 820 m induced by the reservoir impounding only when the dam is under the basic load combination and the special load combination, respectively. All the other horizontal cross sections show similar displacement patterns.

It is found that under the basic load combination, the maximum displacement 35.20 mm of the dam occurs at the crest of the crown cantilever; whereas under the special load combination, the maximum displacement 30.34 mm of the dam occurs at the EL. 820 m of the crown cantilever in contrast to merely 20.89 mm at the crest.

The maximum displacement 13.50 mm of the left dam abutment appears at the EL. 820 m, whereas it is about 17.19 mm at the EL. 800 m (near the fault f_4) of the right abutment.

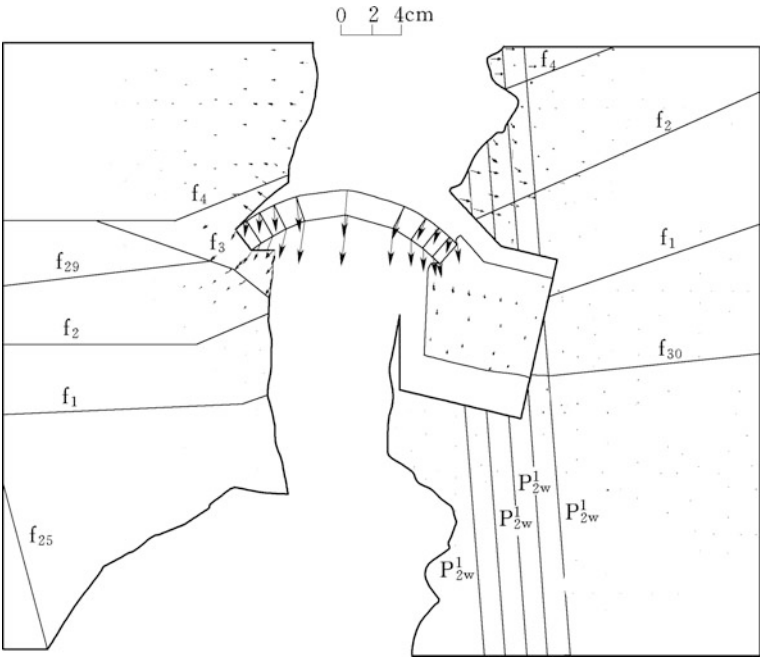

Fig. 11.14 Displacement increments at the EL. 820 m (basic load combination)

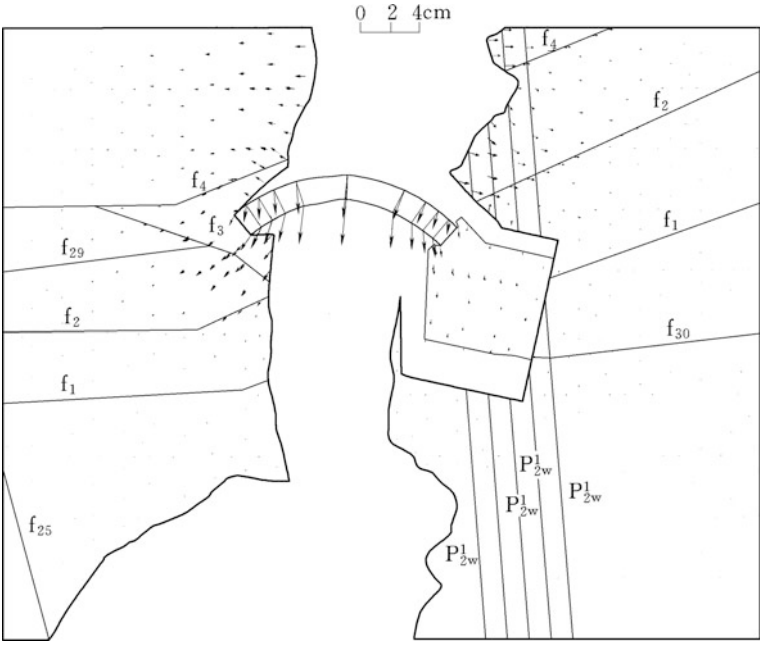

Fig. 11.15 Displacement increments at the EL. 820 m (special load combination)

On the contact face of gravity block pier/arch dam, the pier exhibits river stream oriented displacements of 5.14 mm at the EL. 860 m, 5.60 mm at the EL. 840 m, 7.07 mm at the EL. 820 m, and 6.76 mm at the EL. 800 m.

Attributable to the massive gravity pier across the weak zones, the displacements at the left dam abutment are a bit of smaller than that at the right abutment. It convincingly justifies the important role of the gravity pier in strengthening the left dam abutment.

2. Dam body stresses

Figures 11.16 and 11.17 show the principal stresses on the upstream and downstream surfaces under the basic load combination. The minimum and maximum stresses of the dam are −5.38 MPa and 2.57 MPa demonstrating at the heel and toe of the crown cantilever, respectively.

Figures 11.18 and 11.19 show the principal stresses on the upstream and downstream surfaces under the special load combination. The minimum and maximum stresses of the dam are −5.27 MPa and 2.52 MPa appearing at the heel and toe of the crown cantilever, respectively.

The maximum tensile stress is a bit of higher than the allowable (permissible) value, it means that cracking could manifest at the dam's heel. The suggestion is put forward that further comprehensive analysis should be made by the other available methods with regard to the dam heel cracking problem inclusive the FEM and physical model test. If necessary, the dam's shape should be appropriately adjusted. In Fig. 11.20, a physical model of Dahuashui Arch Dam is shown, on which we

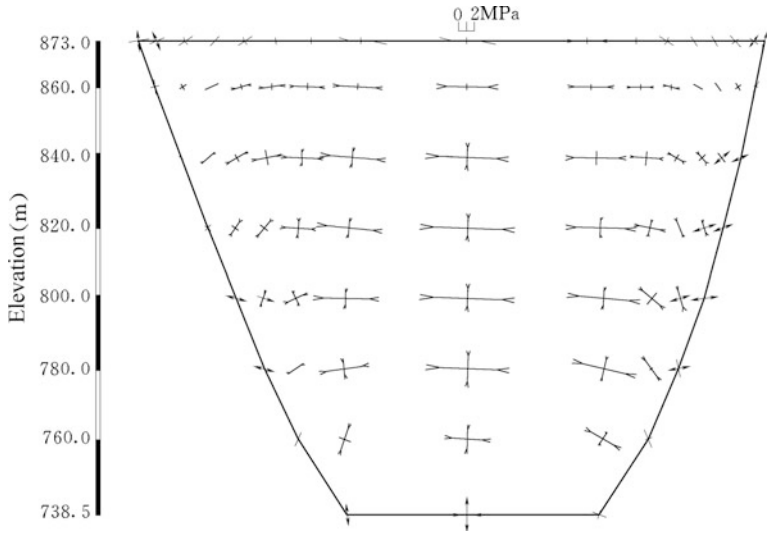

Fig. 11.16 Principal stresses on the upstream dam surface (basic load combination)

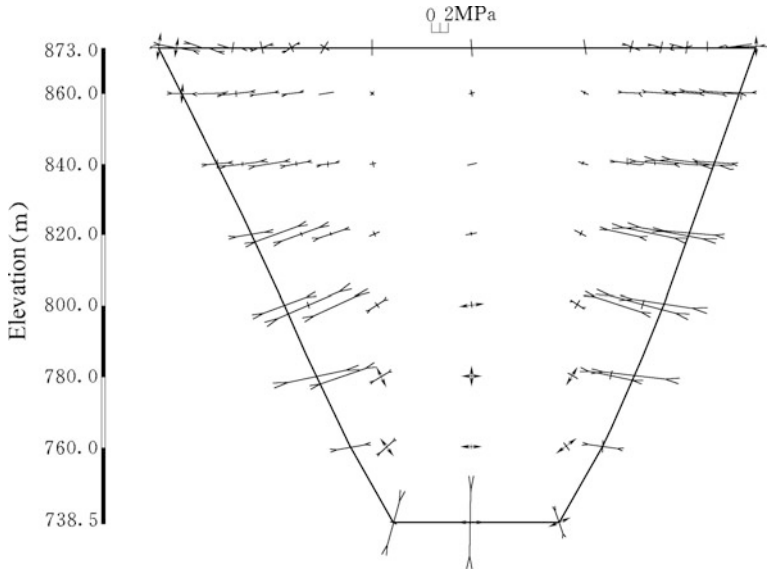

Fig. 11.17 Principal stresses on the downstream dam surface (basic load combination)

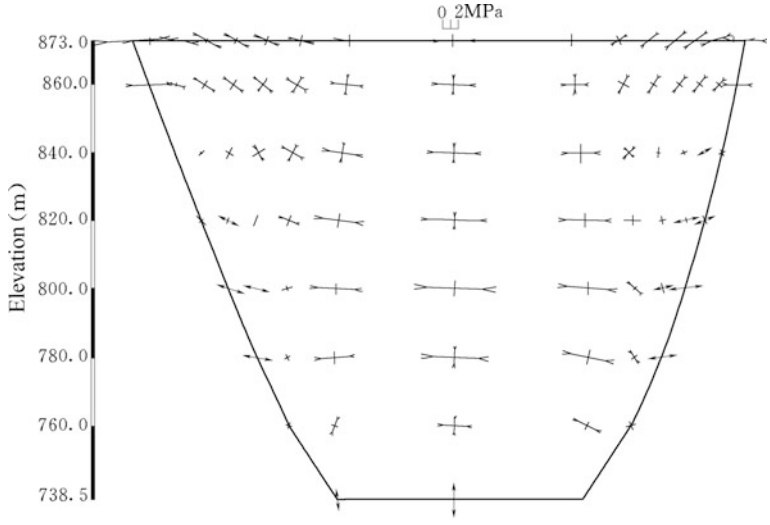

Fig. 11.18 Principal stresses on the upstream dam surface (special load combination)

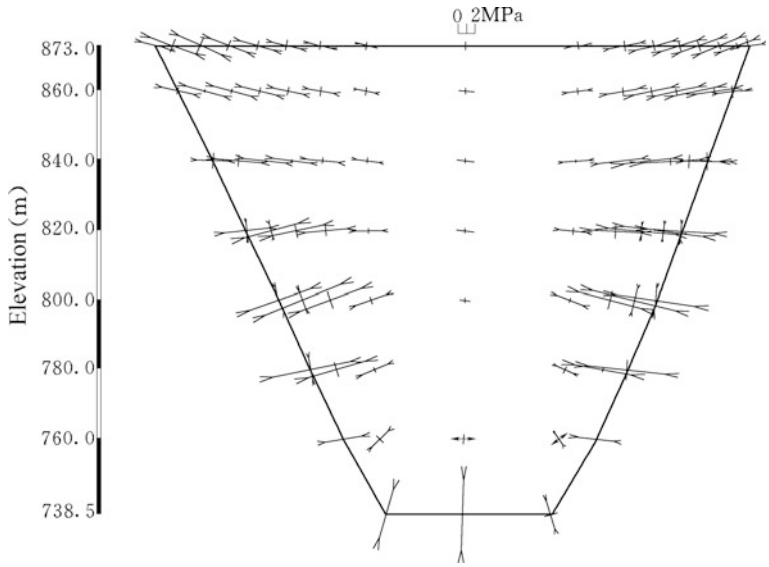

Fig. 11.19 Principal stresses on the downstream dam surface (special load combination)

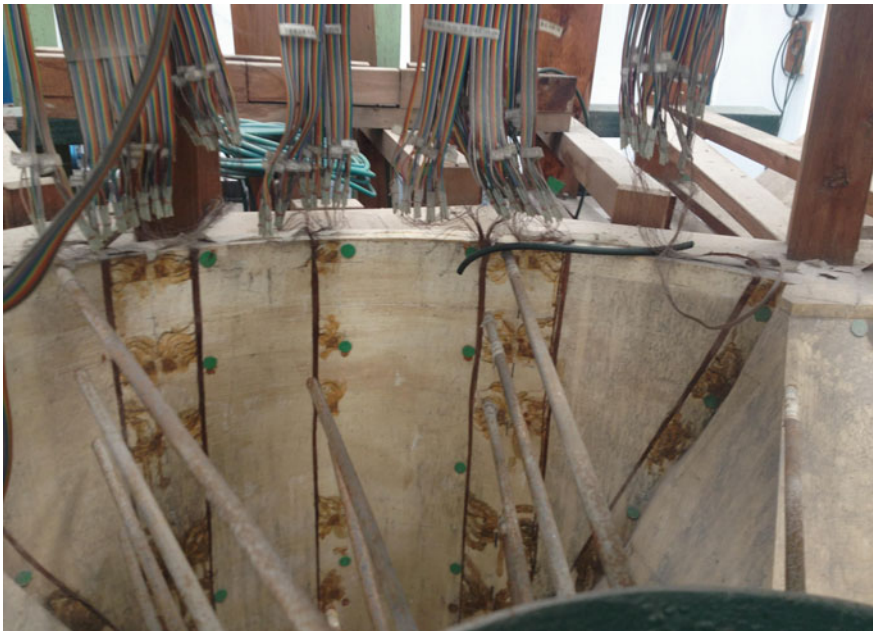

Fig. 11.20 Physical model of Dahuashui Arch Dam (downstream view)

Fig. 11.21 Dahuashui Project in service (downstream view)

conducted a series of tests purposed to the optimal design of crack inducers (inducing joints) for the mitigation of hazardous tensile cracking.

3. Safety factors of abutments against sliding

By the intelligent search (Xu et al. 2000) for blocks or block combinations, 32 main potential failure cases are detected whose safety factors against sliding are relatively lower. The suggestions with regard to the abutment treatment and reinforcement countermeasures are put forward and implemented under the guidance of our study.

After the completion of the project (see Fig. 11.21), it has been working well without any serious problems insofar.

References

Chan HC, Einstein HH. Approach to complete limit equilibrium analysis for rock wedges—the method of "artificial supports". Rock Mech. 1981;14(2):59–86.

Chen SH. The stability of a rock wedge in the slope. MSc thesis, WUHEE, Wuhan, China: 1984 (in Chinese).

Chen SH. Numerical analysis and model test of rock wedge in slope. In: Pasamehmetoglu AG, et al editors. Proceedings of international symposium on assessment and prevention of failure phenomena in rock engineering. Rotterdam, Netherlands: AA Balkema; 1993. p. 425–29.

Chen SH. Hydraulic structures. Berlin, Germany: Springer; 2015.

Chen SH, Xu MY, Shahrour I, Egger P. Analysis of arch dams using the coupled trial load and block element methods. J Geotech Geoenviron Eng, ASCE. 2003;129(11):977–86.

Copen MD, Lindholm EA, Tarbox GS. Design of concrete dams. In: Golzé AR, editor. Handbook of dam engineering. New York, USA: Van Nostrand Reinhold; 1977.

Guzina B, Tucovic I. Determining the maximum three dimensional stability of a rock wedge. Water Power. 1969;21(10):381–5.

Lin SZ, Yang ZH. Load distribution-stiffness method for stress analysis of arch dams. J Hydraulic Eng. 1987;9(1):17–25 (in Chinese).

Londe P. Une method d'analyse o'trois dimensions de la stabilite d'une rive rocheuse. Ann Ponts Chaussees. 1965;135(1):37–60.

Suresh P, Natarajan R. Analysis of laminated composite shell structures by finite element method. Comput Struct. 1981;14(3–4):225–30.

Wang WM, Xu MY, Chen SH. Coupled method of block element and finite element for hydraulic structures. Chinese J Rock Mech Eng. 2001;20(Supp 1):1029–33 (in Chinese).

Xu MY, Chen SH. The improved load-distribution method of arch dam considering the interaction between foundation and dam exactly. In: Kundu T, Desai CS, editors. Proceedings of 10th international conference on computer method and advances in geomechanics. Rotterdam, Netherlands: AA Balkema; 2001. 1641–44.

Xu MY, Wang WM, Chen SH. Research on the dangerous sliding-block combination of rock slopes. Rock Soil Mech. 2000;21(2):148–51 (in Chinese).

Zhu BF, Rao B, Jia JS. Stress analysis of noncircular arch dam with variable thickness. J Hydraulic Eng. 1987;9(11):17–25 (in Chinese).

Chapter 12
Expanding Study on the Block Element Analysis

Abstract In this chapter the principles and algorithms of the BEA are further extended to cover the reinforcement analysis, stochastic analysis, and seismic analysis. This is an important step towards more widespread and practical use of the BEA in hydraulic structures. Looked at as line segments penetrating through or embedding on discontinuities, the positions and/or the intersecting points of reinforcement components (bolts, piles, keys) with regard to discontinuities are pinpointed by the same pre-processor towards block system identification. The force and moment equilibrium equation, deformation compatibility equation and constitutive equation, are employed to establish the governing equation set for such a reinforced block system. In order to assess the reliability of a complex block system, stochastic analysis algorithms with the BEA are formulated using the approaches of the first-order second moment method and the Monte-Carlo method. Seismic analysis algorithm is implemented using a procedure similar to the dynamic FEM, in which the mass matrix, damping matrix and visco-elastic artificial boundary, are employed.

12.1 General

Pre-stress anchors, piles (or bolts), and shear keys are widely employed as reinforcement countermeasures in the stabilization for hydraulic structures. The optimal design requires a large amount of repeated computation with respect to various tentative schemes concerning the excavation procedures and reinforcement deployments. Looking for an efficient and convenient analysis toolkit is therefore of practical importance.

Modern scientific study has shown that it is more reasonable to use reliability theory in structural safety calibration than to use the normal "deterministic" methods such as strength reduction and over load (Ang and Newmark 1977). In recent decades more and more attention has been paid to the stochastic finite element method (Cambou 1975; Ghanem and Spanos 1991). The author of this book also has proposed an elastic-viscoplastic stochastic analysis algorithm based

S.-H. Chen, *Computational Geomechanics and Hydraulic Structures*,
Springer Tracts in Civil Engineering, https://doi.org/10.1007/978-981-10-8135-4_12

on the FEM, towards the reliability assessment of high rock slopes (Chen and Xiong 1990). Although it has been widely accepted that the stochastic finite element method is an powerful analysis tool in engineering practices, yet under certain circumstances its applications are strongly restricted or even unfeasible, especially when the rock mass is delimited by many large scale faults and intercalations into complicated rock block system.

Two types of methods are distinguished in the design specifications for the seismic stability analysis of hydraulic structures (Kramer 1996; Chen 2015), namely the pseudo-static method and dynamic method. The former is simple and convenient, but some important factors such as the frequency and duration of the earthquake, the dynamic and damping characteristics of the rock-like materials, and the acceleration amplification of the structure, are not fully taken into account. The latter often makes use of the finite element method (Bathe 1982; Al-Homoud and Tahtamoni 2000). Although the dynamic FEM has been prevalent in the seismic analysis for a large family of engineering structures, yet in hydraulic structures it is often encountered with difficulties in the simulation of numerous rock discontinuities (faults, joints, etc.) which need to be discretized by special elements. New solutions based on the discrete element methods have been developing fast which enable to simulate a large quantity of discontinuities (Bardet and Scott 1985). At present there are various dynamic methods available for the seismic analysis of multi-block system, of which the DEM (Cundall and Hart 1992) and the DDA (Shi 1992) are typical.

In this chapter the principle and algorithm of the BEA are further extended to cover the reinforcement analysis (Chen 1993), stochastic analysis (Chen et al. 1994), and seismic analysis (Chen et al. 2010). This is an important step towards the practical use of the BEA in hydraulic structures.

12.2 Reinforcement Analysis

12.2.1 Concept

In 1993, Chen proposed a BEA model for the reinforced rock block system. It takes the rock block as a rigid body, while the discontinuities and the reinforcement components possess elasto-viscoplastic characteristics. The governing equations are formulated by the consideration of the force and moment equilibrium conditions of rock blocks, the deformation compatibility conditions between blocks, and the elasto-viscoplastic constitutive laws of the discontinuities and the reinforcement components. This model exploits the simplicity in the relationship of force versus displacement, to describe both the shear and tensile actions of a reinforcement component.

12.2.2 Governing Equations

(1) Assumptions and nomenclatures

Use is made of the following postulations that:

- The rock blocks are rigid, but the discontinuities possess elasto-viscoplastic properties;
- The discontinuity patch $j_{rl,rm}$ on any block surface is regarded as a plane;
- The anchor cables, piles and keys are regarded as line segments;
- At the cross section of cable c or pile p, the stresses are uniformly distributed, along the width of key k, the stresses are uniformly distributed, too.

For a reinforcement component, its straight line segment is geometrically represented by

$$\begin{Bmatrix} X - X_0 \\ Y - Y_0 \\ Z - Z_0 \end{Bmatrix} = \{l\}_i t \quad (i = c, p, k) \tag{12.1}$$

The corresponding direction vector is

$$[l]_i = [\sin\phi_i \sin\theta_i \quad \cos\phi_i \sin\theta_i \quad \cos\theta_i]^T \quad (i = c, p, k) \tag{12.2}$$

where φ and θ = dip direction and dip angle of the reinforcement component, (°).

By the pre-processor towards block system identification (vide Chap. 3), the positions, and/or the intersecting points of reinforcement components with discontinuities, can be extracted in addition to the previous information concerning the position, shape and size of each block.

The nomenclatures of mechanical variables used in the deduction are listed below.

$\{\Delta U\}_{rl}$ displacement increment of block element rl;
$\{\Delta F\}_{rl}$ load increment of block element rl;
$\{\Delta\sigma\}_{j_{rl,rm}}$ stress increment on discontinuity $j_{rl,rm}$;
$\{\Delta u\}_{j_{rl,rm}}$ deformation increment on discontinuity $j_{rl,rm}$;
ΔR_c stress increment of cable c;
Δu_c deformation increment of cable c;
$\{\Delta R\}_{j_{rl,rm},p}$ internal force increments (axial and shear) of pile (or bolt) p where it penetrates discontinuity $j_{rl,rm}$;
$\{\Delta u\}_{j_{rl,rm},p}$ deformation increment of pile (or bolt) p where it penetrates discontinuity $j_{rl,rm}$;
$\{\Delta R\}_{j_{rl,rm},k}$ internal force increments (axial and shear) of key k on discontinuity $j_{rl,rm}$;
$\{\Delta u\}_{j_{rl,rm},k}$ deformation increment of key k on discontinuity $j_{rl,rm}$

(2) Force and moment equilibrium equations

Integrating stress increments on each plane $j_{rl,rm}$ of block element rl into a resultant load vector with respect to the block centroid, we get the equilibrium equation for block element rl

$$\begin{aligned}&\{\Delta F\}_{rl} - \sum_{c} [P]_c \{l\}_c \Delta R_c - \sum_{j_{rl,rm}} J(j_{rl,rm}) \sum_{p} [P]_{j_{rl,rm},p} \{\Delta R\}_{j_{rl,rm},p} \\ &- \sum_{j_{rl,rm}} J(j_{rl,rm}) \sum_{k} \int_{t_k} [P]_{j_{rl,rm},k} \{\Delta R\}_{j_{rl,rm},k} dt_k \\ &- \sum_{j_{rl,rm}} J(j_{rl,rm}) \iint_{\Gamma_{j_{rl,rm}}} [P]_{j_{rl,rm}} \{\Delta\sigma\}_{j_{rl,rm}} dx_{j_{rl,rm}} dy_{j_{rl,rm}} = 0 \\ &(rl = 1, \ldots, n_r)\end{aligned} \tag{12.3}$$

In which

$$\begin{cases} [P]_c = \begin{bmatrix} 1 & 0 & 0 \\ 0 & 1 & 0 \\ 0 & 0 & 1 \\ 0 & -(Z_c - Z_{rl}^0) & (Y_c - Y_{rl}^0) \\ (Z_c - Z_{rl}^0) & 0 & -(X_c - X_{rl}^0) \\ -(Y_c - Y_{rl}^0) & (X_c - X_{rl}^0) & 0 \end{bmatrix} \\ \{l\}_c = \begin{bmatrix} l_{xc} & l_{yc} & l_{zc} \end{bmatrix}^T \end{cases} \tag{12.4}$$

$$\begin{cases} [P]_{j_{rl,rm},p} = \begin{bmatrix} [l]_{j_{rl,rm}}^{-1} \\ [l]_{j_{rl,rm}}^{-1} [P_1]_{j_{rl,rm},p} + [P_2]_{j_{rl,rm},p} [l]_{j_{rl,rm}}^{-1} \end{bmatrix} \\ [P_1]_{j_{rl,rm},p} = \begin{bmatrix} 0 & 0 & y_{j_{rl,rm},p} \\ 0 & 0 & -x_{j_{rl,rm},p} \\ -y_{j_{rl,rm},p} & x_{j_{rl,rm},p} & 0 \end{bmatrix} \\ [P_2]_{j_{rl,rm},p} = [P_2]_{j_{rl,rm}} \end{cases} \tag{12.5}$$

$$\begin{cases} [P]_{j_{rl,rm},k} = \begin{bmatrix} [l]_{j_{rl,rm}}^{-1} \\ [l]_{j_{rl,rm}}^{-1} [P_1]_{j_{rl,rm},k} + [P_2]_{j_{rl,rm},k} [l]_{j_{rl,rm}}^{-1} \end{bmatrix} \\ [P_1]_{j_{rl,rm},k} = \begin{bmatrix} 0 & 0 & y_{j_{rl,rm},k} \\ 0 & 0 & -x_{j_{rl,rm},k} \\ -y_{j_{rl,rm},k} & x_{j_{rl,rm},k} & 0 \end{bmatrix} \\ [P_2]_{j_{rl,rm},k} = [P_2]_{j_{rl,rm}} \end{cases} \tag{12.6}$$

where $\{X\}_c = \begin{bmatrix} X_c & Y_c & Z_c \end{bmatrix}^T$ is the global coordinate of the out-laid head of anchor cable c; $\{X^0\}_{rl} = \begin{bmatrix} X_{rl}^0 & Y_{rl}^0 & Z_{rl}^0 \end{bmatrix}^T$ is the global coordinate of the centroid

of block element rl; $\{x\}_{j_{rl,rm},p}=\begin{bmatrix} x_{j_{rl,rm},p} & y_{j_{rl,rm},p}\end{bmatrix}^T$ is the local coordinate where pile p penetrates through $j_{rl,rm}$; $\{x\}_{j_{rl,rm},k}=\begin{bmatrix} x_{j_{rl,rm},k} & y_{j_{rl,rm},k}\end{bmatrix}^T$ is the local coordinate where the straight line segment representing key k that lies on $j_{rl,rm}$; the other matrices $[P]_{j_{rl,rm}}$, $[P_2]_{j_{rl,rm}}$, $[l]_{j_{rl,rm}}$ have been defined in previous Chapters [see Eqs. (2.13), (9.13) and (9.15)].

(3) Deformation compatibility equations

In addition to the deformation increments $\{\Delta u\}_{j_{rl,rm}}$ on discontinuity $j_{rl,rm}$, the block displacement increments of rl and rm will lead to the deformation increments Δu_c in anchor cable c whose out-laid head is at block element rl, as well as $\{\Delta u\}_{j_{rl,rm},p}$ and $\{\Delta u\}_{j_{rl,rm},k}$ if a pile p or key k penetrates or lies on $j_{rl,rm}$.

By kinematics principles, the relationships between foregoing deformations and displacements can be established as

$$\begin{cases} \Delta\varepsilon_c = \{l\}_c^T[M]_c\{\Delta U\}_{rl} \\ \{\Delta u\}_{j_{rl,rm},p}= J(j_{rl,rm})[l]_{j_{rl,rm}}\left([M]_{rl,p}\{\Delta U\}_{rl} - [M]_{rm,p}\{\Delta U\}_{rm}\right) \\ \{\Delta u\}_{j_{rl,rm},k}= J(j_{rl,rm})[l]_{j_{rl,rm}}\left([M]_{rl,k}\{\Delta U\}_{rl} - [M]_{rm,k}\{\Delta U\}_{rm}\right) \\ \{\Delta u\}_{j_{rl,rm}}= J(j_{rl,rm})[l]_{j_{rl,rm}}\left([M]_{rl}\{\Delta U\}_{rl} - [M]_{rm}\{\Delta U\}_{rm}\right) \end{cases} \tag{12.7}$$

In which

$$[M]_c = \frac{1}{L_c}\begin{bmatrix} 1 & 0 & 0 & 0 & (Z_c - Z_{rl}^0) & -(Y_c - Y_{rl}^0) \\ 0 & 1 & 0 & -(Z_c - Z_{rl}^0) & 0 & (X_c - X_{rl}^0) \\ 0 & 0 & 1 & (Y_c - Y_{rl}^0) & -(X_c - X_{rl}^0) & 0 \end{bmatrix} \tag{12.8}$$

where L_c = length of anchor cable c

$$\begin{cases} [M]_{rl,p} = \begin{bmatrix} 1 & 0 & 0 & 0 & (Z - Z_{rl}^0) & -(Y - Y_{rl}^0) \\ 0 & 1 & 0 & -(Z - Z_{rl}^0) & 0 & (X - X_{rl}^0) \\ 0 & 0 & 1 & (Y - Y_{rl}^0) & -(X - X_{rl}^0) & 0 \end{bmatrix} \\ \begin{Bmatrix} X \\ Y \\ Z \end{Bmatrix} = [l]_{j_{rl,rm}}^{-1}\{x\}_{j_{rl,rm},p} + \{X^0\}_{rl} \end{cases} \tag{12.9}$$

$$\begin{cases} [M]_{rm,p} = \begin{bmatrix} 1 & 0 & 0 & 0 & (Z - Z_{rm}^0) & -(Y - Y_{rm}^0) \\ 0 & 1 & 0 & -(Z - Z_{rm}^0) & 0 & (X - X_{rm}^0) \\ 0 & 0 & 1 & (Y - Y_{rm}^0) & (X - X_{rm}^0) & 0 \end{bmatrix} \\ \begin{Bmatrix} X \\ Y \\ Z \end{Bmatrix} = [l]_{j_{rl,rm}}^{-1}\{x\}_{j_{rl,rm},p} + \{X^0\}_{rm} \end{cases} \tag{12.10}$$

$$\begin{cases} [M]_{rl,k} = \begin{bmatrix} 1 & 0 & 0 & 0 & (Z-Z_{rl}^0) & -(Y-Y_{rl}^0) \\ 0 & 1 & 0 & -(Z-Z_{rl}^0) & 0 & (X-X_{rl}^0) \\ 0 & 0 & 1 & (Y-Y_{rl}^0) & -(X-X_{rl}^0) & 0 \end{bmatrix} \\ \begin{Bmatrix} X \\ Y \\ Z \end{Bmatrix} = [l]_{j_{rl,rm}}^{-1} \{x\}_{j_{rl,rm},k} + \{X^0\}_{rl} \end{cases} \tag{12.11}$$

$$\begin{cases} [M]_{rm,k} = \begin{bmatrix} 1 & 0 & 0 & 0 & (Z-Z_{rm}^0) & -(Y-Y_{rm}^0) \\ 0 & 1 & 0 & -(Z-Z_{rm}^0) & 0 & (X-X_{rm}^0) \\ 0 & 0 & 1 & (Y-Y_{rm}^0) & -(X-X_{rm}^0) & 0 \end{bmatrix} \\ \begin{Bmatrix} X \\ Y \\ Z \end{Bmatrix} = [l]_{j_{rl,rm}}^{-1} \{x\}_{j_{rl,rm},k} + \{X^0\}_{rm} \end{cases} \tag{12.12}$$

The other matrices $[M]_{rl}$, $[M]_{rm}$ and $[l]_{j_{rl,rm}}$ have been defined in previous Chapters (see Eqs. (2.13), (9.17) and (9.18)).

(4) Constitutive equations

According to the potential theory of viscoplasticity, if an explicit time stepping scheme is employed, the deformation and stress increments will observe the following constitutive relations.

– At any point $\left(x_{j_{rl,rm}} \quad y_{j_{rl,rm}}\right)$ on discontinuity $j_{rl,rm}$

$$\begin{cases} \{\Delta\sigma\}_{j_{rl,rm}} = [D]_{j_{rl,rm}} \{\Delta u\}_{j_{rl,rm}} - \{\Delta\sigma^{vp}\}_{j_{rl,rm}} \\ [D]_{j_{rl,rm}} = \begin{bmatrix} k_s & 0 & 0 \\ 0 & k_s & 0 \\ 0 & 0 & k_n \end{bmatrix} \\ \{\Delta\sigma^{vp}\}_{j_{rl,rm}} = \gamma_{j_{rl,rm}} < F_{j_{rl,rm}} > [D]_{j_{rl,rm}} \left\{ \frac{\partial F_{j_{rl,rm}}}{\partial \{\sigma\}_{j_{rl,rm}}} \right\} \Delta t \\ F_{j_{rl,rm}} = \left(\tau_{zx}^2 + \tau_{yz}^2\right)^{1/2} + \sigma_z tg\, \varphi_{j_{rl,rm}} - c_{j_{rl,rm}} \quad for \quad \sigma_z - \sigma_{T_{j_{rl,rm}}} < 0 \\ F_{j_{rl,rm}} = (\tau_{zx}^2 + \tau_{yz}^2 + \sigma_z^2)^{1/2} \quad for \quad \sigma_z - \sigma_{T_{j_{rl,rm}}} \geq 0 \end{cases} \tag{12.13}$$

– For anchor cable c whose out-laid head being located on block element rl

$$\begin{cases} \Delta R_c = A_c E_c \Delta\varepsilon_c - \Delta R_c^{vp} \\ \Delta R_c^{vp} = A_c E_c < F_c > \gamma_c \Delta t \\ F_c = R_c - A_c \sigma_c \end{cases} \tag{12.14}$$

– For pile p penetrating discontinuity j_{rlrm}

$$\begin{cases} \{\Delta R\}_{j_{rl,rm},p} = [D]_{j_{rl,rm},p}\{\Delta u\}_{j_{rl,rm},p} + \{\Delta R^{vp}\}_{j_{rl,rm},p} \\ [D]_{j_{rl,rm},p} = \frac{A_p}{a_{j_{rl,rm}} \cos\beta_p} \begin{bmatrix} G_p & 0 & 0 \\ 0 & G_p & 0 \\ 0 & 0 & E_p \end{bmatrix} \\ \{\Delta R^{vp}\}_{j_{rl,rm},p} = \gamma_p < F_{j_{rl,rm},p} > [D]_{j_{rl,rm},p} \left\{ \frac{\partial F_{j_{rl,rm},p}}{\partial \{R\}_{j_{rl,rm},p}} \right\} \Delta t \\ F_{j_{rl,rm},p} = (R_{zx,p}^2 + R_{zy,p}^2)^{1/2} + R_{z,p} tg\, \varphi_p - c_p A_p / \cos\beta_p \quad for \quad R_{z,p} - \sigma_p A_p / \cos\beta_p < 0 \\ F_{j_{rl,rm},p} = (R_{zx,p}^2 + R_{zy,p}^2 + R_{z,p}^2)^{1/2} \quad for \quad R_{z,p} - \sigma_p A_p / \cos\beta_p \geq 0 \end{cases} \tag{12.15}$$

– For key k located on the discontinuity plane $j_{rl,rm}$

$$\begin{cases} \{\Delta R\}_{j_{rl,rm},k} = [D]_{j_{rl,rm},k}\{\Delta u\}_{j_{rl,rm},k} - \{\Delta R^{vp}\}_{j_{rl,rm},k} \\ [D]_{j_{rl,rm},k} = \frac{B_k}{a_{j_{rl,rm}}} \begin{bmatrix} G_k & 0 & 0 \\ 0 & G_k & 0 \\ 0 & 0 & E_k \end{bmatrix} \\ \{\Delta R^{vp}\}_{j_{rl,rm},k} = \gamma_k < F_{j_{rl,rm},k} > [D]_{j_{rl,rm},k} \left\{ \frac{\partial F_{j_{rl,rm},k}}{\partial \{R\}_{j_{rl,rm},k}} \right\} \Delta t \\ F_{j_{rl,rm},k} = (R_{zx,k}^2 + R_{zy,k}^2)^{1/2} + R_{z,k} tg\, \varphi_k - c_k B_k \quad for \quad R_{z,k} - \sigma_k B_k < 0 \\ F_{j_{rl,rm},k} = (R_{zx,k}^2 + R_{zy,k}^2 + R_{z,k}^2)^{1/2} \quad for \quad R_{z,k} - \sigma_k B_k \geq 0 \end{cases} \tag{12.16}$$

Where $\gamma_{j_{rl,rm}}$, γ_c, γ_p and γ_k = fluidity parameters; $\sigma_{Tj_{rl,rm}}$, σ_a, σ_p and σ_R = tensile strengths; $\varphi_{j_{rl,rm}}$, φ_p and φ_k = friction angles; $c_{j_{rl,rm}}$, c_p and c_k = cohesions; k_n, k_s = normal and tangential stiffness coefficients; E_c, G_p, E_p, G_k and E_k = elastic moduli; A_c and A_p = cross sectional areas of cable c and pile p; B_k = width of key k; β_p = included angle of pile p and outward normal of discontinuity $j_{rl,rm}$; $a_{j_{rl,rm}}$ = mechanical aperture of discontinuity $j_{rl,rm}$.

12.2.3 Equilibrium Equation of Reinforced Block System

Introducing Eqs. (12.13)–(12.16) into Eq. (12.3), then use is made of Eq. (12.7), we obtain

$$[K]_{rl,rl}\{\Delta U\}_{rl} + \sum [K]_{rl,rm}\{\Delta U\}_{rm} = \{\Delta F\}_{rl} + \{\Delta F^{vp}\}_{rl} \quad (rl = 1, 2, \ldots, n_r) \tag{12.17}$$

In which

$$\begin{cases} [K]_{rl,rl} = \sum\limits_{j_{rl,rm}} \iint\limits_{\Gamma_{j_{rl,rm}}} [P]_{j_{rl,rm}} [D]_{j_{rl,rm}} [l]_{j_{rl,rm}} [M]_{rl} dx_{j_{rl,rm}} dy_{j_{rl,rm}} + \sum\limits_{c} A_c E_c [P]_c \{l\}_c \{l\}_c^T [M]_c \\ \qquad + \sum\limits_{j_{rl,rm}} \sum\limits_{p} [P]_{j_{rl,rm},p} [D]_{j_{rl,rm},p} [l]_{j_{rl,rm}} [M]_{rl,p} + \sum\limits_{j_{rl,rm}} \sum\limits_{k} \int\limits_{t_k} [P]_{j_{rl,rm},k} [D]_{j_{rl,rm},k} [l]_{j_{rl,rm}} [M]_{rl,k} dt_k \\ [K]_{rl,rm} = - \iint\limits_{\Gamma_{j_{rl,rm}}} [P]_{j_{rl,rm}} [D]_{j_{rl,rm}} [l]_{j_{rl,rm}} [M]_{rm} dx_{j_{rl,rm}} dy_{j_{rl,rm}} \\ \qquad - \sum\limits_{p} [P]_{j_{rl,rm},p} [D]_{j_{rl,rm},p} [l]_{j_{rl,rm}} [M]_{rm,p} - \sum\limits_{k} \int\limits_{t_k} [P]_{j_{rl,rm},k} [D]_{j_{rl,rm},k} [l]_{j_{rl,rm}} [M]_{rm,k} dt_k \\ \{\Delta F^{vp}\}_{rl} = \sum\limits_{j_{rl,rm}} J(j_{rl,rm}) \iint\limits_{\Gamma_{j_{rl,rm}}} [P]_{j_{rl,rm}} \{\Delta\sigma^{vp}\}_{j_{rl,rm}} dx_{j_{rl,rm}} dy_{j_{rl,rm}} + \sum\limits_{c} [P]_c \{l\}_c \Delta R_c^{vp} \\ \qquad + \sum\limits_{j_{rl,rm}} J(j_{rl,rm}) \sum\limits_{p} [P]_{j_{rl,rm},p} \{\Delta R^{vp}\}_{j_{rl,rm},p} + \sum\limits_{j_{rl,rm}} J(j_{rl,rm}) \sum\limits_{k} \int\limits_{t_k} [P]_{j_{rl,rm},k} \{\Delta R^{vp}\}_{j_{rl,rm},k} dt_k \end{cases} \tag{12.18}$$

For the other blocks there also exist similar foregoing equations. Assemble all of the equations corresponding to the blocks in the reinforced block system, the equilibrium equation set is finally established as

$$[K]\{\Delta U\} = \{\Delta F\} + \{\Delta F^{vp}\} \tag{12.19}$$

In which $\{\Delta U\} = \left[\{\Delta U\}_1^T \ldots \{\Delta U\}_{rl}^T \ldots \{\Delta U\}_{n_r}^T\right]^T$, $\{\Delta F\} = \left[\{\Delta F\}_1^T \ldots \{\Delta F\}_{rl}^T \ldots \{\Delta F\}_{n_r}^T\right]^T$ and $\{\Delta F^{vp}\} = \left[\{\Delta F^{vp}\}_1^T \ldots \{\Delta F^{vp}\}_{rl}^T \ldots \{\Delta F^{vp}\}_{n_r}^T\right]^T$ are the vectors of displacement increment, load increment, and viscoplastic equivalent force increment of the block system, respectively.

12.3 Stochastic Analysis

12.3.1 Concept

In practical engineering, the actual values of design parameters are always affected by a certain degree of uncertainty (Ayyub and Klir 2006). The ability to incorporate non-deterministic properties in computation is hence of great importance in order to allow for realistic reliability assessment of engineering structures.

In most areas related to civil and hydraulic engineering, probability theory is prevalent to handle uncertainties affecting design parameters, and structural reliability is defined as the probable ability of a structure to complete its designed

functions under definite period and working conditions. The structural performance may be treated in probabilistic terms by means of limit state function (LSF) with regard to the most important uncertainties—the basic random variables.

A limit state of a structure entails its loads at which the structure is just on the verge of failing to undertake the intended function, which is given by a set of values of the input random variables

$$Z = g(p_1, p_2, \ldots, p_n) = 0 \tag{12.20}$$

Where Z and $g(\cdot)$ = function of structure (state function); $p_i (i = 1, 2, \ldots, n)$ = random variables that independently contribute to the mathematical model concerning geometry, strength properties and actions.

A LSF is actually the boundary of reliable and unreliable of the structure concerned. It divides the domain of the design model in three sets of safe, limit state and unsafe. Limit state may be distinguished as failure events (collapse) and serviceability deterioration.

The structural reliability P_s with respect to a LSF is defined by

$$P_s = P\{Z \geq 0\} \tag{12.21}$$

Since the cases $\{Z \geq 0\}$ and $\{Z < 0\}$ are complementary, therefore the failure probability P_f is calculated accordingly by

$$P_f = P\{Z < 0\} = 1 - P\{Z \geq 0\} = 1 - P_s \tag{12.22}$$

Equation (12.22) indicates that larger P_f leads to smaller reliability P_s and vice versa. Therefore, the failure probability P_f is customarily employed to gauge the reliability of structures.

Suppose $f_{p_1 p_2 \ldots p_n}(p_1, p_2, \ldots, p_n)$ is the joint probability density function (PDF) of the Z dependent on the random variables $(p_1, p_2, \ldots, p_n)$, then the probability of failure P_f may be determined in terms of

$$P_f = \iiint f_{p_1 p_2 \ldots p_n}(p_1, p_2, \ldots, p_n) \mathrm{d}p_1 \mathrm{d}p_2 \ldots \mathrm{d}p_n \tag{12.23}$$

This integral formula is, however, non-trivial to solve except few cases (e.g. linear LSF and normal distributed variables). Therefore numerical approximations are expedient.

Another commonly employed quantification index—reliability index β, has a simple geometrical interpretation defined as the shortest distance from the origin to the plane (or the hypersurface) forming the boundary between the safe domain and the failure domain. The point on the failure surface with the shortest distance to the origin is commonly termed as the "design point" or "most likely failure point". Where the basic random variables $(p_1, p_2, \ldots, p_n)$ are not independent or not

normally distributed, the function Z is no longer in linear form, and β may only be calculated approximately (e.g. the JC method or design point method) (Zhao and Jin 2000).

In order to assess the reliability of a complex hydraulic structure, the use of numerical integral methods is inevitable because the closed-form solution for the integration of failure probability P_f is seldom accessible. One of the well-known methods for estimating P_f defined in Eq. (12.23) is the Monte-Carlo simulation (MCS) method directly using Eqs. (12.20)–(12.22) (Bjerager 1988), which needs very large amount of evaluations of the LSF defined Eq. (12.20). Since each evaluation is accomplished through a numerical computation using, for example, the FEM or BEA, hence the computational effort will be tremendous with large-scale structures. Another well-known method, namely the first-order reliability method (FORM) (Hasofer and Lind 1974; Rackwitz and Fiessler 1978) also demands a large computation effort, although much more acceptable, when a large number of random variables is involved. In order to alleviate the computational burden, it is more and more prevalent to use a response surface function (RSF) as a surrogate model to approach the LSF (Bucher and Bourgund 1990; Zhao and Qiu 2013).

Another obstacle arise from the applicability of probabilistic approach in hydraulic structures is that available data are normally insufficient or ambiguous, vague or imprecise, to define $f_{p_1,p_2,\ldots,p_n}(p_1, p_2, \ldots, p_n)$ (Moens and Vandepitte 2005). Under such circumstances, uncertainties may be handled using alternative approaches based on non-probabilistic concepts, such as convex models, fuzzy-set theory, interval model, etc. (Elishakoff and Ohsaki 2010; Moens and Hanss 2011; Corotis 2015; Sofi et al. 2015). Since the mid 1990s, the interval model originated from the classical interval analysis (CIA) (Moore 1966) representing the uncertain parameters as interval variables with given lower bound (LB) and upper bound (UB), has been applied in finite element analysis giving rise to the so-called Interval Finite Element Method (IFEM). It can be applied in cases where it is not possible to access reliable probabilistic characteristics of the structure (Rao and Berke 1997; Chen et al. 2002).

The "target reliability" (or design reliability) stipulated in (GB50199-94) "Unified design standard for reliability of hydraulic engineering structures"—the complement of the maximum permissible failure probability, should depend foremost on the measurable consequences of failure in question, which are the injury or loss of life, the direct and indirect economic losses (including repair/replacement expenditures, loss of revenue, compensation for damages, etc.), the environmental pollution and so on. Target reliabilities also should depend on the algorithm of reliability analysis, on the types of uncertainties considered in the analysis, and on the strategies of future maintenance. Due to the difficulties with complicated analysis and insufficient statistics, the "code calibration" is normally employed to evaluate target reliability level, which is determined by the calibration for existing practices (i.e. on existing codes), assuming that these existing practices are optimal. Hydraulic structures such as dams, tunnels, spillways, and cut slopes, that have a history of successful service, can be deemed sufficiently safe, and their reliability levels may be used as the targets for new structures of the same kind.

As a phase of the research activities, stochastic analysis algorithms on the base of the BEA were formulated by the author. These were achieved in two approaches, namely the first-order second moment method and the Monte-Carlo method (Chen et al. 1994).

12.3.2 First-Order Second Moment Method

In the structural reliability theory, the limit state function (LSF) g is generally defined as the difference between the resistance R and the load effect S. The limit state equation entails the case when g is equal to zero

$$g = R - S \tag{12.24}$$

The LSF g must be the function of the N random variables $\{p\} = \{p_1, p_2, \ldots, p_N\}$ which influence the reliability of the structure, i.e.

$$g = g(p_1, \ldots, p_N) \tag{12.25}$$

Transforming all the random variables into standardized form $N(0, 1)$ (normal distribution with zero mean and unit variance) denoted as $\{q_1, q_2, \ldots, q_N\}$, the limit state equation can be interpreted in the N-dimensional space of standardized variables as a hypersurface, the safety index β is then defined as the shortest distance from the origin to this hypersurface

$$\beta = \min. \sqrt{\sum_{i}^{N} q_i^2} \tag{12.26}$$

and the point $\{q_1^*, q_2^*, \ldots, q_N^*\}$ at which β achieves minimum is termed as the "checking point" or "design point".

Since the first-order Taylor series expansion of $g(p_1, \ldots, p_N)$ is adopted for the iteration of the checking point and safety index, and only the means and standard deviations of the random variables are considered, the method gets its name with "first-order second moment".

(1) Random variables

Random variables can be arranged into a vector $\{p\}$

$$\{p\} = [p_1 \ldots p_N]^T \tag{12.27}$$

In which N is the amount of random variables. The mean and variance of $\{p\}$ are

$$\begin{cases} E\{p\} = \{\bar{p}\} = [\bar{p}_1 \ldots \bar{p}_N]^T \\ Var[p] = [Cov(p_{n1}, p_{n2})] \end{cases} \tag{12.28}$$

Following six random variables for discontinuity $j_{rl,rm}$ are considered in our study

$$\begin{cases} p_{6(j_{rl,rm}-1)+1} = k_n \\ p_{6(j_{rl,rm}-1)+2} = k_s \\ p_{6(j_{rl,rm}-1)+3} = c \\ p_{6(j_{rl,rm}-1)+4} = tg\,\varphi \\ p_{6(j_{rl,rm}-1)+5} = \phi \\ p_{6(j_{rl,rm}-1)+6} = \theta \end{cases} \tag{12.29}$$

In fact, external loads are also random variables, but we do not consider their variation at the moment.

The random variables should be normalized at the "checking point" firstly at any iteration step. We keep to denote the normalized random vector using $\{p\}$, and the Cholesky decomposition of a symmetric positive definite $Var[p]$ is made as

$$\begin{cases} Var[p] = [H][H]^T \\ [H] = \begin{bmatrix} h_{11} & \dots & h_{1N} \\ & h_{22} & \dots \\ & & \dots \\ Sym & & h_{NN} \end{bmatrix} \end{cases} \tag{12.30}$$

In which h_{nn} is the standard deviation of the normalized random variable p_n. In this manner the former normalized random vector $\{p\}$ becomes the function of the standardized random vector $\{q\}$

$$\{p\} = [H]\{q\} + E\{p\} \tag{12.31}$$

If we further postulate that all random variables are independent then we will have

$$h_{n1n2} = 0 \quad (n1 \neq n2) \tag{12.32}$$

Under such circumstances, the stochastic algorithm will be simplified greatly.

(2) Limit state function

There are different LSFs according to different failure mechanisms under consideration. If we are focused on the sliding failure of the block system, the LSF will be constructed by the difference of the shear strength against sliding to the driving shear force on the slip planes.

We define a failure mode as a block or block combination sliding along a discontinuity plane or the intersecting line of two discontinuity planes. There will be many failure modes if the amount of blocks is large, and for each failure mode there is a corresponding LSF.

Since it is time consuming and unnecessary to consider all the existing failure modes one by one, deterministic BEA with means of parameters is carried out

firstly to search main failure modes. This is similar to a lower level reliability testing (Ben-Gal et al. 2002) in advance intended to preliminarily estimate failure modes and their probability.

Suppose a main failure mode m is delimited by n_m discontinuity planes, on $j_{rl,rm}$ the resistance to sliding $R_{j_{rl,rm}}$ and the driving shear force $S_{j_{rl,rm}}$ are calculated by the formulas

$$\begin{cases} R_{j_{rl,rm}} = \iint\limits_{\Gamma_{j_{rl,rm}}} CS_{j_{rl,rm}}(c_{j_{rl,rm}} - tg\,\varphi_{j_{rl,rm}}\sigma_z)dx_{j_{rl,rm}}dy_{j_{rl,rm}} \\ S_{j_{rl,rm}} = \iint\limits_{\Gamma_{j_{rl,rm}}} CS_{j_{rl,rm}}\sqrt{\tau_{zx}^2 + \tau_{zy}^2}dx_{j_{rl,rm}}dy_{j_{rl,rm}} \end{cases} \tag{12.33}$$

In which $CS_{j_{rl,rm}} = \cos\,\alpha_{j_{rl,rm}}$, where $\alpha_{j_{rl,rm}}$ is the included angle between the slip direction and the resultant shear force on discontinuity plane $j_{rl,rm}$. The LSF of the main failure mode m therefore can be defined as

$$g_m = \sum_{j_{rl,rm}=1}^{n_m} DIF_{j_{rl,rm}} \tag{12.34}$$

In which

$$DIF_{j_{rl,rm}} = \iint\limits_{\Gamma_{j_{rl,rm}}} CS_{j_{rl,rm}}\left(c_{j_{rl,rm}} - tg\varphi_{j_{rl,rm}}\sigma_z - \sqrt{\tau_{zx}^2 + \tau_{zy}^2}\right)dx_{j_{rl,rm}}dy_{j_{rl,rm}} \tag{12.35}$$

(3) Stochastic algorithm

The LSF in Eq. (12.34) is an implicit function of random vector $\{p\}$ because the stresses σ_z, τ_{zx} and τ_{zy} are all the functions of the random vector. Taken into account of Eq. (12.31), g_m can be further expressed as the function of the vector $\{q\}$

$$g_m = G_m(E\{p\} + [H]\{q\}) \tag{12.36}$$

Denote

$$a_n = \frac{\partial G_m}{\partial q_n}\Big|_{\{q\}=\{q^*\}} = \frac{\partial g_m}{\partial p_n}h_{nn}\Big|_{\{p\}=E\{p\}+[H]\{q^*\}} \tag{12.37}$$

If $\{q^*\}^i$ is the ith iterative value of the checking point, the Lagrangian multiplier method for the minimum value of function will lead to the following well-known iterative algorithm for calculating $\{q^*\}^{i+1}$ (Melchers 1987; Provan 1987).

$$\{q^*\}^{i+1} = \frac{(\{q^*\}^i)^T\{a\}^i - G(\{q^*\}^i)}{(\{a\}^i)^T\{a\}^i}\{a\}^i \tag{12.38}$$

The safety index at any iterative step for the main failure mode m is given by

$$\beta^{i+1} = \sqrt{(\{q^*\}^{i+1})^T \{q^*\}^{i+1}} \tag{12.39}$$

From Eqs. (12.38)–(12.39) it can be seen that for each iteration step the key difficulty lies in the calculation for the derivates of the LSF to the random variables

$$\begin{aligned}\frac{\partial g_m}{\partial p_n} = \sum_{j_{rl,rm}}^{n_m} \iint_{\Gamma_{j_{rl,rm}}} [&\frac{\partial CS_{j_{rl,rm}}}{\partial p_n}\left(c_{j_{rl,rm}} - tg\,\varphi_{j_{rl,rm}}\sigma_z - \sqrt{\tau_{zx}^2 + \tau_{zy}^2}\right) \\ &+ CS_{j_{rl,rm}}(\frac{\partial c_{j_{rl,rm}}}{\partial p_n} - \frac{\partial tg\varphi_{j_{rl,rm}}}{\partial p_n}\sigma_z - tg\varphi_{j_{rl,rm}}\frac{\partial \sigma_z}{\partial p_n} \\ &- \frac{\frac{\partial \tau_{zx}}{\partial p_n}\tau_{zx} + \frac{\partial \tau_{zy}}{\partial p_n}\tau_{zy}}{\sqrt{\tau_{zx}^2 + \tau_{zy}^2}})]dx_{j_{rl,rm}}dy_{j_{rl,rm}}\end{aligned} \tag{12.40}$$

In which the derivates of stresses are given by the accumulation of the derivates of stress increments. From the constitutive relation Eq. (2.126) it can be directly written

$$\frac{\partial\{\Delta\sigma\}_{j_{rl,rm}}}{\partial p_n} = \frac{\partial[D]_{j_{rl,rm}}}{\partial p_n}\{\Delta u\}_{j_{rl,rm}} + [D]_{j_{rl,rm}}\frac{\partial\{\Delta u\}_{j_{rl,rm}}}{\partial p_n} - \frac{\partial\{\Delta\sigma^{vp}\}_{j_{rl,rm}}}{\partial p_n} \tag{12.41}$$

However, to get the derivate items on the right-hand side would be proved the rather cumbersome work. For detailed expression our readers are referred to the literature (Chen et al. 1994).

12.3.3 Monte-Carlo Method

It is essential to reproduce random vectors in Monte-Carlo method. There are various methods of random vector production, and the problem will be simplified if all random variables observe normal distribution, under such circumstances we can use computer produced pseudo-random number series to simulate random vector easily.

The first step is to get the uniform distributed random number series $\{r\}$ on the region (0, 1), statistics test must be carried out to check the independence and uniformity of these pseudo-random number series. The random number series $\{q_{2n}\}$ calculated by the following formulas observes $N(0,1)$ distribution

$$\begin{cases} q_{2n-1} = \sqrt{(-2\,\ln r_{2n-1})}\cos(2\pi r_{2n}) \\ q_{2n} = \sqrt{(-2\,\ln r_{2n-1})}\sin(2\pi r_{2n}) \end{cases} \tag{12.42}$$

After the covariance matrix $Var[p]$ has be resolved into the multiplication of triangle matrix, the sample of random vector $\{p\}$ are calculated by Eq. (12.31).

For each stochastic simulation with a sample of vector $\{p\}$ given in Eq. (12.31), we firstly analyze the block system with the conventional BEA to get the stress and deformation state on the discontinuities, then use is made of Eq. (12.34) to calculate the value of LSF (g_m) of each failure mode m to assess its stability. Suppose that the amount of simulation is N_t, and the failure of block system occurs N_f times, the failure probability will be

$$P_f = N_f/N_t \tag{12.43}$$

The amount of simulation must satisfy

$$N_t > 100/P_f \tag{12.44}$$

From the failure probability P_f the safety index β is easily obtained.

12.3.4 Verifications and Applications

(1) Single rock wedge in slope

The rock wedge in Fig. 9.1 is delimited by four boundary planes inclusive two faults F_1 and F_2 and two exposure surfaces S_1 and S_2. We choose the lower intersecting point of the F_1 and F_2 as the origin of global coordinate system, the means of parameters adopted in the calculation are listed in Table 12.1, the coefficients of variation are listed in Table 12.2, and the calculated results are displayed in Table 12.3.

Table 12.1 Means of parameters

Parameter		F_1	F_2	S_1	S_2
Strike direction (°)		SW210.6	SE161.1	NE90.0	NE90.0
Dip angle (°)		35.6	48.3	10.0	60.0
Stiffness (MN/m^3)	k_n	1138.0	1897.0	–	–
	k_s	379.0	632.0	–	–
Strength	c (kPa)	20.0	20.0	–	–
	φ (°)	20.0	25.0	–	–
	σ_T (kPa)	0.0	0.0	–	–

Table 12.2 Coefficients of variation of parameters

Fault	Strike direction	Dip angle	Stiffness		Strength	
			k_n	k_s	$f = tg\varphi$	c
F_1	0.095	0.281	0.5	0.5	0.2	0.5
F_2	0.124	0.207	0.5	0.5	0.2	0.5

Table 12.3 Failure probability and safety index of the wedge

Method	Monte-Carlo	First-order second moment
P_f	0.149	0.1611
β	1.075	0.99

(2) Multi-block system in slope

The slope located at the downstream left abutment of Baozhusi Gravity Dam (vide Sect. 9.5, Chap. 9) has been studied, its block system considered in the stochastic analysis is shown in Figs. 9.12 and 9.13. Only the variation in the strength parameters of discontinuities is taken into account whose means and coefficients of variation are listed in Tables 12.4 and 12.5.

Both the first-order second moment method and the Monte-Carlo method are exercised for the calibration of this slope. The calculated results are presented in Table 12.6.

Table 12.4 Means of parameters

Parameter		D_1	D_3	F_4	F_{10}	f_{10}
Strike direction (°)		70.0	70.0	15.0	60.0	145.0
Dip angle (°)		SE28.5	SE33.0	NW59.5	NW56.0	SW84.0
Stiffness (MN/m^3)	k_n	22.4	15.0	29.9	9.11	150.0
	k_s	6.41	4.27	8.55	2.6	42.7
Strength	c (kPa)	10.0	10.0	0.0	20.0	0.0
	φ (°)	14.0	14.0	16.7	24.2	16.7
	σ_T (kPa)	1.0	1.0	0.0	2.0	0.0
Volumetric weight of rock γ_r = 26.4 kN/m^3						

Table 12.5 Coefficients of variation of parameters

Parameter	F_4	F_{10}	D_1	D_3
$f = tg\,\varphi$	0.2	0.2	0.2	0.2
c	0.5	0.5	0.5	0.5

Table 12.6 Failure probability and safety index of the slope

Main failure mode	Monte-Carlo		First-order second moment	
	P_f	β	P_f	β
Block 1 + Block 3	0.123	1.16	0.142	1.07
Block 1 + Block 2 + Block 3 + Block 4	0.149	1.04	0.171	0.95
Whole system	0.181	0.91	$0.289 > P_f > 0.171$	$0.95 > \beta > 0.557$

12.3.5 Remarks

As for the comparison between the first-order second moment method and the Monte-Carlo method elaborated in this section, the following points are worthwhile to make that

- The Monte-Carlo method is theoretically a precise method but the first-order second moment method is only an approximate one. In addition, the Monte-Carlo method can calculate not only the safety index of each main failure mode but also that of the whole block system. On the contrary, the first order second moment method can only give some upper and lower bounds with respect to the safety index of the whole block system if there are more than one failure modes appearing in the block system.
- The Monte-Carlo method requires a huge amount of random simulation, particularly where the failure probability is small [see Eq. (12.44)]. For each simulation an elastic-viscoplastic BEA should be undertaken so that the computation time could be extraordinarily long, in some cases it is actually unfeasible for large block system. In contrast, the iteration effort for the checking point in the first-order second moment method is relatively smaller, therefore it is a more feasible tool in solving the problem of large block system with small failure probability.
- Towards the solution of structural system reliability, a promising comprise between the Monte-Carlo method and the first-order second moment method may be achieved by the application of the Bayesian networks (BN) (Pearl 1988; Torres-Toledano and Sucar 1998; Mahadevan et al. 2001) which is a probabilistic directed acyclic graphical model (a type of statistical model) that represents a set of random variables and their conditional dependencies via a directed acyclic graph (DAG).
- At present, we may use the Monte-Carlo method as a standard "benchmark" to check the accuracy of other approximate methods under study.

12.4 Seismic Analysis

12.4.1 Governing Equations

Suppose the block elements are rigid bodies and discontinuities are elastic interlayers, and for the time being the damping is not taken into account. The coordinate system and the deformation compatibility equation as well as constitutive equation are all identical to that in Chap. 9. Only the force and moment equilibrium equation is changed by taking the inertia of block element into account, namely Eq. (9.11) is replaced by

$$\iiint_{\Omega_{rl}} [M]_{rl}^T \{p_i\}_{rl} d\,\Omega + \sum_{j_{rl,rm}} J(j_{rl,rm}) \iint_{\Gamma_{rl,rm}} [P]_{j_{rl,rm}} \{\sigma\}_{j_{rl,rm}} dx_{j_{rl,rm}} dy_{j_{rl,rm}} = \{F(t)\}_{rl}$$

$$(rl = 1, 2, \ldots, n_r) \tag{12.45}$$

In which n_r is the amount of block elements, $\{F(t)\}_{rl}$ is the external load acting at the centroid of block element rl, $\{p_i\}_{rl}$ is the volumetric inertia acting at the centroid of block element rl

$$\{p_i\}_{rl} = -\rho [M]_{rl} \frac{\partial^2 \{U\}_{rl}}{\partial t^2} \tag{12.46}$$

Introducing Eqs. (2.126), (9.16) and (12.46) into Eq. (12.45), the dynamic equilibrium equation of block element rl becomes

$$[m]_{rl} \{\ddot{U}\}_{rl} + [K]_{rl,rl} \{U\}_{rl} + \sum_{rm} [K]_{rl,rm} \{U\}_{rm} = \{F(t)\}_{rl} \quad (rl = 1, 2, \ldots, n_r) \tag{12.47}$$

Where rm runs over all the adjoin block elements around block element rl in corresponding to discontinuity plane $j_{rl,rm}$, and

$$\begin{cases} [K]_{rl,rl} = \sum_{j_{rl,rm}} \iint_{\Gamma_{j_{rl,rm}}} [P]_{j_{rl,rm}} [D]_{j_{rl,rm}} [l]_{j_{rl,rm}} [M]_{rl} dx_{j_{rl,rm}} dy_{j_{rl,rm}} \\ [K]_{rl,rm} = -\iint_{\Gamma_{j_{rl,rm}}} [P]_{j_{rl,rm}} [D]_{j_{rl,rm}} [l]_{j_{rl,rm}} [M]_{rm} dx_{j_{rl,rm}} dy_{j_{rl,rm}} \end{cases} \tag{12.48}$$

$$[m]_{rl} = \iiint_{\Omega_{rl}} [M]_{rl}^T \rho [M]_{rl} d\,\Omega \tag{12.49}$$

Assemble all the block elements governed by Eq. (12.47) in a similar way to the dynamic FEM, the dynamic governing equation set of the elastic block system without damping is formulated as

$$[M]\{\ddot{U}\} + [K]\{U\} = \{F(t)\} \tag{12.50}$$

In which $\{\ddot{U}\} = \left[\{\ddot{U}\}_1^T \quad \{\ddot{U}\}_2^T \quad \ldots \quad \{\ddot{U}\}_{n_r}^T \right]^T$, $\{U\} = [\{U\}_1^T \{U\}_2^T \ldots \{U\}_{n_r}^T]^T$ and $\{F(t)\} = \left[\{F\}_1^T \quad \{F\}_2^T \quad \ldots \quad \{F\}_{n_r}^T \right]^T$ are the acceleration, displacement and load of the block system, respectively.

Damping is normally demanded in practical applications. Similar to the dynamic FEM, we employ the Rayleigh damping (Bathe 1982) in a manner of

$$[C] = \alpha_0[M] + \alpha_1[K] \tag{12.51}$$

In which α_0 and α_1 are defined in Eq. (4.111).

The dynamic governing equation set of the elastic block element system with damping is therefore becomes

$$[M]\{\ddot{U}\} + [C]\{\dot{U}\} + [K]\{U\} = \{F(t)\} \tag{12.52}$$

Where $\{\dot{U}\} = \left[\{\dot{U}\}_1^T \quad \{\dot{U}\}_2^T \quad \ldots \quad \{\dot{U}\}_{n_r}^T\right]^T$ is the velocity of the rock block system.

For the earthquake problem, Eq. (12.52) can be further expressed as

$$[M]\{\ddot{U}\} + [C]\{\dot{U}\} + [K]\{U\} = -[M]\{a\} \tag{12.53}$$

In which $\{a\}$ is the earthquake acceleration of ground.

Equation (12.52) or Eq. (12.53) is formality similar to that of the dynamic FEM. Therefore, the Wilson or Newmark method (Bathe 1982) prevalent in the dynamic FEM can be applied to solve them without difficulty.

12.4.2 Visco-Elastic Artificial Boundary

For many hydraulic structural problems, the calculation is conducted merely in a portion of the foundation or surrounding rock that is cut from the Earth crust. The seismic wave will be completely reflected on the foundation boundary if it is not appropriately handled, which will lead to erroneous results. Therefore, it is necessary to introduce restraints at the boundary to eliminate the boundary reflection. Such restraints are referred to as an "artificial boundary condition" (Clayton and Engquist 1980; Higdon 1986).

Various artificial boundaries are available due to the seminal work of Lysmer and Kuhlemeyer (1969). In our study, the visco-elastic artificial boundary condition proposed by Deeks and Randolph (1994) is adopted for the dynamic BEA, which is the development of the visco boundary condition. The general forms of such condition in the dynamic FEM can be expressed as

$$\sigma_{li}(t) = -K_{li}u_{li}(t) - C_{li}\dot{u}_{li}(t) \tag{12.54}$$

In which $\sigma_{li}(t)$, $u_{li}(t)$ and $\dot{u}_{li}(t)$ are the stress, displacement, and velocity of the node l along the direction i at time t; K_{li} and C_{li} are the elastic modulus and damping factor of the node l along the direction i. They are the functions of the material characteristics.

The physical meaning of the visco-elastic boundary is that at every point along each direction of the boundary, an element containing spring and damping is designed, which is used to simulate the absorption and recovery of the boundary.

In terms of the dynamic BEA, the spring-damping element is put at the boundary as illustrated in Fig. 12.1.

For the block element *rl* contacted to the boundary *j*, the dynamic governing equation can be written as

$$[m]_{rl}\{\ddot{U}\}_{rl} + [C]_{rl,rl}\{\dot{U}\}_{rl} + \sum_{rm}[C]_{rl,rm}\{\dot{U}\}_{rm} + [K]_{rl,rl}\{U\}_{rl} + \sum_{rm}[K]_{rl,rm}\{U\}_{rm} = \{F(t)\}_{rl} + \{p\}_{rl} \tag{12.55}$$

In which $\{p\}_{rl}$ is integrated from the visco-elastic stress $\{\sigma\}_j$ at the artificial boundary *j*

$$\{p\}_{rl} = -\sum_j J(j) \iint_{\Gamma_j} [P]_j \{\sigma\}_j dx_j dy_j \tag{12.56}$$

By the general concept of visco-elastic boundary in Eq. (12.54), we have

$$\{\sigma\}_j = -[D]_j\{u\}_j - [C]_j\{\dot{u}\}_j \tag{12.57}$$

In which $\{u\}_j$ and $\{\dot{u}\}_j$ are the displacement and displacement rate at the artificial boundary *j*.

According to the deformation compatibility condition of the BEA [see Eq. (9.16)], for the block element *rl* contacted to the artificial boundary *j*, we have

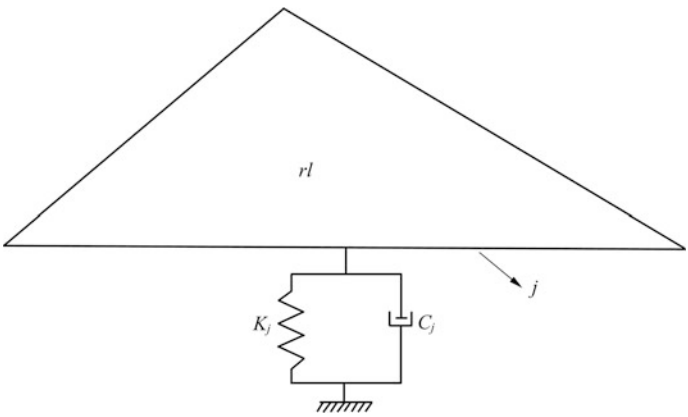

Fig. 12.1 Visco-elastic boundary in the dynamic BEA

$$\{u\}_j = J(j)[L]_j[M]_j\{U\}_{rl} \tag{12.58}$$

$$\{\dot{u}\}_j = J(j)[L]_j[M]_j\{\dot{U}\}_{rl} \tag{12.59}$$

and

$$[D]_j = \begin{bmatrix} k_{sj} & 0 & 0 \\ 0 & k_{sj} & 0 \\ 0 & 0 & k_{nj} \end{bmatrix} \tag{12.60}$$

$$[C]_j = \begin{bmatrix} C_{sj} & 0 & 0 \\ 0 & C_{sj} & 0 \\ 0 & 0 & C_{nj} \end{bmatrix} \tag{12.61}$$

Where k_{nj}, k_{sj} = normal and shear elastic stiffnesses; C_{nj}, C_{sj} = normal and shear dampings.

Introducing Eqs. (12.56)–(12.61) into Eq. (12.55) gives rise to

$$[m]_{rl}\{\ddot{U}\}_{rl} + \left([C]_{rl,rl} + [C]_{rl}\right)\{\dot{U}\}_{rl} + \sum_{rm}[C]_{rl,rm}\{\dot{U}\}_{rm} + \left([K]_{rl,rl} + [K]_{rl}\right)\{U\}_{rl} + \sum_{rm}[K]_{rl,rm}\{U\}_{rm} = \{F(t)\}_{rl} \tag{12.62}$$

In which

$$[K]_{rl} = \sum_j \iint_{\Gamma_j} [M]_{rl}^T[l]_j^T[D]_j[l]_j[M]_{rl}dx_jdy_j \tag{12.63}$$

$$[C]_{rl} = \iint_{\Gamma_j} [M]_{rl}^T[l]_j^T[C]_j[l]_j[M]_{rl}dx_jdy_j \tag{12.64}$$

From Eq. (12.62) we find that the introduction of a visco-elastic artificial boundary condition only changes the diagonal elements of the stiffness and damping matrices.

12.4.3 Verification Example

Figure 12.2 shows a semi-space bar exerted by a pulse action of Dirac differential function $F(t)$ at its left end. The dynamic BEA is conducted for the case when the bar is truncated 50 m in length at its right and restrained with artificial boundary.

The parameters used in the calculation are $E = 80$ MPa, $\mu = 0.25$, $\rho = 2000$ kg/m^3, duration of action time $T = 1.0$ s.

The analytical solution for these ideal bar problem of unlimited length is provided by Eringen and Suhubi (1974)

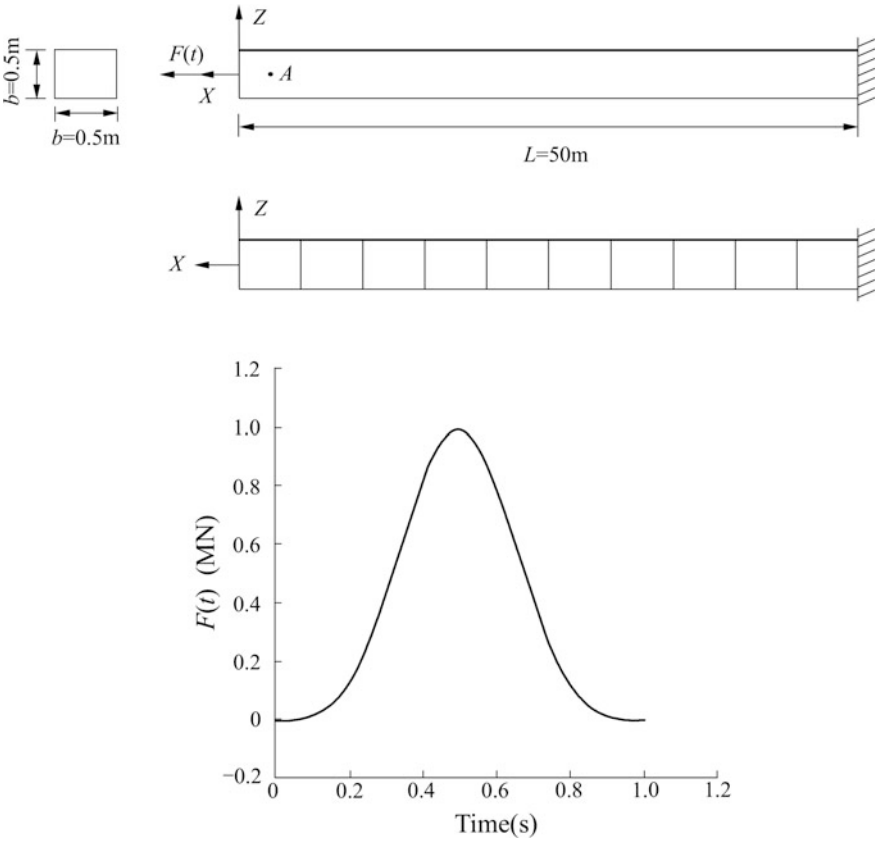

Fig. 12.2 Semi-space bar example

$$u(x)=\begin{cases}0, & \tau<c_s/c_p\\ \dfrac{F(t)}{2\pi Gx}\left[\dfrac{1}{4\left(1-c_s^2/c_p^2\right)}+\displaystyle\sum_{i=1}^{2}\dfrac{K_i\left(1-2v_i^2\right)^2\left(c_s^2/c_p^2-v_i^2\right)^{1/2}}{\left(\tau^2-v_i^2\right)}\right. & \\ \qquad\left.+\dfrac{K_3\left(1-2v_3^2\right)^2\left(v_3^2-c_s^2/c_p^2\right)^{1/2}}{\left(v_3^2-\tau^2\right)}\right], & c_s/c_p<\tau<1\\ \dfrac{F(t)}{\pi Gx}\left[\dfrac{1}{4\left(1-c_s^2/c_p^2\right)}+\dfrac{K_3\left(1-2v_3^2\right)^2\left(v_3^2-c_s^2/c_p^2\right)^{1/2}}{\left(v_3^2-\tau^2\right)}H(v_3-\tau)\right], & \tau>1\end{cases}\tag{12.65}$$

In which $G=\frac{E}{2(1+\mu)}$ is the shear modulus, $H(\tau)$ is Heaviside function, $c_s/c_p=\frac{1}{\sqrt{3}}$ and $c_p=\sqrt{\frac{E}{\rho}}$ are the shear and volumetric wave speeds, $\tau=\frac{c_s t}{x}$ is the dimensionless time, and

$$\begin{cases}v_1^2=\frac{1}{4}\\ v_2^2=\frac{3-\sqrt{3}}{4}\\ v_3^2=\frac{3+\sqrt{3}}{4}\end{cases}\tag{12.66}$$

$$K_i=-\frac{1}{16\left(1-c_s^2/c_p^2\right)\left(v_i^2-v_j^2\right)\left(v_i^2-v_k^2\right)},\quad i\neq j\neq k\tag{12.67}$$

This is a general dynamic problem in terms of the BEA, where the history of load is input in Eq. (12.52). The outputs by the dynamic BEA are the responses in terms displacement, velocity, and acceleration. The vibration history at $x=0.25$ m (point A) is plotted and cross-referenced to the analytical solution [see Eqs. (12.65)–(12.67)] in Fig. 12.3, from which the validation of the dynamic BEM with visco-elastic artificial boundary is evident.

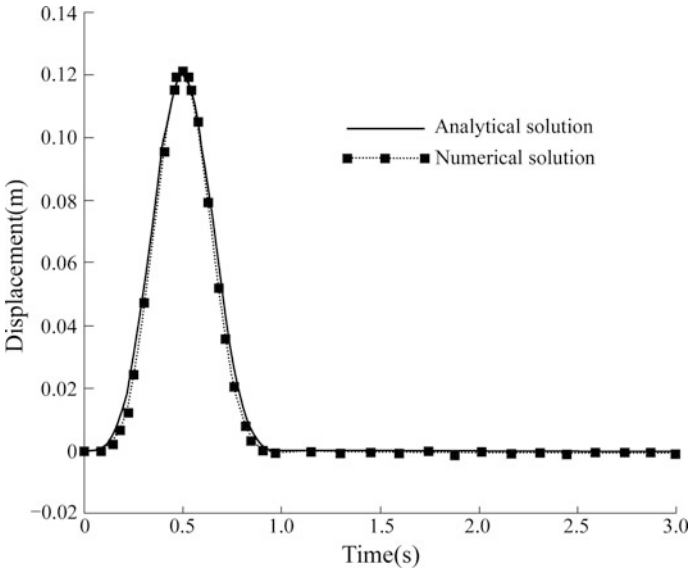

Fig. 12.3 Displacement at the point A of the bar

References

Al-Homoud AS, Tahtamoni WW. Reliability analysis of three-dimensional dynamic slope stability and earthquake-induced permanent displacement. Soil Dyn Earthq Eng. 2000;19(2):91–114.

Ang AHS, Newmark NM. A probabilistic seismic safety assessment of the Diablo Canyon Nuclear Power Plant. Washington, DC, USA: US Nuclear Regulatory Commission; 1977.

Ayyub BM, Klir GJ. Uncertainty modeling and analysis in engineering and the sciences. Boca Raton, USA: Chapman & Hall/CRC, Taylor & Francis Group; 2006.

Bardet JP, Scott RF. Seismic stability of fractured rock masses with the distinct element method. In: Proceedings of the 26th US symposium on rock mechanics. Rapid City, SD, USA; 1985. p. 139–49.

Bathe KJ. Finite element procedures in engineering analysis. New Jersey, USA: Prentice-Hall; 1982.

Ben-Gal I, Herer Y, Raz T. Self-correcting inspection procedure under inspection errors. IIE Trans Qual Reliab. 2002;34(6):529–40.

Bjerager P. Probability integration by directional simulation. J Eng Mech, ASCE. 1988; 114(8):1285–302.

Bucher CG, Bourgund U. A fast and efficient response surface approach for structural reliability problems. Struct Safety. 1990;7(1):57–66.

Cambou B. Applications of first-order uncertainty analysis in the finite element method in linear elasticity. In: Proceedings of 2nd international conference on applications of statistics and probability in soil and structural engineering. Aachen, Germany; 1975. p. 67–87.

Chen SH. Analysis of reinforced rock foundation using elastic-viscoplastic block theory. In: Ribeiro e Sousa L, Grossmann NF, editors. Proceedings on 1993 ISRM International Symposium—EUROCK 93. Rotterdam, The Netherlands: A.A. Balkema; 1993. p. 45–51.

Chen SH. Hydraulic structures. Berlin, Germany: Springer; 2015.
Chen SH, Lian HD, Yang XW. Interval static displacement analysis for structures with interval parameters. Int J Numer Meth Eng. 2002;53(2):393–407.
Chen SH, Shen BK, Huang MH. Stochastic elastic-viscoplastic analysis for discontinuous rock masses. Int J Numer Meth Eng. 1994;37(14):2429–44.
Chen SH, Wang WM, Zheng HF, Shahrour I. Block element method for the seismic stability of rock slopes. Int J Geotech Geoenviron Eng, ASCE. 2010;136(12):1610–7.
Chen SH, Xiong WL. An elastic-viscoplastic stochastic FEM for geotechnical engineering. In: Proceedings of 2nd National symposium on computer geomechanics. Shanghai, China; 1990. p. 256–66 (in Chinese).
Clayton RW, Engquist B. Absorbing boundary conditions for wave equation migration. Geophysics. 1980;45(5):895–904.
Corotis RB. An overview of uncertainty concepts related to mechanical and civil engineering. ASCE-ASME J Risk Uncertain Eng Syst, Part B: Mech Eng. 2015;1(4):040801.
Cundall PA, Hart DH. Numerical modelling of discontinua. Eng Comput. 1992;9(2):101–13.
Deeks AJ, Randolph MF. Axisymmetric time-domain transmitting boundaries. J Eng Mech, ASCE. 1994;120(1):25–42.
Elishakoff I, Ohsaki M. Optimization and anti-optimization of structures under uncertainty. London, UK: Imperial College Press; 2010.
Eringen AC, Suhubi ES. Elastodynamics. NY, USA: Academic Press; 1974.
Ghanem R, Spanos PD. Stochastic finite elements: a spectral approach. NY, USA: Springer; 1991.
Hasofer AM, Lind NC. Exact and invariant second-moment code format. J Eng Mech, ASCE. 1974;100(1):111–21.
Higdon RL. Absorbing boundary conditions for difference approximations to the multi-dimensional wave equation. Math Comp. 1986;47(176):437–59.
Kramer SL. Geotechnical Earthquake Engineering. NJ, USA: Prentice-Hall; 1996.
Lysmer J, Kuhlemeyer RL. Finite dynamic model for infinite media. J Eng Mech Div, ASCE. 1969;95(4):859–77.
Mahadevan S, Zhang R, Smith N. Bayesian networks for system reliability reassessment. Struct Saf. 2001;23(3):231–51.
Melchers RE. Structural reliability analysis and prediction. NY, USA: Wiley; 1987.
Moens D, Hanss M. Non-probabilistic finite element analysis for parametric uncertainty treatment in applied mechanics: recent advances. Finite Elem Anal Des. 2011;47(1):4–16.
Moens D, Vandepitte D. A survey of non-probabilistic uncertainty treatment in finite element analysis. Comput Meth Appl Mech Eng. 2005;194(14–16):1527–55.
Moore RE. Interval analysis. Englewood Cliffs, USA: Prentice-Hall; 1966.
Pearl J. Probabilistic reasoning in intelligent systems. San Francisco, CA, USA: Morgan Kaufmann; 1988.
Provan JW. Probabilistic fracture mechanics and reliability. Dordrecht, The Netherlands: Martinus Nijhoff; 1987.
Rackwitz R, Fiessler B. Structural reliability under combined random load sequences. Comput Struct. 1978;9(5):489–94.
Rao SS, Berke L. Analysis of uncertain structural systems using interval analysis. AIAA J. 1997;35(4):727–35.
Shi GH. Discontinuous deformation analysis: a new numerical model for the statics and dynamics of deformable block structures. Eng Comput. 1992;9(2):157–68.
Sofi A, Muscolino G, Elishakoff I. Special issue on nonprobabilistic treatments of uncertainty: recent developments. ASCE-ASME J Risk Uncertain Eng Syst, Part B: Mech Eng. 2015;1 (4):040301.

Torres-Toledano JG, Sucar LE. Bayesian networks for reliability analysis of complex systems. In: Proceedings of 6th Ibero-American conference on AI (IBERAMIA 98). Lecture notes inartificial intelligence, vol. 1484. Berlin, Germany: Springer; 1998. p. 195–206.

Zhao GF, Jin WL. The theory of structural reliability. Beijing, China: Chinese Industrial Architecture Publishing House; 2000 (in Chinese).

Zhao WT, Qiu ZP. An efficient response surface method and its application to structural reliability and reliability-based optimization. Finite Elem Anal Des. 2013;67:34–42.

Chapter 13
Comprehensive Application of the Block Element Analysis: Xiaowan Project

Abstract Since it is stipulated in China's design specifications that, in addition to the classical structural analyses and the physical model experiments, for high grade hydraulic structures one or two advanced methods should be employed in parallel. Hence in this chapter the systematic study on Xiaowan Project by the BEA is presented, which covers the whole process from the excavation/stabilization of the slopes related to tunnel intakes and arch dam foundation/abutments, to the performance of dam-foundation system.

13.1 General

At the height of 294.5 m and total hydraulic thrust force of 18 million tons, Xiaowan Arch Dam was one of the most challenging dam structures in China (Zou 2010). Studies on this dam had been continuously conducting throughout the design stages as well as the construction and operation periods.

In Chap. 8, the systematic study on Xiaowan Project by the FEM has been presented, which covers the whole procedure from the in situ geo-stress back analysis to the foundation/abutments excavation followed by concrete placement until the impoundment operation. Since it is stipulated in the China's design specifications for high grade hydraulic structures that at least two different methods should be employed for their structural analysis in addition to the classical structural computations and the physical model experiments, therefore the author has been undertaking a parallel study for the key issues with respect to the deformation, strength and stability of the hydraulic structures in Xiaowan Project with the help of the BEA (Chen et al. 2000, 2002, 2003, 2010). A summary of the results are presented in this chapter.

S.-H. Chen, *Computational Geomechanics and Hydraulic Structures*,
Springer Tracts in Civil Engineering, https://doi.org/10.1007/978-981-10-8135-4_13

13.2 Presentation of the Project

Vide Chap. 8.

13.3 Construction Period: Excavation and Reinforcement of the Headrace Intake Slope

13.3.1 Characteristics of the Computation

The headrace intake slope for the underground power plant (installation capacity of 4200 MW) (see Fig. 13.1) is steeply excavated in the sound gneiss rock embedded with various IV grade faults (f_1, f_2, f_3, f_5, f_6, $f_{89\text{-}1}$, $f_{89\text{-}6}$, $gm_{89\text{-}8}$) (see Fig. 13.2) and joint sets of which the dominant one is SN-trending and with high dip angle (nearly 90°). They give rise to the risk of rock block sliding failure, particularly during the excavating period before the mass concrete placement of the intake structure offering extra support to the slope.

After the consideration that all the potential unstable blocks are included, the calculation domain is defined with 200 m along the flow direction (N50°E) and 160 m perpendicular to the flow direction (see Fig. 13.2). The computation parameters are listed in Tables 13.1 and 13.2.

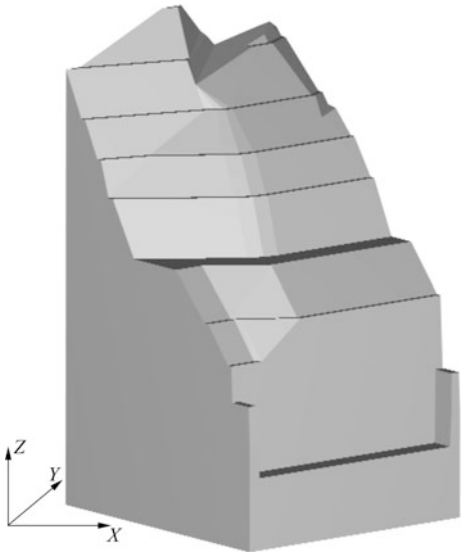

Fig. 13.1 Axonometric drawing of the water intake slope

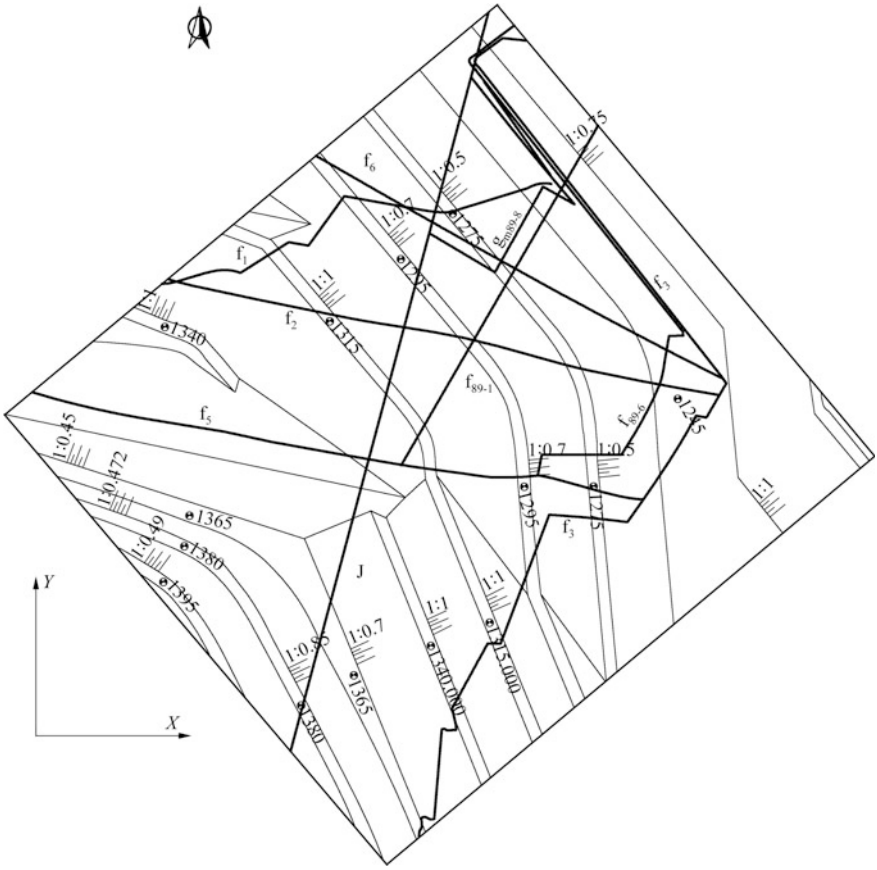

Fig. 13.2 Geological plan showing faults and excavation benches

Table 13.1 Attitude parameters of dominant discontinuities

Discontinuity	Dip direction (°)	Dip angle (°)
f_1	10	65
f_2	15	85
f_3	5	42
f_5	15	82
f_6	30	85
$f_{89\text{-}1}$	300	90
$f_{89\text{-}6}$	0	40
$gm_{89\text{-}8}$	30	46
SN-trending and high dip angle joint J_1	105	90
Virtual joint along the flow direction	320	90

Table 13.2 Mechanical parameters of dominant discontinuities

Discontinuity	Cohesion c (MPa)	Friction coefficient $f = tg\varphi$	Normal stiffness k_n (MPa/m)	Shear stiffness k_s (MPa/m)
f_1	0.04	0.50	10,000	4000
f_2	0.04	0.50	10,000	4000
f_3	0.04	0.45	10,000	4000
f_5	0.04	0.50	10,000	4000
f_6	0.04	0.50	10,000	4000
$f_{89\text{-}1}$	0.045	0.50	10,000	4000
$f_{89\text{-}6}$	0.03	0.40	10,000	4000
$g_{m89\text{-}8}$	0.04	0.045	10,000	4000
J_1	0.125	0.80	15,000	6000

The volumetric weight of the rock is 0.027 MN/m^3

13.3.2 Stability of the Cut Slope Without Reinforcement

Altogether 35 movable blocks are identified. By the search of dangerous slip modes, the block combinations enclosed by the SN-trending and high dip angle joint J_1 and $f_{89\text{-}1}$ possess lower static stability (see Table 13.3). Table 13.4 displays three combinations particularly concerned due to their very low stability factors. Figures 13.3, 13.4, 13.5 and 13.6 illustrate two of them enclosed by f_3-J_1f_5 and f_3-J_1f_6.

13.3.3 Particularities in the Seismic Analysis

In the analysis of the intake slope, particular attention was paid to the three block combinations (f_3-J_1f_6, f_3-J_1f_5 and $f_{89\text{-}6}$-J_1f_2) listed in Table 13.4, to whom the seismic analysis was additionally carried out.

(1) Assumptions

There was no appropriate record of the seismic history in the Xiaowan Dam site at the time being, so the EI Centro earthquake (MC 7.2, California, USA, 1940) N-S wave was used in the seismic analysis of the intake slope (duration time is 10 s). Since the Mercalli intensity of the earthquake stipulated in the Xiaowan Project is 9 with the corresponding peak acceleration of a = 0.4 g (g = 9.81 m/s^2), the input seismic wave is amplified according to the acceleration ratio between these two earthquakes. The horizontal earthquake shake along the X axis (perpendicular to the river valley) is highlighted in the dynamic study of this slope. In the calculation, the curve of earthquake acceleration vs time is input, the general outputs are the response procedures with regard to the displacement, velocity, and acceleration. These messages are further employed to calibrate the seismic safety of the intake slope.

Table 13.3 Block combinations with lower stability

Sequence	Notation	Description of block combination	Volume ($10^4 m^3$)	Static stability	Dynamic stability
1	f_3-J_1f_5	Enclosed by f_3, J_1, f_5	20.44	No	No
5	f_3-$f_{89\text{-}1}f_5$	Enclosed by f_3, $f_{89\text{-}1}$, f_5	10.53	No	Ok
6	f_3-J_1f_2	Enclosed by f_3, J_1, f_2	13.36	No	Ok
10	f_3-$f_{89\text{-}1}f_2$	Enclosed by f_3, $f_{89\text{-}1}$, f_2	5.62	No	Ok
11	f_3-J_1f_6	Enclosed by f_3, J_1, f_6	8.14	No	No
15	f_3-$f_{89\text{-}1}f_6$	Enclosed by f_3, $f_{89\text{-}1}$, f_6	2.82	No	Ok
16	$f_{89\text{-}6}$-J_1f_5	Enclosed by $f_{89\text{-}6}$, J_1, f_5	12.90	No	Ok
20	$f_{89\text{-}6}$-$f_{89\text{-}1}f_5$	Enclosed by $f_{89\text{-}6}$, $f_{89\text{-}1}$, f_5	5.67	No	Ok
21	$f_{89\text{-}6}$-J_1f_2	Enclosed by $f_{89\text{-}6}$, J_1, f_2	8.80	No	No
25	$f_{89\text{-}6}$-$f_{89\text{-}1}f_2$	Enclosed by $f_{89\text{-}6}$, $f_{89\text{-}1}$, f_2	3.25	No	Ok
26	$f_{89\text{-}6}$-J_1f_6	Enclosed by $f_{89\text{-}6}$, J_1, f_6	5.47	No	Ok
30	$f_{89\text{-}6}$-$f_{89\text{-}1}f_6$	Enclosed by $f_{89\text{-}6}$, $f_{89\text{-}1}$, f_6	1.64	No	Ok
31	f_1-J_1	Enclosed by f_1, J_1	1.14	No	Ok
33	$g_{m89\text{-}8}$-J_1f_6	Enclosed by $g_{m89\text{-}8}$, J_1, f_6	1.11	No	Ok
34	$g_{m89\text{-}8}$-J_1f_6	Enclosed by $g_{m89\text{-}8}$, J_1, f_6	0.37	No	Ok

Table 13.4 Rock block element combinations particularly concerned

Block element combination	Description	Static safety factor
f_3-J_1f_6	Enclosed by f_3, SN joint J_1, f_6	0.93
f_3-J_1f_5	Enclosed by f_3, SN joint J_1, f_5	0.92
$f_{89\text{-}6}$-J_1f_2	Enclosed by $f_{89\text{-}6}$, SN joint J_1, f_2	1.04

(2) Dynamic safety factors

Dynamic stability state can be defined on the basis of safety factor or on the permanent displacement (Ang and Newmark 1977). For the elastic dynamic analysis the safety factor is conventionally defined by

$$K_f = \frac{T}{S} \tag{13.1}$$

where T = sliding resistant force; S = sliding driving force.

For the dynamic BEA, the safety factor of any block element combination at time t can be calculated by the formula

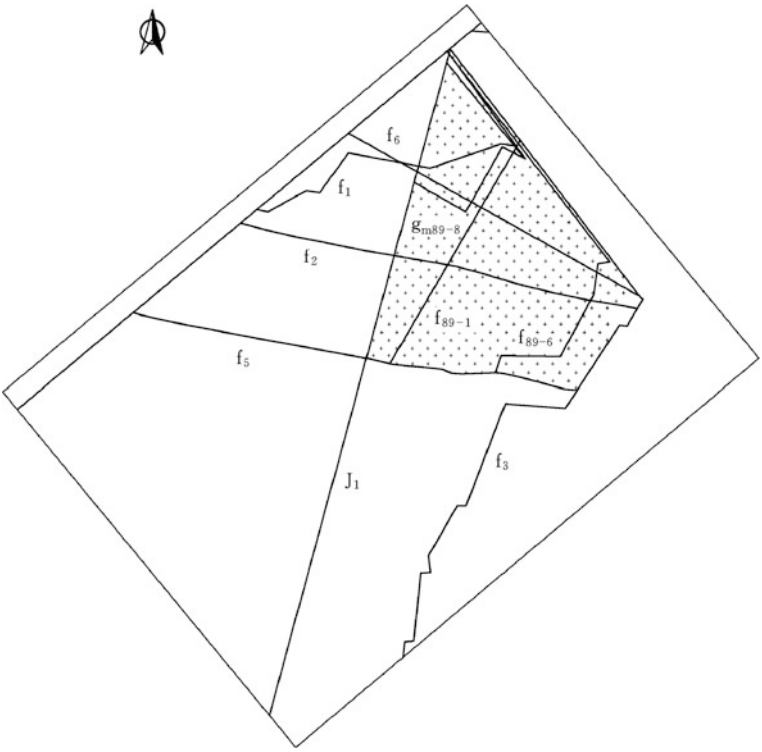

Fig. 13.3 Plan showing block combination f_3-J_1f_5

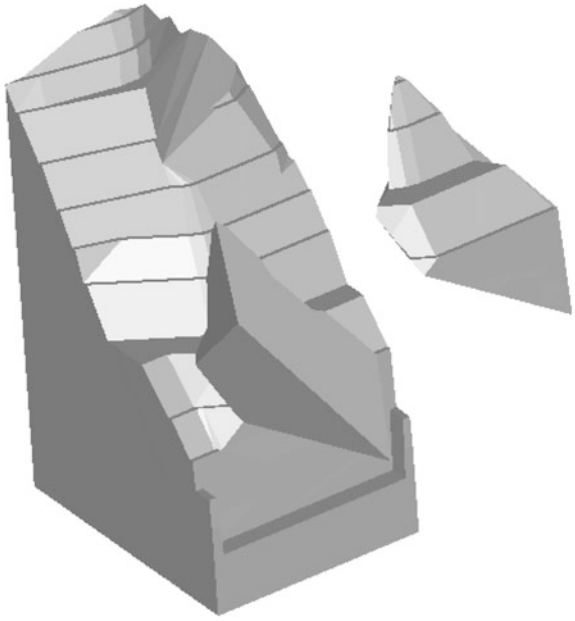

Fig. 13.4 Axonometric drawing of block combination f_3-J_1f_5

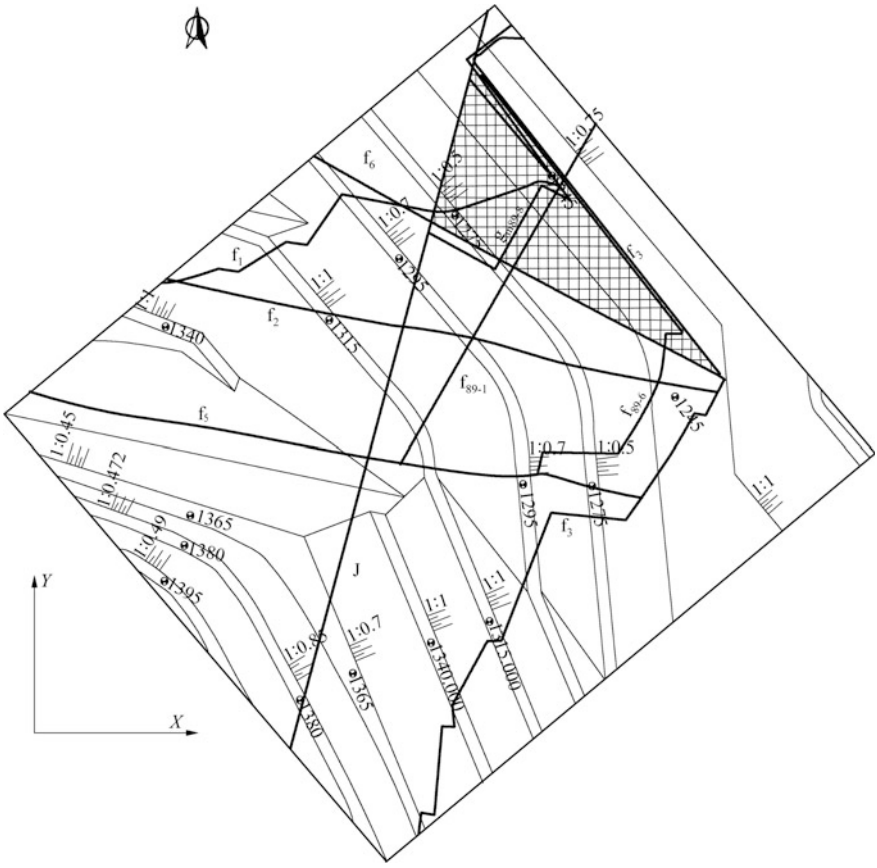

Fig. 13.5 Plan of block combination f_3-J_1f_6

$$K_f = \frac{\sum_{j_{rl,rm}=1}^{n_m} \iint\limits_{\Gamma_{jrl,rm}} CS_{jrl,rm}\left(c_{jrl,rm} - tg\varphi_{jrl,rm}\sigma_z\right)dx_{jrl,rm}dy_{jrl,rm}}{\sum_{j_{rl,rm}=1}^{n_m} \iint\limits_{\Gamma_{jrl,rm}} CS_{jrl,rm}\sqrt{\tau_{zx}^2 + \tau_{zy}^2}dx_{jrl,rm}dy_{jrl,rm}} \tag{13.2}$$

In which $CS_{j_{rl,rm}} = \cos\alpha_{j_{rl,rm}}$ where $\alpha_{j_{rl,rm}}$ is the included angle between the slip direction and the total shear force on the discontinuity plane $j_{rl,rm}$.

Figure 13.7 plots the history of the dynamic stability safety factor of rock block combination f_3-J_1f_6 during the earthquake. It can be found that the dynamic stability safety factor fluctuates around the static one.

Theoretically, if the dynamic stability safety factor is lower than an allowable (permissible) value, the slope is unstable. However, there is no such allowable safety factor stipulated insofar for the dynamic BEA (nor for the dynamic FEM as well) in

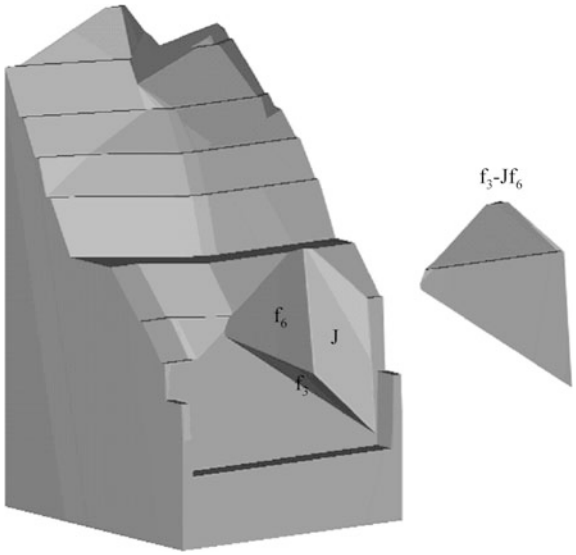

Fig. 13.6 Axonometric drawing of block combination f_3-J_1f_6

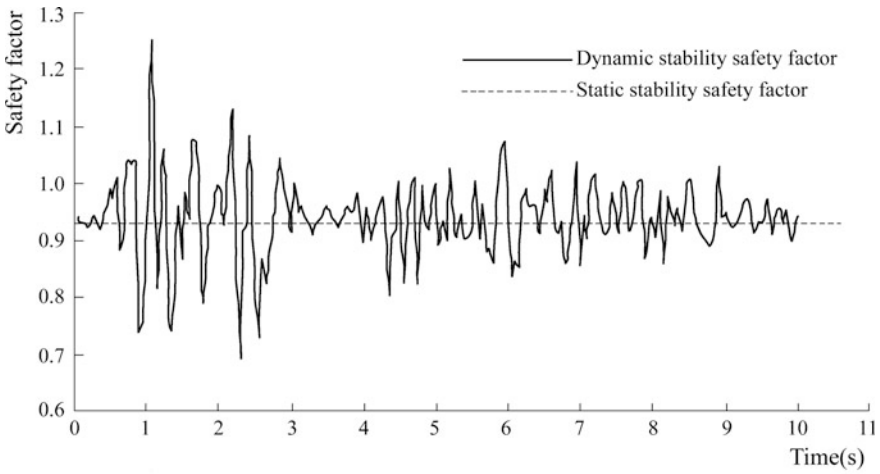

Fig. 13.7 Dynamic stability safety factor of block combination f_3-J_1f_6

the slope design specifications. One possibility to establish the dynamic stability criterion is to make use of permanent displacement (Ang and Newmark 1977) accumulated in the earthquake history, which demands the consideration of plasticity and to stipulate the permissible permanent displacement. Another possibility lies in the fact that, the practitioners are used to the "pseudo-static method" in the design of rock slope under the actions of earthquake. This method calculates the inertia force

through earthquake acceleration first, then a resultant force of this inertia and other static loads is employed in the stability analysis. However, the "pseudo-static method" normally overlooks the difference in the acceleration of the different portions of rock slope. Hence the study on the dynamic amplification factors of the rock block combinations located at different portions of the intake slope is practically important.

(3) Dynamic amplification factors

The dynamic amplification factor is defined as the ratio of output acceleration of the slope to the input earthquake acceleration. Obviously the dynamic amplification factor has complex distribution within the slope and it has relationship with the height and configuration of the slope concerned. Since this factor is paramount in the pseudo-static analysis and is difficult to recommend in the slope design specifications, a case study of the issue would be helpful. Table 13.5 summarizes the amplification factor of each block combination at its geometric center, from which the relationship of the dynamic amplification with the altitude may be elucidated.

13.3.4 Reinforcement Schemes

The reinforcement study is dynamically accomplished via three phases following the progress in the project construction.

(1) First phase

It was initiated from the November 2002 and finished in the March 2003. The block combinations related to the structural planes f_3, $f_{89\text{-}6}$, f_2, f_5, f_6, $f_{89\text{-}1}$ and SN-trending high dip angle joint were designed to be all reinforced by pre-stress cables. The sensitive analysis with regard to the cable dip angle, friction angle of the structural faces, dip direction of f_3, ground water table, etc., were conducted.

The basic reinforcement scheme was proposed to install cables along the flow direction of intake, i.e. dip direction = S50°W. The dip angle of all the cables is −10°. Figure 13.8 shows the zoning of the cable capacity. The total pre-stress force is 1350 MN.

Table 13.5 Dynamic amplification factors

Block element combination	Geometric centre (m) (X, Y, Z)	Dynamic amplification factor
f_3-J_1f_6	(982.81, 836.77, 1177.39)	1.15
f_3-J_1f_5	(972.54, 810.28, 1226.05)	1.18
$f_{89\text{-}6}$-J_1f_2	(962.13, 783.41, 1252.51)	1.20

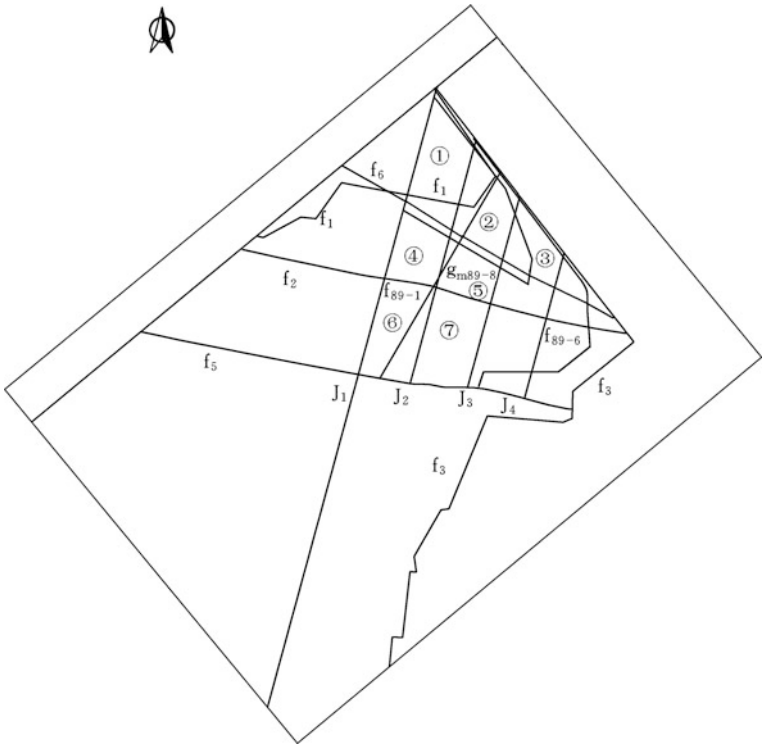

Fig. 13.8 Layout of pre-stress anchor cables: first phase. ①—400 MN; ②—200 MN; ③—200 MN; ④—200 MN; ⑤—150 MN; ⑥—100 MN; ⑦—100 MN

(2) Second phase

It was initiated from the April 2003 and finished in the June 2003. We revised the reinforcement scheme according to the latest geological phenomenon revealed and construction schedule adjusted. The revised scheme was proposed to reinforce the fault f_3 with the combination of cables and shear keys (the concrete replacement of grade C_{35}). The cables of 3MN are employed below the elevation 1245 m, their space is 5 m × 4 m (horizontal × vertical). The layout of the keys on the f_3 is illustrated in Fig. 13.9 and the zoning of the cable capacity is shown in Fig. 13.10. The total pre-stress force is reduced to 630 MN.

(3) Third phase

It was initiated from the July 2003 and finished in the December 2003. We re-checked the reinforcement scheme according to the latest geological phenomenon revealed and construction schedule adjusted. In addition, the sensitive analysis with regard to the dip angles of f_3 and J_1 were conducted.

Through the three phase studies as described above, the conclusions are made for the intake slope that:

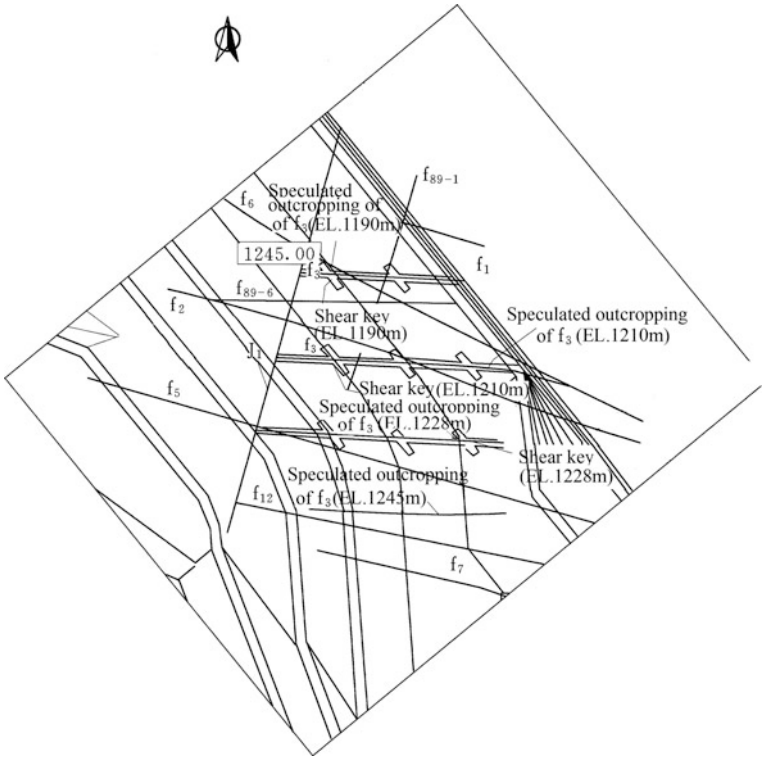

Fig. 13.9 Layout of shear resistance keys: second phase

- Construction excavation is the most critical period of the intake slope.
- The final reinforcement scheme may guarantee the safety of the slope during the construction and service periods.
- The dip angle of cable is not sensitive with regard to the slope stability. If it is additionally dipped down by 5°, the safety factor tends to an augment of 0.02–0.05 only.
- The friction angle of the discontinuities is rather sensitive with regard to the slope stability. Under the circumstances of groundwater table maintaining at 1/4 height of the block, an augment of friction angle 2° results in a safety factor augment around 0.08.
- Dip angle of f_3 is very sensitive with regard to the slope stability. The lower of dip direction of f_3, the higher is the safety factor. Where the dip angle is lowered down from 15° to 10°, a number of block combinations will slide along the two intersected surfaces instead of the formerly single surface slip mode. This will raise the safety factor considerably.
- The groundwater table is very sensitive with regard to the slope stability. The draining holes should be strengthened and elongated in the slope to ensure its stability.

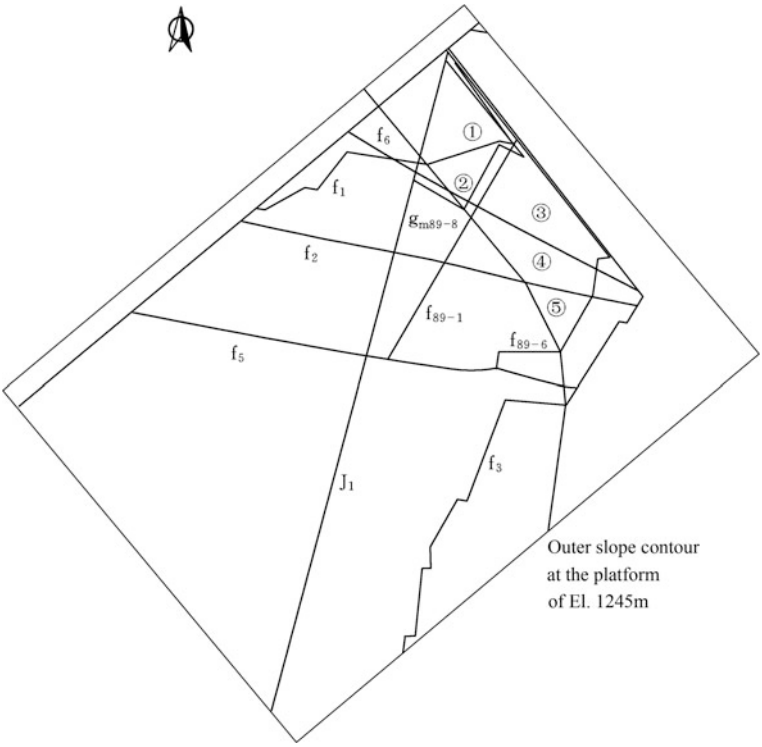

Fig. 13.10 Layout of pre-stress anchor cables: second phase. ①—279 MN; ②—21 MN; ③—198 MN; ④—91 MN; ⑤—51 MN

The slope excavation and reinforcement construction was completed successfully (see Fig. 13.11) under the guidance of the foregoing studies.

13.4 Construction Period: Excavation and Reinforcement of the Dam Abutments

13.4.1 Characteristics of the Computation

During the construction period, the excavated abutment slopes will be temporarily created. The maximum slope height perpendicular to the left spandrel groove is 95–112 m, and the maximum slope height perpendicular to the right spandrel groove is 110–130 m. The stability safety of the abutment slope during the excavation before the completion of dam concrete placement was strongly worried over by the owner, designer and contractor.

Fig. 13.11 Headrace intake after completion (2007–08)

The dominated structural planes influencing the abutment slope stability are that of low angle and SN-trending, high angle and SN-trending (e.g. high angle joint SN, erosion bands), high angle and nearly EW-trending (e.g. III grade faults F_3, F_{11}). They delimit various adverse block combinations that endanger the abutment excavation and concrete placement works (see Fig. 13.12).

For performing the reinforcement optimization, two phases of work were carried out: first, the comparison and screen of alternative reinforcement schemes; then the detailed study on the finial reinforcement scheme.

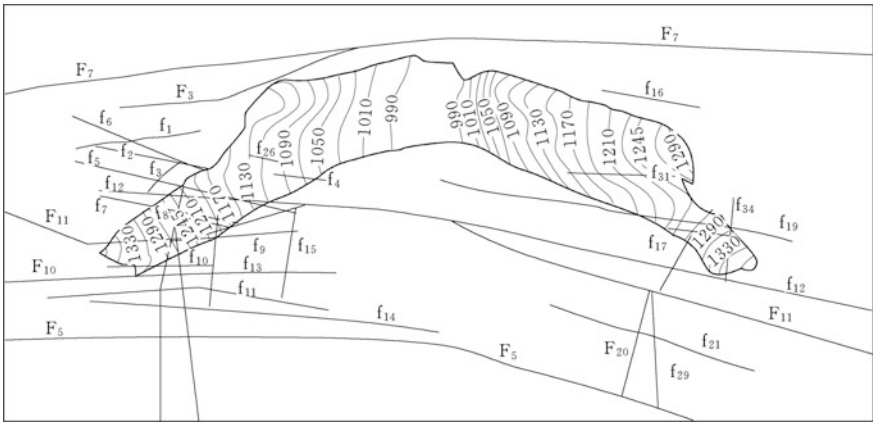

Fig. 13.12 Plan showing excavation benches and faults: phase 1

13.4.2 Comparison and Screen of Alternative Reinforcement Schemes

(1) Emulative schemes

According to the two emulative excavation schemes for the arch dam abutments, altogether 30 faults, 4 geological alteration zones, and three major joint sets are taken into account. The excavation is executed by 22 benches, each bench step is 20 m high.

The pre-processor identifies a block system containing 7873 block elements. The volumetric weight of rock and natural seepage field are considered in the back analysis of in situ geo-stress field first. Then the stress release and the variation of seepage field following the change of exit condition due to abutment excavation as well as the reinforcement component installation, are simulated step by step according to the ongoing of the abutment cut operation.

The excavated slope is reinforced by systematic rock bolts (steel bar Φ25II) and pre-stress cables of 1, 3 and 6 MN. The following three cases are analyzed.

- Case 1. Scheme 1 with reinforcement layout shown in Fig. 13.13 and parameters listed in Table 13.6;
- Case 2. Scheme 2 with reinforcement layout shown in Fig. 13.14 and parameters listed in Table 13.7;
- Case 3. Without reinforcement.

(2) Performances of emulative schemes

1. Displacements

It is found that both the reinforcement schemes perform well in the control of excavating induced displacements. The displacement under the reinforcement

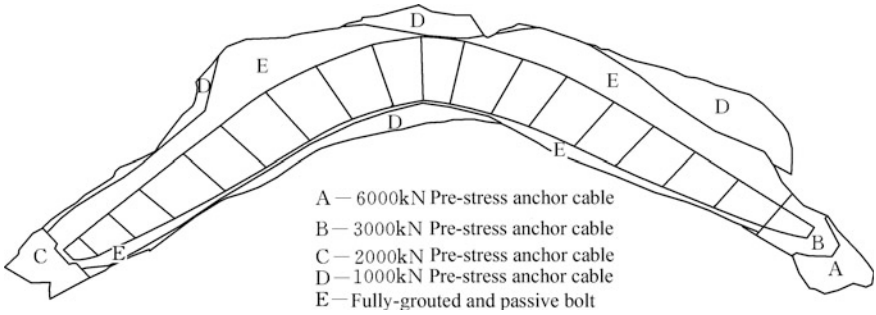

Fig. 13.13 Layout of reinforcement scheme 1

scheme 2 is smaller than that under the scheme 1. The maximum displacements are 4.0 mm for the reinforcement scheme 1, 4.4 mm for the scheme 2, and 5.5 mm for the scheme 3 (without reinforcement).

2. Stability

Use is made of the intelligent search strategy (Xu et al. 2000), altogether 533 potential block combinations with lower safety factors are detected. In Figs. 13.15 and 13.16, we present 14 typical block combinations.

The analysis evidences that without reinforcement the abutment slope failures could manifest because the safety factors are not sufficient for a number of rock block combinations around the areas. In contrast, both the two reinforcement schemes may ensure the stability of the abutment slopes during the excavation. Since the reinforcement scheme 2 demands fewer pre-stress cables and its reinforcement cost is lower compared to the scheme 1, it is recommended as the basic scheme in the formulation of final optimal scheme.

13.4.3 Optimal Analysis for the Finial Reinforcement Scheme

(1) Configuration of the finial scheme

The optimal scheme is the adjustment and expansion of the scheme 2 to include the headrace intake slope and a portion of plunge pool slopes (see Fig. 8.10). Its reinforcement zoning is illustrated in Fig. 8.15 and the correspondent parameters are listed in Tables 8.8, 8.9 and 8.10. The dip angle of pre-stress cables and passive, fully-grouted bolts are all dipped at an angle of 15° downward into the slope surfaces.

Table 13.6 Zoning and reinforcement parameters (scheme 1)

Reinforcement component	6 MN pre-stress cable	3 MN pre-stress cable	2 MN pre-stress cable	1 MN pre-stress cable	Systematic fully-grouted bolt
Length (m)	60	40	35	30	8
Horizontal space (m)	5	5	5	4	3
Vertical space (m)	5	5	5	4	3
Dip direction (°)	Perpendicular to exposure face	Perpendicular to exposure face	Perpendicular to exposure face	Perpendicular to exposure face	Perpendicular to exposure face
Dip angle (°)	10 (downward)	10 (downward)	10 (downward)	10 (downward)	Perpendicular to exposure face
Young's modulus (GPa)	1800	1800	1800	1800	2000
Tensile strength (MPa)	1000	1000	1000	1000	310
Poisson's ratio	0.3	0.3	0.3	0.3	0.3

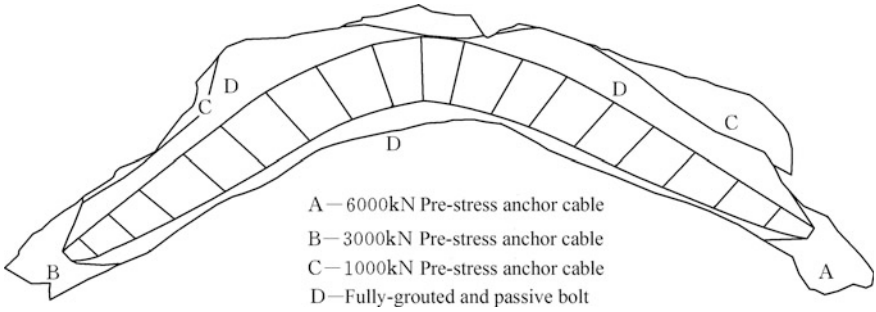

Fig. 13.14 Layout of reinforcement scheme 2

Table 13.7 Zoning and reinforcement parameters (scheme 2)

Reinforcement component	6 MN pre-stress cable	3 MN pre-stress cable	1 MN pre-stress cable	Systematic fully-grouted bolt
Length (m)	60	40	30	8
Horizontal space (m)	5	4	5	3
Vertical space (m)	6	6	8	3
Dip direction (°)	EW	EW	EW	Perpendicular to exposure face
Dip angle (°)	10 (downward)	10 (downward)	10 (downward)	Perpendicular to exposure face
Young's modulus (GPa)	1800	1800	1800	2000
Tensile strength (MPa)	1000	1000	1000	310
Poisson's ratio	0.3	0.3	0.3	0.3

(2) Performances of the final scheme

1. Displacements

The displacement on the upstream slope is large than that on the downstream slope at the left abutment groove. On the contrary, the displacement on the upstream slope is smaller than that on the downstream slope at right abutment groove. With regard to the upstream slopes, the displacement at the left abutment groove is large than that at the right abutment groove. On the downstream slopes, in contrast, the displacement at the left abutment groove is smaller than that at the right abutment groove. The maximum displacement 7.8 cm emerges at the headrace intake.

These conclusions agree well with that from the FEM previously presented in Chap. 8 (Sect. 8.4).

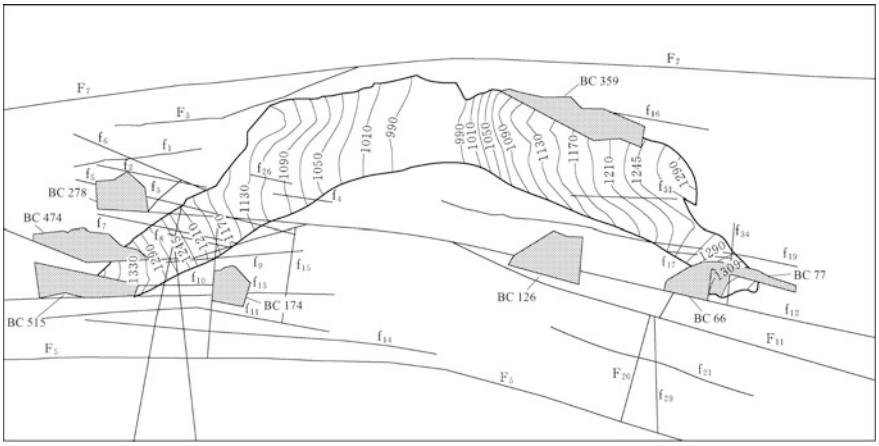

Fig. 13.15 Location of potential failure block combinations (1): phase 1

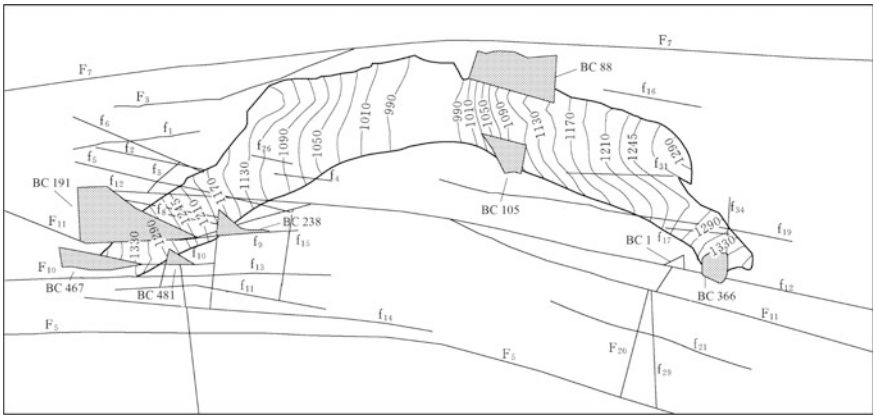

Fig. 13.16 Location of potential failure block combinations (2): phase 1

2. Stability

Altogether 596 potential slip modes are detected and their safety is calibrated. In Figs. 13.17 and 13.18, we present 16 typical slip modes at left and right abutments, respectively.

The computation evidences that the final reinforcement scheme may meet the stability requirements during the construction period. However, the large displacement manifesting at the headrace intake slope sends warning alarm that, during the construction period, the critical portion is the headrace intake slope. Consequently, the particular care should be paid for its reinforcement design, which has been elaborated previously in this chapter (Sect. 13.3).

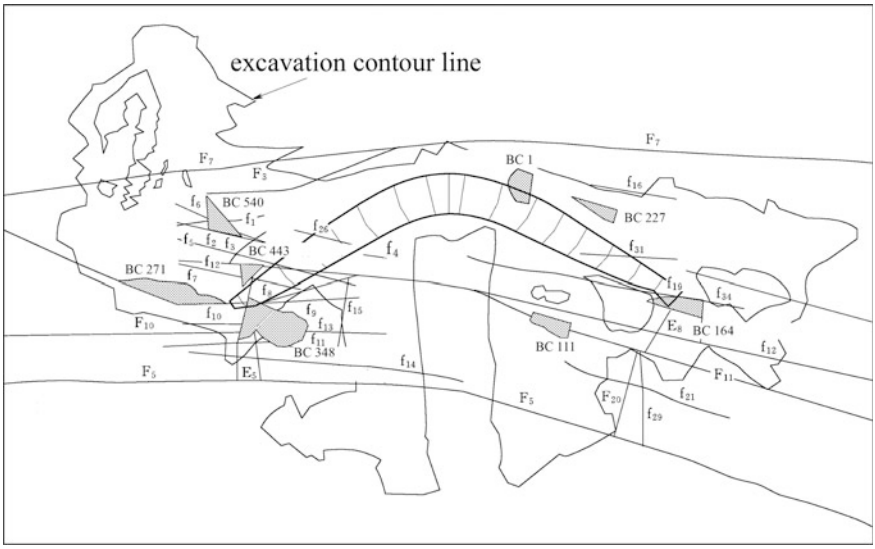

Fig. 13.17 Location of potential failure block combinations (1): phase 2

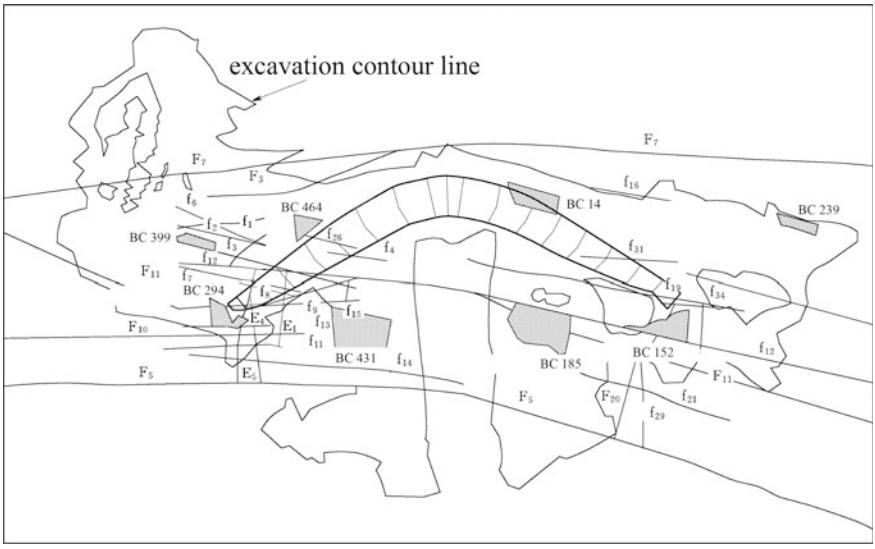

Fig. 13.18 Location of potential failure block combinations (2): phase 2

13.5 Service Period: Abutment Slope Stability

13.5.1 Characteristics of the Computation

Towards the deformation and stability analysis of the abutment slopes under the action of dam thrusts, the block system is identified and illustrated in Figs. 13.19 and 13.20.

Since the rock masses are distinguished into four grades I, II, III and IV (see Table 2.27), the problem is therefore put forward that the parameters of one discontinuity can be changed from a grade of embedded rock to the other. To deal with such variation we construct rock grade boundaries in a similar way to the ground surface using Eq. (3.22). The points for building the boundaries are extracted from geological investigations. They divide the calculated domain into four sub-domains in which a discontinuity can possess different parameters. Each Gaussian quadrature point on a discontinuity is therefore pinpointed to a rock grade zone by its position with respect to the boundary surfaces of the sub-domains (see Fig. 13.21).

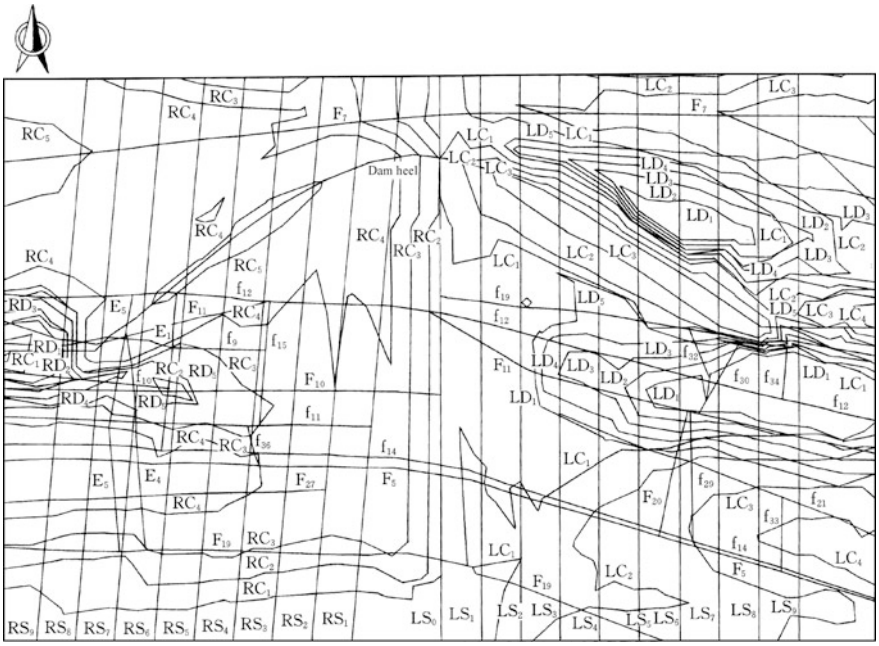

Fig. 13.19 Block system of Xiaowan Arch Dam foundation and abutments: plan

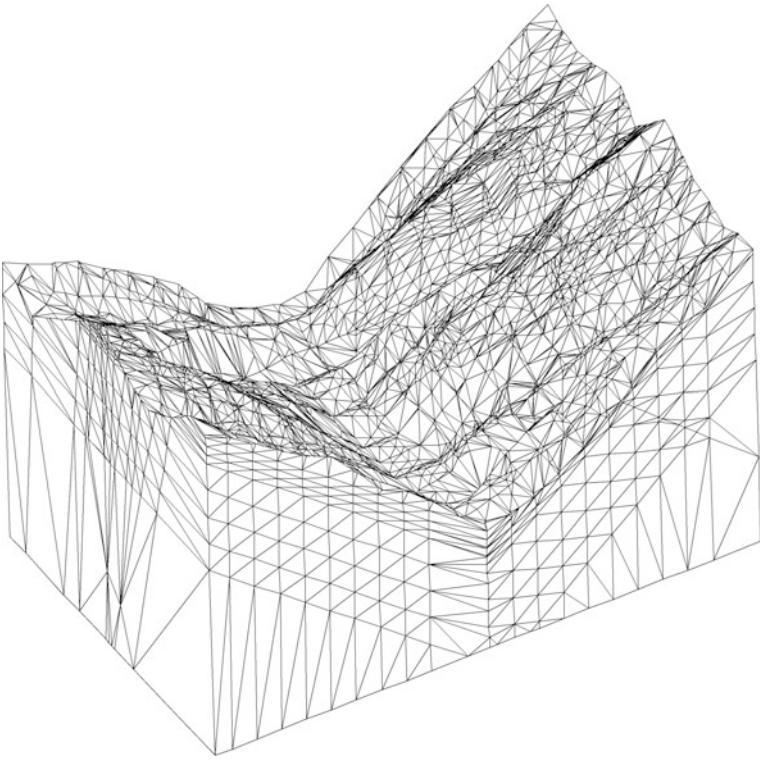

Fig. 13.20 Block system of Xiaowan Arch Dam foundation and abutments: view from downstream left bank

The boundary conditions postulated for the computation of seepage field are that

- The upstream, downstream, and bottom boundary faces are postulated as the second type (without flow exchange);
- The left and the right bank boundary faces are postulated as the first type, on which the groundwater table is 50 m below the ground surface.

13.5.2 Computation Procedure

- The initial seepage field under the natural level of river water is computed with the boundary conditions prescribed;
- The initial in situ geo-stress field is back analyzed taking account of the rock weight and the initial seepage field;
- The dam is constructed and the reservoir is impounded, the thrust forces exerting at the abutment rocks are transferred from the conventional TLM;

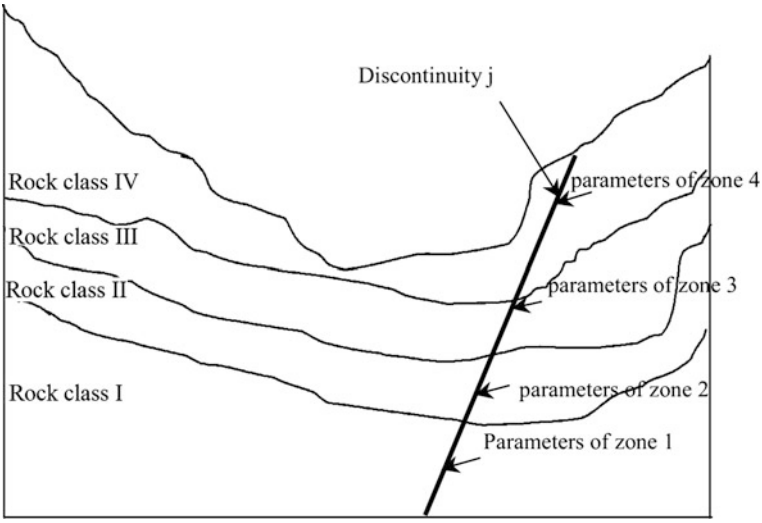

Fig. 13.21 Zoning of discontinuity parameters

– The seepage field is calculated again according to the changed boundary conditions dominated by the reservoir water level;
– Apply the dam thrust forces and seepage force increment after impounding, the deformation and stress of the rock masses are analyzed.

To assess the safety of the dam abutments, the safety factors are calculated by the strength reduction procedure.

13.5.3 Computation Results

(1) Seepage flow

Seepage fields before and after the reservoir impounding are analyzed respectively. The contours of phreatic surfaces are plotted in Figs. 13.22 and 13.23.

It is found that the influence of reservoir impounding is only limited at the vicinity of dam foundation and abutments. Since the groundwater table at the natural state is quite high, the grouting and draining curtains deployed at the dam's foundation and abutments show no significant effect on bringing down the phreatic surface and reducing seepage force in the abutment resistance bodies. Therefore, it is strongly suggested that more attention should be paid to the auxiliary drainage system in the slopes downstream of the abutments (resistance bodies), whose effects may be perceived clearly in Figs. 13.24 and 13.25, where the phreatic surface drops suddenly due to the auxiliary drainage system.

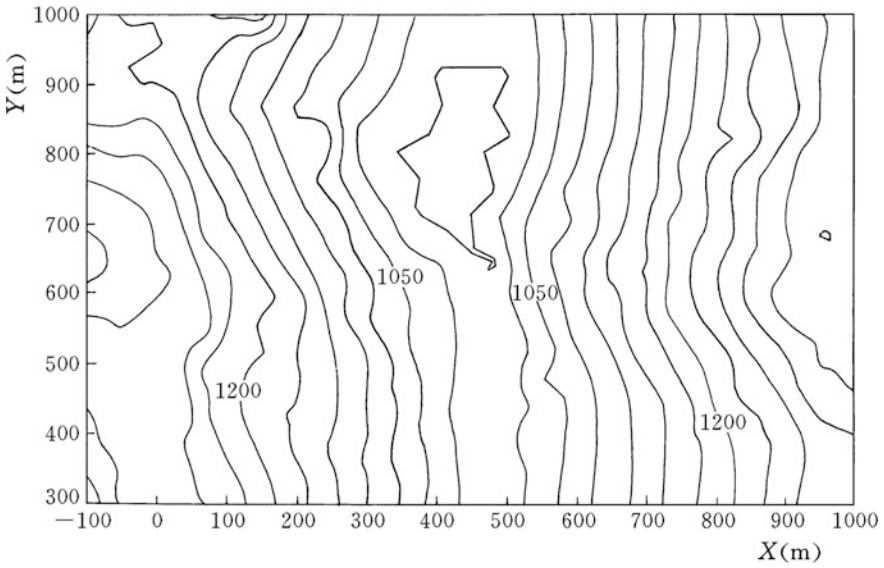

Fig. 13.22 Phreatic surface before reservoir impounding

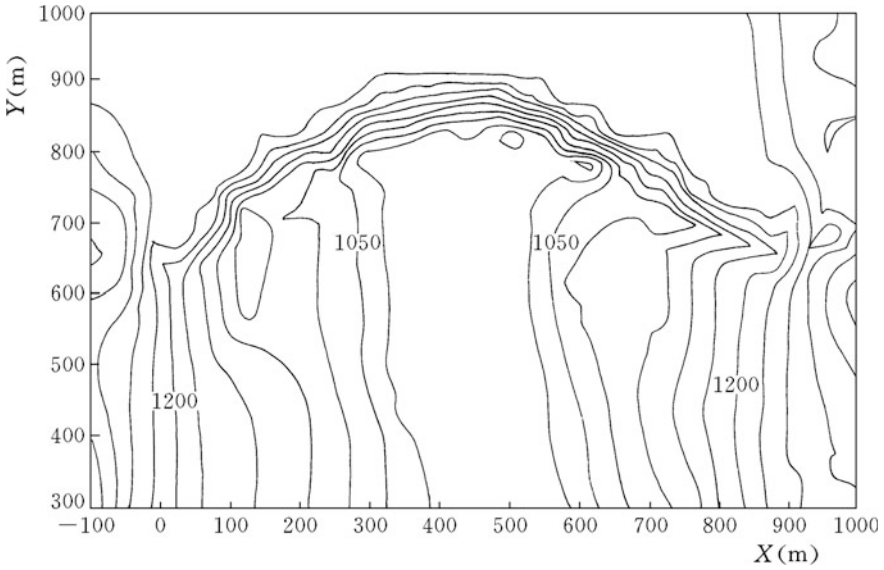

Fig. 13.23 Phreatic surface after reservoir impounding

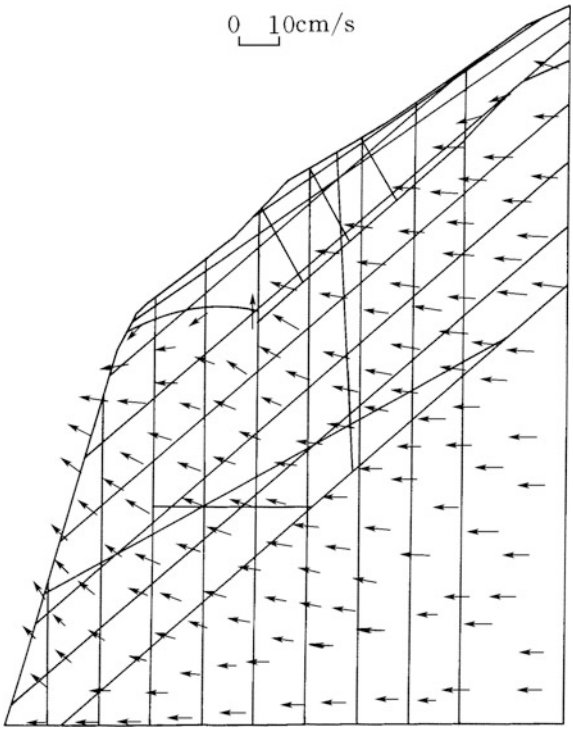

Fig. 13.24 Flow velocity after reservoir impounding in F_{11} (left abutment)

(2) Deformation

When the reservoir is at the normal storage level (NSL) 1240 m, the abutment displacement at the horizontal cross section EL. 1090 m induced by impounding is shown in Fig. 13.26.

The maximum abutment displacement takes place at about the one third of the dam's height, and the displacement at the left bank is greater than that at the right bank. Therefore, it is suggested that more attention should be paid to the left bank abutment in the foundation treatment design.

(3) Stability

Seven modes with higher likelihood of failure formed by block elements or block element combinations, and their corresponding safety factors are summarized in Table 13.8. According to the arch dam design codes of the country, the safety factors of the potential failure modes 4–7 are not sufficiently high since they are lower than 3.5, the strengthened reinforcement measures are therefore desirable for these portions.

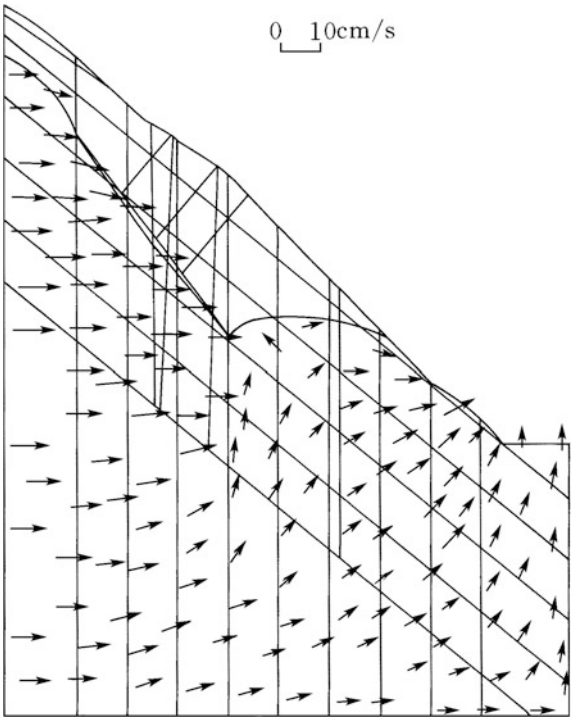

Fig. 13.25 Flow velocity after reservoir impounding in F_{11} (right abutment)

13.6 Service Period: Abutment Stability and Dam Strength

13.6.1 Characteristics of the Computation

(1) Configuration of the dam body

After a long and iterative works, the designer proposed the final optimal scheme of the dam body whose arch rings and layout are provided in Figs. 13.27 and 13.28.

(2) Discretization of the dam and foundation/abutments

The hybrid BEA/TLM system towards the evaluation of dam strength and abutment stability is discretized in Fig. 13.29, in which the block elements for the dam foundation and the arch-cantilever elements for the dam body are displayed. The whole system consists of 2231 block elements and 88 arch-cantilever elements (9 arch rings and 17 cantilevers).

(3) Parameters used in the analysis

The mechanical parameters of the discontinuities are identical to that in Sect. 13.5.

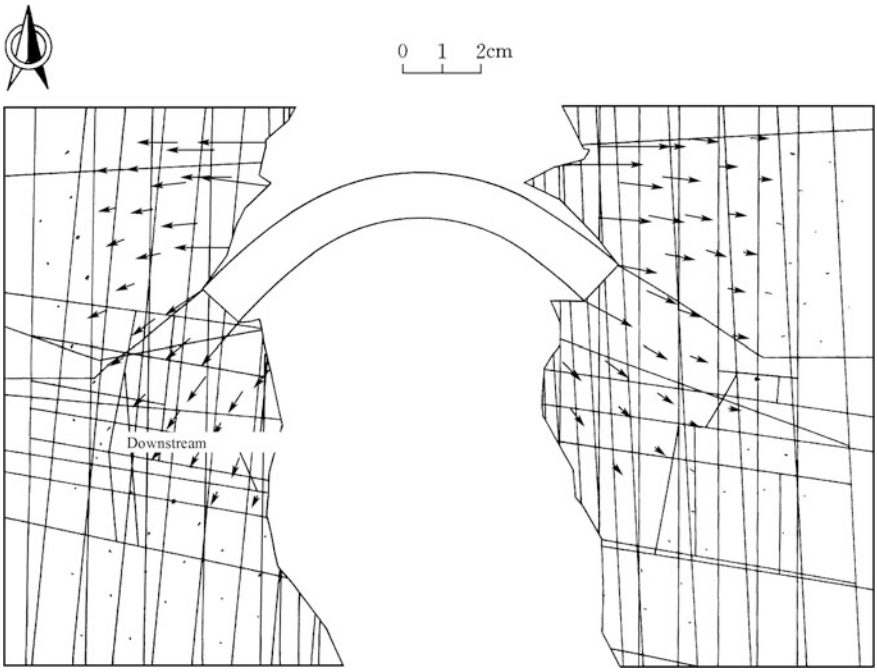

Fig. 13.26 Displacements of the abutments at the cross section EL. 1090 m

Table 13.8 Potential failure modes and corresponding safety factors

Failure mode sequence	Description of the failure mode	Safety factor	
		BEA	LEM
1	Fault F_5, nearly transverse river joint + nearly river trending and low dip joint + nearly river trending and high dip angle joint + ground surface	3.8	5.7
2	Nearly transverse river joint + nearly river trending and low dip angle joint + nearly river trending and high dip angle joint + ground surface	4.2	4.3
3	Nearly transverse river joint + nearly river trending and low dip angle joint + nearly river trending and high dip angle joint + ground surface	3.4	3.9
4	Nearly river trending and low dip angle joint + nearly river trending and high dip angle joint + ground surface	2.0	2.3
5	Nearly river trending and low dip angle joint + nearly river trending and high dip angle joint + ground surface	1.6	2.9
6	Fault f_{12} + fault F_5 + nearly river trending and low dip angle joint + nearly river trending and high dip angle joint + ground surface	2.3	3.0
7	Fault f_{12} + nearly river trending and low dip angle joint + nearly river trending and high dip angle joint + ground surface	1.2	1.6

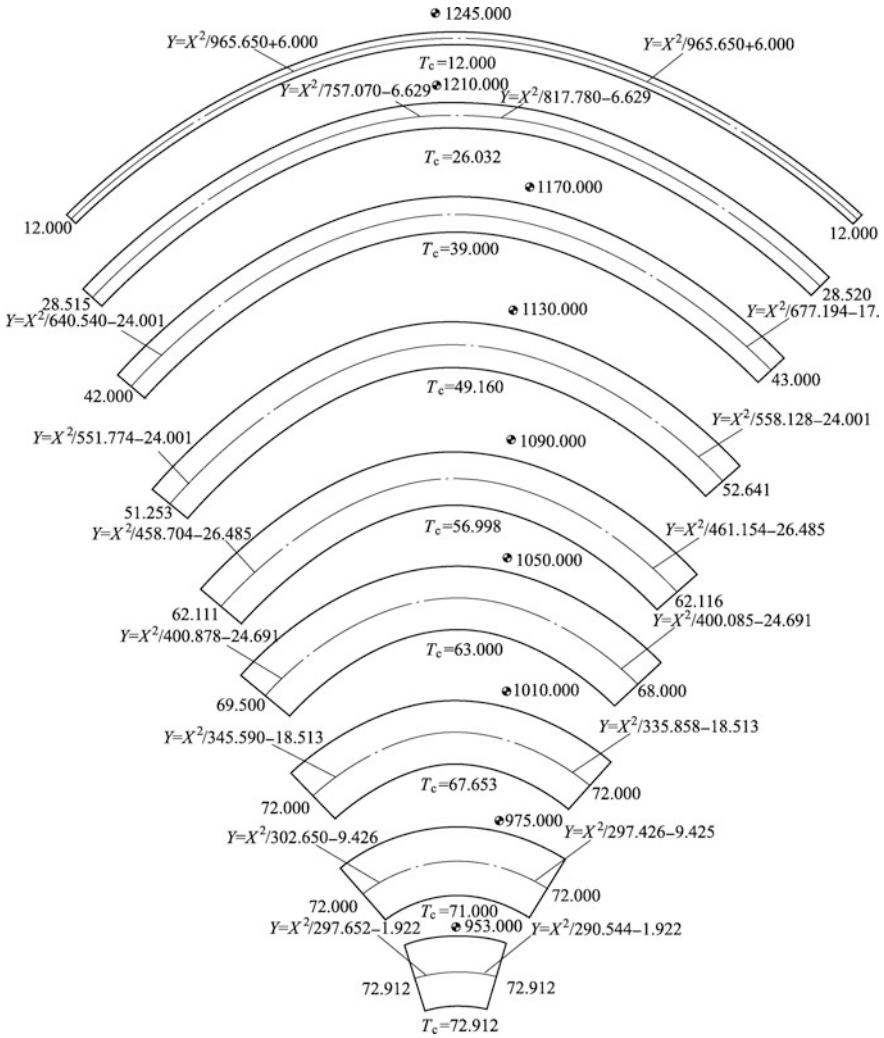

Fig. 13.27 Decomposed arch rings of Xiaowan Arch Dam

The elastic behavior is stipulated for the dam concrete whose Young's modulus and Poisson's ratio are E = 20.78 GPa and μ = 0.18, respectively.

(4) Loads

The calculation is carried out towards the basic load combination comprising: self-weight + water pressure of the normal storage level (∇1240 m) + water pressure of the downstream tail water level (∇1004 m) + silt pressure of the inactive storage level (∇1097 m) + temperature drop + seepage increment.

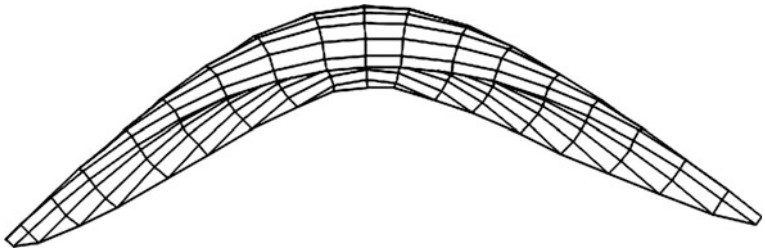

Fig. 13.28 Layout of Xiaowan Arch Dam: plan

The seepage field in the dam foundation and abutments illustrated in the Sect. 13.5 will be employed directly. The mean temperature drop and the linear temperature variation (see Fig. 13.30) are evaluated according to the method stipulated by design specifications SL282-2003 and DL/T5346-2006. For the calculation of other loads, our readers are referred to the literature (Chen 2015).

13.6.2 Computation Results

(1) Displacements

Figures 13.31 and 13.32 present the displacements induced by the reservoir impounding at the cross section of EL. 1090 m and EL. 1245 m, when the reservoir is at the normal storage level 1240 m. All the other cross sections show similar displacement patterns.

It is remarkable that the maximum downstream displacement of the arch dam appears on the crest of the crown cantilever, which is about 0.1544 m. In addition, the displacement of the left bank abutment slope is greater than that of the right bank. For example, the maximum displacements of the abutment slope manifesting at the elevation of 1090–1010 m are 0.027 m at the left abutment and 0.020 m at the right abutment, respectively. The explanation is that there are two deeper gullies at the upstream and downstream of the left abutment. The existence of these gullies makes the rock masses easier to be deflected under the combined actions of self-weight and dam thrust forces. It is, therefore, suggested that more attention should be paid to the left bank in the design of the foundation and abutment treatment.

(2) Stresses

Figure 13.33 plots the contours of the principal stresses at the crown cantilever, Figs. 13.34, 13.35, 13.36 and 13.37 plot the horizontal and vertical stresses on the upstream and downstream dam surfaces meanwhile Figs. 13.38 and 13.39 exhibit the principal stresses. The minimum and maximum stresses of the dam are −16.07 and 3.84 MPa, respectively, which appear at the toe and heel of the crown

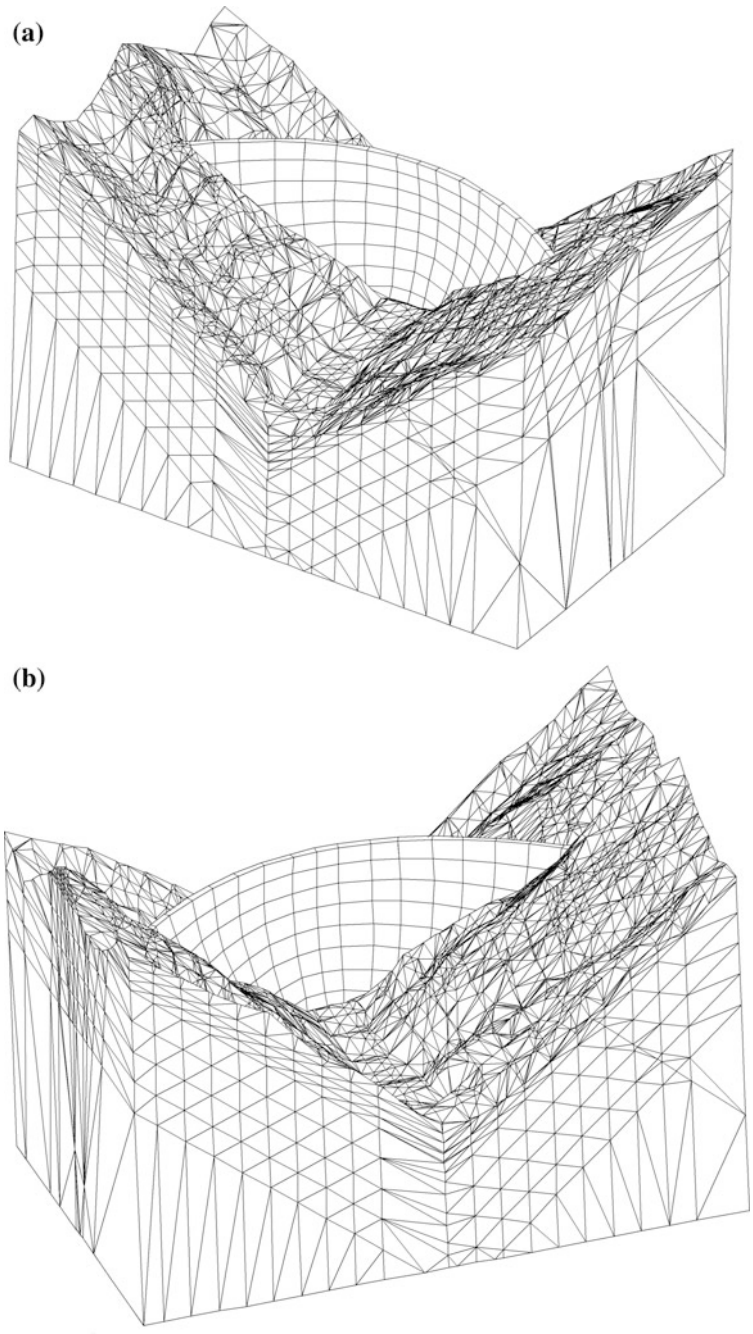

Fig. 13.29 Axonometric perspective of discrete system of Xiaowan Arch Dam. **a** View from downstream left bank; **b** view from downstream right bank

(a) Average temperature drop Unit: ℃

−1.258	−1.258	−1.258	−1.258	−1.258	−1.258	−1.258	−1.258	−1.258	−1.258	−1.258	−1.258	−1.258	−1.258	−1.258	−1.258	−1.258	−1.258	−1.258
	0.037	0.037	0.027	0.018	0.007	0	−0.007	−0.011	−0.014	−0.011	−0.008	−0.002	0.005	0.014	0.025	0.037	0.037	
		0.447	0.447	0.442	0.435	0.43	0.426	0.423	0.422	0.424	0.427	0.432	0.438	0.446	0.455	0.455		
			0.755	0.755	0.751	0.748	0.746	0.744	0.743	0.745	0.748	0.752	0.756	0.762	0.762			
				0.785	0.785	0.779	0.773	0.769	0.766	0.769	0.772	0.778	0.785	0.785				
					0.808	0.808	0.799	0.793	0.788	0.792	0.796	0.804	0.804					
						0.814	0.814	0.807	0.803	0.808	0.814	0.814						
							0.727	0.727	0.726	0.727	0.727							
								1.233	1.233	1.233								

(b) Linear temperature drop Unit: ℃

0	0	0	0	0	0	0	0	0	0	0	0	0	0	0	0	0	0	0
	5.751	5.751	5.719	5.69	5.653	5.628	5.607	5.593	5.584	5.592	5.603	5.622	5.644	5.674	5.711	5.751	5.751	
		8.75	8.75	8.725	8.693	8.671	8.653	8.64	8.631	8.642	8.656	8.68	8.708	8.743	8.787	8.787		
			9.505	9.505	9.485	9.472	9.46	9.452	9.447	9.456	9.468	9.489	9.512	9.542	9.542			
				9.754	9.754	9.719	9.687	9.663	9.647	9.664	9.684	9.718	9.754	9.754				
					9.883	9.883	9.834	9.797	9.771	9.792	9.818	9.859	9.859					
						9.92	9.92	9.881	9.853	9.884	9.92	9.92						
							6.072	6.072	6.064	6.072	6.072							
								5.213	5.213	5.213								

Fig. 13.30 Temperature variation on the dam surface. **a** Average; **b** gradient

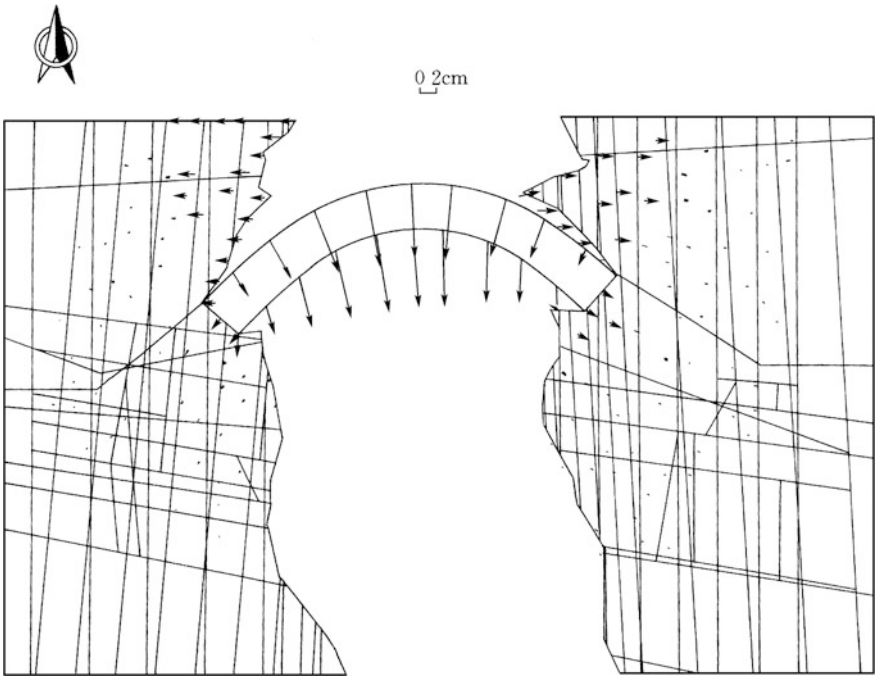

Fig. 13.31 Displacements of dam and abutments at the cross section EL. 1090 m

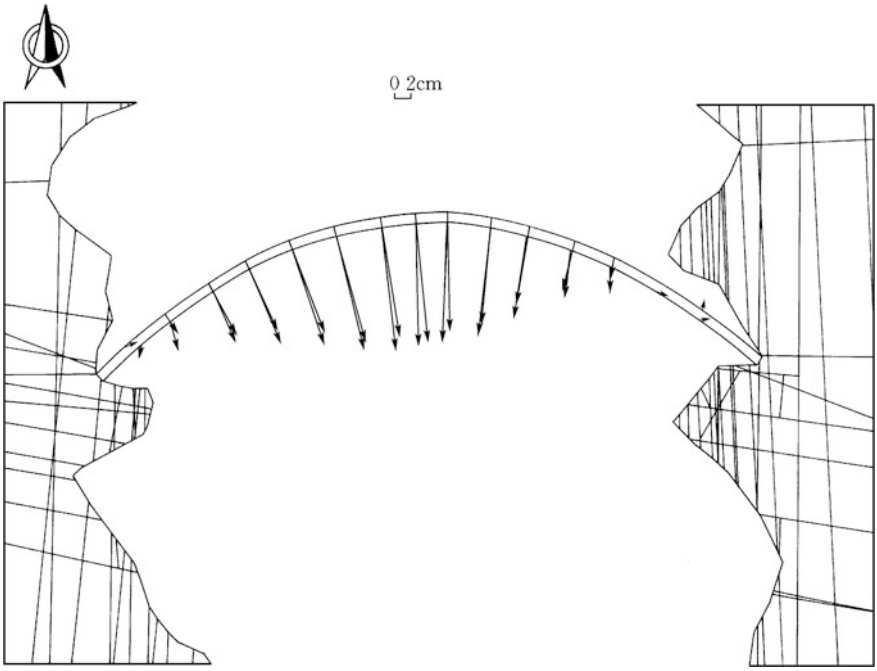

Fig. 13.32 Displacements of dam and abutments at the cross section EL. 1245 m

cantilever. The maximum tensile stress is a bit of larger than the allowable value, it means cracking risk does exist at the dam's heel. The suggestion is therefore put forward that further comprehensive analysis should be made by the other available methods (e.g. FEM, geo-material model test) concerning the dam heel cracking problem. Eventually, a base joint at dam heel is installed near the upstream dam base. This base joint at dam heel may transfer compression stress but has no resistance to the tensile stress. It is actually a variant of peripheral joint (Chen 2015).

(3) Stability

By the intelligent search strategy, 17 modes (blocks or/and block combinations) with higher likelihood of failure are detected whose safety factors are comparatively lower and the reinforcement treatment is desirable. It is also found that more potential failure cases are located at the left abutment (12 modes) than at the right abutment (5 modes). The explanation is that the left abutment is weaker due to the existence of deeper gullies. Figure 13.40 show the location and size of failure mode 4 which possesses a stability safety factor K = 2.1.

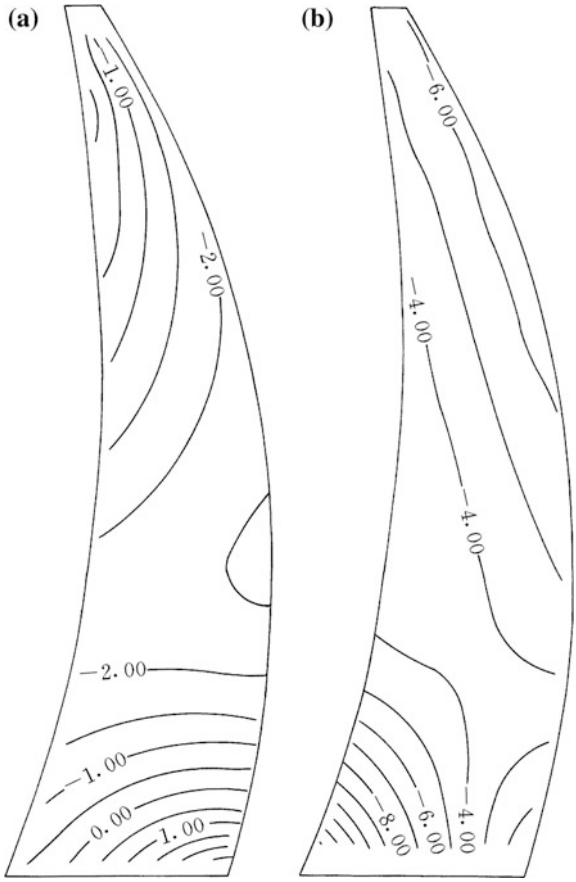

Fig. 13.33 Contours of principal stresses at the crown cantilever (MPa). **a** σ_1; **b** σ_3

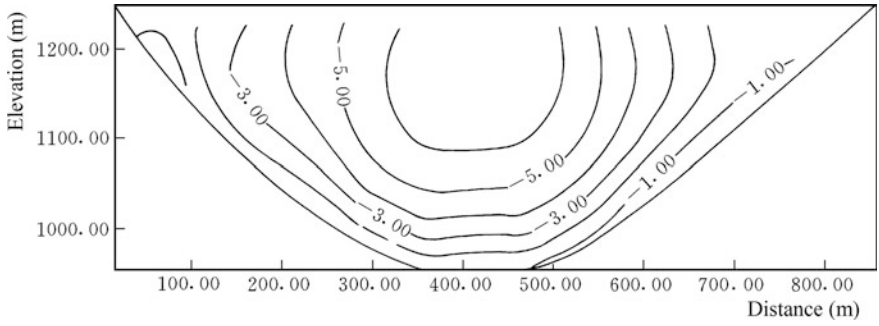

Fig. 13.34 Contours of stress σ_x on the upstream dam surface (MPa)

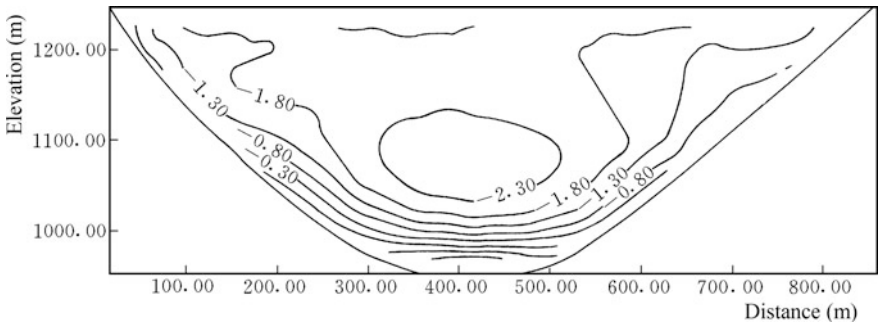

Fig. 13.35 Contours of stress σ_z on the upstream dam surface (MPa)

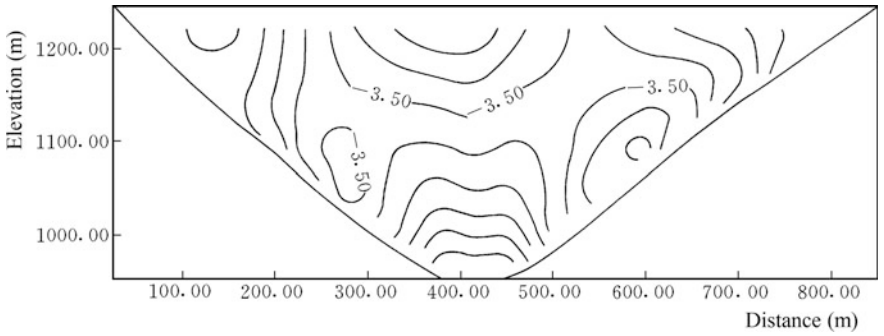

Fig. 13.36 Contours of stress σ_x on the downstream dam surface (MPa)

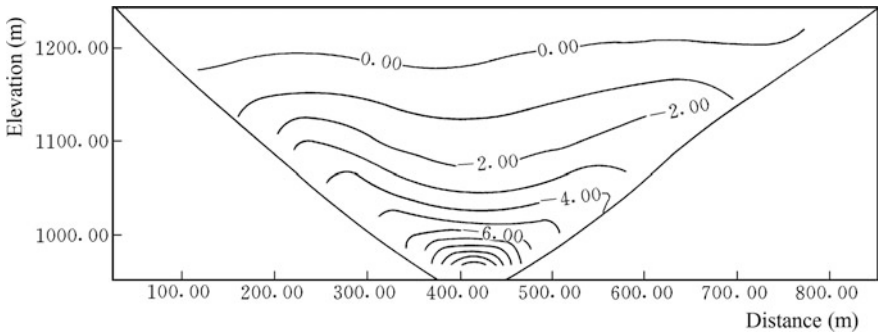

Fig. 13.37 Contours of stress σ_z on the downstream dam surface (MPa)

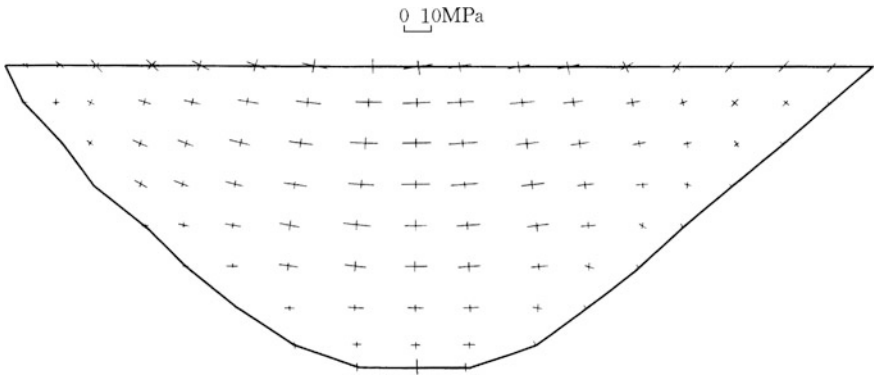

Fig. 13.38 Principal stresses on the upstream dam surface

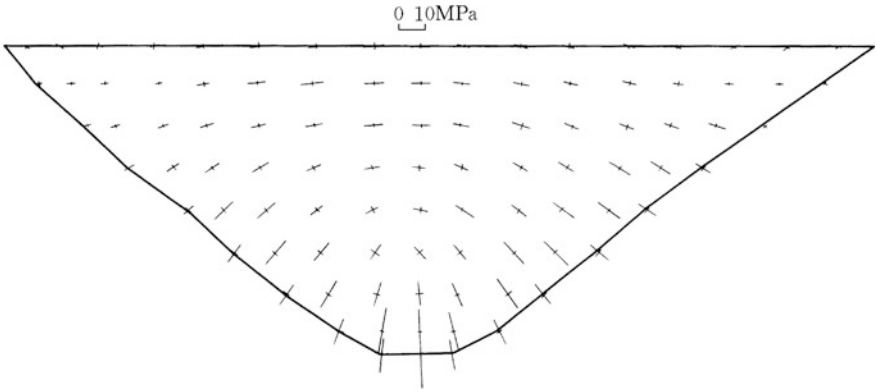

Fig. 13.39 Principal stresses on the downstream dam surface

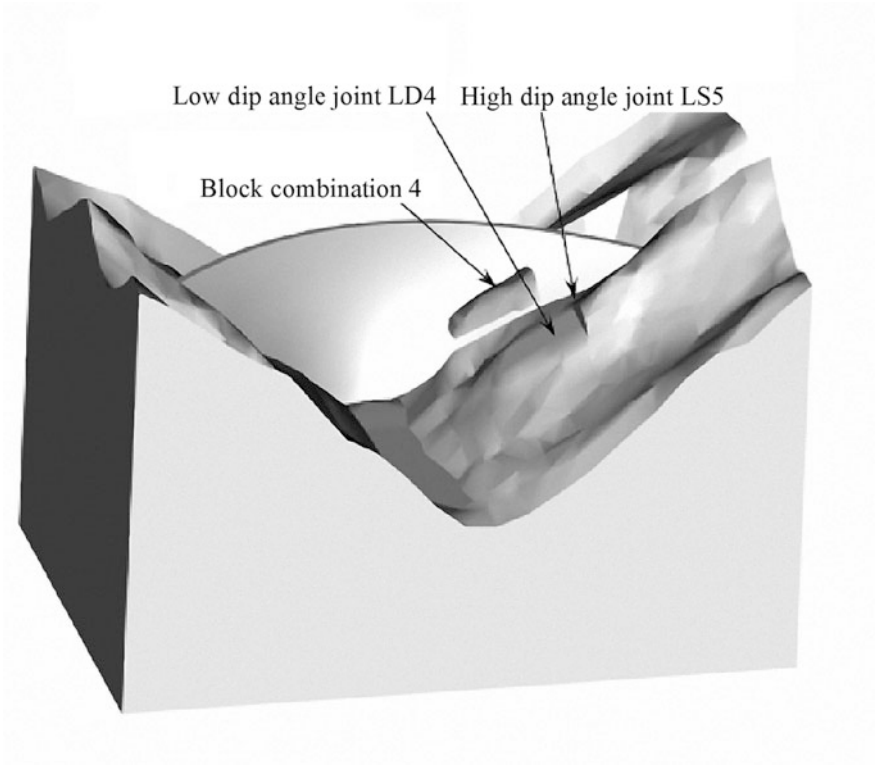

Fig. 13.40 Axonometric drawing of failure mode 4 (K = 2.1): view from downstream right bank

References

Ang AHS, Newmark NM. A probabilistic seismic safety assessment of the Diablo Canyon Nuclear Power Plant. Washington, DC: US Nuclear Regulatory Commission; 1977.

Chen SH. Hydraulic structures. Berlin: Springer; 2015.

Chen SH, Wang WM, She CX, Xu MY. Unconfined seepage analysis of discontinuous rock slope. J Hydrodynamics (Ser B). 2000;12(3):75–86.

Chen SH, Shahrour I, Egger P, Wang WM. Elasto-viscoplastic block element method and its application to arch dam abutment slopes. Rock Mech Rock Eng. 2002;35(3):171–93.

Chen SH, Xu MY, Shahrour I, Egger P. Analysis of arch dams using coupled trial load and block element methods. J Geotech Geoenviron Eng ASCE. 2003;129(11):977–86.

Chen SH, Wang WM, Zheng HF, Shahrour I. Block element method for the seismic stability of rock slopes. Int J Geotech Geoenviron Eng ASCE. 2010;136(12):1610–7.

Xu MY, Wang WM, Chen SH. Research on the dangerous sliding-block combination of rock slopes. Rock Soil Mech. 2000;21(2):148–51 (in Chinese).

Zou LC. Challenge and thinking of constructing Xiaowan Hydropower Project. J Hydroelectric Eng. 2010;36(12):15–9 (in Chinese).

Chapter 14
Fundamentals of the Composite Element Method

Abstract This chapter summarizes the principles related to the composite element method (CEM), which is one of the most promising computational methods in handling discontinuities, bolts, drainage holes, and cooling pipes explicitly to give their detailed description using simple computation mesh. The FE mesh should be generated beforehand to discretize the structure concerned, where the deployment and size of finite elements are dominated by the structure configuration and the gradient of basic variables (displacement, hydraulic potential, temperature). A certain number of sub-elements representing heterogeneous components (joints, bolts, draining holes, cooling pipes) are allocated within an element (standard or hierarchical) that is named as the composite element. The basic variables within each sub-element are interpolated from the correspondent nodal variables bound at the composite element. According to the virtual work or variational principle, the governing equations are established to solve these basic variables. In this manner, less restraint is imposed on the mesh generation with considerable amount of heterogeneous components, which allows for a great simplification in the pre-process work towards the computation for complex hydraulic structures.

14.1 General

As we have discussed in Chap. 6 that in general, the FEM to simulate the discontinuities, bolts and drainage holes fall into the implicit (equivalent) approach which takes into account of their influences on the compliance/permeability tensor but neglects their exact positions (Barenblatt et al. 1960; Snow 1969; Huyakorn et al. 1983; Pande and Gerrard 1983; Guan et al. 1984; Dershowitz et al. 1985; Long et al. 1985; Oda 1986; Sharma and Pande 1988; Chen and Pande 1994; Chen and Egger 1999) and the explicit (distinct) approach which uses special elements to exactly simulate their geological and mechanical properties (Mahtab and Goodman 1970; Wilson and Witherspoon 1974; Duiguid and Lee 1977; Streltsova 1981; Zhu 1982; Du et al. 1984; Fipps et al. 1986; Andersson and Dverstorp 1987; Aydan

S.-H. Chen, *Computational Geomechanics and Hydraulic Structures*,
Springer Tracts in Civil Engineering, https://doi.org/10.1007/978-981-10-8135-4_14

1989; Cacas et al. 1990; Du et al. 1991; Swoboda et al. 1991, 1992; Nordqvist et al. 1992; Wang et al. 1992; Long 1996; Chen and Egger 1997; Wang et al. 2001). The former can be applied to very complex engineering problems with a large quantity of discontinuities and bolts as well as drainage holes, whereas the latter possesses the potentiality to describe them in much more detail and consequently gives more precise solution.

The simulation of bolts within the framework of the discrete element methods was initiated by incorporating the performance of point anchored bolt in the DEM (Lorig 1984, 1985) in which a reinforcement component is simulated by the one-dimensional bar element. Fully bonded reinforcement however, is more difficult to represent in the discrete element methods, as it contributes significant shear stiffness and strength to a discontinuity through which it passes. In Chap. 12, we take the bolt/pile as one-dimensional beam element which applies elasto-viscoplastic restraint to the relative shear displacements of a block with respect to its prescribed adjacent block. The BEA elaborated in this book also simulates the grouting/drainage curtain using a special block stripe with very low/high hydraulic conductivity (see Chap. 9). Although these treatments may extract the overall effects on the stress/stability and permeability of hydraulic structures, yet a portion of details with regard to the reinforcement components and seepage mitigation devices are lost. For example, fully bonded reinforcement is difficult to be satisfactorily simulated, as in addition to the contribution of shear stiffness and strength to discontinuities, it also contributes significant axial stiffness to the block system, which is crucial in the evaluation of its pull-out failure.

The temperature fluctuation in a concrete structure due to the hydration process and thermal flow results in temperature differences (drop or rise) which in turn, produce thermal stresses attributable to the restraint conditions present in the structure. The most adverse effect of the thermal stresses is the concrete cracking (ACI 1987), which is one of the main issues in structural design, in particular when mass concrete is encountered (Chen et al. 2011). Methods often exercised for bringing down the temperature gradients within a structure, and thus also the risk of cracking, are to place concrete in layered column embedded with exposure surfaces (lift joints) and to cool the inner core with embedded cooling pipes in which water performs as the cooling medium. Such techniques were firstly employed to construct Hoover Dam (BOR 1971). Lift joints influence not only the deformation and seepage flow but also the temperature field of mass concrete structures. This is particularly important in the application of Roller Compacted Concrete (RCC) technique (Tatro and Schrader 1985, 1992; Ishikawa 1991; Springenschmid et al. 1994; Zhang and Garga 1996).

To prevent early age cracking, one of the paramount tasks for structure designers is the evaluation of the thermal field and its history in concrete. Based on this evaluation the structural configuration can be adjusted, the protection and cooling requirements also can be proposed. Various methods are reported in the literatures for the thermal analysis of concrete, which are ranged from complex three-dimensional finite element method to simple manual calculation. Today, the FEM is more and more prevalent in the thermal analysis for the hydraulic structures

with complex configuration and construction schedule, of which two approaches are generally distinguished with regard to lift joints (Zhu 1991, 1998, 2006; Huang and Yang 1999; Liu et al. 2008). The first one is to handle the lift joint as a contact face without thickness along which only one layer of nodes is discretized, the nodal temperature at the lift joint is always the average one related to the adjacent old and new concrete elements. This approach is simple and easy to be implemented, but it is unable to take into account of the strong thermal gradient across the new and old concrete lifts. The second approach uses thin transition elements along which two layers of nodes are deployed. This approach is able to simulate the strong thermal gradient across the new and old concrete lifts, but the elementary thickness and parameters are difficult to evaluate, and much larger computation effort is demanded. All the above two approaches have one common drawback, namely the computation mesh generation would be tightly restrained by enormous lift joints.

Similarly, the simulation of cooling pipe lattice can also be distinguished as implicit (or equivalent) approach and the explicit (or distinct) approach. The former looks at a volume of concrete containing cooling pipe segments as negative heat inner source, whose intensity is represented by an average coefficient related to the concrete conductivity, the diameter and the orientation as well as the spacing of pipes (Zhu and Cai 1989; Zhu 1991, 1998; Toshiaki et al. 2000). The latter includes some well known models such as the sub-structure technique (Liu and Liu 1997; Zhu and Zhang 2002; Malkawi et al. 2003; Liu 2004). The implicit approach can be applied to very complicated problems with a large number of cooling pipes, whereas the explicit approach has the potentiality to describe the cooling pipes in detail and consequently gives more precise solution.

From the point view of practitioners, the crucial difficulty in the explicit simulation of fractures/joints as well as bolts/drainage holes/cooling pipes with the FEM lies in the pre-process to discrete the calculation domain. This is arise from the reality that on one hand, there are a large amount of discontinuities/joints of different shapes and sizes, and a large amount of drainage holes, cooling pipes, and bolts of small size (e.g. at a diameter of 3–10 cm) deployed within a small width and largely stretched zone (e.g. spaced at 1.5–3 m); on the other hand, the special elements available possess definite nodes, and some of them should be the common nodes of the host entity elements. Consequently, this, plus the complicity in the configuration and construction of hydraulic structures, will lead to time consuming and tedious pre-process overheads.

In recent decades the composite element method (CEM) has been developed which is good at simulating joints, bolts, drainage holes, and cooling pipes within the structures explicitly (Chen et al. 2002, 2003; Chen and Qiang 2004; Chen et al. 2004, 2004; Xu and Chen 2005; Chen and Feng 2006; Chen et al. 2007, 2008; Chen and Shahrour 2008; Chen et al. 2010, 2011a, b; Ding and Chen 2013; Chen et al. 2015). The most attractive advantage with this method is that it may give a detailed description of the non-homogenous and discontinuous properties within an element using simple computation mesh. In this way less restraint is imposed on the

mesh generation for complicated hydraulic structures with considerable amount of joints/bolts/drainage holes/cooling pipes, which allows for a great simplification in the pre-process work towards the engineering application.

14.2 Strain-Stress Problems

14.2.1 Bolts

Suppose an element (standard or hierarchical) r of rock-like material contains n_b sub-elements representing bolt segments ($n_b = 2$ in Fig. 14.1) and n_g sub-elements representing grout segments ($n_g = 2$ in Fig. 14.1). These sub-elements are not necessarily classical finite elements. The contact face between rock r and grout g is denoted as $j_{r,g}$, meanwhile the contact face between grout g and bolt b is denoted as $j_{g,b}$.

The displacements $\{\Delta u\}_r$, $\{\Delta u\}_g$, $\{\Delta u\}_b$ within each sub-element (see Fig. 14.2) are interpolated from the correspondent nodal displacements bound at the composite element by

$$\begin{cases} \{\Delta u\}_r = [N]\{\Delta\delta\}_r \\ \{\Delta u\}_b = [N]\{\Delta\delta\}_b \quad (b = 1, \ldots n_b) \\ \{\Delta u\}_g = [N]\{\Delta\delta\}_g \quad (g = 1, \ldots n_g) \end{cases} \tag{14.1}$$

In which $[N]$ stands for the shape function matrix (standard or hierarchical) of the FEM defined over the whole composite element (see Eq. 4.57). However, it should be emphasized that the interpolation Eq. (14.1) is valid merely in each of the sub-element respectively.

The loads exerting at each sub-element are transferred to the respective nodal forces at the composite element, then the governing equations are established according to the virtual work principle to relate the nodal displacements with the nodal forces.

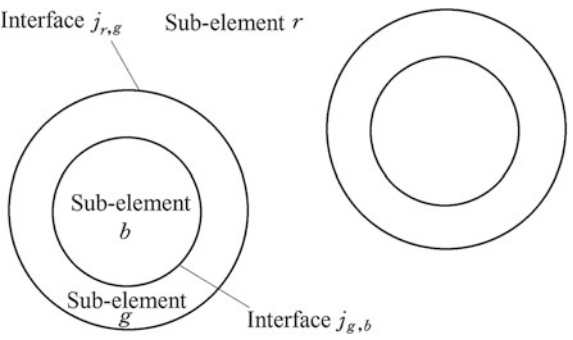

Fig. 14.1 Schematic drawing of a composite element containing fully-grouted bolts

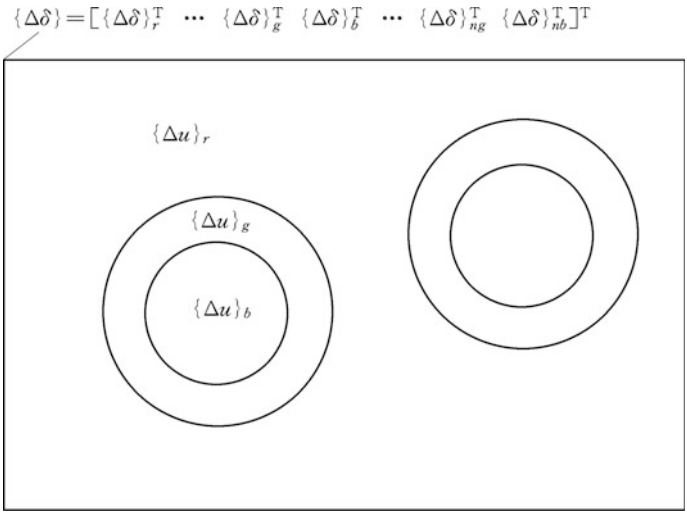

Fig. 14.2 Diagram to the displacement interpolation in a composite element containing fully-grouted bolts

14.2.2 Structural Planes

Finite element mesh should be generated to discretize the structure firstly. The deployment and sizes of elements are dependent on the structure configuration and stress gradient, cares over the existence of the discontinuity system need not to be taken. Then the algebra and geometry calculi will be conducted with the messages of the discontinuity/joint system and the prescribed FE mesh, to construct the CE mesh. In such a CE mesh there are several elements containing discontinuity/joint segments, which are defined as composite elements.

Figure 14.3 shows a composite element containing 4 structural plane segments dividing the element into 4 sub-elements which are not necessarily to be the classical finite elements. Generally, we denote n_r as the number of sub-elements ($n_r = 4$ in Fig. 14.3) and $j_{rl,rm}$ as the discontinuity segment between the sub-element rl and sub-element rm.The displacement $\{\Delta u\}_{rl}$ within each sub-element is interpolated from the correspondent nodal displacements $\{\Delta\delta\}_{rl}$ bound at the composite element (see Fig. 14.4) by

$$\{\Delta u\}_{rl} = [N]\{\Delta\delta\}_{rl} \quad \text{within the sub-element } rl(rl = 1, \ldots n_r) \tag{14.2}$$

In which $[N]$ stands for the shape function matrix of the FEM defined over the whole composite element.

The displacements, the strains and stresses within the sub-element rl are calculated by the corresponding nodal displacements $\{\Delta\delta\}_{rl}$. Meanwhile, the relative displacements, the strains and stresses of the discontinuity segment $j_{rl,rm}$ within the

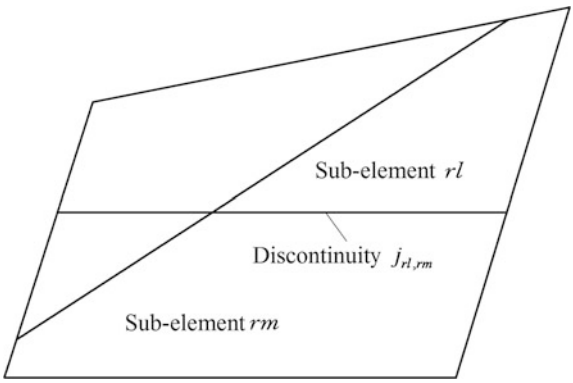

Fig. 14.3 Schematic drawing of a composite element containing structural planes

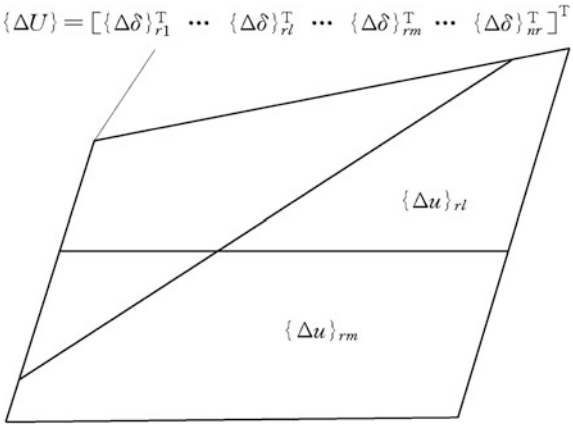

Fig. 14.4 Diagram to the displacement interpolation in a composite element containing structural planes

composite element are calculated by the nodal displacements $\{\Delta\delta\}_{rl}$ and $\{\Delta\delta\}_{rm}$ of its adjacent sub-elements. These displacements can be solved by the governing equations established using the virtual work in a similar procedure of the FEM.

14.3 Seepage Problems

14.3.1 Drainage Holes

Suppose a composite element contains n_d sub-element representing drainage hole segments ($n_d = 2$ in Fig. 14.5). At the boundary of rock/drainage hole there is a virtual interface $j_{r,d}$ leading to the discontinuous characteristics of the hydraulic potential.

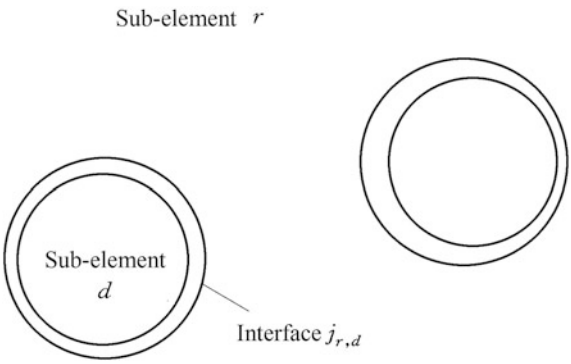

Fig. 14.5 Schematic drawing of a composite element containing drainage holes

The hydraulic potentials in each sub-element ϕ_r and ϕ_d (see Fig. 14.6) respectively are interpolated from their nodal hydraulic potentials $\{\phi\}_r$ and $\{\phi\}_d$ bound at the composite element by

$$\begin{cases} \phi_r = [N]\{\phi\}_r \\ \phi_d = [N]\{\phi\}_d \quad (d = 1, \ \ldots n_d) \end{cases} \tag{14.3}$$

In which $[N]$ stands for the shape function matrix in the FEM defined over the whole composite element. It should be noted that the interpolation Eq. (14.3) is

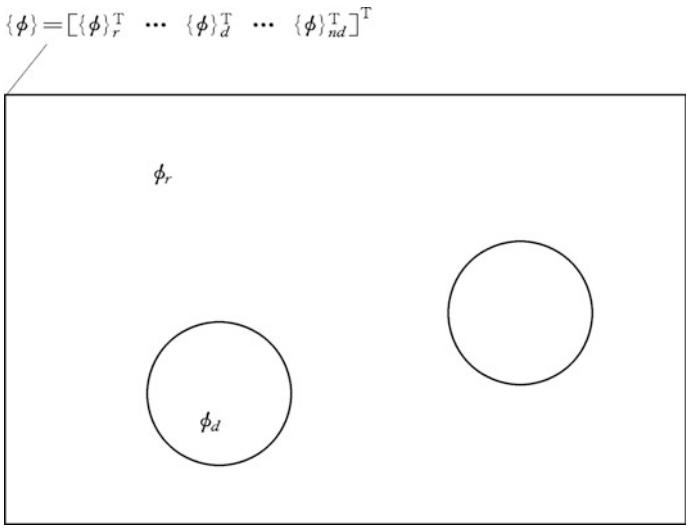

Fig. 14.6 Diagram to the head interpolation in a composite element containing drainage holes

only valid in each of the sub-element respectively. Use is made of the variational principle to establish the governing equations for the solution of $\{\phi\}_r$ and $\{\phi\}_d$.

14.3.2 Structural Planes

Suppose a domain shown in Fig. 14.3 contains n_r sub-elements that probably possess different seepage characteristics. At the boundary of the sub-domains *rl* and *rm* there is an interface $j_{rl,rm}$ representing discontinuity/joint segment. A standard or hierarchical finite element called composite element is defined to cover the whole domain.

The hydraulic potential ϕ_{rl} within each sub-element *rl* (see Fig. 14.7) is interpolated from the correspondent nodal hydraulic potential $\{\phi\}_{rl}$ bound at the composite element as

$$\phi_{rl} = [N]\{\phi\}_{rl} \quad \text{within the sub-element } rl(rl = 1, \ \ldots n_r) \tag{14.4}$$

In which $[N]$ stands for the shape function matrix of the FEM defined over the whole composite element.

By the variation principle, the governing equations can be established to solve the unknown nodal hydraulic potential $\{\phi\}_{rl}$.

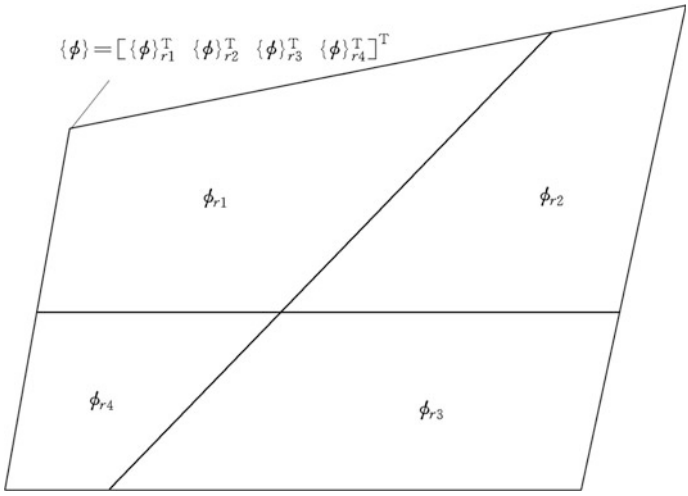

Fig. 14.7 Diagram to the head interpolation in a composite element containing structural planes

14.4 Thermal Problems

14.4.1 Cooling Pipe

The FE mesh should be generated to discretize the structure beforehand. The refinement and sizes of the finite elements are mainly dependent on the structure configuration, concrete placement process, and temperature gradient. Then, the presence of cooling pipes transfers related finite elements into composite elements through geometrical calculi. Figure 14.8 shows such a composite element containing one concrete sub-element c, n_w cooling water sub-elements wi ($n_w = 4$ in Fig. 14.8) and the same number of cooling pipe sub-elements $j_{c,wi}$ looked at as the interface between concrete sub-element c and water sub-elements wi.

There are independent nodal variables (temperatures) for the concrete sub-element and the cooling water sub-elements assembled in a vector $\{T\} = \left[\{T\}_c^T, \{T\}_{w1}^T, \{T\}_w^T, \ldots, \{T\}_{n_w}^T\right]^T$ (see Fig. 14.9), which can be used directly in the temperature interpolations

$$\begin{cases} T_c = [N]\{T\}_c \\ T_{wi} = [N]\{T\}_{wi} \quad (wi = 1, 2, \ldots, n_w) \end{cases} \tag{14.5}$$

The temperature of pipe is not an independent variable and will be averaged by the formula

$$T_{pi} = (T_c + T_{wi})/2 \tag{14.6}$$

In Eq. (14.5), $[N]$ stands for the shape function matrix defined over the whole composite element.

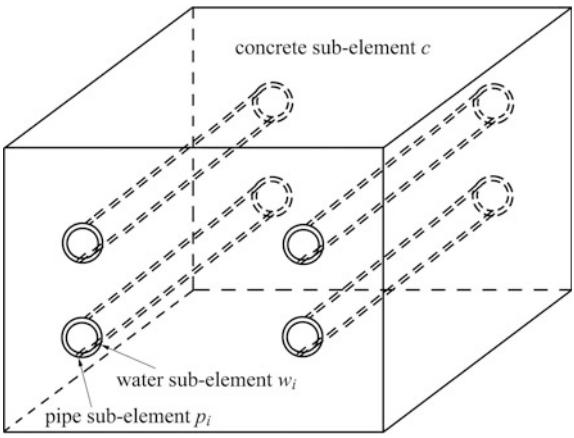

Fig. 14.8 Schematic drawing of a composite element containing cooling pipes

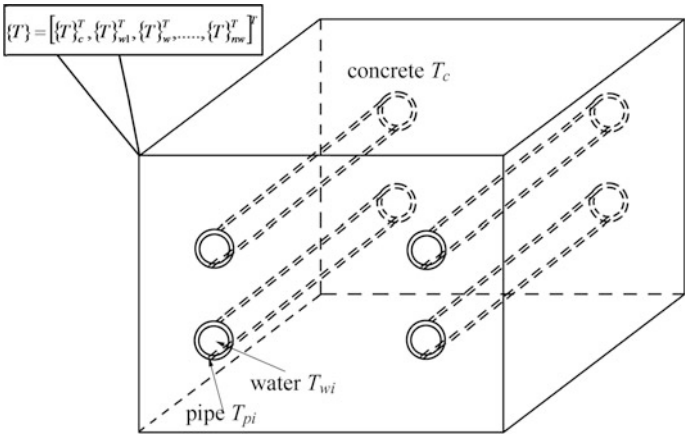

Fig. 14.9 Diagram to the temperature interpolation in a composite element containing cooling pipes

It should be emphasized that the interpolation Eqs. (14.5) and (14.6) are only valid in each of the sub-element merely to ensure the segmental characteristics of the temperature T.

14.4.2 Lift Joints

In the finite element mesh for a concrete structure, the presence of lift joints gives rise to a number of composite elements through the geometric calculation using the messages of the FE mesh and lift joints. Figure 14.10 shows a typical composite element contains n_c sub-elements connected by $n_c - 1$ lift joint segments.

Nodal temperatures are associated to the composite element including both the "real" nodal temperatures and additional temperatures used for the interpolation only. Generally, the DOF of a composite element composed of n_c sub-elements is n_c times that of the conventional finite element. In Fig. 14.11 all the nodal

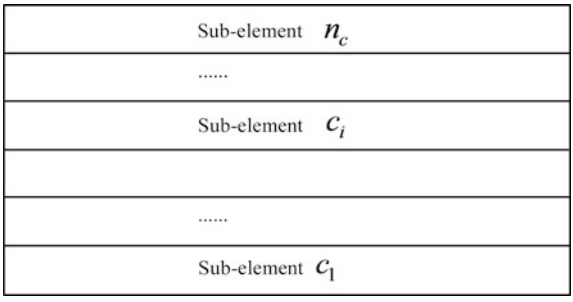

Fig. 14.10 Schematic drawing of a composite element containing lift joints

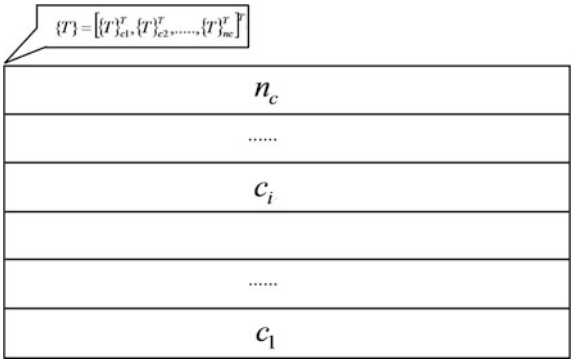

Fig. 14.11 Diagram to the temperature interpolation in a composite element containing lift joints

temperatures of the n_c sub-elements bound at the composite element are arranged as one nodal temperature vector $\{T\} = \left[\{T\}_{c1}^T, \{T\}_{c2}^T, \ldots, \{T\}_{n_c}^T\right]^T$. In the following discussion the subscripts *ci* and $j_{cl,cm}$ will be used for the variables of the concrete sub-element and the lift joint segment between the concrete sub-elements *cl* and *cm*, respectively.

The temperature T_{ci} in each sub-element is interpolated from the nodal temperature $\{T\}_{ci}$ bound at the composite element by

$$T_{ci} = [N]\{T\}_{ci} \quad \text{within the sub-element } ci \; (ci = 1, \ldots n_c) \tag{14.7}$$

In which $[N]$ stands for the matrix of shape function defined in the whole composite element. The nodal temperatures $\{T\}_{ci}$ can be solved by the governing equations based on the variational principle similar to that of the FEM.

References

American Concrete Institute (ACI). Mass concrete. Detroit (USA): ACI Committee 207; 1987.

Andersson J, Dverstorp B. Conditional simulation of fluid flow in three-dimensional networks of discrete fractures. Water Resour Res. 1987;23(10):1876–86.

Aydan O. The stabilisation of rock engineering structures by rockbolts. Ph.D. thesis, Japan: Nagoya University; 1989.

Barenblatt GI, Zheltov IP, Kochina IN. Basic concepts in the theory of seepage of homogenous liquids in fissured rocks. J Appl Math Mech. 1960;24(5):12–8.

Bureau of Reclamation. The story of Hoover Dam. Washington DC (USA): BOR; 1971.

Cacas MC, Ledoux B, De Marsity G, Tillie B, Barbreau A, Durand E, Feuga B, Peaudecerf P. Modeling fracture flow with a stochastic discrete fracture network: calibration and validation, 1. The flow model. Water Res Res. 1990;26(3):479–89.

Chen SH, Egger P. Elasto-viscoplastic distinct modelling of bolt in jointed rock masses. In: Yuan JX, editor. Proceedings of computer method and advances in geomechanics. Rotterdam (Netherlands): AA Balkema; 1997. p. 1985–90.

Chen SH, Egger P. Three dimensional elasto-viscoplastic finite element analysis of reinforced rock masses and its application. Int J Num Anal Meth Geomech. 1999;23(1):61–78.

Chen SH, Feng XM. Composite element model for rock mass seepage flow. J Hydrodyn (Ser. B). 2006;18(2):219–24.
Chen SH, Pande GN. Rheological model and finite element analysis of jointed rock masses reinforced by passive, fully-grouted bolts. Int J Rock Mech Min Sci Geomech Abstr. 1994;31 (3):273–7.
Chen SH, Qiang S. Composite element model for discontinuous rock masses. Int J Rock Mech Min Sci Geomech Abstr. 2004;41(7):865–70.
Chen SH, Egger P, Migliazza R, Giani GP. Three dimensional composite element modelling of hollow bolt in rock masses. In: Dinis da Gama C, Ribeiro e Sousa L, editors. Proceedings of ISRM international symposium rock engineering mount regions—Eurock'2002. Rotterdam (Netherlands): AA Balkema; 2002. p. 753–9.
Chen SH, Zhang GX, Zhu YM. Thermal stresses and temperature control of concrete. In: Zhou JP, Dang LC, editors. Handbook of hydraulic structure design, vol. 5—Concrete Dams (Chapter 6). Beijing (China): China Water Power Press; 2011 (in Chinese).
Chen SH, Shahrour I. Composite element method for the bolted discontinuous rock masses and its application. Int J Rock Mech Min Sci. 2008;45(3):384–96.
Chen SH, He ZG, Egger P. Study of hollow friction bolts in rock by a three dimensional composite element method. In: Merwe JN, editor. Proceedings of 10th ISRM congress—technology roadmap for rock mechanics. Johannesburg (South Africa): ISRM; 2003. p. 203–6.
Chen SH, Qiang S, Chen SF, Egger P. Composite element model of the fully grouted rock bolt. Rock Mech Rock Eng. 2004;37(3):193–212.
Chen SH, Xu Q, Hu J. Composite element method for seepage analysis of geotechnical structures with drainage hole array. J Hydrodyn (Ser B). 2004;16(3):260–6.
Chen SH, Qin WX, Xu Q. Composite element method and application of trace simulation for strain localization bands. Chin J Rock Mechan Eng. 2007;26(6):1116–22 (in Chinese).
Chen SH, Qiang S, Shahrour I, Egger P. Composite element analysis of gravity dam on a complicated rock foundation. Int J Geomech ASCE. 2008;8(5):275–84.
Chen SH, Xue LL, Xu GS, Shahrour I. Composite element method for the seepage analysis of rock masses containing fractures and drainage holes. Int J Rock Mech Min Sci. 2010;47(5):762–70.
Chen SH, Su PF, Shahrour I. Composite element algorithm for the thermal analysis of mass concrete: simulation of lift joint. Finite Elem Anal Des. 2011a;47:536–42.
Chen SH, Su PF, Shahrour I. Composite element algorithm for the thermal analysis of mass concrete: simulation of cooling pipes. Int J Numer Meth Heat Fluid Flow. 2011b;21(4):434–47.
Chen SH, Zhang X, Shahrour I. Composite element model for the bonded anchorage head of stranded wire cable in tension. Int J Num Anal Meth Geomech. 2015;39(12):1352–68.
Dershowitz WS, Gordon BM, Kafritsas JC. A new three-dimensional model for flow in fractured rock. In: Proceedings of memoirs of the 17th international cong of IAH, vol. XVII. Tucson, Arizona (USA): IAH; 1985. p. 441–8.
Ding JX, Chen SH. Simulation and feedback analysis of the temperature field in massive concrete structures containing cooling pipes. Appl Therm Eng. 2013;61(2):554–62.
Du YL, Xu GA, Huang YH. The study of three-dimensional seepage analysis for the complex rock foundation. J Hydraul Eng. 1984;6(3):1–9 (in Chinese).
Du YL, Xu GA, Han LB. Study on applicability of three dimensional method for analysis of seepage in complex rock foundation. Water Resour Hydropower Eng. 1991;1:2–9 (in Chinese).
Duiguid JO, Lee PCY. Flow in fractured porous media. Water Resour Res. 1977;13(3):25–8.
Fipps G, Skaggs RW, Nieber JL. Drains as a boundary condition in finite elements. Water Resour Res. 1986;22(11):1613–21.
Guan JH, Liu JX, Zhu YX. Finite element analysis for an array of wells replaced by a drainage ditch. J Hydraul Eng. 1984;6(3):10–8 (in Chinese).
Huang DH, Yang SH. A study on the methods of setting initial temperature on the joint face of roller compacted concrete. J Hydroelectric Eng. 1999;25(3):25–34 (in Chinese).
Huyakorn PS, Lester BH, Faust CR. Finite element techniques for modeling groundwater flow in fractured aquifers. Water Resour Res. 1983;19(4):1019–35.
Ishikawa M. Thermal stress analysis of concrete dam. Comput Struct. 1991;40(2):347–52.

Liu C. Temperature field of mass concrete in a pipe lattice. J Mat Civil Eng ASCE. 2004;16 (5):427–32.
Liu N, Liu GT. Sub-structural FEM for the thermal effect of cooling pipes in mass concrete structures. J Hydraul Eng. 1997;19(12):43–9 (in Chinese).
Liu YJ, Jia LG, Song YS, Xiao SY. Three dimensional thermal resistance element for simulating heat across interface. In: Xu B, Xiao Y, Ru JP, Ren WX, editors. 10th International symposium on structural engineering for young experts. Beijing (China): Science Press; 2008. p. 1970–4.
Long JSC. Rock fractures and fluid flow. Washington DC (USA): National Academy Press; 1996.
Long JCS, Gilmour P, Witherspoon PA. A method for steady fluid flow in random three-dimensional networks of dice-shaped fractures. Water Resour Res. 1985;21(8):35–40.
Lorig LJ. A simple numerical representation of fully bonded passive rock reinforcement for hard rocks. Comput Geotech. 1985;1(6):79–97.
Lorig LJ. A hybrid computational model for excavation and support design in jointed media. Ph.D. thesis. University of Minnesota (USA); 1984.
Mahtab M, Goodman RE. Three dimensional analysis of joint rock slope. In: Proceedings of 2nd ISRM congress, vol. 3. Beograd (Yugoslavia): Privredni Pregled; 1970. p. 353–60.
Malkawi AIH, Mutasher SA, Qiu TJ. Thermal-structural modeling and temperature control of roller compacted concrete gravity dam. J Perform Constructed Facil ASCE. 2003;17(4): 177–87.
Nordqvist AW, Tsang YW, Tsang CF. A variable aperture fracture network model for flow and transport in fractured rocks. Water Resour Res. 1992;28(6):1703–13.
Oda M. An equivalent continuum model for coupled stress and fluid flow analysis in jointed rock masses. Water Resour Res. 1986;22(13):1845–56.
Pande GN, Gerrard CM. The behaviour of reinforced jointed rock masses under various simple loading states. In: Proceedings of 5th ISRM congress. Melbourne (Australia): Brown Prior Anderson Pty Ltd.; 1983. F217–23.
Sharma KG, Pande GN. Stability of rock masses reinforced by passive, fully-grouted bolts. Int J Rock Mech Min Sci Geomech Abstr. 1988;25(5):273–85.
Snow DT. Anisotropic permeability of fractured media. Water Resour Res. 1969;5(6):1273–89.
Springenschmid R, Breitenbiicher R, Mangold M. Development of the cracking frame and the temperature-stress testing machine. In: Springenschmid R, editor. Thermal cracking in concrete at early ages, international RILEM symposium. London (UK): CRC Press; 1994. p. 137–44.
Streltsova TD. Hydrodynamics of groundwater flow in a fractured formation. Water Resour Res. 1981;17(4):21–6.
Swoboda G, Marence M. FEM modelling of rockbolts. In: Proceedings of computer methods and advances in geomechanics. Rotterdam (Netherlands): AA Balkema; 1991. p. 1515–20.
Swoboda G, Marence M. Numerical modelling of rock bolts in intersection with fault system. In: Proceedings of numerical models in geomechanics, NUMOG 5. Swansea(UK): Pineridge Press Ltd.; 1992. p. 729–38.
Tatro SB, Schrader EK. Thermal analysis for RCC—a practical approach. In: Proceedings roller compacted concrete III. New York (USA): ASCE; 1992. p. 389–406.
Tatro SB, Schrader EK. Thermal considerations for roller-compacted concrete. J Am Concr Inst. 1985;82(2):119–28.
Toshiaki M, Yasuyuki F, Yoshinori M. Control of thermal cracking by pipe-cooling system in concrete structures. In: Proceedings of JSCE (Japan Society of Civil Engineers); 2000, (665):147–63.
Wang L, Liu Z, Zhang YT. Analysis of seepage field near a drainage holes curtain. J Hydraul Eng. 1992;14(4):15–20 (in Chinese).
Wang EZ, Wang HT, Deng XD. Pipe to represent hole–numerical method for simulating single drainage hole in rock masses. Chin J Rock Mech Eng. 2001;20(3):346–9 (in Chinese).
Wilson CR, Witherspoon PA. Steady state flow in rigid networks of fractures. Water Resour Res. 1974;10(2):328–35.
Xu GS, Chen SH. Unconfined seepage analysis with composite element method. Rock Soil Mech. 2005;26(5):745–9 (In Chinese).

Zhang Z, Garga VK. Temperature and temperature induced stresses for RCC dams. Dam Eng. 1996;7(4):336–50.

Zhu BF. The analysis of the effect of drainage holes in the seepage field by means of hybrid elements. J Hydraul Eng. 1982;4(9):32–41 (in Chinese).

Zhu BF. Equivalent equation of heat conduction in mass concrete considering the effect of pipe cooling. J Hydraul Eng. 1991;13(3):28–34 (in Chinese).

Zhu BF. Thermal stresses and temperature control of mass concrete. Beijing (China): China Electric Power Press; 1998 (in Chinese).

Zhu BF. Current situation and prospect of temperature control and cracking prevention technology for concrete dam. J Hydraul Eng. 2006;28(12):1424–32 (in Chinese).

Zhu BF, Cai JB. Finite element analysis of effect of pipe cooling in concrete dams. J Constr Eng Manag ASCE. 1989;115(4):487–98.

Zhu YM, Zhang JB. Study on application of water cooling pipe measures to RCCDs thermal control during continuous construction in high-temperature seasons. J Hydraul Eng. 2002;24 (11):55–9 (in Chinese).

Chapter 15
Reinforcement Analysis Using the Composite Element Method

Abstract This chapter implements the composite element method (CEM) towards the explicit simulation of jointed rock mass reinforced by fully-grouted bolts and pre-stress anchor cables. The joint, bolt/stranded wire, and grout are all embedded within the composite element, meanwhile the bolt/grout and rock/grout interfaces are taken into account. Use is further made of p-refinement to enlarge the shape function space for the complex deformation pattern within a composite element containing reinforcement components and discontinuities. This chapter is closed with a number of validation examples cross-referenced by FEM computation/physical test and two successful engineering application cases related to gravity dam and underground cavern.

15.1 General

Discontinuities or structural planes—the general term of rock faults, joints, beddings, etc., dominate the deformation and stability of dam foundation, cut slope and underground cavern. Rock bolting is widely employed as a principal countermeasure for the stabilization of hydraulic structures. Towards the optimal design of reinforcement scheme, the assessment of both the shear and tension resistances of bolts are crucial. Many laboratory and field tests have been conducted from which the detailed understandings with regard to the interaction mechanism between rock bolts and rock masses are revealed. Based on these understandings, the semi-empirical formulas, the implicit or explicit FEM algorithms (vide Chap. 6), as well as the BEA algorithm (vide Chap. 12), may be elaborated.

However, as has been indicated previously, one of the main difficulties lies in the explicit simulation of bolts using the FEM is the pre-process to discretize the calculation domain, whereas the use of the BEA leads to a partial loss of detailed performance of bolts. The question is naturally put forward that can we, let the special elements representing bolts be located inside conventional elements (standard or hierarchical)? Inspirited by this ideal, we proposed the composite element method (CEM) to explicitly simulate bolts embedded within a finite

S.-H. Chen, *Computational Geomechanics and Hydraulic Structures*,
Springer Tracts in Civil Engineering, https://doi.org/10.1007/978-981-10-8135-4_15

element (Chen et al. 2003, 2004). In this method the bolt and grout are handled with separately, the bolt/grout and rock/grout interfaces are taken into account, and the elasto-viscoplastic deformations are considered. The research then was pushed forward to cover the issues of simulating hollow bolts (Chen et al. 2002, 2003), discontinuities/joints (Chen et al. 2007, 2008), the interaction of bolt and joint (Chen and Shahrour 2008), and the pre-stress stranded wire cables (Chen et al. 2015).

15.2 Fully-Grouted Rock Bolts

15.2.1 Concept

In the computation for a reinforced structure with the CEM, the FE mesh need be generated beforehand without taking into account of the existence of rock bolts. Then the dip directions and dip angles as well as the collar coordinates of the bolts will be put in. By the simple algebra calculations, the intersecting messages of each bolt with the FE mesh can be obtained. Figure 15.1 shows a composite element containing one bolt segment. Within which there are five sub-elements representing the rock material, the grout material, the bolt material, the rock/grout interface, and the grout/bolt interface, respectively.

15.2.2 Coordinate Systems and Transformation

A global coordinate system is defined for the formulation of overall governing equations, with its Y-axis pointing northward, the X-axis pointing eastward, and the

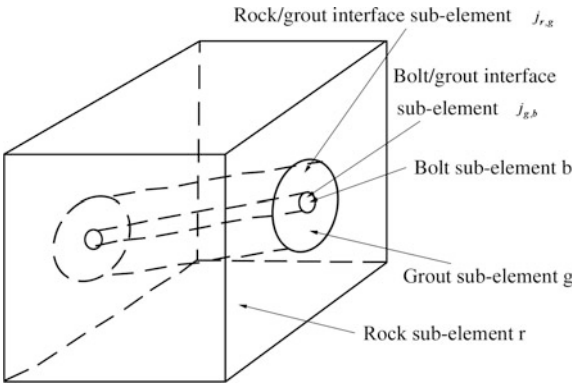

Fig. 15.1 Schematic drawing of a composite element containing five sub-elements

Z-axis being vertical. For each bolt a local Cartesian system and a local Cylindrical system are also needed to simplify the deduction (see Fig. 2.16). The subscripts r, g, b, $j_{r,g}$ and $j_{g,b}$ are employed to denote the variables of rock, grout, bolt, rock/grout interface, grout/bolt interface, respectively; the superscripts ca and cy are used to denote the variables in the local Cartesian system and Cylindrical coordinate system, respectively.

Towards the establishment of governing equations, use is made of the following basic assumptions:

- At the cross section of a bolt (grout as well), there are three stress increments comprising one normal stress (z_b direction) and two shear stresses (x_b and y_b directions);
- At the interfaces of rock/grout and bolt/grout, there are three stress increments comprising one normal stress perpendicular to the interface (r direction) and two shear stresses along the interface (ω and z directions).

For the bolt segment b, the displacement transformation between the global and the local Cartesian coordinate systems is given by

$$\{\Delta u\}_b^{ca} = [l]_b^{ca}\{\Delta u\}_b \tag{15.1}$$

In which the transform matrix $[l]_b^{ca}$ has been defined in Eq. (2.37).

The displacement transformation between the local coordinate systems of Cartesian and Cylindrical is given by

$$\{\Delta u\}_b^{cy} = [l]_b^{cy}\{\Delta u\}_b^{ca} \tag{15.2}$$

In which the transforming matrix $[l]_b^{cy}$ has been defined in Eq. (2.38).

For the grout material around the bolt the transformations are defined similarly

$$\{\Delta u\}_g^{ca} = [l]_g^{ca}\{\Delta u\}_g \tag{15.3}$$

$$\{\Delta u\}_g^{cy} = [l]_g^{cy}\{\Delta u\}_g^{ca} \tag{15.4}$$

Since the transformation matrices $[l]_b^{ca}$ and $[l]_b^{cy}$ are normally identical to $[l]_g^{ca}$ and $[l]_g^{cy}$, therefore in the hereinafter deduction of this chapter, their subscripts b and g are all neglected.

15.2.3 Constitutive Equations

See Eqs. (2.122)–(2.130).

15.2.4 Equilibrium Equations

(1) Relationship between strain increment and nodal displacement increment

There are three sets of nodal displacement increments bound at a composite element if there is one bolt segment, each of them will be employed to interpolate the displacement increments of rock, grout, and bolt, respectively by the formulas

$$\{\Delta u\}_r = [N]\{\Delta\delta\}_r \tag{15.5}$$

$$\{\Delta u\}_g^{ca} = [l]^{ca}[N]\{\Delta\delta\}_g \tag{15.6}$$

$$\{\Delta u\}_b^{ca} = [l]^{ca}[N]\{\Delta\delta\}_b \tag{15.7}$$

In which the shape function matrix $[N]$ is identical to that of the FEM [see Eq. (4.57)].

The strain increments of the rock, grout, and bolt materials are then calculated by

$$\{\Delta\varepsilon\}_r = [B]_r\{\Delta\delta\}_r \tag{15.8}$$

$$\{\Delta\varepsilon\}_g^{ca} = [B]_g[L]^{ca}\{\Delta\delta\}_g \tag{15.9}$$

$$\{\Delta\varepsilon\}_b^{ca} = [B]_b[L]^{ca}\{\Delta\delta\}_b \tag{15.10}$$

where $[B]_r$ is identical to Eq. (4.60), and

$$[B]_b = [B]_g = \left\lfloor [B]_1^{ca} \quad [B]_2^{ca} \quad \cdots \quad [B]_{f_e(p)}^{ca} \right\rfloor \tag{15.11}$$

$$[B]_i^{ca} = \begin{bmatrix} \frac{\partial N_i}{\partial z^{ca}} & 0 & \frac{\partial N_i}{\partial x^{ca}} \\ 0 & \frac{\partial N_i}{\partial z^{ca}} & \frac{\partial_i}{\partial y^{ca}} \\ 0 & 0 & \frac{\partial N_i}{\partial z^{ca}} \end{bmatrix} \tag{15.12}$$

$$[L]^{ca} = \left[([l]^{ca})^T \quad ([l]^{ca})^T \quad \cdots \quad ([l]^{ca})^T \right]^T \tag{15.13}$$

A similar expression for the transformation matrix $[L]^{cy}$ will be employed later is constructed by $[l]^{cy}$ [see Eq. (2.38)].

$$[L]^{cy} = \left[([l]^{cy})^T \quad ([l]^{cy})^T \quad \cdots \quad ([l]^{cy})^T \right]^T \tag{15.14}$$

The displacement increments manifesting in the rock, grout, and bolt materials will give rise to relative displacement increments on the rock/grout interface and the bolt/grout interface, these increments will be expressed in the local Cylindrical coordinate system by

$$\{\Delta u\}_{j_{r,g}}^{cy} = [l]^{cy}[l]^{ca}[N](\{\Delta\delta\}_r - \{\Delta\delta\}_g) \tag{15.15}$$

$$\{\Delta u\}_{j_{g,b}}^{cy} = [l]^{cy}[l]^{ca}[N](\{\Delta\delta\}_g - \{\Delta\delta\}_b) \tag{15.16}$$

(2) Relationship between nodal displacement increment and load increment

Suppose following virtual displacements take place in the rock, grout and bolt that

$$\{\Delta u^*\}_r = [N]\{\Delta\delta^*\}_r \tag{15.17}$$

$$\{\Delta u^*\}_g^{ca} = [l]^{ca}[N]\{\Delta\delta^*\}_g \tag{15.18}$$

$$\{\Delta u^*\}_b^{ca} = [l]^{ca}[N]\{\Delta\delta^*\}_b \tag{15.19}$$

The corresponding virtual strains and relative displacements will be

$$\{\Delta\varepsilon^*\}_r = [B]_r\{\Delta\delta^*\}_r \tag{15.20}$$

$$\{\Delta\varepsilon^*\}_g^{ca} = [B]_g[L]^{ca}\{\Delta\delta^*\}_g \quad (g = 1, \ldots, n_g) \tag{15.21}$$

$$\{\Delta\varepsilon^*\}_b^{ca} = [B]_b[L]^{ca}\{\Delta\delta^*\}_b \quad (b = 1, \ldots, n_b) \tag{15.22}$$

$$\{\Delta u^*\}_{j_{r,g}}^{cy} = [l]^{cy}[l]^{ca}[N](\{\Delta\delta^*\}_r - \{\Delta\delta^*\}_g) \tag{15.23}$$

$$\{\Delta u^*\}_{j_{g,b}}^{cy} = [l]^{cy}[l]^{ca}[N](\{\Delta\delta^*\}_g - \{\Delta\delta^*\}_b) \tag{15.24}$$

The virtual work principle for the composite element will be written as

$$W_r + \sum_{g=1}^{n_g} W_g + \sum_{b=1}^{n_b} W_b + \sum_{g=1}^{n_g} W_{j_{r,g}} + \sum_{b=1}^{n_b} W_{j_{g,b}} = (\{\Delta\delta^*\}_r)^T\{\Delta f\}_r + \sum_{g=1}^{n_g}(\{\Delta\delta^*\}_g)^T\{\Delta f\}_g + \sum_{b=1}^{n_b}(\{\Delta\delta^*\}_b)^T\{\Delta f\}_b \tag{15.25}$$

In which $\{\Delta f\}_r$, $\{\Delta f\}_g$ and $\{\Delta f\}_b$ are the nodal force increments bound at the composite element which are transferred from the load increments exerting at the rock, grout and bolt according to the algorithm identical to the FEM; W_r, W_g, W_b, $W_{j_{r,g}}$ and $W_{j_{b,g}}$ are the virtual works contributed from the embedded components inclusive the rock, grout, bolt, rock/grout interface and bolt/grout interface.

1. Rock material

$$W_r = \iiint_{\Omega_r} (\{\Delta\varepsilon^*\}_r)^T\{\Delta\sigma\}_r \, d\Omega \tag{15.26}$$

Given the constitutive relation in Eq. (2.122) and strain-displacement relation in Eq. (15.8), the virtual work of rock material is

$$W_r = \iiint_{\Omega_r} (\{\Delta\delta^*\}_r)^T [B]_r^T [D]_r ([B]_r \{\Delta\delta\}_r - \{\dot{\varepsilon}^{vp}\}_r \Delta t)\, d\Omega \tag{15.27}$$

2. Grout material

$$W_g = \iiint_{\Omega_g} (\{\Delta\varepsilon^*\}_g^{ca})^T \{\Delta\sigma\}_g^{ca} d\Omega \quad (g = 1, \ldots, n_g) \tag{15.28}$$

Introducing the constitutive relation in Eq. (2.122) and the strain-displacement relation in Eq. (15.9) into Eq. (15.28) gives rise to

$$W_g = \iiint_{\Omega_g} (\{\Delta\delta^*\}_g)^T ([L]^{ca})^T [B]_g^T [D]_g ([B]_g [L]^{ca} \{\Delta\delta\}_g - \{\dot{\varepsilon}^{vp}\}_g^{ca} \Delta t)\, d\Omega \quad (g = 1, \ldots, n_g) \tag{15.29}$$

3. Bolt material

By the similar way to the grout material, the virtual work contributed from the bolt material is

$$W_b = \iiint_{\Omega_b} (\{\Delta\delta^*\}_b)^T ([L]^{ca})^T [B]_b^T [D]_b ([B]_b [L]^{ca} \{\Delta\delta\}_b - \{\dot{\varepsilon}^{vp}\}_b^{ca} \Delta t)\, d\Omega \quad (b = 1, \ldots, n_b) \tag{15.30}$$

4. Rock/grout interface

$$W_{j_{r,g}} = \iint_{\Gamma_{j_{r,g}}} (\{\Delta u^*\}_{j_{r,g}}^{cy})^T \{\Delta\sigma\}_{j_{r,g}}^{cy}\, d\Gamma \tag{15.31}$$

Introducing the constitutive relation in Eq. (2.126) and the strain-displacement relation Eq. (15.15) into Eq. (15.31), we have

$$W_{j_{r,g}} = \iint\limits_{\Gamma_{jr,g}} (\{\Delta\delta^*\}_r)^T - (\{\Delta\delta^*\}_g)^T)[N]^T([l]^{ca})^T([l]^{cy})^T[D]_{j_{r,g}} \\ ([l]^{cy}[l]^{ca}[N](\{\Delta\delta\}_r - \{\Delta\delta\}_g) - \{\dot{u}^{vp}\}^{cy}_{j_{r,g}}\Delta t)\, d\Gamma \tag{15.32}$$

5. Grout/bolt interface

Similar to the rock-grout interface, the virtual work contributed from the grout/bolt interface can be written directly

$$W_{j_{g,b}} = \iint\limits_{\Gamma_{j_{g,b}}} (\{\Delta\delta^*\}_g)^T - (\{\Delta\delta^*\}_b))[N]^T([l]^{ca})^T([l]^{cy})^T[D]_{j_{g,b}} \\ ([l]^{cy}[l]^{ca}[N](\{\Delta\delta\}_g - \{\Delta\delta\}_b) - \{\dot{u}^{vp}\}^{cy}_{j_{g,b}}\Delta t)\, d\Gamma \tag{15.33}$$

We now introduce the component virtual works in Eqs. (15.26)–(15.33) into Eq. (15.25), and arrange the result regarding the different virtual displacements corresponding to the rock sub-element, the grout sub-element, and the bolt sub-element. Remember that the virtual displacements $(\{\Delta\delta^*\}_r)$, $(\{\Delta\delta^*\}_g)$ and $(\{\Delta\delta^*\}_b)$ are arbitrary vectors, the validity of the virtual work principle will leads to

$$\begin{bmatrix} [k]_{r,r}\cdots & [k]_{r,g} & 0\cdots & [k]_{r,n_g} & 0 \\ \cdots & \cdots & \cdots & \cdots & \cdots \\ [k]_{g,r}\cdots & [k]_{g,g} & [k]_{g,b}\cdots & 0 & 0 \\ 0 & [k]_{b,g} & [k]_{b,b}\cdots & 0 & 0 \\ \cdots & \cdots & \cdots & \cdots & \cdots \\ [k]_{n_g,r}\cdots & 0\cdots & 0\cdots & [k]_{n_g,n_g} & [k]_{n_g,n_b} \\ 0\cdots & 0\cdots & 0\cdots & [k]_{n_b,n_g} & [k]_{n_b,n_b} \end{bmatrix} \begin{Bmatrix} \{\Delta\delta\}_r \\ \cdots \\ \{\Delta\delta\}_g \\ \{\Delta\delta\}_b \\ \cdots \\ \{\Delta\delta\}_{n_g} \\ \{\Delta\delta\}_{n_b} \end{Bmatrix} \\ = \begin{Bmatrix} \{\Delta f\}_r \\ \cdots \\ \{\Delta f\}_g \\ \{\Delta f\}_b \\ \cdots \\ \{\Delta f\}_{n_g} \\ \{\Delta f\}_{n_b} \end{Bmatrix} + \begin{Bmatrix} \{\Delta f^{vp}\}_r \\ \cdots \\ \{\Delta f^{vp}\}_g \\ \{\Delta f^{vp}\}_b \\ \cdots \\ \{\Delta f^{vp}\}_{n_g} \\ \{\Delta f^{vp}\}_{n_b} \end{Bmatrix} \tag{15.34}$$

In which

$$
\begin{cases}
[k]_{r,r} = \iiint\limits_{\Omega_r} [B]_r^T [D]_r [B]_r d\Omega \\
\qquad + \sum\limits_{g=1}^{n_g} \iint\limits_{\Gamma_{jr,g}} [N]^T ([l]^{ca})^T ([l]^{cy})^T [D]_{j_{r,g}} [l]^{cy} [l]^{ca} [N] d\Gamma \\
[k]_{g,g} = \iiint\limits_{\Omega_g} ([L]^{ca})^T [B]_g^T [D]_g [B]_g [L]^{ca} d\Omega \\
\qquad + \iint\limits_{\Gamma_{jr,g}} [N]^T ([l]^{ca})^T ([l]^{cy}) [D]_{j_{r,g}} [l]^{cy} [l]^{ca} [N] d\Gamma \\
\qquad + \iint\limits_{\Gamma_{j_{g,b}}} [N]^T ([l]^{ca})^T ([l]^{cy})^T [D]_{j_{g,b}} [l]^{cy} [l]^{ca} [N] d\Gamma \\
[k]_{b,b} = \iiint\limits_{\Omega_b} ([L]^{ca})^T [B]_b^T [D]_b [B]_b [L]^{ca} d\Omega \\
\qquad + \iint\limits_{\Gamma_{j_{g,b}}} [N]^T ([l]^{ca})^T ([l]^{cy})^T [D]_{j_{r,b}} [l]^{cy} [l]^{ca} [N] d\Gamma \\
[k]_{r,g} = -\iint\limits_{\Gamma_{jr,g}} [N]^T ([l]^{ca})^T ([l]^{cy})^T [D]_{j_{r,g}} [l]^{cy} [l]^{ca} [N] d\Gamma \\
[k]_{g,b} = -\iint\limits_{\Gamma_{j_{g,b}}} [N]^T ([l]^{ca})^T ([l]^{cy})^T [D]_{j_{g,b}} [l]^{cy} [l]^{ca} [N] d\Gamma
\end{cases}
\tag{15.35}
$$

$$
\begin{cases}
\{\Delta f^{vp}\}_r = \iiint\limits_{\Omega_r} [B]_r^T [D]_r \{\dot{\varepsilon}^{vp}\}_r \Delta t \, d\Omega + \sum\limits_{g}^{n_g} \iint\limits_{\Gamma_{jr,g}} [N]^T ([l]^{ca})^T ([l]^{cy})^T [D]_{j_{r,g}} \{\dot{u}^{vp}\}_{j_{r,g}}^{cy} \Delta t \, d\Gamma \\
\{\Delta f^{vp}\}_g = \iiint\limits_{\Omega_g} ([L]^{ca})^T [B]_g^T [D]_g \{\dot{\varepsilon}^{vp}\}_g^{ca} \Delta t \, d\Omega + \iint\limits_{\Gamma_{j_{g,b}}} [N]^T ([l]^{ca})^T ([l]^{cy})^T [D]_{j_{g,b}} \{\dot{u}^{vp}\}_{j_{g,b}}^{cy} \Delta t \, d\Gamma \\
\qquad - \iint\limits_{\Gamma_{jr,g}} [N]^T ([l]^{ca})^T ([l]^{cy})^T [D]_{j_{r,g}} \{\dot{u}^{vp}\}_{j_{r,g}}^{cy} \Delta t \, d\Gamma \\
\{\Delta f^{vp}\}_b = \iiint\limits_{\Omega_b} ([L]^{ca})^T [B]_b^T [D]_b \{\dot{\varepsilon}^{vp}\}_b^{ca} \Delta t \, d\Omega - \iint\limits_{\Gamma_{j_{g,b}}} [N]^T ([l]^{ca})^T ([l]^{cy})^T [D]_{j_{g,b}} \{\dot{u}^{vp}\}_{j_{g,b}}^{cy} \Delta t \, d\Gamma
\end{cases}
\tag{15.36}
$$

15.3 Bonded Anchorage Head of Stranded Wire Cable in Tension

Extensive experimental studies concerning the performance of anchors have been reported in numerous literatures (Fuller and Cox 1975; Weerasinghe and Littlejohn 1997; Stheeman 1982; Stillborg 1984, 1994; Goris and Conway 1987; Hassani and Rajaie 1990; Hassani et al. 1992; Hyett et al. 1992, 1995; Kaiser et al. 1992; Benmokrane et al. 1995a, b; Barley 1997a, b; Jarrel and Haberfield 1997; Woods and Barkhordari 1997; Briaud et al. 1998; Kim 2003). They provide important insights into the issues such as the dominant factors in the bond-strength at anchor/grout interface (e.g. interface smoothness, anchor diameter, borehole diameter, steel grade), the effect of the rigidity of host medium on the performance of anchor, the load transfer mechanism from anchor to ground, etc.

Nowadays, the most prevalent approach of anchor cables in the FEM makes use of beam-column models which have been well documented by Desai et al. (1986), Mitri and Rajaie (1990), Mitri et al. (1993). Typical algorithms for cables to investigate their stress and deformation patterns in anchor-solid systems have been provided by these authors, too. To handle the phenomena of interface failure such as slippage and separation, a number of interface models established by Goodman et al. (1968), Mahtab and Goodman (1970), Ghaboussi et al. (1973), Hermann (1978), Desai et al. (1984), Beer (1985), Griffiths (1985), are available. An important progress using fine finite element grid to simulate solid/grout and grout/strand wire interfaces has been achieved, too (Kim et al. 2007). In engineering practice, however, a large amount of anchor cables are ordinarily installed for a hydraulic structure. Under such circumstances, the attempt to deal with all the stranded wires and the interfaces of cables individually would be too ambitious, or even infeasible mainly restrained by pre-process and computation capability.

In Chap. 6 (Sect. 6.5), a simplified model for pre-stress cables to evaluate the reinforced structures in a manner of pre-stress force and additional free-length stiffness has been established. On the out-laid anchor head, concentrated compressive force or distributed pressure of certain pattern is exerted to simulate pre-stress action, meanwhile a concentrated tensile force equal to the pre-stress is exerted at the bonded inside anchorage head—a "bar" or "beam" element with certain length. It is customarily postulated that such a concentrated tensile force is exerted at the intersection of bonded inside anchorage head with free length, for the safe side. In this model, however, the detailed performance of bonded inside anchorage head is totally neglected.

In the following coverage of this section we present an important extension of the CEM for the bonded inside anchorage head of tension cable anchor, in which one composite element contains the sub-elements corresponding to the rock, grout, stranded wires, rock/grout interface and grout/stranded wire interfaces. This kind of composite elements can be easily implemented in FE programs accompanied by the out-laid anchor head force and additional free-length stiffness (vide Sect. 6.5, Chap. 6), to simulate cable reinforced structures much more rationally.

15.3.1 Sub-Element Analysis

(1) Coordinate systems and nomenclatures

Figure 15.2 shows the schematic diagram of the composite element containing a bonded inside cable head with n_w-stranded wires (n_w = 7 in this figure). The entity sub-elements $(\mathrm{w} = 1, 2, \ldots n_w)$ representing n_w stranded wires are connected to the entity sub-element g representing grout through the n_w interface sub-elements of grout/stranded wire $j_{g,w}$ $(\mathrm{w} = 1, 2, \ldots n_w)$. The grout entity sub-element g is, in turn, connected to the host rock sub-element r through the interface sub-element of rock/grout $j_{r,g}$.

The independent displacements corresponding to the sub-elements are bound at the nodes of the composite element as $\{\Delta\delta\} = \left[\{\Delta\delta\}_r^T, \{\Delta\delta\}_g^T, \{\Delta\delta\}_1^T, \{\Delta\delta\}_2^T, \ldots, \{\Delta\delta\}_{n_w}^T\right]^T$ (see Fig. 15.3). In the local coordinate systems, the stress and strain increments are denoted as $\{\Delta\sigma\}_j = [\,\Delta\sigma_r \quad \Delta\tau_{r\omega} \quad \Delta\tau_{rz}\,]^T$ and $\{\Delta u\}_j = [\,\Delta u_r \quad \Delta u_\omega \quad \Delta u_z\,]^T$ for the interface [see Eqs. (2.25) and (2.60)], which means that only compression/tension and shear on the interface are considered; $\{\Delta\varepsilon\}_w = \left[\,\Delta\gamma_{zx} \quad \Delta\gamma_{zy} \quad \Delta\varepsilon_z\,\right]^T$ and $\{\Delta\sigma\}_w = [\,\Delta\tau_{zx} \quad \Delta\tau_{zy} \quad \Delta\sigma_z\,]^T$ for the wire or grout [see Eqs. (2.61)–(2.62) and (2.64)–(2.65)], which means that only compression/tension and shear on the wire section perpendicular to the axis are considered.

The nodal displacement transformation between the global and local Cartesian coordinate systems is defined by

$$\begin{cases} \{\Delta\delta\}_g^{ca} = [L]^{ca}\{\Delta\delta\}_g \\ \{\Delta\delta\}_w^{ca} = [L]^{ca}\{\Delta\delta\}_w \end{cases} \tag{15.37}$$

The transformation matrix $[L]^{ca}$ is identical to that in Eq. (15.13).

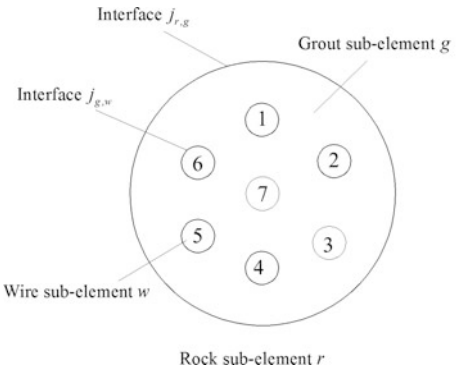

Fig. 15.2 Schematic drawing of the composite element containing $3 + 2 \times n_w$ sub-elements

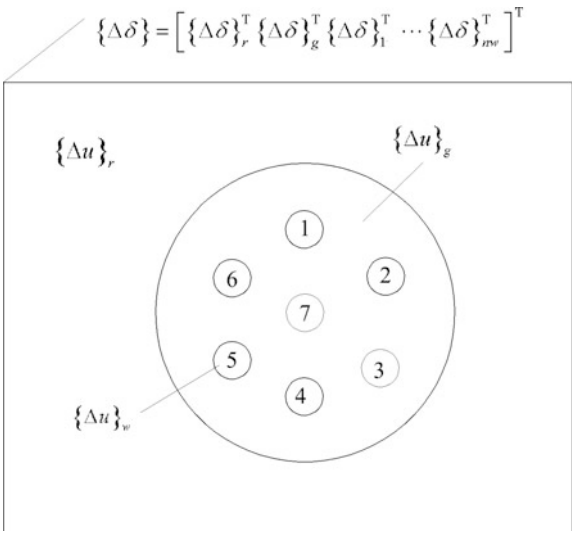

Fig. 15.3 Independent nodal displacements and their interpolation

The nodal displacement transformation between the local Cartesian and Cylindrical coordinate systems with respect to the stranded wire sub-element is defined by

$$\begin{cases} \{\Delta\delta\}_g^{cy} = [L]^{cy}\{\Delta\delta\}_g^{ca} \\ \{\Delta\delta\}_w^{cy} = [L]^{cy}\{\Delta\delta\}_w^{ca} \end{cases} \tag{15.38}$$

The transformation matrix $[L]^{cy}$ has been defined in Eq. (15.14).

(2) Displacement interpolation

The displacement increment in each entity sub-element is interpolated from its corresponding nodal variables bound at the composite element as follows (see Fig. 15.3)

$$\{\Delta u\}_r = [N]\{\Delta\delta\}_r \tag{15.39}$$

$$\{\Delta u\}_g^{ca} = [l]^{ca}[N]\{\Delta\delta\}_g \tag{15.40}$$

$$\{\Delta u\}_w^{ca} = [l]^{ca}[N]\{\Delta\delta\}_w \quad (w = 1, 2, \ldots..n_w) \tag{15.41}$$

where $[N]$ stands for the shape function matrix in the whole composite element [see Eq. (4.57)].

(3) Strain computation

1. Entity sub-elements

The strains of rock, grout, and stranded wire can be calculated in terms of corresponding nodal displacements by

$$\{\Delta\varepsilon\}_r = [B]_r\{\Delta\delta\}_r \tag{15.42}$$

$$\{\Delta\varepsilon\}_g^{ca} = [B]_g[L]^{ca}\{\Delta\delta\}_g \tag{15.43}$$

$$\{\Delta\varepsilon\}_w^{ca} = [B]_w[L]^{ca}\{\Delta\delta\}_w \quad (w = 1, 2, \ldots n_w) \tag{15.44}$$

In which $[B]_r$ is identical to that in Eq. (4.60), $[B]_g$ is identical to that in Eqs. (15.11)–(15.12), and $[B]_w = [B]_g$.

2. Interface sub-elements

For the interface elements ($j_{r,g}$ and $j_{g,w}$), the strains will be replaced by the relative displacements expressed in the local Cylindrical coordinate system

$$\{\Delta u\}_{j_{r,g}}^{cy} = \{\Delta u\}_r^{cy} - \{\Delta u\}_g^{cy} = [l]^{cy}[l]^{ca}[N](\{\Delta\delta\}_r - \{\Delta\delta\}_g) \tag{15.45}$$

$$\{\Delta u\}_{j_{g,w}}^{cy} = \{\Delta u\}_g^{cy} - \{\Delta u\}_w^{cy} = [l]^{cy}[l]^{ca}[N](\{\Delta\delta\}_g - \{\Delta\delta\}_w) \quad (w = 1, 2, \ldots n_w) \tag{15.46}$$

(4) Constitutive equations

See Eqs. (2.122)–(2.130).

15.3.2 Composite Element Analysis

Suppose a virtual displacement increment $\{\Delta\delta^*\}$ manifests at the composite element containing bonded inside cable head, then the corresponding virtual displacements and virtual strains within the sub-elements may be calculated according to Eqs. (15.39)–(15.44). The application of the virtual work principle to the composite element leads to

$$W_r + W_g + \sum_{w=1}^{n_w} W_w + W_{j_{r,g}} + \sum_{w=1}^{n_w} W_{j_{g,w}} = (\{\Delta\delta^*\}_r)^T\{\Delta f\}_r + (\{\Delta\delta^*\}_g)^T\{\Delta f\}_g + \sum_{w=1}^{n_w}(\{\Delta\delta^*\}_w)^T\{\Delta f\}_w \tag{15.47}$$

In which $\{\Delta f\}_r$, $\{\Delta f\}_g$, $\{\Delta f\}_w$ are the nodal forces bound at the composite element that are transferred from the loads exerting on the rock, grout, and stranded

wires according to the similar algorithm of the conventional FEM; W_r, W_g, W_w, $W_{j_{r,g}}$ and $W_{j_{g,w}}$ are the virtual works contributed from the rock, grout, stranded wire, rock/grout interface, and grout/stranded wire interface, which may be respectively expressed by

$$W_r = \iiint_{\Omega_r} (\{\Delta\delta^*\}_r)^{\mathrm{T}}[B]_r^{\mathrm{T}}[D]_r([B]_r\{\Delta\delta\}_r - \{\dot{\varepsilon}^{vp}\}_r\Delta t)d\Omega \tag{15.48}$$

$$W_g = \iiint_{\Omega_g} (\{\Delta\delta^*\}_g)^{\mathrm{T}}([L]^{ca})^{\mathrm{T}}([B]_g)^{\mathrm{T}}[D]_g([B]_g[L]^{ca}\{\Delta\delta\}_g - \{\dot{\varepsilon}^{vp}\}_g\Delta t)\, d\Omega \tag{15.49}$$

$$W_w = \iiint_{\Omega_w} (\{\Delta\delta^*\}_w)^{\mathrm{T}}([L]^{ca})^{\mathrm{T}}([B]_w)^{\mathrm{T}}[D]_w([B]_w[L]^{ca}\{\Delta\delta\}_w - \{\dot{\varepsilon}^{vp}\}_w\Delta t)\, d\Omega \tag{15.50}$$

$$\begin{aligned} W_{j_{r,g}} = \iint_{\Gamma_{j_{r,g}}} &((\{\Delta\delta^*\}_r)^{\mathrm{T}} - (\{\Delta\delta^*\}_g)^{\mathrm{T}})[N]^{\mathrm{T}}([l]^{\mathrm{ca}})^{\mathrm{T}}([l]^{\mathrm{cy}})^{\mathrm{T}}[D]_{j_{r,g}} \\ &([l]^{\mathrm{cy}}[l]^{\mathrm{ca}}[N](\{\Delta\delta\}_r - \{\Delta\delta\}_g) - \{\dot{u}^{vp}\}_{j_{r,g}}\Delta t)\, d\Gamma \end{aligned} \tag{15.51}$$

$$\begin{aligned} W_{j_{g,w}} = \iint_{\Gamma_{j_{g,w}}} &((\{\Delta\delta^*\}_g)^{\mathrm{T}} - (\{\Delta\delta^*\}_w)^{\mathrm{T}})[N]^{\mathrm{T}}([l]^{\mathrm{ca}})^{\mathrm{T}}([l]^{\mathrm{cy}})^{\mathrm{T}}[D]_{j_{g,w}} \\ &([l]^{\mathrm{cy}}[l]^{\mathrm{ca}}[N](\{\Delta\delta\}_g - \{\Delta\delta\}_w) - \{\dot{u}^{vp}\}_{j_{g,w}}\Delta t)\, d\Gamma \end{aligned} \tag{15.52}$$

We introduce Eqs. (15.48)–(15.52) into Eq. (15.47), and arrange the resulted equation regarding the different components of virtual displacements. Bearing in mind that the virtual displacement $\{\Delta\delta^*\}$ is arbitrary, we get

$$\begin{aligned} &\begin{bmatrix} [k]_{r,r} & [k]_{r,g} & 0 & \cdots & 0 \\ [k]_{g,r} & [k]_{g,g} & [k]_{g,1} & \cdots & [k]_{g,n_w} \\ 0 & [k]_{1,g} & [k]_{1,1} & \cdots & 0 \\ \cdots & \cdots & \cdots & \cdots & \cdots \\ 0 & [k]_{n_w,g} & 0 & \cdots & [k]_{n_w,n_w} \end{bmatrix} \begin{Bmatrix} \{\Delta\delta\}_r \\ \{\Delta\delta\}_g \\ \{\Delta\delta\}_1 \\ \cdots \\ \{\Delta\delta\}_{n_w} \end{Bmatrix} \\ &= \begin{Bmatrix} \{\Delta f\}_r \\ \{\Delta f\}_g \\ \{\Delta f\}_1 \\ \cdots \\ \{\Delta f\}_{n_w} \end{Bmatrix} + \begin{Bmatrix} \{\Delta f^{vp}\}_r \\ \{\Delta f^{vp}\}_g \\ \{\Delta f^{vp}\}_1 \\ \cdots \\ \{\Delta f^{vp}\}_{n_w} \end{Bmatrix} \end{aligned} \tag{15.53}$$

where

$$
\begin{cases}
[k]_{r,r} = \iiint\limits_{\Omega_r} [B]_r^T [D]_r [B]_r \, d\Omega + \iint\limits_{\Gamma_{jr,g}} [N]^T ([l]^{ca})^T ([l]^{cy})^T [D]_{j_{r,g}} [l]^{cy} [l]^{ca} [N] \, d\Gamma \\
[k]_{g,g} = \iiint\limits_{\Omega_g} \left([L]^{ca}\right)^T [B]_g^T [D]_g [B]_g [L]^{ca} \, d\Omega + \iint\limits_{\Gamma_{jr,g}} [N]^T ([l]^{ca})^T ([l]^{cy})^T [D]_{j_{r,g}} [l]^{cy} [l]^{ca} [N] \, d\Gamma \\
\qquad + \sum_{w=1}^{n_w} \iint\limits_{\Gamma_{jg,w}} [N]^T ([l]^{ca})^T ([l]^{cy})^T [D]_{j_{g,w}} [l]^{cy} [l]^{ca} [N] \, d\Gamma \\
[k]_{w,w} = \iiint\limits_{\Omega_w} \left([L]^{ca}\right)^T [B]_w^T [D]_w [B]_w [L]^{ca} \, d\Omega \\
\qquad + \iint\limits_{\Gamma_{jg,w}} [N]^T ([l]^{ca})^T ([l]^{cy})^T [D]_{j_{g,w}} [l]^{cy} [l]^{ca} [N] \, d\Gamma \\
[k]_{r,g} = -\iint\limits_{\Gamma_{jr,g}} [N]^T ([l]^{ca})^T ([l]^{cy})^T [D]_{j_{r,g}} [l]^{cy} [l]^{ca} [N] \, d\Gamma \\
[k]_{g,w} = -\iint\limits_{\Gamma_{jg,w}} [N]^T ([l]^{ca})^T ([l]^{cy})^T [D]_{j_{g,w}} [l]^{cy} [l]^{ca} [N] \, d\Gamma
\end{cases}
\tag{15.54}
$$

$$
\begin{cases}
\{\Delta f^{vp}\}_r = \iiint\limits_{\Omega_r} [B]_r^T [D]_r \{\dot{\varepsilon}^{vp}\}_r \Delta t \, d\Omega + \iint\limits_{\Gamma_{jr,g}} [N]^T ([l]^{ca})^T ([l]^{cy})^T [D]_{j_{r,g}} \{\dot{u}^{vp}\}_{j_{r,g}}^{cy} \Delta t \, d\Gamma \\
\{\Delta f^{vp}\}_g = \iiint\limits_{\Omega_g} \left([L]^{ca}\right)^T [B]_g^T [D]_g \{\dot{\varepsilon}^{vp}\}_g^{ca} \Delta t \, d\Omega - \iint\limits_{\Gamma_{jr,g}} [N]^T ([l]^{ca})^T ([l]^{cy})^T [D]_{j_{r,g}} \{\dot{u}^{vp}\}_{j_{r,g}}^{cy} \Delta t \, d\Gamma \\
\qquad + \sum_{w=1}^{n_w} \iint\limits_{\Gamma_{jg,w}} [N]^T ([l]^{ca})^T ([l]^{cy})^T [D]_{j_{g,w}} \{\dot{u}^{vp}\}_{j_{g,w}}^{cy} \Delta t \, d\Gamma \\
\{\Delta f^{vp}\}_w = \iiint\limits_{\Omega_w} \left([L]^{ca}\right)^T [B]_w^T [D]_w \{\dot{\varepsilon}^{vp}\}_w^{ca} \Delta t \, d\Omega - \iint\limits_{\Gamma_{jg,w}} [N]^T ([l]^{ca})^T ([l]^{cy})^T [D]_{j_{g,w}} \{\dot{u}^{vp}\}_{j_{g,w}}^{cy} \Delta t \, d\Gamma
\end{cases}
\tag{15.55}
$$

15.4 Hollow Friction (Swellex) Bolts

The "Swellex" bolt is a hollow metallic tube which is directly connected to the host medium (rock mass). In the structural analysis it is essential to use a bolt element which may simulate the radial expansion and compression effects in addition to the common shear-tension effects along the axis of hollow bolt.

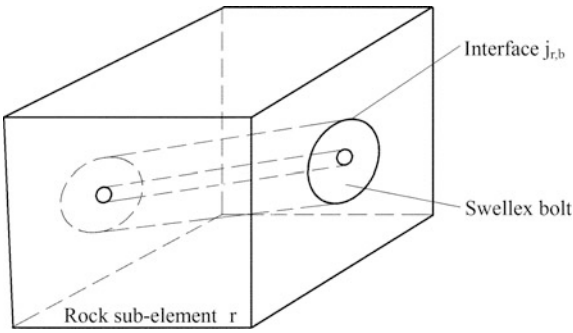

Fig. 15.4 Schematic drawing of the composite element containing one hollow bolt segment

Figure 15.4 shows an element which contains one hollow bolt segment. As we have indicated above, this element can be defined as the composite element, within which there are three sub-elements r, b, $j_{r,b}$ representing the rock material, the bolt material and the rock/bolt interface, respectively.

There are two sets of nodal displacement increments bound at the composite element if there is only one hollow bolt segment, each of them will be used to interpolate the displacement increments of the rock material and the bolt material, respectively by the formulas

$$\{\Delta u\}_r = [N]\{\Delta\delta\}_r \tag{15.56}$$

$$\{\Delta u\}_b^{ca} = [l]^{ca}[N]\{\Delta\delta\}_b \quad (b = 1, \ldots, n_b) \tag{15.57}$$

where $[N]$ = shape function matrix covering the whole composite element identical to the finite element method [see Eq. (4.57)].

The strain increments of the intact rock and bolt materials are then calculated by

$$\{\Delta\varepsilon\}_r = [B]_r\{\Delta\delta\}_r \tag{15.58}$$

$$\{\Delta\varepsilon\}_b^{ca} = [B]_b[L]^{ca}\{\Delta\delta\}_b \tag{15.59}$$

The displacement increments in the rock and bolt materials will result in relative displacement increment on the rock/bolt interface, which is expressed in the local Cylindrical coordinate system as

$$\{\Delta u\}_{j_{r,b}}^{cy} = [l]^{cy}[l]^{ca}(\{\Delta u\}_r - \{\Delta u\}_b) = [l]^{cy}[l]^{ca}[N](\{\Delta\delta\}_r - \{\Delta\delta\}_b) \tag{15.60}$$

By the virtual work principle, the equilibrium equation of the composite element containing n_b hollow bolts can be deduced as follows

$$\begin{bmatrix} [k]_{r,r}\cdots & [k]_{r,b}\cdots & [k]_{r,n_b} \\ \cdots & \cdots & \cdots \\ [k]_{b,r}\cdots & [k]_{b,b}\cdots & [k]_{b,n_b} \\ \cdots & \cdots & \cdots \\ [k]_{n_b,r}\cdots & [k]_{n_b,b}\cdots & [k]_{n_b,n_b} \end{bmatrix} \begin{Bmatrix} \{\Delta\delta\}_r \\ \cdots \\ \{\Delta\delta\}_b \\ \cdots \\ \{\Delta\delta\}_{n_b} \end{Bmatrix} = \begin{Bmatrix} \{\Delta f\}_r \\ \cdots \\ \{\Delta f\}_b \\ \cdots \\ \{\Delta f\}_{n_b} \end{Bmatrix} + \begin{Bmatrix} \{\Delta f^{vp}\}_r \\ \cdots \\ \{\Delta f^{vp}\}_b \\ \cdots \\ \{\Delta f^{vp}\}_{n_b} \end{Bmatrix} \tag{15.61}$$

In which

$$\begin{cases} [k]_{r,r} = \iiint\limits_{\Omega_r} [B]_r^T [D]_r [B]_r \, d\Omega \\ \qquad + \sum\limits_{b=1}^{n_b} \iint\limits_{\Gamma_{j_{r,b}}} [N]^T ([l]^{ca})^T ([l]^{cy})^T [D]_{j_{r,b}} [l]^{cy} [l]^{ca} [N] \, d\Gamma \\ [k]_{b,b} = \iiint\limits_{\Omega_b} \left([L]^{ca}\right)^T [B]_b^T [D]_b [B]_b [L]^{ca} \, d\Omega \\ \qquad + \iint\limits_{\Gamma_{j_{r,b}}} [N]^T ([l]^{ca})^T ([l]^{cy})^T [D]_{j_{r,b}} [l]^{cy} [l]^{ca} [N] \, d\Gamma \\ [k]_{r,b} = [k]_{b,r} = -\iint\limits_{\Gamma_{j_{r,b}}} [N]^T ([l]^{ca})^T ([l]^{cy})^T [D]_{j_{r,b}} [l]^{cy} [l]^{ca} [N] \, d\Gamma \end{cases} \tag{15.62}$$

$$\begin{cases} \{\Delta f^{vp}\}_r = \iiint\limits_{\Omega_r} [B]_r^T [D]_r \{\dot{\varepsilon}^{vp}\}_r \Delta t \, d\Omega \\ \qquad + \sum\limits_{b=1}^{n_b} \iint\limits_{\Gamma_{j_{r,b}}} [N]^T ([l]^{ca})^T ([l]^{cy})^T [D]_{j_{r,b}} \{\dot{u}^{vp}\}_{j_{r,b}}^{cy} \Delta t \, d\Gamma \\ \{\Delta f^{vp}\}_b = \iiint\limits_{\Omega_b} \left([L]^{ca}\right)^T [B]_b^T [D]_b \{\dot{\varepsilon}^{vp}\}_b^{ca} \Delta t \, d\Omega \\ \qquad - \iint\limits_{\Gamma_{j_{r,b}}} [[N]^T ([l]^{ca})^T ([l]^{cy})^T [D]_{j_{r,b}} \{\dot{u}^{vp}\}_{j_{r,b}}^{cy} \Delta t \, d\Gamma \end{cases} \tag{15.63}$$

15.5 Discontinuities

15.5.1 Concept

Now we generalize the concept of composite element to handle discontinuity (structural plane) segments. The finite element mesh should be generated to discretize the hydraulic structure beforehand. The deployment and sizes of the elements are dependent on the structure configuration and stress gradient but without take care of the existence of discontinuity system. Then the algebra and geometry calculation will be conducted with the messages of the discontinuity system and the FE mesh, to construct the corresponding CE mesh in which there are a number of CE elements containing discontinuity segments. Suppose a composite element

contains n_r discontinuity segments ($n_r = 4$ in Fig. 15.1) which delimit it into n_r sub-elements allowing for different mechanical properties. These sub-elements are not necessarily to be the classical finite elements. The loads exerting at each sub-element are transferred to the respective nodal values bound at the composite element as $\{\Delta f\}_{rl}$ and the equilibrium equation is established according to the virtual work principle to solve the nodal displacements $\{\Delta\delta\}_{rl}$, then the strains as well as the stresses in each sub-element can be calculated routinely.

15.5.2 Constitutive Equations

See Eqs. (2.122)–(2.130).

15.5.3 Equilibrium Equations

(1) Relationship between strain increment and nodal displacement increment

The displacement increment $\{\Delta u\}_{rl}$ in the sub-element rl is interpolated from the nodal displacement increment $\{\Delta\delta\}_{rl}$ bound at the composite element using Eq. (14.4).

The strain increments of the intact rock sub-elements are routinely calculated by the formula

$$\{\Delta\varepsilon\}_{rl} = [B]_{rl}\{\Delta\delta\}_{rl} \quad (rl = 1, \ldots n_r) \tag{15.64}$$

In which $[B]_{rl}$ is identical to that in Eq. (4.60).

The displacement increments in the rock sub-elements will give rise to relative displacement increments on the discontinuity segments, which will be expressed in the local Cartesian coordinate system as

$$\{\Delta u\}_{j_{rl,rm}} = [l]_{j_{rl,rm}}(\{\Delta u\}_{rl} - \{\Delta u\}_{rm}) = [l]_{j_{rl,rm}}[N](\{\Delta\delta\}_{rl} - \{\Delta\delta\}_{rm}) \tag{15.65}$$

In which rl and rm are the sub-elements of intact rock separated by the discontinuity segment $j_{rl,rm}$, and the coordinate transformation matrix $[l]_{j_{rl,rm}}$ has been defined in Chap. 2 [see Eq. (2.13)].

(2) Relationship between the nodal displacement and load increments

Suppose virtual displacements manifest in the rock sub-elements

$$\{\Delta u^*\}_{rl} = [N]\{\Delta\delta^*\}_{rl} \quad (rl = 1, \ldots n_r) \tag{15.66}$$

The corresponding virtual strains and relative displacements will be

$$\{\Delta\varepsilon^*\}_{rl} = [B]_{rl}\{\Delta\delta^*\}_{rl} \quad (rl = 1, \ldots n_r) \tag{15.67}$$

$$\{\Delta u^*\}_{j_{rl,rm}} = [l]_{j_{rl,rm}}[N](\{\Delta\delta^*\}_{rl} - \{\Delta\delta^*\}_{rm}) \tag{15.68}$$

And the virtual work principle for the composite element containing discontinuities will be

$$\sum_{rl=1}^{n_r} W_{rl} + \sum_{j_{rl,rm}=1}^{n_j} W_{j_{rl,rm}} = \sum_{rl=1}^{n_r} (\{\Delta\delta^*\}_{rl})^T \{\Delta f\}_{rl} \tag{15.69}$$

where $\{\Delta f\}_{rl}$ are the nodal load increments bound at the composite element which can be transferred from the load increments exerting at the rock sub-elements according to the identical algorithm to the FEM. The component virtual works W_{rl} and $W_{j_{rl,rm}}$ contributed from the rock sub-elements and the discontinuity segments will be elaborated as follows.

1. Rock material

$$W_{rl} = \iiint_{\Omega_{rl}} (\{\Delta\varepsilon^*\}_{rl})^T \{\Delta\sigma\}_{rl} d\Omega \quad (rl = 1, \ldots n_r) \tag{15.70}$$

Take the constitutive relation Eq. (2.122) and the strain-displacement relation Eq. (15.64) into account, the virtual work in the rock material will become

$$W_{rl} = \iiint_{\Omega_{rl}} (\{\Delta\delta^*\}_{rl})^T [B]_{rl}^T [D]_{rl} ([B]_{rl}\{\Delta\delta\}_{rl} - \{\dot{\varepsilon}^{vp}\}_{rl}\Delta t)\, d\Omega \quad (rl = 1, \ldots n_r) \tag{15.71}$$

2. Discontinuity segment

$$W_{j_{rl,rm}} = \iint_{\Gamma_{j_{rl,rm}}} (\{\Delta u^*\}_{j_{rl,rm}})^T \{\Delta\sigma\}_{j_{rl,rm}} d\Gamma \tag{15.72}$$

Introducing the constitutive relation Eq. (2.126) and the strain-displacement relation Eq. (15.65) into $W_{j_{rl,rm}}$, we have

$$W_{j_{rl,rm}} = \iint_{\Gamma_{j_{rl,rm}}} ((\{\Delta\delta^*\}_{rl})^T - (\{\Delta\delta^*\}_{rm})^T)[N]^T ([l]_{j_{rl,rm}})^T [D]_{j_{rl,rm}} ([l]_{j_{rl,rm}}[N](\{\Delta\delta\}_{rl} - \{\Delta\delta\}_{rm}) - \{\dot{u}^{vp}\}_{j_{rl,rm}}\Delta t)\, d\Gamma \tag{15.73}$$

We introduce Eqs. (15.71) and (15.73) into Eq. (15.69), and arrange the resultant equation regarding the different virtual displacements. Because $\{\Delta\delta^*\}_r$ is an arbitrary vector, the validity of the virtual work principle will leads to

$$\begin{bmatrix} [k]_{r1,r1} & .. & .. & .. & [k]_{j_{r1,nr}} \\ .. & .. & .. & .. & .. \\ .. & [k]_{rl,rl} & .. & [k]_{j_{rl,rm}} & .. \\ .. & .. & .. & .. & .. \\ [k]_{j_{nr,r1}} & .. & .. & .. & [k]_{n_r,n_r} \end{bmatrix} \begin{Bmatrix} \{\Delta\delta\}_{r1} \\ \cdots\cdots\cdots \\ \{\Delta\delta\}_{rl} \\ \cdots\cdots\cdots \\ \{\Delta\delta\}_{rm} \\ \cdots\cdots\cdots \\ \{\Delta\delta\}_{n_r} \end{Bmatrix} = \begin{Bmatrix} \{\Delta f\}_{r1} \\ \cdots\cdots\cdots \\ \{\Delta f\}_{rl} \\ \cdots\cdots\cdots \\ \{\Delta f\}_{rm} \\ \cdots\cdots\cdots \\ \{\Delta f\}_{n_r} \end{Bmatrix} + \begin{Bmatrix} \{\Delta f^{vp}\}_{r1} \\ \cdots\cdots\cdots \\ \{\Delta f^{vp}\}_{rl} \\ \cdots\cdots\cdots \\ \{\Delta f^{vp}\}_{rm} \\ \cdots\cdots\cdots \\ \{\Delta f^{vp}\}_{n_r} \end{Bmatrix} \tag{15.74}$$

In which

$$\begin{cases} [k]_{rl,rl} = \iiint\limits_{\Omega_{rl}} [B]_{rl}^T [D]_{rl} [B]_{rl}\, d\Omega - \sum\limits_{rm=1,rm\neq rl}^{n_j} H_1(rl,rm)[k]_{j_{rl,rm}} \\ [k]_{j_{rl,rm}} = -\iint\limits_{\Gamma_{jrl,rm}} [N]^T [l]_{j_{rl,rm}}^T [D]_{j_{rl,rm}} [l]_{j_{rl,rm}} [N]\, d\Gamma \\ H_1(rl,rm) = \begin{cases} 1 & if \quad rl \quad and \quad rm \quad are \quad adjacent \\ 0 & if \quad rl \quad and \quad rm \quad are \quad not \quad adjacent \end{cases} \end{cases} \tag{15.75}$$

$$\begin{cases} \{\Delta f^{vp}\}_{rl} = \iiint\limits_{\Omega_{rl}} [B]_{rl}^T [D]_{rl} \{\dot{\varepsilon}^{vp}\}_{rl} \Delta t\, d\Omega \\ \qquad\qquad - \sum\limits_{rm=1,rm\neq rl}^{n_j} \{\Delta f^{vp}\}_{j_{rl,rm}} \\ \{\Delta f^{vp}\}_{j_{rl,rm}} = -H_2(rl,rm) \iint\limits_{\Gamma j_{rl,rm}} [N]^T [l]_{j_{rl,rm}}^T [D]_{j_{rl,rm}} \left\{\Delta \dot{u}^{vp}\right\}_{j_{rl,rm}} \Delta t\, d\Gamma \\ H_2(rl,rm) = \begin{cases} 1 & if \quad rl > rm \\ -1 & if \quad rl < rm \\ 0 & if \quad rl \quad and \quad rm \quad are \quad not \quad adjacent \end{cases} \end{cases} \tag{15.76}$$

Equations (15.74)–(15.76) govern a composite element containing n_r entity (rock) sub-elements. Generally, if a composite element consists of n_r rock sub-elements, its DOF will be n_r times that of the finite element, whereas if an element contains no discontinuity segments, it will be degenerated automatically to the classical finite element. In this way the composite elements and the finite

elements can be hybrid well in one discrete system and there is no essential difficulty in the computational programming.

15.6 Jointed Rocks Reinforced by Fully-Grouted Bolts

15.6.1 Sub-Element Analysis

(1) Displacement interpolation

Figure 15.5 shows a composite element containing one joint segment and one bolt segment, respectively. This element is composed of two rock material sub-elements cut by the joint segment, two bolt sub-elements connected through the grout/bolt interface with two grout sub-elements, which are in turn, connected through the rock/grout interface with the rock material sub-elements.

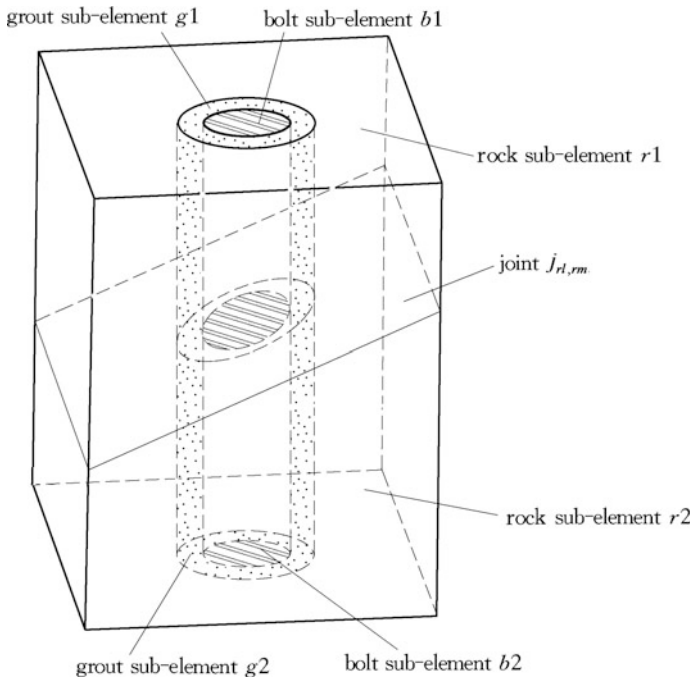

Fig. 15.5 Schematic drawing of the composite element containing one bolt segment and one joint segment

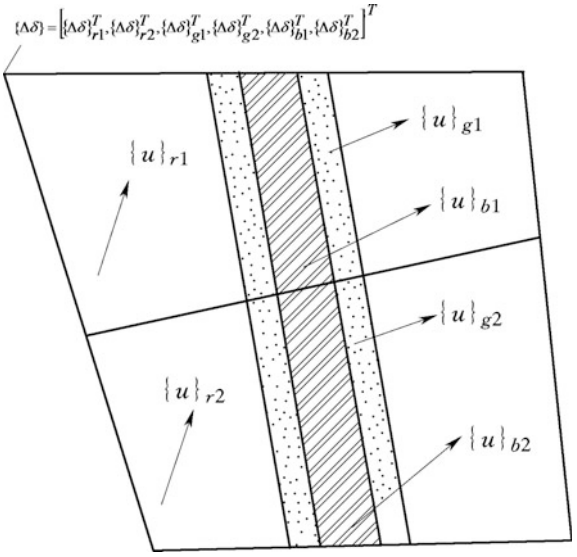

Fig. 15.6 Interpolation of displacement within the composite element containing one bolt segment and one joint segment

The displacements in each sub-element are interpolated from the nodal displacements $\{\Delta\delta\}=\left[\{\Delta\delta\}_{r1}^T \quad \{\Delta\delta\}_{r2}^T \quad \{\Delta\delta\}_{g1}^T \quad \{\Delta\delta\}_{g2}^T \quad \{\Delta\delta\}_{b1}^T \quad \{\Delta\delta\}_{b2}^T\right]^T$ bound at the composite element (see Fig. 15.6) as follows

$$\{\Delta u\}_{rl}=[N]\{\Delta\delta\}_{rl} \quad (rl=1,2) \tag{15.77}$$

$$\begin{cases}\{\Delta u\}_{gl}^{ca}=[l]^{ca}[N]\{\Delta\delta\}_{gl}\\ \{\Delta u\}_{gl}^{cy}=[l]^{cy}[l]^{ca}[N]\{\Delta\delta\}_{gl}\end{cases} \quad (gl=1,2) \tag{15.78}$$

$$\begin{cases}\{\Delta u\}_{bl}^{ca}=[l]^{ca}[N]\{\Delta\delta\}_{bl}\\ \{\Delta u\}_{bl}^{cy}=[l]^{cy}[l]^{ca}[N]\{\Delta\delta\}_{bl}\end{cases} \quad (bl=1,2) \tag{15.79}$$

In which $[N]$ stands for the shape function matrix in the whole composite element. The nodal displacement transformation matrices $[l]^{ca}$ and $[l]^{cy}$ have been defined in Eqs. (2.37) and (2.38) in which the subscript b or g is neglected.

The displacements in the rock sub-elements rl and rm will manifest relative displacement on the joint segment $j_{rl,rm}$, which is expressed in the local Cartesian coordinate system as

$$\{\Delta u\}_{j_{rl,rm}}=[l]_{j_{rl,rm}}(\{\Delta u\}_{rl}-\{\Delta u\}_{rm})=[l]_{j_{rl,rm}}[N](\{\Delta\delta\}_{rl}-\{\Delta\delta\}_{rm}) \quad (rl\neq rm;\quad rl,rm=1,2) \tag{15.80}$$

The transformation matrix $[l]_{j_{rl,rm}}$ is the function of the dip direction $\phi_{j_{rl,rm}}$ and dip angle $\theta_{j_{rl,rm}}$ of the joint defined in Eq. (2.13).

Similarly, the relative displacements at rock/grout and grout/bolt interfaces ($j_{rl,gl}$ and $j_{gl,bl}$) can be expressed in the local Cylindrical coordinate system as

$$\{\Delta u\}^{cy}_{j_{rl,gl}} = \{\Delta u\}^{cy}_{rl} - \{\Delta u\}^{cy}_{gl} = [l]^{cy}[l]^{ca}[N](\{\Delta\delta\}_{rl} - \{\Delta\delta\}_{gl}) \quad (rl = gl = 1,2) \tag{15.81}$$

$$\{\Delta u\}^{cy}_{j_{gl,bl}} = \{\Delta u\}^{cy}_{gl} - \{\Delta u\}^{cy}_{bl} = [l]^{cy}[l]^{ca}[N](\{\Delta\delta\}_{gl} - \{\Delta\delta\}_{bl}) \quad (bl = gl = 1,2) \tag{15.82}$$

(2) Strain computation

The strains in the rock, grout, and bolt sub-elements can be calculated in terms of their nodal displacements

$$\{\Delta\varepsilon\}_{rl} = [B]_r\{\Delta\delta\}_{rl} \quad (rl = 1,2) \tag{15.83}$$

$$\{\Delta\varepsilon\}^{ca}_{gl} = [B]_{gl}[L]^{ca}\{\Delta\delta\}_{gl} \quad (gl = 1,2) \tag{15.84}$$

$$\{\Delta\varepsilon\}^{ca}_{bl} = [B]_{bl}[L]^{ca}\{\Delta\delta\}_{bl} \quad (bl = 1,2) \tag{15.85}$$

In which $[B]_r$ is identical to that in Eq. (4.60), $[B]_{bl}$ and $[B]_{gl}$ is identical to that in Eqs. (15.11)–(15.12).

According to the laboratory tests (Spang and Egger 1990), bending of the bolt at joint becomes predominant even when the shear force is small, which will create two hinges above and below the joint plane. The vertical height of the bended bolt is about 2–4 times the bolt diameter d_b. It is named as "effective height", corresponding to an "effective length" of $L_b = h_b/\cos\theta_b$(see Fig. 6.4). This height depends on the quality of the rock (or the grout mortar) and bolt, as well as on the bolt's diameter and the inclined angle.

It is therefore naturally to assume that for a bolt at joint there is an "effective length" within which nearly all deformations will demonstrate. If we further postulate that the relative displacement between the two hinges is equal to the relative displacement of the joint walls at the intersection point, and the strains are uniformly distributed along the "effective length" L_b (Chen and Egger 1999), then the relationship between the strains and nodal displacements of the bolt b (and grout g as well) is

$$\{\Delta\varepsilon\}^{ca}_{j_{gl,gm}} = [L]^{ca}[N](\{\Delta\delta\}_{gl} - \{\Delta\delta\}_{gm})/L_b \quad (gl \neq gm; \quad gl, gm = 1,2) \tag{15.86}$$

$$\{\Delta\varepsilon\}^{ca}_{j_{bl,bm}} = [L]^{ca}[N](\{\Delta\delta\}_{bl} - \{\Delta\delta\}_{bm})/L_b \quad (bl \neq bm; \quad bl, bm = 1,2) \tag{15.87}$$

(3) Constitutive equations

See Eqs. (2.122)–(2.130).

15.6.2 Composite Element Analysis

Suppose a virtual displacement vector $\{\Delta\delta^*\}$ appears at the composite element, then the corresponding virtual displacements and virtual strains within the sub-elements can be calculated according to Eqs. (15.77)–(15.87).

The application of the virtual work principle to the composite element leads to the following expression

$$\begin{aligned} &W_{r1}+W_{r2}+W_{g1}+W_{g2}+W_{b1}+W_{b2}+W_{j_{r1,r2}}+W_{j_{g1,g2}}+W_{j_{b1,b2}}+W_{j_{rl,gl}}+W_{j_{gl,bl}} \\ &\quad=(\{\Delta\delta^*\}_{r1})^T\{\Delta f\}_{r1}+(\{\Delta\delta^*\}_{r2})^T\{\Delta f\}_{r2}+(\{\Delta\delta^*\}_{g1})^T\{\Delta f\}_{g1} \qquad (rl=gl=bl=1,2) \\ &\qquad+(\{\Delta\delta^*\}_{g2})^T\{\Delta f\}_{g2}+(\{\Delta\delta^*\}_{b1})^T\{\Delta f\}_{b1}+(\{\Delta\delta^*\}_{b2})^T\{\Delta f\}_{b2} \end{aligned} \tag{15.88}$$

In which $\{\Delta f\}_{rl}$, $\{\Delta f\}_{gl}$, $\{\Delta f\}_{bl}$ are the nodal forces bound at the composite element, which can be transferred from the forces exerting at the rock, grout, and bolt materials according to the algorithm identical to the FEM. W_{rl}, W_{gl}, W_{bl}, $W_{j_{rl,rm}}$, $W_{j_{gl,gm}}$, $W_{j_{bl,bm}}$, $W_{j_{rl,gl}}$ and $W_{j_{gl,bl}}$ are the virtual works contributed from the rock, grout in rock, bolt in grout, joint, grout at joint, bolt at joint, rock/grout interface, and grout/bolt interface, respectively

$$W_{rl}=\iiint_{\Omega_{rl}}(\{\Delta\delta^*\}_{rl})^T[B]_{rl}^T[D]_{rl}[B]_{rl}\{\Delta\delta\}_{rl}\,d\Omega \quad (rl=1,2) \tag{15.89}$$

$$\begin{aligned} W_{j_{rl,rm}}=&\iint_{\Gamma_{j_{rl,rm}}}((\{\Delta\delta^*\}_{rl})^T-(\{\Delta\delta^*\}_{rm})^T)[N]^T[l]_{j_{rl,rm}}^T[D]_{j_{rl,rm}}[l]_{j_{rl,rm}}[N](\{\Delta\delta\}_{rl}-\{\Delta\delta\}_{rm})\,d\Gamma \\ &(rl\neq rm;rl,rm=1,2) \end{aligned} \tag{15.90}$$

$$W_{gl}=\iiint_{\Omega_{gl}}(\{\Delta\delta^*\}_{gl})^T([L]^{ca})^T([B]_{gl})^T[D]_{gl}[B]_{gl}[L]^{ca}\{\Delta\delta\}_{gl}\,d\Omega \quad (gl=1,2) \tag{15.91}$$

$$W_{bl}=\iiint_{\Omega_{bl}}(\{\Delta\delta^*\}_{bl})^T([L]^{ca})^T([B]_{bl})^T[D]_{bl}[B]_{bl}[L]^{ca}\{\Delta\delta\}_{bl}\,d\Omega \quad (bl=1,2) \tag{15.92}$$

$$W_{j_{rl,gl}} = \iint_{\Gamma_{j_{rl,gl}}} (\{\Delta\delta^*\}_{rl} - \{\Delta\delta^*\}_{gl})^T [N]^T ([l]^{ca})^T ([l]^{cy})^T [D]_{j_{rl,gl}} [l]^{cy} [l]^{ca} [N] (\{\Delta\delta\}_{rl} - \{\Delta\delta\}_{gl}) \, d\Gamma$$
$$(rl = gl = 1, 2) \tag{15.93}$$

$$W_{j_{gl,bl}} = \iint_{\Gamma_{j_{gl,bl}}} (\{\Delta\delta^*\}_{gl} - \{\Delta\delta^*\}_{bl})^T [N]^T ([l]^{ca})^T ([l]^{cy})^T [D]_{j_{gl,bl}} [l]^{cy} [l]^{ca} [N] (\{\Delta\delta\}_{gl} - \{\Delta\delta\}_{bl}) \, d\Gamma$$
$$(gl = bl = 1, 2) \tag{15.94}$$

$$W_{j_{g1,g2}} = \frac{1}{L_b^2} \iiint_{\Omega_{j_{g1,g2}}} (\{\Delta\delta^*\}_{g1} - \{\Delta\delta^*\}_{g2})^T [N]^T ([l]^{ca})^T [D]_{j_{g1,g2}} [l]^{ca} [N] (\{\Delta\delta\}_{g1} - \{\Delta\delta\}_{g2}) \, d\Omega \tag{15.95}$$

$$W_{j_{b1,b2}} = \frac{1}{L_b^2} \iiint_{\Omega_{j_{b1,b2}}} (\{\Delta\delta^*\}_{b1} - \{\Delta\delta^*\}_{b2})^T [N]^T ([l]^{ca})^T [D]_{j_{b1,b2}} [l]^{ca} [N] (\{\Delta\delta\}_{b1} - \{\Delta\delta\}_{b2}) \, d\Omega \tag{15.96}$$

Since it has been assumed that the strains of the bolt between two hinges are uniformly distributed along the effective length L_a, Eqs. (15.95) and (15.96) can be reduced as

$$\begin{aligned} W_{j_{g1,g2}} &= \frac{1}{L_b^2} \iint_{\Gamma_{j_{g1,g2}}} (\{\Delta\delta^*\}_{g1} - \{\Delta\delta^*\}_{g2})^T [N]^T ([l]^{ca})^T [D]_{j_{g1,g2}} [l]^{ca} [N] (\{\Delta\delta\}_{g1} - \{\Delta\delta\}_{g2}) \, d\Gamma \cdot L_b \\ &= \frac{1}{L_b} \iint_{\Gamma_{j_{g1,g2}}} (\{\Delta\delta^*\}_{g1} - \{\Delta\delta^*\}_{g2})^T [N]^T ([l]^{ca})^T [D]_{j_{g1,g2}} [l]^{ca} [N] (\{\Delta\delta\}_{g1} - \{\Delta\delta\}_{g2}) \, d\Gamma \end{aligned} \tag{15.97}$$

$$W_{j_{b1,b2}} = \frac{1}{L_b} \iint_{\Gamma_{j_{b1,b2}}} (\{\Delta\delta^*\}_{b1} - \{\Delta\delta^*\}_{b2})^T [N]^T ([l]^{ca})^T [D]_{j_{b1,b2}} [l]^{ca} [N] (\{\Delta\delta\}_{b1} - \{\Delta\delta\}_{b2}) \, d\Gamma \tag{15.98}$$

We introduce Eqs. (15.89)–(15.98) into Eq. (15.88), then arrange the equation according to the different components of the virtual displacements. Recall that the virtual displacement vector $\{\Delta\delta^*\}$ is arbitrary, we have

$$[k]\{\Delta\delta\} = \{\Delta f\} + \{\Delta f^{vp}\} \tag{15.99}$$

$$\begin{cases} \{\Delta\delta\} = \left[\{\Delta\delta\}_{r1}^T \quad \{\Delta\delta\}_{r2}^T \quad \{\Delta\delta\}_{g1}^T \quad \{\Delta\delta\}_{g2}^T \quad \{\Delta\delta\}_{b1}^T \quad \{\Delta\delta\}_{b2}^T \right]^T \\ \{\Delta f\} = \left[\{\Delta f\}_{r1}^T \quad \{\Delta f\}_{r2}^T \quad \{\Delta f\}_{g1}^T \quad \{\Delta f\}_{g2}^T \quad \{\Delta f\}_{b1}^T \quad \{\Delta f\}_{b2}^T \right]^T \\ \{\Delta f^{vp}\} = \left[\{\Delta f^{vp}\}_{r1}^T \quad \{\Delta f^{vp}\}_{r2}^T \quad \{\Delta f^{vp}\}_{g1}^T \quad \{\Delta f^{vp}\}_{g2}^T \quad \{\Delta f^{vp}\}_{b1}^T \quad \{\Delta f^{vp}\}_{b2}^T \right]^T \end{cases} \tag{15.100}$$

$$[k] = \begin{bmatrix} [k]_{r1} + [k]_{j_{r1,g1}} + [k]_{j_{r1,r2}} & -[k]_{j_{r1,r2}} & -[k]_{j_{r1,g1}} \\ -[k]_{j_{r1,r2}} & [k]_{r2} + [k]_{j_{r2,g2}} + [k]_{j_{r1,r2}} & 0 \\ -[k]_{j_{r1,g1}} & 0 & [k]_{g1} + [k]_{j_{r1,g1}} + [k]_{j_{g1,b1}} + [k]_{j_{g1,g2}} \\ 0 & -[k]_{j_{r2,g2}} & -[k]_{j_{g1,g2}} \\ 0 & 0 & -[k]_{j_{g1,b1}} \\ 0 & 0 & \end{bmatrix}$$

$$\begin{bmatrix} 0 & 0 & 0 \\ [k]_{j_{r2,g2}} & 0 & 0 \\ -[k]_{j_{g1,g2}} & -[k]_{j_{g1,b1}} & 0 \\ [k]_{g2} + [k]_{j_{g2,b2}} + [k]_{j_{r2,g2}} + [k]_{j_{g1,g2}} & 0 & -[k]_{j_{g2,b2}} \\ 0 & [k]_{b1} + [k]_{j_{g1,b1}} + [k]_{j_{b1,b2}} & -[k]_{j_{b1,b2}} \\ -[k]_{j_{g2,b2}} & -[k]_{j_{b1,b2}} & [k]_{b2} + [k]_{j_{g2,b2}} + [k]_{j_{b1,b2}} \end{bmatrix} \tag{15.101}$$

In which

$$\begin{cases} [k]_{rl} = \iiint\limits_{\Omega_{rl}} ([B]_{rl})^T [D]_{rl} [B]_{rl} \, d\Omega \quad (rl = 1,2) \\ [k]_{bl} = \iiint\limits_{\Omega_{bl}} ([L]^{ca})^T ([B]_{bl})^T [D]_{bl} ([B]_{bl})^T [L]^{ca} \, d\Omega \quad (bl = 1,2) \\ [k]_{gl} = \iiint\limits_{\Omega_{gl}} ([L]^{ca})^T ([B]_{gl})^T [D]_{gl} [B]_{gl} [L]^{ca} \, d\Omega \quad (gl = 1,2) \\ [k]_{j_{rl,gl}} = \iint\limits_{\Gamma_{j_{rl,gl}}} [N]^T ([l]^{ca})^T ([l]^{cy})^T [D]_{j_{rl,gl}} [l]^{cy} [l]^{ca} [N] \, d\Gamma \quad (rl = gl = 1,2) \\ [k]_{j_{gl,bl}} = \iint\limits_{\Gamma_{j_{gl,bl}}} [N]^T ([l]^{ca})^T ([l]^{cy})^T [D]_{j_{gl,bl}} [l]^{cy} [l]^{ca} [N] \, d\Gamma \quad (gl = bl = 1,2) \\ [k]_{j_{g1,g2}} = \frac{1}{L_b} \iint\limits_{\Gamma_{j_{g1,g2}}} [N]^T ([l]^{ca})^T [D]_{j_{g1,g2}} [l]^{ca} [N] \, d\Gamma \\ [k]_{j_{b1,b2}} = \frac{1}{L_b} \iint\limits_{\Gamma_{j_{b1,b2}}} [N]^T ([l]^{ca})^T [D]_{j_{b1,b2}} [l]^{ca} [N] \, d\Gamma \\ [k]_{j_{r1,r2}} = \iint\limits_{\Gamma_{j_{r1,r2}}} ([l]_{j_{r1,r2}})^T [N]^T [D]_{j_{r1,r2}} [N] [l]_{j_{r1,r2}} \, d\Gamma \end{cases} \tag{15.102}$$

$$
\begin{cases}
\{\Delta f^{vp}\}_{rl} = \iiint\limits_{\Omega_{rl}} ([B]_{rl})^T [D]_{rl} \{\dot{\varepsilon}^{vp}\}_{rl} \Delta t \, d\Omega \quad (rl = 1,2) \\
\{\Delta f^{vp}\}_{bl} = \iiint\limits_{\Omega_{bl}} ([L]^{ca})^T ([B]_{bl})^T [D]_{bl} \{\dot{\varepsilon}^{vp}\}_{bl} \Delta t \, d\Omega \quad (bl = 1,2) \\
\{\Delta f^{vp}\}_{gl} = \iiint\limits_{\Omega_{gl}} ([L]^{ca})^T ([B]_{gl})^T [D]_{gl} \{\dot{\varepsilon}^{vp}\}_{gl} \Delta t \, d\Omega \quad (gl = 1,2) \\
\{\Delta f^{vp}\}_{j_{rl,gl}} = \iint\limits_{\Gamma_{j_{rl,gl}}} [N]^T ([l]^{ca})^T ([l]^{cy})^T [D]_{j_{rl,gl}} \left\{\Delta \dot{u}^{vp}\right\}_{j_{rl,gl}} \Delta t \, d\Gamma \quad (rl = gl = 1,2) \\
\{\Delta f^{vp}\}_{j_{gl,bl}} = \iint\limits_{\Gamma_{j_{gl,bl}}} [N]^T ([l]^{ca})^T ([l]^{cy})^T [D]_{j_{gl,bl}} \left\{\Delta \dot{u}^{vp}\right\}_{j_{gl,bl}} \Delta t \, d\Gamma \quad (gl = bl = 1,2) \\
\{\Delta f^{vp}\}_{j_{g1,g2}} = \frac{1}{L_b} \iint\limits_{\Gamma_{j_{g1,g2}}} [N]^T ([l]^{ca})^T [D]_{j_{g1,g2}} \left\{\Delta \dot{u}^{vp}\right\}_{j_{g2,,b2}} \Delta t \, d\Gamma \\
\{\Delta f^{vp}\}_{j_{b1,b2}} = \frac{1}{L_b} \iint\limits_{\Gamma_{j_{b1,b2}}} [N]^T ([l]^{ca})^T [D]_{j_{b1,b2}} \left\{\Delta \dot{u}^{vp}\right\}_{j_{b1,b2}} \Delta t \, d\Gamma \\
\{\Delta f^{vp}\}_{j_{r1,r2}} = \iint\limits_{\Gamma_{j_{r1,r2}}} [N]^T ([l]_{j_{r1,r2}})^T [D]_{j_{r1,r2}} \left\{\Delta \dot{u}^{vp}\right\}_{j_{r1,r2}} \Delta t \, d\Gamma
\end{cases}
\tag{15.103}
$$

15.7 Key Algorithms

The CE approach elaborated in this chapter has been implemented in the software CORE3 in which both the equivalent and explicit FE approaches of the jointed rock masses with reinforcement components (vide Chap. 6) already had been implemented. Towards the implementation of the CE approach, the following algorithms are worthwhile to be explained.

15.7.1 Numerical Integration

Equations (15.35) and (15.36), (15.54) and (15.55), (15.62) and (15.63), (15.75) and (15.76), (15.102) and (15.103) require the integral calculation in irregular sub-elements and discontinuity segments.

It is recommended that solid sub-element is firstly divided into tetrahedrons, then each tetrahedron is further divided into four hexahedrons, in this manner the conventional Gaussian quadrature at the global coordinate system may be applied easily.

Whereas for the discontinuity segment the division into triangles will be undertook firstly, then each triangle is further divided into three quadrilaterals, and the conventional Gaussian quadrature at the local coordinate system can be undertaken. For the sub-elements corresponding to the grout material, bolt material, rock/grout as well as grout/bolt interfaces, the integration conducted at the local Cylindrical coordinate system would be suggestible.

15.7.2 Assemble of Global Stiffness Matrix and Load Vector

When the governing equations of all the composite elements and finite elements have been formulated in a structure system, they can be assembled into the governing equation of the whole discrete system in a manner similar to the FEM.

It is advisable that in assembling the overall stiffness matrix of the whole structure system, the sub-matrices corresponding to the rock sub-elements will be put in the first portion of the overall matrix, the relevant load vector is assembled correspondingly. Then, all the sub-matrices of the grout and bolt sub-elements are put in the second portion. Should the reinforcement scheme be optimized, this assembling procedure allows for repeated calculations of different reinforcement schemes with only a bit change of the stiffness matrix and load vector. This idea is similar to the technique of the p-version refinement FEM.

15.7.3 Hierarchical Refinement

A composite element comprising bolt segments undergoes complicated deformation pattern. Consequently, the use of p-refinement for the CEM may enlarge the function space by the upgrade of basis functions and correspondent virtual nodes, in this way the complex deformation within a composite element containing reinforcement components and discontinuities may be simulated with sufficient accuracy even in a coarse mesh.

In the p-refinement composite element, the general nodes for each sub-element are arranged according to standard nodes and hierarchical edges, faces, and body corresponding to general basis functions. In this manner the p-refinement elaborated in Chap. 5 may be routinely employed (He and Chen 2006).

15.8 Verification Examples

15.8.1 Fully-Grouted Bolt

(1) Characteristics of the computation

Six rock samples at size of 5 m × 5 m × 5 m (length × width × height) has been studied. In the center of sample there is a fully-grouted bolt (see Fig. 15.7) exerted by a pull-out force P on its top.

This bolt is embedded within the composite elements below the pull-out force (see Fig. 15.8). The length of bolt is 3 m, the radii of bolt and grout are 20 and 38 mm, respectively. The pull-out force P is exerted by 4 incremental steps from 300 to 600 kN and 720 kN until 900 kN. The bottom of the sample is fixed and the four vertical surfaces are free.

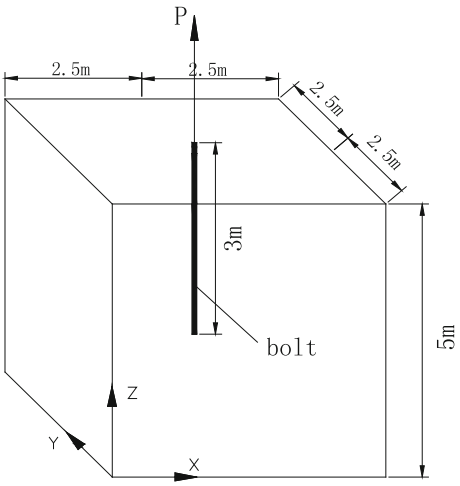

Fig. 15.7 Schematic configuration of the test sample containing a rock bolt

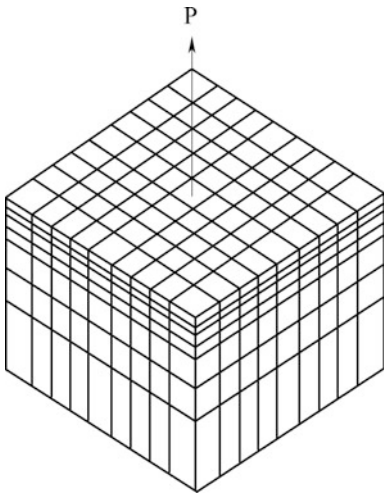

Fig. 15.8 Computation mesh of the test sample containing one rock bolt

These tests were carried out at the excavated rock slope of the ship lock in Three Gorges Project, China (Rong et al. 2001). They are distinguished into two sets: the first set comprises four samples (1, 2, 3, 4), whereas the second set comprises two samples (5, 6). Tables 15.1, 15.2, 15.3 and 15.4 list the mechanical parameters used in the study.

(2) Computation results

During the field experiment, the axial stresses along the bolt and the displacements of the borehole collar are recorded. Unfortunately, the shear stresses and the

Table 15.1 Mechanical parameters of the materials of the first test set (sample 1,2,3,4)

Material	E (GPa)	μ	c (MPa)	φ (°)	σ_T (MPa)	σ_y (MPa)	σ_u (MPa)	γ_u^{vp}
Steel	200	0.25	–	–	–	310	500	0.18
Grout	26.0	0.17	2.5	58.0	1.1	–	–	–
Rock	15.0	0.25	1.1	44.0	1.1	–	–	–

Table 15.2 Mechanical parameters of the interfaces of the first test set (sample 1,2,3,4)

Interface	k_n (MPa)	k_s (MPa)	c (MPa)	φ(°)	ϕ(°)	σ_T (MPa)
Rock/grout	10,000	500	1.0	44	44	1.0
Grout/bolt	10,000	3000	2.0	58	58	1.0

Table 15.3 Mechanical parameters of the materials of the second test set (sample 5,6)

Material	E (GPa)	μ	c (MPa)	φ (°)	σ_T (MPa)	σ_y (MPa)	σ_u (MPa)	γ_u^{vp}
Steel	200	0.25	–	–	–	310	500	0.18
Grout	26.0	0.17	2.5	58.0	1.1	–	–	–
Rock	32.0	0.2	1.7	59	1.1	–	–	–

Table 15.4 Mechanical parameters of the interfaces of the second test set (sample 5,6)

Interface	k_n (MPa)	k_s (MPa)	c (MPa)	φ (°)	ϕ (°)	σ_T (MPa)
Rock/grout	10,000	2000	1.0	50	50	1.0
Grout/bolt	10,000	3000	2.0	58	58	1.0

displacements along the whole bolt cannot be extracted because of the technical difficulties.

Figures 15.9, 15.10, 15.11, 15.12, 15.13 and 15.14 present the experimental and computational results. The experimental results exhibit, as common in the field test for the rock engineering, large variance. However, if the parameters can be evaluated properly, the computation can provide reasonable results.

Figures 15.15, 15.16, 15.17 and 15.18 display the other computed results (without test results for cross-reference) for the second sample set which give us a general idea with regard to the displacements of the whole bolt and grout as well as the shear stresses along the interfaces.

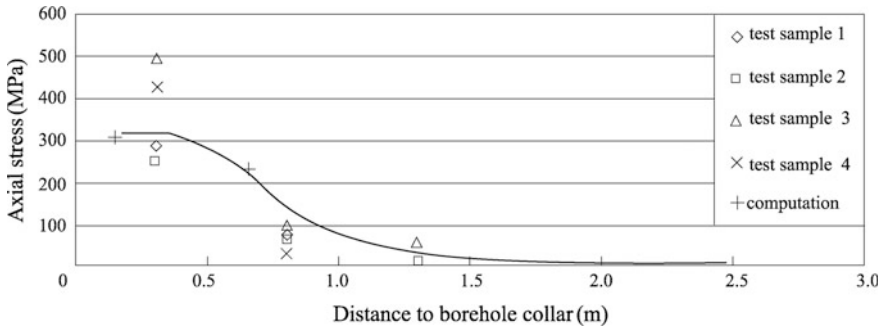

Fig. 15.9 Axial stress distribution along the bolt under 600 kN pull out force (first set)

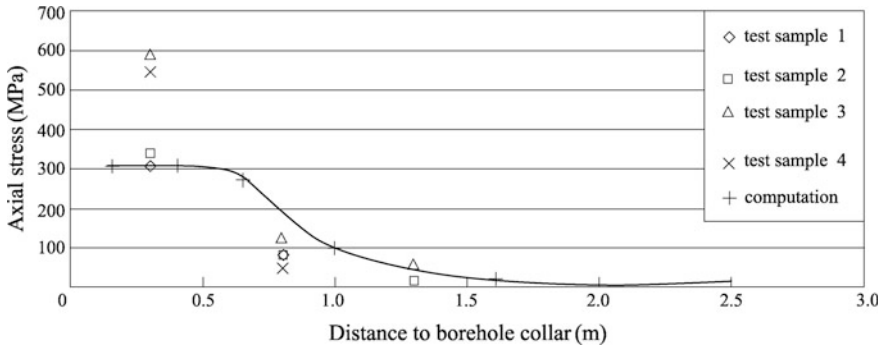

Fig. 15.10 Axial stress distribution along the bolt under 720 kN pull out force (first set)

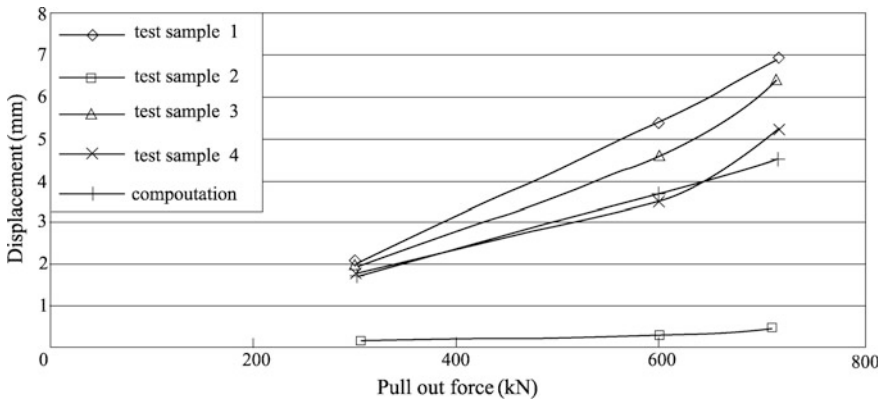

Fig. 15.11 Displacements of the borehole collar against pull out forces (first set)

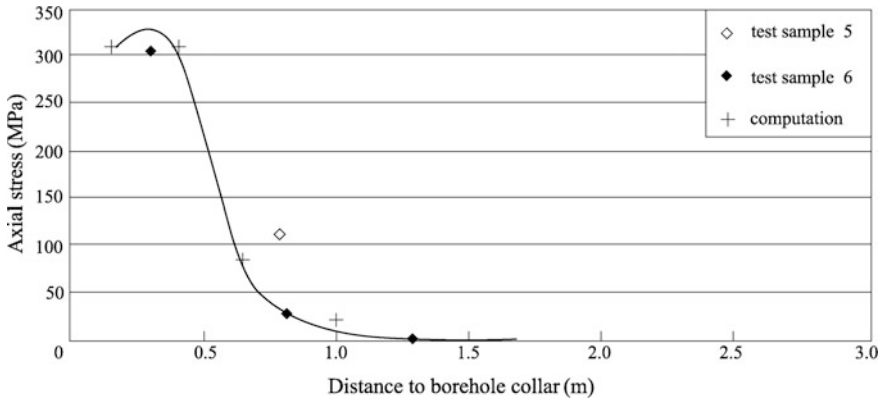

Fig. 15.12 Axial stress distribution along the bolt under 600 kN pull out force (second set)

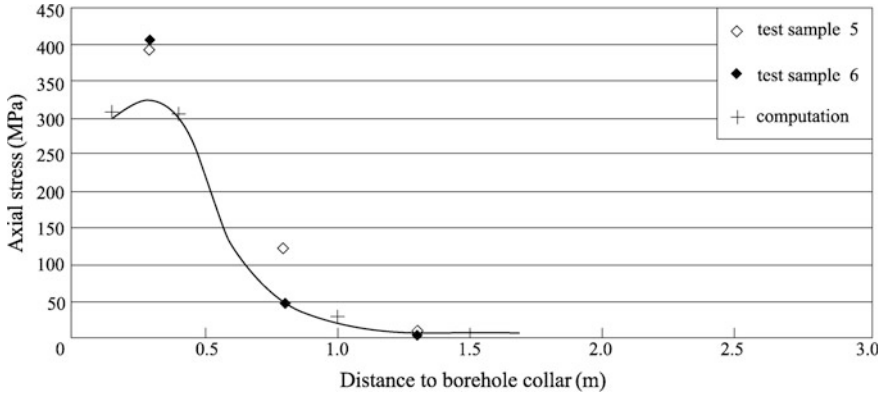

Fig. 15.13 Axial stress distribution along the bolt under 720 kN pull out force (second set)

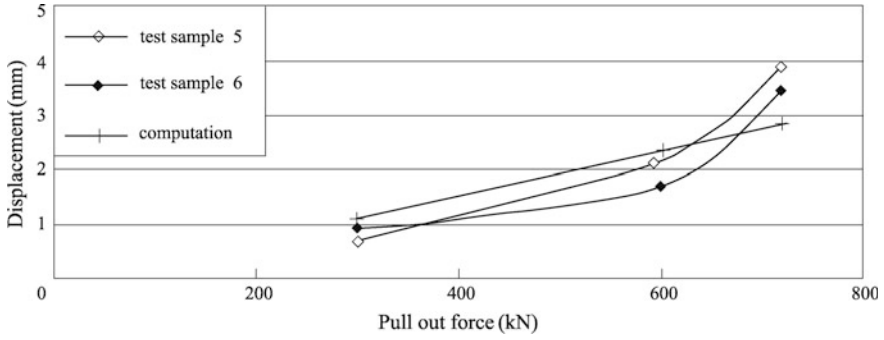

Fig. 15.14 Displacements of the borehole collar against pull out forces (second set)

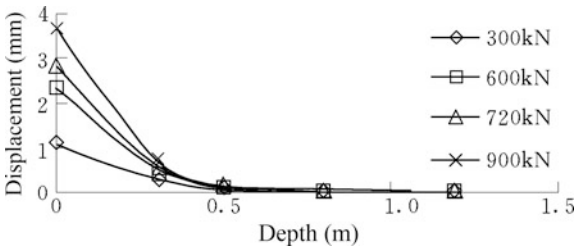

Fig. 15.15 Displacement along the bolt (second set)

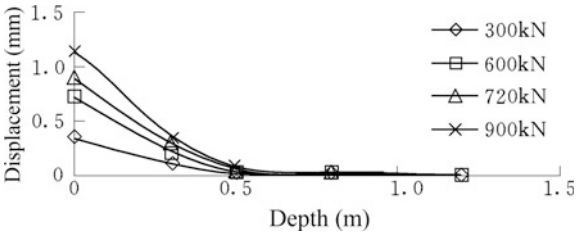

Fig. 15.16 Displacement along the grout (second set)

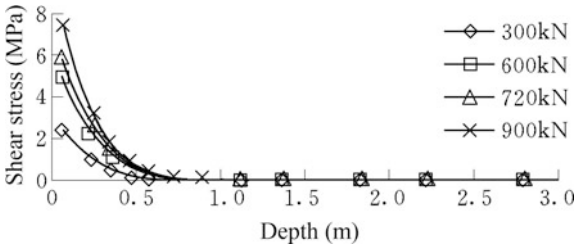

Fig. 15.17 Shear stress along the interface between bolt and grout (second set)

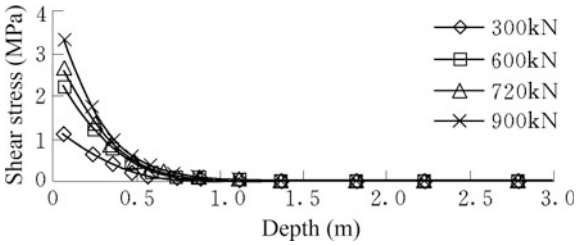

Fig. 15.18 Shear stress along the interface between rock and grout (second set)

15.8.2 Hollow Bolt

The rock sample shown in Fig. 15.7 is analyzed by both the CEM and FEM. In the center of the rock block a hollow bolt is exerted by a pull-out force P at its top extremity. The length of the bolt is 3 m, its interior and exterior diameters are 60 and 70 mm respectively.

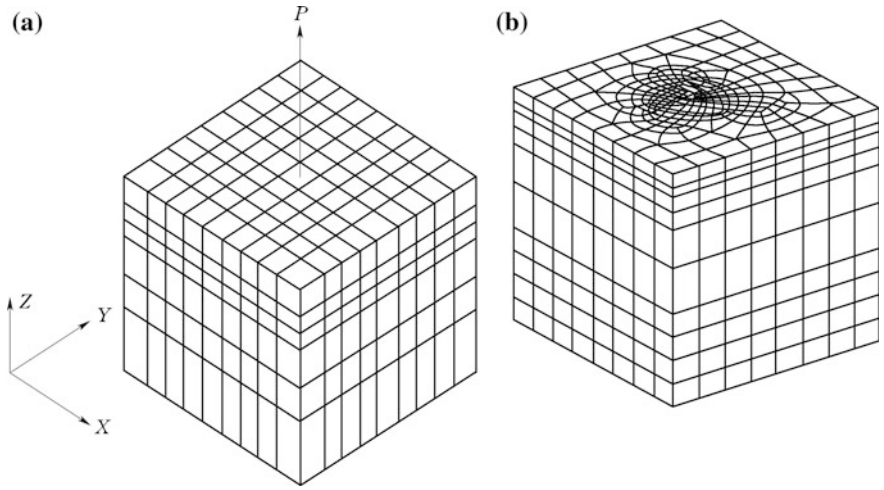

Fig. 15.19 Computation meshes for the sample containing a hollow bolt. **a** CEM (486 elements; 700 nodes); **b** FEM (3274 elements; 3813 nodes)

Table 15.5 Mechanical parameters of the solid materials

Material	E (GPa)	μ	c (MPa)	φ (°)	σ_y (MPa)	σ_u (MPa)	γ_u^{vp}
Steel	200	0.25	–	–	310	500	0.18
Rock	15	0.25	1.1	44	–	–	–

Table 15.6 Mechanical parameters of interface

k_n (MN/m^3)	k_s (MN/m^3)	c (MPa)	φ (°)	ϕ (°)	σ_T (MPa)
10,000	1500	1	44	44	1

In the CE mesh the hollow bolt is embedded in the four top central composite elements (see Fig. 15.19a), whereas in the FE mesh the hollow bolt and rock are all discretized into standard elements meanwhile the rock/bolt interface is discretized into joint elements without thickness (see Fig. 15.19b). Tables 15.5 and 15.6 list the mechanical parameters used in the computation.

Figures 15.20 and 15.21 present the axial and the shear stresses by the CEM and FEM under the pull-out force $P = 200$ kN.

15.8.3 Stranded Wire Cable

(1) CEM versus FEM

Figure 15.22 shows a rock sample with size of 36 m (length) × 5 m (width) × 5 m (height) containing one horizontal anchor cable with 7-stranded wires ($n_w = 7$), each of their diameter is 1 cm. The bonded length is 3 m, and the diameter of the borehole is $D = 10$ cm. A pull-out load $P = 350t$ (3430 kN) exerts on the out-laid anchor head (left end).

Two computation meshes are designed for this sample. The first one (see Fig. 15.23) comprises 36,029 nodes and 35,162 standard finite elements, in which the rock, stranded wires, grout, and interfaces, are all discretized explicitly. The

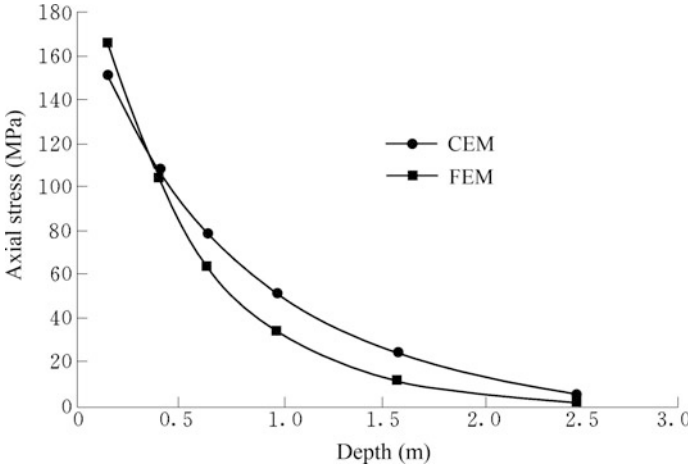

Fig. 15.20 Axial stress along the bolt under the pullout force $P = 200$ kN

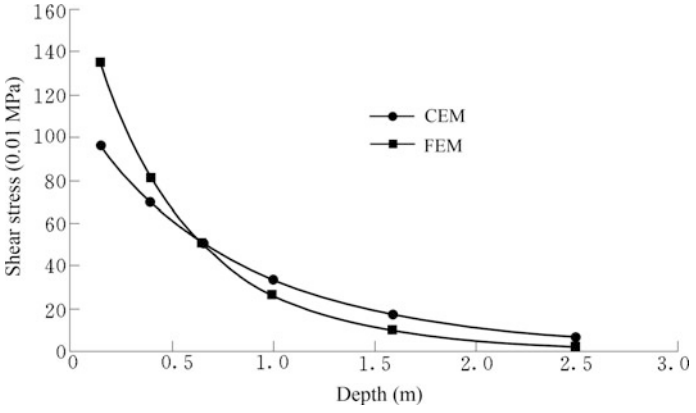

Fig. 15.21 Shear stress along the rock/bolt interface under the pullout force $P = 200$ kN

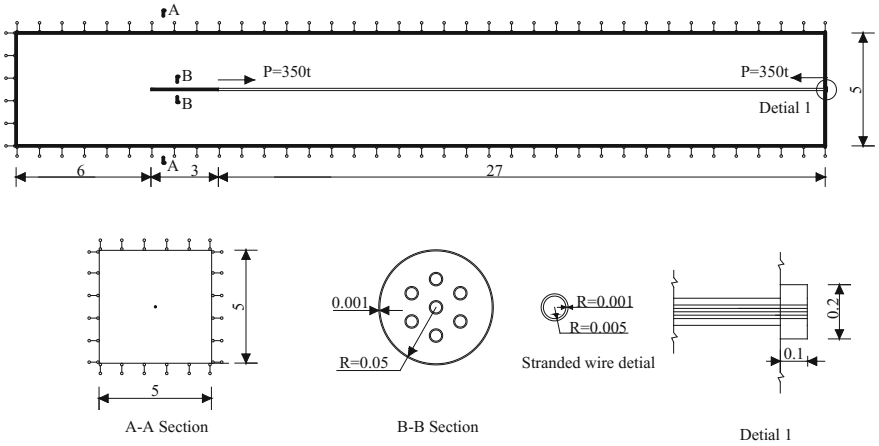

Fig. 15.22 Configuration of the rock sample containing one horizontal anchor cable

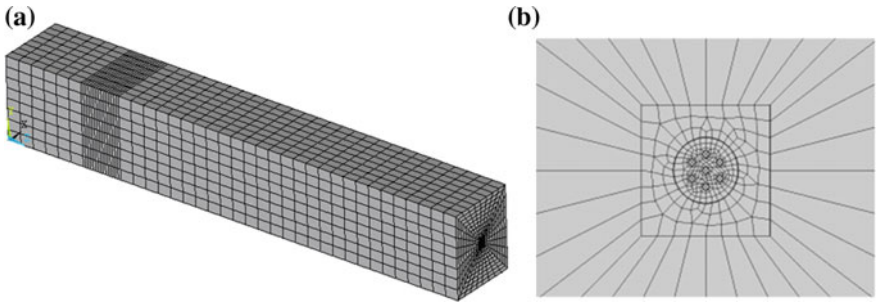

Fig. 15.23 Fine element mesh. **a** Axonometric view; **b** cross sectional view

interfaces are discretized using joint elements without thickness; the intact rock, stranded wires and grout are all discretized using solid (entity) elements. This fine FE mesh performs as a "benchmark" intended to validate the basic algorithm of the composite element method.

The second one (see Fig. 15.24) comprises 4908 nodes and 3971 elements (15 composite elements containing bonded inside anchorage head plus 3956 standard finite elements).

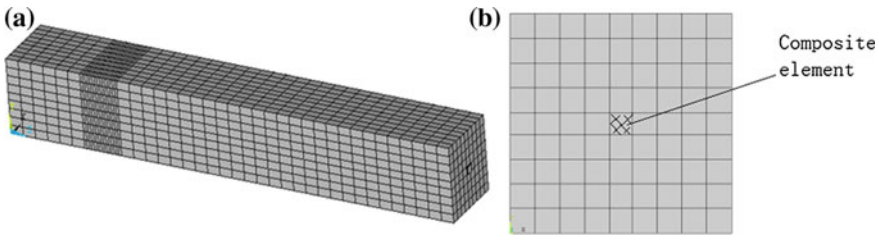

Fig. 15.24 Composite element mesh. **a** Axonometric view; **b** cross sectional view

Table 15.7 Mechanical parameters of materials

Material	Young's modulus E (GPa)	Poisson's ratio μ
Stranded wire	210	0.3
Grout	17.8	0.20
Rock	17.8	0.20

Table 15.8 Mechanical parameters of interfaces

Interface	Normal stiffness k_n (MN/m^3)	Shear stiffness k_s (MN/m^3)
Grout/rock	20,000	10,000
Grout/wire	40,000	20,000

The mechanical parameters used in the computation are listed in Tables 15.7 and 15.8.

The computation results of the stranded wire 7# by the FEM using fine mesh and by the CEM are comparatively drawn in Figs. 15.25, 15.26, 15.27 and 15.28. It is clear that they are very close to each other.

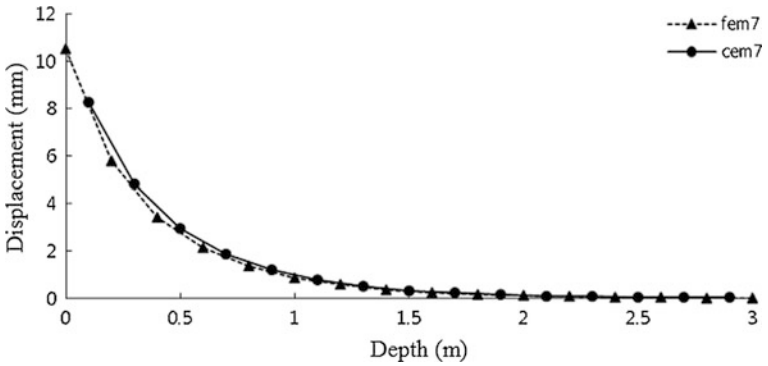

Fig. 15.25 Axial displacement along stranded wire 7#

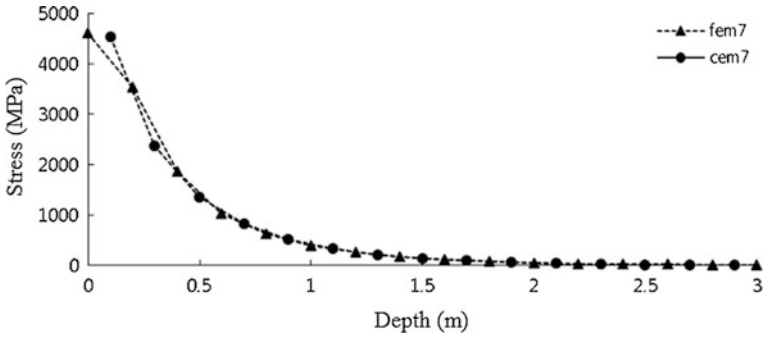

Fig. 15.26 Axial stress along stranded wire 7#

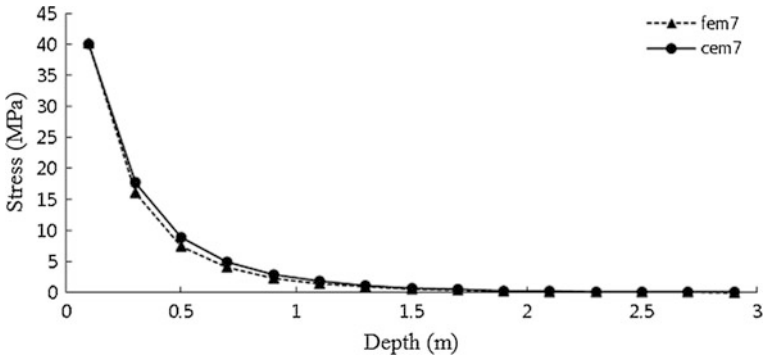

Fig. 15.27 Shear stress along the interface of grout/stranded wire 7#

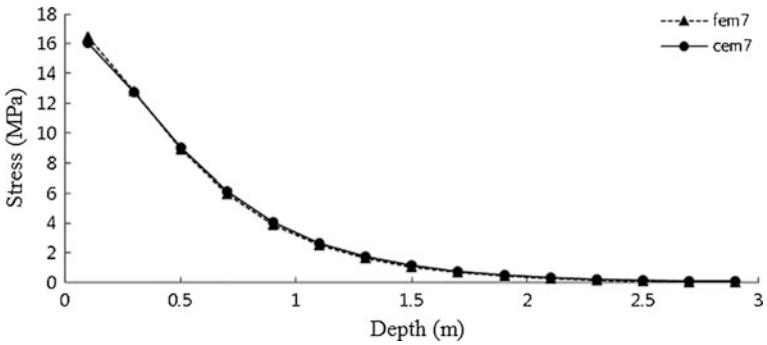

Fig. 15.28 Shear stress along the interface of rock/grout

(2) CEM versus in situ test

The data from the in situ test for a bonded inside anchorage head with 6 stranded wires (see Fig. 15.29, n_w = 6) (Gu et al. 1998) will be used to validate the CEM computation.

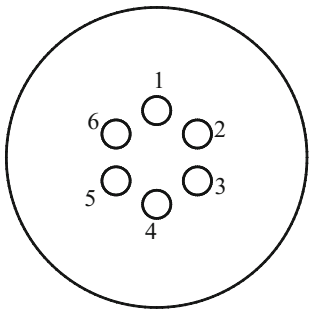

Fig. 15.29 Cross sectional layout of stranded wires

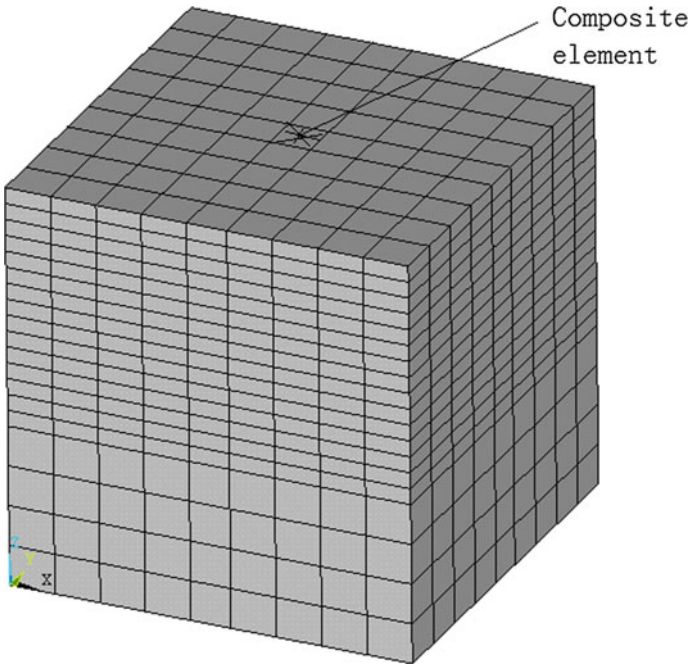

Fig. 15.30 Axonometric view of the CE mesh

A 5 m × 5 m × 5 m cubic rock with the bonded inside anchorage head is discretized in Fig. 15.30. It comprises 2000 nodes and 1539 elements, of which there are 15 composite elements containing bonded inside anchorage head, in a column onset from the center of the top surface. Tables 15.9, 15.10 and 15.11 list the parameters used in the computation.

The distribution of the shear stresses along the interfaces illustrated in Figs. 15.31 and 15.32 is primarily employed for the verification of the CEM

Table 15.9 Geometrical parameters of the bonded inside anchorage head

Stranded wire	Grout	Borehole inclination (°)	Borehole diameter (cm)	Length of bonded inside anchorage head (m)
6Φ5	Cement mortar	0	16	4

Table 15.10 Mechanical parameters of materials

Material	E (GPa)	μ	c (MPa)	φ (°)	σ_T (MPa)
Stranded wire	196	0.25	–	–	1860
Grout	26.3	0.18	2.0	58	2.0
Rock	25	0.20	1.7	59	1.1

Table 15.11 Mechanical parameters of interfaces

Interface	k_n (MN/m^3)	k_s (MN/m^3)	c			φ (°)	ϕ (°)	σ_T (MPa)
			c_i (MPa)	c_r (MPa)	γ_u^{vp} (mm)			
Grout/rock	100,000	35,000	8	0	1	50	50	1.0
Grout/wire	100,000	36,000	25	0	1	58	58	1.0

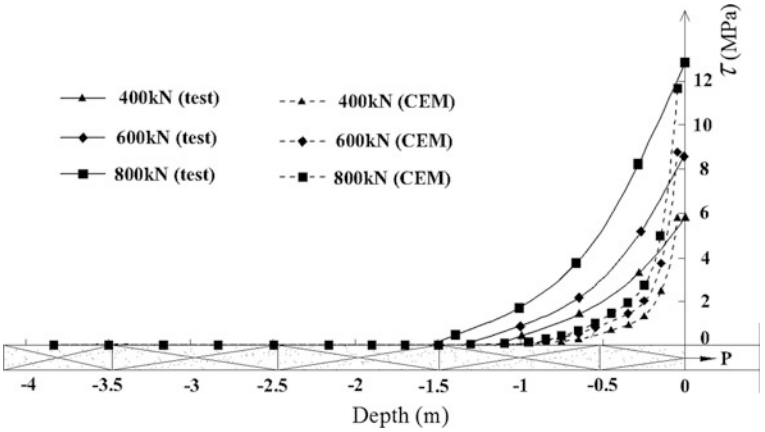

Fig. 15.31 Shear stress along the grout/stranded wire interface

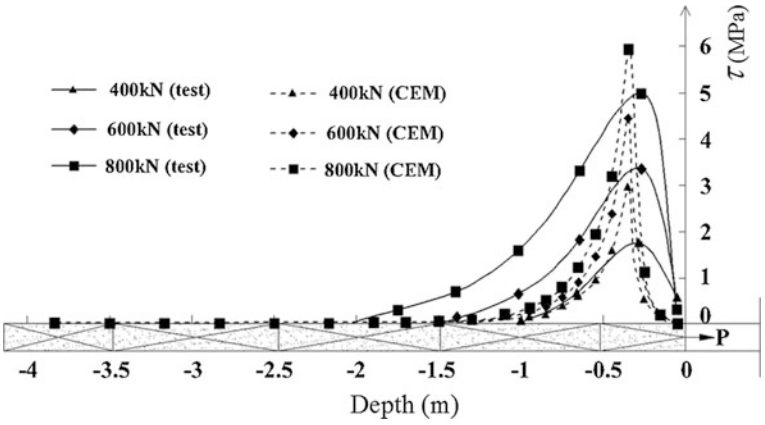

Fig. 15.32 Shear stress along the rock/grout interface

Table 15.12 Parameters used in the computation

Material	Young's modulus E (GPa)	Poisson's ratio μ	Stiffness	
			Normal k_n (GPa)	Shear k_s (GPa)
Rock	25	0.20	–	–
Steel	200	0.25	–	–
Grout/bolt interface	–	–	100	8
Grout/rock interface	–	–	100	5

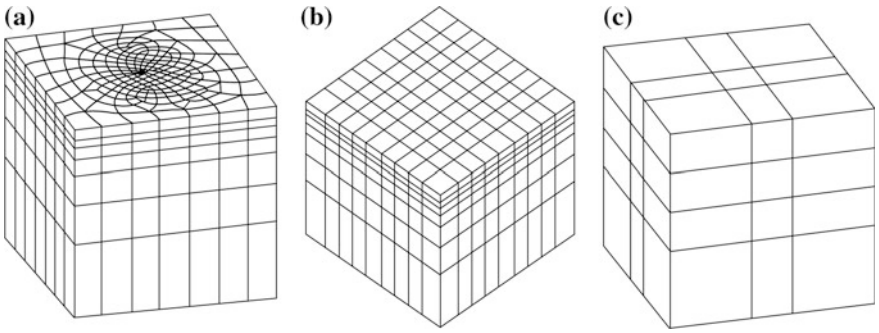

Fig. 15.33 Computation meshes. **a** Standard FEM; **b** standard CEM; **c** hierarchical CEM

algorithm. Generally, the computation results by the CEM agree with the in situ test data well concerning the distribution patterns. However, it is also remarkable that the computed curves always go up or/and down more steeply than the tested ones. The exaggerated high values of the stiffness coefficients and strength parameters (particularly dilatancy angle) of the interfaces, may be probably blamed for these phenomena.

Entailed by the range of pull-out load $P = 400-800$ kN and the parameters stipulated in Tables 15.10 and 15.11, the shear stress distributions on the interfaces exhibit following remarkable features that

– The shear stress of the grout/stranded wire interface keeps maximum at the outermost end and fades away at the innermost end in an approximately exponential pattern, this means that the grout/stranded wire interface maintains elastic bonding. The maximum (peak) shear stress is around 8–10 times of the average one. Since the peak value is kept at the outermost end, it means that the bonding of the grout/stranded wire interface is very well maintained under the pull-out load $P = 400-800$ kN. The pull-out load P is mainly sustained by the outer end portion of the bonded anchorage head within a length of 2 m.

– The shear stress of the rock/grout interface reaches maximum at a depth of 0.4–0.5 m from the outermost end and fades away in both the outer and inner directions, this means that the rock/grout interface around the outer end has entered shear failure state. The maximum (peak) shear stress is around 4–8 times of the average one, and it keeps increase with the increase of the pull-out load P. However, the position where the shear stress reaches maximum value only appears a small shift deeper along with the increase of the pull-out load P (within the tested range). This is probably due to the large dilatancy angle of the interfaces adopted in the computation.

15.8.4 Hierarchical Refinement

(1) Characteristics of the computation

The rock block sample (see Fig. 15.7) with size of 5 m × 5 m × 5 m (length × width × height) has been studied using the p-refinement CEM. The mechanical parameters are postulated in Table 15.12.

Three cases are analyzed using the program CORE3.

1. Standard FEM

Figure 15.33a is the FEM mesh containing 1701 elements and 2064 nodes. The rock, grout and bolt are all discretized with solid elements, the rock/grout and grout/bolt interfaces are all discretized with joint elements without thickness.

2. Standard CEM

Figure 15.33b is the CEM mesh containing 564 standard elements and 800 nodes. From the top, the central six elements in successive column containing bolt segments are defined as the composite elements.

3. Hierarchical CEM

Figure 15.33c is the CEM mesh containing 36 elements and 80 nodes. From the top, the central three elements in successive column containing bolt segments are defined as the hierarchical composite elements. The order of basis functions can be adjusted during the adaptive p-refinement.

(2) Computation results

Figure 15.34 presents the main results extracted from the hierarchical CEM with different polynomial order p using the coarse mesh in Fig. 15.33c. It can be observed that the third order CEM, i.e. $p = 3$, gives rather well distributed stresses and displacements, which are generally in accordance with the theoretical studies of pull-out tests (Farmer 1975): the axial stresses and the displacements of the bolt decline exponentially from the point of loading to its extremity end before a decoupling of the interfaces occurs.

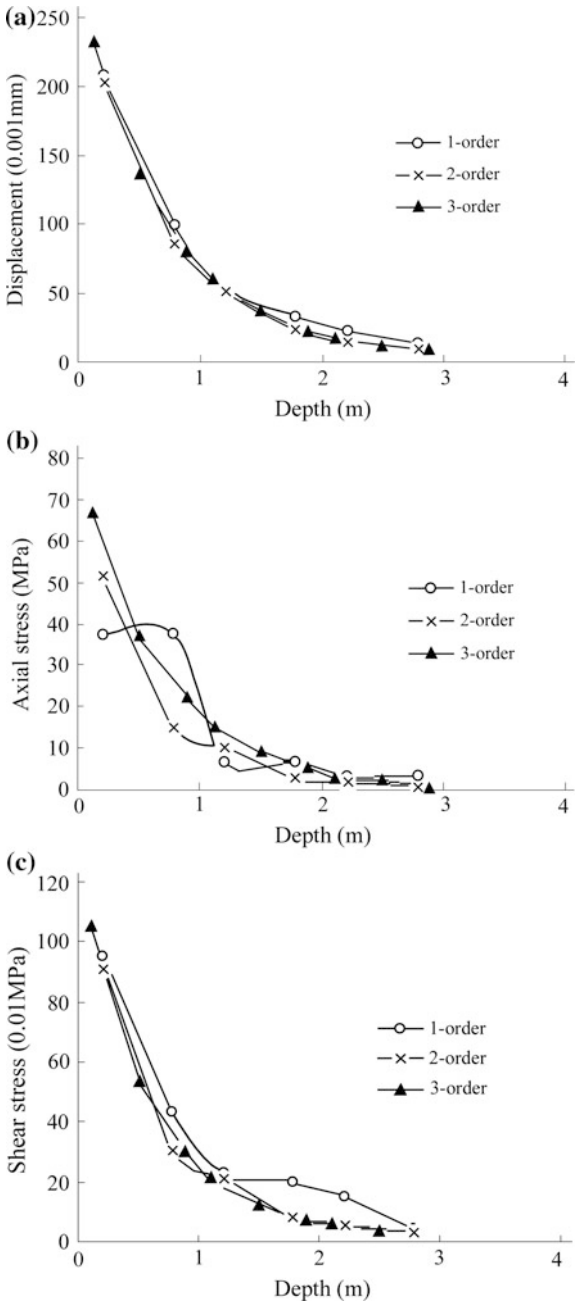

Fig. 15.34 Results by the hierarchical CEM of p-refinement. **a** Displacement of bolt; **b** axial stress of bolt; **c** shear stress of grout/bolt interface

Results obtained with the hierarchical CEM ($p = 3$) are cross-referenced between the standard FEM (see Fig. 15.33a) and CEM (see Fig. 15.33b) in Figs. 15.35, 15.36, 15.37, 15.38 and 15.39. We find that the CEM with the p-refinement technique may provide very good results even on a coarse mesh.

15.8.5 Joint Reinforced by Fully-Grouted Bolt

(1) Characteristics of the computation

The verification work is conducted towards the rock sample of same size in Fig. 15.7, but it contains a horizontal joint in addition to the vertical bolt driven

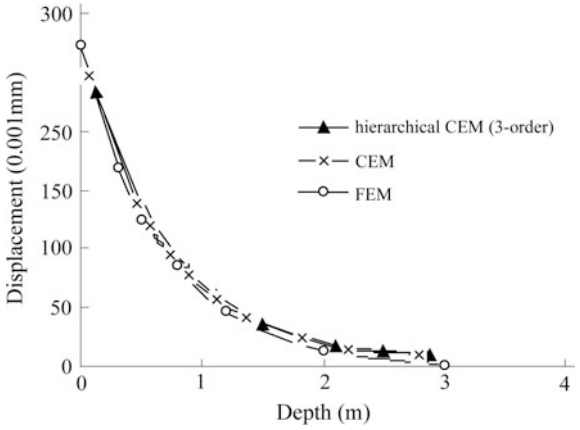

Fig. 15.35 Axial displacement of bolt

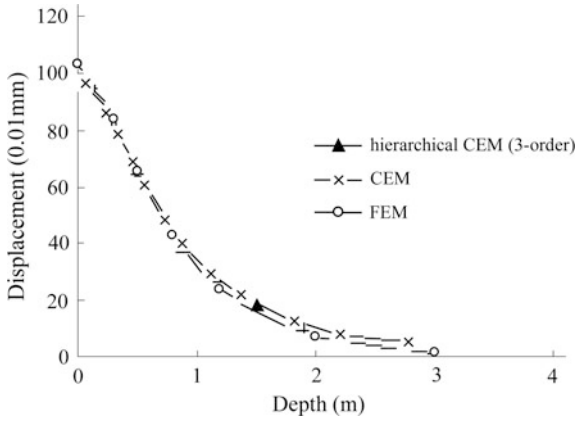

Fig. 15.36 Axial displacement of grout

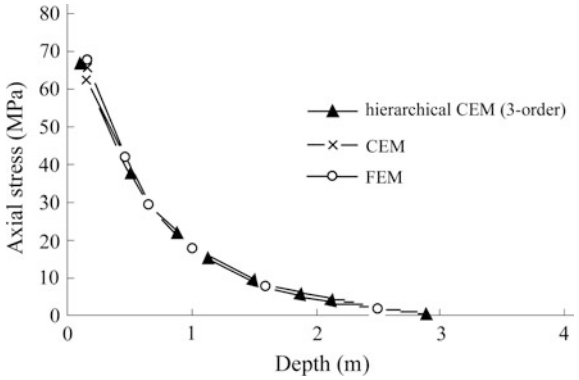

Fig. 15.37 Axial stress of bolt

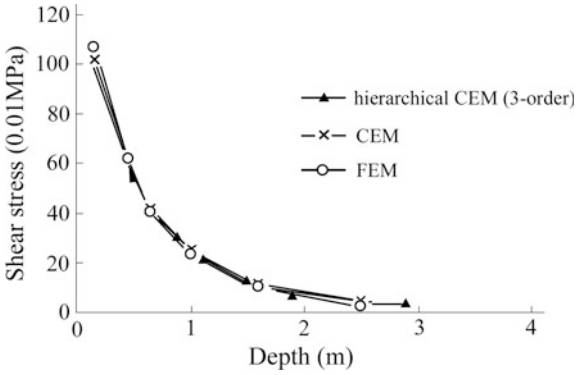

Fig. 15.38 Shear stress along the grout/bolt interface

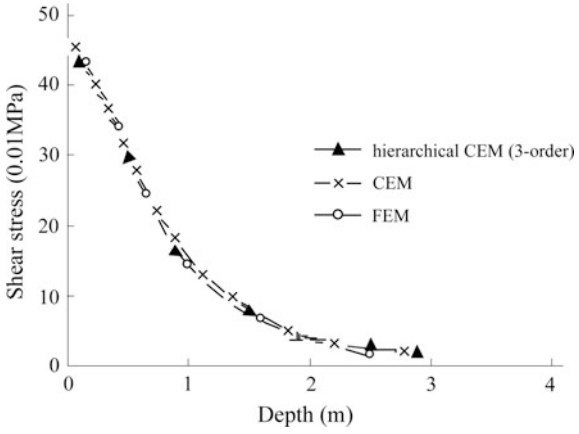

Fig. 15.39 Shear stress along the grout/rock interface

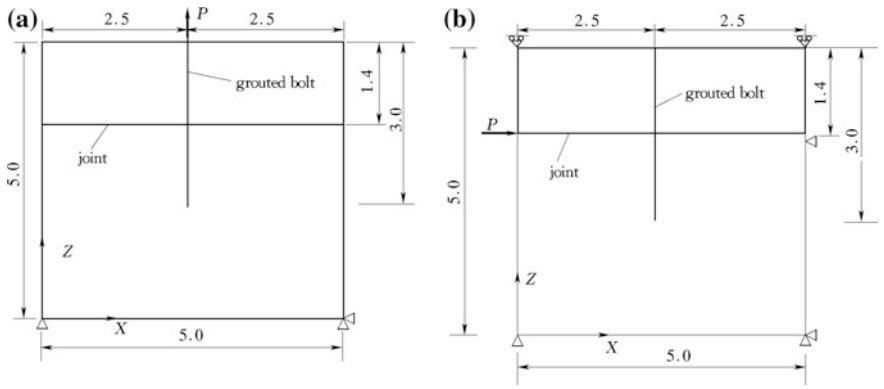

Fig. 15.40 Schematic configuration of the test sample containing a bolt and a joint. **a** Pull-out test; **b** Shear test

Table 15.13 Parameters used in the computation

Material	Young's modulus E (GPa)	Poisson's ratio μ	Stiffness	
			Normal k_n (GPa)	Shear k_s (GPa)
Rock	25	0.20	–	–
Steel	200	0.25	–	–
Joint	–	–	20	1
Grout/bolt interface	–	–	100	8
Grout/rock interface	–	–	100	5

from the top center (see Fig. 15.40). Table 15.13 summarizes the parameters used in the computation.

The computation using the CEM in parallel to the FEM is carried out for the simulation of vertical pull-out test (pull-out force P = 100 kN acting at the top of the bolt, Fig. 15.40a) and the direct shear test (shear force P = 20 MN acting at the upper portion of the block, Fig. 15.40b).

(2) Computation results

Figure 15.41a is the FEM mesh containing 2916 standard elements and 3354 nodes. The rock, grout and bolt are all discretized into solid elements, the interfaces of rock/grout and grout/bolt as well as the joint are all discretized into joint elements without thickness. Figure 15.41b is the CEM mesh containing 567 elements and 800 nodes. From the top, the central six elements in successive column containing bolt segments are defined as composite elements. It is obvious that the FEM mesh is more complicated than the CEM mesh.

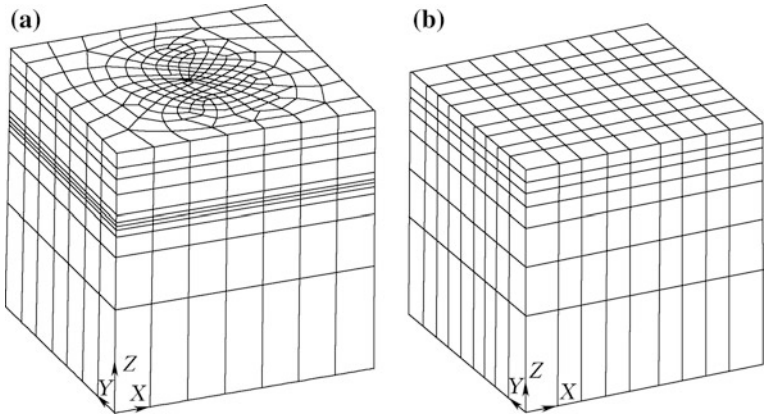

Fig. 15.41 Computation meshes of the test sample containing a bolt and a joint. **a** FEM; **b** BEM

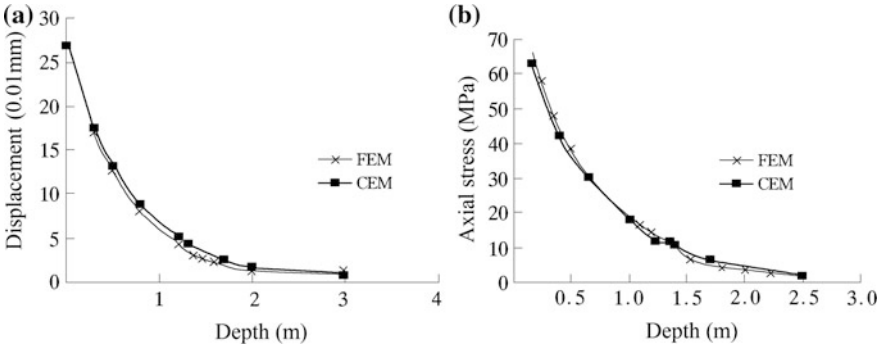

Fig. 15.42 Computation results of the bolt under pull-out action. **a** Displacement; **b** axial stress

Figure 15.42 displays the axial displacements and stresses of the bolt under the pull-out force. It can be observed that the results from the FEM and CEM are very close.

Figure 15.43 shows the axial stresses along the bolt under the shear action. It can be observed that the results by the two methods are very close, too. In Fig. 15.43a, b, the "front axial stress" and "rear axial stress" are corresponding to the axial stresses at the left side and right side of the bolt in the test sample, respectively. The results also validate that under the shear action, the bolt at the joint undergoes very strong bending process, as has been identified in the laboratory tests (Spang and Egger 1990).

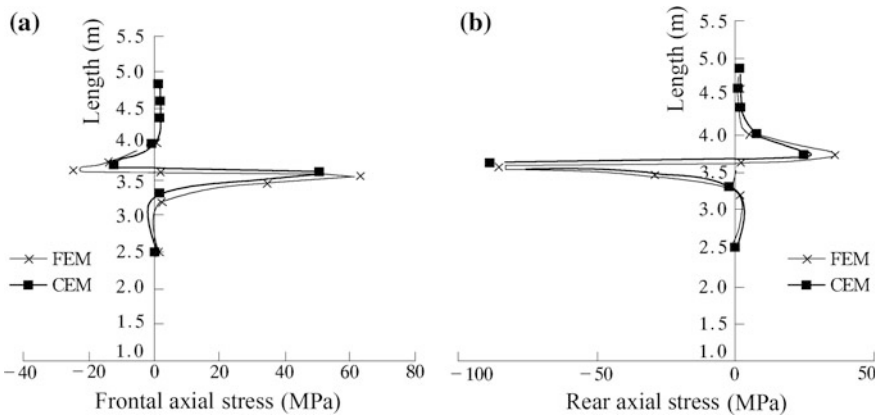

Fig. 15.43 Axial stress along the bolt under the shear action. **a** Frontal axial stress; **b** rear axial stress

15.9 Engineering Applications

15.9.1 Gravity Dam: Baozhusi Project, China

(1) Presentation of the Project

Vide Chap. 9 (Sect. 9.5.1).

(2) Characteristics of the computation

The dam section 17# illustrated in Fig. 10.13 is analyzed in parallel by the FEM and CEM.

The origin of each discontinuity is denoted in Fig. 15.44. It will be used later in the discussion of computation results. Take $O\_F_4\_Down$ and $O\_F_4\_Up$ for example, O means the origin for the distance along the discontinuity, $\_F_4$ denotes the discontinuity, $\_Down$ or $\_Up$ means the lower or upper portion.

These computations may also be validated with the help of the geo-mechanical test illustrated in Chap. 10. The main prototype parameters used in the computation are listed in Tables 10.9 and 10.10. Since the designer of Baozhusi Dam cannot provide the parameter of dilatancy angle, the associated flow rule is adopted in the computation.

The overloading method is executed to explore the failure process and to assess the safety factor of the dam by increasing the water level. The detailed overloading procedures are listed in Table 10.11.

In neglecting the penstock, the dam can be simulated as a two-dimensional structure. Since the program CORE3 is three-dimensional, a dam slice of 1 m thick is cut for the computation. Figure 15.45a is the FE mesh projected at the $X-Z$ plane, it includes 4544 elements and 9420 nodes. Figure 15.45b is the CE mesh

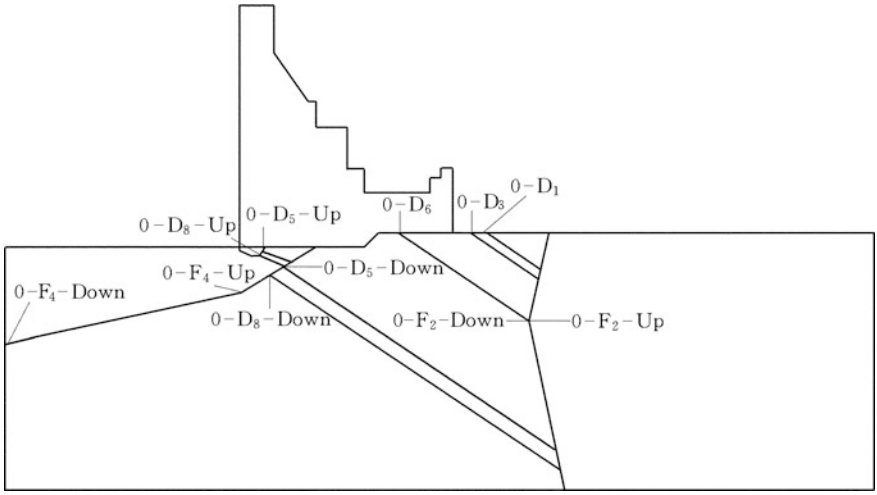

Fig. 15.44 Origins of discontinuities

projected at the $X-Z$ plane, it includes 4897 elements and 10,062 nodes. The displacements along the Y-axis is restrained to ensure the plane strain state.

It can be perceived that the CE mesh is more regular than the FE mesh.

(3) Computation results

The dam is assumed to be built at one concrete placement batch. The load considered after the filling of reservoir is the static hydraulic pressure acting on the upstream dam surface and the reservoir bottom.

1. Displacements

With regard to the working condition under the reservoir impounding, Fig. 15.46 gives the overall displacements in the dam and its foundation meanwhile Table 15.14 gives the displacements at the key points. It can be confirmed that the FEM and the CEM provide rather close results.

Figure 15.47 plots the displacement increments against the overload factor at the gauge points ③ and ④. Again, it may be confirmed that the FEM and the CEM agree with each other well. However, the numerical computation gives larger displacements than the model test. One of the possible explanations is that the deformation modulus used in the model test is a secant modulus including a partial of non-linear deformation, if this deformation modulus is input as elastic modulus in the perfect elasto-viscoplastic computation (FEM and CEM), the stiffness of the structure would be under estimated.

2. Stresses

Under the NSL, Table 15.15 provides the stresses at the Gaussian points close to the dam heel and toe. Figure 15.48 shows the distribution of principal stresses in

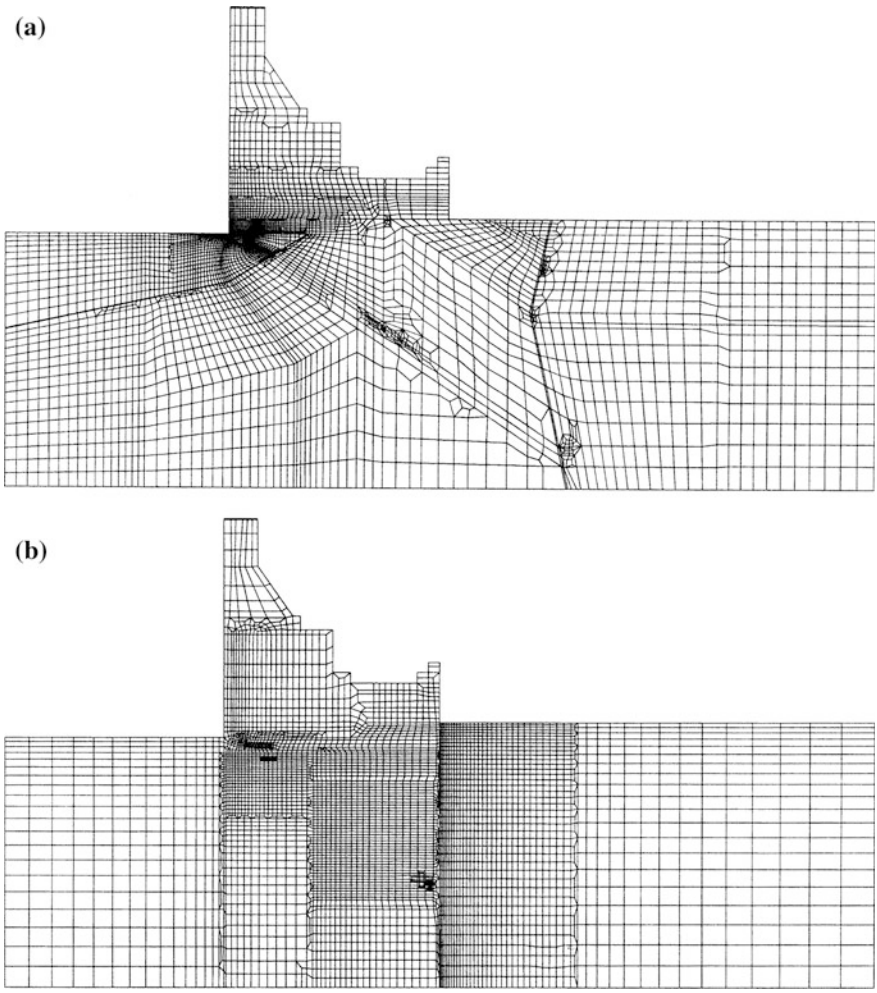

Fig. 15.45 Computation meshes of Baozhusi Gravity Dam. **a** FEM; **b** CEM

the dam. Figures 15.49, 15.50, 15.51 and 15.52 give the distribution of stresses at several typical discontinuities whose origins are defined in Fig. 15.44.

These results validate that

- Generally, the stresses in the dam and foundation by the FEM and the CEM are close to each other. However, the difference in stress is larger than that in displacements, because stresses are more strongly affected by the mesh refinement.
- The stresses at the discontinuities obtained by the FEM and the CEM are close, too. At the intersection points between discontinuities, stresses undergo severe fluctuation due to the complicated deformation patterns around these areas.

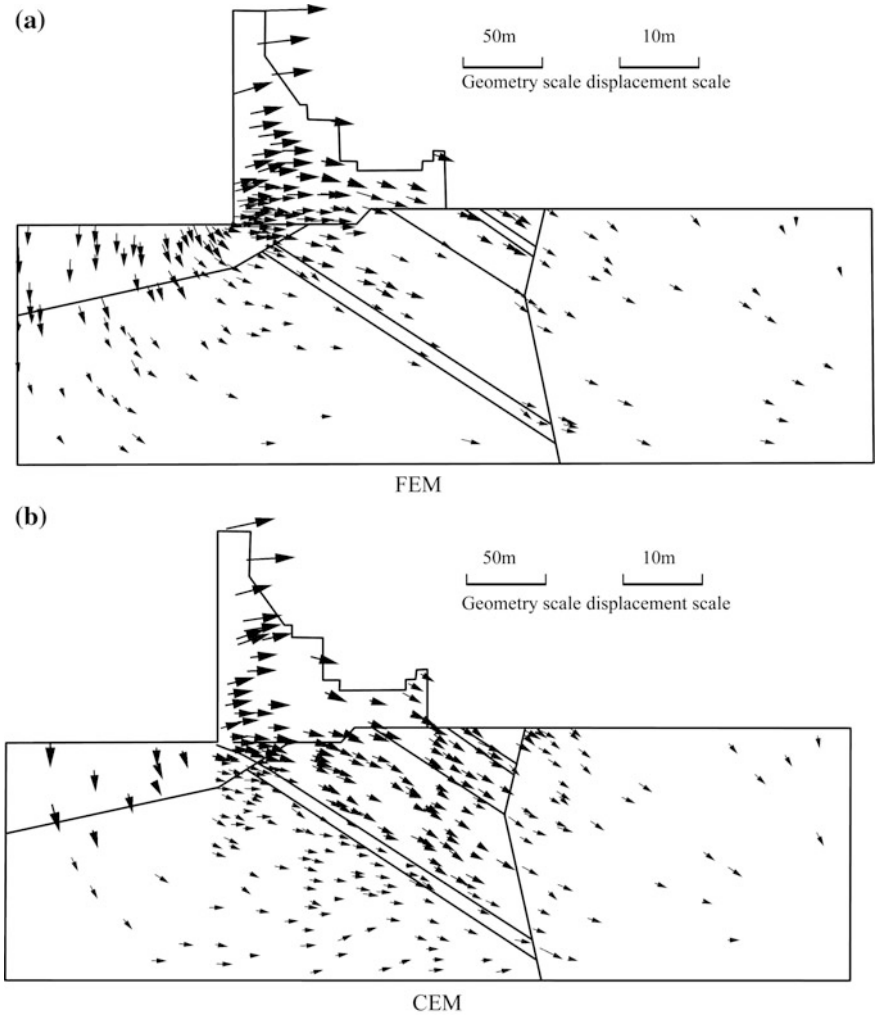

Fig. 15.46 Displacements induced by the reservoir impounding. **a** FEM; **b** CEM

3. Failure mechanism and safety factors

The point (local) safety is defined as the ratio of resistance to the action effect. Given the Drucker-Prager criterion, the point safety factor may be calculated by the formula in Eq. (4.215). In Fig. 15.53 we show the contours of point safety under the actions corresponding to the NSL.

The overloading factor K can be regarded as an index of global (overall) safety. In the laboratory test, the first crack appears at the upstream dam body near the penstock (EL. 558.4 m) when the overloading factor $K = 2.0$. After the overloading

Table 15.14 Displacement at key positions

	Dam crest		Dam toe	
	Horizontal u_X (cm)	Vertical u_Z (cm)	Horizontal u_X (cm)	Vertical u_Z (cm)
FEM	6.77581	1.22786	1.5736	−0.69935
CEM	6.31993	1.12105	1.50264	−0.66740

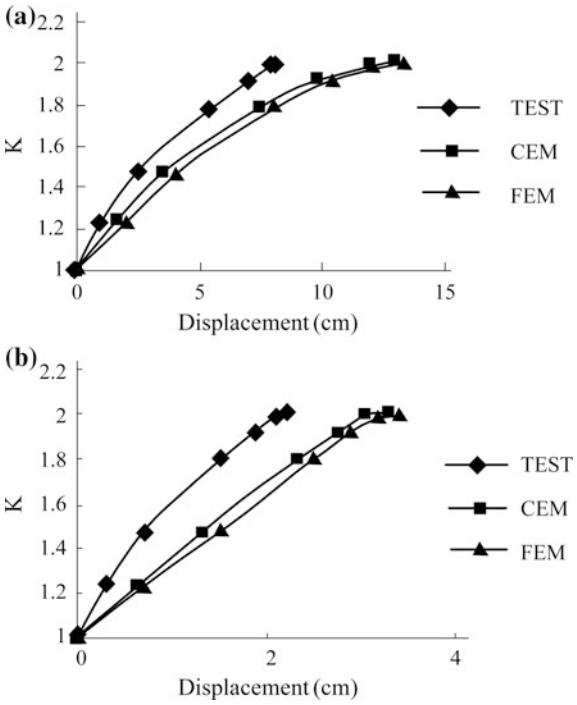

Fig. 15.47 Displacement increments against the overload factor at the gauge points. **a** Gauge points ③; **b** gauge point ④

factor exceeds 2.0, several cracks appear between the penstock and the dam heel. The crack near the penstock propagates fastest and the pressure of upstream jacks cannot be sustained, this means the failure of the dam and the corresponding safety factor can be assessed as $K = 2.0$. From this result it also can be confirmed that the failure mechanism is the crack propagation in the dam, and the stability against the sliding in dam foundation is no longer the major concern attributable to the revision of design.

Figure 15.54 illustrates the tensile yield zones when $K = 2.2$ by the computation. The main crack by the model test is also shown in this figure. In the computation the tensile yield zone near the penstock propagates very fast when the overload factor approaches 2.3, and no convergent results can be obtained. Therefore, the computation gives a safety factor $K = 2.2$ which is higher than that from the model test. This is mainly due to the perfect plasticity (no hardening and

Table 15.15 Principal stresses at the Gaussian points most vicinity to the key positions

	Dam heel			Dam toe		
	σ_1 (MPa)	σ_3 (MPa)	Included angle of σ_1 and X axis (°)	σ_1 (MPa)	σ_3 (MPa)	Included angle of σ_1 and X axis (°)
FEM	−0.736	−3.190	13.54	−0.553	−1.744	33.00
CEM	−0.619	−3.763	10.04	−0.587	−1.699	37.47

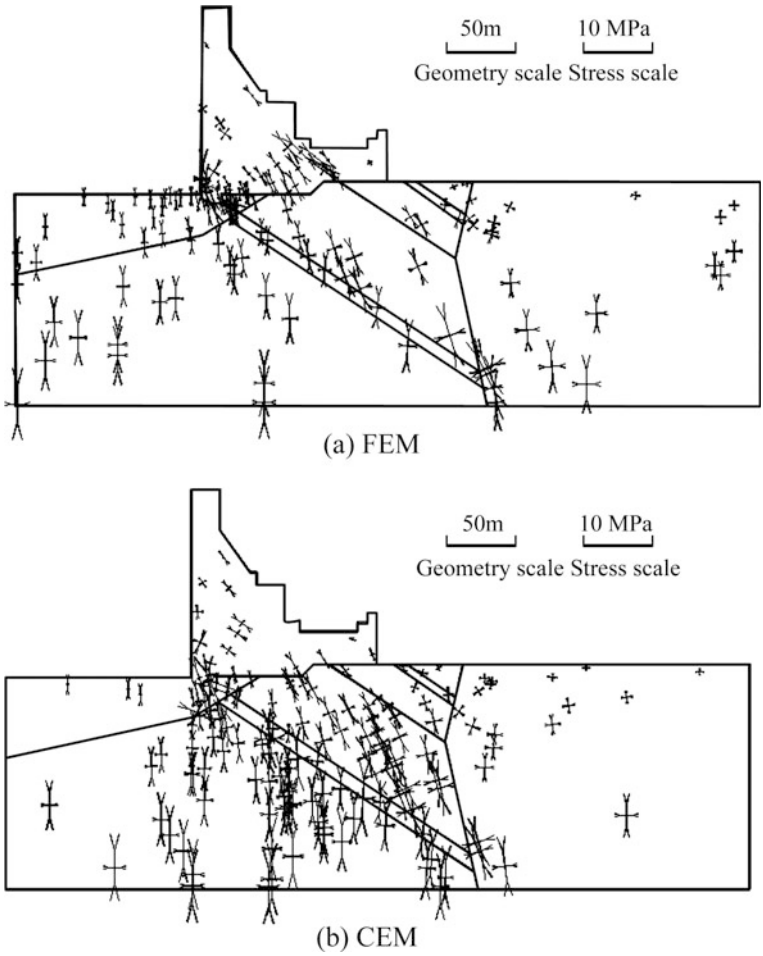

Fig. 15.48 Principal stresses under the NSL. **a** FEM; **b** CEM

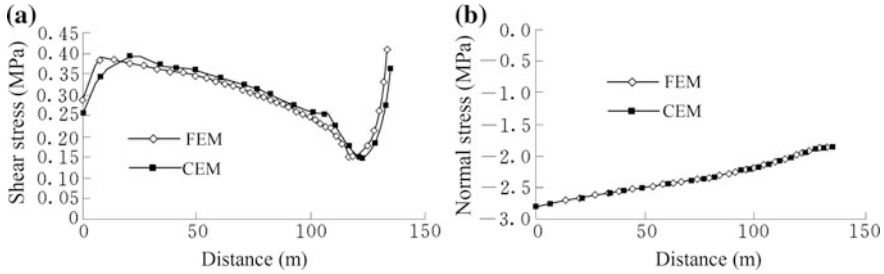

Fig. 15.49 Stress distribution along F_4 (below the EL. 428.98 m) under the NSL. **a** Shear stress; **b** normal stress

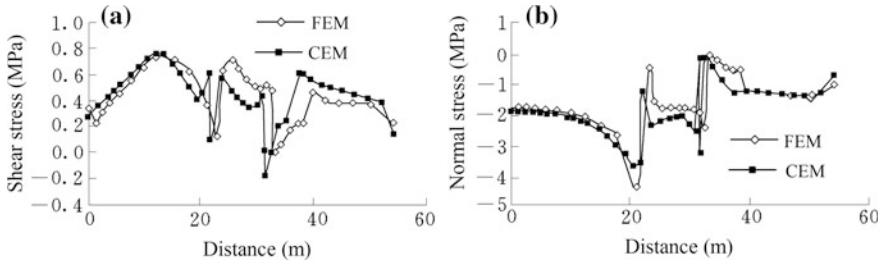

Fig. 15.50 Stress distribution along F_4 (above the EL. 428.98 m) under the NSL. **a** Shear stress; **b** normal stress

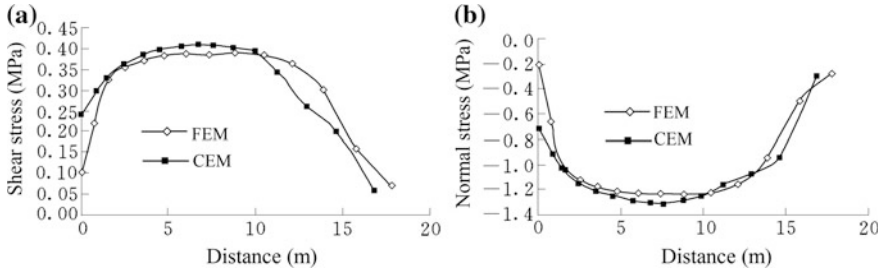

Fig. 15.51 Stress distribution along D_5 (upstream of F_4) under the NSL. **a** Shear stress; **b** normal stress

softening) and associated flow rule adopted in the computation. The other reason for such difference would be the lack of localization trace towards the crack propagation in the computation software hence only wide tensile yield zones may be captured.

The computation also indicates that at the dam heel there is a tensile cracking zone. It will propagate during the overloading procedure, too, but not as fast as that

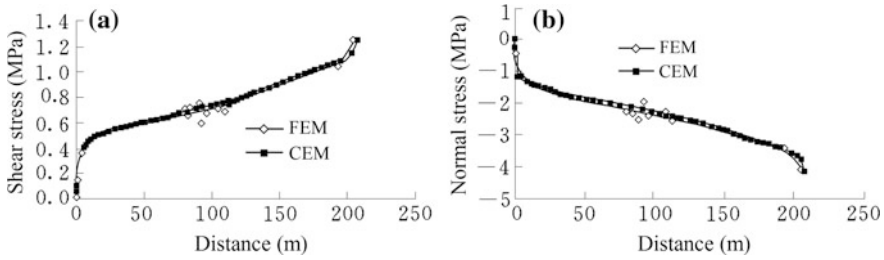

Fig. 15.52 Stress distribution along D_5 (downstream of F_4) under the NSL. **a** Shear stress; **b** normal stress

in the dam body. Therefore it is not the major mechanism dominating the failure of the dam.

15.9.2 Underground Cavern: Saizhu Project, China

(1) Presentation of the project

Saizhu Hydropower Project is the cascade 2 project on the Ximahe River, Yunnan Province, China. It possesses the first double-curved arch dam of full-sectional RCC built on high earthquake risk zone, a headrace (diversion) tunnel of 4.82 km long for the power generation on the right bank, and an underground power station.

The underground power station (see Fig. 15.55) is accommodated in the thick layer limestone with the stratum strike N30°–60°W, dip direction NE and dip angle 10°–20°. The well developed fracture are grouped into set I with attitude N40°–50° W, SW∠70°–80°; set II with attitude N50°–60°E, NW∠50°–70°.

The size of the underground power house is 74.4 m × 17.4 m × 37.6 m (length width × height), the size of the transmission cavern is 58.42 m × 13.6 m × 25.55 m (length × width × height). The overburden rock above the power house is 120–160 m.

(2) Characteristics of the computation

The excavation of the power house is divided into 6 benches illustrated in Fig. 15.56. The excavation and reinforcement procedures are detailed in Table 15.16.

*Φ*25 steel bars are employed for the systematic reinforcement of the caverns, with the space of 1.5 m × 1.5 m and the length of 9 and 6 m alternatively. The bolts reinforcing the crane girder to the rock wall are *Φ*36 steel bars, with a length of 9 m (see Fig. 15.57).

In the design of the rock bolt crane girder (see Fig. 15.58), it is very important to understand the working states with respect to the contact interfaces of girder/rock

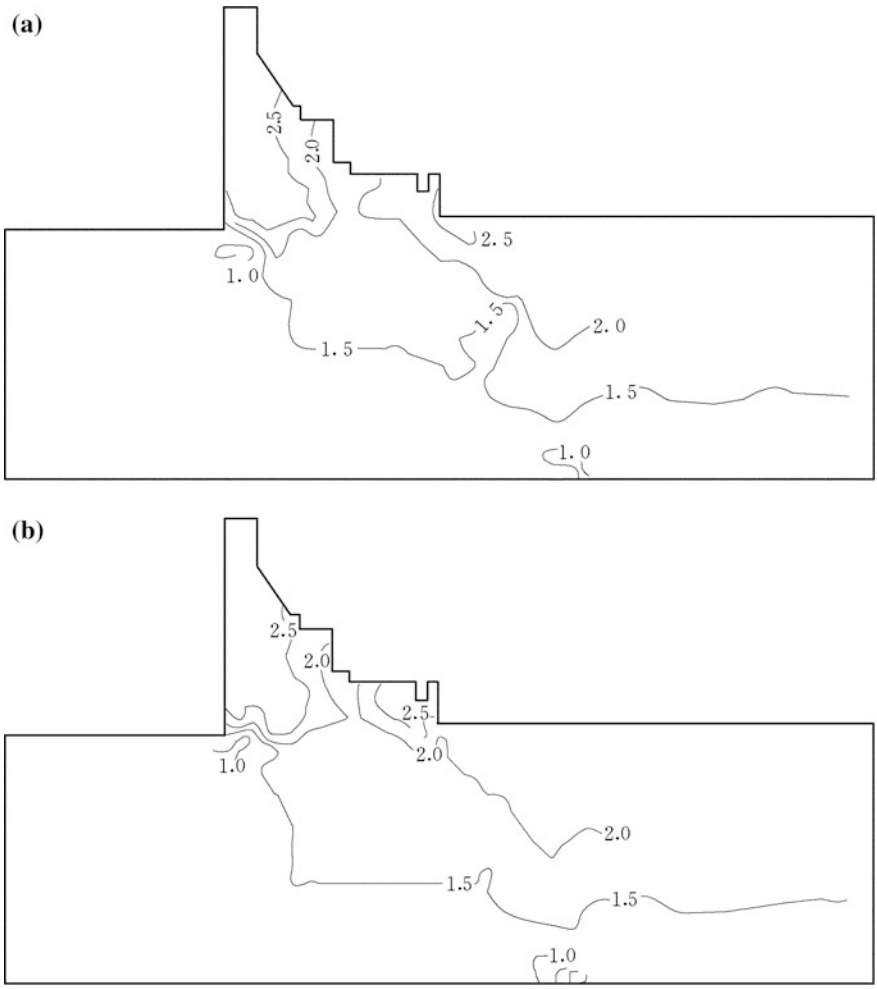

Fig. 15.53 Contours of point safety factors K_p under the NSL. **a** FEM; **b** CEM

and bolt/rock, particularly the bolt's performance at the girder/rock contact interface (Cao et al. 1996). To fulfill these tasks a credible computation appropriately considering excavation procedure and bolting mechanism is demanded.

To help the understanding of the computation results, the local coordinate systems of the supporting bolts and girder/rock contact interface of the crane girder (left wall) are defined in Fig. 15.59, where LUO, LMO, LDO are the origins of the local coordinates of the three girder bolts; LO is the origin of the local coordinate of the girder/rock contact interface.

The in situ geo-stress field is back analyzed under the gravity action only.

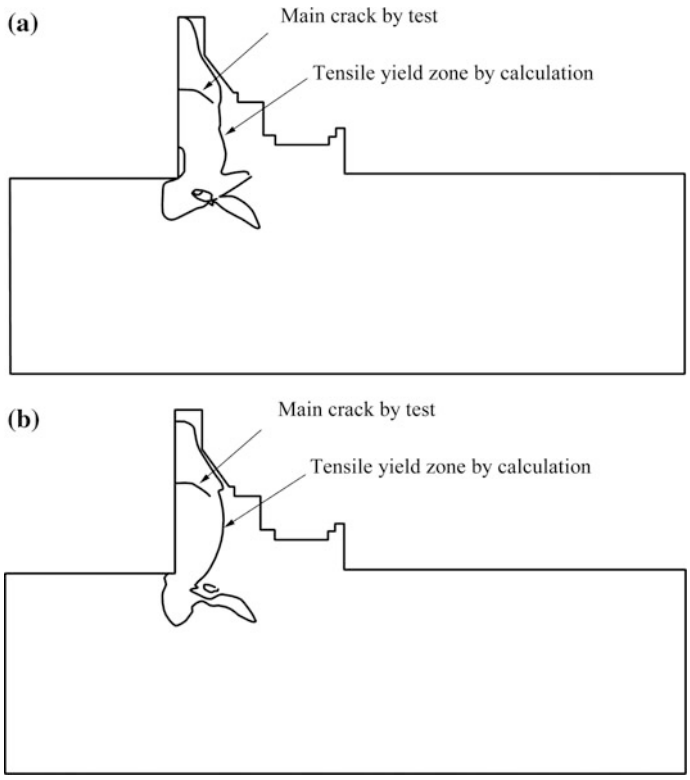

Fig. 15.54 Tensile yield zones by the computation and main crack by the model test (K = 2.2). **a** FEM; **b** CEM

The crane girder is installed after the completion of the third bench excavation. The linear load density exerting at the crane girder is: P(vertical) = 1.0 MPa/m, H (horizontal) = 0.03 MPa/m (see Fig. 15.59).

A slice of 3 m thick along the axis of the caverns is discretized in the study. The systematic bolts around the caverns are approached by the "equivalent model" which takes into account of the influences of the joints (or contact face) and rock bolts but overlooks their exact position (vide Chap. 6). Whereas, the supporting rock bolts which reinforce the crane girder to the rock wall and the girder/rock contact interfaces are simulated by two explicit approaches: the FEM that refines the mesh around the girder area and makes use of special elements (joint element and bar element); plus the CEM that takes no care of the bolts and contact interfaces in the mesh generation, because they are embedded in the composite elements.

The FE mesh and CE mesh generated for the computation are shown in Figs. 15.60 and 15.61, respectively. It is obvious that the FEM mesh is more complicated than the CEM mesh, because the former is restrained strongly by the existence of bolts and contact interface.

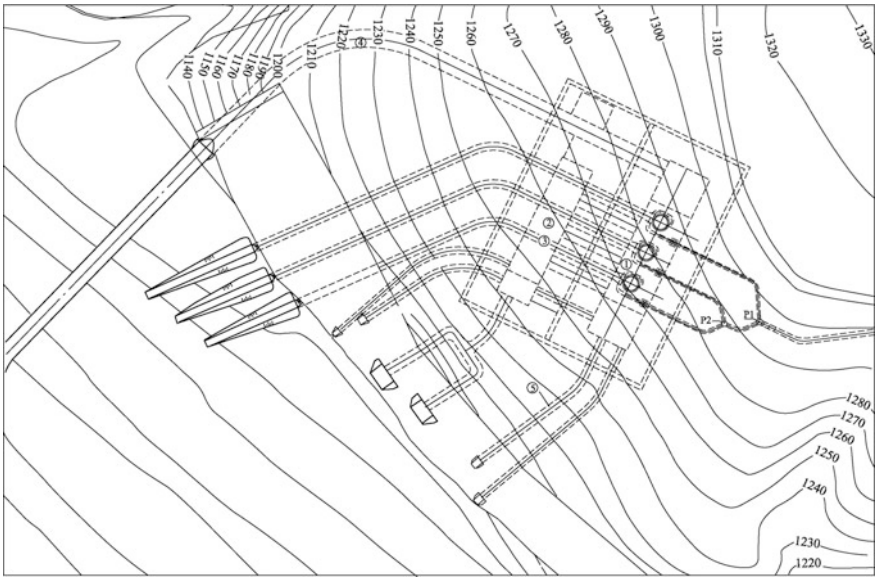

Fig. 15.55 Plan of the underground power station: Saizhu Project, China. ①—main machine hall; ②—main transformer chamber; ③—tailrace tunnel; ④—access tunnel; ⑤—ventilating tunnel

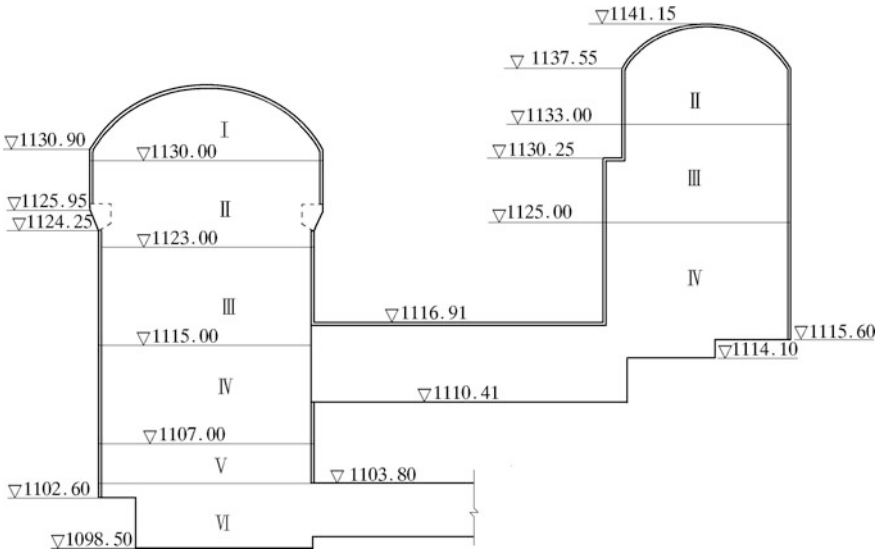

Fig. 15.56 Schematic drawing of the excavation benches

Table 15.16 Excavation and reinforcement procedures of the powerhouse

Excavation step	Power house		Transmission cavern	
	Excavation elevation (m)	Reinforcement elevation (m)	Excavation elevation (m)	Reinforcement elevation (m)
I	1136.10–1130.00	–	–	–
II	1130.00–1123.00	1136.10–1130.00	1141.15–1133.00	–
III	1123.00–1115.00	1130.00–1123.00	1133.00–1125.00	1141.15–1133.00
IV	Installation of girder	1123.00–1115.00	–	1133.00–1125.00
V	1115.00–1107.00	–	1125.00–1115.60	–
VI	1107.00–1103.80	1115.00–1107.00	–	1125.00–1115.60
	–	1107.00–1103.80	–	–

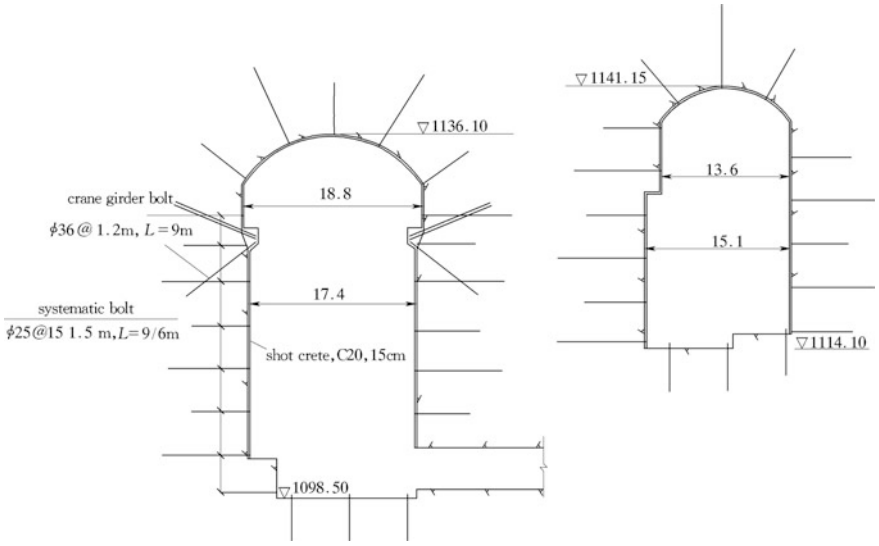

Fig. 15.57 Reinforcement layout of the typical cross section

Fig. 15.58 Details showing the rock bolt crane girder (left wall): Saizhu Project, China

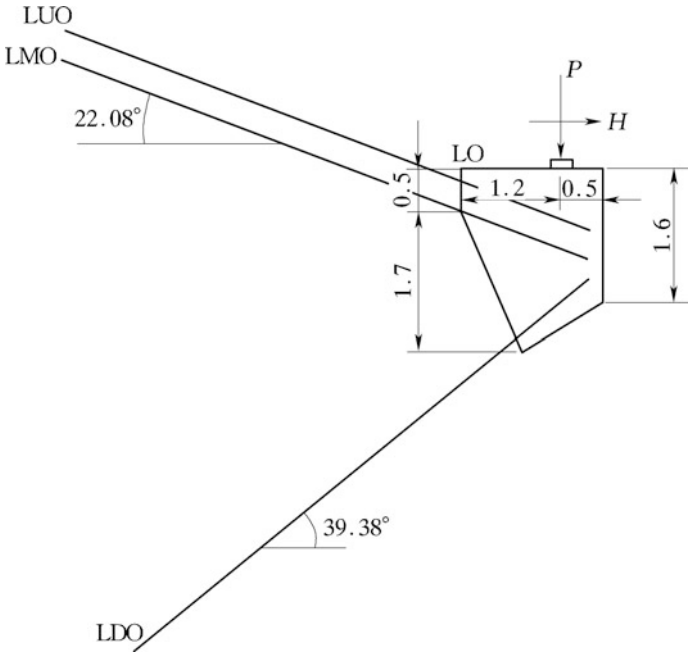

Fig. 15.59 Configuration of the rock bolt crane girder (left wall)

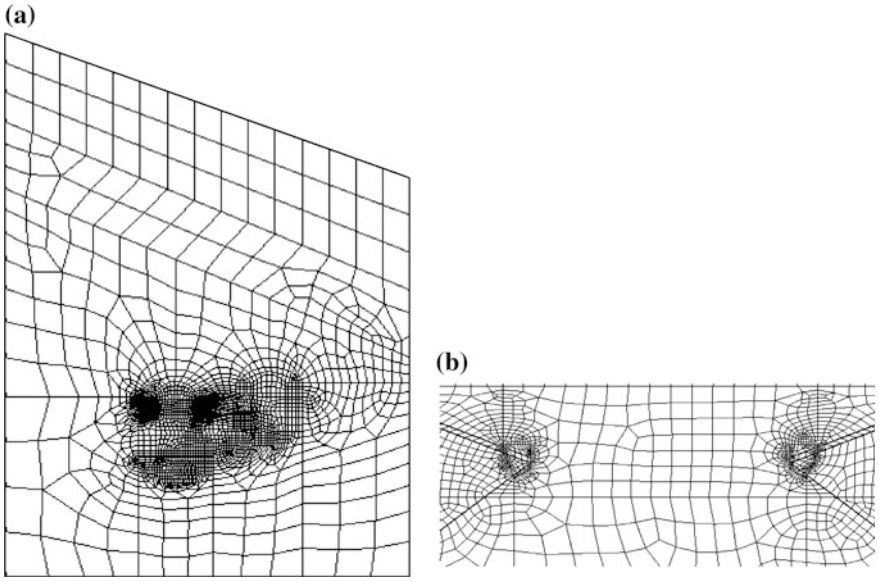

Fig. 15.60 Finite element mesh (17,335 elements; 20,916 nodes). **a** Overall view of the cavern; **b** detailed view around the rock bolt crane girder

The parameters used in the computation are listed in Tables 15.17 and 15.18.

(3) Computation results

1. Displacements

Figures 15.62 and 15.63 show the accumulated displacements in the rock mass and girders after the completion of the caverns.

The FEM and CEM provide nearly identical results. The maximum displacement occurs at the top of the power house, which are 7.02 mm (by FEM) and 6.96 mm (by CEM) respectively. The displacements of the crane girder are 3.00–3.58 mm.

2. Stresses

Figures 15.64 and 15.65 show the stresses in the girders. Generally, the stresses obtained by the FEM and CEM exhibit similar distribution patterns.

The stresses in the surrounding rock mass are ranged within −15 to 1.14 MPa and in the girder are ranged within −15.9 to 4.27 MPa.

Typical axial stresses of the rock bolts (left crane girder only) during the operation period are plotted in Figs. 15.66, 15.67 and 15.68, we can find that they undergo a sudden mounting in the vicinity of the contact interface between rock and crane girder.

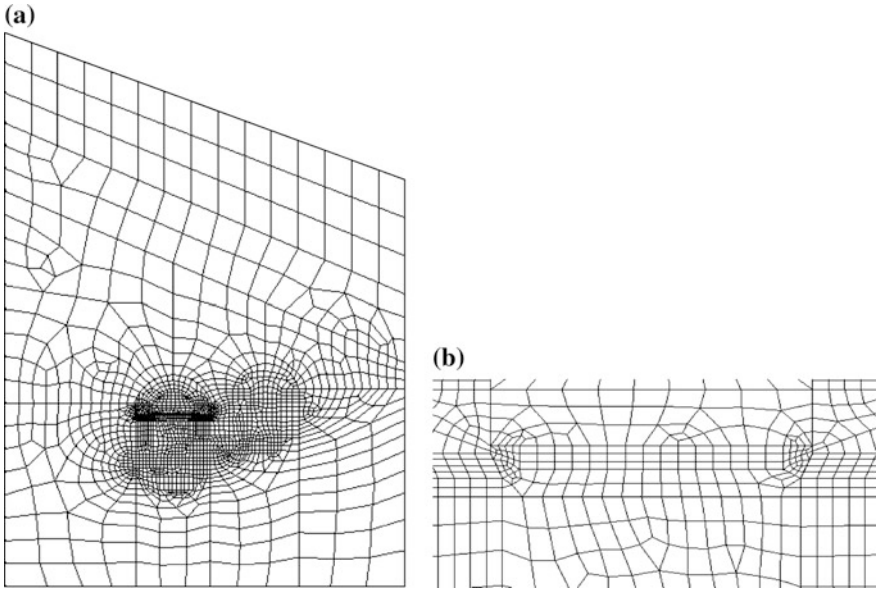

Fig. 15.61 Composite element mesh (5910 elements; 8000 nodes). **a** Overall view of the cavern; **b** detailed view around the rock bolt crane girder

Table 15.17 Parameters used in the computation (rock)

Material	Volumetric weight γ (kN/m^3)	Young's modulus E (GPa)	Poisson's ratio μ	Stiffness	
				Normal k_n (GPa)	Shear k_s (GPa)
Slightly weathering rock	27.0	7	0.28	–	–
Fresh rock		10	0.27	–	–
Girder/rock interface	–	–	–	20	1
Grout/bolt interface	–	–	–	100	8
Rock/grout interface	–	–	–	100	5

Table 15.18 Parameters used in the computation (concrete and bolt)

Material	Young's modulus E(GPa)	Poisson's ratio μ	Volumetric weight γ (kN/m^3)
Concrete	30	0.167	25
Steel	200	0.30	78.5

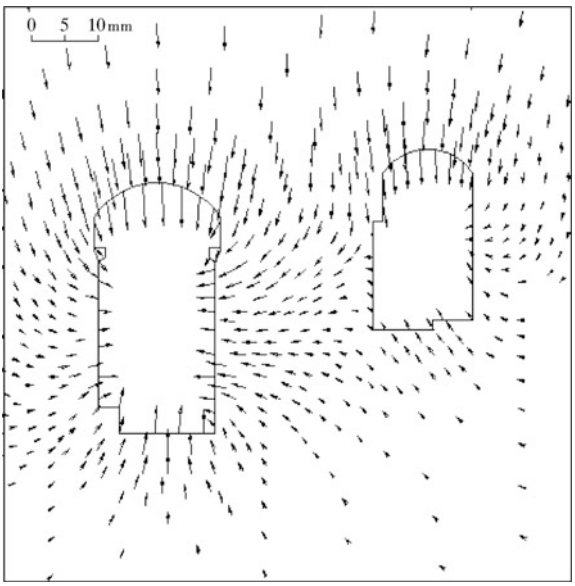

Fig. 15.62 Accumulated displacements of the rock mass and girders (FEM)

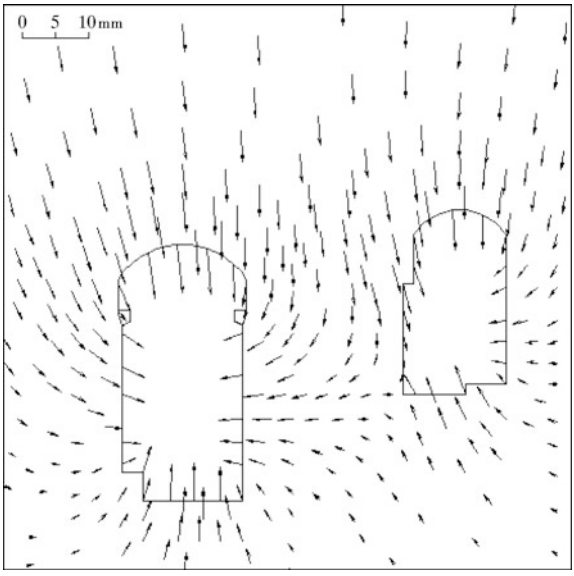

Fig. 15.63 Accumulated displacements of the rock mass and girders (CEM)

Typical shear stresses on the rock/bolt contact interfaces by the CEM (left crane girder only) are plotted in Figs. 15.69, 15.70 and 15.71 which are indispensable in the assessment of the pull-out resistance. These contact shear stresses cannot be provided by the conventional FEM with bar elements.

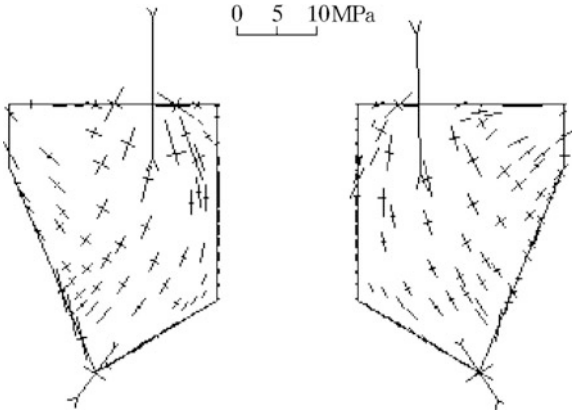

Fig. 15.64 Stresses in girders (FEM)

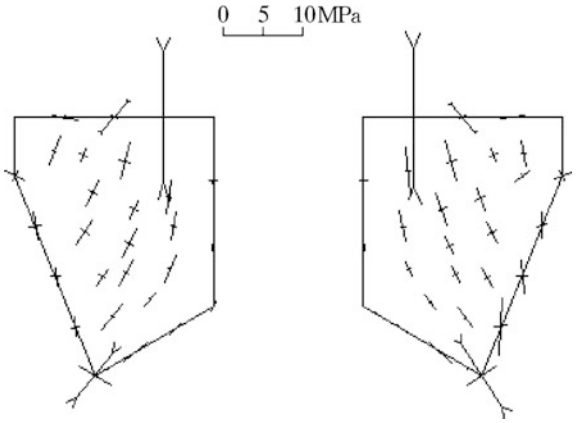

Fig. 15.65 Stresses in girders (CEM)

Typical stresses on the girder/rock contact interfaces are plotted in Figs. 15.72 and 15.73 (left crane girder).

(4) Computation efficiency

The computer used in this study is: P4 CPU, 3.0 GHz, 512MDDR memory. The freedom and the computation time by the FEM and CEM are comparatively presented in Table 15.19, by which it can be concluded that

– For different excavation steps, the difference in the computation time of FEM is attributable to the difference in the DOF;

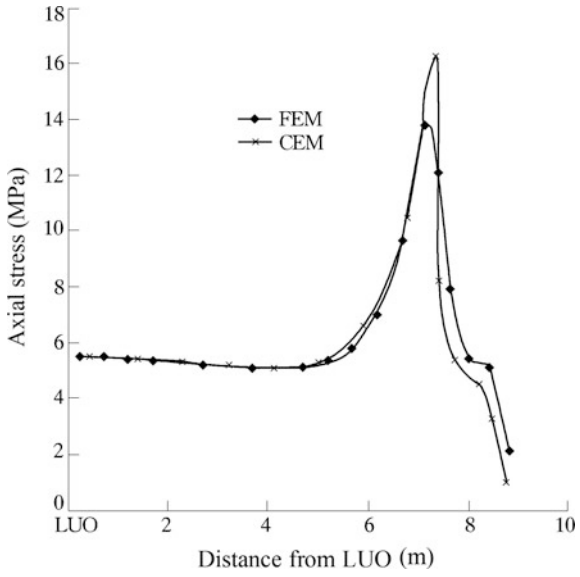

Fig. 15.66 Axial stresses of bolts during the operation period (first row, left crane girder)

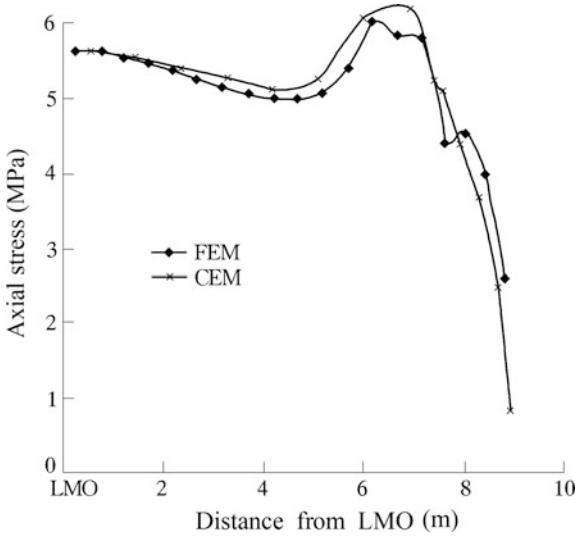

Fig. 15.67 Axial stresses of bolts during the operation period (second row, left crane girder)

- Before the installation of the crane girder, the difference in the computation time of the CEM is attributable to the difference in the DOF, too. However, the installation of the crane girder introduces composite elements containing bolts or/and contact interfaces, which results in a remarkable increase of computation time.
- The CEM actually uses extra calculation overhead to replace a part of pre-process works in the FEM.

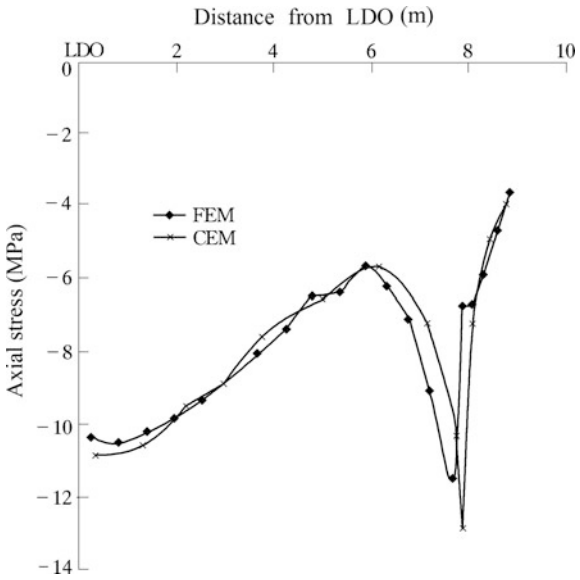

Fig. 15.68 Axial stresses of bolts during the operation period (third row, left crane girder)

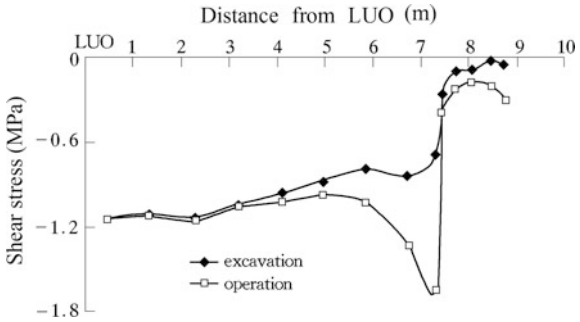

Fig. 15.69 Shear stresses on the rock/bolt interface (first row, left crane girder, CEM only)

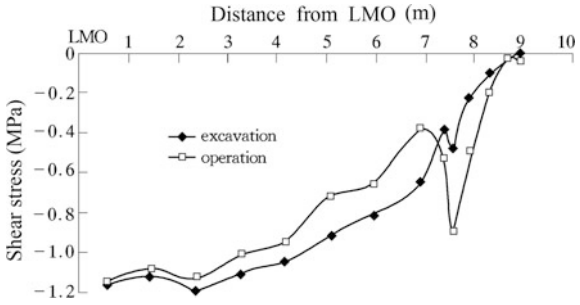

Fig. 15.70 Shear stresses on the rock/bolt interface (second row, left crane girder, CEM only)

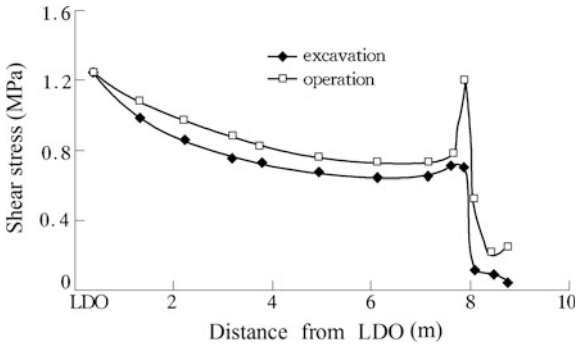

Fig. 15.71 Shear stresses on the rock/bolt interface (third row, left crane girder, CEM only)

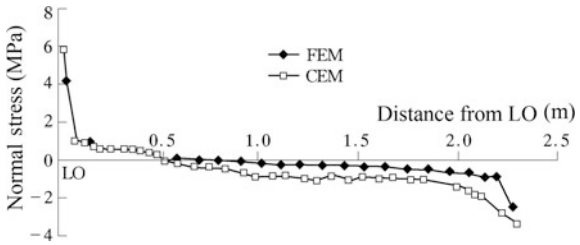

Fig. 15.72 Normal stresses on the girder/rock interface (left crane girder)

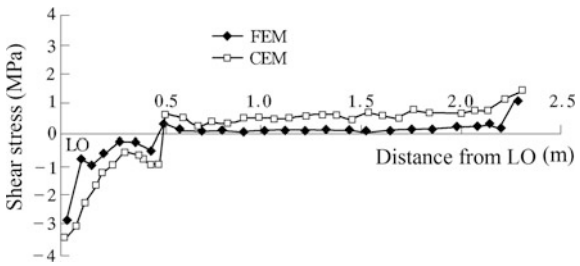

Fig. 15.73 Shear stresses on the girder/rock interface (left crane girder)

Table 15.19 Computation time and degree of freedom (DOF)

		Excavation step I	Excavation step II	Excavation step III	Installation of girder	Excavation step IV	Excavation step V	Excavation step VI	Service
DOF	FEM	55,016	45,112	43,336	47,928	45,912	45,240	44,344	44,344
	CEM	19,768	17,508	16,628	20,032	19,182	18,982	18,712	18,712
Computation time(s)	FEM	99.84	80.25	79.73	90.37	93.31	90.89	89.76	82.20
	CEM	24.17	23.39	22.09	147.17	180.33	162.69	157.44	153.78

References

Barley AD. Properties of anchor grout in a confined state. In: Littlejohn GS, editor. Ground anchorages and anchored structures—proceedings of the international conference on Institution of Civil Engineers (ICE). London: Thomas Telford; 1997a. p. 13–22.

Barley AD. The single bore multiple anchor system. In: Littlejohn GS, editor. Ground anchorages and anchored structures—proceedings of the international conference on Institution of Civil Engineers (ICE). London: Thomas Telford; 1997b. p. 67–75.

Beer G. An isoparametric joint/interface element for finite element analysis. Int J Num Methods Eng. 1985;21(4):585–600.

Benmokrane B, Chekired M, Xu H. Monitoring behavior of grouted anchors using vibrating-wire gauges. J Geotech Eng ASCE. 1995a;121(6):466–75.

Benmokrane B, Chennouf A, Mitri HS. Laboratory evaluation of cement based grouts and grouted rock anchors. Int J Rock Mech Min Sci Geomech Abstr. 1995b;32(7):633–42.

Briaud JL, Powers WF, Weatherby DE. Should grouted anchors have short tendon bond length? J Geotech Geoenviron Eng ASCE. 1998;124(2):110–9.

Cao PF, Liu Y, Peng SZ, Chen MZ. 2D analysis for rock-bolt crane girder in underground power house of Dongfeng plant and its verification. Chin J Rock Mech Eng. 1996;15(4):360–70 (in Chinese).

Chen SH, Egger P. Three dimensional elasto-viscoplastic finite element analysis of reinforced rock masses and its application. Int J Rock Mech Min Sci Geomech Abstr. 1999;23(1):61–78.

Chen SH, Shahrour I. Composite element method for the bolted discontinuous rock masses and its application. Int J Rock Mech Min Sci. 2008;45(3):384–96.

Chen SH, Egger P, Migliazza R, Giani GP. Three dimensional composite element modelling of hollow bolt in rock masses. In: Dinis de Gama C, Ribeiro e Sousa L, editors. Proceedings of the ISRM international symposium on rock engineering mount regions—Eurock'2002. Rotterdam: AA Balkema; 2002. p. 753–9.

Chen SH, He ZG, Egger P. Study of hollow friction bolts in rock by a three dimensional composite element method. In: Merwe JN, editor. Proceedings of the 10th ISRM congress—technology roadmap for rock mechanics. Johannesburg: ISRM; 2003a. p. 203–6.

Chen SH, Qiang S, Chen SF. Study on the three-dimensional composite element model of bolted rock masses. Chin J Rock Mech Eng. 2003b;22(1):1–8 (in Chinese).

Chen SH, Qiang S, Chen SF, Egger P. Composite element model of the fully grouted rock bolt. Rock Mech Rock Eng. 2004;37(3):193–212.

Chen SH, Qin WX, Xu Q. Composite element method and application of trace simulation for strain localization bands. Chin J Rock Mech Eng. 2007;26(6):1116–22 (in Chinese).

Chen SH, Qiang S, Shahrour I, Egger P. Composite element analysis of gravity dam on a complicated rock foundation. Int J Geomech ASCE. 2008;8(5):275–84.

Chen SH, Zhang X, Shahrour I. Composite element model for the bonded anchorage head of stranded wire cable in tension. Int J Numer Anal Methods Geomech. 2015;39(12):1352–68.

Desai CS, Zaman MM, Lightner JG, Siriwardane HJ. Thin-layer element for interfaces and joints. Int J Numer Anal Methods Geomech. 1984;8(1):19–43.

Desai CS, Muqtadir A, Scheele F. Interaction analysis of anchor-soil systems. J Geotech Eng ASCE. 1986;112(5):537–53.

Farmer IW. Stress distribution along a resin grouted rock anchor. Int J Rock Mech Min Sci Geomech Abstr. 1975;12(11):347–51.

Fuller PG, Cox RHT. Mechanics of load transfer from steel tendons to cement based grout. In: Proceedings of the 5th Australian conference on the mechanics of structures and materials. Melbourne: 1975. p. 189–203.

Ghaboussi J, Wilson EL, Isenberg J. Finite element for rock joint interfaces. J Soil Mech Found Div ASCE. 1973;99(SM10):833–48.

Goodman RE, Taylor RL, Brekke TL. A model for the mechanics of jointed rock. J Soil Mech Found Div ASCE. 1968;94(SM3):637–59.

Goris JM, Conway JP. Grouted flexible tendons and scaling investigation. In: Proceedings of the 13th world mining congress. Rotterdam: AA Balkema; 1987. p. 783–92.
Griffiths DV. Numerical modeling of interfaces using conventional finite element. In: Kawamoto T, Ichikawa Y, editors. Proceedings of the 5th international conference on numerical methods in geomechanics. Rotterdam : AA Balkema; 1985. p. 837–44.
Gu JC, Ming ZQ, Shen J. Study on the in situ test of stress characteristic along bolts of pre-stressed anchor cables. Chin J Rock Mech Eng. 1998;17(Suppl.):788–92 (in Chinese).
Hassani FP, Mitri HS, Khan UH, Rajaie H. Experimental and numerical studies of cable bolt support systems. In: Proceedings of the international symposium on rock supports. Rotterdam: AA Balkema; 1992. p. 411–7.
Hassani FP, Rajaie H. An investigation into the optimization of a shotcrete cable bolt support systems. In: Proceedings of the 14th CMMI conference. Edinburgh: Institute of Mining and Metallurgy; 1990. p. 119–29.
He ZG, Chen SH. Study on the bolted rock mass by hierarchical composite element method. Chin J Rock Mech Eng. 2006;25(8):1698–704 (in Chinese).
Hermann LR. Finite element analysis of contact problems. J Soil Mech Found Div ASCE. 1978;104(EM5):1043–57.
Hyett AJ, Bawden WF, Reichert RD. The effect of rock mass confinement on the bond strength of fully grouted cable bolts. Int J Rock Mech Min Sci Geomech Abstr. 1992;29(5):503–24.
Hyett AJ, Bawden WF, Macsporran GR, Moosavi M. A constitutive law for bond failure of fully grouted cable bolts using a modified Hoek cell. Int J Rock Mech Min Sci Geomech Abstr. 1995;32(1):12–36.
Jarrel DJ, Haberfield CM. Tendon/Grout interface performance in grouted anchors. In: Littlejohn GS, editor. Proceedings of the conference on ground anchorages and anchored structures. London : Thomas Telford; 1997. p. 3–14.
Kaiser PK, Yazici S, Nose J. Effect of stress change on the bond strength of fully grouted cables. Int J Rock Mech Min Sci Geomech Abstr. 1992;29(3):293–306.
Kim NK. Performance of tension and compression anchors in weathered soil. J Geotech Geoenviron Eng ASCE. 2003;129(12):1138–50.
Kim NK, Park JS, Kim SK. Numerical simulation of ground anchors. Comput Geotech. 2007; 34(6):498–507.
Mahtab M, Goodman RE. Three dimensional analysis of joint rock slope. In: Proceedings of the 2nd international ISRM congress (vol. 3). Beograd: Privredni Pregled; 1970. p. 353–60.
Mitri HS, Rajaie H. Stress analysis of rock mass with cable support—a finite element approach. In: Proceedings of the conference on stresses in underground structures. Ontario: CANMET; 1990. p. 110–9.
Mitri HS, Edrissi R, Henning J. Finite element modelling of cable-bolted slopes in hard rock underground mines. In: Proceedings of the SME annual meeting. Alburquerque: SME; 1993. p. 94–116.
Rong G, Zhu HC, Yang SL. Field test of rock bolt in the Three Gorges Project ship lock slope. Rock Soil Mech. 2001;22(2):171–5 (in Chinese).
Spang K, Egger P. Action of fully-grouted bolts in jointed rock and factors of influence. Rock Mech Rock Eng. 1990;23(2):201–29.
Stheeman WH. A practical solution to cable bolting problems at the Tsumeb Mine. CIM Bull. 1982;75(838):65–77.
Stillborg B. Experimental investigation of steel cable for rock reinforcement in hard rock. Ph.D. thesis, Lulea University of Technology, Sweden; 1984.
Stillborg B. Professional users handbook for rock bolting. 2nd edition. Clausthal-Zellerfeld: Trans Tech Publications Ltd.; 1994.
Weerasinghe RB, Littlejohn GS. Load transfer and failure of anchorages in weak mudstone. In: Littlejohn GS, editor. Proceeding of the conference on ground anchorages and anchored structures. London: Thomas Telford; 1997. p. 34–44.
Woods RI, Barkhordari K. The influence of bond stress distribution on ground anchor design. In: Littlejohn GS, editor. Proceedings of the conference on ground anchorages and anchored structures. London: Thomas Telford; 1997. p. 55–65.

Chapter 16
Seepage Analysis Using the Composite Element Method

Abstract In this chapter the research interest is directed to the simulation of seepage field, which takes into account of both the discontinuities and drainage holes explicitly located within composite elements. It is an algorithm competent to the structural problems formulated in Chap. 15. As the first step, the "air element" model filled with a virtual matter of much higher permeability is proposed to eliminate the strong dependence of computation mesh on the deployment of drainage holes. Then the presence of discontinuities and drainage holes transfers a number of finite elements into composite elements. The p-refinement is further implemented to enlarge the shape function space, in this way the complex flow pattern in a composite element may be handled appropriately, and the restraints on the mesh generation can be further relaxed. This chapter is closed with a number of validation examples and two successful engineering application cases related to sluice foundation and dam foundation.

16.1 General

Seepage flow is a very important factor influencing the deformation and stability of hydraulic structures. To control its hazardous effects, seepage control devices such as the drainage curtain and grouting curtain, are conventionally installed. The seepage analysis is one of the cornerstones for the design of seepage control system.

In Chap. 15 the composite element method (CEM) has been proposed and implemented towards the simulation of bolts and discontinuities in strain/stress computations. In this chapter a competent algorithm will be elaborated for the seepage field, which takes into account of both the discontinuities and drainage holes explicitly located within composite elements (Chen et al. 2004; Xu and Chen 2005; Chen and Feng 2006; Chen et al. 2010a, b).

S.-H. Chen, *Computational Geomechanics and Hydraulic Structures*,
Springer Tracts in Civil Engineering, https://doi.org/10.1007/978-981-10-8135-4_16

16.2 Air Element for Drainage Holes

The "air element" was initiated for the purpose to eliminate the strong dependence of computation mesh on the deployment of drainage holes, by the simplifications in handling the boundary conditions on the hole wall as well as the judgment/treatment of the hole intersected with the phreatic surface (Hu and Chen 2003).

16.2.1 Concept

Generally, it is supposed that a drainage hole is hollow and filled with air or water. In its explicit modeling, the wall of the drainage hole is taken as a boundary with conditions defined in Eqs. (4.150)–(4.153), and the space within the hole itself will not be included in the variational function defined in Eq. (4.154). This treatment, termed as "exact method", is precise but, as can be anticipated, will impose very strong restraint on the finite element mesh generation, and an system equation with large DOF will be produced. Furthermore, when the phreatic surface is intersected with drainage holes, the iteration procedure using "residual flow method" will demand a huge computation overhead, too.

From the practical point of view, we may imagine that an empty hole makes no essential difference to the hole filled by a kind of material with much higher permeability compared to the host material surrounding the hole. In this manner drainage holes will be included in the variational function defined in Eq. (4.154). Consequently, boundary conditions on the wall of holes will be deleted and the mesh discretization should cover the holes themselves using "air element" (Hu and Chen 2003). These air elements enable to facilitate the pre-process and calculation procedures and may further be incorporated in the composite element method.

The intrinsic question should be answered is that, what should be an appropriate permeability coefficient endued to the virtual filler material in air elements? Towards this question, several examples concerning parametric studies will be presented in the hereafter coverage.

16.2.2 Parametric Studies

Two types of drainage holes are commonly encountered in hydraulic structures. One with water spilling over the hole top, in this case the hydraulic potential on the hole wall is identical to the elevation of the hole top; another with water exiting down from the hole bottom, in this cases the hydraulic potential on the hole wall is identical to the corresponding elevation concerned.

(1) Holes of spilling over

Figure 16.1 shows an entity domain containing one drainage hole with diameter D. Its four lateral sides and top surface are stipulated as the first boundary with specified potential ϕ_0 = 3.5 and 3 m, respectively, the bottom surface is the second boundary without flow rate, i.e. $q = 0$. The permeability coefficient of the entity material is $k_r = 1$, the permeability coefficient k_d of the virtual filler in the hole is variable. The permeability coefficient proportion $R = k_d/k_r$ is employed to describe the relative permeability of the filler in the drainage hole. The computation results by the air element and the exact solution are cross-referenced, the latter discretizes the whole entity with empty hole and specifies boundary conditions on the wall of hole. The error E is defined as the maximum difference in the hydraulic potential on the wall of hole by the air element solution and exact solution.

Figure 16.2 shows the relation of E versus $\lg R$. From the calculation results it can be found that when $\lg R \geq 3$, namely the permeability coefficient of the air element is larger than 1000 times that of the host medium, the computation error is lower than 5%.

According to the Figs. 16.2 and 16.3, the change of the hole diameter D has no significant influence on the computation error E.

Figure 16.4 indicates that the maximum error manifests on the hole wall. Figure 16.5 indicates that the maximum error emerges at the bottom of the hole, where H is the height from the bottom.

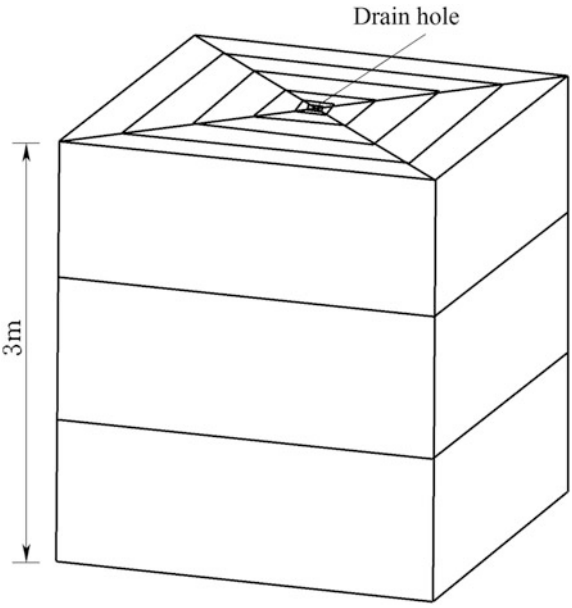

Fig. 16.1 Entity domain containing one over spilling drainage hole

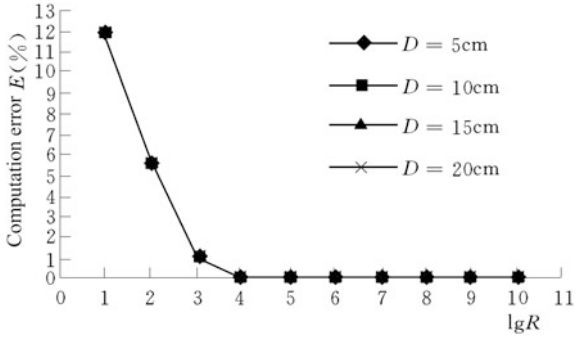

Fig. 16.2 Diagram of E versus lg R

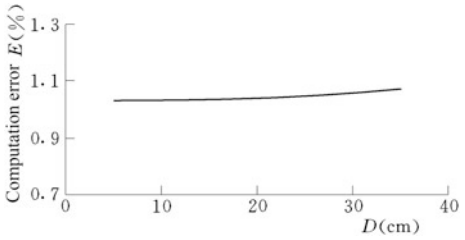

Fig. 16.3 Diagram of E versus D

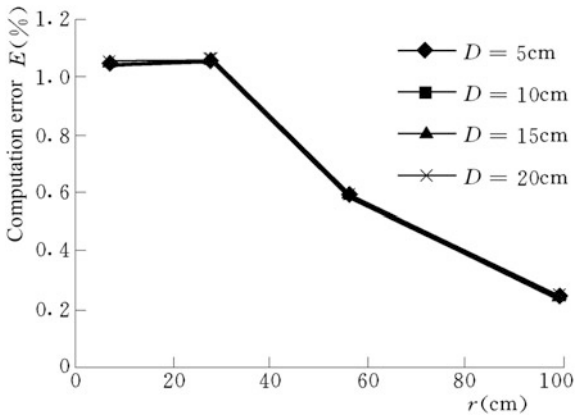

Fig. 16.4 Diagram of E versus r

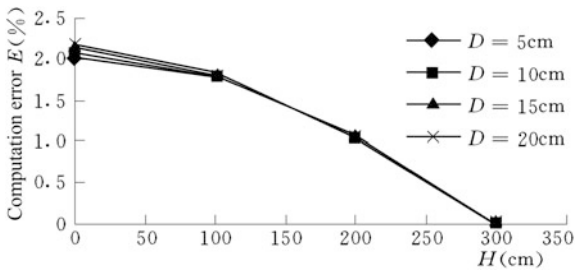

Fig. 16.5 Diagram of E versus H

(2) Holes of exiting down

Figure 16.6 displays a slice of domain embedded with a segment of tunnel and installed with one drainage hole of D= 0.1 m whose exit is at the tunnel crest. The left and right sides are stipulated as the first boundary with specified potential ϕ_0= 15 m, the front and rear sides as well as the bottom surface observe the second boundary condition without flow rate, i.e. $q = 0$. The permeability coefficient of the host medium is $k_r = 1$, whereas the permeability coefficient k_d of the virtual filler in the hole is variable. The computations using the air element solution and exact solution are carried out in parallel.

From the result showing in Fig. 16.7 it may be concluded that when $2.1 < \lg R \leq 2.7$, namely the permeability coefficient of the air element is approximately 300–1000 times the host medium, the error E is lower than 5%.

Figure 16.8 shows the exact solution of isopotential contours at the section through the hole axis, Fig. 16.9 is the corresponding air element solution. They validate that the air element may be employed to simulate drainage holes with

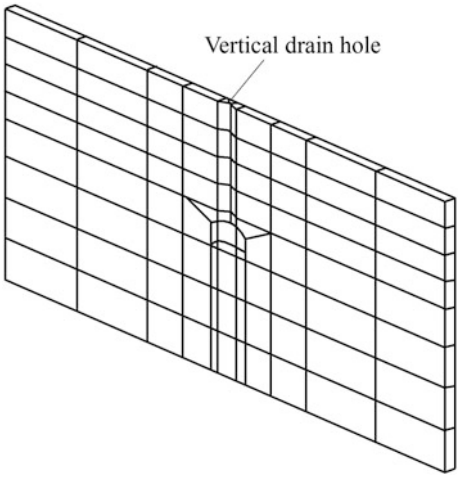

Fig. 16.6 Tunnel installed with one drainage hole on its crown

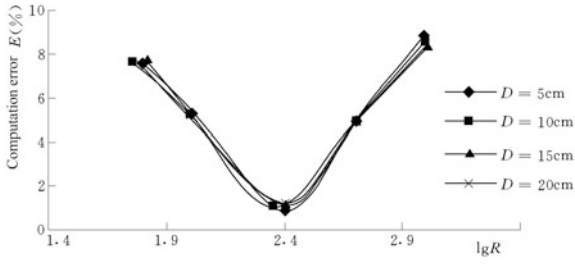

Fig. 16.7 Diagram of E versus $\lg R$

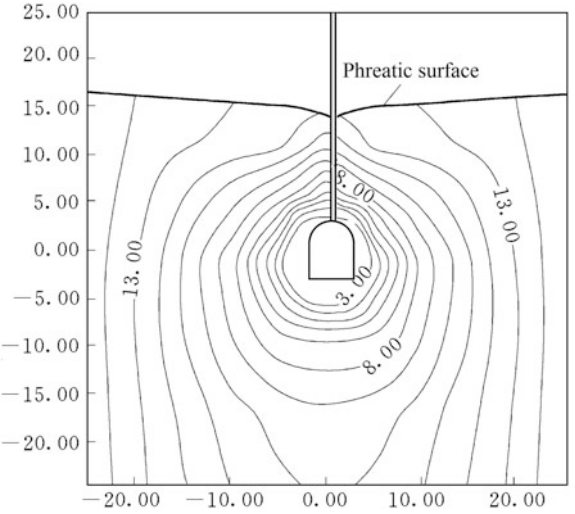

Fig. 16.8 Exact solution of isopotential contours

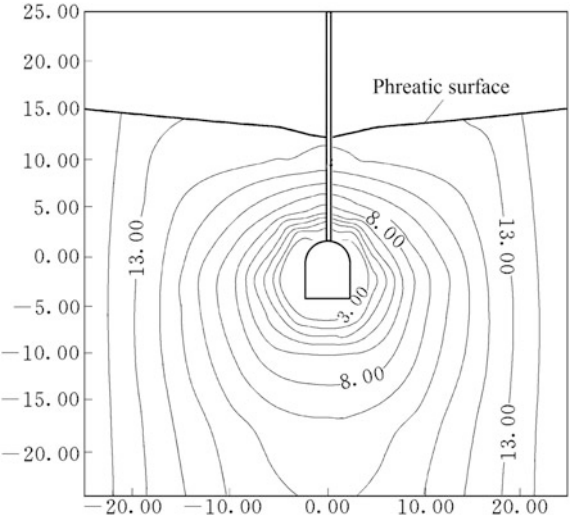

Fig. 16.9 Air element solution of isopotential contours

considerable accuracy, subject to an appropriate selection of the permeability coefficient for the virtual hole filler.

Based on the foregoing studies, it may be generally advised that when the proportion $R = k_d/k_r$ ranges around 10^2–10^3, the solution precision may be satisfactory with the air element for drainage hole of either spilling over or exiting down type.

16.3 Composite Element for Drainage Holes

16.3.1 Coordinate Systems and Nomenclatures

See Fig. 2.5.

16.3.2 Governing Equations

(1) Sub-element element analysis

1. Solid material

The variational function Eq. (4.154) for solid material may be reduced as

$$I(\phi)_r = \iiint_{\Omega_r} \left(\frac{1}{2}(\{S\}\phi_r)^T[k]_r(\{S\}\phi_r) - q_0\phi_r\right) d\Omega + \iint_{\Gamma_r} q\phi_r \, d\Gamma \tag{16.1}$$

where q_0 = inner source; q = boundary flow rate; $\{S\} = \left[\frac{\partial}{\partial X} \quad \frac{\partial}{\partial Y} \quad \frac{\partial}{\partial Z}\right]^T$.

According to the interpolation Eq. (14.3) we have

$$I(\phi)_r = \iiint_{\Omega_r} \left(\frac{1}{2}\{\phi\}_r^T(\{S\}[N])^T[k]_r(\{S\}[N]\{\phi\}_r) - q_0[N]\{\phi\}_r\right) d\Omega + \iint_{\Gamma_r} q[N]\{\phi\}_r \, d\Gamma$$

The application of variational operator gives rise to

$$[h]_r\{\phi\}_r = \{Q\}_r \tag{16.2}$$

In which $[h]_r$ and $\{Q\}_r$ are the conductivity matrix and equivalent nodal flow (or right item) of the solid material (e.g. rock) calculated by

$$[h]_r = \iiint_{\Omega_r} (\{S\}[N])^T[k]_r(\{S\}[N]) \, d\Omega \tag{16.3}$$

$$\{Q\}_r = \iiint_{\Omega_r} [N]q_0 \, d\Omega - \iint_{\Gamma_r} [N]q \, d\Gamma \tag{16.4}$$

2. Drainage hole

For drainage hole d, the variational function Eq. (4.154) may be expressed as

$$I(\phi)_d = \iiint\limits_{\Omega_d} \left(\frac{1}{2}(\{S\}\phi_d)^T[k]_d(\{S\}\phi_d) - q_0\phi_d\right) d\Omega + \iint\limits_{\Gamma_d} q\phi_d \, d\Gamma \tag{16.5}$$

The interpolation using Eq. (14.3) leads to

$$I(\phi)_d = \iiint\limits_{\Omega_d} \left(\frac{1}{2}\{\phi\}_d^T(\{S\}[N])^T[k]_d\{S\}[N]\{\phi\}_d - q_0[N]\{\phi\}_d\right) d\Omega \; + \iint\limits_{\Gamma_d} q[N]\{\phi\}_d \, d\Gamma \tag{16.6}$$

The application of variational operator gives rise to

$$[h]_d\{\phi\}_d = \{Q\}_d \tag{16.7}$$

In which $[h]_d$ and $\{Q\}_d$ are the conductivity matrix and equivalent nodal flow (or right item) contributed from hole d.

$$[h]_d = \iiint\limits_{\Omega_d} (\{S\}[N])^T[k]_d(\{S\}[N]) \, d\Omega \tag{16.8}$$

$$\{Q\}_d = \iiint\limits_{\Omega_d} [N]q_0 \, d\Omega - \iint\limits_{\Gamma_d} [N]q \, d\Gamma \tag{16.9}$$

In Eq. (16.8) the virtual permeability coefficient k_d may be approximately input as 10^2–10^3 times k_r (vide Sect. 16.2).

3. Solid/hole interface

There is no independent nodal hydraulic potential for interface $j_{r,d}$. The differential of the hydraulic potential within the interface in Eq. (4.154) should be expressed by the difference in the nodal values corresponding to the host material and the drainage hole respectively.

Since the hydraulic potential ϕ is a scalar, therefore the variational function in Eq. (4.154) for the interface can be expressed in the local Cylindrical coordinate system as

$$I(\phi)_{j_{r,d}} = \iiint\limits_{\Omega_{j_{r,d}}} \left(\frac{1}{2}(\{S\}\phi)^T[k]_{j_{r,d}}(\{S\}\phi)\right) d\Omega \tag{16.10}$$

In Eq. (16.10) the inner source item and the boundary source item are all ruled out. Normally, the interface possesses a thickness a much smaller compared to the diameter D of drainage hole, therefore it can be postulated that along the thickness direction r (see Fig. 2.5) we have

$$(\{S\}\Phi) = constant \tag{16.11}$$

So Eq. (16.10) in the local Cylindrical coordinate system defined in Fig. 2.5 is transformed into

$$\begin{aligned} I(\phi)_{j_{r,d}} &= \iiint\limits_{\Omega_{j_{r,d}}} \left(\frac{1}{2}(\{S\}^{cy}\phi)^T[k]_{j_{r,d}}(\{S\}^{cy}\phi)\right) rdrd\omega dz \\ &= \frac{D}{2} \times a \times \iint\limits_{\Gamma_{j_{r,d}}} \left(\frac{1}{2}(\{S\}^{cy}\phi)^T[k]_{j_{r,d}}(\{S\}^{cy}\phi)\right) d\omega dz \end{aligned} \tag{16.12}$$

In which D is the diameter of drainage hole, $\{S\}^{cy}$ is the differential operator in the local Cylindrical coordinate system.

$$\{S\}^{cy} = \left[\frac{\partial}{\partial r} \quad \frac{1}{r}\frac{\partial}{\partial \omega} \quad \frac{\partial}{\partial z}\right]^T \tag{16.13}$$

The assumption is further made that in the local Cylindrical coordinate system, the differential of the hydraulic potential ϕ within the interface $j_{r,d}$ will be

$$\begin{cases} \dfrac{\partial \phi}{\partial r} = \dfrac{\phi_r - \phi_d}{a} \times c_1 \\ \dfrac{1}{r}\dfrac{\partial \phi}{\partial \omega} = \dfrac{\phi_r - \phi_d}{a} \times c_2 \\ \dfrac{\partial \phi}{\partial z} = \dfrac{\phi_r - \phi_d}{a} \times c_3 \end{cases} \tag{16.14}$$

In which c_1, c_2, c_3 are deflection coefficients and

$$c_1^2 + c_2^2 + c_3^2 = 1 \tag{16.15}$$

Use is made of Eqs. (16.13–16.14), Eq. (16.12) yields

$$\begin{aligned} I(\phi)_{j_{r,d}} &= \frac{D}{2} \times a \times \iint\limits_{\Gamma_{j_{r,d}}} \left(\frac{1}{2} \begin{Bmatrix} c_1\dfrac{\phi_r - \phi_d}{a} \\ c_2\dfrac{\phi_r - \phi_d}{a} \\ c_3\dfrac{\phi_r - \phi_d}{a} \end{Bmatrix}^T [k]_{j_{r,d}} \begin{Bmatrix} c_1\dfrac{\phi_r - \phi_d}{a} \\ c_2\dfrac{\phi_r - \phi_d}{a} \\ c_3\dfrac{\phi_r - \phi_d}{a} \end{Bmatrix} \right) d\omega dz \\ &= \frac{Da}{4a^2} \iint\limits_{\Gamma_{j_{r,d}}} \left(\begin{Bmatrix} c_1(\phi_r - \phi_d) \\ c_2(\phi_r - \phi_d) \\ c_3(\phi_r - \phi_d) \end{Bmatrix}^T [k]_{j_{r,d}} \begin{Bmatrix} c_1(\phi_r - \phi_d) \\ c_2(\phi_r - \phi_d) \\ c_3(\phi_r - \phi_d) \end{Bmatrix} \right) d\omega dz \\ &= \frac{D}{4a}(c_1^2 k_1 + c_2^2 k_2 + c_3^2 k_3) \iint\limits_{\Gamma_{j_{r,d}}} (\{\phi\}_r - \{\phi\}_d)^T [N]^T [N] (\{\phi\}_r - \{\phi\}_d)\, d\omega dz \\ &= \frac{M}{2} \iint\limits_{\Gamma_{j_{r,d}}} [\{\phi\}_r^T ([N]^T[N]\{\phi\}_r - [N]^T[N]\{\phi\}_d) \\ &\qquad - \{\phi\}_d^T ([N]^T[N]\{\phi\}_r - [N]^T[N]\{\phi\}_d)]\, d\omega dz \end{aligned} \tag{16.16}$$

In which

$$M = \frac{D}{2a}(c_1^2 k_1 + c_2^2 k_2 + c_3^2 k_3) \tag{16.17}$$

where k_1, k_2, k_3 = principal permeability coefficients of interface $j_{r,d}$.

Let $k_1 = k_2 = k_3 = k_{j_{r,d}}$ and use is made of Eq. (16.15), we have

$$M = \frac{D}{2a} k_{j_{r,d}} = \frac{Dk}{2} \tag{16.18}$$

In which k is the conductive coefficient of interface $j_{r,d}$ expressed by

$$k = \frac{k_{j_{r,d}}}{a} \tag{16.19}$$

The permeability coefficient $k_{j_{r,d}}$ can be postulated as equal to k_d of the virtual filler in drainage hole. Theoretically, the interface thickness a should be very small to get the exact solution, however, numerical testing for some very simple examples shows that $R/a = 100$ will lead to precision satisfactory solution in which R is the radium of drainage hole.

The application of variation principle towards the function $I(\phi)_{j_{r,d}}$ defined in Eq. (16.16) gives rise to

$$\begin{cases} [h]_{r,r}\{\phi\}_r + [h]_{r,d}\{\phi\}_d = 0 \\ [h]_{d,r}\{\phi\}_r + [h]_{d,d}\{\phi\}_d = 0 \end{cases} \tag{16.20}$$

In which the hydraulic conductivity matrix and the corresponding right side item of the solid/hole interface are

$$\begin{cases} [h]_{r,r} = M \iint\limits_{\Gamma_{j_{r,d}}} [N]^T [N] \, d\omega dz \\ [h]_{d,d} = M \iint\limits_{\Gamma_{j_{r,d}}} [N]^T [N] \, d\omega dz \\ [h]_{r,d} = -M \iint\limits_{\Gamma_{j_{r,d}}} [N]^T [N] \, d\omega dz \\ [h]_{d,r} = -M \iint\limits_{\Gamma_{j_{r,d}}} [N]^T [N] \, d\omega dz \end{cases} \tag{16.21}$$

(2) Composite element analysis

Based on the above deduction, the variational operator throughout a composite element containing n_d drainage segment will leads to the governing equation below

$$\begin{bmatrix} [H]_{r,r} & [H]_{r,1} & \cdots & [H]_{r,n_d} \\ [H]_{1,r} & [H]_{1,1} & \cdots & 0 \\ \cdots & \cdots & \cdots & \cdots \\ [H]_{n_d,r} & 0 & \cdots & [H]_{n_d,n_d} \end{bmatrix} \begin{Bmatrix} \{\phi\}_r \\ \{\phi\}_1 \\ \cdots \\ \{\phi\}_{n_d} \end{Bmatrix} = \begin{Bmatrix} \{Q\}_r \\ \{Q\}_1 \\ \cdots \\ \{Q\}_{n_d} \end{Bmatrix} \tag{16.22}$$

In which

$$\begin{cases} [H]_{r,r} = [h]_r + \sum_{d=1}^{n_d} [h]_{r,r} \\ [H]_{d,d} = [h]_d + [h]_{d,d} \quad (d = 1, \ldots, n_d) \\ [H]_{r,d} = [h]_{r,d} \\ [H]_{d,r} = [h]_{d,r} \end{cases} \tag{16.23}$$

This elementary governing equation will be further assembled into the overall governing equation of the structure system in a similar way to the FEM.

16.3.3 Numerical Integrations

(1) Solid entity sub-element

The integral domain should be the whole host element minus the space occupied by the holes. Accordingly, in the calculation of $[h]_r$ and $\{Q\}_r$ [see Eqs. (16.3) and (16.4)] the integration will be undertaken as

$$\begin{cases} [h]_r = \iiint_{Z\ Y\ X} (\{S\}[N])^T [k]_r (\{S\}[N])\, dXdYdZ \\ \qquad - \sum_{d=1}^{n_d} \iiint_{z\ \ \omega\ r} (\{S\}[N])^T [k]_r (\{S\}[N])\, rdrd\omega dz \\ \{Q\}_r = \iiint_{Z\ Y\ X} [N] q_0\, dXdYdZ - \iint_{\Gamma_r} [N] q\, d\Gamma \\ \qquad - \sum_{d=1}^{n_d} \iiint_{z\ \ \omega\ r} [N] q_0\, rd\omega drdz + \sum_{d=1}^{n_d} \iint_{\Gamma_d} [N] q\, d\Gamma \end{cases} \tag{16.24}$$

(2) Drainage hole sub-element

The local Cylindrical coordinate system is convenient for undertaking the integral of Eqs. (16.8) and (16.9) in a form of

$$\begin{cases} [h]_d = \iiint\limits_{\omega\ r\ z} (\{S\}[N])^T [k]_d (\{S\}[N])\ r d\omega dr dz \\ \{Q\}_d = \iiint\limits_{\omega\ r\ z} [N] q_0\ r d\omega dr dz - \iint\limits_{\Gamma_d} [N] q\ d\Gamma \end{cases} \tag{16.25}$$

Using the transformation between the local Cartesian and Cylindrical coordinate systems, we may have general integral transformation for any function $F(x, y, z)$ as follows.

$$\iiint\limits_{\Omega_d} F(x, y, z)\ dxdydz = \iiint\limits_{\Omega_d} F(r\ \cos\ \omega, r\ \sin\ \omega, z)\ r dr d\omega dz \tag{16.26}$$

The integration of $[h]_d$ is thus performed with the help of Gaussian quadrature as

$$\begin{aligned} [h]_d &= \iiint\limits_{\Omega_d} (\{S\}[N])^T [k]_d (\{S\}[N])\ d\Omega \\ &= \int\limits_0^{r_d} \int\limits_0^{2\pi} \int\limits_0^{L_d} (\{S\}[N])^T [k]_d (\{S\}[N])\ r dr d\omega dz \\ &= \int\limits_{-1}^{1} \int\limits_{-1}^{1} \int\limits_{-1}^{1} (\{S\}[N])^T [k]_d (\{S\}[N]) r|J|\ d\xi d\eta d\zeta \end{aligned} \tag{16.27}$$

In which L_d is the length of drainage hole within the composite element concerned.

The Gaussian points in the hole are calculated by the formulas

$$\begin{cases} \xi_r = \dfrac{r}{2}(1+\xi) \\ \eta_\omega = \dfrac{2\pi}{2}(1+\eta) \\ \zeta_z = \dfrac{L_d}{2}(1+\zeta) \end{cases} \tag{16.28}$$

where ξ, η, ζ = normalized coordinates of the Gaussian quadrature point in the local Cartesian system; ξ_r, η_ω, ζ_z = coordinates of the Gaussian quadrature point in the local Cylindrical system.

(3) Interface

The matrices $[h]_{r,r}$, $[h]_{d,d}$ and $[h]_{r,d}$ in Eq. (16.21) are expressed in the local Cylindrical system whose quadrature operation is generally undertaken by the formula.

$$\int_0^{2\pi}\int_0^{L_d} F(\omega,z)\,d\omega dz = \frac{2\pi}{2}\times\frac{L_d}{2}\int_{-1}^{1}\int_{-1}^{1} F(\eta,\zeta)\,d\eta d\zeta \tag{16.29}$$

Specifically

$$\begin{cases} [h]_{r,r} = M\iint [N]^T[N]\,d\omega dz \\ \qquad = M\times\dfrac{2\pi}{2}\times\dfrac{L_d}{2}\displaystyle\int_{-1}^{1}\int_{-1}^{1}[N]^T[N]\,d\eta d\zeta \\ [h]_{d,d} = M\iint [N]^T[N]\,d\omega dz \\ \qquad = M\times\dfrac{2\pi}{2}\times\dfrac{L_d}{2}\displaystyle\int_{-1}^{1}\int_{-1}^{1}[N]^T[N]\,d\eta d\zeta \\ [h]_{r,d} = -M\iint [N]^T[N]\,d\alpha dz \\ \qquad = -M\times\dfrac{2\pi}{2}\times\dfrac{L_d}{2}\displaystyle\int_{-1}^{1}\int_{-1}^{1}[N]^T[N]\,d\eta d\zeta \\ [h]_{d,r} = -M\iint [N]^T[N]\,d\omega dz \\ \qquad = -M\times\dfrac{2\pi}{2}\times\dfrac{L_d}{2}\displaystyle\int_{-1}^{1}\int_{-1}^{1}[N]^T[N]\,d\eta d\zeta \end{cases} \tag{16.30}$$

The transformation of the coordinates of the Gaussian point on interface is identical to that of drainage hole [see Eq. (16.28)].

16.4 Composite Element for Discontinuities

16.4.1 Coordinate Systems and Nomenclatures

See Fig. 2.2.

16.4.2 Governing Equations

(1) Sub-element analysis

1. Solid material

The variational function of sub-element *rl* (see Fig. 14.3) is given by

$$I(\phi)_{rl} = \iiint_{\Omega_{rl}} \left(\frac{1}{2} (\{S\}\phi_{rl})^T [k]_{rl} (\{S\}\phi_{rl}) - q_0 \phi_{rl} \right) d\Omega + \iint_{\Gamma_{rl}} q\phi_{rl}\, d\Gamma \quad (rl = 1, \ldots, n_r) \tag{16.31}$$

Introducing Eq. (14.4) into Eq. (16.31) gives rise to

$$I(\phi)_{rl} = \iiint_{\Omega_{rl}} \left(\frac{1}{2} \{\phi\}_{rl}^T (\{S\}[N])^T [k]_{rl} \left(\{S\}[N]\{\phi\}_{rl} - q_0 [N]\{\phi\}_{rl} \right) \right) d\Omega + \iint_{\Gamma_{rl}} q[N]\{\phi\}_{rl}\, d\Gamma \quad (rl = 1, \ldots, n_r) \tag{16.32}$$

The variation operator leads to

$$[h]_{rl}\{\phi\}_{rl} = \{Q\}_{rl} \qquad (rl = 1, \ldots, n_r) \tag{16.33}$$

In which $[h]_{rl}$ and $\{Q\}_{rl}$ are the conductivity matrix and equivalent nodal flow rate of sub-element *rl*, respectively

$$[h]_{rl} = \iiint_{\Omega_{rl}} (\{S\}[N])^T [k]_{rl} (\{S\}[N])\, d\Omega \tag{16.34}$$

$$\{Q\}_{rl} = \iiint_{\Omega_{rl}} [N] q_0\, d\Omega - \iint_{\Gamma_{rl}} [N] q\, d\Gamma \tag{16.35}$$

2. Discontinuity

Suppose discontinuity segment $j_{rl,rm}$ is a contact face of adjacent sub-elements *rl* and *rm*, the variational function in this discontinuity sub-element is given by

$$I(\phi)_{j_{rl,rm}} = \iiint_{\Omega_{j_{rl,rm}}} \left(\frac{1}{2} (\{S\}\phi)^T [k]_{j_{rl,rm}} (\{S\}\phi) \right) d\Omega \tag{16.36}$$

Since the hydraulic aperture $a_{j_{rl,rm}}$ of the discontinuity segment is much smaller than the dimension of composite element, it can be postulated that the hydraulic potential gradient along the aperture of discontinuity is constant, therefore Eq. (16.36) can be reduced as

$$I(\phi)_{j_{rl,rm}} = a_{j_{rl,rm}} \iint\limits_{\Gamma_{j_{rl,rm}}} \frac{1}{2}\left(\{S\}_{j_{rl,rm}}\phi\right)^T [k]_{j_{rl,rm}} \left(\{S\}_{j_{rl,rm}}\phi\right) dx_{j_{rl,rm}} dy_{rl,rm} \tag{16.37}$$

In which $\{S\}_{j_{rl,rm}}$ is the differential operator in the local Cartesian coordinate system of discontinuity segment $j_{rl,rm}$

$$\{S\}_{j_{rl,rm}} = \begin{bmatrix} \frac{\partial}{\partial x_{j_{rl,rm}}} & \frac{\partial}{\partial y_{j_{rl,rm}}} & \frac{\partial}{\partial z_{j_{rl,rm}}} \end{bmatrix}^T \tag{16.38}$$

The hydraulic gradient in the discontinuity segment is simply computed by the formulas

$$\begin{cases} \dfrac{\partial \phi}{\partial x_{j_{rl,rm}}} = \dfrac{\partial\left[\frac{1}{2}(\phi_{rl} + \phi_{rm})\right]}{\partial x_{j_{rl,rm}}} = \dfrac{1}{2}\left(\dfrac{\partial \phi_{rl}}{\partial x_{j_{rl,rm}}} + \dfrac{\partial \phi_{rm}}{\partial x_{j_{rl,rm}}}\right) \\ \dfrac{\partial \phi}{\partial y_{j_{rl,rm}}} = \dfrac{\partial\left[\frac{1}{2}(\phi_{rl} + \phi_{rm})\right]}{\partial y_{j_{rl,rm}}} = \dfrac{1}{2}\left(\dfrac{\partial \phi_{rl}}{\partial y_{j_{rl,rm}}} + \dfrac{\partial \phi_{rm}}{\partial y_{j_{rl,rm}}}\right) \\ \dfrac{\partial \phi}{\partial z_{j_{rl,rm}}} = \dfrac{\phi_{rl} - \phi_{rm}}{a_{j_{rl,rm}}} \end{cases} \tag{16.39}$$

Denoting

$$\begin{cases} \left[N_{x_{j_{rl,rm}}}\right] = \left[\dfrac{\partial N}{\partial x_{j_{rl,rm}}}\right] \\ \left[N_{y_{j_{rl,rm}}}\right] = \left[\dfrac{\partial N}{\partial y_{j_{rl,rm}}}\right] \end{cases} \tag{16.40}$$

And use is made of Eq. (14.4), the variational function of Eq. (16.37) becomes

$$I(\phi)_{j_{rl,rm}} = \frac{a_{j_{rl,rm}}}{2} \iint \begin{pmatrix} \frac{k_x}{4}(\{\phi\}_{rl}^T [N_{x_{j_{rl,rm}}}]^T [N_{x_{j_{rl,rm}}}]\{\phi\}_{rl} + 2\{\phi\}_{rl}^T [N_{x_{j_{rl,rm}}}]^T [N_{x_{j_{rl,rm}}}]\{\phi\}_{rm} \\ + \{\phi\}_{rm}^T [N_{x_{j_{rl,rm}}}]^T [N_{x_{j_{rl,rm}}}]\{\phi\}_{rm}) + \\ \frac{k_y}{4}(\{\phi\}_{rl}^T [N_{y_{j_{rl,rm}}}]^T [N_{y_{j_{rl,rm}}}]\{\phi\}_{rl} + 2\{\phi\}_{rl}^T [N_{y_{j_{rl,rm}}}]^T [N_{y_{j_{rl,rm}}}]\{\phi\}_{rm} \\ + \{\phi\}_{rm}^T [N_{y_{j_{rl,rm}}}]^T [N_{y_{j_{rl,rm}}}]\{\phi\}_{rm}) + \\ \frac{k_z}{a_{j_{rl,rm}}^2}(\{\phi\}_{rl}^T [N]^T [N]\{\phi\}_{rl} - 2\{\phi\}_{rl}^T [N]^T [N]\{\phi\}_{rm} \\ + \{\phi\}_{rm}^T [N]^T [N]\{\phi\}_{rm}) \end{pmatrix} dx_{j_{r,lrm}} dy_{j_{rl,rm}} \tag{16.41}$$

where k_x, k_y,k_z = principal permeability coefficients of the discontinuity.

The operation of the variational principle leads to

$$\begin{cases} [h]_{rl,rl}\{\phi\}_{rl} + [h]_{rl,rm}\{\phi\}_{rm} = 0 \\ [h]_{rm,rl}\{\phi\}_{rl} + [h]_{rm,rm}\{\phi\}_{rm} = 0 \end{cases} \tag{16.42}$$

In which

$$\begin{cases} [h]_{rl,rl} = [h]_{rm,rm} = \frac{a_{j_{rl,rm}}}{2} \iint\limits_{\Gamma_{j_{rl,rm}}} \left(\frac{k_x}{2} [N_{x_{j_{rl,rm}}}]^T [N_{x_{j_{rl,rm}}}] + \frac{k_y}{2} [N_{y_{j_{rl,rm}}}]^T [N_{y_{j_{rl,rm}}}] + \frac{2k_z}{a_{j_{rl,rm}}^2} [N]^T [N] \right) dx_{j_{rl,rm}} dy_{j_{rl,rm}} \\ [h]_{rl,rm} = [h]_{rm,rl} = \frac{a_{j_{rl,rm}}}{2} \iint\limits_{\Gamma_{j_{rl,rm}}} \left(\frac{k_x}{2} [N_{x_{j_{rl,rm}}}]^T [N_{x_{j_{rl,rm}}}] + \frac{k_y}{2} [N_{y_{j_{rl,rm}}}]^T [N_{y_{j_{rl,rm}}}] - \frac{2k_z}{a_{j_{rl,rm}}^2} [N]^T [N] \right) dx_{j_{rl,rm}} dy_{j_{rl,rm}} \end{cases} \tag{16.43}$$

(2) Composite element analysis

The governing equation of the composite element can be obtained through the assemblage of all its sub-elements. Suppose the composite element contains n_r rock sub-elements and n_j structural plane sub-elements, its governing equation relating the nodal displacement vector and load vector will be

$$\begin{bmatrix} [H]_{1,1} & [H]_{1,2} & \cdots & [H]_{1,n_r} \\ [H]_{1,1} & [H]_{2,2} & \cdots & 0 \\ \cdots & \cdots & \cdots & \cdots \\ [H]_{n_r,1} & 0 & \cdots & [H]_{n_r,n_r} \end{bmatrix} \begin{Bmatrix} \{\phi\}_1 \\ \{\phi\}_2 \\ \cdots \\ \{\phi\}_{n_r} \end{Bmatrix} = \begin{Bmatrix} \{Q\}_1 \\ \{Q\}_2 \\ \cdots \\ \{Q\}_{n_r} \end{Bmatrix} \tag{16.44}$$

In which

$$\begin{cases} [H]_{rl,rl} = [h]_{rl} + \sum\limits_{rm=1, rm \neq rl}^{n_r} H(rl, rm)[h]_{rl,rl} \\ [H]_{rl,rm} = H(rl, rm)[h]_{rl,rm} \qquad (rl, rm = 1, \ldots, n_r) \\ H(rl, rm) = \begin{cases} 1 & \text{if } rl \text{ and } rm \text{ are adjacent} \\ 0 & \text{if } rl \text{ and } rm \text{ are not adjacent} \end{cases} \end{cases} \tag{16.45}$$

Generally, if a composite element is composed of n_r rock sub-elements, its degree of freedom (DOF) will be n_r times the classical finite element. Whereas a composite element without discontinuity segments will be retrogressed to the classical finite element. Attributable to this feature the composite elements and the finite elements can joint-work well in one hybrid discrete system and there is no essential difficulty in the algorithm implementation.

16.5 Composite Element for Jointed Rocks Drained by Holes

16.5.1 Concept

The FE mesh should be generated beforehand to discrete the structure concerned, where the deployment and size of finite elements are dominated by the structure configuration and hydraulic potential gradient. Then the presence of discontinuities and drainage holes transfers a number of finite elements into composite elements. Figure 16.10 shows a composite element containing n_r rock sub-elements, n_d drainage sub-elements and n_j joint sub-elements, at its nodes there are independent nodal hydraulic potentials corresponding to rock and drainage sub-elements $\{\phi\} = \left[\{\phi\}_{r1}^T, \{\phi\}_{r2}^T, \ldots, \{\phi\}_{n_r}^T, \{\phi\}_{d1}^T, \{\phi\}_{d2}^T, \ldots, \{\phi\}_{n_d}^T\right]^T$, that are used in the interpolations Eqs. (14.3–14.4).

16.5.2 Sub-element Analysis

(1) Rock sub-element *rl*

See Eqs. (16.33–16.35).

(2) Drainage hole sub-element d_i

See Eqs. (16.7–16.9).

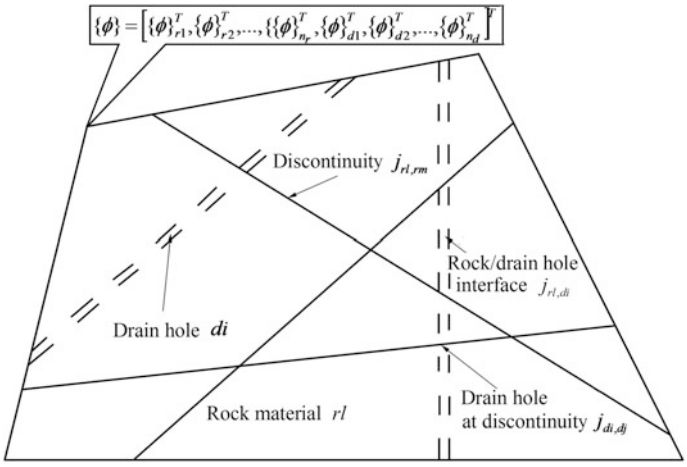

Fig. 16.10 Schematic diagram of a composite element containing discontinuities and drainage holes

(3) Discontinuity sub-element $j_{rl,rm}$

See Eqs. (16.42–16.43).

(4) Solid/hole interface $j_{rl,di}$

See Eqs. (16.20–16.21).

(5) Interface $j_{di,dj}$ between drainage sub-elements di and dj

This interface does only exist when drainage sub-elements di and dj belong to a same drainage hole intersected with discontinuity sub-element $j_{rl,rm}$. The variational function Eq. (4.154) for this interface can be expressed in the local Cylindrical coordinate system as

$$I(\phi)_{j_{di,dj}} = \iiint\limits_{\Omega_{j_{di,dj}}} \left(\frac{1}{2}(\{S\}\phi)^T[k]_{j_{di,dj}}(\{S\}\phi)\right) d\Omega \tag{16.46}$$

The thickness of this interface may be looked at as identical to the hydraulic aperture $a_{j_{rl,rm}}$ of sub-element $j_{rl,rm}$. Since it is normally much smaller compared to the diameter of drainage hole, therefore we can postulate that along the thickness $a_{j_{rl,rm}}$ the flow velocity is constant. By the procedure similar to Eqs. (16.42–16.43) for $j_{rl,rm}$, we obtain

$$\begin{cases} [h]_{di,di}\{\phi\}_{di} + [h]_{di,dj}\{\phi\}_{dj} = 0 \\ [h]_{dj,di}\{\phi\}_{di} + [h]_{dj,dj}\{\phi\}_{dj} = 0 \end{cases} \tag{16.47}$$

$$\begin{cases} [h]_{di,di} = [h]_{dj,dj} = \frac{a_{j_{rl,rm}}}{2} \iint\limits_{\Gamma_{j_{di,dj}}} (\lambda_1 + \lambda_2 + \lambda_3)\, d\Gamma \\ [h]_{di,dj} = [h]_{dj,di} = \frac{a_{j_{rl,rm}}}{2} \iint\limits_{\Gamma_{j_{di,dj}}} (\lambda_1 + \lambda_2 - \lambda_3)\, d\Gamma \end{cases} \tag{16.48}$$

In which $\lambda_1 = \frac{k_d}{2}\left(\frac{\partial[N]}{\partial x^{cy}}\right)^T\left(\frac{\partial[N]}{\partial x^{cy}}\right)$, $\lambda_2 = \frac{k_d}{2}\left(\frac{\partial[N]}{\partial y^{cy}}\right)^T\left(\frac{\partial[N]}{\partial y^{cy}}\right)$, $\lambda_3 = \frac{2k_d}{a^2_{j_{rl,rm}}}[N]^T[N]$; x^{cy} and y^{cy} are the local coordinate of the drainage hole.

16.5.3 Composite Element Analysis

Giving above sub-element analyses, the consideration of the variational principle for the whole composite element will lead to its governing equation as

$$\begin{bmatrix} [H]_{1,1} & [H]_{1,2} & \cdots & [H]_{1,n_r} & [H]_{1,n_r+1} & \cdots & [H]_{1,n_r+n_d} \\ [H]_{2,1} & [H]_{2,2} & \cdots & [H]_{2,n_r} & [H]_{2,n_r+1} & \cdots & [H]_{2,n_r+n_d} \\ \cdots & \cdots & \cdots & \cdots & \cdots & \cdots & \cdots \\ [H]_{n_r,1} & [H]_{n_r,2} & \cdots & [H]_{n_r,n_r} & [H]_{n_r,n_r+1} & \cdots & [H]_{n_r,n_r+n_d} \\ [H]_{n_r+1,1} & [H]_{n_r+1,2} & \cdots & [H]_{n_r+1,n_r} & [H]_{n_r+1,n_r+1} & \cdots & [H]_{n_r+1,n_r+n_d} \\ \cdots & \cdots & \cdots & \cdots & \cdots & \cdots & \cdots \\ [H]_{n_r+n_d,1} & [H]_{n_r+n_d,2} & \cdots & [H]_{n_r+n_d,n_r} & [H]_{n_r+n_d,n_r+1} & \cdots & [H]_{n_r+n_d,n_r+n_d} \end{bmatrix} \begin{Bmatrix} \{\phi\}_1 \\ \{\phi\}_2 \\ \cdots \\ \{\phi\}_{n_r} \\ \{\phi\}_{n_r+1} \\ \cdots \\ \{\phi\}_{n_r+n_d} \end{Bmatrix} = \begin{Bmatrix} \{Q\}_1 \\ \{Q\}_2 \\ \cdots \\ \{Q\}_{n_r} \\ \{Q\}_{n_r+1} \\ \cdots \\ \{Q\}_{n_r+n_d} \end{Bmatrix} \tag{16.49}$$

In which

$$\begin{cases} [H]_{rl,rl} = [h]_{rl} + \sum\limits_{rm=1,rl\neq rm}^{n_r} A(rl,rm)[h]_{rm,rm} + \sum\limits_{di=1}^{n_d} B(rl,di)[h]_{di,di} \quad (rl = 1,\ldots,n_r) \\ [H]_{rl,rm} = A(rl,rm)[h]_{rl,rm} \quad (rl \neq rm; \qquad rl, rm = 1,\ldots,n_r) \\ [H]_{rl,n_r+di} = B(rl,di)[h]_{rl,di} \quad (di = 1,\ldots,n_d; \qquad rl = 1,\ldots,n_r) \\ A(rl,rm) = \begin{cases} 1 & if \quad rl \quad and \quad rm \quad are \quad adjacent \quad sub-elements \\ 0 & if \quad rl \quad and \quad rm \quad are \quad not \quad adjacent \quad sub-elements \end{cases} \\ B(rl,di) = \begin{cases} 1 & if \quad di \quad is \quad within \quad sub-element \quad rl \\ 0 & if \quad di \quad is \quad not \quad within \quad sub-element \quad rl \end{cases} \end{cases} \tag{16.50}$$

$$\begin{cases} [H]_{n_r+di,n_r+di} = [h]_{di} + \sum\limits_{dj=1,dj\neq di}^{n_d} C(di,dj)[h]_{di,dj} + \sum\limits_{rl=1}^{n_r} B(di,rl)[h]_{di,di} \quad (di = 1,\ldots,n_d) \\ [H]_{n_r+di,n_r+dj} = C(di,dj)[h]_{di,dj} \quad (di \neq dj; \qquad di, dj = 1,\ldots,n_d) \\ [H]_{n_r+di,rl} = B(di,rl)[h]_{di,rl} \quad (di = 1,\ldots,n_d; \qquad rl = 1,\ldots,n_r) \\ C(di,dj) = \begin{cases} 1 & if \quad di \quad and \quad dj \quad are \quad connected \quad drainage \quad hole \\ 0 & if \quad di \quad and \quad dj \quad are \quad not \quad connected \quad drainage \quad hole \end{cases} \\ B(di,rl) = \begin{cases} 1 & if \quad sub-element \quad di \quad is \quad within \quad sub-element \quad rl \\ 0 & if \quad sub-element \quad di \quad is \quad not \quad within \quad sub-element \quad rl \end{cases} \end{cases} \tag{16.51}$$

16.6 Hierarchical Refinement

Since a composite element with drainage hole segments exhibits complicated flow pattern, its size should be sufficiently small to ensure the computation accuracy. As a result, the CE mesh will be rather tightly restricted and the advantage of the CEM could be undermined to certain extent.

The motivation to apply the p-refinement for the CEM is to enlarge the function space by upgrading the basis functions and the correspondent virtual nodes, in this way the complex flow pattern in a composite element may be handled appropriately, and the restraints on the mesh generation can be further relaxed (Chen et al. 2010a).

In the p-refinement CEM, the edge based functions, the face based functions, and the body based functions will be successively added to upgrade the order p of basis functions hierarchically. The definition of these basis functions has been given in Chap. 4. Based on the concepts of general nodes and hierarchical shape functions, the formalist algorithm for the permeability problem using the CEM elaborated foregoing sections, is held.

16.7 Validation Examples

16.7.1 Drainage Hole

(1) Characteristics of the computation

The validation study is carried out for a rock block (length 200 m $\times$ width 200 m $\times$ height 4 m) schematically illustrated in Fig. 16.11. It contains a vertical drainage hole with diameter of 0.1 m drilled from its top center. At its four vertical boundary faces the hydraulic potential is fixed to 60 m, meanwhile its top and bottom surfaces are impervious. The hydraulic potential (head) inside the drainage hole is fixed to 10 m.

The classical FEM with fine mesh (see Fig. 16.12) and the hierarchical CEM with coarse mesh (see Fig. 16.13) are carried out in parallel.

Figure 16.12 shows the FEM mesh projected on the $X-Y$ plane. The rock is discretized into solid elements, and the nodes on the drainage hole wall are defined as the first type boundary by Eq. (4.151) ($\phi_0 = 10$ m). This computation is to provide a "benchmark" for the hierarchical CEM computation.

Figure 16.13 shows the CEM mesh projected on the $X-Y$ plane. The central element is defined as the composite element containing drainage hole whose order of shape functions p can be adaptively adjusted.

The permeability coefficients adopted in the computation are $k_r = 1(\mathrm{m/d})$ and $k_d = 1000(\mathrm{m/d})$.

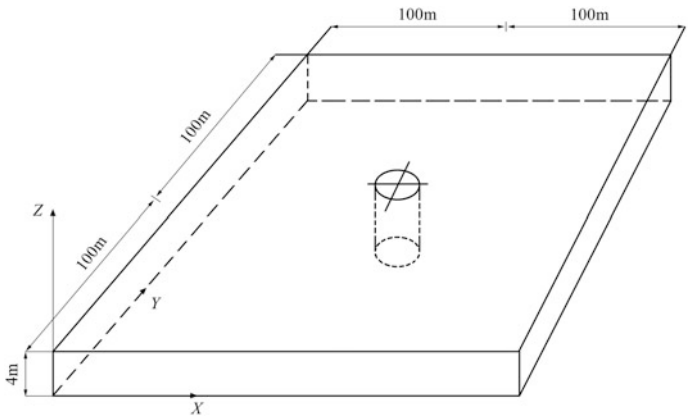

Fig. 16.11 Diagram to the computation of a drainage hole example

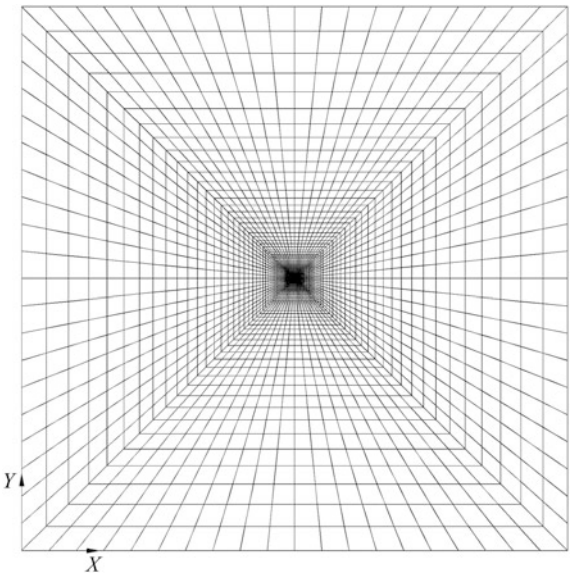

Fig. 16.12 FEM mesh (17,600 elements; 22,025 nodes)

(2) Computation results

Figure 16.14 shows the flow rate on the $X - Y$ plane by the FEM (with fine mesh). Figures 16.15, 16.16, 16.17 and 16.18 show the flow rate at the same horizontal plane by the hierarchical CEM up to $p = 4$. It is clear that by the p-refinement technique, the CEM can present very delicate flow pattern even with coarse mesh.

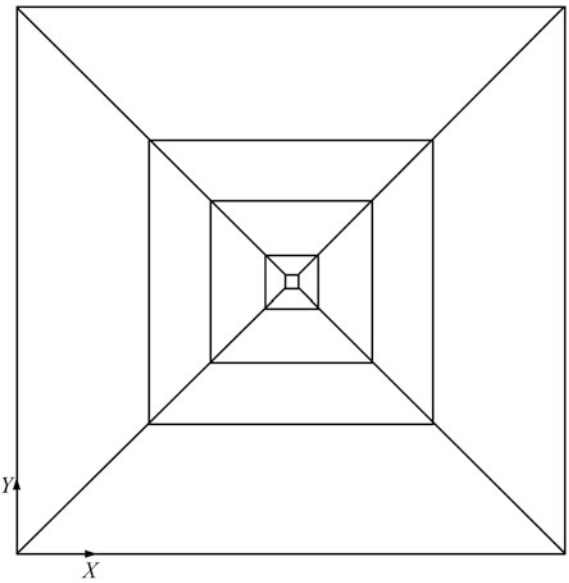

Fig. 16.13 CEM mesh (17 elements; 40 nodes)

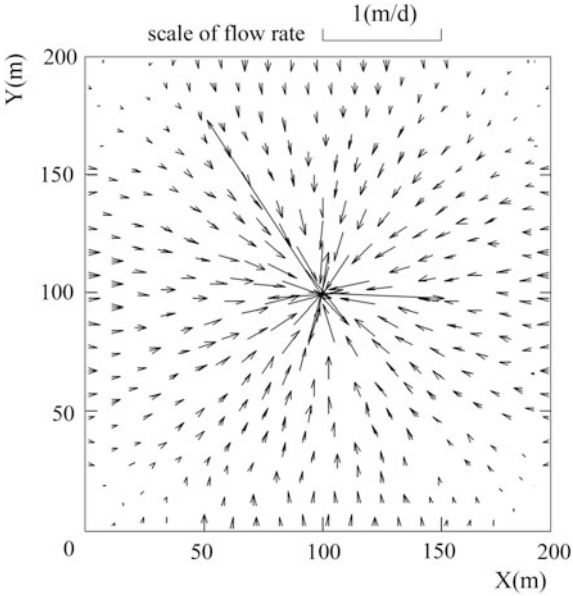

Fig. 16.14 Flow rate on the $X - Y$ plane (FEM)

16.7.2 Jointed Rock Drained by Hole

The rock block (length 15 m × width 5 m × height 2 m) schematically illustrated in Fig. 16.19 is studied using the FEM and CEM in parallel. It contains a horizontal

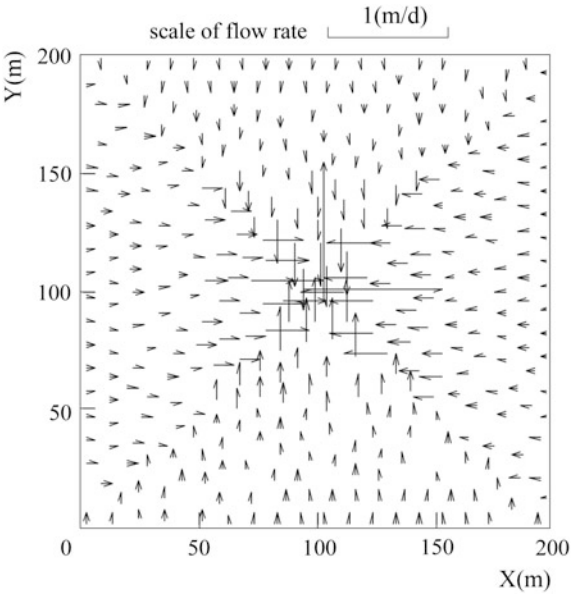

Fig. 16.15 Flow rate on the $X - Y$ plane (CEM, $p = 1$)

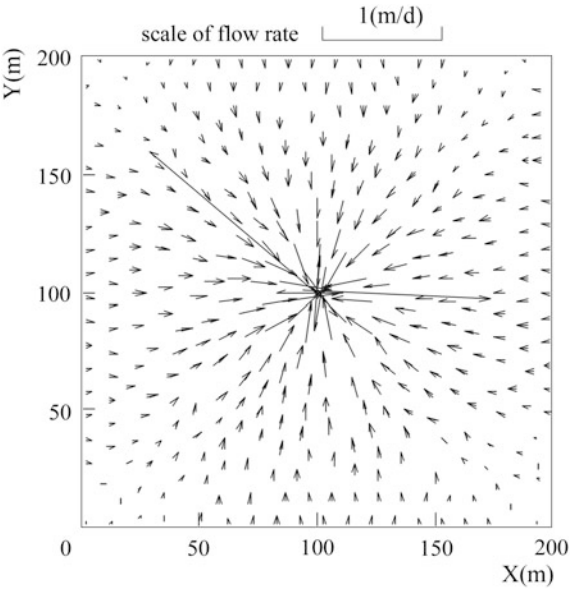

Fig. 16.16 Flow rate on the $X - Y$ plane (CEM, $p = 2$)

fault of thickness 0.1 m and a vertical drainage hole of 0.1 m in diameter. At the upstream face ($X = 0$ m) and the downstream face ($X = 15$ m) the hydraulic potential is fixed to 40 m, the other four faces are isolated without flow exchange.

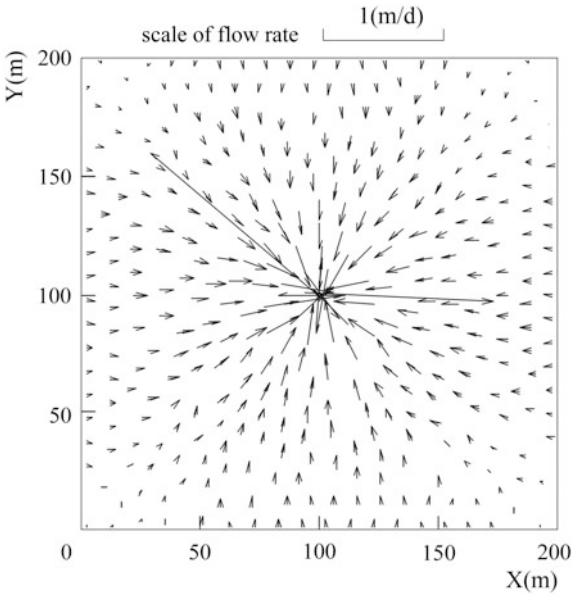

Fig. 16.17 Flow rate on the $X - Y$ plane (CEM, $p = 3$)

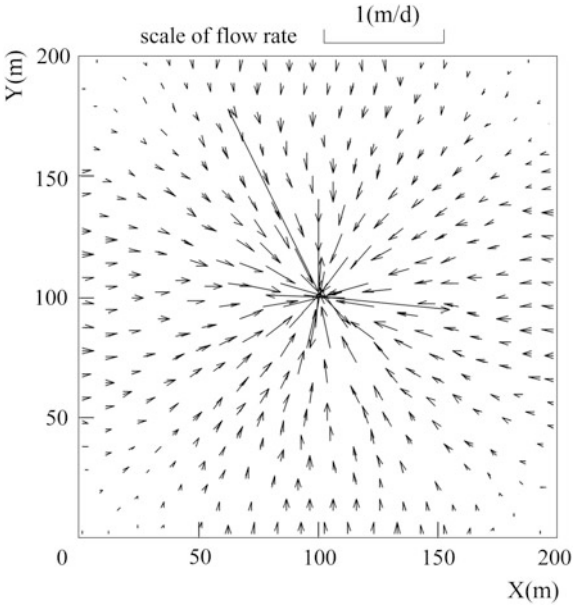

Fig. 16.18 Flow rate on the $X - Y$ plane (CEM, $p = 4$)

Figure 16.20a shows the FEM mesh, in which the rock is discretized into solid elements meanwhile the fault is explicitly discretized into joint elements. The nodes on the hole wall are defined as the first type boundary by Eq. (4.150) ($\phi_0 = 15$ m).

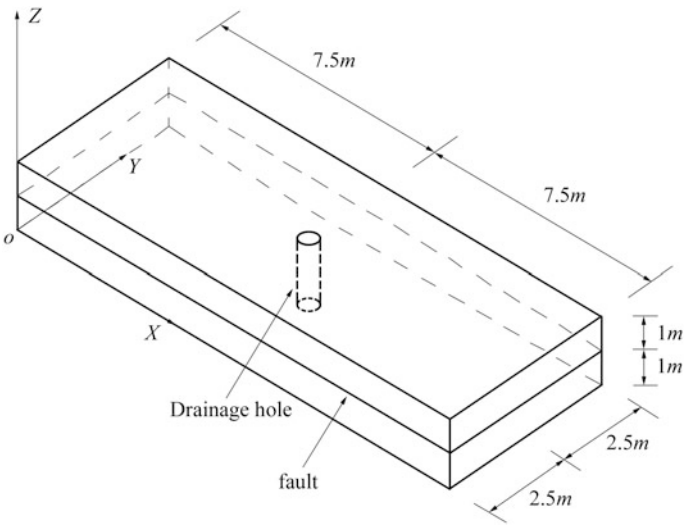

Fig. 16.19 Diagram to the computation of the jointed rock drained by a hole

This computation with fine finite element mesh is to provide a "benchmark" in the verification study.

Figure 16.20b shows the CEM mesh. The drainage hole and fault are embedded within the corresponding composite elements in lieu of explicitly discretization.

The permeability coefficients adopted in the computation are $k_r = 1.15 \times 10^{-5}(\mathrm{m/s})$ for the rock, $k_j = 1.15 \times 10^{-4}(\mathrm{m/s})$ for the fault, $k_d = 1.15 \times 10^{-2}(\mathrm{m/s})$ for the virtual material (filler) in the drainage hole.

The flow rate vectors in Figs. 16.21, 16.22, 16.23 and 16.24 confirm that the computation results by the FEM and CEM are close. It is also validated that the FEM provides a more delicately distributed flow rate field, this is mainly attributable to, on one hand, its fine element density around the fault and drainage hole; on the other hand, its counterpart CEM mobilizing a basis function order $p = 1$ only.

16.8 Engineering Applications

16.8.1 Foundation Drainage: Luohansi Sluice Project, China

(1) Presentation of the project

Built on a sandy foundation, Luohansi Sluice (see Fig. 16.25) is located on the left dyke of the Hanjiang River (Chainage 273 + 400 m), Tianmen City, Hubei Province, China. The principal purpose of this sluice is to intake the river water for

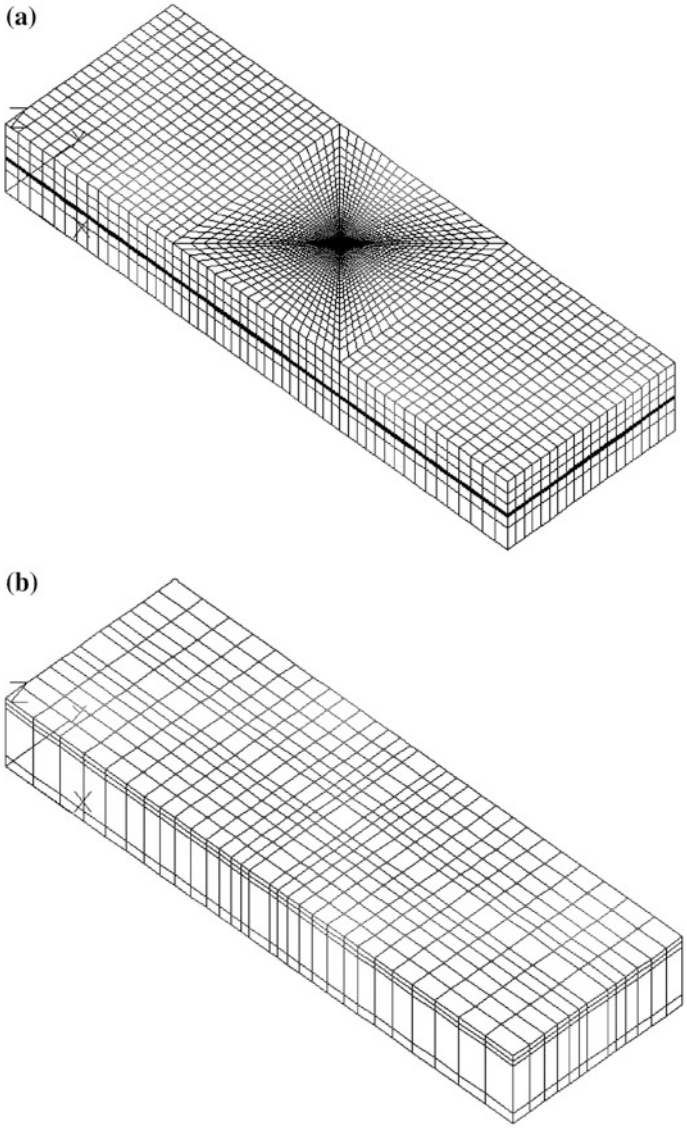

Fig. 16.20 Calculation meshes, **a** FEM (23,040 elements; 27,391 nodes); **b** CEM (1508 elements; 2100 nodes)

the irrigation canal. Since 1961, severe piping incidents in its foundation have frequently manifested. Towards the rehabilitation design of the sluice, 17 pressure relief wells were deployed at the downstream foundation of the sluice, whose functions and effects on the mitigation of piping risk were analyzed using the FEM and CEM.

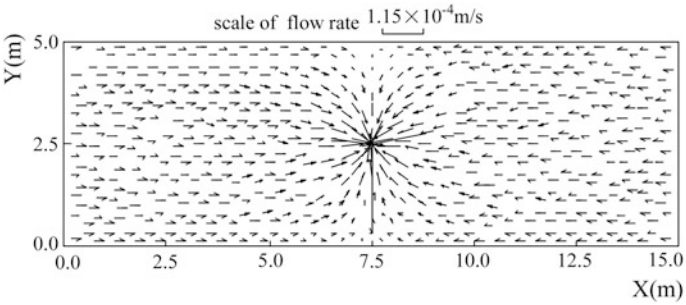

Fig. 16.21 Flow rate on the $X - Y$ plane (FEM, $Z = 1.0$ m)

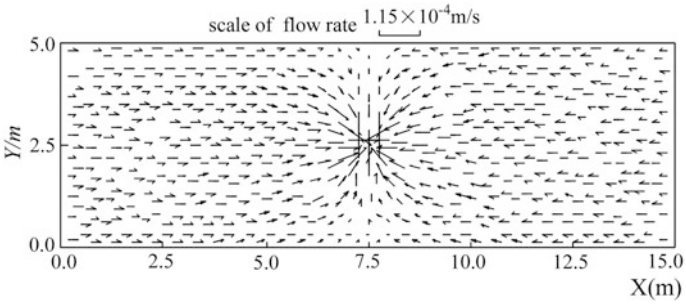

Fig. 16.22 Flow rate on the $X - Y$ plane (CEM, $Z = 1.0$ m)

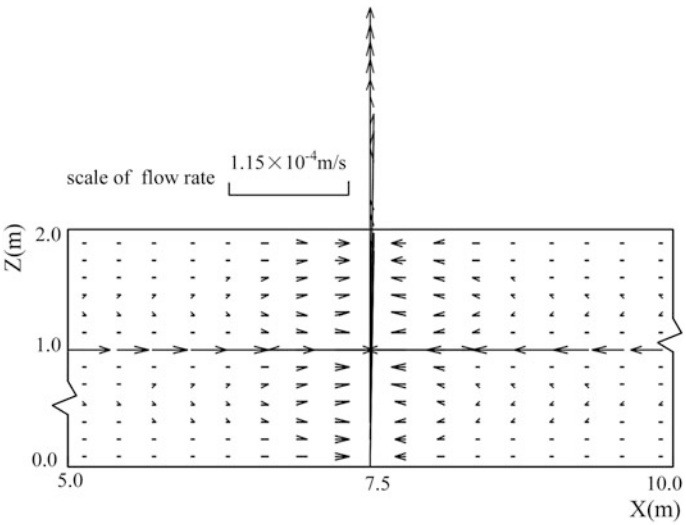

Fig. 16.23 Flow rate on the $X - Z$ plane (FEM, $Y = 2.5$ m)

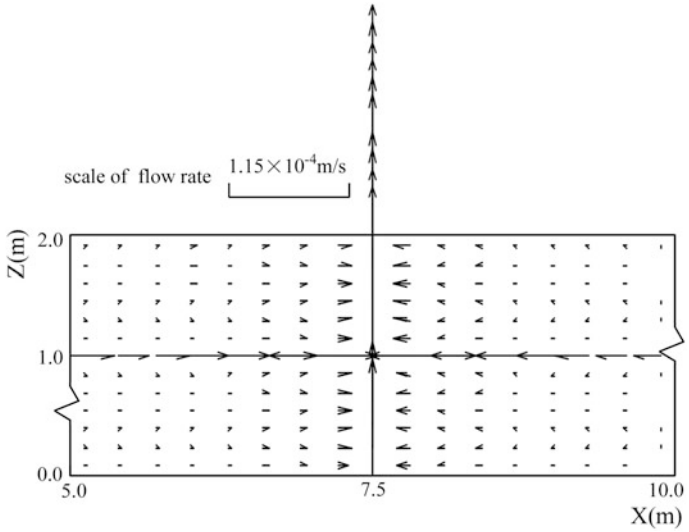

Fig. 16.24 Flow rate on the $X - Z$ plane (CEM, $Y = 2.5$ m)

Fig. 16.25 Bird eye view of Luohansi Sluice, China

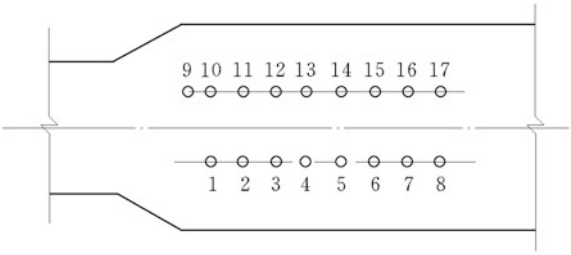

Fig. 16.26 Sequence of the relief wells

(2) Characteristics of the computation

The 17 relief wells of radium 0.127 m are installed by two arrays (see Fig. 16.26).

The soil stratum and their properties are summarized in Table 16.1.

The upstream (Hanjiang River) head water level is 45.56 m, the downstream (canal) tail water level is 34.8 m.

The computation domain is 771 m long along the canal axis and 150 m wide. The bottom is on the top of sand stone stratum.

Figure 16.27 is the FE mesh for exact solution in which the relief well wall is handled as the outflow boundary, Fig. 16.28 shows the detailed local drawing surrounding the relief wells.

Figure 16.29 is the CE mesh for the solution where the wells are filled by a virtual material of high permeable, Fig. 16.30 shows the detailed local drawing surrounding the relief wells.

(3) Computation results

Figure 16.31 plots the seepage pressure contours at the sluice base (EL.27.62 m) without pressure relief wells. Figures 16.32 and 16.33 illustrate the seepage pressure contours with pressure relief wells.

Table 16.1 Soil stratum and their properties

Soil	Distribution	Permeability coefficient (cm/s)
Earth fill	Dyke of the Hanjiang River, dyke of the canal conduit	1×10^{-6}
Clay loam	Dyke of the Hanjiang River, bottom of the sluice between EL. 24.0 and 29.6 m	1.75×10^{-5}
Fine powder sand	Bottom of the sluice between EL. 10.0 and 27.0 m	7.76×10^{-3}
Sand gravel	Bottom of the sluice between EL. 1.0 and −9.0 m	2.5×10^{-2}
Sand stone	Bottom of the sluice between EL. −2.0 and −10.0 m	1×10^{-7}
Filter material	Surrounding the relief well	4×10^{-2}

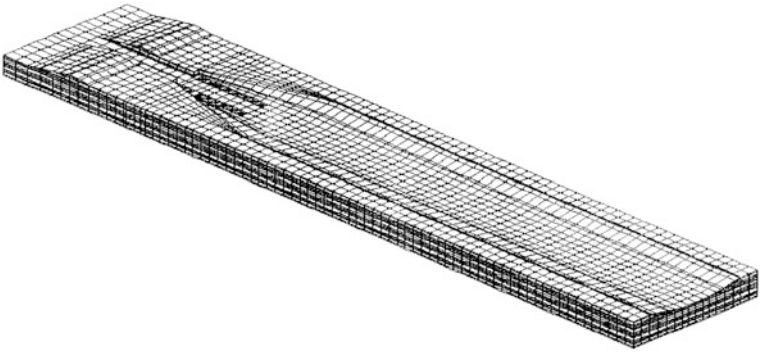

Fig. 16.27 Overall FM mesh (23,954 elements; 27,536 nodes)

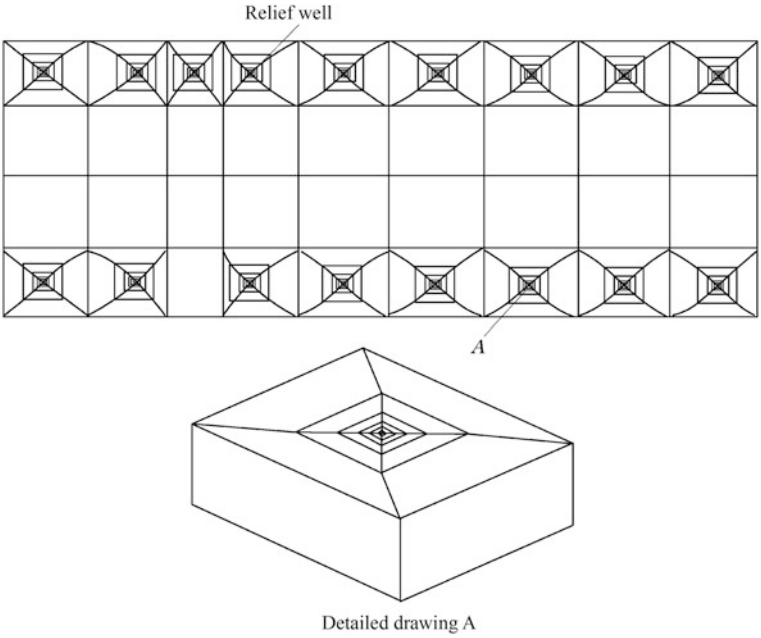

Fig. 16.28 Detailed drawing of local mesh surrounding relief wells (FE solution)

The main conclusions by the computation are that

- The pressure relief wells play an important role in the seepage stabilization for the foundation of Luohansi Sluice;
- The composite element method performs well in the simulation of the sluice foundation drained by relief well array.

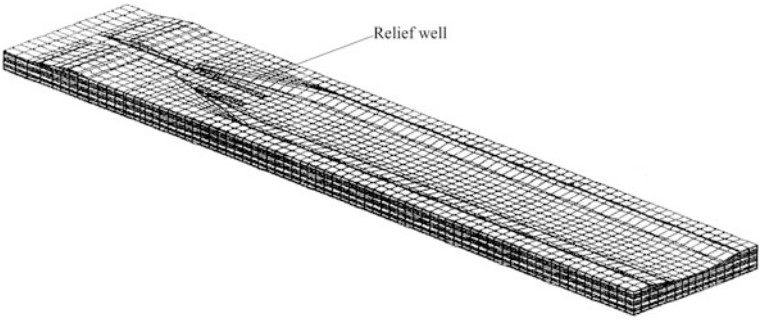

Fig. 16.29 Overall CE mesh (20,189 elements; 22,654 nodes)

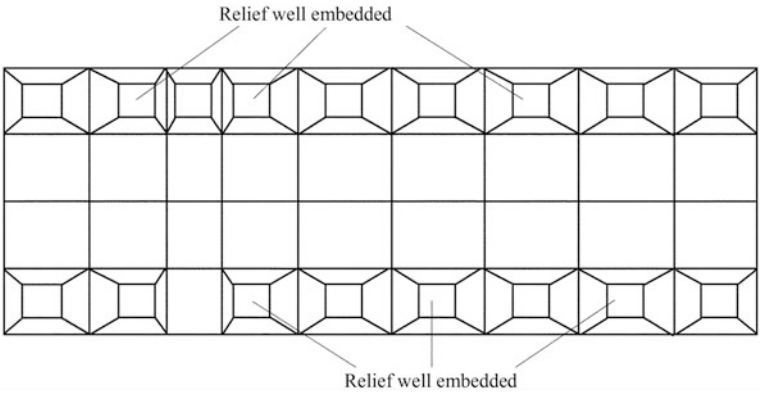

Fig. 16.30 Detailed drawing of local mesh surrounding relief wells (CE solution)

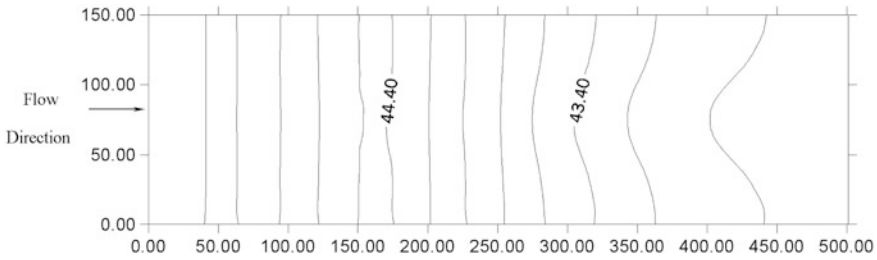

Fig. 16.31 Pressure contours at the sluice base without pressure relief wells (FEM and CEM)

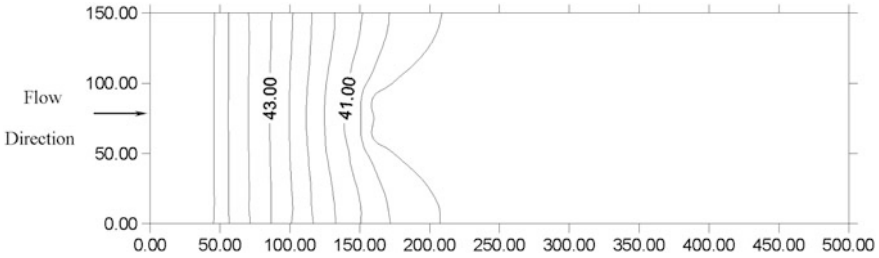

Fig. 16.32 Pressure contours at the sluice base with pressure relief wells (FEM)

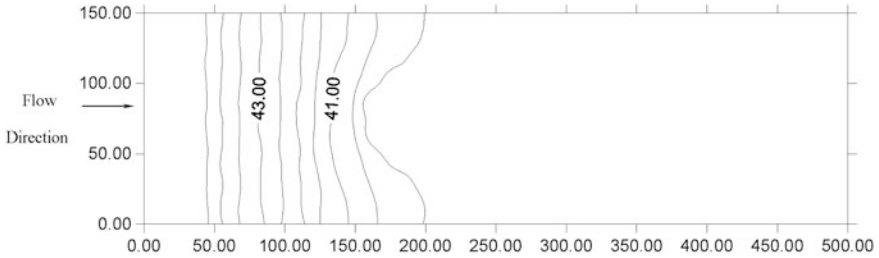

Fig. 16.33 Pressure contours at the sluice base with pressure relief wells (CEM)

16.8.2 Foundation Seepage Control: Baozhusi Project, China

(1) Presentation of the Project

Vide Chap. 9 (Sect. 9.5.1).

(2) Characteristics of the computation

The simplified profile of Baozhusi Gravity Dam with the grouting curtain and drainage curtain installed in the dam foundation is shown in Fig. 16.34. To facilitate the presentation of calculated results, local one-dimension coordinate systems of discontinuities are defined in Fig. 15.44. The permeability coefficients used in the study are given in Tables 16.2 and 16.3.

The grouting curtain is looked at as a continuous cement wall constructed by cement grouting and discretized by solid elements with small permeability coefficient (see Table 16.2). The drainage curtain is actually composed of an array of drainage hole, whose diameter and spacing are 15 cm and 3 m, respectively.

Use is made of the FEM and CEM implemented in the same program CORE3. Figure 16.35 gives the FE mesh in which the rocks and concrete are discretized with solid elements, meanwhile the faults and intercalated layers are all discretized with joint elements. The nodes on the drainage wall are defined as the first type

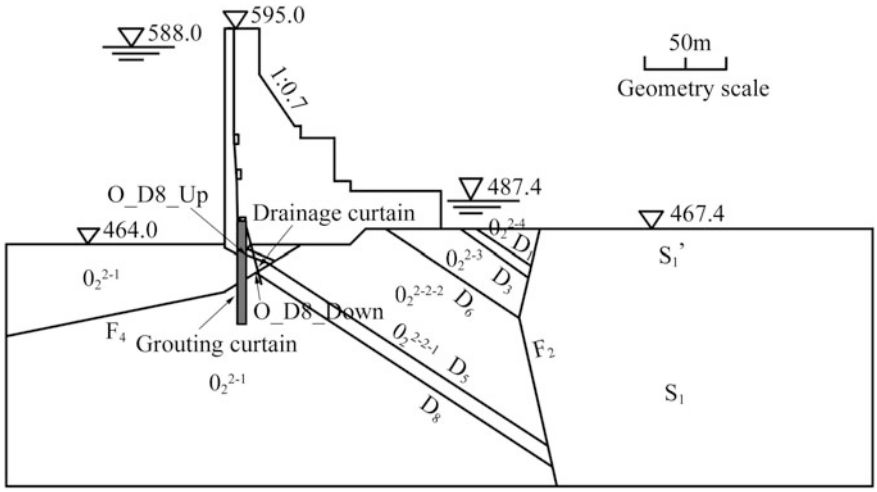

Fig. 16.34 Simplified profile of Baozhusi Gravity Dam, China

Table 16.2 Permeability coefficients of rock masses and concrete

Material	Concrete	Grouting curtain	O_2^{2-1}	O_2^{2-2-1}	O_2^{2-2-2},O_2^{2-3}	O_2^{2-4}	S_1'	S_1
Permeability $k(10^{-5}m/s)$	10^{-6}	10^{-5}	10^{-3}	10^{-3}	10^{-3}	10^{-3}	10^{-3}	10^{-3}

boundary with specified hydraulic potentials according to their positions. Figure 16.36 gives the CE mesh which contains 508 composite elements embedded by faults or/and drainage holes.

(3) Computation results

The flow velocities in the foundation (see Figs. 16.37 and 16.38), as well as the flow velocity distribution along the intercalation D_8 (see Figs. 16.39 and 16.40 where the origins for the distance along discontinuities are defined in Fig. 15.44), all demonstrate that the flow velocities obtained by the FEM and CEM agree each other well. It is also found that at the intersection points of discontinuities as well as at the intersection points of discontinuity/seepage control device, the flow velocity exhibits strong fluctuation due to the complicated flow patterns around these areas.

In Fig. 16.41 we present the uplift distribution at the dam/foundation interface. It is evident that the uplift at the dam/foundation interface by the FEM and CEM are nearly identical, and the grouting and drainage curtains perform well in the control of uplift pressure.

Table 16.3 Permeability coefficients and thicknesses of discontinuities

Discontinuity	$D_{1,3}$	D_6	$D_{7,8}$ (Upstream side of F_4)	$D_{7,8}$ (Downstream side of F_4)	D_5 (Upstream side of F_4)	D_5 (Downstream side of F_4)	F_4	F_2
Thickness (m)	0.01	0.01	0.01	0.01	0.015	0.01	0.5	1.0
Permeability k (10^{-5}m/s)	10^{-1}	10^{-1}	10^{-1}	10^{-1}	10^{-1}	10^{-1}	10^{-1}	10^{-1}

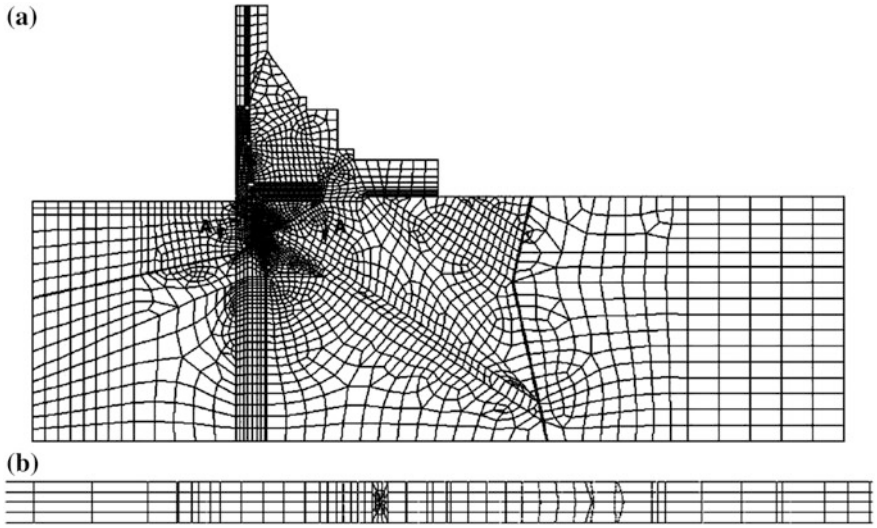

Fig. 16.35 FE mesh of Baozhusi Dam (17,552 elements; 22,307 nodes). **a** Mesh projected on the $X - Z$ plane; **b** mesh of the section A-A

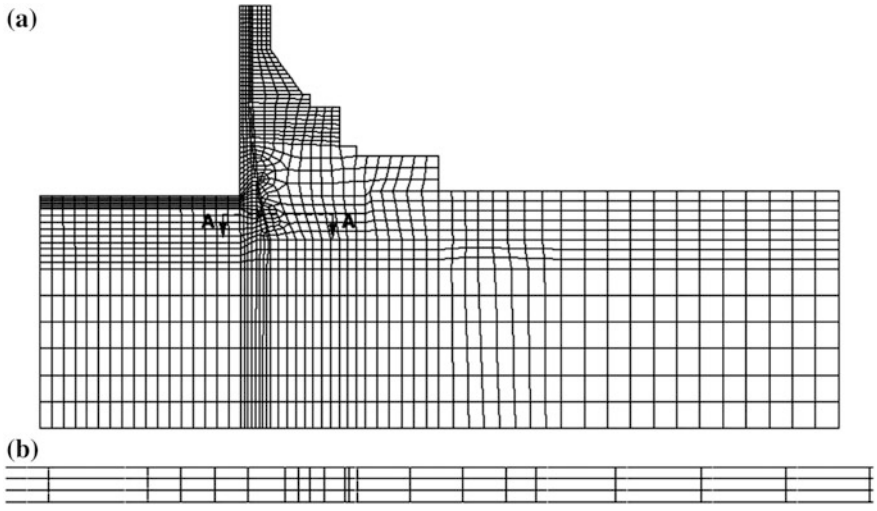

Fig. 16.36 CE mesh of Baozhusi Dam (4170 elements; 7596 nodes). **a** Mesh projected on the $X - Z$ plane; **b** mesh of the section A-A

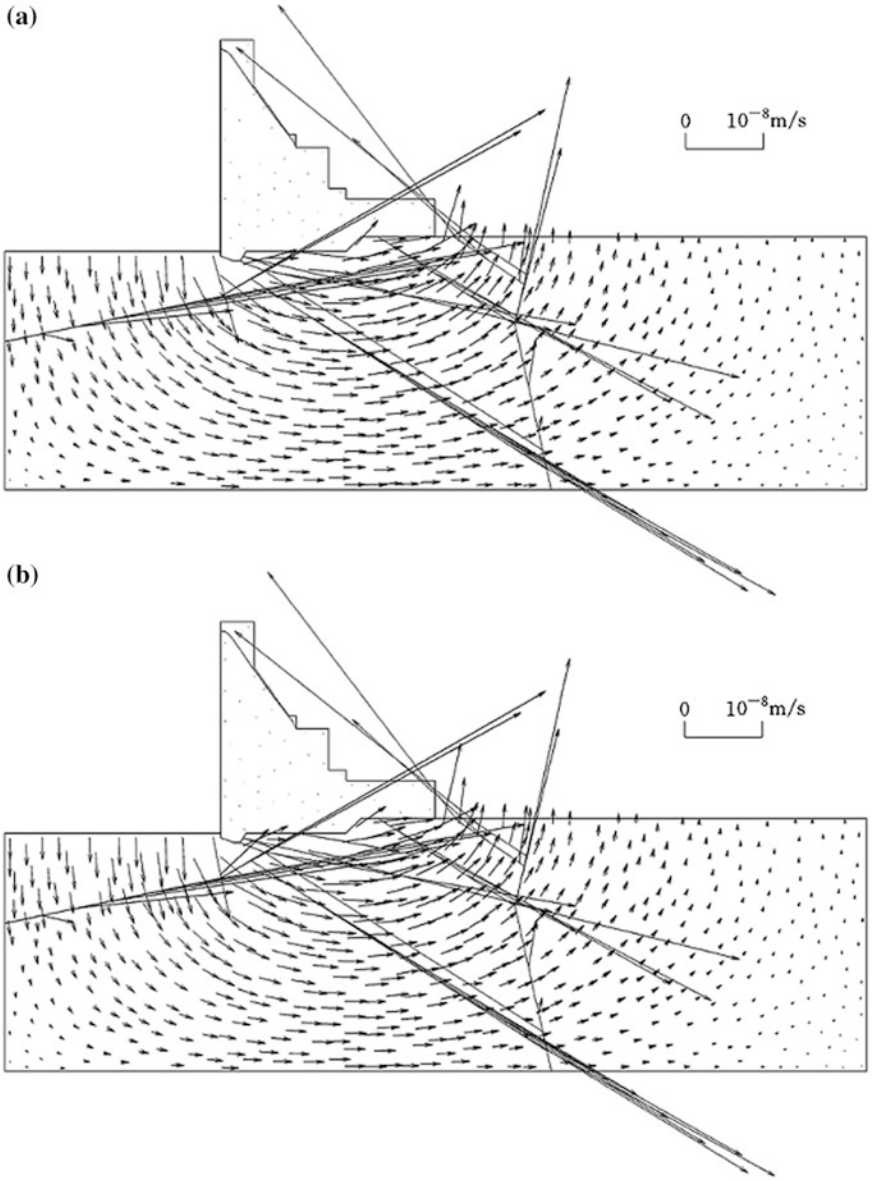

Fig. 16.37 Flow velocities without grouting and drainage curtains. **a** FEM, $Y = 1.5$ m; **b** CEM, $Y = 1.5$ m

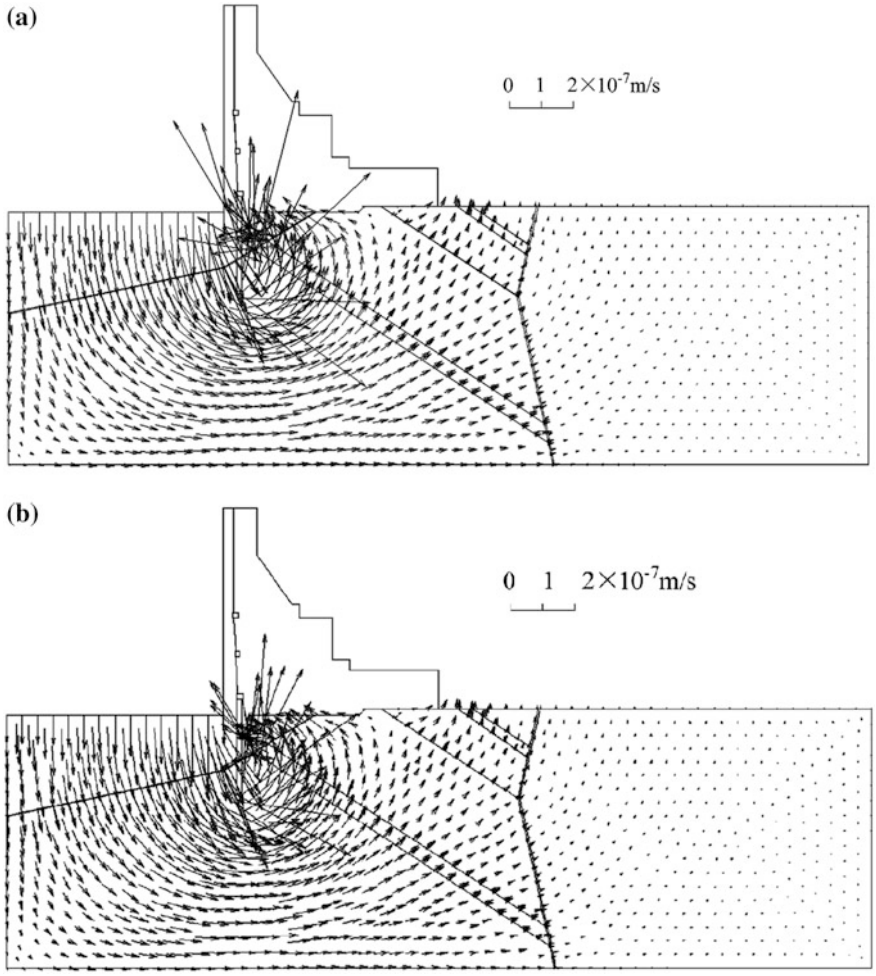

Fig. 16.38 Flow velocities with grouting and drainage curtains. **a** FEM, $Y = 1.5$ m; **b** CEM, $Y = 1.5$ m

The parameters of the PC used in this study is Intel(R) Core(TM)2 Duo CPU E7200, 2.53 GHz, memory 1.95G RAM. The computation time and the degree of freedom (DOF) are summarized in Table 16.4.

According to foregoing results, the conclusions may the derived that:

– If the result by the FEM with special elements and high mesh density is looked at as an "exact solution", the calculation error of the hydraulic potential or uplift by the CEM is below 1%, whereas the calculation error of the flow rate or velocity is approximately 10% with respect to Baozhusi Dam.

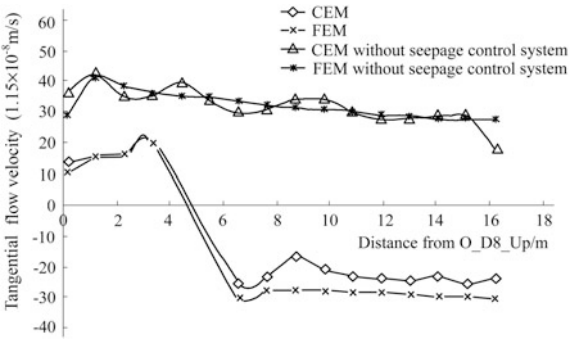

Fig. 16.39 Flow velocity distribution along the fault D_8 (upstream side of F_4)

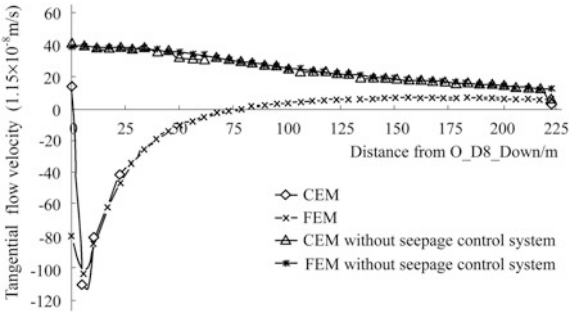

Fig. 16.40 Flow velocity distribution along the fault D_8 (downstream side of F_4)

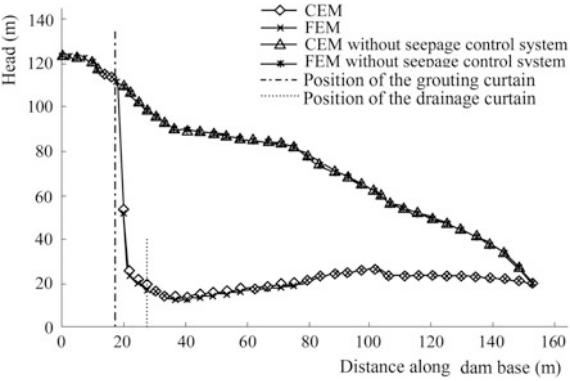

Fig. 16.41 Uplift distribution at the dam/foundation interface

Table 16.4 Computation time and DOF of Baozhusi Dam

	Degree of freedom	Computation time (s)
FEM	22,307	807.05
CEM	9951	943.23

– Since the discontinuities and drainage holes are embedded within composite elements, the computation mesh for the CEM is much simpler, and less restraint is imposed on the mesh generation for complicated hydraulic structures with considerable amount of discontinuities and drainage holes. Actually this is the paramount merit with the CEM.
– The CEM takes more CPU to complete the computation because it uses extra computation effort to replace a portion of pre-process works. This is a remarkable drawback with the CEM.

References

Chen SH, Feng XM. Composite element model for rock mass seepage flow. J Hydrodyn (Ser. B). 2006;18(2):219–24.

Chen SH, Xu Q, Hu J. Composite element method for seepage analysis of geotechnical structures with drainage hole array. J Hydrodyn (Ser. B). 2004;16(3):260–6.

Chen SH, Qin N, Xu GS, Shahrour I. Hierarchical algorithm of composite element containing drainage holes. Commun Numer Methods Eng. 2010a;26(12):1856–67.

Chen SH, Xue LL, Xu GS, Shahrour I. Composite element method for the seepage analysis of rock masses containing fractures and drainage holes. Int J Rock Mech Min Sci. 2010b;47(5):762–70.

Hu J, Chen SH. Air element method for modeling the drainage hole in seepage analysis. Rock Soil Mech. 2003;24(2):281–7 (in Chinese).

Xu GS, Chen SH. Unconfined seepage analysis with composite element method. Rock Soil Mech. 2005;26(5):745–9 (In Chinese).

Chapter 17
Thermal Analysis Using the Composite Element Method

Abstract This chapter presents a further extension of the CEM towards the mass concrete in which a large amount of cooling pipes and lift joints are embedded. The remarkable peculiarity lies in the combination of cooling pipe system or/and lift joint system with the FE mesh, the latter is generated mainly according to the structure configuration and the temperature gradient. A composite element contains several sub-elements defined by cooling pipe segments, lift joint segments, and concrete material itself. The temperature within each sub-element is interpolated from the corresponding nodal temperatures bound at its overlay composite element, which can be solved by the governing equation set established according to the variational principle for thermal field.This chapter is closed with a number of validation examples and two successful engineering application cases related to CVC and RCC dams.

17.1 General

In Chaps. 15 and 16, the composite element method (CEM) has been implemented towards the simulation of rock bolts, rock discontinuities, and drainage holes within hydraulic structures. This chapter will present a further extension towards the mass concrete with large amount of cooling pipes and lift joints embedded within the composite elements (Chen et al. 2011a, b; Ding and Chen 2013). The remarkable peculiarity lies in the combination of cooling pipe system or/and lift joint system with the FE mesh, the latter is generated mainly according to the structure configuration and the temperature gradient. A composite element contains several sub-elements defined by cooling pipe segments, lift joint segments, and concrete material itself. The temperature within each sub-element is interpolated from the corresponding nodal temperatures (see Figs. 14.8, 14.9, 14.10 and 14.11), which can be solved by the governing equations established according to the variational principle. The composite element containing cooling pipes may be retrogressed to a classical finite element automatically after the accomplishment of artificial cooling operation, and may be activated again, if necessary, where the later phase cooling is demanded.

S.-H. Chen, *Computational Geomechanics and Hydraulic Structures*,
Springer Tracts in Civil Engineering, https://doi.org/10.1007/978-981-10-8135-4_17

17.2 Cooling Pipes

17.2.1 Governing Equations

The governing equations with respect to the temperature field in a concrete structure are well known and have been elaborated in Chap. 4. The PDE in Eq. (4.176) together with the boundary conditions [see Eqs. (4.177–4.180)] or their equivalent variational operator [see Eq. (4.182)] may provide solid theoretical basis to formulate the CE algorithm in the form of

$$\delta I = 0 \tag{17.1}$$

where

$$I(T) = \iiint_{\Omega} \left(\frac{a}{2} (\{S\}T)^T (\{S\}T) + \left(\frac{\partial T}{\partial t} - \frac{\partial \theta}{\partial t} \right) T \right) d\Omega + \iint_{\Gamma_3} \bar{\beta} \left(\frac{1}{2} T^2 - T_a T \right) d\Gamma \tag{17.2}$$

In which $\{S\} = \left[\frac{\partial}{\partial X} \quad \frac{\partial}{\partial Y} \quad \frac{\partial}{\partial Z} \right]^T$ is the differential operator; $\bar{\beta} = \beta / c\rho$, β is the surface exothermic coefficient, ρ is the material density and c is specific heat; θ = adiabatic temperature rise; a = thermal diffusivity; T_a = temperature of the water or air; λ = thermal conductivity.

1. Sub-element analysis

Firstly, a FE mesh should be generated to discretize the structure concerned. The sizes of the finite elements are mainly dependent on the structure configuration and temperature gradient. Then the presence of cooling pipes transfers a number of finite elements into composite elements (Fig. 14.8) through geometrical calculation.

For the cooling water and pipe, the local Cartesian and Cylindrical systems are needed to simplify the formulation of algorithm (see Fig. 2.7). The subscript $j_{c,wi}$ will be employed to indicate the pipe (as an interface) between the concrete sub-element c and the water sub-element wi. The superscripts ca and cy are employed to denote the variables in the local Cartesian and Cylindrical coordinate systems, if necessary.

There are independent nodal temperatures for the concrete and the cooling water sub-elements assembled as a elementary vector $\{T\} = \left[\{T\}_c^T, \{T\}_{w1}^T, \{T\}_{w2}^T, \ldots, \{T\}_{n_w}^T \right]^T$ bound at the composite element, which can be used for the temperature interpolations within the sub-elements (see Figs. 14.5, 14.6, 14.7 and 14.8).

(1) Concrete sub-element c

According to Eq. (17.2) the variational function for the concrete sub-element c may be directly expressed as

$$I(T)_c = \iiint_{\Omega_c} \left(\frac{a_c}{2} (\{S\}T_c)^T (\{S\}T_c) + \left(\frac{\partial T_c}{\partial t} - \frac{\partial \theta_c}{\partial t} \right) T_c \right) d\Omega + \iint_{\Gamma_3} \bar{\beta} \left(\frac{1}{2} T_c^2 - T_a T_c \right) d\Gamma \tag{17.3}$$

(2) Cooling water sub-element *wi*

The hydration and boundary effects are neglected for the cooling water in the pipe. Since the temperature is a scalar, the variational function for the cooling water sub-element *wi* may be expressed in the local Cylindrical coordinate system as

$$I(T)_{wi} = \iiint_{\Omega_{wi}} \left(\frac{a_{wi}}{2} (\{S\}^{cy} T_{wi})^T (\{S\}^{cy} T_{wi}) + \frac{\partial T_{wi}}{\partial t} T_{wi} \right) d\Omega_{wi} \quad (wi = 1, 2, \ldots, n_w) \tag{17.4}$$

In which $\{S\}^{cy} = \left[\frac{\partial}{\partial r} \quad \frac{1}{r}\frac{\partial}{\partial \omega} \quad \frac{\partial}{\partial z} \right]^T$ is the differential operator at the local Cylindrical coordinate system.

(3) Cooling pipe sub-element p_i

Looked at as a concrete/water interface $j_{c,wi}$ between the concrete sub-element *c* and water sub-element *wi*, there is no independent nodal temperature for cooling pipe sub-element p_i. We substitute for the differential of the temperature potential within this interface by the difference in the nodal temperatures correspondent to the concrete and cooling water respectively [see Eq. (14.6)], the variational function of the cooling pipe can be written as

$$I(T)_{j_{c,wi}} = \iiint_{\Omega_{j_{c,wi}}} \left(\frac{a_{j_{c,wi}}}{2} \left(\{S\}^{cy} T_{j_{c,wi}} \right)^T \left(\{S\}^{cy} T_{j_{c,wi}} \right) + \frac{\partial T_{j_{c,wi}}}{\partial t} T_{j_{c,wi}} \right) d\Omega \quad (j_{c,wi} = 1, 2, \ldots, n_w) \tag{17.5}$$

Since the thickness t_p of the pipe is rather smaller compared to its diameter, it can be postulated that along the pipe thickness we have

$$\left(\{S\}^{cy} T_{j_{c,wi}} \right) = const. \quad (j_{c,wi} = 1, 2, \ldots, n_w) \tag{17.6}$$

Thus Eq. (17.5) can be transformed to

$$\begin{aligned} I(T)_{j_{c,wi}} &= \iiint_{\Omega_{j_{c,wi}}} \left(\frac{a_{j_{c,wi}}}{2} \left(\{S\}^{cy} T_{j_{c,wi}} \right)^T \left(\{S\}^{cy} T_{j_{c,wi}} \right) + \frac{\partial T_{j_{c,wi}}}{\partial t} T_{j_{c,wi}} \right) r dr d\omega dz \\ &= R t_p \iint_{\Gamma_{j_{c,wi}}} \left(\frac{a_{j_{c,wi}}}{2} \left(\{S\}^{cy} T_{j_{c,wi}} \right)^T \left(\{S\}^{cy} T_{j_{c,wi}} \right) + \frac{\partial T_{j_{c,wi}}}{\partial t} T_{j_{c,wi}} \right) d\omega dz \\ &\quad (j_{c,wi} = 1, 2, \ldots, n_w) \end{aligned} \tag{17.7}$$

In which R is the radius of the cooling pipe.

Additional assumption is further made that in the local Cylindrical coordinate system, the differential of the temperature within the interface will be

$$\begin{cases} \frac{\partial T_{j_{c,wi}}}{\partial r} = \frac{T_c - T_{wi}}{t_p} \\ \frac{1}{r}\frac{\partial T_{j_{c,wi}}}{\partial \omega} = 0 \\ \frac{\partial T_{j_{c,wi}}}{\partial z} = 0 \end{cases} \quad (j_{c,wi} = 1, 2, \ldots, n_w) \tag{17.8}$$

Thus Eq. (17.7) becomes

$$I(T)_{j_{c,wi}} = Rt_p \iint\limits_{\Gamma_{j_{c,wi}}} \left(\frac{a_{j_{c,wi}}}{2} \begin{pmatrix} \frac{T_c - T_{wi}}{t_p} \\ 0 \\ 0 \end{pmatrix}^T \begin{pmatrix} \frac{T_c - T_{wi}}{t_p} \\ 0 \\ 0 \end{pmatrix} + \frac{\partial (T_c + T_{wi})}{2\partial t} \frac{(T_c + T_{wi})}{2} \right) d\omega dz$$

$$(j_{c,wi} = 1, 2, \ldots, n_w) \tag{17.9}$$

2. Composite element analysis

Taking into account of Eqs. (17.3), (17.4) and (17.9), the variational function of the composite element containing n_w cooling pipes is specified below

$$\begin{aligned} I(T) &= I(T)_c + \sum_{i=1}^{n_w} I(T)_{wi} + \sum_{j_{c,wi}=1}^{n_w} I(T)_{j_{c,wi}} \\ &= \iiint\limits_{\Omega_c} \left(\frac{a_c}{2} (\{S\}T_c)^T (\{S\}T_c) + \left(\frac{\partial T_c}{\partial t} - \frac{\partial \theta_c}{\partial t} \right) T_c \right) d\Omega \\ &\quad + \iint\limits_{\Gamma_3} \bar{\beta} \left(\frac{1}{2} T_c^2 - T_a T_c \right) d\Gamma \\ &\quad + \sum_{i=1}^{n_w} \iiint\limits_{\Omega_{wi}} \left(\frac{a_{wi}}{2} (\{S\}^{cy} T_{wi})^T (\{S\}^{cy} T_{wi}) + \frac{\partial T_{wi}}{\partial t} T_{wi} \right) d\Omega \\ &\quad + Rt_p \sum_{j_{c,wi}=1}^{n_w} \iint\limits_{\Gamma_{j_{c,wi}}} \left(\frac{a_{j_{c,wi}}}{2} \left(\{S\}^{cy} T_{j_{c,wi}} \right)^T \left(\{S\}^{cy} T_{j_{c,wi}} \right) + \frac{\partial T_{j_{c,wi}}}{\partial t} T_{j_{c,wi}} \right) d\omega dz \end{aligned} \tag{17.10}$$

Introducing Eq. (14.5) into Eq. (17.10) firstly, then let $\partial I(T)/\partial \{T\}_c = 0$ and $\partial I(T)/\partial \{T\}_{wi} = 0$, finally we discretize the time domain t by implicit differential scheme to produce

$$\begin{cases} \left([H]_c + \sum\limits_{i=1}^{n_w} [H]_{j_{c,wi}}\right)\{T\}_{c,t} - \sum\limits_{i=1}^{n_w} [h]_{j_{c,wi}}\{T\}_{wi,t} = \{f\}_c \\ \left([H]_{w1} + [H]_{j_{c,w1}}\right)\{T\}_{w1,t} - [h]_{j_{c,w1}}\{T\}_{c,t} = \{f\}_{w1} \\ \cdots \\ \left([H]_{wi} + [H]_{j_{c,wi}}\right)\{T\}_{wi,t} - [h]_{j_{c,wi}}\{T\}_{c,t} = \{f\}_{wi} \\ \cdots \\ \left([H]_{n_w} + [H]_{j_{c,n_w}}\right)\{T\}_{n_w,t} - [h]_{j_{c,n_w}}\{T\}_{c,t} = \{f\}_{n_w} \end{cases} \tag{17.11}$$

where

$$\begin{cases} [H]_c = [K]_c + [R]_c + \frac{1}{\Delta\tau}[C]_c \\ [H]_{j_{c,wi}} = [K]_{j_{c,wi}} + \dfrac{[C]_{j_{c,wi}}}{\Delta t} \\ [h]_{j_{c,wi}} = [K]_{j_{c,wi}} - \dfrac{[C]_{j_{c,wi}}}{\Delta t} \\ \{f\}_c = \frac{1}{\Delta t}[C]_c\{T\}_{c,t-\Delta t} + \{F\}_c + \sum\limits_{i=1}^{n_w}\left(\dfrac{[C]_{j_{c,wi}}}{2\Delta t}\{T\}_{c,t-\Delta t} + \dfrac{[C]_{j_{c,wi}}}{2\Delta t}\{T\}_{wi,t-\Delta t}\right) \\ [H]_{wi} = [K]_{wi} + \frac{1}{\Delta t}[C]_{wi} \\ \{f\}_{wi} = \frac{1}{\Delta t}[C]_{wi}\{T\}_{wi,t-\Delta t} + \dfrac{[C]_{j_{c,wi}}}{2\Delta t}\{T\}_{c,t-\Delta t} + \dfrac{[C]_{j_{c,wi}}}{2\Delta t}\{T\}_{wi,t-\Delta t} \quad (wi = 1, \ldots n_w) \end{cases} \tag{17.12}$$

In which $\{T\}_{c,t-\Delta t}$ and $\{T\}_{w,t-\Delta t}$ are the nodal temperatures at time $t - \Delta t$ corresponding to the concrete and cooling water, and

$$\begin{cases} [K]_c = \iiint\limits_{\Omega_c} a_c([S][N])^T([S][N])\, d\Omega \\ [R]_c = \iint\limits_{\Gamma_3} \bar{\beta}[N]^T[N]\, d\Gamma_3 \\ [C]_c = \iiint\limits_{\Omega_c} [N]^T[N]\, d\Omega \\ [K]_{j_{c,wi}} = \dfrac{Ra_{j_{c,wi}}}{t_p}\iint\limits_{\Gamma_{j_{c,wi}}} [N]^T[N]\, d\omega dz \\ [C]_{j_{c,wi}} = \dfrac{Rt_p}{2}\iint\limits_{\Gamma_{j_{c,wi}}} [N]^T[N]\, d\omega dz \\ [K]_{wi} = \iiint\limits_{\Omega_{wi}} a_{wi}([S]^{cy}[N])^T([S]^{cy}[N])\, d\Omega \\ [C]_{wi} = \iiint\limits_{\Omega_{wi}} [N]^T[N]\, d\Omega \\ \{F\}_c = \iiint\limits_{\Omega_c} \dfrac{\partial\theta_c}{\partial t}[N]\, d\Omega + \iint\limits_{\Gamma_3} \bar{\beta}T_a[N]\, d\Gamma \end{cases} \tag{17.13}$$

Equation (17.11) may be further assembled into the global governing equation of the structure system according to the connection among nodes following a similar way of the FEM.

17.2.2 Simplification of the Governing Equations

(1) Simplification step 1

In view that the element size should be very small to simulate concrete placement procedure by lifts, it is desirable and feasible to discretize the CE mesh in a way that each composite element contains one cooling pipe segment only. In this manner Eqs. (17.11–17.13) can be simplified as

$$\left([K]_c+[R]_c+\frac{1}{\Delta t}[C]_c+[K]_{j_{c,w}}+\frac{[C]_{j_{c,w}}}{\Delta t}\right)\{T\}_{c,t}-\left([K]_{j_{c,w}}-\frac{[C]_{j_{c,w}}}{\Delta t}\right)\{T\}_{w,t}$$
$$=\frac{1}{\Delta t}[C]_c\{T\}_{c,t-\Delta t}+\{F\}_c+\frac{[C]_p}{2\Delta t}\{T\}_{c,t-\Delta t}+\frac{[C]_p}{2\Delta t}\{T\}_{w,t-\Delta t} \tag{17.14}$$

$$\left([K]_w+\frac{1}{\Delta t}[C]_w+[K]_{j_{c,w}}+\frac{[C]_{j_{c,w}}}{\Delta t}\right)\{T\}_{w,t}-\left([K]_{j_{c,w}}-\frac{[C]_{j_{c,w}}}{\Delta t}\right)\{T\}_{c,t}$$
$$=\frac{1}{\Delta t}[C]_w\{T\}_{w,t-\Delta t}+\left(\frac{[C]_p}{2\Delta t}\{T\}_{w,t-\Delta t}+\frac{[C]_p}{2\Delta t}\{T\}_{c,t-\Delta t}\right) \tag{17.15}$$

(2) Simplification step 2

The further simplification can be made if the temperature of cooling water is regarded as a separated variable which may be evaluated independently. In this manner, respectively summation of the both sides of Eqs. (17.14) and (17.15) leads to

$$\left([K]_c+[R]_c+\frac{1}{\Delta t}[C]_c+\frac{2[C]_{j_{c,w}}}{\Delta t}\right)\{T\}_{c,t}=\left(\frac{1}{\Delta t}[C]_c+\frac{[C]_{j_{c,w}}}{\Delta t}\right)\{T\}_{c,t-\Delta t}$$
$$+\left(\frac{1}{\Delta t}[C]_w+\frac{[C]_{j_{c,w}}}{\Delta t}\right)\{T\}_{w,t-\Delta t}+\{F\}_c-\left([K]_w+\frac{1}{\Delta t}[C]_w+\frac{2[C]_{j_{c,w}}}{\Delta t}\right)\{T\}_{w,t} \tag{17.16}$$

(3) Simplification step 3

It is also reasonable to postulate that the temperature of the cooling water inside the pipe segment of one composite element is uniformly distributed (i.e. without spatial variation), hence Eq. (17.16) can be simplified as

$$\left([K]_c+[R]_c+\frac{1}{\Delta t}[C]_c+\frac{2[C]_{j_{c,w}}}{\Delta t}\right)\{T\}_{c,t}=\{F\}_c$$
$$+\left(\frac{1}{\Delta t}[C]_c+\frac{[C]_{j_{c,w}}}{\Delta t}\right)\{T\}_{c,t-\Delta t}+\left(\frac{1}{\Delta t}[C]_w+\frac{1}{\Delta t}[C]_{j_{c,w}}\right)\{I\}T_{w,t-\Delta t} \quad (17.17)$$
$$-\left([K]_w+\frac{1}{\Delta t}[C]_w+\frac{2[C]_{j_{c,w}}}{\Delta t}\right)\{I\}T_{w,t}$$

In which $\{I\}$ is the unit vector.

(4) Simplification step 4

Figure 17.1 is the cooling pipe schematically sketched as a straight line. This pipe is discretized into segments sequentially embedded within adjacent composite elements (e). Suppose at any time t the inlet temperature of the cooling water $T^0_{w,t}$ is known, the water temperature increment $\Delta T^e_{w,t}$ of the cooling pipe segment located in the composite element e is given by the heat balance principle

$$c_w\rho_w q_w\Delta T^e_{w,t}=-\lambda\int\frac{\partial T}{\partial r}\,dt \quad (17.18)$$

or

$$\Delta T^e_{w,t}=-\frac{\lambda}{c_w\rho_w q_w}\int\frac{\partial T}{\partial r}\,dt \quad (17.19a)$$

In which c_w, ρ_w, q_w are the specific heat, density and flow rate of the cooling water respectively; λ is the thermal conductivity from concrete to running water. Since the radial temperature gradient may be calculated by $\frac{\partial T}{\partial r}=\frac{T_{c,t-\Delta t}-T_{w,t-\Delta t}}{t_p}$, so we have

$$\Delta T^e_{w,t}=-\frac{\lambda}{c_w\rho_w q_w}\times\frac{T_{c,t-\Delta t}-T_{w,t-\Delta t}}{t_p}\,\Delta t \quad (17.19b)$$

In which t_p is the thickness of pipe.

The cooling water temperatures at composite elements $e+1$ and e are therefore related by

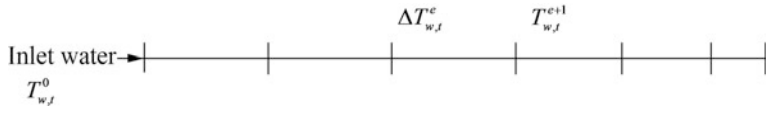

Fig. 17.1 Temperature variation along a cooling pipe

$$T_{w,t}^{e+1} = T_{w,t}^{e} + \Delta T_{w,t}^{e} \tag{17.20}$$

The cooling water temperatures calculated by Eqs. (17.19) and (17.20) are then introduced in Eq. (17.17) for the solution of concrete temperature $\{T\}_{c,t}$.

17.3 Lift Joints

17.3.1 Segmental Form of Variational Function

In Fig. 14.11 all the nodal temperatures of n_c sub-elements bound at the composite element are assembled as one nodal temperature vector $\{T\} = [\{T\}_{c1}^T, \{T\}_{c2}^T, \ldots, \{T\}_{n_c}^T]^T$. The temperature T_{ci} in each sub-element is interpolated by Eq. (14.7).

In the following discussion the subscripts ci and $j_{cl,cm}$ will be employed to denote the concrete sub-element and the lift joint segment between concrete sub-elements cl and cm, respectively.

A global coordinate system (X, Y, Z) is used to formulate the overall governing equations. For each lift joint segment $j_{cl,cm}$, a local coordinate system is defined in Fig. (2.2). The coordinate transformation between the global and local coordinate systems is identically defined in Eqs. (2.12) and (2.13).

The differential equation for the thermal field [see Fig. (4.176)] in a composite element containing n_c sub-elements can be written in a segmental form

$$\frac{\partial T_{ci}}{\partial t} = a_{ci}\left(\frac{\partial^2 T_{ci}}{\partial^2 X} + \frac{\partial^2 T_{ci}}{\partial^2 Y} + \frac{\partial^2 T_{ci}}{\partial^2 Z}\right) + \frac{\partial \theta_{ci}}{\partial t} \quad (i = 1, \ldots, n_c) \tag{17.21}$$

which is subject to appropriate initial condition

$$T_{ci} = T_0 \quad (i = 1, \ldots, n_c) \tag{17.22}$$

and boundary conditions

$$T_{ci} = T_b|_{\Gamma_1} \quad (i = 1, \ldots, n_c) \tag{17.23}$$

$$-\lambda \frac{\partial T_{ci}}{\partial n} = \beta_a (T_{ci} - T_a)|_{\Gamma_3} \quad (i = 1, \ldots, n_c) \tag{17.24}$$

$$-\lambda\left(\frac{\partial T_{ci}}{\partial n}\right) = \frac{1}{R_c}\left(T_{ci} - T_{ci+1}\right)\big|_{j_{ci,ci+1}} = \beta_c\left(T_{ci} - T_{ci+1}\right)\big|_{j_{ci,ci+1}} \quad (i = 1, \ldots, n_c - 1) \tag{17.25}$$

In Eqs. (17.21–17.25), n is the external normal direction to the boundary or lift joint, θ is the adiabatic temperature rise, a is the thermal diffusivity, λ is the thermal conductivity, c is the specific heat, β_a is the concrete surface exothermic coefficient, R_c is the thermal resistance between concrete, T_a is the ambient air temperature, T_b is the reservoir water temperature.

The variational function corresponding to Eqs. (17.21–17.25) is

$$\begin{aligned} I(T)_{c_i} = & \iiint_{\Omega_{ci}} \left\{ \frac{a_{ci}}{2} (\{S\}T_{ci})^T (\{S\}T_{ci}) + \left(\frac{\partial T_{ci}}{\partial t} - \frac{\partial \theta_{ci}}{\partial t} \right) T_{ci} \right\} d\Omega \\ & + \iint_{\Gamma_3} \bar{\beta}_a \left(\frac{1}{2} T_{ci}^2 - T_a T_{ci} \right) d\Gamma \\ & + \iint_{j_{ci,ci+1}} \bar{\beta}_{ci} \left(\frac{1}{2} T_{ci}^2 - T_{ci+1} T_{ci} \right) d\Gamma \\ & + \iint_{j_{ci,ci-1}} \bar{\beta}_{ci} \left(\frac{1}{2} T_{ci}^2 - T_{ci-1} T_{ci} \right) d\Gamma \quad (ci = 1, \ldots, n_c) \end{aligned} \tag{17.26}$$

In which $\{S\} = \left[\frac{\partial}{\partial X} \quad \frac{\partial}{\partial Y} \quad \frac{\partial}{\partial Z} \right]^T$ is the differential operator; $\bar{\beta}_a = \frac{\beta_a}{c\rho}$ and $\bar{\beta}_c = \frac{1}{R_c c \rho}$, ρ is the material density and c is the specific heat.

17.3.2 Governing Equations of the Composite Element Containing Lift Joints

Introducing Eq. (14.7) into Eq. (17.26), then let $\delta I(T)_{c_i} = 0$ followed by the finite difference approximation in the time domain t, we have

$$\begin{aligned} & \left([K]_{ci} + [R]_{ci} + [K]_{ci,ci-1} + [K]_{ci,ci+1} + \frac{1}{\Delta t} [C]_{ci} \right) \{T\}_{ci,t} - [K]_{ci,ci-1} \{T\}_{ci-1,t} \\ & - [K]_{ci,ci+1} \{T\}_{ci+1,t} = \frac{1}{\Delta t} [C]_{ci} \{T\}_{ci,t-\Delta t} + \{F\}_{ci,t} \quad (ci = 1, \ldots, n_c) \end{aligned} \tag{17.27}$$

In which

$$\begin{cases} [K]_{ci} = \iiint\limits_{\Omega_{ci}} a_{ci}(\{S\}[N])^T(\{S\}[N])\, d\Omega \\ [K]_{ci,ci-1} = \iint\limits_{\Gamma_{j_{ci,ci-1}}} \bar{\beta}_{ci}[N]^T[N]\, d\Gamma \\ [K]_{ci,ci+1} = \iint\limits_{\Gamma_{j_{ci,ci+1}}} \bar{\beta}_{ci}[N]^T[N]\, d\Gamma \\ [R]_{ci} = \iint\limits_{\Gamma_3} \bar{\beta}_a[N]^T[N]\, d\Gamma \\ [C]_{ci} = \iiint\limits_{\Omega_{ci}} [N]^T[N]\, d\Omega \\ \{F\}_{ci,t} = \iiint\limits_{\Omega_{ci}} \frac{\partial \theta_{ci}}{\partial t}[N]\, d\Omega + \int\limits_{\Gamma_3} \bar{\beta}_a T_a[N]\, d\Gamma \quad (ci = 1, \ldots, n_c) \end{cases} \tag{17.28}$$

where $[K]_{ci}$ is the heat stiffness (conduction and convection) matrix contributed from sub-element ci itself, $[K]_{ci,ci+1}$ and $[K]_{ci,ci-1}$ are the heat stiffness matrices of sub-element ci contributed from sub-elements $ci+1$ and $ci-1$ through lift joints $j_{ci,ci+1}$ and $j_{ci,ci-1}$ respectively, $[R]_{ci}$ is the convection matrix of sub-element ci, $[C]_{ci}$ is the capacitance matrix of sub-element ci, $\{F\}_{ci}$ is the heat load vector due to the hydration and convection actions of sub-element ci.

By considering the contribution from the n_c sub-elements given in Eqs. (17.27) and (17.28), the governing equations of the composite element containing n_c lifts can be simply constructed as

$$\begin{bmatrix} [H]_{c1,c1} & \cdots & [H]_{c1,ci} & \cdots & [H]_{c1,n_c} \\ \cdots & \cdots & \cdots & \cdots & \cdots \\ [H]_{ci,c1} & \cdots & [H]_{ci,ci} & \cdots & [H]_{ci,n_c} \\ \cdots & \cdots & \cdots & \cdots & \cdots \\ [H]_{n_c,c1} & \cdots & [H]_{n_c,c_i} & \cdots & [H]_{n_c,n_c} \end{bmatrix} \begin{Bmatrix} \{T\}_{c1,t} \\ \cdots \\ \{T\}_{ci,t} \\ \cdots \\ \{T\}_{n_c,t} \end{Bmatrix} = \begin{Bmatrix} \frac{1}{\Delta t}[C]_{c1}\{T\}_{c1,t-\Delta t} + \{F\}_{c1,t} \\ \cdots \\ \frac{1}{\Delta t}[C]_{ci}\{T\}_{ci,t-\Delta t} + \{F\}_{ci,t} \\ \cdots \\ \frac{1}{\Delta t}[C]_{n_c}\{T\}_{n_c,t-\Delta t} + \{F\}_{n_c,t} \end{Bmatrix} \tag{17.29}$$

where

$$\begin{cases} [H]_{ci,ci} = \left([K]_{ci} + [R]_{ci} + [K]_{ci,ci-1} + [K]_{ci,ci+1} + \frac{1}{\Delta t}[C]_{ci} \right) \quad (ci = 2, \ldots, n_c - 1) \\ [H]_{c1,c1} = \left([K]_{c1} + [R]_{c1} + [K]_{c1,c2} + \frac{1}{\Delta t}[C]_{c1} \right) \\ [H]_{n_c,n_c} = \left([K]_{n_c} + [R]_{n_c} + [K]_{n_c,n_c-1} + \frac{1}{\Delta t}[C]_{n_c} \right) \\ [H]_{ci,cj} = \begin{cases} -[K]_{ci,cj} & (j \neq i) \ \ if \ \ ci \ \ and \ \ cj \ \ are \ \ contacted \\ 0 & (j \neq i) \ \ if \ \ ci \ \ and \ \ cj \ \ are \ \ not \ \ contacted \end{cases} \end{cases} \tag{17.30}$$

Equation (17.29) is further assembled with that of other finite elements or composite elements to form the overall governing equation of the structure system. Any composite element contains no lift joint will be retrogressed to the classical finite element automatically.

17.4 Verifications and Applications

17.4.1 Concrete Block Containing a Single Cooling Pipe

This verification study is carried out on the concrete block (1 m in width) illustrated in Fig. 17.2. At its center, a cooling pipe with inner diameter of 0.014 m and outer diameter of 0.016 m is embedded. The parameters used in the computation are: initial temperature of the casted concrete $T_0 = 0$ °C, cooling water temperature $T_w = 0$ °C, $\alpha = 0.0040$ m^2/h, $\lambda_1 = 1.66$ kJ/(m h °C), $\theta(t) = 25(1 - e^{-0.35t})$. All the boundary surfaces are isolated.

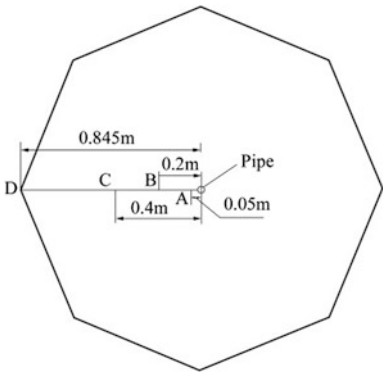

Fig. 17.2 Concrete block containing one cooling pipe

The standard FEM with fine mesh and the CEM with two mesh refinements are generated for the study.

Figure 17.3 shows the FEM mesh projected on the $X - Z$ plane. The concrete is discretized into solid elements, and the nodes on the inner wall of the cooling pipe are defined as the first type boundary [$T_b = 0$ °C in Eq. (4.178)]. This computation is intended to provide a "benchmark" for the CEM computation.

Figure 17.4 shows the fine and coarse CEM meshes projected on the $X - Z$ plane, where the central element is defined as the composite element containing a cooling pipe.

Figure 17.5 displays the history of the temperature averaged over the whole concrete block. It agrees well to the analytical solution (Zhu 1998). Figures 17.6,

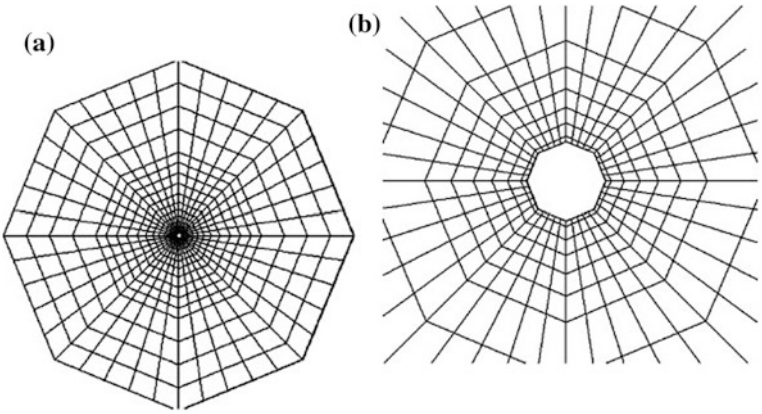

Fig. 17.3 FE mesh projected on the $X - Z$ plane (3800 elements; 4800 nodes). **a** Overall view; **b** detailed view near the cooling pipe

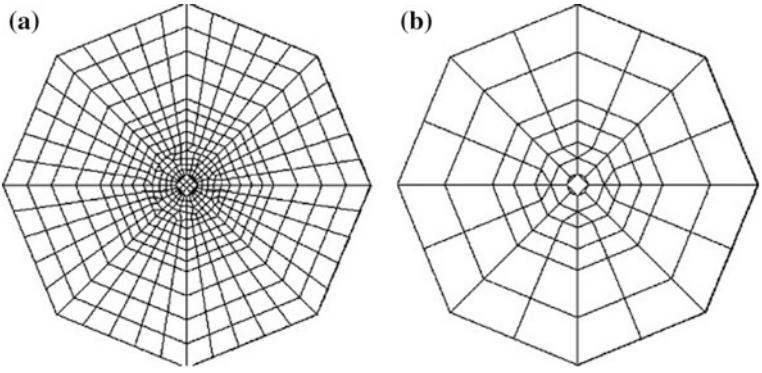

Fig. 17.4 CE mesh projected on the $X - Z$ plane. **a** Fine mesh 1 (514 elements; 1052 nodes); **b** coarse mesh 2 (29 elements; 64 nodes)

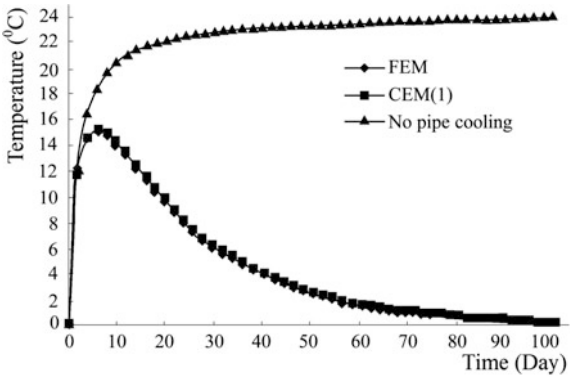

Fig. 17.5 History of the temperature averaged over the whole concrete block

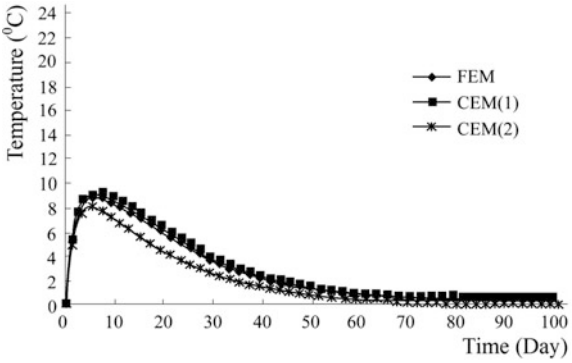

Fig. 17.6 Temperature history at point A

17.7, 17.8 and 17.9 present the temperature histories of typical points A, B, C, D (see Fig. 17.2). It can be found that:

- The nearer to the cooling pipe, the lower is the peak temperature, and the faster is the temperature drop.
- The density of composite elements has remarkable influence on the computation accuracy, especially in the vicinity of the cooling pipe.

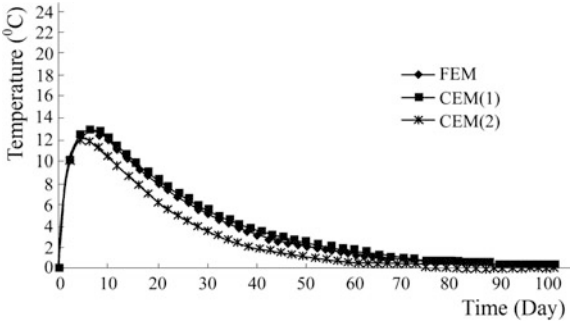

Fig. 17.7 Temperature history at point B

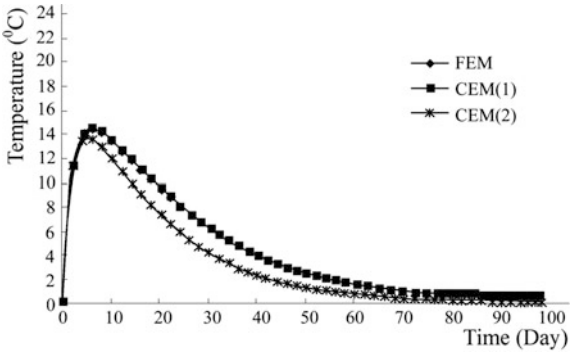

Fig. 17.8 Temperature history at point C

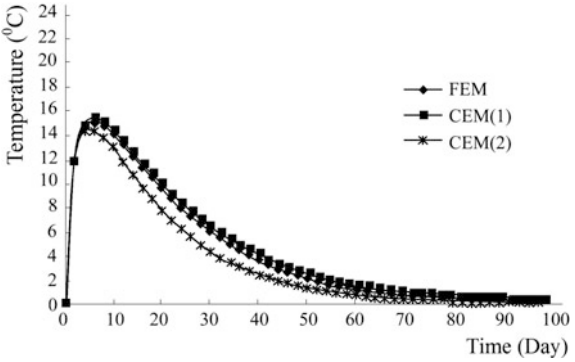

Fig. 17.9 Temperature history at point D

17.4.2 Concrete Block Containing a Single Lift Joint

The size of the concrete block is 10.0 m × 2.0 m × 1.0 m (length × width × height), at $Z = 0.5$ m there is a horizontal lift joint with thickness of 0.05 m (see Fig. 17.10). Two cases are studied to show the precision of the CEM using simpler mesh in contrast to its counterpart FEM using fine mesh with thin-layer elements for the lift joint.

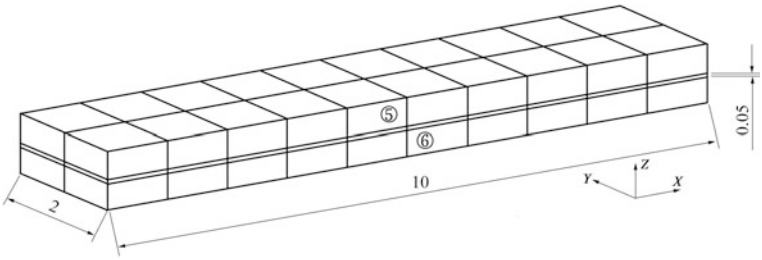

Fig. 17.10 Finite element mesh of case 1 (60 elements; 132 nodes)

(1) Case 1

The initial temperature of the upper lift is 10 °C, and that of the lower lift is 20 °C. All the boundaries are isolated, and hydration heat is not considered.

Figure 17.10 shows the finite element mesh in which the lift joint is discretized by the thin-layer elements of 0.05 m thick. This computation is intended to provide a "benchmark" for the CEM computation. Figure 17.11 shows the composite element mesh. It contains 66 nodes and 20 elements with the lift joint embedded at their horizontal center.

The conductivity coefficient λ of the concrete and lift joint are 200 and 100 kJ/(m.d.) respectively. The thermal resistance R_c is trialed from 0.1 to 0.01 until 0.001 (m^2 h °C/kJ), respectively. The temperature history at the center of the concrete block represented by points ① (CEM) and ⑤ (FEM) is displayed in Fig. 17.12, which validates that a thermal resistance R_c = 0.01 (m^2 h °C/kJ) gives rise to the best agreement between the FEM and CEM.

Figures 17.13 and 17.14 present the temperature history at the dual points located at the vicinity sides of the lift joint (see Figs. 17.10 and 17.11). It can be found that the temperature gradient between two lifts will be lowered down as the ongoing of the time, and the final stable (static) temperature of the whole concrete block is exactly the average of the initial temperature over the two lifts.

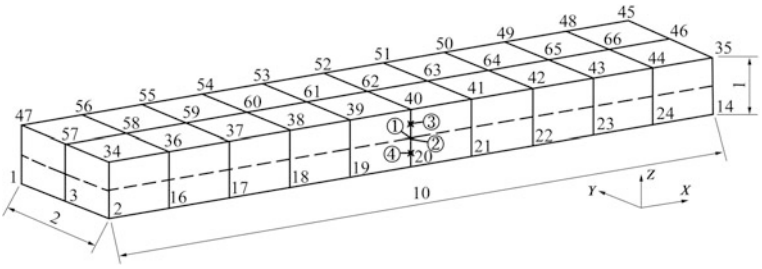

Fig. 17.11 Composite element mesh of case 1 (20 elements; 66 nodes)

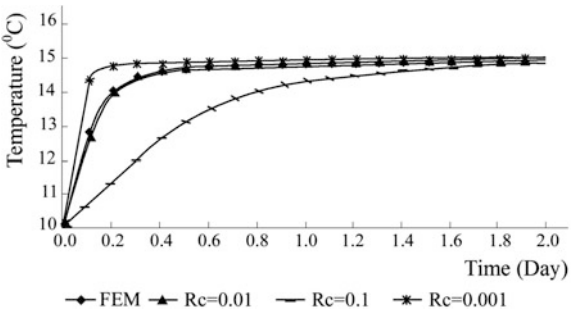

Fig. 17.12 Temperature history at the center of concrete versus thermal resistance R_c

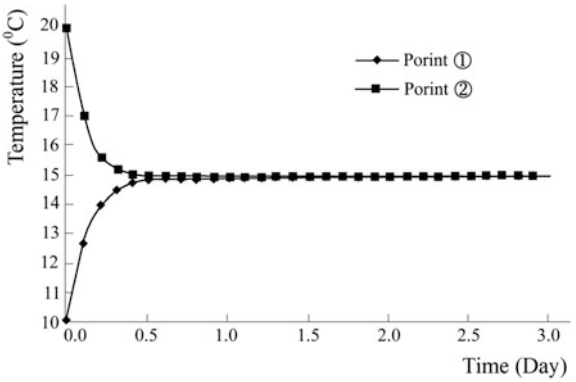

Fig. 17.13 Temperature history at dual points ① and ② (CEM)

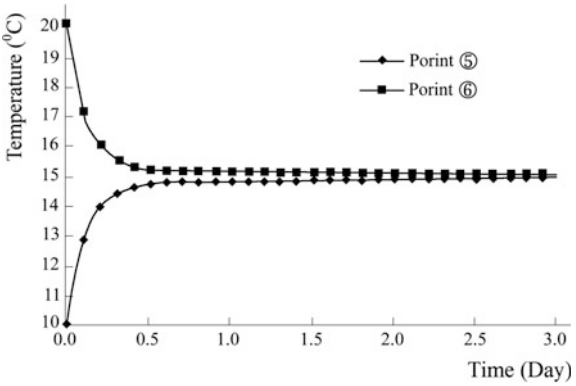

Fig. 17.14 Temperature history at dual points ⑤ and ⑥ (FEM)

(2) Case 2

Suppose the lower concrete lift is old with stable temperature of 20 °C. At initial time $t = 0$ the upper lift is placed with initial temperature 10 °C and with the adiabatic temperature rise given by

$$\theta = 22.42\tau/(2.8 + \tau) \tag{17.31}$$

Figure 17.15 illustrates the temperature history at dual points ① and ②, ③ and ④ (see Fig. 17.11), from which the following phenomena can be observed.

- Point ①. The temperature is influenced both by the old concrete below and the hydration heat of itself. It mounts fast at the beginning, as the time goes on it slows down until to the stable temperature.
- Point ②. The temperature drops first, which is due to the lower placing (initial) temperature of the upper lift. Then the temperature climbs again pushed by the hydration heat from the upper lift.

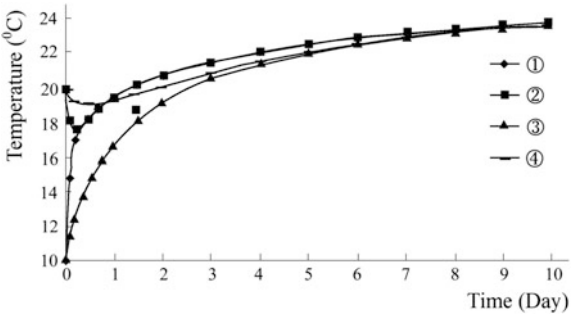

Fig. 17.15 Temperature history at dual points ① and ②, ③ and ④

– Points ③ and ④. The temperature histories at these dual points are similar to that at points ① and ②, but their temperature fluctuations are not so strong, which is attributable to their longer distance from the lift joint.

17.4.3 CVC Arch Dam: Xiaowan Project, China

1. Presentation of the project

Vide Chap. 8.

2. Characteristics of the computation

(1) CE mesh

Among many technical problems need to cope with, the simulation of temperature field is crucial one in each design phase of Xiaowan Arch Dam. It is related to many factors such as the ambient conditions, cooling schemes (see Fig. 17.16), construction and impounding schedules and so on. A 3D model for the 22# dam monolith is presented herein towards the simulation and feedback analysis of the thermal field during the construction period, which is intended to support the design of temperature control and cracking countermeasures.

The 22# dam monolith is simulated from the first concrete batch at base (EL.950.5 m) until the pouring elevation of 1050 m. The CE model is constructed by 452,760 elements and 474,057 nodes, of which 43,846 are composite elements containing cooling pipe segments (see Fig. 17.17). The arrangement of cooling pipes in the CE mesh is illustrated in Fig. 17.18.

(2) Thermal parameters

According to the laboratory test and statistical regression, the thermal parameters of the initially designed concrete are listed in Table 8.5.

Fig. 17.16 Layout of cooling pipes on the lift of dam monolith 22#

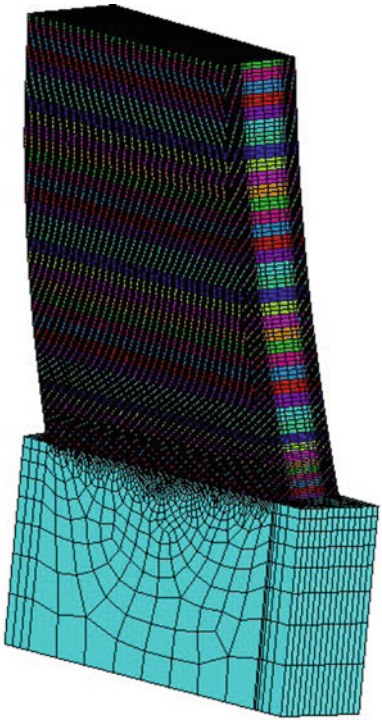

Fig. 17.17 CE mesh of dam monolith 22# (452,760 elements; 474,057 nodes)

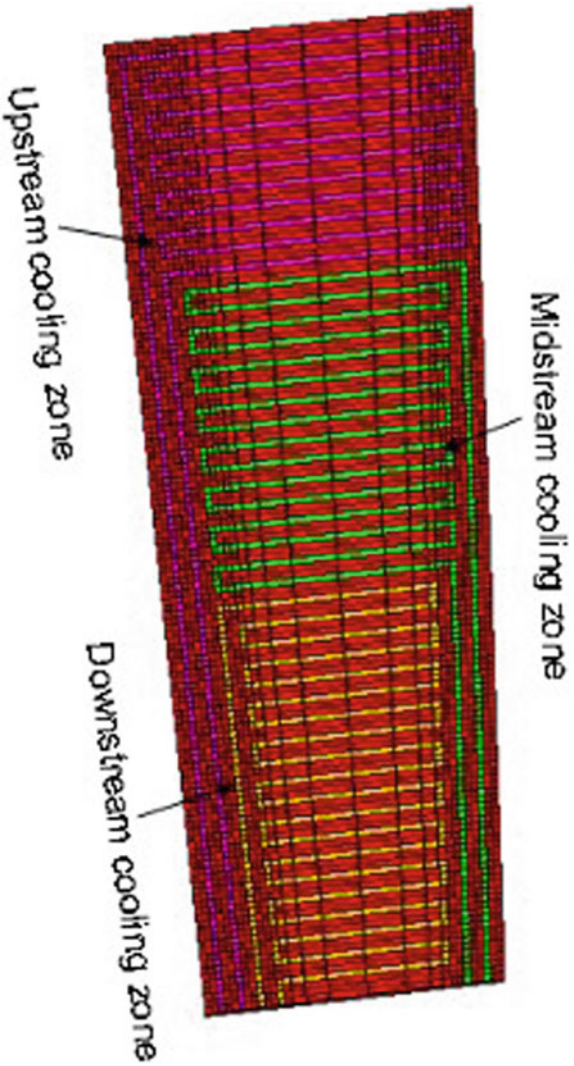

Fig. 17.18 Layout of cooling pipes in dam monolith 22#

(3) Construction schedule

The pouring process of dam monolith 22# is implemented according to Fig. 17.19.

(4) Air temperature

According to the observed data of the meteorological station at Xiaowan Dam site (Fig. 17.20), the air temperature is fitted by the formula

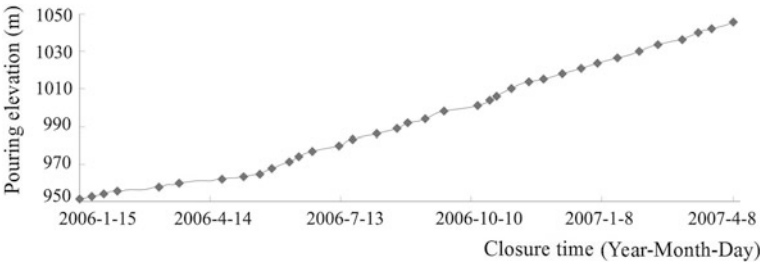

Fig. 17.19 Pouring process of dam monolith 22#

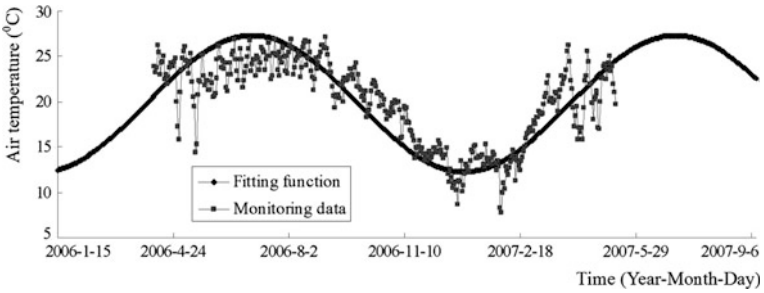

Fig. 17.20 Air temperature history at Xiaowan Dam site

$$T = 19.784 + 7.54 \times \cos[0.0172 \times (t - 169)] \tag{17.32}$$

In which t is the last time (day) from the date 2006-01-15.

(5) Cooling scheme

The specific requirements of Xiaowan Arch Dam for cooling pipes are:

- Material. The metal pipes [the coefficient of thermal conductivity is 262.8 kJ/(m h °C)], and the plastic cooling pipes [the coefficient of thermal conductivity is 1.66 kJ/(m h °C)] are selectively used for cooling.
- Arrangement. Snakelike arrangement is implemented for the layout of cooling pipes, their spacing is 1.5 m × 1.5 m (horizontal × vertical) in restrained zones and 1.5 m × 3.0 m (horizontal × vertical) in unrestrained zones.
- Water. The water flux is 1.3–1.5 m^3/h for single pipe and its flow direction is reverted per 24 h.
- Standard of the first phase cooling. The highest temperature is controlled below 29 °C in the first cooling, the target temperature is 18–20 °C at the end of the first cooling phase. The cooling operation is undertaken within 15–25 days.
- Standard of the second phase cooling. The second cooling phase should be started 45 days before the joint grouting for the arch dam closure, where the cooling water temperature is 6–8 °C, the water flux is 1.2–1.4 m^3/h.

3. Computation results

(1) Parametric inversion

In the inverse (back) analysis for the adiabatic temperature rise, the formula $\theta = \theta_0\tau/(\tau + n)$ is generally applicable. However, we find that the formula $\theta = \theta_0(1 - e^{-m\tau})$ is able to fit the temperature rise better after the second cooling phase. Related parameters by the inverse analysis are summarized in Table 17.1.

The inversion for cooling parameters shows that in the first cooling, the actual cooling water temperature is 7–9 °C and the cooling duration is 18–22 days; while in the second cooling, the actual cooling water temperature is 9–11 °C and the cooling duration is 20–30 days.

(2) Contrast between the computation and monitoring data

There are instrumentation points systematically layout in the 22# dam monolith at different elevations. The typical points at the EL.975 m, EL.1005.5 m, and EL.1030 m are selected for the contrast study (see Figs. 17.21, 17.22, 17.23 and 17.24).

It can be seen that the calculation results are nearly identical to the monitoring data. During the concrete pouring period, the temperature mounts rapidly. Due to the first cooling, the temperature gradually steps down afterwards. Then in the suspension period from the finish of the first cooling phase to the start of the second cooling phase, the concrete temperature rise resumes to a certain extent. In the second cooling, the concrete temperature is further significantly reduced, and after the second cooling, there is solely a minor temperature fluctuation.

Table 17.1 Thermal parameters by the inverse analysis

Grade	Adiabatic temperature rise before secondary cooling θ (°C)	Adiabatic temperature rise after secondary cooling θ (°C)
C40	$\theta = 30\tau/(3.8 + \tau)$ (design)	$\theta = 6.0(1 - e^{-0.006\tau})$ (inversion)
	$\theta = 30.4\tau/(3.92 + \tau)$ (inversion)	

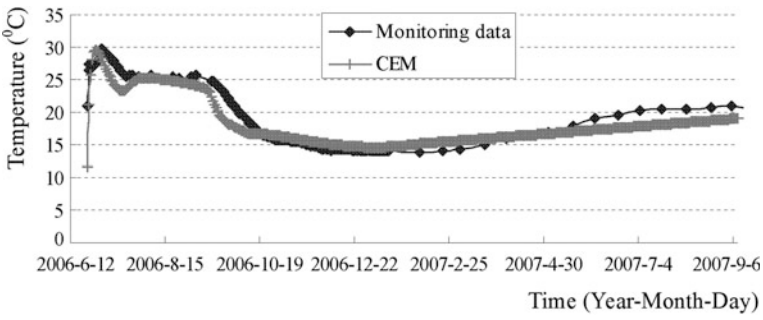

Fig. 17.21 Temperature history at point A (0.1 m from upstream dam surface at EL.975 m)

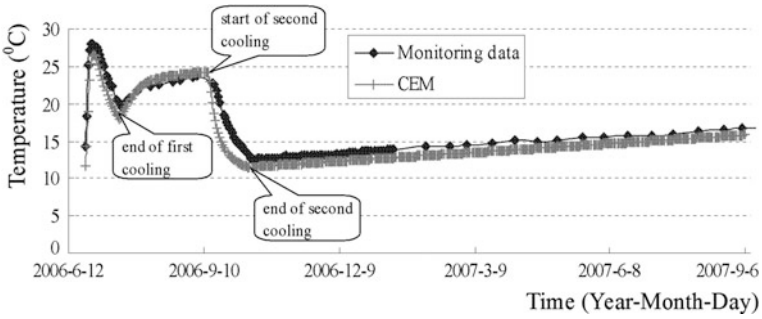

Fig. 17.22 Temperature history at point B (31 m from upstream dam surface at EL.975 m)

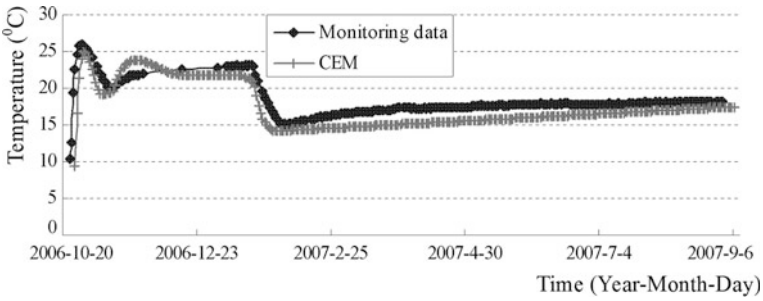

Fig. 17.23 Temperature history at point C (58 m from upstream dam surface at EL.1005.5 m)

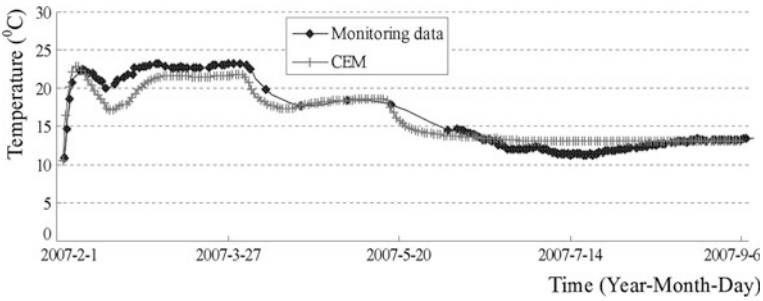

Fig. 17.24 Temperature history at point D (9.4 m from upstream dam surface at EL.1030 m)

In conclusion, the concrete temperature after the first cooling is under the control of stipulated design value. But there is a 3–5 °C residual rise of temperature after the first cooling, which may bring about an adverse effect during the second stage cooling. There is also a residual temperature rise after the second cooling, which may result in an additional compressive stress after the transverse joints grouting.

17.4.4 RCC Gravity Dam: Guangzhao Project, China

(1) Presentation of the project

Guangzhao Hydropower Project with a RCC gravity dam at the height of 200.5 m and with the installated generator capacity of 1040 MW (4 × 260 MW), is located on the Beipanjiang River, Guizhou Province, China. The main purpose of the project is electricity power generation with additional benefits in water regulation and irrigation. The normal storage level (NSL) of the reservoir is EL.745.00 m, and the corresponding reservoir capacity is 3135 million m^3. The dam is accommodated with three spillway chutes on its surface capable of the maximum discharge 9857 m^3/s. The whole crest length is 410 m and the dam consists of 20 monoliths (Fig. 17.25).

The concrete placement was launched in May, 2005, the reservoir impounding was started on December 30, 2007, and the dam construction was completed in July, 2008. Figure 17.26 is Guangzhao Dam during the construction phase (2007-05-15).

In the whole construction period, the feedback analysis for the thermal field and thermal stress field was carried out for the purpose of temperature and crack control.

Figure 17.27 shows the profile of the overflow dam monolith whose thermal study will be demonstrated hereafter.

(2) Characteristics of the computation

There are altogether 58 concrete lifts whose thickness is approximately 3 m. Table 17.2 lists the thermal parameters of the concrete and Table 17.3 displays the construction schedule with placing temperatures.

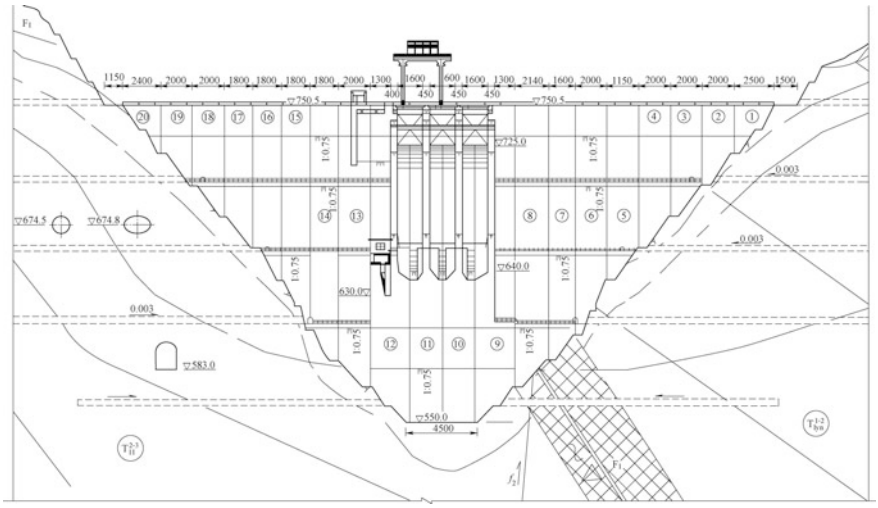

Fig. 17.25 Layout of Guangzhao Project (Downstream elevation view)

Fig. 17.26 Guangzhao Dam during construction (2007-05-15)

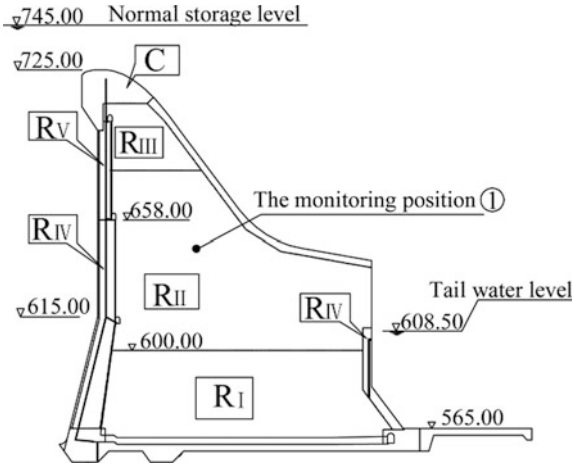

Fig. 17.27 Profile of the overflow dam monolith of Guangzhao Project

Figure 17.28 is the finite element mesh discretized by 5330 nodes and 2379 elements, in which the concrete is discretized into solid elements and the lift joints are discretized into thin-layer elements of 0.05 m thick. Figure 17.29 is the composite element mesh discretized by 1008 nodes and 440 composite elements containing lift joints.

Table 17.2 Thermal parameters of concrete

Concrete	Specific heat c (kJ/kg °C)	Density ρ (kg/m^3)	Thermal diffusivity a (kJ/m h °C)	Adiabatic temperature rise θ (°C)
C_1, C_{b1}, C_{b2}, C_3, C_4	0.97	2450	8.38	$\theta = 22.4\tau/(\tau + 2.80)$
R I	0.956	2445	8.29	$\theta = 20.2\tau/(\tau + 3.02)$
R II	0.935	2438	8.14	$\theta = 17.0\tau/(\tau + 3.25)$
R III	0.917	2464	8.11	$\theta = 16.5\tau/(\tau + 3.50)$
R IV	0.973	2452	8.42	$\theta = 22.0\tau/(\tau + 2.89)$
R V	0.964	2450	8.25	$\theta = 19.6\tau/(\tau + 2.91)$

Table 17.3 Concrete placing temperature versus time since May, 2005

Time (day)	0	28	42	52	59	75	89	96	102	113
Placing temperature (°C)	18.5	20.4	23.4	23.4	22.5	23.5	28	24.5	30	28.1
Time (day)	128	144	158	174	207	215	221	231	244	254
Placing temperature (°C)	30.9	29	30	31	30	29	29	29.6	29.4	29.5
Time (day)	262	273	287	303	313	320	332	338	345	351
Placing temperature (°C)	30	29.5	29.5	26	26	25	20	18	17	18
Time (day)	372	386	393	398	412	448	453	457	467	492
Placing temperature (°C)	17	21	21	22	24	27	26	28	28.5	29.5
Time (day)	499	505	512	518	526	533	539	545	552	599
Placing temperature (°C)	32	32	31.5	29.5	32	31.5	30.5	31.5	32.5	30.5
Time (day)	612	662	667	672	677	682	687	692	–	–
Placing temperature (°C)	28.6	26.8	28.7	23.4	22.5	24.5	18.2	18.2	–	–

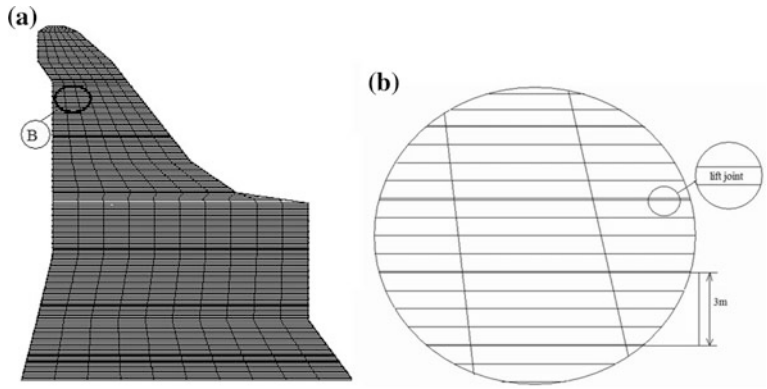

Fig. 17.28 Finite element mesh (2379 elements; 5330 nodes). **a** Overall view; **b** detailed drawing

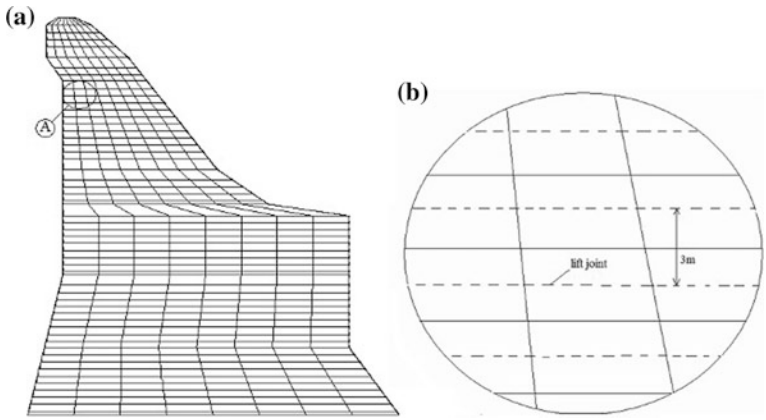

Fig. 17.29 Composite element mesh (440 elements; 1008 nodes). **a** Overall view; **b** detailed drawing

(3) Computation results

Figures 17.30 and 17.31 show the temperature distributions in the dam body on the 400th day after the starting of concrete placement. These results tell us that:

- The thermal fields obtained by the CEM and FEM exhibit similar distributions.
- At the lower and central portion (older concrete) of the dam, the temperature gradient is small.
- The temperature gradient is much larger at the vicinity of the upstream and downstream surfaces. This is mainly due to the difference in the concrete temperature and ambiance temperature. These portions should be tightly monitored to control the surface cracking.

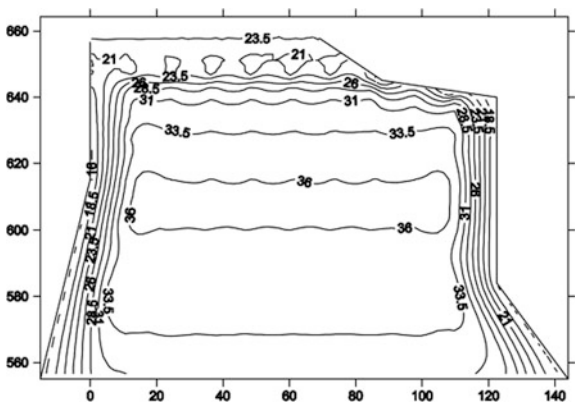

Fig. 17.30 Dam temperature on the 400th day after the starting of concrete placement (FEM)

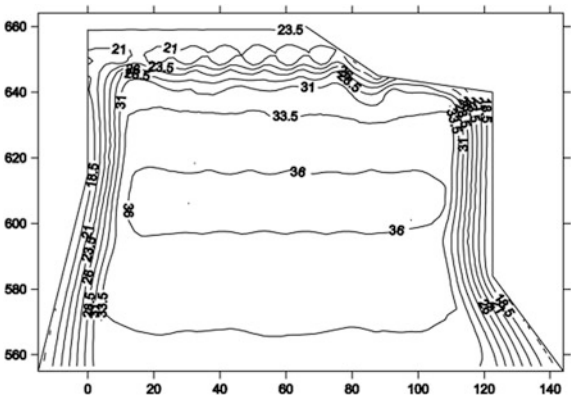

Fig. 17.31 Dam temperature on the 400th day after the starting of concrete placement (CEM)

– The temperature gradient is very large and complicatedly distributed at the vicinity of the top surface of fresh concrete. This is mainly attributable to the difference in the concrete temperature and ambiance temperature, and to the temperature discontinuity between the old/new lifts as well. The vertical cracking could manifest easily if the temperature control countermeasures are not well observed.

Figures 17.32 and 17.33 illustrate the temperature histories on the vicinity sides of a lift joint at monitoring point ① (see Fig. 17.27), which indicate clearly the temperature difference between the upper and lower lifts: it emerges at the beginning of concrete placement, and reaches the maximum after a short period, then decays as the ongoing of time.

Figure 17.34 is the monitored temperature history at the same point. This monitored temperature can be looked at as "averaged" one around the position, since the conventional monitoring facilities are not able to detect the temperature difference between lifts. Bearing this in mind, it can be announced that this monitored temperature provides positive validation for the computation results by both the CEM (see Fig. 17.33) and FEM (see Fig. 17.32).

The RCC gravity dam example justifies that the CEM algorithm, on one hand, is able to provide high precision results concerning the overall spatial-time

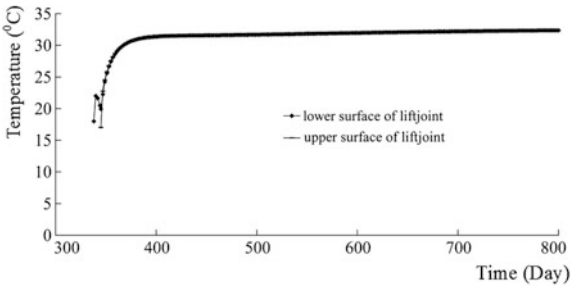

Fig. 17.32 Temperature history at monitoring point ① (FEM)

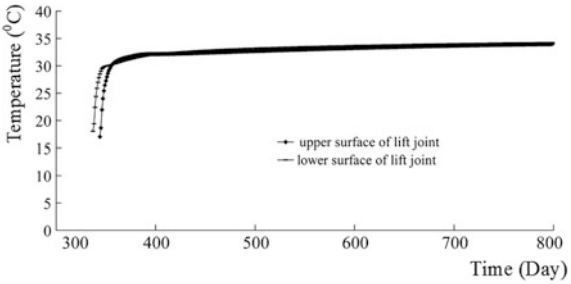

Fig. 17.33 Temperature history at monitoring point ① (CEM)

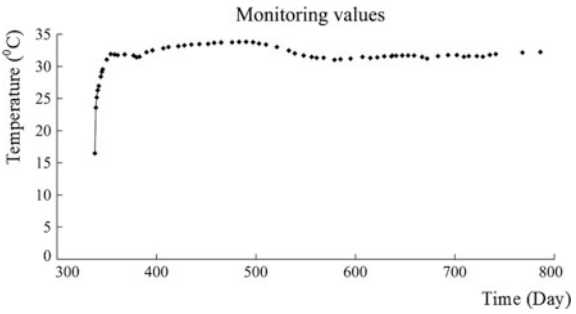

Fig. 17.34 Temperature history at monitoring point ① (monitoring)

distribution of temperature field as well as the detailed characteristics of the temperature gradient across lift joint; on the other hand, is simpler in the pre-process attributable to the abandonment of thin-layer elements demanded by lift joints.

After the accomplishment of Guangzhao Dam (Fig. 17.35), it has been working under perfectly condition insofar.

Fig. 17.35 Guangzhao Dam in service (2009-10-04)

References

Chen SH, Su PF, Shahrour I. Composite element algorithm for the thermal analysis of mass concrete: simulation of lift joint. Finite Elem Anal Des. 2011a;47:536–42.

Chen SH, Su PF, Shahrour I. Composite element algorithm for the thermal analysis of mass concrete: simulation of cooling pipes. Int J Numer Meth Heat Fluid Flow. 2011b;21(4):434–47.

Ding JX, Chen SH. Simulation and feedback analysis of the temperature field in massive concrete structures containing cooling pipes. Appl Therm Eng. 2013;61(2):554–62.

Zhu BF. Thermal stresses and temperature control of mass concrete. Beijing (China): China Electric Power Press; 1998 (in Chinese).

Chapter 18
Comprehensive Application of the Composite Element Method: Numerical Test of Jointed Rock Masses

Abstract With the significant progress in computational geomechanics, multi-scale or multi-level computation termed as the numerical testing (NT) or numerical material (NM), has become more and more acceptable towards the study on the mechanical behaviors of rock-like materials. Nevertheless, it is rather cumbersome that the NT for the properties of rock-like materials demands large computation efforts arise from various sizes of testing specimen and stochastic distributions of aggregate in a concrete mass or discrete fracture network (DFN) in a rock sampling window. Therefore, from practical motivations it is attractive to introduce the CEM with facilitated pre-process into the NT that allows for repeatedly testing on a large number of specimens. In this chapter, the philosophy and roadmap of the NT towards the permeability matrix and elastic compliance matrix as well as their corresponding REV for fractured rocks are elucidated by the hybrid DFN/CEM.

18.1 General

The major tasks in the material property study of rock-like materials are multi-fold including the description of seepage characteristics (Louis 1969; Snow 1969; Long 1996; Hall and Hoff 2012) and deformation/strength characteristics (Zienkiewicz and Pande 1976; Pande and Gerrard 1983; Sitharam et al. 2001; Mehta and Monteiro 2006). As we have previously declared, the computation methods for rock-like materials fall into implicit (or equivalent continuum) approach and explicit (or discrete) approach. The former takes the influences of intrinsic material structures (e.g. discontinuities, aggregates) into account by means of the permeability and elasticity (compliance) matrices but neglects their exact positions; whereas the latter considers the material structures deterministically. The crucial difficulty lies in the explicit approach is the pre-process for generating computation mesh in addition to the consumption of large computer capacity, whereas the applicability of implicit approach is tightly linked with the existence of equivalent parameters such as the permeability tensor and elasticity compliance matrix and the

S.-H. Chen, *Computational Geomechanics and Hydraulic Structures*,
Springer Tracts in Civil Engineering, https://doi.org/10.1007/978-981-10-8135-4_18

corresponding representative element volume (REV). Nevertheless, we have to reluctantly admit that the quantitative solution of them through laboratory and field tests is very difficult and expensive.

With the advance in computer technology, multi-scale or multi-level computation based on numerical methods (e.g. the FEM) termed as the "Numerical Testing" (NT) or "Numerical material" (NM), has become acceptable towards the study on the mechanical behaviors of rock-like materials. Take the "numerical concrete" for example (Roelfstra et al. 1985; Wittmann et al. 1985), it numerically builds meso-scale samples for concrete as a three-phase composite material consisting of coarse aggregates (greater than 4.75 mm in size), mortar matrix, and interfacial transition zone (ITZ) between them. Then the computations emulating the physical tests with regard to stress/deformation, temperature conductivity, and water seepage/absorption, are carried out systematically to explore their response mechanisms, equivalent parameters, and of course, the correspondent REV (Keskin et al. 2011; Zhou et al. 2013; Abyaneh et al. 2014; Li et al. 2016; Xu and Chen 2016; Xu et al. 2017; Li et al. 2017).

In geotechnical literature, a "fracture" is any separation in a geologic formation, such as a joint or a fault, that frequently forms a deep fissure or crevice in the rock and divides the rock into pieces. In this chapter, we observe the convention to use the term "fractures" in lieu of and only for the term "joints" that most frequently occur as joint sets and systems.

The DFN method is a special discrete method that initially considered fluid flow and transport processes in rock masses through a system of connected fractures. It was created in the early 1980s and nowadays is most useful for the study on the flow in fractured rock for the derivation of their equivalent continuum flow and transport properties (Schwartz et al. 1983; Long et al. 1985; Andersson and Dverstop 1987; Dershowitz and Einstein 1987; Zimmerman and Bodvarsson 1996). Solution of flow field for individual fracture in the DFN may been obtained using the closed-form formulas, the pipe models (Cacas et al. 1990) and the channel lattice models (Tsang and Tsang 1987).

The stochastic simulation of fracture system is the geometric basis of the DFN method (Louis and Maini 1970; Baecher et al. 1977; Cruden 1977; Hudson and Priest 1983; Kulatilake and Wu 1984; Hakami and Larsson 1990; Kulatilake et al. 1993; Nicholl et al. 1999). A critical issue is the treatment of bias in the estimation of fracture densities, trace lengths and connectivity from conventional surface or borehole mappings. Development using circular windows also has been reported in Mauldon (1998), Mauldon et al. (2001). Power law has been found to exist for the trace length of fracture and has been applied for representing fracture system connectivity (Renshaw 1999). The fractal concept also has been adopted in order to consider the scale dependence of the fracture system and for up-scaling the permeability properties (Barton and Larsen 1985; Chiles 1988; Barton 1995).

In recent years, computation methods such as the FEM and DEM are exercised for stochastic rock samples containing complicated fracture system to get the permeability tensor (Wei et al. 1995; Zhang et al. 1996; Kulatilake and Panda 2000; Öhman and Niemi 2003; Min et al. 2004) and the elastic compliance matrix

(Wei and Hudson 1986; Kulatilake et al. 1993; Min and Jing 2003) as well as the corresponding REV. The algorithm is generally formulated in the following steps.

- First, a DFN in a sampling window is generated which will be used as the parent stochastic DFN;
- Next, a series of fractured rock blocks with different sizes and orientations are defined as test samples for each stochastic DFN;
- Then the numerical methods (e.g. the FEM or DEM) are applied to the fractured rock samples to evaluate their fluid flow fields or deformation fields;
- Finally the permeability matrices or elastic compliance matrices of the samples are obtained and the existence of REV is verified.

It is obvious that the numerical estimation of permeability tensor or elastic compliance matrix demands large computation efforts related to various sample sizes and orientations. The situation becomes more rigorous if the stochastic characteristics of a rock fracture system are taken into account, where many discrete fracture networks in a sampling window are generated as the parent stochastic DFNs, on which the NT is operated. Therefore, from practical reasons it is attractive to introduce the CEM into the NT that allows for repeatedly tests of rock samples containing stochastic fracture networks, attributable to its greatly facilitated pre-process operation.

In the hereinafter coverage of this chapter, we will be focused on the philosophy and roadmap of the NT towards fractured rocks by the hybrid of the discrete fracture network (DFN) method and the CEM (Chen et al. 2008, 2012).

18.2 Mathematical and Mechanical Tools

18.2.1 Generation of Discrete Fracture Networks

The Monte-Carlo method is employed to generate discrete fracture network (DFN), which includes the following main steps.

- Investigation and record of the fracture system for a sampling window in the geology unit concerned;
- Statistics analysis of the measured data;
- Use is made of the Monte-Carlo method to produce random fractures;
- Construction of the fracture network in the sampling window.

In general, the characteristics (mid position, dip direction, dip angle, trace length, aperture, deformation and strength parameters) of rock fractures are correlated (e.g. fracture length versus aperture), studies on the correlations between the characteristics and fractal dimension may also be found in Charkaluk et al. (1998). These correlations request extra field measuring data which are not easy to be accessed by conventional engineering practices. Without loss of generality, the independent assumption of these characteristics is adopted in this book to simplify the stochastic parent DFN generation.

In the following discussion, N_{sjoint} denotes the amount of fracture sets, N_{joint} denotes the amount of fractures in the fracture set I_{sjoint}, N denotes the amount of stochastic parent DFNs generated in a sampling window. By the assumption that the geometrical characteristics (mid position, dip direction, dip angle, trace length, aperture) of each fracture are independent, the DFN generating algorithm is flow charted in Fig. 18.1.

18.2.2 Seepage Flow in Rock Fracture

Vide Sect. 2.4.2 (Chap. 2).

18.2.3 Characteristics of the Permeability Tensor

For a two-dimensional problem, if the new coordinate system $x' - z'$ rotates by an angle of α with respect to the old coordinate system $x - z$, the transformation of the permeability tensor can be defined as

$$\begin{Bmatrix} k_{x'x'} \\ k_{z'z'} \\ k_{x'z'} \end{Bmatrix} = \begin{bmatrix} \cos^2\alpha & \sin^2\alpha & \sin 2\alpha \\ \sin^2\alpha & \cos^2\alpha & -\sin 2\alpha \\ -\dfrac{\sin 2\alpha}{2} & \dfrac{\sin 2\alpha}{2} & \cos 2\alpha \end{bmatrix} \begin{Bmatrix} k_{xx} \\ k_{zz} \\ k_{xz} \end{Bmatrix} \tag{18.1}$$

If the condition $k_{x'z'} = 0$ is imposed to the third row of Eq. (18.1), the equation for the solution of principal direction can be gotten

$$\tan(2\alpha) = \frac{2k_{xz}}{k_{xx} - k_{zz}} \tag{18.2}$$

And the principal permeability coefficients are calculated according to

$$\begin{cases} k_1 = \frac{k_{xx}+k_{zz}}{2} + \sqrt{\left(\frac{k_{xx}-k_{zz}}{2}\right)^2 + k_{xz}^2} \\ k_2 = \frac{k_{xx}+k_{zz}}{2} - \sqrt{\left(\frac{k_{xx}-k_{zz}}{2}\right)^2 + k_{xz}^2} \end{cases} \tag{18.3}$$

One of the important characteristics of the permeability tensor is the existence of permeability ellipse (2D) or permeability ellipsoid (3D), which can be visualized easily in two-dimensional case. Suppose the x axis and z axis are the principal permeability directions (see Fig. 18.2), then according to Eq. (18.1) the permeability coefficient at the direction forming an included angle of α anti-clockwise with the x axis can be calculated by the formula

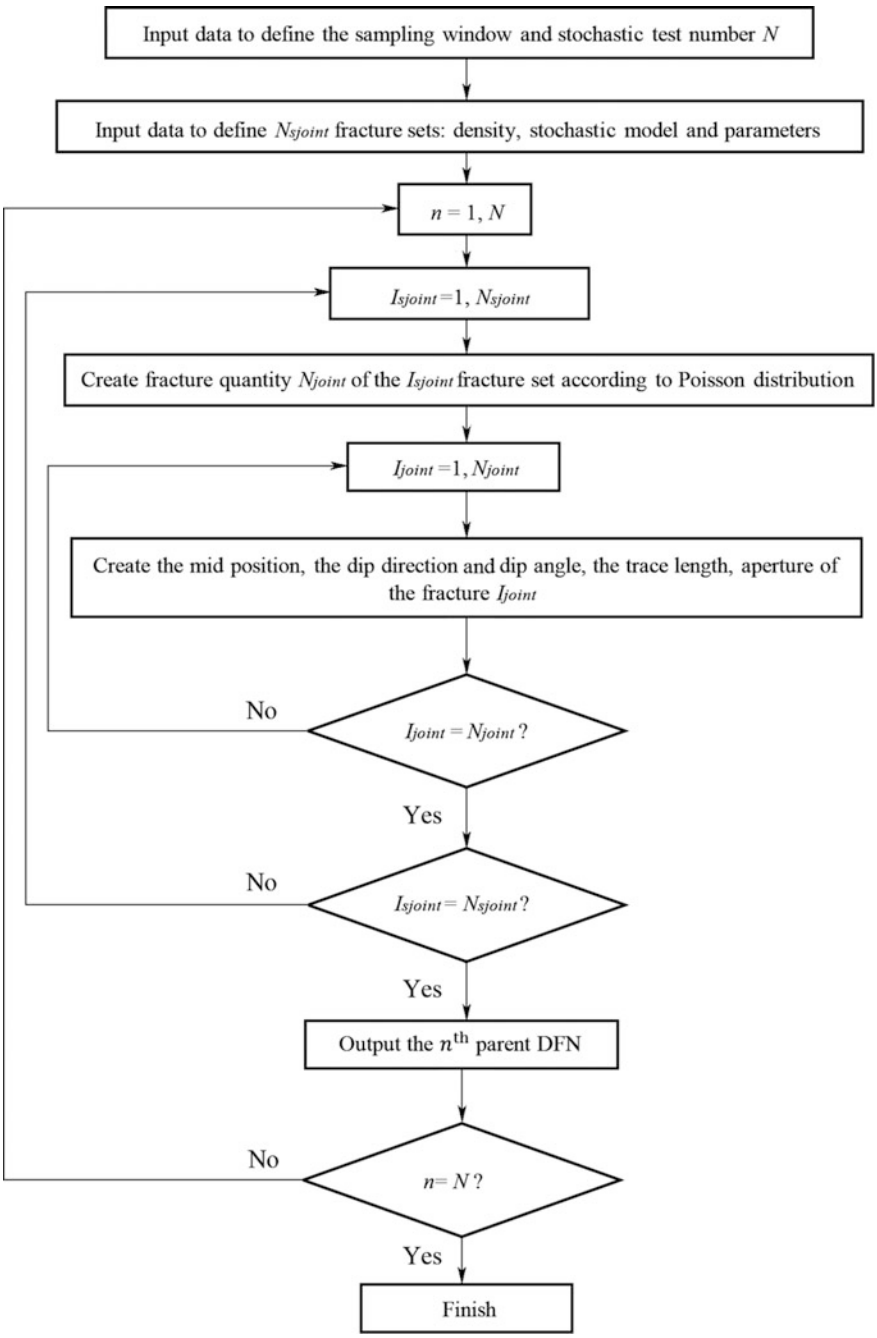

Fig. 18.1 Flow chart for the fracture network generation

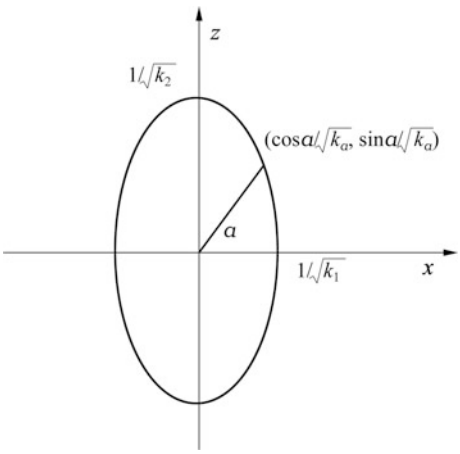

Fig. 18.2 Ellipse of a permeability tensor

$$k_\alpha = k_1 \cos^2 \alpha + k_2 \sin^2 \alpha \tag{18.4}$$

Denoting

$$\begin{cases} x = \cos\alpha/\sqrt{k_\alpha} \\ z = \sin\alpha/\sqrt{k_\alpha} \end{cases}$$

Equation (18.4) becomes

$$\frac{x^2}{(\frac{1}{\sqrt{k_1}})^2} + \frac{z^2}{(\frac{1}{\sqrt{k_2}})^2} = 1 \tag{18.5}$$

Equation (18.5) is visualized by the ellipse in Fig. 18.2, with long axis $1/\sqrt{k_2}$ and short axis $1/\sqrt{k_1}$. At the α direction the length of elliptical radius vector is $1/\sqrt{k_\alpha}$.

18.2.4 Characteristics of the Elastic Compliance Matrix

In the engineering computation, second-order stress and strain tensors are expressed by corresponding vectors, and fourth-order elastic tensor is expressed by elastic matrix. The latter is the inverse of the elastic compliance matrix, i.e.

$$[D] = [C]^{-1} \tag{18.6}$$

For a two-dimensional plane stress problem, if the new coordinate system $x' - z'$ rotates by an angle of α with respect to the old coordinate system $x - z$, the transformation of elastic compliance matrix can be defined by

$$[C'] = \left([T]^{-1}\right)^{T}[C][T]^{-1} \tag{18.7}$$

$$[T] = \begin{bmatrix} \cos^2\alpha & \sin^2\alpha & 2\sin\alpha\cos\alpha \\ \sin^2\alpha & \cos^2\alpha & -2\sin\alpha\cos\alpha \\ -\sin\alpha\cos\alpha & \sin\alpha\cos\alpha & \cos^2\alpha - \sin^2\alpha \end{bmatrix} \tag{18.8}$$

where $[C]$ and $[C']$ are the elastic compliance matrix in the old and the new coordinate systems, respectively; $[T]$ is the transformation matrix.

Any component of the elastic compliance matrix $[C']$ can be plotted against the rotation angle α to form polar diagram. Under the circumstances of orthotropic symmetry where a rock mass contains two sets of orthogonal and continuous fractures in two-dimensional case (see Fig. 18.3), the elastic compliance matrix can be explicitly constructed as

$$[C] = \begin{bmatrix} \frac{1}{E} + \frac{1}{k_{n1}s_1} & -\frac{\mu}{E} & 0 \\ & \frac{1}{E} + \frac{1}{k_{n2}s_2} & 0 \\ Sym. & & \frac{2(1+\mu)}{E} + \frac{1}{k_{s1}s_1} + \frac{1}{k_{s2}s_2} \end{bmatrix} \tag{18.9}$$

In which E is the Young's modulus of the intact rock; μ is the Poisson's ratio of the intact rock; k_{nj} is the fracture normal stiffness; k_{sj} is the fracture shear stiffness; s_j is the fracture spacing.

According to Eqs. (18.7)–(18.9), when the application of normal stress σ is not perpendicular to the fractures (see Fig. 18.3), the compliance component C_α of the

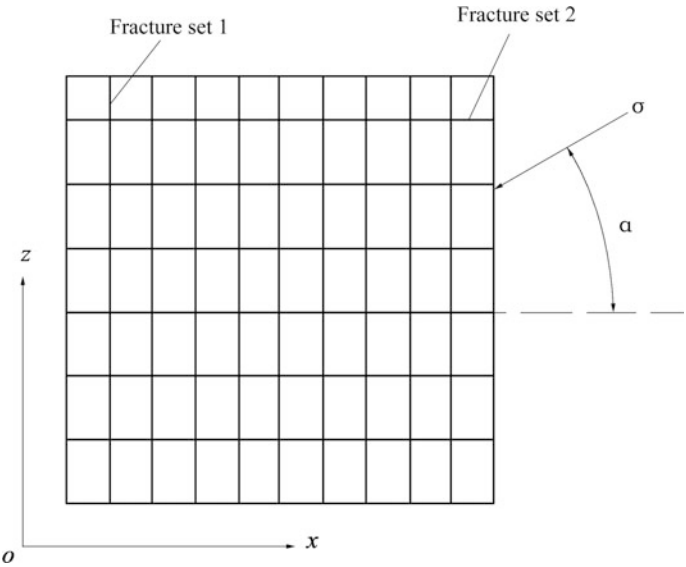

Fig. 18.3 Sketch showing the notations of orthogonal fracture sets

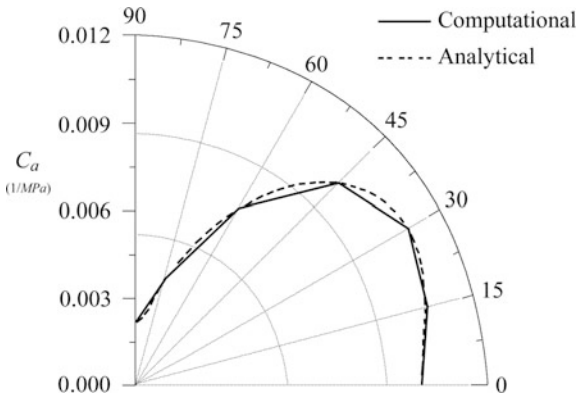

Fig. 18.4 Polar diagram of elastic compliance with two sets of orthogonal persistent fractures

fractured rock mass along the direction of stress with an rotation angle α is calculated by

$$C_\alpha = \frac{1}{E} + \frac{1}{s_1 k_{n1}}\cos^4\alpha + \frac{1}{s_1 k_{s1}}\cos^2\alpha\sin^2\alpha + \frac{1}{s_2 k_{s2}}\cos^2\alpha\sin^2\alpha + \frac{1}{s_2 k_{n2}}\sin^4\alpha \tag{18.10}$$

Suppose that the Young's modulus and the Poisson's ratio of the intact rock are $E = 1.8 \times 10^4$ (Mpa) and $\mu = 0.28$ respectively; the normal stiffness and shear stiffness are k_{n1} = 100 (Mpa/m) and k_{s1} = 50 (Mpa/m) for the first fracture set (vertical), and $k_{n2} = 200$ (Mpa/m) and $k_{s2} = 100$ (Mpa/m) for the second fracture set (horizontal), respectively; the spacing is $s_1 = 1$ (m) for the first fracture set and $s_2 = 1.5$ (m) for the second fracture set, respectively. Figure 18.4 draws the corresponding polar diagram where the solid line is the analytical solution by Eq. (18.10), while the broken line is the NT solution which will be illustrated later in this chapter.

When the fractures are neither orthogonal nor persistent, the analytical form of Eq. (18.9) does not hold. However, by the NT such polar diagram always can be obtained, which is useful for the fluctuation examination of elastic compliance matrix.

18.3 Numerical Test for Permeability Characteristics

18.3.1 Configuration of the Test

For the nth parent DFN in the sampling window, a series of smaller rock samples are extracted, which exhibit different sizes and orientations. Figure 18.5 shows a fractured rock sample which forms an included angle of α referring to the x axis, the regular composite element mesh is also plotted (in broken lines) in this figure.

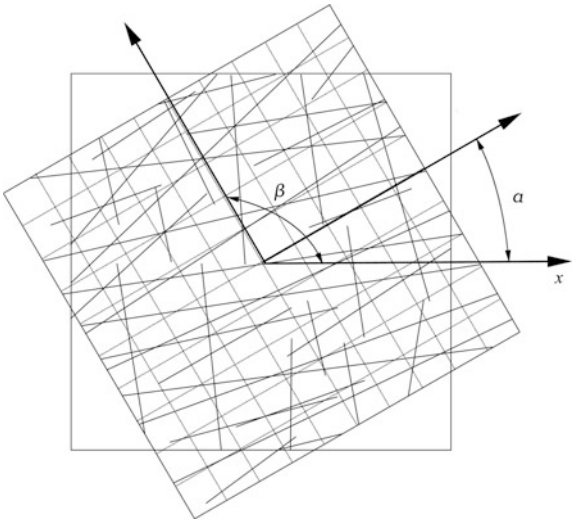

Fig. 18.5 Sample rotated by an angle of α

18.3.2 Computation of Permeability Coefficients

A careful design of the boundary conditions may facilitate the permeability coefficient computation.

We write the general form of the Darcy's law

$$\begin{cases} Q_x = -k_{xx}\frac{\partial \phi}{\partial x}S_{yz} - k_{xy}\frac{\partial \phi}{\partial y}S_{yz} - k_{xz}\frac{\partial \phi}{\partial z}S_{yz} \\ Q_y = -k_{yx}\frac{\partial \phi}{\partial x}S_{xz} - k_{yy}\frac{\partial \phi}{\partial y}S_{xz} - k_{yz}\frac{\partial \phi}{\partial z}S_{xz} \\ Q_z = -k_{zx}\frac{\partial \phi}{\partial x}S_{xy} - k_{zy}\frac{\partial \phi}{\partial y}S_{xy} - k_{zz}\frac{\partial \phi}{\partial z}S_{xy} \end{cases} \tag{18.11}$$

where S_{yz}, S_{xz} and S_{xy} are the areas of the boundary surfaces which can be calculated by

$$\begin{cases} S_{yz} = L_y \times L_z \\ S_{xz} = L_x \times L_z \\ S_{xy} = L_y \times L_x \end{cases} \tag{18.12}$$

Here the pseudo three-dimensional problem is concerned that the sample is a right hexahedron with unit thickness L_y along the y axis. At the $x-z$ plane (see Fig. 18.6), the length along the x axis is L_x and the length along the z axis is L_z. The fracture network is symmetry respecting to the $x-z$ plane, this means that in Eq. (18.11) we may postulate that

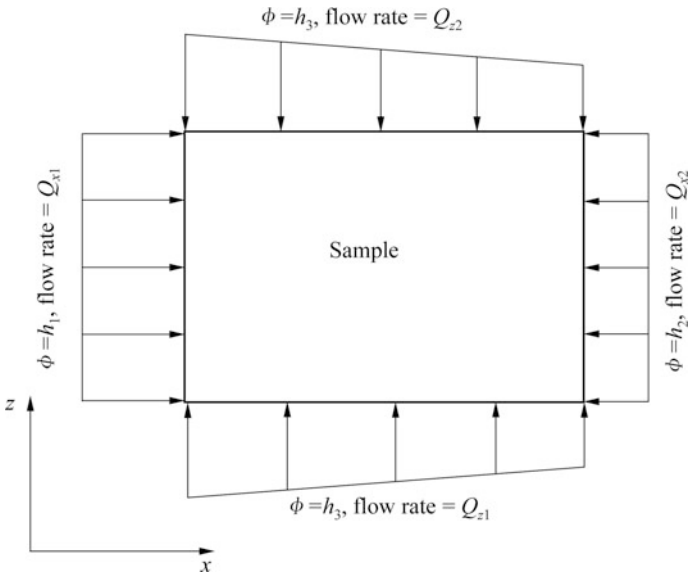

Fig. 18.6 Design of a numerical test sample

$$k_{xy} = k_{zy} = 0 \tag{18.13}$$

The two boundary surfaces perpendicular to the y direction are supposed to be imperious, this further means that in Eq. (18.11) we have

$$Q_y = 0 \tag{18.14}$$

At the two boundary surfaces perpendicular to the x direction, the hydraulic potentials are defined as $\phi = h_1$ and $\phi = h_2$, respectively; at the two boundary surfaces perpendicular to the z direction, the hydraulic potential ϕ varies linearly from h_1 to h_2. The average hydraulic gradients are calculate by

$$\begin{cases} \frac{\partial \phi}{\partial x} = \frac{h_2 - h_1}{L_x} \\ \frac{\partial \phi}{\partial y} = 0 \\ \frac{\partial \phi}{\partial z} = 0 \end{cases} \tag{18.15}$$

According to the calculated flow velocities in the intact rock and fractures, the flow rates at the four pervious boundary surfaces can be obtained. It is worthwhile to point out that usually the flow rates are not identical at the two parallel boundary surfaces, i.e.

$$\begin{cases} Q_{x1} \neq Q_{x2} \\ Q_{z1} \neq Q_{z2} \end{cases}$$

Therefore the average flow rates are calculated as

$$\begin{cases} Q_x = \frac{Q_{x1}+Q_{x2}}{2} \\ Q_z = \frac{Q_{z1}+Q_{z2}}{2} \end{cases} \tag{18.16}$$

According to Eqs. (18.11)–(18.16), the permeability coefficients along and perpendicular to the x direction can be calculated by the formulas

$$\begin{cases} k_{xx} = -\frac{(Q_{x1}+Q_{x2})L_x}{2(h_2-h_1)S_{yz}} \\ k_{xz} = -\frac{(Q_{z1}+Q_{z2})L_x}{2(h_2-h_1)S_{xy}} \end{cases} \tag{18.17}$$

When the sample is subjected to the rotating transformation with an angle of α anti-clockwise (see Fig. 18.5), Eq. (18.17) is held. In this case the permeability coefficients calculated by Eq. (18.17) are that along the directions of α and β, which will be denoted as k_α and k_β, respectively. This rotating operation is important in the study of permeability tensor and its REV.

18.3.3 Identification of Permeability Tensor and REV

The applicability of the equivalent continuum theory dependents on the following conditions: the REV for hydraulic behavior exists and whose size is much smaller than the characteristic dimension of the structure concerned. The REV is theoretically defined as the size beyond which the hydraulic permeability tensor remains unchanged. In the practical study however, the REV is normally identified when the permeability components only exhibit small fluctuation following the augment in the size of rock sample.

Denote v_i as the ith attempt of the REV volume, the procedure for the identification of permeability tensor and REV is flow charted in Fig. 18.7.

18.4 Numerical Test for Deformation Characteristics

18.4.1 Configuration of the Test

For two-dimensional plane stress problem, both the parent DFN and the sampling window are right hexahedron with unit thickness, and all fractures are perpendicular to the plane studied.

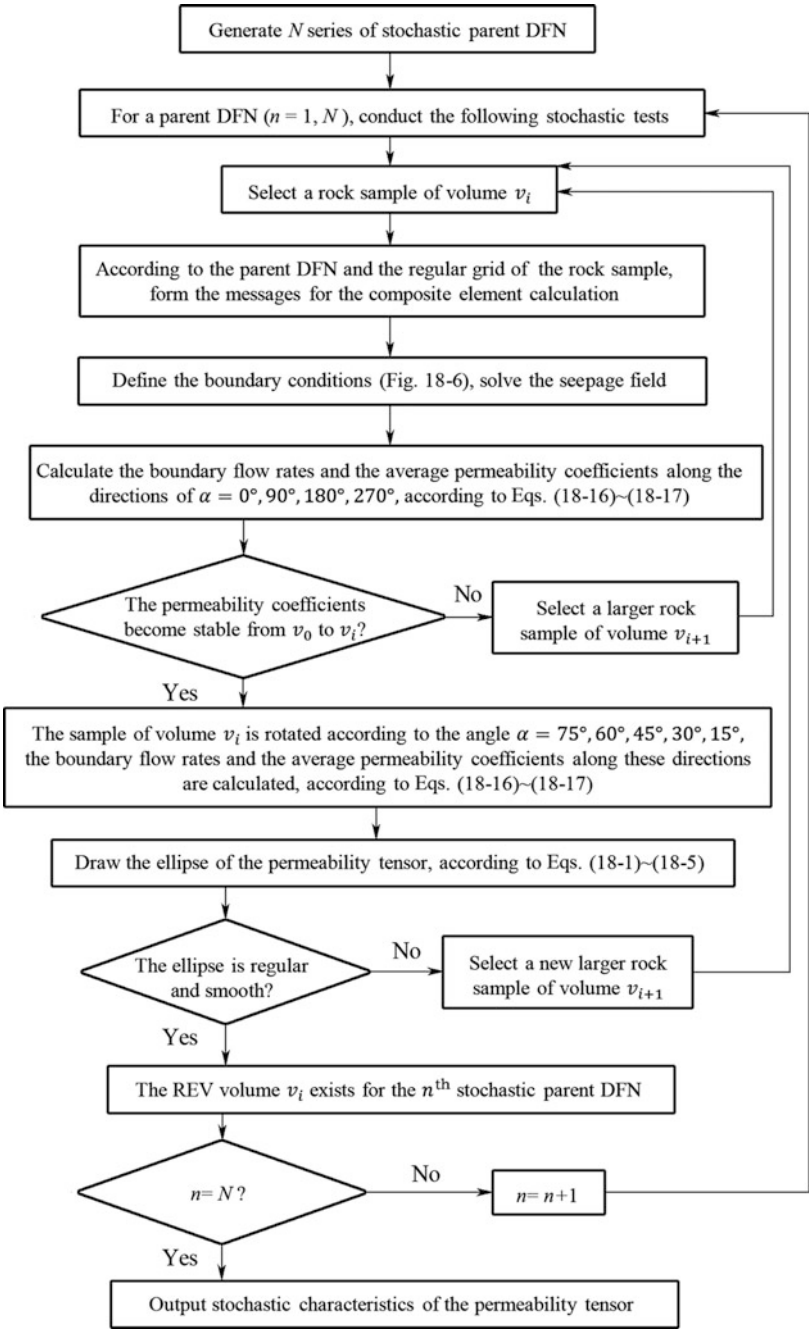

Fig. 18.7 Flow chart for the identification of permeability tensor and REV

The displacement boundary conditions in Fig. 18.8 are so designed to let the sample be statically determinate imposing not extra local stresses within the sample. Figure 18.8 also shows the loads applied on the test sample, which are all uniformly distributed at the sample edges. In Fig. 18.8 the local coordinate system $x' - z'$ for the extracted test sample is defined, too.

In order to obtain the compliance matrix, three independent load combinations are applied respectively. We use three kinds of independent unit load to facilitate the deduction of compliance matrix which are noted in Fig. 18.9, where $\sigma_{x'} = -1$ MPa, $\sigma_{z'} - 1$ MPa and $\tau_{x'z'} = 1$ MPa. Although these boundary unit loads lead to a complicated stress distribution within the sample, yet the equivalent stresses uniformly distributed within the sample can be simply represented by these boundary unit loads.

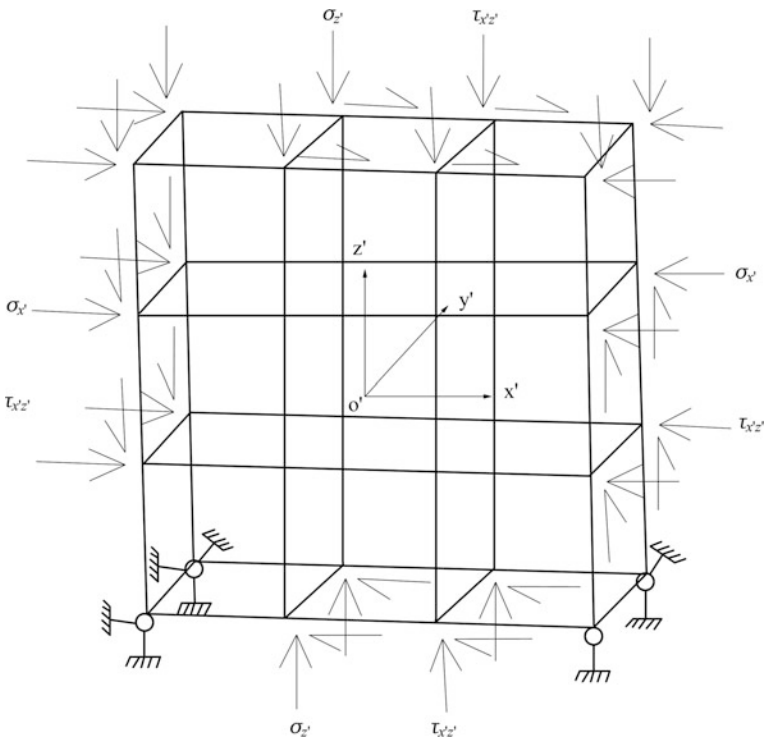

Fig. 18.8 Sketch showing the boundary conditions and loads of a numerical test sample

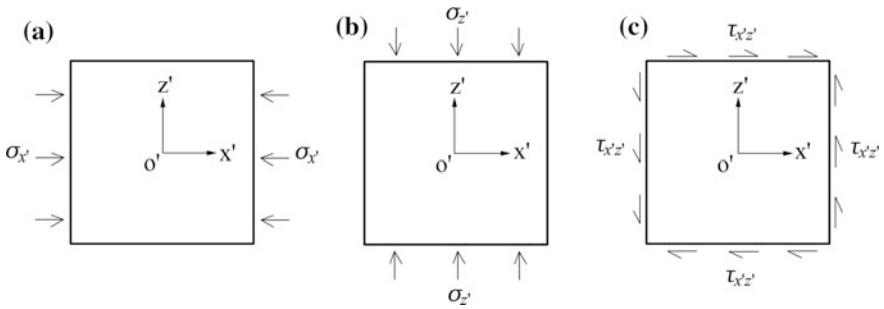

Fig. 18.9 Diagram to illustrate independent unit loads

18.4.2 Computation of Deformation Coefficients

For each unit load the computation using CEM produces an overall displacement field in the sample, then the equivalent strains $\{\varepsilon\}^a$, $\{\varepsilon\}^b$ and $\{\varepsilon\}^c$ corresponding to Fig. 18.9a–c can be calculated accordingly. Use is made of the definition of elastic compliance matrix, three equations can be established to link these equivalent strains and the corresponding unit loads in the form of

$$\begin{Bmatrix} \varepsilon^a_{x'} \\ \varepsilon^a_{z'} \\ \gamma^a_{x'z'} \end{Bmatrix} = [C'] \begin{Bmatrix} \sigma_{x'} \\ 0 \\ 0 \end{Bmatrix} \tag{18.18}$$

$$\begin{Bmatrix} \varepsilon^b_{x'} \\ \varepsilon^b_{z'} \\ \gamma^b_{x'z'} \end{Bmatrix} = [C'] \begin{Bmatrix} 0 \\ \sigma_{z'} \\ 0 \end{Bmatrix} \tag{18.19}$$

$$\begin{Bmatrix} \varepsilon^c_{x'} \\ \varepsilon^c_{z'} \\ \gamma^c_{x'z'} \end{Bmatrix} = [C'] \begin{Bmatrix} 0 \\ 0 \\ \tau_{x'z'} \end{Bmatrix} \tag{18.20}$$

Solution of Eqs. (18.18)–(18.20) offers the elastic compliance matrix $[C']$ in the local coordinate system

$$[C'] = \begin{bmatrix} C'_{11} & C'_{12} & C'_{13} \\ C'_{21} & C'_{22} & C'_{23} \\ C'_{31} & C'_{32} & C'_{33} \end{bmatrix} = \begin{bmatrix} \varepsilon^a_{x'}/\sigma_{x'} & \varepsilon^b_{x'}/\sigma_{z'} & \varepsilon^c_{x'}/\tau_{x'z'} \\ \varepsilon^a_{z'}/\sigma_{x'} & \varepsilon^b_{z'}/\sigma_{z'} & \varepsilon^c_{x'}/\tau_{x'z'} \\ \gamma^a_{x'z'}/\sigma_{x'} & \gamma^b_{x'z'}/\sigma_{z'} & \gamma^c_{x'z'}/\tau_{x'z'} \end{bmatrix} \tag{18.21}$$

Since the elastic compliance matrix should be symmetric, the non-diagonal components of the matrix are averaged in a manner of

$$[C'] = \begin{bmatrix} C'_{11} & (C'_{12}+C'_{21})/2 & (C'_{13}+C'_{31})/2 \\ & C'_{22} & (C'_{23}+C'_{32})/2 \\ Sym. & & C'_{33} \end{bmatrix} \tag{18.22}$$

The elastic compliance matrix $[C]$ and elastic matrix $[D]$ in the global coordinate system can be finally given through the transformation defined in Eqs. (18.6)–(18.8).

When the sample is subjected to the rotating transformation by an angle of α anti-clockwise, a compliance matrix of the rotated sample can be calculated. This rotation testing is important in the study of elastic compliance matrix and REV.

18.4.3 Identification of Elastic Compliance Matrix and REV

The applicability of equivalent or implicit approach in the deformation problem of fractured rock masses depends on the following conditions: REV for the elastic behavior exists and whose size is much smaller than the characteristic dimension of the structure concerned. The REV is theoretically defined as the size beyond which the elastic compliance matrix will be unchanged. In practice the REV is identified when the elastic compliance matrix only exhibits small fluctuation following the augment in the size of rock sample.

Denote v_i as the ith attempt of the REV volume, the procedure for the identification of elastic compliance matrix and REV is flow charted in Fig. 18.10.

18.5 Verification Examples

18.5.1 Permeability Tensor and REV

(1) Probability models and parameters

A numerical sampling window for a statistically homogeneous rock mass is used to elucidate the application of the NT established in this book. To describe the fracture geometry, it is necessary to specify the density, the mid position, the attitude (dip direction and dip angle), the trace length and the aperture, of the fracture sets. The probability models and parameters are listed in Table 18.1 referring to field data. Three fracture sets are considered in the study.

The permeability coefficient of the intact rock is 0.1 m/s. The permeability coefficient of the virtual filler is 1.0 m/s for the first fracture set, and 2.0 m/s for the second and the third fracture sets, respectively.

Altogether $N = 10$ stochastic parent DFNs are generated in a square region of 20 m $\times$ 20 m in size. For each stochastic DFN, a series of rock samples are extracted whose sizes are variable ranging from 6 m $\times$ 6 m to 16 m $\times$ 16 m.

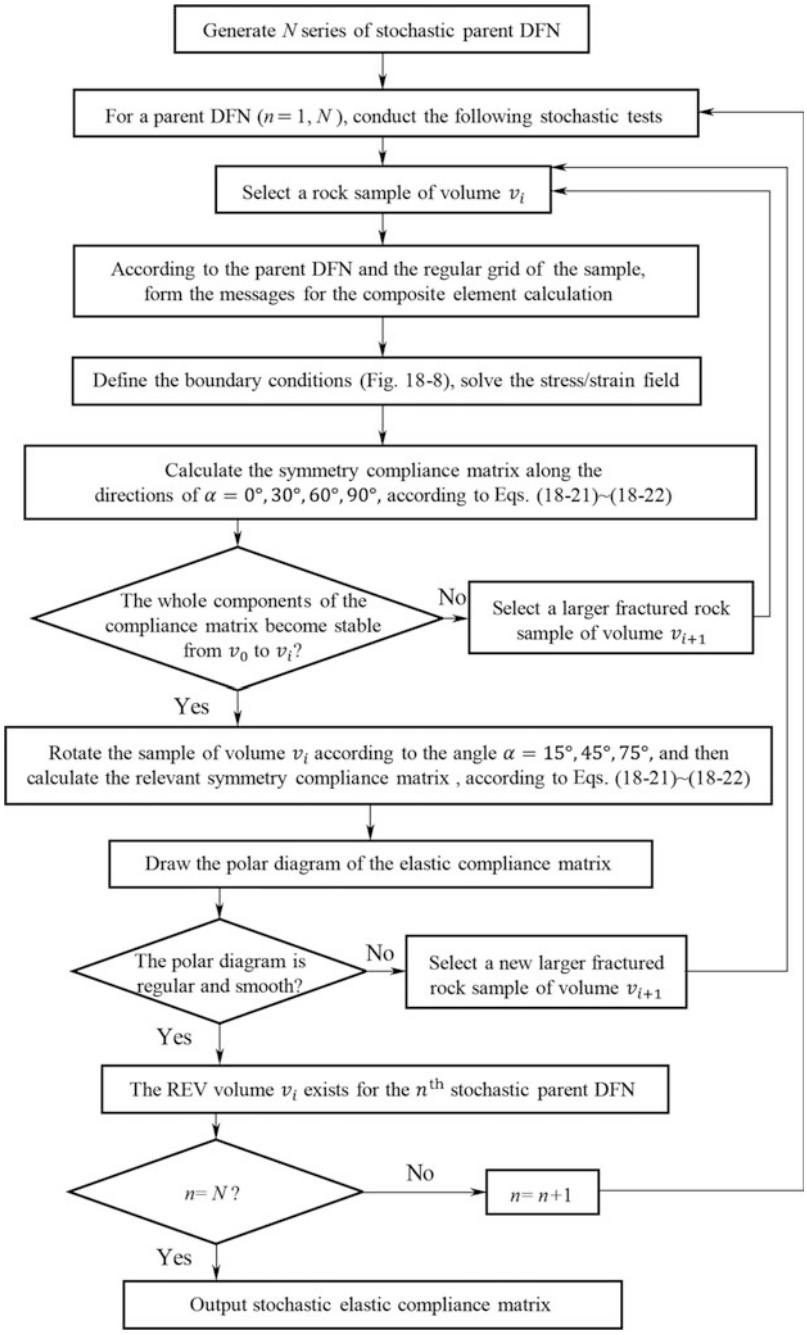

Fig. 18.10 Flow chart for the identification of compliance tensor and REV

Table 18.1 Probability models and parameters of fracture sets

Fracture set	Quantity		Mid position	Trace length		Attitude			Aperture		
	Probability model	Density (m^{-2})		Probability model	μ (m)	Probability model	μ (°)	σ (°)	Probability model	μ (cm)	σ (cm)
1	Poisson	0.14	Uniform	Negative exponent	8.0	Normal	10	5	Logarithm normal	4.0	0.5
2	Poisson	0.18	Uniform	Negative exponent	6.0	Normal	30	5	Logarithm normal	3.0	0.4
3	Poisson	0.16	Uniform	Negative exponent	4.0	Normal	80	10	Logarithm normal	2.0	0.3

The effect of boundaries on the flow patterns and on the overall permeability of the defined fracture networks is avoided when the parent DFN is sufficiently larger than the rock samples.

For each rock sample, the average hydraulic gradient along the direction concerned is 1.0, and those of the other two directions are zero.

The first stochastic DFN ($n = 1$) extracted by the rock sample with size of 10 m $\times$ 10 m is illustrated in Fig. 18.11.

(2) Fluctuation test

Tables 18.2, 18.3, 18.4 and 18.5 collect the calculated permeability coefficients along the directions of $\alpha = 0°, 90°, 180°, 270°$ for the first stochastic DFN ($n = 1$) with different rock sample sizes. Figures 18.12, 18.13, 18.14 and 18.15 display the fluctuation of these permeability coefficients.

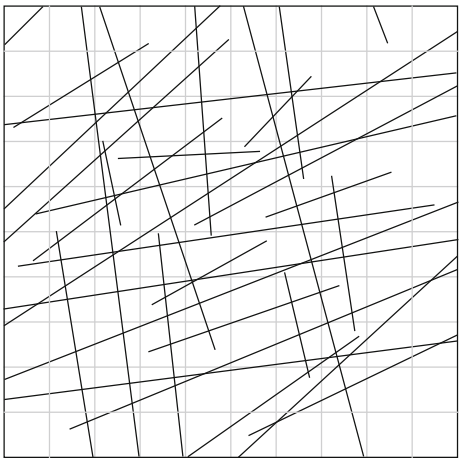

Fig. 18.11 Stochastic DFN at the $x - z$ plane (sample size = 10 m)

Table 18.2 Permeability coefficients along the positive direction of x ($\alpha = 0°$)

Sample size (m)	$Q_{\alpha 1}$ (m^3/s)	$Q_{\alpha 2}$ (m^3/s)	Q_{α} (m^3/s)	k_{α} (m/s)	$Q_{\beta 1}$ (m^3/s)	$Q_{\beta 2}$ (m^3/s)	Q_{β} (m^3/s)	$k_{\alpha\beta}$ (m/s)
6.0	1.0658	1.0965	1.0812	0.1802	0.6807	−0.1355	0.2726	0.0454
8.0	1.1232	1.1325	1.1279	0.1410	0.6684	−0.1484	0.2600	0.0325
10.0	1.3549	1.3556	1.3553	0.1355	0.7096	−0.1795	0.2651	0.0265
12.0	1.5846	1.7328	1.6587	0.1382	0.7787	−0.2054	0.2867	0.0239
14.0	1.9145	1.8501	1.8823	0.1344	0.8919	−0.2143	0.3388	0.0242
16.0	1.9956	2.2346	2.1151	0.1322	0.9891	−0.2735	0.3578	0.0224

Table 18.3 Permeability coefficients along the positive direction of z ($\alpha = 90°$)

Sample size (m)	$Q_{\alpha 1}$ (m^3/s)	$Q_{\alpha 2}$ (m^3/s)	Q_{α} (m^3/s)	k_{α} (m/s)	$Q_{\beta 1}$ (m^3/s)	$Q_{\beta 2}$ (m^3/s)	Q_{β} (m^3/s)	$k_{\alpha\beta}$ (m/s)
6.0	0.7795	0.7337	0.7566	0.1261	0.6983	−0.1068	0.2958	0.0493
8.0	0.7035	0.6919	0.6977	0.0872	0.6351	−0.1698	0.2327	0.0291
10.0	0.8338	0.8370	0.8354	0.0835	0.8249	−0.2168	0.3041	0.0304
12.0	0.9287	0.9710	0.9499	0.0792	0.9826	−0.3584	0.3121	0.0260
14.0	1.0197	1.0376	1.0287	0.0735	1.1245	−0.3764	0.3741	0.0267
16.0	1.1706	1.1833	1.1769	0.0736	1.1874	−0.3692	0.4091	0.0256

Table 18.4 Permeability coefficients along the negative direction of x ($\alpha = 180°$)

Sample size (m)	$Q_{\alpha 1}$ (m^3/s)	$Q_{\alpha 2}$ (m^3/s)	Q_{α} (m^3/s)	k_{α} (m/s)	$Q_{\beta 1}$ (m^3/s)	$Q_{\beta 2}$ (m^3/s)	Q_{β} (m^3/s)	$k_{\alpha\beta}$ (m/s)
6.0	1.1006	1.1206	1.1106	0.1851	0.6626	−0.1298	0.2664	0.0444
8.0	1.1132	1.1309	1.1221	0.1403	0.6729	−0.1518	0.2606	0.0326
10.0	1.3239	1.3681	1.3460	0.1346	0.6935	−0.1883	0.2526	0.0253
12.0	1.5032	1.7319	1.6176	0.1348	0.8153	−0.1928	0.3113	0.0259
14.0	1.9098	1.8667	1.8883	0.1349	0.8822	−0.2174	0.3324	0.0237
16.0	2.0421	2.2117	2.1269	0.1329	1.0302	−0.2646	0.3828	0.0239

Table 18.5 Permeability coefficients along the negative direction of z ($\alpha = 270°$)

Sample size (m)	$Q_{\alpha 1}$ (m^3/s)	$Q_{\alpha 2}$ (m^3/s)	Q_{α} (m^3/s)	k_{α} (m/s)	$Q_{\beta 1}$ (m^3/s)	$Q_{\beta 2}$ (m^3/s)	Q_{β} (m^3/s)	$k_{\alpha\beta}$ (m/s)
6.0	0.7859	0.7746	0.7802	0.1300	0.6892	−0.1114	0.2889	0.0482
8.0	0.7106	0.6918	0.7012	0.0876	0.6989	−0.1711	0.2639	0.0330
10.0	0.8327	0.8430	0.8378	0.0838	0.8383	−0.2027	0.3178	0.0318
12.0	0.9917	0.9724	0.9821	0.0818	1.0826	−0.2184	0.4321	0.0360
14.0	1.0281	1.0417	1.0349	0.0739	1.1358	−0.2272	0.4543	0.0325
16.0	1.1835	1.2009	1.1922	0.0745	1.3167	−0.3055	0.5056	0.0316

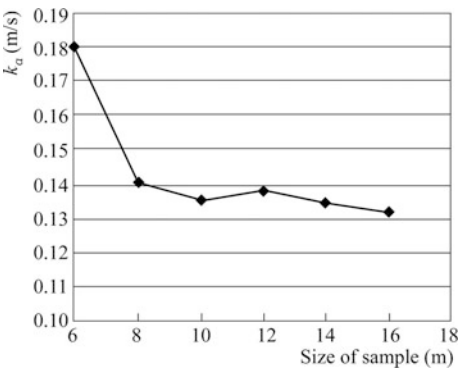

Fig. 18.12 Fluctuation of permeability coefficient at direction $\alpha = 0°$

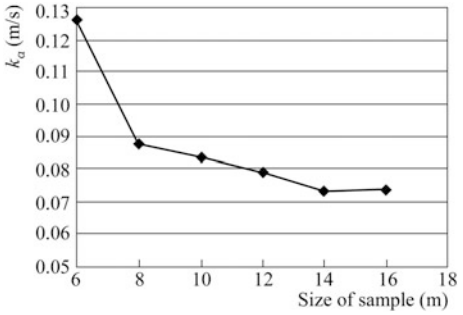

Fig. 18.13 Fluctuation of permeability coefficient at direction $\alpha = 90°$

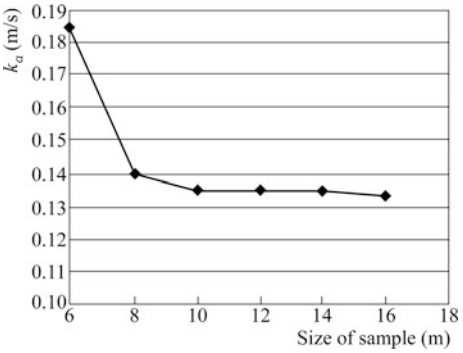

Fig. 18.14 Fluctuation of permeability coefficient at direction $\alpha = 180°$

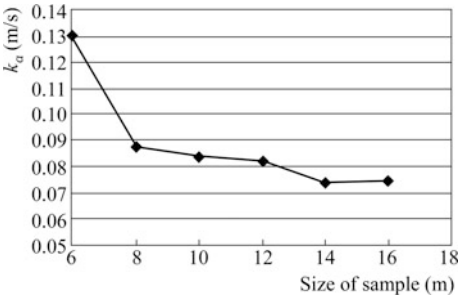

Fig. 18.15 Fluctuation of permeability coefficient at direction $\alpha = 270°$

These fluctuation tests validate that

- The smaller of the sample size, the larger is the permeability coefficients.
- When the sample size is equal to or larger than 10 m, the permeability coefficients start to be stable.
- The size of REV can be estimated preliminary between 8 and 12 m, which is, subject to the further verification using tensor ellipse.

(3) Permeability tensor identification

To identify the permeability tensor and REV, the sample with size of 10 m × 10 m will be rotated by the angle of α. Tables 18.6 and 18.7 present the identification results for the first stochastic DFN ($n = 1$), and Fig. 18.16 shows the corresponding identified permeability ellipse.

Table 18.6 Permeability coefficients of the first stochastic DFN (sample size = 10 m)

α (°)	Direction α		Direction α + 90°		Direction α + 180°		Direction α + 270°	
	k_α (m/s)	$1/\sqrt{k_\alpha}$	k_α (m/s)	$1/\sqrt{k_\alpha}$	k_α (m/s)	$1/\sqrt{k_\alpha}$	k_α (m/s)	$1/\sqrt{k_\alpha}$
0	0.1355	2.7164	0.0835	3.4599	0.1346	2.7257	0.0838	3.4548
15	0.1131	2.9741	0.0649	3.9268	0.1170	2.9231	0.0671	3.8605
30	0.1760	2.3839	0.0584	4.1368	0.1282	2.7925	0.0686	3.8188
45	0.1709	2.4193	0.0522	4.3757	0.1804	2.3546	0.1068	3.0598
60	0.1154	2.9434	0.0724	3.7156	0.1517	2.5672	0.0708	3.7594
75	0.1759	2.3842	0.0724	3.7158	0.1226	2.8559	0.0869	3.3930

Table 18.7 Permeability tensor of the first stochastic DFN (sample size = 10 m)

Principal direction 1		Principal direction 2		Permeability tensor in the $x - z$ plane		
Angle α (°)	Principal permeability (m/s)	Angle β (°)	Principal permeability (m/s)	k_{xx} (m/s)	k_{zz} (m/s)	k_{xz} (m/s)
32.7	0.1484	122.7	0.0649	0.1240	0.0893	0.0380

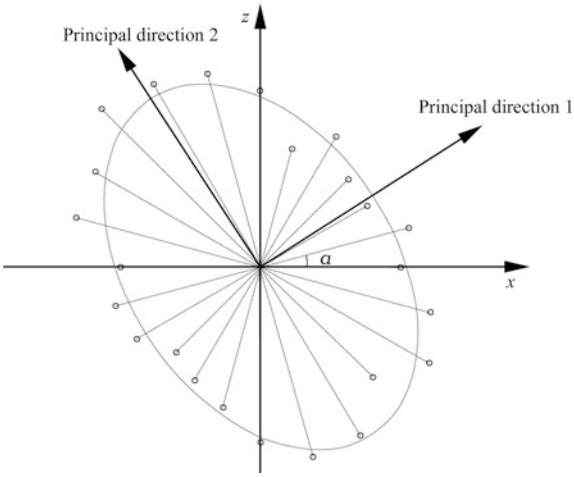

Fig. 18.16 First stochastic permeability ellipse (sample size = 10 m)

(4) Statistic characteristics

To obtain the statistic characteristics of the permeability tensor, altogether 10 stochastic DFNs are used ($n = 1, 2, \ldots 10$). The main results are summarized in Tables 18.8 and 18.9.

The average ellipse $(\alpha, 1/\sqrt{k_\alpha})$ is shown in Fig. 18.17, it validates that when the sample size is 10 m, the permeability tensor can be well fitted.

According to the fitted ellipse, the average permeability tensor on the $x - z$ plane is identified in Table 18.10.

Table 18.8 Statistics of the stochastic tests (sample size = 10 m)

Sequence of stochastic DFN	Principal direction 1		Principal direction 2	
	Angle α (°)	Principal permeability (m/s)	Angle β (°)	Principal permeability (m/s)
1	32.7	0.1484	122.7	0.0649
2	29.1	0.1647	119.1	0.0557
3	28.5	0.1652	118.5	0.0538
4	33.1	0.1255	123.1	0.0706
5	32.9	0.1147	122.9	0.0814
6	26.7	0.1768	116.7	0.0477
7	27.2	0.1882	117.2	0.0516
8	25.8	0.2091	115.8	0.0358
9	35.7	0.0979	125.7	0.0825
10	30.4	0.1331	120.4	0.0702
Mean	30.21	0.1524	120.21	0.0614
Covariance	3.11	0.0330	3.11	0.0143

Table 18.9 Average permeability coefficients at the direction of α (sample size = 10 m)

α (°)	Direction α		Direction $\alpha + 90°$		Direction $\alpha + 180°$		Direction $\alpha + 270°$	
	k_α (m/s)	$1/\sqrt{k_\alpha}$	k_α (m/s)	$1/\sqrt{k_\alpha}$	k_α (m/s)	$1/\sqrt{k_\alpha}$	k_α (m/s)	$1/\sqrt{k_\alpha}$
0	0.1391	2.6808	0.0915	3.3054	0.1502	2.5802	0.0908	3.3180
15	0.1557	2.5344	0.0755	3.6389	0.1819	2.3450	0.0828	3.4757
30	0.1736	2.3998	0.0686	3.8182	0.1747	2.3928	0.0704	3.7702
45	0.1682	2.4380	0.0769	3.6064	0.1860	2.3185	0.0909	3.3167
60	0.1469	2.6092	0.0922	3.2935	0.1588	2.5096	0.0954	3.2369
75	0.1217	2.8662	0.1123	2.9845	0.1260	2.8173	0.1267	2.8092

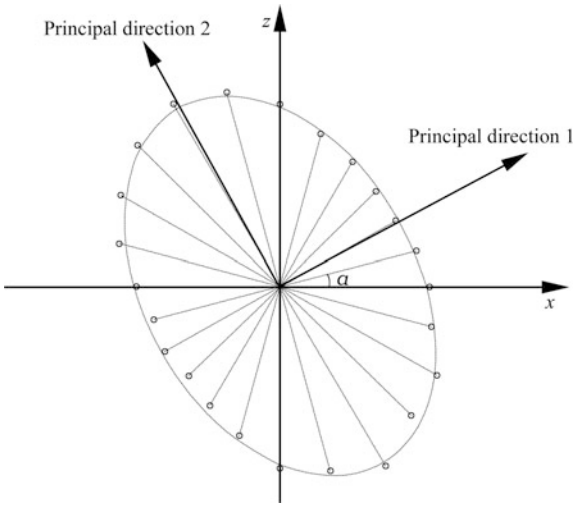

Fig. 18.17 Average permeability ellipse (sample size = 10 m)

Table 18.10 Average permeability tensor (sample size = 10 m)

Principal direction 1		Principal direction 2		Permeability tensor in the $x-z$ plane		
Angle α (°)	Principal permeability (m/s)	Angle β (°)	Principal permeability (m/s)	k_{xx} (m/s)	k_{zz} (m/s)	k_{xz} (m/s)
29.1	0.1668	119.1	0.0729	0.1446	0.0951	0.0399

18.5.2 Elastic Compliance Tensor and REV

(1) Example 1

This example is intended to verify the NT algorithm by an analytical solution of the rock mass containing two orthogonal and continuous fracture sets (see Fig. 18.3). The elastic modulus and the Poisson's ratio of the intact rock are $E = 1.8 \times 10^4$ (Mpa) and $\mu = 0.28$ respectively; the normal stiffness and shear stiffness are $k_{n1} = 100\,(\mathrm{Mpa/m})$ and $k_{s1} = 50\,(\mathrm{Mpa/m})$ for the first fracture set, and $k_{n2} = 200\,(\mathrm{Mpa/m})$ and $k_{s2} = 100\,(\mathrm{Mpa/m})$ for the second fracture set, respectively. No stochastic characteristics are considered.

The outcomes by the algorithm elaborated previously in this chapter show that

- The fluctuation amplitude of elastic compliance matrix decays as the increase in the size of fractured rock samples (see Fig. 18.18);
- When the sample size exceeds 8 m, the maximum fluctuation amplitude of elastic compliance matrix is below 0.0003 (1/MPa), which is much smaller than the analytical solution $C'_{11} = 0.01089\ (1/\mathrm{MPa})$ using Eq. (18.10).

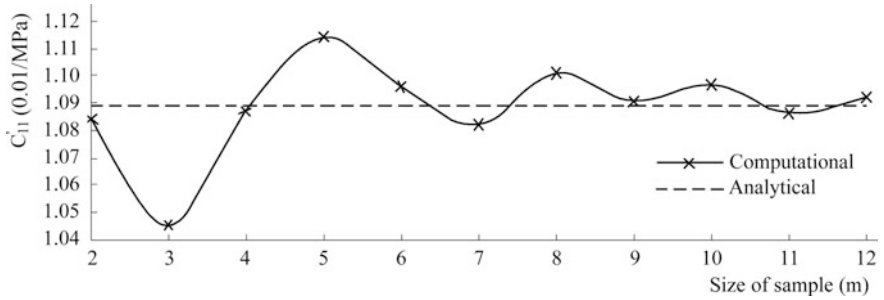

Fig. 18.18 Fluctuation of components of compliance C'_{11} at direction $\alpha = 30°$(example 1)

Table 18.11 Probability models and parameters of fracture sets

Fracture set	Quantity		Mid position	Trace length		Attitude		
	Probability model	Density (m^{-2})		Probability model	μ (m)	Probability model	μ (°)	σ (°)
1	Poisson	0.06	Uniform	Negative exponent	16.0	Normal	10	3
2	Poisson	0.10	Uniform	Negative exponent	8.0	Normal	80	6

The polar diagram by the computation is plotted in Fig. 18.4 (broken line, REV = 8 m × 8 m), and the fluctuation of compliance component C'_{11} (rotation angle $\alpha = 30°$) is shown in Fig. 18.18. It is worthwhile to indicate that the compliance fluctuation by the computation is resulted from the non-uniform augment of volumetric joint count following the increase of sample size. Obviously, this phenomenon is not taken into account in the derivation of Eq. (18.10).

(2) Example 2

This example is to exhibit the ability of the NT algorithm by a complicated sampling window from a statistically homogeneous rock mass.

1 Probability models and parameters

The probability models and parameters are given in Table 18.11 based on the data from field studies. The mechanical parameters of intact rock and fractures are identical to that of the example 1.

Altogether $N = 10$ stochastic parent DFNs are generated in a square region of 60 m × 60 m in size. For each stochastic DFN, a series of fractured rock samples are extracted whose sizes are variable ranging from 2 m × 2 m to 20 m × 20 m. The fractured sample at the $x - z$ plane extracted from the first stochastic parent DFN ($n = 1$) is illustrated in Fig. 18.19, the regular composite element mesh is also plotted (in broken lines) in this figure.

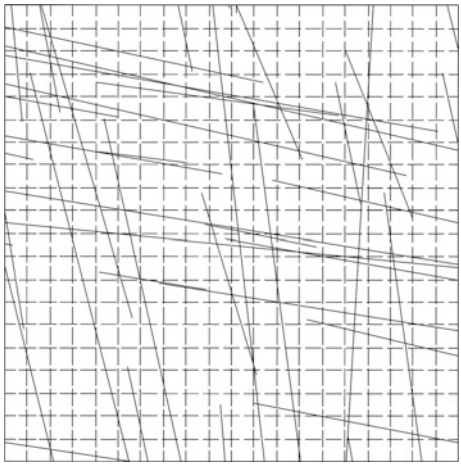

Fig. 18.19 Fractured DFN at the $x - z$ plane (sample size = 10 m)

2 Fluctuation tests

Figures 18.20, 18.21, 18.22 and 18.23 display the fluctuation of the compliance component C'_{11} of the first stochastic ($n = 1$) DFN. All the other components of elastic compliance matrix exhibit similar fluctuation characteristics that

- The fluctuation amplitude of the elastic compliance matrix decays as the increase in sample size.
- The compliance C'_{11} at the direction $\alpha = 90°$ undergoes largest fluctuation.

When the sample size exceeds 10 m, the maximum fluctuation amplitude of the compliance C'_{11} at the direction $\alpha = 90°$ is below 0.0009 (1/MPa), which is much smaller than its stable solution C'_{11} =0.009 (1/MPa) obtained under the sample size exceeding 20 m. Therefore, from the practice standpoint, it may be approximately estimated that REV $\approx$ 10 m $\times$ 10 m.

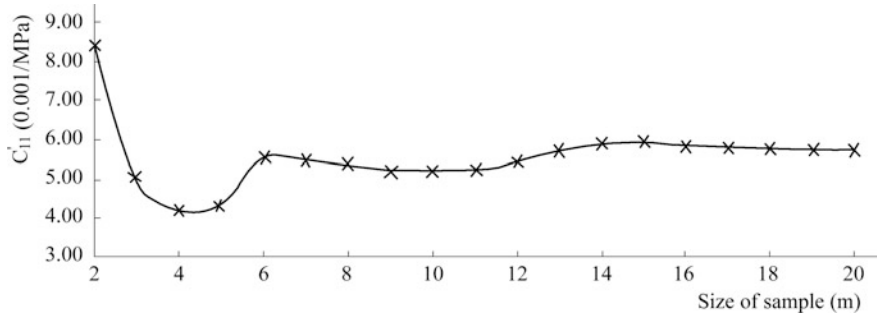

Fig. 18.20 Fluctuation of compliance C'_{11} at direction $\alpha = 0°$

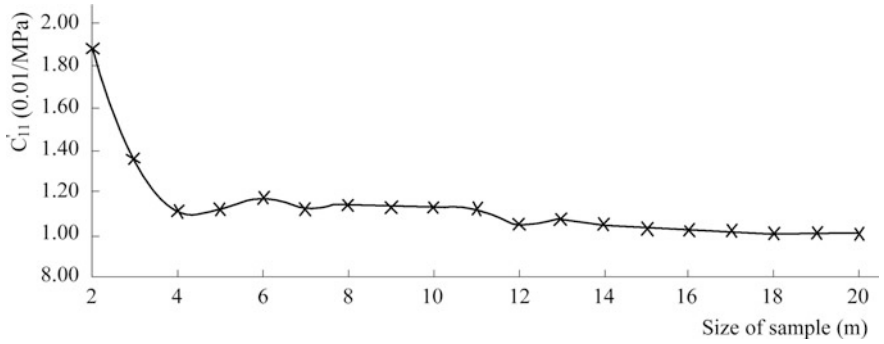

Fig. 18.21 Fluctuation of compliance C'_{11} at direction $\alpha = 30°$

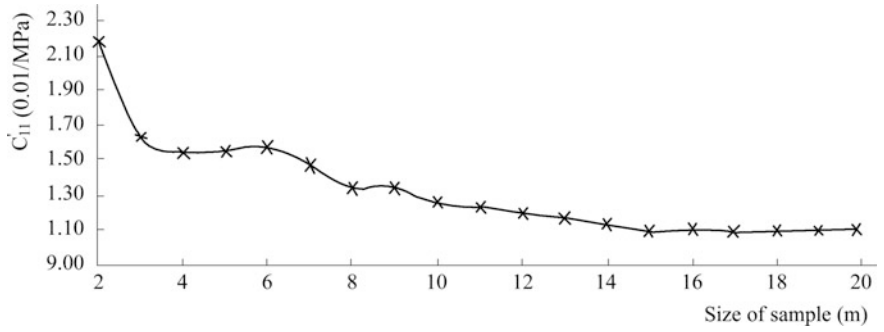

Fig. 18.22 Fluctuation of compliance C'_{11} at direction $\alpha = 60°$

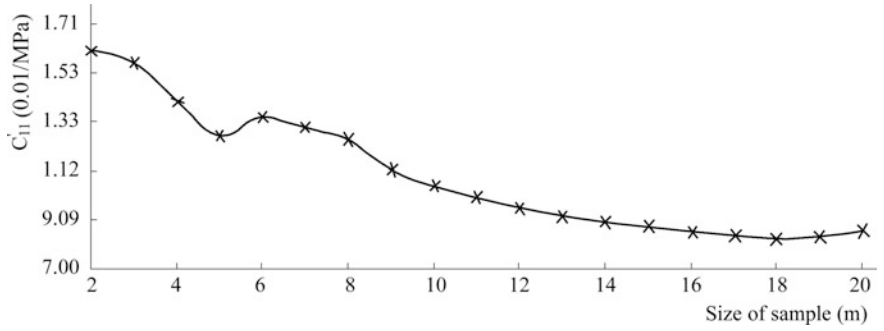

Fig. 18.23 Fluctuation of compliance C'_{11} at direction $\alpha = 90°$

Figure 18.24 displays the polar diagram of the elastic compliance C'_{11} (C_α) when the sample size = 10 m × 10 m, which is plotted according to the computation on the samples rotated at the angles of $\alpha = 0°, 15°, 30°, 45°, 60°, 75°, 90°$, respectively.

3 Statistic compliance matrix

To obtain the statistic compliance matrix, altogether 10 stochastic tests are used ($n = 1, 2, \ldots 10$). The polar diagram of the average results is drawn in Fig. 18.25, the elastic matrix in the global coordinate system ($x - z$ plane) is presented in Eqs. (18.23)–(18.24).

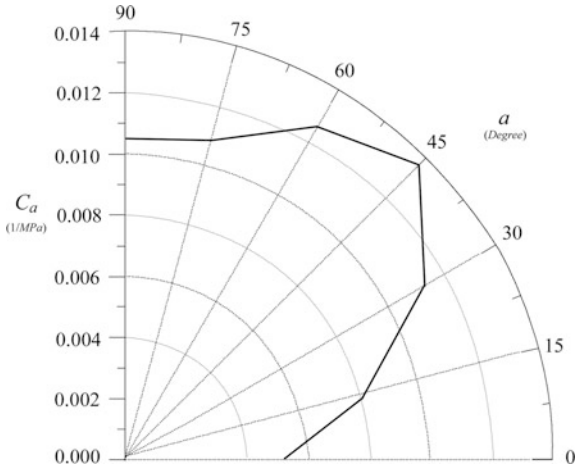

Fig. 18.24 Polar diagram of elastic compliance C_a (sample size 10 m × 10 m)

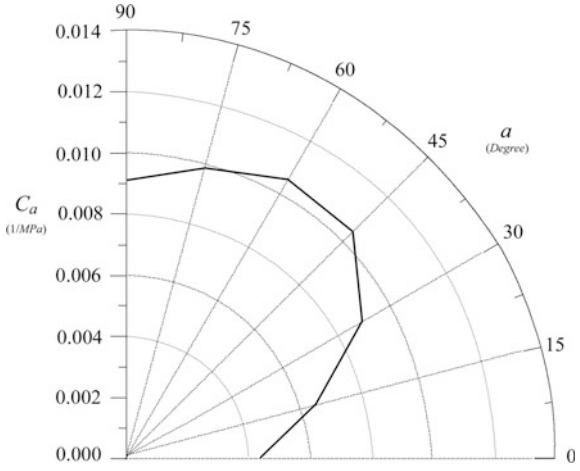

Fig. 18.25 Average polar diagram of compliance matrix with a sample size 10 m × 10 m

$$[C] = \begin{bmatrix} 0.00434 & -0.000362 & 0.00276 \\ & 0.0089 & 0.0013 \\ Sym. & & 0.0218 \end{bmatrix} \left(\text{MPa}^{-1}\right) \tag{18.23}$$

$$[D] = \begin{bmatrix} 253 & 15.1 & -32.9 \\ & 114 & -8.74 \\ Sym. & & 50.5 \end{bmatrix} (\text{MPa}) \tag{18.24}$$

18.5.3 Concluding Remarks

In this chapter we show one possible way to study the permeability and deformation characteristics of fractured rock masses using numerical test procedures established on the hybrid stochastic DFN and CEM. Since it concerns a large quantity of stochastic DFNs and rock samples of different sizes and orientations, the selection of competent computation method with simplified pre-process is essential.

The application of the CEM allows for a large amount of stochastic tests of fractured rock samples: the information of composite element mesh is obtained by the geometrical relation of the stochastic DFN and regular CE mesh, in this way the pre-process is facilitated greatly. Through systematic tests, the stochastic characteristics of permeability or elastic tensor and the existence of representative element volume (REV) can be routinely identified.

It should be admitted that only 10 stochastic tests conducted in our verification examples are not sufficient, and a criterion should be put forward concerning the amount of stochastic tests.

It is also worthwhile to point out that the validation of the NT algorithms is subjected to further study through laboratory and field tests as well as engineering practices. Normally, we can postulate that the principal directions and the proportions of the principal values obtained by the NT are acceptable, whereas the absolute values with respect to the tensor components are desirably to be adjusted through field tests inclusive pumping (or packer) test, plate bearing test, etc.

References

Abyaneh SD, Wong HS, Buenfeld NR. Computational investigation of capillary absorption in concrete using a three-dimensional mesoscale approach. Comput Mater Sci. 2014;87:54–64.

Andersson J, Dverstorp B. Conditional simulation of fluid flow in three-dimensional networks of discrete fractures. Water Resour Res. 1987;23(10):1876–86.

Baecher GB, Lanney NA, Einstein HH. Statistical description of rock properties and sampling. In: Wang FD, Clark GB editors Proc 18th US Symp Rock Mechanics. Colorado (USA): Colorado School of Mines Press, 1977; 5c1–8.

Barton CC. Fractal analysis of scaling and spatial clustering of fractures. In: Barton CC, La Pointe PR, editors. Fractals in the earth sciences. New York (USA): Plenum Press; 1995. p. 141–78.

Barton CC, Larsen E. Fractal geometry of two-dimensional fracture networks at Yucca Mountain, southwestern Nevada. In: Stephansson O, editor. Int symp fund rock joints. Björkliden (Sweden); 1985. 77–84.

Cacas MC, Ledoux B, De Marsity G, Tillie B, Barbreau A, Durand E, Feuga B, Peaudecerf P. Modeling fracture flow with a stochastic discrete fracture network: calibration and validation, 1. The Flow Model WATER Resour Res. 1990;26(3):479–89.

Charkaluk E, Bigerelle M, Iost A. Fractals and fracture. Eng Fract Mech. 1998;61(1):119–39.

Chen SH, He J, Shahrour I. Estimation of elastic compliance matrix for fractured rock masses by composite element method. Int J Rock Mech Min Sci. 2012;49(1):156–64.

Chen SH, Feng XM, Shahrour I. Numerical estimation of REV and permeability tensor for fractured rock masses by composite element method. Int J Numer Anal Meth Geomech. 2008;32(12):1459–77.

Chiles JP. Fractal and geostatistical methods for modelling a fracture network. Math Geol. 1988;20 (6):631–54.

Cruden DE. Describing the size of discontinuities. Int J Rock Mech Min Sci & Geomech Abstr. 1977;14(3):133–7.

Dershowitz WS, Einstein HH. Three dimensional flow modeling in jointed rock masses. In: Herget G, Vongpaisal S, editors. Proc 6th Int ISRM Congress, vol. 1. Rotterdam (Netherlands): AA Balkema; 1987. p. 87–92.

Hakami E, Larsson E. Aperture measurement and flow experiments on a single natural fracture. Int J Rock Mech Min Sci & Geomech Abstr. 1990;33(5):395–404.

Hall C, Hoff WD. Water Transport in Brick, Stone and Concrete. London (UK): Spon Press; 2012.

Keskin RSO, Hover KC, Grigoriu M. Size effects in modeling diffusivity of hardened mortar. Comput Struct. 2011;89(9):713–23.

Hudson JA, Priest SD. Discontinuity frequency in rock masses. Int J Rock Mech Min Sci & Geomech Abstr. 1983;20(2):73–89.

Kulatilake PHSW, Panda BB. Effect of block size and joint geometry on jointed rock hydraulics and REV. J Eng Mech, ASCE. 2000;126(8):850–8.

Kulatilake PHSW, Wang S, Stephansson O. Effects of finite-size joints on the deformability of jointed rock in three dimensions. Int J Rock Mech Min Sci. 1993a;30(5):479–501.

Kulatilake PHSW, Wathugala DN, Stephansson O. Joint network modeling, including a validation to an area in Stripa Mine, Sweden. Int J Rock Mech Min Sci & Geomech Abstr. 1993b;30 (5):503–26.

Kulatilake PHSW, Wu TH. The density of discontinuity traces in sampling windows. Int J Rock Mech Min Sci & Geomech Abstr. 1984;21(6):354–7.

Li XX, Chen SH, Xu Q, Xu Y. Modeling the three-dimensional unsaturated water transport in concrete at the mesoscale. Comput Struct. 2017;190:61–74.

Li XX, Xu Y, Chen SH. Computational homogenization of effective permeability in three-phase mesoscale concrete. Constr Build Mater. 2016;121:100–11.

Long JCS. Rock fractures and fluid flow. Washington DC (USA): National Academy Press; 1996.

Long JCS, Gilmour P, Witherspoon PA. A method for steady fluid flow in random three-dimensional networks of dice-shaped fractures. Water Resour Res. 1985;21(8):35–40.

Louis CA. Study of groundwater flow in jointed rock and its influence on the stability of rock masses (Rock Mechanics Research Report 10). London (UK): Imperial College; 1969.

Louis C, Maini YN. Determination of in-situ hydraulic parameters in jointed rock. In: Proc 2nd ISRM Congress. Belgrade (Yugoslavia): ISRM; 1970. p. 235–245.

Mauldon M. Estimating mean fracture trace length and density from observations in convex windows. Rock Mech Rock Engng. 1998;31(4):201–16.

Mauldon M, Dunne WM, Rohrbaugh MB Jr. Circular scanlines and circular windows: new tools for characterizing the geometry of fracture traces. J Struct Geol. 2001;23(2–3):247–58.

Mehta PK, Monteiro PJM. Concrete: microstructure, properties, and materials, 3rd ed. New York (USA): McGraw-Hill; 2006.

Min KB, Jing LR. Numerical determination of the equivalent elastic compliance tensor for fractured rock masses using the distinct element method. Int J Rock Mech Min Sci. 2003;40 (6):795–816.

Min KB, Rutqvist J, Tsang CF, Jing LR. Stress-dependent permeability of fractured rock masses: a numerical study. Int J Rock Mech Min Sci. 2004;41(7):1191–210.

Nicholl MJ, Rajaram H, Glass RJ, Detwiler R. Saturated flow in a single fracture: evaluation of reynolds equation in measured aperture fields. Water Resour Res. 1999;35(11):3361–73.

Öhman J, Niemi A. Upscaling of fracture hydraulics by means of an oriented correlated stochastic continuum model. Water Resour Res. 2003;39(10):1277–89.

Pande GN, Gerrard CM. The behaviour of reinforced jointed rock masses under various simple loading states. In: Proc 5th ISRM Congress. Melbourne (Australia): Brown Prior Anderson Pty Ltd; 1983, F217–F223.

Renshaw CE. Connectivity of joint networks with power law length distribution. Water Resour Res. 1999;35(9):2661–70.

Roelfstra PE, Sadouki H, Wittmann FH. Le béton numérique. Mater Struct. 1985;18(5):327–35.

Schwartz FW, Smith WL, Crowe AS. A stochastic analysis of microscopic dispersion in fractured media. Water Resour Res. 1983;19(5):1253–65.

Sitharam TG, Sridevi J, Shimizu N. Practical equivalent continuum characterization of jointed rock masses. Int J Rock Mech Min Sci. 2001;38(3):437–48.

Snow D. Anisotropic permeability of fractured media. Water Resour Res. 1969;5(6):1273–89.

Tsang YW, Tsang CF. Channel model of flow through fractured media. Water Resour Res. 1987;23(3):467–79.

Wei ZQ, Egger P, Descoeuders F. Permeability prediction for jointed rock masses. Int J Rock Mech Min Sci & Geomech Abstr. 1995;32(3):251–61.

Wei ZQ, Hudson JA. The influence of joints on rock modulus. In: Tan ZY, editor. Proc int symp eng in complex formations. Beijing (China): Science Press; 1986. p. 54–62.

Wittmann FH, Roelfstra PE, Sadouki H. Simulation and analysis of composite structures. Mat Sci Eng. 1985;68(2):239–48.

Xu Y, Chen SH. A method for modeling the damage behavior of concrete with a three-phase mesostructure. Constr Build Mater. 2016;102:26–38.

Xu Y, Xu Q, Chen SH, Li XX. Self-restraint thermal stress in early-age concrete samples and its evaluation. Constr Build Mater. 2017;134:104–11.

Zhang X, Sanderson DJ, Harkness RM, Last NC. Evaluation of the 2D permeability tensor for fractured rock masses. Int J Rock Mech Min Sci & Geomech Abstr. 1996;33(1):17–37.

Zienkiewicz OC, Pande GN. Time dependent multi-laminated model of rocks – a numerical study of deformation and failure of jointed rock masses. Int J Numer Anal Meth Geomech. 1976;1 (3):219–47.

Zimmerman RW, Bodvarsson GS. Hydraulic conductivity of rock fractures. Transp Porous Media. 1996;23(1):1–30.

Zhou C, Huang B, Shu X. Micromechanical model for predicting coefficient of thermal expansion of concrete. J Mater Civ Eng. 2013;25(9):1171–80.